

## EuPRAXIA Conceptual Design Report

R.W. Assmann<sup>1,a</sup> (editor), M.K. Weikum<sup>1</sup> (editor), T. Akhter<sup>2</sup>, D. Alesini<sup>3</sup>, A.S. Alexandrova<sup>4,5</sup>, M.P. Anania<sup>3</sup>, N.E. Andreev<sup>6,7</sup>, I. Andriyash<sup>8</sup>, M. Artioli<sup>9</sup>, A. Aschikhin<sup>1</sup>, T. Audet<sup>10</sup>, A. Bacci<sup>11</sup>, I.F. Barna<sup>12</sup>, S. Bartocci<sup>13</sup>, A. Bayramian<sup>14</sup>, A. Beaton<sup>4,15</sup>, A. Beck<sup>16</sup>, M. Bellaveglia<sup>3</sup>, A. Beluze<sup>17</sup>, A. Bernhard<sup>18</sup>, A. Biagioni<sup>3</sup>, S. Bielawski<sup>19</sup>, F.G. Bisesto<sup>3</sup>, A. Bonatto<sup>4,20</sup>, L. Boulton<sup>4,15</sup>, F. Brandi<sup>21</sup>, R. Brinkmann<sup>1</sup>, F. Briquez<sup>22</sup>, F. Brottier<sup>23</sup>, E. Bründermann<sup>18</sup>, M. Büscher<sup>24</sup>, B. Buonomo<sup>3</sup>, M.H. Bussmann<sup>25,26</sup>, G. Bussolino<sup>21</sup>, P. Campana<sup>3</sup>, S. Cantarella<sup>3</sup>, K. Cassou<sup>27</sup>, A. Chancé<sup>28</sup>, M. Chen<sup>29</sup>, E. Chiadroni<sup>3</sup>, A. Cianchi<sup>30,31</sup>, F. Cioeta<sup>3</sup>, J.A. Clarke<sup>4,32</sup>, J.M. Cole<sup>33</sup>, G. Costa<sup>3</sup>, M.-E. Couprie<sup>22</sup>, J. Cowley<sup>34</sup>, M. Croia<sup>3</sup>, B. Cros<sup>10</sup>, P.A. Crump<sup>35</sup>, R. D'Arcy<sup>1</sup>, G. Dattoli<sup>36</sup>, A. Del Dotto<sup>3</sup>, N. Delerue<sup>27</sup>, M. Del Franco<sup>3</sup>, P. Delinikolas<sup>4,15</sup>, S. De Nicola<sup>2,37</sup>, J.M. Dias<sup>38</sup>, D. Di Giovenale<sup>3</sup>, M. Diomede<sup>3</sup>, E. Di Pasquale<sup>3</sup>, G. Di Pirro<sup>3</sup>, G. Di Raddo<sup>3</sup>, U. Dorda<sup>1</sup>, A.C. Erlandson<sup>14</sup>, K. Ertel<sup>39</sup>, A. Esposito<sup>3</sup>, F. Falcoz<sup>40</sup>, A. Falone<sup>3</sup>, R. Fedele<sup>2,41</sup>, A. Ferran Pousa<sup>1,42</sup>, M. Ferrario<sup>3</sup>, F. Filippi<sup>3,43</sup>, J. Fils<sup>44</sup>, G. Fiore<sup>2,41</sup>, R. Fiorito<sup>4,5</sup>, R.A. Fonseca<sup>38</sup>, G. Franzini<sup>3</sup>, M. Galimberti<sup>39</sup>, A. Gallo<sup>3</sup>, T.C. Galvin<sup>14</sup>, A. Ghaith<sup>22</sup>, A. Ghigo<sup>3</sup>, D. Giove<sup>11</sup>, A. Giribono<sup>3</sup>, L.A. Gizzi<sup>21,45</sup>, F.J. Grüner<sup>42,46</sup>, A.F. Habib<sup>4,15</sup>, C. Haefner<sup>14</sup>, T. Heinemann<sup>1,4,15,42</sup>, A. Helm<sup>38</sup>, B. Hidding<sup>4,15</sup>, B.J. Holzer<sup>47</sup>, S.M. Hooker<sup>34</sup>, T. Hosokai<sup>48</sup>, M. Hübner<sup>35</sup>, M. Ibison<sup>4,5</sup>, S. Incremona<sup>3</sup>, A. Irman<sup>25</sup>, F. Iungo<sup>3</sup>, F.J. Jafarinia<sup>1</sup>, O. Jakobsson<sup>20</sup>, D.A. Jaroszynski<sup>15</sup>, S. Jaster-Merz<sup>1</sup>, C. Joshi<sup>49</sup>, M. Kaluza<sup>50,51</sup>, M. Kando<sup>52</sup>, O.S. Karger<sup>42</sup>, S. Karsch<sup>53</sup>, E. Khazanov<sup>54</sup>, D. Khikhlikha<sup>55</sup>, M. Kirchen<sup>1,46</sup>, G. Kirwan<sup>4,15</sup>, C. Kitégi<sup>22</sup>, A. Knetsch<sup>1</sup>, D. Kocon<sup>55</sup>, P. Koester<sup>21</sup>, O.S. Kononenko<sup>56</sup>, G. Korn<sup>55</sup>, I. Kostyukov<sup>54</sup>, K.O. Kruchinin<sup>55</sup>, L. Labate<sup>21,45</sup>, C. Le Blanc<sup>17</sup>, C. Lechner<sup>1</sup>, P. Lee<sup>10</sup>, W. Leemans<sup>1</sup>, A. Lehrach<sup>24</sup>, X. Li<sup>57</sup>, Y. Li<sup>20</sup>, V. Libov<sup>42</sup>, A. Lifschitz<sup>56</sup>, C.A. Lindstrøm<sup>1</sup>, V. Litvinenko<sup>58,59</sup>, W. Lu<sup>60</sup>, O. Lundh<sup>61</sup>, A.R. Maier<sup>42,46</sup>, V. Malka<sup>8</sup>, G.G. Manahan<sup>15</sup>, S.P.D. Mangles<sup>33</sup>, A. Marcelli<sup>3</sup>, B. Marchetti<sup>1</sup>, O. Marcouillé<sup>22</sup>, A. Marocchino<sup>3</sup>, F. Marteau<sup>22</sup>, A. Martinez de la Ossa<sup>1</sup>, J.L. Martins<sup>38</sup>, P.D. Mason<sup>39</sup>, F. Massimo<sup>16</sup>, F. Mathieu<sup>17</sup>, G. Maynard<sup>10</sup>, Z. Mazzotta<sup>62</sup>, S. Mironov<sup>54</sup>, A.Y. Molodozhentsev<sup>55</sup>, S. Morante<sup>30</sup>, A. Mosnier<sup>28</sup>, A. Mostacci<sup>63,64</sup>, A.-S. Müller<sup>18</sup>, C.D. Murphy<sup>65</sup>, Z. Najmudin<sup>33</sup>, P.A.P. Nghiem<sup>28</sup>, F. Nguyen<sup>36</sup>, P. Niknejadi<sup>1</sup>, A. Nutter<sup>4,15</sup>, J. Osterhoff<sup>1</sup>, D. Oumbarek Espinos<sup>22</sup>, J.-L. Paillard<sup>17</sup>, D.N. Papadopoulos<sup>17</sup>, B. Patrizi<sup>66</sup>, R. Pattathil<sup>32</sup>, L. Pellegrino<sup>3</sup>, A. Petralia<sup>36</sup>, V. Petrillo<sup>11,67</sup>, L. Piersanti<sup>3</sup>, M.A. Pocsai<sup>12,68</sup>, K. Poder<sup>1,33</sup>, R. Pompili<sup>3</sup>, L. Pribyl<sup>55</sup>, D. Pugacheva<sup>6,7</sup>, B.A. Reagan<sup>14</sup>, J. Resta-Lopez<sup>4,5</sup>, R. Ricci<sup>3</sup>, S. Romeo<sup>3</sup>, M. Rossetti Conti<sup>11</sup>, A.R. Rossi<sup>11</sup>, R. Rossmannith<sup>1</sup>, U. Rotundo<sup>3</sup>, E. Roussel<sup>19</sup>, L. Sabbatini<sup>3</sup>, P. Santangelo<sup>3</sup>, G. Sarri<sup>69</sup>, L. Schaper<sup>1</sup>, P. Scherkl<sup>4,15</sup>, U. Schramm<sup>25</sup>, C.B. Schroeder<sup>70</sup>, J. Scifo<sup>3</sup>, L. Serafini<sup>11</sup>, G. Sharma<sup>71</sup>, Z.M. Sheng<sup>15,29</sup>, V. Shpakov<sup>3</sup>, C.W. Siders<sup>14</sup>, L.O. Silva<sup>38</sup>, T. Silva<sup>38</sup>, C. Simon<sup>28</sup>, C. Simon-Boisson<sup>72</sup>, U. Sinha<sup>38</sup>, E. Sistrunk<sup>14</sup>, A. Specka<sup>16</sup>, T.M. Spinka<sup>14</sup>, A. Stecchi<sup>3</sup>, A. Stella<sup>3</sup>, F. Stellato<sup>30,31</sup>, M.J.V. Streeter<sup>33</sup>, A. Sutherland<sup>4,15</sup>, E.N. Svystun<sup>1</sup>, D. Symes<sup>39</sup>, C. Szwej<sup>19</sup>, G.E. Tauscher<sup>1</sup>, D. Terzani<sup>2,41</sup>, G. Toci<sup>66</sup>, P. Tomassini<sup>21</sup>, R. Torres<sup>4,5</sup>, D. Ullmann<sup>4,15</sup>, C. Vaccarezza<sup>3</sup>, M. Valléau<sup>22</sup>, M. Vannini<sup>66</sup>, A. Vannozzi<sup>3</sup>, S. Vescovi<sup>3</sup>, J.M. Vieira<sup>38</sup>, F. Villa<sup>3</sup>, C.-G. Wahlström<sup>61</sup>, R. Walczak<sup>34</sup>, P.A. Walker<sup>1</sup>, K. Wang<sup>27</sup>, A. Welsch<sup>4,5</sup>, C.P. Welsch<sup>4,5</sup>,

S.M. Weng<sup>29</sup>, S.M. Wiggins<sup>4,15</sup>, J. Wolfenden<sup>4,5</sup>, G. Xia<sup>4,20</sup>, M. Yabashi<sup>73</sup>,  
H. Zhang<sup>4,5</sup>, Y. Zhao<sup>4,20</sup>, J. Zhu<sup>1</sup>, and A. Zigler<sup>74</sup>

- <sup>1</sup> Deutsches Elektronensynchrotron – Hamburg, 22607 Hamburg, Germany
- <sup>2</sup> INFN, Sezione di Napoli, 80126 Napoli, Italy
- <sup>3</sup> INFN, Laboratori Nazionali di Frascati, 00044 Frascati, Rome, Italy
- <sup>4</sup> Cockcroft Institute, Warrington WA4 4AD, UK
- <sup>5</sup> University of Liverpool, Liverpool L69 7ZE, UK
- <sup>6</sup> JIHT of RAS, Moscow 125412, Russia
- <sup>7</sup> Moscow Institute of Physics and Technology, Dolgoprudny 141701, Russia
- <sup>8</sup> Department of Physics of Complex Systems, Weizmann Institute of Science, Rehovot 7610001, Israel
- <sup>9</sup> ENEA – Centro Ricerche Bologna, 40129 Bologna, Italy
- <sup>10</sup> LPGP, CNRS, Univ. Paris-Sud, Université Paris-Saclay, 91405 Orsay, France
- <sup>11</sup> INFN, Sezione di Milano, via Celoria, 16, 20133 Milano, Italy
- <sup>12</sup> Wigner Research Centre for Physics, H-1121 Budapest, Hungary
- <sup>13</sup> Università degli Studi di Sassari, Dip. di Architettura, Design e Urbanistica ad Alghero, 07041 Alghero, Italy
- <sup>14</sup> Advanced Photon Technologies, NIF & Photon Science Directorate, Lawrence Livermore National Laboratory, Livermore, CA 94550, USA
- <sup>15</sup> SUPA, Department of Physics, University of Strathclyde, Glasgow G4 0NG, UK
- <sup>16</sup> LLR, CNRS, École Polytechnique, Palaiseau and Université Paris Saclay, Palaiseau Cedex, France
- <sup>17</sup> LULI, École Polytechnique, CNRS, CEA, Sorbonne Université, 91128 Palaiseau, France
- <sup>18</sup> Karlsruhe Institute of Technology, 76131 Karlsruhe, Germany
- <sup>19</sup> Université de Lille, CNRS, UMR 8523 – PhLAM, Lille, France
- <sup>20</sup> University of Manchester, Manchester M13 9PL, UK
- <sup>21</sup> CNR Istituto Nazionale di Ottica, 56124 Pisa, Italy
- <sup>22</sup> Synchrotron SOLEIL, Gif-sur-Yvette 91192, France
- <sup>23</sup> Euroopportunities OÜ, Sopruuse pst 9, 10615 Tallinn, Estonia
- <sup>24</sup> Forschungszentrum Jülich, 52428 Jülich, Germany
- <sup>25</sup> Helmholtz-Zentrum Dresden-Rossendorf e.V., 01328 Dresden, Germany
- <sup>26</sup> Center for Advanced Systems Understanding (CASUS), Görlitz, Germany
- <sup>27</sup> LAL, CNRS/IN2P3 Univ. Paris Sud, Orsay, and Université Paris Saclay, Orsay, France
- <sup>28</sup> CEA, IRFU, DACM, Université Paris Saclay, F-91191 Gif-sur-Yvette, France
- <sup>29</sup> Shanghai Jiao Tong University, Shanghai 200240, P.R. China
- <sup>30</sup> University of Rome Tor Vergata, 00133 Rome, Italy
- <sup>31</sup> INFN Sezione di Roma Tor Vergata, 00133 Rome, Italy
- <sup>32</sup> STFC Daresbury Laboratory, Sci-Tech Daresbury, Warrington, UK
- <sup>33</sup> John Adams Institute, Blackett Laboratory, Imperial College London, London, UK
- <sup>34</sup> Department of Physics & John Adams Institute, University of Oxford, Oxford OX1 2JD, UK
- <sup>35</sup> Ferdinand-Braun-Institut, Leibniz-Institut für Höchstfrequenztechnik, 12489 Berlin, Germany
- <sup>36</sup> ENEA, Centro Ricerche Frascati, 00044 Frascati, Rome, Italy
- <sup>37</sup> SPIN-CNR, Complesso Universitario di M.S. Angelo, 80126 Napoli, Italy
- <sup>38</sup> GoLP/Instituto de Plasmas e Fusão Nuclear, Instituto Superior Técnico, Universidade de Lisboa, Lisbon, Portugal
- <sup>39</sup> Central Laser Facility, RAL, Didcot, Oxfordshire OX11 0QX, UK
- <sup>40</sup> Amplitude Technologies, 91029 Evry, France
- <sup>41</sup> Università di Napoli “Federico II”, 80126 Napoli, Italy
- <sup>42</sup> Universität Hamburg, 22761 Hamburg, Germany
- <sup>43</sup> ENEA, Centro Ricerche Casaccia, 00124 Santa Maria di Galeria, Rome, Italy
- <sup>44</sup> GSI Helmholtzzentrum für Schwerionenforschung GmbH,
- <sup>45</sup> INFN, Sezione di Pisa, Pisa, Italy

- <sup>46</sup> Center for Free Electron Laser Science, 22607 Hamburg, Germany  
<sup>47</sup> CERN, 1211 Geneva 23, Switzerland  
<sup>48</sup> Osaka University, Osaka Prefecture, 565-0871, Japan  
<sup>49</sup> University of California Los Angeles, Los Angeles, CA 90095, USA  
<sup>50</sup> Helmholtz Institute Jena, 07743 Jena, Germany  
<sup>51</sup> Institut für Optik und Quantenelektronik, 07743 Jena, Germany  
<sup>52</sup> KPSI-QST, Kyoto 619-0215, Japan  
<sup>53</sup> Ludwig-Maximilians-Universität München, 80802 Munich, Germany  
<sup>54</sup> IAP RAS, Nizhnij Novgorod 603950, Russia  
<sup>55</sup> ELI-Beamlines, Dolni Brezany, Czech Republic  
<sup>56</sup> LOA, ENSTA-CNRS-École Polytechnique UMR 7639, Palaiseau F-91761, France  
<sup>57</sup> Deutsches Elektronensynchrotron – Zeuthen, 15738 Zeuthen, Germany  
<sup>58</sup> Brookhaven National Laboratory, Upton, NY 11973, USA  
<sup>59</sup> Stony Brook University, Stony Brook, NY 11794, USA  
<sup>60</sup> Tsinghua University, Beijing 100084, P.R. China  
<sup>61</sup> Lund University, 221 00 Lund, Sweden  
<sup>62</sup> ARCNL, University of Amsterdam, 1098, XG Amsterdam, Netherlands  
<sup>63</sup> Sapienza, University of Rome, 00161 Rome, Italy  
<sup>64</sup> INFN Sezione di Roma 1, Rome, Italy  
<sup>65</sup> Department of Physics, University of York, Heslington YO10 5DD, UK  
<sup>66</sup> CNR Istituto Nazionale di Ottica, I-50019 Sesto Fiorentino, Italy  
<sup>67</sup> University of Milan, 20133 Milan, Italy  
<sup>68</sup> University of Pécs, Institute of Physics, H-7624 Pécs, Hungary  
<sup>69</sup> School of Mathematics and Physics, The Queen’s University of Belfast, BT71NN Belfast, UK  
<sup>70</sup> Lawrence Berkeley National Laboratory, Berkeley, CA 94720, USA  
<sup>71</sup> Diamond Light Source, OX11 0DE Didcot, UK  
<sup>72</sup> Thales Laser S.A., 91400 Orsay, France  
<sup>73</sup> RIKEN SPring-8 Center, Hyogo 679-5148, Japan  
<sup>74</sup> Hebrew University of Jerusalem, Jerusalem, Israel

Received 17 December 2019 / Accepted 21 July 2020

Published online 23 December 2020

**Abstract.** This report presents the conceptual design of a new European research infrastructure EuPRAXIA. The concept has been established over the last four years in a unique collaboration of 41 laboratories within a Horizon 2020 design study funded by the European Union. EuPRAXIA is the first European project that develops a dedicated particle accelerator research infrastructure based on novel plasma acceleration concepts and laser technology. It focuses on the development of electron accelerators and underlying technologies, their user communities, and the exploitation of existing accelerator infrastructures in Europe. EuPRAXIA has involved, amongst others, the international laser community and industry to build links and bridges with accelerator science – through realising synergies, identifying disruptive ideas, innovating, and fostering knowledge exchange. The EuPRAXIA project aims at the construction of an innovative electron accelerator using laser- and electron-beam-driven plasma wakefield acceleration that offers a significant reduction in size and possible savings in cost over current state-of-the-art radiofrequency-based accelerators. The foreseen electron energy range of one to five gigaelectronvolts (GeV) and its performance goals will enable versatile applications in various domains, e.g. as a compact free-electron laser (FEL), compact sources for medical imaging and positron generation, table-top test beams for particle detectors, as well as deeply penetrating X-ray and gamma-ray sources for material testing. EuPRAXIA is designed to be the required stepping stone to possible future plasma-based facilities, such as linear colliders at the high-energy physics (HEP) energy frontier. Consistent with a high-confidence approach, the project includes measures to retire risk by establishing scaled technology demonstrators. This report includes preliminary models for project implementation, cost and schedule that would allow operation of the full EuPRAXIA facility within 8–10 years.

---

<sup>a</sup> e-mail: [ralph.assmann@desy.de](mailto:ralph.assmann@desy.de)

## Contents

Part 1	Executive Summary . . . . .	3686
Part 2	Short Description of EuPRAXIA . . . . .	3690
Part 3	The Research Infrastructure Concept . . . . .	3701
1	Introduction . . . . .	3701
2	Opportunities for Science and Innovation . . . . .	3713
2.1	Flagship Science and Innovation Goals . . . . .	3713
2.1.1	Flagship Innovation Goals . . . . .	3714
2.1.2	Flagship Science Goals . . . . .	3715
2.1.3	Unique Selling Points of EuPRAXIA . . . . .	3716
2.2	The Needs of External Users from the Academic Environment . . . . .	3720
2.2.1	Summary of User Needs and Possibilities . . . . .	3720
2.2.2	Accelerator Science . . . . .	3722
2.2.3	Laser Science . . . . .	3723
2.2.4	Photon Science . . . . .	3725
2.2.5	High-Energy Physics . . . . .	3727
2.2.6	Medical Physics . . . . .	3729
2.2.7	Inspection and Material Studies . . . . .	3731
2.3	The Role of Industry . . . . .	3733
2.4	Added Value for the European Research and Technology Landscape . . . . .	3734
2.5	The Role of EuPRAXIA for Innovation and Science in the Global Environment . . . . .	3736
3	Description of the EuPRAXIA Infrastructure . . . . .	3737
3.1	Introduction . . . . .	3737
3.2	Overview on Design and Performance Parameters . . . . .	3738
3.3	The Concept of Distributed EuPRAXIA Construction . . . . .	3738
3.3.1	EuPRAXIA Clusters for Organising Europe-Wide Work . . . . .	3741
3.3.2	EuPRAXIA Construction and Excellence Sites . . . . .	3751
3.4	EuPRAXIA Construction Footprint (Towards Accelerator Miniaturisation) . . . . .	3753
3.5	EuPRAXIA Digital Footprint (Data Sharing and Management) . . . . .	3756
3.6	Matching EuPRAXIA Needs and Existing Facilities / Capabilities in Europe . . . . .	3759
3.6.1	INFN-LNF: Construction Site for Beam-Driven Plasma Acceleration . . . . .	3760
3.6.2	LAPLACE – France: Excellence Centre for Laser-Plasma Acceleration and 1 GeV FEL . . . . .	3763
3.6.3	IST – Portugal: Excellence Centre for Plasma Simulations and Theory . . . . .	3765
3.6.4	PWASC – UK: Excellence Centre for Advanced Application Beamlines . . . . .	3766
3.6.5	ELI Beamlines: Incubator for the Application of Novel Accelerator Technology to Laser Science Users . . . . .	3769
3.6.6	DESY – Germany: Excellence Centre for Plasma Accelerators and High-Repetition-Rate Developments . . . . .	3771
3.6.7	Possible Candidate Sites for the Laser-Driven Plasma Acceleration Construction Site . . . . .	3773
3.7	Long-Term Scientific Programme . . . . .	3779
4	Preliminary Resource and Financial Plan . . . . .	3781
4.1	Cost Model and Definitions . . . . .	3781
4.2	Summary of Total Costs . . . . .	3782
4.3	Breakdown of Investment Costs Related to the Beam-Driven Plasma Accelerator Site . . . . .	3784

4.4	Breakdown of Investment Costs Related to the Laser-Driven Plasma Accelerator Site . . . . .	3786
4.5	In-Kind Contributions . . . . .	3787
4.6	Operational Costs . . . . .	3787
4.7	Alternative Minimal Systems . . . . .	3788
5	Preliminary Project Organisation and Implementation . . . . .	3789
5.1	Project Schedule . . . . .	3789
5.2	Structure and Governing Model . . . . .	3792
5.3	Operational Model . . . . .	3793
5.4	User Access . . . . .	3794
5.4.1	Types of User Access . . . . .	3794
5.4.2	User Facility Modes . . . . .	3795
5.4.3	User Support . . . . .	3796
5.5	Quality Assurance . . . . .	3797
5.6	Outreach and Communication . . . . .	3797
5.7	Project Risk Assessment . . . . .	3799
5.7.1	General Project Risks . . . . .	3799
5.7.2	Technical Risks . . . . .	3799
6	Impact Assessment . . . . .	3803
6.1	Strategic Significance for European Science and Innovation . . . . .	3803
6.2	Socio-Economic Opportunities . . . . .	3807
6.3	Consistency with the Scientific Strategy of Research Areas . . . . .	3808
6.4	Competition and Worldwide Context . . . . .	3809
6.5	Long-Term Future Accelerator Roadmap and the Role of EuPRAXIA . . . . .	3811
Part 4 Systems Design and Performance . . . . .		3813
7	Technology Background . . . . .	3813
7.1	Plasma-Accelerator Physics . . . . .	3813
7.1.1	Laser-Driven Wakefield Acceleration (LWFA) . . . . .	3814
7.1.2	Beam-Driven Wakefield Acceleration (PWFA) . . . . .	3816
7.1.3	Challenges in Plasma Acceleration . . . . .	3816
7.1.4	Plasma Sources . . . . .	3818
7.2	Laser Science . . . . .	3819
7.3	Free-Electron Lasers . . . . .	3823
8	Description of the Overall Facility Layout and Its Building Blocks . . . . .	3826
8.1	EuPRAXIA Site for Beam-Driven Plasma Acceleration . . . . .	3826
8.2	EuPRAXIA Site for Laser-Driven Plasma Acceleration . . . . .	3829
8.3	Beam Distribution Concept . . . . .	3830
9	Summary Tables of Parameters and Technical Data . . . . .	3832
9.1	Laser System . . . . .	3833
9.2	RF Injector and Accelerator . . . . .	3833
9.3	Plasma Injector . . . . .	3834
9.4	Plasma Accelerator . . . . .	3834
9.5	Beam Transport Line . . . . .	3835
9.6	Free-Electron Laser . . . . .	3836
9.7	Other Radiation Sources . . . . .	3837
9.8	Secondary Particle Sources . . . . .	3837
9.9	Accelerator Start-to-End Simulations . . . . .	3838
10	Laser Systems as Innovative Power Drivers . . . . .	3839
10.1	Introduction . . . . .	3839
10.2	Baseline Design . . . . .	3839
10.2.1	Layout and Amplifiers . . . . .	3839
10.2.2	Front End . . . . .	3841
10.2.3	Power Amplifiers . . . . .	3842
10.2.4	Ti:Sapphire Amplifier Structure and Geometry . . . . .	3842
10.2.5	Pump Lasers . . . . .	3850

10.2.6	Transport to Plasma	3851
10.2.7	Development Paths	3854
10.2.8	Risk-Mitigating Solutions	3856
10.3	Conclusion	3859
11	Laser Control-Command System	3859
11.1	Introduction	3859
11.2	Overview	3860
11.3	Needs and Requirements	3862
11.3.1	Operational Requirements	3862
11.3.2	Personnel Safety System	3867
11.3.3	Electrical Timing and Synchronisation	3868
12	RF Accelerator to 500 MeV as Beam Driver	3870
12.1	Introduction	3870
12.2	S-band RF Photo-Injector	3870
12.2.1	RF Gun	3871
12.2.2	RF Gun Solenoid	3873
12.2.3	Photo-Cathode Drive Laser System	3873
12.2.4	S-band Linac	3874
12.2.5	High-Power System Components	3877
12.3	X-band RF Linac	3878
12.3.1	Introduction	3878
12.3.2	Linac Technology and Gradient Choice	3879
12.4	Accelerating Section Design	3880
12.4.1	X-band Linac Layout	3883
13	Plasma Injector	3884
13.1	Introduction	3884
13.2	Injection Mechanisms	3885
13.3	Low-Energy Plasma Injector	3886
13.3.1	Simulation Results	3887
13.3.2	Plasma Structure	3892
13.4	GeV Plasma Injector	3893
13.5	Implementation in the EuPRAXIA Beamline	3894
13.5.1	Staging Requirements	3894
13.5.2	Laser Removal	3895
13.5.3	Stability	3895
13.5.4	Repetition Rate	3895
13.6	Conclusion	3896
14	RF Photo-Injector	3897
14.1	Introduction	3897
14.2	Laser-Driven External Injection Scheme	3898
14.3	Full RF Compression Scheme	3898
14.4	Hybrid Compression Scheme	3904
14.5	Particle-Driven External Injection Scheme	3906
14.6	Future Plans and Conclusions	3912
15	Sub-Femtosecond Synchronisation of Electrons to the Laser	3913
15.1	A Scheme for Timing Jitter Compensation	3914
15.2	Linear Model	3915
15.3	Numerical Simulations	3916
15.4	Conclusion	3918
16	Laser-Driven Plasma Accelerator	3918
16.1	Introduction	3918
16.2	Parameters of Plasma Accelerator Sections	3920
16.2.1	Density	3920
16.2.2	Interaction Length	3920
16.3	Intense Laser Beam Confinement	3921

16.3.1	Requirements	3921
16.3.2	Possible Waveguides	3921
16.3.3	Example of Waveguide Implementation	3922
16.4	Staged Accelerator Implementation	3923
16.5	Conclusion	3925
17	Beam-Driven Plasma Accelerator	3926
17.1	Start-to-End Simulation for the 1 GeV Case	3927
17.1.1	Plasma Simulation Parameters and Code	3927
17.1.2	Optimum Bunch Acceleration in the Plasma Section	3927
17.1.3	Summary of the Simulation Results	3928
17.2	Numerical Design for the 5 GeV Case	3930
17.2.1	Plasma Parameters	3930
17.2.2	Driver Train Structure and Transformer Ratio	3931
17.2.3	Bunch Acceleration	3932
17.3	Outlook and Further Research and Development	3933
18	Magnets, Undulators, and Plasma Lenses	3934
18.1	Introduction	3934
18.2	Specific Magnetic Elements	3936
18.3	Review of State-of-the-Art Short-Period Undulators	3940
19	Beam Transport and Handling Systems	3950
19.1	Beam Transport for the Low-Energy Beam	3950
19.1.1	Introduction	3950
19.1.2	Compact Beamline with Six Permanent Quadrupoles	3951
19.1.3	Beamline with Eight Permanent Quadrupoles	3953
19.1.4	Beamline with Two Active Plasma Lenses	3954
19.1.5	Beamline with Two Solenoids	3956
19.1.6	Conclusion	3958
19.2	Beam Transport for the High-Energy Beam	3959
19.2.1	Introduction	3959
19.2.2	Scheme 1: LPI-5 GeV	3960
19.2.3	Scheme 2: LPI-150 MeV + LPAS-5 GeV	3961
19.2.4	Scheme 3: RFI-500 MeV + LPAS-5 GeV	3962
19.2.5	Scheme 4: RFI-240 MeV + LPAS-2.5 GeV + Chicane + LPAS-5 GeV	3962
19.2.6	Scheme 5: RFI-500 MeV + PPAS-1 GeV	3967
19.2.7	Conclusion	3969
20	Plasma Diagnostics	3972
20.1	Introduction	3972
20.2	Plasma Diagnostics	3973
20.2.1	Interferometric Density Measurement	3973
20.2.2	Spectroscopic Methods	3978
20.2.3	Group Velocity Measurements	3978
20.2.4	Summary	3978
20.3	Plasma Wave Diagnostics	3979
20.3.1	Longitudinal Probing	3979
20.3.2	Transverse Probing	3981
20.3.3	Summary	3981
20.4	Conclusion	3981
21	Electron Beam Diagnostics	3982
21.1	Introduction	3982
21.2	Charge and Trajectory Measurements	3982
21.3	Transverse Size Measurement	3983
21.4	Longitudinal Diagnostics	3983
21.5	Time-of-Arrival Monitors	3985
21.6	Beam Loss Monitors	3985

21.7	Transverse Emittance Monitors	3986
21.8	Accelerator Diagnostics Layout Before the Plasma-Accelerator Stage	3988
21.9	Accelerator Diagnostics Layout After the Plasma-Accelerator Stage (LPAS / PPAS, relevant for Schemes 1 to 6)	3992
21.10	Conclusion	3995
22	Electron Beam Dump	3996
22.1	Introduction	3996
22.2	The SwissFEL Beam Dumps, Aramis and Athos	3996
22.3	The Plasma Beam Dump	3997
22.3.1	Simulation Study of a Plasma Beam Dump	3998
22.3.2	Passive Beam Dump for EuPRAXIA	3998
22.4	Conclusions	3999
23	Start-to-End Simulations of the Accelerator	4001
23.1	General Aspects	4001
23.2	Study of Injection Techniques	4003
23.3	Study of Acceleration Stages	4005
23.4	Selection of the Configurations to Be Submitted to Start-to-End Simulations	4006
23.5	Preserving Beam Emittance When Matching In and Out of Plasma Stages	4008
23.6	Optimising and Designing Beam Transfer Lines	4010
23.7	Start-to-End Simulations for Scheme 1: LPI-5 GeV	4012
23.8	Start-to-End Simulations for Scheme 2: LPI-150 MeV + LPAS-5 GeV	4021
23.9	Start-to-End Simulations for Scheme 3: RFI-500 MeV + LPAS-5 GeV	4028
23.10	Start-to-End Simulations for Scheme 4: RFI-240 MeV + LPAS-2.5 GeV + Chicane + LPAS-5 GeV	4035
23.11	Start-to-End Simulations for Scheme 5: RFI-500 MeV + PPAS-1 GeV	4041
23.12	Summary of Start-to-End Simulations	4046
24	Photon User Applications	4047
24.1	Free-Electron Laser	4047
24.1.1	Introduction	4047
24.1.2	Features of the Electron Beams at the Plasma Exit and the Transfer Line	4048
24.1.3	Undulator Line Characteristics	4049
24.1.4	FEL Results	4050
24.1.5	Conclusion	4057
24.2	Betatron X-Ray Source	4057
24.3	Compton Source	4063
25	Particle User Applications	4066
25.1	High-Energy Physics Test Beams	4066
25.2	Secondary Particle Sources	4069
25.2.1	Low-Energy Positrons	4069
25.2.2	High-Energy Positrons	4070
26	Additional Innovation Paths	4073
26.1	Hybrid Laser-Beam-Driven Plasma Wakefield Acceleration	4073
26.1.1	Introduction	4073
26.1.2	LWFA Beams as PWFA Drivers	4074
26.1.3	LWFA→PWFA Transition	4075
26.1.4	Experimental Status	4076
26.2	LWFA→PWFA Staging as a Beam Energy and Brightness Transformer	4077
26.2.1	Injector for a Hybrid Plasma Accelerator	4078
26.3	Plasma Injection Mechanisms	4086
26.3.1	Optimisation of Ionisation Injection	4086
26.3.2	Generation of Attosecond Electron Bunches by Density-Gradient- Controlled Injection	4087

26.4	Compact Radiation Generation	4090
26.4.1	Betatron Radiation Control in a Plasma Channel	4090
26.4.2	Schemes for Enhanced Betatron Radiation	4091
26.4.3	Coherent Bright XUV and X-Ray Radiation from LWFA	4091
26.5	Dielectric Technology for Diagnostics & Beam Control	4092
26.6	Additional Application Beamlines	4093
27	Safety and Environmental Impact	4094
27.1	Safety Aspects	4094
27.2	Environmental Impact	4099
Part 5	EuPRAXIA Pre-Construction R&D and Technical Design Phase	4100
28	Necessary Experiments and Prototypes for the EuPRAXIA Design	4100
28.1	Laser System	4100
28.2	Plasma Components	4102
28.3	RF and Accelerator Technology	4103
28.4	Diagnostics	4104
29	EuPRAXIA Consortium Facilities	4107
29.1	APOLLON (France)	4107
29.2	CLARA (United Kingdom)	4108
29.3	COXINEL (France)	4109
29.4	ELBE Centre for High Power Radiation Sources (Germany)	4110
29.5	ELI – Extreme Light Infrastructure	4111
29.6	FLASHForward (Germany)	4113
29.7	HI Jena (Germany)	4114
29.8	ILIL (Italy)	4115
29.9	Imperial College London (United Kingdom)	4116
29.10	KIT (Germany)	4118
29.11	LMU-CALA (Germany)	4119
29.12	LPA-UHI100 (France)	4119
29.13	Lund Laser Centre (Sweden)	4120
29.14	LUX (Germany)	4120
29.15	Queen’s University of Belfast (United Kingdom)	4121
29.16	Rutherford Appleton Laboratory (United Kingdom)	4122
29.17	SCAPA (United Kingdom)	4122
29.18	SINBAD (Germany)	4123
29.19	SPARC_LAB (Italy)	4124
29.20	University of Oxford (United Kingdom)	4126
29.21	Wigner Institute (Hungary)	4127
30	International Consortium Facilities	4128
30.1	Berkeley Lab Laser Accelerator Center (United States)	4128
30.2	Institute of Applied Physics at the Russian Academy of Sciences (Russia)	4129
30.3	Osaka University / KPSI-QST / RIKEN (Japan)	4130
30.4	Shanghai Jiaotong University (China)	4131
30.5	Tsinghua University Beijing (China)	4131
31	Computing Facilities	4132
Part 6	Appendix	4135
32	Further Working Package Results	4135
32.1	Assumptions and Numerical PIC Codes Used	4135
32.2	Further Considerations for High-Gradient Plasma-Accelerator Structures	4144
32.2.1	Introduction	4144
32.2.2	Plasma Stage Parameters	4144
32.2.3	Plasma Creation	4146
32.2.4	Laser Confinement	4151
32.2.5	Injection Techniques for the LPI	4163
32.2.6	Summary: Preliminary Design Elements	4175
32.3	Enabling Laser Design and Optimisation	4176

32.3.1	Introduction . . . . .	4176
32.3.2	Pump Laser Technology . . . . .	4178
32.3.3	Pump Array Layouts . . . . .	4179
32.3.4	Conclusive Remarks . . . . .	4180
32.4	Outreach and Liaison . . . . .	4181
32.4.1	Resources . . . . .	4181
32.4.2	Publications . . . . .	4184
32.4.3	Activities . . . . .	4185
32.5	Experience from PWFA Test Experiments . . . . .	4187
32.5.1	Active Plasma Lenses . . . . .	4187
32.5.2	Plasma Dechirper . . . . .	4190
32.5.3	Plasma Sources . . . . .	4193
32.5.4	Beam-Driven Plasma Wakefields . . . . .	4195
32.6	Use of Other Novel Technologies . . . . .	4196
32.6.1	Possible Alternative Injector Concepts . . . . .	4196
32.6.2	Ultra-Cold Electron Source . . . . .	4196
32.6.3	Dielectric Laser Acceleration (DLA) . . . . .	4197
32.6.4	State of the Art in Fibre Optics Lasers . . . . .	4199
32.7	Experience from FEL Test Experiments . . . . .	4200
32.8	Accelerator Prototyping – Report on Test Experiments . . . . .	4202
32.8.1	Introduction . . . . .	4202
32.8.2	Testing Laser Wakefield Accelerator Sources for EuPRAXIA . . . . .	4203
32.8.3	Non-Destructive Bunch Length Measurement Based on Smith-Purcell Radiation . . . . .	4204
32.8.4	3D-Printed Capillary for a Hydrogen-Filled Discharge for Plasma Acceleration . . . . .	4204
32.9	CAD Model of the Conceptual EuPRAXIA Facility Layout . . . . .	4207
33	EuPRAXIA Publications and Conference Contributions . . . . .	4209
33.1	List of EuPRAXIA Peer-Reviewed Publications . . . . .	4209
33.2	List of EuPRAXIA Conference Proceedings . . . . .	4217
	References . . . . .	4221
	List of EuPRAXIA Partner and Associated Partner Institutes . . . . .	4268
	Commonly Used Acronyms . . . . .	4270
	List of Figures . . . . .	4272
	List of Tables . . . . .	4281

## Part 1

# Executive Summary

The conceptual design of a new European research infrastructure, EuPRAXIA, is presented in this report. The concept has been established over the last 4 years in a unique collaboration of 30 institutes in Europe and 11 laboratories in Asia, Russia, and the United States. EuPRAXIA is the first European project that develops a dedicated particle accelerator research infrastructure based on novel plasma concepts and laser technology. It focuses on the development of particle accelerators and underlying technologies, their user communities, and the exploitation of existing accelerator infrastructures in France, Germany, Italy, and the UK. The conceptual design of EuPRAXIA is timely; recent breakthroughs in laser technology realised through the significant investments by the EU and its member states in the Extreme Light Infrastructure (ELI) and parallel advancements in plasma accelerators worldwide underpin the realisation of a plasma-accelerator-based user facility for science and research. EuPRAXIA has involved the international laser community to build links and bridges with accelerator science as well as to realise synergies, identify disruptive ideas, innovate, and foster knowledge exchange.

The EuPRAXIA project aims at the construction of an innovative electron accelerator using laser- and electron-beam-driven plasma wakefield acceleration that offers a significant reduction in size and possible savings in cost over current state-of-the-art radiofrequency (RF)-based accelerators. EuPRAXIA envisions a beam energy of 1 to 5 gigaelectronvolts (GeV) and a beam quality (single pulse) equivalent to present RF-based linacs.

The worldwide interest in plasma-based electron accelerators is driven by the need of a new technology to overcome the multi-TeV barrier for particle accelerators and the desire to make electron-beam and associated radiation facilities (FELs, synchrotrons, etc.) available to a larger user base. Advancing into the next generation of light sources, a size and cost reduction for the facility of at least one order of magnitude must be realised to harvest the scientific and commercial prospects. EuPRAXIA aims at realising the first laser plasma user facility worldwide, demonstrating feasibility and gaining operational and user experience.

EuPRAXIA will demonstrate high-quality beam generation from a plasma-accelerator module and is therefore the required stepping stone to possible future plasma-based facilities, such as linear colliders at the high-energy physics (HEP) energy frontier, that would combine many such modules. The EuPRAXIA energy range and its performance goals will enable versatile applications in various domains, e.g. as a compact free-electron laser (FEL), compact sources for medical imaging and positron generation, tabletop test beams for particle detectors, as well as deeply penetrating X-ray and gamma-ray sources for material testing.

Consistent with a high-confidence approach, the EuPRAXIA project includes measures to retire risk by establishing scaled technology demonstrators. The EuPRAXIA facility will integrate lessons learned and establish user readiness by 2030. A risk reduction roadmap has been defined and will ensure that risks are minimised and challenges will be addressed by appropriate mitigation measures.

Initial system designs have been developed using start-to-end simulations to achieve the single- and multi-stage acceleration of electron beams, with a quality much superior to present state-of-the-art plasma acceleration experiments. In some parameters, a factor 10 improvement is predicted. At the same time, the design initially realises at least a factor 6 gain in required floor space for the accelerator if compared to existing accelerator facilities. This includes the accelerator system itself and its support infrastructure. A final gain of a factor 10 and more for the accelerator-only footprint seems achievable in a phased approach.

The development and construction of new generations of pulsed lasers with petawatt peak power as drivers for plasma wakefield accelerators will be performed jointly with industry and national laboratories specialised in energetic laser development. These lasers will operate with high stability at 20 to 100 Hz, a modest advancement of a factor 2 to 10 over the current state of the art. The high repetition rate, however, enables laser-based and beam-based fast feedback loops as well as the application of advanced data science techniques, such as machine learning. In parallel, focused R&D activities will be pursued on the rapid development of laser systems that can operate at kHz repetition rates and deliver peak-power levels at 100 TW or more. Such drivers would allow a factor 10 increase in average brilliance and pave the path to even more compact and efficient accelerator systems. The parallel development is envisioned to facilitate innovation in high-repetition-rate plasma-accelerator technology, enabling additional applications and science reach while maintaining the 100 Hz laser systems as a project baseline for a risk-balanced approach. The improved feedback efficiency with such increased repetition rates compared to the current state of the art will allow even better pulse-to-pulse stability control and beam quality.

Finally, EuPRAXIA also includes the development and construction of a compact X-band RF accelerator based on technology from CERN to realise a beam-driven plasma accelerator. Such an X-band linear accelerator will exploit the capabilities with the most compact RF technology available today and provide an excellent science test facility with a complementary technological approach that decouples the plasma accelerator from laser science.

Distributed and versatile user areas will be set up to exploit the inherent advantageous features of the plasma accelerator, for example multiple parallel user lines for laser-driven accelerators, the generation of ultra-fast electron and photon pulses with naturally short pulse lengths, the quasi-point-like emission of X-rays inside plasmas with the potential for ultra-sharp imaging, and unique pump-probe configurations with the synchronised EuPRAXIA particle and laser beams.

The EuPRAXIA project will serve society in a number of ways. The broad and interdisciplinary EuPRAXIA collaboration in Europe and with international partners will create a critical mass of expertise and capabilities in Europe. It will support and further position Europe as a world-leading competitor in accelerator innovation. The EuPRAXIA project will also challenge and support the European and world-wide laser industry to further develop and improve their products on high-power pulsed lasers. New generations of scientists and technicians in the EU will be exposed to innovative and highly challenging technical and intellectual problems in centrally located and well-integrated R&D facilities. The proximity to major universities and laboratories in Europe will amplify the capability of EuPRAXIA to fascinate young generations for science and technology, to foster innovative out-of-the-box thinking, to serve as a high-tech training base, and to strengthen the job base for technical work. Finally, a compact particle accelerator product as a result of the EuPRAXIA project could make accelerators available as versatile tools to new users and in new locations, e.g. laboratory spaces at university, hospitals, mobile platforms, and beyond.

The EuPRAXIA infrastructure is implemented through several components: clusters, excellence centres, and construction site(s).

Clusters of European institutes collaborate jointly to address well-defined challenges and guide the overall R&D and design of the project. This is complemented by EuPRAXIA centres of excellence at existing large infrastructures in Hamburg (DESY – Germany), on the Plateau de Saclay (France), in Lisbon (IST – Portugal), in the UK (CLF and SCAPA), and at ELI Beamlines (Czech Republic). The centres of excellence perform mission-critical R&D, prototyping, testing, and construction tasks bringing in and upgrading their existing infrastructures and delivering fully tested components to the EuPRAXIA construction site(s). As a central component to the

infrastructure concept, one or two construction sites will host new large research facilities, exploiting beam-driven (BPA) and laser-driven plasma-accelerator (LPA) technology. At these construction site(s), the consortium will set up several plasma-accelerator beamlines realising complementary technologies and applications, and providing pilot access to academic and industrial users, once target parameters have been reached. INFN – Frascati (Italy) has been agreed as the construction site for a beam-driven plasma accelerator facility, including several applications, such as a free-electron laser and positron sources. It is ready to proceed and will be realised in the first phase of the project. For the laser-driven construction site, a strong concept has been developed at this stage, and multiple candidate sites have been identified based on the varied research landscape for laser-driven plasma acceleration already existing across Europe. A site decision for the construction of the laser-driven plasma accelerator will be taken during the preparatory project phase of EuPRAXIA.

The EuPRAXIA clusters, excellence centres, and construction sites are coordinated by a lean project management structure. It organises the overall technical design (TD) and prototyping, it oversees construction work, and it links to industrial partners through work at the collaborating institutes.

Funding options for EuPRAXIA start at 68 million euros for a beam-driven and 75 million euros for a laser-driven EuPRAXIA implementation (minimal systems). It is estimated that the full-scale EuPRAXIA facility with two construction sites requires an investment of 320 million euros and about 1,800 FTE person power integrated over an 8–10 year project duration (technical design, prototyping, and construction). The 320 million euro cost includes about 83 million euros that is invested in laser technology with industry. Funding will be leveraged by co-funding from the EuPRAXIA partners. The full-scale EuPRAXIA implementation is a truly European project that realises a major competitive advantage, strong scientific impact, and important societal benefits. Proceeding at full speed, we estimate that the EuPRAXIA research infrastructure would start full operation in 8–10 years. Parts of EuPRAXIA could go into operation at significantly earlier times.

## Role and Structure of the CDR

This report describes the conceptual design of a European plasma accelerator facility EuPRAXIA. It includes technical results and organisational concepts that are required for assessing the feasibility of such a research infrastructure based on plasma acceleration and other technologies. The report does not provide a final technical design of the facility to be implemented, but instead proposes solutions for critical issues, while also identifying additional challenges and developing strategies on how to possibly approach them in the future. Based largely on theoretical and simulation studies, together with in-kind funded experimental activities, the CDR summarises the activities and developments of a large collaboration of research organisations. Most of the concepts developed in the context of EuPRAXIA and presented here have been published as EuPRAXIA articles in scientific journals and are referenced accordingly herein. As an added value, this report brings these findings together and applies them in the context of constructing a compact, large-scale research facility.

On the basis of the outcomes of this report, it is acknowledged that, while some technical issues remain to be solved, several novel solutions have been developed and confirmed in the standard peer review process before publication in journals like *Physical Review Letters*. No fundamental show-stoppers have been identified for the concept of the EuPRAXIA facility. The continuation of the project through a technical design phase will validate the proposed design in more detail. This next phase will also be focused on developing further the detailed technical specifications of

the proposed facility including required prototypes and experimental demonstrations, upon which the final design of the EuPRAXIA implementation will be based.

The remainder of this report consists of five main sections. While the first two present an introductory description of the project suited for non-expert readers, Parts 4 to 6 focus on the technical challenges, proposed solutions and planned experimental demonstrations that determine the strategy for realising the proposed infrastructure.

In this context, Part 2 provides a short description of the EuPRAXIA project, including an introduction to plasma acceleration and the EuPRAXIA Consortium, a definition of the project goals, a summary of the implementation concept of EuPRAXIA and its benefits to participants, as well as an outline of the project's cost, schedule and risk estimates.

Subsequently, the non-technical aspects of EuPRAXIA are presented in Part 3. After an introduction of the project and the field of plasma accelerators in Chapter 1, the case of EuPRAXIA for science and innovation is put forward in Chapter 2 and the concept of the proposed infrastructure is discussed in Chapter 3. Chapter 4 outlines the preliminary financial project planning, whereas Chapter 5 summarises various organisational aspects from schedule and governing model to risk mitigation. Finally, Chapter 6 provides a brief overview of the predicted impact of EuPRAXIA in a scientific and societal context.

Part 4 focuses entirely on the conceptual design of the beamlines foreseen at the EuPRAXIA facility. Chapters 7 to 9 present the technical background, an overview of the facility sub-systems, and a summary of technical parameter tables, respectively, before different machine components are examined in detail in Chapters 10 to 26. Chapter 27.2 summarises aspects relating to the safety and environmental impact of the project.

Consequently, an outlook on the planned technical design phase of EuPRAXIA – dedicated with a large part to prototyping and test experiments – is given in Part 5. After a description of key future activities for different machine sub-systems in Chapter 28, a variety of relevant and suitable test facilities related to the EuPRAXIA Consortium is introduced in Chapters 29 to 31.

Finally, Part 6 presents the Appendix of the CDR, where further details are provided on many of the technical topics discussed in the conceptual design, and a list of EuPRAXIA journal publications can be found.

## Part 2

# Short Description of EuPRAXIA

### Plasma Wakefield Acceleration: A Transformative Technology for Future Particle Accelerators

Plasma wakefield acceleration opens the path to new particle accelerators that can be much more compact and cost-effective. A strong competition is ongoing throughout the world involving laser and accelerator industry.

Europe has played a leading role in the development of particle accelerators since the first radiofrequency (RF) accelerator was built in Aachen in 1927 [1]. Today Europe operates most of the leading particle accelerators in the world. Tens of thousands of users from science, industry, and medicine are provided with beam time and rely on the availability of cutting-edge, high-quality particle and photon beams for performing their work.

Providing particle beams that are competitive on a worldwide scale requires continuous optimisation and the improvement of operating facilities, including strategic research and development. Adopting new ideas and novel technologies has constantly advanced the field of particle accelerators. Prime examples are the 1968 invention of stochastic cooling by Simon van der Meer at CERN [2], opening the route to higher density beams and recognised by the 1984 Nobel Prize in Physics [3]. In 1979, Tajima and Dawson proposed laser-driven plasma accelerators that can produce accelerating fields 1,000 times stronger than in RF accelerators [4], thus opening the possibility for accelerator facilities with a much-reduced size and cost. Such machines have since been realised experimentally and reproducibly demonstrated multi-GeV electron beams with promising beam quality. In parallel, high-power lasers have been developed over the past decades since the invention of chirped pulse amplification and are today produced with European laser industry in a leading position. This innovation in laser technology was awarded with the 2018 Nobel Prize for Physics, going to Donna Strickland and Gérard Mourou [5].

A strong competition is ongoing throughout the world (with the United States, Europe, Japan, and China being the key players) involving laser and accelerator industry. The common breakthrough goal of these activities is an accelerator facility that will support users with particle and photon beams, while demonstrating benefits in size and cost. Such a technology leading to compact accelerators will have unforeseen applications in hospitals, universities, emerging countries, etc., while also being a required stepping stone to future high-energy accelerators for discovery science. EuPRAXIA is the design of such a new facility that offers unprecedented features, enables (if constructed) advances otherwise not possible, and prepares a future with compact accelerators.

### The EuPRAXIA Consortium

EuPRAXIA enables interdisciplinary collaboration in Europe and beyond as a key to success.

The EuPRAXIA Consortium has formed around an EU-funded Horizon 2020 conceptual design study to develop the concept of a “European Plasma Research Accelerator with eXcellence In Applications”. It serves as an open innovation platform bringing together 16 participants and 25 associated partners from Europe, Asia, and

the United States. Among the 41 members of the consortium are international organisations, major national laboratories, and universities combining interdisciplinary expertise from particle accelerators, laser science, plasma physics, theory, simulations, and accelerator-based user facilities.

EuPRAXIA is the first European project that develops a dedicated accelerator research infrastructure based on novel plasma concepts and laser technology. It keeps a strict focus on the development of particle accelerators, their user communities, and the exploitation of existing accelerator infrastructures in France, Germany, Italy, and the UK. The laser community, in particular the Extreme Light Infrastructure (ELI) and its new laser infrastructures, is connected as associated partners, ensuring complementarity and full knowledge exchange.

The EuPRAXIA work is organised in 15 work packages (WP), each led by two senior scientists from European institutes. The consortium also connects to representatives from leading European laser companies through its scientific advisory board and its laser work package, that are, in this way, directly contributing to the project.

## Technical and Scientific Goals

EuPRAXIA will demonstrate compact and highly innovative plasma-accelerator technology for higher energy applications in the European research landscape.

The EuPRAXIA project aims at the construction of an innovative electron accelerator based on plasma wakefield acceleration, with a beam energy of 1 to 5 gigaelectronvolts (GeV), a beam quality (single pulse) equivalent to present RF linacs, and demonstrated benefits in size and cost when compared to RF-based machines.

The EuPRAXIA pilot facilities with improved electron beam quality will establish user-readiness and will deliver electron beams and photons as a first demonstrator to users of this new technology. The EuPRAXIA energy range and its performance goals will enable versatile applications in various domains, e.g. a compact free-electron laser (FEL), compact sources for medical imaging and positron generation, tabletop test beams for particle detectors, and highly mobile but deeply penetrating X-ray and gamma-ray sources for material testing.

EuPRAXIA will demonstrate high-quality beam generation from a plasma-accelerator module and is therefore the required stepping stone to possible plasma-based linear colliders at the high-energy physics (HEP) energy frontier, which would combine many such components.

In more detail, the EuPRAXIA scientific and technical goals include the following:

- Achievement of the single- and multi-stage acceleration of electron beams to final energies between 1 and 5 GeV, with a pulse duration of a few femtoseconds, with transverse emittance of about 1 mm mrad, and with relative energy spread reaching from a few percent down to a few  $10^{-3}$  total and a few  $10^{-4}$  in a 1-micrometre-slice of the beam. The EuPRAXIA specifications approach the regime of modern FELs, open various application paths, and also fulfil basic requirements for a 5 GeV plasma-accelerator stage of a linear collider.
- Implementation of a highly compact machine layout, initially realising at least a factor 3 gain in required floor space for the facility with accelerator and user areas. This includes all necessary components and infrastructure. EuPRAXIA additionally implements a realistic stepwise strategy for the miniaturisation of the particle accelerator itself by a factor 10 and beyond in its most compact version.

- Development and construction of new generations of petawatt-scale pulsed lasers as drivers for plasma wakefields, together with industry and laser institutes. These lasers will operate with high stability at 20 to 100 Hz, therefore enabling laser-based and beam-based fast feedbacks. In parallel, major R&D activities will be pursued on the rapid development of laser systems with higher efficiency, which can operate at kHz repetition rates. Here, we mention the KALDERA system that will be developed at DESY. The new kHz laser system would replace the more conventional 100 Hz laser system during an upgrade of the EuPRAXIA infrastructure and would enable additional applications and science reach. The improved feedback efficiency with such increased repetition rates compared to the current state of the art will allow much better pulse-to-pulse stability control and beam quality.
- Development and construction of a compact beam driver based on X-band RF technology from CERN. The X-band linac foreseen for EuPRAXIA's beam-driven plasma accelerator infrastructure will be the RF linear accelerator with the highest acceleration per metre worldwide.
- Development and construction of distributed and versatile user areas that exploit the inherent advantageous features of the plasma accelerator, namely:
  - the possibility of multiple parallel user lines for laser-driven accelerators,
  - the generation of ultra-fast electron and photon pulses with naturally short pulse lengths,
  - the quasi-point-like emission of X-rays inside plasmas with the potential for ultra-sharp imaging,
  - unique pump-probe configurations with the synchronised EuPRAXIA particle and laser beams.

The EuPRAXIA Consortium has, since 2015, developed and published a number of concepts that describe novel solutions for improved beam quality and will allow reaching these goals (see Chap. 33 for a full list of publications). More controlled electron injection techniques, phase-space manipulation concepts as well as enhanced stability and synchronisation for laser and electron beams, for example, will be combined with conventional, well-established components. Those solutions will be tested in a phased approach during the technical design phase to confirm the validity of the facility concept.

## Societal Goals

EuPRAXIA will involve the European industry and younger generations in inspiring technological challenges close to major universities and research institutions in Europe.

The EuPRAXIA project will serve society in a number of ways:

- The broad and interdisciplinary EuPRAXIA collaboration in Europe and with international partners will create a critical mass of expertise and capabilities in Europe. It will support and further position Europe as a world-leading competitor in accelerator innovation.
- The EuPRAXIA project will challenge and support the European and world-wide laser industry to further develop and improve their products on high-power pulsed lasers. This will strengthen the laser industry overall but in particular also enable European laser companies to stay world leading in a fair and competitive effort.
- New generations of scientists and technicians in the EU will be exposed to innovative and highly challenging technical and intellectual problems in centrally located

and well-integrated R&D facilities. The proximity to major universities and laboratories in Europe will amplify the capability of EuPRAXIA to fascinate young generations for science and technology, to foster innovative out-of-the-box thinking, to serve as a high-tech training base, and to strengthen the job base for technical work.

- A compact particle accelerator product as a result of the EuPRAXIA project could make accelerators available as versatile tools to new users and in new locations, e.g. laboratory spaces at university, hospitals, mobile platforms, and beyond. This would multiply access to accelerators and could create major advances in knowledge and capabilities, some of them yet unimaginable. We can, for example, foresee that ultra-fast X-ray pulses from compact accelerators could serve tens of thousands of PhD students and post-docs to scan features of many million types of viruses and bacteria, materials and medical compounds. The most promising cases would then be studied further and with more accuracy in big science facilities.

## Implementation Concept for EuPRAXIA

EuPRAXIA builds a new kind of European research infrastructure on the foundations of existing facilities and past national investments.

The implementation concept for the EuPRAXIA project has been inspired by the design and construction of large detectors for particle physics, for example ATLAS and CMS for the Large Hadron Collider at CERN. Dozens of institutes form such a detector collaboration; they develop, prototype, and produce the components of the detector and finally assemble the full device at the site of the experiment. During this process, groups of institutes (“clusters”) collaborate on certain well-defined parts of the detector, combining their expertise and involving the local infrastructures at their laboratories. This distributed model of R&D and production has proven very efficient and highly successful for building together some of the world’s most complex scientific installations.

EuPRAXIA aims at implementing such a concept for the common construction of a European plasma-accelerator facility, in the form described below. We also note that such a concept, almost unique in the current scenario of collaborative efforts in the field, is an open innovation approach. As such, following the EU definition, it aims to “open up the innovation process to all active players so that knowledge can circulate more freely and be transformed into products and services that create new markets” [6].

The proposed EuPRAXIA implementation model relies on five pillars:

1. The common goals of the EuPRAXIA Consortium, as described above.
2. Several clusters of institutes that address particular and well-defined challenges in the EuPRAXIA project. International partners are included through bilateral or EU programs, within the rules of funding agencies.
3. A set of EuPRAXIA centres of excellence in plasma-based acceleration, in plasma theory and simulation, and in laser technology. They rely heavily on already-existing large infrastructures active in the field which provide the scientific and technical capabilities required for solving critical R&D challenges for the project in due time. At these facilities, mission-critical R&D, prototyping, testing, and construction tasks are performed, bringing in and upgrading their existing infrastructures.
4. One or two EuPRAXIA site(s) will host the construction of the beam-driven and laser-driven plasma accelerator facility(ies). At these construction site(s)

and possibly also at excellence centres, the consortium will set up several plasma-accelerator beamlines realising complementary technologies and applications and providing pilot access to academic and industrial users once target parameters have been reached.

5. An overarching and lean EuPRAXIA project management structure. It coordinates the overall technical design and prototyping, it oversees construction work, and it links to industrial partners through work at the collaborating institutes (funding passes through existing institutes and administrative structures).

The EuPRAXIA proposal foresees that scientific concepts, technical components, and assemblies are developed and prototyped in existing national facilities in France, Germany, Italy, Portugal, the UK and at ELI Beamlines, close to major universities and research institutions in Europe. This solution will ensure that the existing R&D infrastructure in Europe is fully exploited, it avoids expensive duplication of technical and administrative structures, it optimises the need for investment, and it provides access to a large pool of a technically educated and young work force, which is required for constructing such a facility.

EuPRAXIA proposes clusters of collaborating institutes that solve critical challenges in certain technical areas, including high peak-power laser technology.

The EuPRAXIA Consortium proposes clusters of institutes for addressing the critical challenges in our project. These clusters will bring together the partner institutes to address specific developments of interest for EuPRAXIA; the results will then be shared within the consortium and implemented at the excellence centres and eventually at construction site(s). This model provides a way to extend resources for a specific topic, and benefit the whole consortium. Important clusters proposed include the following:

1. cluster on theory and simulation: start-to-end simulations, performance predictions, evaluation of measured hardware performance, code benchmarking, development of new theoretical concepts, high-performance computing, new codes, and new approaches;
2. cluster on laser technology: R&D, testing, prototyping and construction of final hardware for laser drivers, laser diagnostics, optical components, laser transport lines, and kHz laser technology, all with a link to leading European laser expertise and industry;
3. cluster on plasma components and systems: R&D, testing, prototyping and construction of final hardware for plasma sources, plasma injectors, plasma-accelerator stages, plasma mirrors, and plasma lenses;
4. cluster on RF technology: R&D, testing, prototyping and construction of final hardware for RF drivers, RF injectors, low-level RF, and synchronisation;
5. cluster on magnets and other beamline components: R&D, testing, prototyping and construction of final hardware for magnets, beam transport and manipulation, collimation, and beam dumps;
6. cluster on diagnostics: R&D, testing, prototyping and construction of final hardware for electron diagnostics, positron diagnostics, photon diagnostics, and plasma diagnostics;
7. cluster on applications: R&D, testing, prototyping and construction of final hardware for positron sources, the free-electron laser, undulators, an inverse Compton source, a betatron source, test beam generation, HEP detector testing, and user end stations;
8. cluster on transformative innovation paths: R&D on novel concepts and techniques possibly suitable to implement at EuPRAXIA, including hybrid

accelerators, novel injection and radiation generation mechanisms, multi-pulse LWFA, and plasma-based metrology and diagnostics;

9. cluster on training, outreach, and dissemination: dissemination of results, outreach, education, public engagement, knowledge transfer, training, and user workshops;
10. cluster on layout and implementation: testing, prototyping and, partially, construction of final hardware for the infrastructure of the construction site(s), including the control system, data acquisition, analysis and storage, safety systems, cooling, and other basic support systems.

A more detailed description of these clusters is given in Section 3.3.1.

EuPRAXIA proposes five centres of excellence at existing facilities inside the EU, to be implemented and operated in close collaboration with the technical clusters.

Five EuPRAXIA centres of excellence are being proposed:

1. A EuPRAXIA laser and prototyping excellence centre, located on the Plateau de Saclay, close to Paris in France. A EuPRAXIA prototype laser will be installed by French EuPRAXIA institutes together with the laser industry to generate and accelerate electron beams to 1 GeV. High-quality feedback systems will be devised, acting on the parameters of the laser and the plasma structure developed in the French institutes. The Saclay prototype will be optimised to achieve the required stability goals for EuPRAXIA. In continuation of the COXINEL project in France, FEL quality beams will be demonstrated by generating FEL light. Both the plasma-accelerator technology and the FEL process will then be optimised for EuPRAXIA. In parallel, high-repetition-rate laser applications will be developed.
2. A EuPRAXIA excellence centre for plasma acceleration and high-repetition-rate developments located at DESY. For the past decade, DESY has been building up a program in plasma acceleration and is currently further expanding its capabilities to advance the science and technology of plasma accelerators. It is executing an ambitious development program in both electron beam-driven and laser-driven plasma accelerators, targeted to high electron beam quality, high average power, and first applications. In the context of the EuPRAXIA initiative, DESY is planning to bring in its capabilities and research interests as an excellence centre for plasma acceleration and high-repetition-rate developments. The present and future DESY capabilities relevant for EuPRAXIA include a GeV electron beam driver at a MHz repetition rate at FLASHForward, high peak-power laser pulses ( $>100$  TW) delivered at kHz for an average power at the multi-kW level at KALDERA, ultra-short electron bunches at up to 150 MeV from the S-Band linac ARES, advanced plasma and beam diagnostics, ultra-fast feedback systems, plasma-accelerator components, as well as experimental plasma acceleration setups. Several of these capabilities are supported through the Helmholtz-wide ATHENA project on the laser-plasma accelerator R&D infrastructure in Germany.
3. A EuPRAXIA theory and simulation centre, located at the Instituto Superior Técnico in Lisbon, Portugal. The centre will coordinate EuPRAXIA work on theory and simulations that will be performed at the various partner institutes. Common standards and comparability of results will be ensured. An increase in simulation capabilities through smarter algorithms and access to supercomputers will be essential to establish a full operational model of EuPRAXIA performance, including imperfections, feedback systems, and user needs.
4. A EuPRAXIA advanced application beamline centre, located in the UK. The Central Laser Facility CLF (STFC Rutherford Appleton Laboratory), the CLARA

facility (STFC Daresbury Laboratory), and the SCAPA facility (University of Strathclyde), together with several UK universities, combine unique expertise in plasma accelerators, X-ray-based medical imaging, industrial applications, and schemes for positron production. The UK-based EuPRAXIA consortium will design and prototype EuPRAXIA application beamlines.

5. A EuPRAXIA incubator at a laser centre, located at ELI Beamlines in Prague, Czech Republic, for user aspects and for the transfer of plasma-accelerator technology into ELI. The EuPRAXIA incubator at ELI will provide input and guidance on key components for high-repetition-rate laser-driven FELs from the laser community to EuPRAXIA. In addition, it will provide ELI with a direct open innovation access to the accelerator technology developed inside the EuPRAXIA project, such that it can provide this to its users. Industrial technology transfer from and to the laser industry can pass through ELI but will also directly involve the clusters, excellence centres, and construction site(s) of EuPRAXIA.

It is at the core of EuPRAXIA that the excellence centres will be implemented and operated in close collaboration with the clusters. For example, the laser and prototyping facility will be defined, set up, and operated in collaboration with the cluster on laser technologies, thus ensuring a wide European share of knowledge and work. The concepts, technical designs, technical drawings of prototype devices, and results achieved at the excellence centres listed above and at the construction site(s) (see below) will be made available in the form of open innovation to the whole consortium. The facilities described above will serve as continued development and testing areas during the operation of EuPRAXIA, developing necessary improvements for various components or preparing facility upgrades.

EuPRAXIA proposes a staged approach for the construction of sites for two complementary technical approaches in plasma acceleration. This will ensure competition in technology instead of competition among institutes.

In parallel to and after the technical design and prototyping work, we foresee that the consortium will construct the joint EuPRAXIA plasma accelerator and user facilities. Considering constraints and interests in the collaborating institutes and countries, the conceptual design has converged on the construction of a site devoted to beam-driven acceleration. For the laser-driven construction site, a strong concept has been developed at this stage, and multiple candidate sites have been identified, based on the varied research landscape for laser-driven plasma acceleration already existing across Europe.

1. The EuPRAXIA facility for beam-driven plasma acceleration is proposed to be constructed in Frascati, Italy, and is ready to proceed. The host lab is INFN-LNF, and the electron beam driver will rely on the most compact RF technology available, namely, X-band structures developed at CERN. The Frascati site of EuPRAXIA will build on the investments in beam-driven plasma acceleration at SPARC\_LAB. This proposal also reflects on the Italian interest in an FEL user facility that combines a 1 GeV RF-based FEL option with a plasma-based advanced FEL setup at possibly higher energy. EuPRAXIA@SPARC\_LAB would be the first FEL on the Frascati site. The dual approach will ensure that a new FEL user community at Frascati can be served with maximum availability and particle flux. User applications for EuPRAXIA@SPARC\_LAB will focus on a 1 GeV free-electron laser with an upgrade to 2–5 GeV, an inverse Compton scattering photon source, high-energy positron beams, and test beams.
2. The EuPRAXIA facility for the laser-driven plasma accelerator could be constructed at an excellence centre or at one of the several options described in Section 3.6.7. Laser pulses will be provided from lasers developed in collaboration

with industry and scientific institutes for the EuPRAXIA needs. The laser-driven EuPRAXIA site aims at the most compact accelerator solution for future free-electron lasers, complementing the existing big science FELs at various large research centres in Europe. User applications for EuPRAXIA will focus on a compact 1–5 GeV free-electron laser, plasma-based medical imaging, a compact positron source for material science applications, and highly compact test beams.

The complementary approaches followed in the two construction sites induce some level of competition in technology that will help speed up progress. At the same time, the two approaches offer different benefits and application reach. The two legs of EuPRAXIA will therefore have an excellent and long-term sustainability in technology development and user markets.

The combination of clusters, excellence centres, and construction site(s) will enable a truly European project that integrates the European R&D landscape in this research field and binds together existing facilities and investments. This approach allows the fastest progress in a situation of strong competition throughout the world. It is therefore proposed in the EuPRAXIA CDR and will be refined in the next project phases.

It is a crucial aspect of the EuPRAXIA concept that the implementation model described above is coordinated and governed in the common EuPRAXIA project that we propose. The overall EuPRAXIA management will match tasks across all partner laboratories with available expertise, interests, and capacity. It will ensure that common components will be used in the construction site(s) and the connected facilities, wherever possible. The EuPRAXIA project will thus prevent the duplication of work and loss of resources from internal competition. The proposed EU-wide coordinated project will produce critical mass, synergy, and added value, positioning the EuPRAXIA Consortium as a highly competitive and success-enabled player in the worldwide competition for a new accelerator technology.

## Added Value for EuPRAXIA Participants

EuPRAXIA partners participate in the knowledge creation process, gain in institutional capabilities, share EuPRAXIA intellectual property, and transfer innovations back into their nations.

The participants in the EuPRAXIA project will profit from a number of benefits for their work and their countries:

- Participation in the knowledge creation process that will be fostered by EuPRAXIA with its interdisciplinary and international project team (“attracting and educating the brains for our future”).
- Gain in capabilities in the participant’s laboratory from project tasks performed and from additional resources procured via the EuPRAXIA project.
- Access to EuPRAXIA infrastructures and expertise across the whole project, profiting from larger critical mass and enabling faster progress in R&D activities.
- Institutional share in intellectual property that is generated in the open innovation format of EuPRAXIA.
- Possibility to transfer compact applications to the participant’s country, users, and industry.
- Bringing the competitive advantage of the EuPRAXIA collaboration to the participant’s institute and country in a world-wide race for high technology leadership as well as modern industries and applications.

- Supporting accelerator development using laser plasma technology, bringing together the accelerator community interested in beam quality and the laser plasma physicists interested in high-level advances in laser science.

## Preliminary Cost Estimate

EuPRAXIA is, at full scale, a 320 million euro investment into European compact accelerator innovation and scientific applications, including an 83 million euro investment into laser technology. Depending on budget availability, minimal scenarios include options for a 68 million euro beam-driven and a 75 million euro laser-driven accelerator site.

The EuPRAXIA concept relies heavily on existing R&D facilities at major European laboratories. The institutes operating there today will ensure the availability of the required administrative structures and basic infrastructures. EuPRAXIA can therefore be highly cost-effective and focus on innovation and leadership in technology and science. Using existing large laboratories as hosts guarantees the sustainability of the EuPRAXIA centres and site(s) and opens the possibility of co-funding.

Detailed discussions on funding provisions for the full EuPRAXIA project will only take place after the completion of the Conceptual Design Report (CDR) in October 2019. In Section 4, the CDR provides a preliminary cost estimate for the EuPRAXIA research infrastructure, the required technical design and prototyping. Options start at a cost of 68 million euro for a beam-driven and 75 million euro for a laser-driven EuPRAXIA implementation (minimal systems). It is estimated that the full-scale EuPRAXIA facility with two construction sites requires an investment of 320 million euro and about 1,800 FTE person power integrated over a 8–10 year project duration (technical design, prototyping, and construction). The 320 million euro cost includes about 83 million euro that is invested in laser technology with industry and will be leveraged by co-funding from the EuPRAXIA partners. The full-scale EuPRAXIA implementation is a truly European project that realises the competitive advantage, scientific impact, and societal benefits described above.

The full-scale EuPRAXIA project is a strategic investment into accelerator innovation, laser industry, the technical education of young generations, and European collaboration.

It is explicitly acknowledged that the development of a EuPRAXIA funding scenario will require detailed discussions with decision makers at the national and EU levels. Only the support and injection of significant funding from the European Commission can enable an open innovation infrastructure project like EuPRAXIA, a project that is focused on capital-intensive high technology and operates across Europe.

The interim funding from the completion of the conceptual design report in October 2019 to the possible start of (not yet defined) Horizon Europe funding for the technical design at the end of 2022 is an issue of critical importance. The shift of the next roadmap exercise of the European Strategy Forum for Research Infrastructures (ESFRI) by one year creates a likely gap in funding that should be urgently addressed. A funding of 4 million euro would be sufficient to keep the EuPRAXIA collaboration active and advance preparatory work on concepts and implementation details. Additional funding at the level of a former “Joint Research Activity” (JRA, 15 million euro) would allow the start of urgent R&D work and the performance of critical feasibility demonstrations.

## Schedule

EuPRAXIA is a project that requires a technical design phase of four to six years and a construction phase of four years.

The definition of the EuPRAXIA project phases and the correspondence with European decision processes (such as the ESFRI roadmap) are discussed in Section 5.1. We note that the international race towards compact particle accelerators with applications and progress in back-bone technologies (e.g. high-power lasers from industry) requires a fast decision process. Fast decisions will make it possible to retain the competitive edge. Once funding is available, the EuPRAXIA R&D can start swiftly, based on the work done in the EuPRAXIA conceptual design study and the reliance on existing research infrastructures. It is acknowledged that the EuPRAXIA project is a highly innovative project with a number of risks in technical challenges and project setup. Therefore, a decision process will need to move in a stepwise fashion, from the approval of the technical design phase to a project readiness review and finally the approval for construction.

Proceeding at full speed, we estimate that the EuPRAXIA research infrastructure would start full operation in 8–10 years. Parts of EuPRAXIA could go into operation at significantly earlier times.

## Risk Reduction Roadmap

EuPRAXIA is a highly innovative project and, as such, has areas of technical and managerial risk. A risk reduction roadmap will ensure project success.

The EuPRAXIA project team has identified major risks in various important areas:

1. Laser technology, hardware, and transport might face unforeseen technical problems.
2. The readiness of a user application could be delayed, or user demand might be lower than anticipated initially.
3. One of the novel EuPRAXIA schemes might not work as predicted.
4. Certain EuPRAXIA simulation results might be too optimistic given unavoidable imperfections, new physics processes, and computational limitations.
5. A partner with a relevant commitment for EuPRAXIA might withdraw from the project given funding constraints.
6. A strategic industrial partner might change priorities.

These are just a few major examples. More can be found in Chapter 5.7. Based on these challenges, the EuPRAXIA Consortium has defined a risk reduction roadmap including the following measures:

1. In its CDR, EuPRAXIA relies as much as possible on proven concepts and solutions, requiring challenging but realistic extensions in technology. For example, the baseline EuPRAXIA laser technology is based on an extrapolation of the presently available industrial solutions. Also, the envisaged beam energy in plasma acceleration has been demonstrated. Higher risk solutions have been defined as backup and development paths.
2. Full-scale prototypes of critical components will be tested at EuPRAXIA excellence site(s) before the final construction decision. Examples include the high-power laser, the beamlines, the undulator and FEL performance at 1 GeV, and the plasma targets.

3. The EuPRAXIA concept foresees full and very accurate diagnostics of the laser, the plasma, and the electron beams. Optical control elements and electron beam correctors have been integrated or foreseen to counter performance limitations.
4. Backup options have been defined for critical schemes and can be tested in a timely matter, if needed. Examples include various types of electron sources, various plasma schemes, options for diagnostics, and different transfer line designs.
5. The approach of a distributed construction model guarantees that the consortium can continue operation even if a partner would withdraw from the collaboration.
6. EuPRAXIA has already, in its CDR phase, connected to several companies and will continue relying on multiple industrial partners. This will minimise risks in case of changing priorities in a connected company.
7. EuPRAXIA offers opportunities for outstanding science, innovation, and multiple user applications at excellence centres and site(s). This offers risk mitigation in the case that one science or user application is delayed because of problems in technical parameters.
8. EuPRAXIA has reached out to the user communities in particle physics, photon science, health, and industry to better integrate their insights and needs into the facility design. This effort will be continued.

We are convinced that the combination of a highly innovative EuPRAXIA concept, advanced technologies, new ideas and risk-mitigation strategies will ensure a fully successful project.

# Part 3

## The Research Infrastructure Concept



**Fig. 1.1.** Partners and associated partners of the EuPRAXIA Consortium.

## 1 Introduction

### The EuPRAXIA Consortium

The EuPRAXIA Consortium is a collaboration of 41 institutions across 14 countries (as of November 2018) in Europe and beyond, as shown in Figure 1.1. It consists of 16 full members as well as 25 associated partners, which joined the collaboration after the beginning of the design study and hence have added to the project largely through in-kind contributions.

The EuPRAXIA collaboration came together in a unique attempt to combine interdisciplinary expertise from across all areas relevant for the construction of a novel plasma-based accelerator facility. As such, EuPRAXIA comprises not only international organisations and national laboratories but also research institutes and universities. Its partners have demonstrated excellence in accelerator science and plasma physics as well as laser technology, photon science, and high-energy physics. Finally, through its Scientific Advisory Committee (SAC) as well as more informal partnerships, the EuPRAXIA Consortium is also connected to industry, such as the world-leading laser companies Amplitude, Thales, and Trumpf Scientific, as well as other excellent research hubs like the European XFEL, Fermi, and ALBA light sources, CERN, and the Lawrence Livermore National Laboratory.

The contributions of the consortium partners to the EuPRAXIA conceptual design study have been coordinated through a set of fifteen technical work packages (WPs) with specific foci on the main sub-systems of the EuPRAXIA machine design. In this context, each work package is directed by a WP leader and co-leader, as Figure 1.2 shows, and includes representatives from around two to ten different partner institutes. Work Packages 9 to 15 are not part of the Horizon 2020 project funding; hence, all work carried out by these groups (and, to a large extent, presented in this report) has been entirely based on in-kind contributions.

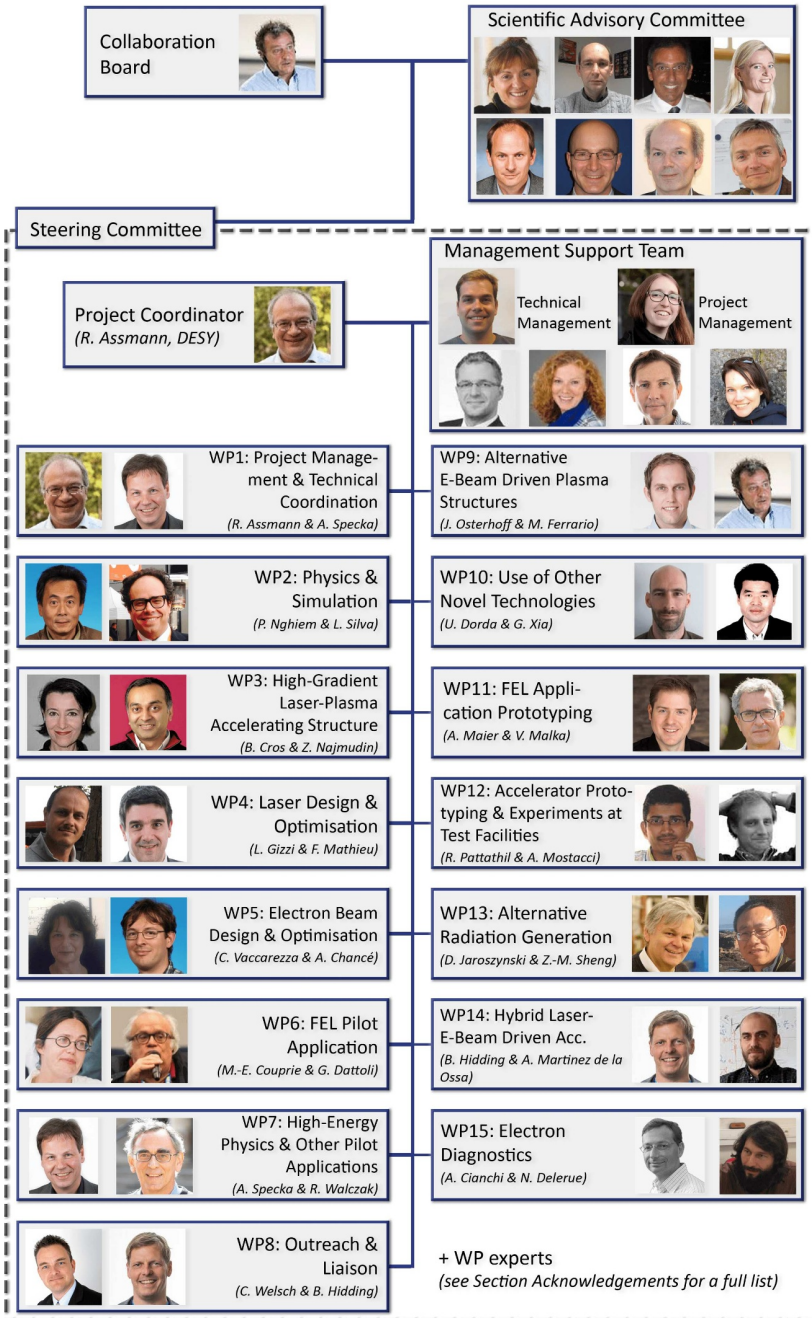


**Fig. 1.2.** Project management structure of the EuPRAXIA design study. The leaders and co-leaders of each work package are shown as well as the project coordinator and the head of the EuPRAXIA Collaboration Board. The Scientific Advisory Committee consists of (top row, from left) C. Biscari (ALBA), F. Falcoz (Amplitude Laser), L. Giannessi (Elettra/ENEA), E. Gschwendtner (CERN), (bottom row, from left) C. Haefner (LLNL), K. Michel (Trumpf Scientific), C. Simon-Boisson (Thales), and T. Tschentscher (European XFEL). The Management Support Team is comprised of (top row, from left) P.A. Walker, M. Weikum, (bottom row, from left) T. Minniberger, R. Rudolph, R. Torres, and A. Welsch.

## State of the Field and Promise for the Future

Particle accelerators are widely used tools for industry, medicine, and science. Today there are around 30,000 particle accelerators in use worldwide, all relying on long-proven and highly developed methods for particle acceleration based on metallic radiofrequency (RF) devices [8]. The possible energy of particles, however, is often limited by practical boundaries on size and cost, for example the available space in hospitals, the available university funding for accelerator-based light sources, or the cost society as a whole can afford for science projects at the energy frontier. In past years, novel acceleration methods with plasma-based structures have demonstrated the acceleration of charged particles in a length reduced by a factor 100–1000. A recent success at Berkeley in the United States, for example, showed an electron beam being accelerated over a distance of 20 cm to 7.8 GeV with a 1 PW laser pulse [9]; in comparison, an RF-based machine requires several tens to hundreds of metres to reach this energy. Many accelerator applications exist at the energy range from 1 GeV to 8 GeV, which could benefit from more compact acceleration technologies. Moreover, the electron pulses from plasma accelerators are short (few femtoseconds), thus opening a groundbreaking route into novel applications for ultra-fast science.

The EuPRAXIA conceptual design study is relying on the impressive progress achieved at LBNL and other laboratories. EuPRAXIA is not aiming at advancing plasma acceleration towards higher beam energies. Instead, it investigates ways for achieving high-quality electron beams and for establishing attractive use cases. To accomplish these goals in a realistic, risk-mitigated manner, the project proposes to combine a mixture of novel concepts, proven phenomena, established technologies, and well-known, yet to be demonstrated solutions.

## Developments in Plasma-Accelerator Research

Plasma accelerators have developed in recent years as one of the most promising novel accelerator technologies capable of overcoming some of the limitations that conventional machines based on radiofrequency acceleration experience, such as limited accelerating field strengths from material breakdown effects and consequently large size and cost at high particle energies. By employing plasmas, i.e. ionised gas targets, instead of vacuum-filled metallic cavities as an accelerating medium, field gradients on the order of tens of gigavolts per metre – up to three orders of magnitude larger compared to RF-based technology – can be achieved. Consequently, plasma wakefield acceleration has the potential to significantly reduce acceleration distances and hence the dimensions and costs of future accelerator-based machines. Figure 1.4 highlights with examples from both RF accelerators and plasma acceleration experiments the order of magnitude of this reduction in acceleration length for various particle beam energies. At the same time, Figures 1.5 and 1.6 visualise the macroscopic and microscopic scales of a plasma-accelerator stage.

Although theoretically proposed already in the late 1970s by Tajima and Dawson [10], it was not until the early 21st century that plasma accelerators demonstrated the first promising experimental results as controllable high-energy electron sources [11–13]. Since then, a rapid development has been observed for both laser-driven (LWFA) and beam-driven (PWFA) plasma accelerators reaching, on the one hand, new energy records, while, on the other hand, significant milestones related to beam quality and applications were achieved. A recent version of the Livingston curve, for example, as shown in Figure 1.7, highlights well how this new technology approaches conventional accelerators in terms of energy still growing at an exponential rate.

Laser-driven plasma acceleration (LWFA) has been linked very closely with the development of laser technology over the last few decades, in particular the invention



**Fig. 1.3.** Participants in the EuroNNac and EuPRAXIA Workshop on a European Plasma Accelerator in Pisa, June 2016. This EuPRAXIA collaboration meeting was organised as a combined event with the European Network for Novel Accelerators EuroNNac [7].

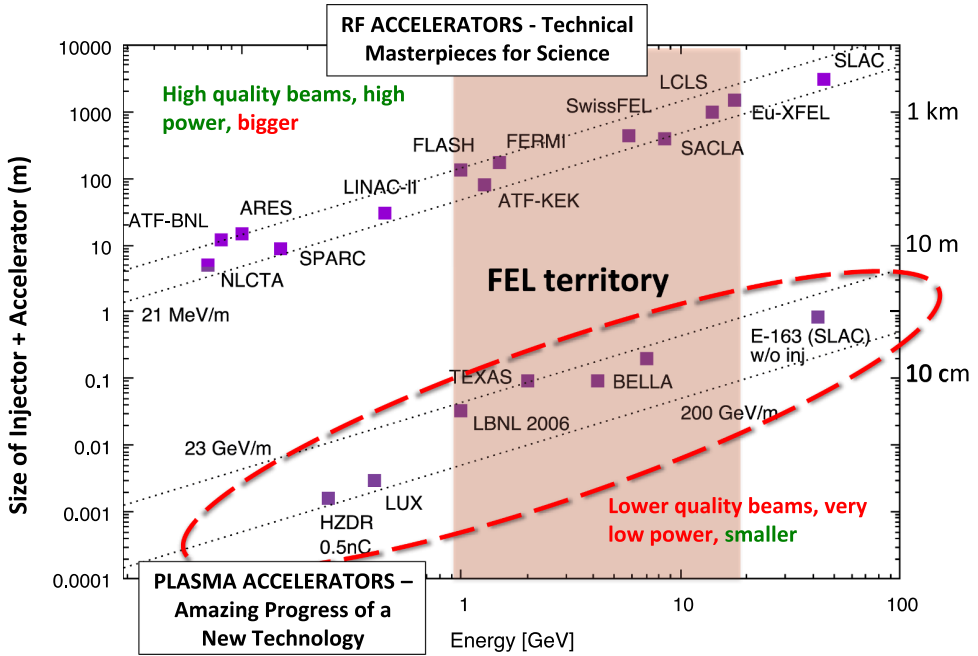


Fig. 1.4. Comparison of size and achievable electron beam energy for different existing radiofrequency and plasma accelerators. It becomes clear that a trade-off between machine size and beam quality at equivalent beam energies distinguished the two technologies to date (image credits: R. Assmann).

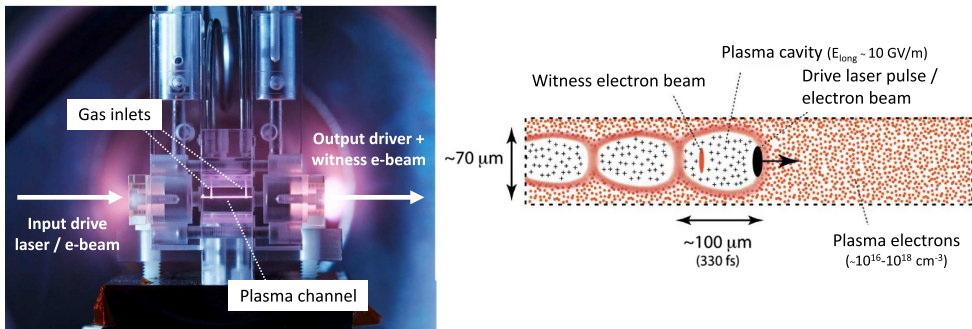


Fig. 1.5. Basic principle of a plasma accelerator. While the left image shows the macroscopic technical components, the schematic on the right highlights the physical process of plasma acceleration on a microscopic scale (image credits: DESY, H. Mueller-Elsner, R. Assmann).

of chirped pulse amplification in 1985 [14], a technique that Donna Strickland and Gérard Mourou received the Nobel Prize in Physics for in 2018 [5]. In LWFA, a short, high-power laser pulse drives the accelerating plasma wakefield, while electron beams can be brought to high energies in this field after injection into the accelerator either from an external source or through generation inside the plasma (self-injection). With the latter, the more prominent method used in experiments in the past, a multitude of different self-injection mechanisms has been developed and tested over the last decade ([15–20] and others), with new ideas and concepts created even today (e.g. [21–23]). Beyond the generally very compact setup, self-injection thus promises flexible options for creating electron beams with varying properties. For external



**Fig. 1.6.** Small, novel plasma accelerator compared to the FLASH accelerator at DESY (Germany) (image credits: DESY, H. Mueller-Elsner).

injection, on the other hand – a technique that is pursued for its improved control over the electron beam quality – theoretical and computational results also show great promise. Most experimental studies are still in preparation [24,25], with some first successful experiments studying beam capture efficiency and other major challenges [26].

Overall, research in LWFA has focused on a broad range of topics, as many small and larger institutes have worked relatively independently on their experimental setups or employed computational methods to study plasma acceleration. Major milestones thus include not only electron acceleration to a few GeV [9,27], but also successful experiments for high-charge beam acceleration [28] and the generation of short electron pulses in LWFA [29–31]. Over the last few years, research has also moved towards improving electron beam quality, one of the main challenges in plasma acceleration. In this context, for example, energy dechirping concepts to remove the typically large correlated energy spread have been developed [32–34], and techniques for preserving electron beam emittance throughout the plasma accelerator are being studied through plasma target shaping [35–37] and high-gradient focusing [38]. Improved diagnostics and plasma characterisation are further topics of interest with successful studies on measuring wakefields [39] and controlling plasma properties [40]. With a view towards reaching even higher beam energies, different concepts for staging multiple plasma accelerators [41,42] are also under development, including, for example, the study of new types of plasma targets that allow acceleration over long distances by keeping the drive laser focused [43,44].

In beam-driven plasma acceleration (PWFA), the community is generally smaller, with experimental infrastructures limited to a few major facilities, such as SLAC, SPARC\_LAB, FLASHForward, and CERN. PWFA uses a relativistic particle beam as a plasma wakefield driver, typically an electron beam from an RF accelerator. This technique comes with some advantages, such as longer possible accelerating distances and hence higher energy gains, but also disadvantages, including the generally very large and expensive experimental setups required. As energy records were achieved

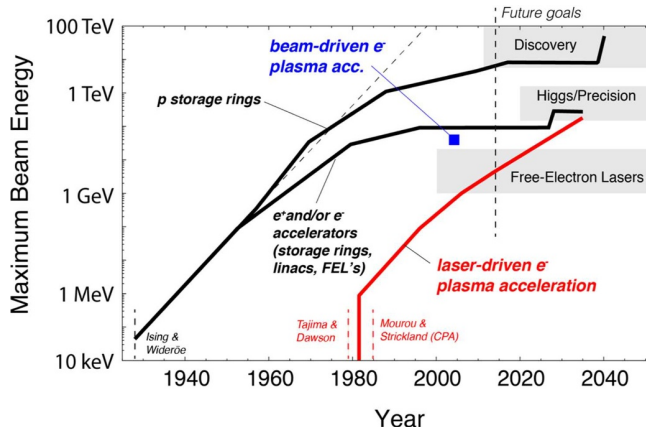


**Fig. 1.7.** Livingston curve for accelerators, showing the maximum reach in beam energy versus time. The grey bands visualise accelerator applications. The left fork shows the progress in conventional accelerators from the first ideas in the 1920s. This main fork splits into two lines for electron/positron machines and for proton accelerators. A new fork of laser-driven plasma accelerators emerged in 1980, reaching multi-GeV energies by now. Beam-driven plasma acceleration results are indicated by the square point. Data beyond 2014 (vertical dashed line) indicate goals for the various technologies (image credits: R. Assmann).

quite early on [45], efforts in recent years have focused experimentally on improving beam quality and controlling beam properties [46,47], in some cases with similar concepts as in LWFA, such as energy dechirping mechanisms [48]. Additionally, with particular promise for high energy physics, efforts have been placed on improving energy gains through improvements in transformer ratio [49]. With a similar goal in mind, other types of particles have been investigated as wakefield drivers, such as proton beams (AWAKE) [50] and even positron beams (both as drivers [51] and witness beams [52]). Finally, more unconventional solutions are also pursued, especially with regard to solving the issue of size and cost of PWFAs. One particular path has been hybrid acceleration, which uses an LWFA to generate a driver for a second PWA. In this context and more generally, recent years have looked at different possible internal injection mechanisms in PWA stages, such as density downramp injection, wakefield-induced ionisation injection [53,54], and Trojan horse injection [55].

As will be shown in the later parts of this report, the EuPRAXIA design brings together many of these developed techniques and combines them with new concepts targeted towards specific remaining issues. The wide range of institutes involved in the collaboration thus plays an essential role in providing the necessary expertise to apply these various developments in a comprehensive and application-driven context, moving from plasma accelerators as experiments towards plasma-based tools and user machines.

## Status of Flagship Free-Electron Laser Experiments

After the first demonstrations of undulator radiation generated by electron beams from a laser-plasma accelerator [56–59], demonstrating free-electron laser (FEL) amplification has become the next goal [60,61]. Theoretical studies [62–64] point out that while the high brightness of an LWFA beam comprises a significant advantage for FEL gain, the comparably high initial values of divergence and energy spread

that are typical for laser-plasma beams generated in the lab today, represent a major obstacle.

To address these issues, the community developed a twofold approach: in addition to the continuous efforts to improve the intrinsic quality of LWFA beams, new concepts have been developed to compensate the inferior characteristics of plasma-generated electron beams by re-distributing the electron phase space in the transport lines. These strategies include the stabilisation of the beam emittance and the spatial sorting of electrons by their energies and form the basis of the experimental projects of LWFA-based FELs currently under development.

Presently, several projects of LWFA-based FELs are either in the commissioning phase or have already started operation. In the framework of EuPRAXIA, the following collaborations are represented:

1. Collaboration of Synchrotron SOLEIL, Laboratoire d'Optique Appliquée (LOA), PhLAM of the University of Lille (all France), and the Weizmann Institute of Science (Israel).
2. Collaboration of the Center for Free-Electron Laser Science and University of Hamburg, Deutsches Elektronen-Synchrotron (both Germany), and ELI Beamlines (Czech Republic).
3. Collaboration of the Karlsruhe Institute of Technology, Helmholtz Institute Jena, and Friedrich-Schiller University in Jena (all Germany).

The experiment of Collaboration 1 is based at the *Salle Jaune* hall of LOA, where a 10-metre electron transport beamline, *COXINEL*, was designed and installed by SOLEIL. The laser-plasma accelerator uses the 60 TW, 800 nm, 30 fs Ti:Sapphire laser of LOA, and an additional laser beam of several mJ is provided to seed the FEL. The electron beam is handled by a series of permanent-magnet variable gradient quadrupoles designed for this experiment, followed by a decompressing magnetic chicane, electro-quadrupoles, and the 18 mm-period undulator U18 of SOLEIL. The chicane-based beam transport follows the strategy of the longitudinal sorting of the electrons by energy to enable FEL amplification for high beam energy spreads.

The UHH-DESY Collaboration 1 operates a dedicated laser-plasma accelerator beamline, *Lux*, driven by the *Angus* Ti:Sapphire laser system with a peak power of up to 200 TW. The beamline and the drive laser are fully integrated into the accelerator controls system available on the DESY campus. The laser beamline has been designed following the DESY machine vacuum standards. It is connectable to the conventional S-band linac machine *Regae*, and, for this, the interaction chamber is equipped with a dedicated differential pumping system for gas extraction, *Evoc*. The beam transport strategy is similar to the one of *COXINEL*, and it comprises several electro-quadrupoles, a decompressing magnetic chicane, and the 5 mm-period short cryogenic undulator *Frosty*.

The third project is developed by the KIT-FSU Collaboration 1 and is based at the 40 TW Jena laser facility *JETI-40*. The beamline is designed targeting an alternative strategy of beam energy-spread compensation. Here, a transverse gradient undulator (TGU) is used, where electron energies are sorted transversely via an achromat-like dogleg chicane. The TGU employed in the experiment is a 40-period superconducting iron-free undulator, fabricated with the coils of wounded Nb-Ti multifilament wires, and installed at the *JETI-40* facility inside a dedicated cryostat filled with liquid helium.

Both the *COXINEL* and *Lux* projects are now fully commissioned, and proper beam transport with first incoherent light was successfully demonstrated at these installations in 2017 [65,66]. At the present time, both projects are actively following scientific programs towards FEL amplification. The KIT-FSU project has, at the

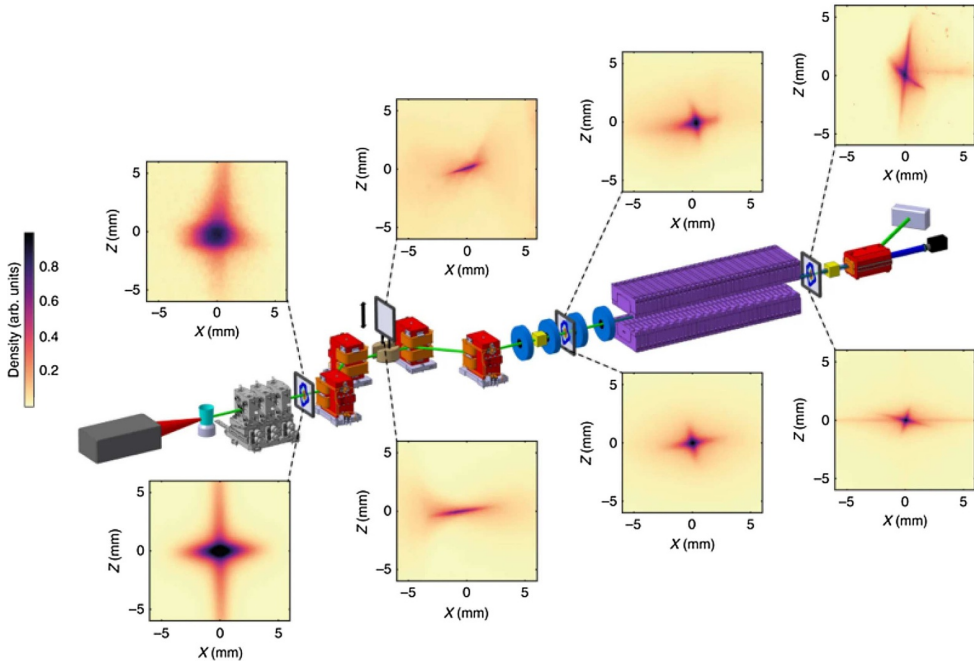


**Fig. 1.8.** Schematic of the COXINEL experiment, including, from left to right, the laser hutch (grey), gas jet (cyan), removable permanent magnet quadrupoles (grey), magnetic chicane (dipole magnet in red) with a slit (brown) inserted in the middle of the chicane, electromagnetic quadrupoles (blue), undulator (purple), cavity beam position monitors (yellow), dipole dump (red), beam dump (grey), and CCD camera (black). Also shown are the measured (top) and simulated (bottom) electron beam profiles at different positions along the line (image reproduced from [65]).

time of writing, successfully demonstrated LWFA beam transport, while the SCTGU device was thoroughly measured and tested at external facilities [67].

## Progress Towards Applications

Besides radiation generation using free-electron lasers, there exists a wide range of other applications typically implemented with the use of particle accelerators. First steps have been undertaken to apply the rapid progress in plasma acceleration to many of these, yet at the same time, new use cases have been identified for such a compact accelerator technology over the last few years.

One particular field of interest is the generation of a compact radiation source based on plasma acceleration, and different technologies have been studied in this context. Besides the use of undulators to generate synchrotron radiation from plasma-accelerated electron beams [56–59], a more compact method is based on betatron radiation. In the latter case, brilliant photon pulses are produced from the intrinsic transverse oscillations that electrons experience inside a plasma accelerator based on their strong radial focusing fields. The radiation properties are thus similar to synchrotron sources with photon energies in the keV range and a broad radiation bandwidth. Successful experiments have also shown that femtosecond-scale pulse duration and source sizes of a few micrometres are typical characteristics of these sources [69–73]. Betatron radiation has been demonstrated to be useful for tomographic and phase-contrast imaging [71,74,75]. Figure 1.9 depicts an example of such

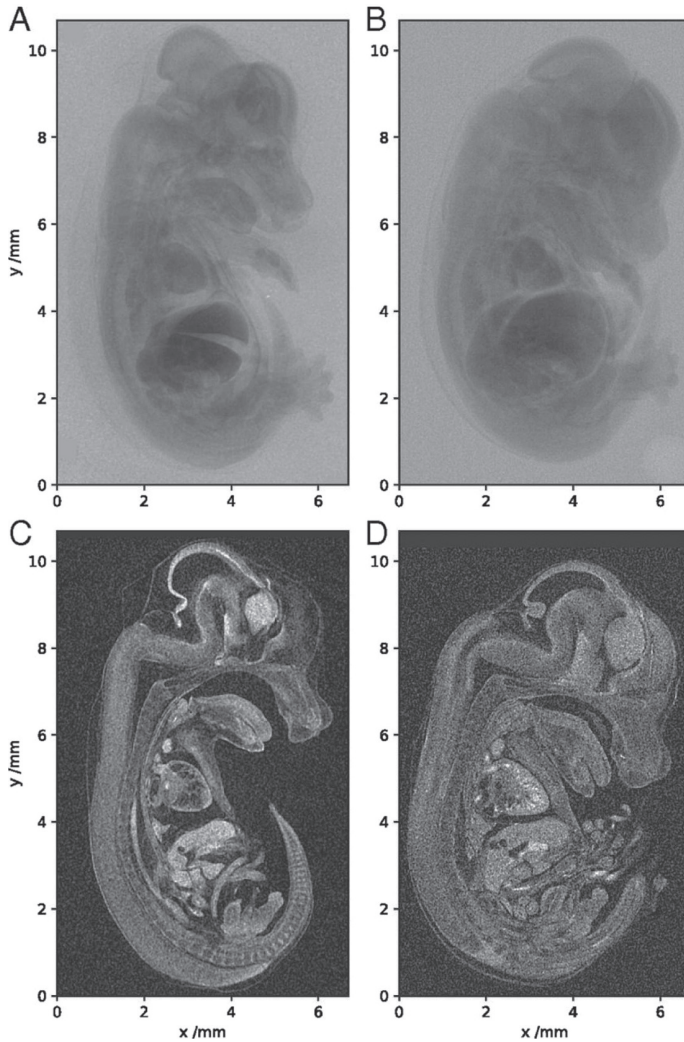


**Fig. 1.9.** Tomographic imaging of a mouse embryo carried out at the Gemini laser at the Science and Technology Facilities Council's (STFC) Rutherford Appleton Laboratory. Single X-ray projections (A and B) and sagittal slices from 3D reconstruction (C and D) are shown, with A and C acquired with a betatron source, and B and D measured with a commercial microfocus scanner (image reproduced from [68]).

an experiment, where a plasma-accelerator-based betatron source was shown to provide beam quality at least equivalent to commercial X-ray sources but with higher photon flux [68]. If such a source could be generated with a higher repetition rate than current plasma-accelerator experiments allow for, it would be extremely useful for fast and detailed medical imaging.

An additional kind of radiation generation that has been studied both theoretically and experimentally with plasma accelerators is inverse Compton or Thomson scattering. By scattering a laser pulse off an accelerated electron beam, this technique produces, depending on setup and laser / electron properties, photons with MeV energies and a quasi-monochromatic distribution [76–78]. With possible applications also in imaging, another interesting use case that has been investigated for this type of

source is the active interrogation of materials and nuclear characterisation [79]. In this context, plasma accelerators could bring possible future improvements to existing techniques thanks to their tunability and compact size.

In medical physics, plasma accelerators have been investigated for cancer treatment. While research in this field is still in the very early stages, using plasma-accelerated electron beams directly as both particle sources [80,81] and for the generation of X-rays is considered [82].

Finally, one of the potentially most promising application fields for compact accelerators is high-energy physics. With RF-based future collider designs reaching ever larger and more expensive scales, a plasma-based particle collider could mitigate these practical size and cost limitations. While a technical design of such a machine will still require considerable and long-term research efforts, first theoretical concepts have already been developed [83,84] and are complemented by many relevant accelerator-based R&D activities, such as plasma staging and multi-GeV acceleration experiments [41–43].

## Open vs. Closed Innovation

Although the term ‘open innovation’ has been originally developed in a business context, it has, in recent years, also found first applications in science [85,86]. A more general definition hence describes it as “open[ing] up the innovation process to all active players so that knowledge can circulate more freely and be transformed into products and services that create new markets” [85]. This stands in contrast to a closed innovation strategy, as traditionally followed by most companies, where the entire innovation and product development process is kept within the institution until a product’s release. All research & development (R&D), intellectual property, and technology is created only within the organisation and remains internal in such a system, at least partially as a historic consequence of the relatively little interaction between research institutions and companies in the past. Many of the arguments speaking for an open-innovation environment in a commercial setting are thus consequences of modern society; the increased mobility of highly educated people makes it hard to retain knowledge exclusively. Equally, the added availability of venture capital and similar concepts today allows to develop ideas and technologies outside of institutions through, for example, spin-offs or licensing agreements. Third, a stronger interconnectivity among institutions in a product or innovation process is required given the increasingly complicated systems and more global markets tackled by most companies [87].

All of these are also relevant topics in academic environments, however, where it is common for research staff to remain mobile throughout their career, for research to be carried out via collaborations of many institutions, and even schemes and programs designed to encourage knowledge exchange and the commercialisation of technologies are becoming more frequent (see, for example, [88] for initiatives in England in 2019/20). At the same time, knowledge-sharing practices are already being pushed strongly in research under the keyword of “open science”, with programs such as the European Open Science Cloud and European Data Infrastructure [89].

Driven by the ambition to act as a stepping stone for future compact accelerator technologies and applications available to new users and new locations, EuPRAXIA could thus provide an ideal platform to combine the more commercial and academic concepts of open innovation and science. As Figure 1.10 shows, there are two main levels of knowledge circulation foreseen within the EuPRAXIA infrastructure. In the first instance, a strong exchange of expertise within the community will be necessary based on the distributed infrastructure concept that EuPRAXIA foresees (more

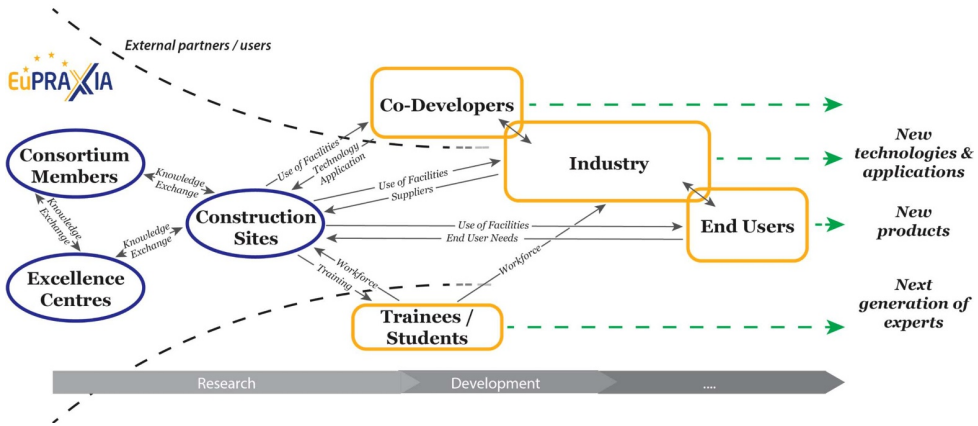


**Fig. 1.10.** Schematic demonstrating the possible integration of the concept of open innovation in the EuPRAXIA research infrastructure [90].

information in Chap. 3). Besides ensuring an optimised facility operation, this will be particularly beneficial for providing a means to reapply the technologies developed for the large-scale machines at EuPRAXIA directly back to the laboratory scale, thus advancing them in the direction of miniaturisation as a long-term goal. Second, the innovation process is opened up at EuPRAXIA further through the facility’s user access, as described in Section 5.4; by defining an access policy and providing an environment suitable for users from across the range of application development, it can provide a unique platform for these different groups to come together and exchange their knowledge, needs, and interests. Including trainees as future researchers, end users, and those working in the technology development stage between – here called co-developers – EuPRAXIA is able to act as a mediator not only providing a testing infrastructure for all but also indirectly helping to streamline the innovation process for plasma-accelerator technologies across all development stages. The long-term goals of the entire process lie directly in line with EuPRAXIA’s societal aims: to enable new technologies and applications, to support European industry in the development of new products, and to foster a new generation of experts.

**EuPRAXIA’s Role in Europe**

Europe is a strong player in accelerator science and especially novel accelerators, but much work in this topic is currently carried out by smaller institutes and universities working in their own laboratories and with their own individual resources. To make progress more efficiently and stay competitive worldwide, it is thus essential to bring the community together more strongly in a collaborative manner. The EuPRAXIA design study has been the first attempt in this direction, with much focus placed on comparing, combining, and optimising the various methods and technologies developed across the different project partners. A EuPRAXIA infrastructure would be the next step by providing a common platform for research with capabilities that are currently not available but are strongly needed for the development of the field.

While the next decade is expected to bring into operation several facilities with similar types of beamlines as EuPRAXIA – such as ELI Beamlines or the Extreme Photonics Applications Centre, recently funded in the UK – these infrastructures, foremost laser facilities in nature, will not be able to provide by themselves the same opportunities as a dedicated plasma-accelerator infrastructure, such as EuPRAXIA,

could. Focusing only partially on plasma acceleration and largely on laser-driven wakefield acceleration, there are significant differences in the scientific aims of these planned or developing facilities compared to EuPRAXIA to an extent that attempting to integrate the latter's goals into these other scientific programs would exceed their capabilities. At the same time, the areas of existing thematic overlap, such as plasma-based free-electron lasers and compact X-ray sources, are fields of significant user demand. For hard X-ray FELs in particular, operational facilities have shown a demand high enough to warrant more than one facility to push this concept, especially as there are expected to be variations in parameters and designs.

A possibly more important argument, however, is the unique synergy and potential for technological innovation that a dedicated common facility for plasma-accelerator technologies would provide. Through a design focused on various applications as well as varying techniques and methods, including both laser- and beam-driven plasma acceleration, a multitude of research avenues can be pursued in a very complementary manner. Setting up this design as a single yet geographically distributed infrastructure additionally provides a strong optimisation between cost-efficiency, which is much higher than for separate national facilities, and the use of existing infrastructures, which is much better than with a new single-site green-field structure. This last point is particularly essential in the design of EuPRAXIA as existing facilities with plasma-accelerator capabilities, such as ELI Beamlines and EPAC, but also smaller centres, such as CALA, SCAPA, and others, are all integrated into this infrastructure and thus allow a very effective exchange of knowledge and competencies beneficial to the development of the field as well as all partners.

Another aspect to consider is the potential future outlook of the project. EuPRAXIA is strongly focused on developing and providing tools for optimising applications, such as techniques for analytical sciences, which it shares with other infrastructures. However, simultaneously, it sets itself up to play a strong role as an intermediary step for future high-energy physics and plasma colliders by implementing important techniques such as external injection and staging, the integration of RF, laser and plasma technologies, and the possibilities for positron beam transport and acceleration experiments. While such milestones have or could be also achieved in smaller laboratories, their implementation in a user test facility opens entirely new perspectives with regard to stability, maintainability, and other operational challenges essential to high-energy accelerators.

Finally, concerning industry, EuPRAXIA will play an important role by guiding demand, thus pushing the European industry but also providing a platform to involve industry more strongly in novel accelerators.

## 2 Opportunities for Science and Innovation

### 2.1 Flagship Science and Innovation Goals

The EuPRAXIA Consortium has produced a conceptual design report of a new kind of European research infrastructure. During the proposed EuPRAXIA phases of technical design (TD), construction, and operation, the facility would achieve a number of important innovation and science goals. While overall ambitious, these aims and planned achievements are supported by the technical solutions presented in detail in the later chapters of this report. To reach the required beam quality for the proposed machine performance and application range, for example, new plasma injection and acceleration schemes have been developed (such as the Resonant Multi-Pulse Ionisation Injection scheme, described in Chap. 23), existing schemes have been improved (e.g. ionisation-induced injection in tailored density

profiles, described in Chap. 13) and experimentally validated (e.g. hybrid acceleration schemes, described in Chap. 26), new dechirping and synchronisation concepts have been defined (described in Chaps. 15 and 23) and a laser system has been designed that not only advances main output parameters, but also incorporates high precision and stability (as described in Chap. 10). This is complemented by design approaches for the electron diagnostics (see Chap. 21) and beam transport systems (see Chap. 19) as other examples, which balance stable performance from well-known technologies with novel, more compact-sized solutions.

Building on these results in a step-wise approach with predicted intermediate milestones, it is foreseen that the innovation goals will be mainly reached during the technical design and construction phases, realising the improved technical components and building up the innovative new concepts and layouts that have been developed for this project. The innovation goals of EuPRAXIA have been defined with the consortium and interested European industry. The completed facility will then, during the operational phase, allow the achievement of science goals that will be pursued with both external and internal users from the European research community.

While the final realisation and exact process of implementation of the proposed EuPRAXIA facility will eventually depend on the available funding and political landscape, the following sections list the most important “flagship” goals foreseen for the project.

### 2.1.1 Flagship Innovation Goals

**Flagship Innovation Goal 1:** EuPRAXIA will develop the first beam-driven and laser-driven plasma-based accelerator facility. Accelerator know-how and methods are used for the design and construction of plasma accelerators. Sufficient investment, especially in laser technology, is provided such that the required new technical developments are performed and the plasma acceleration concept is developed into a usable accelerator technology.

**Flagship Innovation Goal 2:** EuPRAXIA will develop, together with the laser industry, a new generation of high peak-power lasers, advancing the presently leading technology into the regime of 20–100 Hz repetition rates for 100-Joule-class lasers and pulse durations of 50 femtoseconds. The extended repetition rates advance the state of the art by an order of magnitude and will be used for improved feedbacks for higher pulse-to-pulse stability.

**Flagship Innovation Goal 3:** EuPRAXIA will further develop, together with the European Organisation for Nuclear Research (CERN), RF technology at the X-band frequency (12 GHz) and will construct the world’s first 1 GeV X band linear accelerator, demonstrating the most compact electron linac to date, with an average accelerating gradient of 80 MV/m. This linac would be 30% shorter than available today for the same energy.

**Flagship Innovation Goal 4:** EuPRAXIA will construct the required technical schemes for achieving a much-improved quality of the electron beam from a plasma accelerator, leading to a 10-fold increase in the 6D phase space density at best. Predicted performances include 30 pC of charge at 5 GeV beam energy, sub-micron transverse emittances, and an energy spread of below 1% to 0.2% (total) and below 0.1% to 0.03% (for a short slice of the beam).

**Flagship Innovation Goal 5:** EuPRAXIA will demonstrate a factor 7 reduction in the total size for a 5 GeV electron beam facility without a subsequent user beamline. If the FEL undulator and user beamlines are included, the EuPRAXIA facility aims at demonstrating a factor 3 reduction in total size.

**Flagship Innovation Goal 6:** EuPRAXIA will establish a distribution scheme that optimises science return versus investment, minimising the number of expensive items (e.g. lasers, RF electron beams) while distributing less expensive items (e.g. plasma beam/radiation sources). The facility therefore combines the capabilities of relatively high-cost lasers (final pulses easily distributed to various close-by sites), of relatively low-cost plasma sources (up to GeV beams produced locally at end of laser beamlines) and of high-energy electron beams (drivers for plasmas, FEL generation of hard X-rays).

**Flagship Innovation Goal 7:** EuPRAXIA will establish a continuous mode of beam operation for the internal and external users over at least one week (24/7 operating mode) before a maintenance day may occur.

**Flagship Innovation Goal 8:** During its operational phase, EuPRAXIA will perform continuous innovation work to further reduce drastically the total facility footprint required for plasma-based user sources. The aim is to advance the reduction from a factor 6 to a factor 10 and beyond for the accelerator. This will involve, for example, innovative undulator technology, novel beam transfer and diagnostics schemes, and reduced-size optical elements.

**Flagship Innovation Goal 9:** During its operational phase EuPRAXIA will perform continuous innovation work to research and adopt novel laser technology that delivers high peak-power laser pulses at improved efficiency and a higher repetition rate, reaching into the kHz regime.

### 2.1.2 Flagship Science Goals

**Flagship Science Goal 1:** EuPRAXIA will deliver free-electron laser (FEL) X-rays with  $10^9 - 10^{13}$  photons per pulse to user areas, covering wavelengths of 0.2 nm to 36 nm. The EuPRAXIA FEL pulses are naturally short (down to 0.4 fs) and will therefore provide users with tools for investigating processes and structures in ultra-fast photon science at a reduced facility footprint.

**Flagship Science Goal 2:** EuPRAXIA will deliver betatron X-rays with about  $10^{10}$  photons per pulse, up to 100 Hz repetition rate, and an energy of 5–18 keV to users from the medical area. The much-reduced longitudinal length of the X-ray emission area (point-like emission) leads to an important improvement in image resolution compared to other techniques.

**Flagship Science Goal 3:** EuPRAXIA will deliver positron beams at energies from 0.5 MeV to 10 MeV and a repetition rate of 100 Hz for material science studies. Per pulse, about  $10^6$  positrons will be produced in a duration of 20–90 picoseconds on the sample, allowing time-resolved studies. Here, EuPRAXIA will advance the capabilities of existing positron sources in flux and time resolution.

**Flagship Science Goal 4:** EuPRAXIA will deliver electron and positron beams at energies from a few 100 MeV up to 5 GeV for high-energy-physics-related R&D (detectors, linear collider topics). R&D goals include the demonstration of a linear collider stage, a “tabletop” HEP test beam, and studies on positron transport and acceleration towards a linear collider.

**Flagship Science Goal 5:** EuPRAXIA will deliver photons from an inverse Compton scattering (ICS) source. The photons of up to 600 MeV and with a narrow-band spectrum will enable precision nuclear physics and highly penetrative radiography for users.

**Flagship Science Goal 6:** EuPRAXIA will provide access to a multi-stage high-repetition-rate plasma accelerator in the GeV range to users from accelerator science. This R&D platform will allow the testing of novel ideas and concepts, the

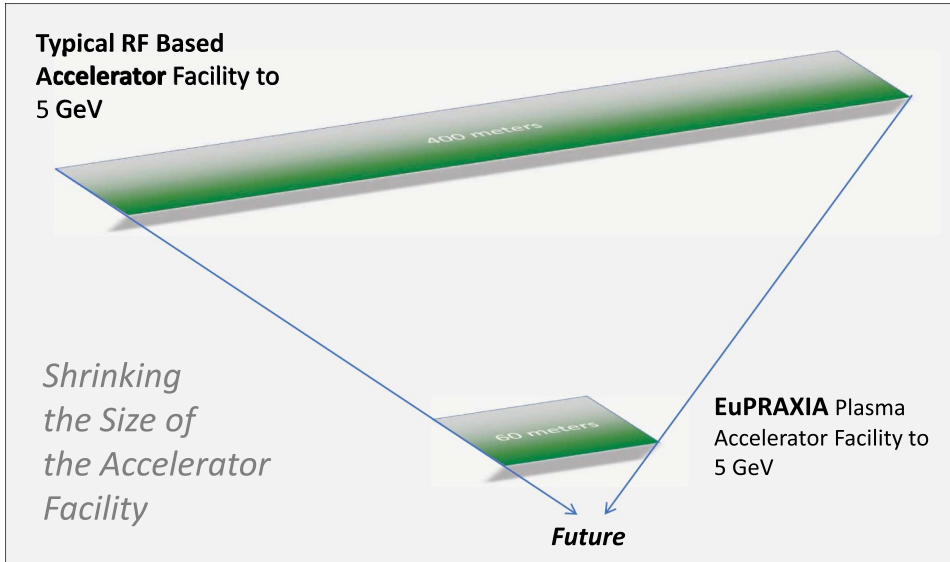


**Fig. 2.1.** The length of a typical RF-based accelerator facility with 5 GeV electron beams (C-band technology including injectors) is compared to the length of the EuPRAXIA 5 GeV design (including injectors). It is noted that undulator sections, target areas, and user areas are not included. Therefore, the miniaturisation factor of EuPRAXIA for the full facility is significantly lower than the factor 6–7 shown here. In EuPRAXIA, we aim at a factor 3 improvement in total facility length.

full optimisation of a plasma collider stage, certain fixed target experiments (also in combination with lasers), and performance studies of conventional versus novel accelerator technology.

**Flagship Science Goal 7:** EuPRAXIA will provide access to cutting-edge laser technology with short pulse length in combination with high-energy photon pulses and short electron/positron bunches. Novel schemes of pump probe configurations and ultra-precise timing will be researched, feeding back into laser science.

### 2.1.3 Unique Selling Points of EuPRAXIA

EuPRAXIA will, as a facility, be the first of its kind. It offers a number of unique selling points.

The technologies of plasma accelerators, electron beams, and high-power lasers enable some unique features and advantages that the EuPRAXIA infrastructure aims to realise:

**Demonstrating a compact facility design in a realistic stepwise approach:** EuPRAXIA exploits plasma, electron beam, and laser technologies to increase accelerating fields by two to three orders of magnitude. While accelerating lengths are reduced by this factor, the total footprint of an accelerator facility includes all the required infrastructure (laser room, shielding, etc.) and user facilities. A “tabletop accelerator” then quickly becomes a large setup with reduced benefits in size, if any. EuPRAXIA is based on a large-scale infrastructure design but reduced in size over conventional technology by a factor of 3 at least. It therefore pushes one of the biggest strengths of plasma-accelerator technology in a realistic stepwise approach, as Figure 2.1 highlights schematically. Once a factor-3 reduction in facility size has

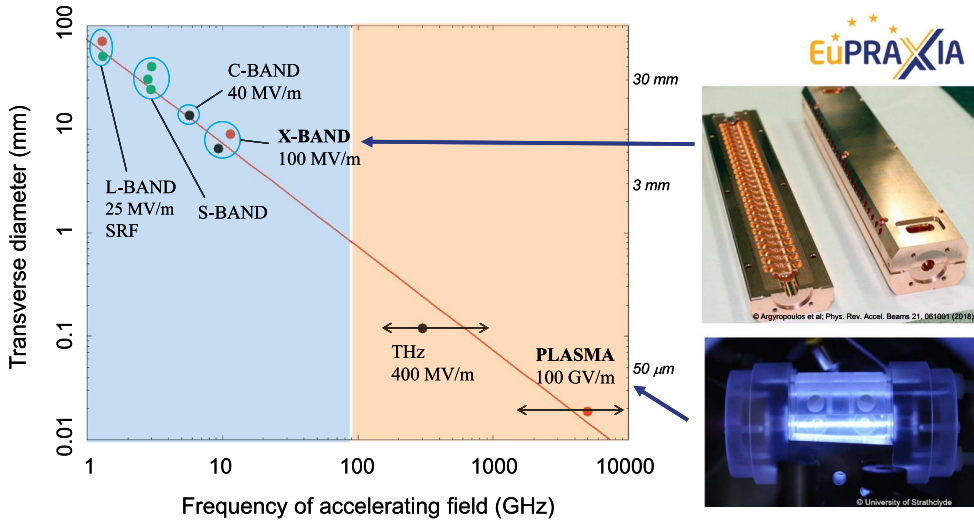


**Fig. 2.2.** Size, frequency, and field strength comparison of different types of RF cavities. It can be seen that both the X-band and plasma technology proposed for EuPRAXIA offer not only smaller structure size but also a higher accelerating gradient, leading to an overall small accelerator for similar energy gain (image credits: the University of Strathclyde and [91]).

been demonstrated, a miniaturisation process towards even more compact designs will be pursued inside EuPRAXIA. A reduction factor of 10 and even 20 for the accelerator itself seems feasible at high beam energy.

**Advancing compact, high-average-power, high-repetition-rate technologies for driving plasma wakefields:** EuPRAXIA includes both high-power lasers and RF technology in the X-band range as drivers (power sources) for exciting the plasma wakefields required for particle acceleration. For high-power lasers, a baseline with development paths has been defined, advancing repetition rates for petawatt-class lasers from 5 Hz today over 20 Hz to 100 Hz and ultimately even into the kHz regime (see Fig. 2.3). In parallel, critical performance parameters will be advanced, for example in terms of shot-to-shot stability and laser pulse quality. EuPRAXIA will pursue work with the laser industry in bringing this key technology to maturity and to the required level for next-generation plasma-accelerator systems. X-band RF technology will be developed with CERN as it is presently the most compact RF technology available for creating high-energy and high-power electron beams, as visualised in Figure 2.2.

**Developing compact user application capabilities of plasma-accelerator systems:** EuPRAXIA will develop user application capabilities of plasma-accelerator systems, including through the parallelisation of user lines, the generation of secondary particle and photon sources, and synchronised pump-probe capabilities. Laser-driven plasma accelerators offer unique possibilities for the parallelisation of user applications: the large laser infrastructure can be centrally located and laser pulses be distributed over 360 degrees into the small-size plasma accelerators and downstream user areas. The scheme of a circular synchrotron light source with dozens of user beamlines could effectively be miniaturised. This is illustrated in Figure 2.4.

**Advancing plasma-accelerator performance:** EuPRAXIA will advance plasma accelerators towards high beam quality, approaching that of conventional accelerators, so that they could then become suitable for existing accelerator applications and open up new application paths. Several novel ideas and concepts are described

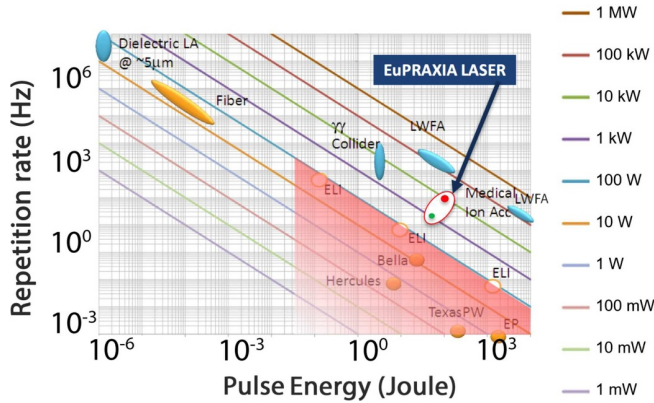


**Fig. 2.3.** Comparison of different lasers and applications in terms of stored energy in a single laser pulse and repetition rate of the laser. The orange dots and areas indicate existing lasers, the blue areas targets for various applications. The red / green dots and the white circle indicate the design goals for EuPRAXIA (reprinted from [92] with the permission of Elsevier).

in the technical part of this CDR. The simulated progress in energy spread with EuPRAXIA is shown in Figure 2.5. It is seen that the EuPRAXIA conceptual design report describes a novel recipe on how to gain a factor 10 in performance and how to approach the beam quality in RF-based free-electron lasers. EuPRAXIA thus presents a design complementary with current FEL facilities – enabling additional sites with reduced peak brightness but compact size, the goal of improved cost efficiency, and promising development opportunities. The approach is also complementary with future collider projects for particle physics – facilitating research into novel, compact collider concepts with adequate beam quality.

**Increasing science performance reach with unique plasma-accelerator features:** Plasma acceleration and the related processes, like betatron radiation, happen necessarily in a small plasma volume given by basic physics processes. The length of the plasma accelerator ranges from a few tens of micrometres (the diameter of a human hair) to a few hundreds of micrometres. Electron beams from plasma accelerators are therefore necessarily short and have pulse durations in the few femtoseconds regime. As such, they are unique tools for investigating processes in ultra-fast science, with additional benefits from pump-probe capabilities enabled by the synchronised EuPRAXIA lasers. Considering betatron radiation in the plasma volume, important gains in resolution can be obtained because of the much more localised emission of X-rays.

**Developing a staging solution and positron sources for high-energy physics:** The EuPRAXIA concept relies in many aspects on plasma-accelerator stages. EuPRAXIA will therefore demonstrate the critical features of coupling in and out of a plasma in the presence of a drive pulse. Of particular importance in this context is the beam-driven construction site of EuPRAXIA, where a compact electron beam driver will power plasma-accelerator stages. At this site also, positron beam generation and acceleration methods will be pioneered and developed. EuPRAXIA will thus construct an essential stepping stone towards high-energy plasma-accelerator applications.

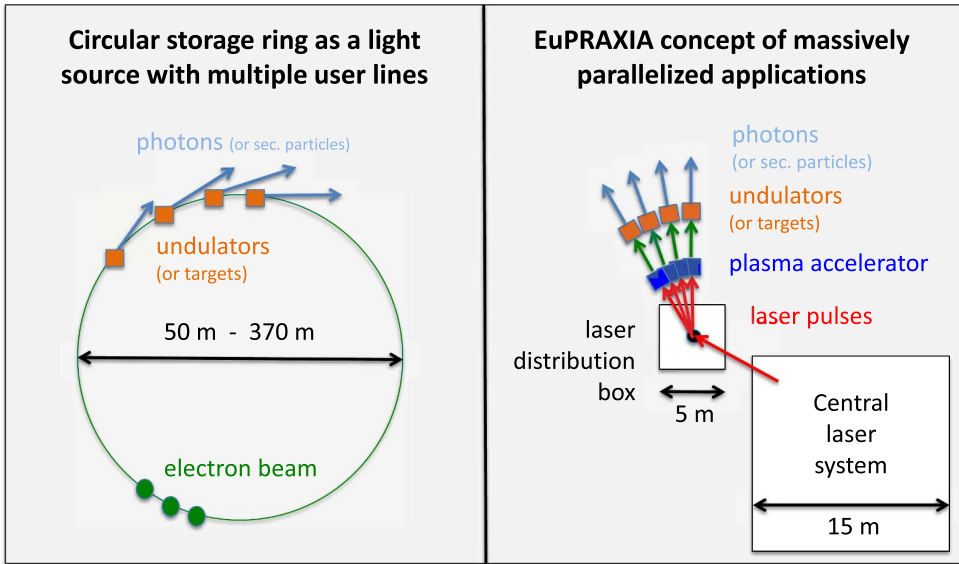


**Fig. 2.4.** Comparison of user concepts in (left) light sources relying on electron storage rings (without injectors) and in (right) the EuPRAXIA laser-driven plasma-accelerator concept. While on the left, the electron beam distribution requires a storage ring of large size, the EuPRAXIA laser distribution can be much more compact, with electrons, photons, and secondary particles being generated with highly compact plasma accelerators locally. The EuPRAXIA concept foresees conventional undulators but could work much more beautifully also with compact undulators that are being developed in the field. The parallel scheme will profit from high-repetition-rate lasers as many lines could be supported by the same laser. EuPRAXIA implements the first basic demonstration of this scheme with up to three beamlines in parallel.

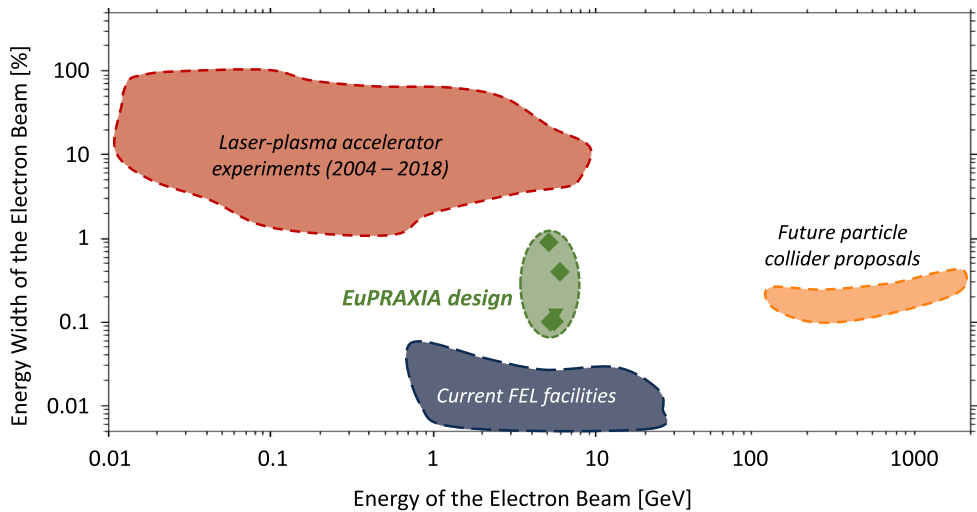


**Fig. 2.5.** Summary of the electron beam energy and relative energy spread for the different EuPRAXIA schemes (from start-to-end simulations). For comparison, the values from typical plasma-accelerator experiments, operational RF-based FEL facilities, as well as proposed future particle collider projects (CLIC, ILC) are also shown.

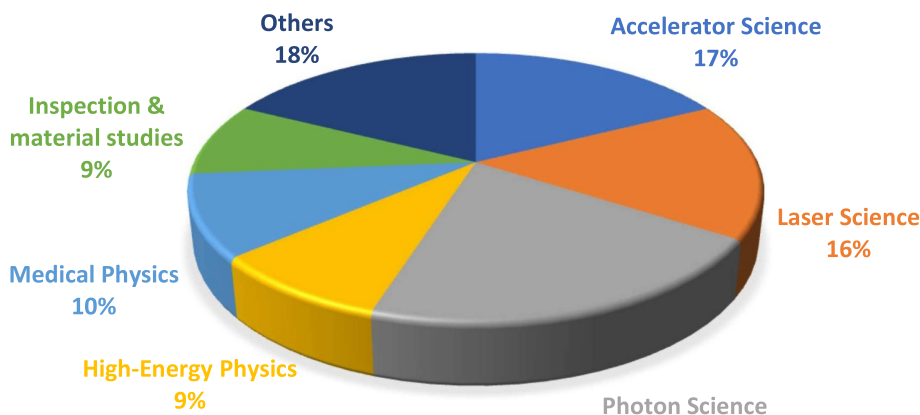


**Fig. 2.6.** Scientific fields for which the EuPRAXIA research infrastructure would be interesting based on an initial survey of potential future EuPRAXIA users. The answers listed under “Others” are shown in Figure 2.7 in further detail.

## 2.2 The Needs of External Users from the Academic Environment

An important aspect in the design of a new research infrastructure is the study of potential user communities to be able to match future user needs and interests with what the planned facility will offer in terms of experimental capabilities and capacity. This section of the CDR presents a qualitative analysis of potential application fields and their current status for EuPRAXIA. It will be complemented by a full quantitative user demand analysis in the future.

### 2.2.1 Summary of User Needs and Possibilities

The EuPRAXIA facility design, as proposed in this report, offers opportunities for a variety of different applications. Scientific fields where EuPRAXIA would be relevant include, in particular, accelerator and laser science, high-energy physics, material processing and analysis, photon science, as well as medicine and life sciences. In most of these areas, accelerators already play an important role; nonetheless, as the following sub-sections will demonstrate, EuPRAXIA aims not only to improve existing capabilities for users but also to open opportunities for new accelerator uses as part of these research directions.

Figure 2.6 demonstrates the significance of the topics above very well based on an initial survey of research groups interested in a future EuPRAXIA infrastructure. All of the fields listed are supported by at least 9% of survey participants. In Figure 2.7, the breadth of relevant subjects is further highlighted by the set of the most common keywords from the survey’s responses given for “other” scientific fields; these range from “Laser Technology” and “Plasma Physics” to “Nanomaterials” and “Molecular Science”, among others. Finally, Figure 2.8 shows that such a new facility as EuPRAXIA could be useful for a diverse set of activities with potential users interested in fundamental research as well as more applied studies and simple test experiments. Thirty groups with a total of more than 1,000 researchers were involved in the survey, demonstrating a clear interest in the European research community for a new facility, such as EuPRAXIA proposes. A larger scale inquiry and discussion with potential users is foreseen during the project’s technical design phase to back up this initial analysis and ensure an optimal agreement between user needs and EuPRAXIA’s facility design.



2. **Machine availability:** The proposed EuPRAXIA research infrastructure may improve the overall availability of certain types of beams and user services. An example for this lies in hard X-ray free-electron laser science, where user beam time is extremely competitive. The future EuPRAXIA facility would not only increase the capacity for FEL experiments but also build a roadmap towards future compact and cost-efficient FEL beamlines.
3. **New features:** The proposed EuPRAXIA research infrastructure may provide machine features and beam properties different from existing facilities. The use of plasma-accelerator technology at EuPRAXIA leads to a series of unique characteristics, such as ultra-short particle and photon beam durations, small beam spot sizes, a small machine footprint, as well as multi-species sources. These could be used, for example, for improved performance in imaging experiments but would also be relevant for the testing of advanced detector systems, both in accelerator science and high-energy physics.

Beyond these well-defined flagship application fields, EuPRAXIA aims to remain open to other types of user experiments. With plasma acceleration as a relatively novel and tunable technology, it can be envisioned easily that entirely new application areas may develop over time, once the facility has come into operation and gained experience with first users.

EuPRAXIA users could come from a range of application fields. They would benefit from improved machine performance, better machine availability, or unique beam properties compared to existing facilities.

### 2.2.2 Accelerator Science

Particle accelerators have been developed and optimised over multiple decades, creating a variety of machine types, components, and technologies, from RF accelerators to novel acceleration schemes, such as plasma and dielectric acceleration (e.g. [93,94]). While, as such, it is a highly developed field, there are still many groups worldwide that investigate and develop new concepts and methods within accelerator science.

Some of these studies, especially on a smaller scale, can be performed at local facilities. For other, especially more complex experiments, however, dedicated accelerator test facilities are required, of which there are a handful in operation currently, as Table 2.1 shows. The parameter overview in the table shows well the variety of available test beams, as is necessary considering the diversity of accelerator-based systems and machines. However, at the same time, it demonstrates clearly that until now, there is a lack of machines producing ultra-short electron beams, a feature that is becoming more and more useful for light-source-related and novel acceleration technologies, for example. This shortage is partially covered by some of the facilities due to come online in the next years, such as the HELL beamline at ELI Beamlines [95], FACET-II [96,97], and SINBAD (with the ARES linac) [98]. EuPRAXIA will thus be another addition to this group of test machines with ultra-short beams, however, bringing further beam properties of interest with it, such as, among others, an increased repetition rate on the scale of 100 Hz (with a possible upgrade to kHz in the long run). For plasma accelerators in particular, this will represent a new regime, thus opening up multiple new research opportunities.

More generally, the EuPRAXIA infrastructure is designed to implement many different techniques and components into one machine, including plasma injectors with different beam energies, multiple staged plasma targets, RF injectors for external injection into a plasma, as well as advanced beam transport lines and diagnostics sections. This makes it uniquely suited for accelerator science experiments, especially

**Table 2.1.** Summary of the electron beam properties of several accelerator test facilities currently in operation or under development. To provide a reasonable comparison with the performance proposed for EuPRAXIA, only infrastructures with beam energies of at least 100 MeV and allowing external users for experiments are considered.

	E [GeV]	$\Delta E/E$ [%]	Q [pC]	$\sigma_\tau$ [fs]	$\varepsilon_n$ [mm mrad]	f [Hz]
<b>Operational</b>						
FLASH Forward [99]	0.4–1.25		50–800	50–6,000	1–3	$4 \times 10^4$ – $3 \times 10^6$
SPARC LAB [100]	0.03–0.15	0.1–0.2	20–1,000	$1 \times 10^4$ – $2 \times 10^4$	1–5	10
CLEAR (CERN) [101]	0.06–0.22	<0.2	10–500	$1.67 \times 10^3$ – $8 \times 10^3$	3–20	1–25
<b>Planned / under development / commissioning</b>						
FACET II [96,97]	10	0.4–1.8	500–3,000	3.3–333		1–30
SINBAD-ARES [98]	0.1		0.5–200	0.8–10	<0.5	50
ELI-Beamlines (HELL) [95]	0.1–5	0.1–10	$10$ – $1 \times 10^5$	1–10		10
EuPRAXIA	0.1–5.9	0.1–4	20–100	0.8–12	0.1–1.5	20–100

for topics related to novel accelerator technologies. Plasma acceleration would likely be the largest user community with, for example, possible proof-of-principle experiments on new plasma injection / acceleration concepts, the prototyping or stability testing of plasma targets and components, as well as R&D into specific accelerator setups. While other sites, especially high-power laser infrastructures, exist in Europe and worldwide where plasma-accelerator studies can be carried out, EuPRAXIA will be, at least in its beginning, the only dedicated plasma-accelerator user facility. This means that, on the one hand, the machine and its properties are all designed specifically for the user operation of plasma accelerators, with very well-characterised beams and components as well as unprecedented system stability. On the other hand, the machine also already includes multiple dedicated and stable plasma-accelerator stages; thus, the acceleration process and generation of electrons, unlike in other facilities, does not have to be part of the experiment, and instead, the experimental focus can be placed on more specific challenges.

There are, however, also other topics in accelerator science that could benefit from a facility such as EuPRAXIA. The development and testing of novel diagnostics, for example, is one such case. The tunability in beam parameters, the availability of various photon and particle beam types, and the overall single-femtosecond duration of these pulses are unique and, as such, will allow for a multitude of varied experiments. Similarly, other types of beamline elements and beam transport concepts could be investigated. Compact accelerator applications in high-energy physics, for example, are discussed as a particular topic of interest [83,84], which will require considerable R&D on the transport and manipulation of beams from such machines. EuPRAXIA would be well suited for these activities.

### 2.2.3 Laser Science

The request for sufficient average particle or photon flux for the envisioned applications of EuPRAXIA will require a rather high repetition rate for the EuPRAXIA laser systems on the order of 20 to 100 Hz. This means that, as a matter of fact, the EuPRAXIA lasers will feature, besides very high peak power, an unprecedented average power. These features pose interesting challenges and, at the same time, will make EuPRAXIA a unique platform for testing novel concepts in the field of ultra-short and ultra-intense laser science.

Research aimed at increasing the average power of ultra-intense lasers, in particular, would greatly benefit from the design and construction of the facility. As it is

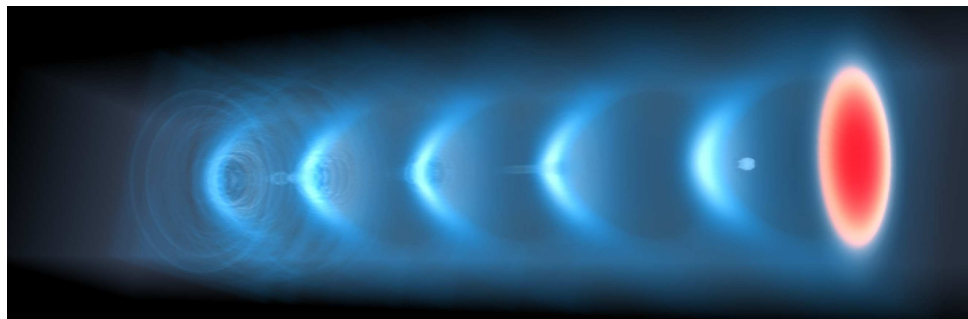


**Fig. 2.9.** 3D visualisation of a plasma wave (blue) excited by a high-intensity laser pulse (red) and accelerating an electron beam generated with the VisualPIC code [102]. There is much potential for exploring new concepts and technologies in both plasma acceleration and RF accelerators as well as the combination of these two (image credits: A. Ferran Pousa, DESY / University of Hamburg).

well known, this is a very active research field since increasing the repetition rate of ultra-short laser systems is seen as a crucial issue for translating laser-driven accelerator technologies to fields as diverse as medicine, material science, and so on, even on a smaller scale than the EuPRAXIA facility, thus allowing a widespread diffusion of advanced, possibly all-optical particle and secondary sources. In this respect, a major research topic is the thermal management in pump and main lasers amplifiers. Substantial improvements beyond the current state-of-the-art architectures are needed to increase the overall laser system efficiency and thus allow their repetition rate and average power to be increased (up to the multi-kW or more range). A lot of efforts are made already toward this goal – an example being the HAPLS laser system, as seen in Figure 2.10 – with several approaches, each at a different stage of maturity. The project would thus certainly give a strong boost to this research field.

Additionally, research related to the transition to diode pumping would benefit from the project. More in perspective, all novel approaches towards an ever-increasing efficiency – such as, for instance, direct pumping, multi-pulse extraction, and so on – would come into play. With this in mind, the possible transition from TiSa-based architectures to new laser materials is of strong interest for the laser community and could benefit significantly from developments at EuPRAXIA.

Besides the energy efficiency issue, other aspects related to thermal management in the laser chain are expected to become relevant for high average and peak-power lasers such as those foreseen for EuPRAXIA. These will require substantial efforts in laser science and technology. As an example, the research in the field of novel grating materials/coatings able to withstand the expected average power without introducing strong wavefront aberrations can be cited.

A rather peculiar aspect of the EuPRAXIA laser systems will be the constraints on their long-term operation; indeed, the combined requirements on the repetition rate and the system availability (uptime) will need new solutions for optical coatings with longer lifetime. Incidentally, the high degree of complexity of the optical architecture of the laser systems coupled with their required reliability in the long term will speed up the availability of advanced technological solutions for the automatic control, alignment, and maintenance procedures of ultra-short laser chains, which would benefit the entire laser community.

One of the critical issues for the EuPRAXIA laser systems given the usage of special target designs and the need for a stable and reliable operation of the beamlines

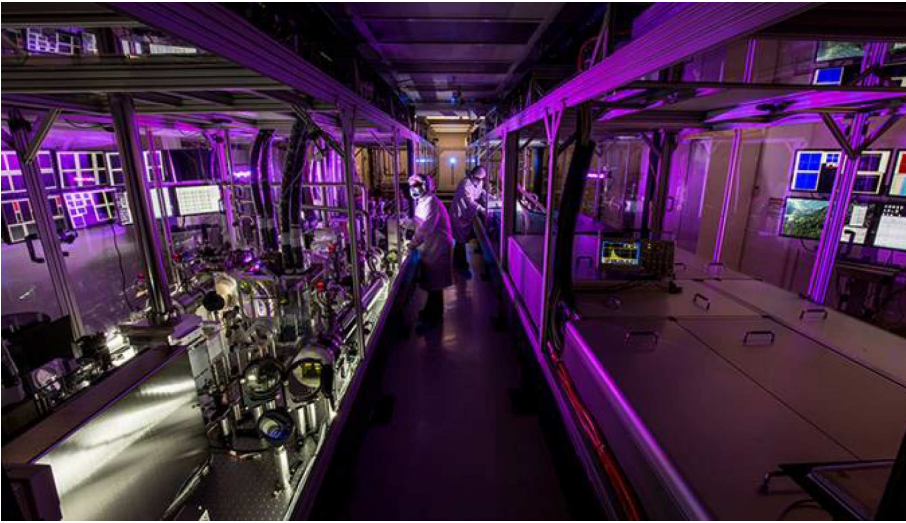


**Fig. 2.10.** HAPLS laser at Lawrence Livermore National Laboratory. Now installed at the ELI Beamlines facility, this laser system is among the current state of the art for petawatt-scale laser systems (image credits: Lawrence Livermore National Laboratory).

for the users will be the pointing stability. Besides already consolidated measures, the search for novel, possibly active techniques will be of interest for laser science.

Another very critical issue for the successful operation of the EuPRAXIA lasers will be the active correction of wavefront distortions, so as to allow a high Strehl ratio to be achieved. Research on both wavefront characterisation techniques and devices and feedback loop algorithms suitable for high-repetition-rate operations would be stimulated.

Finally, we mention here the role that the original design, construction, and further development of the EuPRAXIA lasers may play in the research field of longitudinal diagnostics for ultra-short and ultra-intense pulses. The development of both diagnostics for measuring spectral amplitude and phase as well as diagnostics for the characterisation of pulse contrast could benefit. This is true, in particular, in view of the need for single-shot diagnostics, as well as fast reconstruction algorithms to possibly provide a full shot-by-shot laser pulse characterisation for high-repetition-rate lasers in the future.

#### 2.2.4 Photon Science

The investigation of matter using short-wavelength light sources has benefited from recent developments with the advent of various VUV–X-ray sources. Among them, the X-ray laser [103] as well as high-order harmonic generation in gas (HHG) [104,105] reaching attosecond duration [106] or on solid targets [107] take advantage of the light emission properties of matter. Accelerator-based light sources [108–110] are also valuable tools in this respect.

Third-generation synchrotron light sources rely on synchrotron radiation generated from charged particles in bending magnets or undulators, creating a periodic permanent magnetic field. They are delivering high-brilliance photon beams with partial transverse coherence. These light sources, delivering beams simultaneously to various beamlines, are workhorses for matter investigation. They presently evolve towards low-emittance (picometer-scale) diffraction-limited light sources (DLSR) thanks to

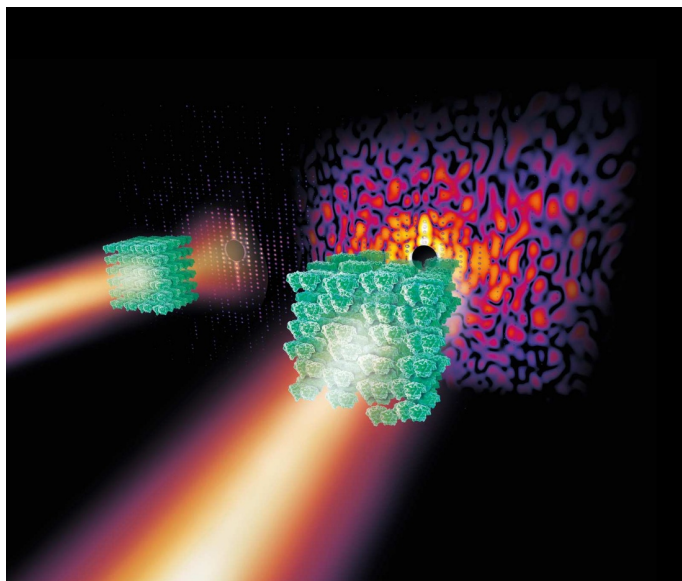


**Fig. 2.11.** Diffraction image of a complex biomolecule under high-intensity X-ray light (image credits: E. Reimann, DESY).

multibend achromat optics requiring high-gradient quadrupoles. The DLSR high brilliance and degree of transverse coherence set a new paradigm and give access to serial crystallography for drug discoveries (pharmaceutical industry) and to new techniques (imaging, spot scanning, small focal spot spectroscopies) for material development, addressing the 21st century societal challenges of health, environment, energy, information technology, and cultural heritage.

Longitudinal coherence, on the other hand, is achieved in free-electron lasers [111] by setting in phase the electrons thanks to an energy exchange between the electrons and a light wave (the spontaneous emission or an external seed), resulting in bunching, coherent emission, and light amplification. Several decades after the laser invention [112,113] and the first free-electron laser (FEL) [114], tuneable high-power X-ray lasers became a reality all over the world. FEL-based fourth-generation light sources presently offer femtosecond tuneable radiation in the X-ray [115–119] and in the VUV to soft X-ray [120–122] domains. These tuneable devices open the path for deciphering unexplored areas of matter and cells (such as protein structure and function) in a time-resolved way. An example of this is shown schematically in Figure 2.11. The League of European Accelerator-based Photon Sources (LEAPS), consisting of 19 research infrastructures in 10 states with 220 beamlines alone, has served more than 24,000 direct users during the last 5 years.

The recent advent of tuneable coherent X-ray FELs (XFELs) [123,124] opened a new era for the investigation of matter [125]. They enable us (1) to decrypt the structure of biomolecules and cells [126–128], (2) to provide novel insight into the electronic structure of atoms and molecules [129–132], and (3) to observe non-equilibrium nuclear motion, disordered media, and distorted crystal lattices thanks to progress in femtosecond spectroscopy [133] and pump-probe techniques [134]. Detailed structural dynamics can be inferred from spectroscopic signatures [135]. XFELs can also reveal movies of chemical reactions. With new imaging techniques [136,137], they are exceptional tools for the investigation of the ultra-fast evolution of the electronic

structure in atoms and provide a deeper insight into the extreme states of matter [138].

Another revolution in the field could now arrive with the emergence of laser-wakefield-accelerator-based free-electron lasers [60,61]. These could provide, on the one hand, compact “laboratory-scale” short-wavelength undulator radiation sources or, on the other hand, new FELs available for the user community. After the first observations of LWFA-based undulator radiation [56–59,63,65], ultra-short VUV to X-ray compact undulator sources can be seen as attractive for the user community [66,139]. Achieving a plasma-accelerator-based FEL is more demanding in terms of electron beam quality, especially in terms of divergence – requiring strong focusing with, for instance, variable permanent magnet quadrupoles [140] – and energy spread – with possible electron sorting with a magnetic chicane [62,141] or a transverse gradient undulator [64]. With the expected improvements of plasma-based electron beam quality, however, the realisation of plasma-accelerator-based FELs could become possible and open up exciting, new opportunities for the ultra-short photon science community.

### 2.2.5 High-Energy Physics

Currently, the largest operational particle collider worldwide is the Large Hadron Collider, a 27 km ring of superconducting magnets at CERN. At its best performance, it provides proton–proton collisions with a centre-of-mass energy of 13 TeV using detectors, such as the one seen in Figure 2.12 to measure the particle interactions occurring in the process. Before that, the Large Electron–Positron Collider (LEP) created electron–positron collisions with a maximum energy of 209 GeV. The Large Hadron Collider’s last most iconic result was the detection of the Higgs boson and the determination of its mass. This represented a brilliant confirmation of the Standard Model (SM) that, however, is known to be incomplete. It does not account for important aspects of fundamental physics observed in cosmology, including dark matter, dark energy, and the excess of matter over antimatter. Additionally, important features of the model, including the spectrum of quark and lepton masses and the presence of a phase transition that breaks its gauge symmetry, are put in by hand rather than being explained from physics principles [142]. To date, the extensive search for additional particles that would generalise the SM has been in vain, and there is a growing need in the community for the next generation of electron–positron colliders that would reach and eventually surpass the TeV barrier.

Conventional RF technology has intrinsic limitations on the maximum accelerating gradients that it can sustain, of the order of tens of MV/m. As an example, the proposed Compact Linear Collider (CLIC) is planning to reach 100 MV/m, implying an overall accelerating length to reach 1 TeV of 100 km. The sheer scale and, subsequently, cost of these machines have motivated the quest for alternative accelerating technologies. Arguably, plasma-based wakefield acceleration is one of the most promising, with landmark results already experimentally obtained for electrons. Accelerating fields of up to 100 GV/m have been demonstrated in a plasma [143]. Recent promising results in this area include, for instance, the demonstration of energy doubling of a 42 GeV electron beam in less than one metre of plasma [45], a 2 GeV energy gain of a positron beam in one metre of plasma [52], and the laser-driven acceleration of electrons up to 8 GeV in only 20 cm of plasma [9]. These promising results have motivated international large-scale projects to study the feasibility of building a plasma-based electron–positron collider. For instance, plasma-based particle acceleration for the next generation of colliders is included as a major area of investment in the Advanced Accelerator Development Strategy Report in the United

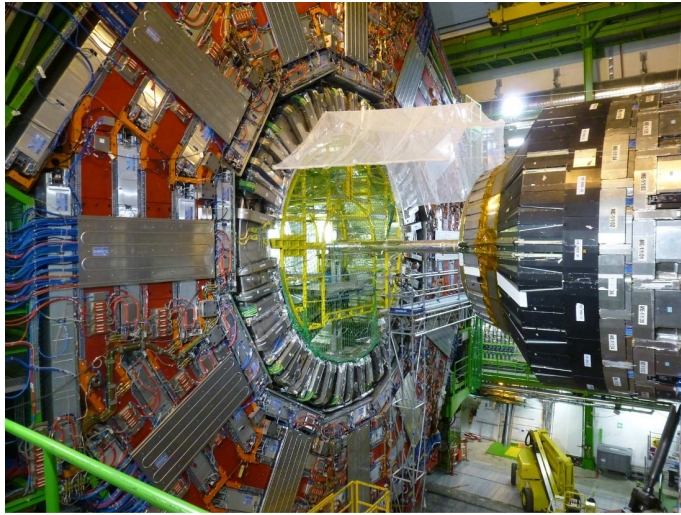


**Fig. 2.12.** CMS detector at the Large Hadron Collider (image credits: Luigi Selmi, CC-BY 2.0, <https://www.flickr.com/photos/susterru/14972545150>).

States [144], it is the main driver for the European consortium ALEGRO (Advanced Linear Collider Study Group) [142], and it is one of the main areas of development identified by the Plasma Wakefield Acceleration Steering Committee (PWASC) in the UK [145].

While the plasma-based acceleration of electrons is rapidly progressing, positron acceleration is far more difficult, mostly because of the intrinsic and strong asymmetry of the wakefields in the plasma. There are four main regimes that are currently being investigated: the quasi-linear regime, the non-linear regime, the hollow channel regime, and the wake-inversion regime. Whilst each regime has its unique advantages and attractive characteristics, any one of them presents significant challenges that must be overcome before reaching maturity. In general, it is challenging to provide a positron beam with sufficient quality to be synchronised with the positron-accelerating region of a plasma wakefield, and this makes experimental progress in this area slow. In particular, one would need low-emittance and short (less than tens of fs) beams with a non-negligible charge. To date, no positron facility suitable for advanced plasma-wakefield studies is available in Europe, and the only facility existing worldwide is FACET [146] in the United States, together with its proposed upgrade, FACET-II [147]. FACET-II is designed to provide a 10 GeV beam containing approximately 1 nC of charge with a transverse normalised emittance of  $20 \times 20$  mm mrad and a duration of 60–70 fs. Currently, the construction of a positron beamline in FACET-II is on hold, with the next stage of funding expected to start after 2021.

The capabilities proposed in the EuPRAXIA facility design, however, could help to close this gap in the international research landscape. The main positron parameters of FACET and FACET-II are shown in Table 2.2 together with beam properties conservatively achievable within EuPRAXIA [148]. Whilst, FACET-II is designed to provide a higher energy beam with a lower normalised emittance, EuPRAXIA will have the capability of providing fs-scale beams at a high repetition rate. The advantage of the design in EuPRAXIA is the absence of a damping ring that, even though it allows for particle storage and therefore a higher bunch charge, introduces a temporal broadening in the beam. The short duration of the beam, however, is of

**Table 2.2.** Main positron beam parameters obtainable in FACET and FACET-II compared with those achievable with EuPRAXIA. EuPRAXIA positron parameters are based on the wakefield accelerated electron beam proposed for the beam-driven site of EuPRAXIA (see details in Chap. 25.2.2).

Quantity	Units	FACET-I	FACET-II	EuPRAXIA
Energy	GeV	21	10	1
Rel. energy spread	%	1.5	0.7	5
Repetition rate	Hz	1	1	100
Average power	W	7.4	10	3
Beam charge	pC	350	1000	1
Transverse spot size in x and y	$\mu\text{m}$	30 x 30	16 x 16	20 x 20
Bunch duration	fs	50	20	>8
Transverse norm. emittance in x and y	mm mrad	200 x 50	20 x 20	500 x 500

critical importance for precision studies of wakefield acceleration for positrons and to ensure maximum energy extraction from the wakefield itself. Moreover, the proposed positron beamline will be the only one available in Europe and thus of fundamental importance for the progress towards the design of a novel TeV-scale particle accelerator, the primary goal of several high-level research projects in Europe, including the European consortium ALEGRO [142].

## 2.2.6 Medical Physics

Particle accelerators have widespread use in medical physics, from the low-energy (tens of MeV) linacs that are used to generate hard X-rays for radiotherapy, to the high-uptime cyclotrons used in the production of short-lived radioisotopes employed in both diagnosis (CT) and treatment.

There is a need for a role for high-precision high-energy electron accelerators for advances in medical physics too. Primarily, EuPRAXIA will be a relatively small-scale FEL that can provide X-ray radiation with unprecedented quality, which can be vital in determining biological pathways and in drug discovery. However, the overall EuPRAXIA facility has a number of other avenues in which it can be of interest to medical physics. Of these, two applications are considered of great interest at the moment: Very High Energy Electron Therapy (VHEET) and phase-contrast imaging (PCI). We expand briefly on some of these applications below.

### FEL Applications for Medical Physics

One of the major uses of X-ray sources lies in determining the structure of biological material at the atomic scale. However, the scattering efficiency of X-rays is low, and to be able to attain enough signal before causing excessive damage to the material, large regular crystals of the material need to be grown, hence the reason this field is usually referred to as *crystallography*. However, this limits the range of materials that can be investigated: some do not form large regular crystals, whilst others change significantly when crystallised as compared to their form when in use, usually in solution. X-ray diffraction with FELs overcomes the restriction on crystal size by allowing strong diffraction from small samples given the very large photon flux they produce. Furthermore, the short temporal duration of the source means that the diffraction takes place before the material under investigation is destroyed by the large radiation flux. These measurements can even be extended to complex structures,

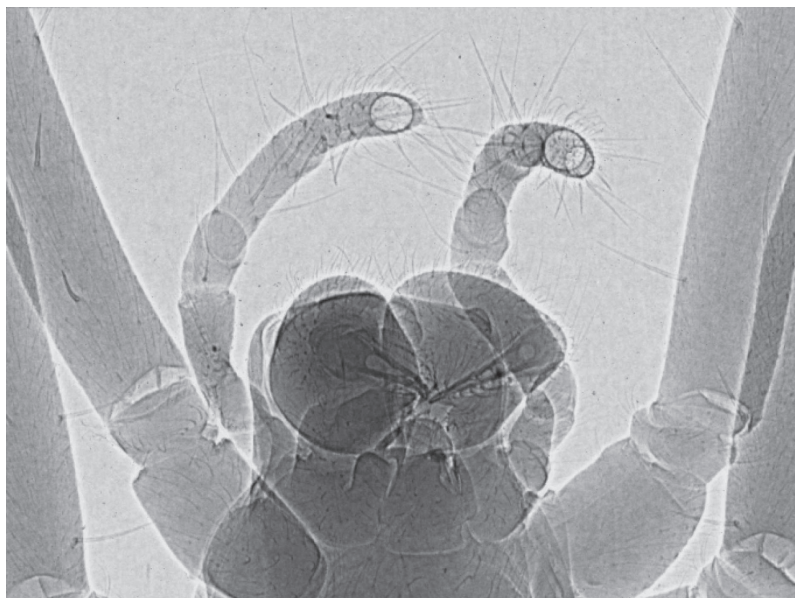


**Fig. 2.13.** Phase-contrast X-ray image of a spider (image credits: Excillum AB, Sweden).

such as viruses, allowing unprecedented knowledge of the working of pathogens and other complex proteins. The ultra-fast nature of FELs also allows movies of these chemicals performing reactions, so in addition to providing structures, they are also elucidating biological pathways. FELs are already revolutionising the knowledge of biochemical processes with its resultant effect on medicine and treatment.

### Very High Energy Electron Therapy

Cancer will affect an ever-increasing proportion of the population as people grow to older age and medicine tackles other diseases and illnesses. More than half of all cancer cases are treated by some form of radiation therapy, where an intense beam of penetrating radiation is directed at the tumour to kill cancerous cells. Again, in the vast majority of cases, this radiation is provided as high-energy photons produced by bremsstrahlung of a low-energy ( $\sim 10$  MeV) electron beam with a solid target. However, photons have a relatively small interaction cross-section as compared to the electrons themselves, and the only reason the electron beam itself is not used is that they do not have sufficient energy to reach deep-seated tumours. For these, electrons of energy in excess of 100 MeV are required, and the cost of a linac producing these energies has been considered to be prohibitive. Wakefield accelerators with their reduced footprint, on the other hand, are considered an interesting source of electrons for VHEET, and a number of studies are underway to demonstrate the use of these devices for this application. The laser-plasma injector (LPI) being developed for the EuPRAXIA facility would be able to produce an electron beam that would be ideal to do experimental work in this area, and a prime goal of EuPRAXIA will be ensuring the reliability and robustness of the electron source, which is vital for this kind of application.

## Imaging Applications

Of course, as important as treatment is the development of techniques to diagnose illness. Many of the advanced techniques now commonly used in hospitals are based on advanced physical techniques, such as PET, CT, or MRI. However, in most cases, the first and most trusted workhorse of medical imaging is the medical X-rays which has mostly remained unchanged in basic operation since the discovery of the X-ray. Yet, with typical X-ray sources, the low resolution and low photon number lead to grainy images which can cause inconclusive and sometimes even incorrect diagnosis. This is especially true when imaging soft tissue, where the contrast between different types of tissue (such as healthy or cancerous tissue) is limited.

High-quality synchrotron and FEL radiation sources have been demonstrated to provide diagnostic capability comparable to invasive and time-consuming biopsies. If the source has additional spatial coherence, then it can be used for phase-contrast imaging, as shown in the example in Figure 2.13. This technique provides extra contrast in soft tissues, such as the ability to detect tumours with high confidence. The radiation sources envisioned for EuPRAXIA, both the FEL and the broadband betatron source, would be able to provide compact and versatile setups that can be applicable to medical imaging. These sources could then be a forerunner of a more widespread adoption of these techniques in hospitals and medical centres.

### 2.2.7 Inspection and Material Studies

Quality assurance and innovation in manufacturing is underpinned by metrological methods and techniques that improve and drive forward the measurement infrastructure available to industry. Metrology is especially important in advanced manufacturing areas producing high-performance and high-value components that are made in and are required to perform under hostile environments. Heat and pressure treatments, new welding methods, radiation exposure, and impact damage are all examples of scenarios that can leave sub-micron defects in materials during advanced manufacturing or extreme performance use.

It is thus highly desirable for industry to be able to assess the uniformity and quality of materials over a wide range of thicknesses, sizes, and composition, ideally while being under significant stress. Moreover, it is vital that any inspection be carried out in a non-destructive manner. Generally speaking, non-destructive inspection can be easily performed at the surface of materials, but several difficulties are encountered when performing sub-surface, volumetric inspections. Several techniques have been developed, which can be classified depending on the particles used to probe the materials: neutron driven, X-ray driven, or positron driven.

Of them all, positron annihilation lifetime spectroscopy (PALS) is arguably the only one that can provide nanometre-scale resolution over a significant range of material thicknesses and detect defects and vacancies in materials down to a few parts per million (Fig. 2.15, left). When in a material, a positron enters a Bloch state, but it is rapidly localised in regions of missing matter; in other words, positrons get easily trapped at vacancy defects. In a timescale of the order of 100 ps, the trapped positron annihilates with an electron in the material, producing annihilation radiation, i.e. two X-ray photons each with an energy close to 511 keV. A sketch of the physical principles behind PALS is given in Figure 2.15 (right). By studying different characteristics of the emitted radiation, such as their spectrum and temporal footprint, one can extract a detailed map of vacancies in the material under study.

Traditionally, positron inspection of materials is carried out using  $\beta^+$  radioactive sources, such as  $^{22}\text{Na}$ . The broadband positron populations that are continuously



**Fig. 2.14.** Accelerators used for inspection and material testing (image credits: FCC / Code of the Universe / CERN / Lois Lammerhuber).

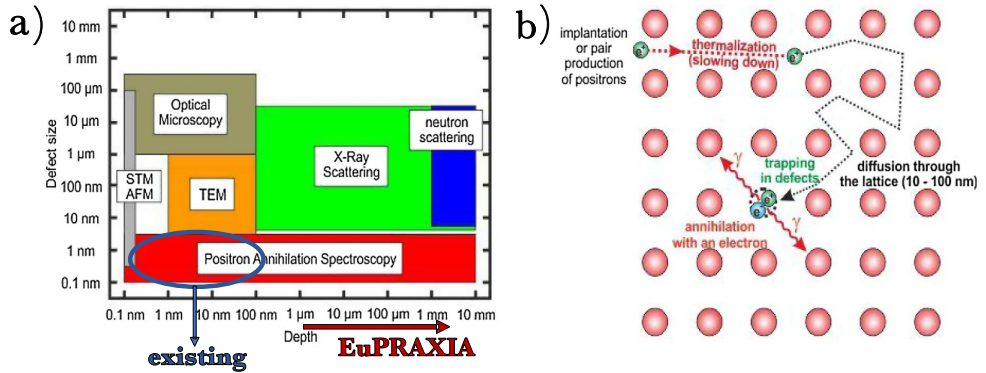


**Fig. 2.15.** Left: Typical range of operation of different methods of material inspection. Positron annihilation techniques allow for the smallest defects to be detected, and the EuPRAXIA facility will allow for micron-to-mm thicknesses to be volumetrically probed. Right: Cartoon of the physical principle behind PALS (image credits: M. Butterling, HZDR).

generated from these atoms are then captured, energy-filtered, and time-gated in bursts with a duration of the order of a nanosecond.

As an example, the ELBE Centre at Dresden-Russendorf provides positron bunches with a duration (FWHM) of 250 ps and an energy tuneable from 0.5 to 15 keV [150]. The SPONSOR area can instead reach up to 36 keV [151]. The maximum intensity achievable by the machine is  $10^6$  positrons per second. The NEPOMUC machine at the Technical University of Munich exploits neutron-induced positron production in  $^{113}\text{Cd}$  and produces approximately  $10^9$  positrons per second with an energy of 1 keV [152]. The PLEPS line in Munich [153] instead provides a DC beam with approximately  $5 \times 10^4$  particles per second. Four minutes are needed to get a full

**Table 2.3.** Calculated positron lifetimes (ps) for perfect lattice (bulk) and monovacancy defects in selected  $ABO_3$  and related materials (adapted from [149]).

Material	Bulk	Defect structure	$V_A$	$V_B$	$V_O$
PbTiO <sub>3</sub>	161	Unrelaxed	292	204	165
		Relaxed	290	185	
SrTiO <sub>3</sub>	152	Unrelaxed	280	195	161
		Relaxed	281	189	
SrRuO <sub>3</sub>	150	Unrelaxed	288	200	161
Sr <sub>3</sub> Ru <sub>2</sub> O <sub>7</sub>	180	Unrelaxed	301	207	187
LaMnO <sub>3</sub>	145	Unrelaxed	282	196	158
TbMnO <sub>3</sub>	152	Unrelaxed	259	199	161
BiFeO <sub>3</sub>	154	Unrelaxed	290	198	161

lifetime spectrum, whereas up to two hours are necessary to get a complete depth profiling, accumulating 25 spectra.

Despite the high performance of these machines and their wide use for industrial applications, it is difficult to produce high-quality positron beams with higher energy (up to a few MeV), able to penetrate deeper into the material under study. Also, the relatively long duration of the beams, comparable to the typical timescales of annihilation in materials (see Tab. 2.3, adapted from [149]), limits the resolution of the systems and makes data extraction rather complicated and prone to uncertainties. This is because it is necessary to deconvolute the signal with the positron duration and the detector response, both on timescales of the order of, if not longer than, 100 ps.

An alternative method to produce high-flux and short beams of positrons has been recently proposed. In a nutshell, the positron production exploits the quantum electro-dynamic cascade initiated by an ultra-relativistic electron beam propagating in a high-Z solid target [154–156]. The positrons escaping the rear surface of the solid target present a duration comparable to that of the primary electron beam, a broad spectrum and divergence, and an overall number of positrons that is a significant fraction of the number of electrons in the primary beam [148].

To generate high-flux, short, and mildly relativistic positron beams, one would then require a primary electron beam with the highest possible charge, modest energy (of the order of 10s to 100 MeV), and short duration. However, higher energy electron beams, as achievable within EuPRAXIA using a multi-staged approach, are also usable for this purpose. On the other hand, the unavoidable spectral broadening introduced by the cascade inside the solid significantly relaxes any requirement on spectral quality of the primary electron beam, which is virtually irrelevant for the positron production. These characteristics are guaranteed by the laser-plasma-based electron beams which are foreseen to be created at the EuPRAXIA infrastructure and which are discussed in more detail in Section 25.2.1.

## 2.3 The Role of Industry

As a relatively young field of science, plasma acceleration has not yet established its own industries, while at the same time relevant existing industry sectors connected to high-power laser and RF accelerator systems have only limited experience with this technology. To push plasma accelerators towards user application and perhaps even eventual commercialisation, closer interactions with industry will thus be essential. In this context, EuPRAXIA can provide an ideal platform for such a development

through involving industry in several different roles. First, with their vision as suppliers of finished and usable equipment, industry partners can help laboratories in the design of robust and reliable products. Thus, they will be able to participate actively in risk-analysis studies and thus identify which activities must be carried out in the prototyping phase to move from a low-technical-readiness to a high-technical-readiness technology. Industry partners may also be able to directly participate in prototyping projects during the EuPRAXIA technical design phase, through collaborative research projects or via students, whether for thermal studies for the laser system (pump laser, mirrors, deformable mirror, gratings), studies on the materials needed for optics or for electron transport and electron diagnostics, just to name a few examples. In addition to these, other topics for collaboration could include operational safety aspects or studies on the integrated logistical support necessary depending on the mission profile and operation mode of the facility to guarantee a controlled operating cost over the lifetime period of the infrastructure. In this way, the manufacturers will be able to commit to the delivery of a turnkey facility for the laser and the functional and reliable installation of particle beam parts in the manufacturing phase thanks to an extensive collaboration in the design. They will also be able to commit more easily to maintenance procedures under operational conditions of the facility over the expected lifetime, as they have already been involved in their development. Additionally, however, industry could also take on a second role as users of the future EuPRAXIA research infrastructure. As the previous sections showed, many of the potential features of the machines designed for EuPRAXIA also have great potential for industrial applications. As such, industrial users could take advantage of this infrastructure, on the one hand, as an analysis or processing tool. On the other hand, they could also see it as a testing ground for applying plasma-accelerator technology to their own facilities and processes, a possibility unique to a facility such as EuPRAXIA thanks to the potential for compactness and cost-efficiency of plasma acceleration. This last point in particular directly links to EuPRAXIA's ambition for open innovation (see Chap. 1) as collaborations and joint projects could foster a unique exchange of knowledge and technology. While providing new research insights and potentially improved performance for EuPRAXIA and its academic users, industry partners could equally benefit from novel R&D results with the potential for future product development opportunities.

## 2.4 Added Value for the European Research and Technology Landscape

The European research and technology landscape features thousands of particle accelerators that provide particle and photon beams to applications in health, industry, and science. State-of-the-art particle beams and the produced photons are used, for example, for cancer therapy in hospitals, for electron beam welding in factories, for security X-ray scans at borders, for investigations of bacteria and viruses in research centres, and, last but not least, for discovering new particles and fundamental forces. Accelerators range in size from a few meters to the 27 km circumference of the Large Hadron Collider at CERN. As undisputed masterpieces of modern technology, they provide indispensable tools to the modern society in Europe, supporting innovation and economical growth.

Today particle accelerators are a mature technology that has started encountering some practical limitations because of size and cost. The application reach of particle accelerators could be dramatically increased if their size and cost could be reduced. For example, the availability of brilliant, time-resolved X-ray pulses in every university could multiply the number of bacteria or virus structures that can be resolved. Young scientists could have early access to powerful research tools, new ideas could

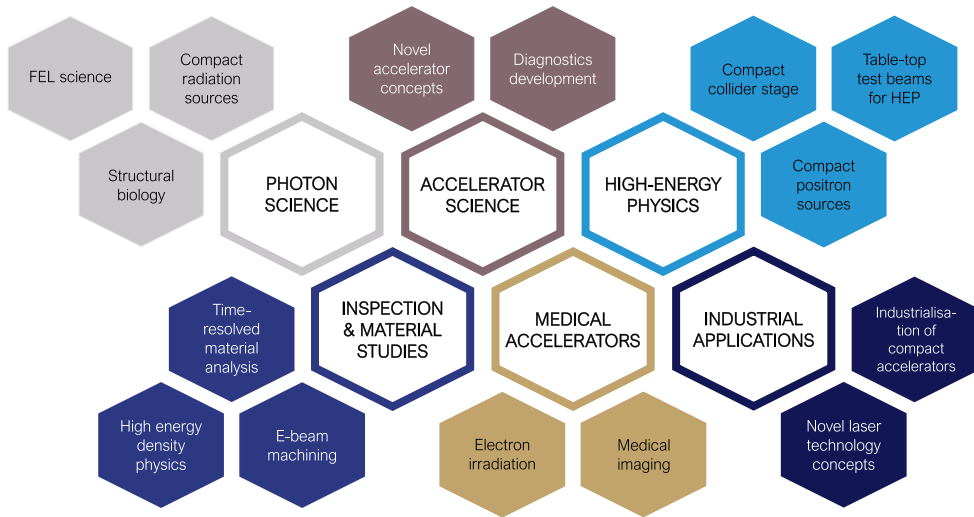


**Fig. 2.16.** Variety of possible topics and application fields available to users to investigate at the EuPRAXIA research infrastructure.

be tested quickly, and unconventional research directions followed. Experience shows that such wider access to powerful research tools will strongly accelerate knowledge gain and innovation. Broader access will also enable more inventions and tests of new solutions, for example in medicine. Once the structure and dynamical behaviour of a bacterium has been understood, new approaches for medication can be developed and tested more quickly.

The EuPRAXIA CDR describes the design of a new European research infrastructure built around the concept of plasma accelerators. Those plasma accelerators aim at enabling a drastic reduction in size and cost for accelerator facilities. EuPRAXIA realises a facility that would, for the first time, demonstrate a gain in facility size while enabling various applications and providing users with additional access to particle and photon beams. As such a demonstration facility, EuPRAXIA targets different application fields in a complementary way with the existing and planned research landscape in Europe. The application fields and particular subjects that are addressed in the EuPRAXIA facility are presented in Figure 2.16.

From Figure 2.16, it becomes clear that EuPRAXIA aims at a broad spectrum of users and therefore also a broad added value for the European research and technology landscape. The added value from EuPRAXIA starts with developing the plasma, accelerator and laser technologies required, thus providing Europe with access to this innovative field and a clear leadership role. Added value continues through collaboration with related industry, which will ensure a swift industrialisation of the required high-tech components. Users from different domains will experience added value, when the highly innovative and novel accelerator technology will be made accessible to them. The users will, on one side, have the benefit of access to the particle and photon beams with some unique features (e.g. access to ultra-fast science). However, the users will also provide feedback on the particles and photon beams, often contributing requests and new ideas.

EuPRAXIA will, last but not least, also generate added value through a coordinating role with its many partner laboratories. EuPRAXIA has been proposed by members of the European Network for Novel Accelerators (EuroNNac) as a European project that ensures the competitiveness of Europe in novel plasma accelerators. It builds on the expertise from several national projects in plasma acceleration, like the

ATHENA project in Germany, the SPARCLab project in Italy, the CILEX project in France, the EPAC project in the UK, and the ELI laser pillars. EuPRAXIA is connected to the LEAPS initiative through the LEAPS task on “Compact Sources”. It is fully complementary to the AWAKE plasma acceleration project, which can only be performed at CERN, with its powerful proton accelerator infrastructure. During its technical design and construction phases, EuPRAXIA will create significant added value by bundling European expertise in a major project with clearly defined common goals and interfaces to alternative approaches.

## 2.5 The Role of EuPRAXIA for Innovation and Science in the Global Environment

Plasma wakefield acceleration is an important research topic in various institutes across Asia and America, many of whom are already involved in EuPRAXIA as associated partners. Continuing and strengthening scientific exchange between EuPRAXIA and the rest of the world could thus strongly advance this field of science.

Several possible avenues for scientific collaboration could be foreseen for EuPRAXIA. A most direct route is, of course, the reciprocal use of experimental facilities. The project’s technical design phase will provide excellent opportunities for common R&D and prototyping projects at different international facilities, such as the PEARL facility in Russia or the Laboratory for Laser Plasmas in China. A more complete list of European and international consortium facilities is given in Sections 29 and 30 in this context. Once the EuPRAXIA infrastructure is set up, it will provide a unique test facility and collaboration partner for users worldwide, especially also those from regions where plasma accelerator or, generally, accelerator facilities do not yet exist in a widespread manner.

In the long term, it could be envisaged that EuPRAXIA will be able to exchange knowledge and technologies with other facilities worldwide. Applying some of the novel techniques from the EuPRAXIA design at other research infrastructures, for example, would demonstrate very well their applicability and user readiness in different setups. At the same time, EuPRAXIA will be in a unique position to share experience in setting up and operating a large-scale test facility based on plasma acceleration. This expertise could be shared through training and knowledge exchange programs as an international effort. A particularly interesting perspective could be offered to developing countries in this way for whom compact accelerator technologies could be ideal entry points to accelerator science considering their reduced cost and size.

Finally, EuPRAXIA brings together and represents a large fraction of the European plasma-accelerator community. As such, it is expected to become an important contact point for international collaborations with European institutes in the field, fostering knowledge exchange and pushing progress for some of the hardest future challenges for novel accelerators, such as diagnostics development, applications, etc.

In the following, some further aspects for EuPRAXIA’s possible role in the global research environment are exemplified with the cases of two collaboration partners in Russia and China.

### Statement from the Institute of Applied Physics in Russia (I. Kostyukov)

Plasma-based acceleration is one of the important directions of research at the Institute of Applied Physics of the Russian Academy of Sciences (IAP-RAS). The scientific exchange programs between EuPRAXIA and the non-European partners could

strongly advance this field of science. Furthermore, the EuPRAXIA infrastructure is excellently suited as a platform for the training of young scientists (not only from European countries but also from non-EU organisations like IAP-RAS), where they will learn advanced techniques for plasma-based acceleration, innovative methods of diagnostics, experiment planning, and organisation.

There are several experimental setups devoted to laser-plasma acceleration in IAP-RAS. Given its flexible structure, the EuPRAXIA facility can be used to repeat and verify experimental results obtained in IAP-RAS facilities (and vice versa) to extend them into new parameter spaces which allows to explore new regimes of acceleration and radiation generation.

The diagnostic methods for experimental investigation of the plasma-based acceleration are still a challenge. The modern methods cannot yet provide the necessary spatial-temporal resolution of laser-plasma structures and phase parameters of the electron bunches during acceleration. The versatile EuPRAXIA infrastructure could make a significant contribution to the development of diagnostic techniques. Moreover, many elements of laser-plasma accelerators like laser targets, laser pulse conditioning and manipulation, electron bunch transportation, etc. can be developed and tested at the EuPRAXIA facility. The developed technologies can then be re-examined and applied in other facilities, like the PEARL facility in IAP-RAS.

### **Statement from Shanghai Jiao Tong University (M. Chen)**

EuPRAXIA will be the most important partner of the key Laboratory for Laser Plasmas (LLP) at Shanghai Jiao Tong University. The two sides will conduct in-depth collaborative research on high-quality electron acceleration (such as two-colour ionisation injection, plasma dechirper devices, etc.), high-efficiency staged wakefield acceleration (such as curved-plasma-channel-based staged laser wakefield acceleration), and the wide applications of electron beams and radiation sources. LLP welcomes EuPRAXIA partners to carry out experimental studies on its 200 TW and the future upgraded 200 + 300 TW laser and target systems. LLP would also like to make theoretical and simulation contributions to EuPRAXIA. LLP looks forward to performing high-quality electron acceleration, X-ray, and electron beam imaging research on EuPRAXIA facilities and sharing the advanced experience of EuPRAXIA in the construction of an acceleration facility and high-average-power laser systems.

## **3 Description of the EuPRAXIA Infrastructure**

### **3.1 Introduction**

In this chapter of the CDR, we describe the envisaged overall EuPRAXIA infrastructure, focusing on the concept of the facility and preliminary ideas on the possible implementation. The technical studies that have been performed for the EuPRAXIA CDR will be described in detail in Part 4. The research field of plasma accelerators is distributed over Europe, and considerable effort has been invested in discussing a model that includes the existing expertise and facilities while delivering a well-defined European research infrastructure. The EuPRAXIA infrastructure and associated project, therefore, will exhibit particular features that are not present in other projects. This is explained and discussed in this chapter.

### 3.2 Overview on Design and Performance Parameters

The EuPRAXIA infrastructure will deliver laser, electron, positron, and photon beams to various users at two central sites. The site concept will be explained later in this chapter. The flagship innovation and science goals have been defined in Chapter 2.1. The detailed performance simulations are discussed later, and multi-page performance tables can be found in Chapter 9. For the convenience of the reader, we show a summary of design and performance parameters in Table 3.1.

Here, we remind the reader of a few main objectives of the EuPRAXIA design study:

1. To develop the disruptive technology of plasma accelerators, modern lasers, and compact beam drivers into a viable option for a new generation of compact and cost-effective accelerators.
2. To solve the beam quality problem of plasma accelerators such that the produced electron beams can support demanding applications like FELs.
3. To demonstrate benefits in terms of the performance, size, and cost of plasma acceleration with respect to RF technology.

While the latter point is discussed in Section 3.4, the expected machine performance of EuPRAXIA is summarised in Table 3.1. It was also visualised in Figure 2.5 for the critical parameter of electron beam energy spread. In the technical part of this design report, various solutions will be presented that allow extending the performance reach of plasma accelerators significantly.

The overview table reflects the two complementary technical approaches of beam-driven and laser-driven plasma accelerators, respectively. Both technologies offer, for example, different benefits on compactness (the laser-driven option is potentially more compact) and stored energy (the beam-driven option stores more energy). The two approaches share a number of common challenges and will be developed together in a synergistic approach. The foreseen user applications have been selected to optimally reflect the benefits of each approach.

### 3.3 The Concept of Distributed EuPRAXIA Construction

As written before, the plasma accelerator community in Europe is dispersed, with some 20 groups and about 15 facilities of 10–30 M€ scale per facility. Major groups and activities exist in France, Italy, Portugal, Sweden, the UK, the Czech Republic, Switzerland, and Germany. The situation can be compared to the field of particle physics detectors that have groups and facilities in various institutes, universities, and countries. The EuPRAXIA concept of distributed construction was therefore inspired by the construction model of big particle physics detectors in Europe:

#### Model of particle physics detectors

- Many groups work together in experimental collaborations; the collaborations are organised in working groups. Working group leaders organise the distributed work and prepare reports.
- The collaboration elects spokespersons that manage agreement on the deliverables of the various institutes and track the overall progress.
- Local institutes in the various countries carry out the R&D work, perform local prototyping and tests, and construct the final components.
- The collaboration assembles the delivered components in the location of the particle physics detector.

**Table 3.1.** Performance summary of the EuPRAXIA design. Further information on the foreseen machine components and properties can be found in the respective sub-system chapters of Part 4, with detailed lists of performance parameters shown in Chapter 9.

Quantity	Baseline Value
<b>Laser systems</b>	
Wavelength	800 nm
Energy on target	5–100 J
Pulse duration	≥20–60 fs
Repetition rate	20–100 Hz
<b>High-energy electron beam from beam-driven plasma accelerator (PWFA)</b>	
Energy	1.0–5.0 GeV
Charge	30–40 pC
Bunch duration	~13 fs
Energy spread	0.4–1.1 %
Normalised emittance	0.7–1.2 mm mrad
<b>High-energy electron beam from laser-driven plasma accelerator (LWFA)</b>	
Energy	5.0–6.0 GeV
Charge	23–30 pC
Bunch duration	3–11 fs
Energy spread	0.1–0.9 %
Normalised emittance	0.1–1.4 mm mrad
<b>Free-electron laser</b>	
Radiation wavelength	0.19–35.9 nm
Pulse duration	0.4–15 fs
Saturation length	16–126 m
Photons per pulse	$1.9 \times 10^9$ – $7.2 \times 10^{11}$
Brightness	$2 \times 10^{28}$ – $4.8 \times 10^{32}$ photons/[mm <sup>2</sup> mrad <sup>2</sup> s(0.1%BW)]
<b>Betatron source</b>	
Photon energy	0.6–110 keV
Source size	1.4–2.4 μm
Photons per pulse	$2 \times 10^8$ – $4 \times 10^{10}$
Peak X-ray brightness	$2 \times 10^{21}$ – $1 \times 10^{26}$ photons/(mm <sup>2</sup> mrad <sup>2</sup> s[0.1%BW])
<b>Inverse Compton source</b>	
Photon energy	≥100 MeV
Pulse duration	~30 fs
Divergence	<1 mrad
<b>Low-energy positron source</b>	
Positron energy	0.5–10 MeV (tunable)
Beam duration	20–90 ps
Positrons per shot	≥ $1 \times 10^6$
<b>High-energy positron source</b>	
Positron energy	≥1.0 GeV (tunable)
Beam duration	≤10 fs
Positrons per shot	~ $1 \times 10^7$

- The collaboration operates the detector and shares in data analysis, common publication, and knowledge gain.

We propose that the EuPRAXIA project would be organised in a similar way:

### Model of EuPRAXIA

- The connected plasma accelerator groups work together in the EuPRAXIA collaboration, which is organised in “technical clusters” (equivalent of working groups). Coordinators of the clusters organise the distributed work and prepare progress reports.
- The EuPRAXIA collaboration appoints the EuPRAXIA project management team. This team organises agreement on the deliverables of the various institutes and tracks the overall progress in clusters and local groups.

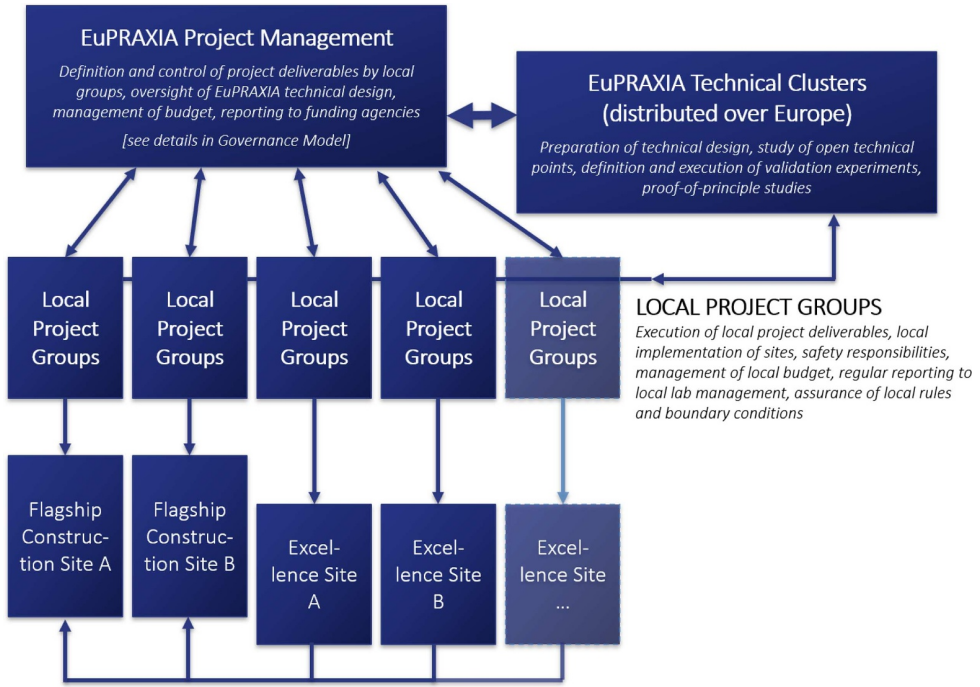


Fig. 3.1. EuPRAXIA facility concept.

- Local project groups in the various countries carry out the R&D work, perform local prototyping and tests, and construct the final components. For this, any available local facility or workshop will be used.
- In addition, EuPRAXIA defines four additional excellence and prototyping sites (at most one per country) that will be upgraded in capability and will focus on aspects of particular importance and difficulty.
- The collaboration assembles the delivered components in the location of the two EuPRAXIA construction sites. Each construction site focuses on a particular technological path such that complementarity is assured.
- The collaboration operates the EuPRAXIA facility and shares in data analysis, common publication, and knowledge gain.

This EuPRAXIA implementation model is visualised in Figure 3.1. More details of the governance model can be found in Chapter 5.2. Here, we describe the model of the EuPRAXIA infrastructure in more detail. It is noted that the consortium found during the CDR work that two complementary and equally promising technological paths can be defined for EuPRAXIA, namely, one relying on a beam-driven plasma accelerator and the other one on a laser-driven plasma accelerator approach. Instead of combining both in one construction site, the consortium proposes to exploit the two paths in two construction sites. Both construction sites shall be located at existing facilities that are upgraded into one leg of the EuPRAXIA infrastructure. Local project groups will coordinate the work per site, in close collaboration with the work of the clusters and institutes around Europe.

The definition of two construction sites maximises the use of existing equipment as one existing site might have important laser infrastructure, and the other existing site might be more focused on RF technology. This minimises the need for duplicating existing infrastructure. In addition, the scientific output is significantly increased,



**Fig. 3.2.** Overview of the proposed technical clusters for EuPRAXIA. More detailed descriptions of each cluster can be found in this chapter.

and the integration of the European research landscape is much improved. The EuPRAXIA concept avoids competition among institutes inside Europe and brings all institutes together with a common scientific goal and shared benefits. Competition is instead defined between two technological paths. This technical competition will produce the fastest possible progress (“competition is good for business”).

### 3.3.1 EuPRAXIA Clusters for Organising Europe-Wide Work

The EuPRAXIA clusters will organise the Europe-wide work similar to working packages in the EuPRAXIA design study. Clusters have been defined along areas of expertise, such that scientists with overlapping expertise are bundled and work together towards the common EuPRAXIA goals. The clusters that were defined are shown in Figure 3.2.

Various institutes of EuPRAXIA have expertise in one or several EuPRAXIA clusters. The mapping of clusters to available competencies in institutes around Europe and Russia is shown in Table 3.2. It is seen that the present EuPRAXIA consortium members cover all the competencies required for the EuPRAXIA technical clusters. A final assignment of institutes to clusters must be done during the preparatory phase of EuPRAXIA and will depend on available project resources.

## I. Theory & Simulation

**Keywords:** start-to-end simulations, performance predictions, evaluation of measured hardware performance, code benchmarking, development of new theoretical concepts, high-performance computing, machine learning and data science, new codes and new approaches

The mission of the “Theory & Simulation” cluster is to study the beam physics and performance throughout the EuPRAXIA machine using theoretical and computational tools. This includes activities on four different topics:

(1) Development and study of new theoretical concepts: These will comprise energy dechirping and external injection concepts, electron injection and acceleration control mechanisms (using e.g. magnetic fields, multiple lasers, and shaped plasma targets), radiation generation techniques in plasma channels from the X-ray to mid-IR regime, and thermodynamics studies of plasma in capillaries.

(2) Start-to-end simulations & theoretical modelling of the beamlines foreseen for the EuPRAXIA facility: Activities additionally flowing into the start-to-end simulations of LWFA-based, PWFA-based, and hybrid designs will include investigations of the FEL performance, detailed error and tolerance studies, the integration of different types of codes across beamline components (e.g. between RF and plasma components), and the development of a theoretical machine model.

(3) Evaluation of the performance of the machine and its components: Benchmarking between different simulation codes will need to be carried out and the measured performance hardware evaluated against theoretical results.

(4) Development of new codes and new computational approaches: Topics of interest are code performance improvements, the design of new, robust, and realistic modelling and simulation tools, high-performance computing (exa-scale computing) developments (using CPU-, GPU-, and cloud-based systems) as well as the integration of machine learning and other data science methods. Areas of particular importance are the integration of plasma density non-uniformities as well as realistic laser pulse and electron beam profiles into simulations.

The “Theory & Simulation” cluster will be active throughout the whole life cycle of the EuPRAXIA facility. Its most essential work will be carried out during the technical design phase by assessing and optimising machine performance through the activities described above. During the implementation and operation phases, the cluster will take on a more supportive role in evaluating and improving the facility. Strong interaction with most of the other clusters involved in the development of specific components will be required to coordinate simulation and modelling tasks. Further cooperation is planned with the “Layout & Implementation” cluster for the development of data analysis and storage capabilities at the EuPRAXIA sites.

## II. Laser Technology

**Keywords:** laser drivers, photo-injector laser, other laser systems, laser diagnostics, optical components, diodes, thermal management, laser transport line, compressor, kHz laser technology (with industry link)

The cluster on laser technologies will deal with all scientific and technical issues related to the EuPRAXIA laser design and, in particular, the transition from the current EuPRAXIA laser conceptual design to the final technical design and construction. The cluster EuP-LASTECH will primarily tackle several aspects of the

**Table 3.2.** List of institutes with interests in particular EuPRAXIA cluster topics. An explanation for each of the institute acronyms can be found in the “List of EuPRAXIA Partner and Associated Partner Institutes” at the end of the report.

	Theory & Simulation	Laser Technology	Plasma Components & Systems	RF Technology	Magnets & Other Beamline Components	Diagnostics	Applications	Transformative Innovation Paths	Training, Outreach & Dissemination	Layout & Implementation
CEA	•		•		•	•				
CNR	•	•				•		•		
CNRS	•	•	•			•	•	•		•
DESY	•	•	•	•	•	•	•	•	•	•
ELI	•		•			•				
ENEA	•						•			
FBH		•								
HIJ				•	•	•	•	•		
HUJI			•							
HZDR			•					•		
IAP-RAS		•								
ICL			•				•	•		
INFN	•	•	•	•	•	•	•	•	•	•
IST	•		•							
JIHT	•									
KIT						•	•			•
LMU			•			•	•	•		
QUB			•				•			
SOLEIL					•	•	•			
STFC		•	•				•	•		•
UHH	•						•			
ULIV						•		•	•	•
UMAN					•	•				
UOXF	•		•	•		•	•	•		
URLS	•			•	•	•				•
URTV				•		•	•			
USTRATH	•		•			•	•	•		
WIGNER	•					•			•	•
YORK			•				•			

laser design, as emerged during the design study phase, through a number of developments and prototyping activities to address and solve critical issues. An initial set of such topics is outlined below, divided into five subject areas concerning the main blocks of the entire laser system, from the amplifiers to the final focusing on the plasma, including manipulations of the initial temporal and spectral properties.

#### Main Scientific and Technical Issues:

- Amplifier configuration:
  - Prototyping of Ti:Sa amplifiers
  - Building a test amplifier to test thermal load and cooling
- Pumping technology:
  - Scaled 100 Hz repetition rate, high-energy pumping
  - Addressing 100 Hz pump lasers developments
- Optical compressor technology:
  - Thermal management of compressor gratings
  - Running high-average-power illumination tests at existing facilities to make assessments on LIDT, thermal load, cooling, and lifetime
- Pointing stability:
  - Stability (pointing and more) and active control
  - Building tools and running tests at existing facilities; defining routes for active stabilisation
- Temporal and spatial shaping:
  - Synchronisation
  - Developing efficient pulse train, temporal contrast, AO control and measurements
  - 3D pulse shaping (formation of triangular, cylindrical, ellipsoidal, etc. pulses)
- kHz repetition rate and beyond:
  - Lasing material development and characterisation
  - Architecture design and modelling
  - Wavelength scaling of applications

The implementation of *development* and *prototyping* activities will be established mainly at participating institutes and will involve a number of leading companies with known expertise in the field. Interested companies include full system manufacturers (AT and Thales) and component manufacturers (Safran, VCS, VacuumFAB, Horiba-JobinYvon, ISP, TRUMPF, Imagine Optic, Dynamic Optics, etc.).

#### Higher Repetition-Rate Developments

The current layout of the EuPRAXIA laser foresees a 20 Hz configuration using arrays of Ti:Sa pumping systems like the DIPOLE or P60. This introduces a significant complexity that could be avoided using pumping systems running natively at 20 Hz, eventually reaching the 100 Hz of the P1 configuration. More generally, >kHz repetition rate is foreseen as a milestone for future laser driver developments. Such higher repetition rates will require major technology developments beyond the simple evolution of current established architectures.

Totally alternative systems are those based on direct diode pumping of different gain media. Yb:YAG and Yb:CaF<sub>2</sub> are being explored and are both candidates as gain media for such systems; however, there are only limited experimental data available on how these approach at high average powers. On the other hand, Tm:YLF is also being considered as a gain material that offers a significant lifetime advantage over the well-established Yb doped materials traditionally used for diode pumped fiber and bulk systems.

The cluster EuP-LASTECH will establish initiatives to support developments of direct-pumping, high-average-power systems in a two-stage approach, starting with a

conceptual design development, supported by existing programmes at participating partners (CNR, CNRS, FBH, LLNL, STFC, etc.), followed by a downselection and a technical design of the chosen architecture.

### III. Plasma Components & Systems

**Keywords:** plasma sources, plasma injectors, plasma-accelerator stages, plasma mirrors, plasma lenses

This cluster brings together experts from partner institutes to develop plasma components and systems requested for the implementation of the EuPRAXIA accelerator and beamlines, in particular: laser-driven plasma injectors (LPIs), laser- and beam-driven plasma accelerators (LPAs & BPAs), and interface components such as plasma mirrors and passive or active plasma lenses. Particular efforts will be oriented towards the development of components providing high-quality, stable electron beams at a high repetition rate. The contribution of identified partners is planned as follows:

#### Development of LPIs

1/ Development of optimised electron injection schemes in tailored density profiles for the EuPRAXIA accelerator baseline: modelling through fluid, PIC and Monte Carlo simulations, design and construction of relevant gas cells, and experimental testing of stable injection schemes; numerical and experimental investigation of optical injection with spatio-temporally controlled laser pulses.

2/ Investigation of physics implications for operation at a higher repetition rate,  $>10$  Hz; development of high-repetition-rate LWFA targets; investigation of strategies for post-acceleration removal and recovery of unused wake energy.

3/ Development of LWFA-integrated targets optimised for betatron radiation and imaging applications (aiming high-quality hard X-ray imaging ( $>50$  keV) and high magnification ( $>20\times$  or sub-micron resolution) with low noise and low dose).

#### Development of LPAs / BPAs

1/ Optimisation of plasma parameters and the development of gas-filled discharge capillaries to reach long plasma channel lengths, typically several tens of centimetres.

2/ Development of novel long low-density plasma channels suitable for multi-GeV accelerator stages operating at high repetition rates.

3/ Guiding of high-intensity laser beams in curved plasma channels: multi-stage capillaries built and tested in guiding experiments; numerical and experimental investigation of curved hydrodynamic optical-field-ionised (HOFI) plasma channels.

4/ Development of all-optical, multi-component, large-volume plasma sources based on (selective) tunneling ionisation (in collaboration with the “Transformative Innovation Paths” cluster).

#### Development of plasma components for laser or electron beam transport and shaping

1/ Development of active plasma lenses and passive plasma lenses for electron beam shaping, plasma lenses for laser focusing; theoretical modeling of plasma channel lenses using a short capillary discharge (2–3 mm) to create a plasma lens, used to increase the intensity of the impinging beam to increase the laser intensity.

2/ Investigation of energy dechirping concepts, including multiple plasma stages.

3/ Plasma mirrors, adaptive mirrors, feedback loops.

#### System integration or prototypes development

Multi-stage design and experiments (LPI and LPA components driven by separate laser beams); full start-to-end analysis to optimise the choice of injection energy, and laser and plasma channel parameters in curved plasma channels.

#### IV. RF Technology

**Keywords:** RF drivers, RF injectors, low-level RF and synchronisation

This cluster is related to the following three topics:

RF gun technology covers the development and optimisation of S-band guns, aiming to reach the best performances in terms of accelerating field gradient and breakdown rate, with particular attention to the new clamping technology that, with the help of special gaskets, allows to avoid the brazing procedure. The study and development of cathode materials like Mg and Yttrium is also covered, besides the more common Cu.

RF accelerating structures technology covers the development and optimisation of the S-band and X-band accelerating structures in terms of feed coupler optimisation for the S-band case, while work for the X-band deals with the design and optimisation of the single cell and of the whole structure in terms of maximum achievable gradient compliant with the optimum compact factor, feeding RF system optimisation and UH vacuum sustainability.

Synchronisation covers the precise synchronisation between components of the RF system as well as with the laser drivers. Feedback mechanisms will be designed and implemented in collaboration with the diagnostics cluster, to ensure the well-controlled and synchronised operation of the EuPRAXIA machines.

For both topics, the cluster will prepare a technical design of the RF technology for the two EuPRAXIA construction sites, carry out test and prototyping experiments, and coordinate the production and delivery of all necessary components for the construction phase.

#### V. Magnets and Other Beamline Components

**Keywords:** magnets, beam transport and manipulation, collimation, beam dumps

This cluster covers magnets, beam transport, and manipulation as well as beam dumps.

Permanent magnet quadrupoles of variable strength, an original design developed at Synchrotron SOLEIL (QUAPEVA), will be investigated and optimised for the EuPRAXIA design, among others.

For the beam transport and manipulation, the different technologies investigated as part of the conceptual design study, from permanent quadrupoles and solenoids to plasma lenses (in collaboration with the cluster on plasma sources and components), will need to be optimised and downselected for a full technical design.

In the case of beam dumps, both conventional designs and plasma-based beam dumps as a possible future upgrade option are under investigation.

In all cases, test experiments and prototypes are planned to develop a robust technical design for the beamlines at the EuPRAXIA sites. Furthermore, the components required throughout the construction phase will be produced and delivered to the respective facility locations in a joint manner.

#### VI. Diagnostics

**Keywords:** electron diagnostics, positron diagnostics, photon diagnostics, plasma diagnostics

This cluster is related to several topics:

Electron and positron beam diagnostics: Electron and positron beam diagnostics cover every acceleration scheme and all the positions along the machine, including the experimental areas. It includes the implementation of conventional diagnostics and R&D on new dedicated instrumentation for plasma acceleration. Non-intercepting or non-disturbing beam diagnostics are in the scope of this cluster. Particular emphasis will be put on innovative single-shot emittance measurement techniques, the development of CBPMs, and several longitudinal diagnostics. Among others, we will focus on the use of coherent radiation (Smith-Purcell-based measurements, implementation of high-throughput THz detector systems and readout electronics, near-field electro-optical sampling) and transverse deflecting structures (X-band TDS, gyrotron/gyrocystron-driven transverse deflecting structures). Betatron diagnostics, passive streakers (metallic or dielectric), and diagnostics based on plasma afterglow are also included in this task.

Photon diagnostics: Photon diagnostics – e.g. for measuring the spectra, divergence and emittance of radiation sources – cover all photons coming from applications, such as FEL, THz sources, X-rays, etc. that can be used to monitor the quality of the source. These diagnostics will be mainly located in the experimental areas. The photon diagnostics for positron experiments for material characterisation are also included.

Plasma diagnostics: Plasma diagnostics are devoted to the measurement of the plasma parameters, to optimise the plasma acceleration process. It includes the measurement of plasma density by the Stark broadening effect, interferometry-based techniques (including novel, robust, real-time second-harmonic interferometry methodology or wavefront measurement techniques for LPIs), and the measurement of the laser driver spectral modulation for the determination of average accelerating fields in long LPA plasmas. Particular emphasis will be placed on the multi-plane few-cycle shadowgraphy of wakefields to retrieve the electron density distribution by in situ interferometry and ex situ interference tomography of non-axisymmetric gas jets. There will also be a focus on diagnostics based on plasma afterglow and ultra-fast plasma diagnostics, which can be used to visualise plasma waves in a beam- or laser-driven electron wakefield accelerator. Here, electromagnetic probe pulses with wavelengths in the visible to mid-IR range will be used to diagnose plasmas covering a wide range of electron densities.

All of these areas of interest include theoretical simulations and mechanical design, device construction, as well as testing and characterisation at selected facilities with beams.

## VII. Applications

**Keywords:** positron generation, free-electron laser, undulators, inverse Compton source, betatron source, THz radiation, high-field physics, test beam generation, HEP detector testing, user end stations

This cluster focuses on the design, prototyping and delivery of all components related to EuPRAXIA's foreseen flagship applications. These include the following eight types of particle / radiation sources:

- free-electron laser beamlines for electron energies between 1 and 5 GeV
- a low-energy, high-charge positron source for material testing and industrial applications
- a high-energy, low-emittance positron source for experimental studies of positron acceleration and transport

- an X-ray betatron source for medical and life science imaging
- a hard X-ray to gamma-ray inverse Compton scattering source for fundamental science and industrial applications
- two electron test beamlines for high-energy physics detector testing, THz radiation, and other detector testing
- high-field physics (as a future development)

For each source, both the transport line of the electron beam to the source and the transfer beamline of the secondary beam after the source need to be designed. After testing and prototyping, the necessary components will be produced collaboratively with the cluster members and delivered to the respective construction sites. The cluster activities will be built on recent work devoted to the optimisation of several aspects of these sources, from their generation and characterisation, to their transport and manipulation, up to their use.

In the case of the free-electron laser, this includes, among others, the undulators and photon beamline. Superconducting undulators (SCU) tailored to EuPRAXIA will be conceptualised, prototyped, tested, and finally implemented according to field measurements. Technological options to be considered are Nb-Ti-based planar SCUs (available technology with the industrial partner Noell), superconducting transverse-gradient undulators, and SCUs with switchable period length (proof of feasibility in the TDR phase) as well as more advanced concepts like laser-scribed HTS tape-stacked undulators.

An additional focus for the cluster will be placed on preparing the user end stations, including general infrastructure (together with the cluster on layout & implementation), as well as the necessary instruments and diagnostics for user experiments. Strong interaction is also planned with the cluster on training, outreach & dissemination regarding the organisation of user workshops as well as with local groups at the host institutes of the construction sites on other topics related to user support.

## VIII. Transformative Innovation Paths

**Keywords:** hybrid accelerators, novel injection and radiation generation mechanisms, multi-pulse LWFA, plasma-based metrology and diagnostics

This cluster concentrates on highly innovative technologies which emerged from EuPRAXIA phase 1 with steep TRL trajectories. These are R&D-intensive thrusts over the next phase and in turn have the potential to transform EuPRAXIA by boosting the quality and efficiency of electron and photon beam output partially by orders of magnitude. An overarching philosophy of this cluster is an “all-plasma” approach, i.e. where suitable using plasma not only for the accelerator, but also for the injector, for diagnostics and for radiation sources.

Here, we highlight six major thrusts or themes:

1. Multi-pulse LWFA. This thrust develops resonant excitation by multiple lower power laser pulses. This may allow using highly efficient high-repetition-rate laser drivers such as thin disk or fibre lasers, (optically) tailored plasma channels, and plasma photo-cathode injectors.
2. Hybrid LWFA $\Rightarrow$ PWFA. This approach combines the best of LWFA and PWFA, centrally utilising high-current electron beams from compact LWFA stages as drivers for PWFA stages. This seeks to unlock key advantages of PWFA such as dephasing-free, practically diffraction-free, dark current-free operation and an abundance of ionisation-based injection mechanisms.
3. Plasma photo-cathodes. Fully or partially decoupled ionisation injection schemes such as the Trojan Horse plasma photo-cathode, plasma torch, 2PII, WII, and

multi-pulse injection schemes, etc., will be developed. A key prospect is the controlled production of ultra-low-emittance, ultra-high-brightness electron beams as the foundation for high-performance applications.

4. Plasma-based metrology and diagnostics. The ultra-low-emittance, ultra-high-brightness beams enabled by the above schemes exceed the metrology capabilities of many established diagnostics. Recent innovations show that ionisation-based and plasma-based detector and amplifier techniques allow minimally invasive, ultra-high sensitivity diagnostics, which will be developed.
5. Plasma undulators and advanced radiation sources. The above-listed technologies combined aim to realise high-efficiency, high-repetition-rate, and ultra-high-brightness electron beams in compact setups. These are ideally suited for driving light sources. Plasma wigglers/undulators (betatron/ICL), ICS, and XFEL based on ultra-high-brightness electron beams will be developed.
6. Plasma-based sources and targets. The above technologies partially require very specific, often multi-component plasma sources with selective ionisation capability and (plasma) density profiles. This theme will develop the corresponding sources in close collaboration with the cluster on plasma components and systems.

## IX. Training, Outreach & Dissemination

**Keywords:** dissemination, outreach, education, public engagement, knowledge transfer, training, user workshops

This cluster will ensure that EuPRAXIA maintains a high profile within the international landscape of scientific facilities. It will promote its activities with the aim of attracting users and collaborators, and help to disseminate its research results to the wider scientific community. A dedicated effort in outreach and public engagement will aim at raising awareness of EuPRAXIA's research goals and its key technologies, maximising its impact on science and society. Moreover, a coordinated training and education programme will ensure a continuous supply of highly skilled scientists and engineers to develop, operate, and continuously optimise the diverse sites and excellence centres of EuPRAXIA.

Publications: Regular contact with all participating partners provides a continuous stream of news articles that will be posted on the central website ([www.EuPRAXIA-project.eu](http://www.EuPRAXIA-project.eu)). All news will be further promoted through social media and targeted online and print articles. News topics include (but are not limited to) research results, journal publications, technological innovations, events, and position vacancies. Items of particular relevance will be selected for publication as feature articles in magazines. The newsletter *The EuPRAXIA Files* is a collection of abstracts from research articles that are relevant to the EuPRAXIA project and will continue to be published three times a year. It will be distributed to all the members of the EuPRAXIA collaboration and made available via the website to disseminate the latest advances in wakefield acceleration and its applications.

Outreach events and educational resources: EuPRAXIA partners will be encouraged to hold public events showcasing the achievements in plasma acceleration. Central support in the form of education material and demo setups will be provided. Based on experiences gained in past pan-European events, a combination of social media campaigns and video live-streams, will be used to engage several institutions at a time and maximise reach and impact. Events set up around a specific theme – such as Physics of Star Wars or Marie Curie Day –, innovative educational materials – like the augmented reality app AcceleratAR, the computer game Surfatron or poster resources that explain the science and technology of EuPRAXIA – will be made available and used to communicate the science of EuPRAXIA to a range

of target audiences and ensure high visibility in the media. The cluster leader will continue to present EuPRAXIA findings at relevant international conferences via the project TEAM based at the Cockcroft Institute.

Training: The cluster members are very experienced in organising complementary skills schools for researchers at different career stages, topical workshops on selected R&D challenges, and international schools that train the next generation of researchers in the science and technology of EuPRAXIA. Online resources such as lectures for undergraduate and postgraduate students, as well as science short films targeting the general public will be part of the wider communication portfolio of EuPRAXIA. Its established YouTube channel will be used to disseminate these materials and coordinate the wider training efforts. Educational material from EuPRAXIA partners will continue to be made available via a dedicated section on the project website. Additionally, the cluster will work on the development of a training program foreseen as one of the user access modes at the future EuPRAXIA facility. In this context, collaborations and connections will be set up with universities and research institutes that can be developed into a full training scheme during the infrastructure's operational phase.

User workshops: Workshops and discussion sessions with potential future users will be organised throughout the different phases of EuPRAXIA. These will aim, first, at attracting future facility users and comparing the users' needs with EuPRAXIA's foreseen capabilities. During the operation phase, such regular user meetings will, in particular, also allow different user groups to exchange experiences, while providing the host sites with feedback on machine performance and possible improvements.

## X. Layout & Implementation

**Keywords:** control system, data acquisition, data analysis and storage, software and hardware development for operation, vacuum, cooling, power distribution, water, site construction, ventilation, support labs, laser safety, radiation safety, general safety, access system

The “Layout & Implementation” cluster covers several topics related to the control and operation, infrastructure, and safety of the future EuPRAXIA machine:

Command control system: The control system and control room for the two EuPRAXIA construction sites will be designed and implemented, with close collaboration with the technical groups at the EuPRAXIA host sites. Moreover, the integration of the laser and accelerator control into one consistent system will be a critical challenge particular to EuPRAXIA.

Data acquisition, analysis, and storage: A robust and reliable data acquisition, analysis, and storage infrastructure suitable for user operation needs to be set up for all EuPRAXIA sites. In this context, it will heavily rely on the extensive experience of some of the project partners in the design and building of DAQ systems, with particular efforts placed on developing fast diagnostic tools and beam analysis techniques based on GPU platforms to better adapt the data acquisition process to plasma-accelerator-based machines. Additionally, the needs and possibilities for data analysis and storage at the future EuPRAXIA facility need to be investigated and assessed, considering, among others, EU policy on open data access. Depending on the results of this investigation, a data analysis and storage system will be designed and implemented for EuPRAXIA. Strong interaction with the clusters on theory and simulation and diagnostics will be considered for this topic.

Infrastructure: The overall infrastructure of the two EuPRAXIA machine sites as well as the experimental support sites that require the setup of sizable, new test beamlines for EuPRAXIA will be targeted. Besides the building design, the utilities of

each new facility need to be considered, including ventilation, heating, air conditioning, electrical power distribution, cooling, and fresh water systems. The cooling and conditioning system needs to be designed and tested carefully, while new concepts for ultra-high-precision water cooling will be explored. For the electrical distribution system, feasible solutions assuring high stability will need to be developed according to best-practice rules. Additional responsibilities include the design and testing of the vacuum system as well as the setting up of a strategy for module and component testing during the construction and commissioning phase. Moreover, the cluster will also evaluate the necessary support laboratories and their infrastructure needs that must be foreseen both for the commissioning phase as well as for the user facility operation. This work will be carried out in close collaboration with the technical groups at the host sites as well as other experienced consortium facilities.

Safety: A safety infrastructure for each of the EuPRAXIA experimental sites will be designed and set up together with local technical groups responsible for safety aspects at the host institutes. This will include, among others, the implementation of interlock and access systems, but also safety procedures for users, safety training, etc. Particular emphasis will be placed on laser safety, coordinated closely with the work cluster on laser technology, and radiation safety. The latter will require detailed radiation protection simulations to be carried out and radiation monitoring to be designed and implemented into the EuPRAXIA machine sites. Because of the short timescale of plasma-generated electron beams and hence any generated radiation, the effects of how electromagnetic pulses in the EuPRAXIA machine can affect the surrounding experimental instrumentation will also be investigated as a potential safety risk.

### 3.3.2 EuPRAXIA Construction and Excellence Sites

The EuPRAXIA facility will be constructed in two central “construction sites”:

1. The EuPRAXIA site with a *beam-driven plasma accelerator, FEL, and other applications*. This site will feature a 1 GeV compact RF linear accelerator, based on the CERN-developed X-band technology. Initially, it has conventional undulators for 1 GeV FEL operation.
2. The EuPRAXIA site with a *laser-driven plasma accelerator, FEL, and other applications*. This site will feature an RF photo-injector, a laser-driven plasma injector, conventional undulators, and three major high-power lasers that drive the plasma accelerator. This facility is designed for producing 5 GeV electron beams and the according FEL radiation.

The two construction sites will be located at existing facilities to maximise reusing already available equipment. As explained before, this approach with two construction sites with complementary technological paths will establish a technical competition but avoids an institutional competition in Europe. There are a number of scientific and technical challenges that are particularly important and difficult. The pursuit of these problems is best performed at EuPRAXIA ‘excellence centres’. The already existing equipment in those locations can be upgraded to the EuPRAXIA needs, local teams can be best integrated into the project work, and the construction sites can focus in parallel on the optimal preparation of EuPRAXIA facility construction and later user operation. These excellence sites will be crucial during the R&D and TDR phases of the project but also during construction (e.g. component testing) and operation (testing and preparation of facility upgrades). They should therefore be operational for the TDR phase but are also a long-term investment into the capabilities of the European research infrastructure landscape, both for EuPRAXIA and other needs. The following excellence sites are envisaged at the moment:



**Fig. 3.3.** Overview of the distributed facility concept for EuPRAXIA proposing two flagship construction sites and five supporting excellence centres.

- an excellence centre for application beamline R&D, prototyping, and testing,
- an excellence centre for laser-plasma acceleration and 1 GeV FEL R&D, prototyping, and testing,
- an excellence centre for plasma accelerator and high-repetition-rate developments,
- an excellence centre for theory and simulation, and
- an incubator for lasers and concepts at ELI Beamlines.

The scheme of the two construction sites, the excellence centres, and the connection to other major European research infrastructures and industry is visualised in Figure 3.3. In the following, we describe the two construction sites in more detail. Additional information on the excellence centres and possible candidates can be found in Chapter 3.6.

### EuPRAXIA Beam-Driven Plasma Accelerator Site

The EuPRAXIA concept of the beam-driven plasma accelerator site is shown in Figure 3.4. The schematic diagram lists the major components of the plasma accelerator, namely, the RF injector for producing electron beams, the RF linear accelerator for accelerating the electron bunch that drives the wakefield in the plasma, and two

plasma accelerators, one aimed at high charge (compromising quality) and one aimed at high beam quality (compromising charge). A line of conventional undulators is used to produce FEL radiation and to send X-rays to two user areas. Alternatively, the high-quality beam can be used to drive an inverse Compton scattering (ICS) gamma-ray source. The high-charge plasma accelerator is used for producing positrons and electron beams for high energy physics detector tests and preparational studies for a plasma linear collider. A full technical description of all components and system simulations can be found in Part 4.

### EuPRAXIA Laser-Driven Plasma Accelerator Site

The EuPRAXIA concept of the laser-driven plasma accelerator site is shown in Figure 3.7. The accelerator infrastructure includes high-power lasers for driving a 5 GeV plasma acceleration, RF and/or plasma injectors for producing electron beams at 150–500 MeV, and two high-energy plasma accelerators for high charge or high beam quality. A conventional undulator line produces X-ray FEL pulses from 1–5 GeV electrons and delivers them to two user areas. In addition, there is a user area for life science, material studies, and medical X-ray imaging. Two other user areas are designed for (1) an ultra-compact positron source and its imaging capabilities and (2) a table-top electron test beam area, e.g. for detector tests from high-energy physics.

The laser-driven plasma accelerator facility in EuPRAXIA will allow the testing of various concepts and approaches for producing high-quality beams in a laser-driven plasma accelerator. The variability of the infrastructure will provide important risk mitigation towards achieving the performance goals in EuPRAXIA. A full technical description of all concepts, components, and system simulations can be found in Part 4.

### 3.4 EuPRAXIA Construction Footprint (Towards Accelerator Miniaturisation)

EuPRAXIA is based on a large-scale infrastructure design but reduced in size over conventional technology by a factor of 3 at least. It pushes one of the biggest strengths of plasma-accelerator technology in a realistic step-wise approach.

It was one of the important goals of the EuPRAXIA design study to demonstrate the benefits of a facility that is based on plasma accelerators for total facility size and cost. Here, we discuss advantages in total facility footprint when including estimates for all relevant infrastructure, like laser laboratories, shielding walls, beam tunnels, conventional undulators, space estimates for X-ray optics, and user laboratories.

To address this task, a database of required components and their space requirements has been set up and was filled with input from collaboration members. The total footprints were calculated both in facility length but also in terms of required surface area. The summary of obtained facility lengths is shown in Table 3.3 where length estimates of RF-based facilities are also given in comparison. These latter values have been guided by existing facilities; for the SRF case we haven taken FLASH (DESY) as an example, whereas SwissFEL is a good example for C-band technology. EuPRAXIA aims at a realistic stepwise approach of miniaturisation. It is based on a large-scale infrastructure design but reduced in size over conventional technology by a factor of 3 at least, as listed in Table 3.3 and also visualised in Figure 3.6. EuPRAXIA therefore pushes one of the biggest strengths of plasma-accelerator technology. Once the expected size reduction by a factor of 3 has been demonstrated, a

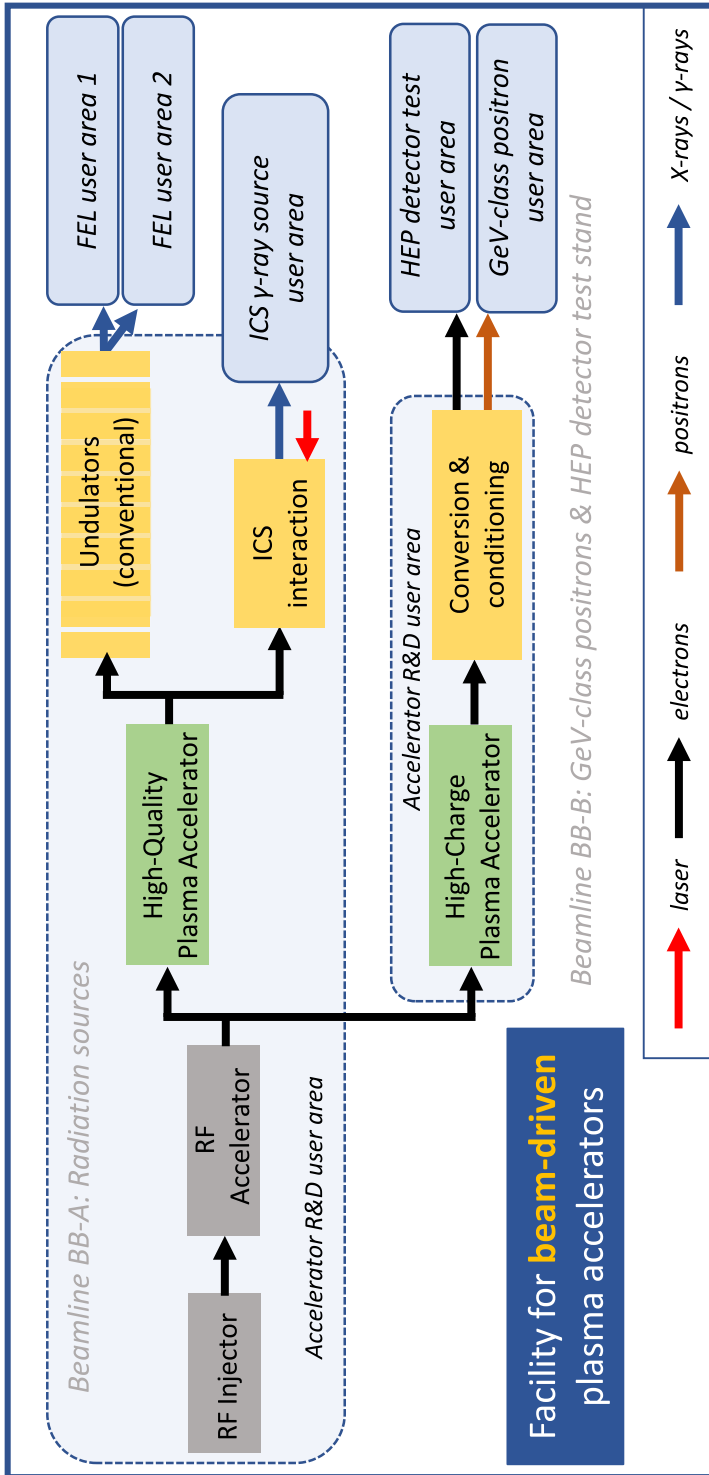


**Fig. 3.4.** Schematic facility layout for the flagship construction site based on beam-driven plasma acceleration.

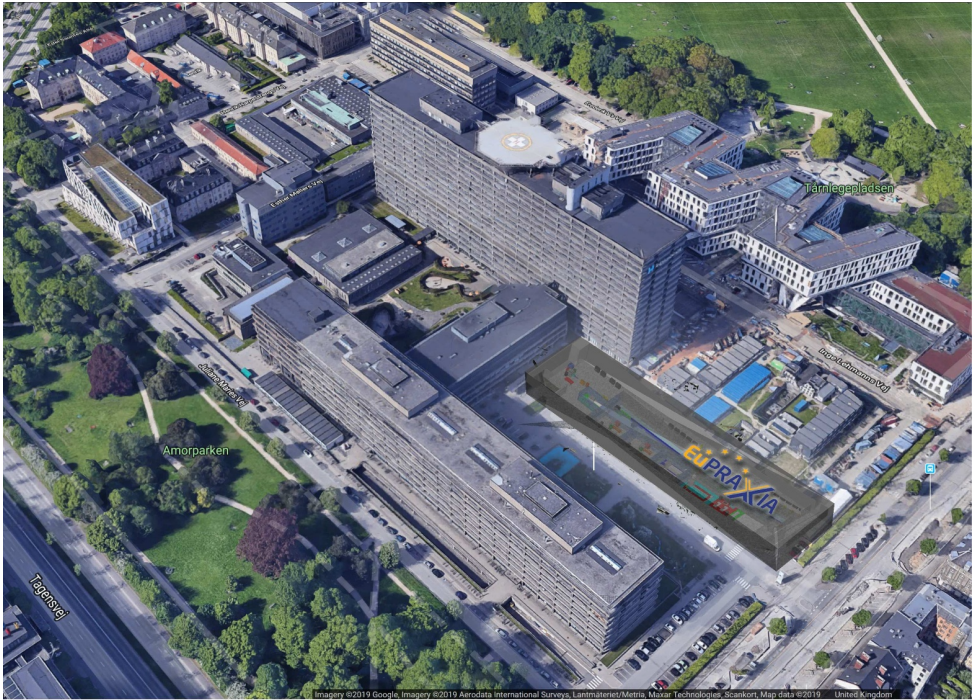


**Fig. 3.5.** Size comparison of the EuPRAXIA infrastructure in relation to a hospital in Copenhagen. The entire EuPRAXIA facility (up to 1 GeV beam energy) would fit onto the parking lot of the building. Note further that the facility footprint could be even smaller if a multi-storey building design is considered (image adapted from Google Maps).

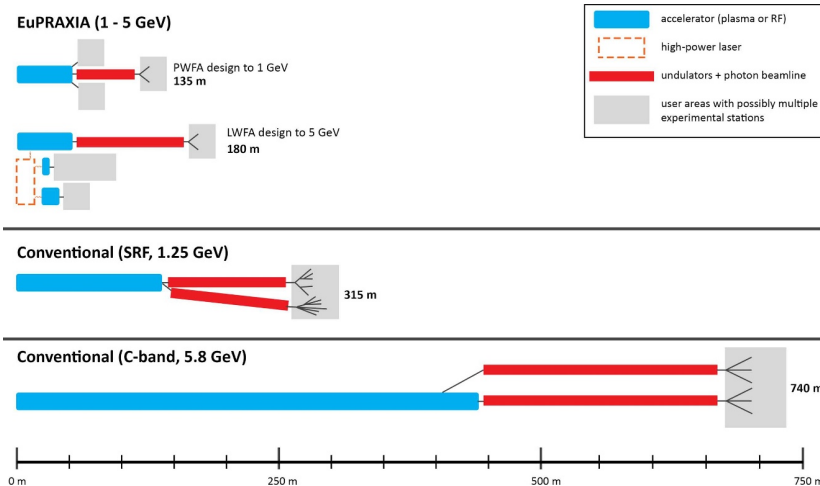


**Fig. 3.6.** Comparison of the expected EuPRAXIA machine length with parameters for facilities of equivalent beam energies based on conventional RF-technologies [157,158]. The transverse size is not to scale. It is noted that such facilities tend to offer FEL performance parameters which are not achievable with the EuPRAXIA design. Gains in size must therefore be put into the context of performance limitations with the EuPRAXIA approach.

**Table 3.3.** Comparison of the expected EuPRAXIA machine size with parameters for facilities of equivalent beam energies based on conventional RF-technologies [157,158]. It is noted that such facilities tend to offer FEL performance parameters which are not achievable with the EuPRAXIA design. Gains in size must therefore be put into the context of performance limitations with the EuPRAXIA approach. The presented EuPRAXIA cases include scenarios with an RF injector to create the electron beam (external injection) as well as an all-optical setup with a plasma injector generating the beam.

	Acc. length		Application length			Total length
	RF / laser	Plasma	Undulators	Photon beamline	User areas	
EuPRAXIA-PWFA ext. injection (1 GeV)	46 m	13 m	39 m	22 m	15 m	135 m
EuPRAXIA-LWFA ext. injection (1 GeV)	42 m	17 m	39 m	22 m	15 m	135 m
EuPRAXIA-LWFA ext. injection (5 GeV)	42 m	17 m	61 m	40 m	15 m	175 m
EuPRAXIA-LWFA all-optical (5 GeV)	20 m	17 m	61 m	40 m	15 m	153 m
Conventional (SRF, 1.25 GeV)	144 m		171 m			315 m
Conventional (C-band, 5.8 GeV)	440 m		300 m			740 m

continuation of the miniaturisation process towards an even more compact facility will be pursued. For example, external and RF-based injectors might be eliminated at some point, more compact undulator designs might become available, and also, laser technology could reduce in size and complexity. A decrease in user area sizes, on the other hand, will not be strived for, as no improvement in compactness is envisaged without having to reduce experimental possibilities significantly. Overall, a size reduction factor for the accelerator of 10 and even 20 thus seems ultimately feasible at high beam energy.

It is concluded that a significant factor of 3 in the reduction of the total facility size has been achieved with the EuPRAXIA design.

### 3.5 EuPRAXIA Digital Footprint (Data Sharing and Management)

EuPRAXIA proposes a data management strategy that will encourage the development of standards and common formats, improve data sharing and provide robust structures for data acquisition, analysis and storage within its facilities.

Accelerator science and, in particular, plasma-accelerator research is a data-intensive field. Experimentally, even compact plasma-accelerator beamlines tend to feature between five and fifteen different diagnostics, each taking images or other measurements with a repetition of a few hertz (with much higher rates expected for EuPRAXIA). This easily leads to the acquisition of multiple petabytes of data for a single experiment. On the theoretical side, plasma acceleration studies are heavily reliant on particle-in-cell (PIC) simulations. Typically run as massively parallelised calculations on CPU- or GPU-based systems at supercomputing facilities, these computational methods also produce several tens to hundreds of gigabytes of data per simulation.

In the past, most research groups have handled and evaluated their data, both experimental and computational, individually as challenges in accessibility (large data volumes, not all analysis / simulation software open source) and reusability (multiple possible techniques and setups to be studied, multiple different simulation codes)

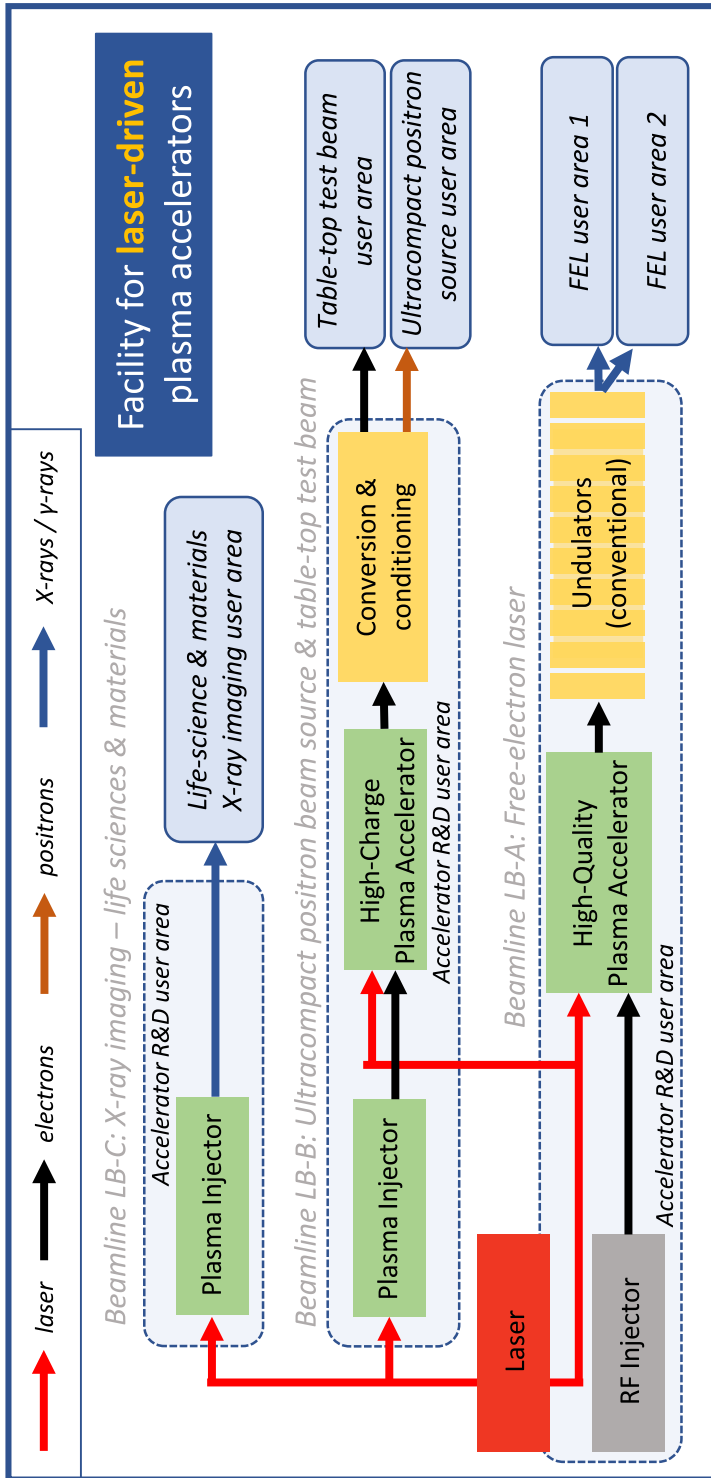


Fig. 3.7. Schematic facility layout for the flagship construction site based on laser-driven plasma acceleration.

have limited the possibility of data sharing among groups and institutes. With the European project EuPRAXIA, however, there is now a unique opportunity to change and optimise this way that data is handled in the field towards a more standardised and more “FAIR” approach [159]. Involving most plasma-accelerator groups in Europe (and worldwide) as project partners or more informal collaborators, EuPRAXIA could be a key factor in bringing together the research community and developing a strategy on how data is collected, evaluated, communicated, and shared in plasma-accelerator research. Such an effort to drive the community’s data management needs and contribute to standards directly from within the research field would also clearly be in line with the European e-IRG Roadmap 2016 recommendations aimed at setting up a common organisation of the electronic infrastructure across Europe in the near future [160].

Some specific points that should be included in EuPRAXIA’s digital strategy are the following:

**Benchmarking:** A multitude of different codes and computational tools exist in plasma-accelerator research. Following on from efforts started during the conceptual design study, the benchmarking of simulation codes with one another as well as with experimental data should be carried out. Moreover, more advanced data science techniques, such as machine learning, could be considered as additions to typical tool sets in the future. With large amounts of related and well-characterised (see next point) test data, EuPRAXIA would provide a great basis for such pursuits.

**FAIR principles:** Not only does the EuPRAXIA Consortium comprise a wide range of experimental and theoretical experts in accelerator, photon, plasma, and laser science, but also, a good number of simulation codes are developed by project partners. As such, the collaboration is in an excellent position to start the discussion on how plasma-accelerator data could be made more consistent with the FAIR (Findable – Accessible – Interoperable – Reusable) principles [159,161]. This should include, for example, the development of common computational formats and standards to improve data characterisation and identification, but also, a better alignment of experimental and computational data would be beneficial. Figure 3.8 highlights several further possible angles to this effort.

**Data acquisition, analysis, and storage:** An important aspect of the design and implementation of the future EuPRAXIA research infrastructure will be the setup of robust data acquisition, analysis, and storage structures for the EuPRAXIA sites, especially those active as user facilities. The realisation of such features will not be trivial in the case of EuPRAXIA requiring the combination of standards, procedures, and capabilities from both laser and accelerator-based infrastructure operation. It will thus set a precedent for future facilities of its kind.

**Data sharing:** An interesting goal for EuPRAXIA’s digital strategy could be the development of a system for sharing and managing data more efficiently within the consortium. Especially during the project’s technical design and construction phases, a large number of studies and measurements will need to be carried out within a limited set of resources. One strategy for tackling this challenge, which is described in more detail in Part 5, will be to design and plan experiments more effectively to consider several research questions in the same measurements. A similar approach, however, could also be employed directly to the data itself by considering data sharing and its possible use for multiple purposes across research groups. Taking a computational example, a single PIC simulation of a multi-GeV laser-driven plasma accelerator stage may cost a few hundred thousand CPU core hours and may be carried out with the aim of studying the dynamics of the injected electron beam. By also sharing this very rich data set with researchers interested in the drive laser evolution, the behaviour of the background plasma,

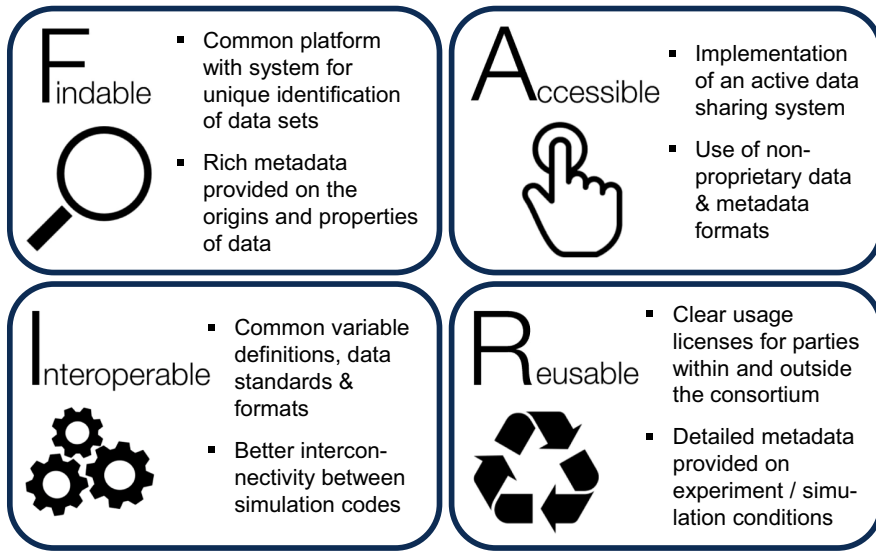


**Fig. 3.8.** Summary of some key strategies to make data management within the EuPRAXIA collaboration more consistent with the FAIR principles [159]. Many of the aspects listed could also have beneficial effects for the plasma-accelerator research community in general (image based on: Sungya Pundir, <http://www.exeter.ac.uk/research/researchdatamanagement/open/fair/>).

or the effectiveness of the target design, resources can be used more efficiently and possibly better results achieved. A first proposed step to implement an appropriate infrastructure for this endeavour will be the setup of a specialist panel to assess specific challenges and possible implementation paths.

**European initiatives:** Finally, besides EuPRAXIA's own initiatives and activities, it will also be important to evaluate how the project can work within and towards the already existing European initiatives for data management. Examples of particular relevance include, among others, the European Open Science Cloud for data storage and sharing as well as the EU Data Infrastructure for high-performance computing [89,160].

Such a digital strategy could be pushed and developed in detail particularly by the technical cluster on theory and simulation (see Sect. 3.3.1) and the excellence centre for theory and simulation (see Sect. 3.3.2) that are proposed for EuPRAXIA.

### 3.6 Matching EuPRAXIA Needs and Existing Facilities / Capabilities in Europe

The European research area features unique infrastructures and capabilities. Those can match all the needs of the EuPRAXIA project. Attractive implementation options have been considered during the EuPRAXIA CDR.

The original goal of the EuPRAXIA design study was a site-independent design of a European plasma-accelerator facility. During the course of the design work, it became apparent that a number of outstanding facilities exist in Europe, that they would be suited to host parts of EuPRAXIA, and that those facilities would also be interested in considering their infrastructure as a EuPRAXIA site option. Therefore, some work has been performed to match the EuPRAXIA concept to existing capabilities and infrastructures in Europe.

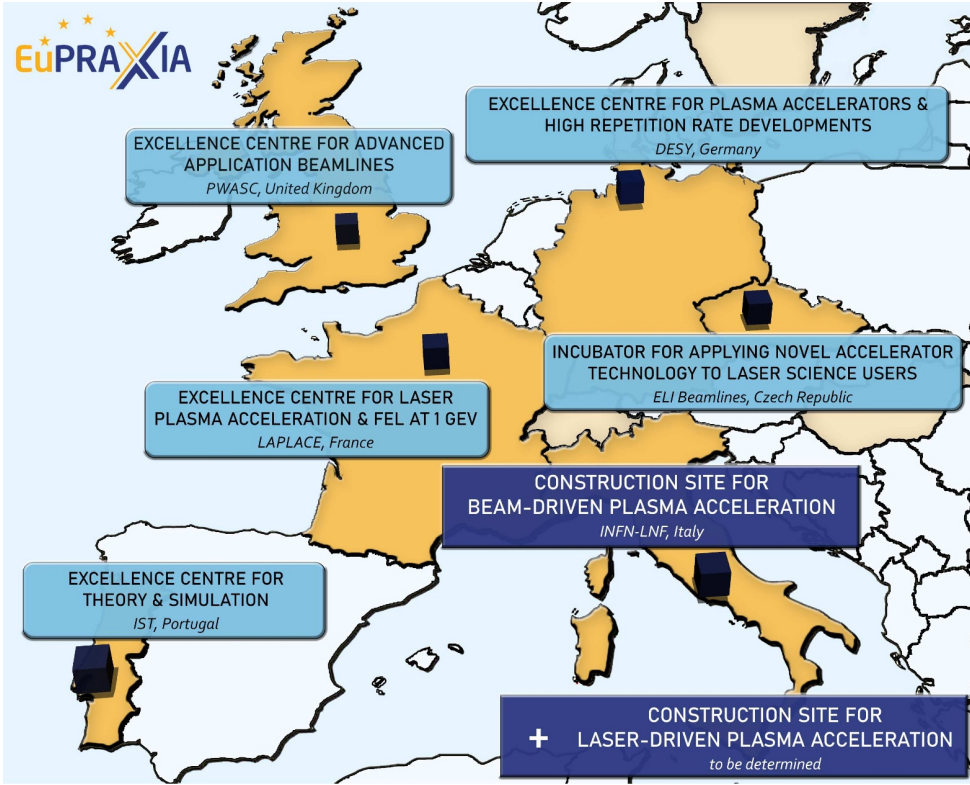


**Fig. 3.9.** Map showing the proposed locations of the different construction sites and excellence centres at existing facilities in Europe. For the construction site for laser-driven plasma acceleration, several possible locations are under consideration; further details can be found in Section 3.6.7.

It is noted that all the considerations here do not imply any commitment of the laboratories involved but are preliminary proposals. Those options can be followed up on if the relevant decision makers in the laboratories, the national funding agencies, and the EU commission would decide so.

In the following sections, a few of the implementation options are being described in more detail. A short overview of the proposed site and centre locations is shown in Figure 3.9.

### 3.6.1 INFN-LNF: Construction Site for Beam-Driven Plasma Acceleration

In this paragraph, we introduce the EuPRAXIA@SPARC\_LAB project [162,163], intended to put forward the Laboratori Nazionali di Frascati (LNF) of the Italian Istituto Nazionale di Fisica Nucleare (INFN) as host of one of the EuPRAXIA European pilot user facilities. The new infrastructure is conceived to be able to accommodate in principle any machine configuration resulting from the EuPRAXIA design study that will find within the new LNF infrastructure the necessary technological background. Nevertheless, a particular emphasis has been addressed to the design of machine in the beam-driven configuration (PWFA) as a complementary facility to the laser wakefield acceleration (LWFA) configuration, developed elsewhere.

**Table 3.4.** Parameters achieved with the start-to-end simulations for the EuPRAXIA@SPARC\_LAB facility.

	Units	1 GeV PWFA
<b>RMS Energy spread</b>	%	1.1
<b>Peak current</b>	kA	2.0
<b>Bunch charge</b>	pC	30
<b>RMS bunch length</b>	$\mu\text{m}(\text{fs})$	3.82(12.7)
<b>RMS normalised emittance</b>	mm mrad	1.1
<b>Slice energy spread</b>	%	0.034
<b>Slice normalised emittance (x/y)</b>	mm mrad	0.57/0.615
<b>Undulator period</b>	mm	15
<b>Undulator strength <math>K(a_w)</math></b>		1.13(0.8)
<b>Undulator length</b>	m	30
<b><math>\rho</math> (1D/3D)</b>	$\times 10^{-3}$	2.5/1.8
<b>Radiation wavelength</b>	nm(keV)	2.98(0.42)
<b>Photon energy</b>	$\mu\text{J}$	6.5
<b>Photons per pulse</b>	$\times 10^{10}$	10
<b>Photon bandWidth</b>	%	0.9
<b>Repetition rate</b>	Hz	10–100

In the PWFA scenario, in which a high-charge (200 pC) electron bunch driver excites the plasma wave ( $\sim 300 \mu\text{m}$ ) to accelerate a low-charge witness bunch (20 pC), the peak accelerating field in the non-linear regime is limited to twice the value of the peak decelerating field within the bunch (transformer ratio  $R_T=2$ ). Therefore, the maximum possible energy gain for a trailing bunch is about twice the incoming driver energy. In this regime, a driver bunch energy of 500 MeV is enough to accelerate the witness bunch up to 1 GeV. This will be the main goal of the EuPRAXIA@SPARC\_LAB project. In the second phase, it will be also possible to run the machine in a configuration with a transformer ratio larger than 4 so that the 5 GeV threshold for the witness beam will be also achievable with a 1 GeV driver and witness injection energy.

The core of the project will be the plasma accelerating module that will consist of a 0.5 m long, 0.6 mm diameter capillary tube in which the plasma is produced by a high-voltage discharge in hydrogen. The accelerating gradient is expected to be in excess of 1 GV/m.

Another fundamental component included in our design is the X-band accelerating technology adopted for the 1 GeV RF drive linac [164]. This choice keeps the overall linac length compact, taking advantage of the high gradient (up 80 MV/m) operation of the X-band accelerating structures.

EuPRAXIA@SPARC\_LAB has been designed to fulfil the 1 GeV EuPRAXIA parameters [220]. To support our design, we have performed start-to-end simulations. In Table 3.4, the achieved parameters are listed (more details also in Chaps. 17 and 24.1). The reported performances show that EuPRAXIA@SPARC\_LAB design is expected to meet the challenging requests for the SASE-FEL synchrotron radiation sources.

To meet the EuPRAXIA requirements, some preparatory actions are underway at LNF:

- provide LNF with a new infrastructure with the size of about  $154 \text{ m} \times 35 \text{ m}$ , as the one required to host the EuPRAXIA facility;

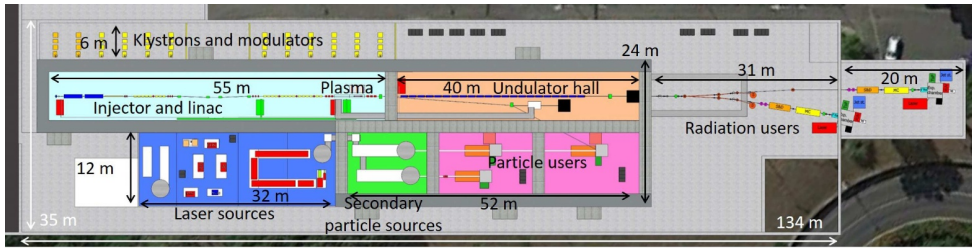


**Fig. 3.10.** Layout of the EuPRAXIA@SPARC\_LAB infrastructure.

- design and build a 0.5–1 GeV, X-band RF linac and an upgraded FLAME laser [165] up to the 0.5 PW range;
- design and build a compact FEL source, equipped with a user beamline at 2–4 nm wavelength, driven by a 1 GeV electron bunch.

The EuPRAXIA@SPARC\_LAB project requires the construction of a new building to host the linac, the FEL, the experimental room, and the support laboratories. The executive project of the building is now in preparation; the construction is expected to start in 2021 and to be completed by mid-2023. The new facility will cover approximately an area of 5,000 m<sup>2</sup>. The layout of the EuPRAXIA@SPARC\_LAB infrastructure is schematically shown in Figure 3.10.

From left to right, one can see a 55 m long tunnel hosting a high-brightness 150 MeV S-band RF photo-injector equipped with a hybrid compressor scheme based on both velocity bunching and magnetic chicane. A chain of high-gradient X-band RF cavities will provide the energy boost from 150 MeV up to a maximum of 1 GeV. At the linac exit, a 5 m long plasma-accelerator section will be installed, which includes the plasma module and the required matching and diagnostics sections. In the downstream tunnel, a 40 m long undulator hall is shown, where the undulator chain will be installed. Further downstream, after a 12 m long photon diagnostic section, the user hall is shown with two end stations. The commissioning of the FEL beamline is expected to be completed by the end of 2026. An additional  $\gamma$ -ray Compton radiation source and a positrons source can be later installed in the other shown beamlines. The upper room in the figure will be dedicated to host klystrons and modulators to drive the X-band linac. In the lower light-blue room will be installed the existing 300 TW FLAME laser, eventually upgraded to 500 TW. The plasma-accelerator module can be driven in this layout either by an electron bunch driver (PWFA scheme) or by the FLAME laser itself (LWFA scheme). A staged configuration of both PWFA and LWFA schemes will be also possible to boost the final beam energy beyond 5 GeV. In addition, FLAME is supposed to drive, in the green room, electron and secondary particle sources that will be available to users in the downstream 30 m long user area.

The local collaboration is carried out with the support of groups from INFN (LNF, LNS, Milano, Roma, Napoli), the Universities of Rome “La Sapienza” and “Tor Vergata”, the University of Milan, ENEA Frascati, CNR-INO Pisa, and the CERN CLIC team. Associated partners are also the University of California at Los Angeles (UCLA) and the Hebrew University of Jerusalem (HUJ). A strong collaboration with the FLASH\_Forward group at DESY will provide additional expertise in the field of PWFA acceleration techniques.

### 3.6.2 LAPLACE – France: Excellence Centre for Laser-Plasma Acceleration and 1 GeV FEL

Following discussions in the frame of the French GDR APPEL group (<http://gdr-appel.fr/>), a proposal to prepare a joint project emerged within the French laser-plasma-acceleration community. The present contribution to EuPRAXIA is based on these discussions and will structure future activities within the French laser-plasma community. The contribution is based on two projects: the Laser PLasma Acceleration CEntre (LAPLACE) bringing together mainly the Laboratoire d’Optique Appliquée (LOA), the Laboratoire de l’accélérateur linéaire (LAL), and SOLEIL, as well as the Prototype Accelerator Laser plASma (PALAS) project including the Laboratoire de l’accélérateur linéaire (LAL), the Laboratoire de Chimie Physique (LCP), the Laboratoire Le Prince Ringuet (LLR), and the Laboratoire d’Optique Appliquée (LOA). The two projects offer a complementary and joint research and development approach. LAPLACE proposes to implement high-repetition-rate laser-plasma-based accelerator developments and high-energy laser-plasma-acceleration studies with associated applications, such as a free-electron laser and pump-probe spectroscopy with X-rays or electrons. The PALAS project, on the other hand, aims to build an accelerator test facility to prototype a GeV multi-stage laser-plasma accelerator. Both the LAPLACE and PALAS projects are currently led by LOA and LAL in association with an open list of partners, including SOLEIL, LLR, the Laboratoire de Physique des Gaz et Plasmas (LPGP), LCP, and CEA. The LAPLACE project aims at developing these two facilities dedicated to laser-plasma accelerators and applications with the following specific aims:

**LAPLACE:** Development of high-repetition-rate LPAs producing tens-of-MeV, femtosecond-scale electron bunches at a minimum of 100 Hz repetition rate as well as high-energy LPAs driven at few-Hz repetition rates with dedicated beam-lines for an FEL and FLASH radiobiology (NanotRad [166]) applications.

**PALAS:** A laser-plasma-accelerator facility for GeV-class laser-plasma accelerator prototyping based on two laser-plasma accelerating sections driven by a 500 TW class laser system with a minimum repetition rate of a few Hz.

The two projects will rely on the upgrade of three main existing facilities, hosted in a renovated building with radiation shielding. In addition, the long focal area of the Apollon laser facility, designed by the CILEX Consortium (LLR, CEA, LULI, LOA, LPGP, Soleil, LAL, etc.), will provide a tool for testing multi-stage, PW-scale laser-driven electron acceleration in plasma.

The proposal is centred on solving several technological bottlenecks and will address optimisation studies with the longer term goals of demonstrating a multi-stage laser-plasma accelerator and short-wavelength FEL gain. It provides an answer to the necessity of rapid prototyping for the EuPRAXIA project, addressing issues such as (i) the reliability of a GeV-class multi-stage laser-plasma accelerator, (ii) the demonstration of FEL gain with a  $> 500$  MeV laser-plasma driver and, finally, (iii) exploring the possibility of laser-plasma acceleration at high repetition rate. Increasing the repetition rate is presently the only way to reach average currents comparable to state-of-the-art room-temperature electron RF accelerators. In the meantime, several other technological challenges must also be addressed in this prototyping phase.

As mentioned above, the LAPLACE and PALAS projects will be developed as an upgrade of three main existing facilities. For the LAPLACE facility, the *Salle Noire* – a 1 TW, kHz-repetition-rate laser driving a few-MeV laser-plasma acceleration beam-line – will be upgraded to a 10 TW laser system with a minimum repetition rate of 100 Hz. In addition, the *Salle Jaune* will be upgraded to a 500 TW-class driver. Depending on the funding, a larger building may be available to provide enough

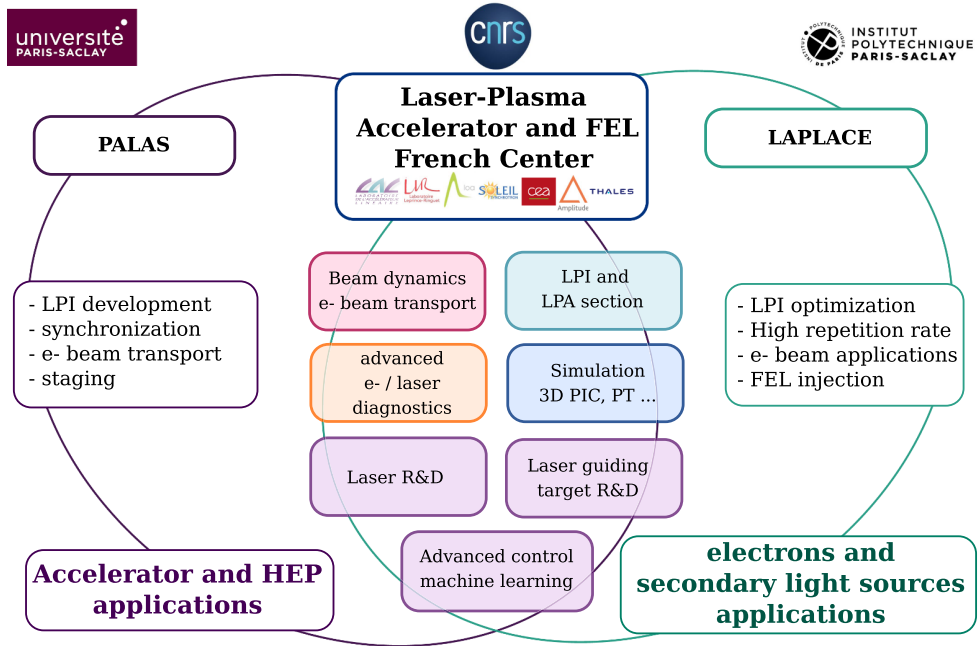


**Fig. 3.11.** Overview of the different partners and activities involved in the LAPLACE and PALAS projects proposed to form the excellence centre for laser-plasma acceleration and a 1 GeV FEL.

space for a short-wavelength FEL. The PALAS project will be based on the existing EXALT laser driver and upgraded pump laser with the last amplifier delivering 15 J to a PW-class optical compressor. The PALAS project could be hosted in the old GeV linac of the LAL injection hall at the DCI ring.

The French scientific and industrial communities have an important role to play in the EuPRAXIA project for the LPA-driven FEL and the development of optimised laser drivers for the optimisation of laser-driven plasma injectors and accelerator stages. The French contribution in the 2020–2025 period to the EuPRAXIA prototyping phase should rely on existing, but *upgraded* facilities with well-adapted technical support. For an efficient and significant contribution, the facilities should be dedicated to LPA development.

The LAPLACE and PALAS projects rely on the LOA and LAL sites for major developments in the EuPRAXIA framework. In addition to LOA and LAL expertise, the two projects and their contribution as an excellence centre to EuPRAXIA will benefit from an exceptional environment, with the accelerator expertise in IRFU-CEA, research and development on laser guiding and plasma components in LPGP, the “Maison de la Simulation” research laboratory for numerical simulations, and, in particular, the SMiLEI [167] team and the Centre for Data Science of the Université Paris Saclay. In addition, proximity and long-term scientific collaborations with the world-leading high-intensity laser industry is strengthening a French contribution to EuPRAXIA to push laser driver developments further. In this particular aspect, a common laboratory is being set up to develop advanced control and expertise on high-intensity laser systems for laser-plasma acceleration. Finally, the ambition to structure the French community is envisioned to bring higher visibility at the European and international level.

In the short term (2020–2023), the LAPLACE and PALAS projects’ research work will be organised in several work packages: WP1 to 5 are foreseen to work with existing facilities and are potentially part of the EuPRAXIA clusters. Completing this part of the project might require relatively modest additional funding that could be obtained via regional or national grants.

**Work Package 1: Laser-plasma injector** – relevant to the EuPRAXIA cluster on plasma components and systems;

**Work Package 2: Numerical simulation** – relevant to the EuPRAXIA cluster on theory and simulation;

**Work Package 3: Electrons beam diagnostics** – relevant to the EuPRAXIA cluster on diagnostics;

**Work Package 4: Advanced control command** – relevant to the EuPRAXIA cluster on layout and implementation;

**Work Package 5 : Optics and lasers** – relevant to the EuPRAXIA cluster on laser technology.

In the long term (2023–2026), more ambitious goals relevant to EuPRAXIA will be addressed. Such a research plan will require a substantial national investment program that we believe should go to the LAPLACE and PALAS projects. This second phase implies crucial upgrades on the current facilities and important infrastructure works. In the context of the LAPLACE and PALAS projects, LAL and LOA have agreed to set up a joint research venture on the development of LPAs, while optimising the different funding sources through the various institutes. A balanced investment could be foreseen and optimised between, on the one hand, the laser upgrades for LAPLACE and PALAS and, on the other hand, the existing building renovation. We estimate that the investment (outside of the cost of the building) would be in the range of 10–13 M€ to acquire the necessary equipment for the LAPLACE and PALAS projects.

**Work Package 6: Short-wavelength FEL gain demonstration with 500 MeV electrons** – relevant to the EuPRAXIA cluster on applications;

**Work Package 7: Multi-stage GeV laser-plasma accelerator** – relevant to the EuPRAXIA clusters on plasma components & systems and magnets & other beamline components;

**Work Package 8: Prototype of a kHz laser-plasma accelerator operating in the 5–50 MeV range** – relevant to the EuPRAXIA cluster on transformative innovation paths

### 3.6.3 IST – Portugal: Excellence Centre for Plasma Simulations and Theory

Computer simulations are the third pillar of the scientific method. In plasma accelerators and in projects with the ambition of EuPRAXIA, the tight interplay and integration between experiments, simulations, and theory is even more critical, as demonstrated by the central role played by simulation in all stages of discovery science and disruptive technology development in plasma accelerators. The maturity of the numerical methods that support R&D in plasma accelerators – capable of taking advantage of enormous computational resources and infrastructures – and the emergence of exascale computing supported by the EU-wide flagship Joint Undertaking EuroHPC open a window of opportunity for the establishment of a world leading centre in plasma simulations and theory in Europe.

At IST, we envision to establish an excellence centre in plasma theory and simulations in the format of a “collaboratorium”, i.e. a platform for coordination, collaboration, and scientific & technical exchange that can i) lead the coordination efforts in

terms of code development and integration, ii) serve as a front end for the EU-wide exascale initiatives in plasma accelerators, and iii) act as a hub for new and disruptive ideas, and explore the future directions for the EuPRAXIA facility through tests and exploration in the simulation realm before application in the laboratory.

The time is ripe for such a collaboratorium. In Portugal, we have a long tradition in plasma theory and simulations – established in close collaboration with the leading theoretical and experimental groups in the world – as the code architects and co-developers of Osiris, a community driven code that defines the gold standard for plasma accelerators employed worldwide, and ZPIC, an open source code designed to train the next generation of plasma-accelerator scientists. These tools have been employed at IST and at all the institutions using our tools for science discovery in plasma accelerators, and their development and exploration represents an outstanding template for a theory and simulation collaboratorium. Moreover, IST is grounded in a vibrant academic and scientific ecosystem for computational sciences and high-performance computing (HPC) with top students in all fields of science and engineering.

The format of the excellence centre will be based on a very light infrastructure which will provide simulation and theoretical support for the EuPRAXIA community. This will include undertaking computational developments, facilitating and coordinating virtual interactions between the different teams in the distributed EuPRAXIA theory & simulation cluster, and running a visiting / workshop program on plasma accelerators, to be modelled after other flagship venues, such as the Kavli Institute for Theoretical Physics in UCSB, Les Houches, or the Barcelona Supercomputing Centre. These can provide advanced training and convene the experts in the field with a combination of senior scientists, post-docs, and PhD students. This excellence centre, which will take the form of a collaboratorium, would take advantage of the unique location of Lisbon (easily accessible from all the European capitals), the support of IST and ULisboa, the integration of Portugal in the EuroHPC initiative, and the leading role plasma-accelerator scientists play in the Portuguese community of HPC.

### 3.6.4 PWASC – UK: Excellence Centre for Advanced Application Beamlines

#### Introduction

For some years, UK research has been strongly oriented towards the development of applications. The UK funding councils are operated through the UK's Department for Business, Energy, and Industrial Strategy (BEIS), and several of the funding streams they control are aligned with industrial applications. Within the field of plasma accelerators, this is evidenced, for example, by the recommendations of the STFC and PWASC roadmaps for accelerator science, both of which identify several applications as near-term goals. As a result, many of the UK research centres in the field of plasma accelerators all emphasise applications: the Centre for Advanced Laser Technology and *Applications* (CALTA), the Scottish Centre for the *Application* of Plasma-based Accelerators (SCAPA), the Compact Linear Accelerator for Research and *Applications* (CLARA), and the Extreme Photonics *Application* Centre (EPAC). Hence the UK is well placed to host the EuPRAXIA Excellence Centre for Advanced Application Beamlines.

The UK has several internationally leading groups working on wakefield acceleration and applications, both laser-driven (LWFA) and beam-driven (PWFA). All these groups collaborate closely with the leading groups across Europe. Many of the UK groups are university based, and several are affiliated with one of the two national

accelerator institutes (the Cockcroft Institute and the John Adams Institute). Since 2016, UK research in this field has been nationally coordinated by the Plasma Wakefield Accelerator Steering Committee (PWASC, see <http://pwasc.org.uk/>), which represents groups at 10 universities (Imperial College London, Lancaster, Liverpool, Manchester, Oxford, Queen's University Belfast, St. Andrew's, Strathclyde, University College London, and York), as well as the Accelerator Science and Technology Centre (ASTeC) and the Central Laser Facility (CLF).

Members of the UK groups have significant leadership roles in major international plasma-accelerator projects. Within EuPRAXIA, UK groups provide leaders and/or co-leaders in three of the eight Work Packages supported by the Horizon 2020 design study. Within the AWAKE programme, UK leadership positions include the deputy spokesperson, a member of the speakers and publications committee, and several task coordinators. UK researchers have held leadership positions or leading roles in many high-profile international experiments, including SLAC FACET I and II, DESY FLASHForward, and AWAKE. The UK has strong representation in several other international efforts, including the ICFA panel on Advanced and Novel Accelerators (ANA), which has formed the Advanced LinEar collider study GROUp (ALEGRO) to coordinate the preparation of a proposal for an advanced linear collider in the multi-TeV energy range. Members of the UK novel accelerator community also provide leadership to large international projects through the co-authorship of technical design reports, e.g. for ELI-NP or for SLAC FACET-II.

The UK groups, in collaboration with their international colleagues, have a strong record of developing high-quality plasma-accelerated electron beams, including the first demonstrations of narrow-band electron beams, the first generation of GeV beams, the successful demonstration of electron acceleration by the AWAKE collaboration, and the first demonstration of the plasma photo-cathode scheme. They have also been strongly involved with developing the applications of these beams. These include applications to the following: betatron radiation for the tomographic imaging of medically relevant samples, security, electron-positron plasma generation, strong-field QED experiments, and tests of radiation reaction.

The application-directed UK funding environment and the strong track record and experience of international collaboration mean that the UK is ideally placed to host the EuPRAXIA Excellence Centre for Advanced Application Beamlines.

## Existing and Future Facilities in the UK

Much of the experimental work by the UK groups on LWFA has been performed at the CLF at the Rutherford Appleton Laboratory (RAL), which hosts the Astra laser (600 mJ, 40 fs laser pulses at a repetition rate of 5 Hz) and the Gemini laser (two synchronised laser beams of 15 J, 50 fs pulses). The experimental facilities at CLF are supported by laser systems based in the university labs, including systems at Strathclyde (SCAPA, three laser systems with a 350 TW / 5 Hz flagship, three bunkers, and up to seven beamlines), Queen's University Belfast (TARANIS-X), Imperial College London, and Oxford. The university-based systems play an important role in developing and testing new concepts, preparing for experiments at national and international facilities, and in training students.

An important project transforming the UK infrastructure for plasma-accelerator research will be the future £81.2 M Extreme Photonics Application Centre (EPAC) at CLF. This new centre will provide a 10 Hz petawatt laser pumped by CLF's world-leading DiPOLE technology, driving plasma accelerators for applications and science. Initially, EPAC will deliver two target areas for enabling experiments on the fundamental and technological aspects of plasma accelerators as well as the development of novel applications: a 40 m long target area dedicated to LWFA and hybrid

PWFA $\Rightarrow$ LWFA as well as another multi-purpose target area with the capability for solid target interactions. The capacity for delivering additional laser sources (e.g. 100 Hz) and a third target area at a later point exist in EPAC. With additional funding opportunities, including the materialisation of EuPRAXIA, EPAC will have the capacity to expand its capabilities and its applications further, including via additional dedicated areas.

To date, the UK groups have also contributed to PWFA R&D via experiments at SLAC FACET and at CERN AWAKE. The CERN AWAKE programme has received funding from the UK institutes and from UK research councils (STFC) since 2012. There is scope to significantly enhance the facilities for PWFA and hybrid LWFA $\Rightarrow$ PWFA research. CLARA, the Compact Linear Accelerator for Research and Applications, is a dedicated R&D facility for developing FEL R&D and to prepare and support UK X-FEL capabilities. CLARA currently produces 50 MeV electron beams and will eventually provide 250 MeV beams. There is also the plan to extract the 250 MeV beam into a beamline dedicated to science experiments requiring short pulses of relativistic beams; this capability could support UK PWFA research by providing a facility for electron-linac-driven PWFA.

### The Proposed UK Contribution

With our European partners, we will continue to take advantage of the positive feedback between pushing the performance of plasma accelerators and developing new, advanced applications. The UK offers world-leading expertise in optimising electron beam quality, aiming at controlled attosecond-scale beams with phase-space control and including the reduction of emittance and energy spread to levels required by FELs. It also has leading programmes on developing strategies for operation at high repetition rates, advanced plasma sources, and beamline diagnostics and beam transport.

The repetition rate requirement for the laser driver for EuPRAXIA is 10 Hz as a minimum, but ideally, it requires a 100 Hz repetition rate and beyond. Diode-pumped solid-state laser (DPSSL) technology is ideal for this task since it aims at delivering unprecedented high peak power ( $>1$  kW) with high repetition rates (10 Hz–1 kHz) and high overall efficiencies ( $>20\%$ ). This is an area in which the UK is currently world leading; the DPSSL technology developed at the CLF (DiPOLE) can already produce 100 J pump lasers that can drive petawatt lasers at 10 Hz, with the final goal of achieving 100 TW, 100 Hz lasers.

For PWFA, linear accelerators such as LCLS, PAL XFEL, and SwissFEL are used to drive FELs at rates between 60 and 120 Hz. The technical challenges associated with operating these precision accelerators at such high rates compared to more typical 5 to 10 Hz accelerators are very significant. The CLARA accelerator is designed to operate at 400 Hz, making it ideally placed to further develop and test EuPRAXIA-related equipment on the quest towards up to 100 Hz plasma-driven systems in the future.

To guarantee the efficient use of beams at such a high repetition rate, significant and fundamental developments in the technology of secondary sources, their characterisation, and their applications have to be pursued hand-in-hand with the development of the accelerator itself. It is necessary to ensure that beam transport and handling lines, beam diagnostics, and detectors are developed to work at matching repetition rates, handling high-flux beams without deteriorating their unique properties, such as the femtosecond, if not attosecond, duration. This applies to the main electron beam as well as to the positron beam and X-ray / gamma ray end stations.

Such high repetition rates also require handling a large amount of data and fast active feedback on the machine. EuPRAXIA can take advantage of the experience available at UK facilities such as the Diamond Light Source and of the active interdisciplinary approach at national facilities for the development of high-repetition-rate technology. Likewise, the handling of big data sets is a UK STFC strength as it is crucial for existing programmes. Finally, there is a wealth of experience in applying machine-learning techniques for beam control and dynamic accelerator control. UK Centres for Doctoral Training had a focus on this technique for several years and are leading in this area.

The EuPRAXIA Consortium has identified the following pilot applications: free-electron laser (FEL), high-energy (GeV) and low-energy (sub-MeV) positron beamlines, a Compton source of MeV gamma-ray beams, and betatron X-ray sources. Several other applications can be envisaged, but these end stations are the ones that allow pursuing specific electron beam parameters that are thought to accommodate the widest range of future applications. The laser-driven construction site will have three laser-driven beamlines: FEL, X-ray medical imaging, and a low-energy positron beamline. Future developments will include accelerator R&D as well as high-field physics experiments. The beam-driven construction site – LNF is a candidate – will host three beam-driven beamlines: FEL, a high-energy positron beamline (including capability for testing novel accelerator technologies and high-energy physics detectors), and a Compton scattering photon source.

In comparison to the state of the art of plasma accelerators today, EuPRAXIA accelerators shall enable a paradigm shift: from R&D accelerators operating usually for a few weeks at a repetition rate often well below 1 Hz to accelerators with industrial beam quality operating 24/7 with a repetition rate of 20 Hz and growing over time to 100 Hz and higher. Given the UK's world-leading expertise in developing high-repetition-rate, high-quality plasma-accelerator technology and applications, we propose that the UK build prototypes, develop all beamlines, and play a major role in their delivery.

## Summary

The conjunction of nationally coordinated world-class expertise, matching funds to upgrade already competitive national and university-scale facilities, and existing programmes in similar areas makes the UK the ideal partner in EuPRAXIA to prototype and develop all beamlines and to play a major role in delivering them.

### 3.6.5 ELI Beamlines: Incubator for the Application of Novel Accelerator Technology to Laser Science Users

The Czech Republic has a long and remarkably impressive history of research and development in the field of high-power short-pulse lasers. As a reflection of this, the European Strategy Forum for Research Infrastructures (ESFRI) supported the location of one pillar of the pan-European Extreme Light Infrastructure (ELI) project, ELI Beamlines, in Dolní Brezany, south of Prague, under the auspices of the Institute of Physics of the Czech Academy of Science. The building for this new facility has been completed, and the envisaged high-repetition-rate lasers with unprecedented opportunities are under development at ELI Beamlines to drive advanced short-pulse optical, IR, X-ray, and particle beams (secondary sources) beyond the state of the art by controlling and extending the parameters of lasers and secondary sources, mainly their intensities, stability, synchronisation, quality, energy range, and repetition rates.



**Fig. 3.12.** ELI Beamlines facility in Dolni Brezany (image credit: ELI Beamlines).

It allows the performance of new investigations spanning the range from fundamental to applied sciences and medicine, ultimately leading to a better understanding of nature and providing future societal benefits. The ELI Beamlines development, as a part of the pan-European ELI project, has two major aspects: enhancing the capabilities and versatility of the laser systems and subsequently using these improved lasers for new experimental possibilities, leading to the interconnectivity / interdependence of lasers and experimental applications. The ELI Beamlines project is a unique endeavour in the field of photonic-based research worldwide and the first large-scale facility in this domain. ELI Beamlines has to innovate in parallel to construction and commissioning to be an incubator for new coming projects, which will be initiated by the prospective user community. The specific nature of the ELI Beamlines user facility is its multi-disciplinary features, opening extremely wide opportunities for the worldwide user community to develop new secondary radiation and particle sources, thus, as a consequence, improving user capabilities at new end stations, creating new paths of applied and fundamental research, pushing the boundaries of science and technology. After the commissioning phase, ELI Beamlines will be able to produce ultra-short laser pulses of a few femtoseconds ( $<30$  fs) duration at the peak power of up to 10 PW. The PW-class laser systems of ELI Beamlines aim to increase the repetition rate to up to 50 Hz in the nearest future. It will lead to the development of new techniques for time-resolved spectroscopy, scattering and diffraction techniques, medical imaging, medical diagnostics, and radiotherapy, including new tools for the design, development, and testing of new materials, as well as improvements in X-ray optics.

Apart from the facility construction and technology development, ELI Beamlines leads the following research activities (research programs):

**RP1 (Lasers):** development of the short-pulse laser systems for all research programs at ELI Beamlines, including the development, implementation, and optimization of the laser systems, their components and subsystems. Short-term activities: development and implementation of four main laser systems of the ELI Beamlines facility. Long-term activities: development of the laser systems to reach world-leading intensities and pulse parameters at high repetition rates.

**RP2 (X-ray sources, driven by ultra-short laser pulses):** development of a new generation of laser-driven secondary light sources from the “vacuum-UV” to the “gamma-ray” energy range. Short-term activities: provide the international user community access to ultrashort secondary light sources for applications in molecular, biomedical, and material science. Long-term activities: continuous development of the radiation sources, including the development of a laser-driven coherent X-ray.

**RP3 (Particle acceleration by lasers):** development of versatile and stable sources of high-energy electrons, protons, and ions, driven by various laser-acceleration mechanisms. Short-term activities: development of laser-driven ion and electron sources with world-leading beam parameters. Long-term activities: development of an ion source as a compact and low-cost laser-driven proton/ion source for cancer therapy. Laser-driven electron acceleration is aimed to develop a laser-driven X-ray FEL.

**RP4 (Applications in molecular, biomedical, and material sciences):** development of setups for time-resolved experiments using high-power lasers, secondary light sources, and a comprehensive set of pump beams for both fundamental and applied research. Short-term activities: implement capabilities in the VUV and soft X-ray range for time-resolved material science, coherent diffraction imaging for atomic molecular, and optical science; implement X-ray instruments for time-resolved scattering, diffraction, absorption spectroscopy, phase-contrast imaging, and pulse radiolysis; use high-intensity lasers directly for advanced optical spectroscopy applications, such as “fsec”-stimulated Raman scattering and 2D spectroscopy. Long-term activities: combine all of these methods with perfect synchronisation for complete investigations of complex phenomena.

**RP5 (Plasma and high-energy density physics):** explore both fundamental science and possible applications in the field of high-energy and high-intensity laser-plasma interaction. Research activities concentrate on ultra-high-intensity laboratory astrophysics, warm dense matter, and plasma optics.

**RP6 (Exotic physics and theory / simulation):** explore theoretical and experimental aspects of the exotic physics expected in the so-called ultra-relativistic regime (above  $1 \times 10^{22} \text{ W cm}^{-2}$ ) of laser-matter interaction. Short-term activities: simulation support for experimental programs in high-energy and high-intensity laser-matter interaction. Long-term activities: explore new horizons in the physics of laser-matter interactions under extreme conditions.

ELI Beamlines has currently over 250 scientific-technical employees, and all of them participate in the development and implementation of the ELI Beamlines systems. All ELI Beamlines achievements will provide input and guidance on key components for the high-repetition-rate laser-driven FEL community, including the worldwide X-ray user community. ELI Beamlines is a platform for the development of new laser technology, the improvement of radiation sources, and the acceleration of particles (protons and electrons) as well as a platform for educating a new generation of scientists and engineers.

### 3.6.6 DESY – Germany: Excellence Centre for Plasma Accelerators and High-Repetition-Rate Developments

DESY has been building up capabilities for plasma-accelerator R&D in the past decade and is currently further expanding these activities. It is executing an ambitious development program in beam-driven and laser-driven plasma accelerators, targeted to high electron beam quality, high average power and first applications. In the context of the EuPRAXIA initiative, DESY is planning to bring in its unique capabilities and research interests as an ‘excellence centre for plasma acceleration and high-repetition-rate developments’. The DESY capabilities are concisely summarised in the following paragraphs.

Particle beam drivers enable high-repetition-rate and high-average-power operation of plasma wakefield accelerators using the high-power accelerator technology

available today. DESY, as the leading laboratory in the development of superconducting radiofrequency resonators, which power many of the world's most advanced particle accelerators, utilises high-average-power technology to enable plasma wakefield accelerators with above 10 kW electron beams at MHz repetition rates in the FLASHForward facility. In particular, FLASHForward aims at realising a plasma booster module in the GeV range that operates at high efficiency, supporting FEL beam quality. To achieve this, research at FLASHForward seeks to demonstrate beam-quality preservation in emittance and energy spread, relying on fine control of the beam properties before plasma interaction and advanced diagnostic capabilities post-plasma. As part of the FLASH FEL user facility, FLASHForward benefits from advanced accelerator controls as well as feedback and feedforward systems that enable high stability and precise tunability for precision experiments. With these capabilities, FLASHForward will become the world's premier plasma wakefield accelerator for the development of high-average-power plasma technology, ultimately opening an avenue for future high-average-power applications.

These developments are synergistically complemented by KALDERA, the high-average-power, high-peak-power laser initiative at DESY. Starting in 2019, it will develop and commission by 2024 a laser system delivering 100 TW peak power at a 1 kHz repetition rate to drive a laser-plasma accelerator generating GeV-level electron beams. DESY has identified a kW average-power laser system as mission critical for the development of laser-plasma acceleration. The leap in repetition rate from today's few Hz to a kHz level will provide electron beams at a level of average power comparable to modern radiofrequency accelerator technology while enabling feedback loops and the active stabilisation of electron beam parameters. It represents a major step for advancing laser-plasma acceleration from a concept to a technology.

To host KALDERA, DESY is currently building a 400 m<sup>2</sup> clean room inside the SINBAD facility. It also prepares an 80 m long radiation-shielded area close by for the installation of a kHz plasma electron target. DESY strongly supports the KALDERA initiative with specialised and user-facility trained technical support personnel for the development of controls, data acquisition, machine protection, safety installations, and technical infrastructure.

The KALDERA system will provide the laser pulses required for the Helmholtz large investment project ATHENA. The ATHENA project builds up infrastructure for implementing a laser-driven electron plasma accelerator flagship at DESY. Inside the SINBAD facility, the capabilities of the high-repetition-rate KALDERA laser system are complemented by the S-band linear accelerator ARES. The ARES linac with beam energy up to 150 MeV is located in the direct vicinity of KALDERA and is presently under commissioning. ARES will provide access to ultra-short electron bunches with a 50 Hz repetition rate and advanced beam diagnostics. Coupling the capabilities of KALDERA and ARES will enable R&D on a compact laser-plasma booster with high-quality electron bunches at beam energies up to 1 GeV, repetition rates of initially up to 50 Hz, and advanced stabilisation systems as developed at DESY. The perspective for such a coupled KALDERA/ARES/ATHENA system aims at the development of a compact free-electron laser at 1 GeV with high beam quality and a repetition rate of 50 Hz initially and later towards the kHz regime.

In summary, the present and future DESY capabilities relevant for EuPRAXIA and partially supported in the Helmholtz ATHENA project include a MHz electron beam driver at FLASHForward, high-average-power laser pulses towards kHz at KALDERA, ultra-short electron bunches at up to 150 MeV from the S-Band linac ARES, advanced plasma and beam diagnostics, ultra-fast feedback systems, plasma accelerator components, as well as experimental plasma acceleration setups. In the context of these capabilities, investments, and research interests, DESY has

been defined as EuPRAXIA’s “excellence centre for plasma acceleration and high-repetition-rate developments”.

### 3.6.7 Possible Candidate Sites for the Laser-Driven Plasma Acceleration Construction Site

Given the strong competition of the laser-plasma accelerator field in Europe, several laboratories are examining the opportunity of hosting the laser-driven plasma acceleration construction site of EuPRAXIA. Developments in the European research and funding landscape are having a direct impact on possible options for EuPRAXIA implementation as boundary conditions are changing. Discussions are ongoing, and a final site concept will need to be worked out during the preparatory and technical design phases of EuPRAXIA. The following section describes some of the present ideas and concepts on specific site proposals. The final concept for EuPRAXIA must also involve additional detailed discussions with decision makers and funding agencies at the national and European level during later phases, as mentioned above.

#### General characteristics and requirements

The final construction site for the laser-driven part of EuPRAXIA shall fulfil a few basic requirements:

- The site shall be at a laboratory with existing infrastructures in one or several of the following areas: RF accelerators, laser installations, user access.
- The site shall have existing groups in place to address all safety requirements (laser, radio-protection, access control) and rules.
- The site shall provide a space of about 175 m in length and 35 m in width (details depending on the choices during the preparatory and technical design phases).
- The site shall provide the required services and facilities for the support of external users.

#### UK: EPAC

The possibility of hosting the laser-driven arm of EuPRAXIA in the UK is now stronger than ever before. The UK has played an internationally leading role in laser wakefield research for many years. The Central Laser Facility at the STFC Rutherford Appleton Laboratory (RAL) has been a major resource for research in this field and a pioneer of European collaboration, with currently 30% European users. It currently hosts Gemini, one of the pre-eminent centres for laser-driven accelerators. Research in CLF is augmented by recent centres, such as SCAPA, and university labs in Queen’s University Belfast, Imperial College London, and Oxford as well as the UK accelerator institutes – the Cockcroft and John Adams Institutes – that develop both conventional and novel accelerator technology. This environment is complemented by STFC’s Daresbury laboratory, which develops the underpinning accelerator and radiation source technology, with a strong track record in delivering key building blocks across the UK and EU, and contributing tailored solutions for plasma wakefield acceleration at CLARA.

The UK government has just invested £81.2 M in a new laser centre at CLF – the Extreme Photonics Applications Centre (EPAC) – in order to exploit the applications of laser-driven novel accelerators in industry and medicine. This facility will host a 10 Hz petawatt laser, pumped by CLF’s world-leading, EU-grown DiPOLE



**Fig. 3.13.** Left: The EPAC facility under development in the UK. Right: Areal view of the EPAC site with space for a potential EuPRAXIA facility next to it (image credits: UKRI, right image adapted from Google Maps).

technology, which will be used for driving plasma accelerators. EPAC will help to develop novel particle and radiation beams for applications in industry, medicine, and security, for example by providing new ways to inspect critical industrial components.

Linking EPAC with EuPRAXIA presents an ideal opportunity to exploit the UK government's investment in this area. EPAC will be a user facility that will be online in 2024, coinciding with the potential construction phase of EuPRAXIA. Initially, EPAC will deliver the 10 Hz petawatt laser to two heavily radiologically shielded target areas for enabling experiments on fundamental and technological aspects of plasma accelerators as well as the development of novel applications: a 40 m-long target area dedicated to LWFA and hybrid LWFA $\Rightarrow$ PWFA as well as a multi-purpose target area with the capability for LWFA and solid target interactions. As currently planned, the EPAC building has a third, additional shielded area, which can host a dedicated beamline for programmes including EuPRAXIA. In addition, it would be possible to build an entirely new building for EuPRAXIA next to EPAC as there is a significant scope for expansion in the construction site with shared basic infrastructure.

In addition to this, as part of a Horizon 2020 programme, the CLF is currently developing the technology for a 100 Hz pump laser for a petawatt-class driver for high-repetition-rate laser wakefield accelerators. With EuPRAXIA funding, it would be possible to deliver a similar laser within the existing EPAC building or in any subsequent expansions to it.

It is clear that the missions of EPAC, CLF, and the UK plasma accelerator groups and university centres align very strongly with EuPRAXIA and its timescales. For example, the existing capabilities in EPAC (10 Hz petawatt laser driving wakefield accelerators for applications) will de-risk EuPRAXIA significantly and it is possible to have dedicated experimental R&D programmes for testing and prototyping EuPRAXIA concepts in EPAC and SCAPA. Further, EPAC will have the capacity for delivering additional laser sources (e.g. a 100 Hz PW-class laser) and a third target area at a later point, once the primary beamlines are commissioned. When additional funding opportunities, such as EuPRAXIA, materialise, EPAC will also have the capacity to expand its capabilities and its applications further, including via additional dedicated, radiologically shielded areas.

As mentioned above, the plasma wakefield acceleration community in the UK has formed a consortium – the Plasma Wakefield Acceleration Steering Committee (PWASC) – to coordinate major activities in this area in the UK, and to amalgamate organisational leadership of research centres and universities. The PWASC has just

published a roadmap that identifies the major research themes and milestones in this area for the next two decades. A clear theme is generating high-energy, high-6D-brightness electron beams that can drive an X-ray FEL (XFEL), ultimately based on compact and high-efficiency laser-plasma wakefield acceleration. While an ecosystem of linked conceptual recipes for this grand challenge exist, and remarkable experimental progress has been demonstrated over the past years through UK-EU-US collaborations, as reported to EuPRAXIA, further R&D, technology development, and implementation require high-energy, high-repetition-rate laser systems that would be available at EuPRAXIA@EPAC. A EuPRAXIA-led, collaborative technology development programme towards this in the UK with a focus on XFEL-ready beams will fully align with the EuPRAXIA goals and complement the efforts from other EuPRAXIA partners and centres of excellence.

This two-pronged proposal from the UK provides EuPRAXIA with a significant de-risking opportunity as well as a future-proofing pathway. The specifications of EPAC are very close to the EuPRAXIA baseline, and basing EuPRAXIA in EPAC will de-risk a key milestone of EuPRAXIA – having a user facility based on LWFA – and tick off its early goals. The ambitious technology development programme towards XFEL-ready beams will ensure that the technology for the upgrade paths of EuPRAXIA is simultaneously developed, making it a very attractive proposition to host EuPRAXIA in the UK.

### Czech Republic: ELI Beamlines

The construction of the ELI Beamlines (ELI-BL) building in Dolni Brezany (near Prague) was finished in 2016. The site area is 65 000 m<sup>2</sup>, including the building area of 28 645 m<sup>2</sup>. The footprint of the experimental building area is 60×100 m<sup>2</sup>. The experimental building has three floors (from top to bottom): the service floor, the laser floor, and the experimental floor, which has six experimental halls. The L3 “HAPLS” laser beam transport from the laser hall to different experimental halls is under preparation now at ELI Beamlines. From November 2019, the L3 “HAPLS” laser beam (see Fig. 3.14), which is the highest repetition-rate PW system worldwide, will be available in the ELI Beamlines experimental areas, starting from the E3 and E4 halls. From the middle of 2020, the L3 “HAPLS” laser beam will be delivered into the E5 experimental hall, dedicated to electron acceleration using a laser wakefield. In addition, the L2 “Amos” laser system of ELI Beamlines, which is under development for the ELI-BL “laser-driven” FEL program (the LUIS project), will be available in the E5 experimental hall starting from the middle of 2021. It will allow to perform LFWA electron acceleration with a repetition rate of up to 25 Hz using an output pulse energy of 10 J with pulse compression down to 30 fs. The LUIS setup is under preparation now in the E5 experimental hall, which is a low-vibration area with a length of 60 m. To accommodate both electron beam and photon beam transport for the laser-driven FEL project, the E5 experimental area can be extended using the existing E6 experimental hall. In this case, the total length of the area, up to 100 m, will be available for the “laser-driven” FEL development at ELI Beamlines, with a possible upgrade in the future of up to 150 m, with a minimal width of 4 m and a height of 5 m (see Fig. 3.14). For this, high thermal stability ( $\pm 0.5$  °C) will be provided to avoid changing the undulator properties in the case of the “Swiss-FEL” type of undulator.

The E5 experimental hall, which has a clean room of ISO Class 7, has fully operating HVAC, lightning, and service distributions. The interlock system will be implemented during the first half of 2020. The floor in the E5 experimental area has superior vibration stability. The rails in the floor are implemented in the E5



**Fig. 3.14.** The L3 “HAPLS” laser system at the ELI Beamlines laser hall (image credit: ČTK).

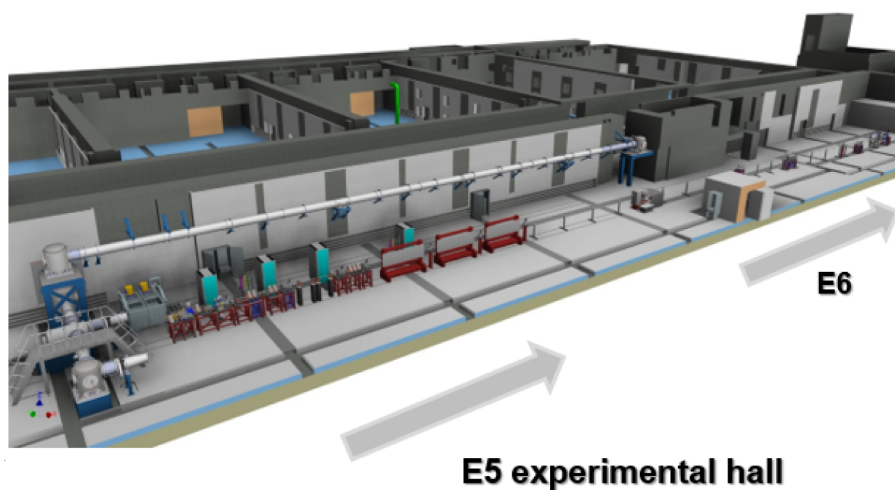


**Fig. 3.15.** Possible allocation of the “laser-driven” FEL elements (both the electron beam transport and the photon beam transport) in the ELI Beamlines experimental areas E5 and E6, with the control room above the experimental area (image credit: ELI Beamlines).

hall, allowing the flexible installation of beamline technologies. The estimated time to complete the E5–E6 merging is 6–12 months.

Taking into account the current status of the ELI Beamlines development (in particular, the readiness of the infrastructure, high-power lasers, and experimental halls), this centre can be considered as a possible option for the laser-driven plasma accelerator construction site and realisation of the EuPRAXIA project.

Italy: CNR-INO

CNR-INO is located inside the CNR Campus in Pisa (Fig. 3.16) and is currently hosting a sub-PW laser laboratory (the Intense Laser Irradiation Laboratory, ILIL [168]) with a fully equipped experimental area (Figs. 3.17 and 3.18) dedicated primarily to laser-plasma acceleration research. The ILIL Laboratory is a founding partner of



**Fig. 3.16.** Map (left) and aerial view (right) of the entire CNR campus in Pisa, with the red arrow indicating the Intense Laser Irradiation Laboratory of the National Institute of Optics (<http://www.area.pi.cnr.it/>).

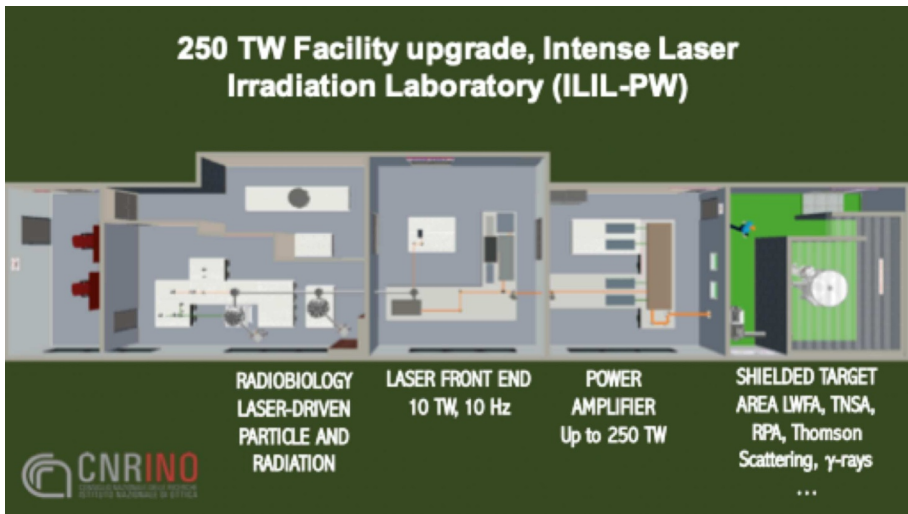


**Fig. 3.17.** A view of the actual layout of the Intense Laser Irradiation Laboratory at CNR-INO in Pisa (<http://ilil.ino.cnr.it/>).

EuPRAXIA and is the first laboratory in Italy where laser-plasma acceleration was demonstrated experimentally in 2007 [169].

The laboratory is also a leading node of the Italian network on the Extreme Light Infrastructure with a focused research programme on medical applications of laser-driven plasma acceleration for advanced radiotherapy and X-ray diagnostic developments. Moreover, ILIL is the proposing institute of the Resonant Multi-Pulse Ionisation Injection scheme (ReMPI) [170] for the generation and acceleration of high-quality electron beams. The ReMPI scheme is one of the priority solutions within the EuPRAXIA model for the 150 MeV injector and represents an effective compact solution as a GeV-scale, fully laser-driven accelerator scheme. The implementation of such a scheme for the 150 MeV injector is already being pursued at the ILIL-PW lab based on the existing 250 m<sup>2</sup> infrastructure and national funding.

At the same time, CNR-INO is also pursuing a fairly large programme for the development of novel high-average-power laser technologies that will be carried out



**Fig. 3.18.** The interaction target chamber (left) and a section of the control room (right) at the Intense Laser Irradiation Laboratory (<http://ilil.ino.cnr.it/>).



**Fig. 3.19.** Map of the CNR campus showing the INO laboratories, including the existing Intense Laser Irradiation Laboratory, compatible with the EuPRAXIA laser-driven accelerator construction site.

in the 2020–2022 timeframe and, eventually, could be part of the final EuPRAXIA layout. In view of these activities, additional upgrades of the laboratory are in order, including a 50 m<sup>2</sup> extension of the shielded target area – an option in the current layout – and the construction of a new 100+100 m<sup>2</sup> clean room to host laser developments, all using already available building space.

From the point of view of local support infrastructures, CNR-INO is located inside the Pisa CNR campus (Area della Ricerca di Pisa), a large multi-disciplinary research site hosting 1,200 staff and unique research capabilities, with established high-quality support facilities and all necessary utilities (engineering, gas supplies, water cooling, UPS, electricity, etc.). The campus also hosts a major medical activity and is the site of the “.it” registration authority.

In view of the above, CNR-INO is an ideal candidate to host the construction of the laser + accelerator + beam transport to establish the EuPRAXIA electron beam

specifications required at the entrance of the undulator for FEL operation. This represents the most challenging milestone of EuPRAXIA and could justify a dedicated, focused effort. Significant additional room would be needed to host the undulator and user beamlines planned for the full EuPRAXIA laser-driven facility and could be available subject to approved construction. Alternatively, the commissioned high-quality accelerator could finally be integrated as an option to drive the undulator at the EuPRAXIA@SPARCLab in Frascati.

The convergence of the ILIL-PW research objectives and the EuPRAXIA main goals is clearly an opportunity for both parties. Further discussion will be needed to finalise the plan of EuPRAXIA at CNR-INO in Pisa and to secure funding for the needed additional dedicated infrastructure and instrumentation developments.

### Italy: INFN-LNF

The EuPRAXIA@SPARC\_LAB project [162,163] of the Italian “Istituto Nazionale di Fisica Nucleare” (INFN) has been described in Section 3.6.1 as the candidate to host the beam-driven plasma acceleration (PWFA) construction site. Nevertheless, in the same infrastructure, the laser-driven plasma acceleration (LWFA) option can be also accommodated, in principle in any configuration resulting from the EuPRAXIA Design Study [171]. Among all the possible LWFA configurations, the EuPRAXIA@SPARC\_LAB project has been investigated in detail by INFN to fulfil the 1–5 GeV EuPRAXIA parameters in the LWFA scheme with the external injection of an electron bunch [162]. This configuration is of particular interest for its promising capability to produce high-quality electron beams and would be very suitable for the INFN site, where a 0.5–1 GeV X-band RF linac is already foreseen to drive the PWFA scheme. To this end, a wide room (32×12 m<sup>2</sup>, light blue in Fig. 3.10) will be devoted to the laser sources, including the 0.5–1 PW upgrade of the existing 300 TW FLAME laser system [165], which will operate at a 5–10 Hz repetition rate and will be synchronised to the RF linac at the fs level.

In the LWFA scenario with external injection, a low-charge (30 pC) electron bunch is accelerated to up to 0.5–1 GeV by the RF linac and then injected into the plasma module that will consist of a 0.5 m long, 0.6 mm diameter capillary tube, in which the plasma is produced by a high-voltage discharge in hydrogen. With a plasma density of  $1 \times 10^{17} \text{ cm}^{-3}$  (quasi-linear regime) and on-target laser parameters of 25 J in a 112 fs (FWHM) long pulse with a 70  $\mu\text{m}$  (RMS) spot size (corresponding to  $a_0 \sim 1.3$ ), the accelerating gradient is expected to be of the order of 10 GV/m. Start-to-end simulations show that the accelerated electron beam at 5 GeV keeps a high quality profile with an RMS normalised slice emittance of 0.35  $\mu\text{m}$ , an RMS energy spread of  $1 \times 10^{-3}$ , and a peak current of 2 kA [172], thus being able to drive a short-wavelength SASE FEL as foreseen for the EuPRAXIA project.

### 3.7 Long-Term Scientific Programme

Considering the challenging nature of the EuPRAXIA project based on its use of novel technologies, most of the design study and consequently this report focus on the baseline design of the proposed EuPRAXIA research infrastructure. However, looking at the long-term sustainability of such a facility, with research infrastructures typically expected to run for several decades, it is also important to keep in view potential future developments and directions of the science at EuPRAXIA.

This section thus presents the first version of a long-term scientific programme. Defining such a strategy relatively early on will allow, on the one hand, the design

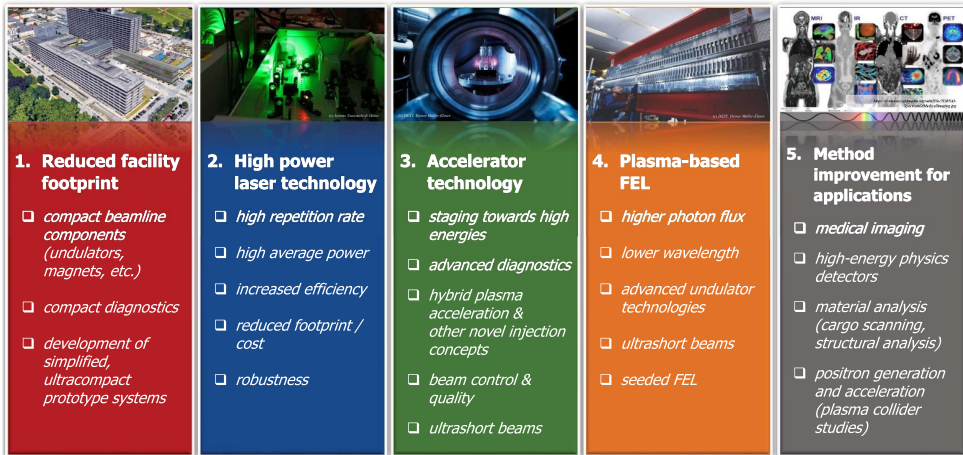


**Fig. 3.20.** The five main pillars of the EuPRAXIA long-term science programme and specific activities towards these topics. Key features that would be targeted in future upgrades are a further reduction in facility size as well as improvements in the machine performance and output beam properties.

and building of the infrastructure with future upgrades in mind. On the other hand, it will also make it possible to already integrate parts of the necessary R&D for these developments very effectively into the technical design phase of the facility.

As Figure 3.20 shows, the proposed long-term programme is built on five main pillars, each of which is foreseen to (1) improve the impact of the EuPRAXIA research infrastructure, (2) ensure that it remains competitive as a facility in the overall research landscape, and (3) open up new possible experimental opportunities at EuPRAXIA:

**Reduced facility footprint:** An important factor limiting a reduction in facility size for the baseline design is the use of many well-tested but relatively large technologies for transport lines, diagnostics, and other parts of the machine. This is a risk-mitigation strategy to ensure that the main R&D efforts can flow into more critical sub-systems, such as the high-power laser and plasma stages. Once robust performance has been achieved for these essential parts, though, a further miniaturisation of the entire machine should be pursued in a stepwise approach, aiming for a size reduction of the accelerator by a factor of 10 or more in the long-term. A promising spin-off of this strategy could also be the development of ultracompact, self-contained accelerator systems based on EuPRAXIA technologies and suitable for testing with collaborating institutes or companies.

**High power laser technology:** The EuPRAXIA laser system is developed to achieve the requirements set by the EuPRAXIA design aims but with technologies at a high technical readiness level to ensure robust and stable performance from the beginning of the facility operation. With this trade-off in mind, future improvements of the high-power laser system will be essential for the competitiveness of EuPRAXIA. Technical challenges of particular interest will, for example, be upgrades to kHz repetition rates and higher efficiency, strategies for which are being developed now (see Sect. 10.2.7).

**Accelerator technology:** A variety of different technological approaches has been investigated as part of the EuPRAXIA conceptual design study, some of which have shown great potential, but are still at a low technical readiness level. By developing these concepts, such as the hybrid plasma acceleration scheme (see

also Chap. 26), further in parallel to the baseline design, a future implementation can be considered to improve the machine properties EuPRAXIA can offer to users with time. Other aspects of accelerator technology, such as beam control and multi-stage acceleration, may not have specific future innovation strategies beyond the baseline yet; nonetheless, it will be important to upgrade these as well, as the overall EuPRAXIA facility develops.

**Plasma-based FEL:** With plasma-based free-electron lasers (FELs) requiring significant research and development to become ready for user operation, the EuPRAXIA FEL design is aimed at achieving an acceptable but in particular also robust performance for this application. Once more experience has been gathered with this new type of radiation source, especially in user experiments, the next natural goal will thus be to improve the properties of the FEL both through optimisation of the beamline and through the integration of more advanced concepts.

**Method improvement for applications:** EuPRAXIA will be an ideal test bed for the secondary beam applications that plasma accelerators can provide based on their specific properties. The user experience gained over time will help to find new ways for improving these imaging and analysis tools at EuPRAXIA in terms of beam properties, reliability, and user-friendliness. Equivalently to the pursued accelerator footprint improvements, an interesting side effect of these developments could also be the prototyping of independent, more specialised, and highly compact accelerator application systems in collaboration with academic or industrial partners.

## 4 Preliminary Resource and Financial Plan

### 4.1 Cost Model and Definitions

EuPRAXIA is, at full scale, a 320 million euro investment into European compact accelerator innovation and scientific applications, including a 70 million euro investment into laser technology. Depending on budget availability minimal scenarios include options for a 60 million euro beam-driven and a 75 million euro laser-driven accelerator site (without R&D costs).

The budget estimate listed in this report is a preliminary estimate that is based on data collected from the consortium on the different required cost items. Here, we explain the categories of spending:

**Category Preparation Costs:** These are costs spent by the laboratories on preparing the sites and centres before the approval of the EuPRAXIA TDR and construction projects. These are costs that are pre-invested by the laboratories in ongoing projects and with the view of preparing the EuPRAXIA site. This category is not included in the EuPRAXIA cost estimate but might become relevant as in-kind contribution.

**Category Investment Costs (R&D and construction):** These are costs spent on hardware, contracts with industry, access to facilities, contractual labor, and other smaller items. These costs are given in 2019 terms in millions of euro.

**Category Personnel Costs (R&D and construction):** This category specifies the labor at collaborating institutes for performing the required tasks in the technical design and construction of EuPRAXIA. These costs are given in full-term equivalents (FTE). One FTE means that one person works full time for the EuPRAXIA project during one year.

**Category Operational Costs:** These are the costs related to hardware commissioning, beam commissioning, and the operation of the proposed facility after the completion of construction.

The major EuPRAXIA costs will incur during the following two phases of the project.

**Costs during Technical Design:** The technical design phase follows the conceptual design that we report on in this document. During the technical design phase, the detailed technical solutions are developed, prototypes will be constructed and tested, components will be industrialised, critical proof-of-principle experiments will be carried out and the construction will be prepared. At the end of this phase, a technical design report (TDR) will describe the detailed facility design.

**Costs during Construction:** This describes the costs that are required for constructing the facilities at the proposed sites as defined in this report. Of particular interest are the two flagship construction projects that realise the complementary technological paths of (1) laser-driven plasma acceleration (LWFA) and (2) beam-driven plasma acceleration (PWFA).

The sections below specify the total cost of the facility and the breakdown into the two main technologies (beam-driven and laser-driven plasma accelerators) as well as the breakdown into major technical systems. Both investments and person-power needs have been estimated from the project participants and are presented. At the end of this chapter, minimal systems are discussed that do not offer the benefits of a European research infrastructure but could be starting blocks for a EuPRAXIA facility. Also, these minimal systems give a first indication of a possible system cost after a successful EuPRAXIA project. For example, the final prize tag of a 5 GeV plasma accelerator after EuPRAXIA will be much lower than the cost of EuPRAXIA as R&D costs will not have to be paid again and central components will be available from the industrial partners of EuPRAXIA.

## 4.2 Summary of Total Costs

The estimated total resources required for the realisation of the EuPRAXIA facility are listed in Table 4.1. The table specifies the integrated investment costs, the personnel needs, and the project duration for the phases of TDR and construction. We note that the project durations for the beam-driven site (8 years) and the laser-driven sites (10 years) are unequal because of the technical readiness level associated with the respective technologies of X-band RF and high-peak-power lasers at 20–100 Hz. More details on the schedule can be found in Section 5.1.

The total costs in Table 4.1 are split into parts related to the site with beam-driven plasma acceleration and laser-driven plasma acceleration. It is seen that the laser-driven leg of EuPRAXIA is more expensive than the beam-driven leg. This is a result of the laser R&D required for realising the more powerful lasers in EuPRAXIA, the cost of laser procurement, and the undulator cost for the 5 GeV FEL user area. This will be explained and discussed in a subsequent section in more detail.

From the data in Table 4.1, a spending profile with yearly tranches of investment budget was estimated. This is shown in Figure 4.1. It is seen that the yearly investment budget would increase over eight years to 55 M€ and then drop in the last two years of the project. The average yearly spending would amount to 32 M€ over the full project duration.

The corresponding person-power effort during the project duration is shown in Figure 4.2. It is seen that this Europe-wide project would require the support of

**Table 4.1.** The estimated integrated costs of the TDR phase and construction are given (a) for the total project, (b) for the parts connected to the beam-driven plasma accelerator site (PWFA) and (c) for the parts connected to the laser-driven plasma accelerator sites.

	TDR phase	Construction phase	Sum
<b>Invest</b>			
<i>Total</i>	119 M€	204 M€	323 M€
<i>Beam-driven</i>	34 M€	85 M€	119 M€
<i>Laser-driven</i>	85 M€	119 M€	204 M€
<b>Personpower</b>			
<i>Total</i>	981 FTE	854 FTE	1835 FTE
<i>Beam-driven</i>	294 FTE	283 FTE	577 FTE
<i>Laser-driven</i>	687 FTE	571 FTE	1258 FTE
<b>Duration</b>			
<i>Total</i>	6 years	4 years	10 years
<i>Beam-driven</i>	4 years	4 years	8 years
<i>Laser-driven</i>	6 years	4 years	10 years

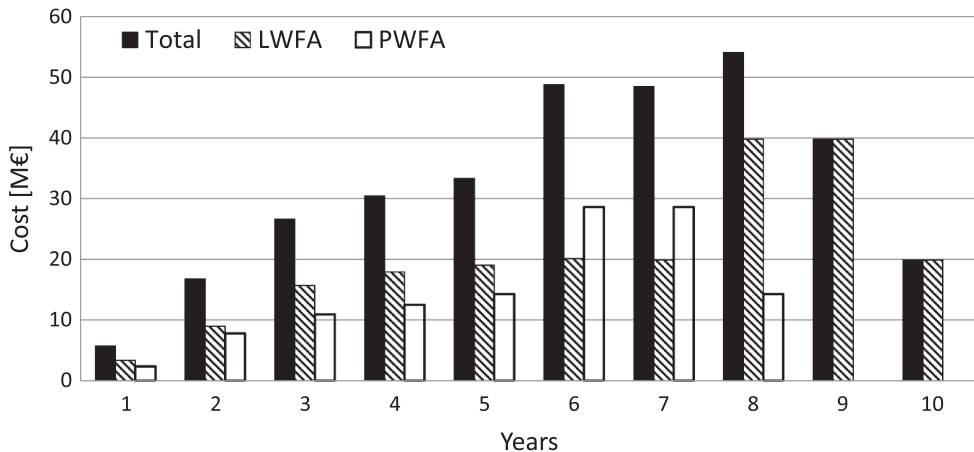


**Fig. 4.1.** The yearly tranches of the required investment costs are shown versus the duration of the project for the total and split by construction site.

184 persons (average) and about 230 persons (peak) for its realisation. This personnel could, in some cases, be contributed by partners in kind and, in other cases, would require funding support from national or European funding agencies. During the EuPRAXIA conceptual design work, about 250 persons have been involved in the work, while an estimated 40 FTE have been invested per year at maximum. The FTE available to EuPRAXIA would therefore need to roughly grow by a factor of 6 in the project realisation phase. The high number of persons associated with this project shows that the required persons and resources in principle exist in the field and in the connected institutions.

It is noted that a final budget planning will be part of the project preparatory phase, which must be performed in parallel to the TDR phase. During the preparatory phase, all budget numbers will be updated, a detailed cost-benefit analysis will be performed, and funding models will be defined. During the CDR phase, we have performed a first study of a possible budget distribution over Europe, grouping the

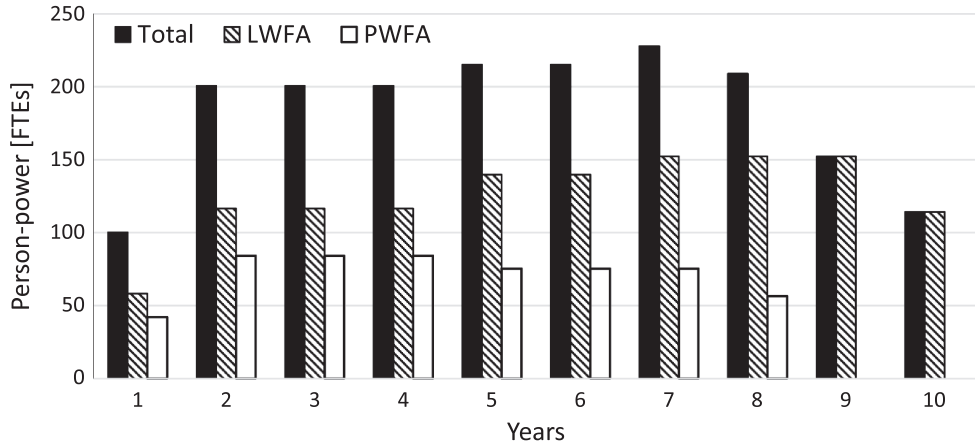


**Fig. 4.2.** The yearly tranches of the required person power are shown versus the duration of the project for the total and split by construction site.

funding by country of the institutes. The result is shown in Figure 4.3, integrating over investment and personnel costs. Here, it is assumed that one FTE costs 100 k€.

It is seen in Figure 4.3 that the project could be implemented with Italy, France, Germany, and the UK as major stakeholders at the 18% to 25% level of share in the total resources. Portugal could share at the 2% level given the mainly theoretical and numerical expertise that the connected institute would bring in. An additional 5% share, including general infrastructure and construction costs, would go to whichever country would host the construction site for laser-driven plasma acceleration. We conclude from this preliminary study that existing groups and facilities in Italy, France, Germany, the UK, Portugal, and other countries have the critical capabilities to support such a EuPRAXIA project if common resources and funding would be made available by the various funding agencies.

### 4.3 Breakdown of Investment Costs Related to the Beam-Driven Plasma Accelerator Site

The overall project costs listed above include a variety of cost items that enable a truly European effort. We first consider the site with the beam-driven plasma accelerator facility (PWFA). The total PWFA cost includes not only the resources required for the construction of the local accelerator facility and the FEL beamline but also prototyping and personnel costs around Europe. These additional resources will support the local construction by prototyping devices, testing them, and then delivering them to the PWFA site. While the cost of the final device should be included in the accelerator construction cost, the prototyping and testing at outside facilities can also be considered separately. The same applies to application beamlines, for example, for positron generation. The positron beamline will be developed, prototyped, and tested in excellence centres in another country with the final beamline delivered to the PWFA construction site.

Table 4.2 provides the breakdown of the PWFA costs into various categories, explained in the caption of the table. We can see, for example, that *the PWFA accelerator plus FEL facility would cost ~68 M€*, which is about half of the total cost. The other half of the total cost funds prototyping and testing activities around Europe, provides the additional application beamlines from non-local partners (thus

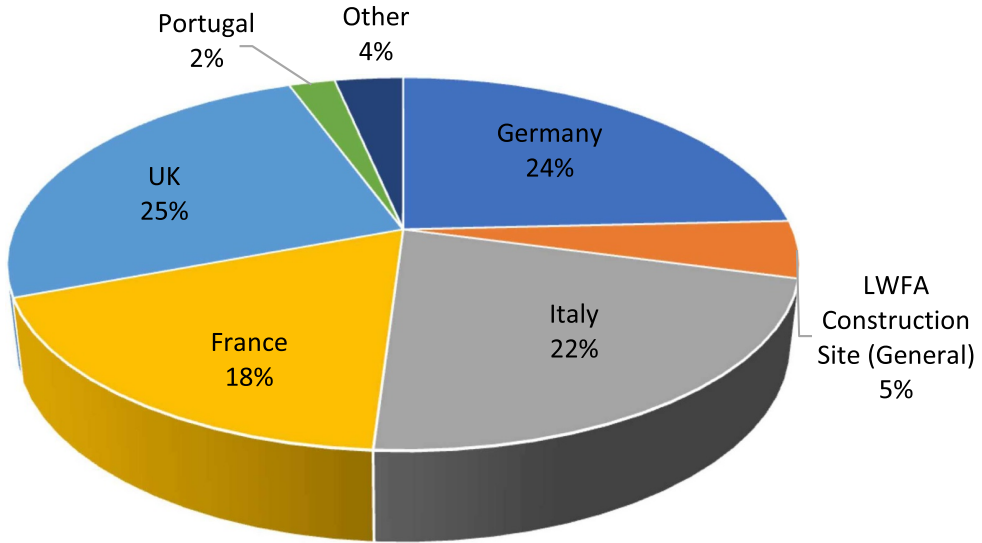


**Fig. 4.3.** A possible share of EuPRAXIA resources (investment plus personnel) over existing groups and facilities in connected European countries is given. General costs for the construction site for laser-driven plasma acceleration (LWFA) are listed separately as their allocation would depend on the location of the site.

**Table 4.2.** The costs of the beam-driven plasma accelerator site are broken down into construction costs of the accelerator (costs of all infrastructure and installed equipment at the construction site), into FEL construction costs (undulators plus user area), into costs for the construction of lines and user areas for other applications (see description in the relevant section), into costs of testing and prototyping at all European partners, and into costs for other innovation parts (for example alternative radiation sources).

Category	Invest	Person-power
<b>Accelerator construction</b>	52 M€	162 FTE
<b>FEL construction</b>	16 M€	22 FTE
<b>Other applications</b>	17 M€	91 FTE
<b>Prototyping EU wide</b>	33 M€	285 FTE
<b>Other innovation paths</b>	1 M€	17 FTE

amplifying the scientific impact of the EuPRAXIA PWFA site), and prepares additional innovation paths.

As noted before, the presented numbers are preliminary estimates that must be detailed and adapted in a preparatory phase of EuPRAXIA. The final numbers will depend on available funding support, the final partners, and implementation details.

It is interesting to consider the breakdown of investment costs also by technical system. Such a breakdown is shown in Figure 4.4. As this concerns the beam-driven plasma accelerator facility, it is seen that, as expected, the main cost drivers are the cost of the linear RF accelerator, infrastructure, and applications.

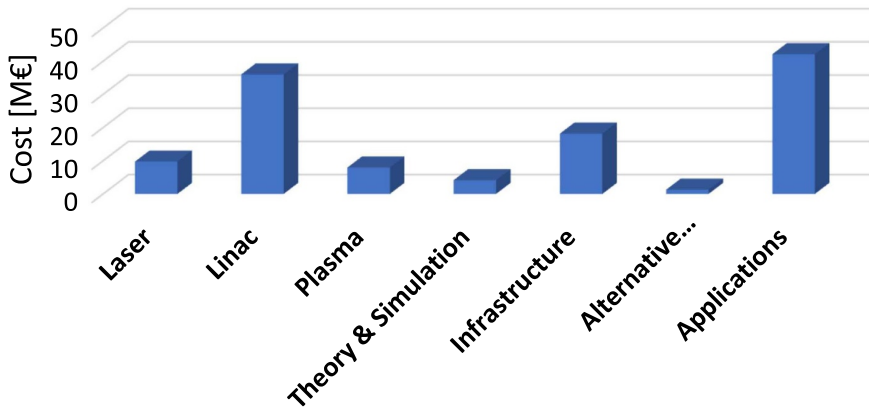


**Fig. 4.4.** The total investment cost related to the beam-driven plasma accelerator facility is broken down into the various major technical systems. Diagnostics and controls costs are contained in the linac and plasma system costs. The listed investment costs include R&D, prototyping, and construction.

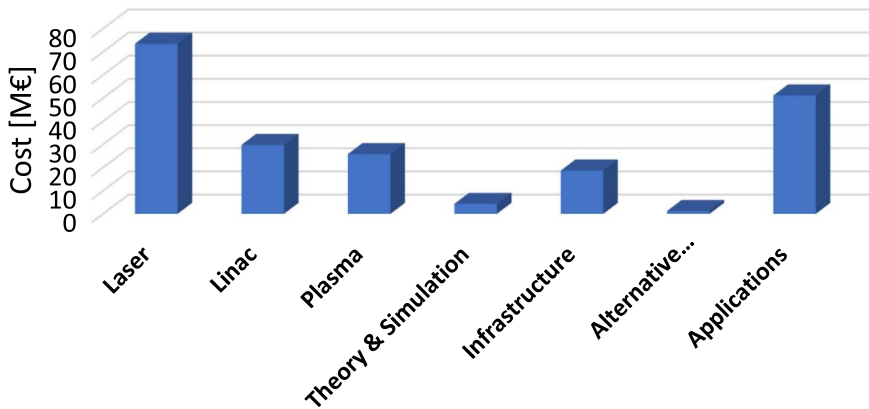


**Fig. 4.5.** The total investment cost related to the laser-driven plasma accelerator facility is broken down into the various major technical systems. Diagnostics and controls costs are contained in the linac and plasma system costs. The listed investment costs include R&D, prototyping, and construction.

**4.4 Breakdown of Investment Costs Related to the Laser-Driven Plasma Accelerator Site**

The breakdown of investment costs by technical systems is shown in Figure 4.5. It is seen that, as expected, the main cost drivers for the laser-driven leg of EuPRAXIA are the costs of the laser systems and of the science applications. The same breakdowns as explained above for the beam-driven plasma accelerator site have been done for the costs related to the laser-driven construction site. Table 4.3 gives the breakdown of the total costs per categories. We can see that the *investment cost of the 5 GeV laser-plasma accelerator facility plus the FEL user area amounts to a total of ~110 M€,* which, again, is about half of the total investment cost. The other half of the cost, similar to the case of the beam-driven plasma accelerator facility, is in part related to the development, prototyping, and testing in European research institutes and in close collaboration with the European laser industry. The laser investment will fertilise technological advances in laser technology and in the laser industry, required

**Table 4.3.** The costs of the laser-driven plasma accelerator site are broken down into construction costs of the accelerator (costs of all infrastructure and installed equipment at the construction site), into FEL construction costs (undulators plus user area), into costs for the construction of lines and user areas for other applications (see description in the relevant section), into costs of testing and prototyping at all European partners, and into costs for other innovation parts (for example alternative radiation sources).

Category	Invest	Person-power
<b>Accelerator construction</b>	86 M€	461 FTE
<b>FEL construction</b>	24 M€	27 FTE
<b>Other applications</b>	9 M€	75 FTE
<b>Prototyping EU wide</b>	84 M€	678 FTE
<b>Other innovation paths</b>	1 M€	17 FTE

for delivering the needed components but also allowing the European laser industry to maintain its world-leading capabilities. Other parts of the additional costs from collaborating institutes around Europe concern additional application beamlines that will again amplify and enhance the scientific potential of the constructed facility. Here, we list the positron-based imaging of materials as an example.

As noted before, the presented numbers are preliminary estimates that must be detailed and adapted in a preparatory phase of EuPRAXIA. The final numbers will depend on available funding support, the final partners, and implementation details.

#### 4.5 In-Kind Contributions

There have been major investments in the infrastructures at the EuPRAXIA institutes in the past. As the EuPRAXIA sites will be located at existing sites, the installed facilities and equipment will be brought into the EuPRAXIA project, and its usage will be considered as in-kind contribution. In addition, new projects on the scale of 20 M€ to 90 M€ are ongoing that enhance the existing investments and possible in-kind contributions even further.

It is immediately clear that the selection of final sites will have an impact on the total costs. For example, if a required laser will be available locally as in kind, the construction cost will be reduced. We assume in this CDR that the required buildings are available and can be adapted to the needs of one of the EuPRAXIA sites. The costs for adaption are included, the building is considered in kind. The INFN/LNF laboratory in Frascati, Italy, is planning to provide the infrastructure (building, air-conditioning, etc.) as an in-kind contribution as a host of the beam-driven plasma accelerator site. A detailed list of in-kind commitments and final budget adjustments must again be performed during the preparatory phase after the CDR.

#### 4.6 Operational Costs

Operational costs require a detailed analysis and study that could not be performed during this CDR. Based on past experience with accelerator-based facilities, a very rough operational cost (material plus operational personnel) can be estimated for the two construction sites:

##### **Operational cost of the beam-driven plasma accelerator facility:**

Estimate:  $\approx 6$  M€ per year

##### **Operational cost of the laser-driven plasma accelerator facility:**

Estimate:  $\approx 12$  M€ per year

It is again stressed that the operational costs listed above are very rough estimates with large errors of uncertainty. The higher operating costs of the laser-driven facility can be assigned to a few arguments:

- The lifetime and mean time to failure of RF modulators and klystrons has been optimised over many decades, and maintenance costs are therefore optimised. On the other side, lasers are a revolutionary and rapidly developing technology that still must be optimised for the lifetime of pump diodes, for example.
- The laser-driven plasma accelerator site of EuPRAXIA includes laser power drivers and undulator length for a beam energy of 5 GeV. The beam-driven leg of EuPRAXIA includes undulators for a beam energy of 1 GeV. Both approaches and sites will profit strongly from new types of innovative and small-size undulators. Strong R&D is supported.

The distribution and financing of the operational costs would need to be defined with the funding agencies during the preparatory phase.

#### 4.7 Alternative Minimal Systems

The EuPRAXIA project has aimed at a risk-minimised approach with a maximised scientific output. *Risk minimisation* is important as up to today, no plasma-accelerated electron beam has been brought into FEL lasing. Also, the available quality of electron beams from plasma accelerators is still quite limited, with up to an order of magnitude improvement required for certain applications, like highest-brilliance FELs. Another area of concern is the achieved repetition rate in plasma accelerators, with 0.5 Hz regularly maintained as average and peak rates of 5 Hz. Risk-mitigation measures are achieved in the EuPRAXIA concept by providing the infrastructure for various approaches of producing high-quality electron beams in a plasma accelerator. Examples include optimised plasma injectors in the bubble regime, plasma sources relying on the new resonance multi-pulse ionisation injection method, the injection of electrons from RF-based photo-cathodes, and novel two-stage acceleration schemes with intermediate phase space rotation.

*Maximised scientific output* is achieved by including various highly promising scientific applications that offer advantages compared to existing facilities. EuPRAXIA does not only include the FEL application but also includes, for example, positron-based imaging, positron beam acceleration, ICS and betatron sources for material and medical applications, etc.

Last but not least, EuPRAXIA brings together institutes and experts from around Europe, with close connections also to partners in Asia, Russia, and the United States. The *collaborational and knowledge-building* aspect of EuPRAXIA is not cost-neutral, but it provides the capabilities to advance faster with such broad support from around Europe. This strengthens the competitive position of Europe in this rapidly advancing technological field but also generates important socio-economic benefits for society. Examples can be the building of European connections, the training of young technicians and scientists in a technically challenging international environment, and last but not least, new jobs for well-trained young people in science and industry.

Given the above features and benefits of EuPRAXIA, it is clear that these come at a cost. We strongly believe that these investments into risk mitigation, science output, and more general socio-economic benefits in the European landscape of high-tech endeavours are well worth the costs. It is, however, interesting to consider minimal scenarios where a local facility targeted to one application only is considered. Cost estimates for a few reduced and minimal cases are summarised in Table 4.4.

**Table 4.4.** The investment costs for the full EuPRAXIA case are compared to estimates of minimal systems. For the beam-driven cases, the applications are reduced to only include the FEL. For the laser-driven cases, the applications in the first scenario are reduced to only include the FEL. In the second step, the mitigation measures on beam quality (multiple laser, RF injector, novel concepts) are reduced to a minimal one-laser, one-stage system. In both cases, the costs of European-wide R&D and prototyping are not included for the reduced scenarios.

Scenario	Invest
<b>Beam-driven plasma accelerator facility</b>	
Full EuPRAXIA proposal	119 M€
Plasma accelerator facility with FEL	68 M€
<b>Laser-driven plasma accelerator facility</b>	
Full EuPRAXIA proposal	204 M€
Plasma accelerator facility with FEL	110 M€
Minimal laser plasma accelerator with FEL	75 M€

## 5 Preliminary Project Organisation and Implementation

### 5.1 Project Schedule

A preliminary timeline for the project has been developed, as shown in Figure 5.2. It assumes that the project technical design, implementation and start of operations can be achieved within 10 years. This estimate as well as the proposed completion date depend strongly on the available financial resources throughout the project development, all of which are currently not clearly foreseeable yet. A certain amount of uncertainty thus needs to be expected from this schedule.

Conceptually, the development of EuPRAXIA as a multi-site infrastructure is divided into two separate yet related timelines. The design and implementation of the five excellence centres is scheduled within the “Technical Design Phase” over the next four to six years, whereas the two user machine sites will begin their technical design and construction at a later point and aim to reach completion at the end of the “Implementation & Construction Phase”. Between the construction sites, the facility based on beam-driven plasma acceleration is expected to require only a four-year technical design compared to six years of R&D and prototyping for the case of the site focused on laser-driven plasma acceleration. This means that the PWFA-based construction site could already be completed after an eight-year period, while the entire research infrastructure, including the LWFA construction site, would be ready by the ten-year mark. The reasons for this temporal separation in the development of the different sites are clear:

1. The excellence centres are smaller setups based strongly on existing infrastructures, thus requiring less design and construction time. Additionally, they are meant as advanced R&D facilities to mature the technologies to be implemented at the user sites, from the plasma-accelerator beamline and feedback systems to the FEL and other applications. They therefore need to be ready for use much earlier than the main machine sites, but not for performance as external user facilities. Figure 5.1 highlights some of the main technical milestones that will need to be achieved either as activities at the EuPRAXIA support facilities or even earlier as R&D at some of the EuPRAXIA Consortium facilities available for smaller testing and prototyping experiments (see Part 5 for more details).
2. The implementation of the laser-driven plasma accelerator construction site is largely dependent on the development of the required high-power,

### Important Technical Milestones

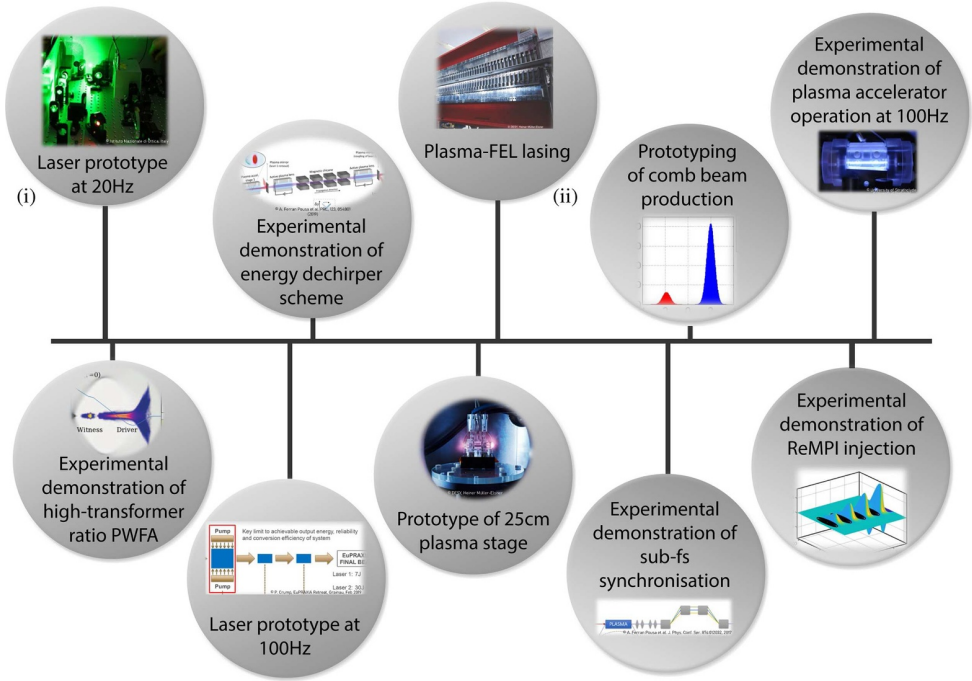


**Fig. 5.1.** Main technical milestones to achieve during the EuPRAXIA technical design phase.

high-repetition-rate laser sources as a significant advance from the current state of the art. This endeavour is expected to require considerable R&D and prototyping efforts. The X-band technology forming the basis of the second construction site for beam-driven plasma acceleration, on the other hand, is, while also a clear extension from the current state, already at a higher technical readiness and supported by long-lasting expertise developed in RF accelerator technology.

Furthermore, given the high degree of novelty in many of the technologies planned for EuPRAXIA as well as in view of funding uncertainties, a phased approach is also foreseen for the implementation and operation of each of the two user machine sites, as indicated briefly in Figure 5.2. With a detailed schedule to be defined during the technical design phase, first ideas for sensible phasing milestones include

- a staggered construction and operation of beamlines and user areas;
- an initial machine operation with 1 GeV electron energy with a later increase to 5 GeV; and
- an initial machine operation at a 20 Hz repetition rate, with a later increase to 100 Hz.

Particularly with regard to user operation, an approximately two-year-long pilot user phase will be extremely beneficial to develop a better understanding of the user and operation needs and challenges of EuPRAXIA as a novel type of plasma-accelerator-based facility. This will be followed by the main user operation phase, with a gradual ramp-up in operation hours, as the stability and performance of the machine is optimised and more beamlines / user areas become available.

Finally, for the long-term operation of the EuPRAXIA infrastructure, future machine upgrades will need to be developed and implemented over time, such as

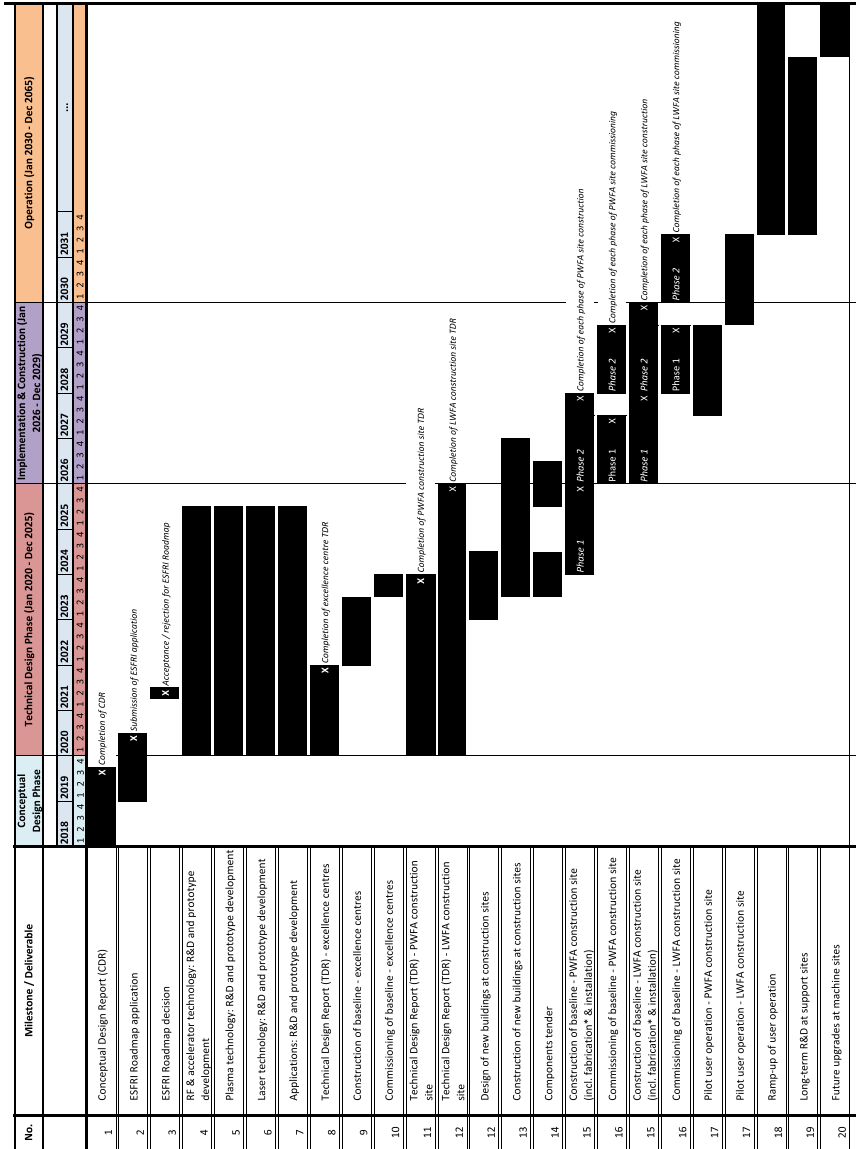
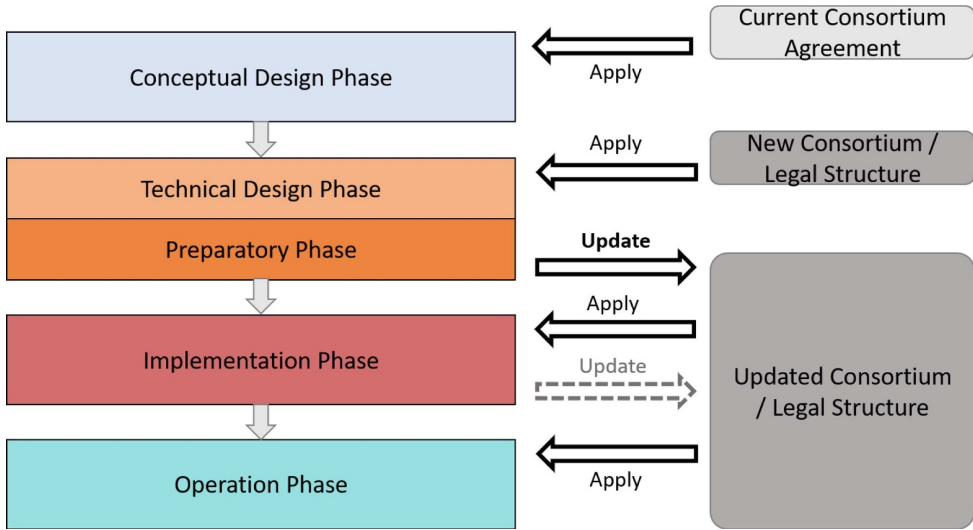
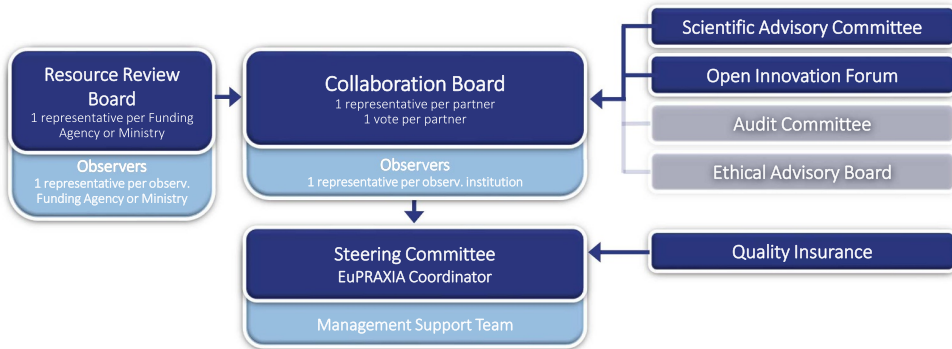


Fig. 5.2. Preliminary timeline for the design, implementation, and operation of EuPRAXIA, including several milestones marked by crosses in the Gantt chart.

high-repetition-rate operation and other topics of interest. These component improvements or machine upgrades will be prepared and optimised at the continuous testing areas of the four EuPRAXIA support facilities with a staggered transfer of technology to the user sites. In this way, the operation disruptions at all facilities are minimised, while a close technological and organisational connection between the many sites remains ensured.



**Fig. 5.3.** Implementation and re-evaluation process for the EuPRAXIA project structure. With the end of the current consortium agreement for the conceptual design study, a new agreement will be set up, which should be updated and revised as necessary throughout the different phases of EuPRAXIA.



**Fig. 5.4.** Planned management structure for the EuPRAXIA Consortium for future project phases. The listed bodies will be integrated as the “project management” within the wider EuPRAXIA infrastructure concept shown in Figure 3.1. Note that the features shown in grey are planned to be implemented only during the construction and operation of the EuPRAXIA facility.

**5.2 Structure and Governing Model**

The following legal and governance model described for EuPRAXIA represents the most suitable option, as foreseeable at this current project stage. Over the course of the design and implementation of the EuPRAXIA research infrastructure, it should be re-examined and possibly revised regularly, as varying external or internal conditions, but also, evolving perspectives within the collaboration may make changes in governance bodies as well as legal structure desirable over time. Figure 5.3 visualises how this continuous implementation and evaluation process for the collaboration structure could work.

The EuPRAXIA collaboration will, for the coming project phases, be structured through a consortium agreement. Following a survey of various international and national legal structures, the decision aligns well with the collaboration's priority to retain a high level of flexibility necessary to accommodate the current uncertainties in terms of funding, schedules, and the implementation of novel technologies still to be validated in the technical design phase. In addition, a consortium agreement will also easily retain the current collaboration constitution, including international partners and many smaller European institutes, without the need to organise the project at a higher, country-based level. Finally, with EuPRAXIA in a relatively early stage of development, the administrative effort associated with the collaboration governance can remain comparably small to develop and expand proportionately as the research infrastructure evolves.

The consortium's governance model is shown in Figure 5.4. It has been largely modelled after the collaboration structure during the conceptual design phase and will consist, among others, of the following bodies:

- The *Collaboration Board (CB)* is the highest decision-making body of the consortium. It is composed of one representative of each consortium member and can host observers. Its main function is to make proposals and decisions on aspects, such as changes to the consortium plan, finances, and intellectual property rights, changes to the consortium composition through withdrawal, default, or entry of a member, suspension or termination of the project, and appointment of positions in the other governance bodies.
- The *Steering Committee (SC)* is responsible for supervising the execution of the project. Similarly to the Collaboration Board, it consists of representatives of the consortium members as well as the Project Coordinator. Its tasks focus on executing and implementing decisions from the Collaboration Board as well as, more generally, overseeing the project progress.
- The bulk of the work carried out within the project is organised via ten *work clusters*, each focusing on a specific technical aspect of the project. Each cluster consists of multiple partner institutes and has a defined set of tasks to be achieved throughout the duration of the project.
- A range of advisory bodies will be set up to oversee the project, such as the *Scientific Advisory Committee* (advising on scientific matters), the *Open Innovation Forum* (connecting EuPRAXIA with industry), and the *Quality Insurance Panel* (overseeing quality control). The *Resource Review Panel* will represent the organisations and ministries funding EuPRAXIA to advise and oversee the project development. As such, it should be set up, once a funding path for implementation and operation is developed.

During the implementation and operation phases, further governance bodies should be installed, in particular the Audit Committee for monitoring consortium finances and the Ethical Advisory Board, overseeing the ethics of user experiments at EuPRAXIA. Moreover, the host institutions of the six EuPRAXIA sites will, of course, be integrated more strongly into the facility governance.

### 5.3 Operational Model

A detailed operational model for the future EuPRAXIA infrastructure will need to be developed, once the facility design, particularly the technical layout and the funding model, has been defined. As a first step, however, several more general arguments can be made regarding the facility operation:

- Both EuPRAXIA construction sites will be opened for user operation in the long term after commissioning and test operation periods are completed. The other

five excellence centres within the infrastructure, however, will be dedicated to research and development instead.

- The entire infrastructure will be coordinated by a lean overarching project management structure, as described in Section 5.2, while much of the day-to-day organisation during operation will be carried out by the host institutions of the individual sites.
- The necessary support structures for user operation – including IT systems, user support, and machine maintenance – will be provided by the host institutions of the construction sites to integrate these services directly into the institutions' existing operational infrastructure.
- It is assumed that the interdependencies between centres will be minimal as the targeted applications for both construction sites are complementary and most users will be interested in only one of the two machines.
- The interdependencies between individual beamlines, on the other hand, need to be examined more carefully during the technical design. For now, it is assumed that, at least during the beginning of the operational phase, each laser system (for the LPA-based site) and each RF accelerator (for the BPA-based site) will only feed one beamline and one user area at a time.
- To fully demonstrate the suitability of plasma acceleration for user experiments, the EuPRAXIA construction sites will aim to operate continuously for several days at a time (24/7), at least during a fraction of the year.

## 5.4 User Access

### 5.4.1 Types of User Access

The proposed EuPRAXIA research infrastructure is not a traditional user facility, but rather a demonstrator for future user infrastructures based on plasma wake-field acceleration. As such, a key goal of the project is the demonstration of high-quality machine performance required for different applications. Once this and other demonstration goals of EuPRAXIA have been achieved, the operation of pilot user experiments is envisaged.

An initial assessment of this potential user community for EuPRAXIA concluded that three main types of user groups can be expected, as Figure 5.5 highlights. Based on this evaluation, some considerations for a possible user access model are described in the following; these will need to be revised and developed in further detail during the preparatory phase of the project.

Beam users – especially in the beginning of the operation phase, a very small user group – correspond to those interested only in the properties of the beams offered at EuPRAXIA. The service that is most relevant for them is beam access, with the technical support of the EuPRAXIA technical staff. What distinguishes this category of users from others in particular is that they are not interested in the use of plasma-accelerator technology. In contrast, the category of users termed co-developers corresponds to those interested in developing and testing novel technologies related to plasma accelerators. EuPRAXIA will be the first user facility where such technologies are in operational use. It is therefore expected to be a reference facility, if not the only facility, where said technologies can be further developed and tested in real conditions. The third category of users is composed of trainees of different origins. As a demonstrator of more compact and economical accelerator technologies, EuPRAXIA is expected to attract (1) accelerator facility staff unexperienced with the new technologies in use at EuPRAXIA, (2) accelerator facility as well as company staff contemplating the adoption of new accelerator technologies in use at

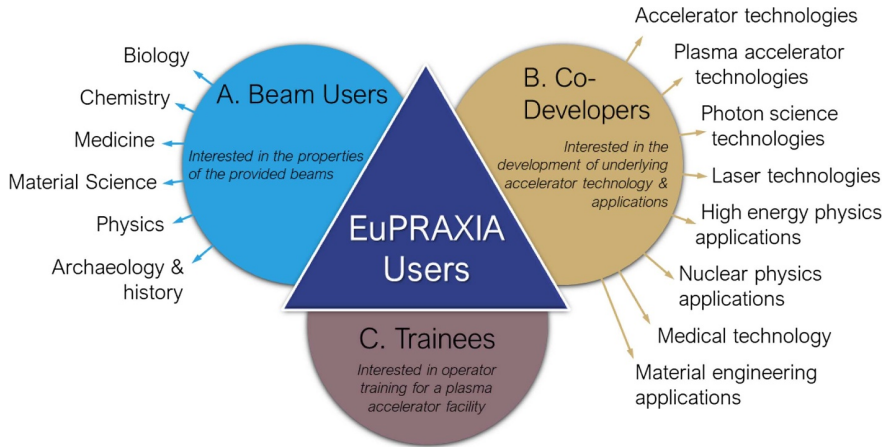


**Fig. 5.5.** Main user categories expected at EuPRAXIA. The access model should be adapted to cater to the different needs of these types of users.

EuPRAXIA, and (3) staff from research and academic institutions with no accelerator facility but interested in developing the theoretical and practical knowledge in view of carrying out experiments in different accelerator facilities. All three of these categories may contain academic as well as industrial users.

Because of their varying objectives for using the EuPRAXIA infrastructure, each user category will have their individual needs in terms of support, duration of beam time, user area setup, etc. To properly accommodate all, it is thus proposed to split access among these groups, offering each more individual services. While co-developers may be interested, for example, in longer experimental periods and more direct access to the accelerator beamline, beam users will be content with being placed in the end user areas, but will expect a reliable, continuously available beam. By assigning specific experimental periods throughout the year to each type of user activity, operation times could thus be optimised and longer maintenance periods in between utilised to adapt the machine setup accordingly.

For the initial period of pilot user operation, a stronger focus on co-developer experiments could be useful as a way to optimise the beamline performance without hindering experiments that are very reliant on strong beam performance or a high number of beam hours.

#### 5.4.2 User Facility Modes

Based on the above categorisation of the expected EuPRAXIA user community, a simple access model can be envisaged encompassing five access modes, as summarised in Figure 5.6 and explained in the following. Note that wide access refers entirely to data and, as such, is discussed in Section 3.5.

It is considered that all access to EuPRAXIA could be organised in three steps: a feasibility review, an evaluation, and scheduling. The feasibility review would be common to all proposals and would be carried out by the EuPRAXIA support staff with the support of EuPRAXIA researchers, if needed. The evaluation step would depend on the access mode and be carried out by external panels. Finally, the scheduling would consist of accommodating all selected proposals within a timeframe compatible with the availability of beamlines, equipment, and other boundary conditions.

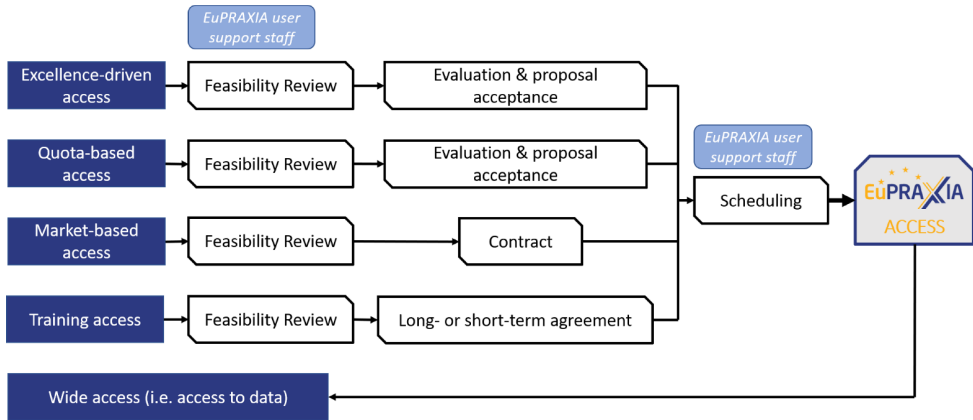


**Fig. 5.6.** Summary of the proposed access modes and procedures for users at EuPRAXIA.

In the excellence-driven access mode, beam time is foreseen to be granted after an assessment of the quality of all experiment proposals by the Research Program Advisory Committee. The acceptance of proposals will be based largely on their scientific excellence, although other criteria featuring into the evaluation could include, for example, consistence with the mission of EuPRAXIA, societal impact, the applicants’ track record, or the diversity of the applicant group. Quota-based access could be handled very similarly but with only proposals endorsed by one or several members of the EuPRAXIA Collaboration Board to be considered. This access mode thus ensures clear benefits for institutions and funding bodies to invest time and resources into EuPRAXIA while, at the same time, preserving the scientific excellence of experiments carried out.

Third, the concept of market-based access is designed specifically for industrial users in respect of the provisions of the General Block Exemption Rules 2014 applying to Research & Development & Innovation and the commission guidelines from the Framework for State Aid for Research and Development and Innovation. As the proposed activities at EuPRAXIA may vary significantly among users in this mode, access should be negotiated individually on a case-by-case basis from the initiation of a non-disclosure agreement and the feasibility review to assessing potential ethical concerns and negotiating a contract with the users. Finally, training at EuPRAXIA could be delivered to industrial users, students, accelerator facility operators, or any other type of users, so again, it makes sense to handle proposals in a customised way. Two main routes, however, could be foreseen: training access through a long-term agreement or through an ad hoc, one-off request. In both cases, a feasibility assessment will be necessary, considering, for example, available resources as well as the proposal’s relevance for EuPRAXIA. Once successful, this can be followed by the definition of a training curriculum, contract negotiation, and training scheduling.

**5.4.3 User Support**

Beyond the actual machine time, further services and support measures will need to be considered and designed for user operation at EuPRAXIA before implementation. These will include, among others, the organisation of user meetings and workshops, a process that has been started already for potential users during the EuPRAXIA conceptual design phase, but should be continued and extended throughout the development of the EuPRAXIA infrastructure. For the operational phase in particular,

the setup of a team of local contacts and machine staff will be essential, who will be responsible for user support before, during, and after experiments as well as for feasibility reviews and scheduling. Furthermore, supporting laboratories and workshops at the construction sites will need to be set up or organised within existing infrastructures, and adequate options for accommodation and catering on site must be ensured.

While most of these measures should likely be integrated into the host institute's existing infrastructure, especially for those institutions that host already other user facilities, details still need to be devised.

## 5.5 Quality Assurance

For EuPRAXIA, an ambitious, innovative project bringing together more than forty institutions across the world, quality assurance is extremely important and will be tackled through a number of dimensions:

- **Governance structures:** EuPRAXIA's proposed governance model (see Sect. 5.2) foresees a number of bodies dedicated to oversight and quality control, most importantly the Quality Insurance Panel. For the implementation and operation phases, the Audit Committee and Ethical Advisory Committee will additionally come into play to ensure adherence to proper spending and ethical principles. On a scientific level, the planned network of technical clusters (see Sect. 3.3.1) will structure the collaboration's research activities and help to avoid inconsistencies or unintentional repetitions among partners.
- **Performance indicators:** As Sections 3.3.1 and 5.1 show, major milestones and deliverables have been defined for the next project phases. This will be extended with a detailed work breakdown structure, schedule, and list of responsibilities for each consortium partner to better measure project progress. Key Performance Indicators as suitable measures for continuous performance will be defined for EuPRAXIA's operational phase.
- **Standards and procedures:** While this design report acts as a comprehensive summary of the design decisions, layout considerations, and project planning to date, more common standards and procedures will need to be defined during the technical design phase in the form of a quality assurance plan. This will include, among others, technical design requirements, procedures for procurement and component testing, employee and user training decisions, and safety regulations (coordinated with the safety organisation described in Chap. 27.1). It will be essential to build on the expertise and existing structures at the project's partner institutions in this context.
- **Validation of scientific results:** A large fraction of the technical design phase will be dedicated to validating the results and concepts proposed in this conceptual design report. Through test experiments, prototyping and further computational studies, a robust comparison between different codes, simulations and experiment results as well as design parameters with fabricated components will become possible.

## 5.6 Outreach and Communication

The EuPRAXIA Outreach and Liaison Group based at the University of Liverpool/Cockcroft Institute will continue to work closely with the Management Support Team and project partners to communicate project results and events internationally.

## Activities

### Existing External and Internal Communication Platforms

The project website [www.eupraxia-project.eu](http://www.eupraxia-project.eu) will be maintained by the Outreach and Liaison Group as the main portal of information of EuPRAXIA for the external world. Relevant news about EuPRAXIA will be promoted via established social media channels. The University of Liverpool's Sharepoint system will continue to be used to facilitate the exchange of documents among the project partners. The group will also continue to showcase EuPRAXIA achievements at workshops and conferences around the world and continue to publish the EuPRAXIA files newsletter three times per year. Existing dissemination material (leaflets, brochures) will be updated on a regular basis and reflect project progress.

### Education and Engagement

The computer game *Surfatron* will be developed into an online version that can be accessed via the project website. Liverpool's pioneering augmented reality application, AcceleratAR (<http://acceleratar.uk/>), which allows building an accelerator by placing paper cubes on a tabletop and then bringing them to life using the app, will be expanded to also include plasma acceleration. This will allow for engaging with primary and secondary schools in a novel and interactive way. Furthermore educational material on the basis of the 2018 Symposium will be developed further and promoted through learning and teaching conferences, as well as publications in journals on education and teaching.

### Outreach

The group, in close collaboration with EuPRAXIA partners, will continue to communicate the specific research challenges and opportunities of plasma accelerators to a range of audiences with the aim to further increase the attractiveness of the field overall. This will include policy makers and funding councils.

The website (<https://marie-curie-day-2017.org/>) that was developed for Marie Curie Day 2017 will be extended to include information about female researchers in accelerator science and technology. There is a number of female researchers in EuPRAXIA at various career stages, and they will be amongst the first to be included. The aim is to establish the website as a careers portal for researchers whilst continuing to promote the posters and talks from the 2017 event.

Another Physics of Star Wars event will be held in November 2019 at the University of Liverpool. Using unique *Star Wars* concepts (hyperspace, the lightsaber, the Force, etc.), the physics and technology of EuPRAXIA will be explained and communicated via media internationally. Communication will benefit from the links that were established in the past and target an even larger audience. Educational material shall be made available for use by schools and university groups.

EuPRAXIA partners will be encouraged to hold public events showcasing the achievements in plasma acceleration, with supporting material and demo setups provided by the Outreach and Liaison Group. Based on experiences gained in past pan-European events using social media campaigns and video live-streams, emphasis will be placed on events involving more than one institution at a time.

## 5.7 Project Risk Assessment

EuPRAXIA needs to consider two different types of risks as part of the project: general project risks and technical risks for specific sub-systems of the machine. While a comprehensive risk assessment for the technical design, implementation, and operation phases of the project is ongoing, this chapter will highlight some of the most important examples.

### 5.7.1 General Project Risks

The general project risks that need to be considered for EuPRAXIA are largely financial, schedule related, or organisational in nature. Table 5.1 shows a few relevant example risks together with possible mitigation strategies. Also listed in each case is a rough assessment of each risk's probability and impact.

### 5.7.2 Technical Risks

With EuPRAXIA as a complex, high-performance machine, the technical risks contained in the project have been analysed carefully. Generally speaking, two particular issues could arise for components of the facility: (1) unforeseen technical problems could occur that limit the final performance of a sub-system, and (2) the expected performance of a component, currently based in many cases on simulations, could be overestimated compared to the experimental output because of computational limitations, new physics processes, or unavoidable imperfections. With these in mind, a set of risk-reduction actions has been defined as a roadmap for the next phases of the project:

1. The EuPRAXIA design is based, as far as possible, on proven concepts and solutions. The baseline for all machine sub-systems is thus either already at a high technical readiness level or an extrapolation of existing technology, particularly for critical components, such as the laser system and the free-electron laser.
2. Test experiments are planned for all machine components, and for the most critical sub-systems, full-scale prototypes will be developed and checked. Further details on the planned prototyping are described in Part 5.
3. The EuPRAXIA accelerators are designed to be very well-characterised machines with a high level of control. Extensive diagnostics, feedback, and correction systems are foreseen to be implemented.
4. Backup options are defined for the most critical sub-systems and will be included in the planning for R&D and prototyping to ensure that they could, if necessary, be implemented with as few changes in cost, schedule, and scope as possible.
5. A wide range of applications with varying levels of complexity and possible step-wise optimisation strategies were defined. This will allow one to fall back initially on less complex user applications, in case of problems with the technical machine performance.

A more detailed risk analysis for each sub-system of EuPRAXIA is provided in the following, with major risks summarised in Figure 5.7. It also shows an estimate of the current technical readiness levels of the components and techniques foreseen for each machine part.

**Table 5.1.** A list of the some of the most relevant general risks for the EuPRAXIA project during its technical design, implementation, and operation phases. Considering the proposed mitigation strategies, in each case, the risk probability and impact is shown on a qualitative scale.

Risk	Description	Mitigation Strategy	Probability	Impact
Failure, bankruptcy or withdrawal of one of the host partners	E.g. due to political circumstances	Development of a strong consortium agreement defining clearly the benefits for partners; early discussions / negotiations with institution higher managements and national ministries; distributed infrastructure concept with responsibilities spread between partners	Very low	High
Failure, bankruptcy or withdrawal of one of the non-host partners			Low	Medium
Delays, difficulties in finalising the research infrastructure (RI) technical design	E.g. due to limited facility access for simulations / test experiments or failure to coordinate individual partners' work	Setup of a strong management structure for the technical design phase; efforts to secure common consortium funding for R&D activities; continuation of current work on prototyping and test experiment coordination through a dedicated panel	Low	Medium
Failure to obtain funding for infrastructure implementation	Assuming the completion of a convincing technical design	Application to ESFRI roadmap; planned discussion with EU representatives and institute management of EuPRAXIA partners on possible opportunities	Very low	Very high
Failure to obtain funding or sufficient guarantees for funding of operational phase	Assuming completion of a convincing technical design and success in obtaining implementation funding	Early negotiation with host institutions / funding bodies	Very low	Very high
Failure to acquire sufficient qualified human resources	Workforce too small to carry out all tasks and deal with all issues for technical design leading to possible project delays	Timely start of recruitment; inclusion of all current EuPRAXIA partners to carry out design work; wide advertisement of positions using also close connections of EuPRAXIA partners and associated labs to university PhD programs	Low	Medium
Failure to timely complete construction	Possibly due to inaccurate schedule estimation or communication / coordination issues between partners	Inclusion of contingencies in cost and schedule planning; building on expertise of collaboration for realistically assessing construction schedule and progress; definition of clear responsibilities during construction	Low	High
Failure to timely procure equipment	Possibly due to delays from external suppliers, underestimation of time requirements for procurement (e.g. through publicly funded procurement processes), failure of supply chain because of economic conditions / limited suppliers or flaws in procured equipment and need for re-procurement	Building on expertise of the many experts in the collaboration in handling procurement	Low	Medium
Increase in equipment cost (or underestimation of costs)	More likely for newly designed equipment	Establishment of an expert committee on accelerator and laser costing to provide best knowledge estimates based on extensive project experience; inquiry of price estimates from industry	Low	Medium
Need for changes / rework of research infrastructure design	Possibly due to mistakes in the final technical design or due to required changes in the project scope (based on changes in user needs, scientific program, etc.)	Thorough validation of components, design and layout during technical design; contingencies in both cost and schedule	Low	Medium
Shift in an industrial partner's priorities	Leading to changing interest / investments in essential technologies	Discussion and collaboration with companies in relevant industries early on since conceptual design study	Low	Medium
Insufficient user base or failure to attract users (academic & industrial)		Early start to user demand analysis through discussions with potential users to align their needs with the design and inform about EuPRAXIA; plans for user / industry workshops during technical design and beyond; development of multiple complementary applications within the RI concept	Very low	High

## Laser System

For the laser system, as one of the most challenging components of the EuPRAXIA machine, a whole range of testing and prototyping exercises is foreseen, as described in more detail in Chapter 10. Three high-level risks, in particular, are being targeted by these activities and need to be considered for backup solutions in case the technical design R&D discovers fundamental performance limitations. First, there is a possibility, although highly unlikely, that the laser stability requirements for a reliable plasma-accelerator operation cannot be fulfilled. In this scenario, a reduction in the plasma density in the LPI and LPAS components would be possible to relax the operational requirements yet at the cost of a lower accelerating gradient and hence larger machine size. A second risk related to the laser stability lies in the possibility that the final focus laser beam handling is insufficient for the staging of multiple plasma targets. While experimental staging tests should provide a clear confirmation of the performance requirements, a final mitigation strategy in case of fundamental issues could foresee the design of an alternative single-stage plasma accelerator. Third, the thermal management of the laser components is a significant challenge and risk to high-repetition-rate operation. As a consequence, the laser design is set up in a stepwise approach with a baseline at 20 Hz, ideal performance at 100 Hz, and a future development option to the kHz level. If the planned R&D activities reveal any physical constraints in this respect, operation at lower repetition rate will thus still be possible, or a redesign of the laser system based on alternative technologies could be considered.

## Plasma Components

Although in general, plasma targets can be produced by now in quite a standardised manner, EuPRAXIA will add some additional challenges to the design and fabrication of components by requiring, on the one hand, particularly long plasma cells with laser guiding capabilities and, on the other hand, components that can withstand significantly higher repetition rates than is usually the case in plasma acceleration experiments. To overcome both of these issues for the target design, several possible technological options have been explored conceptually, as described in Chapters 13 and 16, and will be tested extensively in the coming technical design phase. This strategy will also help to reduce the risk of simulation errors that the current computational approach for estimating the machine performance entails. Additional to experimental testing, the next project phase will focus on cross-checking simulation results with multiple codes as well as carrying out thorough tolerance studies.

## RF Components

The radiofrequency-based sections of the machine layout are some of its more low-risk components and in themselves are integrated in the design as a risk-mitigation strategy. Nonetheless, combining RF injectors with plasma acceleration is a relatively new concept and, as such, brings certain risks with it. It is in particular possible that the conditions on the electron beam properties and synchronisation required for a stable plasma acceleration process, as Chapters 14 and 19 highlight, cannot be met. In this case, again, operation at lower plasma density and hence lower accelerating gradient would be a backup option if consultations with experts and operational accelerator facilities outside the project do not result in alternative conventional accelerator solutions.

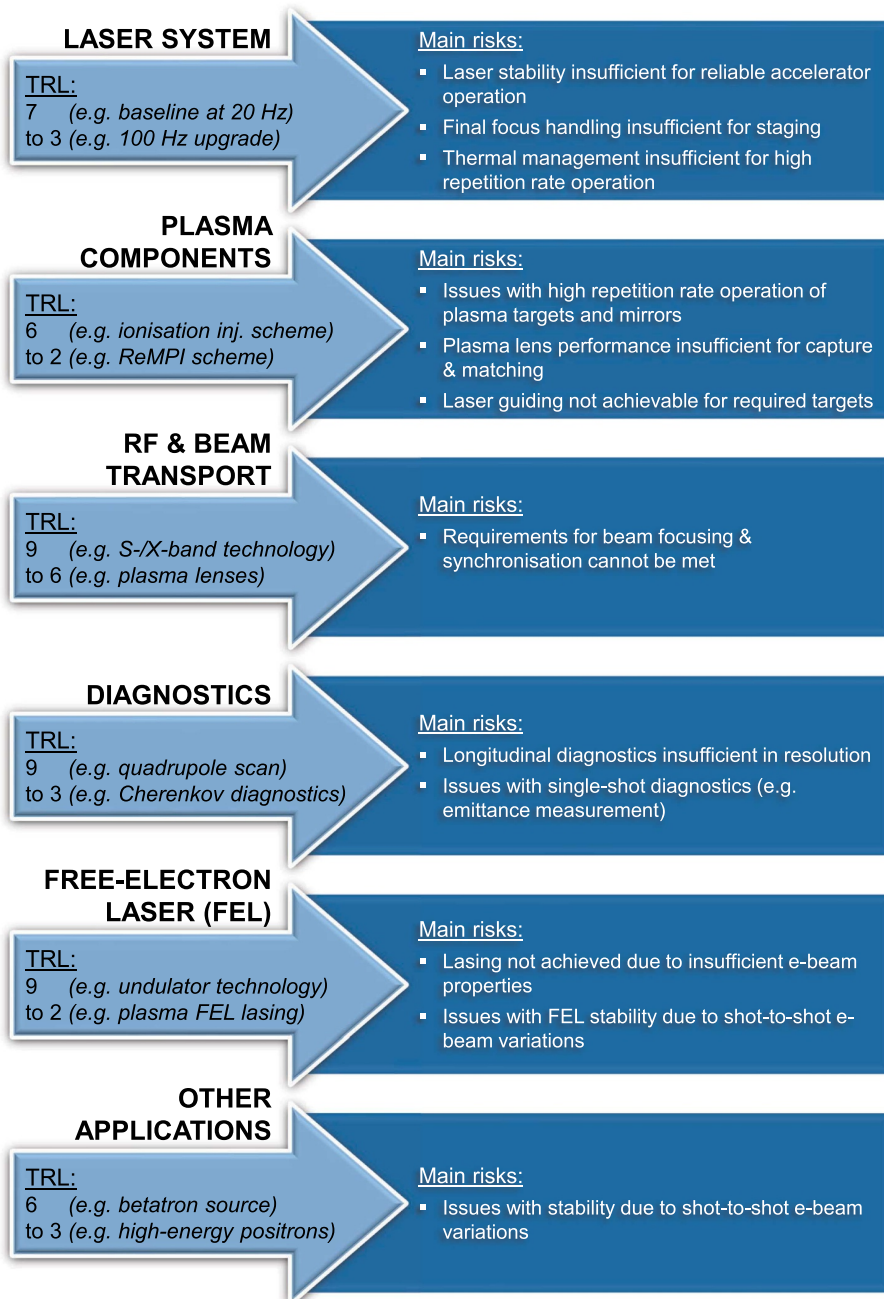


**Fig. 5.7.** List of the main technical risks associated with each major sub-system of EuPRAXIA. General and more specific mitigation strategies for each are described in the main text. Additionally, an estimate of the technical readiness levels (TRL) of the components of each sub-system is listed based on the TRL scale from 1 to 9 defined for Horizon 2020 [173].

## Diagnostics

The diagnostics layout for the EuPRAXIA machine should be customised to the specific properties of the plasma-accelerator-based setup and, as such, involves a large number of novel diagnostic techniques with a compact size and / or the capability to take single-shot measurements (e.g. single-shot emittance measurements, compact cavity BPMs, single-shot coherent radiation-based bunch length measurements). While the testing and prototyping of these devices is planned during the technical design phase, there is a risk that these diagnostics will not perform as well as required for machine operation. As a mitigation strategy, the conceptual design foresees more conventional backup options for the diagnostics sections, which have been validated through operation in other machines but would result in a less compact and less efficient EuPRAXIA accelerator.

## FEL

Lasing with an FEL based on plasma acceleration has not been achieved to date, thus proving one of the most high-risk aspects of EuPRAXIA. As such, multiple mitigation strategies are being pursued in parallel. First, several test experiments are currently ongoing (see Sect. 32.7), with further large-scale prototyping activities planned during the technical design phase. As a second point, conventional undulator technology is chosen as a baseline for the beamline design to minimise risks for this application as much as possible. Third, specific beamline components designed to compensate large energy spread, one of the potential issues with plasma acceleration, are being investigated, such as transverse gradient undulators and decompression chicanes (see Chap. 18). Both could potentially ease the strict electron beam requirements necessary for FEL operation. Finally, if fundamental show-stoppers should emerge based on the studies above, the machine design can be altered during the technical design phase, avoiding, as much as possible, additional costs or schedule delays. For the beam-driven construction site, for example, a backup option is already integrated as the X-band accelerator could be extended to 1 GeV, allowing FEL operation without the need for a plasma acceleration stage.

## Other Applications

Similarly to the free-electron laser application, there is a risk that the electron beam requirements for the other applications foreseen for EuPRAXIA cannot be fulfilled. Beyond the necessary prototyping and testing to reduce this risk, this possible problem is also mitigated by selecting the set of highlight applications chosen for EuPRAXIA based not only on their scientific relevance but also their electron beam requirements. Hence, technically advanced applications with lower requirements, such as the betatron source, can be used, if necessary, as a basis for testing and improving accelerator performance, until it becomes optimised enough for more challenging use cases.

# 6 Impact Assessment

## 6.1 Strategic Significance for European Science and Innovation

### Direct Scientific Impact

The proposed EuPRAXIA research infrastructure will make available several types of particle and radiation beams with capabilities in a number of different scientific fields.

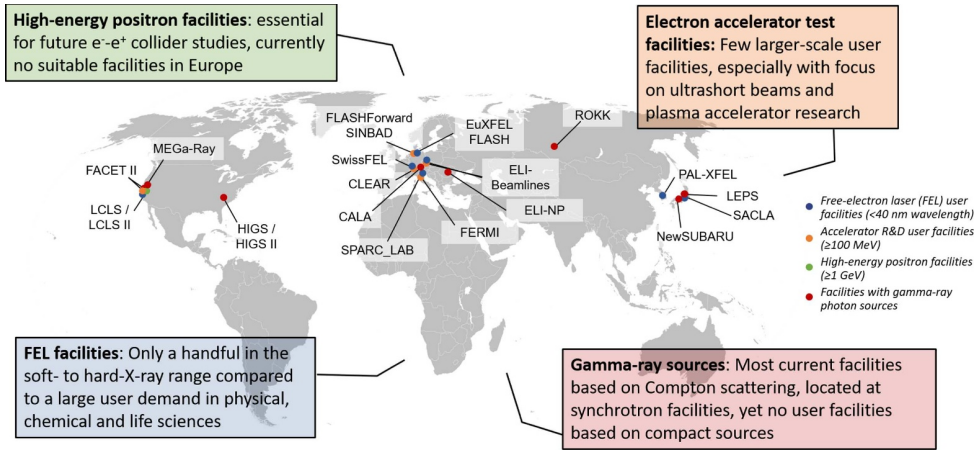


**Fig. 6.1.** Map of large-scale user facilities providing access to similar types of particle and radiation sources as EuPRAXIA will offer (X-rays from free-electron lasers, high-energy electron test beams, gamma rays, and high-energy positrons). The list of facilities shown here is not exclusive, but it does provide an overview of the main research infrastructures of each type.

For many of these, EuPRAXIA will be one of only a few facilities worldwide with such characteristics. As Figure 6.1 shows, for example, there is only a handful of free-electron laser infrastructures in the X-ray regime operational today. Similarly, for the case of electron accelerator R&D, few dedicated user facilities are available in Europe and worldwide; for plasma-accelerator research or studies with ultra-short electron beams, there are even less and none with the capabilities expected at EuPRAXIA. Operational gamma-ray sources for user experiments are almost entirely based on Compton scattering using the GeV-scale electron beams at synchrotron facilities. Hence, both for these as well as high-brightness, non-coherent X-ray sources, largely covered by synchrotrons, EuPRAXIA will be one of the first few compact machines. Finally, to our knowledge, FACET-II will provide the only other high-energy positron source (multi-GeV) in the next years, thus making EuPRAXIA an essential addition to offer similar capabilities within the European research area. It is also important to consider that EuPRAXIA will not only provide access to all of these types of sources and beams but also do so in a single infrastructure (at two locations), thus enabling new types of multi-species experiments which are difficult to coordinate in the current landscape.

A direct scientific impact is therefore expected from the implementation and operation of the EuPRAXIA facilities; the overall capacity for user experiments in photon and accelerator science in Europe will be increased, especially in key scientific areas of strong competition for facility access, such as X-ray free-electron lasers. In addition to a rise in scientific output (through papers and patents) from European research communities, however, these new and increased capabilities of EuPRAXIA could also be beneficial in broadening the community of users of accelerator-based technologies. Through providing beam characteristics not available elsewhere, for example, the entry barrier for accelerator-assisted research can be lowered, allowing access also to research groups typically not making use of large-scale accelerators.

## Impact on Technological Development Capacity of the European Research Area

Plasma accelerators are a highly demanding technology with requirements close to technical feasibility limits in several scientific areas. With significant synergy created from the proposed combination of state-of-the-art plasma acceleration, modern lasers, latest accelerator technology, top-of-the-line environmental control, and promising applications, EuPRAXIA will contribute to strengthening the technological development capacity and effectiveness of the European Research Area at the frontiers of these fields. Technological impact can be expected, among others, on the following topics:

**Ultra-fast synchronisation, electronics, and correction loops:** The timing and accuracy requirements of plasma accelerators are in the femtosecond regime, requiring state-of-the-art synchronisation on the order of single femtoseconds. EuPRAXIA will foster further progress on this technological frontier. Lasers that are timed precisely to an external reference and ultra-fast electronics can be implemented in many technological devices, like laser heaters, laser vibration monitoring, laser wires, ultra-precise timing reference systems, femtosecond stabilisation loops, etc. We note that mechanical miniaturisation (e.g. in nanotechnology or plasma structures) leads to much-reduced stabilisation tolerances and goes hand-in-hand with ultra-fast technologies that must react before tolerances are violated. Ultra-fast technology will thus contribute to the successful development of miniaturised technology.

**Compact accelerator magnets with high field quality:** The need for matching electron beams in and out of plasma channels requires magnetic focusing to a small beam size in the single micrometre regime. While this has been achieved in RF accelerators, the conventional schemes have to be adopted for plasma-accelerator needs. Required are, for example, sufficient flexibility for adapting to changes in plasma focusing fields and small dimensions. Additionally, challenges for the chromatic correction of magnetic beam transport will need to be considered, even with the improved low-energy spread electron beams foreseen from EuPRAXIA. The project will therefore foster developments towards compact accelerator magnets with high field quality, chromatic correction, and a certain tuning range. Both permanent magnets as well as electromagnetic magnets are options that will be considered together with industrial suppliers and accelerator labs. We expect that the magnets and lattice solutions from EuPRAXIA can have many other applications in the 30,000 accelerators around the world.

**Stabilised and high-repetition-rate PW-scale laser technology:** It has recently been demonstrated that the 5 GeV target energy of EuPRAXIA can be achieved with a PW-scale laser [9]. While the peak power in such state-of-the-art systems is sufficient, there are limitations in efficiency, stability, and, in the long term, average power. EuPRAXIA will not consider efficiency problems as these are being addressed in other European efforts. It has, however, investigated laser stability limits and possible design solutions. For example, it is estimated that the laser spot transverse jitter at the location of the beam acceleration can be reduced by optimising the laser transport (e.g. mirror stabilisation) as well as by optimising the laser itself (see Chap. 10). In a similar context, an increase in laser repetition rate up to the 100 Hz to kHz level is expected to significantly improve the feedback capabilities of both the laser system and accelerator-related processes, thus further enhancing machine shot-to-shot reliability. These developments will be carried out in close collaboration with manufacturers and laser institutes, thus opening the path to a broader application of such next-generation laser systems and placing Europe as a leader in laser technology and stability.

**Plasma cell technology:** EuPRAXIA proposes the design of a plasma cell that can be cascaded and fulfils the required tolerances for user applications. The end goal is an “industrial” plasma cell design that provides a path to higher energy by cascading. The in- and out-coupling of the laser is included. EuPRAXIA will thus provide Europe with a technological solution for plasma cell technology to be used with lasers from the European and worldwide industry.

**Compact FELs:** The reduction of length in the acceleration will significantly reduce the length of FELs. However, the undulator sections require significant space and in many cases will determine the length required. EuPRAXIA relies on existing undulator designs for its baseline. However, compact innovative developments and solutions will be followed in parallel, comparing benefits and disadvantages. EuPRAXIA will thus provide Europe with a detailed assessment of compact FELs and, if adequate, with solutions for length-reduced undulators.

**Fast photon science detection technology:** The length of electron bunches in plasma accelerators will necessarily be very short, at around 1 femtosecond, with similarly short photon pulses produced from these beams. This will open a unique science reach into ultra-fast processes that can be analysed at the electronic level without perturbation. The detector technology for ultra-fast photon science has to be adapted to the plasma beam features. EuPRAXIA will foster progress in ultra-fast photon science detection technology, allowing Europe to stay at the leading edge of photon science detectors.

**High-energy physics detector technology:** EuPRAXIA will provide a dedicated application area for developing and commissioning the latest HEP detector technology. Detector components can profit from the additional beam time and the (controllable) high density beam characteristics, either directly in the (collimated) electron beam or after a conversion target. EuPRAXIA will contribute to the development of state-of-the-art HEP detectors for maximum event rate and multiplicity.

**Medical accelerator technology:** Medical applications are included in EuPRAXIA in the form of medical imaging. Compared to other accelerator uses in medicine, such as radiation therapy, this application will allow for the development and demonstration of the required stability of plasma accelerators. This knowledge and these achievements in EuPRAXIA towards stable plasma accelerators can then be directly applied as a path to wider medical applications with a long-term perspective to using plasma acceleration as a technology in hospitals and medical research.

The technical work carried out in EuPRAXIA is thus foreseen to significantly strengthen the technological development capacity and effectiveness as well as the scientific performance, efficiency, and attractiveness of the European Research Area.

### Impact on International Cooperation

EuPRAXIA will develop a model of international cooperation and a strategic vision for bringing plasma accelerators to the users and to the market. The R&D on electron plasma acceleration is carried out in multiple projects in Europe, Asia, and the United States. The relatively small size and cost of a plasma accelerator has attracted a large number of excellent university groups, in addition to major accelerator labs. Scientific results are published at the highest level of journals, including *Nature*, *Science*, and *Physical Review Letters*. Scientific highlight results have often the clear priority over working on already achieved parameters for improving beam quality and demonstrating user readiness. With EuPRAXIA, a new kind of international cooperation has been established in the field of plasma acceleration. The 41

consortium partners in Europe and abroad will continue to team up with the clear goal to bring plasma accelerators to user readiness and to the market. It will establish a common goal for the international field and will give a vision for the funding and implementation of common projects across different universities, labs, and countries. We believe that a common European project on electron plasma accelerators can also contribute to the advancement of the field in other parts of the world. The EuPRAXIA strategy, results, and design choices will be disseminated and discussed widely in the community, especially outside of Europe. The activity can contribute to a global consensus on the best way for bringing plasma accelerators to the users in photon science, high-energy physics, industry, and medicine. It can be used as a basis for improving methodologies and developing standards within this relatively new field within accelerator science. EuPRAXIA will thus foster a new kind of transparent and use-case-oriented international cooperation in the diverse field of plasma accelerators. It will develop a model for the construction of plasma accelerators in a fair and distributed open innovation approach beneficial to consortium partners, industry, as well as researchers beyond the collaboration.

## 6.2 Socio-Economic Opportunities

The opportunities produced by a project such as EuPRAXIA go beyond its scientific impact reaching, as Figure 6.2 shows, into economic, societal, and environmental areas. This is also reflected in the range of societal project goals introduced in the executive summary (see Part 1).

The role of the project for the European high-tech industry as a source for knowledge transfer and technological spillover, for example, should be mentioned. With the high-power laser industry as a most direct beneficiary and partner, EuPRAXIA will help keep Europe's leading position in this field and will contribute to further strengthening the European technological capacity in laser- and accelerator-related industries. European companies will be able to connect to the EuPRAXIA research infrastructure not only as suppliers but also as users or co-developers. It can be envisaged, for example, that industry tests and develops new laser stability measures and other technologies under the very challenging EuPRAXIA conditions and tolerances. The high demands will inspire and foster technological progress, keeping European laser industry at a leading edge. Similar trends can be envisaged also in the area of accelerator systems and components as well as IT and software development, with the latter benefiting particularly from efforts and challenges in plasma simulation.

Additionally, EuPRAXIA will contribute to opening new market opportunities for industry with its concept as an open-innovation platform. The quality improvements, compact size, and cost-effectiveness of plasma accelerators that EuPRAXIA strives to push forward will, in the long term, make accelerators feasible space-wise and/or affordable to additional users. Our future vision based directly on the developments at a future EuPRAXIA research infrastructure includes, for example, compact plasma-based FELs in the basement of every large university, plasma accelerators for fast medical imaging in hospitals, and very compact plasma colliders at high-energy physics laboratories. In many cases, conventional facilities would not be replaced but complemented, and industry could be involved very closely in these developments.

Another important role of a future EuPRAXIA infrastructure will also lie in training and education. On the one hand, the EuPRAXIA collaboration provides an excellent environment for such efforts, with strong cooperation among research centres, universities, and industrial partners across Europe. On the other hand, the EuPRAXIA research infrastructure will also represent one of the first test facilities worldwide with plasma accelerators at its core, thus offering unique expertise with

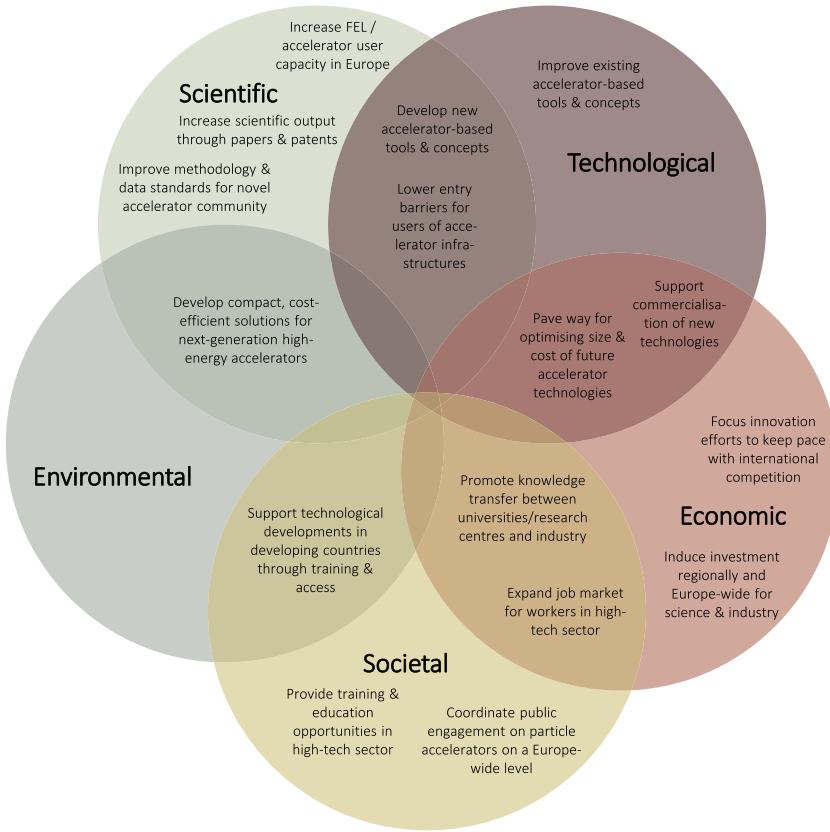


**Fig. 6.2.** Map of areas of impact expected through the implementation and operation of the EuPRAXIA research infrastructure.

regard to the operation and practical challenges of this technology. Both research groups new to particle acceleration as well as more experienced parties established in RF acceleration could therefore benefit from such knowledge. On a more international scale, training and education programs with developing countries are envisaged as an additional, very interesting opportunity; ideas in this context will be developed in further detail as part of the project future stages.

Finally, EuPRAXIA can offer societal opportunities through public engagement and cultural effects. Thanks to its distributed organisation in various countries and regions, outreach campaigns can be designed with broad, geographical impact to inform the general public about plasma accelerators and particle acceleration in general. As Chapters 5.6 and 32.4 demonstrate, the EuPRAXIA Consortium has been very active in this direction already with events at schools, conference centres, and universities and will aim to expand its public engagement program further in the future.

**6.3 Consistency with the Scientific Strategy of Research Areas**

Large accelerator research facilities are at an increasing level encountering practical limitations in size and cost. Proving performance reach and cost benefits of compact accelerator technologies, such as plasma acceleration, has started to play a more and

more visible role in the strategy for future particle accelerators and accelerator applications. The report of the Particle Physics Project Prioritisation Panel on “Building for Discovery – Strategic Plan for U.S. Particle Physics in the Global Context”, from May 2014, for example, states clearly the need for cost-effective particle accelerators: “There is a critical need for technical breakthroughs that will yield more cost-effective accelerators” [174].

The Physics Briefing Book (CERN-ESU-004 [175]) summarises the input for the European Strategy for Particle Physics Update 2020. It lists EuPRAXIA explicitly as a study “of high interest also for possible future HEP applications” (Chap. 10, page 176). EuPRAXIA addresses several of the challenges and near-term goals listed in the briefing book.

LEAPS – the League of European Accelerator-based Photon Sources – is a strategic consortium initiated by the directors of the synchrotron radiation and free-electron laser (FEL) user facilities in Europe (see <https://www.leaps-initiative.eu>). Its primary goal is to actively and constructively ensure and promote the quality and impact of the fundamental, applied and industrial research carried out at their respective facilities to the greater benefit of European science and society. The LEAPS Strategy 2030 [176] lists as one of its future challenges: “A longer-term goal is the development of compact sources based on plasma wakefield acceleration to make some of the capabilities of the current RIs available for industrial applications, hospitals and smaller laboratory environments”.

Plasma acceleration also moved into the focus of national strategies in various European countries, among others with the ATHENA project in Germany, the Extreme Photonics Applications Centre in the United Kingdom, and the EuPRAXIA@SPARCLab project in Italy.

Listed as part of its key goals (see Chap. 2.1), EuPRAXIA aims to assess and advance beam quality, the compactness, and cost benefits of plasma-accelerator technology compared to RF-based machines. The proposed long-term strategy towards high beam quality and miniaturisation is well in line with the strategic demand for a new cost-effective accelerator technology that offers photon science discovery reach, medical applications, industrial potential, and a clear perspective for high-energy physics.

We conclude that the concept and approach of the EuPRAXIA research infrastructure are fully consistent with the strategies in accelerator-based photon science and high-energy physics. It is noted that plasma acceleration and specifically EuPRAXIA are also explicitly mentioned in the landscape analysis of the ESFRI Roadmap 2018.

## 6.4 Competition and Worldwide Context

Important new projects have started in recent years in Europe and worldwide at a total approved investment level of well above 150 M€:

1. The international Advanced Wakefield Experiment (AWAKE) at CERN, a collaboration of 18 institutes, pursues electron plasma accelerators that are driven by high-energy proton beams from the CERN-based SPS accelerator. It aims at very-high-energy electron beams for high-energy physics experiments. AWAKE is fully complimentary with the goals of EuPRAXIA, which aims at applications in the several-GeV energy range (AWAKE: A. Caldwell (MPP), M. Wing (UCL), E. Gschwendtner (CERN), P. Muggli (MMP), K. Lotov (BINP) et al., see <https://awake.web.cern.ch> and [50]).
2. The international ALEGRO study aims at the design of a plasma-based linear collider, the step beyond EuPRAXIA. The ALEGRO roadmap lists EuPRAXIA

- as an intermediate facility on the route to a plasma linear collider (Advanced LinEar collider study GROup ALEGRO: An international study group to promote advanced and novel accelerators for high-energy physics applications; sponsored by ICFA; B. Cros et al, <http://www.lpgp.u-psud.fr/icfaana/alegro>, see also [142]).
3. In the UK, the Plasma Wakefield Accelerator Steering Committee (PWASC) has defined a national roadmap and has proposed the successful EPAC (Extreme Photonics Applications Centre) project. PWASC and EPAC are connected to EuPRAXIA and form part of its consortium (Plasma Wakefield Accelerator Steering Committee (PWASC) in the UK, coordinated by S. Hooker, B. Hidding et al, see [145,177]).
  4. The multi-institutional laser-plasma acceleration project ATHENA in the Helmholtz Association brings together all accelerator-related Helmholtz centres in Germany for the construction of two common flagship plasma accelerators in Hamburg and Dresden. ATHENA is connected to EuPRAXIA, and most of the ATHENA partners are a part of the EuPRAXIA Consortium (Accelerator Technology Helmholtz iNfrAstructure ATHENA, project on laser-driven plasma acceleration by DESY, FZJ, and GSI with HI Jena, HZB, HZDR, and KIT, see <https://www.athena-helmholtz.de>).
  5. The ImPACT program in Japan aims at constructing a laser-driven, multi-stage plasma accelerator that drives a free-electron laser (see Chap. 30 for a more detailed description). The Japanese research labs have joined EuPRAXIA as associated partners.
  6. In China, in the key laboratory for laser plasmas at Shanghai Jiao Tong University, the “Synergetic Extreme Condition User Facility” (SECUF) will install a two-laser-beam system (200 TW + 300 TW) aiming at studies on staged laser wakefield acceleration, non-linear Thomson scattering, and QED-plasma physics. In the next ten years, a 30 PW (/15 PW x 2) laser and target system will be built in the TD Lee Institute in Shanghai. Studies on extreme laboratory astrophysics, such as radiation reaction, positron,  $\gamma$ , and axion generation, will be carried out. Several Chinese institutes have joined EuPRAXIA as associated partners.
  7. In Russia, the “Exawatt Center for Extreme Light Studies” (XCELS) is under study, aiming to use sources of laser radiation with unprecedented giant (exawatt) peak power. The XCELS complex will house laboratories for experiments on the physics of strong fields, high-energy physics, laboratory astrophysics and cosmology, nuclear optics, and neutron physics as well as laboratories for studying the properties of vacuum, attosecond and zeptosecond physics, and fundamental metrology. XCELS includes the investigation of laser-plasma acceleration in the kJ regime of laser energy, including multi-stage acceleration, external injection, and multi-pulse acceleration. Several Russian institutes have joined EuPRAXIA as associated partners.
  8. In the United States, the BELLA facility at LBNL is the world-leading laboratory for laser-driven plasma acceleration in what concerns the maximum beam energy reached. A strong program towards higher beam quality, radiation generation, and applications is under way. LBNL has joined EuPRAXIA as an associated partner.
  9. In the United States, the FACET facility at SLAC is the world-leading facility on beam-driven plasma acceleration, in as far as maximum beam energy for electrons and acceleration of positrons are concerned. Presently, an upgrade of the facility (FACET-II) is being implemented, which will allow improved beam quality and extended positron studies.

It is noted that there are other national projects with significant investments not mentioned above. Some of them are described in Chapters 29 and 30.

The list of competing projects and investments shows that the international landscape for plasma accelerators is rapidly expanding and attracting significant funding support from national governments. This reflects the clear promise in this novel accelerator approach and the worldwide race in bringing the new technology to the market and into the scientific area. It is seen that EuPRAXIA has attracted a large fraction of the relevant international R&D community into its consortium, both at a European and at an international level. This illustrates the strong potential for a European leadership role, for international scientific collaboration, and for a lively yet constructive worldwide competition.

## 6.5 Long-Term Future Accelerator Roadmap and the Role of EuPRAXIA

Several exercises for defining long-term accelerator roadmaps in the domain of plasma accelerators have been undertaken in recent years. In 2017, for example, the European Network for Novel Accelerators, EuroNNAc, published a “European roadmap”, which includes an R&D vision on developing plasma accelerators for the next 35 years [178]. The EuroNNAc roadmap from 2017 lists the EuPRAXIA facility as a required stepping stone for demonstrating high-quality electron beams from plasma accelerators at multi-GeV energies and with a reduced footprint. High beam quality is a necessary prerequisite for applications, which demand high beam brightness such as free-electron lasers, or high luminosity like particle colliders.

The plasma accelerator roadmap has been further detailed and developed in the recent exercise of the ALEGRO study group, as summarised in [179]. ALEGRO is a fully international effort with input from laboratories and experts worldwide, aiming at a broad international consensus. ALEGRO defines a 30 year roadmap towards a high-energy plasma-based linear collider. It defines various critical R&D challenges for arriving at this goal. These include the external injection of a high-quality electron bunch in an accelerator section. Emittances at the mm-mrad level should be produced and maintained, while the final energy spread should be at the percent level or lower. Levels of bunch quality, efficiency, stability, and reproducibility equivalent to those produced by conventional accelerators shall be achieved. Plasma sources with sufficient density uniformity, control, and reproducibility of the density, as well as tapering of the entrance and exit density ramps to assist in beam manipulation between stages should be developed. Operation at high repetition rate is identified as an important step towards a plasma-based linear collider. Challenges in producing high-quality electron ( $e^-$ ) and positron ( $e^+$ ) bunches in the 10 to 20 GeV energy range shall be addressed. Positron capabilities shall be expanded to other facilities beyond FACET-II with its world-leading positron program. The ALEGRO roadmap reviews the existing and planned facilities on plasma accelerator R&D. It lists their capabilities with respect to the challenges that need to be addressed. The EuPRAXIA facility is included, and its role in addressing various critical challenges is described and acknowledged.

We conclude that the EuPRAXIA research infrastructure is part of a long-term future accelerator roadmap. It fulfils an important role in the present R&D roadmaps. The positioning of the project is illustrated in the schematic diagram in Figure 6.3. The EuPRAXIA project will bridge the gap between successful proof-of-principle experiments (today) and a reliable technology with many applications. It should be considered as a ground-breaking, full-scale demonstration facility with first pilot users and unique ultra-fast science features. EuPRAXIA would address several technical shortcomings with novel solutions and prove the potential of plasma accelerators for first users in the multi-GeV energy range. The EuPRAXIA technology could then later be scaled up to higher beam energies, as required for high-energy physics discovery science.

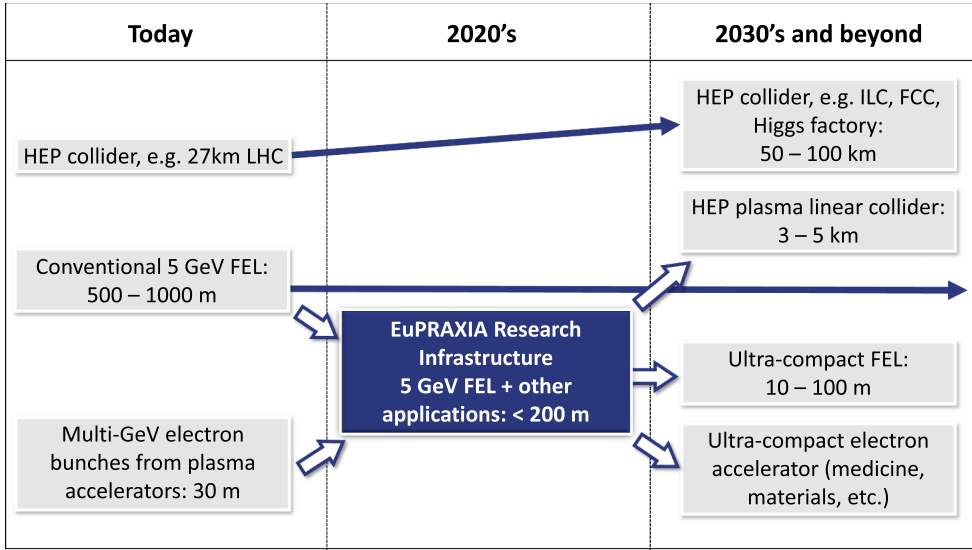


**Fig. 6.3.** Positioning of EuPRAXIA in the technological accelerator landscape of the next decades.

## Part 4

# Systems Design and Performance

## 7 Technology Background

### 7.1 Plasma-Accelerator Physics

While RF accelerators are limited in maximum sustainable field gradient by vacuum breakdown, plasma accelerators do not exhibit this issue as they remove the need for metallic or even dielectric cavities and instead use an underdense plasma as the

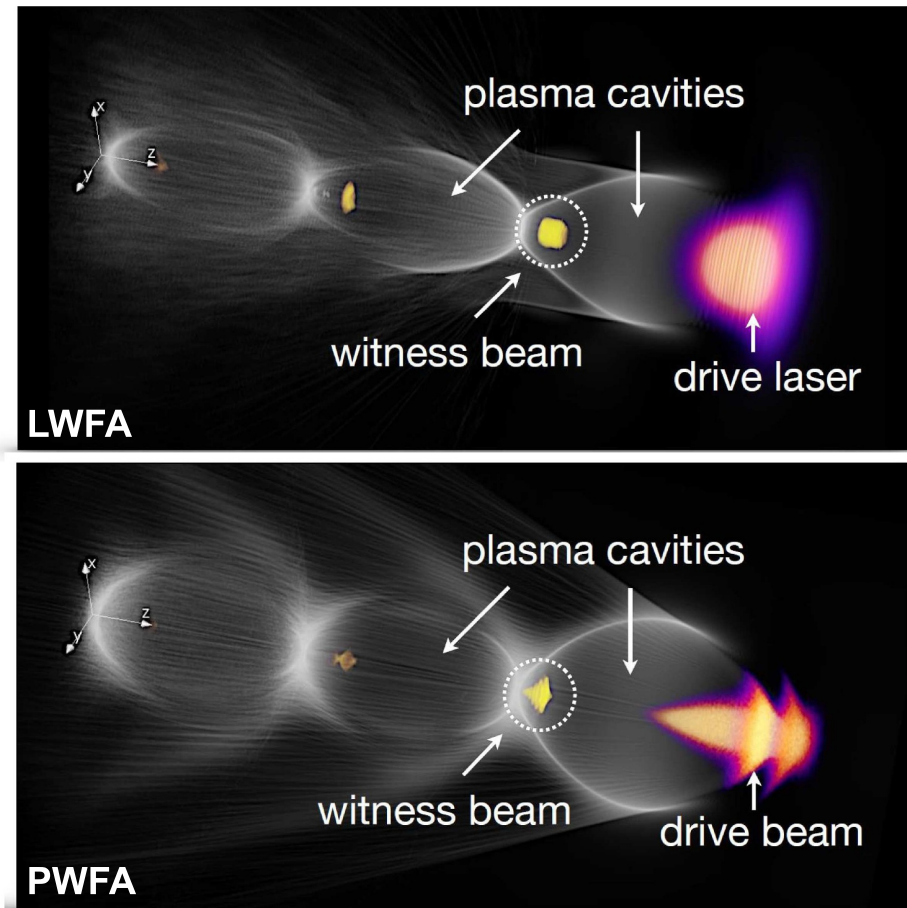


**Fig. 7.1.** Wakefield generation and electron beam acceleration in a plasma accelerator. The top plot shows the behaviour in a laser-driven plasma accelerator (LWFA), while the bottom plot depicts the case of a beam-driven plasma accelerator (PWFA) (image credits: A. Martinez de la Ossa).

acceleration medium. Thus, these devices can exhibit accelerating field gradients on the order of tens to hundreds of GeV/m compared to up to 100 MeV/m with RF-based machines [177].

In plasma acceleration, a drive beam – either a laser pulse (LWFA) or a relativistic electron beam (PWFA) – is propagated through a plasma target, i.e. a jet or confined channel of ionised gas, and in the process induces electron density oscillations, as shown in Figure 7.1. The associated wakefields exhibit field strengths in excess of

$$E_0[V/m] \approx 96\sqrt{n_0[\text{cm}^{-3}]} \quad (7.1)$$

and with a characteristic plasma wavelength

$$\lambda_p = \frac{2\pi c}{\omega_p} = \frac{2\pi c}{e} \sqrt{\frac{m\varepsilon_0}{n_0}} \approx 3.3 \times 10^4 / \sqrt{n_0[\text{cm}^{-3}]}, \quad (7.2)$$

where  $n_0$  is the background plasma density,  $\varepsilon_0$  the vacuum permittivity,  $c$  the speed of light in vacuum, and  $e, m$  the electron charge and mass, respectively. Placed into the correct phase of this plasma wakefield, a short electron beam, termed the witness beam, can be accelerated and focussed simultaneously to reach GeV energies over centimetre to metre distances [180].

As mentioned in Chapter 1, two different mechanisms can be employed to place the witness beam into this plasma wakefield. It can be either generated directly inside the plasma target through a self-injection process or propagated into the plasma from an external source. In the former case of self-injection, a fraction of electrons from the background plasma becomes, through one of several possible injection techniques (further details in Chaps. 13 and 32.2), trapped inside the accelerating wakefield and forms an electron beam that continues to co-propagate with the wakefield and gains energy. The plasma target in this case acts primarily as an injector (laser-plasma injector LPI or particle-plasma injector PPI) creating the electron beam, but can also significantly accelerate it already within the same device. For the case of external injection, the plasma target simply boosts the energy of the pre-generated witness beam as an accelerator stage (laser-plasma accelerator stage LPAS or particle-plasma accelerator stage PPAS). The electron beam itself is created and pre-accelerated in an RF injector or a plasma injector in this scenario. Using such a staged setup, multiple plasma accelerators can be coupled to one another to reach particularly high energies [181,182].

### 7.1.1 Laser-Driven Wakefield Acceleration (LWFA)

In laser-driven plasma acceleration, the plasma wakefield is driven by a TW-scale, fs-duration laser pulse. The properties of the wakefield in this case are largely determined not only by the plasma density but also by the laser parameters,

including, in particular, the laser normalised vector potential  $a_0$ , which can, for a bi-Gaussian pulse, be expressed in practical units as

$$a_0^2 \approx 7.3 \times 10^{-19} (\lambda_l [\mu\text{m}])^2 I_L [\text{W}/\text{cm}^2] \quad (7.3)$$

with  $\lambda_l$  as the laser wavelength and  $I_L$  as the laser intensity. Depending on the value of  $a_0$  in combination with the laser spot size and plasma density, three different operation regimes can be distinguished: a linear regime with  $a_0^2 \ll 1$ , a quasi-linear regime for  $a_0^2 \sim 1$ , and a non-linear regime in the case of  $a_0^2 \gg 1$  [83,180]. The accelerating field gradient increases with higher non-linearity, and in the non-linear regime the self-trapping of background electrons in the plasma can be observed. While the latter may be used in a controlled way for a plasma-based injector, in an accelerator stage with an externally injected electron beam any dark current due to self-injection should be avoided, thus making the linear and quasi-linear regimes typically more suitable [183,184].

Besides the field gradient, another limit to the maximum electron beam energy gain in a plasma accelerator is the acceleration length. This can, depending on the operating regime, be affected by three different phenomena: laser diffraction, electron beam dephasing, and pump depletion. If the natural diffraction of the laser pulse is the dominant process, as is often the case in linear plasma accelerators, the useful acceleration length is limited to a few Rayleigh ranges

$$z_R \approx \pi \frac{w_0^2}{\lambda_l} \quad (7.4)$$

before the laser intensity decreases significantly. Note that  $w_0$  is the laser focal spot size and  $\lambda_l$  the laser wavelength here.

Electron dephasing, on the other hand, often also plays a factor in this regime. It occurs as the accelerated electron beam travels at close to the speed of light  $c$  and outruns the plasma wave, which moves at close to the group velocity of the driving laser pulse within the plasma. Because of this velocity mismatch, the beam eventually slips into the decelerating phase of the wakefield and starts to lose energy, thus limiting the useful accelerating distance to the dephasing length  $L_{dp}$ . In the linear regime, this length can be expressed as [185]

$$L_{dp} \approx \frac{n_{cr}}{n_0} k_p^{-1}, \quad (7.5)$$

with  $\gamma_{ph}$  as the electron beam Lorentz factor,  $n_{cr} = (2\pi c)^2 \varepsilon_0 m / (e \lambda_l)^2$  the critical plasma density, and  $k_p = 2\pi / \lambda_p$  the plasma skin depth.

Finally, pump depletion becomes mostly relevant in the non-linear acceleration regime as the laser energy is lost through driving the plasma wave. The depletion length is defined as the distance over which half of the laser energy is depleted and, in the linear regime, scales as [185]

$$L_{dpl} \approx \frac{n_{cr}}{n_0} k_p^{-1} \frac{\omega_p \tau_L}{a_0^2}, \quad (7.6)$$

with  $\tau_L$  as the laser pulse duration.

### 7.1.2 Beam-Driven Wakefield Acceleration (PWFA)

In beam-driven plasma wakefield acceleration (PWFA), a relativistic charged particle beam is used as a driver generating the plasma wakefield; in the case of EuPRAXIA, it is more specifically an electron beam. Similarly to LWFA, different wakefield regimes can be distinguished depending on the properties of the drive beam. For a bi-Gaussian electron beam, a single value  $\alpha$  as the ratio of peak beam density and background density,  $\alpha = \frac{n_{bunch}}{n_0}$ , is relevant with a value larger than one, designating the blowout regime. For non-ideal drive bunches of a different shape, an additional measure is the reduced charge factor  $Q_{rc}$ , which defines how much charge the drive bunch carries compared to the maximum charge that can be contained in a plasma skin depth volume:

$$Q_{rc} = Q_{bunch} \frac{k_p^3}{n_0 e}, \quad (7.7)$$

where  $k_p$  is the skin depth and  $Q_{bunch}$  the bunch charge. Again, values strongly above one indicate a non-linear response and the formation of a full plasma blowout. Values below or around unity, on the other hand, point to a linear or weakly non-linear wakefield, respectively.

To maximise the accelerating field strength reached in a PWFA stage, the drive beam dimensions can be optimised with an ideal RMS length of  $\sigma_z = \sqrt{2}/k_p$  and an ideal transverse beam size of  $\sigma_{x,y} = \sqrt[4]{2/\gamma} \sqrt{\varepsilon_{n,xy}/k_p}$ .  $\varepsilon_{n,xy}$  is the transverse normalised emittance in this context, as defined below. If these conditions are fulfilled, the radius of the bubble structure in the plasma wakefield can be approximated as

$$R_{bubble} = 2.5\sigma_r\sqrt{\alpha}, \quad (7.8)$$

with  $\sigma_r$  as the radial transverse beam size [186].

Finally, another important variable for efficient acceleration in a beam-driven plasma accelerator is the transformer ratio  $R_T$ . It is defined as the ratio between maximum accelerating field in the witness bunch and maximum decelerating field in the driver bunch [49,187]. In practical terms, it determines the ratio between energy gain by the witness beam and energy loss by the driver, thus defining the maximum energy gain of the witness bunch inside the beam-driven wakefield as  $\Delta E_{wit,max} = R_T \times \Delta E_{driv,max}$ , with  $\Delta E_{driv,max}$  as the average particle energy loss in the driver bunch. With the acceleration length being another practical limitation to the energy gain, the goal for efficient PWFA is to achieve a high transformer ratio and to continue the acceleration process until the drive beam reaches depletion. As symmetrical drive beams have a limit in  $R_T$  of at maximum 2, PWFA setups, including also EuPRAXIA, typically work with asymmetric beams. Specific ways to reach higher transformer ratio values include, for example, bunch shaping [188–191] as well as the use of shaped bunch trains [192], which is explored further in this design report.

### 7.1.3 Challenges in Plasma Acceleration

Besides the usual challenges of particle acceleration, plasma accelerators exhibit several issues specific to their technology. These have been tackled with particular focus during the conceptual design study, with solutions presented throughout the remainder of this part.

## Bunch length and energy spread

Because of the high accelerator frequency – on the order of THz instead of GHz as for most RF accelerators – the accelerating section of the wakefield in plasma-based devices is only a few tens of micrometres in size, hence limiting the acceptable witness bunch durations to fs and tens of fs. In plasma injectors, such bunch lengths are produced naturally; however, with RF injectors bunch compressors need to be implemented, and space-charge forces can become an issue at lower energies. At the same time, given the short accelerating field period, the variation of the accelerating field along the electron beam is typically large enough to generate a significant correlated energy spread of at least a few percent in the beam. This common feature constitutes a major issue for many applications, such as free-electron lasers, but also proves, for example, challenging for electron beam transport due to chromatic dependences in most beamline components.

Several concepts to remove this correlated energy spread (energy chirp) either inside the plasma [33] or through beam manipulation outside the target [34] have been proposed. One relatively old strategy involves beam loading, i.e. using the witness beam's own electric field, which has an opposite curvature to the plasma wakefield, to level the overall accelerating field shape that the beam experiences [28,193]. Through tuning the electron beam shape and charge, this effect can, in principle, be optimised to create a flat field along the beam; however, over longer acceleration distances, additional factors such as the evolution of the driver, plasma wave, and witness beam shape also need to be taken into account.

## Transverse matching

Another particular challenge for staged acceleration is presented by transverse beam matching into plasma targets. In accelerator physics, the transverse dynamics of an accelerated electron beam are typically described by two specialised quantities: the transverse beam emittance and Courant-Snyder (Twiss) parameters [194,195]. The normalised transverse RMS emittance  $\varepsilon_n$  is defined in this context (exemplary in the horizontal direction  $x$ ) as

$$\varepsilon_{n,x} = \frac{1}{mc} \sqrt{\langle x^2 \rangle \langle p_x^2 \rangle - \langle xp_x \rangle^2} \quad (7.9)$$

with  $\langle x^2 \rangle = \sum x_i^2/N$ ,  $\langle p_x^2 \rangle = \sum p_{x,i}^2/N$ , and  $\langle xp_x \rangle = [\sum x_i p_{x,i}/N] - [(\sum x_i \sum p_{x,i})/N^2]$ , where  $x_i$  and  $p_{x,i}$  are the  $x$ -positions and  $x$ -momenta of the  $N$  electrons within the beam. A second measure for the transverse beam distribution is the normalised trace-space emittance (again exemplary for the horizontal  $x$ -direction):

$$\varepsilon_{tr,n,x} = \frac{\bar{p}_z}{mc} \sqrt{\langle x^2 \rangle \langle x'^2 \rangle - \langle xx' \rangle^2}, \quad (7.10)$$

where  $\bar{p}_z$  is the mean longitudinal momentum in the  $z$ -direction, whereas  $x' = p_x/p_z$  is the horizontal divergence. The Courant-Snyder (or Twiss) parameters are then expressed as

$$\alpha_x = -\frac{\langle xx' \rangle}{\varepsilon_{tr,x}} \quad \beta_x = \frac{\langle x^2 \rangle}{\varepsilon_{tr,x}} \quad \gamma_x = \frac{\langle x'^2 \rangle}{\varepsilon_{tr,x}}, \quad (7.11)$$

with  $\varepsilon_{tr,x} = \varepsilon_{tr,n,x}(mc/\bar{p}_z)$ . In all cases, equivalent values can be calculated for the vertical direction  $y$ .

As the inward-focussing forces on the electron beam need to match its outward space-charge forces for stable beam propagation, the transition from one beamline

element to the next with differing focussing fields requires the transverse beam size and divergence to be adapted and matched to the element. The following matching conditions in particular need to be fulfilled for the witness beam in a plasma – in the blowout regime, assuming negligible beam loading – to avoid oscillations of the beam envelope:

$$\beta_{\text{matching}} = \frac{\sqrt{2\gamma_{ph}}}{k_p} \quad (7.12)$$

$$\sigma_{\text{matching}} = \sqrt{\frac{\beta_{\text{matching}}\varepsilon_n}{\gamma_{ph}}} \quad (7.13)$$

where  $\sigma$  is the transverse electron beam RMS size. As discussed further in Chapters 14 and 19, these matching values are extremely small for plasma-accelerator stages, thus requiring strong and well-controlled focussing before the plasma entrance. Similarly, the electron beam is also strongly focussed when it leaves the plasma stage, thus putting considerable challenges on the capturing and transport line behind the plasma accelerator / injector where the matched beam size increases again.

#### 7.1.4 Plasma Sources

Targets for plasma accelerators can be broadly classified as waveguide or non-waveguide targets, specifically for LWFA, depending on whether they are designed with a guiding mechanism for the drive laser. For the non-waveguide target, typically used for plasma injectors or low-energy accelerators, most often, a gas jet or a simple gas cell is used. Waveguide targets, on the other hand, mostly in use for high-energy acceleration, include a variety of different technologies, such as capillary discharge waveguides, plasma channels formed by hydrodynamic expansion, and gas-filled capillaries (more details in Chaps. 16 and 32.2). Each type of target can be further divided into being pre-ionised, almost always the case in PWFA, or being ionised by the driving laser. Further additional features can be important to implement in plasma targets to improve their performance, such as structures for controlling the injection of electrons into the wakefield, longitudinal variations of the plasma density for extending acceleration beyond the dephasing length for LWFA, or for controlling the properties of the electron bunch as it leaves the acceleration stage [196].

The specific properties of the plasma target depend on the following constraints:

- Plasma length: For LWFA stages, the acceleration length is usually optimally set to the dephasing length  $L_{dp}$ , thus determining the density and length of the stage. However, in some circumstances, it may be preferable to accelerate at lower intensities (e.g. to prevent target damage, to minimise emittance growth, etc.). This necessitates increasing the target length. For PWFA, both the length and the density are determined almost entirely by the desired final beam energy. The depletion length is an important parameter to name in this context as the distance over which the beam driver has lost all of its energy through driving the wake, thus representing the scenario of most efficient energy transfer between driver and witness.
- Density profile: For a laser wakefield electron injector, a tailored density profile can be useful; for example, injection can be assisted by a density downramp [15]. Similarly, density upramps can provide an energy boost at the end of a stage, and density profile shaping can be used to control the self-focussing and self-compression of the drive laser. Moreover, gradients can be used in the LWFA injector to compensate the energy chirp of the injected electron bunch and therefore reduce the energy spread [32]. Controlling the density profiles at both the

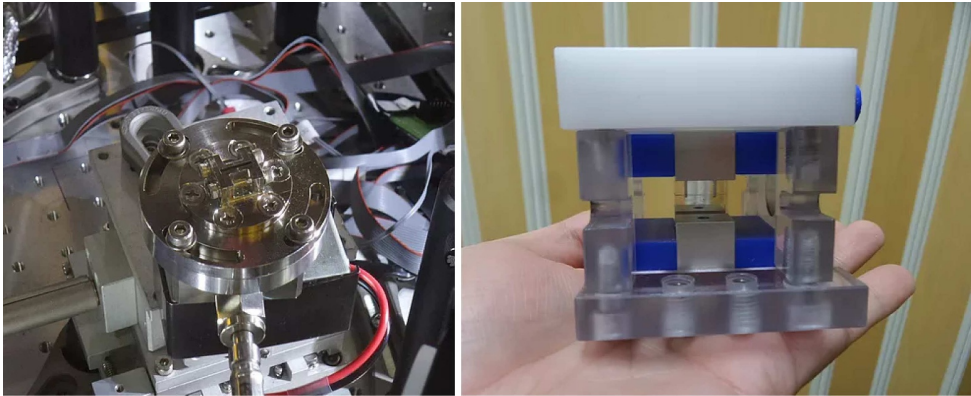


**Fig. 7.2.** Examples of different types of plasma sources used in plasma injectors and accelerators. The image on the left-hand side shows a setup used to produce a gas jet, while the image on the right-hand side depicts a capillary gas cell (image credits: Gwangju Institute of Science and Technology, Korea).

entrance and the exit of plasma-accelerator stages is also vital to properly couple accelerated beams between stages [35,36].

- Density stability: It has been shown that the plasma electron density is a key parameter for the stability of the injector [197,198]. For EuPRAXIA, the acceptable level of fluctuations on the value of the density has been examined in a preliminary numerical tolerance study [171]. Further, more detailed investigations will be carried out in the future.
- Target repetition rate and lifetime: Most plasma accelerators currently operate at only a few Hz repetition rate, but for EuPRAXIA, this should be increased to a baseline of 20–100 Hz. For the plasma stages, this means that either targets should directly sustain hundreds of thousands of shots, or a remotely interchangeable target must be designed that can be replaced after a smaller number of shots without interrupting the operation.

## 7.2 Laser Science

As it has been pointed out in the previous chapters, the EuPRAXIA infrastructure will require several laser beamlines with peak power up to some petawatts (PW), pulse energy in the range of tens to hundreds of Joules, pulse duration in the range of some tens of femtoseconds up to 100 femtoseconds, and pulse repetition rates of 20 or 100 Hz. The implementation of the foreseen plasma acceleration schemes will require the simultaneous operation of up to three laser beamlines, with tight synchronisation requirements. The purpose of this chapter is to provide a general overview of the available laser technologies that can be employed to achieve the performance level exposed above. It must be pointed out that no system in the world is currently capable to achieve these requirements, in particular at a high repetition rate. Existing PW laser systems can achieve even higher energies or even shorter pulse duration but at a very low repetition rate (from a single shot to a few Hz at maximum).

All the existing high-peak-power ( $>$  few TW) laser technologies are based on the so-called chirped pulse amplification (CPA) technique. A short (e.g. tens of fs), broadband, low-energy seed laser pulse is first temporally stretched in a suitable delay line (stretcher), up to several hundreds of thousands of fs; then it is amplified in a

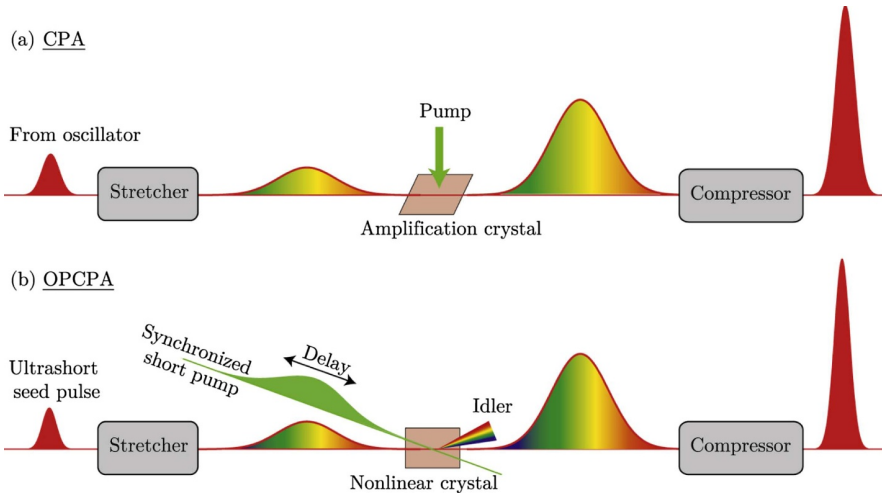


**Fig. 7.3.** Operating principle of chirped pulse amplification (CPA) and optical parametric chirped pulse amplification (OPCPA) (image credits: [200]).

laser amplification chain up to the desired energy level. Finally, it is compressed to (about) the original pulse duration in a second delay line (compressor) conjugated with the stretcher. CPA (invented by G. Mourou, recently awarded the Nobel Prize for this achievement [199]) allows one to reach very high peak-power levels, avoiding severe non-linear optical effects in the amplifiers that would spoil the pulse duration and the laser beam quality and eventually could destroy the amplifier itself.

Following this approach, the architectures for the laser systems envisaged in EuPRAXIA will comprise at least a master oscillator, a pulse stretcher, one or more pre-amplification stages, one or more high-energy amplification stages, a pulse compressor, a beam transport system, and a final focussing system. As it will appear in the following parts, one of the most critical elements for the achievement of the required laser parameters is the pulse amplification system (in its broader meaning, i.e. including the gain elements, the pump system, and the cooling system), which must sustain the high-average-power regime imposed by the desired performance and keep non-linear optical effects below a given threshold. Another critical element is the pulse compression system, mainly because of the high-peak-power density handled by its last stage. Conversely, the master oscillator and the pre-amplifier stages appear less critical, given the lower average power involved, the relatively long pulse duration required, and the relatively low coherent contrast ratio. It must be underlined that the required repetition rate of 20 Hz is at the border between two alternative technologies for the pumping system. A repetition rate of 20 Hz on the desired energy range can still be obtained with flashlamp pumped systems. Under this limit, flashlamps still have advantages in terms of initial cost and operation costs with respect to solid state pumping (laser diode arrays), and are then a viable option. Above 20 Hz, pumping with laser diode arrays is probably the only option.

The available solid-state high-energy laser pulse amplification technologies that can be reasonably adopted for the development of the laser source foreseen by the project can be classified in the following main streamlines:

**Ti:Sapphire-based systems:** In this case, the gain medium is titanium-doped Al<sub>2</sub>O<sub>3</sub> (Sapphire). Given the broad gain bandwidth, this gain medium allows the generation of laser pulses with a duration down to a few fs and the amplification in the timescale of a few tens of fs at a wavelength of about 800 nm.

On the other hand, Ti:Sapphire must be pumped in the visible (typically in the range of 500–550 nm), which is commonly obtained by using frequency-doubled Q-switched lasers operating in the near infrared (e.g. Nd:YAG, Yb:YAG). As a consequence, the wall plug efficiency of the pumping system is usually quite low, in particular when flashlamp pumped lasers are used. Moreover, the quantum defect between the pump photon energy and the fluorescence photon energy is quite high (about 34%). This imposes a relatively high level of thermal load on the gain medium, the effects of which are nonetheless mitigated by the high thermal conductivity of the host. For these reasons, the operation at high average power of these systems can be quite challenging. Finally, the development of a high-energy laser system will require large aperture gain elements. Ti:Sapphire can only be produced as a single crystal, and this can be a limitation for the size of the gain elements. Anyhow, Ti:Sapphire crystals with a size exceeding 7 inches were already delivered by Crystal System for ELI-NP and Apollon (see below) to reach up to 200 J of energy (corresponding to 100 J on target). Currently operating PW laser systems based on Ti:Sapphire amplification are, for instance, APOLLON [201] and LASERIX in France [202], BELLA in the United States [203], PULSER in South Korea [204], and Xtreme Light III in China [205].

**Yb-based systems:** Compared to Ti:Sapphire, Yb-based gain media have many advantages in terms of pumping efficiency. First of all, they allow direct pumping by semiconductor lasers in the wavelength region of 930–970 nm without further wavelength conversion stages. Moreover, the quantum defect between the pump photon energy and the laser photon energy is rather low (around 10%) because the emission wavelength (usually 1030–1050 nm, depending on the host) is close to the pumping wavelength. This reduces the thermal load on the gain medium, and thus, the power dissipation requirements. Both of these elements are advantageous in view of a high-average-power operation regime. The main drawback of Yb-based gain media is the reduced gain bandwidth, which makes it difficult to achieve the desired pulse duration of 100 fs for high energy pulses, whereas operation in the range of 100–200 fs is more easily achieved. Moreover, in Yb-doped media, the saturation fluence of the laser transition often largely exceeds the damage threshold of the host; in these cases, the amplification stage cannot operate in saturation, which limits the energy extraction and jeopardises the overall system efficiency [206]. Two high-energy sub-PW laser systems, both based on amplification in Yb:CaF<sub>2</sub>, have been realised in Germany, namely, PENELOPE [207] and POLARIS [208].

**Nd:glass-based systems:** Some high-energy laser systems adopt Nd:glass as a gain medium for the final power amplification stages. Nd-doped glasses provide a gain bandwidth suitable for the generation and amplification of pulses in the 100 fs time range. Large gain elements can be produced with glasses more easily than with crystal growth technologies. Moreover, Nd:glasses can be directly pumped with semiconductor lasers, which is advantageous for the overall efficiency and power dissipation requirements of the pump system. On the other hand, even though the thermally dissipated pump power fraction is moderate (around 20%), the operation at high-average-power levels of Nd:glass bulk amplifiers is hampered by the poor thermal conductivity of the glass host, which makes the cooling of the gain elements difficult, unless special provisions are adopted. An example of a PW laser system based on this technology is the Texas Petawatt Laser in the United States [209].

**OPCPA systems:** An alternative method for the amplification of high-peak-power pulses is based on parametric light amplification in non-linear optical crystals (optical parametric chirped pulse amplification, OPCPA) [210,211]. Instead of using ordinary laser media (based on the excitation/de-excitation of an atomic

**Table 7.1.** Main parameters of some PW laser systems worldwide. Operational systems are shown in bold. The energy value is reported after compression.

System	Country	Ampl. medium (last stage)	Wavelength (nm)	Energy (J)	Pulse length (fs) (FWHM)	Peak power (PW)	Rep. rate (Hz)	Contrast
<b>APOLLON</b>	FRA	Ti:Sa	800	150	15	10	0.017	10 <sup>10</sup>
ALPS HF*	HUN (EU)	Ti:Sa	800	34	<17	2	10	10 <sup>11</sup>
<b>BELLA</b>	USA	Ti:Sa	800	40	30	1	1	10 <sup>10</sup>
HAPLS L2*	CZE (EU)	OPCPA	800-850	18	15	1	10	N/A
HAPLS L3*	CZE (EU)	Ti:Sa	800	30	30	1	10	N/A
HPLS*	ROM (EU)	Ti:Sa	800	200	20	10	0.017	10 <sup>12</sup>
<b>LASERIX</b>	FRA	Ti:Sa	800	40**	50	0.8	0.1	N/A
<b>PEneLOPE</b>	GER	Yb:CaF2	1035	150*	140	1*	1	N/A
<b>POLARIS</b>	GER	Yb:CaF2	1030	17	<100	0.17	0.02	10 <sup>9</sup>
<b>PULSER</b>	KOR	Ti:Sa	820	83	20	4	0.1	10 <sup>9</sup>
QUIANG- GUANG 5 PW	CHN	Ti:Sa	800	138***	27***	5.1***	0.0083	N/A
RAL 10Hz PW*	UK	Ti:Sa	800	30	30	1	10	10 <sup>10</sup>
<b>SHENGUANG II</b>	CHN	OPCPA	808	37	21	1.76	S.S.	N/A
<b>TEXAS PW LASER</b>	USA	Nd Glass	1060	186	<170	1.1	0.0017	10 <sup>5</sup>
VULCAN 20 PW*	UK	OPCPA	1053	300	30	10	0.0011	N/A
<b>XTREME LIGHT III</b>	CHN	Ti:Sa	800	32.3	29	1.16	0.0083	10 <sup>6</sup>

\*Design specifications. \*\*Before compression. \*\*\*Small-scale test.

transition), the amplification is based on optical difference frequency generation in non-linear crystals. Compared to standard amplification, OPCPA has several specific features that can be potentially advantageous, including a very high amplification factor of chirped pulses (up to 3–4 orders of magnitude per pass in terms of energy) and a high contrast because the parametric gain exists only when the pump pulse is present. Finally, the process is non-dissipative because the energy difference between the pump (highest energy) photon and the amplified signal (lower energy photon) is emitted as a third photon (the so-called idler), and it is not dissipated into the crystal, as it happens in the stimulated emission process. Therefore, the parametric amplification process imposes a much lower thermal load on the amplified medium with respect to amplification based on the emission from atomic transitions. The amplification of high-energy pulses requires large aperture crystals; this limits the choice of possible non-linear materials, mainly to KDP, DKDP, and LBO. OPCPA is used in the last amplification stage of the Shenguang II laser system in China [212].

Table 7.1 shows a synopsis of the emission parameters of several PW laser systems worldwide, currently operating or in advanced construction phase, in alphabetical order. Data are derived from published papers [213] and documentation available on the websites of the various facilities.

Many of the above approaches to high-average-power amplification are developing fast and hold the promise to deliver revolutionary performances to drive plasma acceleration and other major applications of such high-intensity lasers. However, in the perspective of a short-term approach, a driver for a plasma accelerator capable of outstanding parameters, like those required by the EuPRAXIA laser, should be based on components with a high technology readiness level (TRL), ideally sourcing from a lab environment where specific technologies have been explored in depth. Ti:Sa technology is currently used in the HAPLS system (ELI Beamlines) to deliver today's highest available average power (design value: 300 W) and is certainly the preferred platform that can lead to the required specifications by scaling existing systems.

However, as anticipated, scaling to kW average power still requires innovative solutions for high repetition rate, including a transition from a flashlamp to fully DPSSL-based pumping and efficient thermal management in both the amplifier and the whole transport chain from the compressor to the target plasma. kW-scale lasers suitable for pumping Ti:Sa in the 10–20 Hz repetition rate range are just emerging with industrial systems, like the P60 by Amplitude Technologies (FR), or prototypes, like the DiPOLE system developed at the Central Laser Facility (UK), and can be integrated into advanced Ti:Sa amplifier designs, provided a geometry with efficient cooling ensures heat removal from the amplifier head. This is a crucial issue that is taking much of the design effort. In fact, existing amplifier architectures, including those successfully used in systems, like HAPLS, feature cooling schemes (e.g. multi-slab with gas cooling) that cannot be easily scaled to the required heat removal capacity for a kW-scale system. Possible solutions include the use of liquid cooling, requiring a major effort in counteracting the depletion of beam quality stemming from propagation through a non-uniform, highly refractive material, or implementing alternative cooling concepts to avoid propagation through the cooling liquid, like the “active mirror” concept used in the P60 system.

Both pumping schemes and cooling architectures are key conceptual aspects of the laser design that have an impact on both the complexity and the compactness of the final system.

### 7.3 Free-Electron Lasers

Relativistic charged particles moving subject to a magnetic field lose energy, while emitting synchrotron radiation, an intrinsic limiting factor to accelerate electrons at high energy with circular machines that turn out to have an increasingly important role in many areas of basic and applied sciences. In particular, the kinetic energy of a relativistic electron beam is transformed into an intense laser beam of electromagnetic radiation by wiggling the electrons transversely in a long undulator: the free-electron laser (FEL) [215–218]. An FEL consists of a laser where the basic emission process does not occur in a bound atomic or molecular system with population inversion. Such machines are becoming the main source of tunable, intense, and coherent photons of either ultra-short time resolution or ultra-fine energy resolution on a broad band of frequencies that cannot be covered with most of other conventional light sources. In existing facilities, they can cover a range from the terahertz to the hard X-ray regime.

An electron beam is associated with a power equal to the product of beam energy  $E$  and current  $I$ :

$$P_E[\text{MW}] = I[\text{A}] E[\text{MeV}]. \quad (7.14)$$

Such power is delivered to the beam by the particle accelerator. The magnetic field associated with an undulator with period  $\lambda_u$  and on-axis peak field  $B_0$ , on the other hand, is

$$\mathbf{B} = \left( 0, B_0 \sin \frac{2\pi z}{\lambda_u}, 0 \right). \quad (7.15)$$

The Lorentz force due to the undulator field introduces a transverse component in the electron motion, described by the deflection strength parameter  $K$ ,

$$K = \frac{eB_0\lambda_u}{2\pi m_e c} \simeq 0.943 B_0[\text{T}] \lambda_u[\text{cm}], \quad (7.16)$$

where  $e$ ,  $m_e$ , and  $c$  are, respectively, the electron charge, the electron mass, and the speed of light in vacuum. For a single electron of given energy  $E = \gamma m_e c^2$  and Lorentz

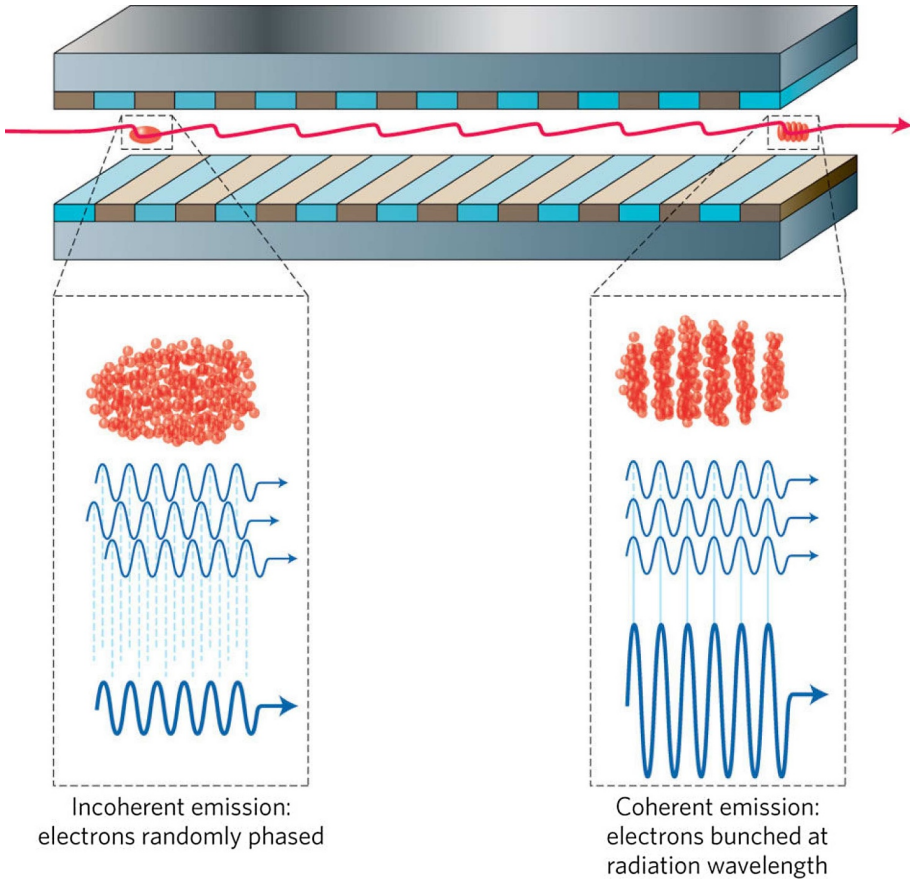


**Fig. 7.4.** Operating principle of a free-electron laser (FEL) (image credits: [214], reprinted with permission of Springer Nature).

factor  $\gamma$ , the resonance condition on the wavelength  $\lambda_0$  of the emitted radiation is

$$\lambda_0 = \frac{\lambda_u}{2\gamma^2} \left( 1 + \frac{K^2}{2} \right) \tag{7.17}$$

The efficiency of the energy transfer from electrons to the radiation field, and the gain of the process are described by the FEL Pierce parameter  $\rho$ :

$$\rho = \frac{1}{4\pi\gamma} \sqrt[3]{2\pi \frac{J}{I_0} (\lambda_u K f_b(K))^2} \simeq \frac{8.36 \times 10^{-3}}{\gamma} \sqrt[3]{(\lambda_u[\text{m}] K f_b(K))^2 J \left[ \frac{\text{A}}{\text{m}^2} \right]}, \tag{7.18}$$

where  $f_b(K) = J_0(\xi) - J_1(\xi)$  is the planar undulator Bessel correction factor with the argument  $\xi = \frac{K^2}{2} \frac{1}{2+K^2}$  and  $I_0 = 17\text{ kA}$  as the Alfvén current. The beam current is expressed in terms of the bunch root mean squared (RMS) time duration  $\sigma_\tau$  and the bunch charge  $Q_b$  as

$$I[\text{A}] = \frac{Q_b[\text{C}]}{\sigma_\tau[\text{s}]\sqrt{2\pi}} \tag{7.19}$$

The current density  $J$  is given by

$$J \left[ \frac{\text{A}}{\text{m}^2} \right] = \frac{Q_b[\text{C}]}{\sigma_r[\text{s}]\sigma_x[\text{m}]\sigma_y[\text{m}](2\pi)^{3/2}} \quad (7.20)$$

where  $\sigma_{x,y}[\text{m}]$  is the RMS transverse size of the electron beam.

Equation (7.18) plays a crucial role in the theory and design of high-gain self-amplified spontaneous emission (SASE) FEL devices as it specifies efficiency, laser growth rate, bandwidth, and the role of inhomogeneous broadening. In fact, estimates of the SASE FEL bandwidth  $\Delta\omega/\omega$  and saturation power  $P_S$  are, respectively, provided by

$$\frac{\Delta\omega}{\omega} \approx \rho \quad \text{and} \quad P_S \simeq \sqrt{2}\rho P_E. \quad (7.21)$$

The gain length determining the FEL growth rate can be expressed in terms of  $\rho$  as follows:

$$L_g = \frac{\lambda_u}{4\pi\sqrt{3}\rho}. \quad (7.22)$$

The power growth can be expressed [219] in terms of the following logistic equation:

$$P(z) = P_0 \frac{A(z)}{1 + \frac{P_0}{P_S} [A(z) - 1]}, \quad (7.23)$$

$$A(z) = \frac{1}{9} \left[ 3 + 2 \cosh\left(\frac{z}{L_g}\right) + 4 \cos\left(\frac{\sqrt{3}z}{2L_g}\right) \cosh\left(\frac{z}{2L_g}\right) \right],$$

with  $P_0$  being the input seed and  $z$  the longitudinal propagation coordinate. Accordingly, the length of the undulator section needed to reach the saturated power, the so-called saturation length, is

$$L_S \simeq 1.066L_g \ln\left(\frac{9P_S}{P_0}\right). \quad (7.24)$$

The effects of inhomogeneous broadening – namely, the gain deterioration because of non-ideal electron beam qualities, in particular significant energy spread and emittance values – are embedded in the previous formulae by means of the  $\mu$  parameters. These quantify the main contributions to the effective  $\rho$  reduction, and so to the gain length increase, leading to  $L_{g,\varepsilon}$  as an effective quantity.

Regarding the energy spread, we have the following:

$$L_{g,\varepsilon}(\chi) = \chi L_g, \quad \chi \simeq 1 + \frac{0.185\sqrt{3}}{2} \mu_\varepsilon^2, \quad (7.25)$$

$$\mu_\varepsilon = 2 \frac{\sigma_\varepsilon}{\rho}, \quad \sigma_\varepsilon = \frac{\Delta E}{E}, \quad \Delta E = \sqrt{\langle E^2 \rangle - \langle E \rangle^2}.$$

A reliable estimate of  $L_S$  requires also to consider inhomogeneous broadening effects due to three-dimensional diffraction contributions, which modify the Pierce parameter by introducing the  $\mu_D$  diffraction parameter, as described below:

$$\mu_D = \frac{\lambda\lambda_u}{(4\pi\sigma_T)^2\rho}, \quad \rho_D = \mathcal{F}(\mu_D)\rho, \quad \mathcal{F}(\mu_D) = \frac{1}{\sqrt[3]{1 + \mu_D}}, \quad (7.26)$$

where we considered a transversely symmetric electron beam with  $\sigma_x = \sigma_y = \sigma_T$  and  $\varepsilon_x = \varepsilon_y$ .

Together with these formulae describing the fundamental harmonic, similar expressions are found regarding the non-linear higher harmonics generation FEL mechanism, characterised by the  $n^{\text{th}}$  harmonic radiation wavelength as follows:

$$\lambda_n = \frac{\lambda_u}{2n\gamma^2} \left( 1 + \frac{K^2}{2} \right) \quad (7.27)$$

The theory described above has been used for guiding the FEL design of EuPRAXIA. Specific performance estimations and simulations with numerical codes are described in Section 24.1.

## 8 Description of the Overall Facility Layout and Its Building Blocks

The conceptual design presented in this part is focussed on the two machine sites of EuPRAXIA and based on complementary plasma-accelerator technologies, as introduced in Section 3.3.2.

In the following chapters, the main components foreseen for the two construction sites are presented, and an overview over the technical solutions found in each case is given. Figures 8.1 and 8.2 highlight the main technical sub-systems envisaged for each site and provide a reference to the respective chapters and sections where further information on these components can be found. Six types of sub-systems are considered, in this context, in the facility design:

- laser systems
- RF injectors and accelerators
- plasma injectors and accelerators
- transport lines for different types of beams (electrons, positrons, photons)
- beamline sections for generating secondary sources or conditioning the beams
- user areas

Some of these, such as the electron beam transport lines, have very similar characteristics in both sites and are thus described in a general way. Others, such as the plasma injectors and accelerators, are targeted to a specific site only. For certain components, as described in the following, multiple design options are considered, with some foreseen as baseline solutions, while others are backup options or paths for future developments. A further down-selection of the proposed techniques and components is planned only during the technical design phase, once further test experiments and prototyping have validated the performance of the different technical options. This strategy takes into account the potential and excellent computational results for the solutions considered while, at the same time, mitigating the risk of building a machine based on technologies not tested in a user-operation setting before.

### 8.1 EuPRAXIA Site for Beam-Driven Plasma Acceleration

Before going into the technical details and tables of parameters, here, we first summarise the main building blocks from an overview perspective. As Figure 8.1 highlights, the following sub-systems and design solutions are proposed for the EuPRAXIA site for beam-driven plasma acceleration:

**RF injector and accelerator:** The *baseline* design for the RF-based accelerator consists of an S-band injector with velocity bunching combined with an X-band

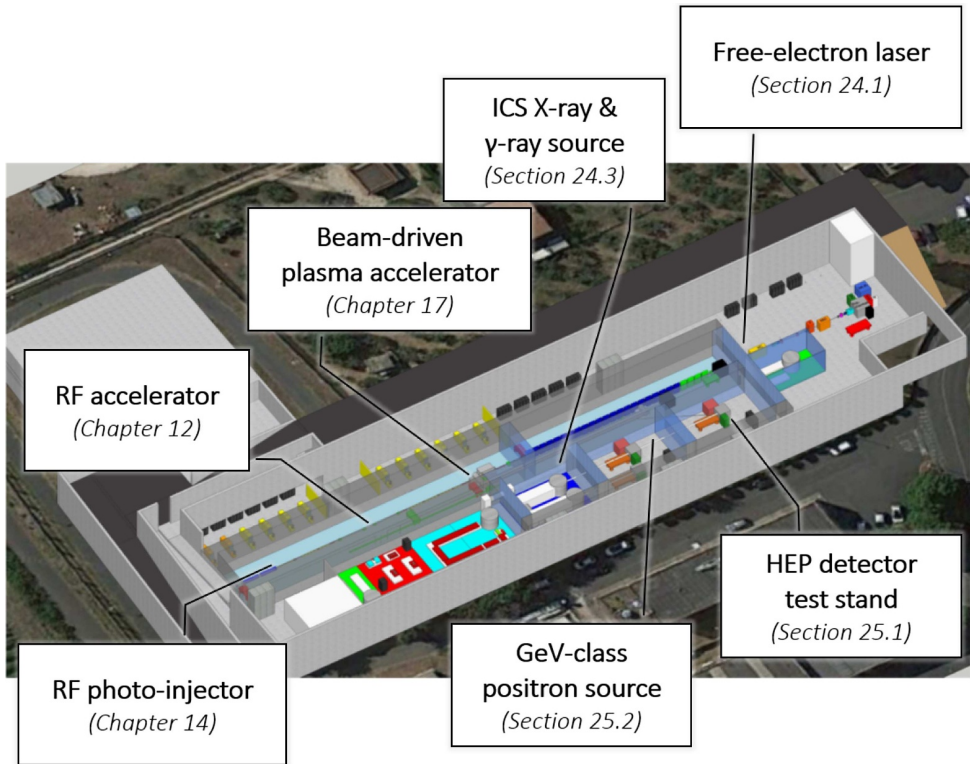


**Fig. 8.1.** Overview layout of the EuPRAXIA site for beam-driven plasma acceleration.

linac producing electron beams with energy of around 500 MeV. An extension of the accelerator to 1 GeV is further considered as an *upgrade / backup option* as the plasma accelerator stages could be omitted or used to reach higher energies than with the baseline design. More details on the RF injector and accelerator for generating the driver and witness electron beams at the PWFA site can be found in Chapters 14 and 12, respectively.

**Plasma accelerators:** Two types of plasma accelerators are foreseen at the PWFA site of EuPRAXIA: one focussed on high beam quality for radiation generation and the other aiming to produce high-charge, high-average-power electron beams suitable for positron generation and as test beams. The *baseline* in both cases considers the external injection of the electron drive and witness beams from the RF accelerator into a weakly non-linear plasma stage to achieve beam-driven wakefield acceleration up to 1 GeV. The generated electron bunches based on current results comply with the requirements for both types of accelerator stages but could be optimised further towards high charge or high quality in the future. A detailed design is described in Section 17. Additionally, potential *future development paths* are foreseen through (1) increasing the energy reach to 5 GeV (see Sect. 17.2) as well as (2) improving the beam quality further, for example through using the RF-accelerated electron beam as a driver in a beam-driven plasma wakefield injector based on the Trojan horse injection mechanism (more details in Sect. 26).

**Free-electron laser:** The EuPRAXIA facility *baseline* foresees the use of conventional undulators in all of its FEL beamlines as a risk-mitigating measure, as described in Chapters 18 and 24.1. The adoption of more compact, novel

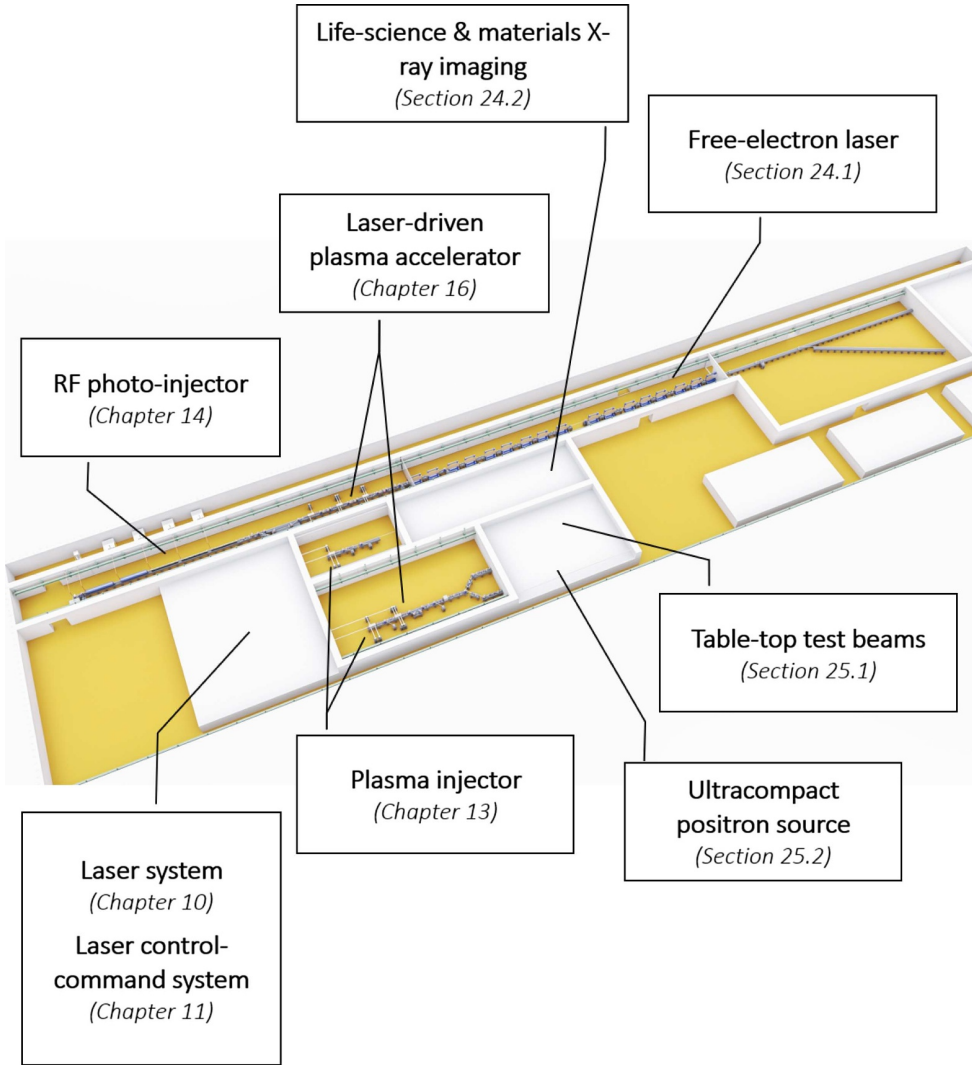


**Fig. 8.2.** Overview layout of the EuPRAXIA site for laser-driven plasma acceleration.

undulator concepts, at least for parts of the undulator line, will be examined as a potential *future development path*.

**ICS  $\gamma$ -ray source:** The inverse Compton scattering (ICS) interaction section and considerations for the user area are described in Section 24.3.

**HEP detector testing and GeV-class positron source:** The high-energy physics (HEP) detector testing application and the generation of high-energy positron beams are foreseen with a common beamline as complementary user applications. The section comprises two parts the first of which is a target and transport line for the conversion of the high-energy electron beam to a positron beam, its energy filtering, and collimation. Second, the remaining electron beam is conditioned for use in detector testing and transported to the respective user area. Detailed designs for both aspects are presented in Sections 25.1 and 25.2.2.

## 8.2 EuPRAXIA Site for Laser-Driven Plasma Acceleration

Similarly to the PWFA site, here, we first summarise the main building blocks of the design of the laser-driven construction site from an overview perspective, before going into the technical details and tables of parameters. The main sub-systems proposed for the EuPRAXIA site for laser-driven plasma acceleration are shown in Figure 8.2. The following design solutions are considered for each component:

**Laser system:** The high-power laser system design of EuPRAXIA consists of three sub-systems optimised for the different types of plasma stages on site: (1) a 5–7 J laser suitable to drive a plasma injector; (2) a 15–30 J targeted for plasma acceleration to 1 GeV; and (3) a 50–100 J laser for plasma acceleration to 5 GeV. Two performance levels are foreseen as part of the *baseline*, including, among others, operation at 20 Hz and 100 Hz. A main *future development path* for the laser system will be towards higher average power and repetition rate at the kHz level. Further details are presented in Chapter 10.

**RF injector:** The *baseline* design for the RF injector line consists of an S-band injector combined with a hybrid bunch compression scheme (combining velocity bunching and magnetic compression) producing electron beams with energy of around 250 MeV. A second presented option is the same setup as foreseen for the PWFA construction site; here, an S-band injector with velocity bunching is combined with an X-band linac to reach an electron beam energy of  $\sim 500$  MeV. Both designs are described in Chapter 14.

**Plasma injector:** Three *baseline* designs are under consideration for the plasma injector with electron beam energy variable between 140 and 250 MeV:

1. Resonant multi-pulse ionisation (ReMPI) injection
2. Density downramp injection
3. Ionisation injection with a density gradient

As detailed in Chapter 13 and, partly, Chapter 23 (start-to-end simulations), for all three schemes, state-of-the-art performance is predicted, while space and cost requirements are similar and very small compared to the overall beamline. It is thus foreseen to validate and optimise all three designs during the coming technical design phase before making a decision on the injection technique implemented for the final design.

**High-quality plasma accelerator:** Similarly to the plasma injector, three *baselines* with excellent performance have been identified for the high-quality plasma accelerator and will be optimised during the technical design, as Chapters 23 (start-to-end simulations) and 16 demonstrate:

1. External injection of the RF-accelerated electron beam into two consecutive plasma-accelerator stages separated by a chicane-based dechirping mechanism
2. External injection of the RF-accelerated electron beam into a single plasma-accelerator stage
3. External injection of an electron beam generated from a plasma injector into a single plasma-accelerator stage

In all three cases, the final electron beam energy is 1 GeV during the first preliminary operation phase before increasing to 5 GeV during full operation. Note that given the small size of the plasma stages, all three concepts are compatible with a single beamline layout, as the first plasma-accelerator stage in the first proposed scheme can easily be removed for setup number two or replaced by a plasma-injector stage to achieve the third setup, thus not affecting the size and cost estimation of the machine significantly. Furthermore, several *upgrade / backup options* are investigated for this challenging beamline design, including

the use of different plasma-injector techniques. Finally, a hybrid plasma accelerator with a laser-driven plasma injector producing the driver beam for a second beam-driven, high-energy plasma-injector stage is further studied as a potential *development path* (see Chap. 26). Three types of injection mechanisms for the second beam-driven injector stage are, in this case, considered as promising solutions.

**High-charge plasma accelerator:** For this type of setup, focussed less on beam quality and more on large beam charge but benefiting strongly from a compact design, an all-optical *baseline* is proposed with a plasma injector followed by external injection into a single plasma-accelerator stage, accelerating the beam to 5 GeV. As with the high-quality accelerator, different techniques for the plasma injector – such as ReMPI injection, downramp injection, and ionisation injection – are examined as different options. A *future development path* is a high-energy plasma injector based on the ReMPI injection mechanism where electrons could be internally injected and accelerated up to 1 to 5 GeV, achieving an extremely compact setup.

**Free-electron laser:** Equivalently to the PWFA site design, the *baseline* for the LWFA-driven FEL will also use conventional undulators, as described in Chapters 18 and 24.1. The implementation of more compact, novel undulator concepts will be a common *future development path*.

**Life-science and materials X-ray imaging:** A compact X-ray source based on betatron radiation inside a plasma target is foreseen for this application. As a *baseline*, the radiation can be directly created inside the plasma injector used for electron beam generation leading to a relatively simple and flexible beamline setup. *Future development paths* will focus on the optimisation of the source, for example, through separating the electron beam injection process from the radiation generation, with an additional dedicated plasma target as a betatron source. The design for this part of the beamline is described in Section 21.7.

**Ultracompact positron source and tabletop test beams:** Similarly to the PWFA site, both of these applications, the generation of an ultra-compact positron source, and the creation of tabletop test beams are foreseen with a common beamline. The section comprises two parts the first of which is a target and transport line for the conversion of the high-energy electron beam to a positron beam, its energy filtering (keeping the low-energy part of the positron beam), and collimation. Second, the remaining electrons are conditioned for use as test beams. They could be used in a similar way to the high-energy physics detector test stand at the PWFA site but will also be suitable for other applications yet to be determined. Detailed designs for both aspects are presented in Sections 25.1 and 25.2.1.

### 8.3 Beam Distribution Concept

Throughout many of the following chapters, describing the detailed design of machine components, six possible accelerator and beam distribution configurations are considered. They are shown schematically in Figure 8.3 and listed with their abbreviated names in Table 8.1. Further details are also included in Chapter 23 in the context of start-to-end simulations of the accelerator.

The following schemes are foreseen as possible beamline configurations for one or several of the proposed beamlines at EuPRAXIA:

**Scheme 1** is a laser-driven plasma injector (LPI) where the electron beam is generated and also accelerated up to 5 GeV in a single plasma stage.

**Table 8.1.** Naming convention of the different accelerator schemes investigated as part of the EuPRAXIA conceptual design study. In each case, the energy value after a stage’s name indicates the electron beam energy at the end of this stage. Different stages are connected by transport lines, which are detailed in Chapter 19. The following abbreviations are used: LPI = laser-plasma injector, RFI = radiofrequency injector, LPAS = laser-driven plasma-accelerator stage, PPAS = beam-driven plasma-accelerator stage.

Scheme no.	Short descriptive name
1	LPI-5 GeV
2	LPI-150 MeV + LPAS-5 GeV
3	RFI-500 MeV + LPAS-5 GeV
4	RFI-240 MeV + LPAS-2.5 GeV + chicane + LPAS-5 GeV
5	RFI-500 MeV + PPAS-1 GeV
6	LPAS-3 GeV + PPAS-5 GeV

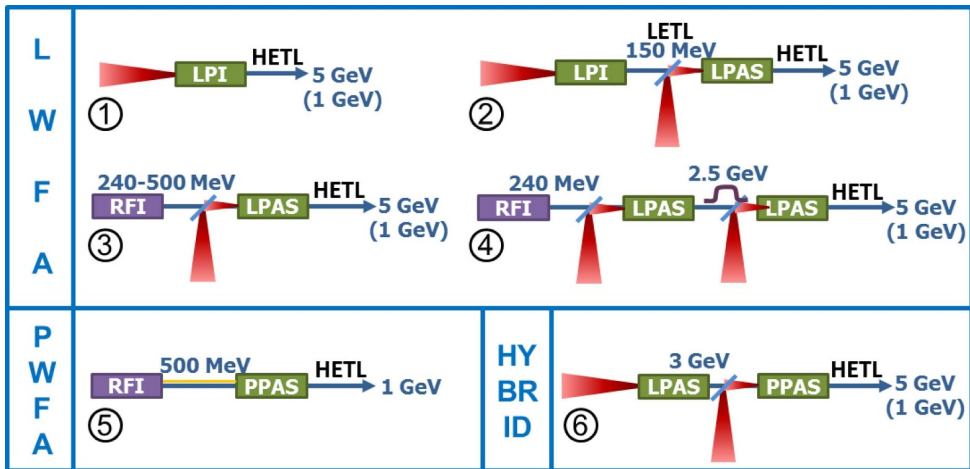


**Fig. 8.3.** Beam distribution and acceleration configurations under consideration for the various EuPRAXIA beamlines. The following abbreviations are used besides those listed in the main text: LETL = low-energy transport line, HETL = high-energy transport line. A detailed description and assessment of the performance of each of these schemes as a whole is presented in Chapter 23 (image credits: [171]).

**Scheme 2** is a staged setup where the electron beam is generated in a laser-driven plasma injector (LPI), then transported and injected into a laser-driven plasma-accelerator stage (LPAS), where its energy is boosted up to 5 GeV.

**Scheme 3** is a staged setup where the electron beam is generated in an RF photo-injector and pre-accelerated in an RF linac (RFI), then transported and injected into a laser-driven plasma accelerator stage (LPAS) where its energy is boosted up to 5 GeV.

**Scheme 4** is a staged setup where the electron beam is generated in an RF photo-injector and pre-accelerated in an RF linac (RFI), then transported and injected into two consecutive laser-driven plasma-accelerator stages (LPAS); in each stage the beam experiences an energy gain of approximately 2.5 GeV, while propagation through a magnetic chicane in the transport between the LPAS induces an energy dechirping process.

**Scheme 5** is a staged setup where two electron beams – a driver and a witness – are generated in an RF photo-injector and pre-accelerated in an RF linac (RFI), then

transported and injected into a beam-driven plasma-accelerator stage (PPAS), where the energy of the witness beam is boosted up to 5 GeV.

**Scheme 6** is a staged hybrid accelerator setup where a laser-driven plasma injector (LPAS) generates an electron beam that is in turn used as the beam driver in a second beam-driven plasma injector (PPAS); in the latter a higher quality electron beam is generated and accelerated up to 5 GeV.

Schemes 1 to 4 are all based on laser-driven plasma acceleration and are thus relevant for implementation at the laser-driven construction site of EuPRAXIA. For a versatile and optimised layout, it is foreseen that different beamlines will be designed based on different schemes; the central laser system of EuPRAXIA will allow to feed several of these lines in parallel. Scheme 5, on the other hand, is a beam-driven plasma accelerator configuration and forms the baseline for the accelerator at the beam-driven construction site. Multiple user areas can be served by splitting the central line either before or after the plasma-accelerator stage (PPAS). In the former case, the plasma sections could be customised to each application, while, in the latter scenario, the transport of the beam may be less challenging. Finally, Scheme 6 provides a potential future development option for both sites with a configuration that combines laser-driven and beam-driven plasma acceleration, with the promise of exceptional electron beam quality.

## 9 Summary Tables of Parameters and Technical Data

The design of the technical components for EuPRAXIA has been guided by a set of goal parameters defining successful performance through the realisation of key applications. A particularly challenging target in this context has been identified with the capability to run an FEL and this has consequently been chosen as a baseline goal for the electron accelerator performance. Considering that most of the other applications foreseen for EuPRAXIA have comparably relaxed conditions for the more challenging beam parameters in plasma acceleration, such as energy spread and emittance, they should thus also be attainable through fine-tuning such an FEL-capable machine. Table 9.1 summarises the key goal parameters for the electron accelerator following this derivation (see [220] for the original complete parameter list, some updates to which have been made since its publication).

**Table 9.1.** Estimated goal parameters of the electron beam at the entrance of an undulator for FEL lasing. These values have been determined by the EuPRAXIA collaboration and form an updated version of the original design concept in [220]. Most of the design work on technical components has been informed by these aimed performance ranges.

Quantity	Baseline Goal	Range of Exploration
Energy	5 GeV	$\geq 1$ GeV
Charge	30 pC	5–100 pC
Bunch length (FWHM)	10 fs	$\leq 30$ fs
Peak current	3 kA	2–5 kA
Energy spread	1 %	$< 1$ %
Normalised emittance in x,y	1 mm mrad	$< 1$ mm mrad
Slice energy spread	0.1 %	$< 0.1$ %
Normalised slice emittance in x,y	$< 1$ mm mrad	$\ll 1$ mm mrad

Based on the goals of Table 9.1, in-depth conceptual solutions have been developed and the expected performance of different working points has been simulated in detail. The resulting performance predictions are summarised in the parameter tables following in this chapter. Experimental results are also taken into account in this context, as far as possible (e.g. for the plasma injector). More detailed explanations of the origins of the listed values can be found in the relevant component chapters, as defined in the respective table captions.

## 9.1 Laser System

**Table 9.2.** Summary table of parameters and technical data of the laser system. More detailed parameters and further context are found in Chapter 10.

Quantity	Baseline Value
Laser 1 – Energy on target	$\leq 5\text{--}7\text{ J}$
Laser 1 – Pulse duration	$\geq 20\text{--}30\text{ fs}$
Laser 2 – Energy on target	$\leq 15\text{--}30\text{ J}$
Laser 2 – Pulse duration	$\geq 20\text{--}30\text{ fs}$
Laser 3 – Energy on target	$\leq 50\text{--}100\text{ J}$
Laser 3 – Pulse duration	$\geq 50\text{--}60\text{ fs}$
Wavelength	800 nm
Repetition rate	20–100 Hz
Energy stability (RMS)	0.6–1 %
Pointing stability (RMS)	$\sim 1\text{ }\mu\text{rad}$

## 9.2 RF Injector and Accelerator

**Table 9.3.** Summary table of parameters and technical data of the RF injector and accelerator. More detailed parameters and further context are found in Chapters 12 and 14.

Quantity	Baseline Value
<b>RF Injector / Accelerator – Full RF Compression Scheme (for LWFA / PWFA)</b>	
Photoinjector – Operating frequency	2.856 GHz
Photoinjector – Gun field amplitude	$120\text{ MV m}^{-1}$
Photoinjector – Gun output beam energy	5.6 MeV
Photoinjector – TW sections field amplitude	$20\text{--}28\text{ MV m}^{-1}$
Photoinjector – solenoid magnetic field (gun, linac)	3.0–3.05 kG, 0.32–0.52 kG
Photoinjector – Length	12 m
Linac – Operating frequency	$\sim 12\text{ GHz}$
Linac – Field amplitude	$\geq 60\text{ MV m}^{-1}$
Linac – Length	10 m
<b>Witness Electron Beam Parameters after the RF Injector / Accelerator</b>	
Charge	30 pC
Energy	535–570 MeV
Energy spread (RMS)	0.07 %
Bunch length (RMS)	17–20 fs
Peak current (FWHM)	3.0 kA
Normalised emittance in x,y (RMS)	0.5–0.7 mm mrad (x), 0.44–0.9 mm mrad (y)
<b>Driver Electron Beam Parameters after the RF Injector / Accelerator</b>	
Charge	200 pC
Energy	580 MeV
Bunch length (RMS)	20 fs
Normalised emittance in x,y (RMS)	4.0 mm mrad (x), 6.4 mm mrad (y)
<b>RF Injector – Hybrid Compression Scheme (for LWFA)</b>	
Photoinjector – Operating frequency	2.856 GHz
Photoinjector – Gun field amplitude	$110\text{ MV m}^{-1}$
Photoinjector – Gun output beam energy	5 MeV
Photoinjector – TW sections field amplitude	$25.5\text{ MV m}^{-1}$
Photoinjector – Length	12 m
<b>Witness Electron Beam Parameters after the RF Injector</b>	
Charge	29.8 pC
Energy	240.8 MeV
Energy spread (RMS)	0.27 %
Bunch length (RMS)	7.5 fs
Peak current (FWHM)	4.0 kA
Normalised emittance in x,y (RMS)	0.81 mm mrad (x), 0.46 mm mrad (y)

### 9.3 Plasma Injector

**Table 9.4.** Summary table of parameters and technical data of the plasma injector. More detailed parameters and further context are found in Chapter 13.

Quantity	Baseline Value
<b>Low-energy LPI</b>	
Plasma electron density	$3 \times 10^{18} - 8 \times 10^{18} \text{ cm}^{-3}$
Plasma length	0.6–1.6 mm
Plasma entrance / exit ramp length	0.3–0.8 mm
Normalised laser vector potential on target	1.4–4.5
Beam energy at injector exit	140–250 MeV
Beam charge at injector exit	27–32 pC
Beam energy spread at injector exit	0.9–4%
Bunch length at injector exit	3–8 fs
Beam norm. emittance in x,y at injector exit	0.1–0.8 mm mrad (x), 0.15–1.8 mm mrad (y)
<b>High-energy LPI</b>	
Plasma electron density	$10^{18} - 6 \times 10^{18} \text{ cm}^{-3}$
Plasma length	9–30 mm
Plasma entrance / exit ramp length	0.9–2.1 mm
Normalised laser vector potential on target	1.2–3.9

### 9.4 Plasma Accelerator

**Table 9.5.** Summary table of parameters and technical data of the plasma accelerator stages. More detailed parameters and further context are found in Chapters 16 and 17.

Quantity	Baseline Value
<b>Laser-Driven Plasma Accelerator (LPAS)</b>	
Plasma electron density	$\sim 10^{17} \text{ cm}^{-3}$
Plasma length	0.25–1 m
Plasma entrance / exit ramp length	3.5–7 mm
Normalised laser vector potential on target	1.0–2.0
Accelerating field gradient	$\sim 10 \text{ GV m}^{-1}$
Beam energy at accelerator exit	5.0–6.0 GeV
Beam charge at accelerator exit	23–30 pC
Beam energy spread at accelerator exit	0.1–0.9%
Bunch length at accelerator exit	2.9–11 fs
Beam norm. emittance at accelerator exit	0.09–1.38 mm mrad
<b>Beam-Driven Plasma Accelerator (PPAS)</b>	
<b>PPAS to 1 GeV</b>	
Plasma electron density	$10^{16} \text{ cm}^{-3}$
Plasma length	40 cm
Plasma entrance / exit ramp length	$\sim 0.5 \text{ cm}$
Accelerating field gradient	$1.1 - 3.0 \text{ GV m}^{-1}$
Beam energy at accelerator exit	1.03 GeV
Beam charge at accelerator exit	30–34 pC
Beam energy spread at accelerator exit	1.1%
Bunch length at accelerator exit	13 fs
Beam norm. emittance in x,y at accelerator exit	0.96 mm mrad (x), 1.2 mm mrad (y)
<b>PPAS to 5 GeV</b>	
Plasma electron density	$2.5 \times 10^{16} \text{ cm}^{-3}$
Plasma length	2.4 m
Plasma entrance / exit ramp length	$\sim 1 \text{ cm}$
Accelerating field gradient	$1.6 - 2.7 \text{ GV m}^{-1}$
Beam energy at accelerator exit	5.0 GeV
Beam energy spread at accelerator exit	0.4%
Beam norm. emittance at accelerator exit	$\sim 0.7 \text{ mm mrad}$

## 9.5 Beam Transport Line

**Table 9.6.** Summary table of parameters and technical data of the beam transport. More detailed parameters and further context are found in Chapter 19.

Quantity	Baseline Value
<b>Low-Energy Transport Line (LETL)</b>	
Six-quadrupole setup: magnetic field gradients	(211/-189/86/-101/190/-161) T m <sup>-1</sup>
Six-quadrupole setup: length	0.7 m
Eight-quadrupole setup: magnetic field gradients	(97/-182/162/-62/-67/-161/ -171/94) T m <sup>-1</sup>
Eight-quadrupole setup: length	2.04 m
Active-plasma-lens setup: magnetic field gradients	(316/301) T m <sup>-1</sup>
Active-plasma-lens setup: length	2.02 m
Solenoid setup: magnetic field	(7.6/-7.3) T
Solenoid setup: length	2.2 m
Beam energy spread after LETL	2.2–3.1 %
Bunch length after LETL	3.7–4.7 fs
Beam norm. emittance in x,y after LETL	0.45–0.66 mm mrad (x), 0.38–0.67 mm mrad (y)
<b>High-Energy Transport Line (HETL)</b>	
Length	8 m
Number of quadrupoles	7
Transport line length	6–8 m
Beam energy after HETL (beam core)	4.96–5.9 GeV
Energy spread after HETL (beam core)	0.10–0.32 %
Bunch length after HETL (beam core)	0.3–3.5 fs
Norm. emittance in x,y after HETL (beam core)	0.087–1.64 mm mrad (x), 0.085–0.88 mm mrad (y)

## 9.6 Free-Electron Laser

**Table 9.7.** Summary table of parameters and technical data of the free-electron laser. More detailed parameters and further context are found in Chapter 24.1.

Quantity	Baseline Value
<b>Free-Electron Laser – 1 GeV</b>	
<b>Long-Wavelength Setup</b>	
Undulator period	30 mm
K parameter	4.36
Peak undulator field	1.56 T
Radiation wavelength	34.5–35.9 nm
Pierce parameter	0.45–0.57 %
Saturation power	2.5–4.9 GW
Saturation length	~16–23 m
Linewidth	0.5–3.6 %
Pulse duration	~7.8–15 fs
Photons per pulse	$1.6 \times 10^{11}$ – $3.1 \times 10^{11}$
Brightness	$2 \times 10^{28}$ – $8.6 \times 10^{29}$ photons/[mm <sup>2</sup> mrad <sup>2</sup> s(0.1%BW)]
<b>Short-Wavelength Setup</b>	
Undulator period	20 mm
K parameter	1.5
Peak undulator field	0.81 T
Radiation wavelength	4.67–4.86 nm
Pierce parameter	0.19–0.24 %
Saturation power	1.29–1.94 GW
Saturation length	16–28 m
Linewidth	0.25–0.59 %
Pulse duration	2.0–2.4 fs
Photons per pulse	$1.3 \times 10^{10}$ – $2.3 \times 10^{10}$
Brightness	$8 \times 10^{28}$ – $5 \times 10^{29}$ photons/[mm <sup>2</sup> mrad <sup>2</sup> s(0.1%BW)]
<b>Free-Electron Laser – 5 GeV</b>	
<b>Long-Wavelength Setup</b>	
Undulator period	30 mm
K parameter	4.36
Peak undulator field	1.56 T
Radiation wavelength	1.40–1.67 nm
Pierce parameter	0.2–0.23 %
Saturation power	14–17.8 GW
Saturation length	20–26 m
Linewidth	0.3 %
Pulse duration	0.7–2.2 fs
Photons per pulse	$4.2 \times 10^{10}$ – $7.2 \times 10^{11}$
Brightness	$2.8 \times 10^{31}$ – $4.8 \times 10^{32}$ photons/[mm <sup>2</sup> mrad <sup>2</sup> s(0.1%BW)]
<b>Short-Wavelength Setup</b>	
Undulator period	20 mm
K parameter	1.5
Peak undulator field	0.81 T
Radiation wavelength	0.19–0.30 nm
Pierce parameter	0.084–0.099 %
Saturation power	1.75–4.39 GW
Saturation length	38–126 m
Linewidth	0.18–0.23 %
Pulse duration	0.4–2.0 fs
Photons per pulse	$1.9 \times 10^9$ – $3.2 \times 10^{10}$
Brightness	$3.7 \times 10^{30}$ – $4.0 \times 10^{31}$ photons/[mm <sup>2</sup> mrad <sup>2</sup> s(0.1%BW)]

## 9.7 Other Radiation Sources

**Table 9.8.** Summary table of parameters and technical data of the betatron and inverse Compton scattering sources. More detailed parameters and further context are found in Sections 24.2 and 24.3.

Quantity	Baseline Value
<b>Betatron Source</b>	
Photon energy	0.6–110 keV
Source size	1.4–2.4 $\mu\text{m}$
Divergence	0.7–70 mrad
Peak X-ray brightness	$2 \times 10^{21}$ – $1 \times 10^{26}$ photons/( $\text{mm}^2\text{mrad}^2\text{s}[0.1\% \text{BW}]$ )
Photons per pulse	$2 \times 10^8$ – $4 \times 10^{10}$
<b>Inverse Compton Source</b>	
Photon energy	>100 MeV
Pulse duration	$\sim 30$ fs
Source size	single $\mu\text{m}$
Divergence	<1 mrad

## 9.8 Secondary Particle Sources

**Table 9.9.** Summary table of parameters and technical data of the secondary particle sources. More detailed parameters and further context are found in Section 25.

Quantity	Baseline Value
<b>Low-Energy Positron Source</b>	
Positron energy	0.5–10 MeV (tunable)
Energy bandwidth	$\pm 50$ keV
Beam duration	20–90 ps
Beam size at user area	2–5 mm
Positrons per shot	$\geq 10^6$
<b>High-Energy Positron Source</b>	
Positron energy	$\geq 1.0$ GeV (tunable)
Energy bandwidth	$\pm 5\%$
Beam duration	< 10 fs
Beam size at user area	20 $\mu\text{m}$
Positrons per shot	$\sim 10^7$

## 9.9 Accelerator Start-to-End Simulations

**Table 9.10.** Summary table of parameters from the start-to-end simulations of different acceleration schemes. All parameters are given for the beam core at the end of the final transport line matched exemplarily to the undulator entrance. The following abbreviations are employed: RFI = RF injector, LPI = laser-plasma injector, LPAS = laser-driven plasma accelerator, PPAS = beam-driven plasma accelerator. Slice parameters and peak current are calculated based on 0.1  $\mu\text{m}$  long slices. More detailed parameters and further context are found in Chapter 23.

Quantity	Baseline Value
<b>Scheme 1: LPI-5 GeV</b>	
Beam energy	5.0 GeV
Charge	30 pC
Peak current	3.8 kA
Bunch duration	2.9 fs
Energy spread	0.9 %
Normalised emittance in x,y	0.10 mm mrad (x), 0.06 mm mrad (y)
Energy spread (best slice)	0.08 %
Normalised emittance (best slice)	0.07 mm mrad (x), 0.04 mm mrad (y)
<b>Scheme 2: LPI-150 MeV + LPAS-5 GeV</b>	
Beam energy	5.0 GeV
Charge	5 pC
Peak current	3.3 kA
Bunch duration	0.4 fs
Energy spread	0.1 %
Normalised emittance in x,y	0.76 mm mrad (x), 0.88 mm mrad (y)
Energy spread (best slice)	0.08 %
Normalised emittance (best slice)	0.85 mm mrad (x), 1.00 mm mrad (y)
<b>Scheme 3: RFI-500 MeV + LPAS-5 GeV</b>	
Beam energy	5.3 GeV
Charge	22 pC
Peak current	3.3 kA
Bunch duration	2.9 fs
Energy spread	0.11 %
Normalised emittance in x,y	0.32 mm mrad (x), 0.29 mm mrad (y)
Energy spread (best slice)	0.03 %
Normalised emittance (best slice)	0.32 mm mrad (x), 0.32 mm mrad (y)
<b>Scheme 4: RFI-240 MeV + LPAS-2.5 GeV + chicane + LPAS-5 GeV</b>	
Beam energy	6.0 GeV
Charge	23.8 pC
Peak current	5.1 kA
Bunch duration	3.1 fs
Energy spread	0.39 %
Normalised emittance in x,y	1.50 mm mrad (x), 0.69 mm mrad (y)
Energy spread (best slice)	0.06 %
Normalised emittance (best slice)	0.85 mm mrad (x), 0.40 mm mrad (y)
<b>Scheme 5: RFI-500 MeV + PPAS-1 GeV</b>	
Beam energy	1.1 GeV
Charge	10.5 pC
Peak current	2.0 kA
Bunch duration	0.6 fs
Energy spread	0.26 %
Normalised emittance in x,y	0.91 mm mrad (x), 0.68 mm mrad (y)
Energy spread (best slice)	0.07 %
Normalised emittance (best slice)	0.62 mm mrad (x), 0.48 mm mrad (y)

## 10 Laser Systems as Innovative Power Drivers

### 10.1 Introduction

The use of lasers as power drivers for plasma accelerators has been emerging dramatically in the past decades, not only for the well-known effectiveness in exciting and driving plasma waves, but also for the fast-developing technologies that drive the continuous improvement in performances.

Beyond that, entirely new technologies are also maturing while we write, laying the foundations for the migration of laser drivers from the context of pioneering laser-driven acceleration R&D to the realm of viable drivers for plasma accelerators. In fact, while currently available off-the-shelf technology is limited in average power and repetition rate, new pump power approaches based on robust solid-state technologies are already emerging as powerful alternative solutions to overcome such limitations.

In view of that, the proposed EuPRAXIA infrastructure relies on a range of unique petawatt-power, ultra-short pulse laser systems to drive plasma acceleration in a range of different configurations, including a 150 MeV injector and 1 and 5 GeV accelerators. For the development of the conceptual design, we have investigated a broad range of technologies, concepts, and approaches to petawatt laser technology capable of fulfilling the specifications set by the design of the injector and the accelerators. In doing so, a technology survey has been carried out (see [221]), and the main conclusions are presented in Sections 7.2 and 32.3 of this report. In the study, an accurate examination of relevant laser developments was carried out, identifying applicable technologies and corresponding technology readiness levels (TRL). The requirement of ultra-short pulse duration, down to 30 fs, combined with the significant energy per pulse needed by the three laser-driven schemes, finally made Ti:Sa emerge as the most suitable technology based on the foreseen temporal constraints. The baseline design of the main EuPRAXIA lasers could be delivered using Ti:Sa laser technology and exploiting the fast ongoing developments in pump lasers, i.e. lasers capable of delivering ns pulses with approximately 100 J energy per pulse at a 100 Hz repetition rate. The baseline concept includes the main amplifiers, a description of the key components and sub-components, and the analysis of all the main transport sections, from the compressor down to the interaction point. At the same time, a number of development paths for alternative technologies for longer term solutions were also tackled given the potential further exploitation of laser drivers in terms of efficiency, very high repetition rate, compactness, and overall cost.

This chapter delivers the baseline design of the laser system and identifies the pivotal development paths with step-by-step instructions for the transition to the technical description.

### 10.2 Baseline Design

#### 10.2.1 Layout and Amplifiers

The development of the laser driver for EuPRAXIA relies on chirped pulse amplification (CPA) and uses Ti:Sapphire (Ti:Sa) as a gain medium. The required performance and reliability is currently beyond the state of the art of available industrial or prototype systems, especially for what concerns the 100 Hz operation. However, in recent years, a number of advancements have been consolidated or are in progress, making it possible not only to conceive a viable design but also to identify the development

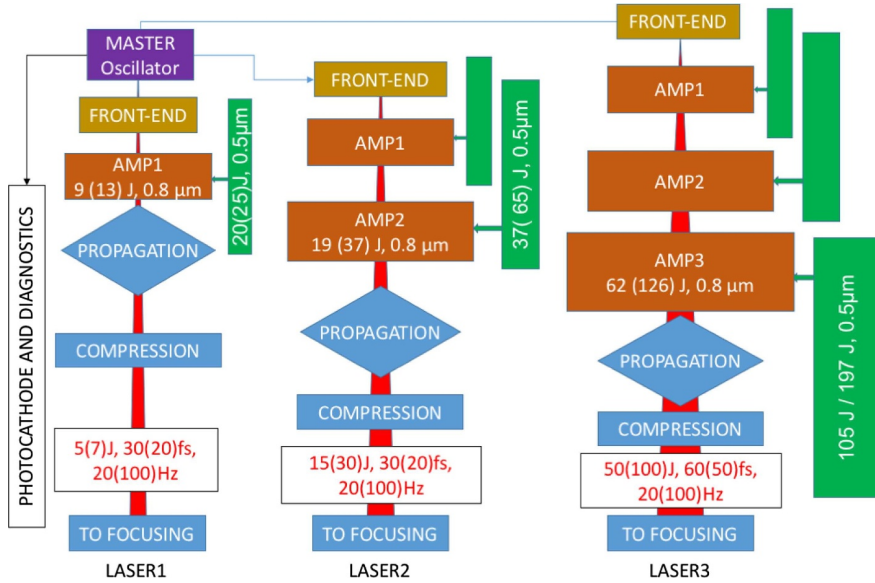


Fig. 10.1. Block diagram of the three laser driver chains.

path to take this design to a technical level in a few years, a time compatible with the envisaged construction of EuPRAXIA.

The implementation of the plasma acceleration schemes considered in EuPRAXIA requires the simultaneous use of up to three different laser beamlines with accurate relative synchronisation to ensure controlled plasma acceleration. Auxiliary laser beams for diagnostics and a photocathode laser, tightly synchronised with the three main laser pulses, are also included. The overall architecture of the EuPRAXIA laser system is shown in Figure 10.1. It consists of three different laser chains, with different output pulse parameters (LASER1, LASER2, and LASER3) to drive three different plasma acceleration configurations. Each laser chain consists of a front-end segment, an amplification section – made of one, two, or three amplification stages depending on the required output energy – a beam shaping segment, a compressor, and the final transport system to the target.

The three laser chains share a common master oscillator to ensure intrinsic synchronisation accuracy; the front-end segments share a similar design but are separated to allow independent control on seed pulse properties.

Our design focussed on the following aspects of the layout:

- the technology for the laser systems for pumping the Ti:Sa amplifiers at a high repetition rate;
- the design of the Ti:Sa amplifiers, especially for the thermal load management and cooling strategies, and the optimisation of the extraction efficiency; and
- the design of the pulse compression system, mainly in relation with the optical damage and thermal management of the gratings.

For each system, two levels of performance have been envisaged, with different energy levels and pulse repetition rates:

- (a) Low-performance level (named P0), featuring low pulse energy and a 20 Hz repetition rate
- (b) High-performance level (called P1), with higher energy at a repetition rate of 100 Hz

**Table 10.1.** Laser parameters for the three laser driver beamlines envisaged for laser plasma injection and acceleration stages, at the performance levels P0 and P1. The maximum output energy has been calculated from the requirements of energy on target, assuming an overall efficiency of 80% of the compression and the beam transport system.

<b>LASER1 – Injector 150 MeV</b>			
<b>Parameter</b>	<b>Unit</b>	<b>P0</b>	<b>P1</b>
<b>Wavelength</b>	nm	800	800
<b>Max Energy on Target</b>	J	5	7
<b>Max Total Output Energy</b>	J	8.8	12.5
<b>Shortest Pulse Duration</b>	fs	30	20
<b>Repetition Rate</b>	Hz	20	100
<b>Energy Stability RMS</b>	%	1	0.6
<b>LASER2 – Injector 1 GeV</b>			
<b>Parameter</b>	<b>Unit</b>	<b>P0</b>	<b>P1</b>
<b>Wavelength</b>	nm	800	800
<b>Max Energy on Target</b>	J	15	30
<b>Max Total Output Energy</b>	J	18.8	37.5
<b>Shortest Pulse Duration</b>	fs	30	20
<b>Repetition Rate</b>	Hz	20	100
<b>Energy Stability RMS</b>	%	1	0.6
<b>LASER3 – Accelerator 5 GeV</b>			
<b>Parameter</b>	<b>Unit</b>	<b>P0</b>	<b>P1</b>
<b>Wavelength</b>	nm	800	800
<b>Max Energy on Target</b>	J	50	100
<b>Max Total Output Energy</b>	J	62.5	125
<b>Shortest Pulse Duration</b>	fs	60	50
<b>Repetition Rate</b>	Hz	20	100
<b>Energy Stability RMS</b>	%	1	0.6

The performance level P0 is less challenging in terms of required technologies. According to our study, it can be implemented with the currently available technologies, requiring mainly integration efforts and optimisation. Level P1 is more challenging and can be considered as lying one step ahead with respect to the current technological capabilities, in particular regarding the repetition rate of the pump sources. The target performances of the three laser chains, at the level of performances P0 and P1, are reported in Table 10.1.

The performance level P0 can be implemented with the currently available technologies, requiring mainly integration efforts and optimisation.

### 10.2.2 Front End

The design of the front-end segment, at the performance levels P0 or P1, is based on commercially available configurations. It includes a common master oscillator shared among the three systems. A first CPA stage is devoted to the amplification of the pulse at the 1 mJ level, which is required to efficiently pump a PW stage immediately downstream. The resulting pulse, with typical energy of the order of 10–100  $\mu$ J, is then seeded into the main CPA chain. A regenerative amplifier and two multi-pass amplifiers increase the energy up to about  $>1$  J needed to efficiently seed the first stages of the three amplification chains.

### 10.2.3 Power Amplifiers

The amplification of the pulses generated by the front end is based on chirped pulse amplification (CPA) in Ti:Sapphire pumped by frequency-doubled, solid-state Nd- or Yb-based lasers with an emission in the range of 515–532 nm. The basic amplifier configuration is similar to many of the systems operating worldwide, with the significant difference of the very high repetition rate of 20–100 Hz compared to the typical Hz or sub-Hz repetition rate of current petawatt systems. This results in high average pump power requirements, thus placing a severe thermal load on the amplification stages.

The thermal load management was therefore the main driver in the design of the amplification stages, in particular for the cooling strategy. The baseline design foresees the use of a fluid cooling of the end surfaces of the amplification crystals shaped as disks, with a relatively large diameter-to-thickness ratio, to provide an adequately large surface for heat exchange. Water at near room temperature is used as the cooling fluid, following an approach that was recently proposed in the framework of the ELI-ALPS developments [222].

Effort was also directed towards the optimisation of the extraction efficiency to reduce the pump energy needed for a given level of output energy, thus reducing both the requirements on the pump lasers and the overall thermal load. This optimisation has been pursued by a careful repartition of the amplification level between the different amplification stages and by implementing the extraction during pumping (EDP) method to prevent the build-up of excessive transverse gain and thus the occurrence of energy losses from transverse parasitic lasing [223,224].

Finally, modularity and scalability were included in the design, conceiving the amplifiers as a set of amplification modules arranged in different combinations dimensioned to operate at the highest level of performance (P1, see Tab. 10.1), provided that a sufficient pump pulse energy is available. This approach was deemed as advantageous in view of an industrial development of the system, and of the scaling up of its performance during the facility lifetime. Following this approach, as shown in Figure 10.1, the amplification chain of LASER1 consists of a single amplification stage (named AMP1). The amplification chain of LASER2 consists of two amplification stages, AMP1 and AMP2, the first one having the same design of the single amplification stage of LASER1 and operating at the same seed pulse energy, pump energy, and output pulse energy. Finally, LASER3 consists of three amplification stages (AMP1, AMP2, and AMP3), the first two being identical to LASER2, and the third one featuring a dedicated design.

### 10.2.4 Ti:Sapphire Amplifier Structure and Geometry

A dedicated analysis was carried out to define the geometrical layout of the multi-pass amplifier suitable for the required cooling management. As exposed above, one of the main outcomes of the conceptual design is that the amplifying crystals need to be water-cooled with a high flow speed to remove the heat generated by the pumping process. For this purpose, the amplifying crystals must be shaped as thin disks with a high diameter-to-thickness ratio. Cooling must be applied on the crystal faces to have a sufficient heat-exchange surface. To achieve sufficient pump absorption and energy storage, several disks (2 to 4) must be used in each amplification stage, depending on the pump energy and repetition rate. To achieve efficient amplification and energy extraction, the amplified beam must cross the crystal several times, from 4 to 6 passes, depending on the configuration. As for the cooling strategy, two possible approaches were considered for the disks: a transmission geometry and a reflection geometry.

**Table 10.2.** Amplified beam diameters, Ti:Sapphire crystal diameter and clear aperture (CA), crystal thickness, and number of passes for the various amplification stages.

Amplifier	Beam FWHM (mm)	CA/diameter (mm)	Thickness (mm)	Passes P0 or P1
<b>AMP1</b>	4.5	50/60	6	6/6
<b>AMP2</b>	8	100/120	10	6/6
<b>AMP3</b>	12.8	160/180	16	6/4

In the transmission geometry, the amplifying crystal is water-cooled on both faces, and both the pump beams and the amplified beam cross the crystal, the water-cooling flow, and the flow containment windows. This solution has been proposed and numerically analysed in [222]. It offers a good performance in terms of heat extraction and allows for the implementation of simpler layouts from the geometrical point of view, but it presents a potential drawback because the amplified beam crosses the cooling flow and is potentially subjected to optical aberrations due to turbulences as the fluid flows at high values of the Reynolds number.

In the reflection geometry, one of the faces of the crystal is highly reflective for the amplification beam. The amplified beam enters in the crystal from the front face, and it is reflected back in the incoming direction on the back surface. The same occurs with the pump beams. The reflective surface is water-cooled, whereas the front face is uncooled, as shown in Figure 10.2. In this way, the beam path does not cross the turbulent cooling flow, so no optical aberrations occur. On the other hand, this arrangement allows for a less favourable surface/volume ratio for cooling and requires a more complex optical geometry.

Details of the amplifiers in the transmission geometry have been described in a previous paper [225] [Gizzi 2018]. Both reflection and transmission geometry designs are still under consideration on the basis of theoretical considerations and simulations, and they will be addressed by suitable pilot studies. The laser modules were dimensioned by means of numerical simulations using the code MIRO, developed by CEA [226], using the built-in amplification model for Ti:Sapphire. The simulations were validated by comparison with real laser systems [224,227]. These case studies were considered relevant because the operating parameters of these systems are similar in terms of pump fluence, single-pass gain, and output energies. As a baseline design, all the amplifying modules feature a multi-pass amplification architecture with four passes, depending on the stage.

## Transmission Geometry

The structure of the amplifier crystals for the transmission geometry is similar for all three amplifying stages, and it is shown schematically in Figure 10.3. The gain length is split into two elements to increase the available cooling surface. For each surface, the flow of cooling water is contained between the surface of the crystal and a transparent window made of glass or fused silica. The crystals are surrounded by a layer of index matching, absorbing fluid to suppress optical feedback from the side surfaces and prevent parasitic lasing. The size of each crystal of the pair is reported in Table 10.2.

The thickness of the cooling flow is dictated by fluid-dynamic considerations, and it is in the range of 5 to 7 mm, regardless of the diameter of the disks. For the geometrical layout of the amplifiers in the transmission geometry, the classical bowtie arrangement was adopted. The paths of the various passes of the amplifier are multiplexed in angle in a plane perpendicular to the crystal faces, as shown in the

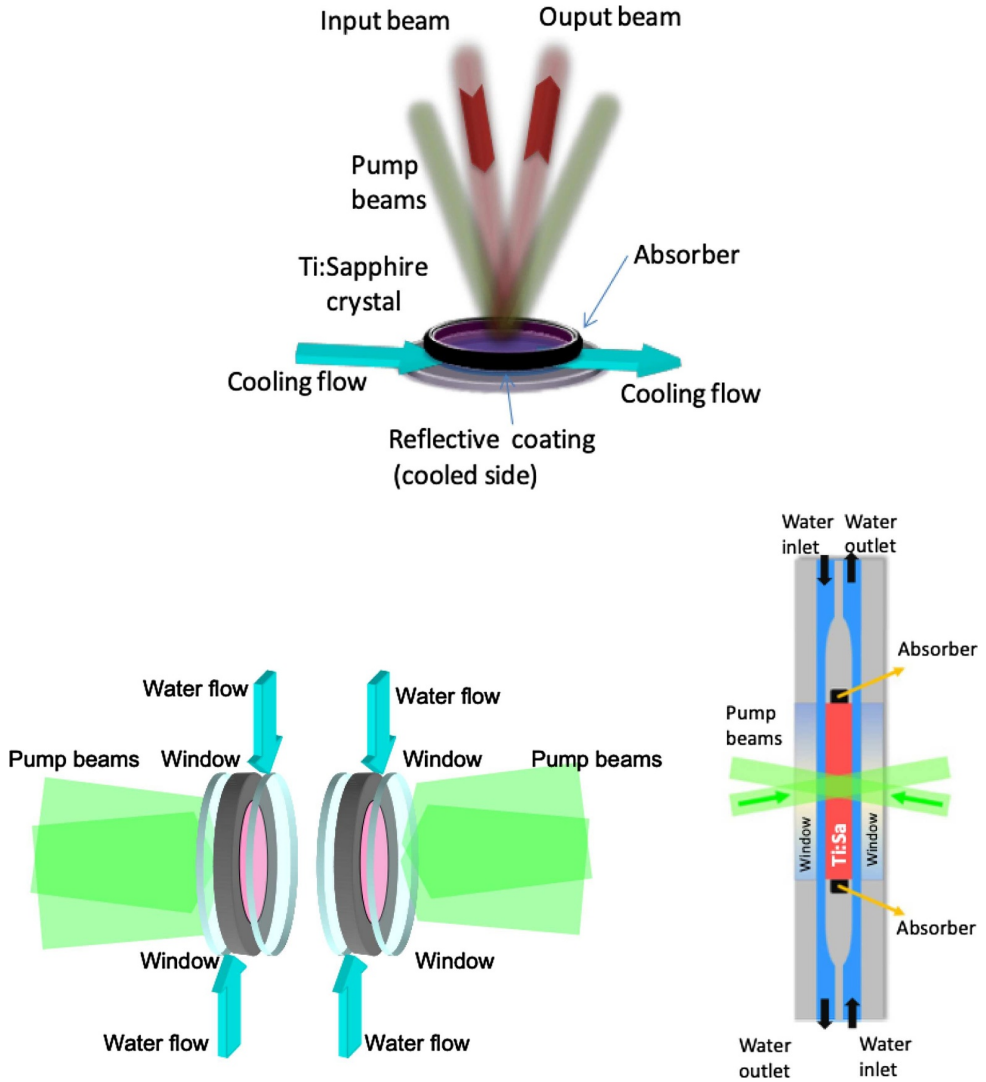
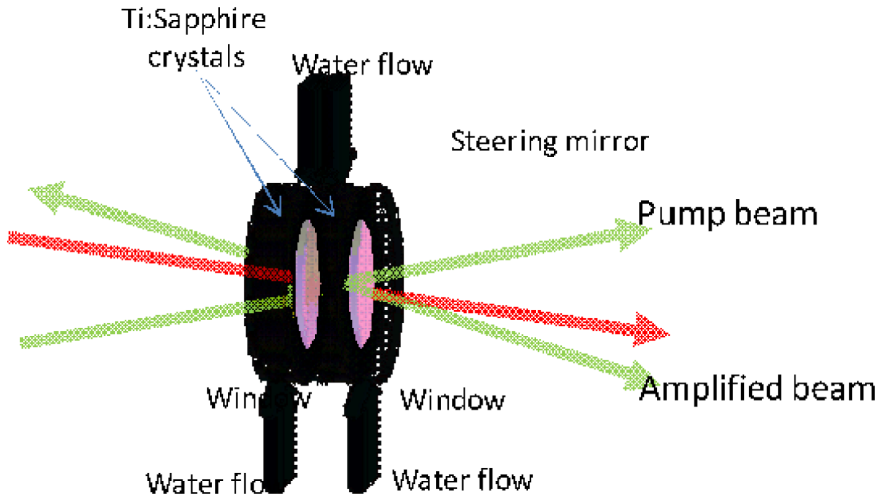


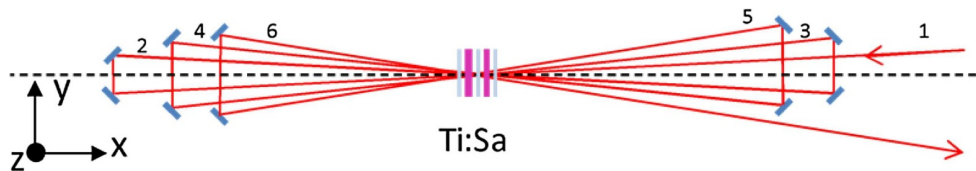
Fig. 10.2. Investigated geometries of the amplifier head with disk gain material and water cooling. Top: Reflection geometry. Bottom: Transmission geometry.

diagram in Figure 10.3, for a six-pass arrangement (the reduction to the four-pass case is straightforward). This scheme is common to all the amplifiers (AMP1, AMP2, AMP3) at both performance levels P0 and P1. For increasing the size of the crystals and cross-section of the beams, the geometry is scaled proportionally, keeping fixed values for the offset angles.

For increasing the number of passes, the angle of the beam path with respect to the crystal axes increases from  $1.2^\circ$  (passes 1,2) to  $2.4^\circ$  (passes 3,4) to  $3.6^\circ$  (passes 5,6). To obtain a sufficient separation of the beams at the steering mirrors (i.e. to avoid mechanical obstructions), the overall length of the system is 4 m for AMP1, 5 m for AMP2, and 8 m for AMP3. Regarding the pump injection path, as said before, the pulse coming from each pump source must be split into two parts, which must arrive at the crystal at different times: the first one just before the injection of



**Fig. 10.3.** Schematic structure of the twin amplifying crystals in the transmission geometry, along with the cooling flow arrangement. Some passes of the pump beams and of the amplified beam are also shown.



**Fig. 10.4.** Top view of the general layout of the amplifier crystals for the transmission geometry for a six-pass arrangement. The red line is the beam path of the amplified beam, which lies in the x-y plane of the drawing. The numbers exemplify the sequence of passes. The pump beam's path is not shown for clarity. The dashed line indicates the axis of the crystals.

the seed pulse, the second one just before one of the subsequent amplification passes (the third and fourth depending on the amplification stages).

The recombination of the two sub-pulses on the same beam path after the splitting was considered technically too complicated as it would require large-aperture active components, such as Pockel's cells, with fast-switching capabilities. For this reason, the sub-pulses will be sent to the Ti:Sapphire crystals along different beam paths using angular multiplexing, as exemplified in the diagrams below (Fig. 10.5). To avoid obstruction from the steering optics of the amplified beam, the beam paths for the pump beams are slanted with respect to the horizontal plane (i.e., the plane of the amplified beam passes).

Moreover, each sub-pulse is further split into two equal parts before the injection in the amplifier. The two parts enter the crystals from opposite directions to obtain a more uniform pump density distribution needed to mitigate parasitic lasing effects. Two passes of the pump beam across the crystals are needed to roughly obtain complete pump absorption.

It must be noted that the diagram of Figure 10.5 shows the beam path for the pulse generated by a single pump source. The different stages are pumped by at least two and up to eight individual pump sources. This requires four to sixteen separated pump beam paths with different incidence angles at different offsets in the horizontal and vertical planes. The transverse size (i.e. along the y-axis of Figs. 10.4 and 10.5)

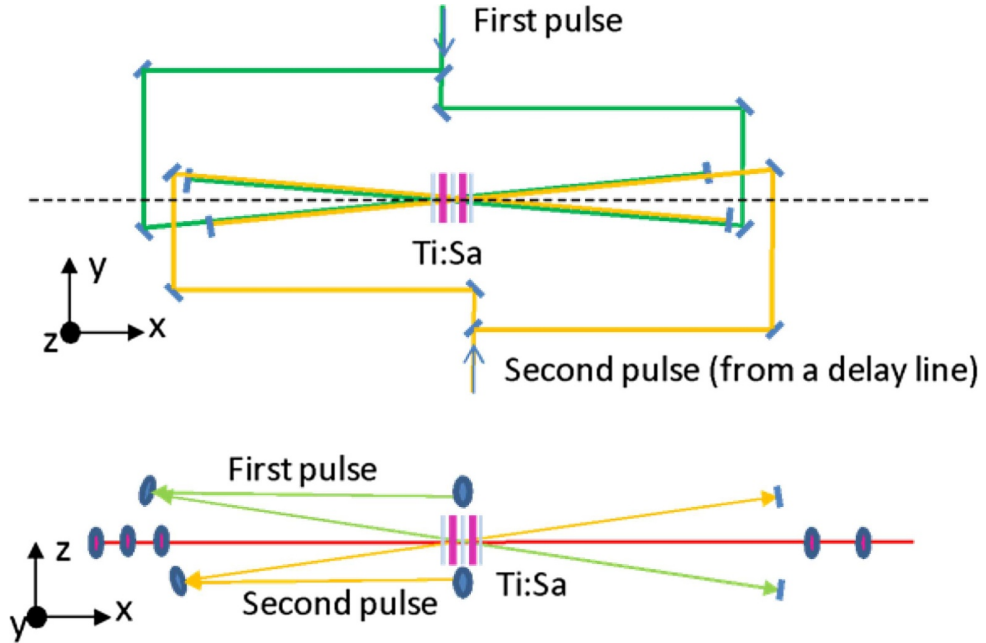


**Fig. 10.5.** Beam paths for the injection in the Ti:Sapphire crystals. The upper frame shows the top view, evidencing the beam paths for the first (green line) and for the second (yellow line) delayed pump sub-pulses. The lower frame shows the side view, evidencing the angular offset in the vertical direction of the pump beam paths. The path and the steering mirrors for the amplified beam are also shown (red line).

of the amplifiers is determined by the pump injection beam paths, and it can be estimated to be about 1 m for AMP1 and AMP2 and 1.5 m for AMP3. Overall, the footprint of the amplification stages is about 4 m<sup>2</sup> for AMP1, 5 m<sup>2</sup> for AMP2, and 12 m<sup>2</sup> for AMP3.

**Reflection Geometry**

The most challenging performance is set by AMP3, which is the amplifying module running at the highest energy and power level and therefore requiring a demanding design of the thermal management. In our design, the unit consists of three equal amplification disks. The main parameters are reported in Table 10.3 for the performance levels P0 and P1. A possible geometrical layout of the disk arrangement is shown in Figure 10.6, which depicts separately the amplified beam path (left) and the pump beam path (right). The seed pulse enters the first disk of the chain, and it is routed to the second and third disks by a suitable steering mirror arrangement. After a first pass along the disk sequence, the pulse travels along a delay line, and then it is sent backward along the chain, meeting the three disks in reverse order. Angular multiplexing is used to separate the forward and the backward beam paths.

The three disks are pumped with the same amount of energy, equally distributed from the same pump pulse by the two beam splitters of Figure 10.6. On each disk, the pump pulse is partially absorbed on the first two passes and then reflected back on the disks for two further passes to achieve almost complete energy absorption. The path of the pump beams is slanted in the vertical (z) with respect to the horizontal (x-y) plane to avoid obstruction by the steering mirrors for the amplified beam. The

**Table 10.3.** Main design and operational parameter for the amplifier AMP3 in the reflection configuration.

Parameter	P0	P1
Crystal diameter (cm)	16	16
Crystal clear aperture (cm)	13.2	13.2
Crystal thickness (mm)	10.7	10.7
Crystal doping (% Wt)	0.045	0.045
Beam diameter FWHM (cm)	12	13
Pump beam energy (J)	109	198
Seed pulse energy (J)	18.8	37.5
Output pulse energy (J)	62	126.7
Pulse bandwidth (FWHM)	27	23

distance between the steering mirrors and the Ti:Sa disks is about 4 m, and the angles of the amplified beam path with respect to the normal to the disks' surface are  $1.2^\circ$  and  $2.4^\circ$ .

The pump beam path includes suitable delay lines so that the arrival of the pump pulse on each disk is synchronised with the arrival of the amplified pulse. The extraction during pumping (EDP) strategy can be implemented by temporal multiplexing; through a proper synchronisation between the injection of the seed pulse and that of the pump pulse, the amplification on the first reflection on each disk can be made to occur when only the desired fraction of the pump energy has been absorbed, leaving the remaining part available for the next pass. To obtain this result on all disks, the transit time of the pump pulse from one disk to the next one must match the transit time of the amplified pulse, hence the need for delay lines on the pump beam path. This is shown in the diagram of Figure 10.7, which represents the time of arrival of the amplified pulses, of the pump pulses, and of the stored energy in each disk.

### Fluid-Cooling Simulations

A simulation of the temperature distribution and of the thermomechanical stresses affecting the amplifier disks was carried out by means of a finite element analysis (FEA) software available in a commercial software package, i.e. LAS-CAD (ver. 3.6.1), developed by LAS-CAD GmbH ([www.las-cad.com](http://www.las-cad.com)). The FEA thermal modelling was used to calculate the spatial temperature distribution in the gain material resulting from the heat input given the pump absorption and from the cooling at the surfaces. The stress mechanical modelling was then used to calculate the stress distribution and the deformation distribution in the crystal, induced by the thermal expansion. This allowed for the calculation of the thermal aberrations computing the optical path difference (OPD) distribution across the crystal aperture, resulting from the variation in the optical path length due to the variation of the refractive index with temperature integrated along the crystal length and the variation in the crystal thickness due to thermal expansion and thermally induced stresses. Thermally induced birefringence [229] was not considered, and the dependence of the thermal and mechanical parameters of the Ti:Sapphire from the temperature was neglected, as well as the slight anisotropy of some parameters in the orientation with respect to the crystalline axes. Detailed results of this approach are described in [225]. A key point to obtain meaningful results from the FEA simulations outlined above is the modelling of the heat exchange between the solid and the fluid.

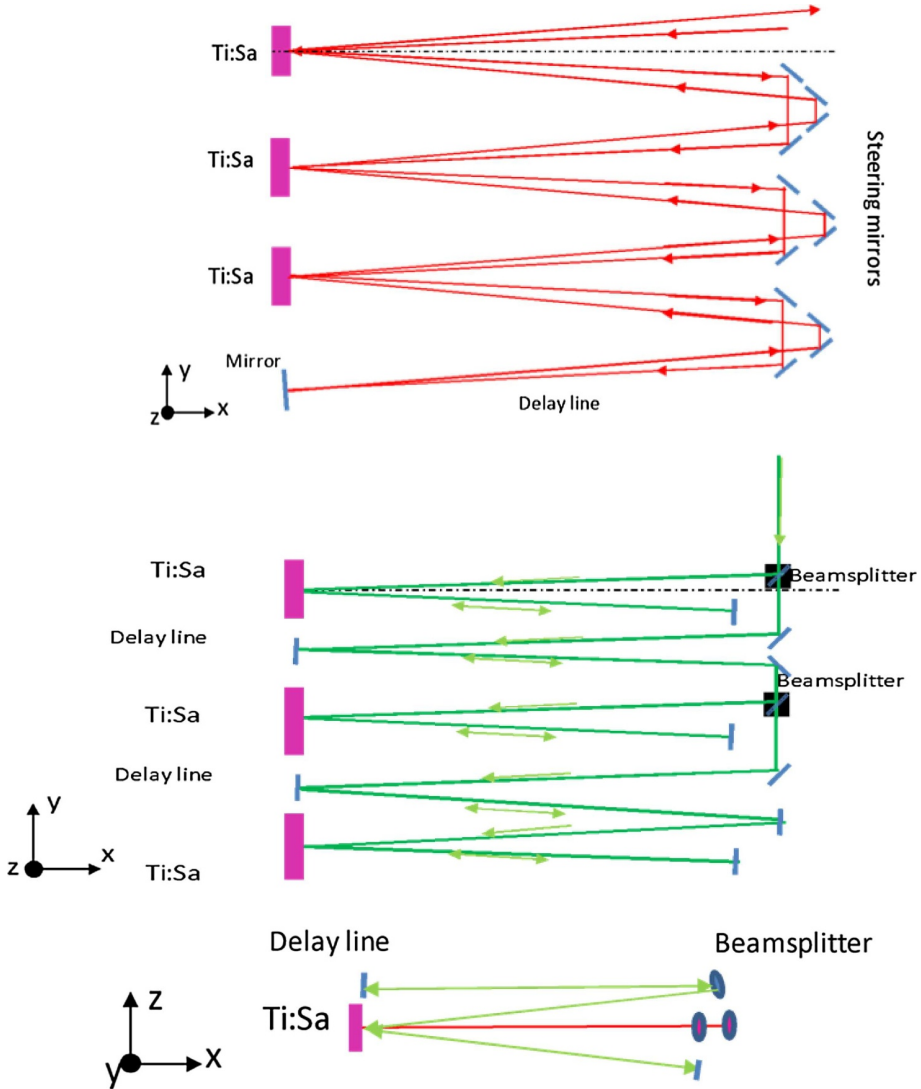


**Fig. 10.6.** Top view of the seed beam path through the sequence of Ti:Sapphire disks (top). Side view of the pump beam through the sequence of Ti:Sapphire disks (middle). Top view of the combined seed and pump layout (bottom) [228].

In these simulations, the heat exchange between the fluid and the solid was modelled by means of a film coefficient  $k=Q/\Delta T$ , where  $\Delta T$  is the local difference of temperature between the solid surface and the fluid and  $Q$  is the power per unit surface transferred from the solid to the fluid. This is an approximated approach yet very effective to reduce the computational effort to acceptable levels, in particular when full 3D problems are modelled. The heat transfer process between the fluid and the solid was studied by means of dedicated fluid-dynamical simulations in 2D geometry, to obtain reliable values for the heat transfer coefficient used in the full 3D simulation. The computational method was a numerical solution of the Navier–Stokes equations for mass and energy transport, using the so-called Low Reynolds  $k-\epsilon$  method capable of a quite accurate simulation of the behaviour of the fluid–solid

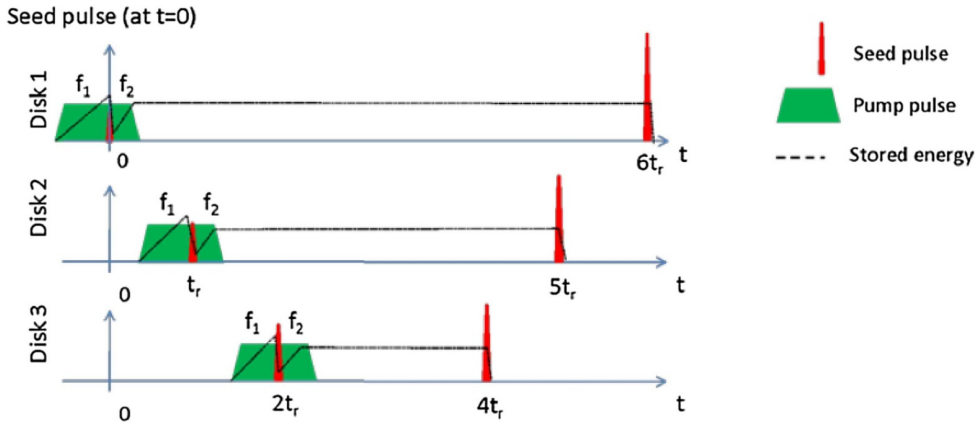


**Fig. 10.7.** Overview of the synchronisation scheme for the implementation of the EDP strategy. The red peaks represent the amplified pulses, the green trapezoids represent the pump pulses, and the dashed line is the stored energy. The time is the pulse transit time from one disk to the other (24 ns for AMP3). The fraction of stored energy  $f_1 / f_2$  available for the amplification on the first/second transit can be adjusted by finely tuning the delay between the arrival of the amplified pulse and the pump pulse on each disk [228].

interface layer with a reasonable computational effort. The fluid-dynamics simulations were carried out using a commercial software package (COMSOL Multiphysics Version 5.3a). An example of these simulations is shown in Figure 10.8 depicting the fluid flow in contact with the back (reflective) surface of the disks. The calculated temperature distribution of the boundary layer of the water flow in contact with the Ti:Sapphire surface is shown in Figure 10.9. It depicts the temperature profile at the heated interface calculated for different flow speeds at a constant heat input of  $25 \text{ W/cm}^2$ . Under fully developed heat-transfer conditions, the temperature increase in the surface is about spatially proportional to the heat input. This allows for the calculation of an effective film coefficient as  $k=Q/\Delta T$  (where  $Q$  is the heat input in  $\text{W/cm}^2$  and  $\Delta T$  is the temperature increase with respect to unperturbed fluid), which expresses the cooling capability of the fluid flow. The effective film coefficient was found to be independent from the heat input and proportional to the flow speed (proportionality constant of about  $0.04 \text{ J cm}^{-3}$ ). The simulations show that with the channel configuration presented in Figure 10.8 (i.e. parallel walls), only a very thin layer of fluid near the surface is actually involved in the heat-exchange process. To improve the cooling performance, other channel configurations were studied with ridges meant to enhance the fluid turbulence and increase the heat exchange. An example is shown in Figure 10.10. The channel profile of Figure 10.8 was modified by introducing triangular protrusions on the upper wall (height 2 mm, base 4 mm, spaced by 10 mm). The fluid speed distribution shows strong turbulence caused by the unevenness of the upper channel wall, which stirs the water, locally increases the fluid velocity up to about two times the input velocity, and improves the heat transfer from the lower surface. As a result, the temperature increase in the heated surface is significantly lower (more than a factor of 2) than in the case of the smooth channel for the same heat-input conditions. This results in a roughly threefold increase in the film coefficient  $k$ . Such a configuration can be applied for the cooling of the disks in the reflection configuration as the back face of the cooling channel is not crossed by the light beams, so it can be shaped to optimise heat-exchange processes.

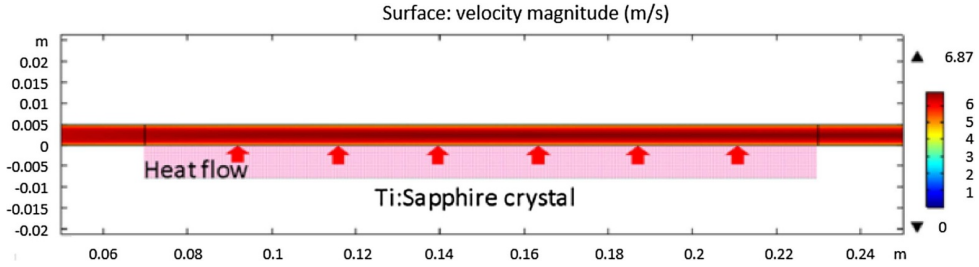


**Fig. 10.8.** Fluid velocity distribution in the cooling channel under the simulation conditions specified in the text. The position of the Ti:Sapphire crystal is shown for clarity, but in the thermal simulation, it is considered only as a thermal boundary condition for the fluid flow (constant surface heat flux).

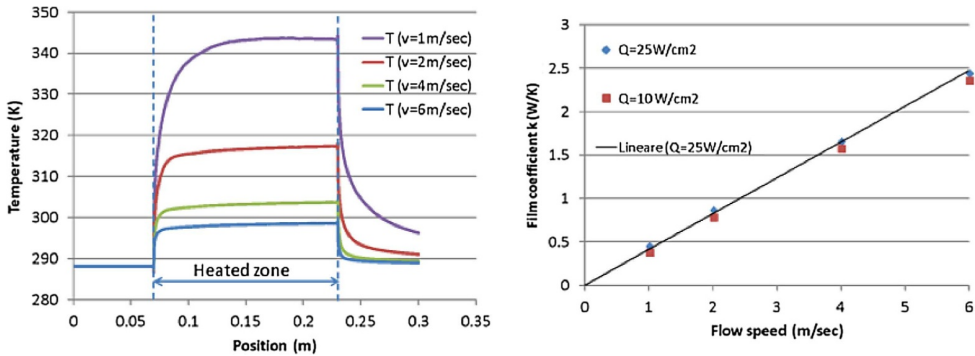


**Fig. 10.9.** Left: Temperature profile along the Ti:Sapphire crystal surface for different flow speeds, at a heat input of  $25 \text{ W/cm}^2$ , with an input temperature of  $288.15 \text{ K}$  ( $15^\circ\text{C}$ ). Right: Effective film coefficient calculated for various flow speeds and heat input values.

### 10.2.5 Pump Lasers

Pump laser requirements are a critical aspect of our design. Our approach was to minimise pump laser needs while optimising extraction efficiency and relying on efficient transport and compressor throughput and optimised second harmonic conversion efficiency of pump lasers. The compressor throughput was assumed to be 80%, achievable with a single grating reflectivity better than 95%. Such a value is not far from current commercial grating technology [230] providing dielectric or gold-coated gratings with demonstrated reflectivity between 90% and 94% at 800 nm. We also assumed a conversion efficiency from  $1 \mu\text{m}$  pump energy to  $0.5 \mu\text{m}$  of 70%, a conservative value if compared to the 80% conversion efficiency demonstrated recently [231]. Based on these assumptions, we obtain average IR pump power requirements ranging from 0.5 kW for the first amplifier module AMP1 at 20 Hz to approximately 30 kW for the last amplifier module AMP3 at 100 Hz. The corresponding total pulse energies at  $0.5 \mu\text{m}$  range from 20 J to 200 J, resulting in an IR pump pulse energy ranging from 27 J to 280 J.

The choice of suitable pump lasers capable of delivering these performances was based on an extensive evaluation of currently available technologies. A detailed analysis of potentially suitable pumping technologies was included in the previous technology survey [221]. Moreover, a similar analysis was carried out in the framework of the k-BELLA project [232]. These investigations consistently suggest that diode-pumped Yb-based systems are emerging as candidates to sustain the envisaged average power.

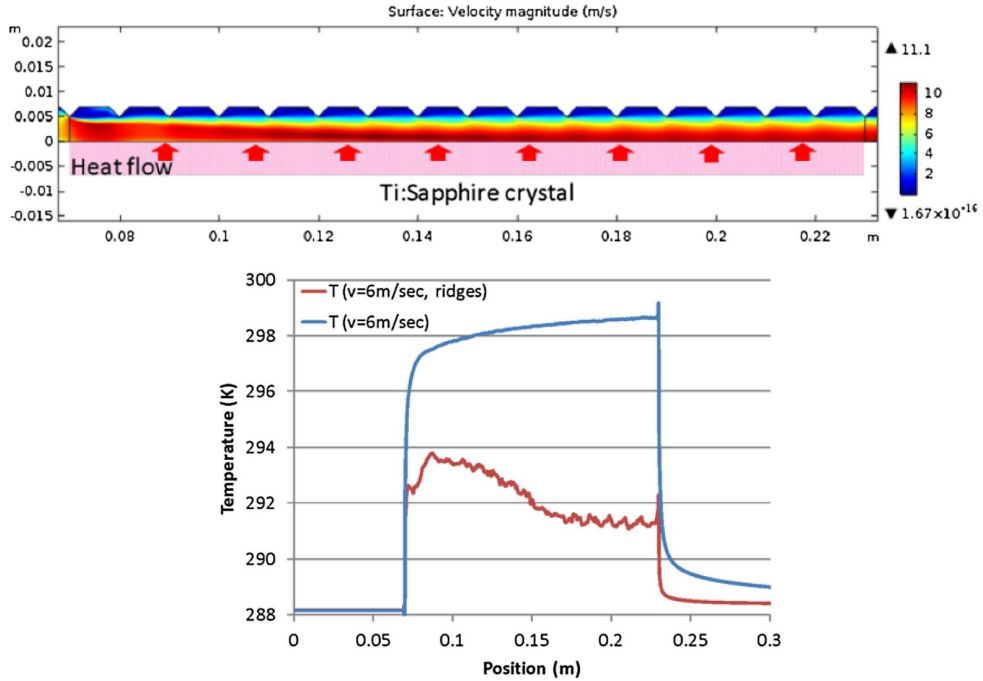


**Fig. 10.10.** Top: Fluid velocity distribution in the cooling channel, with triangular ridges on the upper wall. The thickness of the channel between the ridges is 7 mm, with an input flow speed of  $6 \text{ m s}^{-1}$ . The position of the Ti:Sapphire crystal is shown for clarity, but it is considered in the thermal simulation only as a thermal boundary condition for the fluid flow (constant surface heat flux). Bottom: Temperature profile along the channel position at the interface between the fluid and the Ti:Sapphire for the case of the smooth channel (blue line) and for the case of the ridged channel (red line). The other conditions of the simulation are the same [228].

At the same time, Nd-based systems also proved to be capable of rep-rated operation at average power levels relevant for our aims. At this stage, we can identify three different pumping systems and technologies for the three EuPRAXIA lasers, all based on diode pumping or adaptable to diode pumping and all having been demonstrated at a sufficient average power level to give confidence on their readiness. A detailed description of pump laser technology is given in Section 32.3.

### 10.2.6 Transport to Plasma

This section is dedicated to the beam transport from the last amplifier output towards the plasma cell. The equipment that will be installed for each laser includes the following:

- a deformable mirror (DFM) to ensure a good wavefront phase at the input of the compressors and to be sure to be able to reach the required pulse duration;
- a telescope with a pinhole to act as a spatial filter for high frequencies coming from the Ti:Sa crystals [this will expand the beam to the required beam diameter at the compressors to respect the laser induced damage threshold (LIDT) of the gratings and relay the image plane of the deformable mirror into the compressor];
- a change polarisation system, if needed, depending on the technology of the gratings;

- a compressor to reach the required pulse duration;
- a series of mirrors to transport the beam from the output of the compressor to the final focussing optic; and
- a focussing optic, the focal length of which will be calculated to meet the  $a_0$  required on target, taking into account the beam profile, the energy, and the pulse duration.

From each amplifier section, we will arrive with an average power for the P1 level of the following:

- LASER1: 1.2 kW (12 J @ 100 Hz), needed 20 fs after compression (62 nm bandwidth), spectral acceptance required: 140 nm
- LASER2: 4 kW (40 J @ 100 Hz), needed 20 fs after compression (62 nm bandwidth), spectral acceptance required: 140 nm
- LASER3: 13 kW (130 J @ 100 Hz), needed 60 fs after compression (23 nm bandwidth), spectral acceptance required: 60 nm

For the deformable mirror (DFM), we can use a DFM based on the mechanical actuator principle. Mechanical actuators use macroscopic part displacements, which create a change of the force applied on the back of the DFM. This change of the applied force creates a nanometric displacement of the front surface of the mirror. In this way, a macroscopic displacement is converted into a microscopic change of the mirror's surface shape. However, this technology is today limited in repetition rate, and since we will have probably some thermal effects in the membrane of the DFM, it will be needed to cool down. Today there is very limited work carried out on cooling down a membrane linked to actuators. The beam diameter on these DFMs will be, respectively, 4.5 cm for LASER1, 8 cm for LASER2, and 12 cm for LASER3.

The beam diameter in the compressor for each laser is determined by the laser induced damage threshold (LIDT) of the gratings. This LIDT depends on the gratings technology, but it is around  $250 \text{ mJ cm}^{-2}$ . As we know that we will have modulations in the beam profile and temporal spatial modulations, we will consider a mean fluence of  $100 \text{ mJ cm}^{-2}$ . Once we have determined a range of possible beam diameters, we have to check that the intensity on the gratings remains below  $1 \times 10^{14} \text{ W cm}^{-2}$ . Then we have to check that the size of the gratings is compatible with existing technology, since we do not want to tail the gratings, as is done on PETAL, because of the difficulty in operating for pulse durations under 100 fs. Following this process, we have determined that the beam size (FWHM) in the compressor will be 12 cm for LASER1, 19.5 cm for LASER2, and 34 cm for LASER3.

With this size, it is easy to design the spatial filter. The spatial filters would be set up with a  $45^\circ$  off-axis parabola in a Z-configuration for LASER1 and LASER2 since the pulse duration is below 30 fs and chromatism will be of importance. For LASER3, refractive optics (doublet) can be used.

For the compressor configuration, we have to take into account the compression ratio, and the size of the vacuum vessel that will keep the gratings under  $1 \times 10^{-5}$  to  $1 \times 10^{-6}$  mbar. Doing so, we have chosen for the three lasers a two-gratings compressor folded by a vertical retro-reflector with gold gratings with 14801/mm. This design leads to a very compact compressor with a size of around  $1 \times 1 \times 1 \text{ m}^3$  for LASER1,  $1.5 \times 1.5 \times 2 \text{ m}^3$  for LASER2, and  $1.5 \times 1.5 \times 2.5 \text{ m}^3$  for LASER3. However, for LASER2 and LASER3, a design with four gratings will have to be considered if thermal studies show that the heating in the gratings is too dominant, even if we envisage to cool them down. Considering the material for the gratings, we stay with gold gratings for now as a fallback solution. Indeed, MMLD and MD gratings could be a good solution, but we do not have enough experience on their LIDT. MLD could also be an interesting option if a large-enough bandwidth can be demonstrated, especially for LASER3, where the pulse duration is 60 fs and, for some acceleration

schemes, may rise up to 100 fs. Using MLD gratings will avoid having to turn the polarisation between the amplifiers and the compressor. It should also be noted that for LASER1, we could increase the size of the beam to reduce the average intensity under  $10 \text{ W/cm}^2$  and avoid the necessity of cooling down the gratings.

Concerning the beam transport and the focussing system to reach the plasma target, the main requirements are the transmission, pointing stability, and intensity at the target. The transmission has to be 83% for LASER1, 88% for LASER2, and 89% for LASER3. For the transmission, we have to take into account the energy directly in the spot on target. Some recent results require a reassessment of the need of a second deformable mirror on this transport line (publication in preparation). Indeed, the results showed that the impact of wavefront correction with a deformable mirror before the compressor to get a focal spot in the target chamber with a Strehl ratio better than 0.85 is less than 1 fs on the pulse duration after compression. It is to be noticed that in existing facilities currently operated and working on plasma acceleration, there is typically only one deformable mirror placed before compression (BELLA, APOLLON). However, not having a deformable mirror after the compression would make it impossible to shape the focal spot as needed for specific applications. Another point is that a Strehl ratio of 0.85, an already very good value, is not sufficient to reach the required 83–89% transmission. Further studies will thus be necessary on this point to decide whether or not a second deformable mirror is necessary. For the following sections, we will consider a Strehl ratio of 0.9, which has been demonstrated at several existing facilities. In this case, the transmission of the other mirrors and the focussing system has to be 92% for LASER1, 97.8% for LASER2, and 98.9% for LASER3.

Given the laser energy and pulse duration, the focal spot size has to be  $15 \mu\text{m}$  for LASER1,  $33 \mu\text{m}$  for LASER2, and  $130 \mu\text{m}$  for LASER3. To reach such spot sizes, the focussing system has to have an equivalent focal length of 3.5 m for LASER1, 9 m for LASER2, and 75 m for LASER3. For LASER1 and LASER2, our preferred design is to use an off-axis parabola. The axis could go from  $10^\circ$  to  $45^\circ$ , keeping in mind that the larger the angle is, the more expensive the parabola becomes. The off-axis parabola will be defined once the layout of the laser and the target chamber (with all the laser and electrons diagnostics) is established. In this way, it will be possible, with three mirrors and the focussing parabola, to reach the required transmission with a reflectivity of 99.4%. For LASER2, because the parabola is too expensive, we may envisage a telescope with a flat pinhole mirror and an on-axis parabola (or an on-axis spherical mirror for reduced cost). Another reason to envisage another design could be the footprint of the system which will be higher with an off-axis parabola. However, using a flat mirror with a pinhole would decrease the transmission of the system by about 6%, meaning that the desired 97.8% transmission cannot be reached and that less than 30 J pulse energy reaches the target. For LASER3, if we want to keep the design compact and cheap, we may have to change the optical system to focus the beam, except if the beam path is along the beamlines. If not, it is suggested to use a zoom design with spherical concentric mirrors. This design has the advantage of being very compact, but a lot of energy is lost because of the secondary mirror (around 15%). Thus, for this design, we will need to increase the energy at the output of the amplifier, which is not desirable since it will increase the average power. Another way could be to envisage a different design for the gas jet, e.g. to not use a capillary and decrease the spot size to reduce the focal length. More detailed studies for optimising and testing this aspect are planned during the technical design phase.

Finally, regarding stabilisation, an active system will not be easy to implement since it will require either to tip-tilt a big and heavy mirror at a high repetition rate or to tip-tilt a small mirror, the image of which is placed through the optical system of all laser beamlines on the target. Alternatively, we envisage passive stabilisation as

an option. Besides the current techniques to minimise instabilities from mechanical parts, a new technology could allow the gain of one order of magnitude on the stability by dumping the mechanical deformation and transforming it into thermal energy. This technique has been demonstrated by CEA and the company ISP but so far only for operation in air. The development of this technique to work under vacuum is also planned. Additionally, LULI and UNIMI have developed a new apparatus to measure mechanical instabilities over a range of 0.1 Hz to MHz to detect instabilities of the order of 100 nrad [233]. This diagnostic will need to be implemented in the transport section and the nearby focal spot region.

### 10.2.7 Development Paths

With the high average power required by systems like the EuPRAXIA laser, both the optical-to-optical and the overall wall-plug efficiency of the laser system become increasingly important; the laser cooling capacity and complexity of the laser amplifier design scales with the amount of energy directly converted into heat in the laser gain medium. The output energy of a pulsed diode-pumped laser system can be written as follows:

$$E_{out} - E_{in} = E_{elec} \eta_{DC} \eta_P \eta_{EO} \eta_{PT} \eta_{abs} \eta_{QE} \eta_{QD} \eta_{decay} \eta_{ext} \eta_{MO} \eta_{trans}, \quad (10.1)$$

where  $E_{elec}$  is the electrical input energy,  $\eta_{DC}$  is the overall efficiency of the laser diode power supply,  $\eta_P$  is the efficiency of the pulse forming network for pulsed laser diodes (if applicable),  $\eta_{EO}$  is the electrical-to-optical efficiency of the laser diode arrays,  $\eta_{PT}$  is the pump light transfer efficiency to the amplifier gain medium,  $\eta_{abs}$  is the gain medium absorption efficiency,  $\eta_{QE}$  is the quantum efficiency (QE), the number of upper laser-level ions produced for each pump-laser photon absorbed by the active ions,  $\eta_{QD}$  is the laser gain medium quantum defect efficiency,  $\eta_{decay}$  is the decay efficiency, defined as the fraction of the excited upper-state population that remains when the extraction pulse arrives,  $\eta_{ext}$  is the fraction of the excited-state population that is extracted on each pulse,  $\eta_{MO}$  is the pump-to-extraction mode-coupling efficiency, and  $\eta_{trans}$  is the passive optical system transmission efficiency. For architectures that rely on laser-pumped lasers (e.g., Nd:YAG-pumped Ti:Sa systems), efficiencies for each laser frequency converter and optical transfer must be included and eventually become a limiting factor because of prohibitive electricity requirements. For this reason, our baseline Ti:Sa design is accurately designed, adopting the most effective strategies to minimise power needs to acceptable levels while providing a viable solution compatible with EuPRAXIA's construction timeframe.

On the other hand, in view of an evolutionary infrastructure design, we also consider the possibility of extending laser performances, e.g. increasing the repetition rate to the kHz level, further improving efficiency and enabling a long-term use of the facility. In this perspective, one way to reduce electricity power needs is to replace the two-step DPSSL-laser-pumped laser architecture with a single-step DPSSL-pumped architecture using lasing materials that can be pumped directly with diodes. This direct CPA option would ideally provide high wall-plug efficiency, lower complexity, dramatically lower thermal loading, and improved mean time to failure.

Indeed, in a comparison of system efficiency for a CW-diode-pumped direct CPA laser system vs. a diode-pumped indirect CPA laser system, the energy losses per joule of output energy are shown in Figure 10.11, where estimated losses have been grouped into logical categories to emphasise waste heat pathways. Finally, to calculate the overall wall-plug efficiency of the laser, the power consumption of the laser support systems (e.g. cooling and the laser control system) must be factored in. It is important to note that the cooling system size and cost, power consumption, and

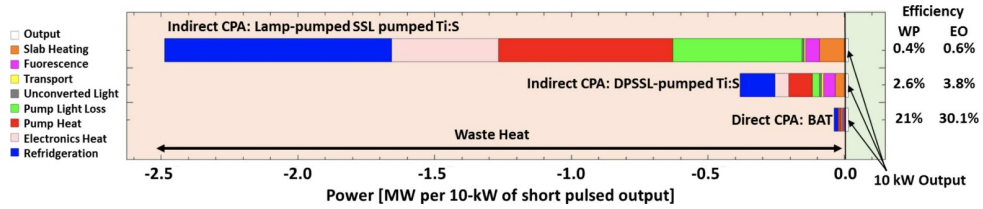


**Fig. 10.11.** Wall-plug efficiency comparison between direct CPA (here: Multi-Pulse-Extraction, Big Aperture Thulium (BAT) laser architecture utilising multi-pulse extraction), a pulsed, diode-pumped, indirect CPA system (here based on Nd:glass-pumped Ti:Sa) and a flashlamp-pumped Ti:Sa (image credits: C. Siders, European Advanced Accelerator Concepts Workshop 2017).

overall contribution to the system wall-plug efficiency scale with the waste heat to output energy ratio.

This possibility was, in fact, examined within Work Package 4 of the EuPRAXIA project and is discussed in further detail in Section 7.2. It is, in particular, emphasised that besides Ti:Sa technology, an alternative/complementary configuration involves direct CPA with mixed glass or other materials, directly pumped with semiconductor lasers. Several issues, mainly concerning the available gain bandwidth, prevented these architectures from developing at a level to compete with Ti:Sa technology. However, since then, significant innovation has been shown in this area of direct CPA, successfully addressing key uncertainties and significantly mitigating the risk of this approach for EuPRAXIA. In addition to the technology platform discussed in the Section 7.2, we outline here an additional possible solution based on Tm:YLF as a paradigmatic approach to the EuPRAXIA development path towards a higher repetition-rate laser driver solution.

A careful analysis of factors introduced above, determining the final output laser energy, identifies Tm:YLF as a laser amplifier medium with specifications compatible with a long-term solution for an efficient laser wakefield driver. As shown in Figure 10.12, Thulium (Tm)-doped gain media offer a significant lifetime advantage over the well-established Yb-doped materials traditionally used for diode-pumped fiber and bulk systems [234].

Interestingly, Tm multi-pulse extraction becomes efficient at repetition rates  $>1$  kHz, making it a well-matched evolutionary solution beyond the 100 Hz limit of Ti:Sa-based architectures.

A key requirement for Tm-based concepts to be relevant for sub-100-fs applications is clearly the gain bandwidth of Tm in the chosen laser host material – that must be  $>100$  nm – which is satisfied by most of the host materials considered. Among the relevant host materials, YLF offers several attractive properties, including a negative  $dn/dT$ , low linear and non-linear refractive indices, and natural birefringence. These properties support laser architectures that exhibit high-fidelity laser pulses with very low non-linear phase accumulation, low wavefront aberration, and high polarisation purity at very high average power (up to hundreds of kW).

Tm is characterised by a long upper-state lifetime (15 ms), and above all, Tm can easily be pumped with commercially available, technologically mature, high-brightness, continuous-wave laser diodes that operate at 800 nm. CW pumping of the gain material eliminates laser diode pulse-forming networks (pulsers) and associated electrical losses. Furthermore, the overall brightness requirement is reduced given the longer time available for storing the pump energy in the gain media. Because of the well-known cross-relaxation process, pumping in the  $\sim 800$  nm band yields approximately two excited state ions per pump photon, resulting in an effective quantum

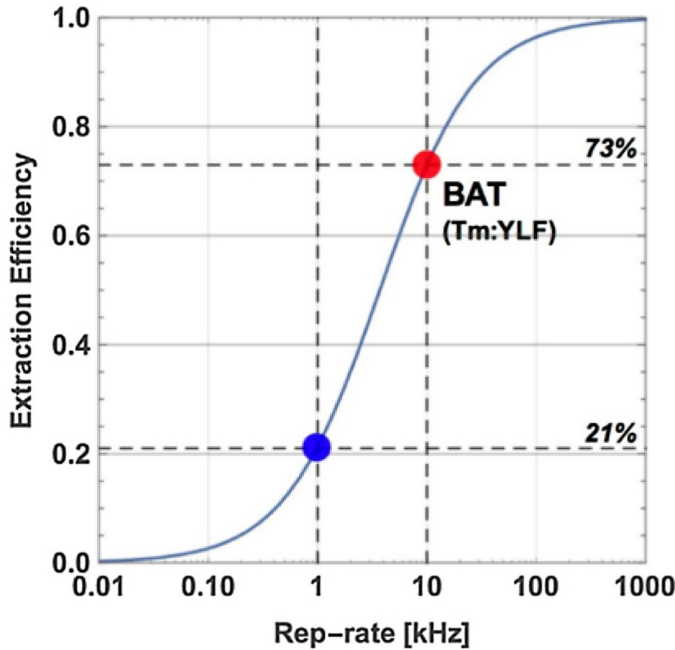


**Fig. 10.12.** Extraction efficiency (stimulated emission rate divided by the sum of stimulated emission rate and spontaneous decay rate). In multi-pulse extraction, higher repetition rates (while maintaining the extraction fluence) are beneficial to the overall wall-plug efficiency [234].

defect of  $\sim 84\%$  (depending on doping), so only 16% of the pump energy is converted to heat [235,236]. Therefore, the quantum defect for Tm lasers is comparable to the quantum defect for Nd lasers. Furthermore, Tm:YLF is commercially available in boule sizes consistent with 300 kW average-power operation of 30 J, compressed at 10 kHz, or up to 160 J at lower repetition rates.

A novel aspect of the Tm dopant in YLF is the lasing wavelength of  $\sim 1.9 \mu\text{m}$ . Considering that most of the experimental work carried out so far in the laser-plasma acceleration of electrons was driven by the availability of intense radiation from Ti:Sa systems at 800 nm, the possibility of using 1.9  $\mu\text{m}$  calls for an exploration of the wavelength-scaling properties of candidate acceleration and injection schemes. Preliminary considerations emerged from the EuPRAXIA community, in particular from the theory and modelling work package, and indicate that while the change of wavelength may have a major impact on current models, no obvious drawbacks exist, and some benefits related to the longer wavelength may arise.

### 10.2.8 Risk-Mitigating Solutions

The current laser conceptual design builds mostly on high technical readiness level (TRL) components. A full technical design will, however, need some targeted work to address open issues, currently in the development stage at leading institutions of the EuPRAXIA collaboration. This will ensure that progress in the respective areas is immediately reflected in the design work.

## Prototyping of Ti:Sa Amplifiers

As discussed above, the EuPRAXIA preliminary laser driver design is foreseen to consist of a Ti:Sa main amplifier pumped by frequency-doubled DPSSL-pumped lasers. A preliminary development of all components is needed prior to the definition of the architecture of the Ti:Sa amplifier head. R&D is crucial for the definition of the design of the main amplifier(s), the testing of key components and the prototype demonstration using established expertise at existing facilities and in collaboration with industry (e.g. Amplitude and Thales). A definition of the preliminary architecture of a Ti:Sa amplifier head based on scaled but similar systems will be developed using numerical simulations to address thermal management and reach a stable configuration for the baseline EuPRAXIA parameters.

A risk-mitigating solution here includes building a prototype of this system to validate numerical modelling. This will be done in close collaboration with laser developer groups involved in EuPRAXIA Work Package 4, using existing equipment with the partial integration of EuPRAXIA-specific components. This activity will provide details of the architecture of the baseline laser for EuPRAXIA to be included in the final laser design. At the same time, it will help to make a robust assessment of the possibility of reaching the higher repetition rate (100 Hz) expected for the goal of the laser configuration.

## Addressing 100 Hz Pump Laser Developments

Demonstrated DPSSL laser technology is already capable of providing kW-scale systems at 10 Hz. With moderate additional investment in R&D, the pump light required for LASER3 at P0 can be delivered by a reduced number of units, such as the DiPOLE 100 (from the Central Laser Facility, UK) or the P60 (from Amplitude Technologies, France) systems, possibly scaled to the 20 Hz repetition rate required by the P0 specification level. Delivering pump pulses at 100 Hz for the >100 J energy level design should be feasible, but is likely to be very costly given the large number of laser systems required or would require the timely introduction and qualification of alternative higher performance diode laser technology. In view of these considerations, both new diode laser pump approaches (such as alternative cooling and diode laser technology) and also new amplifier approaches (such as liquid cooling and room-temperature operation) should be considered.

Alternative amplifier concepts, such as BAT, will also require the timely introduction of new diode laser pumps at a potential cost in overall performance and commercial availability. These new approaches will require substantial R&D investment and have the potential to significantly reduce the number of lasers and therefore the cost required for a given amount of average power. This is a high-priority task that will require the EuPRAXIA laser community to promote and support necessary developments at participating laboratories and in cooperation with industry.

## Thermal Management of Compressor Gratings

As discussed above, the laser drivers for the EuPRAXIA accelerator will need to operate at a high repetition rate between 20 Hz and 100 Hz with the goal of industrial beam quality in mind. Higher laser repetition rates will allow for an increase in stability in operation parameters and enable feedback loops for active monitoring and control not only for the laser system itself but also for enabling feedback loops and active control over parameters in the electron-generating plasma stage. In today's

laser-plasma acceleration experiments, the repetition rate is practically limited to a fraction of 1 Hz. One crucial limiting factor is the performance of the laser compressor gratings, which includes the yet not fully understood limitations due to laser-induced single-shot catastrophic damage threshold, limitations in average power, and thermal management of the gratings required for long-term operation. These are all issues that need to be fully understood and controlled to enable the driver laser for EuPRAXIA. A detailed design study for the modelling of the thermal properties of the EuPRAXIA laser compressor under high-average-power operation will help us to define the most crucial technical bottlenecks and assist us in the preparation of an experimental campaign which will reveal the parameters for safe operation at high repetition rates and high average powers.

A preliminary indication of the steps to be followed to mitigate the risk includes the modelling of the thermal effects and their impact on compression using established modelling capabilities at existing partner institutes, tests at existing facilities to compare with models, and the design of a new setup to manage the thermal load, including options for a suitable new gratings design (without gold and metal). Following this path, the goal of reliably determining the configuration for the operation of the EuPRAXIA laser compressor will be safely achieved.

### Stability and Active Control

As specified in the requirement tables, EuPRAXIA will require an outstanding stability of the laser driver beam spatial properties, including in terms of beam pointing, intensity distribution in the focal spot, longitudinal focal spot position, etc. Current standard laboratory LPA systems exhibit moderate to poor stability specifications, and depending on the specific system architecture, special measures are required to enable any sort of repetitive operation. Knowledge concerning current state-of-the-art laser parameter stability is needed to develop novel control and correction schemes to reach EuPRAXIA requirements, including dedicated development activities for the design, implementation, and testing of diagnostic and control systems as well as active stabilisation systems as required. These activities are crucial to the definition of the interface between the laser system and the plasma stage, where laser coupling with the target plasma is being optimised.

### Driver Pulse Temporal Shaping and Synchronisation

The control of temporal issues of the laser pulse – e.g. multi-pulse (pulse train) development, laser pulse contrast, and chirped pulse control for the delivery of 100 fs pulses – are aspects relevant for laser-driven plasma acceleration. Multi-pulse operation is explored as a way to efficiently drive plasma waves, relying on the use of a train of moderate-intensity ultra-short pulses. This is foreseen as an alternative to current schemes based on a single high-intensity laser pulse and would allow advanced schemes based on ionisation injection to be investigated, potentially providing injection stages delivering bunches with very low energy spread and ultra-low emittance. The aim here is to investigate the generation of a train of ultra-short pulses, with 100 fs delays to one another, starting from a single ultra-short pulse and relying on easy-to-implement optical schemes, e.g. wave-front division. The design and prototyping of time-manipulation techniques, including testing at existing facilities at EuPRAXIA-participating institutions, are being planned. Available and novel schemes for multi-pulse operation will be designed and tested, including interaction with plasmas to demonstrate effectiveness. Pulse stretching will be explored

for the delivery on target of longer pulses, and plasma interaction models will be implemented in LWFA experiments under scaled conditions to test numerical models. Finally, temporal contrast at different time-scales will be tested at existing labs, and a comprehensive set of values will be given for the stability of such parameters. Where required, the implementation of established or newly developed temporal contrast control techniques will be taken into account to meet additional EuPRAXIA requirements, especially for what concerns the use of high-contrast lasers for solid target interactions and the control of pre-ionisation in gases. These activities are crucial to the definition of the interface between the laser system and the plasma stage, where laser coupling with the target plasma is being optimised.

### 10.3 Conclusion

The first generation of high-quality laser-plasma accelerator designs is progressing rapidly towards a user infrastructure and needs a new generation of ultra-short pulse laser drivers with high average power and high stability. A range of candidate technology paths are being considered and developed according to the timescales available for implementation and the required driver performance. A step-like evolution of a widely explored Ti:Sa based system is proposed as a viable short-term solution for kW-scale drivers with a repetition rate of up to 100 Hz. The proposed system will enable a robust operation of the EuPRAXIA facility, establishing plasma acceleration technologies at an industrial level. As for higher repetition-rate (kHz and beyond), higher average-power (10 kW and beyond) solutions, these will build on highly efficient direct DPSS CPA laser technologies.

## 11 Laser Control-Command System

### 11.1 Introduction

This chapter gives an overview of the control-command system for the laser system, keeping in mind that it will have to be interfaced with the control-command of the EuPRAXIA facility. The design will evolve in the future with the definition of the control-command system of the EuPRAXIA facility and with the definition of the laser system itself. More general aspects on machine operation, data management, and safety are described in Sections 5.3, 3.5, and 27.1, respectively. Aspects of the control-command system specific to the particle beam are not described here since they will be very similar to existing accelerator facilities, such as SOLEIL and ESRF.

This document gives a list of the requirements that this system will have to fulfill and defines the interface with the control-command system of the EuPRAXIA facility. This document further provides an account of the laser diagnostics and a general outline of the proposed system structure. Such an outline is based upon available information from existing laboratories and/or facilities (or those under construction) where laser systems with an architecture conceptually analogous to that envisioned for EuPRAXIA are employed. In particular, a broad overview of the kind of devices needed to be controlled for most of the EuPRAXIA laser diagnostics will be given, as well as a conceptual description of the timing and synchronisation architecture.

It is to be noted that the laser control-command system (LCC) will have to be interfaced with the general EuPRAXIA facility control-command system (FCC). In this context, since the control-command system of the facility has not been defined yet, we emphasise the following points:

- The implementation details – such as, for instance, the suggested toolkit (TANGO, EPICS, etc.) of the EuPRAXIA laser control-command system – may be better defined at a later stage at a higher (facility) level. For this reason, it is too early to provide details on the software and protocols implementation and related issues such as the following:
  - the way to develop, upgrade, and integrate different software or data-analysis methods;
  - the way to exchange information; and
  - the way to access databases, configuration data, and results data.
- The mission profile of the facility has to be better deepened yet. In particular, the user profiles, types of experiments, and operation modes have to be better identified to identify the possible links between the laser- and beam-related parts of the control-command infrastructure. In this context, different user categories may possibly be identified, having access (through the FCC) to different laser operation modes and / or parameter-tuning modes (laser energy, laser shot sequences, etc.). The envisioned LCC must take into account different levels of external (i.e., by the FCC) actions.

## 11.2 Overview

Figure 11.1 gives an overview of the hardware architecture of the EuPRAXIA laser control system. Vertically, the system can be divided into several layers:

PSS: Personal Safety System

SSS: Synchronisation and Sequencing System (also including pump lasers)

ALS: Alignment Systems

DLS: Laser Diagnostics Systems

VFS: Vacuum and Fluids Systems

TAS: Target Areas Systems (one per experiment hall)

For some of the subsystems, a stand-alone operation mode may be needed; to this purpose, local GUI stations are required. In all operation modes, the PSS and SSS are needed to generate laser beams. The VFS can work independently, only providing interlock signals to the LCC. The blue line in Figure 11.1 gives the perimeter of the control-command system.

Starting from the top, we first find Level 2 with servers and operator workstations. The operator console and servers are localised in control rooms. Local operator stations are also necessary, to be used during initial setup, new components integration phases, laser warming up, and maintenance periods. Through the GUI, operator workstations display data exchanged with front-end computers at Level 1. At Level 1, we find the front-end processors (FEPs) running software modules, such as device drivers and local interfaces. FEPs control process devices, sensors, and actuators through specific electronic drivers and can be operated locally by laser operators. Finally, at Level 0, we find the facility with all devices under control.

Taking into account the number of systems to control and the size of the facility, the control system must be a scalable and distributed control system.

Programming technologies have to use object-oriented programming, and the system must support common object-oriented programming languages (Python and C/C++). In addition, bindings should be available for commonly used commercial software, such as Labview, Matlab, and supervisory software, if necessary. Protocols used for communications must enable separate pieces of software written in different languages and running on different computers to work with one another like a single application or set of services.

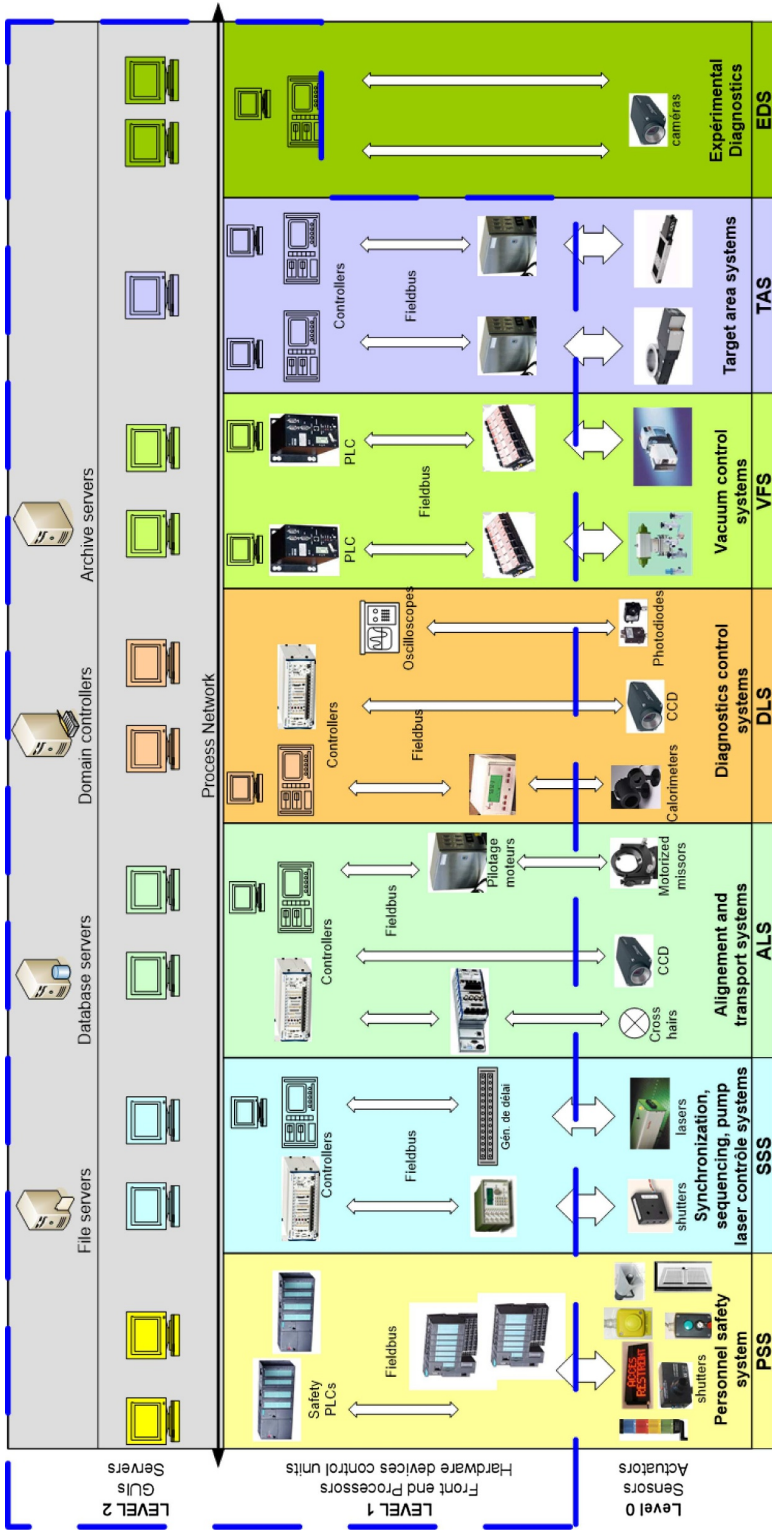


Fig. 11.1. Possible hardware architecture for the control-command system.

This control system must have a centralised database containing properties of the devices to control and tools to administer the system through the network.

### 11.3 Needs and Requirements

#### 11.3.1 Operational Requirements

##### Operational Modes

Different laser(s) operation modes will be defined according to the different phases of laser operation: warming up, different phases of beam alignment (from the front end to the target), and end user needs (for instance, in terms of pulse energy, pulse train generation, etc.). Operation modes should differ with respect to one another, roughly speaking, for the status of actuators (for instance, those activating beam shutters), electronic trigger timings and triggering, as well as optical attenuators (for instance, those protecting CCDs).

Since the mission profile of the facility is not defined yet, the definition of these operation modes has to be postponed to a later stage.

##### Laser Alignment/Setup and Tuning

Laser beam characteristics are defined by parameters which have to be adjusted from control systems. For particular parameters, it can be expected that they can only be adjusted using local computers not connected to the central system. In this case, the drawbacks are (1) the inability to save and have an overview of the global setup to control the setup integrity, and (2) the inability to verify the conformity between the shot model and user needs.

So the facility needs to have within the control system a centralised set of setup data allowing control over the setup before launching a sequence.

##### Sequencing and Machine Protection System

The repetition rate of the EuPRAXIA laser systems will be between 20 Hz and 100 Hz as a baseline. In some circumstances, pulse sequences may be needed on demand, i.e. depending on final user needs. This demand is described by a sequence which can have all the topologies coming from continuous shot to complex bursts. Sequences should be configurable.

Setting up a shot sequence includes the following:

- parameters of sequence timing: sequencer setup;
- energy variations: action on pump lasers (delay);
- pulse duration variations: action on motors on stretcher/compressors;
- delay variations between beams: action on motors of delay lines;
- number of beams: action on beam shutters;
- targets: action on target holder motors.

##### Supervision Functions

General supervision functions are necessary to monitor the laser operation. Graphic user interfaces (GUI) display graphic objects to control and visualise laser operation.

Except for dedicated and stand-alone software and computers, all instrumented systems can be controlled over the control network. CCD cameras are expected to be the most widely used detector for the diagnostics so that graphic objects are supplied with basic image-processing functions.

## Data Acquisition and Devices to Control

### *Instrumentation buses*

Diagnostics supply data through specific buses which can be serial bus, USB, or GPIB. In most cases, Ethernet is recommended when it is available.

### *Pump laser control system*

Many pump lasers will be used in the EuPRAXIA laser system. Some of them will be delivered with their stand-alone control software, some with a GUI, but most of them should be interfaced with the distributed control system to ease operation.

### *Vacuum systems*

A great number of devices (pumps, valves, gauges, etc.) for vacuum systems will be used for laser beam transport, compressors, and interaction chambers.

Vacuum processes need to be subdivided into several subsystems. Each of them covers a perimeter defined by specific operation and maintenance requirements. These subsystems are:

- spatial filter vacuum systems in the amplification section,
- compressors,
- beam transport,
- switchyard,
- 150 MeV beam transport and target chamber,
- 1 GeV beam transport and target chamber, and
- 5 GeV beam transport and target chamber.

There are also other vacuum devices in the front end and the pump laser, but this kind of equipment does not need a control system, or it is controlled by the pump laser control system itself.

Vacuum processes are controlled by industrial programmable logic controllers (PLCs) programmed with languages defined in the CEI 61131-3 norm. The PLCs used will communicate through a local network. Vacuum devices can be controlled from supervision through a distributed control system with communication software modules (OLE for process control and device servers) between PLCs and the fieldbus.

### *Cameras*

Digital cameras will be widely used in the EuPRAXIA facility. Gigabit standard CCD cameras are the preferred choice. Gigabit cameras will be widely used in the laser beam alignment and diagnostics systems. Cameras included in automatic alignment loops will be directly connected to the hosted FEP, while cameras included into diagnostics systems will be connected to the dedicated gigabit cameras VLAN.

### *Motion devices*

In the long run, more than 100 motors will be in operation in the EuPRAXIA laser subsystem. Motors are located in motorised mirror mounts, stretchers, compressors, and alignment and diagnostics sensors. The electronic motor controller/driver must be selected to supply a universal solution for most applications by taking into account the capacity to drive bipolar stepper motors, and to read data from absolute or incremental encoders, maintenance, features, and durability. The chosen solution must be interfaced with the distributed control system.

### *Automatic closed loops*

Alignment functions may consist of manual and automatic controls. Manual alignment by an operator with the control systems consists of centring or pointing the laser beam by observing an image and controlling a motorised mirror. The automatic alignment loop is the same except that software replaces the operator. This software analyses a CCD image, then calculates and sends the corrections to the motorised mirrors. Many iterations could be necessary. The speed of the loop is adjusted according to the requirements of the localisation of the correction. Most of them have to correct slow deviation due to thermal variation. However, some of them require faster loops to correct laser beam pointing fluctuations caused, for example, by the laser itself or by air turbulence.

Another example is wavefront correction. This system is usually a dedicated system. The interconnection and data exchange with the distributed control system of such a system is to be studied.

### *Specific diagnostics*

To deliver a usable electron beam, it is mandatory to control the laser performances. In this document, we will not present the loop that allows to control the laser parameters based on the electron beam parameters. The relationship between laser and electron beam performance needs to be further studied during a prototyping step.

To do so, it is crucial to implement a complete series of diagnostics and control tools along the three laser beamlines. Diagnostics are needed to characterise the energy, laser pulse duration, spectral and spatial phase, wavefront, and spatial profile.

In this section, we describe the main controls/diagnostics that are considered mandatory along the laser chain. A description of their actual implementation (possibly with the addition of further controls) will be addressed when the final architecture will be defined and validated.

At the current stage, it appears that the alignment will be mainly controlled on (a) the Ti-Sa crystal (assuming the baseline design) to ensure that the pump and the signal beams are well overlapped, and (b) the input of the compressor since the angle of incidence has to be maintained around  $\pm 20 \mu\text{rad}$  in the target plane.

A description of the set of main diagnostics is given in Table 11.1. It does not take into account the alignment process. The repetition rate of operation of each diagnostic is also given in the table and designated by the following numbers and abbreviations:

- (1): Near field and far field are intended to be displayed on monitors at 100 Hz. The raw data of the near field will be processed at 100 Hz just to check the peak intensity (hot spots) (see the section on system security below for more details). However, only the raw data will be saved at 100 Hz on text files or other formats, which will allow a post-treatment of data. We will not save images to avoid the excessive use of disk space to handle at 100 Hz since the facility mission profile is 7 days a week, 24 hours a day.
- (2): These measurements will be performed by using a relay imaging insertable system.
- (3): This is the ns, ps, and fs contrast measurement.
- (4): This is the measurement of the ns contrast only to check if some coatings are evolving in time.
- (TBD): To be defined. The synchronisation between different lasers at the focal plane (i.e. in the target chamber) will be defined according to the specific experimental configuration when available.

**Table 11.1.** Set of laser diagnostics, their proposed positioning along the beamline, and data taking rates. Note that “once a week” here means that we will store the data only one time a week; “x” means no measurement. Some of those diagnostics will have to be performed just after maintenance, requiring the replacement of optics. The footnotes in the table are explained in the main text.

		Energy	Near Field	Far Field	Spectrum	Temporal Contrast	Wavefront sensor	Pulse Duration	Synchronization	Pointing Stability
Front-End Oscillator	Fs oscillator	100 Hz	100 Hz (1)	x	100 Hz	x	x	x	x	x
Front-End 1st CPA	Before AOPDF	x	x	100 Hz (1)	x	x	x	x	x	x
Front-End 1st CPA	Output AOPDF	x	100 Hz (1)	x	100 Hz	x	x	x	x	x
Front-End 1st CPA	Before compressor	100 Hz	100 Hz (1)	x	100 Hz	x	x	x	x	x
Front-End XPW	Before XPW	x	x	100 Hz (1)	x	x	x	x	x	x
Front-End XPW	Output XPW	100 Hz	100 Hz (1)	x	100 Hz	Once a week	x	x	x	x
Front-End 2nd CPA	Output Stretcher	100 Hz	x	100 Hz (1)	100 Hz	x	x	x	x	x
Front-End 2nd CPA	Output Regen	100 Hz	100 Hz (1)	100 Hz (1)	x	x	x	x	x	x
Front-End 2nd CPA	Output Multipass	100 Hz	100 Hz (1)	100 Hz (1)	x	x	x	x	x	x
Front-End 2nd CPA	Output Front-End	100 Hz	100 Hz (1)	x	x	x	x	100 Hz	x	x
Amplification Section	Before AMP1	100 Hz	100 Hz (1)	100 Hz (1)	100 Hz	Once a week (4)	x	x	x	x
Amplification Section	Before AMP2	100 Hz	100 Hz (1)	100 Hz (1)	100 Hz	Once a week (4)	x	x	x	x
Amplification Section	Before AMP3	100 Hz	100 Hz (1)	100 Hz (1)	100 Hz	Once a week (4)	x	x	x	x
Amplification Section	Before compressor	100 Hz	100 Hz (1)	100 Hz (1)	100 Hz	Once per hour	Once per hour (3)	x	x	x
Propagation	Before beam focusing	100 Hz	100 Hz (1)	100 Hz (1)	100 Hz	Once per hour	Once per hour (3)	100 Hz	x	100 Hz
Experimental Chamber	At focal spot	x	x	Once a week during 1000 shots (2)	Once a week during 1000 shots (2)	x	Once a week during 1000 shots (2)	x	(TBD)	Once a week during 1000 shots (2)

**Table 11.2.** A strategic view of protection measures put into place along the laser chains.

	<b>Spectrum</b>	<b>Beam Profile</b>	<b>Vacuum Level</b>
<b>AMP1</b>	if outside reference limits: block the beam	if outside reference limits: block the beam	
<b>AMP2</b>	if outside reference limits: block the beam	if outside reference limits: block the beam	
<b>AMP3</b>	if outside reference limits: block the beam	if outside reference limits: block the beam	
<b>Compressor</b>	if outside reference limits: block the beam		if $> 1 \times 10^{-5}$ mbar: block the beam
<b>Beam Transport</b>			if $> 1 \times 10^{-5}$ mbar: block the beam

Some of these diagnostics will be used to set up a system security control, as explained in the next paragraph.

We still have to define on which component we will act to close the loop with these diagnostics. For this, we need to perform a detailed model of the performances. We plan to achieve this task before the end of the final design.

Pump lasers are considered as industrial products. So we do not describe here all the internal diagnostics that will be needed to drive their performance. However, we need to check at the output of those pump lasers the near field and the energy. Associated with these measurements, we will need to have a view of the main amplifying crystals to monitor depletion levels.

### Security – Protection from Damage of Laser Components

For security reasons, we will implement a check of the spectrum of the main beam and the vacuum level in the vacuum chambers and vacuum transport lines. If the pressure in the vacuum chamber of the compressors gets higher than  $1 \times 10^{-5}$  mbar, there is a risk of damage to the gratings. The system needs to guarantee that the pressure stays below  $1 \times 10^{-5}$  mbar. In the relay imaging system stages in the beam propagation and in the presence of real foci (e.g. spatial filters), it needs to ensure that the pressure in these stages is below  $1 \times 10^{-3}$  to  $1 \times 10^{-2}$  mbar to avoid any plasma creation.

For the same reasons, we need to check the spectrum along the amplification section to be sure that there is no distortion of the spectrum of the chirped pulse, implying modifications in the temporal shape of the pulse (in particular, pulse narrowing) and possibly leading to a high risk of damages on the mirror and/or the crystals.

Additionally, the diagnostics of the beam profiles can be used to implement a safety lock; a deviation from the expected beam profile (both in shape and in pointing) can lead to the formation of hot spots with a risk of damage on the mirrors, on the crystal, and on the gratings. We thus need to check the beam profile in real time and stop the beam if it shows an excessive deviation from a reference profile.

To avoid any damage, we will have to block the beam between the front end and the amplification section (to be confirmed) and block the pump beam before entering the amplifiers (to be confirmed). A schematic view of the conditions and actions put in place in strategic points of the laser chains is given in Table 11.2.

Finally, we will implement closed loop stauts for every piece of equipment that could be inserted in the beam, such as a cross hair needed for the alignment of the beam or a mirror to inject a cw laser as a reference.

## Data Archiving

A huge amount of data is expected to be produced during the EuPRAXIA operations, from both the laser side and the experimental areas. Data from the lasers must be archived for two main purposes. First, we need to follow the laser operation by making statistics and an analysis to detect a decrease in performances and prevent failures. For that, we need a historical data-archiving system recording laser shot results. In this case, data are supplied by instrumented laser diagnostics dispatched over the four subsystems: front end, amplification section, compression section, and transport and focussing system.

Second, a part of this data is needed to optimise the laser-driven acceleration. For this purpose, only data supplied by diagnostics looking at the output beams are useful. All laser data are stored in databases.

To preserve data integrity and allow data access from office computers, data-archiving servers may have a duplication system from a control network of the machine to the laboratory network.

### *Computerised maintenance management system*

The EuPRAXIA laser system is composed of a large quantity of optical, electrical, and mechanical components and pieces. For maintenance, inventory, and stock management purposes, a maintenance team needs a computerised maintenance management system.

This system will be based on a commercial product or developed by a database software developer to have a customised system.

## 11.3.2 Personnel Safety System

The aim of the Personnel Safety System (PSS) is to secure a particular area of the laser facility when risks are too high for workers; this system has to be designed to make it the least intrusive possible, to avoid any unnecessary laser halt. A balance between safety and service must be sought.

We do not know yet how the PSS of the facility will work at EuPRAXIA. However, it is clear that the laser sub-system will have to send data to this system and will have to answer to some commands from the PSS of the facility.

Based on risk studies conducted at other laser facilities, a Safety Integrity Level of 2 [237] seems to be the minimum required. This level is applied to every security loop: sensors -> cables and fieldbus -> digital input modules -> fail-safe CPU -> digital output modules -> cables and fieldbus -> actuators.

The facility will have to define levels of risk and define for each level the protection needed. From this study, it will be possible to determine which data the laser sub-system will have to display. The following scheme is an example of a risk outside a zone:

In this case, the entry door of Zone 3 is opened in spite of the fact that it is strictly forbidden (third level of laser risk, meaning that no one could be in the presence of the laser). The PSS activates the laser beam shutter No. 1. If we assume this shutter does not work, then PSS activates laser beam shutter No. 2 to secure both Zones 2 and 3. Finally, if necessary, the laser interlock is opened by the PSS to stop every laser light emission. With this example, we show that the laser system will have to be

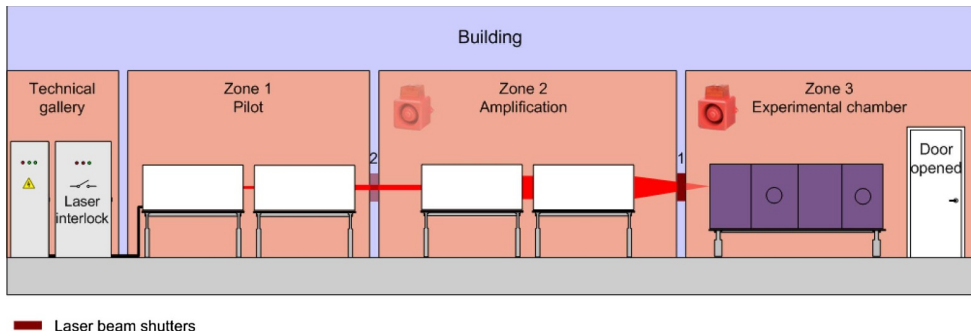


**Fig. 11.2.** Schematic of the beamline divided into different zones.

able to “say” which level of risk is triggered and will let the PSS control the interlock to stop the beam.

### 11.3.3 Electrical Timing and Synchronisation

#### Overview

##### *Synchronisation of the laser sub-system*

The EuPRAXIA laser has several pump lasers with different frequencies in the range of 1 kHz to 20 (100) Hz. Each pump laser needs at least two synchronisation signals, one for flashlamps or diodes and one for the Qswitch with, respectively, 1 ns and 100 ps uncertainty. Laser components which need the best temporal precision are chopper Pockels cells with 100 ps peak-peak uncertainty; a better temporal precision should be useful to improve contrast.

Other components needing synchronisation are diagnostics: calorimeters, CCDs, and spectrometers but with no specific temporal requirements.

Another feature of the EuPRAXIA laser is the large distances between systems, more than 50 m in most cases. Thus, synchronisation signals must be distributed over the entire facility with the same uncertainty and reliability.

##### *Synchronisation of interaction area systems*

Interaction areas need also synchronisation signals to trigger diagnostics, such as CCDs, scopes, and more specific diagnostics. These diagnostics need the same temporal precision as the laser diagnostics. Slow timing signals will occur up to a few tens of ms before each laser pulse. The pulse duration is up to 10  $\mu$ s for fast timing signals and 10 ms for slow timing signals.

Target shots are delivered and controlled by specific opto-mechanics shutter devices with programmable sequences. All sequence topologies must be generated and are characterised by a given number of parameters not yet defined.

Finally, it will be necessary to control the synchronisation of the laser beams with the particle beams. While this topic will need to be investigated further in considerable detail in the future, a possible solution for sub-femtosecond synchronisation is described in Chapter 15. Clearly, the main emphasis here will be on the control and monitoring of the jitter value, which will need to remain on the fs level or below.

##### *Architecture*

The synchronisation system will be designed to operate with large distances between the modules. Typically, the distances between the laser sub-system and the interaction chambers will exceed several hundred metres by taking into account the length of the cable trays layout.

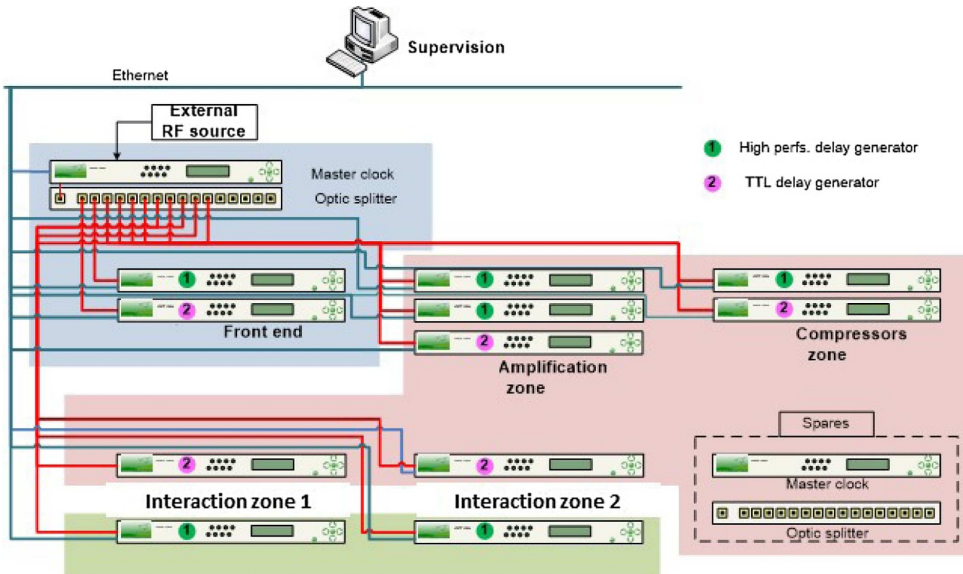


**Fig. 11.3.** Scheme of timing and synchronisation. The master and the delay generators are controlled via Ethernet.

Signals between modules are transmitted through optical fibers to obtain a high immunity from electromagnetic interferences generated by interaction, particle creation, and high voltage pulsed systems. The architecture of the synchronization system could be similar to the one described in Figure 11.3.

The system will be designed to be compliant with the possibility to manage three delay generators in each location, and all fiber optic links will be redundant. Wherever it is necessary, we use distribution amplifiers to duplicate triggers which do not need separate adjustments of both the delay and the amplitude, especially for CCD cameras.

#### *Reference master*

The first solution, as shown in Figure 11.3, is to master the system by a reference clock with a high-stability reference clock based on an oven-controlled crystal oscillator (OCXO). The stability and aging (for one day) required are  $\pm 0.1$  ppm.

The second solution could be to use an external RF signal from the oscillator. Long-term stability requirements of this RF signal must be defined. To achieve this stability, slow frequency drifts due to the temperature of the oscillator cavity need to be compensated.

The master delivers a serial data stream synchronised to the RF signal. The data stream contains coded information to generate at least frequencies between 20 Hz and 1 kHz. This data stream is used by delay generators to deliver delayed signals.

#### *Delay generators*

Delay generators receive from the master a serial data stream through a mono-mode optic fibre. The limits of the system are 1 km between the master and delay generators and 2048 simultaneous channels. The type of delay generator is not yet defined.

#### *Time stamping*

Time stamping is based on a clock signal supplied by the SSS to a counter/timer card mounted in the host. This card receives a signal at at least 100 Hz from a delay generator. The counter value is incremented by one with each pulse of this signal.

This value is used to time-stamp the acquired data. With this time-stamping system, for each sensor, a subsystem should archive data at 100 Hz. A list of data to be archived in such a system has been defined and is described in [238]. The codification for the names of the data is not yet defined.

An acquisition can be made at different frequencies or can follow the sequence. So, to catch the counter value at the right time, the counter cards receive a trigger signal. This signal is delivered by a delay generator and can have a frequency of 100 Hz or less, or it can be synchronous with the sequence.

To reset counters, two signals are used – a gate and a reset signal. These two signals are generated by the SSS. To ensure the synchronisation of all counters, we need to reset them and restart counting at the same time. The gate signal is put on a high level to stop counting; when the counters stop to count, a reset signal is sent to reset the counter values. When the counter values are initialised, the gate signal is put on a low level, and the counters restart counting.

## 12 RF Accelerator to 500 MeV as Beam Driver

### 12.1 Introduction

The RF accelerator of the EuPRAXIA facility is meant to provide a maximum energy of 500 MeV for electron bunches generated at a laser-illuminated photo-cathode. It consists mainly of two parts:

1. an S-band RF photo-injector made up of an RF gun equipped with a photo-cathode and followed by an S-band linac booster for a maximum final energy of 170 MeV and
2. an X-band RF linac to raise the electron beam energy up to a maximum final value of 500 MeV by means of X-band RF sections providing accelerating gradients of the order of  $E_{acc} \geq 50 MV/m$ . In the following paragraphs, the two systems are described in detail.

### 12.2 S-band RF Photo-Injector

The RF photo-cathode gun and associated systems are meant to reliably produce, at the most critical point in the injector, the extremely high-quality beam demanded by the EuPRAXIA facility. For this reason, it has to be based on technology that is both proven and, at the same time, at the cutting edge. Similar considerations apply to the other critical components associated with the beam generation and emittance compensation process, i.e. the photo-cathode drive laser and the solenoid after the gun itself. The EuPRAXIA electron bunches will be generated by an injector with a maximum energy of 170 MeV, which consists of a 1.6-cell RF gun cavity, followed by three accelerating structures. The system will operate at the frequency of 2.856 GHz, which is the same frequency as the SPARC photo-injector in operation at LNF since 2005. The RF gun has a metallic photo-cathode, located in the high electric field region of the cavity and illuminated by short ps-scale UV laser pulses at a 50 Hz repetition rate.

**Table 12.1.** Main parameters of the RF gun.

Gun Parameter	Unit	Value
Resonant frequency	GHz	2.856
$E_{cath}/\sqrt{P_{diss}}$	MV/(m·MW <sup>0.5</sup> )	37.5
RF input power	MW	14
Cathode peak field	MV/m	120
Repetition rate	Hz	50
Quality factor		14600
Coupling coefficient		3
RF pulse length	$\mu s$	1.0
Mode separation	MHz	41.3
$E_{surf}/E_{cath}$		0.9
Pulsed heating	°C	<30
Average diss. power	W	400
Working temperature	°C	30

### 12.2.1 RF Gun

A robust solution for the RF gun of the EuPRAXIA facility can be a 1.6-cell gun of the BNL–SLAC–UCLA type [239,240], with modifications foreseen and implemented during the last years for the gun developed for the ELI-NP GBS project [241] and integrated in the new gun recently developed for the SPARC photo-injector. With respect to the original design [239,240], this gun, whose parameters are given in Table 12.1, will implement several features described in the following.

The iris profile has been designed with an elliptical shape and a large aperture to simultaneously reduce the peak surface electric field, increase the frequency separation between the two resonant modes (i.e. the working  $\pi$ -mode and the so-called 0-mode), and improve the pumping efficiency on the half-cell. Furthermore, a high-frequency separation of the resonant modes strongly reduces the residual field of the 0-mode due to the transient regime, which is particularly important if the structure is fed with short pulses [242]. The coupling window between the rectangular waveguide and the full cell has been strongly rounded to reduce the peak surface magnetic field and, as a consequence, the pulsed heating [243]. Figures 12.1b and 12.1c show, respectively, the magnetic field in the coupler region at a 120 MV/m cathode peak field and the longitudinal accelerating field profile. The input coupling coefficient ( $\beta$ ) has been chosen to be equal to 3 to reduce the filling time, allowing an operation with short RF pulses [241]. Finally, to compensate the dipole field component, induced by the presence of the coupling hole, a symmetric port (connected to a circular pipe below cutoff) has been included in the gun [244–246] and is also used as a pumping port. The residual quadrupole field component from the presence of the two holes does not significantly affect the beam quality [247].

The electromagnetic design of the gun has been carried out using 2D and 3D electromagnetic codes (Superfish [248] and HFSS [249]). Figure 12.1a shows the HFSS geometry of the gun with its main dimensions.

A new fabrication technique for this type of structure has been recently developed at LNF [250] and successfully applied to the realisation of two RF guns: the ELI-NP gun and the first prototype gun currently in operation at UCLA at a low repetition rate (i.e. 5 Hz) and a relatively low cathode peak field [251]. The new technology is based on the use of special RF-vacuum gaskets, which allow a brazing-free realisation process, avoiding copper annealing from the brazing process itself, with the advantage of potentially reaching higher accelerating field with a lower breakdown rate [252].

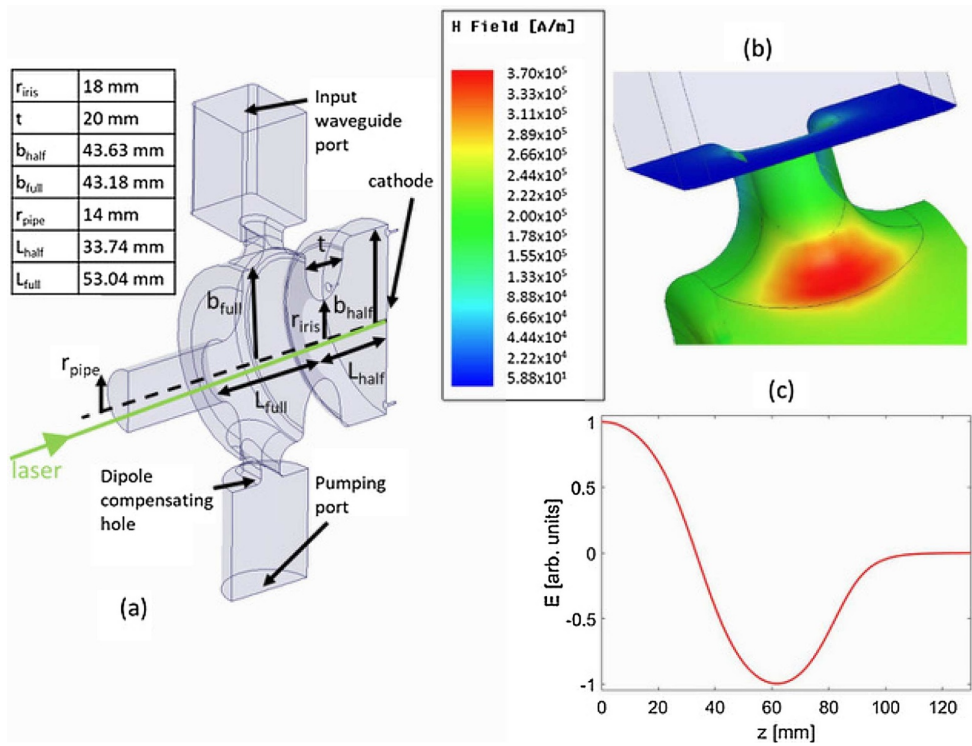


**Fig. 12.1.** (a) HFSS geometry of the gun; (b) H field in the coupler region; (c) longitudinal accelerating field profile.

The photo-cathode is centred on the flange that closes the half-cell. The requirement of a short response time of the cathode to allow electron beam shaping through laser pulse manipulation limits, in the case of the EuPRAXIA photo-injector, the choice of the cathode materials to metals that usually present response times of the order of a few tens of femtoseconds [253]. Based on the results so far obtained worldwide in different laboratories, the most promising candidate metals that can be used as sources for electron generation are copper (Cu) [254], magnesium (Mg) [255], and yttrium (Y) [256]. One of the parameters that is critical for the final choice and operation of the photo-cathode is represented by the quantum efficiency (QE) at the drive laser wavelength. The QE of these metals has been measured in similar conditions under UV laser irradiation at 266 nm, resulting in values of about  $4 \times 10^{-5}$  [257],  $5 \times 10^{-4}$  [255], and  $\sim 2 \times 10^{-4}$  [256] for Cu, Mg, and Y, respectively.

In the first phase of EuPRAXIA, a copper cathode can be adopted. Copper is a robust material with well-proven photo-emissive behaviour that guarantees uniformity of the emission distribution over the laser spot illuminated by the laser. Its drawback is the low emission efficiency (i.e. quantum efficiencies of the order of  $5 \cdot 10^{-5}$ ), which entails large laser pulse energy. Different cathode materials (e.g. Mg, Y) can be used in future phases once their reliability is demonstrated for operation in user facilities. In any case, all types of cathodes demand very good vacuum conditions, at the level of  $10^{-9}$  mbar during high-gradient operation, which typically implies that the vacuum without RF should be even better by one order of magnitude. These demands are to be met by stringent control of the gun manufacturing and cleaning processes and by implementing a pumping system with high pumping

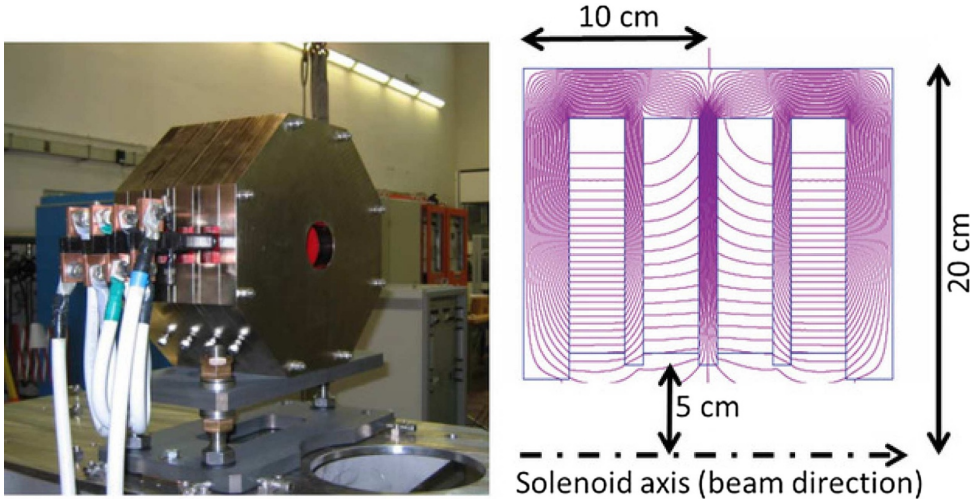


**Fig. 12.2.** Left: Photo of the SPARC gun solenoid. Right: The solenoid field distribution in the SPARC configuration  $++-$ , as computed by the Poisson-Superfish code.

**Table 12.2.** Parameters of the gun solenoid.

Parameter	Unit	Value	Conditions
Typical operation axial field peak (+ + -)	Gauss	2700 (-2700)	@ 14.3 cm (25.0 cm)
Residual axial field @ cathode	Gauss	<10	@ 2700 Gauss field peak
Maximum coils current (typical)	A	~280 (180)	
Distance cathode to solenoid edge	cm	9.6	
Solenoid bore	cm	7.6	

speed through direct pumping ports on the accelerating cells waveguide and cathode flange.

### 12.2.2 RF Gun Solenoid

The design of the solenoid, immediately after the gun, together with the gun design itself, is crucial for the emittance compensation process [258] and final beam performances at the linac exit. The proposed design consists of four coils, embedded and separated by iron armatures, that can be powered independently. In this way, it is possible to shape the magnetic field profile and move the field peak around the central position. This solenoid design, as tested at SPARC\_LAB, allows one to power the coils with alternate signs (e.g.  $+-+-$  or  $+-+-$ ), giving a better compensation for alignment errors and multi-polar components. The magnetic field lines of the solenoid, as computed using the Poisson-Superfish FEM code [259], are shown in Figure 12.2, while the main design parameters are reported in Table 12.2.

The solenoid will also be mounted on a movable support to allow a beam-based fine alignment of the magnetic centre with a precision below  $\sim 10 \mu\text{m}$  in the transverse planes.

### 12.2.3 Photo-Cathode Drive Laser System

The EuPRAXIA photo-injector is required to produce both single and comb-like electron bunches, with a charge ranging from tens to a few hundreds of pC, with a

high peak current and normalised transverse emittance  $<1$  mm mrad. Therefore, the laser pulses have to be tailored to minimise the beam emittance and, at the same time, have enough power to produce relative high-current bunches.

Photo-cathode drive lasers for high-brightness electron beam applications must have very specific capabilities driven by two major considerations: (1) the low photo-emission efficiency for robust photo-cathodes requires high UV pulse energy to generate the needed charge; and (2) the emittance compensation process is most successful with a uniform temporal and spatial laser energy distribution. Additionally, low amplitude and time jitters from pulse to pulse, as well as pointing stability are needed to ensure repeatable SASE FEL performance. The laser pulses have to be synchronised with the master oscillator to extract electrons at the specified phase of the RF wave. Other laser systems will be used at EuPRAXIA for laser-driven plasma acceleration, electron and photon diagnostics, and a variety of possible pump and probe experiments. All these lasers are required to be synchronous within very tight tolerances. The timing and synchronisation of the laser system are discussed in more detail in Chapters 11 and 15. The allowed variations in parameters concerning the laser system and its relationship to the RF system have been specified with the aid of simulation codes.

The laser system for EuPRAXIA is required to deliver energies per pulse in excess of  $\sim 150 \mu\text{J}$  at a wavelength of 266 nm to the photo-cathode at a repetition rate of up to 50 Hz. This energy requirement comes from the typical quantum efficiency of a copper photo-cathode. Indeed, the drive laser supplies photons that are absorbed by electrons within the RF gun cathode, producing via the photo-electric effect emitted electrons only if their kinetic energy exceeds the material's work function. The energy per laser pulse  $U$  (J) needed to produce a bunch of charge  $q$ (C) using photons of energy  $E_\gamma$  (eV) incident on a cathode surface with quantum efficiency  $QE$  is given by  $U = q E_\gamma / QE$ . A cathode's quantum efficiency depends on many conditions, such as material, preparation, excess of photon energy over the work function, RF field, and vacuum levels. Nevertheless, we may extrapolate the needed performance of the photo-cathode drive laser based on our experience at SPARC\_LAB. Assuming a typical quantum efficiency value of  $5 \times 10^{-5}$  for copper,  $20 \mu\text{J}$  are required to produce a  $400 \text{pC}$  electron beam; allowing for an energy overhead of one order of magnitude, this implies that  $200 \mu\text{J}$  of laser energy are necessary. This required value at the photo-cathode must be considerably larger at the harmonic-generation crystal exit as light will be absorbed by various optical elements needed for pulse shaping and transport to the photo-cathode. In addition, the emittance compensation scheme requires that the laser pulse must show a uniform transverse and longitudinal profile to compensate the non-linear space-charge field with a proper magnetic focussing. The temporal and spatial flat-top laser energy distribution on the cathode has been demonstrated to reduce the emittance [256,257]. We foresee to change the pulse length on a range between 100 fs to a few ps (RMS) and the number of pulses from one to five to explore different machine working points based on the different foreseen experiments.

#### 12.2.4 S-band Linac

The EuPRAXIA photo-injector is finally completed with three S-band accelerating structures that allow one to accelerate and manipulate the beam through the velocity-bunching compression scheme. RF compression or velocity bunching [260] consists of compressing the beam by injecting it in the first RF structure ahead of the field crest with a phase near the zero of the accelerating field; the beam slips back up to acceleration phases undergoing less than a quarter of synchrotron oscillation and



**Fig. 12.3.** Solenoid coils embedding the first accelerating S-band structure; the upper iron shield is removed.

is compressed. The emittance growth occurring during the compression can be controlled by the proper shaping of an additional magnetic field around the accelerating structures. For this purpose, two solenoids around the first two structures are used for emittance compensation. Simulations show that compression factors larger than three require an accurate tuning of the coils composing the solenoids embedding the structures, as also experimentally demonstrated at SPARC\_LAB [261].

The solenoid structure will be covered by de-mountable soft iron magnetic shields to shield the fringing field that, at a distance of 80 mm from the beam axis, is still not negligible ( $\approx 150$  Gauss). Figure 12.3 shows the solenoid coils around the first linac sections with the shielding opened. The advantages of this configuration are the following:

- a higher magnetic field, about 1900 Gauss, as opposed to 1660 Gauss with the same number of ampere-turns;
- a sharper magnetic fringe field tail;
- an improved transverse alignment of the solenoid as it will depend partially on machined iron, not simply on wound coils with dielectric coatings;
- no fringing field outside the structure, i.e. no constraints for materials, external apparatus, and personnel safety;
- the iron shielding, realised by means of semi-annular rings, which can be easily removed for checks, tests, or other necessities; and
- thermal confinement of the accelerating structure, which means less sensibility to ambient temperature variations.

The main parameters of each solenoid are summarised in Table 12.3.

The accelerating structures of the EuPRAXIA S-band linac are travelling wave (TW), constant gradient (CG),  $2\pi/3$ , and 3 m long operating at 2.856 GHz. These types of accelerating sections, known as SLAC-type structures [262], are made of a series of 86 RF copper cells, joined with a brazing process performed in high-temperature vacuum furnaces. The cells are coupled by means of on-axis circular irises with decreasing diameter, from input to output, to achieve the constant-gradient field profile in case of uniform input power. The RF power is transferred to the accelerating section through a rectangular slot coupled to the first cell. The power not dissipated

**Table 12.3.** Characteristics of the solenoid focussing magnets per linac section.

Parameter	Unit	Value
Number of coils		12
Inner diameter	mm	308
Outer diameter	mm	632
Coil cross-section (insulated)	mm <sup>2</sup>	162.82
Nominal Cu conductor size	mm <sup>2</sup>	7.5-7.5
Nominal cooling hole diameter	mm	5
Turns per solenoid		200
Maximum excitation current	A	200
Current density	A/mm <sup>2</sup>	5.05
Maximum voltage	V	30.15
Power per coil	W	5580
Hydraulic circuits per coil		5
Water velocity	m/s	0.9
Water flow per magnet	m <sup>3</sup> /s	9·10 <sup>-5</sup>
Water temperature rise	°C	15
Pressure drop per circuit	MPa	0.19

**Table 12.4.** Technical specifications of the S-band accelerating sections.

Parameter	Unit	Value
Structure type		Constant gradient, TW
Working frequency	GHz	2.856
Number of cells		86
Structure length	m	3
Working mode		TM <sub>01</sub> -like
Phase advance between cells		2 $\pi$ /3
Max. average accelerating gradient	MV/m	22 (S1)/ 25 (S2)/ 28 (S3)
Average RF input power ( $P_{IN}$ )	MW	<40 (S1) / <50 (S2)/ <60 (S3)
Shunt Impedance per unit length	M $\Omega$	53-60
Phase velocity		$c$
Normalised group velocity	$v_g/c$	0.0202-0.0065
Filling time ( $\tau_F$ )	ns	~850
Structure attenuation constant	neper	0.57
Operating vacuum pressure (typical)	mbar	10 <sup>-8</sup> -10 <sup>-9</sup>
Repetition rate	Hz	50
Average dissipated power	kW	~1.3

in the structure (about 1/3) is coupled out from the last RF cell and dissipated on an external load. To meet the severe emittance requirements for the injector, the single-feed couplers (foreseen in the original SLAC-type structures) will be replaced by a dual-feed design [263] to minimise the multipole field effects generated by the asymmetric feeding, which induces transverse kicks along the bunch causing beam emittance degradation.

The maximum achievable accelerating gradient is the most important parameter of such devices. To reach the maximum required nominal energy of about 180 MeV, the average accelerating field in the three SLAC-type sections S1, S2, and S3 needs to be 22, 25, and 28 MV/m, respectively. The beam loading is negligible because of the very small average beam current (energy extracted by the beam is maximum 40 mJ per section; stored energy in each section is about 40 J).

Technical specifications of the S-band accelerating sections are reported in Table 12.4.

**Table 12.5.** Main specifications of the S-band klystrons.

Parameter	Unit	Value
Frequency type	GHz	2.856
RF pulse duration	$\mu s$	4
Repetition rate	pps	50
Cathode voltage	kV	350–370
Beam current	A	400–420
HV pulse duration	$\mu s$	6
RF peak power	MW	60

### 12.2.5 High-Power System Components

Two RF power stations are needed to feed all of the S-band active devices. The first one will power the RF gun and one RF deflecting cavity used for beam longitudinal phase-space diagnostics (see Chap. 21). Both devices are standing wave (SW) cavities, requiring  $\approx 1.5\mu s$  long RF pulses of  $\approx 15MW$  and  $\approx 5MW$  power, respectively. Because of the pulse length and the moderate power request, this station will not be equipped with a pulse compressor. A total power of  $\approx 25MW$  is sufficient to provide a comfortable safety margin for operation. A circulator will protect the klystron itself against the power reflected by the standing wave cavities. Given the fact that this device employs ferrite materials, it usually operates in a pressurised atmosphere of sulfur-hexafluoride (SF6) to guarantee the required insulation. The waveguide vacuum system will be separated from the circulator SF6 insulating system by means of RF ceramic windows. This type of window will also be used to separate the accelerator and waveguide vacuum systems. A capillary distributed interlock/alarm system, managed by a complex of programmable logic controllers (PLC), will protect the linac and the RF stations in the case of malfunction.

A second RF station will power the three accelerating sections S1, S2, and S3. The total power required is  $\approx 150MW$  in  $0.85\mu s$  long pulses, which can be obtained by compressing a  $\approx 4\mu s$  long,  $60MW$  pulse produced by a single klystron. Although the nominal accelerating fields are not extreme, they nevertheless require the use of selected materials, precise machining, a high-quality brazing process, surface treatments and cleaning, ultra-pure water rinsing, careful vacuum, and RF low-power tests. To keep the accelerating structures and the pulse compressor cavities precisely tuned, they need to be kept at a very constant temperature, i.e.  $\Delta T = \pm 0.1^\circ$ , by means of regulated cooling water systems.

Three manufacturers – Thales (France), CPI (U.S.), and Toshiba (Japan) – produce 60 MW peak-power S-band klystrons, which meet the requirements of the second station of the EuPRAXIA S-band linac. A set of klystron parameters is given in Table 12.5. Each klystron, equipped with beam-focussing coils, will be supplied by a high-voltage (HV) modulator. As already mentioned the second klystron will be connected to a pulse compressor (SLED), which is used to increase the peak power, feeding the three accelerating structures in parallel. An important specification of the SLED system is the peak power gain, which usually ranges around 7.4 dB, with maximum values of 7.8 dB. The power at the SLED output increases therefore, on average, by a factor of 3, while the pulse length is reduced to  $0.85\mu s$ , corresponding to one filling time of the S-band TW structures.

A network of rectangular WR284 copper waveguides distributes the RF power from the klystrons to the gun, SLEDs, and accelerating structures. The waveguides are pumped down to  $1 \times 10^{-8}$  mbar with a distributed pumping system and are

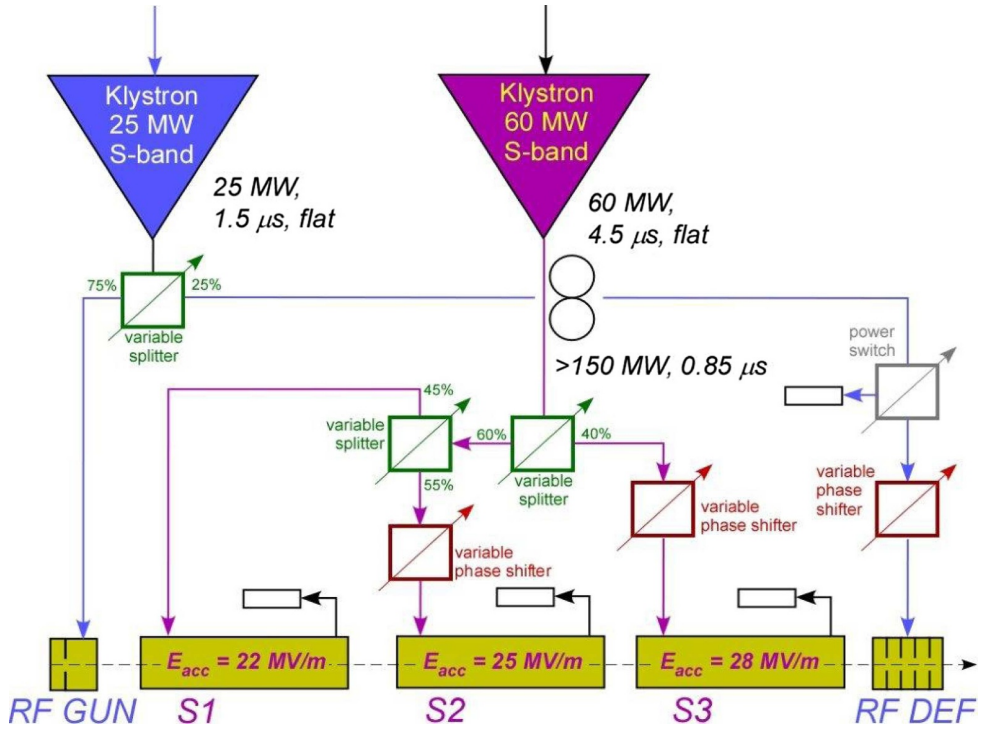


**Fig. 12.4.** Layout of the EuPRAXIA@SPARC\_LAB RF power station as an example for the RF power distribution for the photo-injector.

connected to the accelerating structures through ceramic windows to protect the beamline vacuum.

Variable phase shifters and splitters will be used to allow a fully independent phase and amplitude regulation of the three TW accelerating structures. This option is critical in the optimisation of the machine performance and, in particular, in providing all the capabilities needed for velocity-bunching and chicane-bunching working points. The phase shifter and splitter/attenuators located in the waveguide arms are high-power devices capable of operating in vacuum, and are commercially available. The variable power splitter/attenuators can be integrated in the waveguide network to route in each distribution arm the required power level. Figure 12.4 shows a scheme of the RF power distribution for the photo-injector.

### 12.3 X-band RF Linac

#### 12.3.1 Introduction

The EuPRAXIA linac is the core of the accelerator. It is designed to accept the beam coming from the injector and to accelerate it to the final energy with the proper beam characteristics to match the requirements of the various specific applications. In this respect, the linac needs to be flexible enough to cope with different scenarios: (1) injection of a beam comb into a neutral plasma to both excite a plasma wave and exploit it to accelerate the last (or “witness”) bunch of the train (PWFA case) and (2) injection of a single bunch into a plasma wave excited by a laser pulse (LWFA case). The linac RF design is driven by the need of a high accelerating gradient,

i.e. a gradient well above the operational values of the existing FEL sources. This is required to achieve facility compactness, which is one of the main goals of the EuPRAXIA project. Thus, the high-gradient operation motivates the choice of the linac technology. In fact, the use of high RF frequencies is the most suitable and efficient solution for high gradients. C-band technology ( $f \approx 6$  GHz) is the chosen baseline of most recent room-temperature FEL source facilities, such as SACLA at Spring 8 (Japan) and SwissFEL at PSI (Switzerland), while X-band ( $f \approx 12$  GHz) is the proposed baseline for CLIC, the CERN multi-TeV linear collider project. In principle, both technologies could fulfill EuPRAXIA requirements. The baseline chosen for the EuPRAXIA project, however, is X-band for various reasons: it is more efficient, it has operated at higher gradients, its development is supported by a stronger international effort, and experimental data are more abundant. Moreover, the possibility to establish a partnership with CERN represents an added value to the project. Nevertheless, it has to be mentioned that, at present, some X-band RF components are more expensive than C-band ones, although costs are decreasing as the technology is being adopted by different laboratories, and cavity fabrication and alignment tolerances are becoming more stringent.

### 12.3.2 Linac Technology and Gradient Choice

The total space required for a  $\sim 500$  MeV linac accelerating section (with  $\sim 100$  MeV gain in the photoinjector and  $\sim 400$  MeV gain in the linac itself) is  $\sim 10$  m, corresponding to an active length of  $\sim 8$  m, with the remaining space required to accommodate beam diagnostics, magnetic elements, vacuum equipment, and flanges plus the room foreseen for upstream and downstream lattice-matching sections and magnetic chicanes. The minimum gradient required to accomplish the 0.5 GeV scenario is therefore 50 MV/m. However, the linac accelerating sections and the whole RF system need to be designed to ultimately reach a higher gradient to guarantee a comfortable safety margin during operation. The need of generating such high accelerating gradients (i.e. in the range of  $\geq 50$  MV/m) has been indeed the strongest motivation addressing the RF technology choice.

In the last 25 years, a huge effort has been invested in the development and consolidation of X-band as a fully reliable RF technology for future linear colliders, initially at SLAC and KEK (NLC/JLC projects) and then at CERN (CLIC project) [264]. The work has led to a better understanding and control of high-gradient phenomena, such as breakdown, as well as to the development and extensive experimental testing of all RF components necessary to build a complete RF accelerating system. This includes RF power sources, pulse compressors, waveguide networks, and vacuum components. To perform long-term tests on various prototypes of the CLIC accelerating structures, three test stand stations, the so-called “X-boxes”, have been put into operation at CERN. Many of the tested structures have exceeded the 100 MV/m threshold, with a breakdown rate compliant with CLIC specifications ( $\leq 3 \times 10^{-7}$  in units of breakdowns per pulse per metre of active length) [265,266].

The development work on C-band technology instead has been more focussed on the performances required by FEL source facilities [267–269] so that less data are available on the ultimate achievable gradients with this approach compared to X-band.

Starting from these considerations, X-band RF technology has been evaluated to be the most appropriate choice for the EuPRAXIA linac. In this regard, INFN has set up a collaboration agreement with CERN for a wide exchange of technical information, expertise, and components. Short-term goals of the collaboration are the refinement of the EuPRAXIA linac RF design and the construction at LNF of an additional X-box to test accelerating structure prototypes.

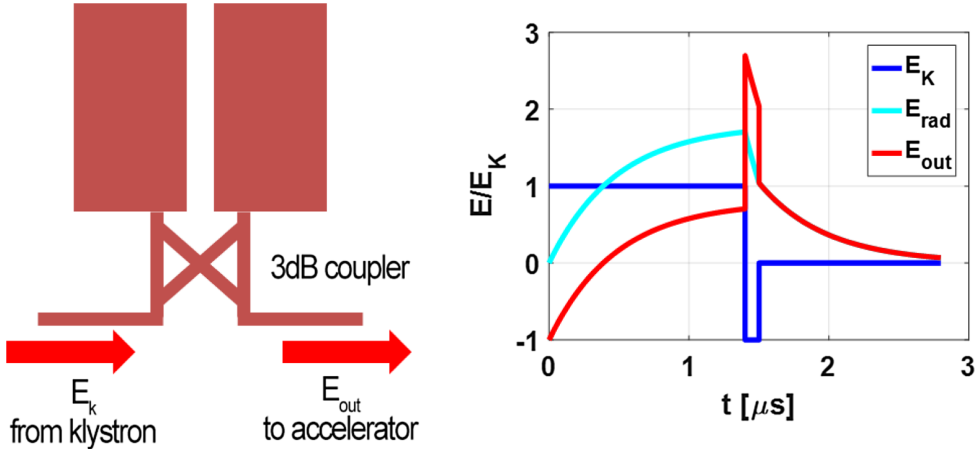


Fig. 12.5. Pulse compression with a SLED-type system.

### 12.4 Accelerating Section Design

The RF system for the EuPRAXIA linac has been designed using the following procedure:

- define the optimal filling time of the structures, considering the necessity to use pulse compressors in the system;
- choose the iris aperture according to beam dynamics considerations (this allows to determine the dimensions of a single cell and the total length of the accelerating structure); and
- define the layout of the complete RF system based on the following:
  - optimised TW section parameters;
  - RF power source (klystrons) parameters; and
  - the various operating scenarios that the linac must support.

The accelerating sections are of the travelling wave (TW) type, and will be powered by means of pulse compression systems. This choice maximises the overall efficiency and decreases costs by reducing the number of power sources required to produce the necessary peak power [270]. Pulse compressors are widely used devices in RF systems of room-temperature linacs. By constructively interfering reflected power pulses of very high-Q cavities with properly phase-modulated forward pulses, it is possible to concentrate a large portion of a klystron RF pulse energy in a small fraction of the original pulse duration, as shown in Figure 12.5.

The peak power in the shortened RF pulse is considerably higher than the original one, and the shorter the pulse, the larger the peak power. On the other hand, the shorter the RF pulse, the smaller the fraction of its energy exploited for acceleration by the TW section. The optimal pulse length of the TW section powered by a compressed pulse can be calculated and depends on the klystron pulse duration and the Q factors of both the accelerating sections and the pulse compressor cavities. For typical values of an X-band system ( $f_{RF} \approx 12GHz$ ,  $\tau_{kli} \approx 1.5\mu s$ ,  $Q_{TW} \approx 6500$ ,  $Q_{SLED} \approx 180000$ ), the optimal duration of the compressed pulse can be derived from the plots shown in Figure 12.6.

The plots on the left side show the values of the “effective” shunt impedance per unit length  $R_s$  normalised to the ordinary shunt impedance per unit length  $R$  as a function of the parameter  $\tau_s = \alpha \cdot L_s = (\omega_{RF}/2Q) \cdot \tau_F$ , with  $\alpha$  as the linear attenuation coefficient of the structure,  $L_s$  its length, and  $\tau_F$  the structure filling

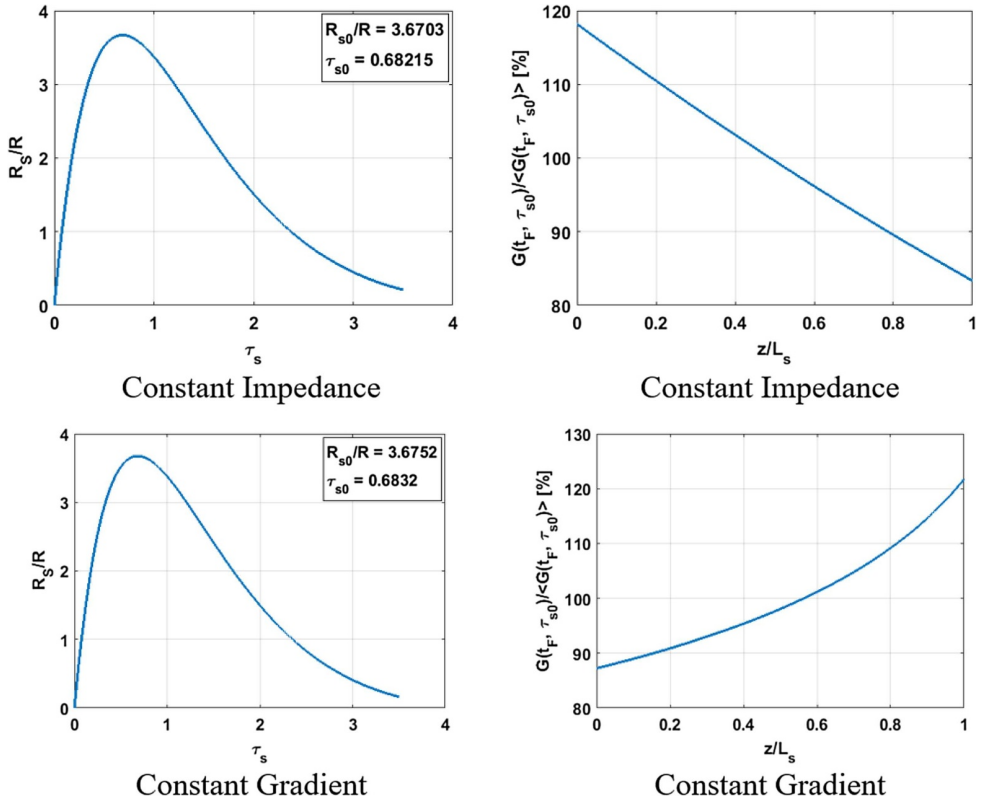


**Fig. 12.6.** Effective shunt impedance as a function of the section attenuation and resulting accelerating field profile.

time. The definitions of  $R$  and  $R_s$  are the following:

$$R = \frac{E_{acc}^2}{|dP/dz|}; \quad R_s = \frac{\langle E_{acc}^2 \rangle_{avg}}{P_{in}/L_s} \quad (12.1)$$

The maximum value of the  $R_s/R$  ratio is  $\sim 3.67$ , a number larger than 1 since it accounts for the peak power gain factor provided by the pulse compressor. It is reached when  $\tau_{s0} \sim 0.68$ , which corresponds to a filling time value of  $\tau_F \approx 120$  ns. The values obtained with constant impedance and constant gradient sections are similar, so this parameter does not determine the choice between the two options. The dimensions of the basic cell of the TW accelerating section have been parametrised and simulated with the HFSS code to calculate all the characteristic parameters of the structure. The cell model for simulations is shown in Figure 12.7. The aim of the simulations was to scan the structure characteristics for iris radius values  $a$  varying in the  $\tau_F \approx 120$  ns range. For each value of  $a$ , the cell has been tuned to the nominal frequency ( $\tau_F \approx 120$  ns) by varying the cell radius  $b$ , while the other dimensions have been kept fixed. The chosen phase advance of the TW structure is  $2\pi/3$ , so that the length  $d$  of the cell is  $1/3$  of the RF wavelength.

The main characteristic parameters of the TW structure (such as attenuation constant, group velocity, shunt impedance per unit length, Q factor, and modified Poynting's vector) have been calculated as functions of the iris radius  $a$  and are reported in the plots in Figure 12.8. The attenuation constant and group velocity depend critically on the iris aperture, while the shunt impedance per unit length

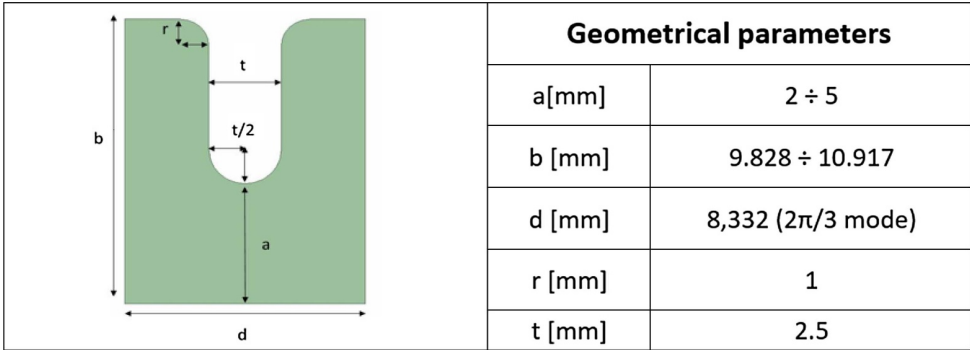


Fig. 12.7. Basic EuPRAXIA X-band accelerating cell.

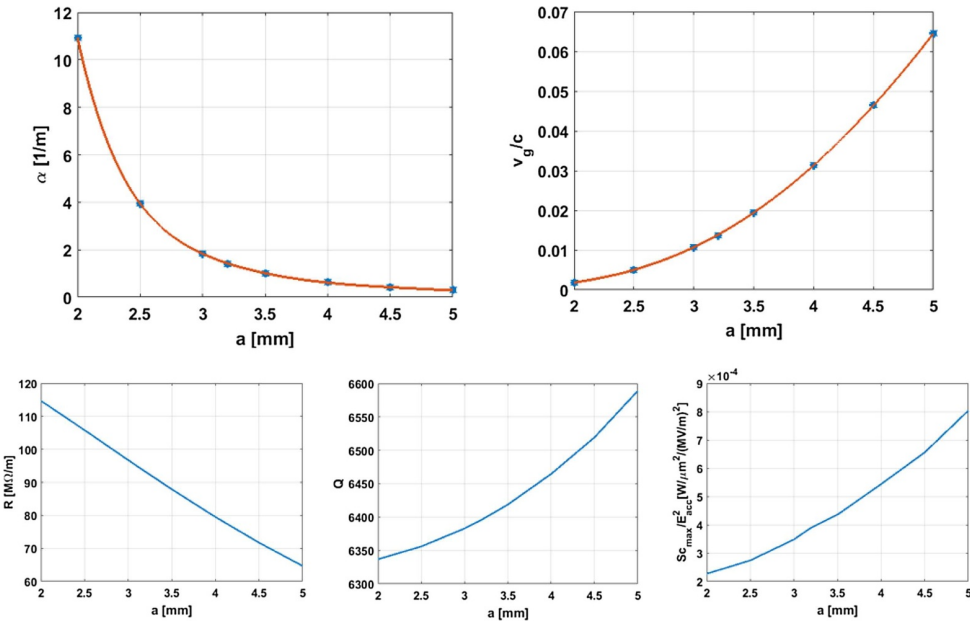


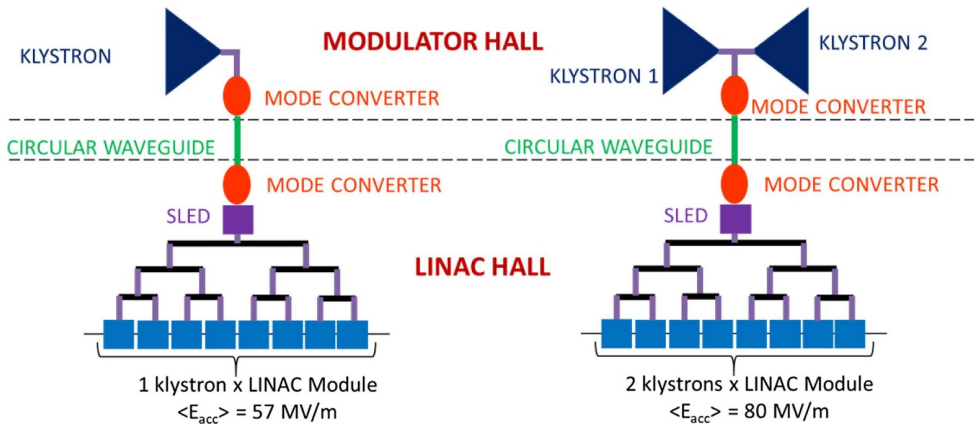
Fig. 12.8. Characteristics of the TW accelerating section as a function of iris radius.

shows an approximately linear dependence, and the Q-factor excursion is very limited (~5%) in the explored range.

The choice of the iris aperture design value is a trade-off between efficiency, pushing towards small values of  $a$ , and different technical and beam dynamics-related considerations (such as energy spread, emittance growth, beam stay-clear margins, alignment tolerances and so on), pushing towards larger values of  $a$ . In particular, calculations on beam breakup (BBU) limits caused by the transverse wakefield of the accelerating sections scaled to the EuPRAXIA beam parameters have led to a minimum acceptable value of the iris aperture of  $a = 3.2\text{mm}$  [271,272]. This value, together with the optimal total attenuation and filling time reported in Figure 12.6, is sufficient to complete the TW section design. The main parameters characterising a constant gradient TW X-band section for the EuPRAXIA linac are summarised in Table 12.6.

**Table 12.6.** Characteristics of the EuPRAXIA constant gradient accelerating section.

Accelerating section parameter	Symbol	Unit	Value
Average iris radius	$\langle a \rangle$	mm	3.2
Structure length	$L_s$	mm	500
Quality factor	$Q$		6400
Normalised group velocity	$v_g/c$	%	2.5–0.77
Filling time	$\tau_F$	ns	121
Number of cells	$N_c$	–	60
Average shunt impedance per unit length	$\langle R \rangle$	$M\Omega m^{-1}$	90
Effective shunt impedance per unit length	$R_s$	$M\Omega m^{-1}$	330

**Fig. 12.9.** Schematics of an 8-section RF module powered either by one (left) or two (right) klystrons.

#### 12.4.1 X-band Linac Layout

The TW X-band accelerating sections optimised for the EuPRAXIA application are 0.5 m long and show an effective shunt impedance per unit length of  $330 M\Omega/m$ , a value that accounts also for the peak power gain provided by the pulse compressor. The fraction of the klystron RF power required by each accelerating section to reach the  $\approx 57$  MV/m average gradient (i.e. the minimum needed to provide a  $\approx 0.5 GeV$  beam to the magnetic undulator without plasma contribution) is then:

$$P_{in} = \frac{\langle E_{acc}^2 \rangle_{avg}}{R_s/L_s} = 4.9 \text{ MW}. \quad (12.2)$$

Commercially available X-band klystrons provide up to 50 MW peak power in  $\approx 1.5 \mu s$  long pulses.

RF losses in the waveguide distribution system are estimated to reduce the available klystron power to the accelerating sections by  $\approx 20\%$  so that a single tube can actually deliver  $\sim 40$  MW. Thus, up to 8 TW structures can be fed in parallel at the required gradient by a single klystron. For this reason, the basic RF module of the EuPRAXIA X-band linac can be conveniently composed by a group of 8 TW sections assembled on a single girder and powered by a single klystron connected to a pulse compressor system and a waveguide network splitting and transporting the RF power to the input couplers of the sections. Each RF module will provide an active length of 4 m, while its actual physical length will be 5 m to accommodate flanges, vacuum equipment, beam diagnostics stations, and magnets. The 500 MeV

**Table 12.7.** Main parameters of the X-band linac RF system for different scenarios: injection in the plasma (LPWA – PWFA) and ultimate performance.

	Parameter	Unit	Value	
$N_s$	Number of sections		16 (2 modules x 8 sections)	
$P_k$	RF power available per klystron	MW	50 (at klystron output couplers) 40 (at section input couplers)	
			PWFA – LWFA	Ultimate
$\langle E_{acc} \rangle$	Max. average gradient	MV/m	57	80
$P_{RF}$	Total RF power required	MW	79	155
$N_k$	Number of klystrons		2 (reduced power)	4 (full power)

linac will host 2 RF modules in total, corresponding to 16 accelerating sections. This configuration (2 RF modules driven by 2 klystrons) is already sufficient to provide the minimum nominal beam energy for the different operational scenarios; however, its optimisation is still in progress.

The linac energy could be increased by doubling the RF power on one or more modules by simply adding a second klystron. Upgraded modules could run with an increased gradient up to 80 MV/m. Thanks to the modularity of the RF system, the RF power upgrade of the modules can be planned in various steps according to the needs of the facility. This will provide a gradient overhead that could be exploited to increase the operation flexibility and, ultimately, to reach higher beam energies. A sketch of one RF module powered in initial (left) and upgraded (right) configurations is shown in Figure 12.9, while the main parameters of the X-band linac RF system are reported in Table 12.7.

The RF system layout and the waveguide network distribution will remain unchanged downstream of the 2-klystron power combiner. The standard WR-90 rectangular waveguide supporting the TE<sub>10</sub> mode at 12 GHz shows a  $\approx 0.1$  dB/m attenuation. Thus, the choice is not suitable for long-distance connections, such as the one between the RF power station (klystron gallery) and the RF module (accelerator hall). For this reason, the majority of this length will be covered by a round overmoded WC-50 waveguide, showing a much lower attenuation of  $\approx 0.013$  dB/m. Two mode converters need to be placed to interface the two waveguide standards. The pulse compressor (SLED) will be placed downstream of the low attenuation connection, just in front of the power splitter network feeding the 8 TW structures.

## 13 Plasma Injector

### 13.1 Introduction

A laser-driven plasma-wakefield accelerator can be used as a laser-plasma injector (LPI) stage by trapping electrons from the plasma source. This would then form the first component of the accelerator in place of a conventional photo-cathode. During the in-plasma injection process, a small fraction of electron trajectories are such that they become trapped in the focussing and accelerating field structure of the plasma wakefield set up by the bulk motion of the plasma. This happens naturally when the plasma oscillation is driven to a large enough amplitude, such as in the ground-breaking “dream beam” papers of 2004 [11, 12, 273]. Thus, in its simplest form, an LPI can be constructed by focussing a short, relativistically intense laser pulse into a uniform plasma. By ensuring that the laser pulse is focussed to the dimensions of a relativistic plasma wave ( $\approx \lambda_p \equiv 2\pi c/\omega_p$ ), the laser pulse can efficiently drive an electron plasma wave with

**Table 13.1.** Target parameters for electron bunches generated by LPIs.

Beam parameter	Symbol	unit	Baseline	Range (accept-best)
Bunch Charge	$Q$	pC	30	$\geq 30 \rightarrow 100$
Bunch total energy spread	$\Delta E/E$		5%	$\leq 10\% \rightarrow 1\%$
Bunch transverse emittance	$\varepsilon_{N,\perp}$	mm mrad	1	$\leq 10 \rightarrow 1$
Bunch length	$\tau$	fs	5	$10 \rightarrow 3$
Repetition rate	$f$	Hz	10	$1 \rightarrow 100$

a phase velocity equal to the group velocity of the laser pulse. The normalised vector potential  $a_0$  of the laser pulse determines the nature of the plasma response, and for  $a_0 \gg 1$ , the plasma wave amplitude becomes large, with the motion of the plasma electrons becoming highly relativistic. Indeed, the velocities can become so large that there can be trajectory crossing, and the plasma wave is said to “break” in analogy to water waves breaking at the sea shore. By controlling the laser and plasma parameters, this wave breaking can be harnessed to inject a bunch of charge, which is then accelerated in the longitudinal field of the plasma wave.

To build a high-quality and stable LPI for a potential user facility, control of the injection process has to be maintained to industrial standards. Experimental results over the past 15 years have explored various methods of achieving controlled injection. The main methods considered for a EuPRAXIA LPI are density-downramp injection, ionisation injection, and a new technique called resonant multi-pulse ionisation injection (ReMPI). The first two techniques affect the injection process in complementary ways and can further be incorporated into a single plasma source design, leading potentially to greater control on beam properties. With an emphasis on experimental data, this chapter will focus largely on the techniques of density-downramp and ionisation injection, both demonstrated in test experiments in the past, while the ReMPI technique will be discussed further via simulation studies in Chapter 23.

Two scales of LPI will be implemented in EuPRAXIA: a “low-energy” injector producing electron beams in the range of 150–400 MeV and a 1 GeV injector. Evidently, the low-energy injector is less challenging and can be accomplished with a lower-energy laser driver. However, the GeV injector allows extra versatility for EuPRAXIA, such as enabling a lower transformer ratio or single-stage plasma wakefield acceleration. The GeV injector could also be directly used for some of the secondary applications proposed for the facility. Apart from the energy, the specifications for the electron beam produced by these two LPIs are similar, as summarised in Table 13.1.

## 13.2 Injection Mechanisms

To generate high-quality electron beams, the region over which injection occurs must be small and controlled. The latter implies that a large quantity of charge is placed into a small region of the accelerator, leading to small bunch energy spread and emittance. In addition, the injection ideally happens at a point that is both reproducible and repeatable, leading to high stability in energy and charge. The outcome should be a high-brightness beam with good shot-to-shot stability. LPI beams are most commonly generated by self-injection, whereby the plasma wave amplitude grows so large that wavebreaking can provide the trapped electrons [11,12,273]. This process, however, relies on the non-linear evolution of the laser pulse in the plasma and so can be sensitive to small changes in input parameters [274]. By tailoring the plasma source, injection can be decoupled from the laser pulse evolution, leading to increased stability.

Density-downramp injection can be used to decrease the plasma wave phase velocity over a specific region featuring a negative density gradient [15,275]. As the drive laser propagates through this region, the plasma wavelength increases, and so the back of the plasma wave moves at a reduced velocity. This temporarily decreases the potential required for trapping since a slower moving wave more readily accelerates particles to the velocity required to be trapped. Hence, injection can occur at lower plasma wave amplitudes than pure self-injection, so the electron beam quality can be higher. It also ensures that the injection is localised to the region of the density transition, thereby increasing energy stability [276]. In addition, by fixing the injection point physically in the plasma, the electron beam timing relative to the laser pulse is more precisely defined, allowing for a greater temporal synchronisation of subsequent stages.

Ionisation injection in a laser wakefield accelerator provides further control and increased flexibility by allowing injection only from a high-Z dopant gas species [277–280]. The dopant gas, e.g. nitrogen, is mixed to a concentration of a few percent in a background gas of hydrogen or helium. The outer levels of the dopant atoms are easily ionised at low intensity, and so the electrons are released in the rising edge of the laser pulse and form the plasma wakefield structure along with the electrons from ionisation of the H/He gas. However, the inner electrons of the high-Z dopant are only ionised near the peak of the laser and are therefore born inside the wakefield. They can then be born with a longitudinal velocity greatly different from the background plasma electrons which form the plasma waves. Hence, these electrons can be trapped at wave amplitudes well below the usual trapping threshold [281], and the process can be largely decoupled from the non-linear evolution of the laser pulse. The amount of trapped charge can be adjusted through control of the level of gas impurity, and the location of the injection can be controlled by allowing only a small physical extent to the mix region [282]. This process may also be further controlled by combining it with a negative density gradient to produce the highest level of control and stability.

Either mechanism or a combination of both can achieve the minimum requirements for the LPI stage. Ionisation injection, however, allows a far easier adjustment of electron beam charge and potentially greater stability of output beam parameters. In addition, a plasma source incorporating downramp injection may be easily modified to allow ionisation injection by merely changing the target gas to a mixture of species.

The LPI stage of EuPRAXIA will employ controlled injection. Both downramp and ionisation injection will be able to produce beams of acceptable quality. In addition, a combination of injection mechanisms could produce beams which can directly achieve the target parameters.

### 13.3 Low-Energy Plasma Injector

The plasma parameter range can be determined from simple considerations. Using scaling laws [185], for an LPI driven by a laser pulse with  $a_0 = 2$ , the plasma density required to achieve a 150 (400) MeV energy gain is estimated to be  $n_e \sim 5.0(1.9) \times 10^{18} \text{ cm}^{-3}$ , and the corresponding dephasing length is  $L_{\varphi} \sim 1.5(6.5) \text{ mm}$ . Short pulse Ti:sapphire laser drivers with power as little as 30 TW should be sufficient, though powers in excess of 100 TW provide greater versatility.

A crucial property of the electron bunch exiting the LPI is the emittance of the beam. To mitigate emittance growth at the exit of the injector, the density gradient at the plasma to vacuum transition should have a characteristic length larger than the betatron wavelength  $\lambda_{\beta} = \sqrt{2\gamma_e}\lambda_p$ , where  $\gamma_e$  is the electron Lorentz factor and  $\lambda_p$  the plasma wavelength [283].

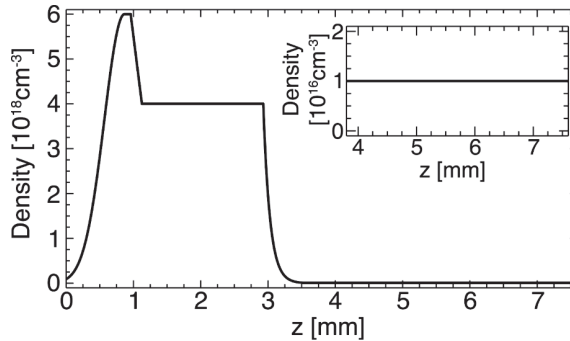


**Fig. 13.1.** Optimal plasma profile used in simulations for the LPI using a density downramp to inject the beam before further acceleration. The inset shows a zoom of the profile in the passive plasma lens region.

These values are indicative and will need to be tuned when the electron energy is specified. Published experimental or numerical results relevant to EuPRAXIA plasma properties [28,284,285] as well as specific simulation studies described below and in Chapter 23 are in agreement, giving confidence that these parameters can be achieved.

### 13.3.1 Simulation Results

Complementary to the scalings described above, three specific plasma injector scenarios were simulated using particle-in-cell codes. While injection using the resonant multi-pulse ionisation injection (ReMPI) technique is described in detail as part of the start-to-end simulations in Chapter 23.8, the following shows the predicted performance for an LPI based on density downramp and ionisation injection.

#### Density-Downramp Injection

This chapter presents simulation results for the injector stage where a plasma density transition is used to inject a bunch of electrons in the wakefield. After injection, the beam is accelerated for a few millimetres, reaching an energy of 250 MeV, and then is prepared to be captured at the transfer line after the plasma target. Below, the laser and plasma parameters used in our optimal simulation are described. The simulation was carried out with the PIC code OSIRIS (see Sect. 32.1 for details), and the beam parameters at end of the plasma (i.e., right before the transfer line) are presented.

The plasma profile is similar to the ones obtained in fluid simulations of gas cells [286], and it is shown in Figure 13.1. It consists of an upramp with a Gaussian profile and total length of 1 mm, where the density rises from 0 to  $6 \times 10^{18} \text{ cm}^{-3}$ . This is followed by a downramp with 150  $\mu\text{m}$  length, which brings the density to  $4 \times 10^{18} \text{ cm}^{-3}$ , where it reaches a plateau. As the plasma wave expands during the downramp, some electrons at the back of the wakefield are injected in the accelerating structure and form a beam. This beam is accelerated in the plateau for 1.8 mm. We considered a plasma exit with an exponential profile and a total length of 500  $\mu\text{m}$  coupled with a 5 mm long  $1 \times 10^{16} \text{ cm}^{-3}$  plasma, which works as a passive plasma lens (see inset of Fig. 13.1). The plasma exit and lens prepare the beam for the transport to the next acceleration stage.

The laser vacuum parameters are the following: wavelength  $\lambda = 800 \text{ nm}$ , pulse duration  $\tau_{\text{FWHM}} = 30 \text{ fs}$ , and beam waist and normalised vector potential at the

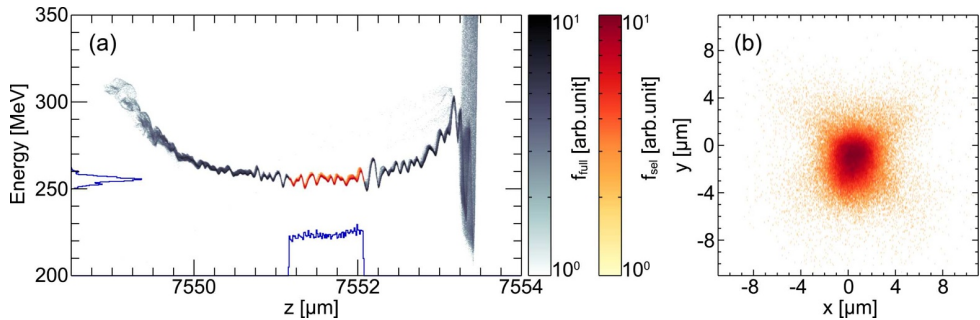


**Fig. 13.2.** Beam energy distribution along its length at the end of the density profile of Figure 13.1. The region highlighted in red (between circa 7551.1 μm and 7552.1 μm) is able to fulfill all the requirements for the injector stage. The blue curves along the energy- and z-axes are the integrated profile of the red region.

**Table 13.2.** LPI using a density downramp: beam parameters at the end of the plasma lens.

	Units	Values		Units	Values
<b>Energy</b>	MeV	255.3	<b>Energy Spread</b>	–	0.78%
<b>Charge</b>	pC	30.66	<b>Peak Current</b>	kA	10.22
<b>RMS norm. emittance x</b>	μm	0.13	<b>RMS norm. emittance y</b>	μm	0.16
<b>RMS <math>\gamma</math> Twiss x</b>	m <sup>-1</sup>	190.6	<b>RMS <math>\gamma</math> Twiss y</b>	m <sup>-1</sup>	181.9

focus of  $w_0 = 18 \mu\text{m}$ , and  $a_0 = 1.8$ , respectively. The laser is linearly polarised and focussed at  $200 \mu\text{m}$  into the plasma profile of Figure 13.1. Simulations show that the laser is greatly affected by the plasma; the normalised vector potential gets as high as  $a_0 \approx 4$  before the density downramp due to self-focussing.

The beam charge injected at the density transition is  $163 \text{ pC}$ . While beam loading for the whole beam was not achieved simultaneously, the accelerating field in the central region is nearly constant. If we observe the beam energy distribution along its length at the end of the plasma lens (Fig. 13.2a), the full beam profile (in grey) has regions of high energy spread at the leading edge and tail. In the centre, however, the energy spread is small. The region highlighted in red is able to fulfill all the requirements of the injector stage, as shown in Table 13.2. The integrated profiles for this section are shown in the blue curves in Figure 13.2a, and the transverse beam profile for the selected electrons is shown in Figure 13.2b. One possible way to separate the particles in this region from the ones at the leading edge and tail is the use of magnetic fields, which is possible because the electron energy is higher compared to the centre. The remaining unwanted electrons could be lost at the transfer line or the next plasma stage since they might not be matched to those elements. Details of such a scheme will be developed and tested as part of the technical design phase of EuPRAXIA.

### Ionisation Injection

A parametric study was carried out of the main physical parameters for ionisation injection in order to identify optimised configurations. For this parametric study, the laser is assumed to have a Gaussian form both in space and in time. Non-Gaussian forms will be considered in future studies. Except for this Gaussian form, specific care was taken in choosing configuration parameters already validated in experiments, both for the laser and for the target.

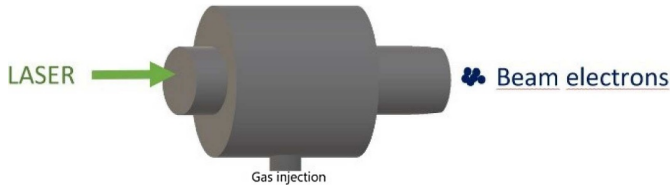


**Fig. 13.3.** Schematic view of the target cell used in the simulation.

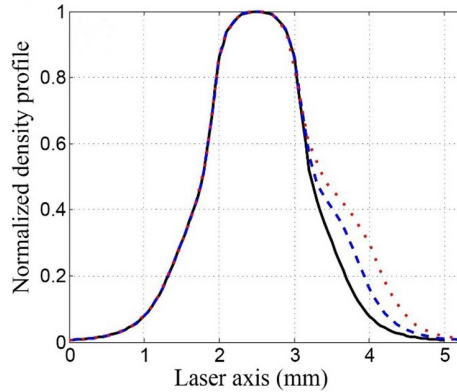


**Fig. 13.4.** Longitudinal density profile for different lengths of the exit tube: 500  $\mu\text{m}$  (black solid line), 750  $\mu\text{m}$  (dashed blue line), and 1000  $\mu\text{m}$  (dotted red line) [285].

As described above, in the ionisation injection scheme (IIS), the gas medium in the target is composed of hydrogen with a small amount of high-Z atom (generally nitrogen). If ionised by the laser, the inner-shell electrons of the high-Z atom are more easily trapped in the plasma wakefield. The laser intensity is then adjusted to trap and accelerate only these inner-shell electrons. A simple way for controlling the accelerated charge is through the percentage of the impurity gas. By increasing this percentage, the amount of trapped charge increases. Because the size and duration of the electron bunch should be kept at small values for accelerator applications, the increase in the trapped charge generates an increase in the space-charge fields. As pointed out in [281], when these space-charge fields become significant, their increase yields a reduction of the final electron energy and an enhancement of energy dispersion. The objective of this study is thus to perform a detailed quantitative analysis of this effect within a configuration in accordance with the EuPRAXIA requirements.

#### *Simulation parameters*

The laser configuration is similar to existing multi-TW laser systems. The laser wavelength is 0.8  $\mu\text{m}$ ; in the focal plane, its maximum intensity is  $5.5 \times 10^{18} \text{ W cm}^{-2}$  with a waist of 16  $\mu\text{m}$ . Its duration is 20 fs FWHM, resulting in a total energy of 0.47 J and a maximum power of 22 TW. The target gas cell is shown in Figure 13.3. It is similar to ELISA (ELECTron Injector for compact Staged high energy Accelerator), as described in [280]. It is composed of a central tube with a large radius and a variable length adjusted to a value of 1 mm to reach the required energy range. This cell is connected to the vacuum chamber through two tubes of 600  $\mu\text{m}$  in diameter. It has been verified experimentally that with this diameter, the tubes are not affected by the high-intensity laser. The length of the tube at the entrance is fixed at 500  $\mu\text{m}$ . Different tube lengths can be used at the exit to modify the density gradient. The density profile has been determined by fluid simulations using the OpenFoam

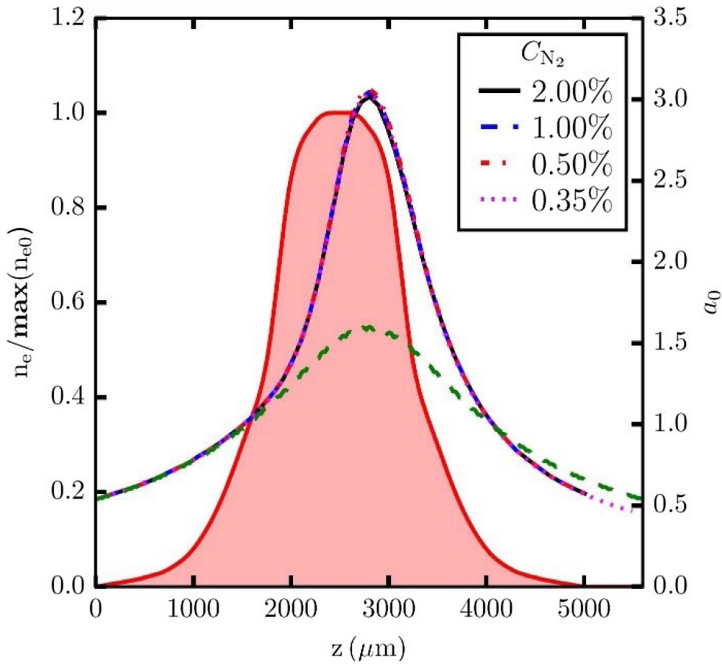


**Fig. 13.5.** Laser evolution inside the ionisation injection plasma target. The red area indicates the longitudinal density profile of the gas cell (left axis). The evolution of  $a_0$  (right vertical axis) in vacuum (dashed green line) and in plasma is shown for different values of CN2 [285].

software. Examples of the obtained density profiles are shown in Figure 13.4. The target gas is composed of hydrogen with a small percentage CN2 of nitrogen. Simulations have been performed for CN2 = 2, 1, 0.5 and 0.35%, keeping the density of all the outer-shell electrons constant, with a maximum value of  $4 \times 10^{18} \text{ cm}^{-3}$  electron density.

The numerical simulation has been performed with the PIC code Warp using the azimuthal Fourier decomposition algorithm in cylindrical geometry with 3 Fourier modes (0,  $\pm 1$ ) (see Sect. 32.1 for further details, also [287]), whereas field ionisation rates are calculated with the ADK model. In our PIC calculations, the numerical grid is a moving window  $130 \mu\text{m}$  in radius,  $58.4 \mu\text{m}$  in length, and with 36 macroparticles per species and per cell. The mesh resolution is chosen to be  $\lambda_L/25$  and  $\lambda_L/6$  in the longitudinal and transverse directions (with  $\lambda_L$  the laser wavelength). A mesh resolution of  $\lambda_L/30$  and  $\lambda_L/10$  has also been used for the most optimal case for confirmation and for a more precise evaluation of the second-order beam properties, such as the beam emittance. The calculations were performed on 140 cores at the Mésolum computing centre of University Paris-Sud and on 1000 cores of the Curie supercomputer at the TGCC-CEA centre. Using these machines, the required computing time for describing the 5 mm interaction length in the plasma was between 10,000 and 30,000 CPU hours.

### Results and discussion

In Figure 13.5, the evolution of the maximum normalised laser vector potential is reported for the different values of CN2. We observe that this evolution is nearly identical for all values. This indicates that by keeping the same total density of outer-shell electrons, the plasma wave is independent of CN2. It allows a direct

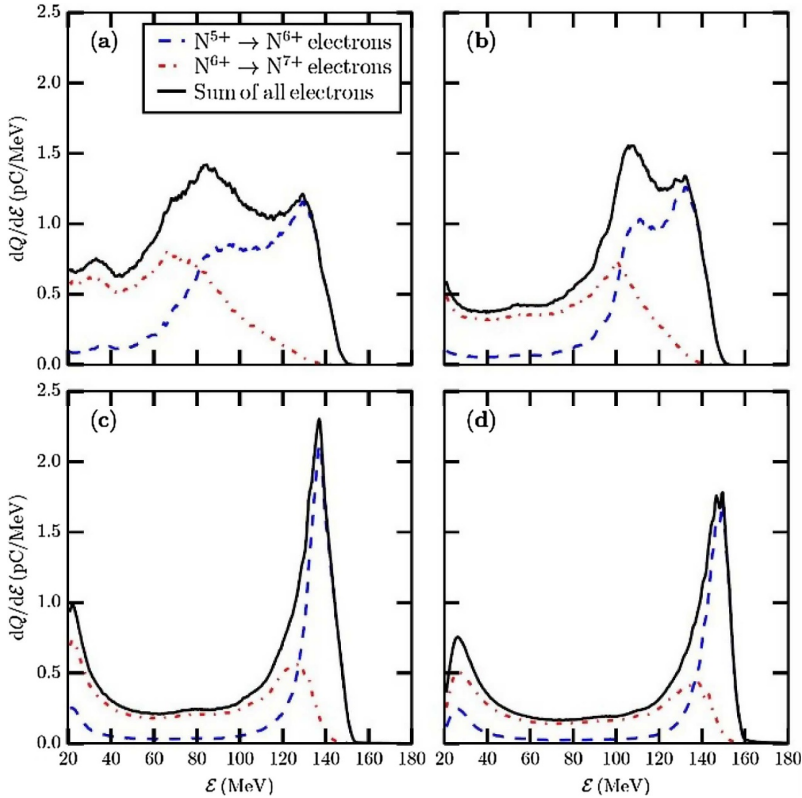


**Fig. 13.6.** Energy distribution of the electrons at the exit of the target. Each plot corresponds to a specific value of CN2. (a) 2%; (b) 1%; (c) 0.5%; (d) 0.35 % [285].

identification of the contribution of the space-charge field induced by the trapped electrons. The energy distributions of accelerated electrons at the exit of the injector for different values of CN2 are shown in Figure 13.6. We observe a strong influence of CN2 on the energy distribution. Figure 13.6 also shows that electrons coming from N6+ yield the main part of the low-energy pedestal. To obtain a low energy spread, their contribution has to be minimised by avoiding large laser intensities. The main characteristic of the high-energy peak, defined by the energy range of the maximum of the curve  $\pm$  the FWHM width, are reported in Table 13.3. As in [281], we observe a decrease in the average energy and an increase in the energy dispersion with CN2. Only the two smallest values of 0.5 and 0.35% have an energy spread within the EuPRAXIA requirements, as described in Chapter 23. Note that these values of CN2 are smaller than the ones reported in several experimental works. In particular, at CN2 = 1% the energy spread is already much too large. Looking at the other beam characteristics at CN2 = 0.35–0.5%, we observe that they are all in accordance with the EuPRAXIA requirements, except for the normalised emittance  $\varepsilon_{N,y}$  in the laser polarisation direction, which is larger by a factor of two. In fact in all calculations that we have performed for ionisation injection, a minimum value close to  $\varepsilon_{N,y} = 2$  mm mrad has been observed (see also [288]). This relatively large value of  $\varepsilon_{N,y}$  is mainly generated during the trapping process.

### Conclusions

A parametric study has been performed for the LPI with ionisation injection to determine the best conditions to meet the requirements of the EuPRAXIA design.

**Table 13.3.** Main characteristics of the electron bunch for different values of CN2.  $\langle E \rangle$ : average energy;  $Q$ : charge;  $\delta E$ : RMS width of the energy;  $\nu_{\text{arepsilon}} \epsilon_{N,x(y)}$ : normalised emittance;  $\theta_{x(y)}$ : RMS transverse divergence;  $\tau_t$ : RMS bunch length.

$C_{N2}$ (%)	$\langle E \rangle$ (MeV)	$Q$ (pC)	$\delta E / \langle E \rangle$ (%)	$\epsilon_{N,x}$ (mm.mrad)	$\epsilon_{N,y}$ (mm.mrad)	$\theta_x$ (mrad)	$\theta_y$ (mrad)	$\tau_t$ (fs)
2	93	108	29	2.6	3.9	4.5	5.6	7.0
1	114	72	15	1.9	2.3	3.7	4.0	3.4
0.5	135	37	5	1.1	1.9	2.8	3.1	3.0
0.35	142	27	4	0.8	1.8	2.2	2.9	2.9

We found that in our configuration, the space-charge field imposes a severe limitation on the beam charge, with a maximum value below 40 pC. For a charge between 20 and 40 pC, the properties of the electron bunch are within the EuPRAXIA requirements except for the normalised emittance in the laser polarisation direction, which is larger by a factor of two. Additional calculations also showed that the case with the lowest charge (here 27 pC) is the most robust when considering variations of the laser-plasma configuration. The next step will be to consider a more realistic description of the laser pulse by using data from experimental diagnostics. The final step will be devoted to a detailed analysis of the sensitivity of the injector performances on the fluctuations of the physical parameters (target and laser) planned as part of the technical design.

### 13.3.2 Plasma Structure

For a 150–250 MeV injector, a short plasma target of the order of 1 mm is considered. Both gas jets and gas cell targets could provide such a medium, and both have their own benefits (more details in Sect. 32.2). Gas jets exhibit an open geometry convenient for transverse probing and in-line density control. They can be used in conjunction with a sharp edge to generate a density transition to trigger electron trapping [284]. However, small-scale flow non-uniformities are thought to lead to a degradation of the injector’s electron beam quality [22]. Also, the typical sharp density gradients obtained from supersonic gas jets [289] are not adequate for mitigating emittance growth at the exit of the injector [283], which would reduce the coupling efficiency of the two stages.

To avoid emittance growth at the exit of the injector, the density gradient at the plasma-to-vacuum transition should have a characteristic length larger than the betatron wavelength  $\lambda_\beta = \sqrt{2\gamma_e} \lambda_p$ , where  $\gamma_e$  is the electron Lorentz factor of the accelerated electrons. In the case of 150 MeV electrons accelerated in plasma densities in the range  $n_e \simeq [10^{18}; 10^{19}] \text{ cm}^{-3}$ , the betatron wavelength is:

$$\lambda_\beta \simeq \begin{cases} 800 \mu\text{m} & \text{for } n_e = 10^{18} \text{ cm}^{-3}, \\ 253 \mu\text{m} & \text{for } n_e = 10^{19} \text{ cm}^{-3}. \end{cases}$$

Gradients with such characteristic lengths, larger than a few hundred  $\mu\text{m}$ , can be achieved in gas cells or capillaries by adjusting the geometry of the transition volume between the inside of the target and the vacuum of the experimental chamber. Cells with various geometries can be used to confine the gas, but the probing of density profiles is more challenging. However, the walls of the gas cell can be in proximity to the laser path and are thus more susceptible to laser ablation of the target in case of misalignment or poor laser beam quality. Clearly, in the context of EuPRAXIA, as

**Table 13.4.** Experimental parameters for the low-energy LPI.

Experimental parameter	Symbol	unit	LPI at 150 MeV	LPI at 400 MeV
Plasma electron density	$n_e$	$10^{18} \text{ cm}^{-3}$	3–8	3–5
Plasma length	$L_p$	mm	0.6–1.5	0.8–1.6
Exit gradient length	$L_{\text{grad}}$	$\mu\text{m}$	300–500	600–800
Laser intensity	$I_L$	$10^{18} \text{ Wcm}^{-2}$	4.2–16.8	15–43
Normalised vector potential	$a_0$		1.4–2.8	2.6–4.5

high reliability is necessary, laser stability and quality should be specified to be good enough for using gas cells.

Both gas cells and gas jets, being quite inexpensive to manufacture, could be implemented in the final design and even share the same target positioning system. However, a different gas injection and extraction system would be needed for each target due to the different backing pressure ranges required. In particular, gas jets typically produce greater demands on the vacuum pumping system, and added to the aforementioned concerns on stability, it is not recommended to use gas jets in the base configuration for the facility. This makes gas cells, fashioned either in capillaries or in a more open geometry, the baseline configuration for the LPI stages. The electron injection scheme considered for this stage – likely relying on density gradient injection, ionisation-induced injection, or a combination of both – should be readily implemented in these different cell configurations.

Table 13.4 summarises the experimental parameter ranges based on scaling laws and published results required to achieve the EuPRAXIA plasma properties for the low-energy injector. It also gives the exit gradient length corresponding to the density range and electron energy.

Both gas cell and capillary targets would be suitable for the low-energy injector. Published results with existing laser systems show that generating these beams is possible with present experimental techniques.

### 13.4 GeV Plasma Injector

Similar to the considerations for the low-energy injector, we can determine experimental parameters to achieve 1 GeV electron beams at the exit of the LPI through scaling laws [185] and published results [19,290]. These well-studied results fix the density and plasma length. The requirements for mitigation of the emittance growth at the exit of the injector are also pertinent for the 1 GeV LPI. However, as the electron energy is higher, the exit gradient section has to be longer.

The length of the 1 GeV injector stage will range between 10 and 40 mm depending on the plasma density lying between  $\sim 1 \times 10^{18} \text{ cm}^{-3}$  and  $\sim 4 \times 10^{18} \text{ cm}^{-3}$ . Laser power between 40 and 250 TW has been reported as necessary to reach these output energies [19,290], though it is likely that powers in excess of 100 TW will be required to be less dependent on non-linear laser evolution [290]. Nevertheless, for the length of target being considered here, it may be preferable to house the injector in some form of laser-guiding structure, such as a capillary discharge or capillary tube. This, though, must be weighed against the potentially shorter lifetimes of these devices as compared to open gas cells. Injection will be achieved in a similar way to the low-energy injector, i.e. ReMPI, downramp, ionisation injection, or a combination of these two schemes. The particular scheme in use will depend on the specific application of the injector and whether one wants to optimise a particular parameter such as charge, energy spread, etc.

**Table 13.5.** Experimental parameters for the 1 GeV LPI.

Experimental parameter	Symbol	unit	LPI at 1 GeV
Plasma electron density	$n_e$	$10^{18} \text{ cm}^{-3}$	1–6
Plasma length	$L_{\text{acc}}$	mm	9–30
Exit gradient length	$L_{\text{grad}}$	mm	0.9–2.1
Laser intensity	$I_L$	$10^{18} \text{ Wcm}^{-2}$	3.1–32.5
Normalised vector potential	$a_0$		1.2–3.9

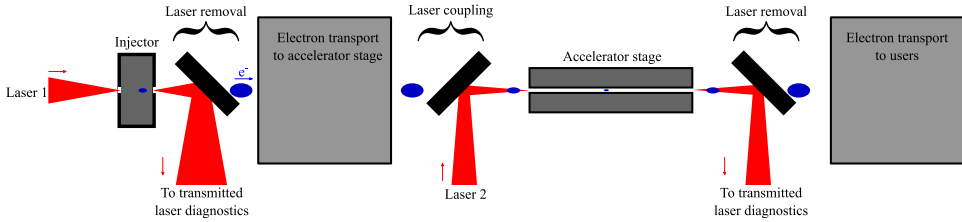


**Fig. 13.7.** Schematic of the laser removal and coupling in a multi-stage configuration.

The emittance growth considerations at the exit of the plasma also apply for this stage, and as the betatron wavelength scales as  $\lambda_\beta \propto \gamma_e^{1/2} n_e^{-1/2}$ , the exit gradient length should be longer. For 1 GeV electrons and plasma electron density in the range  $n_e \simeq [10^{18}; 4 \times 10^{18}] \text{ cm}^{-3}$ , the betatron wavelength is:

$$\lambda_\beta \simeq \begin{cases} 2 \text{ mm} & \text{for } n_e = 10^{18} \text{ cm}^{-3} \\ 1 \text{ mm} & \text{for } n_e = 4 \times 10^{18} \text{ cm}^{-3} \end{cases}$$

Table 13.5 shows the experimental parameter range to achieve the EuPRAXIA plasma properties for the 1 GeV LPI. Note that in the range indicated in Table 13.5, the higher values of  $a_0$  correspond to the shortest plasma length because of a larger accelerating field. These values may need to be tuned to meet all EuPRAXIA target properties.

The GeV stage will share some commonality with the low-energy stage but ideally would be driven at higher laser power (>250 TW). Efficiency and reliability in beam pointing can be enhanced by using a guiding plasma target but will result in more regular target replacement.

### 13.5 Implementation in the EuPRAXIA Beamline

#### 13.5.1 Staging Requirements

As schematically presented in Figure 13.7, after each plasma stage, the transmitted laser light has to be removed from the axis, and the laser driving the following stage has to be coupled into the plasma. The high intensities limit the proximity of the removal/coupling device to the plasma target, whereas the electron transport prescribes that the electron capture should be as close to the plasma as possible to limit the emittance growth (see [291]). As a mirror placed close to the laser focus would suffer damage from heating and ionisation, plasma mirrors are considered as a solution to remove the laser from the electron axis.

### 13.5.2 Laser Removal

After the LPI interaction, a significant fraction of the laser pulse energy remains and is capable of damaging downstream components. The most compact way to remove the laser pulse is to use a thin mirror to reflect the laser pulse shortly after the interaction. The foil will be damaged upon reflecting and absorbing the laser, and so must be rapidly replenished. A commonly used device for this purpose is a tape drive, which allows a thin foil to be easily translated between shots so that each laser pulse interacts with a fresh surface. A similar device can be used for laser in-coupling for later laser-plasma accelerator stages. However, in the case of out-coupling, since all that is being reflected is spent laser energy, it is not necessary to have a high reflectivity or good reflected wavefront quality as long as the transmitted energy is low. Hence the requirements here are not as demanding.

A metal-coated plasma tape can be used, with the substrate ( $\sim 10\ \mu\text{m}$ ) and metal coating ( $\sim 20\ \mu\text{m}$ ) kept as thin as possible to reduce scattering of the traversing particle beam. It may be necessary to allow some drift space at the end of the plasma source so that the plasma density at the foil surface is low. Otherwise, a wakefield driven by the reflecting laser pulse may interact with the electron bunch and reduce its beam quality. This distance will be determined by the plasma density profile at the gas cell exit, and the tape itself will add a further  $\sim 5\ \text{mm}$  drift space to the first electron capture optic. Therefore, the total distance before the next downstream element will be 5–10mm depending on the LPI scheme employed. A beam pipe will be required to propagate the laser pulse in vacuum until the laser intensity has dropped sufficiently to be absorbed by a permanent laser dump.

There remains a possibility for the electron beam quality to be degraded because of bremsstrahlung or by interaction with the fields generated by the laser at the beam dump. Further studies will be required to determine the effect of this interaction and if any steps are required to minimise potential adverse effects.

Laser drivers require the coupling of the optical pulses to the accelerator beamline. For removing spent laser energies, plasma mirrors can be used with little drawback.

### 13.5.3 Stability

In order to achieve reproducibility of the electron energy from shot to shot, the external electron beam issued from the LPI should be injected in the same phase-space volume of the LPAS with every shot. This implies a need to control the position of the injected electron beam relative to the plasma wave, both transversely and longitudinally. This is determined by the pointing stability, and relative timing jitter of the laser driver *as well as* the pointing stability, transverse emittance, and timing jitter of the generated electron beam. The reproducibility of the plasma wave amplitude is controlled by the reproducibility of laser intensity and plasma electron density.

Table 13.6 summarises the main parameters of interest for the generated electron beam on the left, and the accelerator properties that have a direct influence on their stability on the right.

### 13.5.4 Repetition Rate

To achieve a high-repetition-rate operation of gas targets in a high-vacuum environment, it may be necessary to use differential pumping to reduce the gas load on the main chamber. This has been demonstrated with a 5 Hz gas jet in laser-plasma

**Table 13.6.** Beam parameters and the accelerator properties that impact their stability.

Beam parameter	Injector and accelerator constraints
Particle energy	Accelerating phase stability Drive laser stability Beam loading effect Plasma density and length stability
Bunch charge	Laser stability at injection Plasma properties at injection
Emittance	Laser and plasma properties at injection Plasma matching sections
Transverse size	Laser beam quality Transverse density profile Longitudinal density profile
Divergence	Laser pointing stability Input electron pointing stability Plasma transverse gradient stability Laser pulse front tilt stability

experiments at the CLF [292] and LWFA experiments at LUX [66]. The LUX design uses a continuous flow target and a differential pumping system which can achieve  $10^{-6}$  mbar vacuum pressures at a distance of 1.5 m from the plasma source. Adopting such an approach would allow for a very-high-repetition-rate operation, limited by recombination and pressure equilibration time, and provides compatibility with accelerated beamline vacuum requirements. However, gas jet targets generally produce high loads on the vacuum system, and smaller targets, such as gas cells and capillaries, can significantly reduce pumping requirements. However, as noted before, this must be weighed with the potentially shorter life-times of such targets. Further tests will be required to determine how to construct a tailored plasma structure in a way which is robust to laser damage. This will be critically important for continuous high-repetition-rate performance with petawatt-class laser systems, such as may be used for the GeV LPI stage.

Numerous factors can affect the repeatability and control of plasma accelerators, and EuPRAXIA should demand state-of-the-art control on all of these parameters.

## 13.6 Conclusion

Though LPI electron sources have only been demonstrated relatively recently as a source of high-energy electrons, they may offer remarkable benefits to the proposed EuPRAXIA beamlines. Their unique nature promises short, relatively high-brightness electron beams in an extremely compact configuration. This can have important beneficial repercussions for the delivery of EuPRAXIA beams, especially to other laser-driven accelerator structures. Furthermore, not only are they suitable for injection into successive plasma accelerator stages, but also, given their potentially high currents, they can be considered as drivers for plasma wakefield stages (see Chap. 26).

However, the novelty of these structures also produces many challenges. Transporting the short and often divergent beams produced in LPIs will be a challenge, especially while maintaining their ultra-short duration. Also, whilst many of the properties required for the EuPRAXIA injectors have been reached in proof-of-principle

experiments, no single experiment has yet simultaneously achieved all of the necessary parameters in one demonstration. Furthermore, most of these experiments have taken place at existing high-power laser facilities where shot-to-shot reproducibility is not emphasised.

Clearly, whilst the methodology is demonstrated and injectors for high-quality beams can be produced in simulation, the direct regular operation of LPIs suitable for EuPRAXIA is a remaining challenge to demonstrate during the technical design phase.

## 14 RF Photo-Injector

### 14.1 Introduction

Multi-GeV acceleration, both laser- and particle-beam-driven, has been already demonstrated in cm-scale plasma structures [11,45,290,293]. Great efforts are currently ongoing in several groups [294–297] worldwide for the acceleration of high-brightness electron beams, which need to be captured from plasma or RF injectors. In all cases, the control of electron injection into the plasma accelerator module is mandatory for efficient acceleration; the beam must satisfy the transverse matching condition at the plasma entrance to prevent envelope oscillations that may cause emittance growth. In particular, the following condition for the Twiss parameters of the witness beam holds in the blow-out regime and assuming negligible beam loading [298]:

$$\beta_{\text{matching}} = \frac{\sqrt{2}\gamma}{k_p} \quad (14.1)$$

where  $k_p = 2\pi/\lambda_p$  is the inverse plasma skin depth, with the plasma wavelength depending on the plasma background density as  $\lambda_p(\mu\text{m}) \sim 3.3 \cdot 10^{10} n_p^{-1/2} (\text{cm}^{-3})$ ;  $\gamma$  is the Lorentz factor for the electron beam. The matching condition for the beam transverse size is:

$$\sigma_{\text{matching}} = \sqrt{\frac{\beta_{\text{matching}} \varepsilon_n}{\gamma}} \quad (14.2)$$

with the typical numbers involved, e.g.  $\gamma=1000$ ,  $n_p=10^{16} \text{ cm}^{-3}$ , and  $\varepsilon_n=1 \text{ mm mrad}$ ; the beam transverse size is of micrometre scale.

Here, a fully external injection scenario is considered, meaning that bunches (witness for the LWFA case and both driver and witness for the PWFA case) are externally produced by an RF photo-injector and then delivered to the plasma-accelerating section (Schemes 3 to 5, as described in Chap. 8). Studies for the accelerator and start-to-end simulations of the electron beam dynamics from the photo-cathode to the plasma entrance have been performed by means of numerical codes, and they are described in detail in the following sections.

Beam parameters – e.g. charge, emittance, peak current, and energy spread, except for the final energy – must be guaranteed at the plasma entrance.

Concerning the LWFA case (Scheme 3: RFI-500 MeV + LPAS-5 GeV and Scheme 4: RFI-240 MeV + LPAS-2.5 GeV + chicane + LPAS-5 GeV), we have investigated two methods for satisfying the requirements on the peak current, thus on the bunch length, while preserving the beam quality. One method is based on a full RF compression scheme, occurring in the first two S-band traveling wave (TW) sections, and a boost to a final energy of about 500 MeV in the X-band linac. The second method is based on a hybrid compression scheme, combining moderate RF compression in the first S-band TW section and magnetic compression at higher energy through a

**Table 14.1.** Target values for the 1 GeV electron beam parameters to drive a SASE FEL.

	<b>Units</b>	<b>1 GeV case</b>
<b>Bunch charge</b>	pC	30
<b>Peak current</b>	kA	3
<b>Repetition rate</b>	Hz	10
<b>RMS normalised emittance</b>	$\mu\text{m}$	1
<b>RMS energy spread</b>	%	1
<b>RMS bunch length</b>	fs	10
<b>Slice normalised emittance</b>	$\mu\text{m}$	<1
<b>Slice energy spread</b>	%	0.1
<b>Slice length</b>	$\mu\text{m}$	0.75
<b>Radiation wavelength</b>	nm	4
<b>Pierce parameter <math>\rho</math></b>	$1 \times 10^{-3}$	>1
<b>Undulator period</b>	cm	1.5
<b>Undulator strength K</b>		0.872

chicane. The two methods have been optimised for slightly different layouts, but with proper design, only one layout could host both compression schemes.

## 14.2 Laser-Driven External Injection Scheme

In this section, we will discuss two possible RF injector layouts for the successful operation of a laser-driven wakefield accelerator (LWFA), based on the external injection of high-brightness electron bunches (Scheme 3: RFI-500 MeV + LPAS-5 GeV and Scheme 4: RFI-240 MeV + LPAS-2.5 GeV + chicane + LPAS-5 GeV). The requirements at the plasma-accelerating module for the 1 GeV case have been identified in the framework of the EuPRAXIA collaboration and are listed in Table 14.1.

The two layouts differ in the compression scheme adopted for the achievement of kA peak current, while preserving the normalised transverse emittance at the plasma entrance.

## 14.3 Full RF Compression Scheme

At the EuPRAXIA facility, the main challenge for the RF photo-injector comes from the request of producing ultra-short, high-quality electron beams. A case of interest foresees 500 MeV witness beam energy at the plasma interface, with a slice emittance of much less than 1 mm mrad and 30 pC charge in a 10 fs FWHM length, which turns into a peak current of up to 3 kA. Except for the final energy, these parameters are those requested to generate SASE FEL radiation at 3 nm with a 1 GeV electron beam.

A pure RF compression, applying the velocity-bunching scheme, has been considered to produce in one stage a 3 kA beam at the end of the S-band TW sections with 100 MeV.

High-quality electron beams can be achieved in RF photo-injectors by means of RF guns, equipped with laser-driven photo-cathodes, followed by booster sections. An emittance compensation scheme [258] based on a focussing solenoid at the exit of the RF gun can be used in photo-injectors to control emittance growth from space-charge effects. In addition to the invariant envelope theory [299], a proper matching of the

transverse phase space of the electron beam, injected in the downstream accelerating sections (booster), can help to control the transverse emittance oscillations during the acceleration. Under the conditions of an invariant envelope and proper phasing of space-charge oscillations [300], the final emittance is almost compensated down to the thermal emittance value given by cathode emission with an expected emittance scaling like  $\varepsilon_n \sim \sigma_{cath} \sim \sqrt{Q}$ , where  $\sigma_{cath}$  is the laser spot size on the photocathode, and  $Q$  the extracted electron charge. A compression stage can be employed to shorten the beam length so as to achieve the required high peak current. The so-called velocity-bunching method [301] has opened up a new possibility of compressing the beam inside an RF structure and, when integrated in the emittance compensation process [260], can provide the desired bunch current values with the advantage of compactness of the machine and the absence of coherent synchrotron radiation (CSR) effects present in a magnetic compressor [302].

It is interesting to notice that a shortened beam length also permits the containment of the energy spread dilution due to RF curvature degradation; indeed, the energy spread depends on the bunch length,  $\sigma_z$ , and the accelerating frequency,  $f_{RF}$ , as  $\frac{\Delta\gamma}{\gamma} \sim 2(\pi f_{RF} \sigma_z / c)^2$ , where an on-crest operation in full relativistic conditions has been considered. To avoid the energy spread dilution from RF curvature degradation effects, a bunch length of  $\sigma_z \leq 130\mu\text{m}$  must be injected in the X-band linac, ensuring  $\frac{\Delta\gamma}{\gamma} \leq 0.1\%$ .

One proposed layout for the EuPRAXIA photo-injector is based on the experience at the SPARC\_LAB test facility [296] in operation at INFN laboratories at Frascati, and devoted to plasma-based experiments [303–305], both to accelerate and focus charge particle beams, and to generate advanced radiation, such as from a multi-color FEL [306–309],  $\gamma$ -rays through Thomson backscattering [310,311], and both broad- and narrow-band high-peak-power THz radiation [312,313].

The layout of the S-band photo-injector [314], operating at 2.856 GHz, is shown in Figure 14.1; it consists of a 1.6-cell UCLA/BNL/SLAC-type standing-wave RF gun, including a copper photo-cathode with an emittance-compensating solenoid followed by 3 m long SLAC-type travelling-wave sections operating at 2.856 GHz [262]. The first two accelerating sections are embedded by a solenoid; each solenoid is composed of 13 coils, with the first coil and the other twelve coils, in groups of three, independently supplied. The beamline matching foresees a proper set of the emittance compensation solenoids and of the S-band cavity gradients in the velocity-bunching scheme [301], according to the invariant envelope criteria [299]. In this configuration, the first and second TW sections can operate far from the crest in the velocity-bunching regime, enabling the RF compression of the beam length, while the third section operates almost on crest to let the electron bunch gain energy and freeze its phase-space quality.

The main operating parameters of this EuPRAXIA photo-injector for the optimised witness beam in case of LWFA in external injection are summarised in Table 14.2.

A photo-cathode laser pulse with a Gaussian longitudinal profile of RMS length of  $\sigma_z = 105\mu\text{m}$  and a transverse uniform distribution with a spot size  $\sigma_r = 175\mu\text{m}$  has been chosen, as reported in Figure 14.2. The velocity-bunching regime is applied to the first two S-band structures to shorten the beam length from  $102\mu\text{m}$  (on crest) to  $\sim 3\mu\text{m}$  (RMS), both cavities working close to the zero crossing of the field. The emittance minimisation is obtained, setting the gun solenoid at  $\sim 3\text{ kG}$  and those surrounding the first and second S-band cavities at  $0.32\text{ kG}$  and  $0.50\text{ kG}$ , respectively. A slightly off-crest operation of the third S-band cavity further reduces the energy spread at the injector exit. In this configuration, the design electron beam parameters at the photo-injector exit are listed in Table 14.3, as obtained from beam dynamics

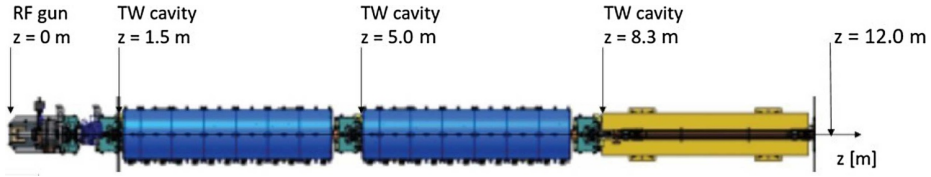


**Fig. 14.1.** Layout of the SPARC-like RF photo-injector: a 1.6 cell UCLA/BNL-type SW RF gun, equipped with a copper photo-cathode and an emittance compensation solenoid, followed by three S-band TW SLAC type sections; another two compensation solenoids surround the first and the second structures for the operation in the velocity-bunching scheme.

**Table 14.2.** Main photo-injector parameters.

Parameter	Unit	Value
Gun electric field amplitude	MV/m	120
Gun electric field operation phase	deg	30
Output gun beam energy	MeV	5.6
Amplitude of electric field in the three TW sections	MV/m	20.0/20.0/28.0
Magnetic field in the emittance compensating solenoid	kG	3.05
Magnetic field in the linac solenoids	kG	0.32/0.50
Total photo-injector length	m	12

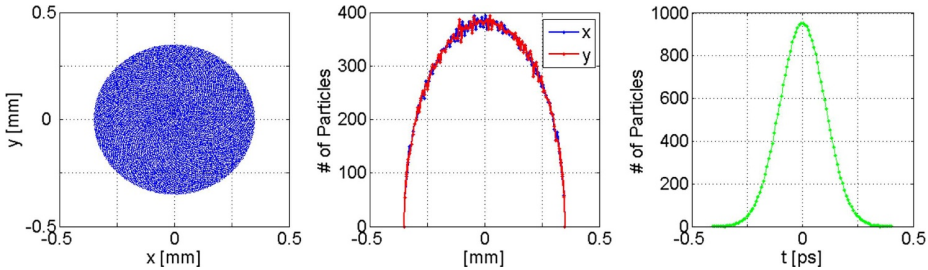


**Fig. 14.2.** Charge distribution at the cathode surface produced by the photo-cathode laser pulse, as obtained with 2D TStep simulations.

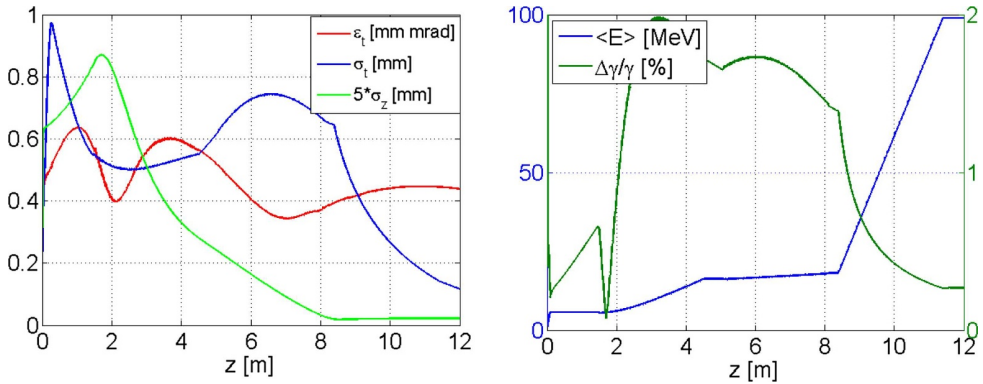
simulations using 30k macro-particles with the code TStep [315]. The simulation results are shown in Figure 14.3 for the optimised witness-like beam; the left plot shows the evolution of the transverse normalised emittance (red line), spot size (blue line), and longitudinal bunch length (green line), while the right plot illustrates the energy (blue line) and energy spread (green line) from the cathode down to the photo-injector exit, as obtained with the TStep code.

The longitudinal and transverse phase spaces at the photo-injector exit are reported in Figure 14.4. The longitudinal profile of the beam exiting the photo-injector is typical of the velocity-bunching process showing a spike of current at the head of the bunch and a long tail, with a FWHM bunch length of 3  $\mu\text{m}$ .

The 100 MeV beam exiting the photo-injector is then matched to the X-band linac to boost the energy up to about 500 MeV. The X-band linac mainly consists of two sections located before and after the magnetic chicane, named as L1 and L2, respectively. Twelve X-band accelerating sections, 50 cm long, are foreseen for L1 and twenty for L2. According to the RF power system design, the maximum accelerating gradient applied might be up to  $\sim 80$  MV/m. For the study of this working point, a more conservative accelerating gradient,  $\sim 60$  MV/m, has been considered. Between

**Table 14.3.** Witness beam parameters at the end of the photo-injector in the case of pure RF compression.

Parameter	Unit	Value
Charge	pC	30
Energy	MeV	100
RMS energy spread	%	0.27
RMS bunch length	fs	10
Peak current (FWHM)	kA	4.0
RMS normalised emittance	mm mrad	0.44
Repetition rate	Hz	10

**Fig. 14.3.** Evolution along the injector of the electron beam transverse normalised emittance ( $\epsilon_T$ , red line), envelope ( $\sigma_T$ , blue line), and longitudinal bunch length ( $\sigma_z$ , green line), as obtained with the TStep code in the case of pure RF compression. The right-hand plot shows the evolution of mean energy ( $\langle E \rangle$ , blue line) and energy spread ( $\Delta\gamma/\gamma$ , green line).

L1 and L2, a 10 m long magnetic chicane is foreseen for phase-space manipulation and / or longitudinal compression of the bunch in case hybrid compression schemes want to be addressed; at the same time, when the chicane dipoles are switched off, the straight beamline accommodates the middle energy diagnostic station for beam parameter measurements. Note that this setup is somewhat different from the minimum linac configuration described in Chapter 12. Compared to the latter, a longer X-band section was chosen in this particular design to allow more flexibility in selecting between different compression schemes and beam energies (through variations in the accelerating gradient) without underestimating the potential linac length in the final design.

The following simulations have been performed with the chicane between the two linac sections off. The two linac sections L1 and L2 have been optimised to provide the required beam acceptance, from the photo-injector and after the magnetic chicane, for the considered working points described in this chapter; the best focussing strength for the lattice has been found with a betatron phase advance per cell of  $15^\circ$  and  $28^\circ$  for L1 and L2, respectively. In Table 14.4, the L1 and L2 main parameter list is reported.

For this working point, the X-band RF linac is meant to provide at the plasma module an electron beam of  $Q = 30$  pC,  $I = 3$  kA (FWHM), with a transverse spot size of  $4\ \mu\text{m}$ ; the electron bunch is fully compressed in the photo-injector by means of the velocity-bunching operation scheme. An accelerating gradient of  $E_{\text{acc}} \sim 20\text{--}36\text{m}^{-1}$

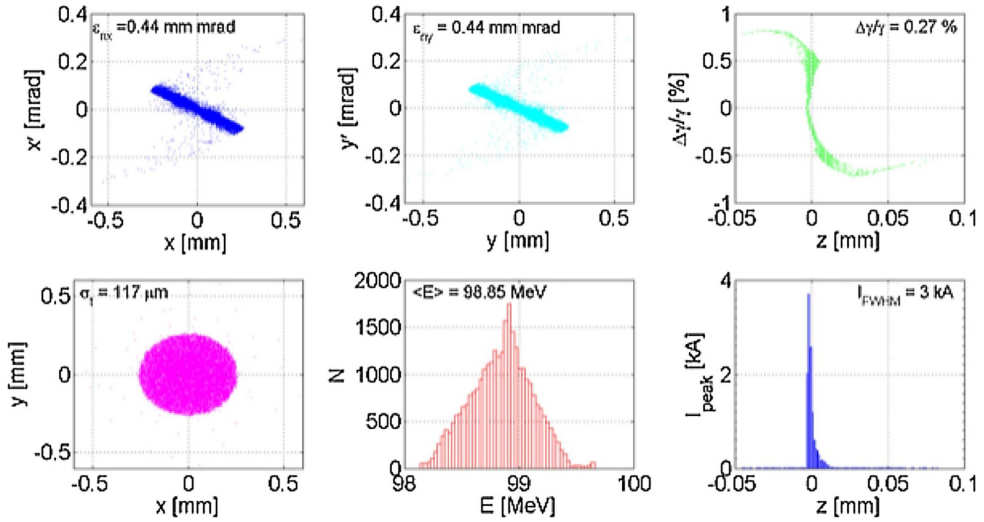


**Fig. 14.4.** Upper plots: transverse and longitudinal phase spaces. Lower plots: transverse (x and y) distribution, energy, and current profile. The results are outputs from the TStep code at the photo-injector exit.

**Table 14.4.** L1 and L2 linac parameter list.

Beam Parameter	Unit	L1	L2
		LWFA	PWFA
Initial energy	GeV	0.098	0.212
Final energy	GeV	0.212	0.550
Active linac length	m	6.0	10.0
Accelerating gradient	MV/m	20.0	36.0
RF phase (0 crest)	deg	-20.0	-19.5
Initial energy spread	%	0.27	0.15
Final energy spread	%	0.15	0.07
Final bunch length	mm	0.005	0.005

is applied in the L1 and L2 linac sections, respectively (see Tab. 14.4), and the final electron beam energy is  $E_{L_2\text{exit}} \sim 550$  MeV, with an energy spread of less than 0.1% (Fig. 14.5).

Before entering the plasma capillary, a focussing triplet of permanent magnet quadrupoles (PMQ) is foreseen at a distance of a few centimetres from the plasma entrance to obtain a typical  $\beta_{x,y} \sim 1\text{--}5$  mm. The gradient of the first three PMQs is around  $G \sim 300$  T/m with a magnetic length of 5–10 cm; the emittance dilution due to chromatic effects in the quadrupoles is the main concern of the final focussing stage. A longitudinal position adjustment setup to tune the strength of the final focus array and latest generation of tunable permanent quadrupoles are under study to increase as much as possible the tunability of the magnet arrangement and widen the energy acceptance of the transfer line.

This working point for the RF photo-injector has been optimised and validated by means of its integration into a start-to-end simulation, which included the plasma-accelerating module and the matching sections to provide the complete evolution of the bunch transverse and longitudinal properties from photo-cathode to the undulator entrance; the results are reported in Figures 14.6 and 14.7, respectively.

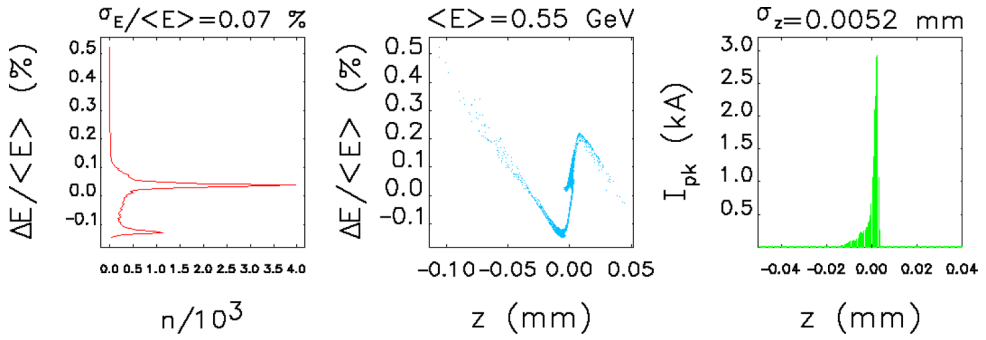


**Fig. 14.5.** Longitudinal phase space of the LWFA-accelerated electron beam at the L2 linac exit.

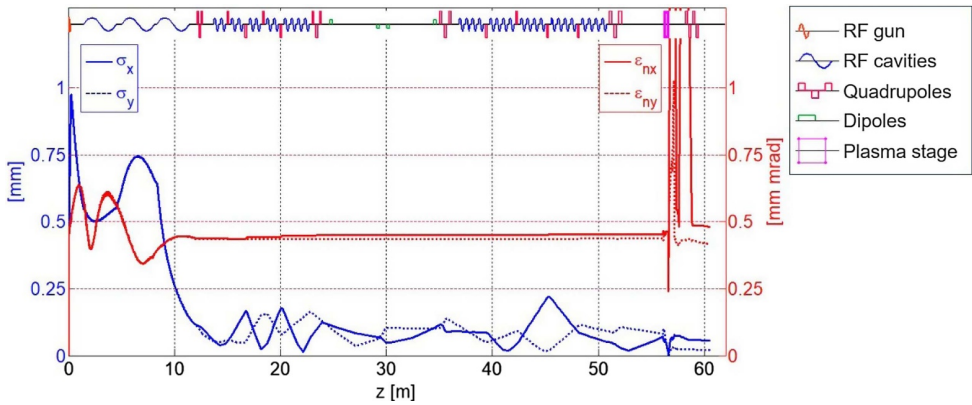


**Fig. 14.6.** Start-to-end simulation results for the witness bunch from the photo-cathode to the undulator entrance: evolution of the electron beam transverse normalized emittance ( $\epsilon_{nx}$  red line,  $\epsilon_{ny}$  red dotted line) and spot sizes ( $\sigma_x$  blue line,  $\sigma_y$  blue dotted line).

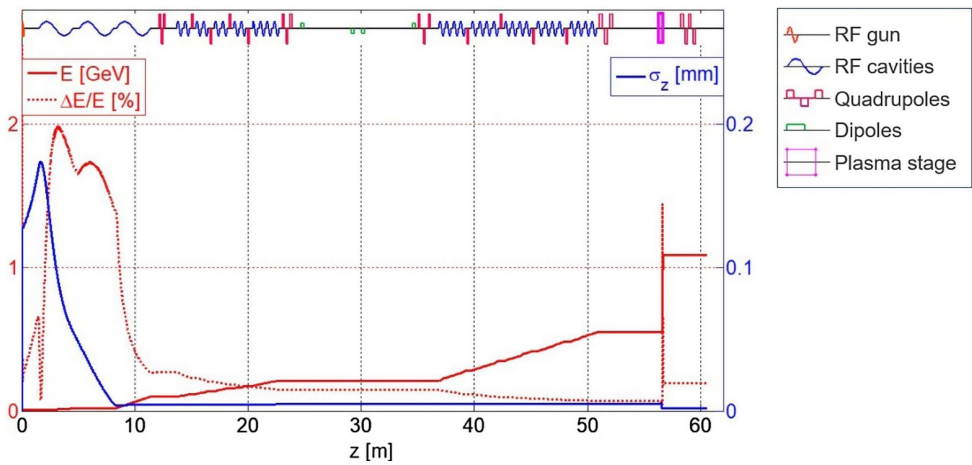


**Fig. 14.7.** Start-to-end simulation results for the witness bunch from the photo-cathode to the undulator entrance: evolution of the energy ( $E$  red line) and energy spread ( $\Delta E/E$  red dotted line) as well as longitudinal bunch length ( $\sigma_z$  blue line).

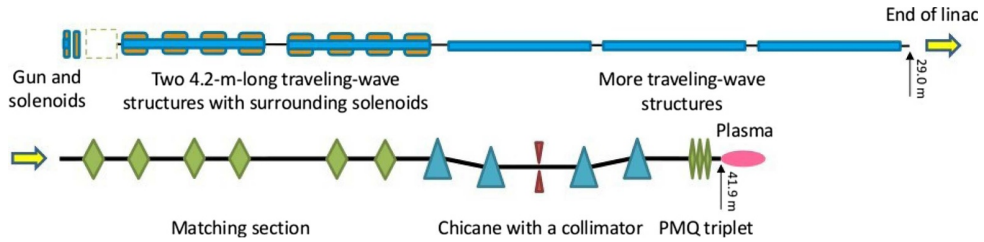


**Fig. 14.8.** Injection layout for the hybrid compression scheme.

#### 14.4 Hybrid Compression Scheme

An alternative to full RF compression is the integration of a hybrid compression scheme, consisting of RF based at low energy and magnetic based at higher energy, to finalise the longitudinal compression. In this regard, the layout of the RF photo-injector is based on the ARES linac [316] at the SINBAD facility [317], hosted by DESY Hamburg.

The layout of the proposed RF injector is shown in Figure 14.8. The electron bunch generated by the 1.5-cell S-band photo-cathode RF gun is velocity bunched and accelerated by five 4.2 m long S-band traveling wave structures. The first two structures are surrounded by solenoids in order to provide better emittance compensation and focussing. Afterwards, the bunch is matched into the magnetic chicane compressor with an  $R_{56}$  of about 9 mm for further compression. To match the electron beam at the plasma module, the final focus section consists of a triplet of permanent magnet quadrupoles (PMQ) 3 cm in length and with gradients of 300 T/m, 600 T/m, and 600 T/m, respectively.

The electron bunch is compressed using a two-stage hybrid compression scheme, i.e. the beam is compressed by means of velocity bunching [260] in the first S-band structure and magnetic compression successively. The initial bunch charge at the photo-cathode is 50 pC; to meet the beam requirements at the plasma module (see Tab. 14.1) and, in particular, a bunch charge of 30 pC, a slit collimator is located in the middle of the chicane with a full width of 0.6 mm. Situated at a position of maximum horizontal dispersion inside the chicane, the slit collimator is used to control both charge and bunch length by allowing only the central slice of the dispersed bunch to pass through [318,319]. The two-stage compression scheme, with a slit collimator integrated in the magnetic chicane, also helps to reduce the non-linearity of the longitudinal phase space in case strong bunch compression is required (i.e.  $\sim$  fs bunch duration). Compared to the pure magnetic compression scheme, the hybrid compression scheme has a much lower charge loss at the slit collimator. In addition, since a much smaller amount of charge is required to be extracted from the photo-cathode, the beam emittance will be smaller. Finally, this scheme helps to reduce both the energy and peak current jitter after bunch compression [318]. The energy jitter affects the longitudinal location of the focal point, while the peak current jitter affects the beam loading effect as well as the FEL output after the LWFA stage.

Preliminary studies have been performed to define the minimum injection energy at the plasma module based on the requirements listed in Table 14.1, in particular to guarantee at the plasma entrance the 3 kA peak current,  $<1$  mm mrad slice normalised emittance, and  $\ll 1\%$  energy spread needed to drive a SASE FEL. In addition, to meet the plasma matching condition of equation (14.2), the transverse beam size must be in the  $\mu\text{m}$  range. Afterwards, start-to-end simulations have been performed by using the combination of two codes. The beam dynamics from the photo-cathode to the linac exit was simulated using ASTRA [320] with a two-dimensional

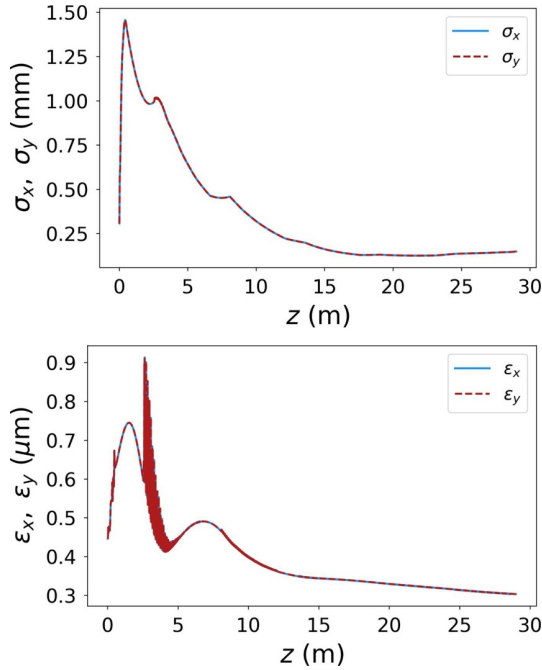


**Fig. 14.9.** Evolution of the transverse beam size and the normalised emittance (here defined as  $\epsilon_{x,y}$ ) from the photo-cathode to the linac exit.

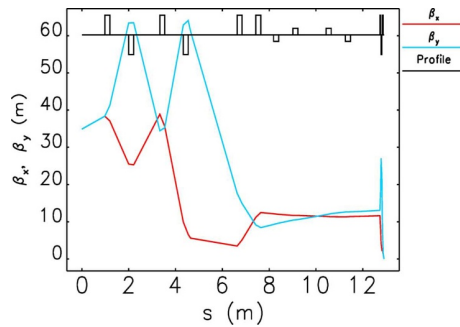


**Fig. 14.10.** Beam optics from the linac exit to the injection point.

cylindrical-symmetric space-charge algorithm. Afterwards, it was simulated up to the plasma by using IMPACT-T [321] with a 3D space-charge algorithm and 1D CSR model. The photo-cathode laser pulse was assumed to have a Gaussian longitudinal shape with an RMS duration of 3 ps and a uniform transverse laser intensity distribution ( $\sigma_x = \sigma_y \sim 0.17$  mm) taken at the photo-cathode. The maximum gradient of the 1.5-cell S-band RF gun was assumed to be 110 MV/m. By operating the five structures with the same gradient of 25.5 MV/m and different off-crest phases ( $-487.0$ ,  $-55.0$ ,  $-41.0$ ,  $-41.0$ , and  $-41.0$ ) in degrees, the final beam energy is about 240 MeV. The evolution of the transverse beam sizes and emittances from the photo-cathode to the linac exit are shown in Figure 14.9.

The beam optics from the linac exit to the injection point is shown in Figure 14.10. The beam parameters at the linac exit and the injection point are summarised in Table 14.5, and the transverse and longitudinal phase spaces are shown in

**Table 14.5.** Beam parameters at the linac exit and the injection point.

	Linac exit	Injection point
Energy (MeV)	242.0	240.8
Bunch charge (pC)	50.0	29.8
RMS bunch length (fs)	160.0	7.5
Peak current (kA)	0.13	4.0
Projected emittance $\varepsilon_{n,x}/\varepsilon_{n,y}$ ( $\mu\text{m}$ )	0.30/0.30	0.81/0.46
Slice emittance $\varepsilon_{n,x}/\varepsilon_{n,y}$ ( $\mu\text{m}$ )	0.28/0.28	0.59/0.34
$\beta_x/\beta_y$ (mm)	/	3.1/3.0
RMS energy spread (%)	0.50	0.27
Slice RMS energy spread (%)	0.05	0.23

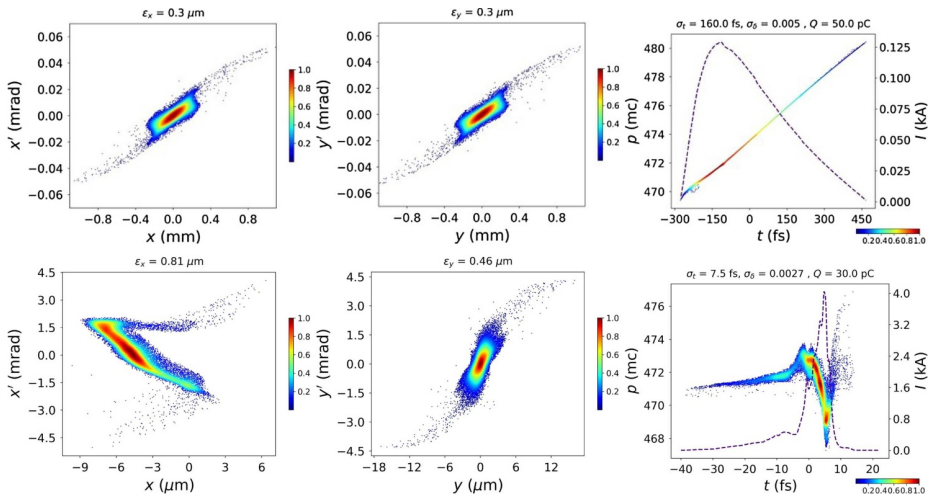
**Fig. 14.11.** Transverse and longitudinal phase spaces of the beam at the linac exit (upper row) and the injection point (lower row). The normalised emittance is defined as  $\varepsilon_{x,y}$  here.

Figure 14.11. The FWHM bunch length at the injection point is only 5 fs. However, there is merely one  $0.75 \mu\text{m}$  long slice with a peak current higher than 3 kA. The influence of the space-charge effects after bunch compression is found to be significant. From the chicane exit to the injection point, the RMS energy spread of the bunch increases from 0.18% to 0.27%, and the vertical slice emittance increases from  $0.27 \mu\text{m}$  to  $0.34 \mu\text{m}$ . However, it is interesting to find out that the horizontal slice emittance decreases slightly in this region. The decrease in the horizontal slice emittance could be caused by the cancellation of the correlations built by the strong CSR effect in the chicane. It should be noted that the chromatic aberration at the PMQ triplet also contributes considerably to the vertical emittance growth [322].

## 14.5 Particle-Driven External Injection Scheme

For the beam-driven external injection case (Scheme 5: RFI-500 MeV + PPAS-1 GeV), a comb-like configuration for the electron beam, consisting of a 200 pC driver followed by a 30 pC witness bunch, has been explored with the aim to optimise the witness parameters and to set the longitudinal distance between the two bunches at the desired value.

The comb-like operation foresees the generation of two or more bunches within the same RF accelerating bucket through the so-called laser-comb technique

**Table 14.6.** L1 and L2 linac parameter list for the PWFA external injection scheme.

Beam Parameter	Unit	L1	L2
Initial energy	GeV	0.102	0.222
Final energy	GeV	0.222	0.582
Active linac length	m	6.0	10.0
Accelerating gradient	MV/m	20.0	36.0
RF phase (0 crest)	deg	0.0	0.0
Initial energy spread	%	0.15	0.11
Final energy spread	%	0.11	0.07
Final bunch length	mm	0.006	0.007

[323,324], consisting of a train of laser time-spaced pulses that illuminate the photo-cathode. The witness arrives earlier than the driver on the photo-cathode, and then they are reversed in time at the end of the velocity-bunching process, during which the longitudinal phase space is rotated. Experimental results have been obtained at SPARC LAB, where the laser-comb technique is routinely used to produce trains of multiple electron bunches [325] for narrow-band THz generation [326], two-color FEL experiments [327,328], and resonant particle-driven plasma acceleration [303].

Computational studies have been dedicated to provide at the plasma module two bunches, i.e. driver and witness, separated by at least 0.55 ps, which corresponds to  $\lambda_p/2$  with the plasma wavelength  $\lambda_p = 330 \mu\text{m}$  for a plasma background density  $n_p = 10^{16} \text{cm}^{-3}$ . Both driver and witness bunches must be compressed down to  $\sim 50$  fs and  $\sim 10$  fs (FWHM), respectively; the witness bunch length must be much less than the plasma wavelength to minimise the energy spread growth. In addition, one more request is on the minimisation of the emittance growth, which unavoidably occurs because of the witness and driver overlapping during the velocity-bunching regime.

A linac setup equal to the one described in Chapter 14.3 is assumed in this scenario. The same accelerating gradient of  $E_{acc} \sim 20\text{--}36 \text{MeV m}^{-1}$  is applied in the L1 and L2 linac sections, respectively; the final electron beam energy is  $E_{L2\text{exit}} \sim 580 \text{MeV}$ , with an energy spread of less than 0.1%. The linac parameters are listed in Table 14.6, and the longitudinal phase space at the end of the linac is depicted in Figure 14.12.

The photo-cathode laser has been shaped to provide at the cathode a witness and a driver bunch separated by 4 ps. A Gaussian longitudinal distribution with  $\sigma_z = 120 \mu\text{m}$  (RMS) and a uniform transverse distribution of radius  $r = 0.35 \text{mm}$  have been assumed for the witness pulse at the cathode. Figure 14.13 depicts the transverse and longitudinal distributions of the photo-cathode laser at the cathode surface. The photo-cathode laser has been shaped via the laser-comb technique, also in intensity to provide at the cathode a 30 pC witness beam (red) separated by 4 ps from the 200 pC driver bunch (blue).

On the other hand, the driver spot size on the cathode has been chosen, looking at the witness quality, as the witness emittance and longitudinal profile are dependent on it. The optimal value for the driver transverse dimension at the cathode surface, in terms of emittance and duration of the witness beam at the injector exit, is  $\sigma_{rD} = 350 \mu\text{m}$ .

Besides an appropriate shaping and relative spacing of the laser comb pulses at the cathode surface, a proper set of active and passive accelerator elements allows us to obtain the required comb beam at the photo-injector exit. The choice of the accelerator setup starts from the optimised witness working point illustrated in Section 14.3, with additional fine-tuning of accelerating cavity RF phases and solenoid magnetic

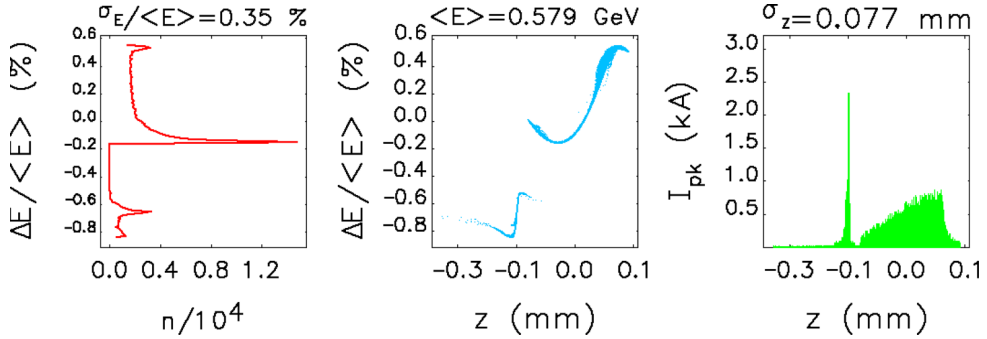


**Fig. 14.12.** Longitudinal phase space of the PWFA-accelerated electron beam at the L2 linac exit.

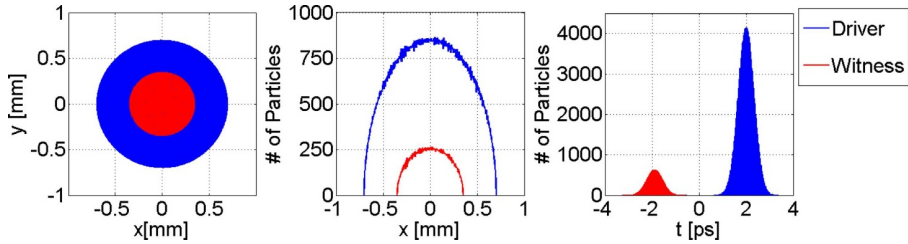


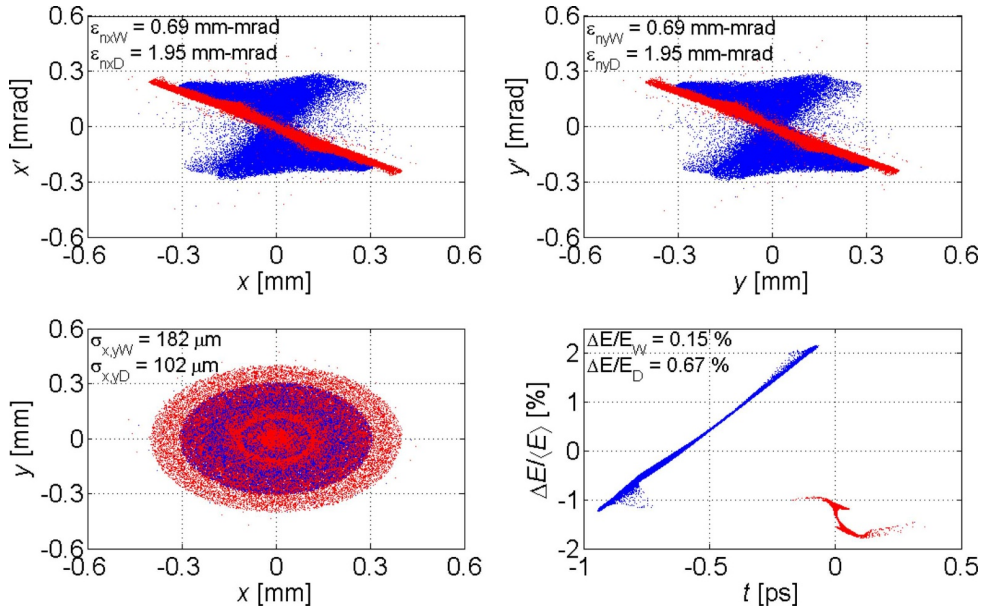
**Fig. 14.13.** Transverse and longitudinal distributions of the photo-cathode laser at the cathode surface. The photo-cathode laser has been shaped via the laser-comb technique, also in intensity to provide at the cathode a 30 pC witness beam (red) separated by 4 ps from the 200 pC driver bunch (blue).

**Table 14.7.** Main photo-injector parameters.

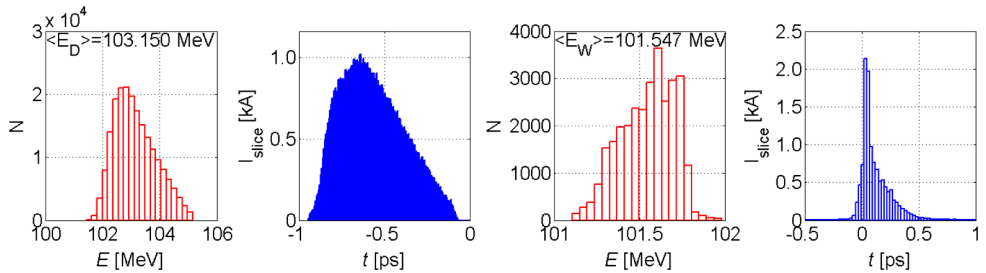
Parameter	Unit	Value
Gun electric field amplitude	MV/m	120
Gun electric field operation phase	deg	32
Output gun beam energy	MeV	5.6
Amplitude of electric field in the three TW sections	MV/m	20.0/20.0/28.0
Magnetic field in the emittance compensating solenoid	kG	3.0
Magnetic field in the linac solenoids	kG	0.34/0.52
Total photo-injector length	m	12

fields. The main operating parameters of the EuPRAXIA photo-injector for the optimised comb beam in case of PWFA are summarised in Table 14.7.

The best compromise in terms of final spacing and witness profile has been obtained with a laser-comb operation, with two laser pulses spaced by  $\Delta t = 4.8$  ps on the cathode. In this configuration, adopting the setup described in Section 14.3, the beam crossing occurs in the second TW accelerating cavity, and a fine-tuning of the RF phases suffices to provide 0.55 ps spaced beams, corresponding to  $\lambda_p/2$ , and the desired witness and driver longitudinal lengths, i.e.  $3 \mu\text{m}$  (FWHM) and in the range of 30–50  $\mu\text{m}$  (RMS), respectively.



**Fig. 14.14.** Upper plots: Transverse phase space (x and y). Lower plots: transverse distribution and longitudinal phase space for a comb-like beam at the photo-injector exit. The blue and red dots are related to the driver and witness, respectively.

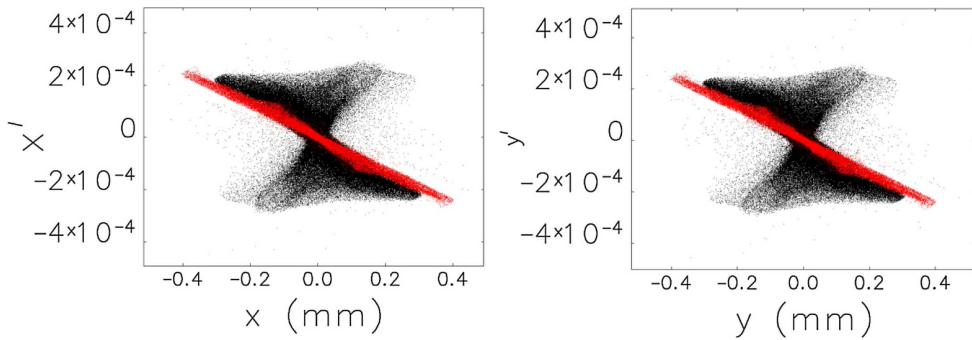


**Fig. 14.15.** Driver (left plots) and witness (right plots) beam energy and current profiles (red and blue lines, respectively) after velocity bunching.

Both witness and driver bunches have been simulated with 30 k and 200 k macroparticles, corresponding to 30 pC and 200 pC, respectively. In the described configuration, the driver arrives 0.58 ps earlier than the witness at the X-band booster. The parameters of both witness and driver beams at the X-band linac entrance are listed in Table 14.8; it is worth noticing that the witness length is about  $3 \mu\text{m}$  (FWHM) with a normalised transverse emittance of  $\sim 0.7 \text{ mm mrad}$ . Figure 14.14 reports longitudinal and transverse phase spaces at the photo-injector exit for both witness and driver beams as obtained with TStep. Figure 14.15 shows the energy and current profiles for both driver and witness bunches as naturally produced by the velocity-bunching regime, i.e. a spike-like distribution with the charge gathered on the head of the bunch. Even though this longitudinal particle distribution is suitable for the witness beam to take profit of the beam loading, it is not the optimum for the driver beam. Indeed, to increase the transformer ratio, the opposite charge distribution, i.e. low charge on the head and maximum charge on the tail, is mandatory. In this regard, further manipulation of the longitudinal phase space is required for the driver.

**Table 14.8.** Driver and witness beam parameters at the end of the photo-injector.

Parameter	Unit	Witness	Driver
Charge	pC	30	200
Energy	MeV	101.5	103.2
RMS energy spread	%	0.15	0.67
RMS bunch length	fs	12	20
Peak current (FWHM)	kA	6.0	0.37
RMS normalised emittance	mm mrad	0.69	1.95
Repetition rate	Hz	10	10

**Fig. 14.16.** Horizontal and vertical phase-space distribution of the PWFA driver (black dot) and witness (red dot) beams at the L1 linac entrance.

The X-band RF linac has to provide an electron beam for injection in the plasma capillary with  $Q = 30$  pC,  $I = 3$  kA (FWHM), and  $1\text{--}2\ \mu\text{m}$  of transverse spot size; the comb-like electron beam undergoes deep over-compression in the photo-injector by means of the velocity-bunching scheme.

The driver and witness bunches are characterised by a high charge / low current and a low charge / high current, respectively. Moreover, the initial matching conditions for the injection in the X-band linac are quite different for the two bunches, as shown by their transverse phase space at the linac entrance (i.e. injector exit) and depicted in Figure 14.16. In this regard, an efficient sharing of the same lattice is achieved by means of a mild transverse focussing that aims to keep the RMS size of the comb beam compatible with the beam stay-clear aperture throughout the X-band accelerator, as seen in Figure 14.17.

The same argument applies also to the focussing stage, with the permanent quadrupoles at the entrance of the plasma capillary, where a residual asymmetry between the horizontal and vertical planes for the witness beams is present, as shown in Figures 14.18 and 14.19, unavoidable up to now if not at the expense of a much greater dilution of the transverse emittance of the driver bunch; optimisation and improvement of the lattice are due in progress to minimise the issue.

This working point for the RF photo-injector in the laser comb configuration has been optimised and validated by means of its integration into a start-to-end simulation, which included the plasma-accelerating module and the matching sections to provide the complete evolution of both driver and witness bunches. The transverse properties from the photo-cathode to the undulator entrance for both bunches are reported in Figures 14.20 and 14.21, respectively.

The longitudinal properties from the photo-cathode to the undulator entrance for both bunches are reported in Figures 14.22 and 14.23, respectively.

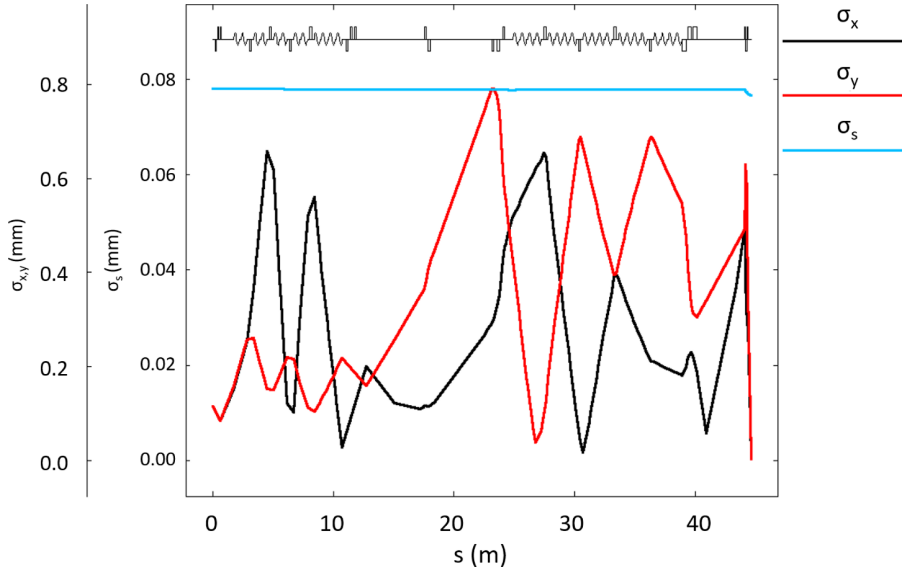


**Fig. 14.17.** Transverse RMS size of the electron beam (driver plus witness) along the linac.

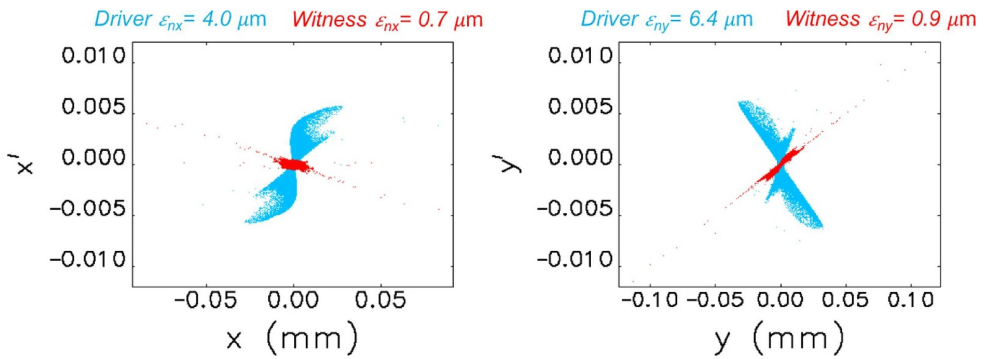


**Fig. 14.18.** Horizontal and vertical phase-space distribution of the PWFA driver (cyan dot) and witness (red dot) beams at the capillary entrance.

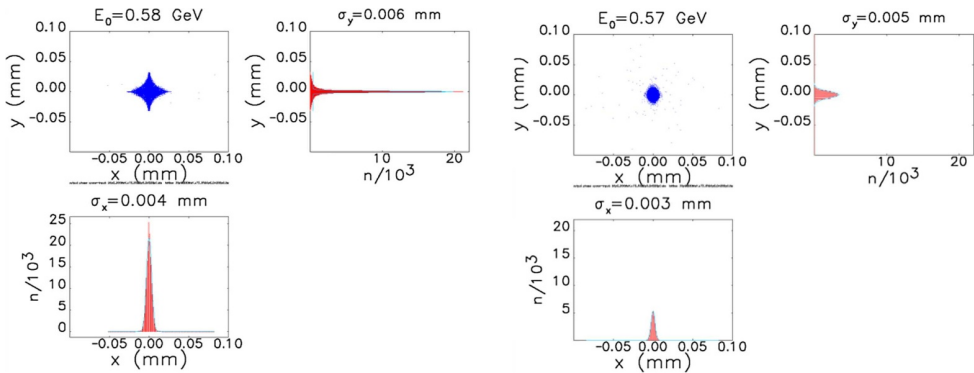


**Fig. 14.19.** Transverse horizontal and vertical distribution of the PWFA driver (left) and witness (right) beams at the capillary entrance.

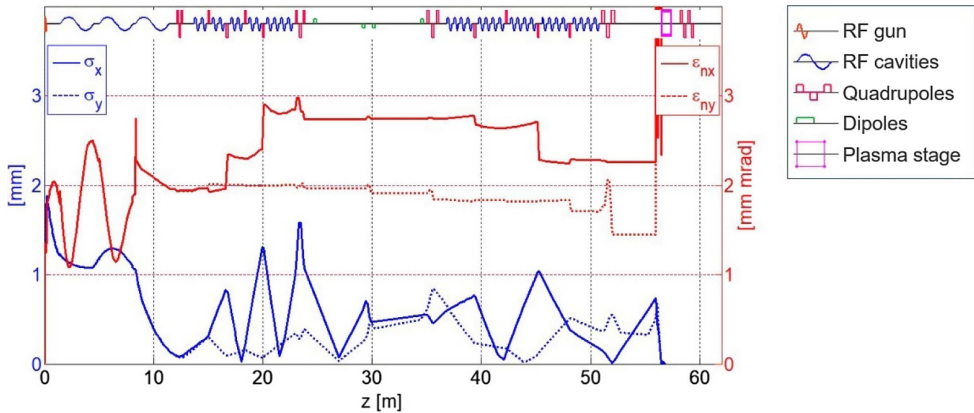


**Fig. 14.20.** Start-to-end simulation results for the driver bunch from the photo-cathode to the undulator entrance: evolution of transverse normalised emittance ( $\epsilon_{nx}$  red line,  $\epsilon_{ny}$  red dotted line) and spot size ( $\sigma_x$  blue line,  $\sigma_y$  blue dotted line).

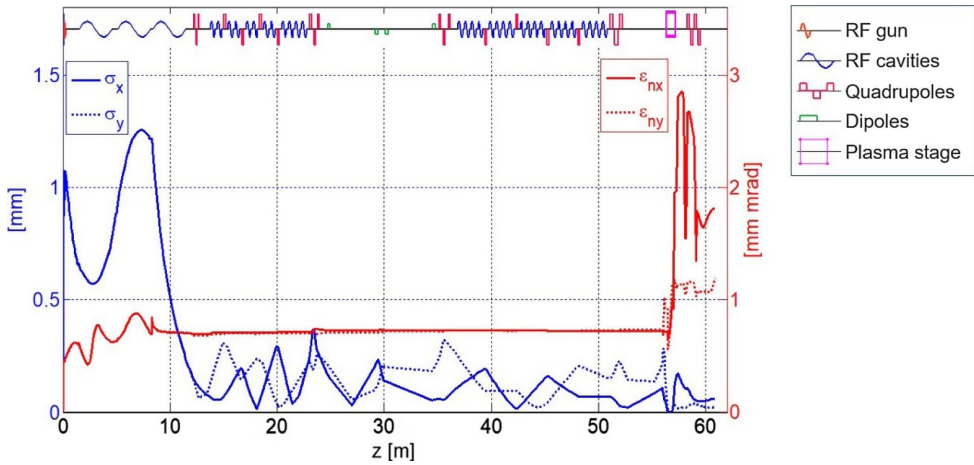


**Fig. 14.21.** Start-to-end simulation results for the witness beam from the photo-cathode to the undulator entrance: evolution of transverse normalised emittance ( $\epsilon_{nx}$  red line,  $\epsilon_{ny}$  red dotted line) and spot size ( $\sigma_x$  blue line,  $\sigma_y$  blue dotted line).

## 14.6 Future Plans and Conclusions

Further studies are ongoing to optimise the current distribution in particular for particle-driven plasma acceleration, and to better control the matching of both driver and witness beams along the machine up to the plasma entrance. Additional studies will be dedicated to the definition of a unique solution for the photo-injector layout to integrate both compression schemes and guarantee optimal performances for both external injection acceleration schemes. The start-to-end simulations shown here have taken profit from the collaboration and synergy with other work packages, mainly WP2 and WP9.

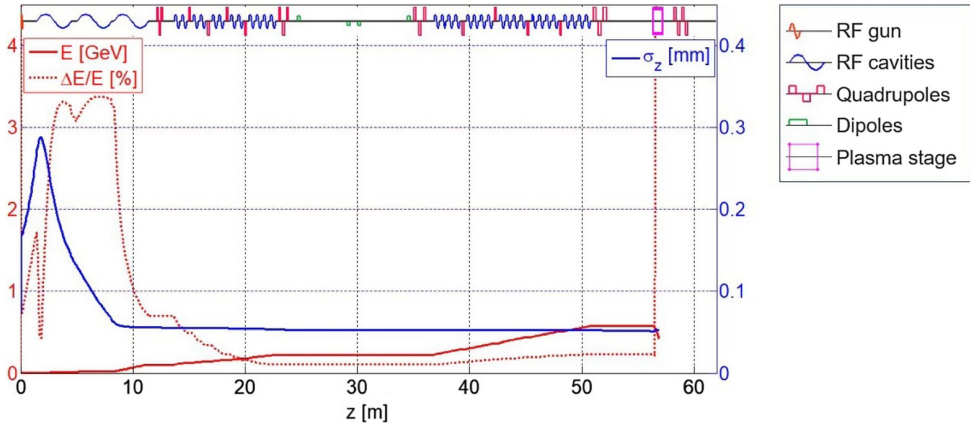


**Fig. 14.22.** Start-to-end simulation results for the driver bunch from the photo-cathode to the undulator entrance: evolution of the energy ( $E$  red line) and energy spread ( $\Delta E/E$  red dotted line) as well as longitudinal bunch length ( $\sigma_z$  blue line).

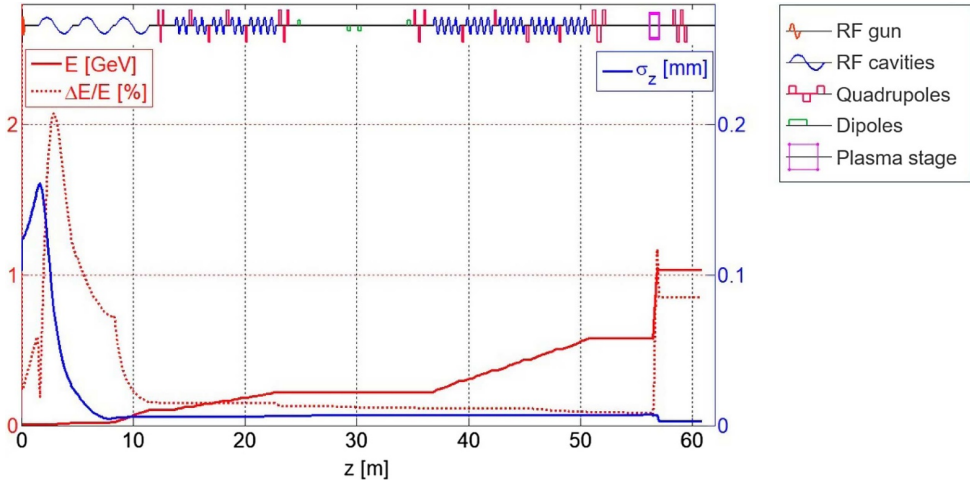


**Fig. 14.23.** Start-to-end simulation results for the witness beam from the photo-cathode to the undulator entrance: evolution of the energy ( $E$  red line) and energy spread ( $\Delta E/E$  red dotted line) as well as longitudinal bunch length ( $\sigma_z$  blue line).

## 15 Sub-Femtosecond Synchronisation of Electrons to the Laser

One of the proposed methods for improving beam quality in EuPRAXIA is to use an external injection scheme, where the electron beam is provided by an external RF linac rather than produced within the plasma (Schemes 3 and 4, as described in Chap. 8). This allows good control of the beam properties so that the emittance and energy spread growth during acceleration can be minimised by properly shaping [329] and matching [35,330] the beam into the plasma.

However, operating a plasma accelerator with external injection brings in new technical challenges. In particular, it requires an extremely low timing jitter between the drive laser and witness beam. Given the small size of the accelerating plasma buckets (typically on the order of 10–100  $\mu\text{m}$ ) and the steep field gradients in them, an accuracy on the femtosecond level is required, smaller than what is available today in state-of-the-art setups. In this context, a new timing jitter compensation scheme

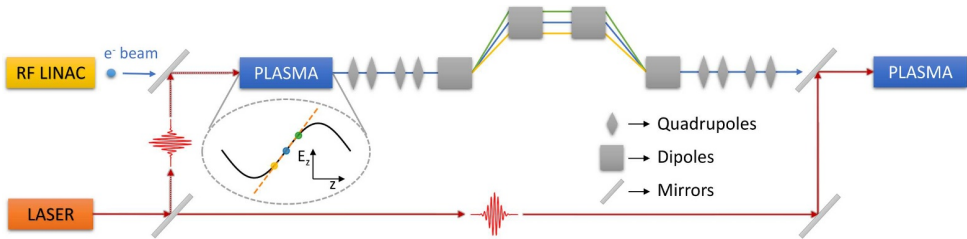


**Fig. 15.1.** Schematic view of the synchronising stage.

to control synchronisation between the RF-generated electron bunch and the laser-driven plasma wakefield was developed by A. Ferran Pousa et al. [331]. The scheme is based on the same underlying idea already explored in previously proposed concepts [332–334], but with an already pre-bunched and ultrashort beam. In the following, the results from this first paper on the synchronisation mechanism are reproduced with the authors' permission.

### 15.1 A Scheme for Timing Jitter Compensation

We propose a new concept for external injection that would allow the achievement of unprecedented sub-femtosecond timing jitter between the laser and the witness beam. The scheme, as seen in Figure 15.1, relies on adding an intermediate synchronising stage before the main plasma acceleration module.

In this concept, the laser pulse is initially split into two, with one of them containing only a small fraction of the energy (e.g.  $\sim 5\%$ ). These two pulses are intrinsically synchronised and will serve different purposes: the weak one will be used in the synchronising stage, while the strong pulse will be used as a driver in the main plasma acceleration module.

As seen in Figure 15.1, the main idea is to use the weak pulse to drive the first plasma stage, in which the electron beam will get a small energy change proportional to its arrival time. In the speed-of-light frame,  $\xi = z - ct$ , beams with an offset  $\Delta\xi_i = \xi_i - \xi_0$  with respect to the zero crossing,  $\xi_0$ , of the accelerating field,  $E_z$ , will gain or lose energy depending on whether they arrived too late ( $\Delta\xi_i < 0$ ) or too soon ( $\Delta\xi_i > 0$ ), therefore correlating arrival time and beam energy.

Due to this correlation, a magnetic chicane will then be able to correct the initial offsets thanks to the differences in path length for each beam energy, virtually removing the timing jitter between the electron beam and the main laser pulse for injection into the second plasma stage.

Additionally, the scheme contains two quadrupole sections to match the beam into and out of the plasma modules.

The laser parameters should be such that the weak pulse is able to excite a linear wake in the first plasma stage, so powers on the order of 1–10 TW should suffice. For the strong one, the necessary power will depend on the desired final energy of the beam after acceleration.

The design energy of the chicane,  $E_0$ , should be selected as the energy, after the first plasma, of a beam with  $\Delta\xi = 0$ . In case of no beam loading, this means that  $E_0 = E_i$ , where  $E_i$  is the initial energy of the beams coming from the linac.

## 15.2 Linear Model

In the first plasma stage, beams will get an energy deviation  $\delta = \frac{E-E_0}{E_0}$  depending on their longitudinal position. For small offsets, this can be approximated as

$$\delta = -\frac{eE'_z L_p}{E_0} (\xi_i - \xi_0), \quad (15.1)$$

where  $e$  is the electron charge,  $E'_z = \partial_\xi E_z$  is the slope of the accelerating field around  $\xi_0$ , and  $L_p$  is the length of the plasma stage.

To the first order, the final position of the beam after the chicane will be given by

$$\xi_f = \xi_i - R_{56}\delta, \quad (15.2)$$

where the minus sign comes from the fact that in the co-moving coordinate  $\xi$ , as commonly used in plasma acceleration, the bunch head is on the right.

Then, in order to correct the initial offsets,  $\xi_f = \xi_0$  should be imposed. This, together with equation (15.1), yields

$$R_{56} = -\frac{E_0}{eE'_z L_p}. \quad (15.3)$$

For a plasma in the linear regime ( $a_0 \ll 1$ ) [180,335] and a circularly polarised Gaussian pulse,  $a^2 = a_0^2 \exp(-\xi^2/2\sigma_z^2)$ , the slope of the field  $E_z$  around its zero crossing is

$$E'_z = \frac{mc^2}{e} \sqrt{\frac{\pi}{2}} a_0^2 k_p^3 \sigma_z e^{-\frac{k_p^2 \sigma_z^2}{2}}, \quad (15.4)$$

where  $m$  is the electron mass,  $c$  is the speed of light,  $a_0$  is the peak amplitude of  $a$ , the laser's normalised vector potential,  $k_p$  is the plasma wavenumber, and  $\sigma_z$  is the laser RMS length. In the case of linear polarisation,  $a_0^2$  should be replaced by  $a_0^2/2$ . By substituting this into equation (15.3), one finds the general expression

$$R_{56} = -\sqrt{\frac{2}{\pi}} \frac{E_0}{mc^2 a_0^2 k_p^3 \sigma_z L_p} e^{\frac{k_p^2 \sigma_z^2}{2}}. \quad (15.5)$$

Now if the laser pulse length satisfies the resonant condition ( $\sigma_z k_p = 1$ ), one can find a simplified equation which, written in a convenient way, reads,

$$R_{56} [\text{mm}] = -7.27 \times 10^{13} \frac{E_0 [\text{MeV}]}{a_0^2 n_p [\text{cm}^{-3}] L_p [\text{mm}]}. \quad (15.6)$$

In reality, depending on the beam energy, it might be necessary to take into account the path length effect given the deviation from the speed of light not being negligible. This would decrease the necessary  $R_{56}$  at the chicane, but a precise value can only be given once the full geometry of the beamline up to the second plasma has been decided. Also, Eqs. (15.5) and (15.6) do not take into account beam loading, so if this effect becomes significant,  $R_{56}$  might have to be determined from the chirp of  $\delta$  as obtained from simulations.

Another important remark is that the quality of the jitter correction will depend on the stability of the parameters in equation (15.5) as well as the pointing jitter of the electron beam after the first plasma. For the case presented below, assuming the pointing jitter does not exceed the natural beam divergence, the resulting maximum timing jitter would be around 0.2 fs per metre of beamline downstream of the plasma, still on the sub-fs range.

Moreover,  $\delta$  should always be much bigger than the intrinsic energy spread of the beam; otherwise, its longitudinal phase space might be perturbed in the chicane.

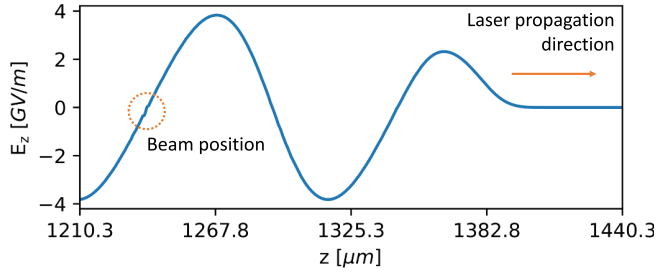


**Fig. 15.2.** On-axis longitudinal electric field after 1.2 mm of propagation in the plasma, with the electron beam placed at the zero crossing (case with  $\Delta\xi = 0$ ).

### 15.3 Numerical Simulations

In order to test this method, a series of start-to-end simulations going from the injection of the beam into the first plasma until the end of the chicane have been performed.

The simulation of the plasma stage was performed in 3D with the fully relativistic particle-in-cell code OSIRIS [336] using the Ponderomotive Guiding Center (PGC) algorithm [337]. WinAGILE [338] and MAD-X [339] were used for the optimisation of the quadrupole section, and the tracking of the electron beam from the plasma exit until the end of the chicane was done with ELEGANT [340].

Effects derived from coherent synchrotron radiation (CSR) at the dipoles have been taken into account, but a full treatment including space charge after exiting the plasma has not yet been possible. However, because of the low charge density of the beam after the plasma and its relativistic energy, strong space-charge effects are not expected.

#### Main Parameters

The electron beam after the linac is Gaussian with a charge of 0.1 pC in 1 fs, an energy of 100 MeV with 0.1% relative energy spread, a normalised emittance  $\varepsilon_{n,x,y}$  of 0.3  $\mu\text{m}$ , and initial offsets due to timing jitter between -20 and 20 fs. These parameters were chosen to avoid significantly perturbing the plasma wakefield with the beam (see Fig. 15.2) and are within the range of those expected to be produced at the SINBAD facility at DESY [322,341,342]. The first plasma stage has a length of 2 mm with a density of  $1 \times 10^{17} \text{ cm}^{-3}$ , and the laser parameters are based on those considered for the EuPRAXIA conceptual design (see Chap. 10), using only around 3.5% of its energy for the synchronising stage. This means an 800 nm linearly polarised pulse of 3.5 J with an  $a_0$  of 0.6, a waist  $w_0$  of 54  $\mu\text{m}$ , and a length of 93 fs (FWHM in intensity), having a peak power of 35 TW. With these parameters, the matched beam size for emittance preservation [35] is  $\sigma_x = 1.3 \mu\text{m}$  for the focussing fields around  $\xi_0$ .

#### Quadrupole Section

The set of magnets is placed 4 cm after the plasma and consists of 4 permanent quadrupoles with a width of 1 cm separated by drifts of 4, 6, and 4 cm. Their strengths were left as free parameters for optimisation in order to achieve, as seen in Figure 15.3, a beam waist at the centre of the chicane and a beta function,  $\beta_{x,y} = \gamma_r \sigma_{x,y}^2 / \varepsilon_{n,x,y}$ , as constant as possible, where  $\gamma_r$  is the Lorentz factor of the beam.

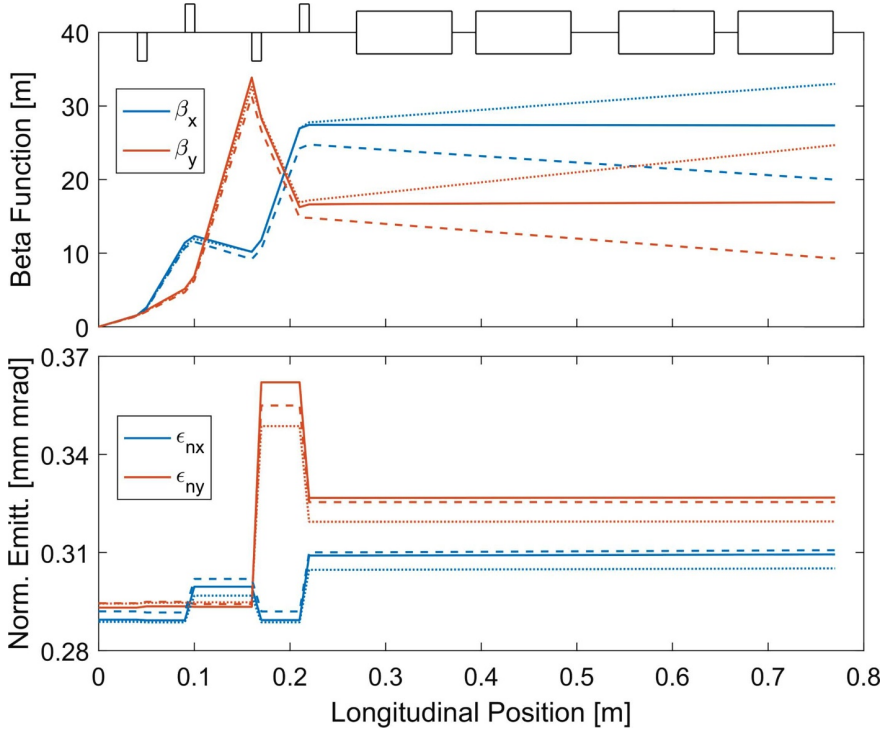


**Fig. 15.3.** Beta function and emittance evolution for beams with different offsets. The solid line corresponds to  $\Delta\xi_i = 0$ , while the dashed and dotted lines represent offsets of 20 and -20 fs, respectively.  $z=0$  represents the end of the plasma stage.

The resulting geometric strengths of the quadrupoles read, from first to last, -878, 1406, -1497, and 823 in units of  $\text{m}^{-2}$ , which, for this beam energy, translate into field gradients of up to 500 T/m, requiring tight apertures.

### Chicane Setup

For this case, equation (15.5) predicts an  $R_{56} = -0.222$  mm. However, for higher accuracy, the slope of  $\delta$  was directly measured from the simulation results (see Fig. 15.4), obtaining an  $R_{56} = -0.267$  mm. This could be due to the laser  $a_0$  being 0.6, slightly high for the linear theory to hold, since  $a_0 \ll 1$  is assumed.

The bending angle  $\theta$  of the dipoles was determined from

$$R_{56} = -2\theta^2 \left( L_d + \frac{2}{3}L_m \right) \quad (15.7)$$

by assuming a magnet length  $L_m = 10$  cm and a drift length  $L_d = 2.5$  cm, obtaining  $\theta = 2.19^\circ$ .

### Simulation Results

As seen in Figure 15.4, the plasma stage correctly imprints a linear kick to the beam energy depending on its initial offset, allowing the chicane to compensate the jitter.

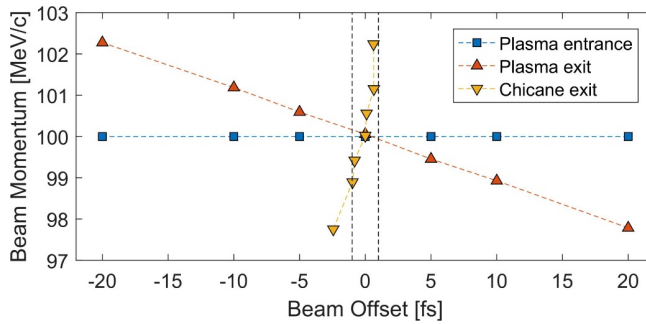


**Fig. 15.4.** Jitter correction thanks to plasma stage and chicane. The vertical lines delimit a 1 fs jitter.

All beam offsets between  $\pm 10$  fs have been reduced to sub-fs level, showcasing the potential of this method.

In terms of quality, as seen in Figure 15.3, the beam experiences an increase in emittance of around 10–20% due to chromatic effects at the quadrupoles. Additionally, given the strong focussing, the beam develops a slightly curved shape in the transverse plane, increasing its RMS length to about 0.5 fs.

Also, as seen in Figure 15.3, beams with  $\Delta\xi_i \neq 0$  will present variations in the evolution of the beta function because of their different energies, so some way of compensating this chromatic effect before the second plasma stage will be required.

## 15.4 Conclusion

A new scheme for arrival time jitter minimisation between laser pulse and witness beam for LWFA with external injection is presented. Simulation results show that jitters of 10 fs can be reduced to the sub-femtosecond level with minimal loss of beam quality.

Further studies are required to determine the stability and tolerances of the setup, as well as the influence of space-charge effects and finding ways of matching the beam into the second plasma stage, taking into account the variations in beta function seen in Figure 15.3.

Also, although only ultra-short beams have been tested, it is possible that for longer beams ( $\sigma_z \sim 10$  fs), this scheme could be used both for synchronisation and compression.

## 16 Laser-Driven Plasma Accelerator

### 16.1 Introduction

The plasma accelerator stages form the heart of the EuPRAXIA facility. As will be discussed, these structures can readily support accelerating fields exceeding 5 GV/m. The direct consequence of this is the ability to attain particles with multi-GeV gain in a fraction of the distance that would be required by more conventional techniques.

Figure 16.1 demonstrates the location of the plasma acceleration structures within the proposed accelerator developments, with those of long length (which here means  $> \text{cm}$  length) circled in red. The structures will be driven either by intense laser or electron beams. For beam-driven plasma acceleration experiments, the accelerating structures, though similar in concept to the laser-driven structures, have some

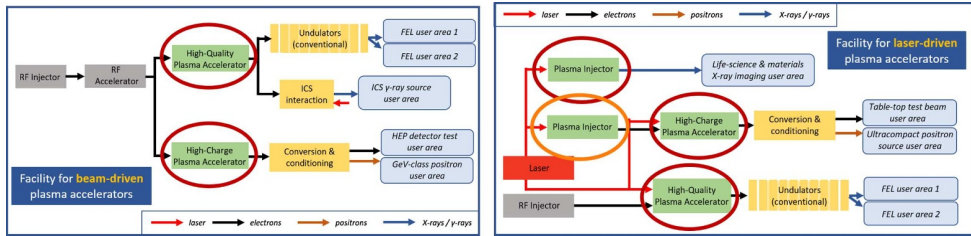


**Fig. 16.1.** Schematic of the proposed developments at the two EuPRAXIA construction sites, with the plasma accelerator stages circled. Those circled in darker red are where longer acceleration stages ( $> \text{cm}$  length) will be employed.

key differences. Their characteristics are generally dependent on their driver, and so they are more naturally discussed in Chapter 17, dedicated to particle-beam-driven wakefield acceleration in EuPRAXIA.

This chapter describes the general requirements to implement plasma-accelerating structures driven by laser beams. Therefore, these discussions primarily apply to the developments planned at the construction site for laser-driven plasma acceleration, where there will be an availability of co-located particle and laser beams.

There are also two types of plasma components to consider for laser wakefield accelerators. Components of the first type are those operated for a *laser-plasma injector* (LPI), which is typically designed to have relatively low output energy ( $< \text{GeV}$ ). These LPIs are of less than a centimetre in length and are thus close to the natural diffraction (Rayleigh) length of the laser used to drive the accelerating fields inside them. As such, the use of advanced techniques for the guiding of high-power laser beams is usually considered unnecessary. The electrons accelerated in these devices originate from the plasma, which hosts the accelerating structure. Numerous schemes have been devised and tested to facilitate this injection of electrons into the accelerating structure, and they have been investigated in detail both numerically and in experiments. The strengths and weaknesses of the different approaches are discussed further in Chapter 13, as well as developments to optimise these devices for implementation as an injector for EuPRAXIA.

The second function, as which plasma accelerators will be implemented, is as a *laser-plasma accelerator stage* (LPAS).

In EuPRAXIA, the laser-plasma accelerator stage(s) (LPAS) will take sub-GeV beams and accelerate them to 1 to 5 GeV. Given the need to couple electron and laser beams, these stages form a beamline that must be designed to holistically incorporate electron and laser optics. Also, the need to operate these structures for distances which will exceed tens of centimetres means that some form of laser beam guiding is required to maintain large-amplitude plasma wave growth over the whole length of the accelerator stage.

We will begin by providing the parameters of interest for development of these plasma-accelerator stages since little experimental work in this area exists at the present for laser-driven structures. The parameters are determined predominantly from the limits of well-tested scaling laws and, where appropriate, through confirmation via simulations. These parameters have to be refined when including stability considerations and tolerances, which is a task begun in simulations performed in the frame of Work Package 2 on ‘‘Physics and Simulation’’.

## 16.2 Parameters of Plasma Accelerator Sections

### 16.2.1 Density

Within the laser-driven components of the EuPRAXIA facility, plasma components, as highlighted in Figure 16.1, with the following energy gain characteristics need to be considered:

- i.  $\Delta W = 1$  GeV injector and accelerator primarily for application beamlines;
- ii.  $\Delta W = 0.85 - 4.85$  GeV for a test beam;
- iii.  $\Delta W = 0.85 - 4.85$  GeV for FEL applications.

The LPAS will thus have to accelerate the electron beam to an energy of  $\Delta W = 0.85 - 4.85$  GeV for a test beam or FEL applications. In general, these stages will be some form of laser wakefield accelerator [4]. To limit non-linear effects, the accelerator stages will usually be operated in the linear ( $a_0 < 1$ ) or quasi-linear ( $a_0 \simeq 1$ ) regime, where the energy gain is given by the following:

$$W_{\max} = 2a_0^2 \gamma_{ph}^2 mc^2 \approx a_0^2 (n_{cr}/n_e) \text{ MeV}, \quad (16.1)$$

where  $\gamma_{ph}$  is the Lorentz factor associated with the plasma wave. Operating in the linear regime ensures higher reproducibility and predictable energy gain. The energy gain is mainly determined by the laser intensity ( $a_0$ ) and the ratio of critical density to plasma density ( $n_{cr}/n_e$ ), the first because it determines the amplitude of the plasma wave, and the latter because it determines its velocity.

An energy gain up to 4 GeV is required; setting  $a_0 \simeq 1$  ensures the maximum acceleration whilst remaining in the linear regime, for  $n_e \approx 2.5 \times 10^{-4} n_{cr} \approx 4 \times 10^{17} \text{ cm}^{-3}$ . These plasma densities are readily obtained by laser ionisation of near-atmospheric-density gas targets and thus determine the type of targets required for the LPA stages.

### 16.2.2 Interaction Length

The length over which this acceleration is achieved is optimally set, in an LPAS, by dephasing. This is the length over which the accelerated electrons, travelling at close to the speed of light  $c$ , outrun the plasma wave, which travels at close to the group velocity of the driving laser pulse within the plasma. In the linear regime, the dephasing length is approximately given by

$$L_{dp} \approx \gamma_{ph}^2 \lambda_p \approx (n_{cr}/n_e)^{3/2} \lambda_0 \quad (16.2)$$

for a plasma wave of wavelength  $\lambda_p$ . For the 4 GeV gain required,  $(n_{cr}/n_e) \approx 4000$ , and so this increases to  $L_{dp} \approx 25$  cm.

This can be compared to the distance over which a high-intensity laser pulse naturally diffracts, the Rayleigh range:

$$z_R \approx \pi w_0^2 / \lambda_0. \quad (16.3)$$

Typically, one focusses the laser pulse to a spot size  $w_0 \approx \lambda_p = (2\pi c/\omega_p) \approx 30(60) \mu\text{m}$  for 1(4) GeV acceleration. This gives  $z_R \approx 3(12)$  mm, which means that the interaction length  $L_{dp} \approx 10(20) z_R$ , motivating the need for some form of guiding of the laser pulse to maintain a high-intensity interaction over the necessary length.

We note that 4 GeV energy gain in a length of 25 cm corresponds to an average acceleration of 16 GeV/m, demonstrating the remarkable accelerating potential of laser-plasma accelerators.

The EuPRAXIA LPA stages will typically operate at densities down to  $n_e \approx 1 \times 10^{17} \text{ cm}^{-3}$  over lengths up to  $\sim 1$  m. Hence, they will be formed in gaseous targets with the requirement of some form of laser pulse guiding at high intensity.

## 16.3 Intense Laser Beam Confinement

### 16.3.1 Requirements

As noted above, the laser drivers for the EuPRAXIA LPA stages will need to be focussed with spot sizes in the range of 10–100  $\mu\text{m}$  for distances up to one metre in length, which corresponds to many tens of Rayleigh ranges. Thus, some form of radial confinement of the laser pulse is required to maintain the high-intensity interaction or guide the laser pulse over these lengths.

The guiding of short laser pulses in an underdense plasma requires modification of the plasma refractive index, such that it has a maximum on axis, i.e.  $\partial\eta/\partial r < 0$ . This causes the laser wavefronts to be retarded on axis, countering the natural tendency of the focussed laser pulse to diffract. In the weakly non-linear regime ( $n_e \ll n_{cr}; a_0 < 1$ ), the refractive index of the plasma is given by

$$\eta \simeq 1 - \frac{\omega_p^2}{2\omega_0^2} \left( 1 - \frac{a^2}{4} + \frac{\Delta n_p}{n_e} + \frac{\delta n}{n_e} \right) \quad (16.4)$$

for a linearly polarised laser. Equation (16.4) shows there are three methods for producing the necessary refractive index modification: an increase in intensity ( $a$ ), a self-generated decrease in axial density ( $\delta n$ ), or an initially applied density modification ( $\Delta n_p$ ). The relativistic (intensity) dependent and ponderomotive (self-generated density depression) effects come naturally in laser wakefield acceleration. Since they depend only on the applied laser beam, they are termed collectively as self-guiding. However, relying on self-guiding by itself makes the accelerator highly dependent on the quality and reproducibility of the laser driver. Hence, it is preferable to enforce some kind of guiding structure (which is captured by the last term in equation (16.4)), such as plasma channels and capillary tubes. In the low-intensity (linear) regime, this increases the efficiency of guiding too. This is because the density increase in the front of the plasma wave has a defocussing effect on the laser pulse, which is detrimental to guiding short pulses [343,344]. These externally applied guiding structures are discussed in more detail below.

### 16.3.2 Possible Waveguides

Several types of configurations are candidates for the LPA stages of EuPRAXIA and are described in detail in Chapter 32.2. The main features and most promising options are highlighted in this section.

The transverse refractive index variation required to guide a laser pulse can be created prior to the arrival of the LPA-driving laser pulse by suitable modification of the density profile. A column of plasma, in which  $n_e(r)$  increases smoothly with radial distance from the axis, will have a refractive index which decreases away from the axis. As such, each transverse slice of the plasma column acts as a positive lens, focussing the light as it propagates. This *plasma channel* is therefore an example of a gradient refractive index (GRIN) waveguide.

An alternative configuration, known as a *hollow plasma channel*, is one, in which the plasma column comprises a uniform density core surrounded by a coaxial cylinder

of higher density. Light propagating at sufficiently small angles to the axis of this structure will experience total internal reflection at the core-cladding boundary and hence be guided. This is an example of a step-index waveguide and is analogous to a standard silica optical fibre.

The most widely used type of plasma channel waveguide is the *capillary discharge*. A gas filled capillary discharge readily spans the densities of interest with the required matched spot size and over the lengths suitable for the LPA stages of EuPRAXIA. Although the parameters of interest have not yet been achieved simultaneously, it can be assumed that these parameters will be available. Furthermore, with recent advances in reproducibility, these targets should be able to operate many days at EuPRAXIA repetition rates without the need for replacement.

Plasma channels can also be formed by the *hydrodynamic expansion* of a hot plasma column into a cold gas [345]. More recently optical-field-ionised (OFI), hydrodynamically generated plasma channels have been investigated [346–349]. Here, the initial plasma is formed by the direct field ionisation of a short, more intense laser pulse ( $I > 1 \times 10^{15} \text{ W cm}^{-2}$ ). This allows access to fully ionised media such as hydrogen and helium plasmas. The channel is formed by plasma expansion due to the above-threshold ionisation heating of the ionised electrons. As well as allowing access to a wider range of target material, the plasma can be formed in common targets such as gas jets and gas cells, offering ease of operation. Additionally, OFI-generated channels can be relatively easily diagnosed since they offer unhindered transverse access.

Another device for guiding a high-intensity laser is a *capillary tube*. In these devices, a laser beam can be guided by reflections at the inner wall of the capillary, and so the laser guiding can be achieved either in vacuum or at low plasma density [350]. This does not rely on laser power or plasma density and provides the opportunity to explore a large domain of laser-plasma parameters. An important aspect associated with the use of a capillary tube is the material damage threshold at the inner wall where reflection occurs. For a glass capillary, the maximum intensity on axis which can be guided by a capillary of 50  $\mu\text{m}$  radius in the fundamental  $\text{EH}_{11}$  mode without wall ionisation is  $\sim 10^{19} \text{ Wcm}^{-2}$ , which is at least 10 times higher than the one required for LPAS.

For LPA stages, some form of laser confinement is required. Gas-filled capillary discharges and gas-filled capillaries are the two leading candidates. Their operation has been demonstrated over the density range and lengths required for the EuPRAXIA LPAS.

Hydrodynamically generated waveguides are an interesting alternative for the testing and optimisation of the LPA stages for EuPRAXIA due to their improved diagnostic access.

### 16.3.3 Example of Waveguide Implementation

Figure 16.2 shows examples of the two types of waveguides, a capillary discharge waveguide and a dielectric capillary tube that can be envisaged to create plasmas for accelerator stages. The capillary discharge waveguide scheme relies on a pulsed high-voltage discharge to ionise the gas and on plasma relaxation to create a plasma density channel to ensure laser guiding, as shown in Figure 16.2a.

In dielectric capillary tubes, wall reflections ensure laser guiding. The plasma creation relies on the ionisation of gas by the drive laser. Figure 16.2b illustrates the gas distribution in the stationary regime achieved inside a glass capillary tube. The gas density is constant along the axis between the two slots, shown by the red area in Figure 16.2b.

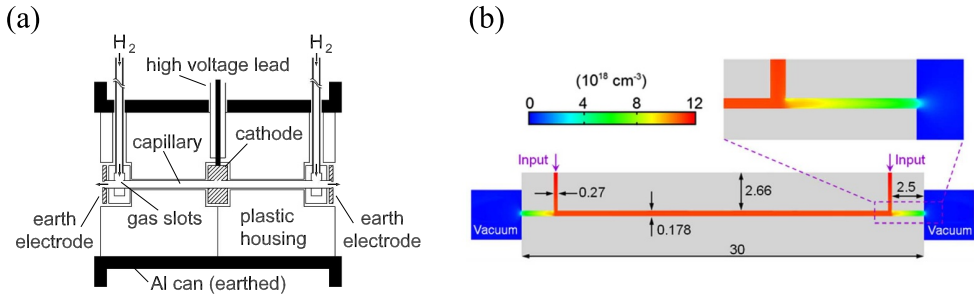


**Fig. 16.2.** (a) Example of hydrogen-filled capillary discharge waveguide from [351] (copyright (2002) by the American Physical Society); (b) Simulation of gas distribution in a dielectric capillary tube from [352] (reprinted with permission of AIP Publishing).

Some form of density variation can be accommodated in both types of targets by having unbalanced fill pressures at either end. Additionally, specialised regions of high density or different gas species can also be easily accommodated in both designs by having extra inlets. These sections can be used for dechirping the beam, providing additional energy gain, reducing emittance growth from the plasma exit, and for internal injection into the LPAS from the plasma. The latter subject is covered in detail in the section on laser-plasma injectors (LPIS).

The targets for the EuPRAXIA LPAS will be either laser-ionised or discharge plasmas. Uniform density gas capillaries, either discharge or laser-ionised, will be the baseline configuration for the EuPRAXIA LPA stages. Many different advanced options exist integrating density ramps and localised areas of high density or special gases. The EuPRAXIA facility will allow many of these schemes to be tested under directly comparable conditions.

## 16.4 Staged Accelerator Implementation

Despite the many possibilities, the baseline recommendation for the LPA stages for the EuPRAXIA facilities should be based on gas-filled dielectric capillaries or gas-filled capillary discharges as these are proven technologies for guiding the laser pulse over the 10–100 cm lengths required here. Actual experimental demonstrations of acceleration to the scale required in EuPRAXIA are not yet available, but the feasibility of both approaches has been demonstrated in numerical simulations. Useful scaling and physics considerations for the design of plasma-accelerating stages in the quasi-linear regime can also be found in [83]. The table below details possible operating parameters for both of the external guiding schemes found for EuPRAXIA, as determined from simulations.

The first option, based on WAKE-EP simulations described in [353], uses dielectric capillary tubes to guide the laser beam and excite a wakefield to accelerate a 50 MeV externally injected electron bunch up to 5 GeV. The second option is based on simulations with WARP, described in [354], to accelerate electrons to 10 GeV over 0.75 m from an injected bunch at 100 MeV. These parameter sets are a starting point and are being refined using specific simulations with EuPRAXIA parameters performed by WP2.

For a 1 GeV stage, it would be straightforward to downscale the parameters given above, ideally scaling up the required density to ensure extraction at close to the dephasing length.

**Table 16.1.** Example of parameter sets to achieve an energy gain of the order of 5 GeV in a laser-driven plasma-accelerator stage.

Type of guiding	Dielectric capillary based on [353]	Plasma channel based on [354]
$n_e$ ( $\text{cm}^{-3}$ )	$1 \times 10^{17}$	$1 \times 10^{17}$
Plasma characteristic length (m)	$\sim 1$	$\sim 0.4$
Guiding	Capillary walls	Density distribution
Gas	H <sub>2</sub>	H <sub>2</sub>
$I_L$ ( $\text{W}/\text{cm}^2$ )	$4.3 \times 10^{18}$	$4.3 \times 10^{18}$
$a_0$	1.42	1.41
$\tau_L$ (FWHM fs)	40	47
$w_0$ (FWHM $\mu\text{m}$ )	118	74
$E_L$ (J)	29	27

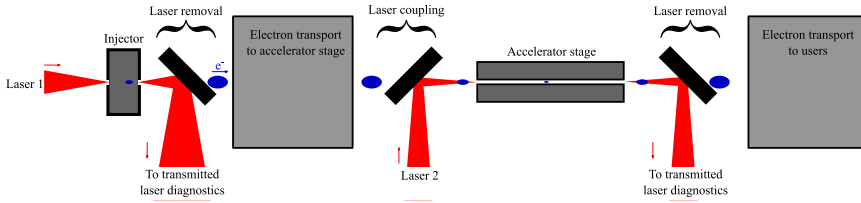


**Fig. 16.3.** Schematic of the laser removal and coupling in a multi-stage configuration.

A schematic of the functional implementation of the accelerator, including the injector stage, is presented in Figure 16.3.

The figure shows some of the key challenges common to all staged wakefield acceleration proposals:

- Transport of the electron beam to the accelerator stage
- Transport of the driver (high-intensity laser) to the accelerator stage
- Diagnosis of the interaction
- Separation of the accelerated beam from the spent driver

Some other important considerations include the following:

- The whole interaction should take place in vacuum to prevent degradation of the laser driver and injected particle beam.
- The target and beams should be positioned, ideally, to sub-micron precision, and spatial movement of both should be below this level.
- Diagnostics should be non-invasive where possible but also easily translated if not, for example in the case of an electron spectrometer.

As schematically presented in Figure 16.3, at each plasma stage, the laser driving the accelerator stage has to be coupled to the plasma, and the transmitted laser light has to be removed from the axis after the interaction. The high intensities limit the proximity of the removal / coupling device to the plasma target. However, the electron transport prescribes that the electron capture should be as close to the plasma as possible to limit the emittance growth. There are two main options for the coupling of the laser to the accelerator.

A *perforated mirror* can be used to couple the second laser beam to the accelerator plasma stage. A hole in the centre of the mirror would free the electron path, and the outer part would reflect the laser beam on to the electron axis. With typical parameters considered for the EuPRAXIA facilities, the operating distance of this coupling mirror would be at least of the order of metres. This can greatly increase the

overall length of the accelerator, consequently reducing the average acceleration. Also, care must be taken that the mirror perforation does not contribute to the unwanted degradation of the driver profile on the target, which will be a serious consideration for some of the targets that may be used. Nevertheless, a perforated mirror is the technically proven solution for laser-beam coupling, and the EuPRAXIA facilities should provide sufficient space to accommodate this solution.

As a mirror placed close to the laser focus would suffer damage from heating and ionisation, *plasma mirrors* are considered as a solution to remove the laser from the electron axis. These are mirror surfaces which become almost instantaneously over-dense plasmas and hence become highly reflecting on irradiation with a high-intensity laser. Such plasma mirrors have long been in use as pulse contrast enhancers [355] but are conventionally constructed of AR-coated fused silica blocks which must be rastered between laser shots in order to expose a fresh optical-quality surface to the laser. This motion limits the repetition rate at which the plasma mirror can operate, and the number of pulses which can be reflected before the mirror is replaced.

Many different schemes for plasma mirrors exist and are being considered for implementation at EuPRAXIA. However, the greatly reduced operating distance of the plasma mirrors is very important. Not only does it maintain the compactness of the facility, but also by making the distance to transport optics for the accelerated beams shorter, it greatly reduces emittance growth in the drift sections. This may prove very important for achieving the high brightness projected for the EuPRAXIA facility.

Another important consideration for a wakefield acceleration facility is the stability of the device. Staged acceleration places exacting requirements on the positioning and timing of laser and particle beams. Spatial positioning to micrometre precision and a temporal overlap down to 10 fs is anticipated. This places high pointing and wavefront constraints on the laser system ( $< \mu\text{rad}$ ). Also, though beams may be derived from the same initial source, the system should be devised to avoid or at least compensate long-term drifts. In addition, spatio-temporal properties of the laser, such as pulse front tilts, must be monitored and controlled to maintain high beam quality and pointing stability.

For the implementation of the staged approach to plasma acceleration that forms the basis of the design of the EuPRAXIA facilities, the coupling of driver and particle beams is of paramount importance. We note that for reasons of reliability and field-proven performance, conventional solutions, such as high-damage-threshold perforated optics for laser beam transport and quadrupole transport lines for particle beam focussing should be accommodated in the EuPRAXIA LPA beamlines. This will necessitate allocating sufficient distances to manoeuvre these components in the base designs.

However, we note that in keeping with the ethos of the EuPRAXIA facilities, the application of plasma technology, e.g. plasma lenses for laser transport and plasma lenses for particle beam transport, will allow dramatic improvements in compactness and potentially performance. Hence, the ability to assimilate these technologies should be made in the design phase.

## 16.5 Conclusion

The plasma accelerator stage would be operated in the quasi-linear regime to prevent the additional internal injection of electrons which would be detrimental to bunch quality. As a consequence, the plasma electron density for this stage would be of the order of  $10^{17} \text{ cm}^{-3}$ . The laser normalised vector potential would be around  $a_0 \simeq 1.4$ , which corresponds to an intensity of  $I_L \simeq 4.3 \times 10^{18} \text{ Wcm}^{-2}$ . The low density and

intensity considered imply that the acceleration length should be of the order of 0.5–1 m.

To sustain accelerating gradients over such a long distance, the laser beam has to be transversely confined to prevent diffraction. A self-guiding scheme relies on the non-linear self-focussing effect and requires laser power in excess of the critical power  $P_{cr} = 17.4 (n_{cr}/n_e)$  GW. At the density considered for the accelerating stage,  $n_e = 10^{17} \text{ cm}^{-3}$ , the critical power is around  $P_{cr} \sim 100 \text{ TW}$ , which is below the laser power considered for this stage,  $\sim 0.5 - 1 \text{ PW}$  (see Chap. 10). However, as self-guiding relies on non-linear effects, it is sensitive to fluctuations of laser power and spatial profile. In the context of building an accelerator to provide electron beams of industrial quality, this can add undesired instability. Hence, for a robust accelerator, one should operate in the linear or near (quasi-)linear regime of  $a_0 \simeq 1$ , with some form of external guiding.

An external confining structure, such as a plasma density channel or dielectric capillary tube, would be beneficial, as it can help tame fluctuations caused by non-linearities, such as pointing instabilities. In an extreme case, the laser power can be operated below the self-focussing threshold so that the guiding and acceleration are only determined by the properties of the guiding channel. In that case, good shot-to-shot reproducibility of the guiding structure is imperative to maintain reproducible acceleration.

One issue for applying external guiding structures is their susceptibility to damage due to a poor laser structure and pointing instabilities. For the case of a capillary tube, the angular variation between the laser axis and the capillary tube should be less than 5 mrad, and the displacement of the laser spot centre to the capillary centre should be less than 10% of  $R_{cap}$ . This imposes stringent requirements on the beam quality of the high-power lasers that will drive the LPA stages of EuPRAXIA.

The coupling of laser and particle beams to the accelerator stage is another area of important consideration for the EuPRAXIA developments. Though laser beams can be directed by mirrors with perforation along the axis to allow the ingress of the particle beams, necessarily, EuPRAXIA should be designed with the possibility of using some form of plasma mirror due to the dramatic reduction in size that this affords. Continued research in the area of plasma mirror development is necessary. Similarly, particle beam coupling can be designed based on conventional fixed magnet optics, quadrupoles, etc., but given the space and challenging beam parameter constraints of the LPA beams, it is unlikely that these optics can provide an adequate solution for compact beam transport. In this case, the advent of plasma lenses based on capillary discharges offers equally important potential savings in space and complexity. Considering the rapid developments on these systems, it is now considered likely that they will form an important component of the EuPRAXIA developments.

## 17 Beam-Driven Plasma Accelerator

For the beam-driven case, acceleration to 1 GeV can be achieved in a single-stage plasma accelerator that is coupled with an RF linac operating at 500 MeV (Scheme 5, as described in Chap. 8). This stage is a few centimetres long, has a plasma density of approximately  $10^{16} \text{ cm}^{-3}$ , to produce electric fields of 1–2 GV/m, and with a plasma wavelength of  $\lambda_p \sim 330 \text{ }\mu\text{m}$ , which allows for the acceleration of electron bunch trains with the use of the laser-comb technique [323].

For the 5 GeV case, a transformer ratio of 5–6 is essential, and a single plasma stage would have to be a few metres long. The high transformer ratio is, in this scenario, accomplished with the use of a shaped train of bunches as the driver. This bunch structure guarantees a higher transformer ratio [192] that can be used to

accelerate the trailing bunch beyond the energy-doubling limit for symmetric bunches (see Sect. 7.1). In the design study, we assume an ideal train of bunches generated by the RF linac to an energy of 1.2 GeV, which is then boosted in a plasma stage with a plasma density of approximately  $2.5 \times 10^{16} \text{ cm}^{-3}$ , to produce electric fields of 1–2 GV/m and with a plasma wavelength of  $\sim 210 \text{ }\mu\text{m}$ .

## 17.1 Start-to-End Simulation for the 1 GeV Case

A sequence of several codes has been used to study beam-driven plasma acceleration through start-to-end simulations without any phase-space manipulation or remapping. The TStep code is used to simulate the generation and transport of both driver and witness bunches in the photo-cathode section. The ELEGANT code is used to track particles up to the plasma entrance (see Chap. 14); the particle phase space is then imported into the Architect code for the evolution in the plasma section. A summary of these results is presented in Chapter 23. In the following, the study of the beam-driven plasma accelerator stage (PPAS) is discussed.

### 17.1.1 Plasma Simulation Parameters and Code

The state-of-the-art code Architect is used for the plasma stage [356,357]. Given the necessity to run long simulations, a classical particle-in-cell approach was computationally too expensive. Architect is a reduced model code relying on a fluid background (see Sect. 32.1 for more details), which has been tested and verified against a classical particle-in-cell code for the parameter range of interest [357]. Simulations described in this section for the 1 GeV case have been performed with a longitudinal resolution of 1  $\mu\text{m}$  and a transverse resolution of 0.4  $\mu\text{m}$  in a mesh that allows resolving the fine structure at a reasonable computational cost. The advancing time step is 1.1 fs, and the average number of particles per cell is 30 and 100 for the driver and the witness, respectively.

### 17.1.2 Optimum Bunch Acceleration in the Plasma Section

The driver and the witness have been designed to perform for optimum acceleration in terms of both quality and energy transfer (*transformer ratio*,  $R_T$ ) [358]. To maximise the energy transfer, the bunches, particularly the witness, have been designed with a *triangular* [298,359] shape, which is an optimised profile to limit the energy spread growth.

Then the bunches are imported into Architect for the plasma evolution. The aim is to transport and accelerate the witness bunch through the plasma section, preserving the original bunch quality. The witness has also been designed with a *triangular* current shape to limit the energy spread growth. In addition to the triangular shape, the peak current influences the optimisation of the longitudinal density profile, which minimises the increase in energy spread during the propagation. Bunch shaping with high accuracy is not, however, a trivial task. In our case, a pseudo-triangular shape is produced where the front part of the profile consists of high-current slices for FEL lasing. From the FEL requirements standpoint, it is these high-current slices that need to be transported with as small a phase-space dilution as possible.

Additionally, to maintain the bunch quality and to ensure that both bunches evolve through the plasma with as little deterioration as possible, they have to be

injected at matching conditions. As introduced in Section 7.1, this plasma transverse matching condition is given by

$$\sigma_{x,\text{matching}} = \sqrt[4]{\frac{2}{\gamma}} \sqrt{\frac{\varepsilon_{n,x}}{\kappa_p}} \quad (17.1)$$

where  $\varepsilon_{n,x}$  is the normalised RMS emittance (in the transverse plane) in mm mrad while  $\kappa_p = 2\pi/\lambda_p$  is the plasma wavenumber. Equation (17.1) indicates transverse micron-size bunches. For our case, assuming  $n_p = 10^{16} \text{ cm}^{-3}$  as a nominal density background, we calculate  $\sigma_{x,D\text{-matching}} = 4 \text{ }\mu\text{m}$  and  $\sigma_{x,W\text{-matching}} = 1.55 \text{ }\mu\text{m}$ . We have assumed a driver with a normalised emittance of 3 mm mrad and a witness with a normalised emittance of 1 mm mrad.

Two geometrical conditions must also be met. (1) The bunch has to be as symmetric as possible, i.e.  $\sigma_x \sim \sigma_y$ . (2) The driver length must meet the longitudinal matching condition:  $\kappa_p \sigma_{z,D} = \sqrt{2}$  [360] (see also Sect. 7.1). The longitudinal matching condition is used to maximise the transformer ratio and to limit the quantity of driver charge recalled within the self-wake (head-tail acceleration process):  $\sigma_{z,D} = 75 \text{ }\mu\text{m}$ .

The foreseen design is planned to operate in the so-called *weakly non-linear regime*, where the electric field induced by the driver bunch has neither a full sinusoidal behaviour nor a full saw-tooth shape. The parameter we used to measure the degree of non-linearity is the *reduced charge parameter* [361,362], as introduced in Section 7.1,  $Q_{rc} = \frac{N_b}{n_p} \kappa_p^3$ , with  $N_b$  as the electron bunch number (bunch charge divided by the elementary charge). For the foreseen case,  $Q_{rc} \sim 0.8 - 0.9$  for a driver that is carrying a charge of 200 pC. Therefore, we need to leverage on both linear regime scaling laws as well as the non-linear regime scaling laws to identify the best parameter space for the accelerating stage. The injection phase  $\varphi_0$ , calculated for the maximum accelerating field, in a linear regime can be found as  $\varphi_0 \approx \frac{Q_{\text{witness}}}{Q_{\text{driver}}}$ . The calculation assumes that a driver bunch produces a linear wake  $E_{\text{acc}} = G \cos(k_p \xi)$ , while the witness produces a decelerating self-wake  $E_{\text{dec}} = -g \sin[k_p(\xi_0 + \sigma_z - \xi)]$ , with  $G$  and  $g$  as the accelerating and decelerating fields, respectively, where  $\xi$  is the longitudinal co-moving coordinate. By requiring that the electric field felt by a particle located at the witness front  $\xi = \xi_0 + \sigma_z$  experiences the same accelerating field of a particle in the centre of the bunch  $\xi = \xi_0$ , we retrieve the given solution. Then the injection phase is close to half of the plasma wavelength for the maximum decelerating driver field. Since the witness charge is fixed by the upstream FEL applications, simulations identify that beam loading is compensated for a driver-witness distance of 184  $\mu\text{m}$ , corresponding to a plasma density of  $0.55 \times \lambda_p (n_p = 10^{16} \text{ cm}^{-3})$ .

Our setup, specifically the driver, is characterised not only by a reduced charge factor that is just below 1 but also by a peak density that is about 10 times larger than the plasma background density. At the plasma entrance, the driver core is characterised by  $n_b/n_p = 10 - 15$ , where  $n_b$  is the peak bunch density. This condition, as discussed in [53], suggests that it is also possible to achieve a transformer ratio larger than 2 with a single bunch. The transformer ratio, for our optimised distance, is estimated to be around 3, while the accelerating gradient is estimated to reach around 1.1 GV/m.

### 17.1.3 Summary of the Simulation Results

In the simulations presented here, density ramps on the order of 0.5 cm are considered, which is experimentally feasible. The length of the ramps is below the betatron

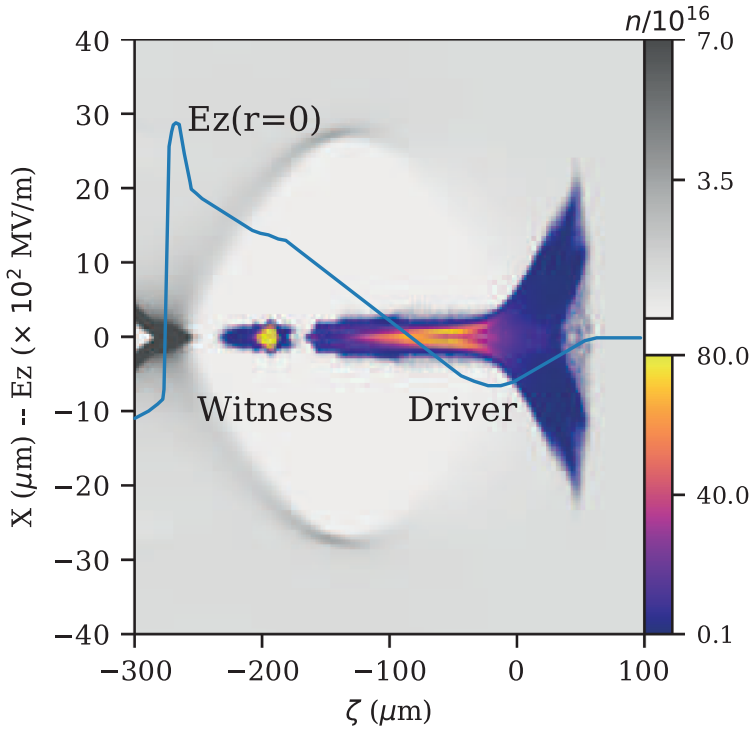


**Fig. 17.1.** Bunch and background density after 5 mm propagation within the plasma. The bunch density is plotted with a *plasma* colour map, while the background is plotted with a grey colour map. The longitudinal accelerating electric field on axis is over-imposed with a solid blue line. For the purpose of scaling,  $E_z$  is plotted in hundreds of MV/m.

wavelength, assuring that bunch oscillations are not present to increase acceleration robustness.

The witness is delivered at the plasma entrance with the required triangular shape. In the transverse direction, the bunch is relatively symmetric in size and in emittance (see Tab. 17.1), both of which are tuned to the plasma requirements and to preserve the beam brightness. The driver exhibits a weaker degree of geometrical symmetry, and it is delivered at the plasma entrance with a larger parameter than the matching condition because the RF linac has been optimised to deliver the witness bunch specifications at the plasma entrance (more details in Chaps. 12 and 14). The strict requirements for the witness naturally result in the driver to be away from the optimal conditions. However, since the driver will be removed after the acceleration, the lower quality is acceptable. Additionally, at the entrance of the plasma, the front part of the driver, which corresponds to 1/3 of the total beam charge, is highly convergent and will result in expansion within the plasma channel, producing a unique funnel shape which can be seen in Figure 17.1. Nonetheless, the driver is capable of driving a weakly non-linear wake with a maximum effective field that peaks around 2.5–3.0 GV/m (see Fig. 17.1).

The maximum field is achieved at the bubble closure where the witness is placed. The positioning of the witness would significantly change the bubble structure [186, 298, 363]. In the case of interest here, where a witness with a given peak current for FEL applications is desired, positioning the witness closer to the driver and meeting the beam-loading condition allows for better control of the energy spread. The wider bubble width also reduces the chance of quality deterioration. On the downside, such

**Table 17.1.** PWFA bunch parameters at plasma entrance and at plasma exit. The best slice value is also reported.

Beam	Units	Driver-IN	Driver-OUT	Witness-IN	Witness-OUT
<b>Charge</b>	pC	200	200	30	30
$\sigma_x$	$\mu\text{m}$	8	6.4	1.47	1.42
$\sigma_y$	$\mu\text{m}$	3.1	10	3.17	1.4
$\sigma_z$	$\mu\text{m}$	52	50	3.85	3.8
$\varepsilon_{n,x}$	mm mrad	2.56	4.1	0.6	0.96
$\varepsilon_{n,y}$	mm mrad	4.8	11.4	0.55	1.2
$\sigma_E$	%	0.2	20	0.07	1.1
<b>E</b>	MeV	567	420	575	1030
<b>Best Slice</b>					
<b>Current</b>	kA			2	2.0
$\varepsilon_{n,x}$	mm mrad	N/A	N/A	0.59	0.57
$\varepsilon_{n,y}$	mm mrad			0.58	0.62
$\sigma_E$	%			0.011	0.034

placement will limit the transformer ratio. The central part of the driver that mostly contributes to generating the wake loses about 150 MeV after a 40 cm distance; the witness gains about 460 MeV at the same time. This value indicates that the accelerating gradient is about 1.1 GV/m and that a transformer ratio of about 3 is achieved.

The electron beam properties from the simulations reaching 1 GeV beam energy are shown in Figure 17.2. Note that the rolling slice analysis technique was used here to estimate the witness bunch slice properties. Rather than defining a fixed binning across the longitudinal distribution of the bunch, which may misidentify high- or low-quality portions of the beam if they are split between bins, separate values are defined in this method for the bin size (L) and the step size with which to move the bin across the beam length (dz). Slice values are thus calculated in steps of size dz along the longitudinal beam distribution, while the region of macroparticles taken into account for each slice is defined by the length  $L \geq dz$  (e.g. corresponding to the cooperation length of an FEL). This provides a larger number of points at which slice parameters are calculated without having to reduce the number of macroparticles considered in each slice, therefore providing a better sampling of the bunch properties.

## 17.2 Numerical Design for the 5 GeV Case

### 17.2.1 Plasma Parameters

Simulations for the 5 GeV case have been performed assuming ideal bunch shapes. The simulations described in this section have been run with a longitudinal and transverse resolution of 1.0  $\mu\text{m}$  with a mesh that allows one to reasonably resolve the witness bunch structure at a moderate computational cost. The advancing time step is 0.59 fs. The drivers and the witness bunches use 200k and 30k particles, respectively.

The simulation includes focussing via a plasma ramp before the plateau; thus, the discretisation corresponds to  $\approx 1$  particle per cell at the initialisation reaching  $\approx 1000$  particles per cell at the plateau. The plasma channel is ideal, composed by a  $\sim 2.4$  m plateau with a plasma density of  $n_p = 2.5 \cdot 10^{16} \text{ cm}^{-3}$ , preceded by a 1 cm long injection ramp with a density that varies from zero to  $n_p$  with a  $\cos^2$  shape and a constant transverse dimension of 160  $\mu\text{m}$ .

In this section, less attention has been given to the transverse evolution of the bunch since for ideal bunch shapes, it is always possible to find a matching condition

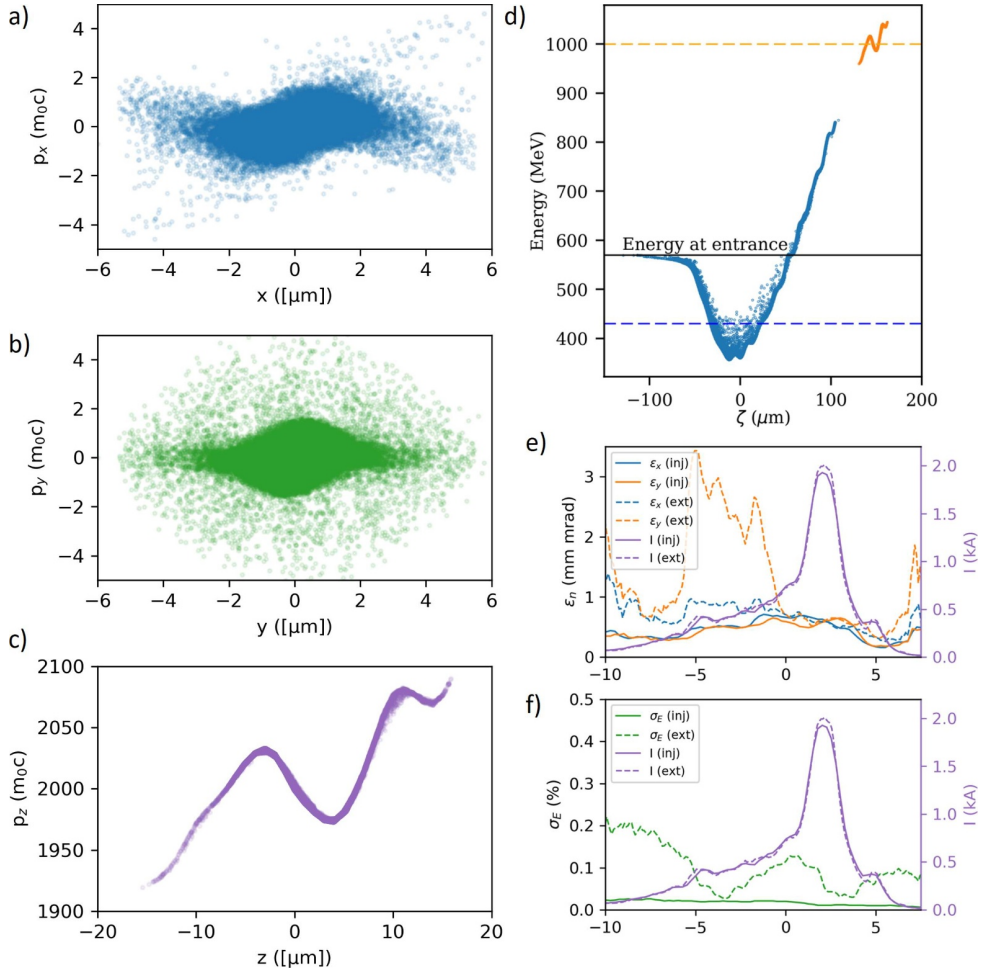


**Fig. 17.2.** Witness phase-space plots at the exit of the plasma-accelerating section (a–c). Longitudinal phase space at the plasma exit, plot of both the driver and the witness (d). Rolling slice analysis for the witness bunch at the plasma entrance (solid line) and at the plasma exit (dashed line). The top panel (e) shows the emittance in both transverse planes as well as the current. The bottom panel (f) plots the energy spread and the current. The corresponding current axis is the right  $y$ -axis.

for the preservation of the total transverse emittance [364]. In future full start-to-end simulation studies, where the accomplishment of such conditions is not trivial, the required attention will be dedicated to emittance preservation.

### 17.2.2 Driver Train Structure and Transformer Ratio

We assume a train of driver bunches generated by an X-band RF linac up to the energy of 1.2 GeV. Increasing energy transfer in a PWFA stage requires a driving structure with a higher transformer ratio  $R_T$  than the 1 GeV case. This condition can be obtained by utilising a train of drive electron bunches [192]. An energy increase from 1.2 GeV to 5 GeV requires an effective transformer ratio of  $R_T \approx 3.2$ , whereby “effective” means the transformer ratio is evaluated using the average field acting on

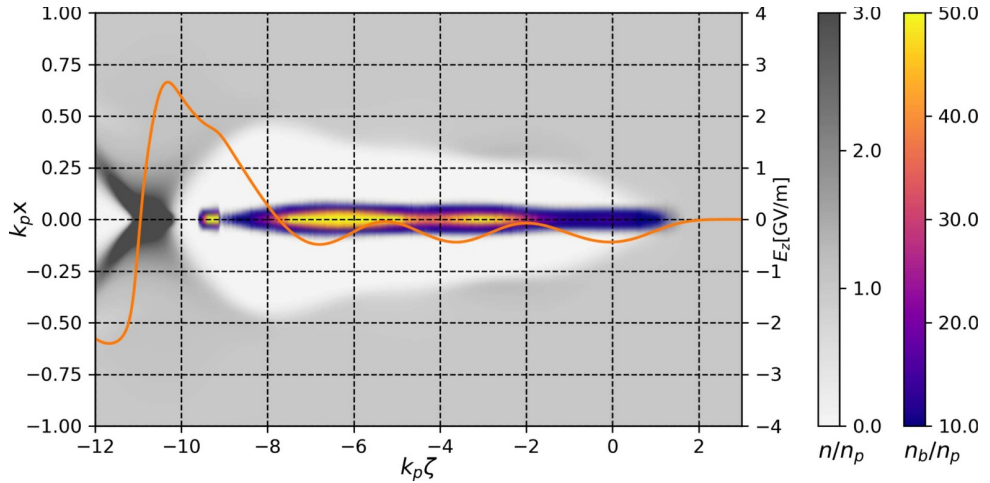


**Fig. 17.3.** Electron bunch and background density after 15 mm propagation within the plasma. The bunch density is plotted with a *plasma* colour map, while the background is plotted with a grey colour map. The longitudinal accelerating electric field on axis is over-imposed with a solid orange line.

the witness, including the beam-loading effect. Given the high current of the witness (3 kA), the beam-loading effect generates a critical reduction of the accelerating field and consequently reduces the effective transformer ratio. To avoid this problem, we designed an ideal train of 3 drivers with ramped increasing charge densities. Theoretically, this configuration allows reaching a transformer ratio of  $R_T = 2N$ , where  $N$  is the number of drivers. The bunch length for any bunch is  $\sigma_z = 33 \mu\text{m}$ , to have the condition for the maximum accelerating gradient  $k_p \sigma_z = 1$ . The separation between the bunches is constant, with  $\Delta\xi = 0.5\lambda_p$ , corresponding to  $\Delta\xi \approx 106 \mu\text{m}$ . The transverse injection condition is calibrated in order to have bunch focussing inside the ramps, reaching the matching condition (Eq. (17.1)) at the beginning of the plateau (Twiss functions  $\alpha_{x,y} \approx 1$ ,  $\beta_{x,y} \approx 22 \text{ mm}$  for all bunches). The transverse emittance of the two bunches is chosen arbitrarily as  $\varepsilon_{n,xy} = 1 \text{ mm mrad}$ . The charges are  $Q_1 = 40 \text{ pC}$ ,  $Q_2 = 140 \text{ pC}$ , and  $Q_3 = 270 \text{ pC}$ . They are properly calibrated to obtain a maximum decelerating field within the bunches that is constant for all drivers. In this configuration, without the trailing witness bunch, the transformer ratio is  $R_T \approx 7.5$ .

### 17.2.3 Bunch Acceleration

The witness is designed with the energy of  $E = 1.2 \text{ GeV}$  and an initial uncorrelated energy spread of  $\sigma_E = 0.7 \%$ . As in the 1 GeV case, a triangular current shape is chosen to reduce the energy spread growth with an RMS bunch length of  $\sigma_z = 3.6 \mu\text{m}$ . The transverse emittance is arbitrarily chosen as  $\varepsilon_{n,xy} = 0.7 \text{ mm mrad}$ , and the Twiss functions are  $\alpha_{x,y} \approx 1$  and  $\beta_{x,y} \approx 22 \text{ mm}$ , to reach the matching condition from equation (17.1) at the beginning of the plateau. The peak field is located at the bubble closure with a value of  $E_z \approx 2.7 \text{ GV/m}$  (see Fig. 17.3). The bunch separation between the centroids of the last driver and the witness is set as  $0.46 \lambda_p$ , corresponding to  $\approx 97 \mu\text{m}$  in order to minimise the energy spread growth. With this fixed, the mean accelerating gradient acting on the witness is  $E_z \approx 1.6 \text{ GV/m}$ . The maximum decelerating field acting on the drivers is  $\approx 450 \text{ MV/m}$ , leading to an

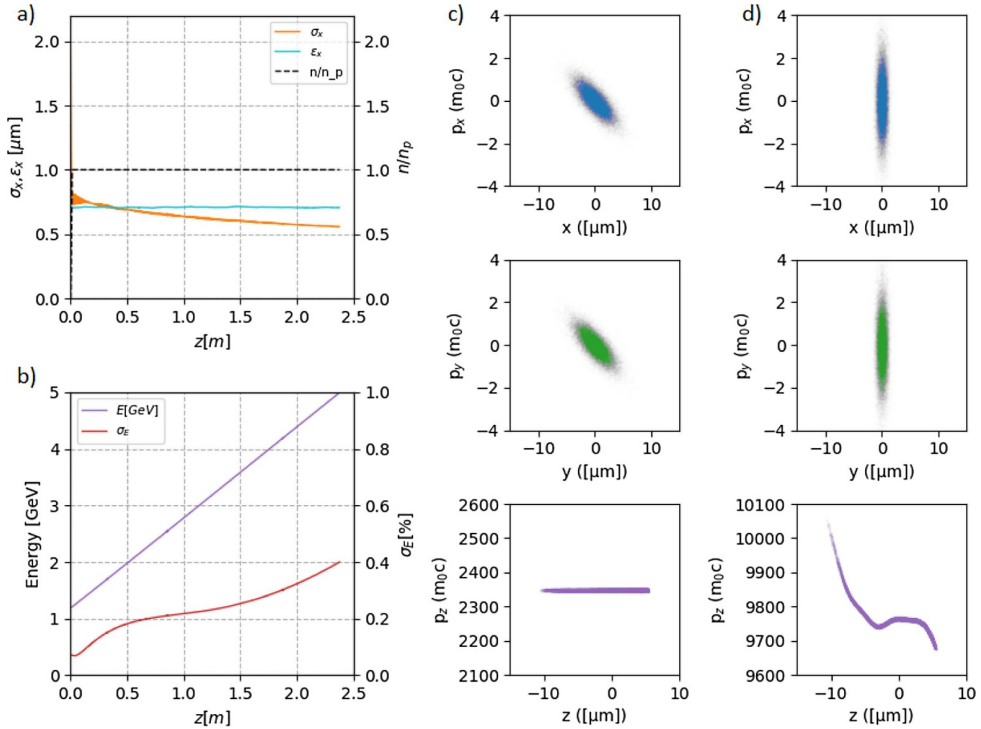


**Fig. 17.4.** Evolution of the spot size and the transverse emittance of the witness bunch (a), energy and energy spread of the witness bunch (b), phase space of the witness at injection (c), and phase space of the witness at the final step of the plasma target (d). Note that the normalised transverse emittance is defined as  $\epsilon_x$  here.

effective transformer ratio of  $R_T = 3.5$ . The witness is accelerated up to 5 GeV in a 2.4 m long accelerating structure. The evolution of the integrated parameters and the phase space can be seen in Figure 17.4. The slice parameters can be observed in Figure 17.5. The transverse phase-space quality is preserved completely. The energy spread increases to  $\sigma_E \approx 0.4\%$ . The highest energy spread growth is in the tail of the bunch, where the current is at a minimum.

### 17.3 Outlook and Further Research and Development

A further improvement of the beam parameters as presented in the previous subsections will further increase possibilities for a practical use of beam-driven plasma wakefield accelerators. From the studies presented here, it is evident that accelerating the electron beam to energies beyond 5 GeV in a single stage of the EuPRAXIA design may degrade its quality. Therefore, a strong focus for future studies on staging, its challenges, and mitigation techniques is essential.

To this aim, currently, operational R&D beam-driven facilities such as FLASH-Forward and SPARC-LAB have dedicated experiments for the investigation and evaluation of cutting-edge mitigation techniques and diagnostics. These studies are still ongoing. A selection of the most recent developments has been summarised in Section 32.5. The section also discusses some more practical considerations regarding the plasma sources required for a beam-driven wakefield accelerator.

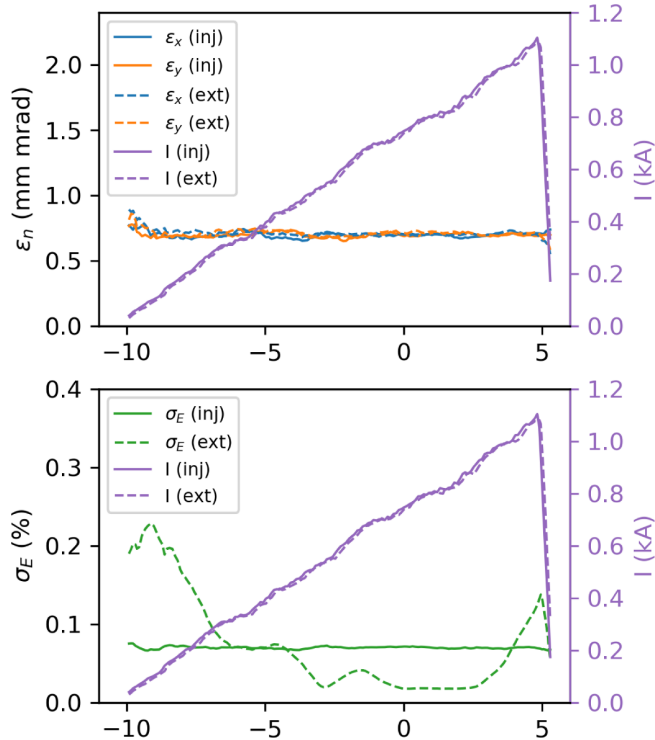


**Fig. 17.5.** Rolling slice analysis in the 5 GeV case for the witness bunch at the plasma entrance (solid line) and at the plasma exit (dashed line). The top panel reports the normalised emittance in both transverse planes as well as the current. The bottom panel plots the energy spread along with the current. The corresponding current axis is the right  $y$ -axis.

PWFAs in comparison to LWFAs are especially promising for high-average power free-electron laser applications and linear colliders considering their capabilities in energy transfer efficiency, average power, and repetition rate. It is crucial that future studies at PWFA test installations explore this potential in a complementary fashion beyond the goals set for EuPRAXIA. For example, at FLASHForward, it is possible to drive the plasma wakefield by high-current-density electron beams extracted from the FLASH L-band superconducting RF accelerator at up to a 3 MHz repetition rate with an average power well exceeding 10 kW. Such activities will synergistically complement future EuPRAXIA activities and help to maximise a successful implementation of PWFA technology into operational accelerators for users.

## 18 Magnets, Undulators, and Plasma Lenses

### 18.1 Introduction

Proposed in 1979, the laser-plasma accelerator (LPA) [4] enables the creation of ultra-high accelerating fields capable of generating electron beams with up to several GeV energy, short beam size (fs), excellent emittance at the plasma-vacuum interface ( $<1$  mm mrad), and a high peak current (1–10 kA) within centimetre scale. The concept of the LPA [4] is based on the focussing of an ultra-intense laser pulse used to drive large-amplitude plasma waves that then act as accelerating structures for

particles. Since then, various LPA configurations have been conceived and realised, like the laser wakefield accelerator (LWFA) [4], the plasma beat wave accelerator (PBWA) [4], the self-modulated laser wakefield accelerator [365], wakefields driven by multiple pulses [180], and the highly non-linear regime of electron cavitation [366]. The so-called LWFA bubble (or blowout) regime [367] is very efficient since it preserves the normalised emittance of an accelerated electron bunch as the focussing force can be very large, is linear and provides charges of the order of hundreds of pC with mrad-level divergences, fs bunch durations, and good electron energy tunability. Two stages (injection and acceleration) can be differentiated in LPAs. The injection, where the electrons are introduced into the acceleration structure and the acceleration, is crucial to better control the resulting electron bunch characteristics. Specific acceleration techniques can thus be developed in multiple injection schemes. Ponderomotive injection [368] uses a laser to generate the plasma wakefield via LWFA and a second one to drive electrons into the wakefield, which allows for good injection control. Trapping in the self-modulated LWFA regime [369] uses a single laser to cause self-trapping and the generation of sub-ps electron bunches by trapping background plasma electrons in the wakefield. Colliding pulse injection [370] uses a three-laser system for plasma wave generation; backward and forward injection is used to generate a slow beat wave which heats and traps background electrons that are injected in a fast wakefield. Density transition injection [275] uses a downward transition in the plasma density to induce local self-trapping in the plasma wave, allowing for the generation of well-collimated, short electron bunches with narrow energy spread. Ionisation injection [280] uses a simple scheme where a target medium of low  $Z$  with a small proportion of high- $Z$  gas is used, so that in front of an intense laser the outer shell of the high- $Z$  gas is ionised contributing mainly to the plasma wave, and the inner-shell electrons ionised at the intensity peak are easily trapped by the plasma wave. Table 1 shows some experimental results for LPA electrons from the hundreds of MeV to the GeV level.

When considering implementing a free-electron laser based on electrons that are produced through LWFA [180], several new issues arise. The electron beam being of rather short duration, one should lengthen the electron beam in a chicane for the light not to escape from the electron bunch due to slippage. The electron beam also presents an energy spread which is typically one hundred times larger than the one generally accessible on linear accelerators used for short X-ray FELs [124]. To handle this issue, some electron beam manipulation has to be performed, either prior to the undulator with a demixing chicane [141,371] or directly inside the undulator using a transverse gradient undulator [64].

A relativistic electron passing through a planar undulator of period  $\lambda_u$  and peak field  $B_u$  is subjected to a sinusoidal trajectory and emits synchrotron radiation because of its acceleration in the transverse plane. The emitted radiation interferes and tends to add constructively depending on the phase lag between the electron and the front of the emitted wave train. This interference produces higher harmonics, leading to a harmonic spectrum. The radiation spectrum in the forward direction is not continuous but nearly monochromatic, i.e. it is composed of narrow spectral lines at well-defined frequencies caused by the harmonics. The resonant wavelength of these harmonics is given by  $\lambda = \lambda_u(1 + K_u^2/2)/2\gamma^2$ , with  $K_u$  as the deflection parameter and  $K_u = 0.934\lambda_u(\text{cm})B_u(T)$ . A planar undulator leads to a linear polarisation in the plane of the electrons. An elliptical polarised undulator (EPU) produces a periodic magnetic field in both the vertical and horizontal planes, with variable dephasing and helical polarisation.

The periodic magnetic field of an undulator is created by either permanent magnets or electromagnets (superconducting or warm magnets) placed next to each other and separated by equal distance. The various technologies available to build an

undulator for an LPA-based FEL include cryogenic undulators [372,373], superconducting undulators, as well as exotic systems and technologies under development such as microfabricated undulators, plasma undulators, and transverse gradient undulators. For an FEL application, different undulator figures of merit are considered. First, a correct trajectory should be achieved for the radiation of the different period to interfere properly and ensure a proper natural bandwidth. The phase error, caused by the magnetic field errors along the undulator axis, such as variations in the peak field or the period length from one period to another [374,375] (mechanical changes, thermal effects, random effects due to magnetic defects, angular errors, etc.) has to be considered. It can cause a change in the length of the electron trajectory and yields a phase lag between the electron and the photon, resulting in destructive interference. In the framework of EuPRAXIA studies, a particular interest concerns the push towards higher magnetic fields with shorter undulator periods since one aims to minimise the slippage because of the shorter electron bunches produced by laser-plasma acceleration in order to avoid the light from escaping the electron bunch along the progression in the undulator. While reducing the period, one should keep, however, a deflection parameter value slightly larger than 1 to produce harmonics. So typically, one naturally considers cryogenic or superconducting undulators. In addition, depending on the strategy chosen for handling the initial large energy spread, transverse gradient undulators are of particular interest. Then one tries to define baseline undulator parameters to be used for the FEL pilot application of EuPRAXIA.

## 18.2 Specific Magnetic Elements

### Issues to Be Handled for LPA-Based FELs

An LPA-based FEL [60,61,376] appears attractive and conceivable, even though the properties of the beams cannot be directly used for FEL and, as a result, the beams should be first adapted and transported to the undulator.

Electron beam performance should thus fulfill the electron beam requirements imposed by the FEL. For an FEL [111] to be achieved, a relative slice energy spread  $\sigma_\gamma$  over one coherent length of less than  $\sigma_\gamma/\gamma < \rho$  is needed, with  $\gamma$  as the relativistic factor and  $\rho$  as the Pierce parameter. This condition is difficult to achieve since energy spreads on the percent level have been measured for MeV–GeV LPA electron beams. So to use these beams for FEL, the slice energy spread should be reduced, for example, by cutting a part of the initial distribution [377], using a demixing chicane to separate longitudinally the energies and select them [65] or opting for a different approach with the use of transverse gradient undulators (TGU) [64,378]. There is no specific issue regarding the dipoles of the chicane. The transverse gradient undulator has been reviewed in previous EuPRAXIA reports.

A problem arises regarding the transport of these beams towards the undulator. Even though the beam at the plasma-vacuum interface has a low emittance when leaving the interaction region, the normalised emittance suffers a strong deterioration, which makes the beam transport very difficult if not quickly mitigated [377,379]. So as the Twiss beta function  $\beta_T = \sigma_x/\varepsilon$  (with  $\varepsilon$  as the geometric emittance and  $\sigma_x$  as the transverse beam size) is of sub- $\mu\text{m}$  magnitude in the drift, the transverse beam correlation increases quadratically with distance due to a divergence of the order of mrad and becomes a predominant term in the emittance. The high divergence also causes a constant rapid increase in the beam size. The approach for calculating normalised emittance as  $\varepsilon_n = \langle \gamma \rangle \varepsilon$  used for a drift in conventional accelerators is no more correct for LPA electron beams, and one has to employ the general definition

**Table 18.1.** Typical quadrupole specifications.

	LPA
Gradient G (T/m)	200
G tuneability (%)	$\pm 20$
Gradient homogeneity over 5 mm	$10^{-2}$
Bore diameter (mm)	10.5
Magnetic axis excursion ( $\mu\text{m}$ )	$< 10$
Length (cm)	30

[194] given by

$$\varepsilon_n^2 = \langle x \rangle^2 + \langle \beta^2 \gamma^2 x'^2 \rangle + \langle x \beta x' \gamma \rangle^2 \quad (18.1)$$

with  $x$  and  $x'$  as the transverse position and divergence, respectively,  $\beta = v/c$ , and  $\gamma$  as the relativistic factor. If the correlation between energy and transverse position is negligible and assuming relativistic electrons ( $\beta=1$ ), one can write,

$$\varepsilon_n^2 = \langle \gamma \rangle^2 + (\sigma_\gamma^2 \sigma_x'^2 \sigma_x^2 + \varepsilon^2) \quad (18.2)$$

with  $\sigma_x'$  as the beam transverse divergence. Assuming that the beam is at a waist at the plasma-vacuum interface ( $\sigma_x(s) = \sigma_x' s$ ), with  $s$  as the longitudinal beam position, equation (18.2) becomes

$$\varepsilon_n^2 \approx \langle \gamma \rangle^2 + (\sigma_\gamma^2 \sigma_x'^4 s^2 + \varepsilon^2). \quad (18.3)$$

This rapid emittance increase is linked to the fact that the betatron frequency of the beam strongly depends on the energy. During the drift, each energy component rotates with a different velocity in the transverse phase space, increasing the area occupied by the bunch, resulting in a position and energy spread dependence of the normalised emittance. The projected normalised emittance of an LPA bunch of percent slice energy spread and mrad divergence causes a rapid increase in normalised emittance in a short drift distance, causing the beam to become emittance dominated and making it difficult to transport. A way to avoid a fatal emittance worsening of the beam is to capture and control the beam using strong focussing magnetic fields as close as possible to the plasma-vacuum interface with conventional accelerator techniques (e.g. the use of FODO with quadrupoles) [61] or active plasma lenses (APL) [380,381]. In both cases, a high magnetic gradient is necessary to control the beam emittance.

## Different Conventional Quadrupole Technologies

### *Typically Required Quadrupoles Strength*

It is relevant to consider conventional accelerator technology to handle the beam divergence. One can consider typical quadrupole requirements, as indicated in Table 18.1.

### *Electromagnetic Technology*

Mature resistive magnets, with copper conductors wrapped around soft iron poles, enabling one to tune the strength by simply changing the current with significant associated power consumption, are mostly used nowadays. Superconducting magnets producing very large magnetic fields require a costly helium infrastructure to keep the magnets in a superconducting state at a few Kelvin in temperature.

**Table 18.2.** Characteristics of fixed-gradient quadrupoles.

Labs/Projects	Gradient (T/m)	Bore diameter (mm)
PLEIADES ICS	550	5
FEL LPA	500	6
CLIC	575	8.25
SLAC/Kyoto	285	14
CESR	25.4	67
CESR	27.5	67
ESRF	82	24

### *Permanent Magnet Technology*

Permanent magnet quadrupoles (PMQs) can offer high fields in a very compact design, free of the need for a power supply and electricity consumption. Wide tunability, high field homogeneity, and cost optimisation are still challenges to be faced.

### Permanent-Magnet-Based Quadrupoles of Fixed Strength

Permanent-magnet-based quadrupoles (PMQs) mainly consist of  $Nd_2Fe_{14}B$  magnets because of their high remanent field and coercivity. Several Halbach-based PMQs with a fixed gradient were designed and built recently at facilities worldwide (see Tab. 18.2). Using the strong permanent magnet material NEOMAX, made from  $Nd_2Fe_{14}B$  (Sumitomo Special Metal Co, Ltd), a PMQ was fabricated (at Kyoto University/SLAC) with a modified Halbach configuration [382]. A high-gradient miniature PMQ is built for a laser-based tabletop free-electron laser at the Mainz electron accelerator (MAMI) [383]. It has a bore diameter of 6 mm with a magnetic length of 17 mm producing a field gradient of 503 T/m. The quadrupole field is defined by four radially magnetised wedges of  $Nd_2Fe_{14}B$  with a remanence field of 1.5 T.

In addition, various PMQs have been built at the Cornell Electro-Positron Storage Ring (CESR). A permanent magnet with a 16-sector Halbach system with 1.22 remanence-field  $Nd_2Fe_{14}B$  magnets of 67 mm bore diameter and 92 mm magnetic length, providing an integrated gradient of 2.5 T, was built [384]. At PLEIADES ICS, a 16-sector Halbach system of 5 mm bore diameter and maximum gradient of 560 T/m with adjustable focussing by longitudinal translation of the PMQ triplet has been designed and built [385]. At the Department of Physics in Munich, two 12-sector Halbach ring permanent-magnet systems using four radially magnetised magnets of 17 mm (15 mm) length, 6 mm bore diameter, 500 T/m gradient, and 7.5 T (8.5 T) integrated gradient have been built for tabletop FEL application [383]. Within a CLIC-CERN collaboration, a modified 12-sector Halbach permanent magnet with a Permendur mainframe that also works with poles of 100 mm (300 mm), 8.25 mm bore diameter, and 575 T/m gradient has been designed [386]. At ESRF, a compact PMQ with a hybrid-undulator-type design of 24 mm bore diameter and 82 T/m gradient for use in a storage ring has been constructed [387].

### Permanent-Magnet-Based Quadrupoles of Variable Strength

Various original designs were proposed and developed for a PMQ with a variable gradient (see Tab. 18.3) [388]. A modified Halbach-configuration PMQ with a variable gradient has been built in collaboration between Kyoto University and the Stanford Linear Accelerator Center (SLAC) for the final focus lens in a linear collider [389]. The quadrupole consists of an inner and outer ring, where the outer one is rotated to change the integrated gradient. The quadrupole bore diameter is 20 mm, with a magnetic length of 200 mm, generating a maximum gradient of 115 T/m with a tunability of 98 T/m.

**Table 18.3.** Characteristics of variable gradient quadrupoles.

Labs/Uni	Gradient (T/m)	G (T)	Bore diameter (mm)
ILC	115	98.5	20
COXINEL	208	93	11
NLC	135	27	12.7
SLAC	115	102	13
ILC	120	98	20
CLIC beam driver	60.4	45.4	27.2

An adjustable PMQ prototype has been designed and built in collaboration between CERN and the STFC Daresbury Laboratory [390]. The design incorporates a novel method of adjustment based on moving the permanent magnets. The field is generated by four permanent magnets at an angle of  $40^\circ$  to the horizontal, and each pair is attached by a wedge-shaped bridge of ferromagnetic material, where the gradient strength is varied by moving the bridge and permanent magnets vertically away from the centre to increase the gap. The bore diameter is 27.2 mm, with a magnetic length of 241 mm providing a maximum gradient of 60.4 T/m with a tunability of 45.4 T/m. A lower-strength version is also designed with the same bore diameter but with a 194 mm magnetic length. The maximum gradient attained is 43.8 T/m, with a tunability of 40.9 T/m.

Other designs of PMQs with variable gradients have been proposed and developed, such as a design (SLAC-Fermilab collaboration) based on four permanent magnet blocks and four soft iron poles, with the possibility to retract linearly the permanent magnet blocks, enabling an integrated gradient variation between 7 T and 68.7 T (gradient between 13 T/m and 115 T/m) for a 6.5 mm bore radius [391]. A ‘super hybrid quadrupole’ concept (28 T/m, 7 T integrated gradient, and 27.5 mm bore radius) combining permanent magnetic material, coils, and soft magnetic material with 30% variability has also been built [392]. A high-reliability prototype quadrupole for the Next Linear Collider (NLC) of 12.7 mm bore with a range of integrated strengths from 0.6 T to 132 T, a maximum gradient of 135 T/m, and an adjustment range of 0 to  $-20\%$  with a  $1\ \mu\text{m}$  magnetic centre stability has been built and fully tested [393].

A new patented [394] concept of compact hybrid permanent magnet quadrupoles of variable focussing strength for accelerators has been developed in the frame of the ERC COXINEL project for handling the large divergence of the electron beams produced by LPA while aiming at FEL application [141]. These so-called QUAPEVAs provide a large gradient (up to 200 T/m) and a wide tunability range ( $\sim 45\%$ ) [140,395–398]. They are mounted on translation tables for fine alignment and combine a Halbach-type quadrupole surrounded by four motorised rotating cylindrical magnets, enabling the gradient adjustment and plates behind for magnetic field shielding. Seven systems have been built and measured. The measurements confirmed the expected performance and successfully enabled the LPA electron transport for COXINEL [65]. The magnetic centre excursion, while varying the gradient, is kept within the  $\pm 10\ \mu\text{m}$  range.

### Prospects Offered by Active Plasma Lenses

First discussed by Baker and Panofsky in 1950 [399], active plasma lenses (APLs) have been extensively used for ion beams, for example by using z-pinch discharges [400]. Now with the necessity of a transport strategy for LPA electron beams, the use of APL is already being seriously considered to substitute quadrupoles [380,381]. The high gradient fields of the order of kT/m, high tunability, and radial focussing symmetry allow for cm-scale focal lengths for MeV and GeV electron beams.

Recent works comparing state-of-the-art permanent magnet quadrupole triplets and active plasma lenses [401] have been carried out at LBNL in California, USA. A PMQ triplet positioned 17 cm away from the LPA source and 1.73 m from the spectrometer entrance with a 25 mm bore, 39, 54.5, and 25.5 mm lengths, 51.9, -50.9, and 51.3 T/m gradients in the x-direction, and -51.3, 51.0, and -51.1 T/m gradients in the y-direction is compared with an APL positioned 24 cm from the LPA source of  $L_{APL}=1.5$  cm length and a  $R_{APL}=500$   $\mu\text{m}$  radius and with different densities.

Experiments and simulations show a lower energy dependence (chromaticity) in the APL-based line. Given the limited acceptance of around  $\pm 2$  mrad, the electron beam wings for the APL are cut. The APL aperture also reduces the effective source divergence to approximately 1.8 mrad RMS and makes the charge throughput more sensitive to pointing fluctuations. Other effects on the electron beam caused by the APL walls lead to changes in charge density and a slight increase in emittance for large beam sizes with respect to the APL.

APLs favour smaller beams, but the effect can be reduced with low-density APLs of  $n < 10^{17}$   $\text{cm}^{-3}$ , short capillaries, and low beam densities (larger longitudinal length beams). A study of an APL transport line design that keeps the emittance degradation to 0.4  $\mu\text{m}$  is being researched [401], two-stage LPA setups using APL are being used [380], and numerous experiments to characterise APL and their capabilities for electron bunch transport are being carried out in numerous laboratories [305,381].

## Conclusion

The transport of an LPA electron beam requires strong focussing right after the plasma. The technological solutions based on permanent magnet quadrupoles have been presented. The first results of comparing active plasma lenses with quadrupoles are also discussed. For EuPRAXIA, in view of robustness, it appears that the solution based on permanent magnet quadrupoles of variable gradients and variable strengths is the most suitable, since it enables the compensation for alignment errors of the components of the transfer line and of the electron beam pointing changes [65].

## 18.3 Review of State-of-the-Art Short-Period Undulators

### Development of State-of-the-Art Cryogenic Undulators

#### *Permanent-Magnet-Based Undulators*

Permanent magnet undulators (PMUs) [402] are able to function at room temperature and attain a fair magnetic field depending on the magnet material. PMUs are typically on-air devices with comparably large undulator gaps, which limits the on-axis magnetic field. Most pure permanent magnet undulators (PPMUs) use the Halbach geometric design [403]. Introducing poles between the magnets of a permanent magnet undulator makes it a hybrid type and enhances its magnetic peak field [404]. Poles are usually made of Vanadium Permendur material, i.e. cobalt-iron-vanadium alloys which saturate rather easily and have a high permeability and very high flux density at saturation.

Achieving a short-period undulator design with a sufficiently high magnetic field sets requirements for the magnetic material. Shortening the period implies a magnet-size reduction that results in a lower magnetic field. The magnetic remanence increase is at the expense of the coercivity (i.e. resistance against demagnetisation). So in-vacuum undulators [405–407] which avoid the beam pipe undulator gap limitation

**Table 18.4.** Typical characteristics of permanent magnets used for undulators.

Magnets	$B_r$ (T)	$H_c$ (kA/m)
SmCo <sub>5</sub>	0.8–0.9	2400
Sm <sub>2</sub> Co <sub>17</sub>	1.05–1.15	1700–2000
Nd <sub>2</sub> Fe <sub>14</sub> B	1.0–1.4	1000–2600
Pr <sub>2</sub> Fe <sub>14</sub> B	1.1–1.37	1000–1300

were adopted to reach a small gap with a sufficient magnetic field in placing the magnetic arrays in vacuum. The mechanical design should thus handle the magnetic forces due to larger fields and be vacuum compatible. The carriage can consist of a metallic base and a frame on which two external girders are fixed. A system of rods and flanges enables one to connect the internal girders where the magnet arrays are installed to external girders fixed to the carriage, which is designed to handle the magnetic forces. The carriage is equipped with motors for the movement of the gap (entrance and exit) and eventually for the movement of the offset to adjust vertically the magnetic axis of the undulator to the electron beam axis. Linear and rotated encoders are currently used to read the absolute gap. In addition, a vacuum chamber and pumping system should provide a good vacuum. Usually, the in-vacuum undulators are baked, so the magnet grade should handle being heated; tests with an unbaked in-vacuum undulator showed that beam conditioning can improve rapidly the vacuum [408]. The undulator vacuum chamber is connected to the standard chamber with specific RF tapers [409] for preserving a proper value of the impedance with or without water cooling. A liner (generally in Ni-Cu) is laid on the magnet arrays to prevent the heat load from the image current because of wakefields or up-stream synchrotron radiation [410].

#### *Magnet Choice*

Permanent magnets are characterised by their remanence  $B_r$  (strength of the magnetic field), coercivity  $H_c$ , energy product  $BH_{max}$  (density of magnetic energy), and Curie temperature  $T_c$  (temperature at which the material loses its magnetism). Permanent magnets [411,412] used for undulators combine rare-earth (RE) ferromagnetic elements with incomplete f-shells and transition metals with d-shells such as iron, nickel, and cobalt. The rare-earth magnets present a crystalline structure with a very high magnetic anisotropy (stable alignment of the atoms), enabling an easy magnetisation along one direction and a high resistance along the other. High magnetic moments at the atomic level combined with the high anisotropy result in a high magnetic field strength. The typical performances of SmCo<sub>5</sub> [413], Nd<sub>2</sub>Fe<sub>14</sub>B [414–416], and Pr<sub>2</sub>Fe<sub>14</sub>B magnets are presented in Table 18.4.

Magnets' resistance to demagnetisation [417,418] and heat budget are an issue, in particular for in-vacuum undulators, for which intermediate grades of Nd<sub>2</sub>Fe<sub>14</sub>B ( $B_r \leq 1.26$  T;  $H_c = 1900$  kA/m) could be used. A choice of Nd<sub>2</sub>Fe<sub>14</sub>B with high coercivity avoids demagnetisation at UHV baking and radiation damage. A small inclusion of Dysprosium also allows for a larger coercivity. Typically, one should consider a coercivity larger than 1000 kA/m to avoid demagnetisation at room temperature and larger than 2000 kA/m to prevent it at 120°C (393 K), i.e. in baking conditions.

The idea of cooling down RE<sub>2</sub>Fe<sub>14</sub>B rare-earth permanent magnets, which increases the remanent field and coercivity, was proposed [419], leading to the concept of cryogenic undulators. For example, typical temperature coefficients for RE<sub>2</sub>Fe<sub>14</sub>B are  $-0.11\%/^{\circ}\text{C}$  for the remnant field and  $-0.58\%/^{\circ}\text{C}$  for the coercivity, i.e. decreasing the temperature by a factor of two enables one to increase the remanent field by 10% and the coercivity by more than 50%. As the increase in coercivity is larger than

the one of the remanent field, one can even take a magnet grade that is less resistant at room temperature but presents a higher remanent field.

Measurements [407,420] of remanent field and coercivity for different grades of  $RE_2Fe_{14}B$  permanent magnets versus temperature were performed. The grades for each material slightly differ in field remanence and coercivity but show similar behaviour as a function of temperature. For Neodymium grades at low temperature (130–140 K), the remanent field starts to decrease because of the so-called spin re-orientation transition (SRT) phenomenon [421–423], which exhibits a negative dependence of remanent fields against temperature below 130–140 K due to a change in the preferred direction of the magnetisation with respect to the easy axis of magnetisation. In contrast to the Praseodymium grades, the remanent field continues to increase at low temperatures down to 30 K. These magnets can be cooled down to 30 K, and attain a high coercivity ( $\sim 7300$  kA/m) and high field remanence (1.7 T) [424,425]. The coercivity of all grades maintains increasing with lower temperature [426].

#### *Cryogenic Permanent-Magnet-Based Prototype Undulators*

Several cryogenic permanent magnet undulator (CPMU) prototypes were built at different locations. At SPring-8 [427], a  $40 \times 15$  mm period  $Nd_2Fe_{14}B$  system has been built and optimised, with  $3.3^\circ$  and  $3.2^\circ$  RMS phase errors at 300 K and 130 K, respectively. The temperature control at 140 K was enabled thanks to sheath heaters. It then appeared quite attractive to use  $Pr_2Fe_{14}B$  magnets for being able to operate at lower temperature, thus with a larger magnetic field and coercivity. The first prototype of  $8 \times 14.5$  mm period NSLS [428] using  $Pr_2Fe_{14}B$  magnets (NEOMAX 53CR) and Vanadium-Permendur poles has been measured in the Vertical Test Facility at liquid nitrogen and He temperatures with a slight increase in the RMS phase error at lower temperature ( $3.1^\circ$  at room temperature and  $3.5^\circ$  at 77 K). The second system [429] developed at NSLS-II, using a grade of  $Pr_2Fe_{14}B$  magnet that can be baked (NEOMAX CR47) led to a higher field than the previously employed grade (at 80 K : 1.12 T for the CR47 and 1.22 T for the CR53). Several CPMU prototypes were built at SOLEIL [430]. The first one [431], a  $4 \times 20$  mm period hybrid  $Nd_2Fe_{14}B$  system, shows a 11.5% increase in the magnetic field between room temperature and a cryogenic temperature of 140 K, the operation temperature. The second one [432] ( $4 \times 18$  mm period) and the third one [433] ( $4 \times 15$  mm period) of the  $Pr_2Fe_{14}B$  hybrid type (NEOMAX CR53), take advantage of the absence of SRT phenomena. The magnetic field grows by 13% between room temperature and a cryogenic temperature of 77 K. A  $20 \times 9$  mm period  $(Pr, Nd_2)Fe_{14}B$  (Vacuumschmelze /Vacoflux50) cryogenic undulator [434,435] with  $Co_{49}Fe_{49}V_2$  poles with a saturation magnetisation of 2.35 T, built jointly by the Helmholtz-Zentrum Berlin and the Ludwig-Maximilian-University München (LMU), shows an increase in the remanence by 20% and of the peak field at the fixed gap of 2.5 mm by 11 %, with a partial saturation of the pole pieces from 300 K to 30 K. The second prototype with modified poles exhibits a larger field [436] and it enabled the observation of synchrotron radiation [437] using the MAMI-B beamline with a 855 MeV beam.

#### *State of the Art of Cryogenic Permanent-Magnet-Based Full-Scale Undulators*

The construction of full-scale devices to be installed for beamlines has started at ESRF [438–441] with a 2 m long full-scale 18 mm period  $Nd_2Fe_{14}B$ -magnet (NEOREM 595t) hybrid CPMU. The peak field is increased by 6% when cooled down from 273 K to 150 K at a gap of 6 mm. The RMS phase error slightly increases from room temperature ( $4.8^\circ$ ) to 150 K ( $5.7^\circ$ ), because of a residual longitudinal temperature gradient. It is the first full-scale (2 m length) CPMU to be built and installed for operation with an electron beam and a liquid nitrogen closed loop for

**Table 18.5.** Width of magnets and poles for different periods and coefficients of the fitting curves, a, b and c, shown in Figure 18.2. The magnetic field is fitted with the equation  $B_{peak} = a \exp(b\frac{g}{\lambda_u} + c(\frac{g}{\lambda_u})^2)$ , where  $g$  is the magnetic gap.

Period (mm)	Magnet Width (mm)	Pole Width (mm)	a	b	c
18	6.5	1.25	3.74306	-4.0533	0.69459
15	5	1.25	0.389558	-4.0222	0.52895
12	4	1	3.98608	-4.0874	0.67293
10	3.5	0.75	3.5308	-3.6476	0.40497

cooling. A second CPMU has been built and installed at ESRF. Two additional  $Pr_2Fe_{14}B$ -based hybrid undulators are under construction.

At the Paul Scherrer Institute [442–444], a full-scale 1.7 m long 14 mm period CPMU using  $Nd_2Fe_{14}B$  (Hitachi NMXS45SH) magnets and Vanadium-Permendur poles, cooled with LN2, had been measured with SAFALI (Self-Aligned Field Analyser with Laser Instrumentation). The measured phase error of  $1.1^\circ$  is similar to the one measured at room temperature, thanks to an in situ correction method.

SOLEIL [445,446] had built and measured the first  $Pr_2Fe_{14}B$  (CR53)-based full-scale hybrid cryogenic undulator (2 m long, 18 mm period) cooled down to 77 K with LN2. The phase error at a 5.5 mm gap at room temperature of  $2.8^\circ$  RMS increases up to  $9^\circ$  at 77 K, but has been corrected down to  $3^\circ$  by shimming the rods. It is the first  $Pr_2Fe_{14}B$  full-scale cryogenic undulator installed in a synchrotron radiation facility, in use at the Nanoscopium long beamline. SOLEIL is in the process of building three new cryo-ready devices with a different  $Pr_2Fe_{14}B$  grade with an enhanced coercivity (1912 kA/m): a second 2 m long U18 CPMU that has been successfully installed for use at COXINEL [447,448] at room temperature as well as a 3 m long U15 CPMU [433] enabling a 1.65 T at 77 K for a 3 mm gap.

At DIAMOND [449], a 17.7 mm period full-scale  $Nd_2Fe_{14}B$  (Vacodym 776TP)-based hybrid CPMU has been built by Danfysik [450]. As the temperature is decreased from 300 K to 157 K, the field is increased by 7.03% at a 4 mm gap, while for a gap of 10 mm the increase in field is 8.69%. At 157 K, the RMS phase error is measured to be  $3.5^\circ$  at a gap of 4 mm.

Based on earlier prototypes, HZB [451–453] has built one full-scale cryo-cooled CPMU of dimensions  $175 \times 17$  mm and with a gap of 5 mm [454] and is building another one with a 15 mm period length and 2 mm gap, investigating two cooling concepts based on liquid nitrogen and single-staged cold heads, respectively.  $(Pr,Nd)_2Fe_{14}B$  magnets (Vacuumschmelze) treated with a grain boundary diffusion process for an enhanced stability and Co-Fe poles are used. The gap size is measured using an optical micrometer. CPMU15 is developed for a plasma-driven FEL experiment in close cooperation with Hamburg University.

The National Synchrotron Radiation Research Center (NSRRC) [455] is developing a 22 mm period CPMU. A CPMU magnetic measurement bench is developed and tested, with a carriage and optical components being redesigned to improve the reproducibility.

A 2 m long cryogenic undulator with 140 periods of length 13.5 mm is to be built for the High-Energy Photon Source Test Facility (HEPS-TF) in Korea [456]. This undulator consists of  $Pr_2Fe_{14}B$  magnets and will be cooled down to liquid nitrogen temperatures (80 K), reaching a magnetic field of 1 T at a gap of 5 mm.

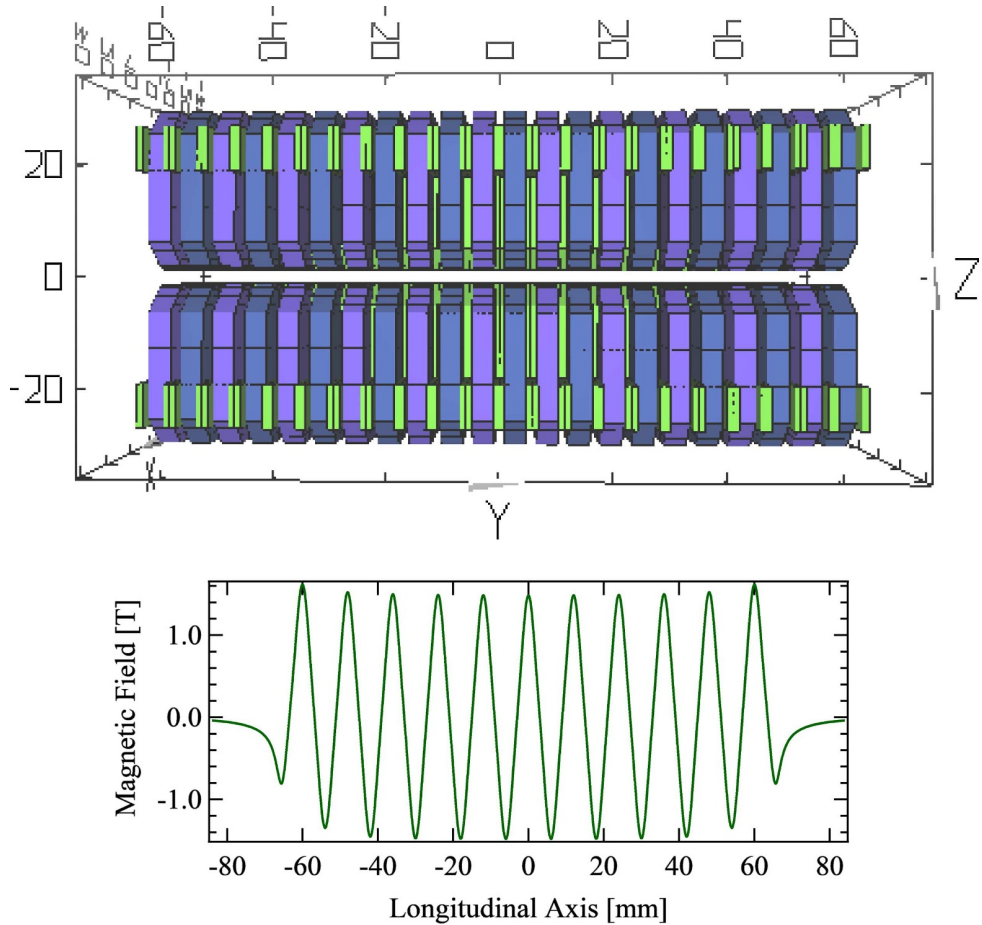


**Fig. 18.1.** (a) RADIA model of a cryogenic undulator with a 12 mm period: the remanent field is 1.57 T, the dimensions (x, z, s) are the following: half-poles:  $56 \times 1 \times 26 \text{ mm}^3$ , magnets:  $50 \times 4 \times 30 \text{ mm}^3$ . (b) Magnetic field of this undulator for a 3 mm gap.

#### *Magnetic Fields Generated by Cryogenic Permanent-Magnet-Based Full-Scale Undulators for EuPRAXIA*

The peak field-to-gap relationship of undulators with different periods have been computed using the RADIA software [457]. The model is presented in Figure 18.1 (top).

The peak field versus the gap for a 12 mm period has been computed using the RADIA software, as shown in Figure 18.1 (bottom).

Figure 18.2 depicts the deflection parameter versus the undulator gap and period. The magnetic field is fitted with the following equation:  $B_{peak} = a \exp(b \frac{g}{\lambda_u} + c (\frac{g}{\lambda_u})^2)$ , where  $g$  is the magnetic gap, and  $a, b, c$  are the fitting coefficients (see Tab. 18.5). Typically, one can get 1.65 T on axis with a U15 at a 3 mm gap, or 1.52 T on axis with a U15 at a 3 mm gap.

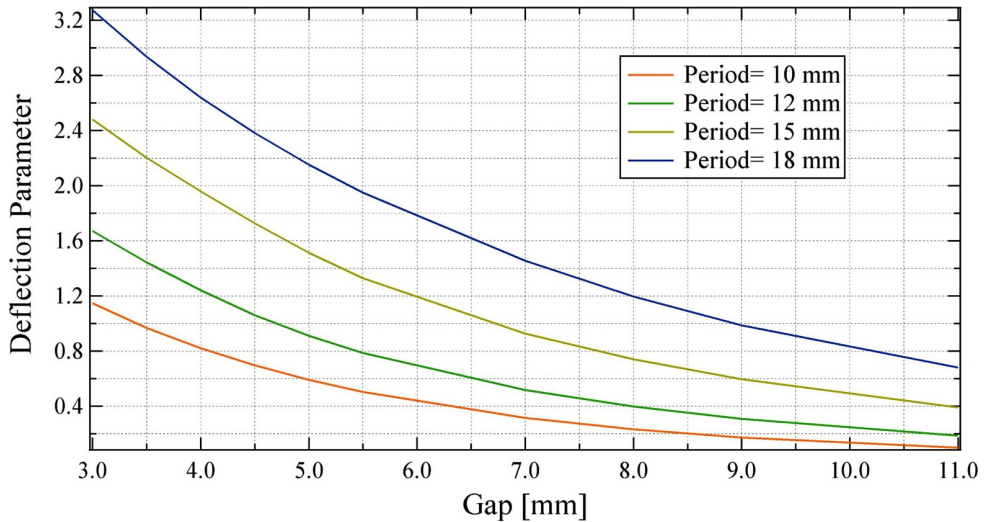


**Fig. 18.2.** Deflection parameter versus gap for different period undulators using RADIA (image credits: A. Ghaith).

### Progress on Superconducting Undulators

Superconducting technology is routinely applied to the development of high-field-strength magnets for applications such as magnetic resonance imaging (MRI) and particle physics accelerators and detectors. Short-period superconducting undulators (SCUs) are still not a mainstream solution for accelerator-based light sources, with just a few examples being in use today. The reason for this rather slow uptake is, in large part, due to the extremely successful application and ongoing improvements in permanent magnet undulator technology rather than any specific shortcomings in superconducting technologies. Despite the undoubted success of permanent magnet systems, there is still a clear margin in performance advantage to be gained through the application of superconducting materials, and it is for this reason that a number of groups around the world have been actively pursuing the detailed development of short-period, high-field SCUs for light source applications over the past ten years or more [458]. This research and development effort has led to the construction of a few SCUs which are now installed and in daily use on storage ring light sources in Germany [459] and the United States [460]. These particular examples have exhibited very good operational performance in terms of reliability, stability, and user experience, and this has increased confidence within the accelerator community that national FEL light source facilities, such as LCLS-II, should carefully assess employing SCUs rather than permanent magnet alternatives in their baseline configurations [461]. The specific advantages of SCUs over PMUs highlighted by the LCLS-II team are the higher magnetic fields at a short period, allowing superior FEL performance or reduced undulator length, the radiation hardness compared to PMUs offering long lifetime and smaller magnet gaps, the anticipated reduction in resistive wakefields due to the cold bore, the much lower vacuum pressure from cryo-pumping, reducing gas scattering, the smaller footprint and simpler magnet field control compared with the massive adjustable-gap PMU, and the easy reorientation for vertical polarisation, if desired. The project team estimated that the LCLS-II hard X-ray undulator could be shortened by up to 70 m using an SCU in place of a PMU. Still, LCLS-II undulators are permanent magnet based.

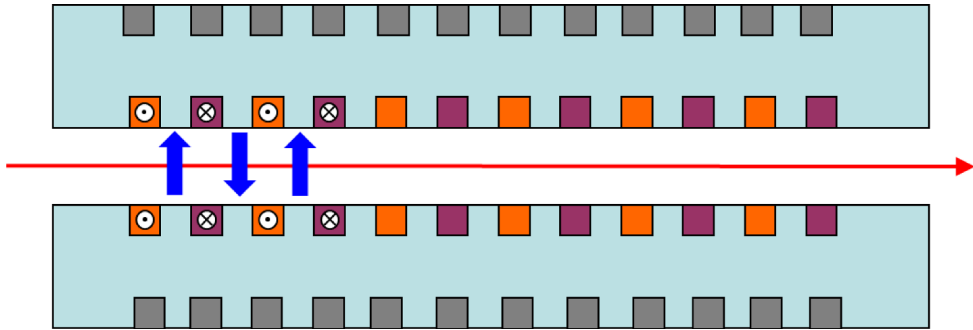


**Fig. 18.3.** Typical magnet design for an SCU viewed from the side, with the electron beam direction indicated by the red horizontal arrow. The superconducting windings close to the electron beam are perpendicular to the beam direction and generate the periodic fields indicated by the blue vertical arrows. The windings on the outside of the steel former (shown as grey rectangles) are for the convenience of simplifying the winding configuration.

The magnetic design of planar SCUs is very straightforward, with a similar approach being adopted by all of the research groups working in this area. The typical arrangement is shown in Figure 18.3. Two independent sets of superconducting windings on steel formers are arranged such that the current flows transversely orthogonal to the electron beam and so generates the periodic magnetic field required [462]. The two sets of windings are held apart by a non-magnetic mechanical arrangement, which is not shown in the figure.

The former is made of a good magnetic steel, and the superconducting wire employed is either NbTi or Nb<sub>3</sub>Sn. The SCU typically operates at between 2 and 4 K. NbTi is more commonly used as it is far easier to work with in terms of winding, insulation, and stability. Nb<sub>3</sub>Sn has to be heat-treated after winding to create the superconducting alloy and afterwards is rather fragile. Nb<sub>3</sub>Sn also suffers from instability issues at the field levels required by SCUs (below  $\sim 5$  T) as it is primarily targeted at far stronger magnetic field applications [463]. Research on the use of special grades of Nb<sub>3</sub>Sn better suited to SCU applications is ongoing at LBNL [464].

Although the magnetic design of SCUs is straightforward, the engineering challenges are severe, and this is the area which has held back SCUs from widespread adoption so far. The mechanical tolerances are very tight, and these must be maintained as the magnet is cooled down from room temperature to  $\sim 4$  K. The gap separation between the two sets of windings is typically between 5 to 10 mm, with no room for a standard vacuum chamber, and so the SCU is, in effect, another type of in-vacuum undulator. The coils are at  $\sim 4$  K, and any heat transfer from the electron beam to the coils because of wakefields or synchrotron radiation must be minimised to prevent magnet quenching. This is generally resolved through the insertion of a very thin beam screen between the beam and the windings at an intermediate temperature of 10 to 20 K to absorb any power from the electron beam. A further issue is that the magnetic field quality is not just determined by the steel pole shape and location but also strongly dependent upon the superconducting wire placement. The accurate placement of individual wires, to a tolerance of a few tens of micrometres, is a painstaking process and difficult to maintain over a length of more than a few tens of centimetres. For this reason, and also to achieve the required machining tolerances, the complete SCU magnet is often made up of shorter sections which couple together to form a longer device [465]. Post-assembly magnet shimming, which is a standard technique for permanent magnet undulators, is not easy to implement in an SCU. Many schemes have been proposed, but they add an extra layer of complexity which

teams try to avoid if at all possible [466]. In addition, the proposed schemes often require additional windings or use valuable space within the magnet gap and so also serve to lower the maximum possible peak field that the SCU can achieve. For these reasons, several groups aim to construct SCUs that have excellent field quality on first assembly and have no shimming capability. This is only possible by working to very tight tolerances at all stages of manufacture and assembly but has been shown to be a practical approach.

An example of an SCU installed in a storage ring is the SCU15 in the ANKA synchrotron radiation facility [456]. The SCU15 was installed in the storage ring during the December 2014 shutdown and has been in operation with beam since the beginning of 2015. The SCU15 has a period length of 15 mm and 100 full periods. Since at ANKA, during electron beam injection and energy ramping, a vertical beam stay-clear of 15 mm is needed and at the full energy of 2.5 GeV, a minimum gap of 7 mm is allowed, the beam vacuum chamber is movable from a 7 mm to a 15 mm vacuum gap. The magnetic peak field measured at the maximum coil current of 150 A is 0.73 T. This value is claimed in the paper to be 16% higher than the peak field of 0.62 T achieved with a CPMU using the best available material for the permanent magnets (PrFeB) with the same period length and beam stay-clear of 7 mm. From Figure 18.2, one reaches 0.66 T with a CPMU U18 at 7 mm, reaching 10% increase with superconducting technology for a 7 mm gap. However, it is meaningless to use a CPMU only at a 7 mm gap, as it can reach a much larger field (larger than 1.5 T) at a smaller gaps, for which it is intended to operate.

Another example of a recent SCU installed and successfully operating in a storage ring is SCU1 in the APS. It built upon the experience gained from the 30 cm long SCU0 device, which was their first SCU to be installed [460]. SCU1 has an 18 mm period and a fixed magnet gap of 9.5 mm, achieving a peak field of 0.97 T. For the same gap, the CPMU U18 would give at 9.5 mm a field of 0.53 T, but the design is not optimised. The magnetic length is 1.1 m. The magnet is wound using round NbTi wire with a diameter of only 0.6 mm. Nevertheless, the SCU comfortably operates at a current of 450 A, well within the maximum current achieved of 520 A.

## Advanced and Novel Undulators

Even though unlikely to be used for an LPA-based FEL as a baseline case, more exotic undulators can be considered, such as RF undulators, micro-machined undulators, and plasma undulators.

### *Sub-Millimetre Period Undulators*

A dramatic reduction of the undulator period is actively investigated using various techniques and concepts, such as the microstructure-driven laser undulator [467], the surface micro-machined undulator [468], the micro-machined magnet undulator [469–471], the RF undulator [472], and the optical undulator [473]. However, because of the magnetic field value and short period, the low value of the deflection parameter limits the emission intensity and the harmonics operation. There could be some issues with wakefields with these extremely low gaps and with magnetic measurements. Because of the low-deflection parameter values and the associated technical challenges, they will not be considered for EuPRAXIA.

### *Plasma Undulators*

Plasmas represent electromagnetically active media which can produce and sustain very high static fields and give rise to the strong collective phenomena such as channel formation and plasma waves with strong charge separation fields, and for that, they attract high interest for beam applications. The idea to apply plasma fields to operate

and, in particular, to undulate electrons dates back to the 1980s–1990s. In this period, several concepts were proposed involving the oscillations of electrons guided in ion channels [474] or to impose a wiggling motion by coupling an electron beam to plasma waves [475,476]. In these approaches, the plasmas were considered to be created by a high-intensity laser focussed in gas targets. The wavelength corresponding to such gaseous plasmas with densities of  $1 \times 10^{15}$ – $1 \times 10^{17} \text{ cm}^{-3}$  corresponds to wiggler periods of  $\lambda_w \sim 1 \times 10^{-1}$ – $1 \times 10^2 \text{ }\mu\text{m}$ , and the calculated wiggler strength for to-date laser parameters (intensities of  $\sim 1 \times 10^{14} \text{ W/cm}^2$ ) could already reach  $a_w \sim 0.1$ – $1$ . Such parameters may potentially provide the conditions to generate X-rays using relatively low-energy electron beams with limited collimation quality.

One of the principal challenges identified in these early studies was the low number of oscillation periods which could be produced for realistic parameters, hindering developments of these concepts to the point of FEL applications. Moreover, in the “plasma wave” approach, the laser energy required to create the corresponding plasma wave front has turned rather big, thus requiring high-energy laser systems. Finally, the stability of laser plasmas, which affects directly the reproducibility of interaction conditions, presents another challenge for the experimental tests.

In recent years, the concept of underdense plasma undulators has been revised in more detail. The “plasma wave” scheme has been studied by coupling to the laser-plasma-accelerated electrons with a more advanced numerical approach. In one such study [477], the possibility of keV photon generation along 25 wiggler periods with realistic experimental parameters has been demonstrated. Another approach, derived from the “channel” scheme, consisted of applying to electrons the wakefields of a laser pulse injected off axis into a plasma channel in such a way that the laser centroid oscillates transversely [478]. Potentially, this scheme can be coupled to an LPA and can provide a few tens of  $\lambda_w \sim 1$ – $2 \text{ mm}$  wiggler periods with a strength of  $a_w \sim 1$ . Further numerical studies revealed the potential tunability of such a source in terms of wavelength and polarisation of the produced radiation [479,480].

Recently, an alternative concept of the plasma undulator based on an overdense plasma was proposed [481]. The solid target is composed of nanowires with a sub-micrometre diameter and a few tens of micrometers length, which are arranged in a chessboard fashion on the axis of the LPA, close to its exit. The laser driver of the LPA ionises the wires, producing strong, spatially alternating electrostatic fields on the following electron beam, providing an undulator strength of  $a_w \sim 1$ . The period of such an undulator does not rely on the plasma density but is fixed only by the target design and can be chosen in the range of  $\lambda_w \sim 10$ – $100 \text{ }\mu\text{m}$ .

The main interest in plasma undulators is related to their potential to produce strong undulating fields with sub-millimetre periods. In the present state, these schemes remain mainly theoretical concepts, and in the short term, their experimental validation for synchrotron light production is required. For these reasons, plasma undulators are not yet ready to be considered as the candidates for the EuPRAXIA project.

### Transverse Gradient Undulators

Transverse gradient undulators (TGU) are considered to be a promising solution for free-electron lasers (FEL) which aim at utilising electron beams with large energy spread such as beams generated by laser-plasma accelerators (see Fig. 18.4). The TGU enables in principle to restore FEL gain impacted by the energy spread of an electron beam. Some technical issues still remain (e.g. independent tuning of K and gradient) but are in the process of being fixed. Some other points have to be studied in detail, such as the effect on the beam dynamics [482] of additional multipolar terms (not a pure gradient) coming from the finite pole width and the gap variation in the

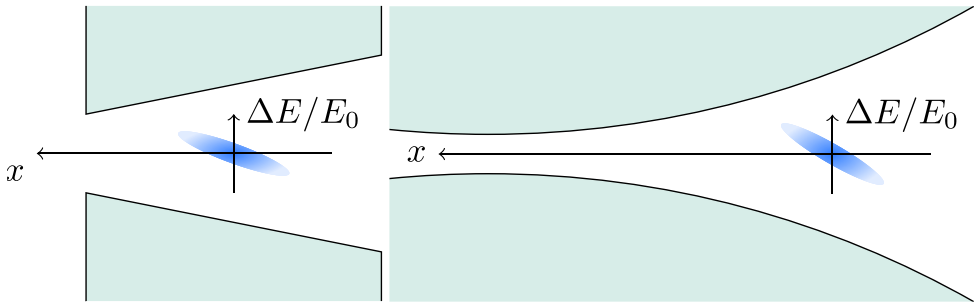


**Fig. 18.4.** Transverse gradient undulator scheme (image credits: A. Bernhard, KIT).

horizontal plane. As a consequence, TGUs can be proposed for linac-based FELs but hardly for recirculating FELs while the latter point is not clarified. The TGU is considered for LPA-driven FELs and will be further investigated in the context of EuPRAXIA.

The first concept was presented in the latest seventies [483], where it was proposed, on the one hand, to disperse transversally the electrons following their own energy and, on the other hand, to vary transversally the magnetic amplitude of the field of the undulator by generating a gradient. An adequate value of the dispersion and the field gradient minimises the effect of the electron beam energy spread on the FEL resonance condition, leading to a strong increase in the gain. The main interest of the TGU is to keep electrons always energy resonant even at a very large energy spread ( $>50\%$ ) leading to a shorter saturation length, a higher saturation power, and a narrower bandwidth [64]. However, dispersing the particles increases the beam size in the direction of dispersion (usually the horizontal direction) and reduces the transverse coherence of the FEL radiation. Therefore, a dispersion value of only a few centimetres must not be exceeded and undulators producing transverse gradients of many tens of  $\text{m}^{-1}$  are necessary to minimise this effect.

Many magnetic designs of TGUs have been proposed, but only two have been built or are under development presently. The first solution, proposed at SINAP, is based on a classical PPM / hybrid undulator whose magnetic system has been transversally tilted [484]. Four fixed-gap TGUs composed of 75 periods of 20 mm have been completely constructed, leading to a K value of 1.15 and a transverse gradient of  $50 \text{ m}^{-1}$ . The main drawback is that this solution leads to a compromise between the tilt angle ( $<10^\circ$ ) and the good gradient region. A second TGU based on off-axis operation of a cylindrical superconducting undulator is in the commissioning phase at KIT [67]. The undulator is composed of 40 periods of 10.5 mm, with a K value of 1.07 and a transverse gradient of  $149.5 \text{ m}^{-1}$  in a limited region of 5 mm. Both technical solutions do not presently enable the independent tuning of the K value and the transverse gradient, which presently represents a mechanical challenge.

The TGU on-beam impact has also been studied [482]. The presence of the transverse gradient generates a ponderomotive drift [485], which deviates the electrons quadratically from the magnetic axis. The global result is the increase in the transverse beam size if not corrected and, in turn, a drop of the FEL gain. Nonetheless, this effect can be corrected by means of long correction coils inserted in the magnetic structure.

## Conclusion

From the above presented systems, one can pick out from the technologically feasible undulator parameters the most appropriate characteristics for FEL operation in different spectral ranges. Cryogenic undulators seem to be the solution of choice for an FEL project to be realised over the next 10 years. They represent a technological advance over currently used on-air warm permanent magnet undulators used in FEL facilities worldwide. Yet, the underlying technology is, although still cutting-edge, well understood and under control. The combination of short periods with comparably high on-axis magnetic fields could enable plasma-driven FELs at water-window photon energies and relatively low-energy electron beams of 1 GeV, provided proper electron beam parameters can be reached. In the case where it is more preferable to achieve a high field, superconducting magnets are a good choice to satisfy such a goal; however, these undulators are limited by the minimum magnetic gap reached, which is almost 7 mm so far with a total length shorter than 1.5 m. At 7 mm, cryogenic undulators can obtain a peak field of almost 0.5–0.7 T, but the advantage of such a device is that one is able to reach a magnetic gap of almost 3 mm depending on the magnetic period, and with such a gap, the peak field is enlarged to almost 1.5–1.8 T, with lengths up to 2 m so far. A 12(10) mm CPMU provides a deflection parameter ranging between 1.67 and 0.91 (1.15 and 0.59) from a 3–5 mm gap. A CPMU is more sustainable than an SCU in regards to the operating cost. Since superconducting undulators offer great possibilities and open up the parameter ranges, one could consider also an alternative U12 SCU for EuPRAXIA. Other, more exotic undulator concepts, should, given their early stage of development, currently not be considered for driving a EuPRAXIA FEL facility.

## 19 Beam Transport and Handling Systems

### 19.1 Beam Transport for the Low-Energy Beam

#### 19.1.1 Introduction

The low-energy beam transport line (LETL) is relevant for transferring the electron beam from the injector stage (either an RF or plasma injector) to a second plasma-accelerator target (laser-driven or beam-driven) for energy boosting in a staged accelerator setup. With transport from a plasma injector the more challenging scenario, this will be focussed on in the remainder of this section using the example of a plasma injector with the ReMPI technique (Scheme 2, see Chap. 23 for details). The transport lines between the injector and accelerator stages in a setup with an RF injector, on the other hand, are described in Chapter 14.

At low energy (150–250 MeV), space-charge forces are not negligible. A measure of the relative importance of space-charge effects versus emittance pressure is given by the laminarity parameter, defined as the ratio between the space-charge term and the emittance term [486] as follows:

$$\rho = \frac{\hat{I} \sigma^2}{2I_A \gamma \varepsilon_n^2}, \quad (19.1)$$

where  $I_A = 4\pi\varepsilon_0 \frac{m_e c^3}{e} \approx 17$  kA is the Alfvén current,  $\hat{I}$  is the peak beam current,  $\sigma$  is the RMS beam size,  $\varepsilon_n$  is the normalised emittance, and  $\gamma$  is the Lorentz factor. When  $\rho$  greatly exceeds unity, the beam behaves as a laminar flow – all beam particles move on trajectories that do not cross – and transport and acceleration require a

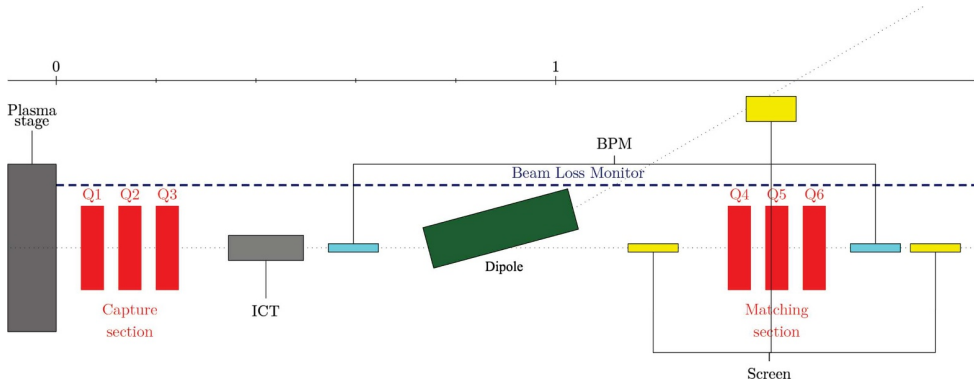


**Fig. 19.1.** Layout of the low-energy beam transfer line (in red: permanent quadrupoles in the capture and matching sections, in green: dipoles, in cyan: BPMs, in gray: ICTs, and in yellow: screens).

careful tuning of focussing and accelerating elements to keep laminarity. A correlated emittance growth is typical in this regime, which can be made reversible if proper beam matching conditions are fulfilled.

The values for the low-energy beam of EuPRAXIA are  $\hat{I} \approx 1$  kA,  $\gamma \approx 300$ ,  $\sigma \approx 50$   $\mu\text{m}$ ,  $\varepsilon_n \approx 0.5$   $\mu\text{m}$ . After calculation, we find  $\rho \approx 2$ ; the beam dynamics is thus driven by space-charge effects. Nevertheless, minimising momentum spread and beam divergence at the plasma exit will help because a smaller beam divergence implies a smaller average beam size and thus a smaller laminarity parameter.

The beam transfer line will be made up of one capture section consisting of a triplet or a quadruplet of permanent quadrupoles, and one matching section also consisting of a triplet or a quadruplet of permanent quadrupoles. Both capture sections will be separated by a section of at least 1000 mm in length to insert different diagnostics and correctors, like a spectrometer, a dipole corrector, or a beam position monitor (BPM). A sketch of the low-energy transfer line is shown in Figure 19.1.

The electron beam is generated in a laser-plasma injector (LPI) by the ReMPI (Resonant Multi-Pulse Ionisation) technique, then accelerated in the same plasma target to 150 MeV in the quasi-linear regime [170]. The laser beam is split into two pulses, the first of small energy for ionising the gas and the second containing the main part of the energy itself decomposed into a series of several sub-pulses to excite the wakefield without ionising the gas. Start-to-end simulations for this setup have been performed (see Chap. 23), and the final distribution, after further energy boosting in a laser-driven plasma-accelerator stage (LPAS), has been transported to the user areas. We propose in this section to describe the optimised LETL between the LPI and the LPAS. The high-energy beam transport line from the LPAS to the user application will be described in Section 19.2.

### 19.1.2 Compact Beamline with Six Permanent Quadrupoles

The transfer line in this scenario is made of two triplets separated by a drift. The first triplet is used to capture the beam after the LPI, whereas the second triplet is used to match the beam into the LPAS. Matching conditions at the entrance of the LPAS are  $\beta_{xy} = 30$  mm and  $\alpha_{xy} = 1$  (see Sect. 7.1 for the general equations).

The distance between the triplets and the plasma stages is to be as short as possible to minimise the emittance growth; betatron functions scale as the square of this distance, beam sizes scale linearly with it, and space-charge effects grow as a

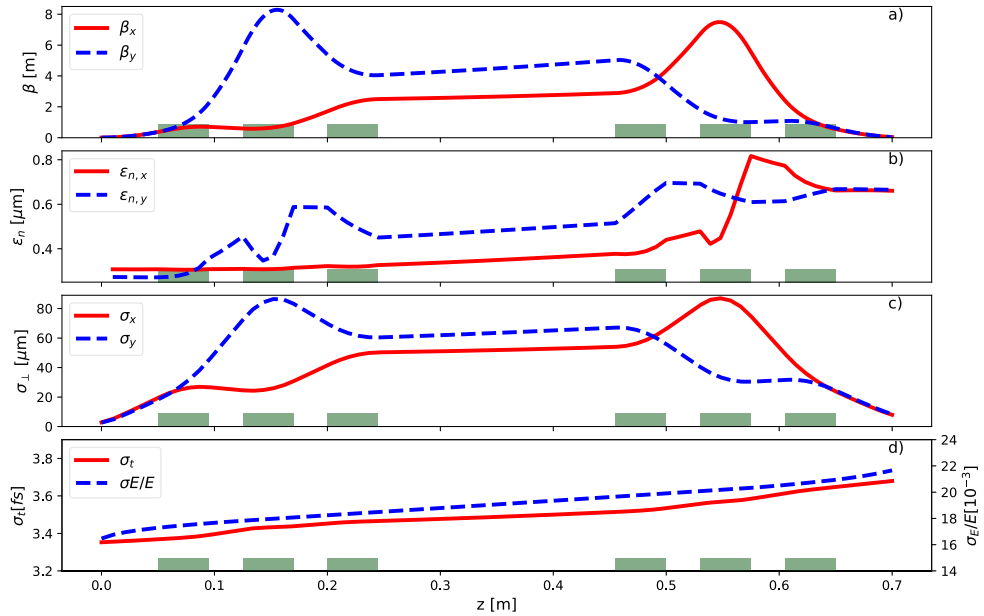


**Fig. 19.2.** Low-energy transfer line: Beam beta function (a), normalised emittance (b), transverse size (c), and bunch duration and energy spread (d) of the core beam along the transport line between the two plasma stages in Scheme 2 (assuming a beam energy of 150 MeV, a total length of 700 mm, and 6 quadrupoles). The calculations were performed with the tracking code TraceWin.

**Table 19.1.** Parameters of the focusing elements in the low-energy transport line between the two plasma stages of Scheme 2, in the case of six quadrupoles and a total length of 700 mm.

Quadrupole	Q1	Q2	Q3	Q4	Q5	Q6
Length [mm]	45					
Gradient [T/m]	211	-189	86	-101	190	-161

power of the beam size and thus also as a power of this distance. We have assumed a minimum distance between the LPI and the triplet of 50 mm. For start-to-end simulations, the length of the transfer line is 700 mm. As explained above, the drift should host diagnostics like BPMs, screens, or a spectrometer to measure the energy spectrum.

Nevertheless, the distance between both triplets is too short here to insert all diagnostics. The parameters of the quadrupoles are summarised in Table 19.1. The evolution of the beam distribution along the transport line is shown in Figure 19.2, whereas the evolution of the properties of the electron beam slices is shown in Figure 19.3. The final beam properties are summarised in the third column of Table 19.4. If the drift is made longer to host diagnostics (for instance with a total length of 1400 mm) with a parallel beam in between, space-charge effects increase and the emittance growth becomes even larger. The final emittance is then 0.9  $\mu\text{m}$  (compared to 0.66  $\mu\text{m}$  with a total beamline length of 700 mm). Another solution is to over-focus the beam with the first capture section to reach a phase advance between both sections, which cancels the variation of betatron functions with energy.

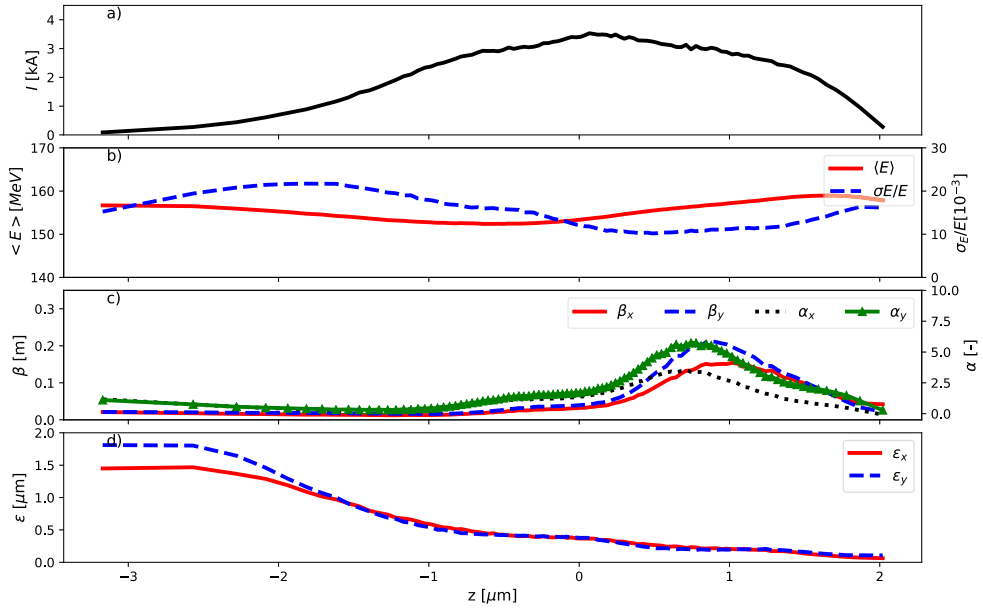


**Fig. 19.3.** Low-energy transfer line: Profile of the current (a), mean energy and energy spread (b), Twiss parameters (c), and normalised emittance (d) along the beam slices at the entrance of the second plasma stage of Scheme 2 (assuming a beam energy of 150 MeV, a total length of 700 mm, and six quadrupoles). The calculations were performed with the tracking code ASTRA.

### 19.1.3 Beamline with Eight Permanent Quadrupoles

This transfer line is also made of two quadruplets separated by a drift. The first quadruplet is used to capture the beam after the LPI, whereas the second quadruplet is used to match the beam into the LPAS. As before, matching conditions at the entrance of the LPAS are  $\beta_{xy} = 30$  mm and  $\alpha_{xy} = 1$ .

An additional constraint is to have a phase advance of roughly  $90^\circ$  between both capture sections. Indeed, initial and final Twiss parameters are quite close, which requires similar capture sections. The main contribution of the trace emittance growth comes from the quadrupoles (and more particularly the variation of Twiss parameters with energy). The pulsation of the betatron wave is twice the phase advance; in other terms, if the phase advance between two points is  $\phi$ , the phase shift of the perturbation of the Twiss parameters is  $2\phi$ . Therefore, a perturbation of the Twiss parameters in the first capture section will be cancelled by the second capture section if the phase advance in between is  $90^\circ$  (and thus  $180^\circ$  for the phase advance of the betatron wave). To reach a phase advance of  $90^\circ$ , it is necessary to have  $\alpha_{x,y} \approx 0$  and  $\beta_{x,y} \approx L_d/2$ , where  $L_d$  is the length of the drift between both capture sections. A second iteration is then performed to match the beam and to minimise the final emittance with a tracking code. It is worth remarking that this condition is more difficult to fulfil with permanent quadrupoles than with plasma lenses or solenoids because a quadrupole is focusing only in one plane. The cancellation of the betatron wave cannot be perfect because of space-charge effects; this constraint means that only the emittance growth coming from the optics itself can be cancelled and not from collective effects.

We have assumed a minimum distance between the LPI and the triplet of 50 mm. As explained above, the drift should host diagnostics like BPMs, screens, or a spec-

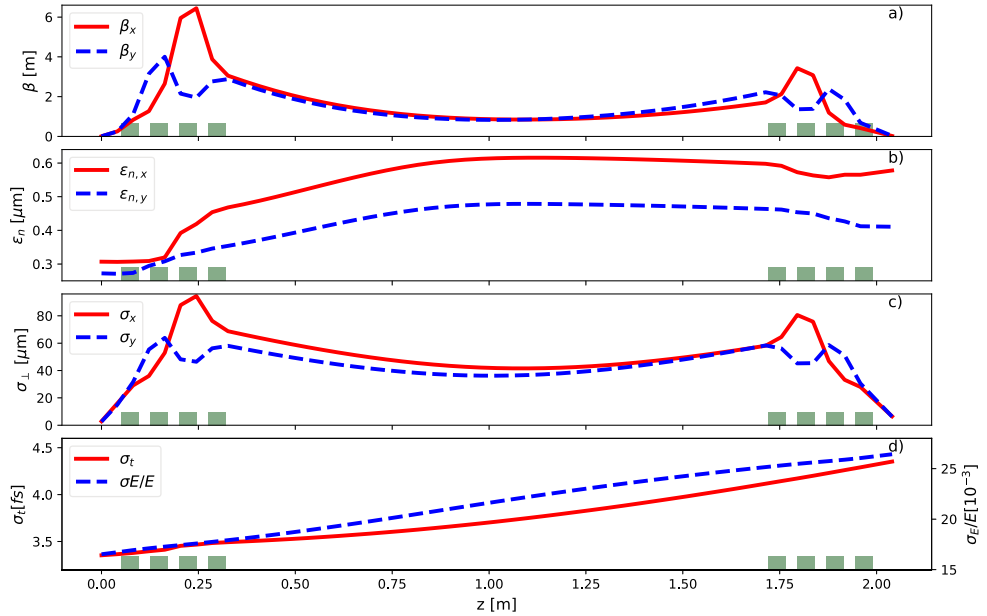


**Fig. 19.4.** Low-energy transfer line: Beam beta function (a), normalised emittance (b), transverse size (c), and bunch duration and energy spread (d) of the core beam along the transport line between the two plasma stages in Scheme 2 (assuming an electron beam energy of 150 MeV, a total length of 2040 mm, and eight quadrupoles). The calculations were performed with the tracking code TraceWin.

**Table 19.2.** Parameters of the focusing elements in the low-energy transport line between the two plasma stages of Scheme 2 in the case of eight quadrupoles and a total length of 2040 mm.

Quadrupole	Q1	Q2	Q3	Q4	Q5	Q6	75	Q8
Length [mm]	45							
Gradient [T/m]	96.6	-182	162	-61.6	-66.7	-161	-171	94

trometer to measure the energy spectrum. Hence, the low-energy beam transfer line has now been lengthened with a total length of 2040 mm. The parameters of the quadrupoles are summarised in Table 19.2. The evolution of the beam distribution along the transport line is shown in Figure 19.4 with the evolution of the properties of the electron beam slices depicted in Figure 19.5. As we can see, the final emittance growth is smaller despite a longer total length. The variation of the betatron functions along the slice is also flatter. The variation of the betatron functions for the slices with  $z > 0.5 \mu\text{m}$  comes from the initial variation of the Twiss parameters. The final beam characteristics are summarised in the fourth column of Table 19.4.

#### 19.1.4 Beamline with Two Active Plasma Lenses

The use of active plasma lenses (APL) has also been considered for the beam capture and final focus (one for each task), as these devices suffer less from chromatic aberrations compared to other focusing systems [38], and are therefore well suited for high-energy-spread beams. Currently, this beamline contains only two APLs. To keep the possibility to separately match horizontal and vertical planes, weak quadrupoles

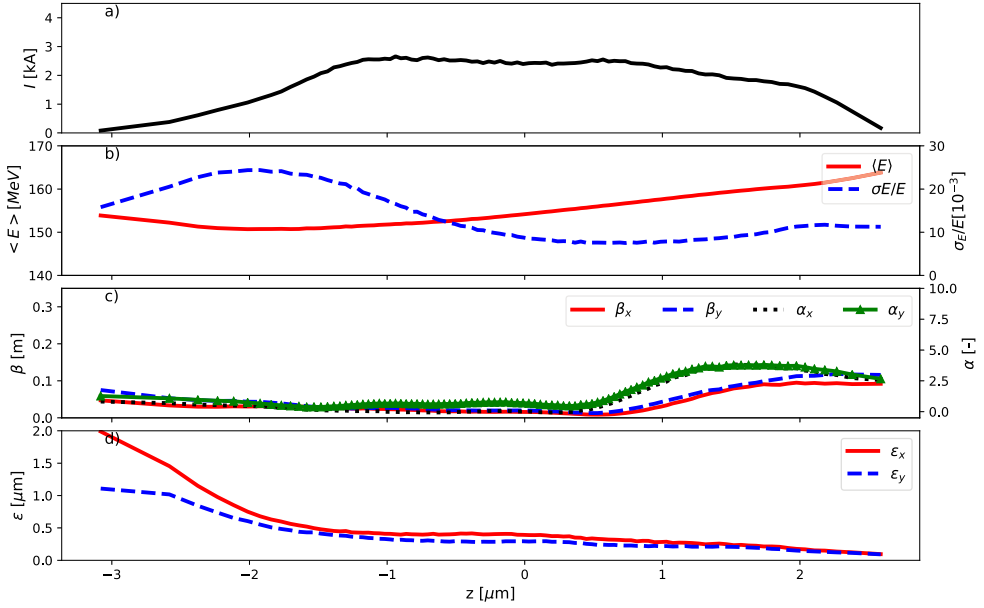


**Fig. 19.5.** Low-energy transfer line: Profile of the current (a), mean energy and energy spread (b), Twiss parameters (c), and normalised emittance (d) along the beam slices at the entrance of the second plasma stage in Scheme 2 (assuming an electron beam energy of 150 MeV, a total length of 2040 mm, and eight quadrupoles). The calculations were performed with the tracking code ASTRA.

should be inserted in between. Their impact should be low on the final beam emittance.

Nevertheless, at low energy, the needed gradient is reduced and special care must be taken to check that the wakefield generated by the beam itself in the plasma lens is negligible compared to the focusing gradient. We should have the following relation [488]:

$$g_{APL} \gg g_{WF}, \quad (19.2)$$

$$g_{WF} \approx -\frac{e\mu_0 c}{2} \min \left( n_0, \frac{N k_p^2 \sigma_z}{\pi \sigma_r^2 \left( 1 + \frac{k_p^2 \sigma_r^2}{2} \right) \left( 1 + \sqrt{8\pi} k_p^2 \sigma_z^2 \right)} \right), \quad (19.3)$$

$$g_{APL} \approx \frac{\mu_0 I}{2\pi R^2}, \quad (19.4)$$

where  $\mu_0$  is the vacuum permeability,  $c$  is the speed of light,  $g_{WF}$  the maximum wakefield, and  $g_{APL}$ ,  $I$ ,  $R$ ,  $n_0$ ,  $k_p$  are, respectively, the gradient, the current, the radius, the plasma density, and the plasma wavenumber of the APL.  $\sigma_r$  is the RMS beam size,  $\sigma_z$  is the RMS bunch length, and  $N$  is the electron population of the bunch.

The APL gradient in the case of a uniform current, a discharge current of 1 A, and a diameter of 1 mm is shown in Figure 19.6. The gradient linearly scales with the discharge current. For the simulations with ASTRA, a more realistic profile has been used, as explained in [487].

To decrease the wakefield in the APL, the plasma lens should be as short as possible and should be located far enough from the LPI exit to increase the beam size. Nevertheless, a trade-off must be found between a small wakefield in the APL

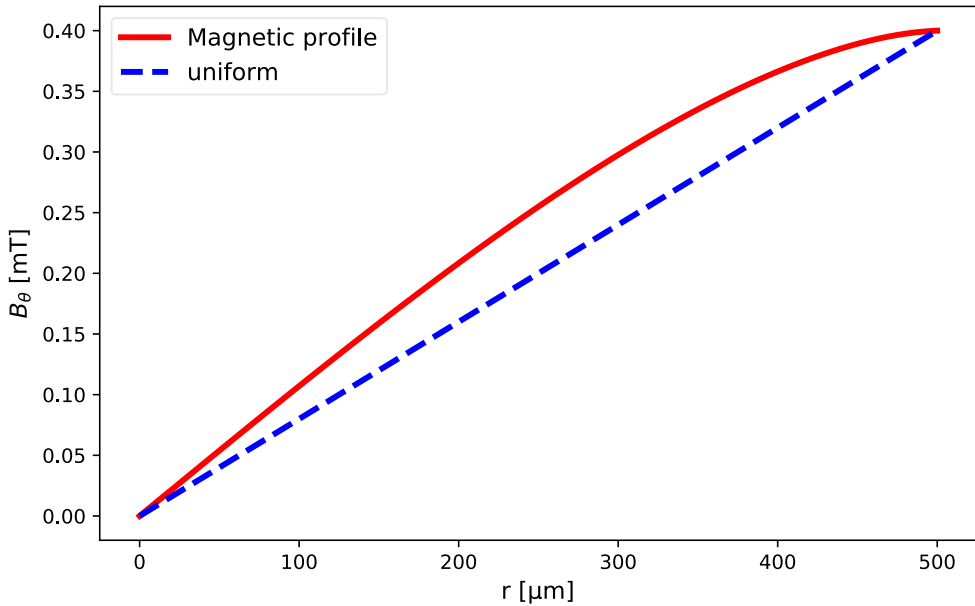


**Fig. 19.6.** Magnetic field profile in a 1 mm diameter active plasma lens using the simplified model given in [487] (plotted as solid red curves). One can observe an approximately 35% enhancement in B-field gradient compared to the model with uniform current in the APL. The magnetic field corresponds to a discharge current of 1 A.

(with a large beam size), small chromatic effects (small beam size), and efficient focussing in the APL (small beam size). A first guess is to put the APL at 200 mm from the LPI. At this position, the beam size is about  $80\ \mu\text{m}$ , which is roughly  $1/6$  of the APL radius and thus a good compromise.

The evolution of the beam distribution along the transport line is shown in Figure 19.7. The evolution of the properties of the electron beam slices is shown in Figure 19.8. The parameters of the APLs are summarised in Table 19.3. As we can see, the final emittance growth is smaller thanks to reduced chromatic effects in the APLs. The variation of the betatron functions along the slice is also flat. The final beam characteristics are summarised in the fifth column of Table 19.4.

The order of magnitude of the gradient in the APLs is  $300\ \text{T/m}$ . If we consider a typical plasma density of  $1 \times 10^{17}\ \text{cm}^{-3}$ , a bunch length of  $1\ \mu\text{m}$ , a beam size of  $80\ \mu\text{m}$ , and a bunch charge of  $33.5\ \text{pC}$ , equation (19.3) gives a gradient of  $76\ \text{T/m}$  for the wakefield, which is 25% of the APL gradient. Some solutions to mitigate the effect of the wakefield are to shorten the APL – but a length of 10 mm is already small and little room is possible – or to put the APL farther – with a larger beam size but increased chromatic effects. The wakefield is thus not negligible and more accurate simulations (with FBPIC [489] for instance) should be performed.

### 19.1.5 Beamline with Two Solenoids

The case of a beamline with two solenoids has also been investigated. The advantage of the solenoid is to be focussing in both planes (same advantage as the APL) and to use a more mature technology. Quadrupoles can also be used to match the beam in both planes after focusing. Nevertheless, at 150 MeV, superconducting solenoids are to be used to keep a compact beamline. The positions of the centre of the solenoids is

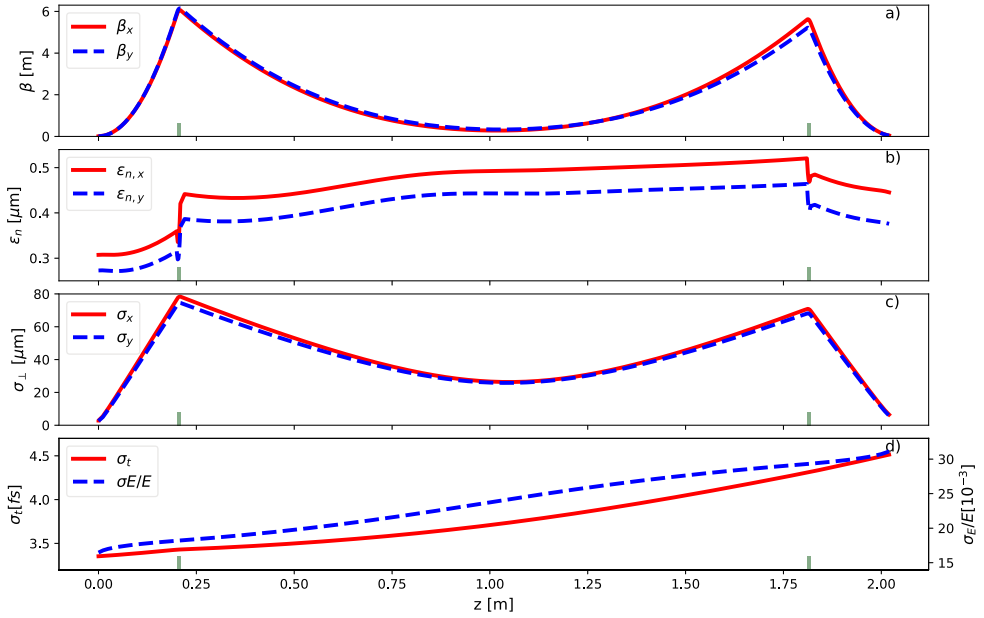


**Fig. 19.7.** Low-energy transfer line: Beam beta function (a), normalised emittance (b), transverse size (c), and bunch duration and energy spread (d) of the core beam along the transport line between the two plasma stages of Scheme 2 (assuming an electron beam energy of 150 MeV, a total length of 2020 mm, and two APLs). The calculations were performed with the tracking code TraceWin.

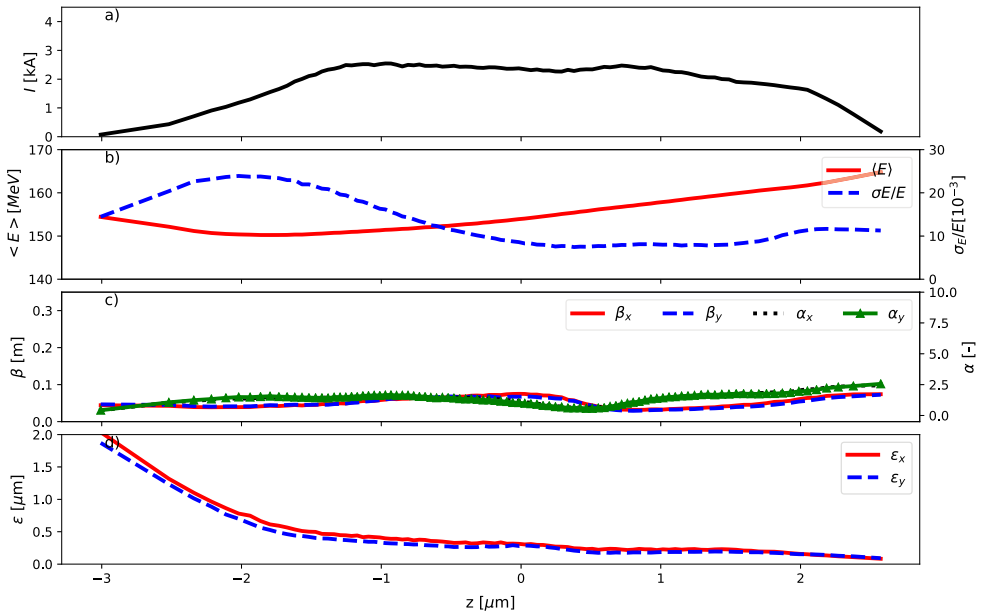


**Fig. 19.8.** Low-energy transfer line: Profile of the current (a), mean energy and energy spread (b), Twiss parameters (c), and normalised emittance (d) along the beam slices at the entrance of the second plasma stage in Scheme 2 (assuming an electron beam energy of 150 MeV, a total length of 2020 mm, and two APLs). The calculations were performed with the tracking code ASTRA.

**Table 19.3.** Parameters of the focusing elements in the low-energy transport line between the two plasma stages of Scheme 2 in the case of two APLs and a total length of 2010 mm.

APL		APL1	APL2
Length	[mm]	10	
Current	[A]	301	286
Gradient	[T/m]	316	301

**Table 19.4.** Comparison of the beam parameters at the end of the LPI and at the entrance of the LPAS for the four different low-energy transfer line configurations investigated. The bunch core contains 33.5 pC of charge.

		LPI exit	LPAS entrance			
			6 quads (700 mm)	8 quads (2040 mm)	2 APLs (2020 mm)	2 solenoids (2200 mm)
$\beta_x$	[m]	0.008	0.029	0.029	0.028	0.030
$\beta_y$	[m]	0.008	0.032	0.030	0.027	0.030
$\alpha_x$	–	–0.22	0.816	0.945	0.95	0.965
$\alpha_y$	–	–0.13	0.908	1.041	1.01	1.061
$\varepsilon_{n,x}$	[ $\mu\text{m}$ ]	0.31	0.66	0.59	0.45	0.58
$\varepsilon_{n,y}$	[ $\mu\text{m}$ ]	0.27	0.67	0.41	0.38	0.51
Mean Energy	[MeV]	154	154	154	154	154
$\sigma_\gamma/\gamma$	[ $10^{-3}$ ]	16.5	21.6	29.3	31.1	30.0
$\dot{I}$	[kA]	4.2	3.5	2.7	2.5	2.6
$\sigma_\tau$	[fs]	3.3	3.7	4.5	4.5	4.7

at 200 mm and at 2000 mm. The total length of the beamline in this case is 2200 mm. The considered solenoids are 150 mm long, have an inner radius of 15 mm, an outer radius of 40 mm, and a maximum current density of 300 A/mm<sup>2</sup>, which gives a maximum on-axis magnetic field of 8.8 T. The optimisation of the line is similar to the baseline: a waist is generated at the centre of the drift to obtain a phase advance of about 90° between both solenoids. After optimisation, the needed magnetic fields are, respectively, 7.55 T and –7.31 T. The final beam characteristics are summarised in the last column of Table 19.4. The solution with solenoids does not provide better results than the solution with eight quadrupoles. Hence, the solution with eight quadrupoles is preferred, as it enables to differentiate between the horizontal and vertical planes. Nevertheless, it is simpler to tune the beamline with solenoids and thus to reach a phase advance of 90° between them.

### 19.1.6 Conclusion

The beamline between two plasma stages has been optimised and presented. Different schemes have been discussed: a compact beamline with two quadrupole triplets, a longer beamline with two quadrupole quadruplets (to host diagnostics and to get a larger phase advance between both capture sections), a beamline with two active plasma lenses, and a beamline with two solenoids.

The beamline with two APLs gives the best final properties, i.e. minimum emittance growth. However, the wakefield generated by the beam itself in the APL was not taken into account in the simulations. First estimations show it is not negligible and emittance degradation is likely. Further calculations are thus necessary to validate this concept.

**Table 19.5.** Electron beam matching parameters at the entrance of the undulator section in the case of a short-wavelength design (undulator period:  $\lambda_u = 20$  mm, module length:  $L_u = 2$  m, distance between modules: 360 mm).

	$\langle\beta_{x,y}\rangle$ [m]	$\beta_x$ [m]	$\beta_y$ [m]	$\alpha_x$	$\alpha_y$
<b>Scheme 1: LPI-5 GeV</b>	5	3.16	7.31	-0.697	1.556
<b>Scheme 2: LPI-150 MeV + LPAS-5 GeV</b>	5	3.16	7.31	-0.698	1.556
<b>Scheme 3: RFI-500 MeV + LPAS-1 GeV</b>	5	3.39	6.89	-0.613	1.174
<b>Scheme 3: RFI-500 MeV + LPAS-5 GeV</b>	5	3.16	7.31	-0.698	1.556
<b>Scheme 5: RFI-500 MeV + PPAS-1 GeV</b>	5	3.40	6.87	-0.608	1.155

Solutions with two quadruplets or two solenoids use mature technology and require less R&D. The final emittance is slightly worse, but stays within specifications. The beamline with solenoids should add some weak quadrupoles to make a fine-tuning between horizontal and vertical planes possible.

Finally, an open problem remains how to remove the laser of the LPI and how to inject the laser for the LPAS. This will be addressed in future studies.

## 19.2 Beam Transport for the High-Energy Beam

### 19.2.1 Introduction

A sketch of the high-energy transfer line (HETL) is shown in Figure 19.9. This is the section transporting the electron beam after its final acceleration stage to an application beamline, here exemplarily assumed to be the entrance of an undulator. Other applications would require slightly different beam parameters, yet the procedure and general beamline layout would be the same.

The transfer line can be divided into three sections: a capture section, a C-chicane, and a matching section.

The capture section is made of permanent quadrupoles and is aimed to capture the electron beam at the plasma exit and focus it. Most of the emittance growth occurs in this section. Careful optimisation must then be performed to minimise this emittance growth. An integrated current transformer (ICT) is inserted behind the capture section to measure the beam current.

The C-chicane is made up of four straight dipoles and is aimed to separate the witness beam from the laser beam (in the case of LWFA), or from the electron drive beam (in the case of PWFA). A collimator will be used for the laser or beam driver removal in these cases. The chicane's other main purpose is to protect the undulators from possible failures at the plasma exit, such as large misalignment errors or energy fluctuations; in these cases the beam will then be dumped into the collimator. Simulations should be performed to validate this concept.

Finally, two doublets are used to match the beam to the undulator entrance. The two magnet pairs are separated by a distance greater than 2 m to enable the insertion of different diagnostics: a BPM to measure the beam position, an X-band transverse deflecting structure (TDS) to measure the time structure [490], and a deflecting dipole to measure the energy spectrum, when needed (see Chap. 21 for details on the diagnostics).

At high electron-beam energy, space-charge forces can be neglected. A python script has been written to match the beam to the undulator and to minimise the emittance growth along the machine. The matching constraints at the entrance of the undulator for the different schemes are given in Table 19.5 for the case of

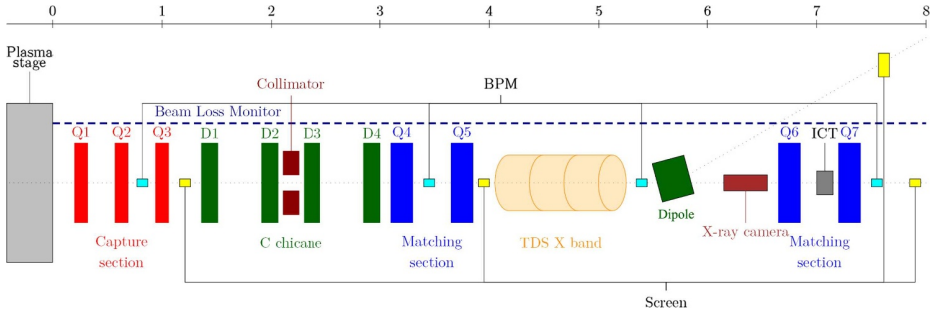


**Fig. 19.9.** Layout of the high-energy beam transfer line (in red: permanent quadrupoles in the capture section, in blue: electromagnet quadrupoles in the matching sections, in green: dipoles (designated as dipole and D1-D4), in cyan: BPMs, in gray: ICTs, and in yellow: screens).

**Table 19.6.** Matching parameters at the entrance of the undulator section in the case of a long-wavelength setup (undulator period:  $\lambda_u = 30$  mm, module length:  $L_u = 2.1$  m, distance between modules: 360 mm).

	$\langle\beta_{x,y}\rangle$ [m]	$\beta_x$ [m]	$\beta_y$ [m]	$\alpha_x$	$\alpha_y$
<b>Scheme 1: LPI-5 GeV</b>	5	3.08	7.44	-0.668	1.545
<b>Scheme 2: LPI-150 MeV + LPAS-5 GeV</b>	5	3.07	7.45	-0.670	1.559
<b>Scheme 3: RFI-500 MeV + LPAS-1 GeV</b>	4	2.69	5.35	-0.382	0.627
<b>Scheme 3: RFI-500 MeV + LPAS-5 GeV</b>	5	3.07	7.45	-0.670	1.559
<b>Scheme 5: RFI-500 MeV + PPAS-1 GeV</b>	4	2.75	5.26	-0.361	0.561

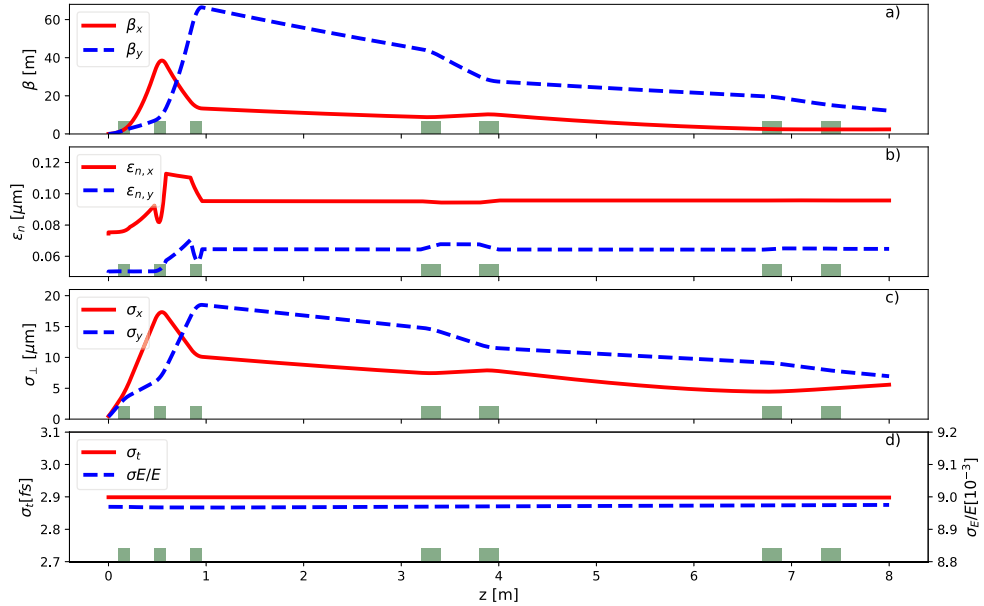
a short-wavelength undulator setup and in Table 19.6 for the case of a long-wavelength undulator design. Further details on the undulator parameters are given in Section 24.1. The optimisation is based, in a first instance, on particle swarm optimisation (PSO) [491] to find initial conditions near a global minimum, then, in a second stage, on the conjugate gradient method [492] to speed up the convergence near a minimum; finally, it uses a tracking code, like TraceWin [493], elegant [340] or ASTRA [320]. The variables are the quadrupole gradients and the positions of the different elements. The constraints are the total length of the machine (8 m in our case), minimum and maximum gradients (500 T/m for permanent quadrupoles and 50 T/m for electromagnet quadrupoles), and the minimum distance between elements (30 mm between permanent quadrupoles and 300 mm between electromagnetic quadrupoles of the same doublet to insert BPMs and correctors in between, 2 m between permanent quadrupoles and electromagnetic quadrupoles to insert a C-chicane in between, and 2.5 m between both doublets to insert long diagnostics like the TDS or a spectrometer). Finally, the beam transfer line is optimised with the tracking code TraceWin [493] to match the beam to the undulator entrance and to minimise the emittance growth. This optimisation takes into account the entire beam distribution with no assumptions on the initial conditions.

### 19.2.2 Scheme 1: LPI-5 GeV

The LPI uses the ReMPI injection technique to generate an electron beam inside the plasma and accelerate it to a final energy of 5 GeV. The transfer line is made of one triplet of permanent quadrupoles, used as a capture section, one C-chicane, and four electromagnetic quadrupoles as a matching section. The drive laser will be

**Table 19.7.** Parameters of the focusing elements in the high-energy transport line to the undulator for the case of Scheme 1 (LPI to 5 GeV).

Quadrupole		Q1	Q2	Q3	Q4	Q5	Q6	Q7
Length	[mm]	120			200			
Gradient	[T/m]	-468	487	-266	-20.0	29.9	-12.3	5.34

**Fig. 19.10.** High-energy transfer line – Scheme 1: Beam beta function (a), normalised emittance (b), transverse size (c), and bunch duration and energy spread (d) of the core beam along the transport line for the case of a single LPI to 5 GeV. The calculations were performed with the tracking code TraceWin.

removed at the middle of the C-chicane. Optical functions have been matched at the undulator entrance to the values given in Table 19.5.

The length of the transfer line is 8 m. The evolution of the beam distribution along the transport line is shown in Figure 19.10, whereas the evolution of the slice properties along the longitudinal beam distribution is shown in Figure 19.11. Beam properties are well preserved along the transfer line. The parameters of the quadrupoles are summarised in Table 19.7. The final beam characteristics are listed in Table 19.7.

### 19.2.3 Scheme 2: LPI-150 MeV + LPAS-5 GeV

In this scheme, electrons are first transported from one LPI to the LPAS, as described in Section 19.1. Electrons are then injected into an LPAS to be accelerated up to 5 GeV. As in the previous case, the transfer line is made of one triplet of permanent quadrupoles, used as a capture section, one C-chicane, and four electromagnet quadrupoles used as a matching section. The drive laser is removed at the middle of the C-chicane. Electron beam optical functions have been matched at the undulator entrance to the values given in Table 19.5.

The length of the transfer line is 8 m. The evolution of the beam distribution along the transport line is shown in Figure 19.12, whereas the evolution of the

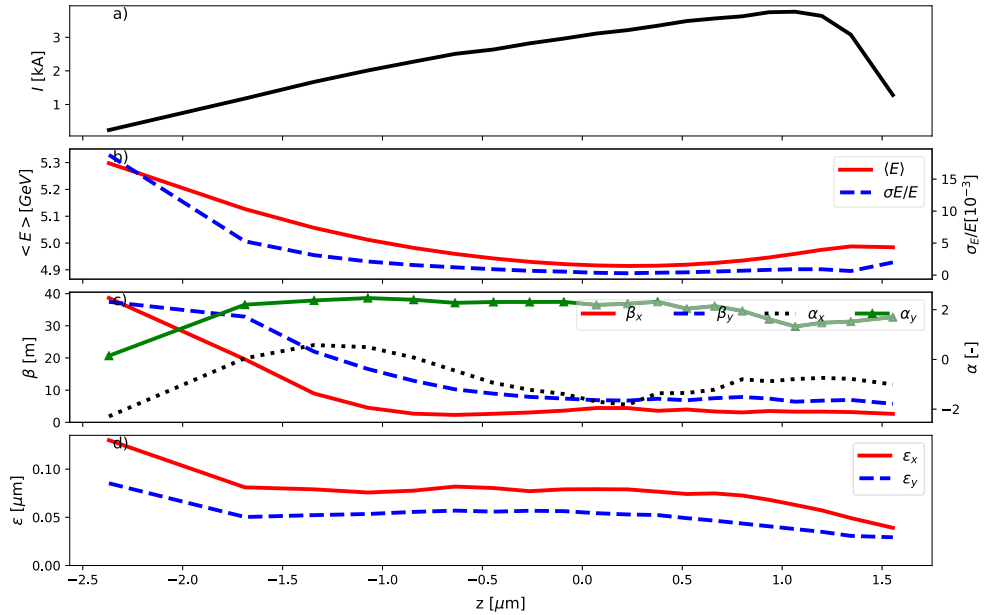


**Fig. 19.11.** High-energy transfer line – Scheme 1: Profile of the slice current (a), mean slice energy and slice energy spread (b), slice Twiss parameters (c), and normalised slice emittance (d) along the beam length at the entrance of the undulator for the case of a single LPI to 5 GeV. The calculations were performed with the tracking code ASTRA.

slice properties along the longitudinal beam distribution is depicted in Figure 19.13. Beam properties are well preserved along the transfer line. The parameters of the quadrupoles are summarised in Table 19.9. The final beam characteristics, on the other hand, are presented in Table 19.9.

#### 19.2.4 Scheme 3: RFI-500 MeV + LPAS-5 GeV

Electrons are injected from one RFI at 500 MeV to be accelerated up to 5 GeV inside the plasma stage in this scenario. The high-energy transfer line has the same standard setup: made of one triplet of permanent quadrupoles, used as a capture section, one C-chicane, and four electromagnetic quadrupoles used as a matching section. The drive laser is removed at the middle of the C-chicane. Electron beam optical functions have been matched at the undulator entrance to the values given in Table 19.5.

The length of the transfer line is 8 m and the evolution of the beam distribution along the transport line is shown in Figure 19.14. The evolution of the slice properties along the longitudinal beam distribution is shown in Figure 19.15. Beam properties are well preserved along the transfer line. The parameters of the quadrupoles are summarised in Table 19.11, while the final beam characteristics are depicted in Table 19.11.

#### 19.2.5 Scheme 4: RFI-240 MeV + LPAS-2.5 GeV + Chicane + LPAS-5 GeV

The current configuration considers splitting the acceleration process into two identical LWFA stages providing a  $\sim 2.5$  GeV energy gain in each to an externally injected electron beam. This layout is based on the multi-stage dechirping concept presented

**Table 19.8.** High-energy transfer line – Scheme 1: Comparison between the beam parameters at the LPI exit and at the entrance of the undulator. These parameters have been calculated considering only the beam core, i.e. only an 11.1 fs long slice in  $z$  around the peak current. This bunch core contains 30 pC of charge. The slice parameters and peak current are calculated assuming 0.1  $\mu\text{m}$  long slices.

		LPI exit	Undulator entrance
$\beta_x$	[m]	0.030	3.17
$\beta_y$	[m]	0.029	7.28
$\alpha_x$	–	–1.06	–0.70
$\alpha_y$	–	–1.03	1.57
$\varepsilon_{n,x}$	[ $\mu\text{m}$ ]	0.075	0.095
$\varepsilon_{n,y}$	[ $\mu\text{m}$ ]	0.050	0.064
Mean Energy	[GeV]	4.96	4.96
$\sigma_\gamma/\gamma$	[ $10^{-3}$ ]	9.0	9.0
$\hat{I}$	[kA]	3.8	3.8
$\sigma_\tau$	[fs]	2.9	2.9
$\varepsilon_{n,x}$ (slice)	[ $\mu\text{m}$ ]	0.069	0.068
$\varepsilon_{n,y}$ (slice)	[ $\mu\text{m}$ ]	0.041	0.041
$\sigma_\gamma/\gamma$ (slice)	[ $10^{-3}$ ]	0.8	0.8

**Table 19.9.** Parameters of the focusing elements in the transport line to the undulator for the case of Scheme 2 (LPI + LPAS to 5 GeV).

Quadrupole	Q1	Q2	Q3	Q4	Q5	Q6	Q7
Length [mm]	100			200			
Gradient [T/m]	–347	471	–297	1.18	22.7	–39.5	–25.4

in [494], where the energy chirp given to the electron beam in the first LWFA is inverted by a subsequent magnetic chicane, thus allowing it to be compensated in the second accelerating stage. A simplified representation of the beamline considered for this scheme can be seen in Figure 19.16. The details of the transport line between the two LPAS as well as the transport to the undulator are presented in the following. In the first case, the simulations were performed with the particle tracking code ASTRA [320] for the drifts, quadrupoles, and dipoles, taking into account 3D space-charge effects, while the plasma lenses were simulated with FBPIC [489]. CSRtrack simulations of the chicane were also performed to confirm that CSR effects do not have a significant impact on the beam. The second beamline for the beam transport to the undulator was simulated with the ASTRA code.

### Transport Line Between LPAS

The beam transport between the two plasma acceleration stages is crucial for the performance of this scheme. This beamline has to capture a highly divergent and high-energy-spread beam from the first LPAS, properly transport it through the chicane so that the energy chirp can be effectively inverted, and focus the beam again for injection into the second LPAS. All of this needs to be carried out, while preserving the beam properties, mainly its emittance and current profile.

To achieve this, APLs have been considered for the beam capture and final focus (one for each task), as these devices suffer less from chromatic aberrations compared

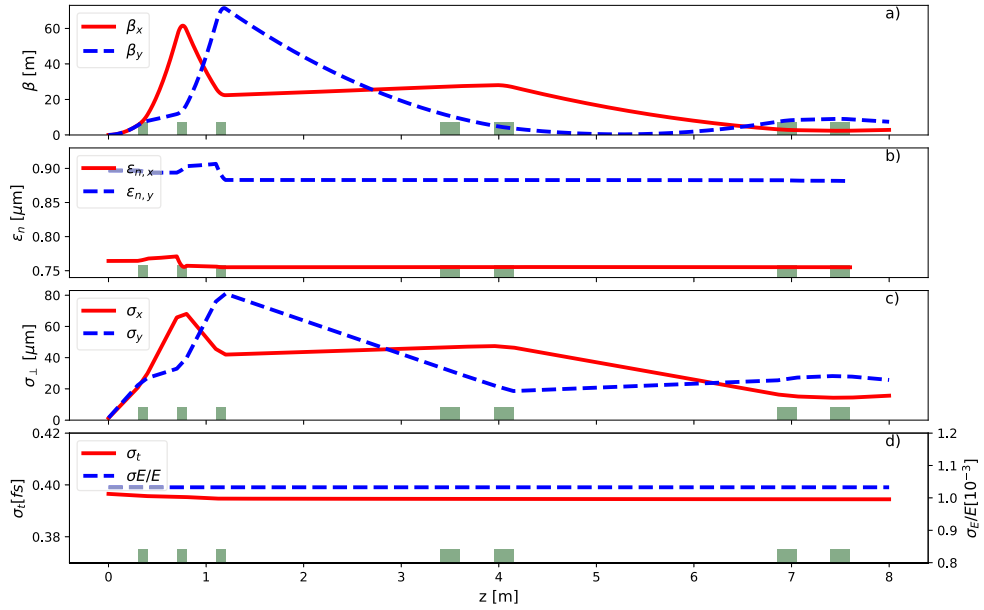


**Fig. 19.12.** High-energy transfer line – Scheme 2: Beam beta function (a), normalised emittance (b), transverse size (c), and bunch duration and energy spread (d) of the core beam along the transport line for the case of an LPI + LPAS to 5 GeV. The calculations were performed with the tracking code TraceWin.

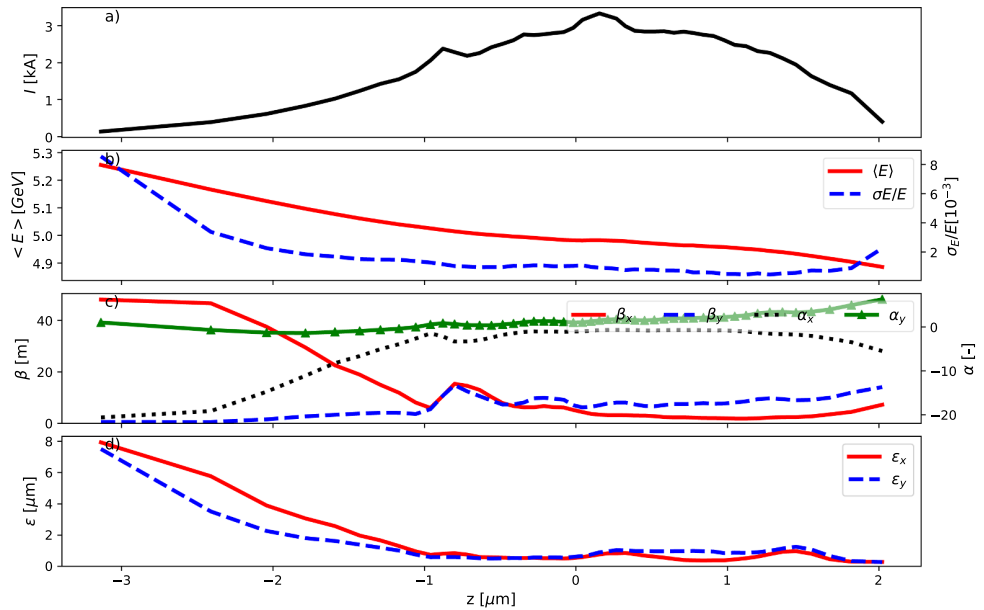


**Fig. 19.13.** High-energy transfer line – Scheme 2: Profile of the slice current (a), mean slice energy and slice energy spread (b), slice Twiss parameters (c), and normalised slice emittance (d) along the beam length at the entrance of the undulator for the case of an LPI + LPAS to 5 GeV. The calculations were performed with the tracking code ASTRA.

**Table 19.10.** High-energy transfer line – Scheme 2: Comparison between the beam parameters at the LPAS exit and at the entrance of the undulator. These parameters have been calculated considering only the beam core, i.e. only a 1.4fs long slice in  $z$  around the peak current. This bunch core contains 5pC of charge. The slice parameters and peak current are calculated assuming 0.1  $\mu\text{m}$  long slices.

	LPAS exit	Undulator entrance
$\beta_x$ [m]	0.021	3.16
$\beta_y$ [m]	0.023	7.33
$\alpha_x$ –	–0.48	–0.70
$\alpha_y$ –	–0.54	1.56
$\varepsilon_{n,x}$ [ $\mu\text{m}$ ]	0.76	0.76
$\varepsilon_{n,y}$ [ $\mu\text{m}$ ]	0.90	0.88
Mean Energy [GeV]	4.98	4.98
$\sigma_\gamma/\gamma$ [ $10^{-3}$ ]	1.0	1.0
$\hat{I}$ [kA]	3.2	3.3
$\sigma_\tau$ [fs]	0.4	0.4
$\varepsilon_{n,x}$ (slice) [ $\mu\text{m}$ ]	0.86	0.85
$\varepsilon_{n,y}$ (slice) [ $\mu\text{m}$ ]	1.00	1.00
$\sigma_\gamma/\gamma$ (slice) [ $10^{-3}$ ]	0.85	0.76

**Table 19.11.** Parameters of the focusing elements in the transport line to the undulator for the case of Scheme 3 (RFI + LPAS to 5 GeV).

Quadrupole	Q1	Q2	Q3	Q4	Q5	Q6	Q7
Length [mm]	120			200			
Gradient [T/m]	–331	489	–275	4.26	–15.1	46.1	–4.63

**Table 19.12.** High-energy transfer line – Scheme 3: Comparison between the beam parameters at the LPAS exit and at the entrance of the undulator. These parameters have been calculated considering only the beam core, i.e. only a 13fs long slice in  $z$  around the peak current. This bunch core contains 22pC of charge. The slice parameters and peak current are calculated assuming 0.1  $\mu\text{m}$  long slices.

	LPAS exit	Undulator entrance
$\beta_x$ [m]	0.034	3.16
$\beta_y$ [m]	0.034	7.32
$\alpha_x$ –	–1.79	–0.70
$\alpha_y$ –	–1.83	1.56
$\varepsilon_{n,x}$ [ $\mu\text{m}$ ]	0.31	0.32
$\varepsilon_{n,y}$ [ $\mu\text{m}$ ]	0.28	0.29
Mean energy [GeV]	5.41	5.41
$\sigma_\gamma/\gamma$ [ $10^{-3}$ ]	1.1	1.1
$\hat{I}$ [kA]	3.4	3.3
$\sigma_\tau$ [fs]	2.9	2.9
$\varepsilon_{n,x}$ (slice) [ $\mu\text{m}$ ]	0.35	0.35
$\varepsilon_{n,y}$ (slice) [ $\mu\text{m}$ ]	0.32	0.32
$\sigma_\gamma/\gamma$ (slice) [ $10^{-3}$ ]	0.28	0.27

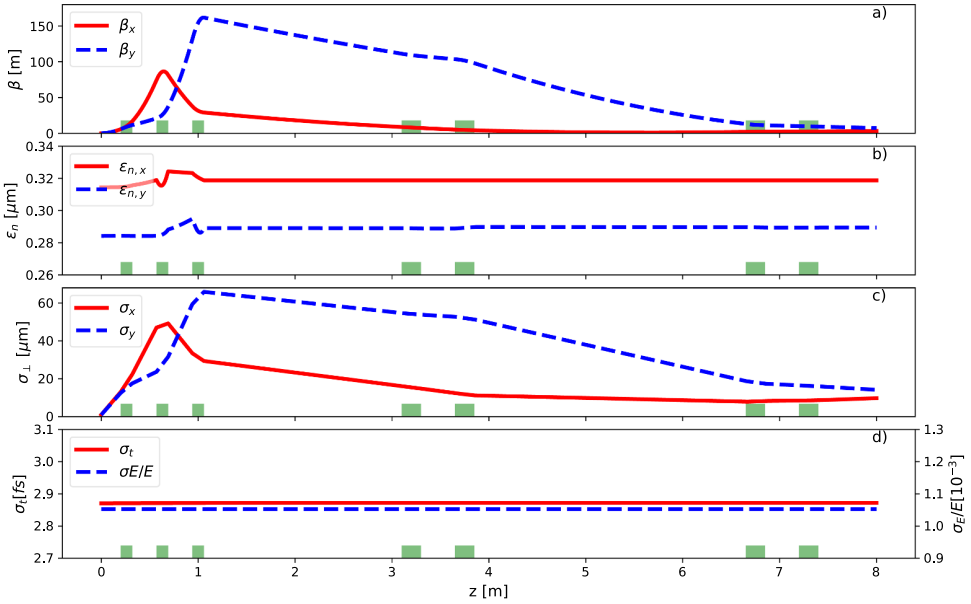


**Fig. 19.14.** High-energy transfer line – Scheme 3: Beam beta function (a), normalised emittance (b), transverse size (c), and bunch duration and energy spread (d) of the core beam along the transport line for the case of an RFI + LPAS to 5 GeV. The calculations were performed with the tracking code TraceWin.

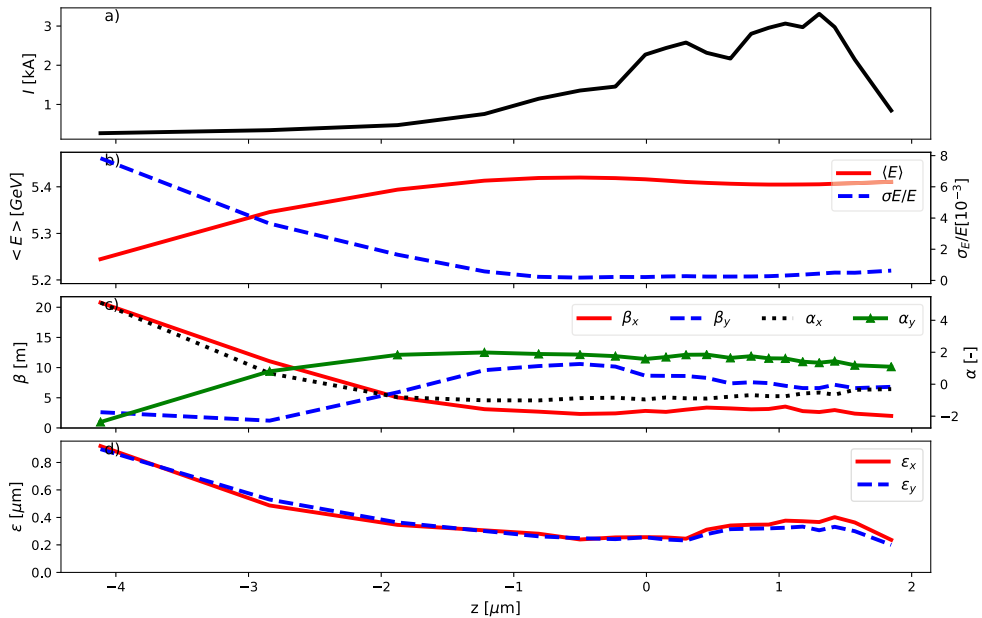


**Fig. 19.15.** High-energy transfer line – Scheme 3: Profile of the slice current (a), mean slice energy and slice energy spread (b), slice Twiss parameters (c), and normalised slice emittance (d) along the beam length at the entrance of the undulator for the case of an RFI + LPAS to 5 GeV. The calculations were performed with the tracking code ASTRA.

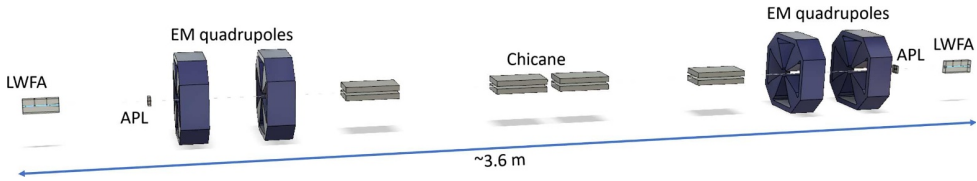


**Fig. 19.16.** Illustrative representation of the accelerator beamline of Scheme 4.

**Table 19.13.** Parameters of the focusing elements in the transport line between the two LPAS stages in Scheme 4.

Element	APL 1	Q1	Q2	Q3	Q4	APL 2
Length [cm]	1	20	20	20	20	1
Gradient [T/m]	3000	-35.47	29.07	25.59	-32.46	3000

to other focusing systems [38] and are therefore well suited for high-energy-spread beams. These two devices are the main components of the transport line and could, in theory, be sufficient to successfully transport the beam. However, since they provide the same focusing in both  $x$  and  $y$  planes and the beam parameters (Twiss parameters  $\alpha$  and  $\beta$ ) are different in each transverse direction, the presence of quadrupoles is required to properly guide the beam. In addition, including quadrupoles in the beamline provides a higher tunability of the transport line, since now the APLs are only needed to perform the initial capturing and final focusing of the beam. The quadrupoles, on the other hand, can be tuned to transport the beam through the chicane (achieving a beam waist, i.e.  $\alpha_x = \alpha_y = 0$ , at the chicane centre) and can be adapted for different beamline designs. The parameters of the focussing elements in the beamline, as currently considered in the simulations, can be seen in Table 19.13. The four chicane dipoles are all equal, having a length of 200 mm and a magnetic field of 0.4 T. The evolution of the beam parameters along this transport line is shown in Figure 19.17 and a comparison of the beam current profile before and after the chicane can be seen in Figure 19.18.

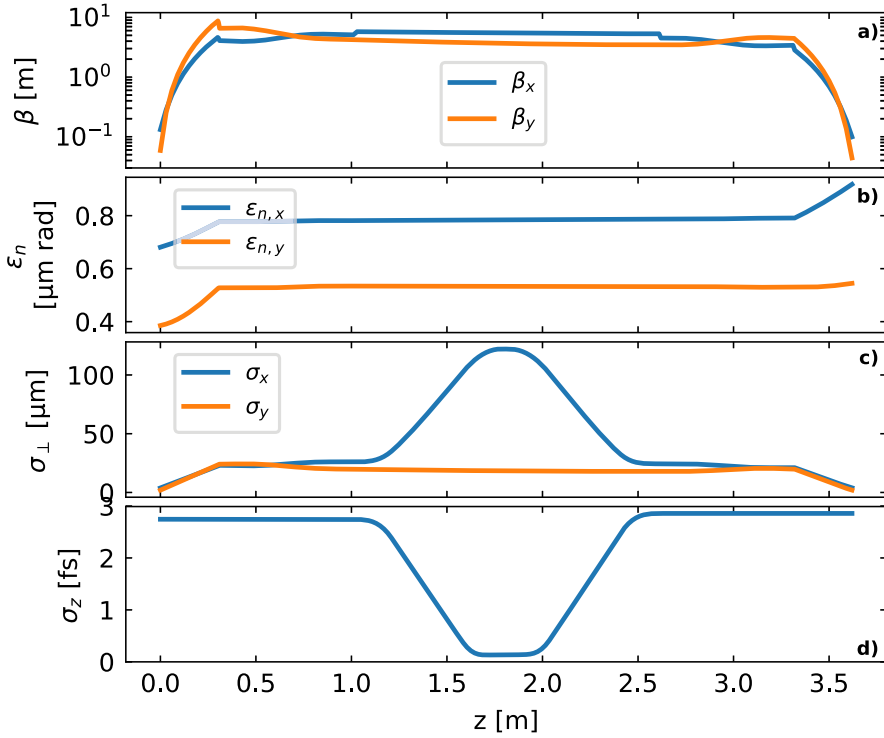
### Transport to Undulators

Similarly to the other schemes, this transfer line is made of one triplet of permanent quadrupoles, used as a capture section, one C-chicane, and four electromagnetic quadrupoles used as a matching section. The drive laser is removed in the middle of the C-chicane. Electron beam optical functions have been matched at the undulator entrance to values similar to those given in Table 19.5.

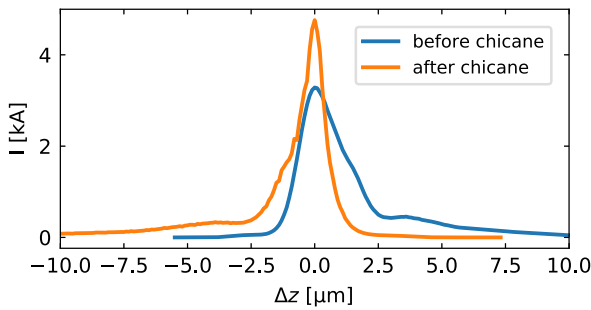
The length of the transfer line is 8 m. The evolution of the beam distribution along the transport line is shown in Figure 19.19 and the evolution of the slice properties along the longitudinal beam distribution is shown in Figure 19.20. Beam properties are well preserved along the transfer line. The parameters of the quadrupoles are summarised in Table 19.15, while the final beam characteristics are depicted in Table 19.15.

### 19.2.6 Scheme 5: RFI-500 MeV + PPAS-1 GeV

Two electron bunches (one driver and one witness) are injected from one RFI at 500 MeV to accelerate the witness up to 1 GeV inside a beam-driven plasma stage



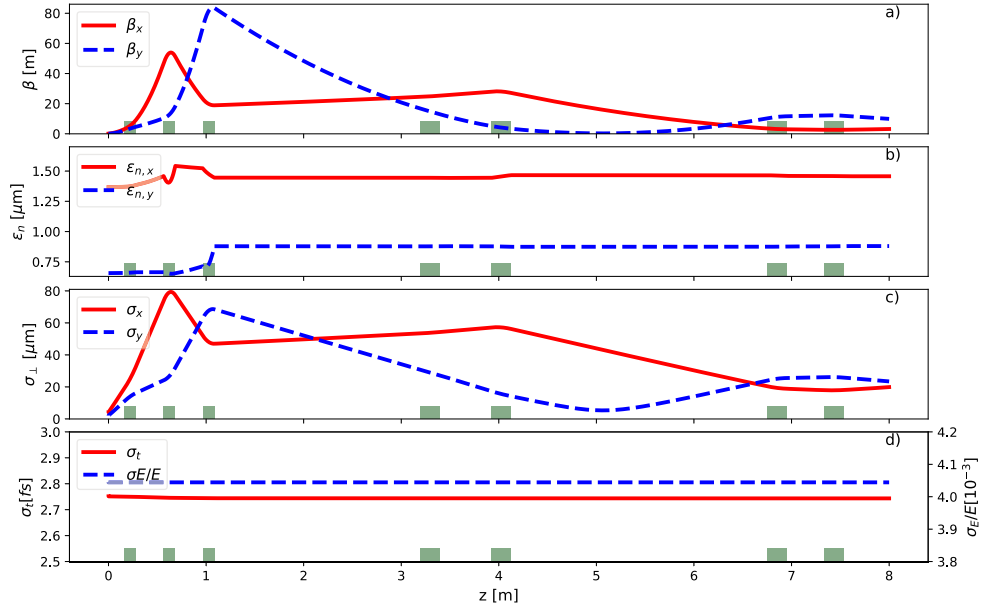
**Fig. 19.17.** High-energy transfer line – Scheme 4: Beam beta function (a), normalised emittance (b), transverse size (c), and bunch duration (d) along the transport line between the two LPAS. It should be noted that, although the actual simulations of the beamline were performed with ASTRA and FBPIC, due to the small amount of saved time steps along the transport line in those simulations (insufficient to get a clear picture of the beam evolution), the data shown in this plot come from a simulation performed with the particle-tracking code Wake-T [495]. However, since the effect of space-charge forces and wakefields in the APL on the beam parameters is very limited, the actual beam evolution does not significantly differ from the one shown in this figure.



**Fig. 19.18.** Current profile of the beam before and after the chicane in Scheme 4.

**Table 19.14.** Parameters of the focusing elements in the transport line to the undulator for the case of Scheme 4 (RFI + LPAS + LPAS to 5 GeV).

Quadrupole		Q1	Q2	Q3	Q4	Q5	Q6	Q7
Length	[mm]	120			200			
Gradient	[T/m]	-336	500	-317	-4.11	34.0	-48.6	-26.0

**Fig. 19.19.** High-energy transfer line – Scheme 4: Beam beta function (a), normalised emittance (b), transverse size (c), and bunch duration and energy spread (d) of the core beam along the transport line for the case of an RFI + two LPAS to 5 GeV. The calculations were performed with the tracking code TraceWin. Note that small variations in the average beam parameters in this figure compared to Figure 19.20 and Table 19.15 are a consequence of particle filtering; the beam core in this figure has been defined as the particles within 4 sigma of the beam centre.

(PPAS). The transfer line is made of one triplet of permanent quadrupoles, used as a capture section, one C-chicane, and three electromagnetic quadrupoles used as a matching section. The driver is removed at the middle of the C-chicane, where the dispersion is maximum (driver and witness have different energies then, with 500 MeV and 1 GeV, respectively). Electron beam optical functions have been matched at the undulator entrance to the values given in Table 19.5.

The length of the transfer line is 8 m. The evolution of the beam distribution along the transport line is shown in Figure 19.21. The evolution of the slice properties along the longitudinal beam distribution is shown in Figure 19.22. Beam properties change slightly along the transfer line. The parameters of the quadrupoles are summarised in Table 19.16, while the final beam characteristics are depicted in Table 19.17.

### 19.2.7 Conclusion

The high-energy beamlines from plasma stages to user applications (such as the FEL) have been optimised and presented. The optimisation procedure is now well

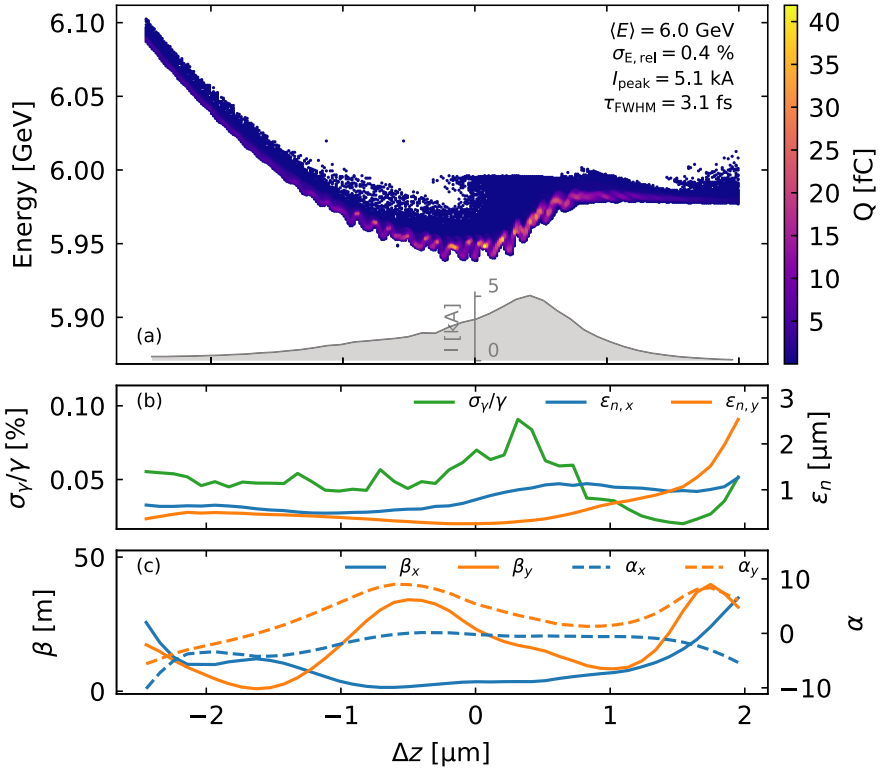


**Fig. 19.20.** High-energy transfer line – Scheme 4: (a) Longitudinal phase space and current profile of the beam core, (b) slice energy spread and normalised slice emittance along the beam, and (c) slice Twiss parameters. This particle distribution corresponds to the beam at the entrance of the undulator for the case of one RFI + two LPAS (5 GeV). The calculations were performed with the tracking code ASTRA.

**Table 19.15.** High-energy transfer line – Scheme 4: Comparison between the beam parameters at the exit of the second LPAS and at the undulator entrance. These parameters have been calculated considering only the beam core, as defined in the main text. The slice parameters and peak current are calculated assuming 0.1 μm long slices.

	2 <sup>nd</sup> LWFA exit	Undulator entrance
$Q$ [pC]	23.7	23.8
$\beta_x$ [m]	0.15	4.07
$\beta_y$ [m]	0.08	7.73
$\alpha_x$ –	-3.27	-0.98
$\alpha_y$ –	-1.91	1.63
$\epsilon_{n,x}$ [μm]	1.50	2.19
$\epsilon_{n,y}$ [μm]	0.69	0.90
Mean energy [GeV]	6.0	6.0
$\sigma_{\gamma/\gamma}$ [ $10^{-3}$ ]	4.1	3.9
$I_{\text{peak}}$ [kA]	4.9	5.1
$\tau_{\text{FWHM}}$ [fs]	3.1	3.1
$\epsilon_{n,x}$ (slice) [μm]	0.77	0.85
$\epsilon_{n,y}$ (slice) [μm]	0.40	0.40
$\sigma_{\gamma/\gamma}$ (slice) [ $10^{-3}$ ]	0.54	0.55

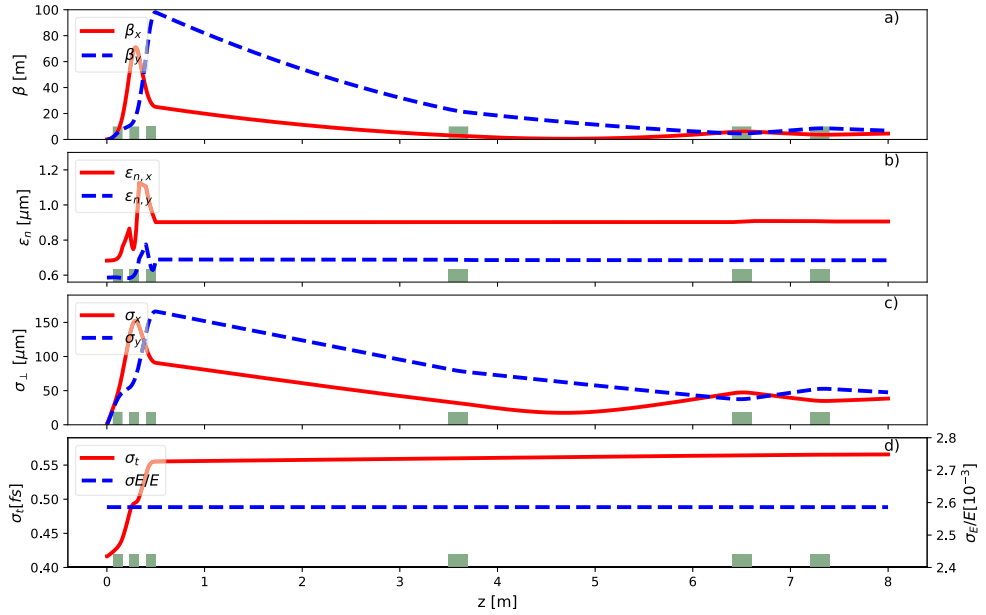


**Fig. 19.21.** High-energy transfer line – Scheme 5: Beam beta function (a), normalised emittance (b), transverse size (c), and bunch duration and energy spread (d) of the core beam along the transport line for the case of an RFI + PPAS to 1 GeV. The calculations were performed with the tracking code TraceWin.

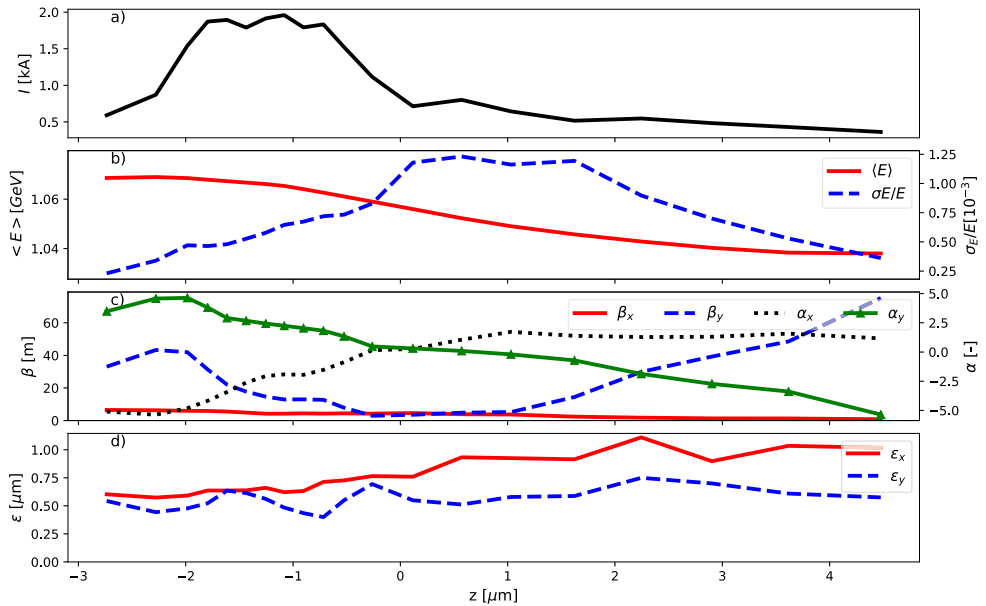


**Fig. 19.22.** High-energy transfer line – Scheme 5: Profile of the slice current (a), mean slice energy and slice energy spread (b), slice Twiss parameters (c), and normalised slice emittance (d) along the beam length at the entrance of the undulator for the case of an RFI + PPAS to 1 GeV. The calculations were performed with the tracking code ASTRA.

**Table 19.16.** Parameters of the focusing elements in the high-energy transport line to the undulator for the case of Scheme 5 (RFI + PPAS to 1 GeV).

Quadrupole		Q1	Q2	Q3	Q4	Q5	Q6
Length	[mm]	100			200		
Gradient	[T/m]	-267	288	-153	2.89	15.6	-10.1

**Table 19.17.** High-energy transfer line – Scheme 5: Comparison between the beam parameters at the PPAS exit and at the entrance of the undulator. These parameters have been calculated considering only the beam core, i.e. only electrons in the range  $\pm 5$  MeV around the mean energy. This bunch core contains 10.5 pC of charge. The slice parameters and peak current are calculated assuming 0.1  $\mu\text{m}$  long slices.

		PPAS exit	Undulator entrance
$\beta_x$	[m]	2.175	3.39
$\beta_y$	[m]	4.2664	6.88
$\alpha_x$	–	0.004	-0.61
$\alpha_y$	–	1.072	1.16
$\varepsilon_{n,x}$	[ $\mu\text{m}$ ]	0.68	0.91
$\varepsilon_{n,y}$	[ $\mu\text{m}$ ]	0.59	0.68
Mean Energy	[GeV]	1.06	1.06
$\sigma_\gamma/\gamma$	[ $10^{-3}$ ]	2.6	2.6
$\hat{I}$	[kA]	2.06	1.96
$\sigma_\tau$	[fs]	0.42	0.56
$\varepsilon_{n,x}$ (slice)	[ $\mu\text{m}$ ]	0.66	0.62
$\varepsilon_{n,y}$ (slice)	[ $\mu\text{m}$ ]	0.55	0.48
$\sigma_\gamma/\gamma$ (slice)	[ $10^{-3}$ ]	0.33	0.65

established and transfer lines integrate diagnostics. Results show that, in most of the cases, beam properties can be preserved and the beam is matched to the user application requirements with state-of-the-art elements.

Nevertheless, correction schemes have not been implemented yet and should be addressed in the future. This work will have a direct impact on the diagnostics requiring a validation of the positioning of diagnostics (BPMs for instance). Laser removal is another critical topic and the required space to inject and remove the laser driver should be discussed in the near future.

## 20 Plasma Diagnostics

Diagnostics techniques capable of providing information on plasma density and accelerating field amplitude in the plasma structures envisaged for injectors and accelerators in the EuPRAXIA beamline are described in this chapter.

### 20.1 Introduction

Diagnostic tools suitable for real-time monitoring and control of plasma density are necessary to achieve the long-term stable operation of the accelerator as required for a user facility.

Interferometric diagnostics can be used for the determination of gas or plasma density in a variety of configurations, giving access to the range of parameters required for injector and accelerator plasma modules. Their respective sensitivities are compared, and practical considerations are discussed.

Spectroscopic methods and group velocity measurements have the capability to diagnose plasma density in waveguides and are better suited for the accelerator plasma.

The spectral analysis of the laser driver after interaction with the plasma in the quasi-linear regimes provides a measurement of the averaged accelerating field and is thus a precious tool for monitoring the quality of the accelerator during operation.

Plasma diagnostics are required both in the development stage and in the operation stage of a facility like EuPRAXIA. They can be classified as diagnostics used for the following:

- **Alignment, A:** in the preparation phase or start-up after an interruption of operation.
- **Tuning, T:** to monitor plasma parameters while tuning, changing operation mode, or optimising electron beam parameters.
- **Operation, O:** to monitor plasma parameters for measuring reproducibility and stability, and detect any potential deviation during operation.

Controlling and measuring the density of a plasma with a precision better than 10% at the instant of interaction with the short laser or particle pulse is extremely challenging. This report examines several diagnostic techniques that could be useful for either injector or accelerator stages. As plasma density, volume, regime of interaction, and accessibility to detection are different for injectors and accelerators, different techniques may be used. In the quasi-linear regime of the accelerator stage, a measurement of the amplitude of the accelerating field can also be envisaged.

## 20.2 Plasma Diagnostics

Diagnostic tools suitable for a real-time monitoring and control of plasma density are necessary in order to achieve long-term stable operation of the accelerator as required for a user facility. The plasma target envisaged for the EuPRAXIA accelerator stages will be composed of hydrogen gas [220]. Assuming full ionisation, the electron density in the plasma will then be double the neutral particle number density [286], which may be a simpler quantity to measure in some circumstances.

In this section, we consider simple diagnostic methods not requiring sophisticated implementation (e.g. anti-vibration systems) which may be applicable to the plasma preparation phase or resuming after an interruption (A), when changing / optimising parameters (T), and when monitoring parameters for measuring reproducibility / stability (O).

### 20.2.1 Interferometric Density Measurement

In interferometric methods, the density is inferred from measurements of the phase shift acquired by an optical ray when passing through the target. This is possible as the refractive index of the sample  $\eta(n)$  is dependent on its particle number density  $n$ ; in particular, the refractivity  $\eta(n) - 1$  is proportional to the particle number density of the atoms / molecules in a gas or free electrons in a plasma. For a plasma,  $\eta_e(\lambda, n_e) - 1 = -e^2 \lambda^2 n_e / (8\pi^2 m_e \varepsilon_0 c^2)$ , where  $e$  is the electron charge,  $\lambda$  is the light wavelength,  $m_e$  is the electron mass,  $\varepsilon_0$  is the vacuum permittivity, and  $c$  is the speed of light. For neutral atoms / molecules, from the Lorentz-Lorenz equation,

$\eta(\lambda, n) - 1 = (\eta_0(\lambda) - 1) \times n/n_0$ , where  $\eta_0(\lambda)$  is the refractive index at a particle number density  $n_0$  taken as reference value. The additional phase acquired by a light beam when passing through a sample of length  $L$  is then  $\phi = (2\pi/\lambda) \int_L (\eta(\lambda) - 1) d\ell$ . Therefore, with an interferometric measurement, the information acquired is the line-integrated particle density.

Interferometric measurements can be performed over an extended area using an optical imaging system to acquire a 2D interferogram, from which it is possible to retrieve a 2D map of the line-integrated phase shift imparted by the target. Two-dimensional phase retrieval can lengthen the data analysis and introduce some uncertainty in the measurement due to the algorithm used to analyse the interferogram but allows for the reconstruction of complex density profiles which may be most appropriate during the alignment (A) and tuning (T) of the system.

It is also possible to perform a 1D interferometric measurement over a single line of sight, i.e. integrating over the entire light beam using a photodiode or PMT as a light detector, in which case a spatially averaged density will be retrieved. One-dimensional measurements are faster to acquire and process and therefore may be more suitable during operation (O), e.g. to monitor in real time the gas particle number density.

Three classes of interferometric diagnostics are in common usage.

### Two-Arm Interferometer (TAI)

In two-arm interferometers (TAIs), the phase shift is measured relative to the phase of an optical ray not passing through the sample. The two-arm method can be implemented in various configurations depending on the optical design adopted:

- Standard two-arm design, e.g. Mach-Zehnder and Fizeau interferometers, where the light beam is split into two distinct beams following different paths, one of which passes through the target, which then recombine and interfere [352].
- Modified two-arm interferometers, also called two-arm folded interferometers, where the light beam is split into two after passing through the target and interference take place between parts of the beam with and without the sample [496,497]. This method provides more control on the fringe spacing and angle and is often used in LWFA experiments.
- Nomarski interferometer, similar to the two-arm folded interferometer, but the beams are split using a Wollaston polariser or a bi-prism after the target [498,499].

The standard two-arm interferometers suffer from high sensibility to environmental conditions, e.g. mechanical vibration and temperature changes, while the last two methods are relatively more robust. The typical sensitivity of an ultra-fast-imaging two-arm interferometer can be hundredths of a fringe, i.e.  $\sim 100$  mrad.

### Wavefront (WF) Sensor

A versatile and robust method is based on wavefront (WF) sensors, e.g. the commercial quadri-wave lateral shearing interferometer (Phasics, Fr) [500]. This instrument measures the differential phase among two adjacent points of the light beam on the wavefront detector. In fact, it is sensitive to the phase gradients along two orthogonal directions, and the actual phase map is retrieved by analysing the data with a proprietary software. Finally, the phase shift is calculated by subtracting the phase map of an undisturbed beam, acquired in a separate measurement without the plasma [501]. It is a single-arm method since interference takes place only at the detector and therefore is a very robust method, allowing for a relatively high phase sensitivity,

**Table 20.1.** Measuring capability of interferometric methods. Phase shift after passing through 1 cm of medium.

Method	Neutral gas at $10^{19} \text{ cm}^{-3}$	Plasma electrons at $10^{17} \text{ cm}^{-3}$
Two-arm, 800 nm	4 rad	2.2 rad
Two-arm, 400 nm	8.3 rad	1.1 rad
Second harmonic, 800 nm	0.3 rad	3.4 rad

which is claimed to be  $<2$  nm, i.e.  $<30$  mrad at 400 nm [502]. An RMS sensitivity of 11 mrad has been estimated at 400 nm over 188 acquisitions [503]. It is noted that no single-acquisition value has been reported, so a conservative value of 30 mrad at 400 nm is assumed.

The wavefront sensor measures only the gradient of the density and therefore is not a straight forward analytical relation between the measured quantity and the density. In reference [503], a comparison between wavefront-based sensors and a modified two-arm interferometer resulted in a difference in the absolute value of the measured density of 10–20%. From the WF data sheet, 15 nm accuracy, i.e. 0.24 rad at 400 nm, is claimed, which can explain the deviation with respect to the TAI measurement. Thus, the WF sensor-based instrument would require an accurate calibration before being used for an absolute measurement of density.

### Second-Harmonic Interferometer (SHI)

Another kind of interferometer is the so-called second-harmonic (or dispersion) interferometer (SHI), which has a fully common-path design and measures the phase difference acquired by the fundamental and second-harmonic beams when passing collinearly through the sample [504,505]. The measured phase shift is given by  $\Delta\phi_{SHI} = (4\pi/\lambda) \int_L \Delta\eta(\lambda) d\ell$ , where  $\Delta\eta(\lambda) = \eta(\lambda) - \eta(\lambda/2)$ . It is a very robust method against mechanical and thermal vibrations, with a sensitivity  $\leq 1$  mrad for 1D measurements [506], though there are no data available in the literature regarding sensitivity of the SHI for 2D imaging [507,508]. Here, we assume a conservative sensitivity value of 10 mrad for quadrature detection [509].

Spectral-domain second-harmonic interferometry (SDSHI) has recently been successfully applied to measure the line-integrated longitudinal plasma density. Significantly, the measurement of the group delay in SDSHI at 800 nm results in a sensitivity of 2.84 rad, while a simultaneous measurement of the spectral phase allows one to get a sensitivity of 63 mrad without the need of a fringe-tracking procedure [510].

### Comparison of the Measurement Capability

Given that the refractivity of hydrogen at the fundamental and second-harmonic wavelength of a Ti:sapphire laser are  $1.374 \times 10^{-4}$  and  $1.426 \times 10^{-4}$ , respectively [511],  $\Delta\eta(800 \text{ nm}) = \eta(400 \text{ nm}) - \eta(800 \text{ nm}) = 52 \times 10^{-7}$  at standard temperature and pressure.

The measuring capability of the various techniques, measured as phase shift per centimetre of medium, are compared in Table 20.1.

In Figures 20.1 and 20.2, the capabilities of the various interferometric methods are graphically shown for neutral hydrogen and free electrons, respectively; the lower full lines represent the lower detection limit set by the sensitivity, while the upper dashed lines represent the upper limit within a single fringe measurement, i.e.  $\Delta\phi <$

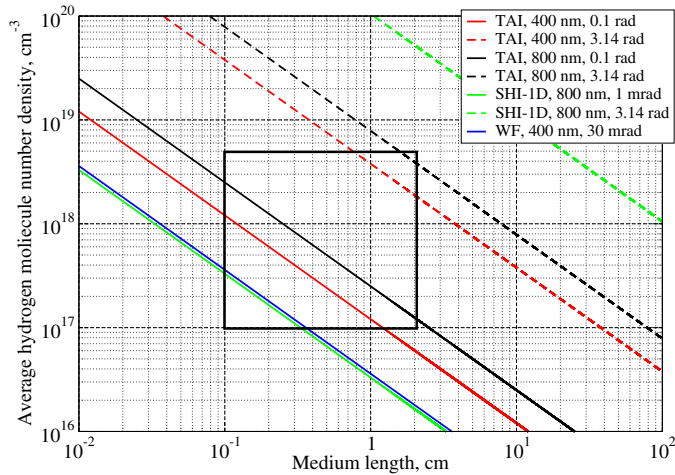


**Fig. 20.1.** Interferometric measurement capability for neutral molecular hydrogen. The solid lines correspond to the minimum detectable phase while the dashed-lines correspond to the sub-fringe limit, as indicated by the phase value reported in the legend.

$\pi$ . The black boxes represent the parameters space indicated for free-electron density  $n_e$  for EuPRAXIA,  $2 \times 10^{17} - 1 \times 10^{19} \text{ cm}^{-3}$ , with a neutral gas density half of it. Interferometry is performed usually transversally to the main laser and the electron beam. In such a case, the plasma length seen by the interferometer lies between  $10 \mu\text{m}$ , roughly the dimension of the main laser beam spot, and hundreds of  $\mu\text{m}$ . In case of a centimetres-long plasma channel/waveguide, e.g. for the accelerator module, longitudinal interferometry may be considered. The length of neutral gas seen by the interferometer can range from a millimetre, e.g. for a pulsed jet [512], to tens of millimetres, as in flowing gas cells [40,513].

From Figure 20.1, it is evident that the SHI and the WF sensors are capable of measuring low-density values even for paths of a few millimetres. The SHI allows a very fast measurement of neutral hydrogen in 1D (acquisition time  $\sim 1 \mu\text{s}$ ) and therefore can be implemented as a sensor in a closed-loop gas flow regulation system. This is very important for gas cells as repetitive shots of the high-power main laser beam may eventually modify the cell's orifice, altering the gas flow dynamics and therefore the internal number density for a pre-set backing pressure [286]. On-line regulation of the gas supply system is therefore necessary to achieve a stable and reproducible laser-plasma acceleration process. A 1D measurement with an SHI can achieve a sensitivity  $< 1 \text{ mrad}$ , therefore enabling the measurement of density around  $10^{17} \text{ cm}^{-3}$  over a 1 mm length [506]. In comparison, a wavefront sensor is suitable for 2D density mapping for densities above  $10^{17} \text{ cm}^{-3}$  gas lengths above several millimetres.

For one-shot measurements of the free-electron density, Figure 20.2 shows that only the imaging SHI with 10 mrad sensitivity would be suitable to measure the lowest free-electron density in the range of a few  $10^{17} \text{ cm}^{-3}$  for a plasma length  $< 100 \mu\text{m}$ . However, such an instrument has not yet been tested, and further development is necessary to assess the actual sensitivity achievable with an imaging SHI, though ultra-fast SHI has been presented in the literature [514]. The wavefront sensor is suitable for the measurement of free-electron densities above  $10^{18} \text{ cm}^{-3}$  and a plasma longer than hundreds of  $\mu\text{m}$ , and it can readily work with ultra-fast light sources [503].

Concerning plasma channels / waveguides, the measurement of the group delay in SDSHI results in a sub-fringe resolution (2.84 rad), with a simultaneous measurement

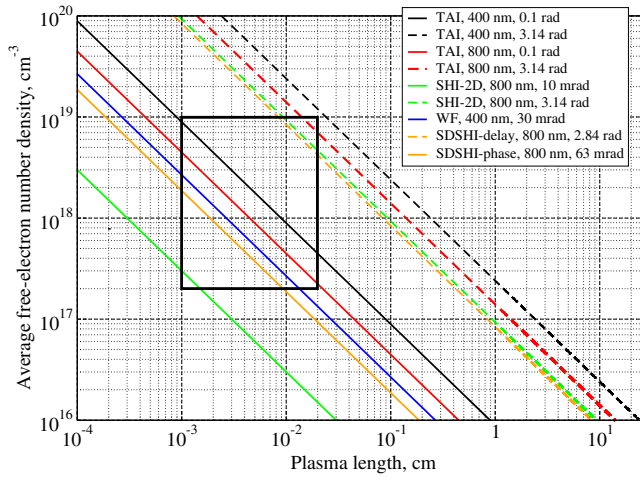


**Fig. 20.2.** Interferometric measurement capability for free electrons. The solid lines correspond to the minimum detectable phase, while the dashed lines correspond to the sub-fringe limit, as indicated by the phase value reported in the legend, except for the SDSHI, for which both spectral phase and group delay measurements capability are shown by solid and dashed lines, respectively.

**Table 20.2.** Comparison of interferometric methods.

Diagnostic	Advantages	Disadvantages
Two-arm	Ultra-fast compatible 2D measurement	Sensitive to environmental conditions Requires multiple beams
Second-harmonic	Single beam Compact Easy to implement High phase sensitivity High absolute accuracy	Ultra-fast and 2D imaging versions to be tested
Wave-front	Single beam Compact Easy to implement Ultra fast compatible 2D measurement	Low absolute phase accuracy Processing frequency < 3 Hz

of the spectral phase to achieve a phase resolution of 63 mrad over multiple fringes without any fringe tracking procedure [510]. These data are also included in Figure 20.2 for better comparison with the other interferometric methodologies.

The advantages and disadvantages of each interferometric method are summarised in Table 20.2.

### Practical Considerations

To retrieve the actual density from an interferometric measurement, some assumptions on the geometry of the sample have to be made. There are two typical cases: cylindrically symmetric samples, e.g. pulsed gas jet from circular nozzles and plasma created by a laser beam, and uniform samples, e.g. gas-filled cells. For uniform and homogeneous samples, the actual density is simply related to the measured phase

shift. For cylindrically symmetric samples, the measured phase shift must be symmetrised and Abel-inverted to extract the radial density profile [497]. The density distribution of anisotropic samples must be measured using tomographic methods [515].

All interferometric methods require a line of sight through the sample. For a freely expanding gas jet, interferometry is easy to implement, while in the case of confined samples – e.g. gas cells, capillaries, and tubes – flat optical side windows are necessary in order to provide the optical path for transverse interferometry. This issue must be considered when designing the geometry of the accelerator stage. Longitudinal interferometry may be adopted [352,510], potentially for aligning (A) / tuning (T), but not during operation (O) because of the geometrical constraints due to the main laser / electron bunch propagation.

### 20.2.2 Spectroscopic Methods

In the case when there is not a straight optical path through the sample, e.g. cylindrical capillaries or tubes, other optical diagnostics to monitor density can be considered. Stark broadening measurements may be envisaged to monitor the free-electron density in this situation [516]. It has to be noted, however, that the data analysis in this case depends (in a mild way) on the electron temperature. Therefore, a direct measure or estimate of the electron temperature may be necessary in parallel with Stark broadening measurements. Spatially resolved emission spectroscopy (along a line) can be implemented using an imaging spectrometer, and measurements at the nanosecond time scale can be achieved using a fast (intensified) camera. For example, the Stark broadening of hydrogen lines (e.g.  $H_\beta$  at 486.1 nm) allows for the determination of the local electron density down to the  $10^{16} \text{ cm}^{-3}$  range with a medium-resolution spectrometer.

### 20.2.3 Group Velocity Measurements

For a discharge capillary waveguide producing a radial plasma density distribution, laser group velocity measurements can be used to measure the plasma density [517–519]. This measurement relies on interferometry in the spectral domain between a reference beam travelling in vacuum and a beam probing the plasma. The reference beam and the probe beam are achieved by a 50/50 beam splitter in front of the capillary. The capillary beam is focussed by a lens into the capillary entrance and imaged on a spectrometer. The reference beam is transported in vacuum to a delay stage before being imaged on the same imaging spectrometer. A reference measurement is done with the capillary out and compared to the same measurement, with the capillary guiding the laser to deduce the delay introduced by the lower group velocity ( $v_g$ ) inside the capillary plasma. Particular attention must be put into the laser spot size as laser size fluctuations during its propagation in the capillary discharge can indeed increase the optical path. Simulations of the laser propagation inside the plasma channel must be performed to take this effect into account.

### 20.2.4 Summary

In summary, the methods described above are appropriate for different types of plasma targets:

- For the LPI, flowing gas cells with an electron density of  $2 \times 10^{17} \text{ cm}^{-3}$  for a 1 GeV baseline and  $3 \times 10^{18} \text{ cm}^{-3}$  for a 150 MeV baseline are considered a promising

target. For the lower density case, the 2D SHI is a potentially useful diagnostic, but further development is necessary to develop the required ultra-fast and 2D capability. At higher density / plasma length, a wavefront sensor is suitable for 2D mapping with ultra-fast capability. Concerning neutral gas density measurements in the range  $10^{17} - 10^{19} \text{ cm}^{-3}$ , 1D SHI provides the best solution for real-time monitoring, while the wave-front sensor is suitable for 2D measurements. TAIs are less suitable during operation because of their limited sensitivity but may be useful during the aligning / tuning of the system.

- Small-diameter plasma channels created with a laser pre-pulse at densities of  $10^{17} - 10^{19} \text{ cm}^{-3}$  are open structures compatible with transverse interferometry. At lower density, only the ultra-fast 2D SHI may prove useful, while at higher density, a wavefront sensor will work.
- Plasma channels created by a discharge in a capillary or the grazing incidence capillaries do not allow for transverse interferometry; in these cases, Stark broadening measurements and / or longitudinal interferometry may be adopted [352,510,520]. TAIs are less suitable during operation but may be useful during aligning / tuning.

### 20.3 Plasma Wave Diagnostics

The primary diagnostic of electric field and thus plasma wave amplitude in the plasma accelerator is likely to come from the injection and acceleration of fast particles into the structures. However, in the absence of a particle beam, which will be true in preparatory phases (A), optical diagnosis can provide a great amount of information about the relativistic plasma wave. This can be achieved with both longitudinally and transversely directed beams.

#### 20.3.1 Longitudinal Probing

##### Spectral Characterisation of the Driver Beam

The plasma wave amplitude can be diagnosed by analysing the spectrum of the transmitted laser radiation after interaction over a long distance in the quasi-linear regime. Laser pulses transmitted through gas jets [521] and gas-filled capillary tubes exhibit broadened spectra [522]. In the range of parameters relevant to the accelerator plasma, spectral modifications of the laser pulse driving the plasma wave, after propagating in the plasma over a large distance, are mainly related to changes in the index of refraction of the plasma during the creation of the plasma wave. The front of the laser pulse creates an increase in electron density as plasma electrons are pushed in front of the intense laser pulse by its ponderomotive push. This leads to a blueshift at the very front of the pulse, sometimes called photon acceleration [523]. However, the main body of the laser pulse sits in a region of decreasing electron density, away from the first maximum. In this region, the laser pulse is redshifted, indicating that the laser photons are transferring energy to the growth of the plasma wave (i.e. “photon deceleration”). This shift of the spectrum toward longer wavelengths is thus a signature of plasma wave excitation.

The average wavelength shift  $\Delta\lambda(l)$  over a propagation length  $l$  can be expressed as a function of the laser spectrum  $S(\lambda, l)$  as follows [524]:

$$\Delta\lambda(l) = \frac{\int_0^\infty \lambda S(\lambda, l) d\lambda}{\int_0^\infty S(\lambda, l) d\lambda} - \lambda_L$$

with  $\lambda_L = \int_0^\infty \lambda S(\lambda, l = 0) d\lambda / \int_0^\infty S(\lambda, l = 0) d\lambda \simeq 2\pi c / \omega_L$  as the laser centre wavelength. For a laser pulse well above the ionisation threshold so that the blueshift

caused by ionisation can be neglected and the wavelength shift is small compared to the laser wavelength, the shift is related to the energy of the plasma wave electric field  $E_p$  through

$$\frac{\Delta\lambda(l)}{\lambda_L} \simeq \frac{1}{16\pi E_{out}} \int_V E_p^2 dV$$

with  $E_{out}$  as the transmitted laser energy and  $V$  as the interaction volume. For a Gaussian laser pulse propagating in a monomode dielectric capillary of radius  $r_c$ , the wavelength shift can be expressed analytically as follows:

$$\Delta\lambda(l) \simeq \left[ 0.178 + 1.378 \frac{c^2}{(\omega_p r_c)^2} \right] \left( \frac{\omega_p}{\omega_L} \right)^3 a_L^2 D(\Omega) l$$

with  $D(\Omega) = \Omega \exp(-\Omega^2/4)$  and  $\Omega = \omega_p \tau_L / \sqrt{2 \ln 2}$ ,  $\omega_p$  as the plasma angular frequency and  $\tau_L$  as the laser pulse duration;  $c$  is the velocity of light in vacuum and  $a_L$  the peak normalised amplitude of the laser field.

The measurement of the total energy and spectral composition of the transmitted laser pulse can therefore be used to diagnose the amplitude of the plasma wave [525]. This diagnostic can be used to adjust plasma and laser parameters for optimum acceleration.

### Photon Acceleration Probe

This process can be extended by the use of secondary laser beams to probe the plasma density. A long laser pulse can be sent behind the short pulse drive, which generates the wakefield, so that it copropagates with the wakefield. Frequency shifts along the length of the probe beam caused by the varying refractive index can be compared to the simulation to allow the plasma wave shape to be unfolded [526]. Alternatively, full spectral-phase measurements can be performed with an instrument such as a FROG (frequency-resolved optical gating) to allow the variation in phase along the plasma wave to be determined [527]. This can then be directly related to the density of the plasma wave causing the phase shifts.

Problems with this technique, which are common with those for diagnosing the transmitted beam, are the longitudinal displacement of photons due to group velocity dispersion, photon trapping, and instabilities such as Raman scattering. These become particularly an issue over long interaction lengths. Sending the probe beam at an angle to limit the interaction length has also been considered to overcome some of these problems.

### Frequency Fomain Interferometry

These measurements can be extended by directly measuring the phase shifts rather than spectral shifts using frequency-domain interferometric methods. The 1D structure of the wave can be found by stepping an ultra-short probe through the plasma wave so that the plasma density can be interrogated as a function of longitudinal displacement [528,529]. An extension of this technique is the overlapping of a long probe pulse with one that has not been through the plasma to produce a complete spatio-temporally resolved image in three-dimensions of the plasma wave in a technique called frequency-domain holography (FDH) [530]. FDH is particularly useful for diagnosing linear plasma waves over limited distance, but again, when spectral and phase shifts become too large because of long interaction lengths or strong density gradients in the plasma wave, then the same limitations as other longitudinal plasma wave density measurements exist.

### 20.3.2 Transverse Probing

Recently, it has been demonstrated that the same transverse probing techniques used for imaging plasma channels can be used for measuring the density profiles of relativistic plasma waves as well [531–533]. An ultra-short probe can essentially freeze the motion of the plasma wave. Since the plasma wave can be as short as 30 fs in temporal duration at a plasma density of  $1 \times 10^{19} \text{ cm}^{-3}$ , then this demands that the probe beam should be much shorter. Typically, probe beams of duration  $< 10$  fs are employed using the latest pulse-compression techniques. Additionally, polarisation measurements can allow sensitive measurements of the magnetic field within the plasma wave [531,532], which can be produced as a combination of the self-generated fields of the plasma wave as well as the magnetic field of an accelerating bunch. Indeed, this has allowed an injected bunch inside a plasma wave to be imaged for the first time [532], and is a useful diagnostic of the injection process [533]. The short pulse means that interferometry is relatively difficult in this configuration, since the short pulse length necessitates a large bandwidth. The short pulse length limits the spatial extent over which interference occurs, and the broad bandwidth can reduce fringe visibility. As a result, these first experiments have relied on transverse probe deflection (shadowgraphy) for imaging the plasma wave.

The difficulty with transverse probing is that the relatively short interaction distances mean that the sensitivity of this technique is less than that of longitudinal techniques. Indeed, until now, it has only been operated at high density ( $> 1 \times 10^{19} \text{ cm}^{-3}$ ) and for non-linear plasma waves. However, the use of longer wavelength probes, which increases sensitivity, and the use of advanced techniques, such as SHI or wavefront sensors, would allow these techniques to be extended to lower plasma density stages.

### 20.3.3 Summary

In summary, a number of optical techniques have been developed to diagnose the full 3D structure of an accelerating relativistic plasma wave. Generally, these techniques make use of the variation in refractive index associated with the plasma density modulations of the plasma wave. Probing longitudinal to the plasma wave can allow an integrated effect, allowing for a particularly high sensitivity. This will be particularly important for the long low-density plasmas, which are envisaged for the high-energy stages for EuPRAXIA. These density modulations can then be diagnosed using a combination of spectral and interferometric techniques. In turn, this will allow both a longitudinal and a transverse characterisation of the accelerating fields excited in the wake of the laser pulses over the long distances necessary for the efficient acceleration of electrons to high energies.

## 20.4 Conclusion

A set of diagnostics for monitoring plasma density and plasma wave amplitude with EuPRAXIA parameters can be designed from existing techniques. The final choice of diagnostics will depend on the choice of target: (i) gas cell or gas jet for the injector; and (ii) type of waveguide for the accelerator. A detailed implementation will depend on the compatibility with other components such as coupling and removal devices for the high-power laser beam, electron diagnostics or coupling, and transport components.

## 21 Electron Beam Diagnostics

### 21.1 Introduction

A plasma accelerator sets new and interesting challenges for every device, including diagnostic tools. While our investigation of electron beam diagnostics found reasonable solutions with state-of-the-art devices, we also focus on ongoing R&D to develop new diagnostics tailored to plasma accelerators.

The EuPRAXIA machine will produce electron beams with high brightness, accelerated by one or several plasma-accelerator stages. The inherent instability of plasma acceleration, observed in experiments in the past, lends itself to single-shot measurements. Additionally, diagnostics must measure beam transverse dimensions of the order of  $\mu\text{m}$  (RMS) and bunch lengths of the order of a few fs (FWHM), ideally with single-shot devices. This is not trivial and exceeds, in certain cases, the state of the art.

Different schemes can be foreseen to inject electron beams into the plasma booster stage, some including an RF accelerator. However, even the performance of this RF-based machine will be far from conventional, as the high accelerating gradient, the need to operate at very high frequencies (in the X-band range), requests to control the beam trajectory position / transverse size at the  $\mu\text{m}$  level and bunch lengths at the fs level set a very high standard for the diagnostics, even if multi-shot measurements were foreseen.

Finally, in a compact machine, all the components must be compact as well to avoid wasting space and increasing the overall machine length. This is reflected in a complete redesign and re-engineering of many existing devices, as described in this chapter.

### 21.2 Charge and Trajectory Measurements

One of the first questions in the commissioning of a new accelerator is the number of particles in the machine, i.e. the beam intensity. This fundamental property, which can be obtained by measuring the beam current (charge), is important for the beam transmission and for avoiding beam losses. For laser wakefield accelerators and particle wakefield accelerators, charges of a few pC have to be measured. Many technologies exist to measure such values.

Integrated current transformers (ICTs, [534]) measure the magnetic field of the beam using magnetic induction to effectively detect intensity variations. The measurement is linear, perfectly adapted for low charges and in line with the single-shot requirement. Additionally, charge can be determined in absolute terms. However, many studies reported that ICTs can overestimate the beam charge compared to a measurement based on imaging plates and scintillating screens [535,536]. The source of this discrepancy is mainly attributed to the electromagnetic pulse (EMP) from the laser-plasma interaction. However, a more recent investigation [537] presents a good correlation between an ICT and a Lanex screen. Authors explained this agreement with their particular focus on separating the EMP from the laser-plasma interaction, direct particle/radiation hits on the ICT, and low-energy electrons. A new generation of ICTs called Turbo-ICT, developed by Bergoz, can be a good choice to detect low charges (few pC) in a single bunch mode.

Faraday cups (FC) are another charge diagnostic. They use an absorber block (usually made of copper) to absorb the beam. The block is connected to the ground through an ammeter to measure the total charge deposited by the beam. Unlike ICTs, they intercept the beam and thus can only be installed at the end of the beamline. Especially in the commissioning phase, a Faraday cup will be very useful.

Beam alignment and intensity measurements are essential operations for particle accelerators and can be carried out with a beam position monitor (BPM) as a non-destructive element. For LWFA, because of beam shape fluctuations and beam instabilities, those devices must allow an extended detection area and be as insensitive as possible to the bunch profile. Several LWFA and PWFA accelerator experiments have used stripline BPMs [538]. These can offer a good resolution of tens of  $\mu\text{m}$  with a charge of a few pC. However, those devices are not very compact to be inserted into a plasma-accelerator beamline, where an increase by every centimetre leads to a growth of the machine length and a decrease in the effective accelerating gradient.

For LWFA and PWFA machines, a resolution of a few  $\mu\text{m}$  with a few pC is mandatory, and cavity BPMs show a better resolution than their stripline and button counterparts. For this reason, the choice of cavity BPM seems to be an interesting option for the beam position measurement. In the EuPRAXIA project, a re-entrant cavity BPM [539] can be a good choice in particular for the beam orbit measurement because of its mechanical simplicity and excellent resolution.

### 21.3 Transverse Size Measurement

Transverse diagnostics can perform two types of measurements: emittance and envelope. The envelope is very important to properly match the beam along the machine comparing the measured dimensions with the simulated ones. Usually, scintillator screens, like YAG:Ce or optical transition radiation (OTR) monitors, are in use for such a task. The LWFA community is also using Kodak Lanex fast and Gd<sub>2</sub>O<sub>2</sub>S:Tb screens [537]. YAG screens in particular are a must, when the beam charge is below a few tens of pC due to their better photon yield. OTR is a prompt surface effect proportional to the number of charges, while scintillator light is emitted isotropically, and the process involves the material bulk. In the latter case, there is a limit on the charge amount beyond which the emission is not linear anymore.

We plan to use scintillator screens, where the resolution and the saturation are not an issue. OTR screens will be employed to produce radiation useful for longitudinal diagnostics and wherever high-resolution conditions demand a different choice of screen other than scintillator-based ones.

### 21.4 Longitudinal Diagnostics

A bunch of electrons can only be successfully accelerated without a large energy spread by a plasma if the bunch length is much shorter than the plasma wavelength. Additionally, particular longitudinal shaping can be used in order to increase the transformer ratio in a beam-driven plasma accelerator. There are several techniques that can be fruitful to thus measure the bunch length and profile. Some of them are single shot, while others are not intercepting. Usually, a certain redundancy is needed in every machine; hence, it makes sense to use several different techniques.

#### Transverse Deflection Structures

Transverse deflection structures (TDS), often called RF deflectors, are RF cavities providing a time-dependent transverse force. The longitudinal distribution of an electron beam injected into such a structure is mapped onto the transverse dimension thanks to the transversely deflecting field. The transverse distribution of the beam can be measured using a screen placed downstream of the cavity. This device is

**Table 21.1.** Electron bunch parameters at different diagnostic points (DP1 to DP3) along the beamline, as defined in the main text. When the properties in x-y are different, the average value is given.

Parameter	DP1	DP2	DP3
Charge [pC]	30	30	30
Normalised RMS emittance [ $\mu\text{m}$ ]	0.44	0.46	0.5
RMS bunch length [fs]	10	7.5	16
Beam energy [MeV]	100	240	550
$\sigma_{x,y}$ [mm]	0.125	0.100	0.06
$\beta_{x,y}$ [m]	7	10	8

used for longitudinal diagnostics, such as bunch length measurements, longitudinal charge profile measurements, longitudinal phase-space measurements (in combination with a dipole spectrometer), slice emittance, and slice transverse phase-space reconstruction measurements (in combination with quadrupole scan techniques or a multi-screen lattice). The slice parameters that can be retrieved are relative to the plane perpendicular to the streaking direction of the RF field.

In Table 21.1, we report illustrative beam parameters at different energies obtained for some of the working points analysed in the design of the RF injector:

- DP1 (Diagnostic Point 1) is taken at the exit of the *SPARC-like* photo-injector (Sect. 14.3).
- DP2 (Diagnostic Point 2) is taken at the exit of the *ARES-like* photo-injector, considered for the hybrid compression scheme (Sect. 14.4).
- DP3 (Diagnostic Point 3) is taken at the exit of the X-band accelerator designed after the *SPARC-like* photo-injector (Sect. 12.3).

Those working points are not exhaustive but give an overview of typical electron beam parameters that we can expect at different locations of the accelerator considering the different RF designs that are discussed within EuPRAXIA. More challenging transverse parameters are expected at the plasma input, where a spot size on the order of a few  $\mu\text{m}$  RMS is required.

X-band TDS cavities are reliable tools that are currently being operated in many facilities worldwide [540,541] and have been proven to be capable of achieving sub-fs temporal resolution. In FEL facilities, RF deflectors can be placed after the undulators and thus allow for the reconstruction of the X-ray pulse profile [542,543]. Moreover, measurements of the longitudinal phase space of the electron bunch driver and witness in plasma wakefield accelerators have been planned in projects, such as FLASHForward [544] and SINBAD-ARES [317] at DESY. Such a use of this diagnostic could also be of potential interest for EuPRAXIA.

More recently, a new project [545] has been born thanks to the collaboration of three institutes – namely, DESY, CERN, and PSI – for the development of a novel type of TDS called PolariX TDS, having the potential of changing the streaking direction of the field [546]. The prototype of this novel cavity design is currently being characterised and tested [547] and, if successful, would open up opportunities for a more complete characterisation of the phase space of the beam. One possible application of such a technology would, for example, be the multi-shot reconstruction of the 3D charge density distribution of an electron bunch, which would be of extreme interest as a diagnostic tool for visualising the properties of the electron beam before the injection into the plasma [548,549]. This technology fits very well with a plasma-accelerator design, and we plan to use such a device in our project.

## COTR-Based Methods

The ability to produce ultra-short electron bunches in plasma acceleration opens yet another possibility of using coherent transition radiation (COTR) spectroscopy techniques in the infrared or even optical wavelength range, where well-established spectrum characterisation methods exist. Such schemes have already been demonstrated, even as single-shot diagnostics, in [550,551], where the CTR spectrum was directly measured using a far-infrared spectrometer based on a dispersive prism, or in [552], where a cascaded grating setup was used.

Another method based on coherent radiation uses Smith-Purcell radiation. This type of radiation occurs when a relativistic beam of charged particles passes near a metallic diffraction grating [553]. The phenomenon is described in detail in [554]. When the bunch is short enough, the radiation emitted will be coherent, and like in similar phenomena, it will encode the electron bunch length in the radiation pulse. Several experimental demonstrations have been performed [555–558]. Beams of a few hundred femtoseconds in duration have been characterised, and it is believed that shorter beams could be measured if suitable test facilities were found.

## 21.5 Time-of-Arrival Monitors

Measuring the beam arrival time is of great importance, especially in a facility that wants to drive an FEL, because it can supply crucial information for the beam-based feedback system. The best result in this field (with a resolution of a few fs) is achieved with beam-arrival monitors (BAMs) developed at DESY for XFEL; we refer mainly to this system reported in [559]. The BAM system is composed of three parts: the RF unit, the electro-optical unit (EOM), and the data acquisition (DAQ) system. In a BAM, the electromagnetic field induced by an electron bunch is captured by four broadband pickups. The electro-optical unit then combines the signals from the RF unit and a reference signal provided by an external source to perform the measurement. The result is finally stored in the DAQ system.

Another possible diagnostic tool for measuring the time of arrival is electro-optical sampling (EOS), a technique widely used to monitor electron bunch length [560–562]. It relies on the modification of the refractive index of a crystal, placed very close to the beamline, caused by the strong electric field co-propagating with the electron beam. The polarisation of a probe laser is rotated by the non-linearity induced in this crystal. Orthogonal polarisers are then placed before and after the crystal, so the probe laser signal is recorded only when there is a polarisation rotation, i.e. when there is an interaction with the beam. A decoding scheme transforms the measured polarisation rotation into the bunch profile.

By using as a probe laser the same laser source that arrives on the photo-cathode and produces the electron emission or an optically linked oscillator, there is a natural self-synchronisation between the laser and the electrons. In this way, the fluctuations in time, that are always measured in the readout are linked only to the beam jitter, and they are a direct measurement of the beam arrival time. A resolution of a few fs has already been demonstrated [563], highlighting the great feasibility of this monitor in measuring the time of arrival in different machine configurations and helping in optimising jitters and synchronisation.

## 21.6 Beam Loss Monitors

Beam loss monitors are very important in plasma acceleration. In the commissioning phase, for instance, the beam can easily be lost, and better knowledge of its fate

is of paramount importance to properly tune the plasma parameters. In brief, the principle of optical beam loss monitors (oBLMs) depends upon on-line measurements, taken along the whole beamline by optical fibres laid on or near the beam pipe. The detection of fast charged particles lost from the beam is by Cherenkov light emitted when an electron traverses a medium at speeds greater than that of light in the medium. Photons emitted within the critical angle will be totally internally reflected down the fibre and so are able to reach the end, where they are detected by a silicon photo-multiplier (SiPM) device.

## 21.7 Transverse Emittance Monitors

In a linac, there are several methods to measure the beam emittance, the main one being multiple screen measurements with a quadrupole scan [564]. This method is the most commonly used worldwide. Unfortunately, it is a multi-shot method, whereas we are more interested in single-shot measurements in the context of EuPRAXIA. While in the operational phase of the machine, a multi-shot technique may be feasible, during the commissioning of a plasma accelerator, single-shot techniques are needed. However, so far, there is a lack of this kind of technique for emittance measurements. To fill this gap, the EuPRAXIA collaboration is developing and investigating possible new instrumentation methods, brief descriptions of which are presented in the following.

### High-Energy Pepper Pot

The low-energy limitation of the pepper-pot technique comes from the penetration depth of high-energy particles in matter. In recent years, it has been proposed to use pepper pots at several hundreds of MeV in energy [565]. Several experiments have confirmed the validity of this approach at energies up to 3 GeV [566], and higher energies could be considered with a suitable test beam. Of course, an accurate analysis of the angular acceptance of the device must be carried out depending on the beam energy and transverse beam parameters. It should be noted that thick masks can cut the phase space, resulting in an underestimation of the beam emittance.

### Multiscreen OTR Measurement

The beam transverse emittance can also be measured by inserting quasi-non-destructive screens at several locations. These screens can measure the beam envelope at different positions in a single shot, from which the transverse emittance can be deduced. The method has been demonstrated experimentally [567] at 3 GeV, and there is no upper limitation on the energy that could be reached. On the other hand, for lower energies, multiple scattering will be a limiting factor. Also, in order to have enough betatron phase advance for the measurement, a large distance between screens is needed.

### Multiscreen OTR Measurement with Active Plasma Lens

The simultaneous measurement of beam size on different screens in the same shot, described in the section above, is very attractive. However, as with all the other diagnostics in a plasma accelerator, it must be very compact, occupying the smallest possible space in the beamline. Conventional quadrupoles have focal lengths on the order of metres and this results in screens placed at roughly this distance. Plasma

lenses [38,305] have regained significant interest in recent years because they are able to focus in both planes at the same time with a strength at least one order of magnitude better than permanent quadrupoles. A recent study [568] demonstrated the possibility to use a plasma lens without appreciable emittance dilution. Additionally, the focal length of these devices can be tuned with the current and can be on the order of a few centimetres. This fact paves the way to replace conventional quadrupoles with plasma lenses in multi-screen measurements.

The main advantage of this setup is the extreme compactness. The screens can be very thin (about 1  $\mu\text{m}$ ), and they can be used in the same shot, realising a single-shot emittance measurement. However, further investigations are needed to better validate the working principle of plasma lenses, to study their chromatic aberration – which will, in any case, be less important than in a conventional quadrupole – and side effects, such as beam misalignment, plasma density fluctuations, and so on.

### Permanent Quad Scan

In a conventional quadscan, the current of the quadrupoles is varied. In a multi-screen setup, on the other hand, the position of the measurement is varied by using different screens. If we consider a beam with high energy spread (more than 1%) and we use permanent quadrupoles with a dipole, we can focus the beam in different transverse positions after the dipole, corresponding to different energies and different parts of the beam. With the beam dimension depending on the quads' focal length and this focal length depending on the beam energy, we find that particles at different energies are focussed with different spot sizes. In this way, we do not need to change the focal length of the quads or the position of the measurement, but the inherent energy spread already produces different beam sizes at the same measurement position.

This method was first introduced a few years ago [569] and later successfully implemented by several groups [570,571]. We consider using this method in the commissioning phase of the plasma injector because in this scenario, with an energy spread likely on the order of 1% or worse, this system can offer a single-shot emittance measurement. As the technique is already implemented by several other groups, we can also benefit from their experience. However, with the goal of the whole project being the production of a high-quality electron beam with reduced energy spread with respect to these mentioned values, we do not plan to reserve room in the final accelerator for this scheme.

### Measurements Using Cherenkov Radiation

Recently, a breakthrough paper has been published [572] about the use of Cherenkov radiation as a non-intercepting monitor for beam size measurements. A high-purity fused silica slab is placed along the beamline at a mm-range distance to the electron beam. The electromagnetic field, co-propagating with the electron bunch, interacts with the crystal and produces Cherenkov radiation. By observing the crystal from above, it is possible to see a bright line, the thickness of which corresponds to the electron beam size.

The ultimate resolution of this system is still unknown because so far, there exists no analytic expression for the spread point function yet. A beam size of about 70  $\mu\text{m}$  has been measured and positively cross-checked with other methods. One of the crucial points to further investigate is a possible dependence between resolution and beam energy.

## Measurements Using Betatron Radiation

Measurements inside the plasma cell can be performed by making use of the betatron radiation generated during the acceleration process (see Sect. 24.2 for more details on betatron radiation). Diagnostics based on betatron radiation [573] have been developed in recent years in several laboratories, relying on the measurement of the radiation spectrum (see for instance [574]) or on the diffraction of the radiation from a knife edge [575].

However, these systems were able to measure just the beam profile and divergence, neglecting the correlation term. Only recently, a new algorithm has been developed to retrieve the correlation term [576]. Using the simultaneous measurement of the electron and radiation energy spectrum together with the plasma density, it is possible to reconstruct the whole phase space.

To collect the betatron radiation, we have to, sooner or later, separate the radiation from the electron beam with a dipole. Unfortunately, the bending of the beam produces synchrotron radiation, and its spectrum can overlap with the betatron photons. Usually, the betatron radiation is much stronger than the synchrotron radiation though, and there is an additional degree of freedom from the bending angle. The possibility to increase the magnetic field also allows to move the peak of the synchrotron radiation to a higher frequency, resulting in a better separation from the betatron radiation. However, an open problem remains with the separation between the betatron radiation coming from the witness beam and that from the driver in a beam-driven plasma acceleration scheme. In this case, the driver contains much more charge with respect to the witness, and so only a clear energy separation of the two spectra can solve the problem. In the case of laser-driven plasma acceleration, this problem obviously disappears.

### 21.8 Accelerator Diagnostics Layout Before the Plasma-Accelerator Stage (Plasma Booster)

Laser Plasma Injector (LPI, relevant for Scheme 2: LPI-150 MeV + LPAS-5 GeV)

Before the installation of the plasma booster, temporary diagnostics will be placed after the LPI, as seen in Figure 21.1.

A driver exclusion and removal zone is foreseen to almost completely remove the laser and to protect the following instrumentation. The length and the schemes employed in this removal section are outside the scope of this chapter and will be defined as part of the technical design.

The beamline is schematically shown in Figure 21.1. A triplet of permanent quads will follow the exclusion region. They can be used both to capture the beam for the following diagnostics and to allow for a single-shot emittance measurement following the scheme in Section 21.7 by using the downstream dipole and the screen on the dogleg.

After the triplet, a view screen will be placed, including the possibility to host an EOS station. EOS will be used as a time-of-arrival monitor, while the view screen allows the measurement of the beam envelope. A couple of cavity BPMs are needed to properly measure the beam trajectory, while a Faraday cup at the end of the line will give us a measurement of the total charge. Two electromagnetic quadrupoles will be used to properly adjust the optics, providing also the possibility of a multi-shot measurement with a quadrupole scan. A pepper-pot station will be implemented as well to have the possibility to perform single-shot high-energy emittance measurements. The bunch length can be evaluated in the range down to 50 fs by means of

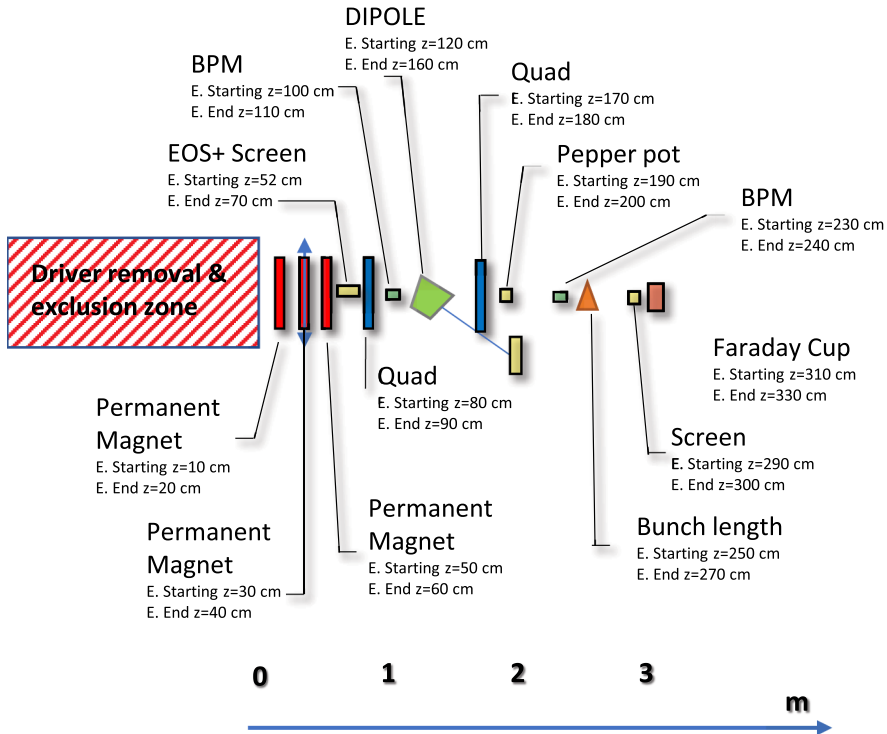


**Fig. 21.1.** Temporary beamline for the electron diagnostics after the LPI.

EOS, while for shorter bunches, a longitudinal single-shot coherent radiation-based measurement setup or a Smith-Purcell device can be located in the chamber placed 2.5 m behind the beginning of the beamline. The overall length of this line is not a critical point because it will be removed later. However, the need to have several different diagnostics to cover a large range of beam parameters as well as the requirement to easily move the setup downstream later prevents us from building a longer beamline.

Eventually, a second stage for plasma acceleration will be placed behind the plasma injector. In the space between the LPI and the LPAS and after the laser mirror, a dedicated and permanent beamline will be placed. This line must contain not only the diagnostics setup but also the permanent capture optics for the electron beam. A conceptual layout is thus shown in Figure 21.2.

The triplet of permanent quads shown in Figure 21.2 can be one of the two already foreseen for the capture optics. However, the distance between two quads must, in this case, be increased to at least 1 m, which should not be a critical issue as the gradient of the permanent quadrupole design can be adjusted accordingly. Even further in the future, when active plasma lenses [38,305] will be routinely used in operational machines and even higher gradients will be available, longer spacing between magnetic elements should not be a critical issue anymore. It should be noted that in our layout, the driver removal zone is considered prohibited for the diagnostics. Behind this region, a couple of cavity BPMs will track the orbits, while an ICT will measure the charge bunch by bunch. A permanent but removable dipole can be inserted to drive the beam into a spectrometer arm to measure its energy and energy spread. Furthermore, view screens can be used to image the beam and check the envelope for proper beam matching in the section following the diagnostics.

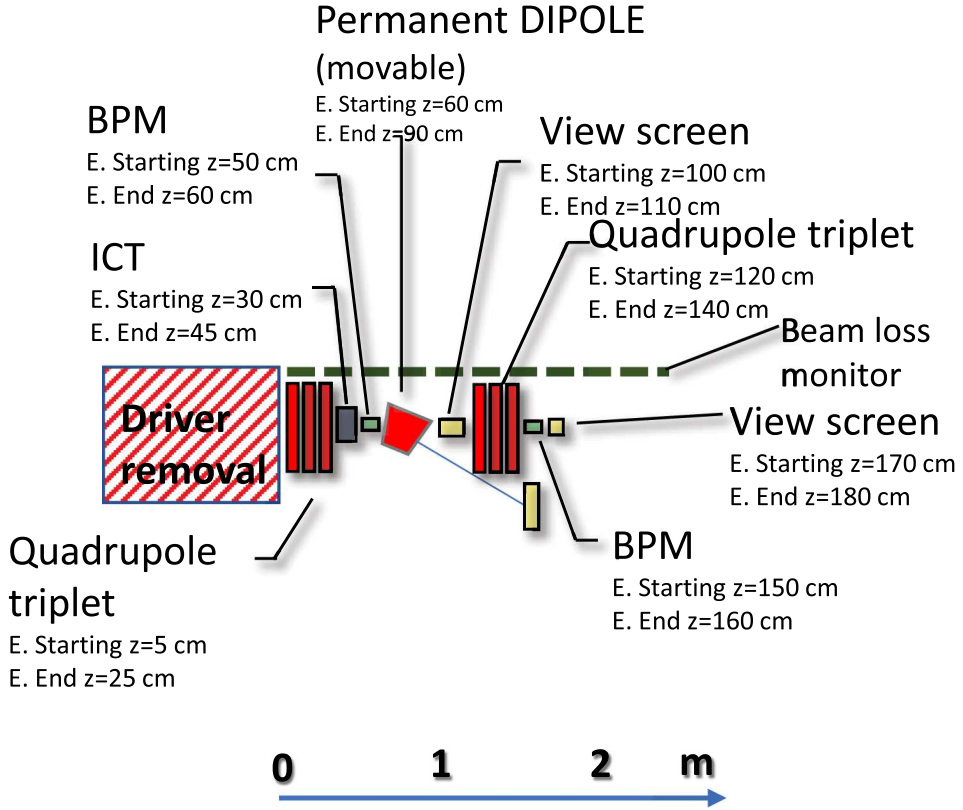


**Fig. 21.2.** Layout of the permanent beamline for electron diagnostics between the LPI and LPAS.

In one of the dedicated positions, a bunch length measurement setup by means of COTR will also be placed. A beam loss monitor will be located around the beamline to measure beam losses and help in aligning the beam.

RF Injector (relevant for Schemes 3 to 5)

The RF injector, even if it will be built using emerging technologies like X-band structures, is a conventional machine from the point of view of diagnostics. However, there are two main issues: orbit control and 6D phase-space control at the plasma injection point, where the bunch size will be on the  $\mu\text{m}$  level and the bunch length in the few fs range. We consider two possible approaches to the RF injector using the designs developed in two projects of the collaboration partners INFN and DESY (EuPRAXIA@SPARC\_LAB and SINBAD-ARES, respectively).

In EuPRAXIA@SPARC\_LAB, the linac is realised with an S-band injector, followed by a X-band linac, equivalent to the proposed design in Chapter 12. The conceptual layout of the injector diagnostics is shown in Figure 21.5.

Stripline or button BPMs are inserted before and after every S-band structure, while an ICT will measure the bunch charge. The layout of part of the linac is shown in Figure 21.6.

The rest of the linac, about a factor of 2 longer, will be a repetition of this structure. After a section with a TDS and a dipole for single-shot longitudinal phase-space

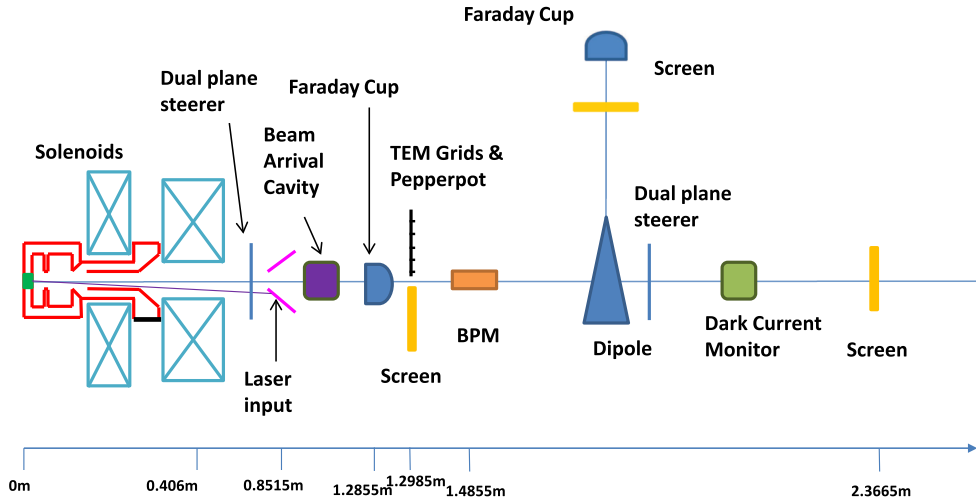


Fig. 21.3. Layout of the diagnostics in the electron gun section of SINBAD-ARES.

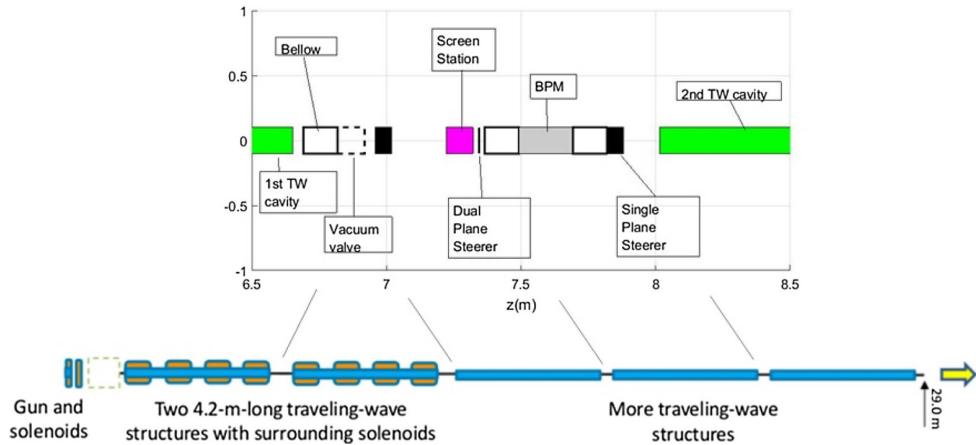


Fig. 21.4. Layout of the diagnostics in the linac section of ARES.

measurements, there are cavity BPMs (CBPMs) placed after every two accelerating structures and view screens after every four. High-resolution OTR monitors will be implemented before the plasma channel. Critical measurements, like emittance or bunch length, will be carried out with diagnostics placed after the plasma, while turning the plasma off. They will thus be discussed in the next chapter.

The gun area in the ARES-like linac (equivalent to the described design in Sect. 14.4) is shown in Figure 21.3.

The diagnostics setup in this region is standard with BPMs, view screens, a pepper pot for emittance measurements, a spectrometer, a BAM monitor, and a Faraday cup, with the latter also useful as a beam dump.

In the linac section, a 1.36 m long empty space is available between every two accelerating modules. A view screen and a BPM can be placed in these positions. Moreover, one toroid for charge measurement can be placed additionally between the second and third RF cavities of the linac.

The linac is followed by a matching and collimation section to prepare the beam for entering the plasma-accelerator stage. Between these two sections, a spectrometer

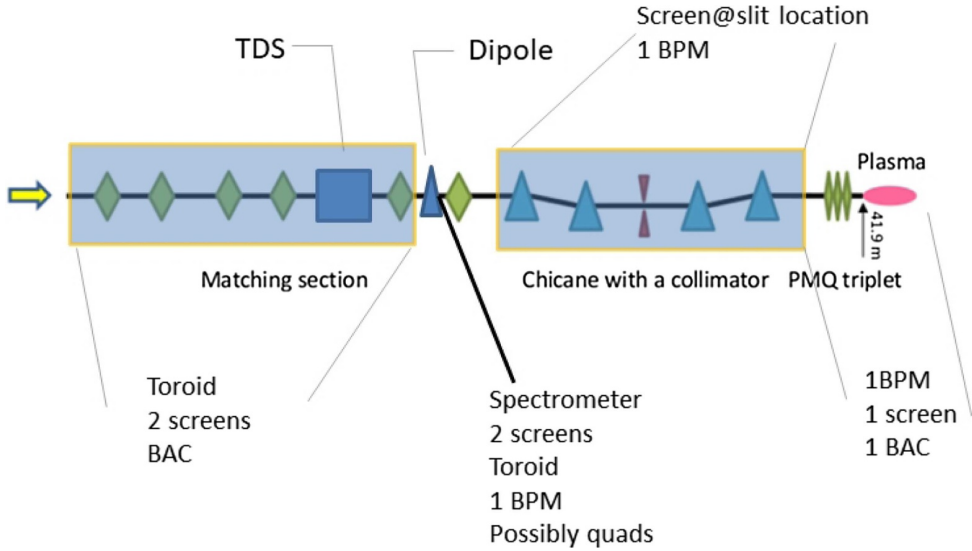


**Fig. 21.5.** Layout of the diagnostics for the RF injector at EuPRAXIA@SPARC\_LAB.

is placed in the following configuration: a dipole is followed by one BPM, two view screens, and a toroid for charge measurement. The presence of a TDS in the matching section can further allow the measurement of the full longitudinal phase space in single-shot mode. In the matching section, a toroid, two BPMs, a beam arrival time monitor, and a view screen will be placed. Additionally, it is foreseen to include a view screen and a BPM in the middle part of the magnetic bunch compressor. After the bunch compressor, if allowed by space constraints, we foresee one additional BPM and / or a view screen as well as a beam arrival time cavity.

### 21.9 Accelerator Diagnostics Layout After the Plasma-Accelerator Stage (LPAS / PPAS, relevant for Schemes 1 to 6)

After the plasma booster and the driver removal, a diagnostics section is needed to fully characterise the 6D beam phase space and to properly match the beam to the undulator or other applications. As we pointed out previously, there exist so far some examples of single-shot longitudinal phase-space measurements that can be considered almost state of the art. However, only few experiments were already carried out on the topic of single-shot transverse emittance measurements. Hence, in this beamline, we consider the use of not only novel techniques under development but also well-established, multi-shot approaches to the emittance measurement. We will use only betatron radiation to characterise the emittance at the plasma exit, while we plan to measure the emittance and the Twiss parameters of the beam before its entrance into the undulator. This choice arises from the need to capture the beam emerging from the plasma as soon as possible, thus avoiding emittance dilution [577].

One of the fundamental requirements of the diagnostics layout must be the compatibility with the capture optics. A couple of permanent quadrupoles will be followed by several electromagnetic quadrupoles. To avoid wasting space and to keep the machine as compact as possible, we tailored our diagnostics following this layout, as can be seen in the diagnostics sketch in Figure 21.8.

A beam loss monitor will be placed around the system along the full length of this section to measure any beam losses. An ICT will check the charge of the bunch

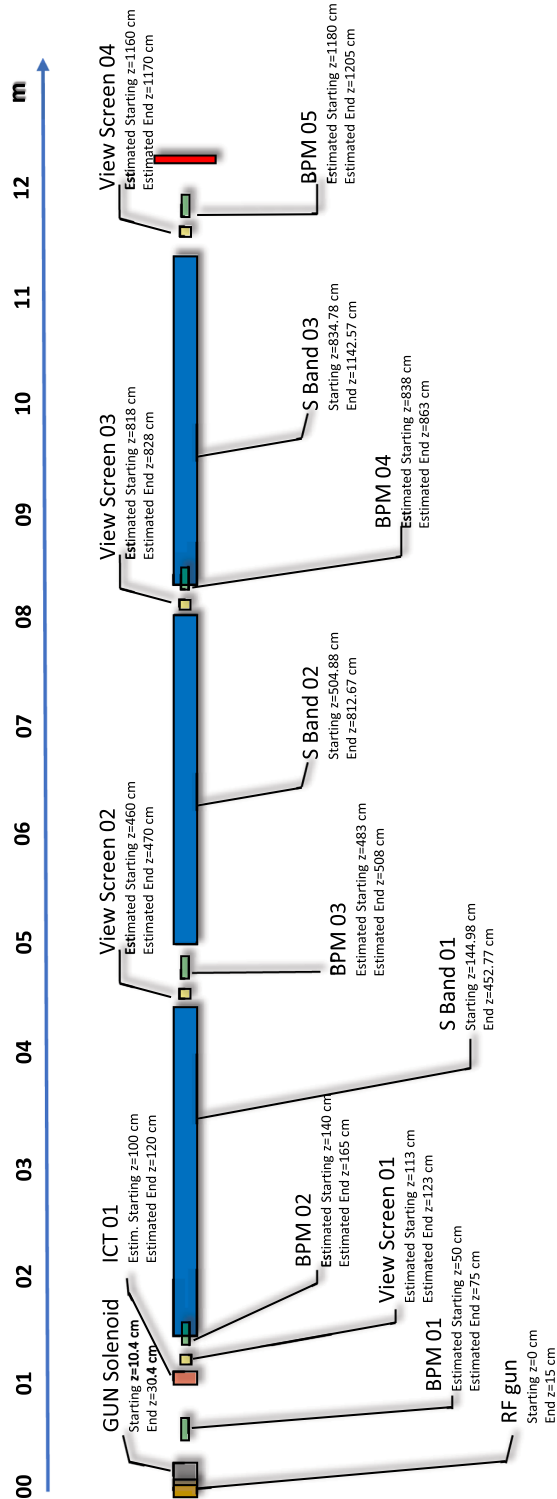


Fig. 21.6. Layout of the diagnostics for a section of the linac at EuPRAXIA@SPARC\_LAB.

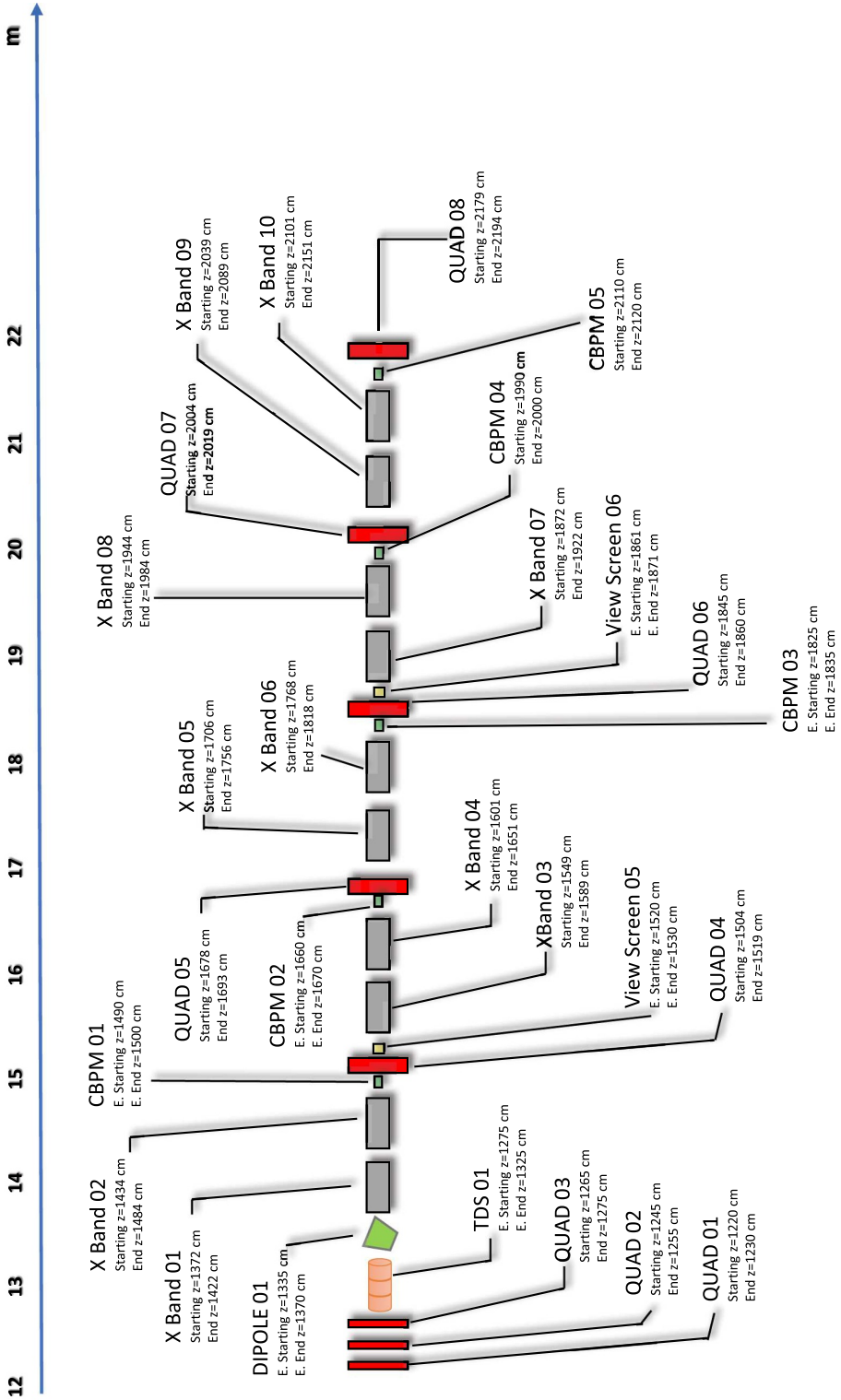
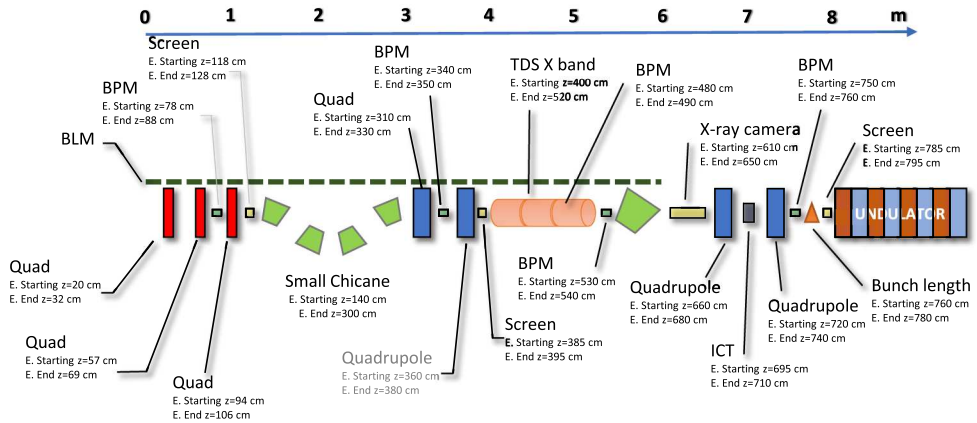


Fig. 21.7. Layout of the diagnostics in the beam-matching section of SINBAD-ARES.



**Fig. 21.8.** Layout of the matching optics and diagnostics setup behind the plasma booster.

emerging from the plasma interaction. Along the beamline, there are also view screens and cavity BPMs foreseen. Additionally, an X-band TDS can be placed here during the commissioning and later, during operation, moved behind the undulator chain. This setup is followed by a spectrometer to measure the energy, energy spread, and longitudinal phase space. A separate station to measure the longitudinal profile also in parasitic mode will be placed after the dipole in the main line. To collect and analyse betatron radiation to measure the transverse phase space at the plasma exit, we need to place a chamber with an X-ray camera and a proper set of filters and attenuators into the beamline. This chamber should be transversally very wide so that the camera can be moved onto the beamline only for this kind of phase-space measurement and only with the dipole in operation. Until the new methods will be ready to be implemented, it is planned to measure the emittance using a multi-shot method with a quadrupole scan (where one of the available quads in the line can be employed).

## 21.10 Conclusion

We have made an extensive survey of the tools available to measure the beams to be produced at EuPRAXIA. We identified diagnostics to measure the bunch charge, the bunch position, the transverse envelope, the transverse emittance, and the longitudinal profile. We also identified means of measuring the bunch arrival time and beam losses along the accelerator. Following this survey, we concluded that the existing diagnostics are sufficient for basic beam measurements. However we also found that for some advanced measurements, especially single shot (e.g. transverse emittance and longitudinal profile), significant additional R&D is still needed.

We also investigated how these diagnostics could be used at EuPRAXIA, and we produced conceptual designs of the main beamlines. This required iterative work with the beam transport group, and in most cases, we succeeded in finding a suitable layout. In some cases, it was found that the design of individual diagnostics should be made more compact, a task to be completed as part of the technical design.

Overall, at this conceptual stage, we find that from a diagnostics point of view, we are ready to build EuPRAXIA, although additional research on some diagnostics in the future will allow better performances.

**Table 22.1.** Parameters of the electron beam hitting the beam dump.

		EuPRAXIA	Beam Dump Beam Dump	Beam Dump Beam Dump
Nominal electron energy [GeV]	$E_0$	1–5	5.8	3.4
Nominal charge per bunch [pC]	$N_e$	30	200	200
Repetition rate [Hz]		100	100	100
Maximum no. of bunches per RF pulse		1	1	1
Average beam power [W]	$P_{ave}$	3–15	116	68

## 22 Electron Beam Dump

### 22.1 Introduction

The electron beam dump is one of the most important components for any particle accelerator facility to absorb or dispose beam kinetic energy in a safe way. Expertise from similar existing machines can be used when looking at a conventional design of the electron beam dump [158] with the basic concept and functions of a beam dump summarised as follows [578]:

- to disperse the beam by magnets in front of the beam entry, i.e. decreasing the power density by means of beam defocussing / spreading;
- to stop the beam part by part in a spatially separated block, i.e. reducing the power deposition in small regions of the beam dump, for example by designing the absorber with a decreasing transverse cross-section diameter to deposit the beam energy in subsequent steps; and
- to minimise the induction of radioactivity, i.e. eliminating the use of water to stop the beam. The electron beam parameters to be taken into account are reported in Table 22.1, together with values related to the SwissFEL beam dumps. With similar requirements, these can be taken as examples, although overestimated, for the EuPRAXIA case, thus showing clearly that conventional solutions for the beam dump design exist. While first estimates and considerations are discussed below, the development of a specific design of beam dumps for EuPRAXIA will be carried out as part of the technical machine design.

Besides the conventional systems, an innovative proposal based on a plasma beam dump is also reported here. This will be considered as a complementary option to conventional solutions and could possibly, depending on further prototyping and test experiments, be implemented as a future upgrade of the facility.

### 22.2 The SwissFEL Beam Dumps, Aramis and Athos

At the end of each undulator line, a permanent beam dump is foreseen by means of which the beam is deflected for a few degrees towards the ground and stopped in a copper block. To shield against produced secondary radiation, the core block is surrounded by layers of iron and heavy concrete. The setup scheme adapted from the SwissFEL CDR [158] is shown in Figure 22.1.

According to the SwissFEL operation modes, the full electron beam is dumped in two beam dumps. During the beam tuning, a smaller fraction of the beam is stopped in the beam stopper to protect the undulator magnets. There is also one stopper for each beamline. For a conservative estimate of the residual activation, the beam energy has been set to 7 GeV and the beam power to 560 W for the beam dump and 14 W for the beam stopper (Aramis line case). Like at SLS, a 30 % downtime of the

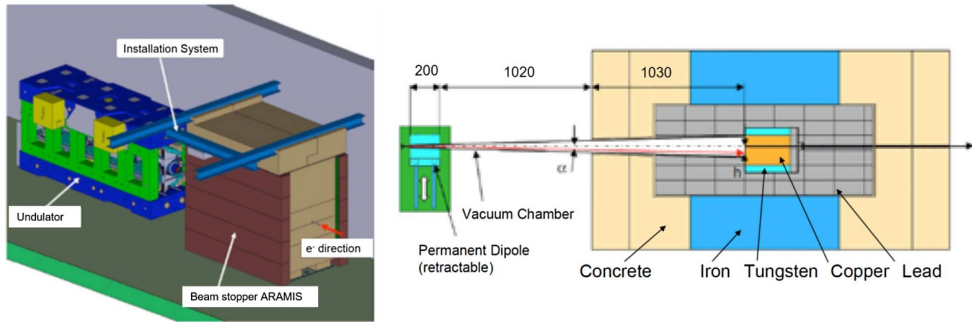


**Fig. 22.1.** SwissFEL Aramis beam stopper in front of the first undulator (left). A dipole magnet is inserted in the beamline to deflect the electrons on a copper target surrounded by shielding materials (right) (image credits: [158]).

facility has been assumed, which is used as the downtime for the beam dump. The calculation of the residual dose rates has been carried out with FLUKA based on the design of the beam dump and stopper. The layout used for the beam dump consists of a cylindrical carbon core surrounded by iron. The outer layer consists of normal concrete. At the very front, a small layer of PE suppresses low-energetic neutrons to protect electronic devices for diagnostics. From the calculations, the dose rates after 1 day on the outer sides of the beam dump are of the order of a few  $\mu\text{Sv h}^{-1}$  and therefore acceptable for a controlled zone. The beam stopper has a copper core of 20 cm thickness followed by 10 cm of tungsten, which can be moved in and out of the beam. It is surrounded by steel and finally normal concrete of about half a metre on each side. With this design, the residual dose rates should be low after 1 h of beam-off.

As a corollary, the nuclide inventory also needs to be calculated for every material block in view of the disposal after the operation shutdown to estimate the time to wait before dismantling the beam dump and the beam stopper. The residual activation and resulting dose rates should also be considered for the safety requirements during deconstruction.

### 22.3 The Plasma Beam Dump

Since a conventional beam dump can affect the overall compactness of a machine, such as EuPRAXIA, aiming for a small footprint, an alternative design is proposed with the implementation of a plasma target to absorb the kinetic energy of the EuPRAXIA electron beams. Such a setup would improve the overall compactness of the facility and generate less radioactivity. In this section, some simulation results of a plasma beam dump based on EuPRAXIA beam parameters are briefly described.

The development of laser-plasma-based compact high-quality electron accelerators have already attracted tremendous interest worldwide. The initial idea was proposed by Tajima and Dawson 40 years ago [4]. The basic principle behind this is to inject a beam of electrons behind the driver pulse to achieve an extremely high acceleration gradient, usually three orders of magnitude higher than the field in conventional accelerators. Nowadays, an electron beam of several GeV energy can be routinely generated in laser wakefield accelerators within centimetre-long plasma targets by using petawatt laser drivers [9,290].

On the other hand, the use of plasma wakefields for the compact deceleration of relativistic beams has not been fully explored yet. In 2010, Wu et al. proposed

the collective deceleration of electron beams in plasma for the first time [579]. The idea is to utilise the large decelerating wakefields, with amplitudes as high as those of the accelerating fields, to absorb the beam energy as fast as possible. This would allow beam deceleration to be achieved in a short distance if compared to equivalent conventional beam dumps. Moreover, it could help to mitigate the requirements of conventional beam dumps, which often suffer from complicated designs and large sizes (and costs), when the beam power is high. Moreover, the use of a low-density plasma greatly reduces radio-activation hazards if compared to conventional beam dumps, in which energetic particles interact with dense media, such as metals, graphite, or water, causing nuclear reactions and the production of secondary particles.

### 22.3.1 Simulation Study of a Plasma Beam Dump

Generally speaking, there are two types of plasma beam dumps: the so-called passive plasma beam dump (PPBD) and the active plasma beam dump (APBD) [580]. For the PPBD, a relativistic particle bunch propagates in a uniform plasma and excites its own wakefield. As a consequence, the head of the bunch will experience no decelerating field due to the finite response time of the plasma, while particles closer to the bunch tail will experience a decelerating field. After some time, the fraction of the bunch experiencing the maximum decelerating field will become non-relativistic, and it will fall behind the rest of the bunch until it reaches an accelerating phase of the wakefield. This causes beam re-acceleration, which leads to the saturation of the beam net energy loss [581]. On the other hand, in the APBD, this drawback is eliminated in the following way. A laser pulse is employed to excite a wakefield in the plasma prior to beam propagation in such a way that the combination of both laser-driven and beam-driven wakefields flattens the decelerating field along the bunch. This enables a uniform energy extraction, thus preventing the formation of re-acceleration peaks. Although the energy extraction is more efficient in the APBD, the need for a laser pulse and the precise synchronisation required between this laser and the beam causes this scheme to be far more complex to be experimentally implemented than the PPBD.

### 22.3.2 Passive Beam Dump for EuPRAXIA

To simplify the design, we propose to use a passive beam dump system for the EuPRAXIA facility. We aim to absorb most of the energy from most of the particles in the bunch by tailoring the plasma density profile. Typical EuPRAXIA beam parameters were used in our studies, as follows [582]: beam energy of 1 GeV, bunch charge of 30 pC, transverse beam size of 1.4  $\mu\text{m}$ , longitudinal bunch length of 2  $\mu\text{m}$ , beam energy spread of 1%, and angular divergence of  $1 \times 10^{-5}$ . This corresponds to a beam density of  $3 \times 10^{18} \text{ cm}^{-3}$ . The 2D particle-in-cell code EPOCH is used to perform simulations of beam-plasma interaction [583]. As a first step, we choose the plasma density of  $4.4 \times 10^{17} \text{ cm}^{-3}$  so that the wakefield excited is in the quasi-linear to non-linear regime. The results show that the particles lose their energy very fast. After about 8 cm in plasma, the particles at the tail of the bunch lose most of their energy and reach energy loss saturation. As a result, the bunch length increases during the energy dump. If the bunch continues to propagate further in the plasma, the particles at the tail of the bunch will reach the acceleration phase of the wakefield and start to absorb energy again.

Figure 22.2 shows the beam longitudinal phase space after propagating 8.5 cm in plasma. It can be seen clearly that the beam energy at the head of the bunch does not

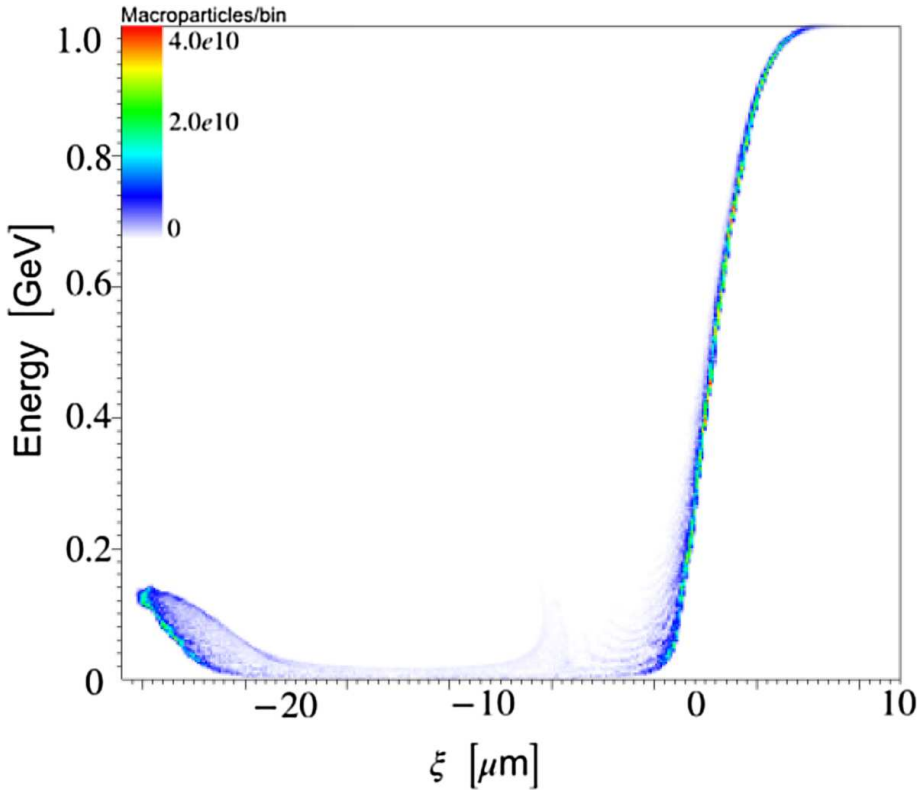


**Fig. 22.2.** Beam longitudinal phase space after 8.5 cm in plasma.

change, while the particles at the tail start to gain energy. To eliminate the particles gaining energy from the wakefield, the plasma density is tuned just before energy loss saturation occurs. In doing so, the low-energy particles at the bunch tail will move to the defocussing phase of the wakefield, being ejected by the transverse wakefield. Figure 22.3 shows a typical plasma density profile in which the density starts to increase quadratically at about 7.5 cm and reaches a value 10 times higher than the initial density of  $n_0 = 4.4 \times 10^{17} \text{ cm}^{-3}$ . As a comparison, the beam longitudinal phase space after 21 cm in the plasma is shown in Figure 22.4. It is found that the re-acceleration peak (as shown in Fig. 22.2) is removed and particles continue to lose their energy in the plasma.

Figure 22.5 provides the beam energy as a function of propagation distance in the plasma for the plasma density profile shown in Figure 22.3. The results demonstrate that the total beam energy is reduced to 12% of its initial energy. Almost 80% of the beam's initial energy is deposited in the plasma, and only approximately 10% of the initial beam energy is transversely ejected. This plasma density tailoring scheme will guarantee a relatively low beam energy deposited in the plasma vessel, ensuring a safe operation of the plasma beam dump.

## 22.4 Conclusions

The study shown here demonstrates the viability of the PPBD for the EuPRAXIA 1 GeV beam. It shows that a 21 cm plasma with a density ramp can absorb most of the total beam energy ( $\approx 80\%$ ) through the passive beam dump scheme. The PPBD

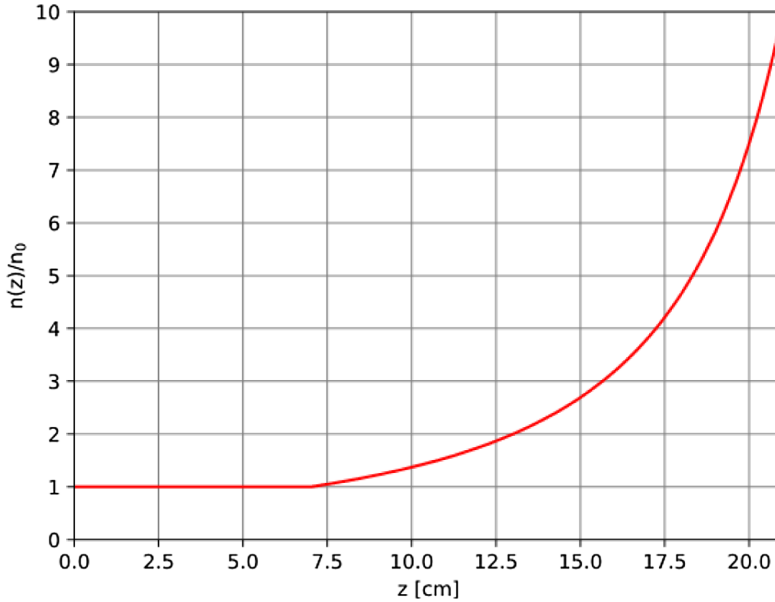


**Fig. 22.3.** Density profile used to eliminate the re-acceleration of particles in the bunch tail.

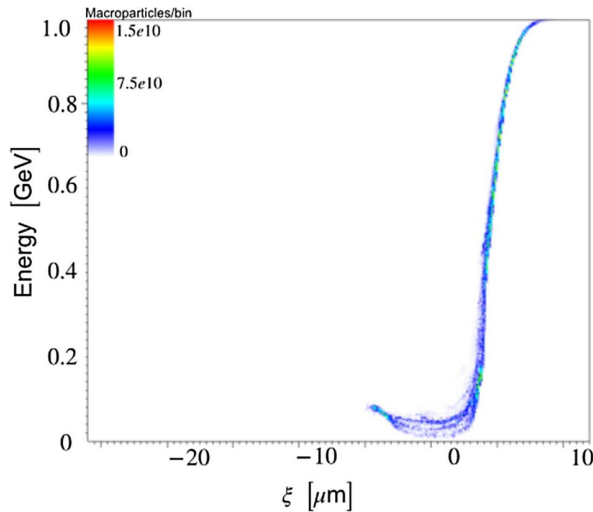


**Fig. 22.4.** Beam longitudinal phase space after 21 cm in plasma. The plasma density exhibits quadratic growth starting from  $z = 7.5$  cm and reaches a value 10 times higher at  $z = 21.0$  cm, compared to initial plasma density.

set up can make the overall facility compact and less radioactive. On the other hand, we have not discussed the APBD scheme here given its complexity. However, if an active beam dump could be used for the EuPRAXIA machine, where a laser pulse can drive the plasma wakefield for beam deceleration, in principle, almost 100% of the beam energy could be absorbed inside the plasma dump. In addition, recent experiments performed at Rutherford Appleton Laboratory (RAL) on multiple laser pulses driving a plasma wakefield have shown the possibility of energy recovery by the trailing laser pulse picking up energy from the plasma [584]. All these possibilities

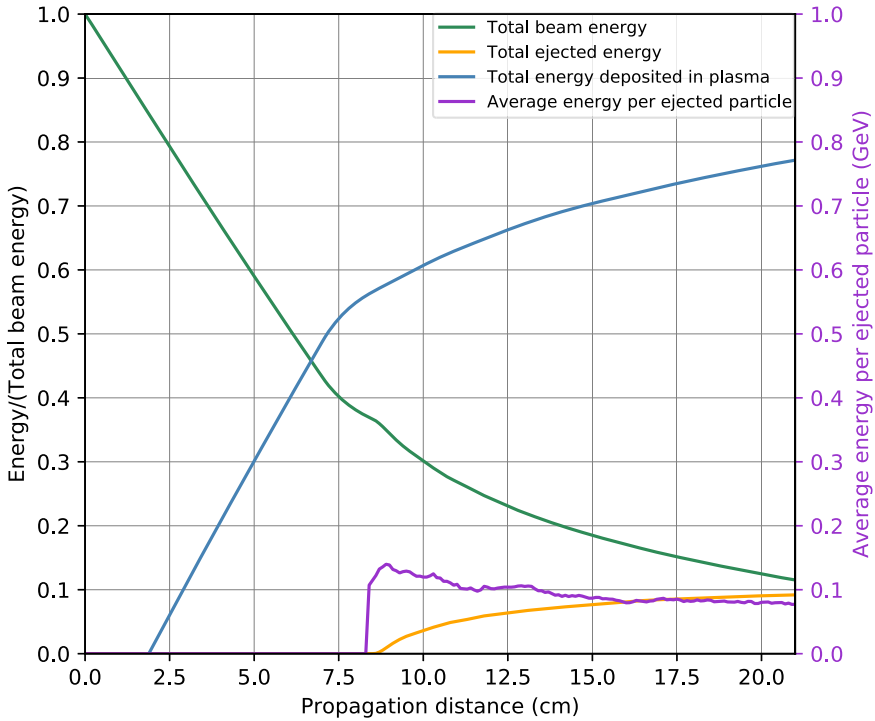


**Fig. 22.5.** Energy as a function of propagation distance in plasma, for the plasma density profile shown in Figure 22.3.

could pave the way for a future very compact and green beam dump facility and will be investigated further as part of the technical design.

## 23 Start-to-End Simulations of the Accelerator

### 23.1 General Aspects

The continuous progress in plasma-based acceleration would suggest that the era of plasma-based accelerators is approaching. However, from plasma acceleration as a physics experiment towards accelerators as part of a facility delivering beams to user communities, important challenges remain to be solved. The advanced components of such a plasma accelerator, in particular the plasma and laser systems, need to be designed and constructed in a way to ensure reproducibility and reliability beyond the start of the art. On the user end of the accelerator, the machine must be capable of providing high beam energy, high charge, and exceptional beam quality for a variety of applications and user experiments. Table 23.1 summarises the main requirements that were defined for the EuPRAXIA design based on the needs of foreseen applications and expected technological developments. They are provided for three different points along the machine: the electron beam at the exit of the injector, which can be either (1) a laser-plasma injector or (2) a radiofrequency (RF) injector; and (3) at the accelerator exit just before the application beamlines. We can see that these beam characteristics, suitable for a highly demanding application such as a free-electron laser, are particularly challenging as they require simultaneously a high final beam energy of 5 GeV (with a commissioning step at 1 GeV), a high charge of 30 pC in a

**Table 23.1.** Main requirements for the electron beam at the exit of the injector, which can be either a laser-plasma (LP) injector or a radiofrequency (RF) injector, and at the accelerator exit, which means at the user applications.  $E$ ,  $Q$ ,  $\tau$ (FWHM),  $\sigma_E/E$ ,  $\sigma_{E,s}/E$ ,  $\varepsilon_n$ , and  $\varepsilon_{n,s}$  stand, respectively, for beam energy, charge, length (full width at half maximum), energy spread, slice energy spread, normalised phase-space emittance, and slice normalised phase-space emittance. Note that slice values are driven by application requirements and are therefore only defined at the accelerator exit.

Parameter	LP Injector Exit	RF Injector Exit	Accelerator Exit
$E$	150 MeV	250–500 MeV	5 GeV (1 GeV)
$Q$	30 pC	30 pC	30 pC
$\tau$ (FWHM)	10 fs	10 fs	10 fs
$\sigma_E/E$	5%	0.2%	1%
$\sigma_{E,s}/E$	N/A	N/A	0.1%
$\varepsilon_n$	1 mm mrad	1 mm mrad	1 mm mrad
$\varepsilon_{n,s}$	N/A	N/A	1 mm mrad

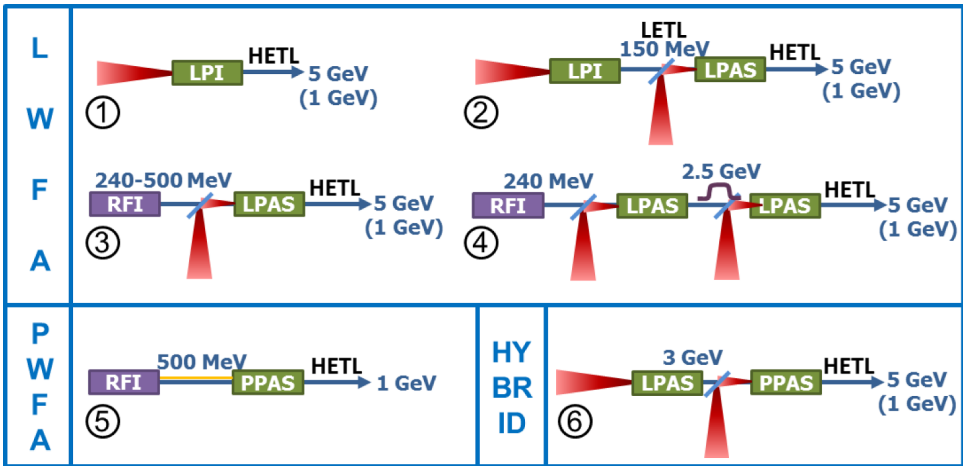


**Fig. 23.1.** The accelerator schemes under investigation. Schemes 1 to 4 are based on laser-driven wakefield acceleration where the laser beam is represented in red. Scheme 5 is based on beam-driven wakefield acceleration. Scheme 6 is a hybrid configuration mixing laser-driven and beam-driven acceleration. RFI stands for radiofrequency injector, LPI for laser-driven plasma injector, PPI for beam-driven plasma injector, LPAS for laser-driven plasma acceleration stage, and PPAS for particle-driven plasma acceleration stage. The energy at the different stages is also given [171].

short length of 10 fs (i.e. producing a high peak current of 3 kA), a low emittance of  $\leq 1$  mm mrad, a low energy spread of  $\leq 1\%$ , and an even lower slice energy spread of 0.1%.

In order to meet those challenging requirements, it was decided to explore broadly various plasma injection and acceleration schemes in order to down-select subsequently. This necessary but long procedure is only feasible thanks to the many contributors of the EuPRAXIA collaboration.

The main schemes under investigation are sketched in Figure 23.1, where the final beam energy is also indicated at each stage exit. Schemes 1 to 4 refer to LWFA, laser-driven wakefield acceleration, where the electron beam can be internally injected (Scheme 1) or else externally generated by a laser-plasma injector (Scheme 2) or an RF

**Table 23.2.** Naming convention of the different accelerator schemes investigated as part of the EuPRAXIA conceptual design study. In each case, the energy value after a stage's name indicates the electron beam energy at the end of this stage. Different stages are connected by transport lines which are detailed in Chapter 19. The following abbreviations are used: LPI = laser-plasma injector, RFI = radiofrequency injector, LPAS = laser-driven plasma-accelerator stage, and PPAS = beam-driven plasma-accelerator stage.

Scheme no.	Short descriptive name
1	LPI-5 GeV
2	LPI-150 MeV + LPAS-5 GeV
3	RFI-500 MeV + LPAS-5 GeV
4	RFI-240 MeV + LPAS-2.5 GeV + chicane + LPAS-5 GeV
5	RFI-500 MeV + PPAS-1 GeV
6	LPAS-3 GeV + PPAS-5 GeV

injector (Schemes 3 and 4). Acceleration to the final beam energy can be achieved in a single laser-plasma accelerator stage (LPAS) (Schemes 2 and 3) or split into two symmetric parts separated by a magnetic chicane for energy dechirping (Scheme 4). The laser considered in all cases is a Ti:Sa laser system operating at  $0.8\ \mu\text{m}$  wavelength, described in detail in Chapter 10. Scheme 5 refers to PWFA, particle-driven wakefield acceleration, where this chapter only examines a final beam energy of 1 GeV using a 500 MeV RF injector for external injection; a scenario for an acceleration to 5 GeV is presented in Section 17. Finally, Scheme 6 describes a hybrid configuration where the first LWFA plasma stage generates a 3.5 GeV particle beam to drive the wakefield in the second PWFA plasma stage, accelerating witness electrons to 5 GeV. Table 23.2 gives a short summary of the naming conventions for each scheme.

Further configurations with multiple plasma-accelerator stages were also considered initially. First simulations of the LWFA schemes showed, however, that acceleration to 5 GeV is quite accessible in one plasma-accelerator stage. It is therefore generally not useful to consider schemes with two acceleration stages that will need one more transfer line between the two stages (with the exception of Scheme 4, as described in Sect. 23.10).

Four LWFA schemes, one PWFA scheme, and one hybrid scheme have been studied in detail and are presented here.

In the following, various injection and acceleration techniques, studied for the different schemes of Figure 23.1, are presented. Based on the beam requirements in Table 23.1, the most promising configurations, i.e. combinations of a given scheme and given injection / acceleration techniques, are selected for the next studies. Consequently, theoretical considerations for an optimised electron beam extraction / transport are derived and applied to these selected configurations. Finally, start-to-end simulation results for the most promising machine setups are described, involving injector stages, acceleration stages, and beam transport lines.

## 23.2 Study of Injection Techniques

Two different *RF injectors* have been optimised so as to provide electron beams with 240 or 500 MeV energy and beam parameters meeting the requirements indicated in Table 23.1:

- (a) An S-band linac with a hybrid compression scheme combining RF and magnetic compressors is studied. It shows that an electron bunch of 30 pC, 7.5 fs RMS

length, and  $\sim 0.5$  mm mrad emittance, as required, can be obtained at the plasma injection point. This is achieved by accelerating the beam up to the energy of 240 MeV where space-charge forces are less harmful [585].

- (b) Another strategy with pure RF compression (using velocity bunching) [260] has been considered to produce in one stage a 100 MeV, 3 kA beam at the end of a set of S-band travelling wave sections [262]. An additional X-band linac with an accelerating gradient of  $\geq 60$  MV/m further boosts the beam energy to  $\sim 500$  MeV, while proper matching conditions at the plasma entrance are achieved with a triplet of permanent quadrupoles. For the beam-driven plasma acceleration case, a laser-comb configuration [262,323] has been applied for producing two electron bunches, a 200 pC driver followed by a 30 pC witness bunch. By illuminating the photo-cathode with a train of laser pulses with well-controlled timing, two or more electron bunches can be generated within the same RF accelerating bucket. The witness is created earlier than the driver on the photo-cathode, but then they are reversed in time at the end of the velocity-bunching process, during which the longitudinal phase space is rotated.

A detailed description of both RF injector designs is found in Chapter 14.

For the laser-plasma injector (LPI), on the other hand, the following five different injection techniques have been simulated and optimised:

- (a) Wave-breaking injection and acceleration in the non-linear regime. This is a self-injection technique that arises when the speed of the electrons in the plasma is higher than that of the wakefield [586]. Simulations have been performed with the PIC code SMILEI [587].
- (b) Shock-front injection and acceleration in the bubble regime. The principle is to focus the laser beam on a plasma density plateau, which is preceded by a steep upramp followed by a downramp of around  $100 \mu\text{m}$  length [588]. Simulations have been performed with the PIC code CALDER-Circ [589].
- (c) Ionisation injection and acceleration in the quasi-linear regime. This study is based on an experimental setup composed of a 5 mm long gas cell equipped at both ends with variable length tubes of smaller radius allowing to adjust the plasma ramps [285,590]. Simulations have been performed with the 3D PIC code WARP [354].
- (d) Downramp injection and acceleration in the blowout regime. The principle is similar to that of the shock-front technique in (b), but a smoother and longer density step is used, with more parameters to adjust to improve the beam quality at the injection. The acceleration afterwards occurs in a  $\sim 2$  mm long plasma density plateau. Simulations have been performed with the 3D PIC code OSIRIS [336].
- (e) Resonant multi-pulse ionisation injection (ReMPI). This technique relies on the localised ionisation of gas as in (c) above, but the laser beam is, in this case, split into three components: the main one (decomposed in four sub-pulses) to drive the plasma wakefield, a second small component to ionise the gas, and a third tiny component with perpendicular polarisation to symmetrise the beam [170,584,591]. Simulations have been performed with the 3D PIC ALaDyn [592] and QFluid [593] codes, the latter having been benchmarked with the FBPIC code [489].

More detailed descriptions of the simulation codes used are provided in the appendix, in Section 32.1.

### 23.3 Study of Acceleration Stages

The acceleration stages of the four *LWFA schemes* have been studied with the following different acceleration techniques leading to various and revealing results.

- (a) The LPI in Scheme 1 has been studied with the ReMPI technique detailed above. However, to accelerate an electron beam with the required parameters up to 5 GeV, a more sophisticated configuration is considered [594]: the drive laser is decomposed into eight sub-pulses, the fourth harmonic of the ionisation laser is used, and the plasma is split into two components, a gas jet for ionising the doped gas and trapping the ionised electrons followed by a 25 cm long capillary for acceleration.
- (b) The LPAS in Scheme 2 has been studied in the quasi-linear acceleration regime with external injection. In the first step, the injected beam considered has a bi-Gaussian density profile and parameters as required in Table 23.1 [582,595]. Simulations have been performed with the 3D PIC code WARP [354] in the boosted frame. In the second step, the considered input beam directly comes from simulations of the 150 MeV LPI applying the ReMPI technique (described in the previous section) and transferred by a dedicated transport line. Simulations have been performed with the quasi-3D code FBPIC [489].
- (c) The LPAS in Scheme 3 has also been studied in the quasi-linear acceleration regime with external injection. Two input beams have been considered, coming from the two RF injectors at 240 and 540 MeV described in the previous section. Simulations have been performed, respectively, with the quasi-3D code FBPIC [489], and hybrid fluid-PIC tools – the QFluid code [596] and the LAPLAC code [597,598]. In the latter codes, the plasma is assumed to behave like a cylindrically symmetric fluid, while the electron beam is treated using a full 3D PIC model.
- (d) The setup of two LPAS separated by a magnetic chicane in Scheme 4 has been studied in the blowout acceleration regime with external injection. Two input beams have been considered: the first one is an ideal Gaussian beam and the second one is a beam coming from the RF injector at 240 MeV, described in the previous section. Simulations are performed with the FBPIC code for the plasma stages as well as the ASTRA [320] and CSRtrack [599] codes for the magnetic parts.

The acceleration stage of the *PWFA Scheme 5* has been studied in the weakly non-linear regime, characterised by a wakefield departing from a sinusoidal wave tending toward a saw tooth profile. The objective is to accelerate the bunch from 540 MeV to 1 GeV without phase-space dilution. Simulations have been performed with the Architect code [600], where the electron bunch is treated in a 3D PIC model and the plasma background in a cylindrical fluid model.

The *hybrid Scheme 6* is based on two plasma stages. The first LPAS generates a high-charge electron beam which is used as a driver for the second PPAS. The injection process in the second stage is studied with three different injection techniques:

- (a) Plasma torch injection (PTI) is a specific type of density downramp injection. Instead of shaping the plasma through gas jet configurations or a knife edge, a low-power laser pulse is used to ionise helium in a hydrogen / helium mixture. This process generates a steep density downramp, which can be used for the injection [601].
- (b) Wakefield ionisation injection (WII) is a specific type of ionisation injection [602]. The accelerated beam from the first stage drives a strong wakefield in the second stage, ready for accelerating witness electrons in the bubble regime. The same wakefield presents a location where its amplitude combined with an optimised dopant gas concentration allows the injection of electrons with very high beam

**Table 23.3.** Laser and electron input beam parameters of the LPAS.  $P_L$ ,  $E_L$ ,  $a_{0L}$ , and  $\tau_{FWHM}$  stand for, respectively, the power, energy, strength, and duration at full width at half maximum of the laser pulse(s).  $E$ ,  $\varepsilon_{x,y}$ ,  $\sigma_E/E$ , and  $\tau_{FWHM}$  stand for, respectively, the energy, emittance, RMS energy spread, and duration of the input electron beam.

LPAS	Laser beam				Electron input beam			
	$P_L$	$E_L$	$a_{0L}$	$\tau_{FWHM}$	$E$	$\varepsilon_{x,y}$	$\sigma_E/E$	$\tau_{FWHM}$
Scheme 2	341 TW	45 J	2.0	132 fs	150 MeV	1.0 $\mu\text{m}$	2 %	7 fs
Scheme 3	225 TW	25 J	1.15	110 fs	537 MeV	0.4 $\mu\text{m}$	0.06 %	11 fs
Scheme 4 (for laser: per LPAS)	750 TW	40 J	3.0	50 fs	241 MeV	0.8, 0.5 $\mu\text{m}$	0.3 %	6.5 fs

quality [53]. Simulations have been carried out with the 3D PIC code OSIRIS [336].

- (c) Trojan horse injection (THI) is a specific type of plasma photo-cathode injection [603]. A PPAS containing a hydrogen / helium gas mixture is considered, fed by an upstream LPAS and a 10 GW laser beam [603]. The latter ionises the hydrogen gas to generate the witness beam. The LPAS, itself fed by two laser beams, delivers (i) a driver beam that ionises the helium gas by means of its self-field and simultaneously generates a blowout acceleration regime, and (ii) a large-size escort beam at the location where the witness beam already reaches a high enough relativistic energy [48]. Simulations have been performed with the 3D PIC code VSim [604].

### 23.4 Selection of the Configurations to Be Submitted to Start-to-End Simulations

From the extensive results obtained by the broad exploration described above on various injection and acceleration schemes, we will proceed to the down-selection of those configurations producing results closest to the EuPRAXIA requirements.

With the laser-plasma injector (LPI) using wave-breaking injection, a very big charge of 1 nC can be self-injected, then accelerated to 204 MeV after only 1.35 mm propagation. This results, however, in a normalised emittance of 7 mm mrad and 15% energy spread, both well outside the requirements of Table 23.1. Using shock-front injection, a witness beam of 80 pC charge can be created and accelerated to more than 100 MeV with an emittance of 1.5 mm mrad, but an energy spread of around 15%. Again, this latter parameter is well above the required value. The three other injection techniques give results much closer to the requirements. The beam parameters at the LPI exit obtained with those techniques are presented in Figure 23.2, where the parameter requirements are shown as orange bars. While ionisation injection still produces beams with emittance slightly above the required value in the laser polarisation direction, both downramp injection and ReMPI meet all the requirements.

The results obtained by the different acceleration techniques up to 5 GeV are gathered and compared to the parameter requirements (marked as orange bars) in Figure 23.3 (results from the PWFA scheme are not shown here). We can see that the two hybrid schemes lead to very good beam quality but low beam charge around 10 pC. In contrast, the five LWFA schemes, both with external and internal injection, all exhibit results closer to the requirements: four of them, in particular, meet almost all requirements, although only with a small margin. Not shown here are the LWFA Scheme 1 results using wave-breaking and shock-front injection techniques; these were found to accelerate a big charge up to 1 GeV, but with insufficient beam quality.

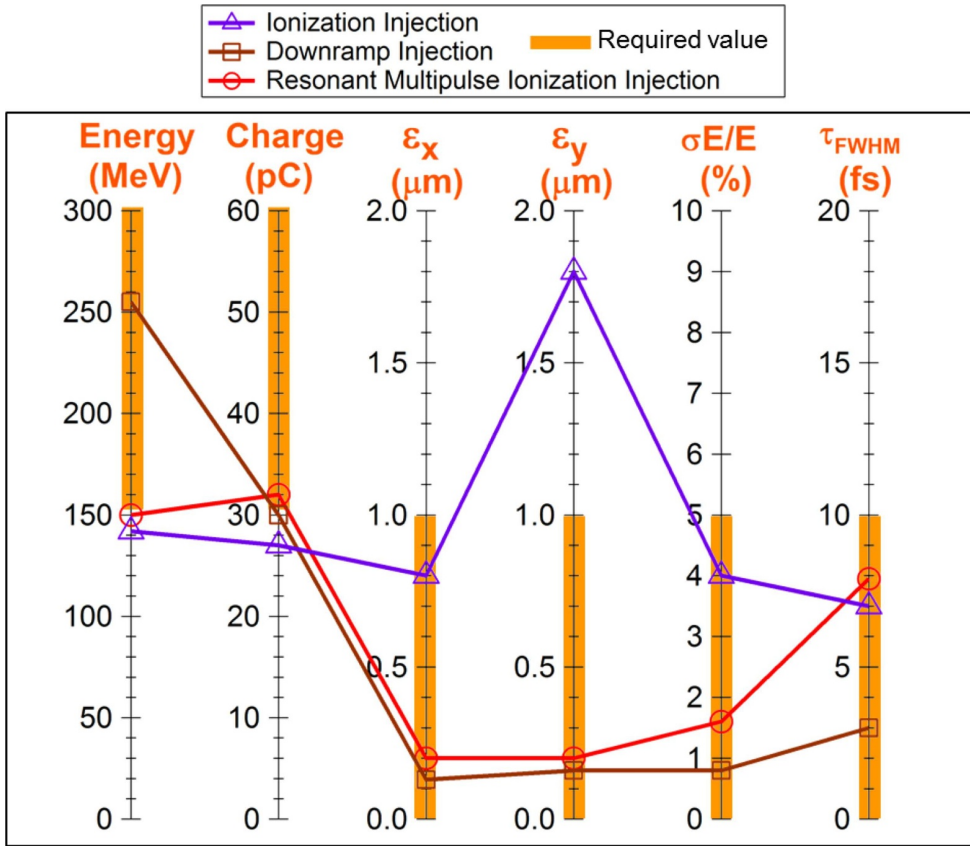


**Fig. 23.2.** Beam parameters obtained at the LPI exit, compared to the requirements, for three different injection techniques.

It is also important to note that, in many of the LWFA schemes, the quasi-linear acceleration regime is applied within the LPAS, although simulations are performed with three different simulation codes and both plasma and laser parameters vary to some extent. The fact that, even with these differences and input electron beams at varying energies, the witness beams at the LPAS exit demonstrate similar properties is a very positive indicator towards the robustness of the simulated results. Not only do the simulation codes appear to be consistent with each other, but also the acceleration process in the quasi-linear LPAS seems to be largely unaffected by moderate variations in the input parameters. We will aim to quantify these indications further in future studies on the robustness of the machine to errors and parameter fluctuations.

The PWFA Scheme 5, accelerating an externally injected witness beam to 1 GeV (from a 500 MeV RFI), demonstrates, although not shown in the figure, results quite close to the requirements. The LWFA Scheme 3 reaching 5 GeV with a 500 MeV RFI has also been optimised for reaching a final beam energy of 1 GeV. Here, the beam parameters meet all output requirements as well. The other acceleration schemes have not yet been thoroughly optimised for 1 GeV, but first results show that, a priori, equivalent beam quality could be reached as for the 5 GeV cases.

In summary, the following configurations have been selected for start-to-end simulations:

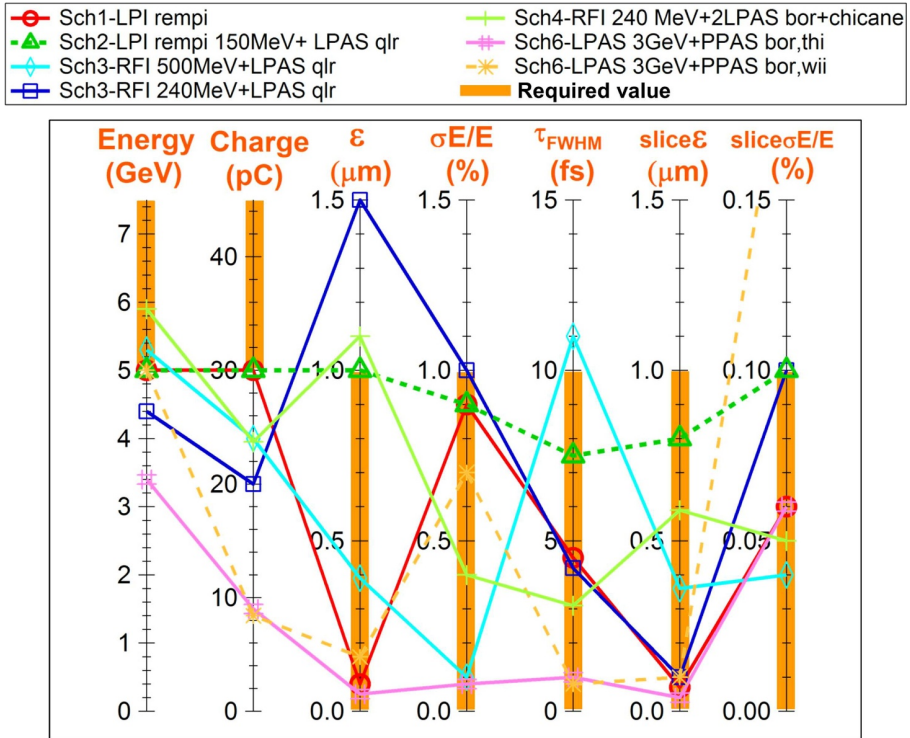


**Fig. 23.3.** Beam parameters obtained at the 5 GeV LPAS exit, compared to the requirements, for seven different acceleration techniques and beam injection mechanisms. “qlr”, “bor”, “thi”, and “wii” stand for quasi-linear regime, blowout regime, Trojan horse injection, and wakefield ionisation injection, respectively.

- Scheme 1: LPI with ReMPI injection to 5 GeV
- Scheme 2: LPI with ReMPI injection to 150 MeV + LPAS with quasi-linear acceleration to 5 GeV
- Scheme 3: RFI with RF bunching to 540 MeV + LPAS with quasi-linear acceleration to 5 GeV
- Scheme 4: RFI with RF and magnetic bunching to 240 MeV + LPAS in two sections separated by a magnetic chicane, with blowout acceleration to 5 GeV
- Scheme 5: RFI with the COMB technique to 500 MeV + PPAS with weakly non-linear acceleration to 1 GeV

### 23.5 Preserving Beam Emittance When Matching In and Out of Plasma Stages

As seen above, the EuPRAXIA requirements can be met considering well-optimised injection and acceleration stages. An important concern for full start-to-end simulations, however, is the preservation of these beam properties when transporting the beam from one plasma stage to another or towards the application beamlines (see Sect. 7.1.3). It is indeed well known that the transverse beam emittance can grow very strongly, by a factor up to 10 or more, when the beam abruptly leaves a plasma wakefield area with very strong focussing to enter into free space [605]. Although this is a very well-known phenomenon and many theoretical studies [35,194] have

been dedicated to study mitigation through smooth adiabatic plasma density transitions [36], a consistent description and strategy to fully understand the emittance growth and its mitigation for the concrete cases studied in EuPRAXIA should be developed. It is, for example, important to be clear which emittance, trace- or phase-space emittance, increases the most, and whether this occurs pre-dominantly in the free drifts or the focusing elements of the transfer lines. Additionally, the adiabatic transitions were studied only without beam loading effects, which are not applicable to EuPRAXIA's high-charge beams. For these reasons, a thorough study has been performed to understand emittance growth and to mitigate it in the most general case [606].

Based on the definitions in Section 7.1, let us recall that the trace-space emittance  $\varepsilon_{tr}$  and the normalised trace-space emittance  $\varepsilon_{tr,n}$  are defined as:

$$\begin{aligned}\varepsilon_{tr} &= \sqrt{\langle x^2 \rangle \langle x'^2 \rangle - \langle xx' \rangle^2}, \\ \varepsilon_{tr,n} &= \beta_r \gamma_r \varepsilon_{tr},\end{aligned}\tag{23.1}$$

where  $x$  and  $x'$  are the particle position and momentum angle, and  $\beta_r$  and  $\gamma_r$  are the relativistic coefficients (not to be confused with the Twiss parameters  $\alpha, \beta, \gamma$ ).

Equivalently, the phase-space emittance and the normalised phase-space emittance are defined as:

$$\begin{aligned}\varepsilon_{ph} &= \sqrt{\langle x^2 \rangle \langle p_x^2 \rangle - \langle xp_x \rangle^2}, \\ \varepsilon_{ph,n} &= \frac{\varepsilon_{ph}}{m_0 c},\end{aligned}\tag{23.2}$$

where  $p_x$  is the particle momentum,  $m_0$  the electron rest mass, and  $c$  is the speed of light.

Based on these relations, the following three conclusions can be derived:

1. When the Twiss parameter  $\alpha$  equals zero, i.e. at a beam waist where the beam changes from divergent to convergent and vice versa, the two normalised emittance values are equal:

$$\varepsilon_{ph,n} = \varepsilon_{tr,n} \quad \text{when} \quad \alpha = 0.\tag{23.3}$$

2. Through a free drift of length  $l$ , the trace-space emittance remains constant, whereas the phase-space emittance varies (subscript 0 corresponds to the drift entrance and no subscript to the drift exit):

$$\begin{aligned}\varepsilon_{tr,n}^2 - \varepsilon_{tr0,n}^2 &= 0, \\ \varepsilon_{ph,n}^2 - \varepsilon_{ph0,n}^2 &= \varepsilon_{tr0,n}^2 \left(\frac{\sigma_p}{p_0}\right)^2 \gamma_0 l (\gamma_0 l - 2\alpha_0).\end{aligned}\tag{23.4}$$

3. Inversely, through a thin lens of integrated normalised gradient  $k$ , the phase-space emittance remains constant, whereas the trace-space emittance varies (subscript 0 corresponds to the lens entrance and no subscript to the lens exit):

$$\begin{aligned}\frac{\varepsilon_{tr,n}^2 - \varepsilon_{tr0,n}^2}{\varepsilon_{tr0,n}^2} &= \beta_0^2 k^2 \left(\frac{\sigma_p}{p_0}\right)^2, \\ \varepsilon_{ph,n}^2 - \varepsilon_{ph0,n}^2 &= 0.\end{aligned}\tag{23.5}$$

Equation (23.4) points out that the variation of phase-space emittance in a drift is higher when the initial trace-space emittance, the energy spread, or the Twiss  $\gamma_0$  is larger. Those parameters are known to be particularly large in plasma accelerators. We thus propose to take advantage of this equation by using a plasma downramp for

minimising  $\gamma_0$  at the drift entrance in order to minimise the phase-space emittance growth.  $\varepsilon_{tr0}^2$  and  $\sigma_p^2$ , on the other hand, must be minimised upstream in the wakefield acceleration process, and, of course, it is helpful to reduce the drift length  $l$  as much as possible.

Equation (23.5) exhibits the well-known chromaticity effect. Due to the energy spread, there is a jump in the trace-space emittance when crossing a focussing element. To limit this increase, the focussing gradient  $k^2$  should be as low as possible (smoothest focussing), and the beam beta function at the element's entrance,  $\beta_0^2$ , should be as small as possible. Notice that the latter condition can be met by minimising the Twiss parameter  $\gamma$  in the drift section preceding the focussing lens.

Regarding these two results, minimising  $\gamma$  at the plasma exit must be the key strategy; it is doubly beneficial, for minimising the phase-space emittance growth when going through a free drift, and for minimising the trace-space emittance growth when crossing a thin lens. Seeing that  $\gamma$  is very large within the accelerating plasma and is necessarily constant in a consequent free drift, the only location to minimise this parameter is right at the plasma exit.

The above studies show precisely the relation between the two beam emittances, which emittance grows in which context, and all the parameters governing these growths. Equations (23.4) and (23.5) enable one, furthermore, to distribute different roles to each component of a multi-stage accelerator in the emittance preservation task.

The three key tasks are the following:

1. Minimising the emittance and energy spread during acceleration, therefore this should be the exclusive role of the acceleration section of the plasma-accelerator stage.
2. Minimising the Twiss parameter  $\gamma_0$  at the transfer line entrance, i.e. at the plasma exit, therefore this should be the exclusive role of the density downramp of the plasma-accelerator stage, with the reservation that the latter would not itself induce significant emittance growth.
3. Minimising the total length and the integrated focussing strength in the transfer line, therefore this should be the exclusive role of the focussing elements in the transfer line.

It is important here to consider the exclusive role of each stage. Once the best is achieved at each of those three components as recommended, the emittance growth is ensured to be minimised. The advantage is that optimisation can be achieved separately at each stage without affecting the next stage. On the contrary, if optimisation is not carried out correctly at a given stage, the effects cannot be compensated elsewhere. These minimisation procedures will be pursued all along the following start-to-end simulations.

### 23.6 Optimising and Designing Beam Transfer Lines

At least one type of transfer line is needed to drive the electron beam at high energy from the last acceleration stage to the application beamlines. In the case of external injection, a second type is needed, which drives the beam at low energy from the injector (LPI or RFI) to the acceleration stage (LPAS or PPAS). A general strategy for optimising and designing these two transfer lines is discussed in the following (see also [606]). Detailed calculations and design considerations for both transfer lines, on the other hand, are found in Chapter 19.

## The Number of Constraints and Quadrupoles

In both cases of transfer lines, the inputs are the beam parameters at the entrance of the transport section, and the constraints are the beam parameters at the section's exit, required either by the LPAS or the application beamline. In addition, as derived in Section 23.5, the transfer line should be as short as possible and should provide the smoothest focussing possible in order to minimise the emittance growth.

Gathering all these points, three constraints in each transverse direction must be considered at the end of the transfer line: the RMS beam size, divergence, and emittance. This leads to six constraints in total and, therefore, the transfer line should be designed with at least six quadrupoles.

For the low-energy transfer line, linking two plasma stages that have beam sizes and divergences on the same order of magnitude, a good solution is to use two triplets with antisymmetric polarities. As the divergence is rather high, short and strong magnets are needed. Two triplets, including six permanent magnets, should be used. We will see in the following that a section of  $\geq 0.7$  m length is the minimum length for the EuPRAXIA schemes, with a place reserved for diagnostic devices in between the triplets where the beam envelopes are parallel.

For the high-energy transfer line, as the required beam parameters on the application side (in particular for the beam propagation into the undulator section) are very different from those on the plasma side – the beam size is much bigger for the former, whereas the beam divergence is much bigger for the latter – a doublet of permanent magnets can be used to capture the beam, followed by a quadruplet of electromagnets. This offers the needed flexibility to shape the beam according to various user demands. We will see in the following that, for the different EuPRAXIA cases, a minimum section length of  $\geq 4$  m is adequate.

With six constraints and six degrees of freedom, the solution found for the quadrupole gradients should be unique once their lengths, positions, and polarities are fixed and when considering only their linear effects, as is the case here. However, in order to ensure that there are no better configurations with other quadrupole lengths and positions, or even with more quadrupoles, we have explored different possibilities.

## Exploration of Solutions with More Quadrupoles

When using more than six quadrupoles, we are in a situation where the number of free parameters is larger than the number of constraints. There is thus an infinite set of solutions. For example, two close quadrupoles with various strengths can produce the same effect, as long as the difference between their strengths is the same. Searching for the best solution in this context means searching the minimum of a function that is on a hyper-surface in a multidimensional space, where it is essential to find out the lowest minimum while avoiding the local minima. The particle swarm optimisation (PSO) algorithm [491] is well suited for this kind of problem as it employs an “army of swarms” to explore the topology of the studied space before converging toward the lowest minimum.

A code based on the PSO algorithm has thus been written in Python to optimise the transfer lines. When the program is near converging, a gradient conjugate method is used to speed up the convergence. Although requiring massive simulations, this optimisation code is not very time-consuming because it relies uniquely on analytical transfer matrices (see [606]) so that no particle tracking has to be performed. Only once the solution is found, the latter is checked with the tracking codes TraceWin [493] and ASTRA [320], where space-charge effects are taken into account.



**Fig. 23.4.** Scheme 1 using a single-stage injector / accelerator generating an FEL-quality 5 GeV beam.

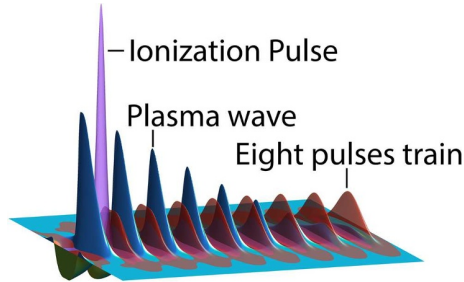


**Fig. 23.5.** The ReMPI scheme: The incoming laser pulse passes through a beam splitter; a portion of it is time-shaped as a train of eight pulses (transparent surface), while a smaller portion in the fourth harmonic is tightly focused in the rear of the train (purple surface) and is used to extract electrons from the Argon dopant. The driver train resonantly excites a high-amplitude plasma wave (black line), which traps and accelerates the electrons (reprinted from [594] with permission, copyright IOP Publishing).

This extensive procedure demonstrates that the solution using six quadrupoles for achieving six constraints (beam size, divergence, and emittance in  $x$  and  $y$ ) is adequate for a compact beamline aiming at transferring the beam from one stage to another. More complex beam transport solutions, adding extra space for diagnostics or using more unconventional components, can also be considered. They are described in some of the following start-to-end simulation cases as well as, in detail, in Chapter 19.

### 23.7 Start-to-End Simulations for Scheme 1: LPI-5 GeV

In the single-stage injection-and-acceleration scheme, the electron beam is trapped and further accelerated inside the plasma, without propagation in vacuum after the injection occurs and, therefore, without the need of beam transport optics. This approach has the disadvantage of being less flexible than one based on two stages, where both the injection and acceleration parts can be optimised independently. The single-stage scheme, however, offers the possibility to avoid potential beam quality degradation occurring at the plasma exit for low-energy electron beams and during the beam transport line, which has a sizeable impact, particularly on the beam emittance.

In the following, we will show that a single-stage setup in the ReMPI configuration [170] is flexible enough to generate, after a 25 cm long acceleration distance in a guiding capillary, a 5 GeV beam with a charge of 30 pC and FEL-compliant quality [594] as shown in Table 23.4.

The selected working configuration (see [594] for further details) is based upon a 1 PW Ti:Sa laser system, whose pulses are shaped as a train of eight pulses in the fundamental harmonics, each delivering about 6.5 J in 55 fs. Moreover, a tightly focussed

**Table 23.4.** Requested beam quality (see Tab. 23.1) and quality parameters obtained by means of the simulations reported in this section. The relative energy spread,  $\delta E_{rms}/E$  and  $\delta E_{rms|slice}/E$ , and normalised emittance,  $\varepsilon_n$  and  $\varepsilon_n|_{slice}$ , are also shown as projected and slice parameters.

Parameter	$\delta E_{rms}/E$	$\varepsilon_n$	$\delta E_{rms slice}/E$	$\varepsilon_n _{slice}$	Charge	Peak Current
Requested	$< 10^{-2}$	$< 1 \mu\text{m rad}$	$\leq 10^{-3}$	$\ll 1 \mu\text{m rad}$	$\geq 30 \text{ pC}$	$> 1 \text{ kA}$
Obtained	$0.9 \cdot 10^{-2}$	$0.085 \mu\text{m rad}$	$0.3 \cdot 10^{-3} \text{ (min)}$	$0.085 \mu\text{m rad}$	$30 \text{ pC}$	$2.5 \text{ kA}$

**Table 23.5.** Parameters of the driver train and the ionisation pulse. The total delivered energy (E in J), the FWHM duration of the pulse(s) (T in fs), the minimum waist ( $w_0$  in  $\mu\text{m}$ ), the pulse-to-pulse delay (in fs), and the normalised pulse amplitude  $a_0$  are shown.

Pulse parameters	E	T	$w_0$	Delay	$a_0$
Driver pulse	50 J	55 fs	$90 \mu\text{m}$	250 fs	0.64
Ionisation pulse	0.06 J	45 fs	$5.9 \mu\text{m}$	85 fs	0.25

45 fs long “ionisation” pulse in the fourth harmonic, obtained by an amplified portion of the same master pulse of the train, is propagated just behind the driver. Considerations for the realisation of such a laser setup are described in Section 10.2.8. The experimental arrangement of the time shaper could make use either of multiplexing techniques for the amplified pulse [584,607–609], or of pulse shaping at an early stage of the amplification chain, as in the TEMPI scheme proposed by L. Labate et al. and numerically tested with start-to-end simulations [228]. The TEMPI scheme results in a more compact and stable setup with respect to the methods handling the full-power version, yet it should operate with an energy conversion efficiency marginally below 100%. Finally, we point out that, as the driving train and the ionisation pulse are amplified replicas of the same master pulse, no standard synchronisation jitter issues are expected, except for femtosecond-level fluctuations due to  $\mu\text{m}$ -size mechanical vibrations. Table 23.5 collects the main laser driver and ionisation pulse parameters.

The plasma target consists of two contiguous sections. In the first section (an Ar 50% + He 50% filled gas cell), K-shell electrons are extracted by the ionising pulse field and trapped in the plasma wave excited by the driver train. In the adjacent He-filled capillary, the pulse train remains focussed and excites the plasma wave for about 25 cm [9]. The background plasma density is set to  $n_e = 2.1 \times 10^{17} \text{ cm}^{-3}$  in the whole gas cell and along the capillary axis, thus sustaining a plasma wave linear wavelength of about 75  $\mu\text{m}$ .

Simulations beyond 25 cm of propagation in the plasma have been performed with the quasi-static, hybrid fluid / PIC code QFluid [593]. QFluid simulations assume a 2D *cylindrical* symmetry of the fields, while particles of the bunch move in a full 3D space. QFluid is equipped with a mesh-refining technique, which is activated in the longitudinal portion of the cylinder where the bunch is placed. The bunch is sampled with  $N_b \approx 10^6$  macro-particles and the simulation cylinder has a radius and length of 320  $\mu\text{m}$  and 690  $\mu\text{m}$ , respectively. The resolution of the whole (coarse) cylinder is  $dz_{coarse} = 0.47 \mu\text{m}$  (longitudinal) and  $dr_{coarse} = 0.93 \mu\text{m}$  (radial), while the refined cylinder spacings are  $dz_{fine} = 0.0125 \mu\text{m}$  and  $dr_{fine} = 0.1 \mu\text{m}$ .

We remark also that the laser pulses’ complex envelope space / time evolution [610] has been performed maintaining the second order derivative in the time evolution, thus ensuring the most accurate description of the pulse evolution.

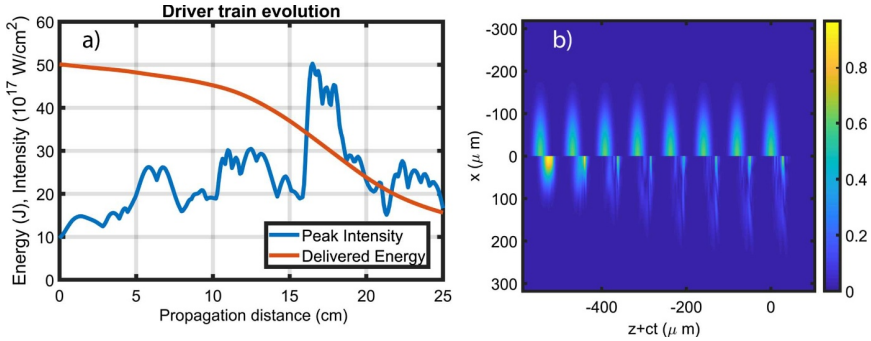


**Fig. 23.6.** Driver train evolution. a) Peak intensity and overall pulse energy evolution. b) Initial (upper) and final (lower) maps of the pulse envelope. Pulses move from the left to the right (reprinted from [594] with permission, copyright IOP Publishing).

### Evolution of the Driving Pulse Train

The evolution of the driver train is highly non-trivial, due to the propagation of the pulses in a plasma perturbed by the preceding parts of the train. This can lead to either focussing or a defocussing of different portions of the pulses, especially in the rear side of the train where the plasma wave amplitude reaches its maximum [594].

In the simulation, the evolution of the pulses at the train tail is stabilised through an optimisation procedure. During the 20 cm of propagation in the capillary, the peak intensity of the train, nonetheless, experiences large fluctuations (see Fig. 23.6a), and severe pump depletion of about 70% of the laser energy occurs, mostly due to the erosion of pulses in the tail (see Fig. 23.6b). The lead pulse, on the other hand, becomes strongly self-focussed, yet only experiences a depletion of around 10% (not shown). Overall, a large-amplitude plasma wave is excited by the train for almost all of its propagation distance, as will be apparent in the next section.

### Extraction of the Electrons by the Ionising Pulse

In the first target section (gas cell containing Argon), it is supposed that the nanosecond and picosecond laser pre-pulses, as well as the first few cycles of the first driver pulse, are able to ionise the Argon atoms up to the 8<sup>th</sup> level. The large jump of the ionisation energy occurring in the passage to the K-shell (i.e. to the 9<sup>th</sup> electron,  $U_{i,9} \simeq 422$  eV) realises the conditions for the controlled extraction of the K-shell electrons with a large-amplitude electric field. This is accomplished by tightly focussing the fourth-harmonic “ionisation” pulse just behind the train, tuning its electric field in the vicinity of the  $Ar^{8+} \rightarrow Ar^{9+}$  transition threshold. In the following, a pulse converted to the fourth harmonic (see [594] for details) will be considered, along with the resulting normalised amplitude  $a_{0,ion} = 0.25$  and a minimum waist of  $w_{0,ion} = 5.82$   $\mu\text{m}$ . As the electric field amplitude of the laser is inversely proportional to its wavelength, this design choice allows a sufficient field amplitude despite the low  $a_0$  value.

As the electron leaves the atom, it starts quivering in the laser field. After the ionising pulse overtakes it, a residual transverse momentum along the polarisation axis remains, thus constituting a source of bunch emittance. Simulations and analytical results (see [611]) show that the normalised emittance achievable by using a linearly polarised pulse can be as low as

$$\varepsilon_n \simeq 2^{-\frac{1}{2}} w_{0,ion} \cdot a_{0,ion} \cdot \Delta^2 = 2^{-\frac{1}{2}} w_{0,ion} \cdot a_{0,ion}^2 / a_c \quad (23.6)$$

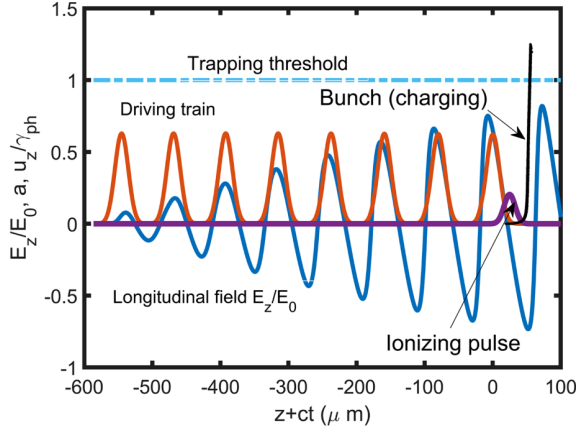


**Fig. 23.7.** On-axis snapshot at the early stage of bunch trapping. A line-out of the driving train (red line) and ionising pulse (purple line) normalised amplitudes, as well as a line-out of the longitudinal normalised electric field  $E_z/E_0$  are shown. The Lorentz factor  $\gamma$  associated with the wakefield is  $\gamma_{ph} \simeq 90$ . The longitudinal phase space of the bunch (black dots) is  $(z + ct[\mu\text{m}], u_z/\gamma_{ph})$ , where  $u_z = -p_z/mc$ . Particles with  $u_z/\gamma_{ph} \geq 1$  are trapped by the wave (reprinted from [594] with permission, copyright IOP Publishing).

where  $\Delta \equiv \sqrt{a_{0,ion}/a_c}$  and  $a_c \simeq 0.108 \cdot \lambda_{ion}(U_i/U_H)^{3/2}$  ( $U_H \simeq 13.6 \text{ eV}$ ; see Eqs. (26) in [611] and (4) in [170]). In our configuration, equation (23.6) predicts a minimum achievable emittance of  $\varepsilon_{n,min} \simeq 0.05 \mu\text{m rad}$ . However, other mechanisms than initial quivering can be responsible for an emittance increase. Among them, we mention a residual non-linearity of the transverse ponderomotive force and non-linear dependence of the radial force on the transverse coordinates. In our QFluid simulations, an emittance of  $\varepsilon_{nx} = 0.08 \mu\text{m rad}$  at the end of the gas-cell section has been obtained, which should be compared with the minimum value of  $0.05 \mu\text{m rad}$  deduced by equation (23.6).

### Beam Trapping and Energy Boosting Up to 5 GeV

Electrons leaving the  $Ar^{9+}$ -ion with a negligible speed start to quiver in the ionising pulse polarisation plane and slip back into the plasma wave while they are accelerated by the longitudinal electric field. Particle trapping occurs if electrons reach the plasma wave phase speed  $v_{ph}$  before they slip into the de-accelerating region of the wave. In our configuration, the newborn electrons reach the plasma wave speed close to the longitudinal electric field peak, which means that trapping occurs close to the “strong” trapping threshold [170] regions. In Figure 23.7, the bunch longitudinal phase space in the middle of the gas cell containing Argon is shown. A portion of the bunch (black dots) is already trapped, while most of the particles still have a longitudinal momentum  $u_z = -p_z/mc$  well below the trapping threshold  $\gamma_{ph} = (1 - \beta_{ph}^2)^{-\frac{1}{2}} \simeq 90$ . In Figure 23.7, the driving pulse train (red line) and ionisation pulse (purple line) are also shown. After the passage of the last train pulse, a moderately non-linear wave (blue line) with amplitude  $E_z/E_0 \simeq 0.7$  is excited (here  $E_0 = mc\omega_p/e$  is the non-relativistic wave-breaking limit).

Close to the end of the gas cell, the fully trapped beam experiences both longitudinal and transverse phase-space rotations. As the bunch is fully trapped by the wave,

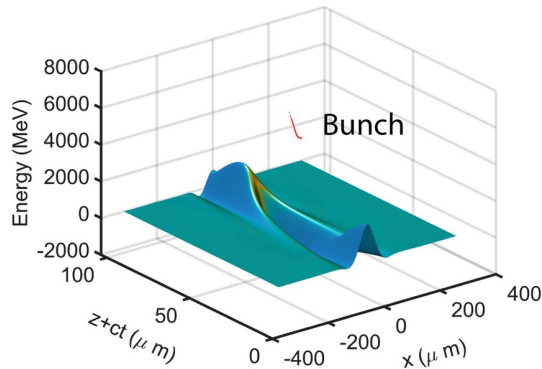


**Fig. 23.8.** The phase space  $((z + ct)[\mu\text{m}], x[\mu\text{m}], E[\text{MeV}])$  of the bunch at the end of the 25 cm long capillary. The longitudinal electric field map is also shown (reprinted from [594] with permission, copyright IOP Publishing).

a longitudinal phase-space rotation occurs, resulting in a quasi-monochromatic beam adiabatically squeezed down to a (quasi-round) beam of about  $0.8\ \mu\text{m}$  in diameter.

Just after the phase-space rotations, the driving train and the bunch enter into the helium-filled capillary “booster”, which guides the laser for more than 20 cm. Inside the capillary, an average longitudinal electric field of  $\simeq 46\ \text{GV/m}$  is obtained, corresponding to a mean normalised field of  $E_z/E_0 \simeq 0.46$ . At the capillary exit, the driving train energy is depleted by 70% and the bunch energy is about 5 GeV, with a tiny increase in the normalised emittance up to  $\varepsilon_{nx} = 0.086\ \mu\text{m rad}$  and  $\varepsilon_{ny} = 0.081\ \mu\text{m rad}$ . The longitudinal electric field map (in the bucket containing the bunch), as well as the bunch longitudinal phase-space at the end of the capillary are shown in Figure 23.8.

### Final Beam Quality

An FEL-driving beam should be analysed from both the projected and slice perspectives. While the former provides relevant information about quality degradation during the beam transport [379,606] up to the undulators, the latter shows if some slices of the bunch are suitable for lasing [219].

In Figure 23.9, several snapshots of the six-dimensional final phase space are shown. Cuts in the  $x - y$  and  $x - u_x$  planes show that a (quasi)-round and matched beam was obtained (see [591] for details). The  $z - u_z$  cut highlights an high-energy tail with a fractional charge of 8% (see Fig. 23.10). This tail, however, can be easily removed through simple fine-tuning of the transfer line energy acceptance. Finally, the transported beam (with about 92% of the total charge) complies with all the requirements of the “Requested” raw in Table 23.4, comprising a projected energy spread of  $\sigma_E/E = 9 \cdot 10^{-3}$ .

Figure 23.11a shows the slice current profile as well as the 5D brightness ( $B_{5D} \equiv 2I/(\pi^2 \varepsilon_{nx} \times \varepsilon_{ny})$ ) and 6D brightness ( $B_{6D} \equiv B_{5D}/(\sigma_E/E/10^3)$ ) of the beam. We mention here that our definition of brightness includes a  $1/\pi^2$  factor, so the comparison of peak brightness values found in the literature must be performed with care. Moreover, the current distribution shows a gently varying profile with a peak value of 3.5 kA. In Figure 23.11b, the normalised emittances along the  $x$  (ionisation) and  $y$  (driver) polarisation axes are reported. At the peak current, i.e. at a longitudinal position of about  $1\ \mu\text{m}$  from the bunch centre of mass, emittances of  $0.066\ \mu\text{m rad}$  and  $0.041\ \mu\text{m rad}$  along the  $x$ - and  $y$ -axes are reported. Remarkably, the slice energy

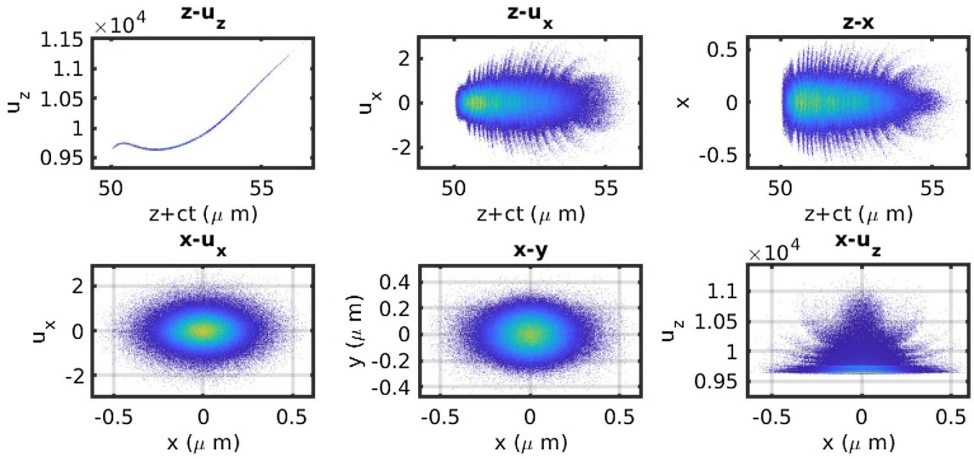


**Fig. 23.9.** Phase-space cuts of the final beam. Here,  $u_{x,y} = p_{x,y}/mc$  and  $u_z = -p_z/mc$ . The bunch moves from the left to the right (reprinted from [594] with permission, copyright IOP Publishing).

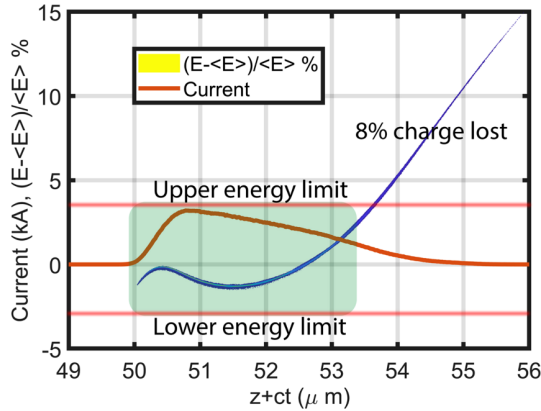


**Fig. 23.10.** Longitudinal phase-space plot ( $(z + ct)[\mu\text{m}]$ ,  $(E - \langle E \rangle)/\langle E \rangle$ ) and current profile of the final beam. By using a standard beam optics for selecting a maximum energy below  $1.3 \times \langle E \rangle$ , about 92% of the bunch charge is transported to the final undulator stage for lasing (reprinted from [594] with permission, copyright IOP Publishing).

spread reported in Figure 23.11c shows that more than 80% of the bunch charge lies in slices with an energy spread below the upper limit of  $10^{-3}$ , required for FEL lasing (see [594] for further details).

### Optimisation of Beam Transfer in the HETL

The final objective for the proposed beamline for Scheme 1 is to transfer the output beam from the plasma target towards the application beamlines, e.g. the FEL entrance, while preserving the beam quality. In particular, the beam emittance should practically not be degraded. The optimisation in this sense is described in detail in Chapter 19. The adopted solution is an 8 m long line with 7 quadrupoles: three as a capture section right behind the plasma target and another four used for matching the beam to the application. They are separated by a C-chicane right after the capture section.

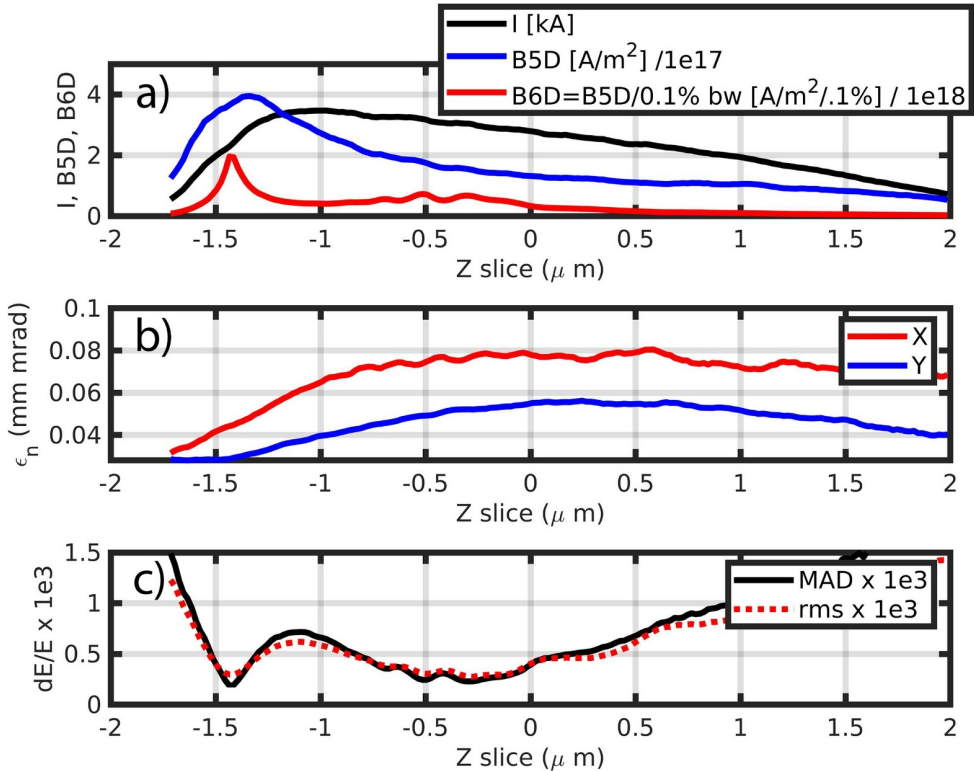


**Fig. 23.11.** Slice analysis with a slice thickness of  $0.1 \mu\text{m}$ . The longitudinal axis corresponds to the slice position with respect to beam centre of mass. a) Current (black), 5D brightness  $B_{5D} \equiv 2I/(\pi^2 \epsilon_{nx} \times \epsilon_{ny})$  (blue), and 6D brightness  $B_{6D} \equiv B_{5D}/(\sigma_E/E/10^3)$  (red). b) Emittances in the  $x$  (red) and  $y$  (blue) directions. c) Energy spread using the RMS estimator (red, dashed) or the Mean Absolute Deviation robust indicator (black) (reprinted from [594] with permission, copyright IOP Publishing).

The resulting evolution of the beam envelope, normalised emittance, and other beam parameters along the HETL is shown in Figure 23.12. The properties of the transport line components are listed in Section 19.2.2, while the final electron beam parameters are given in Table 23.6, reproduced from Chapter 19.

### Sensitivity of the Final Beam to Parameter Fluctuations

The final beam quality can be affected in an LWFA stage by several laser and target parameters. Fluctuations of the laser pulse energy are directly linked to variations in both the accelerating field amplitude and phase of the plasma wave, while (even tiny) fluctuations of the background plasma density can affect the resonance condition for the wave excitation. A full evaluation of the final beam parameter stability against the relevant working point parameters has already been performed for a setup related to the 150 MeV injector for Scheme 2 (LPI-150 MeV + LPAS-5 GeV), where a background density of about  $1 \times 10^{18} \text{cm}^{-3}$  was used. In that context, we found that the selected working point is stable, provided that reasonable requirements for laser / target fluctuations are satisfied [591,594]. The multi-pulse nature of the wake-field excitation introduces more constraints on the suitable parameter space, with the pulse-to-pulse delay  $T_D$  jitter, for example, being responsible for the loss of the

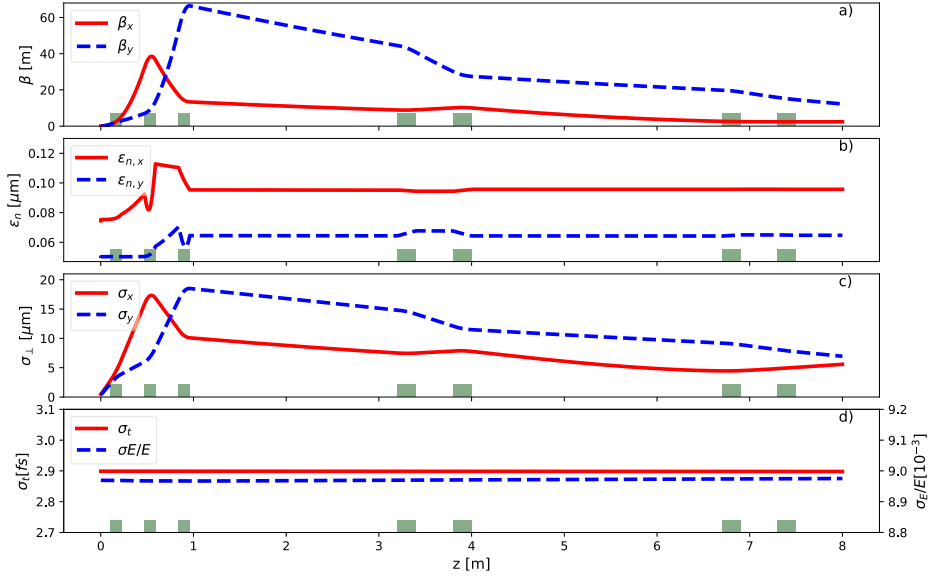


**Fig. 23.12.** High-energy transfer line for Scheme 1: Beam beta function (a), normalised emittance (b), transverse size (c), and bunch duration and energy spread (d) of the core beam along the transport line for the case of one LPI (5 GeV). The calculations were performed with the tracking code TraceWin.

**Table 23.6.** High-energy transfer line for Scheme 1: Comparison between the beam parameters at the end of the LPI and at the entrance of the undulator. These parameters have been calculated considering only the beam core, i.e. only a 11.1 fs long slice in  $z$  around the peak current. This bunch core contains 30 pC of charge. The slice parameters and peak current are calculated assuming 0.1  $\mu\text{m}$  long slices.

	LPI exit	Undulator entrance
$\beta_x$ [m]	0.030	3.17
$\beta_y$ [m]	0.029	7.28
$\alpha_x$ -	-1.06	-0.70
$\alpha_y$ -	-1.03	1.57
$\varepsilon_{n,x}$ [ $\mu\text{m}$ ]	0.075	0.095
$\varepsilon_{n,y}$ [ $\mu\text{m}$ ]	0.050	0.064
Mean Energy [GeV]	4.96	4.96
$\sigma_\gamma/\gamma$ [ $10^{-3}$ ]	9.0	9.0
$\hat{I}$ [kA]	3.8	3.8
$\sigma_\tau$ [fs]	2.9	2.9
$\varepsilon_{n,x}$ (slice) [ $\mu\text{m}$ ]	0.069	0.068
$\varepsilon_{n,y}$ (slice) [ $\mu\text{m}$ ]	0.041	0.041
$\sigma_\gamma/\gamma$ (slice) [ $10^{-3}$ ]	0.8	0.8

resonance condition (see [594] for further details). Therefore, the time shaper that generates the driver train must possess a very good stability. In our selected configuration, the TEMPI scheme shows a negligible pulse-to-pulse jitter, since the replicas of the stretched pulse (about 1 ps long) are produced by a mechanically stable stack

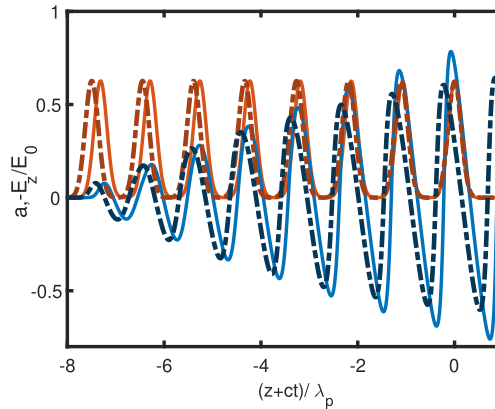


**Fig. 23.13.** Sensitivity of the accelerating field (blue lines) on the resonance condition mismatch. The horizontal axis refers to the number of plasma periods, and in the vertical axis both the accelerating field and pulse amplitude (orange) are shown. While in the optimised case (solid lines) the peak accelerating field reaches the value of  $E_{z,ref} = 0.7E_0$ , the wakefield excited in a plasma with a background density increased by 5% (dashed lines) has a peak value of  $E_z = 0.55E_0$ , showing a reduction of more than 20% (reprinted from [594] with permission, copyright IOP Publishing).

of birefringent crystals and polarisers. We also mention that the time jitter between the pulse train and the ionising pulse possesses potential detrimental effects on the beam quality. However, in our proposed setup, only mechanical vibrations can lead to this jitter, limited to a few  $\mu\text{m}$ , because the driver and ionisation pulses are amplified replicas of the same master pulse. The phase jitter of the bunch in the plasma wave is therefore very low for a plasma wavelength of  $\lambda_p \simeq 75 \mu\text{m}$ .

We point out that target density fluctuations represent the most severe source of beam-quality fluctuations. The resonance condition is related to the plasma wavelength, which is dependent on the local background density  $n_0 = n_{0,ref} + \delta n_0$ . As the efficient resonant excitation of the wave can be expressed as  $\delta n_0/n_{0,ref}/2 + \delta T_D/T_{D,ref} \ll 1/N$ , where  $N$  is the number of pulses in the train (see [594]), very low background density fluctuations on the percent level can be acceptable. This is emphasized in Figure 23.13, where the pulse train and its excited wakefield are shown in two different scenarios: the optimised case with the pair of parameters  $(T_{D,ref}, n_{0,ref})$  (solid lines) and a case with the “perturbed” pair  $(T_{D,ref}, n_{0,ref} + \delta n_0)$  with  $\delta n_0 = 5 \cdot 10^{-2} n_{0,ref}$  (shown with dashed lines). From Figure 23.13, we can infer that a variation of  $5 \times 10^{-2}$  of the plasma density, or equivalently a variation of about  $2.5 \times 10^{-2}$  of the time delay between all the pulses, will induce a reduction of more than  $20 \cdot 10^{-2}$  in the plasma wave amplitude, thus reinforcing the claim that the background plasma density must be controlled at an approximately 1% level.

#### Summary of start-to-end simulations for Scheme 1: LPI-5 GeV:

Start-to-end simulations have been carried out for this configuration. All parameters from the LPI to the HETL let us conclude that this scheme is fully compatible with the EuPRAXIA objectives. Currently, the margin with regard to the required beam parameters is still quite narrow, but further optimisation and thorough tolerance studies are planned in the future.

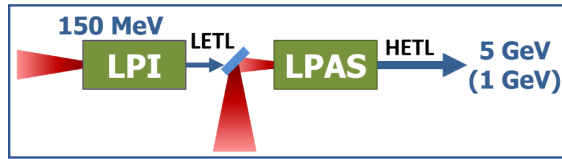


**Fig. 23.14.** Scheme 2 combining a 150 MeV laser-plasma injector with an LPAS to 5 GeV.

### 23.8 Start-to-End Simulations for Scheme 2: LPI-150 MeV + LPAS-5 GeV

This configuration includes two laser-plasma stages, a laser-plasma injector (LPI) with an output beam energy of 150 MeV, and a laser-plasma acceleration stage (LPAS) with 5 GeV (and also 1 GeV) output energy. These are connected by two transfer lines: a low-energy one (LETL) transporting the witness electron beam from the LPI to the LPAS, and a high-energy one (HETL) driving the beam from the LPAS to the application beamline. Again these include both FEL and other applications, but the FEL case is chosen exemplarily due to its more demanding requirements. As concluded in Section 23.3, the quasi-linear acceleration regime is considered here for the LPAS.

#### Optimisation of Particle Injection and Acceleration Within the LPI

The injection scheme considered for the LPI in this case is resonant multi-pulse ionisation injection (ReMPI) [170,591]. It is an injection / acceleration scheme aiming at generating high-quality electron bunches in a flexible fashion in terms of final energy, charge, and duration. Due to beam-loading effects, a configuration with relatively high emittance (about 0.3 mm mrad normalised emittance) and high charge (about 30 pC) is achieved. With a final RMS bunch duration of 3.2 fs, the peak current after the LPI is about 4 kA, while the energy spread has been limited down to 1.7%, well below the 5% limit stated in Table 23.1.

To operate the ReMPI scheme, a single pulse needs to be delivered by a Ti:Sa laser system. This pulse is split into three sub-pulses: a small fraction of laser energy is used to ionise the gas in the plasma target (pre-ionised nitrogen 5+) in order to extract the electrons; another tiny fraction with perpendicular polarisation is used to make the electron beam transversely symmetrical; the remaining main part of the laser is split further into four micro-pulses to resonantly drive the wakefield, as shown in Figure 23.15. The ionising pulse is frequency-tripled by a non-linear crystal and tightly focused behind the wake-driving pulse train. The extracted electrons are quickly trapped by the wake and accelerated up to a final energy of 150 MeV. A round beam is preferred for both the next optics / boosting stages and for minimising beam loading in the current stage; this can be achieved through the application of the perpendicularly polarised laser sub-pulse. No intrinsic timing jitter will be present, as all the laser pulses are fractions of the single initial pulse.

The injection process lasts across a distance of about 250  $\mu\text{m}$ , as a snapshot of the longitudinal field and the electron phase space shows in Figure 23.16 (left). Afterwards, a 31 pC bunch is trapped and longitudinally compressed. After the acceleration phase (about 3 mm from the ionisation pulse focus), the electron bunch is tightly focused (with an RMS size in x, y of about 0.5  $\mu\text{m}$ ) and the longitudinal phase-space plot is now as shown in Figure 23.16 (right).

The remarkably low value of 1.6% (RMS) energy spread has been obtained after optimising the density profile according to the non-linear variation of the plasma

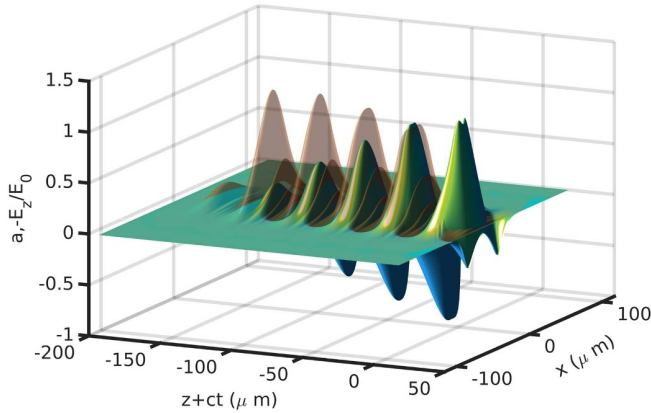


**Fig. 23.15.** The longitudinal normalised electric field, resonantly excited by a train of laser pulses (red surface).

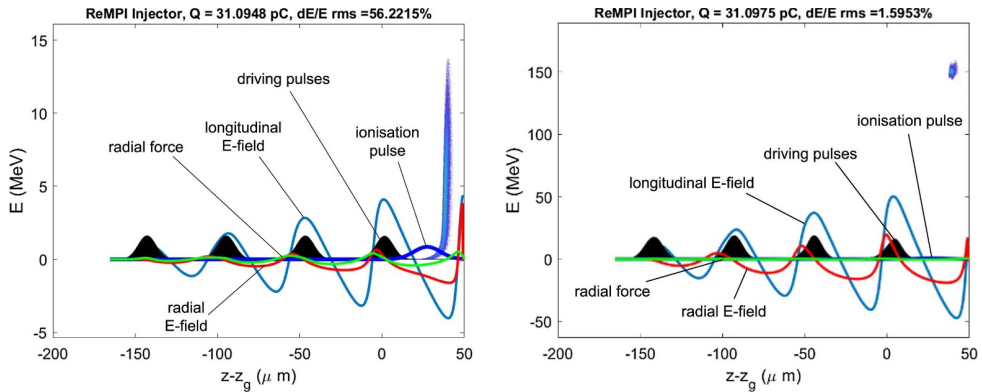


**Fig. 23.16.** The longitudinal phase-space density of the bunch close to the end of the injection process (left) and at the end of the acceleration phase (right). The laser pulses and the electron bunch move from the left to the right. The four driving pulses are represented in black. The amplitudes (a.u.) of the longitudinal electric field on axis, the ionisation pulse, the radial electric field, and the radial force on the relativistic particles are represented by the thin blue, thick blue, red, and green lines, respectively.

wavelength due to relativistic quivering. Moreover, a partial flattening of the accelerating gradient due to beam loading assisted further in reducing the final energy spread. The transverse phase space evolves smoothly as a round beam with a stable size. Unfortunately, beam loading introduces non-linear transverse gradients close to the beam axis, which induces emittance growth up to about 25% in a 2.5 mm propagation distance.

As a final result, the projections of the bunch phase space at the end of the acceleration section of the LPI can be found in Figure 23.17 together with the relevant wakefields.

Optimisation of the Downramp and Passive Plasma Lens at the LPI Exit

Although this beam has all the features to be properly injected into the next LPAS, its Twiss parameter  $\gamma = 5000 \text{ m}^{-1}$  is still too big, i.e. its divergence is too large.

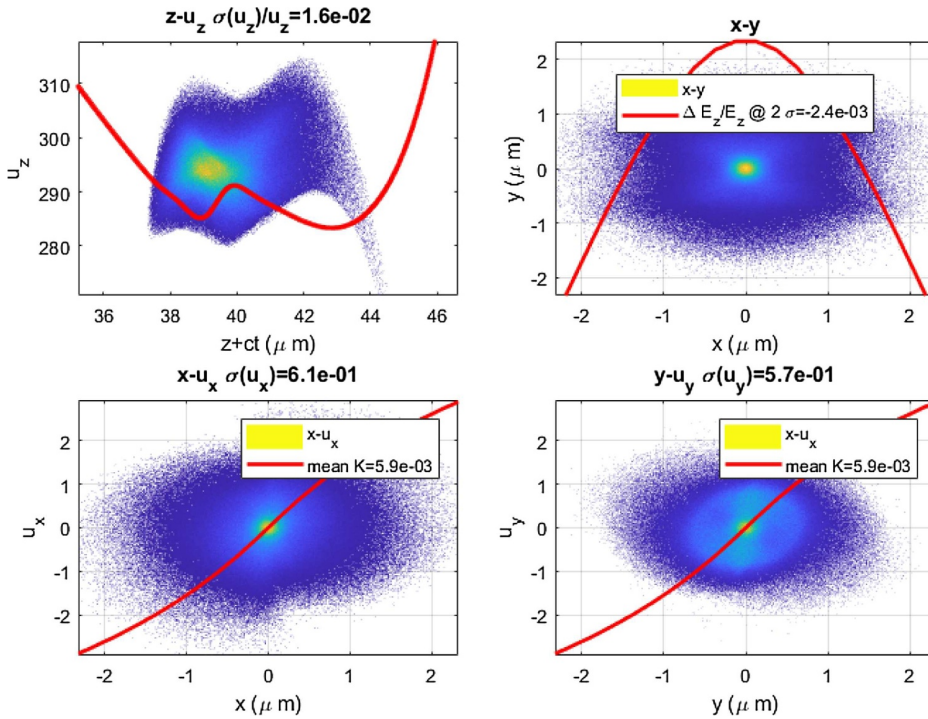


**Fig. 23.17.** Electron beam phase space (position vs. normalised momentum  $p/mc$ ) at the end of the acceleration phase. Red lines represent the longitudinal electric field on axis (top left), the longitudinal electric field at the centre of the beam (top right), and the radial force at the centre of the beam (bottom).

Combined with the 1.6% energy spread, this makes it difficult to transport the beam to the LPAS entrance without significant degradation in beam quality. According to the recommendations in Section 23.6, a density downramp assisted by a passive plasma lens (Fig. 23.18) has thus been introduced to drastically reduce  $\gamma$  to  $130 \text{ m}^{-1}$ .

Due to the resonance condition, the mean electric field acting on the bunch varies in a different manner from a single-pulse case, as the density reduces on the ramp. After an optimisation of the density downramp scale, an optimum scale length of 1 mm has been found. At the end of a density downramp of length 1.3 mm, the energy spread has increased up to a value of 1.7% and the Twiss  $\gamma$  reaches  $1700 \text{ m}^{-1}$ , which is definitely still too large for a successful beam transport. A flat-density passive plasma lens has been, therefore, inserted just after the downramp so as to gently stabilise the electron beam evolution. The passive plasma lens effect strongly reduces the Twiss parameter by more than a factor of 10 in less than 3 mm of propagation with a tiny increase in normalised emittance.

### Main Features of Particle Injection and Acceleration in the LPI and Downramp

In the following, the laser and plasma parameters used in the simulation study of the LPI are listed together with the achieved output electron beam properties:

- **Laser:** bi-Gaussian, ionising laser: 3<sup>rd</sup> harmonic,  $P = 1 \text{ TW}$ ,  $E = 0.07 \text{ J}$ ,  $a_0 = 0.53$ ,  $w_0 = 3.8 \text{ }\mu\text{m}$ ,  $\tau_{FWHM} = 45 \text{ fs}$ ; symmetrisation laser: 3<sup>rd</sup> harmonic, delay 40 fs,  $P = 0. \text{ TW}$ ,  $E = 0.02 \text{ J}$ ,  $a_0 = 0.14$ ,  $w_0 = 11 \text{ }\mu\text{m}$ ,  $\tau_{FWHM} = 25 \text{ fs}$ , drive

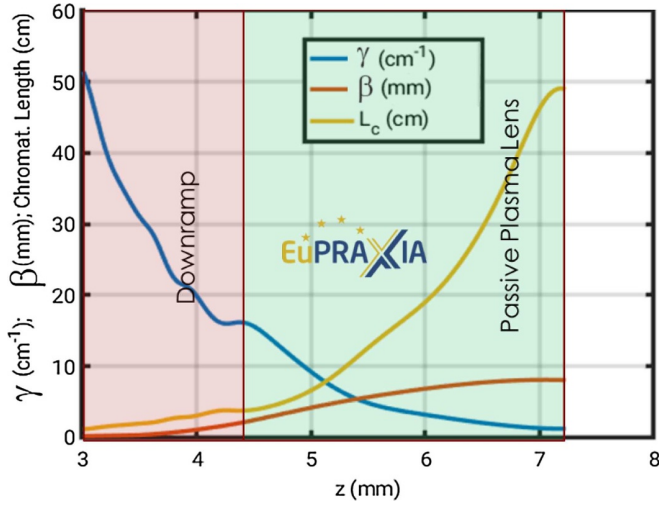


**Fig. 23.18.** Twiss parameters and chromatic length along the plasma downramp and the passive plasma lens.

laser: delay 160 fs, 4 pulses, each of them has  $P = 30$  TW,  $E = 0.98$  J,  $a_0 = 1$ ,  $w_0 = 30$   $\mu\text{m}$ ,  $\tau_{FWHM} = 30$  fs (the total need is  $P=240$  TW,  $E=8$  J, because of a 50 % conversion efficiency to 4 pulses)

- **Plasma:**  $n_0 = 5 \times 10^{17}$   $\text{cm}^{-3}$ , N pre-ionised up to 5+, radially uniform, 3.5 mm length + 1 mm downramp + 3 mm passive plasma lens, where  $n_0 = 1.4 \times 10^{16}$   $\text{cm}^{-3}$
- **Output electron beam:**  $Q = 31$  pC,  $E = 150$  MeV,  $\varepsilon_{n,x,y} = 0.31, 0.27$  mm mrad,  $\beta_0 = 0.008$  m,  $\gamma_0 = 130$   $\text{m}^{-1}$ ,  $\sigma_E/E = 1.7\%$ ,  $\tau_{FWHM} = 7.9$  fs

### Optimisation of Beam Transfer in the LETL

Several different setups for the low-energy transfer line have been investigated and are described in detail in Chapter 19. A clear decision on the optimal design will require further analysis and experimental testing; a decision on a final configuration will thus need to be taken during the technical design phase. For the current setup, the following transfer line design has been used exemplarily in the simulation study.

The objective here is to transfer the output beam from the LPI plasma lens, where  $\beta = 0.008$  m,  $\gamma = 130$   $\text{m}^{-1}$ , and  $\sigma = 2.9$   $\mu\text{m}$ , to the LPAS entrance, where  $\beta = 0.03$  m,  $\gamma = 67$   $\text{m}^{-1}$  and  $\sigma = 10.0$   $\mu\text{m}$ , while preserving all other beam qualities. In particular, the beam emittance should practically not be degraded. The optimisation process in this sense is described in Section 23.5. The proposed solution is a 0.7 m long line with six permanent quadrupole magnets: one triplet to catch the divergent beam on the LPI side and another triplet to symmetrically refocus the beam on the LPAS side. These are connected by a drift section in between, where the beam is round and parallel, reserved for diagnostic devices. Note that, instead of six quadrupoles, also two strong solenoids or two active plasma lenses could be used, as discussed in Chapter 19.

The particle distribution at the plasma lens exit looks compact without any tail. The whole distribution can thus be used. The charge and normalised emittance at the LETL exit are  $Q = 31$  pC and  $\varepsilon_{tr,n} = 0.61$  mm mrad. The evolution of the beam envelope and normalised emittance along the LETL are shown in Figure 23.19. The

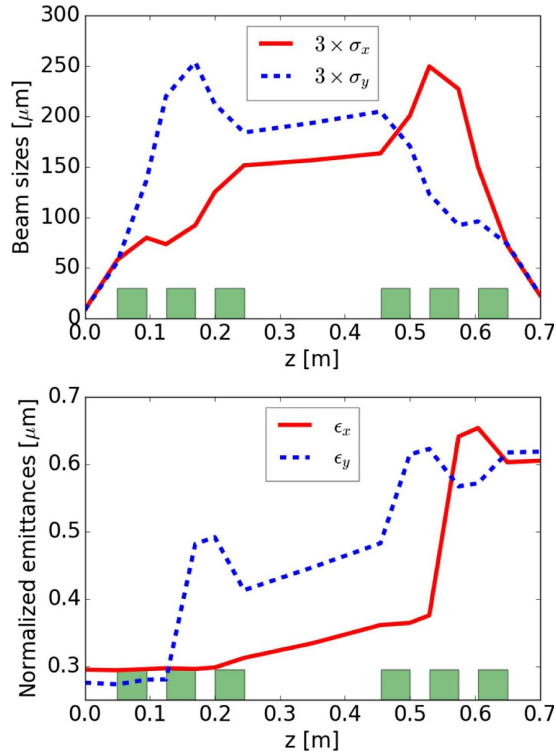


**Fig. 23.19.** Evolution of the beam size and emittance along the LETL. The six quadrupoles are symbolised by the green boxes.

LETL setup can be seen in this figure as well. The six permanent quadrupoles are each 45 mm long with a 211 T/m maximum gradient.

### Optimisation of Particle Acceleration Within the LPAS

This LPAS was optimised in parallel with the LPI, when the optimised input beam coming from the latter was not yet available. In waiting, a 6D-Gaussian beam with characteristics as required in Table 23.1 at 150 MeV was used for the optimisation. The obtained results are described in the following, and first results with the LPI beam will be given subsequently.

The objective of the LPAS is to boost the witness electron beam to 5 GeV with the required high beam charge and low emittance, low divergence, and low energy spread [582]. The technique of quasi-linear acceleration in a parabolically pre-formed plasma is applied. The laser and plasma parameters are defined following the scaling laws for a resonant wakefield. The plasma depth is defined to match the laser injection. The transversal beam size is defined to minimise emittance growth, and the longitudinal beam size is defined to minimise the energy spread by using the beam-loading effect [595]. The obtained transverse and longitudinal phase spaces after acceleration in the LPAS are shown in Figure 23.20. Simulations have been performed with the 3D PIC code Warp, where the boosted-frame technique is used to speed up the computation [354].

For an acceleration up to only 1 GeV, only a very first study was performed. Starting from the 5 GeV configuration, the first optimisation based uniquely on scal-

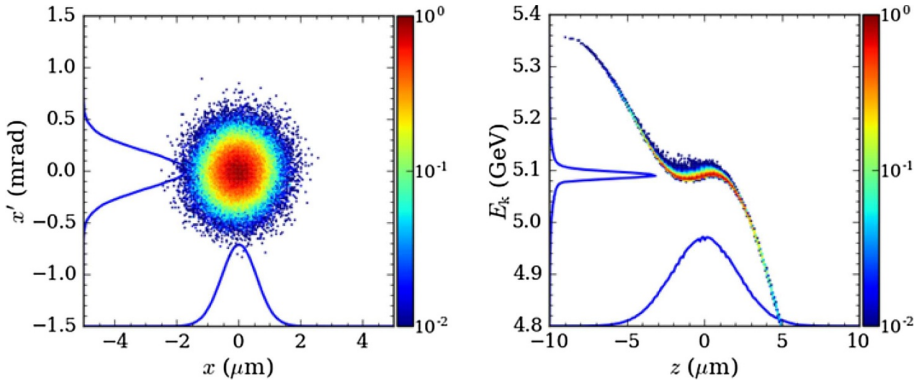


**Fig. 23.20.** Transverse and longitudinal phase spaces at the plasma exit of Scheme 2 (LPI 150 MeV + LPAS 5 GeV).

ing laws allows one to already obtain a 1 GeV beam with all the parameters meeting the EuPRAXIA beam requirements, except for the slice energy spread. The latter could be improved by tuning more carefully the beam length to take profit of the beam-loading effect, as explained above.

### Optimisation of the Up ramp at the LPAS Entrance

At the LPAS entrance, it is mandatory to have a matched input beam in order not to deteriorate the beam emittance upon entering the plasma. If no up ramp is considered, i.e. with a sharp edge plasma, this matched beam should obey two constraints:

- its Twiss parameter  $\alpha$  must be equal to zero (waist);
- its RMS size must be equal to the inverse of the square root of the wakefield focussing strength at the start of the LPAS, i.e.  $\sim 1 \mu\text{m}$ .

Such a small beam size at the waist implies a strong focussing in the upstream LETL inducing a significant emittance growth there (see Eq. (23.5)). It is thus mandatory to consider a density up ramp to smoothly increase the plasma density from zero to its maximum value in the density plateau to relax the two constraints above. We set ourselves the objective to relax the required beam size by a factor of 10.

Symmetrical at the LPAS exit, exponential profiles with different lengths have also been studied. It is found in [606] that, for each ramp length, there exists an optimal divergence resulting in a minimum emittance growth. First semi-analytical investigations with the ASTRA code [320] show that the longer the ramp, the smaller the emittance growth, but the minimum is more peaked, meaning that it should be more precisely achieved. 3D PIC simulations were conducted with the Warp code [354] in the boosted frame. In order to save computation time, a comparably short ramp of 7 mm characteristic length is studied with different  $\alpha_0$  Twiss parameters at the plasma entrance. The evolution of the beam emittance and beam size along the up ramp is shown in Figure 23.21. It is interesting to note that, no matter how well the beam is matched, the beam size always converges to its matched value, because of the presence of the very strong plasma wakefield focussing gradient. However, the stronger the beam size oscillates before it reaches its equilibrium value, the more the emittance increases. A minimum emittance growth of 4% is obtained for  $\alpha_0 = 2.0$ . Those results are obtained with a 6D-Gaussian beam.

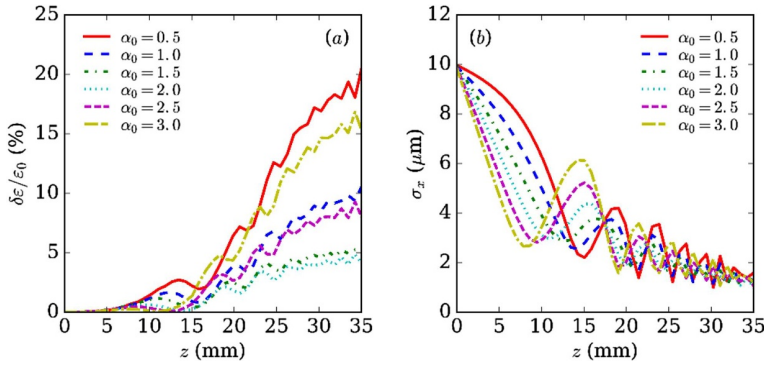


**Fig. 23.21.** Beam emittance (a) and RMS size (b) evolution along the upramp of the LPAS.

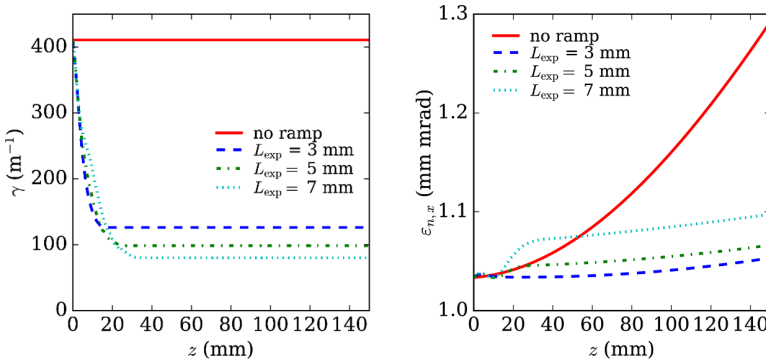


**Fig. 23.22.** Evolution of the Twiss parameter  $\gamma$  and the normalised phase-space emittance  $\epsilon_{ph,n}$  along the downramp and the downstream drift for exponential density profiles with characteristic lengths of  $L = 3, 5,$  and  $7$  mm, compared to the case without ramp.  $z = 0$  mm is the downramp entrance.

### Optimisation of the Downramp at the LPAS Exit

Although the witness beam at the LPAS exit meets all the requirements dictated for an FEL application, its Twiss parameter  $\gamma = 400 \text{ m}^{-1}$  is still too large, i.e. its divergence is too big. Combined with the 1% energy spread, this means that it is extremely difficult to transport the beam to the FEL entrance without significant emittance degradation. According to the recommendations of Section 23.5, a density downramp with different types of profiles and lengths has been considered. It turns out that, independent of the profile shape, it is enough to roughly tune the length of the density downramp to drastically decrease  $\gamma$ , while deteriorating only marginally the emittance. Figure 23.22 shows the effect of varying ramp lengths on  $\gamma$  and the beam emittance. For example, an exponential shape with a 7 mm characteristic length allows one to decrease  $\gamma$  from 400 down to  $80 \text{ m}^{-1}$  [606]. This beam distribution is taken for the HETL entrance.

### Main Features of Particle Acceleration in the LPAS, Upramp, and Downramp

The following parameter list summarises the laser, plasma and input electron beam parameters assumed in simulations of the LPAS. It also shows the output beam properties at the LPAS exit:

- **Laser:** bi-Gaussian,  $P = 341$  TW,  $E = 45$  J,  $a_0 = 2$ ,  $w_0 = 50$   $\mu\text{m}$ ,  $\tau_{FWHM} = 132$  fs
- **Plasma:**  $n_0 = 1 \times 10^{17}$   $\text{cm}^{-3}$ , radially parabolic with  $\Delta n/n_c = 0.35$ , 26 cm long, 7 mm long up- and downramps
- **Input electron beam:** 6D-Gaussian,  $Q = 30$  pC,  $E = 150$  MeV,  $\varepsilon_{n,x,y} = 1$  mm mrad,  $\varepsilon_{n,x,y,S} = 1$  mm mrad,  $\beta_0 = 0.03$  m,  $\gamma_0 = 67$   $\text{m}^{-1}$ ,  $\sigma_E/E = 2\%$ ,  $\tau_{FWHM} = 7$  fs
- **Output electron beam:**  $Q = 30$  pC,  $E = 5$  GeV,  $\varepsilon_{n,x,y} = 1.07$  mm mrad,  $\varepsilon_{n,x,y,S} = 1.1$  mm mrad,  $\beta_0 = 0.13$  m,  $\gamma_0 = 79$   $\text{m}^{-1}$ ,  $\sigma_E/E = 0.8\%$ ,  $\sigma_{E,S}/E = 0.1\%$ ,  $\tau_{FWHM} = 7$  fs

Note that the first simulation studies of the LPAS have also been carried out with an input beam coming directly from the LPI simulations, as described in Section 23.8, and transferred by the LETL described in Section 23.8. While the setup is not fully optimised yet, small changes in the configuration (e.g. a reduction of the upramp length to 6 mm) already achieved good output beam properties, as shown below:

- **Output electron beam:**  $Q = 30$  pC,  $E = 5$  GeV,  $\varepsilon_{n,x,y} = 1.0$  mm mrad,  $\varepsilon_{n,x,y,S} = 0.8$  mm mrad,  $\beta_0 = 0.02$  m,  $\gamma_0 = 60$   $\text{m}^{-1}$ ,  $\sigma_E/E = 0.9\%$ ,  $\sigma_{E,S}/E = 0.1\%$ ,  $\tau_{FWHM} = 7.8$  fs

### Optimisation of Beam Transfer in the HETL

The objective here is to transfer the output beam from the LPAS downramp as described above, i.e. with the Twiss parameters  $\alpha = 3.04$  and  $\beta = 0.13$  m, towards the FEL entrance, while preserving the beam quality. In particular, the beam emittance should practically not be degraded. The optimisation in this sense is described in detail in Chapter 19. The adopted solution is an 8 m long line with 7 quadrupoles: three as a capture section right behind the plasma target and another four used for matching the beam to the application. They are separated by a C-chicane right after the capture section.

The particles with energies in the tail of the distribution will also have its Twiss parameters far from those in the inner core. They must be removed in the optimisation of the HETL, which consists of matching those Twiss parameters. The remaining charge is  $Q = 25$  pC.

The resulting evolution of the beam envelope, normalised emittance, and other beam parameters along the HETL is shown in Figure 23.23. The properties of the transport line components are listed in Section 19.2.3, while the final electron beam parameters are given in Table 23.7, reproduced from Chapter 19.

#### Summary of start-to-end simulations for Scheme 2: LPI-150 MeV + LPAS-5 GeV:

Start-to-end simulations have been carried out for this configuration. All parameters from the LPI, LETL, LPAS, and HETL let us conclude that this scheme is fully compatible with the EuPRAXIA objectives. Currently, the margin with regard to the required beam parameters is still quite narrow, but further optimisation as well as thorough tolerance studies are planned in the future.

### 23.9 Start-to-End Simulations for Scheme 3: RFI-500 MeV + LPAS-5 GeV

This configuration includes a radiofrequency injector (RFI), which produces an electron beam of energy 500 MeV to be injected into the laser-plasma acceleration stage

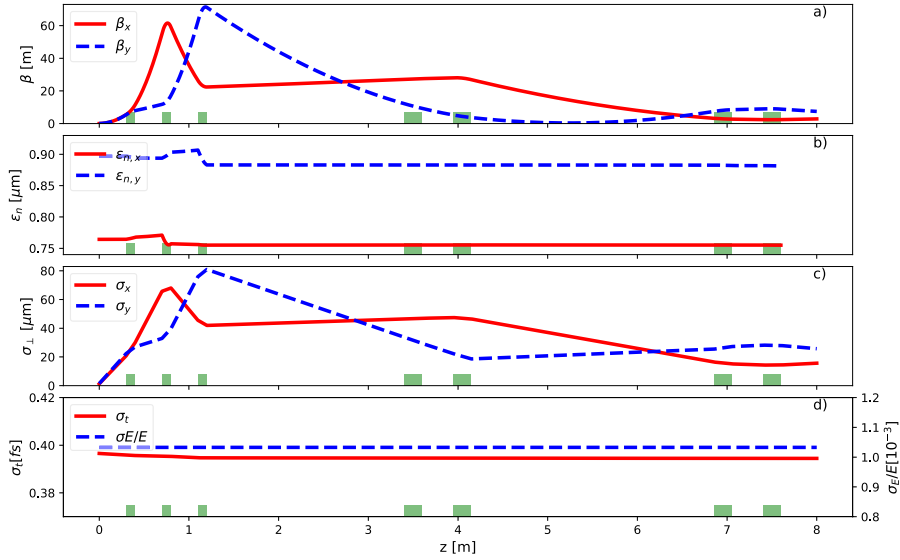


**Fig. 23.23.** High-energy transfer line for Scheme 2: Beam beta function (a), normalised emittance (b), transverse size (c), and bunch duration and energy spread (d) of the core beam along the transport line for the case of one LPI + LPAS (5 GeV). The calculations were performed with the tracking code TraceWin.

**Table 23.7.** High-energy transfer line for Scheme 2: Comparison between the beam parameters at the end of the LPAS and at the entrance of the undulator. These parameters have been calculated considering only the beam core, i.e. only a 1.4 fs long slice in  $z$  around the peak current. This bunch core contains 5 pC of charge. The slice parameters and peak current are calculated assuming 0.1  $\mu\text{m}$  long slices.

	LPAS exit	Undulator entrance
$\beta_x$ [m]	0.021	3.16
$\beta_y$ [m]	0.023	7.33
$\alpha_x$ –	-0.48	-0.70
$\alpha_y$ –	-0.54	1.56
$\epsilon_{n,x}$ [ $\mu\text{m}$ ]	0.76	0.76
$\epsilon_{n,y}$ [ $\mu\text{m}$ ]	0.90	0.88
Mean Energy [GeV]	4.98	4.98
$\sigma_\gamma/\gamma$ [ $10^{-3}$ ]	1.0	1.0
$\vec{I}$ [kA]	3.2	3.3
$\sigma_\tau$ [fs]	0.4	0.4
$\epsilon_{n,x}$ (slice) [ $\mu\text{m}$ ]	0.86	0.85
$\epsilon_{n,y}$ (slice) [ $\mu\text{m}$ ]	1.00	1.00
$\sigma_\gamma/\gamma$ (slice) [ $10^{-3}$ ]	0.85	0.76

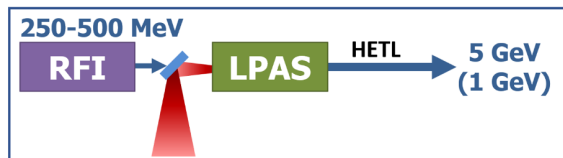


**Fig. 23.24.** Scheme 3 combining a 500 MeV RF injector with an LPAS to 5 GeV.

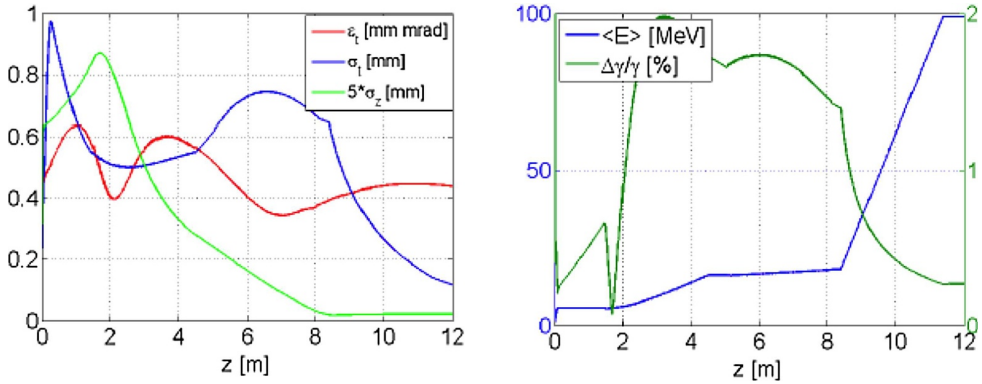


**Fig. 23.25.** Evolution of the beam parameters along the RF injector. The graphs show the electron beam transverse normalised emittance ( $\varepsilon_n$ , red line), envelope ( $\sigma_t$ , blue line), and longitudinal bunch length ( $\sigma_z$ , green line), as obtained with the TStep code for the case of pure RF compression.

(LPAS). The LPAS, in turn, accelerates the beam to 5 GeV (and also 1 GeV). It is followed by a high-energy transfer line (HETL) driving the beam to the application beamlines. The latter include FEL or other applications, but as the FEL requirements are more demanding, these will be considered primarily here. As concluded in Section 23.3, the quasi-linear acceleration regime is considered for the LPAS.

### Optimisation of the RFI

The main challenge for the RF photo-injector comes from the request to produce ultra-short, high-quality electron beams. The RF injector foreseen for this setup is described in detail in Section 14.3. It generates a witness electron beam of 500 MeV energy at the plasma interface with much less than 1 mm mrad slice emittance and 30 pC charge in a 10 fs FWHM length, which is equivalent to a peak current up to 3 kA. Pure RF compression, applying the velocity-bunching scheme [260], is used to produce in one stage a 3 kA beam at the end of the S-band travelling wave (TW) sections at 100 MeV. The S-band photo-injector [314], operating at 2.856 GHz, consists of a 1.6-cell UCLA/BNL/SLAC-type standing wave (SW) RF gun, including a copper photo-cathode with an emittance-compensating solenoid followed by 3 m long SLAC-type travelling wave (TW) sections operating at 2.856 GHz [262]. The beam-line matching foresees a proper set of emittance compensation solenoids and S-band cavity gradients in the velocity bunching scheme [301], according to the invariant envelope criteria [299]. In this configuration, the first and second TW sections can operate far from the crest in the velocity-bunching regime, enabling the RF compression of the beam length, while the third section operates almost on crest to let the electron bunch gain energy and freeze its phase-space properties. Velocity bunching is used in the first two S-band cavities to shorten the beam length from 102  $\mu\text{m}$  (on crest) to  $\sim 3 \mu\text{m}$  (RMS), both cavities working close to the zero-crossing of the field. Emittance minimisation is achieved by setting the gun solenoid to a 3 kG magnetic field and those surrounding the first and second S-band cavities to 0.32 kG and 0.50 kG, respectively. A slightly off-crest operation of the third S-band cavity further reduces the energy spread at the injector exit (see Fig. 23.25).

An additional X-band linac boosts the beam energy up to  $\sim 500$  MeV, as needed at the plasma entrance with proper matching conditions. The X-band linac mainly consists of two sections, L1 and L2; twelve X-band accelerating sections, 50 cm long,

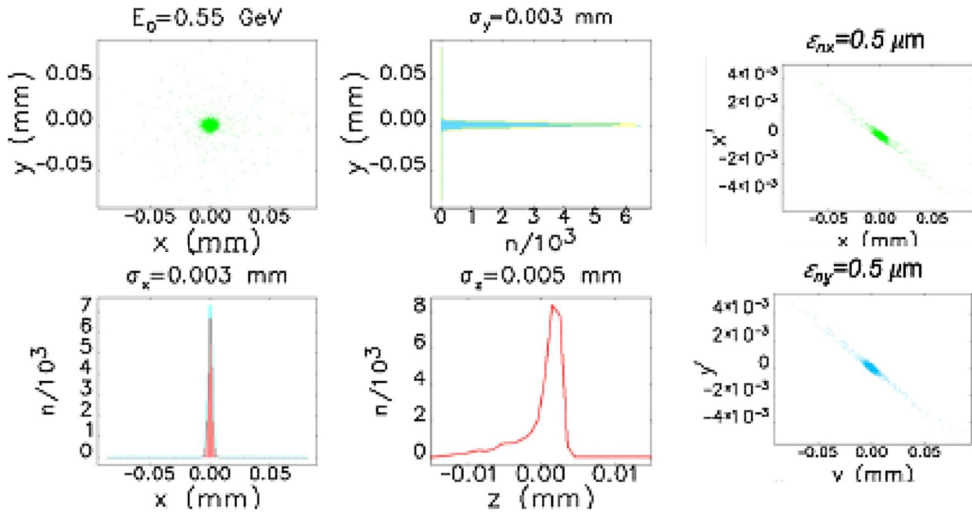


**Fig. 23.26.** Left: Transverse and longitudinal distribution of the electron beam at the capillary entrance. Right: Transverse phase space of the beam at the capillary entrance.  $E_0$  is the mean energy,  $\sigma_x$  and  $\sigma_y$  the RMS transverse size at the plasma capillary entrance, and  $n$  is the number of occurrences.

are foreseen for L1, and twenty for L2. According to the RF power system design, the maximum accelerating gradient applied is  $\sim 60$  MV/m through all of L1 and L2 to reach the required energy and energy spread for the electron beam in the conventional RF operation scheme. An increased power configuration can also be implemented progressively in a machine upgrade plan to provide overhead and flexibility to the operation, and ultimately, to reach higher beam energies with the accelerating gradient raised up to  $\sim 80$  MV/m.

For this working point, the X-band RF linac provides an electron beam with the following parameters:  $Q = 30$  pC,  $I = 3$  kA (FWHM),  $E = 550$  MeV, and energy spread less than 0.1% (see Fig. 23.26). Before entering the plasma capillary, a focussing triplet of permanent magnet quadrupoles (PMQ) is foreseen at a distance of a few centimetres from the plasma entrance to obtain a typical beta function of  $\beta_{x,y} \sim 1\text{--}5$  mm. The gradient of the first three PMQs is around  $G \sim 300$  T/m with a magnetic length of 5–10 cm; the emittance dilution due to chromatic effects in the quadrupoles is the main concern of the final focussing stage.

### Optimisation of Particle Acceleration Within the LPAS

The goal at the end of the plasma-accelerator stage is to produce a witness electron beam at 5 GeV energy with the required high beam charge and low emittance, low divergence, and low energy spread, as indicated in Table 23.1. The technique of quasi-linear acceleration in a parabolically pre-formed plasma is applied.

The plasma target profile is comprised of equally shaped, exponential input and output ramps, and a constant density plateau. The presence of the ramps helps both in matching the bunch to the plasma at the input and to reduce its divergence at the exit. Their characteristic length of 3.5 mm is chosen to be half of the bunch betatron wavelength at injection. This length is both realistic and has been shown to yield the same results, in terms of beam parameters, as longer ramps [612].

The plasma density is set to  $n_0 = 1 \times 10^{17}$  cm $^{-3}$  so that the plasma wavelength is much longer than the beam length, to avoid excessive energy spread increase while

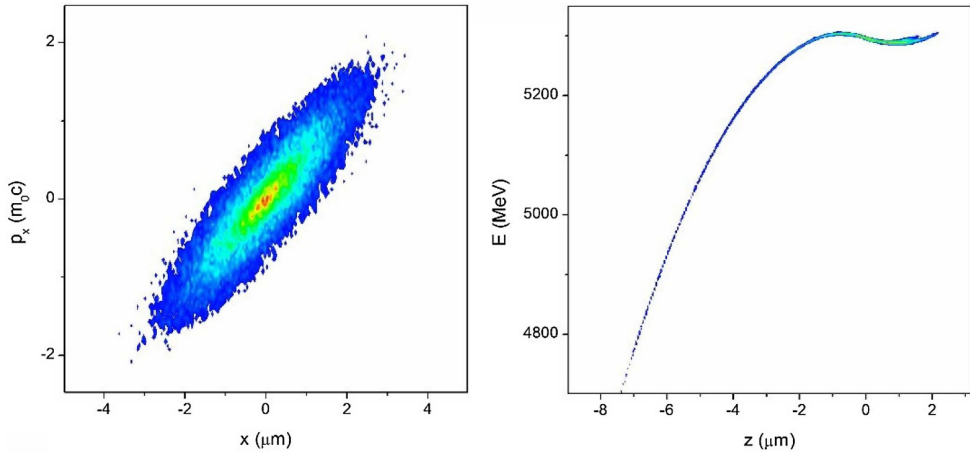


**Fig. 23.27.** Transverse and longitudinal phase spaces at the exit of the Scheme 3 (RFI 500 MeV + LPAS 5 GeV).

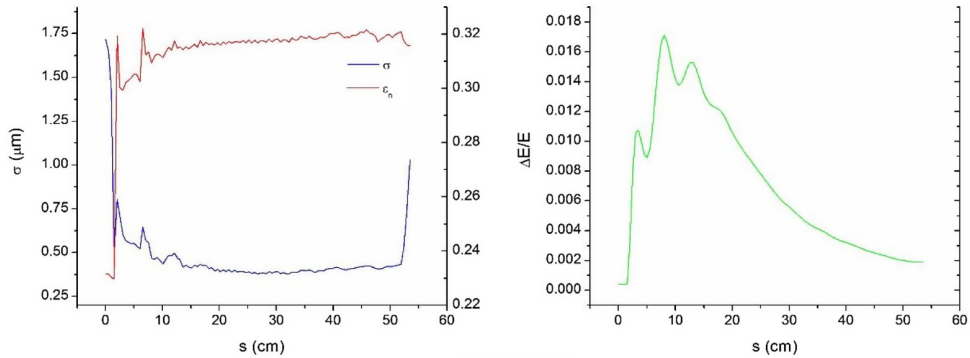


**Fig. 23.28.** Evolution of some electron beam parameters during plasma acceleration. Left: transverse size (blue) and emittance (red) evolution. Right: energy spread evolution.

retaining an accelerating gradient around 10 GV/m. The laser parameters are set to  $E = 24.4$  J,  $w_0 = 70$   $\mu\text{m}$  and  $\tau = 112$  fs (FWHM), and  $a_0 \sim 1$ , to both increase the dephasing length and maximise the laser-to-plasma energy transfer.

The obtained transverse and longitudinal phase spaces are shown in Figure 23.27. Figure 23.28 reports on the optimised beam parameters throughout the acceleration in the plasma, after performing a 20% charge cut in the bunch tail. Figure 23.29 shows the final slice phase-space emittance and energy spread parameters. For an acceleration up to only 1 GeV, equivalent results can be obtained with even higher charges. Results have been reported in [612].

### Main Features of Particle Acceleration in the LPAS

The following laser and plasma parameters have been used in the simulation of the LPAS. Also listed are the input electron beam parameters, as achieved from the RF injector above, and the output parameters of the LPAS simulations:

- **Laser:** bi-Gaussian,  $P = 225$  TW,  $E = 24.5$  J,  $a_0 = 1.15$ ,  $w_0 = 70$   $\mu\text{m}$ ,  $\tau_{FWHM} = 110$  fs

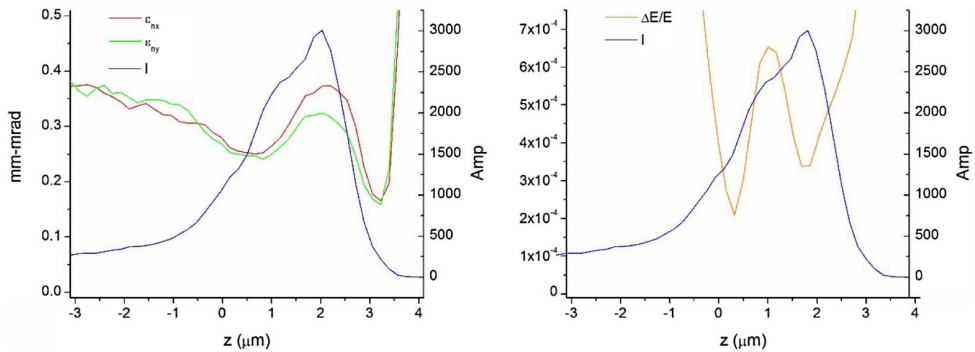


**Fig. 23.29.** Slice characteristics along the beam. Left: slice normalised emittances (red, green). Right: slice energy spread (orange). In both plots, the slice current is plotted in blue.

- **Plasma:**  $n_0 = 1 \times 10^{17} \text{ cm}^{-3}$ , radially parabolic, 50 cm long, exponential up- and downramp
- **Input electron beam** (from RFI):  $Q = 30 \text{ pC}$ ,  $E = 536.5 \text{ MeV}$ ,  $\varepsilon_{n,x,y} = 0.4 \text{ mm mrad}$ ,  $\beta_0 = 0.023 \text{ m}$ ,  $\gamma_0 = 93 \text{ m}^{-1}$ ,  $\sigma_E/E = 0.06\%$ ,  $\tau_{FWHM} = 11 \text{ fs}$
- **Output electron beam:**  $Q = 24 \text{ pC}$ ,  $E = 5.3 \text{ GeV}$ ,  $\varepsilon_{n,x,y} = 0.39 \text{ mm mrad}$ ,  $\varepsilon_{n,x,y,S} = 0.36 \text{ mm mrad}$ ,  $\beta_0 = 0.033 \text{ m}$ ,  $\gamma_0 = 110 \text{ m}^{-1}$ ,  $\sigma_E/E = 0.1\%$ ,  $\sigma_{E,S}/E = 0.04\%$ ,  $\tau_{FWHM} = 11 \text{ fs}$

### Optimisation of Beam Transfer in the HETL

The objective here is to transfer the output beam from the LPAS downramp as described above, i.e. with the Twiss parameters  $\alpha = 1.62$  and  $\beta = 0.033 \text{ m}$ , towards the FEL entrance while preserving the beam quality. In particular, the beam emittance should practically not be degraded. According to Chapter 19, the adopted solution is an 8 m long line with 7 quadrupoles: three as a capture section right behind the plasma target and another four used for matching the beam to the application. They are separated by a C-chicane right after the capture section.

The particles with energies in the tail of the distribution will also have its Twiss parameters far from those in the inner core. They must be removed in the optimisation of the HETL, which consists of matching those Twiss parameters. The remaining charge is  $Q = 24 \text{ pC}$ .

The resulting evolution of the beam envelope and normalised emittance along the HETL is shown in Figure 23.30. The properties of the transport line components are listed in Section 19.2.4, while the final electron beam parameters are given in Table 23.8, reproduced from Chapter 19.

#### Summary of start-to-end simulations for Scheme 3: RFI-500 MeV + LPAS-5 GeV:

Start-to-end simulations have been carried out thoroughly for this configuration. All parameters achieved from the RFI, LPAS, and HETL let us conclude that this scheme is fully compatible with the EuPRAXIA objectives. Currently, the margin with regard to the required beam parameters is still quite narrow, but further optimisation and thorough tolerance studies are planned in the future.

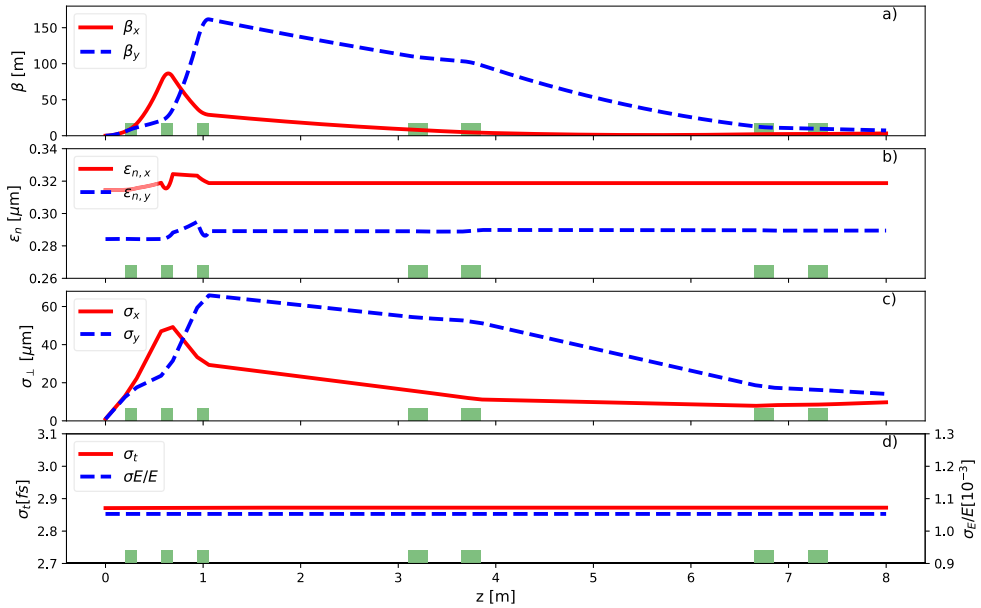


**Fig. 23.30.** High-energy transfer line for Scheme 3: Beam beta function (a), normalised emittance (b), transverse size (c), and bunch duration and energy spread (d) of the core beam along the transport line for the case of one RFI + LPAS (5 GeV). The calculations were performed with the tracking code TraceWin.

**Table 23.8.** High-energy transfer line for Scheme 3: Comparison between the beam parameters at the end of the LPAS and at the entrance of the undulator. These parameters have been calculated considering only the beam core, i.e. only a 13 fs long slice in  $z$  around the peak current. This bunch core contains 22 pC of charge. The slice parameters and peak current are calculated assuming 0.1  $\mu\text{m}$  long slices.

	LPAS exit	Undulator entrance
$\beta_x$ [m]	0.034	3.16
$\beta_y$ [m]	0.034	7.32
$\alpha_x$ –	-1.79	-0.70
$\alpha_y$ –	-1.83	1.56
$\varepsilon_{n,x}$ [0.1 $\mu\text{m}$ ]	0.31	0.32
$\varepsilon_{n,y}$ [0.1 $\mu\text{m}$ ]	0.28	0.29
Mean Energy [GeV]	5.41	5.41
$\sigma_\gamma/\gamma$ [ $10^{-3}$ ]	1.1	1.1
$\dot{I}$ [kA]	3.4	3.3
$\sigma_\tau$ [fs]	2.9	2.9
$\varepsilon_{n,x}$ (slice) [0.1 $\mu\text{m}$ ]	0.35	0.32
$\varepsilon_{n,y}$ (slice) [0.1 $\mu\text{m}$ ]	0.35	0.32
$\sigma_\gamma/\gamma$ (slice) [ $10^{-3}$ ]	0.28	0.27

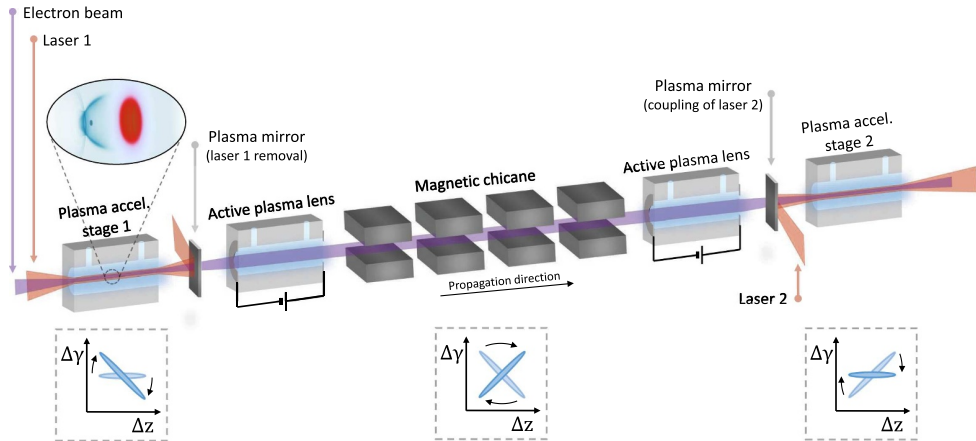


**Fig. 23.31.** Overview of the proposed acceleration scheme (not to scale) and the evolution of the longitudinal phase space of the beam.

### 23.10 Start-to-End Simulations for Scheme 4: RFI-240 MeV + LPAS-2.5 GeV + Chicane + LPAS-5 GeV

Achieving a low beam energy spread below the 0.1% level, as required by the EuPRAXIA design parameters, is one of the major current challenges for plasma-based acceleration. One of the main reasons contributing to this issue is the large slope of the accelerating fields in the plasma wake as a consequence of their high amplitude and small wavelength. This slope imprints a large energy–position correlation along the beam (known as *chirp*), which leads to a large energy spread. Although several possible solutions to mitigate this chirp have been proposed [33,48,613–616], achieving an energy spread below 0.1% has not yet been demonstrated.

Motivated by this challenge, a new design concept for plasma accelerators has been proposed and developed within the EuPRAXIA framework, which could overcome this issue. The proposed scheme, published in the journal *Physical Review Letters* [34], considers performing the acceleration of an externally injected beam in two identical plasma stages joined by a magnetic chicane, as represented in Figure 23.31. This chicane inverts the beam energy chirp generated in the first plasma stage, which can therefore be naturally compensated in the second. Numerical simulations of a first conceptual implementation of this scheme show that 5.5 GeV electron beams with energy spreads of 0.12% (total) and 0.028% (slice) could be produced while maintaining a sub-micrometre emittance. This energy spread is at least one order of magnitude below the current state of the art and would satisfy the EuPRAXIA requirements. Given these promising initial results, a EuPRAXIA layout based on this chirp compensation method has been designed and is presented in this section.

#### Design of a Two-Stage Beamline

The first conceptual implementation of the scheme, presented in [34], showed that a number of potential issues such as space charge or coherent synchrotron radiation (CSR) had a negligible influence on the simulated case, and that the energy chirp could be effectively compensated for in the second stage. This initial setup, with a total length of only 1.5 m, was, however, not meant as a prototype for an experiment, as it did not take into account certain aspects such as space for diagnostics and for the laser in- and outcoupling. In addition, the plasma-to-vacuum transitions (or ramps)

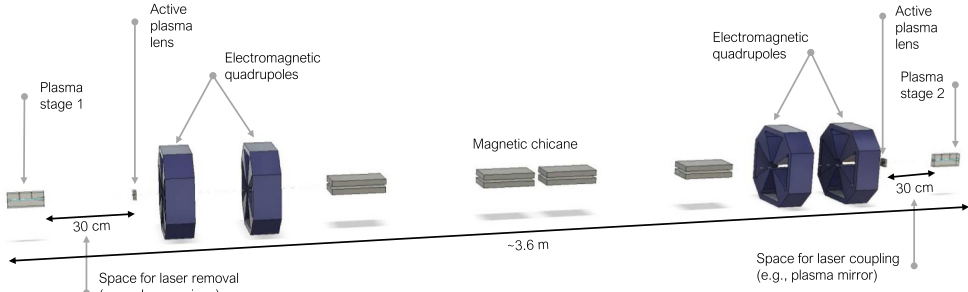


**Fig. 23.32.** Overview of the two-stage accelerator beamline for EuPRAXIA.

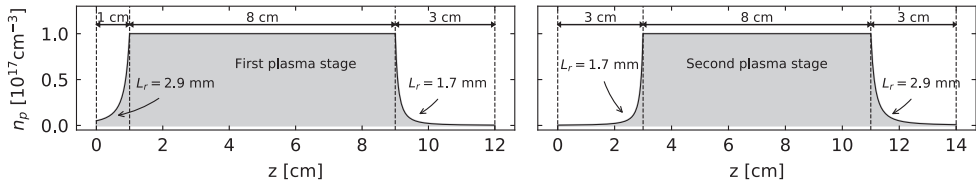


**Fig. 23.33.** On-axis density profile of the two plasma stages.

were not considered and the beam transport between accelerating stages relied solely on active plasma lenses. For these reasons, a dedicated conceptual design of this scheme for EuPRAXIA has been developed, which goes a step further towards a realistic implementation by taking all of these issues into account. A simplified view of the accelerator layout can be seen in Figure 23.32. In the following, details of each beamline section are given.

### Plasma-Accelerating Stages

As in the case presented in [34], the two plasma-accelerating stages have a length of 8 cm and operate with an on-axis plasma density at the plateau of  $n_{p,0} = 10^{17} \text{ cm}^{-3}$ , with a parabolic transverse profile  $n_p(r) = n_{p,0} + r^2/\pi r_e w_0^4$  for laser guiding, where  $r$  is the radial coordinate,  $r_e$  the classical electron radius, and  $w_0$  the spot size of the laser driver. The experimental generation of parabolic transverse profiles in this range of parameters has been recently demonstrated by means of laser pre-pulses [44,349]. In addition, the plasma ramps have now been taken into account and optimised for beam matching at the plasma entrance and divergence minimisation at the exit. No transverse guiding profile was assumed in the plasma ramps, while their longitudinal shape was assumed to follow the expression  $n_{p,ramp}(z) = n_{p,0}/(1+z/L_r)^2$ , which was found to provide good performance for matching and emittance preservation [617]. The total ramp length and the decay parameter  $L_r$  were optimised to offer the best possible matching at the injection (minimising emittance growth) and minimise the beam divergence at extraction. The values of these two parameters and the on-axis density profile of the plasma cells can be seen in Figure 23.33. Regarding the laser driver, the same parameters as in [34] have been considered; i.e. a 40 J pulse per stage with a FWHM duration of 50 fs (peak power of 0.75 PW), a spot size of  $w_0 = 50 \mu\text{m}$ , and a peak normalised vector potential of  $a_0 = 3$ . These parameters are, however, above what is in principle required to achieve a 2.5 GeV energy gain per stage, and preliminary simulations indicate that other designs based on 20 J of laser energy per stage would also be feasible.

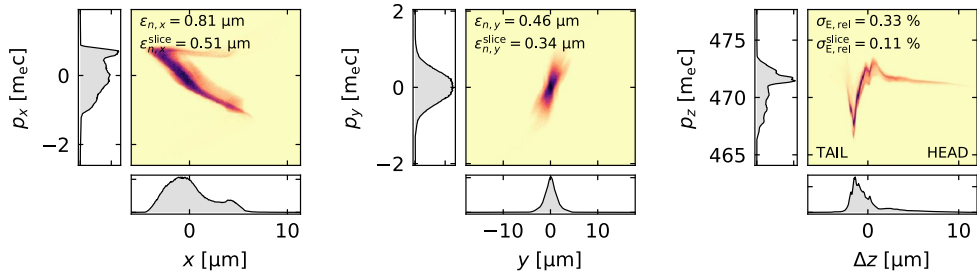


**Fig. 23.34.** Transverse and longitudinal phase space of the electron beam as delivered by the RF linac at the entrance of the first plasma.

### Space for Laser Removal

Thanks to the plasma downramp in the first stage, the divergence of the beam can be significantly reduced with respect to the original design. This reduces the emittance growth rate after the plasma stage and allows the first plasma lens to be placed farther away. In this case, a distance of 30 cm was chosen (in comparison to only 3 cm in the original design). This provides additional space for placing a plasma mirror and allows the laser pulse to diverge more, reducing its peak intensity from  $\sim 2 \times 10^{19} \text{ W cm}^{-2}$  to  $\sim 3 \times 10^{16} \text{ W cm}^{-2}$  after 25 cm. This greatly minimises the magnetic fields generated by the laser on the plasma mirror [618] and thus the risk of emittance increase. In this regard, the use of liquid crystal mirrors [619] instead of tapes would also be strongly beneficial to mitigate emittance growth caused by multiple scattering [620], as they can be much thinner (a few nm vs. a few  $\mu\text{m}$ ). The same considerations apply for the coupling of the second laser into the next plasma stage.

### Transport Line Between Stages

The transport line, in this case, has been designed to allow for a higher degree of tunability. Instead of relying only on two active plasma lenses, two pairs of electromagnetic quadrupoles have been added. In this way, the role of the plasma lenses is only to control the beam divergence after the plasma stage to suppress further emittance growth and to provide the last strong focus for the injection into the second stage. The beam transport through the chicane is, instead, performed by the quadrupoles. This allows for an independent control of both transverse planes of the beam, which might feature different properties at the plasma exit, as well as the possibility of increasing the length of the transport line to, for example, accommodate diagnostic devices simply by optimising the quadrupole strengths and positions. The full details of the transport line can be found in Section 19.2.5.

### Start-to-End Simulation Results

Initial simulations to optimise the shape of the plasma ramps and the transport line were performed with Wake-T [495], a particle-tracking code with simplified models for plasma-based accelerators, which was developed within the framework of this work to be able to quickly simulate and optimise this kind of beamlines combining plasma and conventional devices. After the initial optimisations, fully detailed simulations of the beamline have been carried out with a combination of several numerical codes.

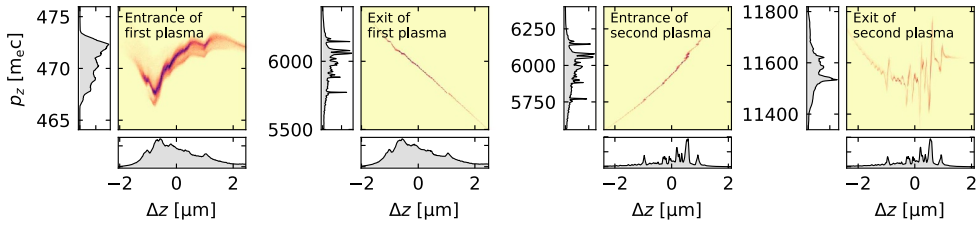


**Fig. 23.35.** Evolution of the longitudinal phase space of the externally injected electron beam along the beamline. The phase-space distribution is shown at the entrance and exit of each plasma stage. The development of an energy modulation and the micro-bunching are clearly visible. Only the central core of the beam along  $z$ , which contains  $\sim 80\%$  of the charge and is the relevant part for lasing, is shown.

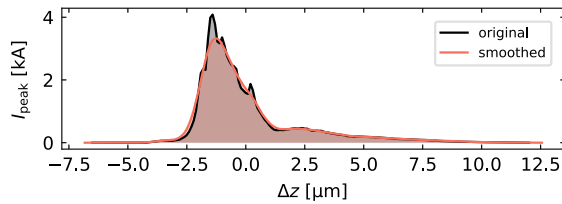


**Fig. 23.36.** Comparison of the current profiles of the original and smoothed beams.

The plasma elements, i.e. the accelerating stages and the active plasma lenses, have been simulated with the particle-in-cell code FBPIC [489], while the drifts between them as well as the transport line were simulated with the particle tracker ASTRA [320] in order to account for 3D space-charge effects. In addition, the transport line was also simulated with CSRTRACK [599] to check for possible CSR effects.

The externally injected electron beam, whose phase space can be seen in Figure 23.34, comes from the linac described in Section 14.4. Using this beam as-is led, however, to problems in the current profile and energy distribution of the beam after acceleration. As seen in Figure 23.35, the sharp peaks in the initial current profile of the beam lead to a slight energy modulation at the end of the first plasma stage caused by longitudinal space-charge effects. In the chicane, this energy modulation is translated into a charge-density modulation with sharp peaks or micro-bunches, which, in turn, generate an even larger energy modulation in the second stage. As a result, even though the energy chirp is compensated, the large energy modulation leads to a high average slice energy spread above 0.3% (for 0.1  $\mu\text{m}$  long slices), which does not fulfil the target requirements.

In order to solve this issue, an improved version of the electron beam was created by smoothing its current profile as shown in Figure 23.36. This is something that could, in principle, be achieved by introducing a laser heater before the bunch compressor in the linac, which is a technique used in FEL facilities to prevent the onset of micro-bunching. As a result of this smoothing, the energy modulation is greatly minimised and a final average slice energy spread of  $\sim 0.05\%$  (for 0.1  $\mu\text{m}$  long slices) is achieved, fulfilling the EuPRAXIA requirements.

The evolution of the parameters of this improved version of the beam along both plasma stages can be seen in Figure 23.37, while its final phase space is shown in Figure 23.38. The parameters and distributions shown in these figures as well as the following table correspond to the bunch core. This has been defined because there is a small number of particles that are far from the axis and therefore give an unrealistic calculation of beam parameters. In addition, the beam also has a long tail with a small fraction of particles that have a significantly different energy from the rest. This

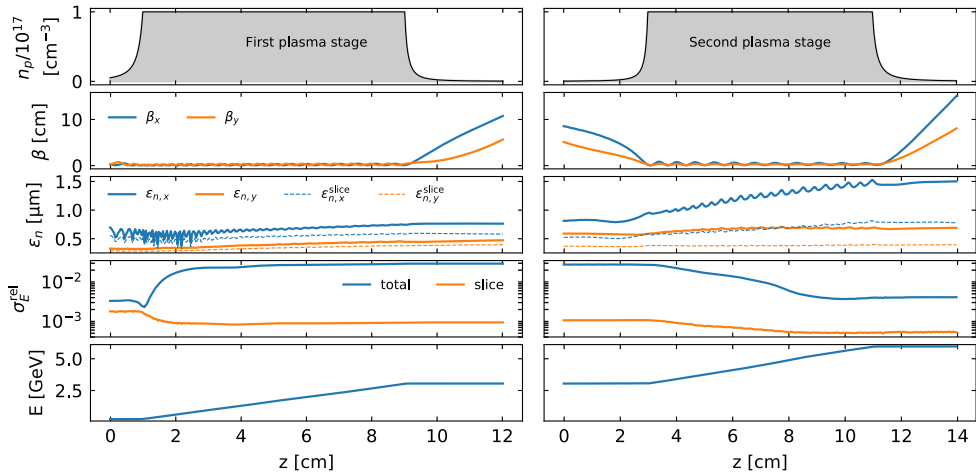


**Fig. 23.37.** Evolution of the parameters of the core part of the beam along both plasma stages. The noisy behaviour of the emittance at the beginning of the first plasma is due to the particle filtering applied to remove halo particles when computing the beam parameters.

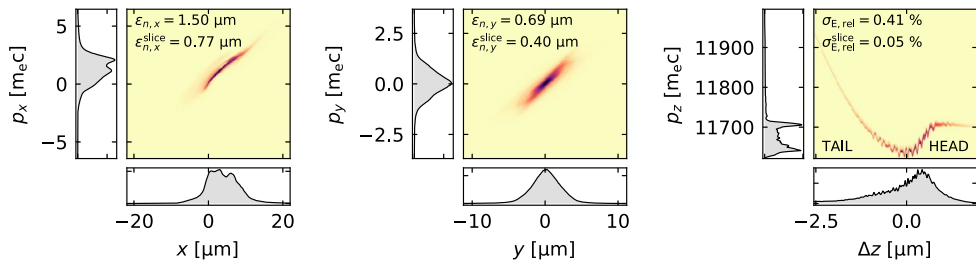


**Fig. 23.38.** Transverse and longitudinal phase space of the improved (smoothed) beam after the second plasma stage. Only the core of the beam is shown, as defined in the text.

**Table 23.9.** Final parameters of the core of the improved (smoothed) beam at the end of the second plasma.

Parameter	$Q_{\text{core}}$	$I_{\text{peak}}$	$\tau_{\text{FWHM}}$	$E$	$\sigma_{E,\text{rel}}$	$\sigma_{E,\text{rel}}^{\text{slice}}$	$\epsilon_{n,x}$   $\epsilon_{n,y}$	$\epsilon_{n,x}^{\text{slice}}$   $\epsilon_{n,y}^{\text{slice}}$
Units	pC	kA	fs	GeV	%	%	$\mu\text{m}$	$\mu\text{m}$
Value	23.7	4.9	3.1	6.0	0.41	0.05	1.50   0.69	0.77   0.40

core, which contains  $\sim 80\%$  of the charge and is the relevant part of the beam for the FEL process, has been obtained by removing the particles that are more than 5 sigma away from the axis in the transverse phase space and taking into account only a 12 fs long region around the position of the current peak, as seen in the figures.

The high-energy transport line after the last plasma stage is described in detail in Chapter 19. It consists of an 8 m long line with 7 quadrupoles: three as a capture section right behind the plasma target and another four used for matching the beam to the application. They are separated by a C-chicane right after the capture section. Table 23.10 shows the electron beam parameters achieved after the beam transport and ready for use in one of the applications foreseen for EuPRAXIA. The beam distribution at the undulator entrance is shown in Figure 23.39.

**Table 23.10.** High-energy transfer line – Scheme 4: Comparison between the beam parameters at the exit of the second LPAS and at the undulator entrance. These parameters have been calculated considering only the beam core, as defined in the main text. The slice parameters and peak current are calculated assuming 0.1  $\mu\text{m}$  long slices.

	2 <sup>nd</sup> LWFA exit	Undulator entrance
$Q$ [pC]	23.7	23.8
$\beta_x$ [m]	0.15	4.07
$\beta_y$ [m]	0.08	7.73
$\alpha_x$ –	–3.27	–0.98
$\alpha_y$ –	–1.91	1.63
$\varepsilon_{n,x}$ [ $\mu\text{m}$ ]	1.50	2.19
$\varepsilon_{n,y}$ [ $\mu\text{m}$ ]	0.69	0.90
Mean energy [GeV]	6.0	6.0
$\sigma_\gamma/\gamma$ [ $10^{-3}$ ]	4.1	3.9
$I_{\text{peak}}$ [kA]	4.9	5.1
$\tau_{\text{FWHM}}$ [fs]	3.1	3.1
$\varepsilon_{n,x}$ (slice) [ $\mu\text{m}$ ]	0.77	0.85
$\varepsilon_{n,y}$ (slice) [ $\mu\text{m}$ ]	0.40	0.40
$\sigma_\gamma/\gamma$ (slice) [ $10^{-3}$ ]	0.54	0.55

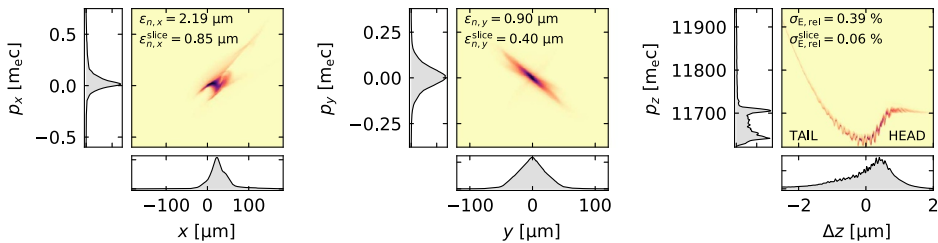


**Fig. 23.39.** Transverse and longitudinal phase space of the improved (smoothed) beam at the undulator entrance. Only the core of the beam is shown, as defined in the text.

## Conclusion

Start-to-end simulations of the two-stage layout, based on the dechirping concept presented in [34], show that 6.0 GeV beams satisfying the EuPRAXIA requirements and with a slice energy spread of  $\sim 0.05\%$  could be produced. Achieving this beam quality requires, however, to prevent the onset of micro-bunching in the magnetic chicane, which might require an upgrade of the RF linac to include a laser heater. It is also possible that this issue would not be as strong in reality as the linac simulations might be enhancing it given the limited amount of beam particles that were considered. Further detailed studies of this effect should therefore be carried out.

### Summary of start-to-end simulations for Scheme 4: RFI-240 MeV + LPAS-2.5 GeV + chicane + LPAS-5 GeV:

Start-to-end simulations have been carried out thoroughly for this configuration. All parameters achieved from the RFI, two LPAS stages, LETL and HETL let us conclude that this scheme is fully compatible with the EuPRAXIA objectives. Currently, the margin with regard to the required beam parameters is still quite narrow, but further optimisation and thorough tolerance studies are planned in the future.

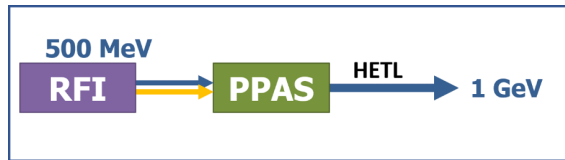


**Fig. 23.40.** Scheme 5 combining a 500 MeV RF injector with a PPAS to 1 GeV.

### 23.11 Start-to-End Simulations for Scheme 5: RFI-500 MeV + PPAS-1 GeV

This configuration includes one radiofrequency injector (RFI) injecting a 500 MeV witness beam and a driver beam to the particle-driven plasma-acceleration stage (PPAS), which, in turn, accelerates the witness beam to 1 GeV, and one high-energy transfer line (HETL) driving the beam to the end users. The latter include FEL or other applications, but as the FEL requirements are more demanding, these will be considered primarily here. The weakly non-linear acceleration regime is considered here for the PPAS.

#### Optimisation of the RFI

A laser-comb configuration [323,324] has been explored for producing two electron bunches: a 200 pC driver followed by a 30 pC witness bunch. By illuminating the photo-cathode with a train of laser pulses with well-controlled timing, two or more electron bunches can be generated within the same RF accelerating bucket. The witness is created earlier than the driver on the photo-cathode, but then they are reversed in time at the end of the velocity-bunching process, during which the longitudinal phase space is rotated.

This optimisation process consists of setting the parameters of the two electron bunches and the longitudinal distance between them as desired at the next plasma acceleration stage to be at least  $\lambda_p/2$ , where the plasma wavelength is  $\lambda_p = 330 \mu\text{m}$  for a plasma background density of  $n_p = 1 \times 10^{16} \text{cm}^{-3}$ . For this purpose, the fine-tuning of the accelerating cavity RF phases and solenoid magnetic fields has been computed. The results are summarised in Table 23.11. The RFI and the X-band boosting sections are the same as for the LWFA case. Details of these components are reported in Chapters 12 and 14.3.

The parameters of both witness and driver beams at the X-band linac entrance are listed in Table 23.12; it is worth to notice that the witness length is about  $3 \mu\text{m}$  FWHM with a normalised transverse emittance of  $0.7 \text{mm mrad}$ .

The X-band RF linac has to provide a witness beam for injection in the plasma capillary with  $Q = 30 \text{pC}$ ,  $I = 3 \text{kA}$  (FWHM), and a final beam energy of  $E_{L2exit} \sim 580 \text{MeV}$ , with an energy spread of less than 0.1%.

The driver and witness bunches are characterised by a high charge / low current and a low charge / high current, respectively. Moreover, the initial matching conditions for the injection in the X-band linac are quite different for the two bunches. In this regard, an efficient sharing of the same lattice is achieved by means of a mild transverse focusing that aims to keep the RMS size of the comb beam (formed by both witness and driver) compatible with the beam stay-clear aperture through all the X-band accelerator. The same argument applies also to the focussing stage with the permanent quadrupoles at the entrance of the plasma capillary, where a  $1\text{--}2 \mu\text{m}$  transverse spot size is required; in this case a residual asymmetry between the horizontal and vertical planes for the witness beam is present (see Figs. 23.41 and 23.42).

**Table 23.11.** Main photo-injector parameters.

Parameter	Unit	Value
Gun electric field amplitude	MV/m	120
Gun electric field operation phase	deg	32
Output gun beam energy	MeV	5.6
Amplitude of electric field in the three TW sections	MV/m	20.0/20.0/28.0
Magnetic field in the emittance compensating solenoid	kG	3.0
Magnetic field in the linac solenoid	kG	0.34/0.52
Total photo-injector length	m	12

**Table 23.12.** Driver and witness beam parameters at the end of the photo-injector.

Parameter	Unit	Witness	Driver
Charge	pC	30	200
Energy	MeV	101.5	103.2
RMS energy spread	%	0.15	0.67
RMS bunch length	fs	12	20
Peak current (FWHM)	kA	6.0	0.37
RMS normalised emittance	mm mrad	0.69	1.95
Repetition rate	Hz	10	10

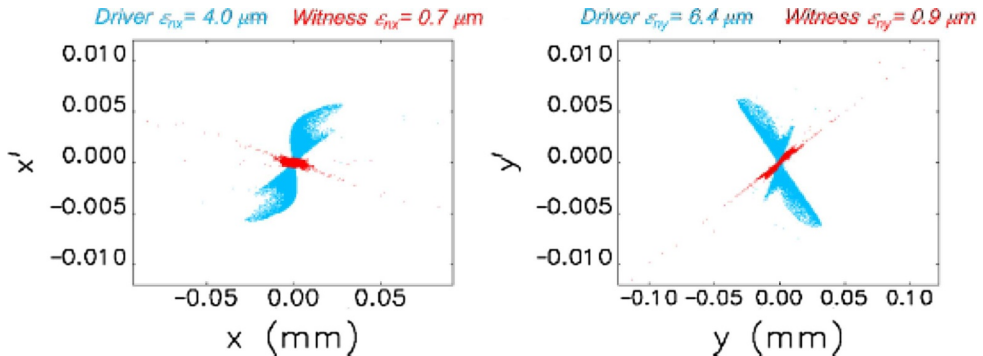


**Fig. 23.41.** Horizontal and vertical phase-space distribution of the PWFA driver (cyan dots) and witness (red dots) beams at the capillary entrance.

Optimisation of Particle Acceleration Within the PPAS

The objective is to accelerate the bunch to 1 GeV without phase-space dilution, with the required high beam charge and low emittance, low divergence, and low energy spread as indicated in Table 23.1. The so-called weakly non-linear regime is applied,

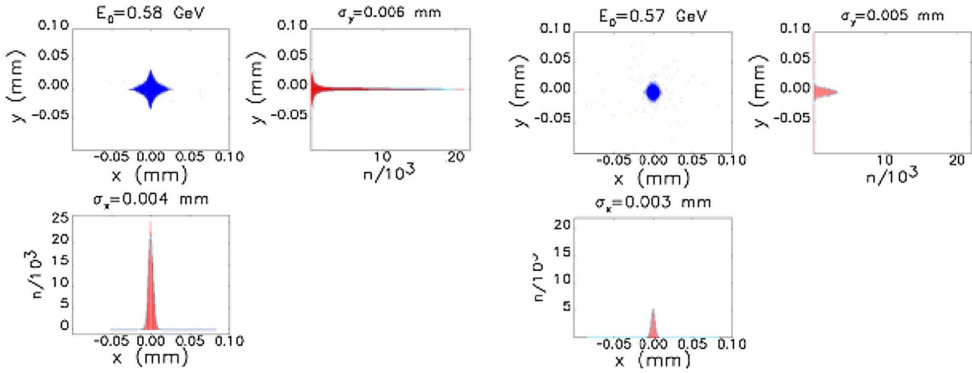


**Fig. 23.42.** Transverse horizontal and vertical distribution of the PWFA driver (left) and witness (right) beams at the capillary entrance.

characterised by an electric field wave departing from a sinusoidal wave, tending toward a sawtooth profile.

The parameter we used to measure the degree of non-linearity is the reduced charge parameter, which is the beam charge normalised to the electron charge located in a cubic plasma skin depth  $Q_{RC} = N_b k_p^3 / n_p$  [361,362]. For the foreseen case with a driver carrying about 200 pC of charge, the reduced charge is about  $Q_{RC} = 0.8 - 0.9$ . Moreover, recalling that the witness charge is fixed by the downstream applications, simulations identify that beam loading is compensated for a driver–witness distance of 184  $\mu\text{m}$ , which corresponds to  $0.55 \lambda_p$  for a  $1 \times 10^{16} \text{ cm}^{-3}$  number density. With this parameter choice, the accelerating field experienced by the witness beam is around 1.1 GV/m, as reported in Figure 23.43.

The following setup specifically allows to produce a maximum field on the order of 2.5–3.0  $\text{GV m}^{-1}$  at the bubble closure. The maximum peak is achieved at the bubble closure, where the room to allocate the witness will be limited and where the positioning of the witness would significantly change the bubble structure. We recall that the accelerating field together with the plasma wavelength depend upon the plasma number density  $n_p$  as  $\propto n_p^{1/2}$  and  $\propto n_p^{-1/2}$ , respectively. The technology related to the capillary plasma discharge is quickly evolving, suggesting that it will be possible to control the density within the capillary with great accuracy and also to compensate for some fluctuations such as the distance between driver and witness. A flat density profile at the required density is achieved with a capillary tube. The capillary tube, confining the ejected gas, permits a high degree of control, to which we can rely on for experimental on-site optimisation.

Much care has been taken to deliver the witness at the plasma entrance according to the transverse and longitudinal matching conditions of a plasma channel. For the case of interest, a witness with a given current for FEL application, requires a closer position to the driver to control at some level the energy spread. The non-bubble-rear witness positioning has some advantages and some disadvantages. The transformer ratio is limited, however, the positioning well inside the bubble allows for a wider room to place the witness, avoiding that any part of the transverse distribution hits the bubble edge with a consequent quality deterioration. In an accelerating length of 40 cm within the plasma, the witness gains about 460 MeV, so as to reach about the 1 GeV desired energy. This value indicates that the accelerating gradient is about 1.1 GV/m and that its transformer ratio is about 3.

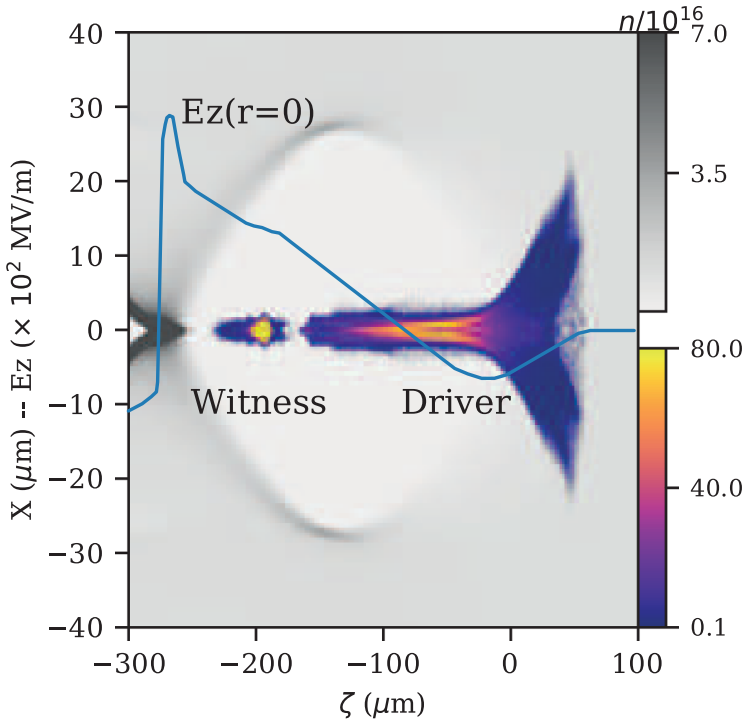


**Fig. 23.43.** Driver and witness density contour plots with the position of the accelerating electric field overlaid.

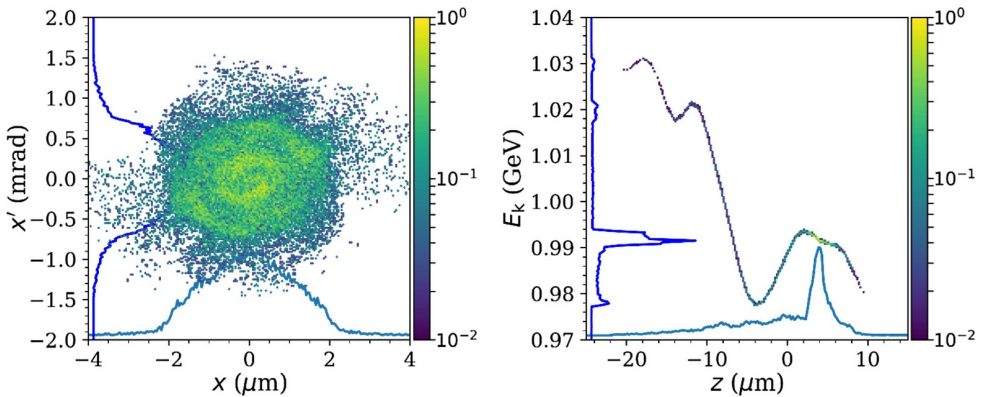


**Fig. 23.44.** Transverse and longitudinal phase spaces at the plasma exit of Scheme 5 (RFI 500 MeV + PPAS 1 GeV).

The transverse and longitudinal phase spaces obtained at the plasma exit are shown in Figure 23.44. Simulations have been performed with the Architect hybrid code [600,621].

Main Features of Particle Acceleration in the PPAS

- **Injected bunch 1 (driver):** bi-Gaussian,  $Q = 200$  pC,  $E = 567$  MeV,  $\epsilon_{n,x,y} = 3$  mm mrad,  $\sigma_E/E = 0.2\%$ ,  $\tau_{FWHM} = 313$  fs

**Table 23.13.** High-energy transfer line for Scheme 5: Comparison between the beam parameters at the end of the PPAS and at the entrance of the undulator. These parameters have been calculated considering only the beam core, i.e. only electrons in the range  $\pm 5$  MeV around the mean energy. This bunch core contains 10.5 pC of charge. The slice parameters and peak current are calculated assuming 0.1  $\mu\text{m}$  long slices.

		PPAS exit	Undulator entrance
$\beta_x$	[mm]	2.175	3.39
$\beta_y$	[mm]	4.2664	6.88
$\alpha_x$	–	0.004	–0.61
$\alpha_y$	–	1.072	1.16
$\varepsilon_{n,x}$	[ $\mu\text{m}$ ]	0.68	0.91
$\varepsilon_{n,y}$	[ $\mu\text{m}$ ]	0.59	0.68
Mean Energy	[GeV]	1.06	1.06
$\sigma_\gamma/\gamma$	[ $10^{-3}$ ]	2.6	2.6
$\hat{I}$	[kA]	2.06	1.96
$\sigma_\tau$	[fs]	0.42	0.56
$\varepsilon_{n,x}$ (slice)	[ $\mu\text{m}$ ]	0.66	0.62
$\varepsilon_{n,y}$ (slice)	[ $\mu\text{m}$ ]	0.55	0.48
$\sigma_\gamma/\gamma$ (slice)	[ $10^{-3}$ ]	0.33	0.65

- **Injected bunch 2 (witness):** triangular,  $Q = 34$  pC,  $E = 575$  MeV,  $\varepsilon_{n,x,y} = 0.6$  mm mrad,  $\sigma_E/E = 0.07\%$ ,  $\tau_{FWHM} = 12$  fs
- **Plasma:**  $n_0 = 1 \times 10^{16}$   $\text{cm}^{-3}$ , 40 cm long with a 0.5 cm long plasma ramp
- **Output electron beam:**  $Q = 34$  pC,  $E = 1.03$  GeV,  $\varepsilon_{n,x,y} = 0.96$  mm mrad,  $\varepsilon_{n,x,y,S} = 1.2$  mm mrad,  $\beta_0 = 0.0038$  m,  $\gamma_0 = 406$   $\text{m}^{-1}$ ,  $\sigma_E/E = 1.1\%$ ,  $\sigma_{E,S}/E = 0.036\%$ ,  $\tau_{FWHM} = 12$  fs

### Optimisation of Beam Transfer in the HETL

The objective here is to transfer the output beam from the PPAS downramp as described above, i.e. with the Twiss parameters  $\alpha = 0.74$  and  $\beta = 0.0038$  m, towards the FEL entrance, while preserving the beam quality. In particular, the beam emittance should practically not be degraded. The optimisation in this sense is described in Chapter 19. The adopted solution is an 8 m long line with 7 quadrupoles: three as a capture section right behind the plasma target and another four used for matching the beam to the application. They are separated by a C-chicane right after the capture section.

The particles with energies in the tail of the distribution will also have their Twiss parameters far from those in the inner core. They must be removed in the optimisation of the HETL, which consists of matching those Twiss parameters. The remaining charge is  $Q = 28$  pC.

The resulting evolution of the beam envelope and normalised emittance along the HETL are shown in Figure 23.45. Table 23.13 shows the electron beam parameters achieved after the beam transport and ready for use in one of the applications foreseen for EuPRAXIA. The properties of the transport line components are listed in Section 19.2.

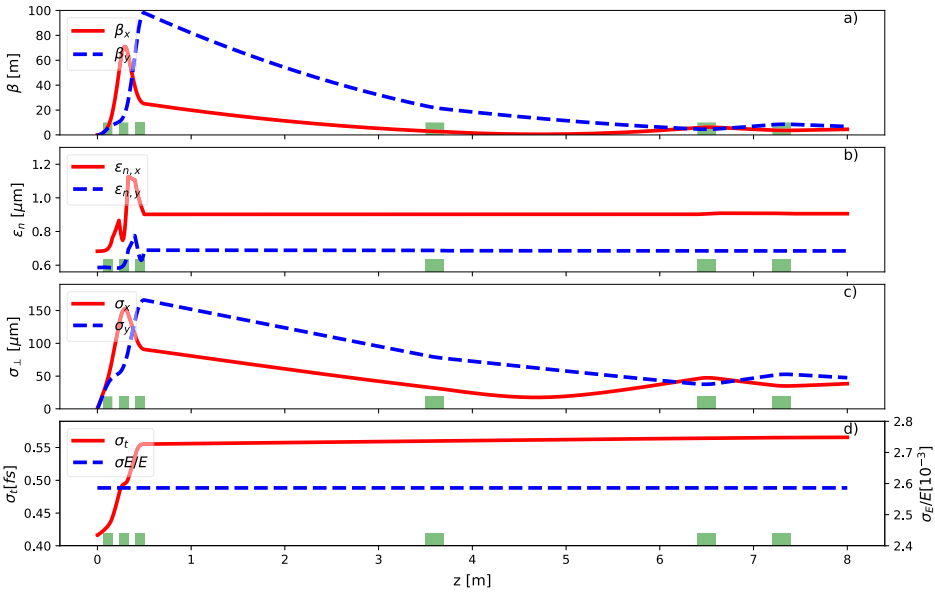


**Fig. 23.45.** High-energy transfer line for Scheme 5: Beam beta function (a), normalised emittance (b), transverse size (c), and bunch duration and energy spread (d) of the core beam along the transport line for the case of one RFI + PPAS (1 GeV). The calculations were performed with the tracking code TraceWin.

### Summary of start-to-end simulations for Scheme 5, RFI-500 MeV + PPAS-1 GeV:

Start-to-end simulations have been carried out thoroughly for this configuration. All parameters achieved from the RFI, PPAS, and HETL let us conclude that this scheme is fully compatible with the EuPRAXIA objectives. Currently, the margin with regard to the required beam parameters is still quite narrow, but further optimisation and thorough tolerance studies are planned in the future.

In addition, the present start-to-end simulation also considers the injection into a conventional undulator based on permanent magnets to successfully produce SASE FEL radiation at 3 nm, as requested for the FEL user application. This is described further in detail in Section 24.1.

## 23.12 Summary of Start-to-End Simulations

The main conclusions that can be drawn from the start-to-end simulation studies described in this chapter are, for each of the acceleration schemes under investigation, as follows:

**Scheme 1 – LPI-5 GeV:** Start-to-end simulations of Scheme 1 have demonstrated good performance with the final witness electron beam parameters aligning well with the EuPRAXIA requirements. As the scheme has not been tested experimentally and, as a single stage, promises slightly less tunability, it is considered as a development option.

**Scheme 2 – LPI-150 MeV + LPAS-5 GeV:** Full start-to-end simulations of Scheme 2 have not yet been carried out thoroughly yet. Nonetheless, the performance of the LPI, LPAS, and connecting transfer line sections demonstrates

promising results in line with the EuPRAXIA requirements. This option should therefore be considered as a baseline configuration, under the condition that full start-to-end simulations can confirm the beamline performance.

**Scheme 3 – RFI-500 MeV + LPAS-5 GeV:** Start-to-end simulations of Scheme 3 have demonstrated good performance with the final witness electron beam parameters aligning well with the EuPRAXIA requirements. This configuration is considered as a baseline option.

**Scheme 4 – RFI-240 MeV + LPAS-2.5 GeV + chicane + LPAS-5 GeV:** Start-to-end simulations of Scheme 4 have demonstrated good performance with the final witness electron beam parameters aligning well with the EuPRAXIA requirements. This configuration is considered as a baseline option.

**Scheme 5 – RFI-500 MeV + PPAS-1 GeV:** Start-to-end simulations of Scheme 5 have been carried out thoroughly. The expected performance from this configuration fits well with the EuPRAXIA requirements, thus making it a baseline option for the EuPRAXIA design for acceleration to 1 GeV.

More studies remain to be completed to improve and consolidate the results described in this chapter. With further progress expected, most of the proposed schemes may be, for example, further optimised and tested for their robustness.

It should be noted that all the studies presented here have been performed in close collaboration between the EuPRAXIA work packages WP2 (“Beam Physics and Simulation”) and WP5 (“Electron Beam Design and Optimisation”). Intense exchanges and discussion, including the sharing of large particle files, have been necessary between colleagues in different European institutes and between experts in plasma acceleration physics and conventional RF accelerator physics. This collaboration should be extended to the next studies on error effects and tolerance analyses. Considering the important number of parameters subject to errors and the very time-consuming simulations in plasma acceleration, such studies will only be possible in close collaboration between the future clusters on plasma structures, laser technology, and applications.

## 24 Photon User Applications

### 24.1 Free-Electron Laser

#### 24.1.1 Introduction

Free-electron lasers use ultra-relativistic free electrons travelling in a periodic magnetic field shaped by an undulator as a gain medium [111,114]. Among the recent trends of free-electron laser (FEL) developments, compact designs are in rapid development for replacing relevant elements with alternative accelerator concepts or novel schemes [622]. Within the EuPRAXIA concept [295], the interest is to consider a plasma-based accelerator to drive an FEL. When considering to implement an FEL based on electron bunches produced by plasma acceleration [180], several new issues have to be considered:

- the electron beam presents an energy spread inherent to the dynamics of plasma acceleration, which is typically one order of magnitude larger than that generally available at conventional linear accelerators driving FELs;
- external injection schemes promise to provide a more reliable control of the beam quality, with emphasis on those effects inducing beam-emittance deterioration [379];
- in order to minimise the energy spread and divergence increase, a high brightness injector is needed and particular care must be taken of the bunch length;

- Twiss parameters have to be chosen such that the  $\beta$  parameter is large enough at the plasma exit to allow beam manipulation, but then such that both a decrease in divergence and an increase in size at an almost fixed emittance take place at the undulator entrance.

In the present work, reproduced from [623] with the authors' permission, we analyse the FEL performance of some of the most promising schemes based on laser- and particle-driven plasma acceleration investigated for EuPRAXIA. We also compare the FEL results of the electron beams targeting the same resonant wavelength.

#### 24.1.2 Features of the Electron Beams at the Plasma Exit and the Transfer Line

The main EuPRAXIA objective in terms of beam energy lies in providing electron bunches:

- at 1 GeV, perfectly available for FEL applications as a commissioning step;
- at 5 GeV, meeting final FEL user requirements in terms of wavelength and short-pulse duration.

The performance of several schemes has been investigated in this context in terms of beam quality and subsequent efficient light production.

**LPI-150 MeV + LPAS-5 GeV (Scheme 2):** This scheme includes two plasma stages: the laser-plasma injector to produce electrons with beam energy of 150 MeV, and a laser-plasma acceleration stage to accelerate particles to the final energy of 5 GeV. In particular, the beam distribution under study, and denoted hereafter as Scheme 2-5 GeV, is injected with the resonant multi-pulse ionisation technique [170,624] and accelerated through a single stage in the quasi-linear regime [582,595].

**RFI-500 MeV + LPAS-1 / 5 GeV (Scheme 3):** In this scheme [304], a 500 MeV electron beam is injected from an RF section [625] into the plasma acceleration stage, which, in turn, accelerates the electrons up to either a beam distribution with 1 GeV [612] energy, denoted hereafter as Scheme 3-1 GeV, or a beam distribution with 5 GeV energy, denoted hereafter as Scheme 3-5 GeV.

**RFI-500 MeV + PPAS-1 GeV (Scheme 5):** In this scheme, a laser-comb configuration [323,324] produces two electron bunches: a 200 pC driver and a 30 pC witness bunch. Both are injected into the plasma acceleration stage, which, in turn, accelerates the witness bunch up to 1 GeV energy [626]. The resulting beam distribution is denoted hereafter as Scheme 5-1 GeV.

These beam distributions are analysed in terms of the main parameters driving the FEL performance. Values of emittance, energy spread, and peak current are calculated over the width of a single slice in order to have reasonable performance predictions. More in detail, the electron distribution slice with the highest current density is identified and denoted as the “best slice”. Table 24.1 shows the parameter values of the best slice at the plasma exit of the beams under study regarding FEL applications, where  $\varepsilon_{n,x(y)}$ ,  $\sigma_{x(y)}$ ,  $I_{peak}$ , and  $\sigma_E/E$  are the slice values of the normalised emittance in  $x(y)$ , the RMS size in  $x(y)$ , the peak current, and the RMS energy spread for the specified slice length  $\ell_s$ , respectively.

The best slice results are evaluated assuming that the FEL dynamics in one slice are not affected by the electron distribution in another slice if the two slices are significantly separated. However, bunch collective effects could, in principle, affect this picture and should be considered at the stage of a technical design.

The transfer line from the plasma exit stage, where the bunch leaves strong focussing fields to drift into free space, towards the undulator section is designed [606, 627] according to the following considerations:

**Table 24.1.** Best slice values of the relevant parameters at the plasma exit.

Name	$E$ [GeV]	$I_{peak}$ [kA]	$\sigma_E/E$ [%]	$\varepsilon_{n,x}$ [ $\mu\text{m}$ ]	$\varepsilon_{n,y}$ [ $\mu\text{m}$ ]	$\sigma_x$ [ $\mu\text{m}$ ]	$\sigma_y$ [ $\mu\text{m}$ ]	$\ell_s$ [ $\mu\text{m}$ ]
Scheme 2-5 GeV	4.98	2.93	0.108	0.53	0.59	0.87	0.92	0.11
Scheme 3-5 GeV	5.41	2.85	0.046	0.38	0.32	1.06	0.98	1.3
Scheme 5-1 GeV	1.07	1.95	0.098	0.67	0.59	0.83	0.98	0.9
Scheme 3-1 GeV	1.09	1.88	0.923	0.4	0.41	2.2	2.2	1.2

- the growth of both emittance and energy spread has to be minimised along the line;
- the maximum total length is 8 m and the focussing gradients are chosen to be 700 T/m for the permanent magnet and 100 T/m for the electromagnetic quadrupoles.

Moreover, each beam distribution in Table 24.1 has to be properly matched to the undulator configurations to be discussed in the following section. Further details on the beam transfer lines to the undulator section are also found in Chapter 19.

### 24.1.3 Undulator Line Characteristics

In an FEL, electromagnetic radiation is attained by wiggling the electrons, subject to the periodic magnetic field of an undulator and specified by the undulator period  $\lambda_u$  and the deflection strength parameter  $K$ . These quantities define the resonant FEL wavelength  $\lambda_R$  as

$$\lambda_R = \frac{\lambda_u}{2\gamma^2} (1 + a_u^2), \quad K = \frac{eB_0\lambda_u}{2\pi m_e c}, \quad (24.1)$$

where  $\gamma$  is the beam energy Lorentz factor,  $a_u = K/\sqrt{2}$  ( $a_u = K$ ) for planar (helical) undulators,  $B_0$  is the peak magnetic field value, and  $e$ ,  $m_e$ , and  $c$  are the electron charge, the electron mass, and the speed of light, respectively.

The main parameter quantifying FEL performance is the Pierce parameter  $\rho$  [219, 628–631]. It depends on undulator parameters and on the bunch current density  $j$ , from which the cooperation length  $L_c$  is derived as follows:

$$\rho \propto \frac{\sqrt[3]{j (\lambda_u K f_b(K))^2}}{\gamma}, \quad L_c = \frac{\lambda_R}{4\pi\rho\sqrt{3}}, \quad (24.2)$$

where  $f_b(K) = J_0(\xi) - J_1(\xi)$  is the planar undulator factor, with the argument

$$\xi = \frac{K^2}{2} \frac{1}{2 + K^2}$$

described in terms of the Bessel  $J_{0,1}(\xi)$  functions.

Each previously discussed beam distribution is analysed and matched to two different undulator configurations, to probe the beam phase-space features with two different cooperation lengths: one at the shortest reasonable  $\lambda_R$  and the other such that  $L_c \sim \mathcal{O}(1\%)$  at  $E = 5$  GeV and  $L_c \sim \mathcal{O}(10\%)$  at  $E = 1$  GeV. Table 24.2 shows the features of the chosen undulator configurations.

These values are perfectly feasible [632,633] with the present undulator technology, for both superconducting and cryogenic permanent magnet devices, assuming a

**Table 24.2.** Undulator configurations used for the FEL environment.

$E$ [GeV]	$\lambda_R$ [nm]	$\lambda_u$ [mm]	$K$	$B_0$ [T]
5	0.22	20	1.5	0.81
5	1.65	30	4.36	1.56
1	5.5	20	1.5	0.81
1	41	30	4.36	1.56

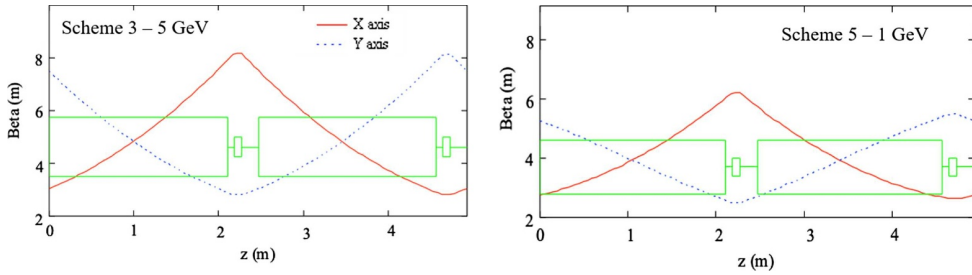


**Fig. 24.1.** Magnetic unit cell of a system made up of an undulator as well as focussing and defocussing quadrupoles for the  $\lambda_u = 3$  cm configuration, associated with the specified electron beams and superimposed with the longitudinal profiles of their Twiss  $\beta_x$  (solid red line) and  $\beta_y$  (dotted blue line) functions.

minimum undulator gap of 6 mm. This choice mitigates the wakefield-deteriorating effects inside undulators. In-vacuum undulators are expected to provide slightly smaller  $B_0$  and  $K$  values compared to those of Table 24.2. A more detailed analysis of different possible undulator technologies can also be found in Chapter 18. At both 1 GeV and 5 GeV electron beam energies, the natural focussing of the undulator is rather weak. In order to maintain a small transverse size of the electron beam, the periodic magnetic cell thus has to include alternate gradient quadrupoles between undulator modules.

As an example, Figure 24.1 shows the resulting  $\beta_{x,y}$  values as a function of  $z$  when matching the electron beams of Table 24.1 to the undulator configuration with  $\lambda_u = 3$  cm and  $K = 4.36$ .

The strategy to match the beams is based on minimising the difference between average Twiss  $\beta$  values,  $|\langle\beta_x\rangle - \langle\beta_y\rangle|$ , while also featuring reasonable magnetic gradients for both the short- and the long- $\lambda_u$  configurations. The undulator period and strength clearly define the Twiss  $\alpha$  and  $\beta$  parameter values that the electron beams should have at the undulator entrance to be correctly matched.

#### 24.1.4 FEL Results

After a proper transport of the beams to the undulator entrance, the best slice parameters have the values described in Table 24.3. As a first step, these values are used to estimate the FEL performance by means of semi-analytical formulae [219,628–631].

Within this picture, the main parameters quantifying the FEL performance are the gain length  $L_{G,3d}$  and the saturation power  $P_{sat}$ , both depending on the Pierce parameter in the following way:

$$L_{G,3d} \simeq \chi\left(\rho, \frac{\sigma_E}{E}, \langle\varepsilon_n\rangle, \langle\beta\rangle\right) \frac{\lambda_u}{4\pi\rho\sqrt{3}}, \quad P_{sat} \simeq \Phi\left(\rho, \frac{\sigma_E}{E}, \langle\varepsilon_n\rangle, \langle\beta\rangle\right) \rho P_E, \quad (24.3)$$

**Table 24.3.** Best slice values of the relevant parameters at the undulator entrance and expected cooperation lengths.

Name	$E$ [GeV]	$I_{peak}$ [kA]	$\sigma_E/E$ [%]	$\langle \epsilon_n \rangle$ [ $\mu\text{m}$ ]	$\langle \beta \rangle$ [m]	$L_c^2$ [cm]	$L_c^3$ [cm]
Scheme 2-5 GeV	4.96	2.63	0.052	0.58	5	20	61
Scheme 3-5 GeV	5.41	2.74	0.052	0.34	5	14	42
Scheme 3-1 GeV	1.09	1.75	0.103	0.44	4	140	430
Scheme 5-1 GeV	1.07	1.06	0.047	0.55	4	320	990

**Table 24.4.** FEL semi-analytical results for the short-undulator-period configuration based on the best slice parameters of Table 24.3.

Name	$\lambda_R$ [nm]	Pierce $\rho$ [%]	$L_{G,3d}$ [m]	$P_{sat}$ [GW]
Scheme 3-5 GeV	0.19	0.099	1.7	4.39
Scheme 2-5 GeV	0.3	0.084	2.74	1.75
Scheme 3-1 GeV	4.67	0.236	0.59	1.94
Scheme 5-1 GeV	4.86	0.188	0.63	1.29

where  $\chi$  and  $\Phi$  are correction functions accounting for energy spread and emittance contributions, and  $P_E$  is the power associated with the electron beam. Then, as a second step, the full longitudinal behaviour of each electron beam distribution is analysed in the self-amplified spontaneous emission (SASE) mode, and the FEL performance is evaluated with the PERSEO simulation code [634], which allows to perform a full time-dependent simulation of the FEL dynamics in a fast way, taking into account the proper energy, current, and energy spread profiles along the bunch. This feature is of particular relevance for the electron bunches under study as the current distribution is not Gaussian and with long asymmetric tails, and as the energy spread distribution exhibits abrupt variations. Furthermore, the time-dependent analysis allows a reliable estimate of the FEL pulse duration and spectrum line width, improved with the aforementioned longitudinal dynamics-deteriorating effects.

Figures 24.2 and 24.3 show the longitudinal slice profiles of energy, current, energy spread, and normalised emittance for the 5 GeV and 1 GeV beam distributions, respectively. In all cases, the normalised emittance is assumed to be constant as the associated variations affect the effective saturation length less dramatically.

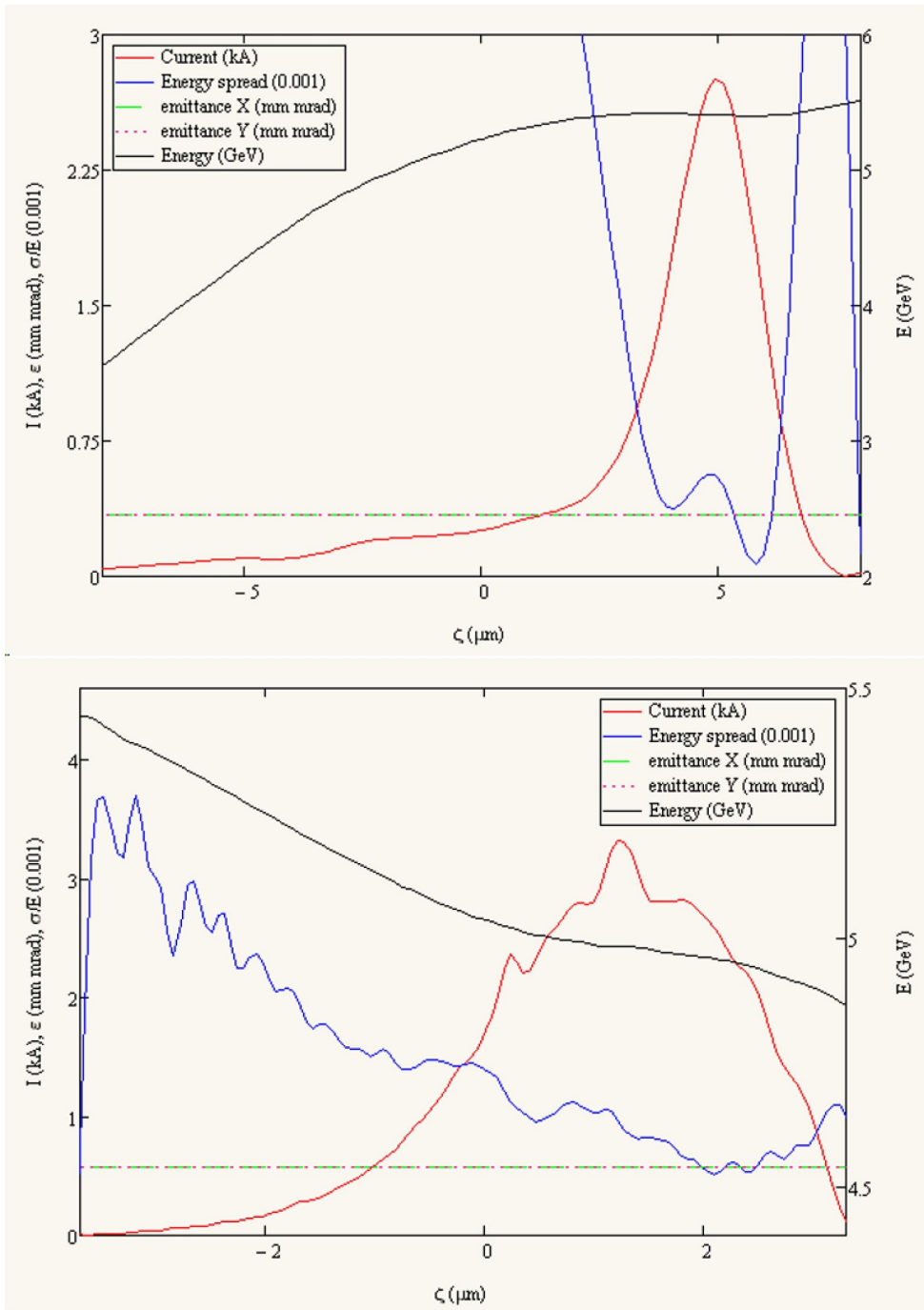
## Results with the Short-Undulator-Period Configuration

Table 24.4 shows the FEL results on gain length and saturation power targeting the short resonant wavelength, featuring inhomogeneous broadening effects based only on the best slice parameters.

The normalised emittance value in Scheme 2-5 GeV, which is higher than in Scheme 3-5 GeV, results in a higher gain length and lower saturation power.

The results of the time-dependent simulations obtained with longitudinal dynamics are shown in Table 24.5. The already mentioned argument of a high normalised emittance in Scheme 2-5 GeV is enforced in the time-dependent analysis resulting in a long saturation length and in a small number of photons per pulse. At saturation, Scheme 3-1 GeV and Scheme 5-1 GeV have a similar number of photons per pulse; a lower current profile in Scheme 3-1 GeV is compensated by a smaller normalised emittance than in Scheme 5-1 GeV.

Figures 24.4 and 24.5 show the evolution of the SASE FEL energy per pulse for the beam distributions matched to the short-undulator-period configuration, for



**Fig. 24.2.** Energy, current, energy spread, and normalised emittance slice profiles as a function of the intra-bunch  $\zeta$  coordinate, for the beam distributions of Scheme 3-5 GeV (top) and Scheme 2-5 GeV (bottom) at the undulator entrance.

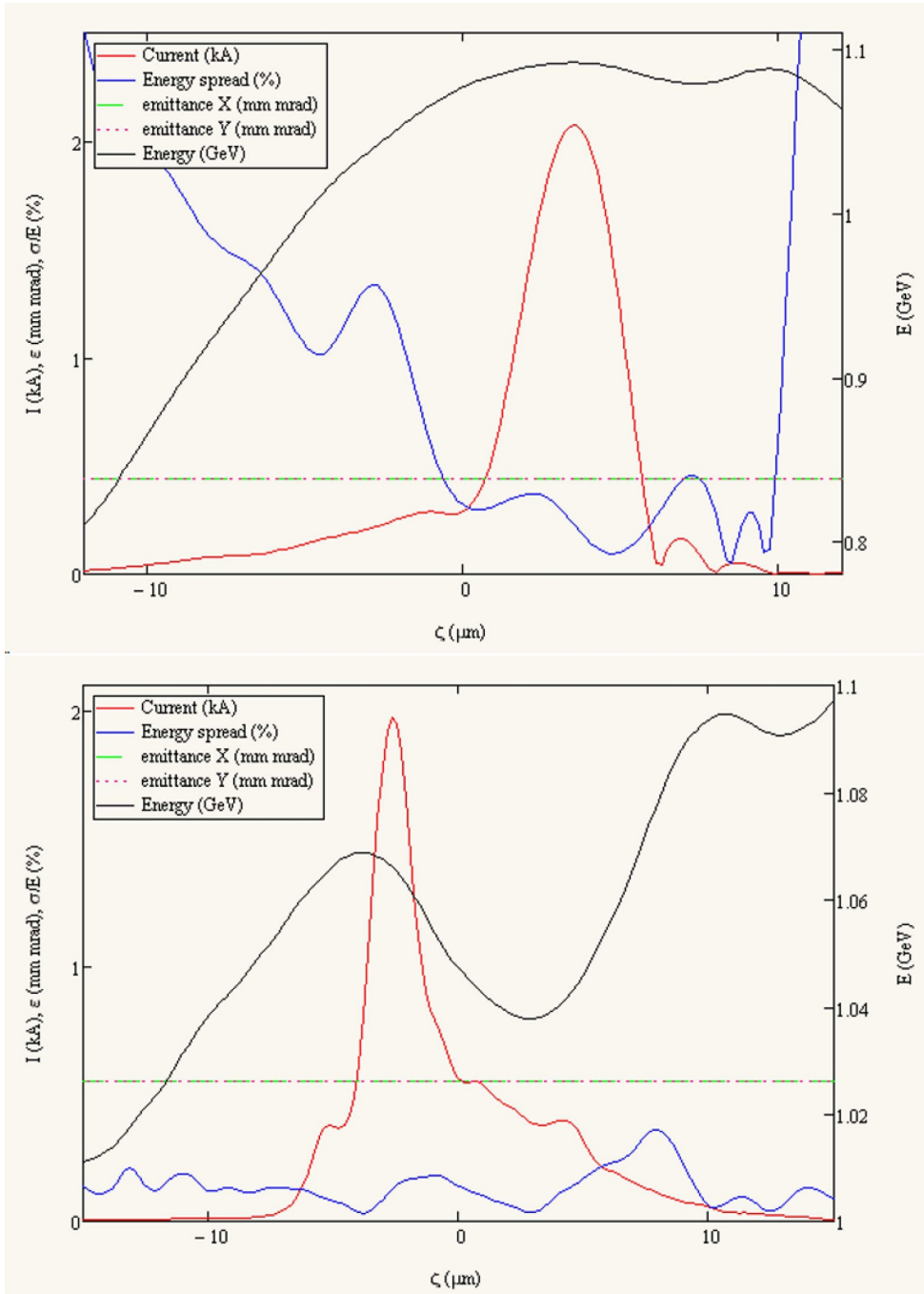


**Fig. 24.3.** Energy, current, energy spread, and normalised emittance slice profiles as a function of the intra-bunch  $\zeta$  coordinate, for the beam distributions of Scheme 3-1 GeV (top) and Scheme 5-1 GeV (bottom) at the undulator entrance.

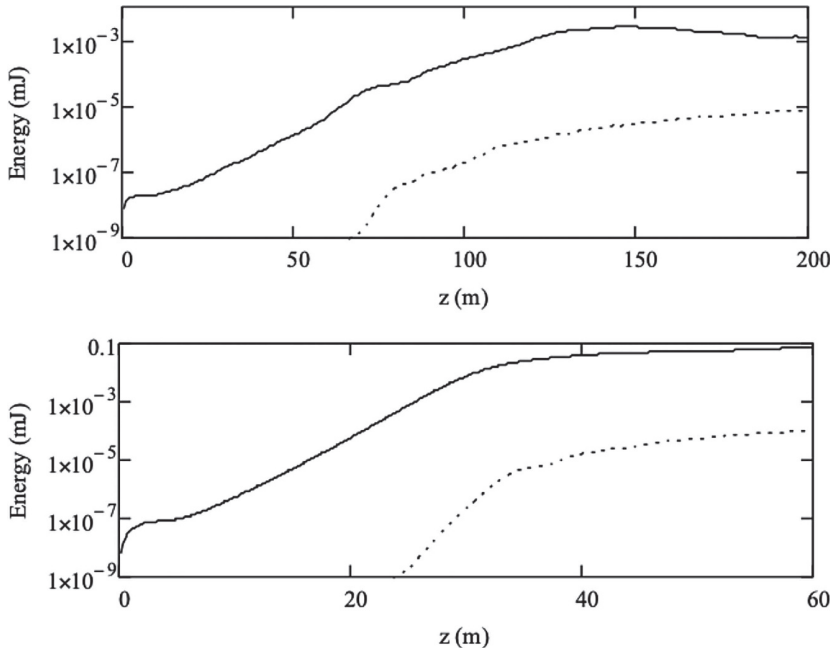


**Fig. 24.4.** Growth of the SASE FEL energy per pulse of Scheme 2-5 GeV (top) and Scheme 3-5 GeV (bottom) beam distributions with the short-undulator-period configuration. The fundamental (solid line) and third (dotted line) harmonics are shown.

**Table 24.5.** Results of the time-dependent simulations with longitudinal dynamics, obtained with PERSEO, for the short-undulator-period configuration.

Name	Saturation length [m]	Linewidth [%]	Pulse duration [fs]	Photons per pulse [ $10^{10}$ ]	Brightness [ $\times 10^{30} \text{ s}^{-1} (\text{mm mrad})^{-2} (0.1\% \text{bw})^{-1}$ ]
Scheme 2-5 GeV	126	0.18	0.4	0.19	3.7
Scheme 3-5 GeV	38	0.23	2.0	3.2	40
Scheme 3-1 GeV	28	0.25	2.4	2.3	0.5
Scheme 5-1 GeV	16	0.59	2.0	1.3	0.08

both fundamental and third harmonics. The curves suggest that targeting the shorter resonant wavelength is within reach for 1 GeV beams, while it demands extremely high-quality 5 GeV beam distributions, with very low energy spread and normalised emittance values.

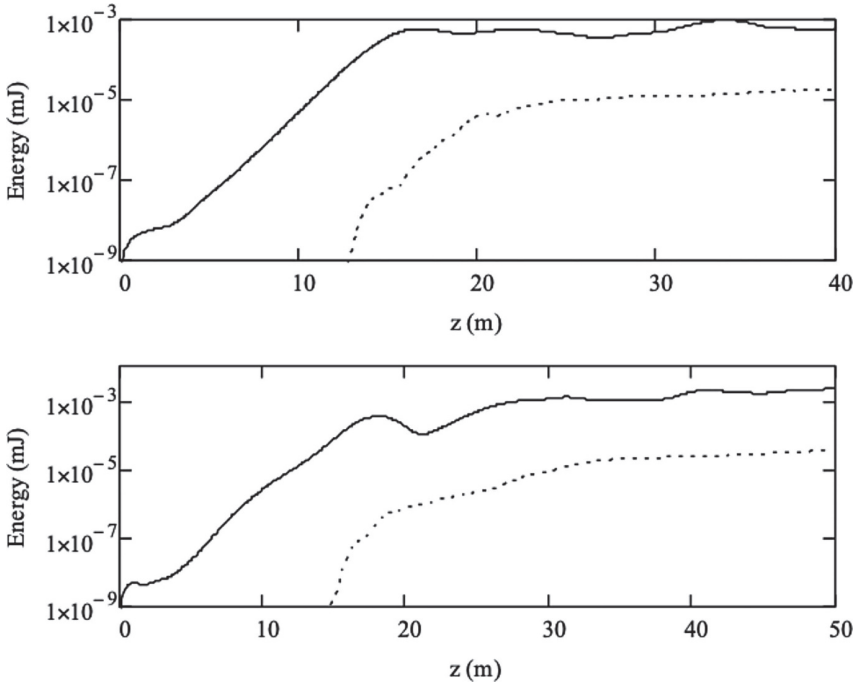
### Results with the Long-Undulator-Period Configuration

Table 24.6 shows the FEL results on gain length and saturation power targeting the long resonant wavelength, featuring inhomogeneous broadening effects based only on the best slice parameters.

The considerations described discussing Table 24.4 above apply also to this case.

The results of the time-dependent simulations obtained with longitudinal dynamics are shown in Table 24.7.

A larger undulator period and strength yield a significantly larger Pierce  $\rho$  parameter in each beam distribution. The effective result is a significantly better FEL performance in terms of saturation length, brightness, and photons per pulse, while



**Fig. 24.5.** Growth of the SASE FEL energy per pulse of Scheme 5-1 GeV (top) and Scheme 3-1 GeV (bottom) beam distributions for the short-undulator-period configuration. The fundamental (solid line) and third (dotted line) harmonics are shown.

**Table 24.6.** FEL semi-analytical results for the long-undulator-period configuration based on the best slice parameters of Table 24.3.

Name	$\lambda_R$ [nm]	Pierce $\rho$ [%]	$L_{G,3d}$ [m]	$P_{sat}$ [GW]
Scheme 3-5 GeV	1.4	0.23	0.83	17.8
Scheme 2-5 GeV	1.67	0.2	0.94	14
Scheme 3-1 GeV	34.5	0.57	0.36	4.94
Scheme 5-1 GeV	35.9	0.45	0.44	2.51

**Table 24.7.** Results of the time-dependent simulations with longitudinal dynamics, obtained with PERSEO, for the long-undulator-period configuration.

Name	Saturation length [m]	Linewidth [%]	Pulse duration [fs]	Photons per pulse [ $10^{10}$ ]	Brightness [ $\times 10^{30}$ $s^{-1}(\text{mm mrad})^{-2} (0.1\% \text{bw})^{-1}$ ]
Scheme 2-5 GeV	26	0.3	0.71	4.2	27.6
Scheme 3-5 GeV	20	0.3	2.2	72	475
Scheme 3-1 GeV	16	0.54	7.8	31	0.86
Scheme 5-1 GeV	23	3.6	15	16	0.02

keeping a good quality spectrum line width and pulse duration, clearly targeting a significantly longer resonant wavelength at a given beam energy. Figures 24.6 and 24.7 show the evolution of the SASE FEL peak power for the beam distributions matched to the long-undulator-period configuration, for both fundamental and third harmonics. All beam distributions conceptually show a fair performance in realising compact SASE FEL facilities driven by a plasma-acceleration stage.

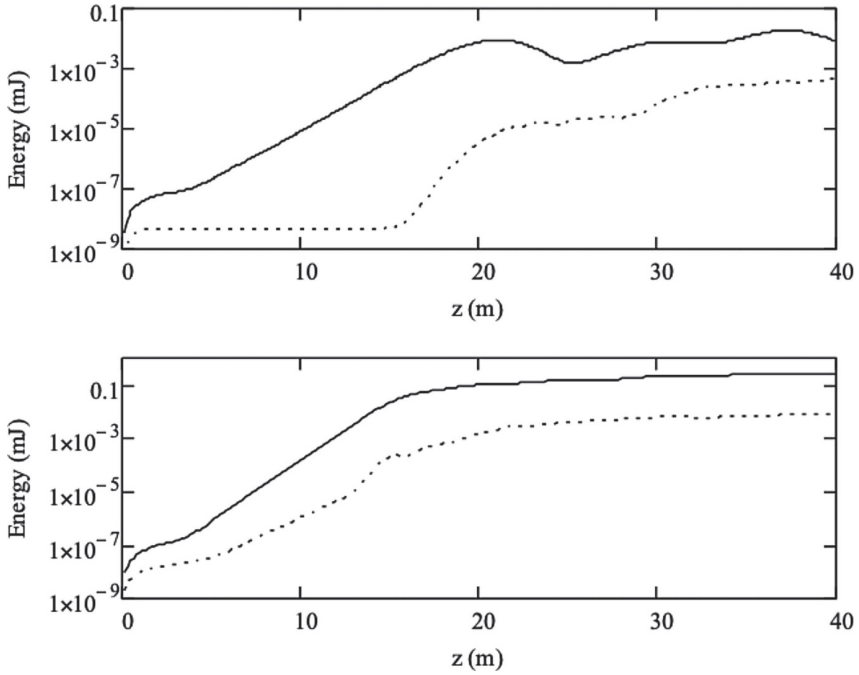


**Fig. 24.6.** Growth of the SASE FEL energy per pulse of Scheme 2-5 GeV (top) and Scheme 3-5 GeV (bottom) beam distributions for the long-undulator-period configuration. The fundamental (solid line) and third (dotted line) harmonics are shown.

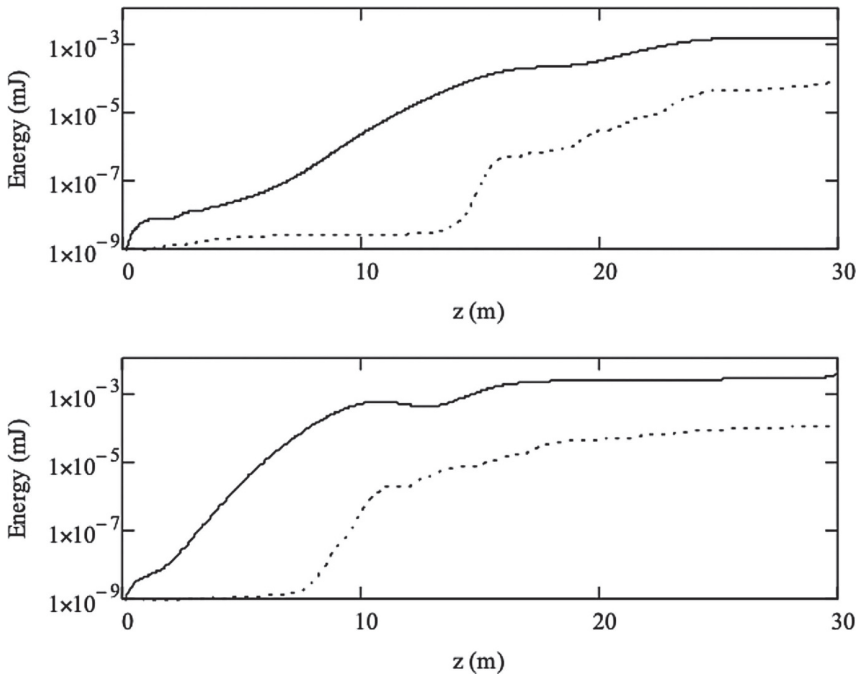


**Fig. 24.7.** Growth of the SASE FEL energy per pulse of Scheme 5-1 GeV (top) and Scheme 3-1 GeV (bottom) beam distributions for the long-undulator-period configuration. The fundamental (solid line) and third (dotted line) harmonics are shown.

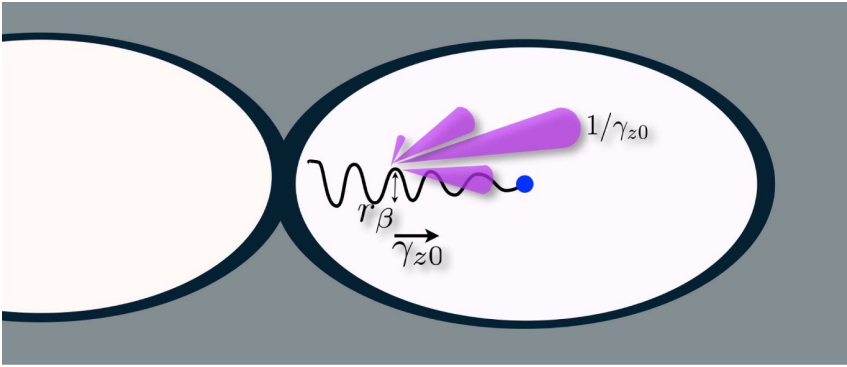


**Fig. 24.8.** Cartoon of the trajectory of an electron with maximum Lorentz factor  $\gamma_{z0}$  being accelerated in a non-linear wakefield with an offset of  $r_\beta$ , which leads to a strong synchrotron emission within a cone angle of  $1/\gamma_{z0}$ .

#### 24.1.5 Conclusion

We have analysed some of the most promising electron beam distributions arising from dedicated design studies on injection and – both laser- and particle-driven – plasma acceleration stages, adopting present and near-future solutions for the undulator technology and producing FEL radiation in the SASE configuration. In particular, we have performed time-dependent simulations with full longitudinal dynamics for each beam distribution, targeting two different resonant wavelengths.

At a given beam energy, short resonant wavelengths demand for extremely high-quality beams, with the highest current density and lowest energy spread characteristics extended over many slices of the bunch. In more detail, wavelengths of the order  $\mathcal{O}(1 \text{ nm})$  are perfectly within reach in such a FEL facility operating in the SASE mode and matching to a rather compact undulator section.

## 24.2 Betatron X-Ray Source

### Betatron Radiation from Wakefield Accelerators

Plasma wakefield accelerators typically exhibit a strong focussing force for forward-going electrons, created by the radial displacement and longitudinal motion of the plasma wave electrons. Electrons with an initial offset from the central axis of the accelerator, or with some initial transverse momentum, will thus oscillate around this axis as they propagate, as shown in Figure 24.8. The resulting wiggling motion leads to the emission of synchrotron radiation, referred to as “betatron radiation”.

Betatron radiation from plasma accelerators has some unique features as compared to other synchrotron radiation sources. In much the same way as the accelerating forces in a plasma accelerator are greater than those in a conventional accelerator, so are the focussing forces also many orders of magnitude greater. They typically reach an order of  $E \approx E_0 = mc\omega_p/e \approx 0.1 \cdot [n_e (\text{m}^{-3})] \text{ Vm}^{-1}$ . For a plasma of density of  $10^{18} \text{ cm}^{-3}$ , this creates fields of magnitude  $\approx 10^{11} \text{ Vm}^{-1}$  over distances on the scales of tens of micrometres. In these fields, the electrons wiggle with a betatron frequency and wavelength given by the following:

$$\omega_\beta = \omega_p / \sqrt{2\gamma_{z0}}; \quad \lambda_\beta = \sqrt{2\gamma_{z0}} \lambda_p,$$

where  $\gamma_{z0}$  is the Lorentz factor due to the longitudinal motion of the electron. For typical densities used to generate GeV-scale electron beams ( $n_e \approx 10^{18} \text{ cm}^{-3}$ ), a 1 GeV electron would have  $\lambda_\beta \approx 2 \text{ mm}$ . This compares to the undulation period of conventional (magnet-based) undulators, which can be of the order of tens of millimetres. Hence, plasma-based undulators can be much more compact, in the same way that plasma-based accelerators have advantages in scale.

But, of course, the short undulation period and thus correspondingly high betatron frequency mean that the radiation produced is also of higher frequency. For low amplitude undulation, the emitted energy is just the Doppler-upshifted photon energy,  $E_u \simeq 2\gamma_{z0}^2 \hbar\omega_\beta$ . For this to be valid, the undulator parameter  $\alpha_\beta$  (also often denoted as  $K$ ) given by,

$$\alpha_\beta = \gamma_{z0} r_\beta \omega_\beta / c,$$

should be less than one ( $\alpha_\beta < 1$ ).  $\alpha_\beta$  is a measure of the transverse momentum of the oscillation and thus is analogous to the normalised momentum discussed for electrons in a laser field. To have large oscillations, betatron sources commonly use self-injection where the injected electrons are those which were initially part of the plasma-wave motion. Hence, they have energies when arriving on axis comparable to the ponderomotive potential, which generated the plasma wave  $E_{\text{pond}} \simeq a_0 m c^2$ . As the electrons are accelerated, the oscillation amplitude  $r_\beta$  decreases due to the relativistic increase in the electrons inertia but the energy associated with the transverse motion stays almost unchanged. This means that  $r_\beta$  is typically of the order of micrometres at the point where the electrons have their highest energy [635]. This is important because this is when the electrons are also radiating the most, and so the source size is also of the order of  $1 \mu\text{m}$ . This small source size has some advantages, which will be discussed later.

Yet, despite these small excursion sizes caused by the high betatron frequency for the parameters given before (GeV electrons accelerated in  $n_e \approx 10^{18} \text{ cm}^{-3}$  plasmas),  $\alpha_\beta \approx 10$ , and the resulting motion is strongly non-linear. As  $\alpha_\beta$  becomes greater than 1, the non-linearities induced in the electron motion produce harmonics of the fundamental Doppler-upshifted undulator radiation. The higher  $\alpha_\beta$ , the higher the harmonic content, and including the effect of the increasing electron energy and the range of  $r_\beta$  that would be present (not all electrons are injected with the same momentum), a continuous spectrum is formed similar to the usual synchrotron spectrum [635,636]. The synchrotron spectrum has a peak in the spectral brightness and is usually characterised by a *critical energy* as follows:

$$E_{\text{cr}} = \frac{3}{2} a_\beta \gamma_{z0}^2 \hbar\omega_\beta,$$

which is defined as the point in the spectrum, where half of the energy is located above and half is below. The critical energy is close to the energy with the peak spectral brightness. Note that the frequency of this radiation scales as  $\gamma_{z0}^3$  times the betatron frequency because of the dependence of  $\alpha_\beta$  on  $\gamma_{z0}$ . This means that, even for modest electron energies, the radiation is in the multi-keV range [637]. For example, in experiments performed at the Gemini facility at the Rutherford Appleton Laboratory, acceleration of electrons to  $\sim \text{GeV}$  energies ( $\gamma_{z0} \approx 2000$ ) in plasmas of densities  $n_e \approx 10^{18} \text{ cm}^{-3}$  led to critical energies in excess of 20 keV [75,638]. Indeed, the photon energies from betatron radiation exceed those of most synchrotron sources except in specialised beamlines.

The (mean) power radiated by an electron experiencing this undulating motion is given by the following equation:

$$\bar{P} = \frac{e^4 \gamma_{z0}^2 \kappa^2 r_\beta^2}{12\pi \epsilon_0 m^2 c^3},$$

**Table 24.8.** Important properties of a plasma betatron-radiation source and their implications.

Property	Symbol	Characteristic Value	Implication
Hard photon energy	$E_{\text{crit}}$	$> 25 \text{ keV}$	Deeply penetrating
Small source size	$r_{\beta}$	$\sim \mu\text{m}$	Exhibits high spatial resolution
Small divergence	$\theta$	$\sim 10 \text{ mRad}$	Makes beamline
Short pulse	$\tau$	$\sim 10 \text{ fs}$	Ultra-fast dynamics
Bright	$N_{\text{ph}}$	$> 10^9$ (photons per shot)	Single-shot imaging

where  $\kappa$  is the gradient of the focussing field strength. Despite the small oscillation amplitudes, the strong fields give rise to a substantial photon yield, with almost one photon produced per electron. A single shot can produce upwards of  $10^8$  photons, more than enough to do single-shot imaging of moderately sized objects ( $\sim \text{cm}$ ).

The high photon energy is not the only interesting property of these sources. Given the small spatial scales of the accelerator, the region from which the radiation is emitted is also very small, both transversely and longitudinally. The length of the X-ray beam can be controlled by changing the distance over which electrons are injected and accelerated. In addition, high-charge (100 pC) electron beams can be readily produced with a bunch duration that is less than half of the plasma period [639]. Experimental measurements have shown that electron bunches can be a few femtoseconds in duration with peak current of a few kA [550]. The emitted radiation is set by the electron bunch duration and so is a highly attractive source for measurements on the finest temporal scales.

Furthermore, the transverse extent of the radiation is also small, comparable to the amplitude of the undulator oscillation when the electrons reach their highest energy. This is, as noted above, typically of the order of  $\sim \mu\text{m}$ . This small source size allows for high-resolution imaging in a compact imaging setup, without the need for expensive and difficult-to-align X-ray optics. Furthermore, the X-rays are “beamed” by the relativistic electrons that emit them, which enables high-magnification imaging without sacrificing imaging brightness greatly. But perhaps the most interesting manifestation of this small source size, is that it allows the beam to exhibit spatial coherence in a compact arrangement. This enables enhanced imaging modalities, specifically phase-contrast imaging, which will be discussed in more detail below.

Table 24.8 lists some of the interesting properties of the plasma betatron-radiation sources and also the implications of these properties.

In the next section, we expand a little on these interesting properties of betatron-radiation sources, and outline a plan for implementing a dedicated betatron beamline within the applications area of the EuPRAXIA facility. Finally, we give some example applications.

## Implementation of a Betatron Source at EuPRAXIA

The first measurements of betatron radiation from a plasma accelerator were made by S. Wang and co-workers on the E-157 plasma-wakefield experiment at SLAC [640]. They measured  $\approx 15 \text{ keV}$  photons produced by 28.5 GeV electrons. Betatron radiation was soon measured from laser-wakefield-acceleration experiments. Using a laser with many tens of TW power to produce electrons with energies up to 200 MeV, Rousse and co-workers at the LOA in France [573] were able to measure photons with critical energies in the few keV range [641]. The high densities that these LWFA experiments



**Fig. 24.9.** Conceptual visualisation of a betatron beamline at the proposed EuPRAXIA laser-driven construction site (based on the CAD model in Sect. 32.9 of the appendix).

work at mean that the scale of the source was reduced from the metre-length E-157 experiment down to sub-centimetre scales.

A step forward in usability of these sources was achieved by using a plasma accelerator in the self-injecting self-guiding mode (“bubble regime”). In these experiments, a significant increase in spectral brightness (by more than three orders of magnitude) was achieved by being able to accelerate large numbers of particles to high energy [637]. More than  $10^8$  photons per shot were produced, which was more than sufficient for single-shot imaging [637]. Performing these measurements with greater than 100 TW lasers has allowed the critical energy to be extended to well over 30 keV, which allows for uses in studying dense media [75,638].

Considerations for radiation emission in this highly non-linear regime gives scalings of electron beam energy, betatron critical energy, and photon number, which increase monotonically with laser power. These scalings have now been thoroughly tested in numerical simulations [635] and in experiments. Though petawatt lasers are already operational, there has been little work in the strongly driven regime, which is ideal for betatron applications.

Both plasma-wakefield beams and laser-wakefield drivers can be used as drivers for betatron radiation sources, but, as noted, the significantly higher densities of operation of laser drivers to reach the bubble (“blow-out”) regime is advantageous in terms of photon energies, numbers, pulse lengths, and source sizes. Hence, it is proposed that the LWFA driver that will be usually used to drive a laser-wakefield stage be redirected to a dedicated applications area where a betatron source can be installed. A conceptual visualisation of such a beamline is shown in Figure 24.9.

Using the considerations given in the first section and some of the scalings presented in [575], Table 24.9 gives the expected scalings in photon properties for the PW-class laser that will drive the laser accelerators in EuPRAXIA.

### Applications of Betatron Sources

As we have noted, there are numerous synchrotron facilities, each with beamlines dedicated to enhance their applicability for particular uses. But an application beamline based on a betatron radiation source has a number of useful intrinsic properties that

**Table 24.9.** Scalings for betatron radiation from established scaling laws ([575]). The figures for 10 and 100 TW systems agree well with reported measurements.

Laser power	10 TW	100 TW	1 PW
Pulse duration $\tau$ (fs)	12	37	120
Spot size $w_0$ ( $\mu\text{m}$ )	4	10	35
Plasma density $n_e$ ( $\text{cm}^{-3}$ )	$5 \times 10^{19}$	$5 \times 10^{18}$	$5 \times 10^{17}$
Plasma length (mm)	$90 \times 10^{-3}$	3	90
Peak electron energy $\gamma m_e c^2$ (MeV)	60	600	$6 \times 10^3$
Beam charge (nC)	0.1	0.4	1
X-ray energy (keV)	0.6	8	110
Source size ( $\mu\text{m}$ )	1.4	1.8	2.4
Divergence $\theta$ (mrad)	70	7	0.7
Undulator parameter $\alpha_\beta$	7	9	12
Peak X-ray brightness *	$2 \times 10^{21}$	$3 \times 10^{23}$	$1 \times 10^{26}$
Photon number	$2 \times 10^8$	$3 \times 10^9$	$4 \times 10^{10}$

\*Units for peak X-ray brightness are photons /( $\text{mm}^2 \text{mrad}^2 \text{s}^{-1} 0.1\% \text{BW}$ ).

can be exploited for particular investigations. Furthermore, the relatively small size and cost of a betatron facility could mean that applications of synchrotron radiation could become more widespread if such facilities were developed. In particular, synchrotron techniques could supplant widespread X-ray techniques that are based on first-generation X-ray sources. Of particular note is the short pulse length, high photon energy, synchronised secondary beams and small source size, which make certain applications relatively easy to implement using a betatron source as compared to other X-ray radiation sources. Though many of these applications have or are being pursued in proof-of-principle experiments, the higher energy, relatively high repetition rate, and industrial robustness of the (laser) drivers would mean a betatron source based on EuPRAXIA would be a major step towards dedicated betatron radiation facilities.

### Synchrotron Applications

The EuPRAXIA betatron source would have sufficient average photon yield to allow various types of experimental stations for spectroscopy, diffraction, and imaging experiments, as are common in existing synchrotron facilities. In particular, it would potentially be the first betatron source to be run at a consistent repetition rate (minimum of 10 Hz) promising time-averaged photon brightness in excess of  $10^{13}$  photons /( $\text{mm}^2 \text{mrad}^2 \text{s}^{-1} 0.1\% \text{BW}$ ), many orders of magnitude greater than available with other common laboratory sources [75].

### Lensless Imaging

The small source size and high photon energy already make betatron radiation sources interesting for standard radiography applications. It allows the high-resolution imaging of dense matter, such as bone specimens or materials of interest in industrial manufacturing with a compact size [75]. The petawatt betatron source at EuPRAXIA offers to take this a step further, with its higher photon energy. This allows imaging of even denser objects, in particular in vivo imaging of humans, which takes photon energies in excess of 100 keV. For such a high photon energy, optics are not readily

available, so coupling the small sources to a beam with reasonable divergence allows high-resolution imaging in a compact size. This can be a considerable advantage over other synchrotron sources, where the beam has to be conditioned to offer similar abilities.

The other advantage of the small source size is that it offers an appreciable degree of spatial coherence. This can be most readily taken advantage of in free-propagation phase-contrast imaging (PCI). Again, the natural properties of the source allow X-ray PCI to be carried out without additional optics such as gratings, which are required for other X-ray sources. Phase-contrast imaging offers increased contrast and the ability to demarcate features in specimens which offer relatively little absorption contrast. This has been demonstrated on small biological [637,642] and industrial samples, especially those of low-Z materials, such as carbon fibres, and those made by additive manufacture. The higher repetition rate of EuPRAXIA offers full 3D tomographic reconstruction capabilities of such objects in a fraction of the time that it takes with many other PCI solutions [643]. The higher energies available make it possible to visualise soft tissue such as cancerous liver or kidney lesions, removing the need for a contrast agent. Though the advantages of PCI for this type of work have been proven, progress has been held back due to the lack of suitable X-ray sources with the necessary spatial coherence properties or due to the requirement for cumbersome imaging techniques. A EuPRAXIA-based synchrotron source using betatron radiation would make a valuable contribution to advancing this field.

### Coherent Imaging

Of course, it is well known that the small wavelength of X-rays allows imaging features of size comparable to the radiation wavelength. In the case of hard X-rays produced by a petawatt betatron source, we can expect to be able to resolve features in the nanometre to ångström range. For objectives approaching the wavelength of the radiation, direct imaging is not possible, but instead we rely on diffractive imaging. Even when specimens do not crystallise, computational techniques can be used in a lensless imaging scheme to infer the structure of a specimen from the diffraction pattern so long as the X-ray probe is temporally and spatially coherent. Again, considering the often large scattering angle, it is impractical to use X-ray optics, and so lensless imaging configurations are ideal. Temporal coherence is inversely proportional to spectral width and can be achieved with crystal monochromators, as used in other synchrotron facilities. Though this can greatly reduce the available flux – typical monochromators will reduce the spectral brightness by at least  $10^6$  –, this can be compensated somewhat by the higher repetition rate proposed for the EuPRAXIA beamline. Spatial coherence increases proportionally with the distance from the source and with the inverse of the source size. This means conventional X-ray tubes and even synchrotron light sources must be apertured, which becomes difficult for hard X-rays, thus reducing the available photon flux and increasing the required exposure time. Once again, the inherent small size of betatron sources makes them attractive for this application.

### Ultra-Fast Studies

As has been noted, the inherently ultra-fast nature of the betatron source, coupled to the fact that it can be synchronised to numerous other radiation sources, makes it an attractive platform for numerous pump-probe experiments. The secondary radiation source can be other laser beams, but also particle beams that can be generated with lasers. There are two types of dynamic processes, which could be particularly interesting to implement on a betatron beamline.

The first are ultra-fast processes, where an interaction initiated by a secondary source is then followed over subsequent steps by taking multiple shots with varying delay between the pump and a betatron probe. This has been used in proof-of-principle experiments to study the propagation of shocks in dense media. The betatron beam need not only be used in imaging mode, but can also be used for X-ray Thomson scattering, or even for spectroscopy. Indeed, the broad bandwidth of the betatron source is ideal for ultra-fast absorption spectroscopy.

The other type of interaction, where a high-repetition-rate, short-pulse X-ray source is advantageous, is in the study of longer-scale dynamic effects. Examples for this are the motion in biological systems, e.g. the respiration of insects and the motion of wings, as well as gradual material effects, e.g. the growth of dislocations in materials, annealing and nucleation processes. Here the pulsed nature of the betatron sources is useful in reducing motion blur.

## Gamma-Rays

The availability of petawatt laser energies at EuPRAXIA will extend photon energies to beyond 100 keV, which is not widely available in synchrotron laboratories. As already noted, the greater penetration of these photons can be used in imaging macro-scale objects, such as cracks in airplane wings. They can also be used to identify high-Z materials, such as for use in the discrimination of glass fragments for forensic analysis, which require photon energies in excess of 100 keV. Indeed, the higher end of this photon spectrum can be considered as  $\gamma$ -rays and can be used for nuclear-induced applications. Gamma radiation can be used to identify and study nuclear materials. It can also be used in nuclear resonance fluorescence to study the nuclear structure or identify isotopes, potentially even pumping a gamma laser. Finally gamma-ray radiography is routinely used to scan cargo for security applications.

The EuPRAXIA laser-plasma beamlines based on industrially robust laser systems offer the opportunity to have a first generation of user experiments based on plasma-accelerator technologies. One of the premier applications for this type of system will be a betatron beamline that can provide high quality X-rays for a number of different types of experiments. Betatron radiation sources could potentially be the first type of plasma-based accelerator device to be used as the basis of an accelerator facility.

## 24.3 Compton Source

### Applications of Gamma Sources

The inverse Compton scattering (ICS) end station at EuPRAXIA will aim to generate unique sources of high-energy ( $>100$  keV) photons, which, in theory, would be tunable up to 300 MeV. The low divergence and small source size allow the study of nuclear physics as well as the interrogation of high-areal-density samples, which may be of interest for security screening at ports.

High-quality, high-energy photon sources are important for nuclear physics as demonstrated by the success of the Hi $\gamma$ S facility at TUNL. With photon energies in excess of 100 MeV, it will be possible to produce pions and perhaps even heavier exotic particles from the “clean” photon rather than particle collisions.

The highly penetrating nature of such gamma-rays also allows for the interrogation of high-areal-density materials for security purposes.

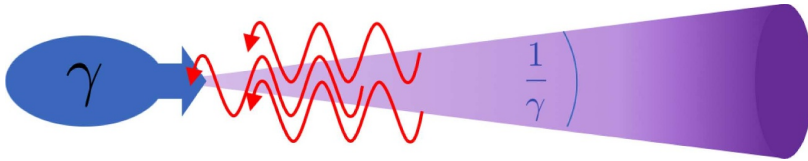


**Fig. 24.10.** Cartoon of the collision of an electron with Lorentz factor  $\gamma$  with a laser resulting in MeV radiation emission from a small spot and within a cone angle  $1/\gamma$ .

## Inverse Compton Scattering

### Introduction

Inverse Compton scattering (ICS) is the process by which light may be upshifted in frequency through collision with a moving electron. The process of X-ray production is straightforward in the photon picture, with the emitted photons experiencing a double relativistic Doppler upshift: once due to the reflection in the electron rest frame, and a second time as the interaction is transformed back into the lab frame. The emitted photon energy,  $E_\gamma$ , is dependent on the Lorentz factor of the relativistic electron,  $\gamma$ , and the angle of collision,  $\theta$ , where  $\theta = 0$  in the co-propagating geometry. This gives the following relation:

$$E_\gamma = \hbar\omega_0 \times [\gamma(1 - \cos\theta)]^2, \quad (24.4)$$

where  $\hbar\omega_0$  is the energy of the incident photon with radial frequency  $\omega_0$ . This results in the generation of high-energy (greater than 100 keV) photons from the collision of an optical laser ( $\approx$  eV) with electrons of energy above 100 MeV. Since the radiation may be considered isotropic in the rest frame of the electron, the transformation into the lab frame also results in the radiation being beamed into a small cone. The cone angle may be approximated by  $\frac{1}{\gamma}$ , as illustrated by the cartoon in Figure 24.10.

Simplifying the expression for the emission energy, by considering only the counter-propagating geometry, we obtain the following simple expression for the maximum radiation energy:

$$E_\gamma = 4\gamma^2\hbar\omega_L \quad (24.5)$$

### ICS from Wakefield Accelerators

Inverse Compton scattering from LWFA electron bunches has been demonstrated in various experiments. Ta Phuoc et al. [644] demonstrated that reflecting the LWFA drive laser from a foil at the end of the accelerator allows guaranteed temporal and spatial overlap of the electron and laser pulse. In this work, the linear scattering generated sources in the tens of keV. Such sources were also generated with a secondary laser [645] by the Umstadter group, who then extended the accessible photon energy to the MeV range by scattering from higher energy electrons [646]. In 2014, Sarri et al. reported the first instance of non-linear ICS, where the scattering laser was sufficiently intense to generate harmonics of the scattering frequency [647].

The increased interest in ICS from LWFA is driven by the uniqueness of the sources which may be generated. Much of the discussion in previous sections about the advantages of LWFA-based photon sources also apply to ICS. For example, the duration of the emission is restricted to the duration of the electron bunch allowing for radiation source durations in the range of few femtoseconds. In addition, since

**Table 24.10.** Unique properties of plasma-accelerator-based ICS radiation sources, and their implications.

Property	Symbol	Characteristic Value	Implication
High photon energy	$E_\gamma$	> 100 MeV	Deeply penetrating
Small source size	$r_{\text{ICS}}$	$\sim \mu\text{m}$	High spatial resolution
Low divergence	$\theta$	< 1 mrad	Localised irradiation
Short pulse	$\tau$	$\sim 30$ fs	Ultra-fast dynamics

the scattering comes from the laser focus, the source size can be restricted to order of 1 micrometre.

Table 24.10 lists some of the interesting properties of plasma-based inverse Compton scattering radiation sources, and also the implications of these properties.

### Considerations of ICS Source Quality from a Single Electron

Here, each property of the ICS is addressed in more realistic terms. In equation (24.5), an expression is given to demonstrate the unique photon energies accessible through ICS at EuPRAXIA. However, taking into account the observer angle,  $\theta$ , the laser strength parameter,  $a_0$ , and the electron recoil, encapsulated in  $\Delta$ , a more accurate expression is given by the following [648]:

$$E_\gamma \cong \frac{4\gamma^2 \hbar \omega_L}{1 + \gamma^2 \theta^2 + \frac{a_0^2}{2}} (1 - \Delta) \quad (24.6)$$

### Preservation of Low Bandwidth

From equation (24.6), it is clear that the bandwidth of an ICS source is only small, even in the idealised linear case, when the observation angle is small. To retain spectral selectivity, a hard aperture will be required for the beam.

In addition, if a small bandwidth is required, it will be important to ensure that the intensity of the scattering laser is low such that the spectrum is not broadened by an increase in  $a_0$ . This low laser intensity regime will also facilitate a small  $\Delta$ .

### Small Source Size and Short Pulse Duration

An advantage of ICS over other radiation mechanisms lies in the importance of the scattering laser. Since the radiation only emanates from the focal spot, the size and duration of the laser at focus will determine the size and duration of the radiation source.

### Low Divergence

As illustrated in Figure 24.10, the divergence of the emission from an electron is given by  $\frac{1}{\gamma}$ . Again, this is only preserved for scattering at linear laser intensities ( $a_0 < 1$ ).

## Electron Bunch Considerations

Thus far, arguments for high beam quality have been based on the simplistic picture of a single electron. While it is expected that the beam quality in EuPRAXIA will be high, there are some fundamental beam parameters which must be considered when designing an ICS source. All of the above parameters rely on every electron in the bunch being identical in terms of energy, position, and angle relative to the laser pulse. The deviation from this idealised case may be quantified by the electron beam emittance.

When scattering from a 5 GeV electron beam ( $\gamma \sim 10,000$ ), in order to limit the bandwidth of the source, the acceptance angle of the end station must be limited to  $<0.1$  mrad. If the divergence of the electron beam is greater than this, it will not be possible to limit the bandwidth of any ICS source. This does not erase the applicability of the source, rather imposing limitations on how the source is implemented and requiring flexibility in both electron energy and laser energy / intensity in order to fully access regimes of interest. The study of electron beam quality on ICS sources has been considered [648,649].

## Implementation of an ICS Source at EuPRAXIA

From the previous section, it is clear that a range of photon sources will be feasible from the ICS end station. As with many aspects of facility use, the parameter selection will be a compromise, whereby an increase in flux (through higher  $a_0$ ) or higher photon energy (through higher electron energy) will each come at the price of increased bandwidth. The conclusion from this argument is that flexibility in electron and laser parameters will allow access to a range of unique sources unavailable at other facilities. The specific parameters available at the ICS end station will be sufficiently sensitive to electron beam parameters the precise knowledge of which will be essential.

## Electron Beam Diagnostics

In addition to the plethora of applications outlined thus far, the relationship between emittance and bandwidth, as intimated above, provides an opportunity for a novel beam diagnostic. Measuring the angularly resolved ICS emission from a well-characterised laser focus will provide a complementary transverse emittance measurement of the wakefield-accelerated beam.

# 25 Particle User Applications

## 25.1 High-Energy Physics Test Beams

As complex high-tech devices, modern large particle detectors, such as those used for measurements at the Large Hadron Collider at CERN, typically require extensive R&D, simulation, and testing, before they can start operation. Test beams suitable for such work, however, are only available at large accelerator laboratories. The electron-positron synchrotron DESY II, for example, is one of such test beam facilities, although it is also used as an injector for the PETRA III synchrotron. With a circumference of 293 m, it generates particle beams with energies up to 6.3 GeV,  $\sim 5\%$  energy spread,  $\sim 1$  mrad divergence and around 1000 particles per  $\text{cm}^2$  in bunch

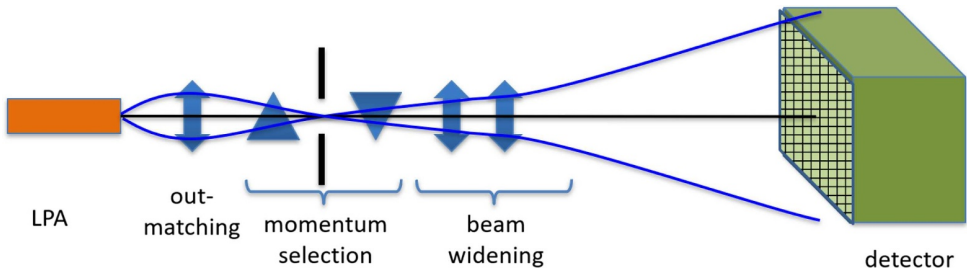


**Fig. 25.1.** Schematic layout for the electron test beamline, which could be used, for example, for HEP detector timing calibration and testing.

lengths around 30 ps [650]. In view of increasing the availability and reducing the cost of such test beam facilities, plasma accelerators could provide an interesting alternative, pioneering complementary ways to develop and test detectors.

There are indeed a number of differences between electron beams generated from plasma accelerators and RF-based machines. Conventional test beams can consist of a variety of particle species, from protons and neutrons to electrons, positrons, photons, and other more exotic particles. Plasma accelerators, on the other hand, have been shown so far to generally only produce few particle species at the same time in the form of electrons and photons, as well as, in the case of EuPRAXIA (as discussed below), positrons. Additionally, the beam distribution from plasma accelerators is quite unusual for test beams due to its short bunch duration, fs-level synchronisation and compact transverse beam size leading to a large number of particles arriving at the same time and same spot at the detector.

These particular characteristics could, however, be turned into an advantage and allow new types of detector test and timing calibration studies. In the following, three particular use cases are proposed.

**Parallel irradiation of large detectors:** Using a high-flux beam, but with a low flux density, larger areas of a detector could be irradiated simultaneously instead of scanning across the detector area in many small steps. Such an approach would be not only be significantly faster or allow for significantly more data-taking, but also make it possible to calibrate the timing measurement uniformity across the detector. Additionally, the high-flux beam could be used as an excellent tool to stress-test the data acquisition system of the detector under realistic conditions given the high, but tunable number of particles.

**High-flux-density scanning of detector elements:** Using a focussed high-flux beam from a plasma accelerator, high flux density can be reached to study fine effects within individual detector elements. This could be used, for example, to test the saturation and linearity of an active element response, but may also be interesting for studying particle beam effects on the embedded read-out electronics in the detector in an extreme high-density scenario.

**Testing of the uniformity of the timing response:** A third possible use case of plasma-accelerated electron beams is for timing tests of the detector. Thanks to their short bunch duration, a good temporal resolution could be achieved and it could be envisaged to be able to scan through different bunch durations by stretching the electron beam in a controlled way along the transport beamline to the detector measurement.

At EuPRAXIA, several of these testing scenarios could be realised. In the generation of low- and high-energy positron beams at both construction sites, part of the incoming electron beam will remain after propagation through the converter

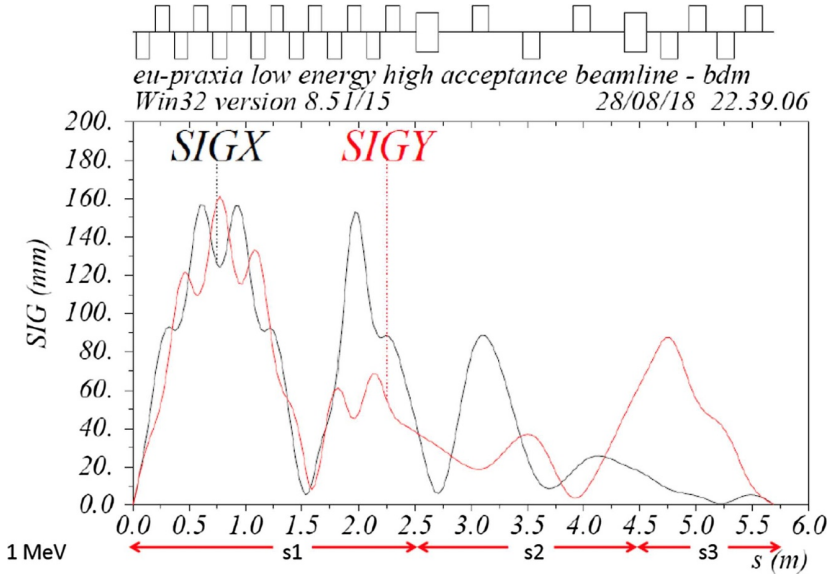


**Fig. 25.2.** Conceptual design of the low-energy positron beamline to be installed at the laser-driven plasma acceleration construction site. The laser (red cone on the left) is focussed on a plasma target to generate an ultra-short ( $\sim$ fs) and ultra-relativistic electron beam that, after conditioning and potential second acceleration, is sent onto a high-Z converter. A beamline for both the electrons and positrons escaping the solid target is sketched after that.

target. This beam will be of GeV-scale energy, with charge between a few particles and several pC (depending on the converter target thickness), and limited beam quality in terms of energy spread and transverse emittance. It is foreseen to separate this electron beam from the positrons in a dogleg setup, described in more detail in Section 25.2, transport it through a conditioning beamline, and finally direct it into a user area for detector calibration and other test experiments. While a detailed design still needs to be developed during the technical design phase, a schematic beamline layout can be seen in Figure 25.1 showing the key elements of the conditioning line. As Figure 25.5 in the next section shows to some extent, a set of quadrupoles will be used for capturing the electron beam after the converter target and separating it from the positron beam through a dipole section. The latter could also be expanded for momentum selection to fine-tune the energy and energy spread of the electron beam as well as filtering out a specific beam charge. Beam focussing can be tuned downstream through further focussing optics. Finally, a controlled bunch lengthening system would need to be implemented for timing studies, a feasibility study for which remains to be carried out. The combination of these conditioning elements and their potential for tuning the beam properties will thus enable such unique studies, as high-flux-density scans, large-area detector irradiation and uniformity-of-timing tests, as described above. Additionally, this setup could provide a very interesting ground, more generally, for experiments with ultra-short, tunable electron test beams, for example for studying novel diagnostics or beam manipulation elements. It is thus foreseen to implement a test beam user area along the shared positron beamlines at each of the two EuPRAXIA construction sites, thus allowing for more user time and increased flexibility.

Regarding the test beam user areas, several essential requirements can be defined, based on discussions with potential future users during the “EuPRAXIA Workshop

**Table 25.1.** Expected properties of the low-energy positron beam generated at the EuPRAXIA beamline.

Positrons/shot (50 keV bandwidth)	Energy	Repetition rate	Beam size at sample	Beam duration	Positrons/s
$10^6$	tunable: 0.5–10 MeV	100 Hz	2–5 mm	90 ps 1 MeV 20 ps 2 MeV	$10^8$

on Pilot Applications of Electron Plasma Accelerators (PAEPA)” in 2016 and include the following:

- large manipulation space both horizontally and vertically,
- presence of a crane and movable table for large components,
- presence of an accurate timing signal, e.g. through adequate synchronisation with a reference laser,
- presence of several specific diagnostics, including a flux monitor,
- presence of cooling water in the user area.

The current conceptual layout of EuPRAXIA has been developed with these features in mind and a detailed design will be realised together with the technical specification of the conditioning beamline during the next phases of EuPRAXIA.

## 25.2 Secondary Particle Sources

### 25.2.1 Low-Energy Positrons

Using baseline values for the EuPRAXIA plasma injector (charge: 30 pC, duration: 10 fs, energy: 150 MeV – 5 GeV, depending on the number of acceleration stages), one can obtain, after propagating through a mm-scale Pb target, up to 10 pC of positrons with a broad energy spectrum extending up to the maximum electron energy, and a sub-ps duration. The repetition rate of the positron source would be identical to that of the laser beam driving the acceleration of the primary electrons, and is designed to be of the order of 100 Hz. The broadband spectrum of the positrons [148] can be used as an advantage since, with the appropriate beam handling, one can select the energy required, virtually seamlessly from sub-MeV to a few MeV – the spectral region where most of the positrons are present. In Figure 25.2, a conceptual design of the beam handling after the converter, including collimation and energy selection, is shown. After approximately 6 m of beamline, one can achieve a mm-size positron beam with a tuneable energy from 0.5 to 10 MeV and a bandwidth of  $\pm 50$  keV. The simulated evolution of the transverse size of the positron beam through the beamline (both along the x and y axes) is shown in Figure 25.3.

Once the positrons exit the conditioning beamline, they will enter a dedicated target area with an approximate footprint of  $8 \times 15$  m<sup>2</sup>. The electrons escaping the target will instead be directed along a different beamline and will be finely characterised, on-shot, to provide a live diagnostic of the generated positron beam. Finally, the arrival of the X-ray radiation escaping the solid converter will be used as a definition for time-zero, i.e., the time the positrons are implanted in the sample. The end-user target area will comprise a vacuum vessel where the sample to be studied will be mounted on a 5-D motorised stage, allowing for its fast alignment and scanning, both transversally and in depth. A suite of detectors will be used to perform typical positron-induced material inspections, which include positron annihilation spectroscopy and Doppler-broadening spectroscopy.



**Fig. 25.3.** Simulated evolution of the transverse size of the positron beam, in  $x$  and  $y$  (designated as SIGX and SIGY), through the low-energy beamline shown in Figure 25.2 (after the converter).

Due to the different penetration depths of different positron energies, this allows one to perform the *volumetric* scanning of materials, a feature that is unavailable at the sub-relativistic positron factories currently operational. Moreover, the high positron flux per shot (of the order of  $10^6$  positrons in a 50 keV bandwidth) and the considerable repetition rate of 100 Hz result in a considerably high flux of the order of approximately  $10^8$  positrons/s.

The intrinsic short duration of the laser-wakefield electron beam, implies that the positron duration at the sample will be predominantly dictated by the temporal spreading during propagation through the beamline. Assuming a 6 m long beamline (see Fig. 25.3), a  $2 \text{ MeV} \pm 50 \text{ keV}$  ( $1 \text{ MeV} \pm 50 \text{ keV}$ ) positron beam will have a duration at the sample of the order of 20 ps (90 ps), which is currently unattainable by more conventional positron factories and, indeed, shorter than the typical timescales of positron annihilation in materials (see Tab. 25.1).

This will not only lead to much higher resolution but can also allow to study real-time dynamic effects in material under stress on picosecond time-scales, a unique feature that would represent a step change in the designing and manufacturing of materials under extreme conditions. A summary of the positron parameters that can be reached in this end-station of EuPRAXIA is given in Table 25.1.

It must be noted here that the number of positrons will scale linearly with the charge of the primary electron beam, making it desirable to have a higher charge in a broader spectrum. Moreover, the number of positrons will scale, empirically, with the square root of the energy of the primary electron beam. Extending the electron beam energy from 150 MeV to 5 GeV, as possible using a multi-staged approach, would thus increase the number of positrons by a factor of approximately 6.

### 25.2.2 High-Energy Positrons

We propose here to use the main electron beam designed for the beam-driven plasma acceleration construction site of EuPRAXIA to drive high-quality and high-energy positron beams that can be used as seed beams for advanced studies of laser wakefield

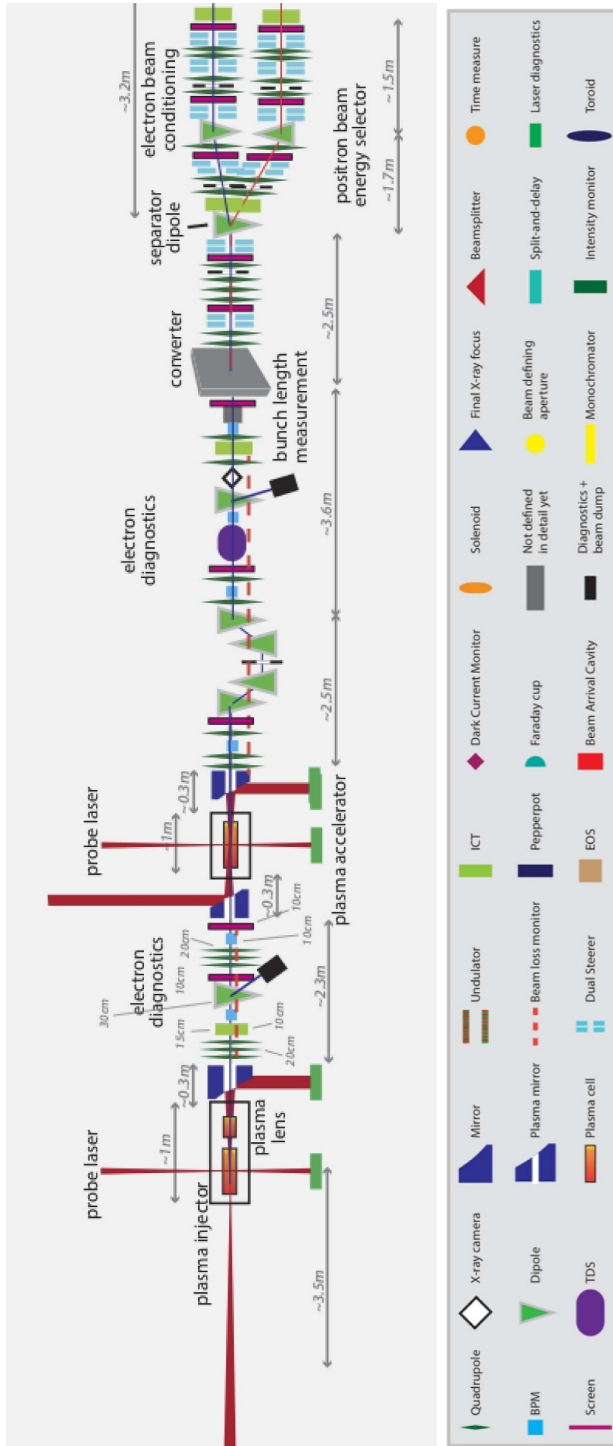


**Fig. 25.4.** Conceptual visualisation of the positron and test electron beamline at the proposed EuPRAXIA laser-driven construction site (based on the CAD model in Section 32.9 of the appendix).



the current design for the positron line is given in Figure 25.5. The electron beam will be steered by a magnetic dipole onto a high-Z solid target (lead) with a thickness of the order of a few millimetres. The quantum electrodynamic cascade inside the solid target will generate a high-flux photon beam and dense populations of electrons and positrons. The positrons escaping the target will present a broad spectrum and energy-dependent duration, source size, and divergence. In a 5% bandwidth around 1 GeV, one expects approximately  $10^7$  positrons with a duration comparable to that of the primary electron beam, a source size of 20  $\mu\text{m}$  and a divergence of 10 mrad [148]. The resulting geometrical emittance at 1 GeV at source is then 0.25 mm mrad (normalised emittance of 500 mm mrad). The positron duration at 1 GeV will be comparable to that of the primary electron beam, i.e., sub-10 fs [148]. The simulated evolution of the transverse size of the positron beam at 1 GeV through the beamline illustrated in Figure 25.5 is given in Figure 25.6.

The beamline can be tuned in order to maximise the collection efficiency, which can be as high as 50%. Moreover, tuning of the magnetic components in the beamline allows for a certain level of freedom in tuning the final energy of the positrons, in the range of hundreds of MeV up to 1 GeV. At the end of the beamline, the positron beam will then enter the user area with the following characteristics: an energy of 1 GeV  $\pm 5\%$ , a duration of  $<10$  fs, a beam size of 20  $\mu\text{m}$ , and a charge of the order of 1 pC. A versatile area with a footprint of  $10 \times 20 \text{ m}^2$  will then be dedicated to experiments in high-energy physics, with a specific focus on providing a test beam for experiments in advanced schemes of positron acceleration. Several plasma columns and plasma cells will be available in vacuum vessels to study laser-driven and particle-driven wakefield acceleration. A dedicated high-power laser system will be installed and synchronised with the positron beam for laser-wakefield studies (800 nm laser system providing 30 J in pulses with a duration of 30 fs and a repetition rate of 10 Hz). It must be noted then that a high-charge electron beam ( $>10$  pC) synchronised with the positron beam will also be collected by the proposed beamline, and thus available in the area for particle-driven wakefield experiments.

## 26 Additional Innovation Paths

### 26.1 Hybrid Laser-Beam-Driven Plasma Wakefield Acceleration

#### 26.1.1 Introduction

PWFA has various well-known important advantages when compared to LWFA, such as dephasing-free, dark-current-free operation, and enables unique injection schemes such as the plasma photo-cathode, which promises improved output electron beam qualities such as brightness by a factor of 1,000 to 100,000 better than the state of the art.

PWFA can be realised at linac-driven facilities, such as SLAC FACET(-II), DESY, Daresbury Laboratory, and INFN, where the EuPRAXIA PWFA construction site is foreseen. Linac-driven PWFA is well-established and potentially allows beam acceleration at high repetition rate with stable beams, but also has drawbacks such as the large size of the accelerator due to the linac system, which produces the electron beam used to drive the PWFA stage, and limited synchronisation between electron beam driver and laser systems, which is desirable e.g. for FEL seeding, pump-probe-experiments, and the realisation of plasma photo-cathodes.

In EuPRAXIA's Work Package 14 on "Hybrid Laser-Electron-Beam Driven Acceleration", forward-looking and potentially disruptive approaches were developed, which combine the best of LWFA and PWFA (Scheme 6, as described in Chap. 8).

In addition, hybrid solutions across LWFA and PWFA also strengthen synergies and coherence of the overall EuPRAXIA design. They are a bracket around the key EuPRAXIA approaches and sites for LWFA and PWFA.

Hybrid plasma accelerators unite the best of LWFA and PWFA and offer a symbiosis between the two main underlying technologies of EuPRAXIA.

Dramatic progress has been seen in applying this novel hybrid philosophy over the lifetime of the EuPRAXIA study (2015–2019) both conceptually but also experimentally. While key concepts [53,601,603,651,652] had been experimentally unproven at the beginning of the project, a major important subset of them could recently be successfully demonstrated experimentally [653,654]. This constitutes a jump in technology readiness level (TRL) from approximately TRL 2 (conceptual) to TRL 6 (experimental technology demonstration) and is a very strong sign of its viability and capability to fulfil the main EuPRAXIA aim of a “Compact European Plasma Accelerator with Superior Beam Quality”.

### 26.1.2 LWFA Beams as PWFA Drivers

The main concept of hybrid LWFA→PWFA staging is to use the electron beam output from LWFA as a driver for PWFA. PWFA requires energetic, dense electron beams with high currents as drivers. This is precisely what LWFAs can inherently deliver: ultra-short, multi-kiloampere current electron bunches. While the sizeable energy spread and emittance of electron bunches from current state-of-the-art LWFAs impose serious challenges to realise key applications, such as free-electron lasers, these properties are excellent prerequisites to realise compact PWFA, as they offer improved resilience to instabilities [655,656]. In this hybrid approach, the electron beam (or beams) produced in an LWFA stage is inserted into a subsequent PWFA stage, which can be less than a millimetre away from the LWFA stage, or further away when an electron beam transport beamline is employed.

Figure 26.1 shows the schematic underlying concept. First, a short high-current and high-density electron beam is produced via LWFA. This capability is an inherent advantage of LWFA: the short duration of high-power laser pulses makes it possible to work at a wide range of plasma densities ( $10^{17} - 10^{19} \text{ cm}^{-3}$ ) to drive a resonant plasma wave. In particular at high densities, the laser pulse group velocity is significantly reduced with respect to the speed of light, which together with the high accelerating and transverse plasma wakefields, favours self-injection and the rapid acceleration of high-current-density electrons. An alternative strategy lies in operating at lower plasma densities to prevent self-injection and exploit the implementation of more controlled injection techniques for tunability [18,279,657–660]. In particular, ionisation-based injection techniques [279,661] allow for a direct control of the amount of injected charge, which can be tuned to find nearly optimal beam-loading conditions for a reduced correlated energy spread along the witness beam [329]. A relatively recent LWFA experiment at the Helmholtz Centre Dresden-Rossendorf (HZDR) employing a  $\sim 100$  TW laser system demonstrated that electron beams with around 300 pC charge can be produced at a reduced energy spread [28] by adjusting the loaded charge. With a duration of  $\sim 10$  fs, these LWFA beams deliver tens of kiloamperes of current at around 300 MeV mean energy. Multi-kA level electron beams from LWFA can also be obtained by other LWFA installations, e.g. in the UK at the Scottish Centre for the Application of Plasma-based Accelerators and the Central Laser Facility, in Germany at LMU Munich and in France at LOA Paris. A high current density is the critical requirement for PWFA drivers, as it allows the PWFA system to operate in the highly non-linear “blowout” regime [367]. This regime

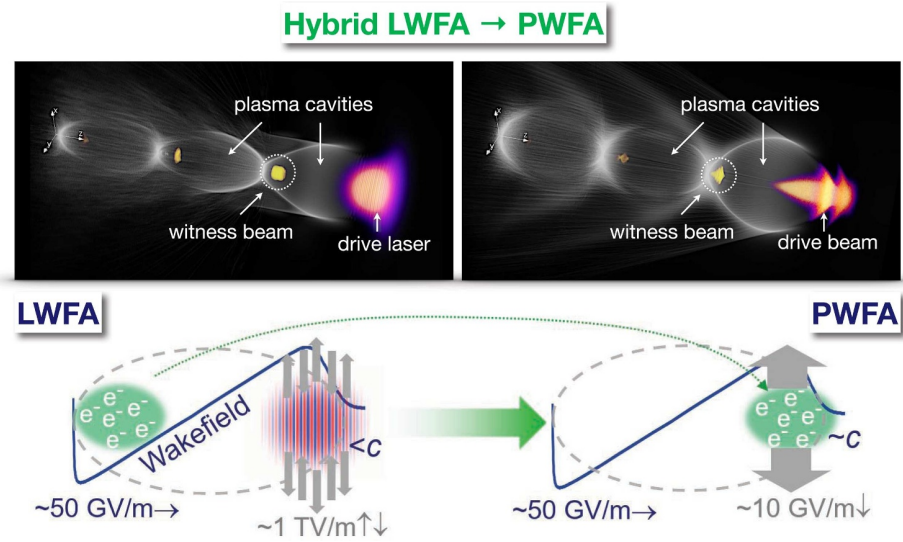


**Fig. 26.1.** Three-dimensional electron density maps, extracted from particle-in-cell simulations with OSIRIS [336], for LWFA (left) and PWFA (right). The schematic shows the underlying principle of the hybrid approach. In LWFA, laser pulses in plasma propagate at a velocity significantly smaller than  $c$ , and their oscillatory field structure excite the plasma wave via the ponderomotive force. In PWFA, the drive beam moves with  $\sim c$  and its space-charge fields excite the plasma wave, such that the driving field values involved in the process are orders of magnitude lower than in LWFA. This enables unique injection methods based on field ionisation for electron bunch production with ultra-high quality [601,603,652].

offers key advantages for the production of high-quality beams from PWFA, such as the possibility for advanced injection techniques [54,601,603,652,662] and a particularly steady wakefield formation for beam-loading control [48,53]. While in LWFA, the currently achievable levels of energy spread and normalised emittance constrain the application of LWFA beams, e.g. for X-ray lasing in an FEL setup, this is not a critical aspect for using LWFA beams as PWFA drivers. In fact, a significant initial energy spread and emittance of the electron beam driver have advantageous implications for PWFA as they offer improved resilience to well-known instabilities [655,656]. These features suggest that LWFA-generated electron bunches are extremely promising candidates to realise PWFA and explore its physics [653,663].

LWFA-generated electron beams are natural near-ideal drivers for PWFA.

### 26.1.3 LWFA→PWFA Transition

One challenge of hybrid LWFA→PWFA staging is the transition between LWFA and PWFA. LWFA-generated electron beams typically have relatively large divergence ( $>1 \text{ mrad}$ ), which is due to the strong focussing fields inside the plasma-wakefield cavity that compress the electron beam to a small transverse size on the  $\mu\text{m}$ -scale. For this reason, the LWFA beam will quickly diverge after its release in vacuum, thus decreasing quadratically its charge density as the spot size grows linearly with the propagation distance. As mentioned above, maintaining a high beam current density is crucial for driving a strong PWFA, and therefore, the distance to the PWFA stage shall be minimised. Although a gradual transition from plasma to vacuum at

the end of the LWFA stage permits to significantly reduce the divergence of the beam [664], a capture and transport line between the LWFA and PWFA stages may be desirable. Such a beamline interface will provide control over the focal position of the beam in the PWFA stage, while at the same time alleviating the requirements for out-coupling the spent drive laser and in-coupling assisting lasers for injection in the PWFA stage. As an alternative to capturing the electron beam from LWFA with permanent magnet quadrupoles, passive [665] and active [666] plasma lenses are under development. These tasks are synergistic with LWFA approaches, which attempt to directly use the electron beam output for applications.

A direct transition from LWFA to PWFA could also be achieved during the plasma upramp in a PWFA stage placed close by, providing capturing and re-focussing of the LWFA electron beam [663,665]. The diverging remnant laser pulse from the LWFA stage can either be used to pre-ionise the PWFA stage immediately prior to arrival of the electron beam or it can be blocked by a thin foil or tape [653,663,667,668]. The space-charge field of the electron beam itself can then be sufficient to self-ionise the PWFA stage in an elegant solution, yet there are drawbacks, such as an increased head erosion and a strong sensitivity to shot-to-shot jitter of the LWFA output. Substantially more control can be provided by a separate pre-ionisation laser pulse for the PWFA stage, as it is done in conventional linac-driven PWFA, such as [46,654,669]. Several options exist for the implementation of the pre-ionisation laser, for example using axicons, axilenses, or simply Gaussian focussing in a collinear geometry [46,653,654,669]. More comprehensive discussions of complementary advantages and combinations of LWFA and PWFA can be found, for example, in [602,670,671].

#### 26.1.4 Experimental Status

A transition from LWFA to PWFA was first observed experimentally within a single plasma stage, naturally occurring when the field strength of the accelerated electron beam became stronger than the depleting laser. However, only indirect signs of PWFA were obtained in this kind of single-stage experiments, based on either electron energy measurements [672], pulse duration measurements [673], or X-ray emission diagnostics [674]. An experimental milestone towards a well-defined and controllable LWFA→PWFA transition is the physical separation of the LWFA and PWFA stages with two different gas reservoirs. This has been demonstrated, for example, in [665], where a passive plasma lensing effect driven by the LWFA beam in the second gas reservoir was observed; in [667], where self-ionisation and electron beam deceleration in the second gas reservoir has been demonstrated; and in [653], where the unambiguous observation of a plasma wave driven by laser-accelerated electrons has been achieved using few-cycle shadowgraphy.

#### Proof-of-Concept Experiment at HZDR

The actual feasibility of the hybrid LWFA→PWFA concept is being tested through a proof-of-concept experiment implemented at HZDR [602,663], using the DRACO [675] laser system for the LWFA stage and the thereby produced electron beam as driver of a subsequent PWFA stage. As a proof of concept, the first goal of the experiment is to demonstrate the injection and acceleration of a new witness beam in the PWFA stage driven by the LWFA beam. Ultimately, the resulting PWFA beam is ought to feature a substantially higher energy and brightness than the initial LWFA beam [602].

The experimental setup consists of two consecutive supersonic gas jets, one for the generation of a high-current electron beam in an LWFA stage driven by the DRACO

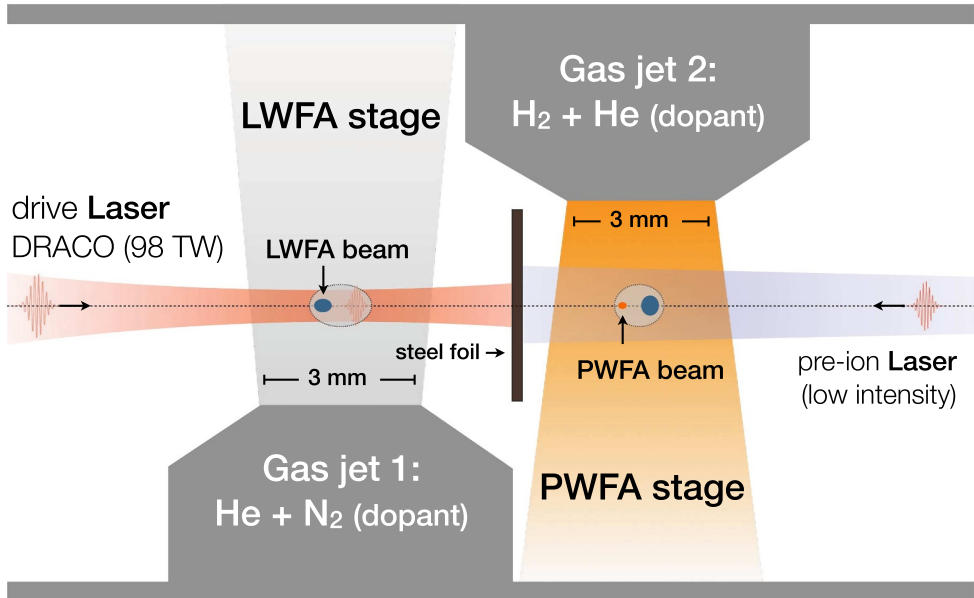


**Fig. 26.2.** Schematic of the double-jet plasma target for the LPWFA proof-of-concept experiment at HZDR. In the first gas jet, an LWFA stage is driven by the DRACO laser for the generation of a high-current electron beam. In the second gas jet, the LWFA-produced electron beam drives a PWFA for the production of a new electron beam with largely improved energy and brightness [602].

laser, and a second jet for the injection of a new electron beam in a PWFA stage, driven by the previously produced electron beam (see Fig. 26.2). A thin foil made of steel is placed at the entrance of the second jet, aiming to reflect the main laser from the second stage, while letting the electron beam go through with a tolerable impact on its transverse size and emittance. A counter-propagating low-intensity laser can be used in order to fully pre-ionise the hydrogen to facilitate the beam re-focussing and enhance the blowout formation in the second stage.

Promising results have been obtained during the experimental campaigns of 2018, where conclusive evidence for the witness beam acceleration in a PWFA driven by LWFA beams has been achieved, in both self-ionised and pre-ionised PWFA regimes [T. Kurz, T. Heinemann et al., to be submitted]. This result represents a breakthrough milestone in the development and for future implementations of hybrid LWFA→PWFA. The goal is to use those as beam brightness and energy transformers, delivering high-quality beams at multi-GeV energies while maintaining a compact setup [53,602,603,651,663,670,671]. Such electron beams would meet the quality requirements for driving compact free-electron lasers powered by plasma beams, one of the major goals of EuPRAXIA.

## 26.2 LWFA→PWFA Staging as a Beam Energy and Brightness Transformer

Beyond the original prospects for mono-energetic energy doubling in a hybrid LWFA→PWFA setup [651], novel concepts for PWFA powered by LWFA beams aim for largely improved beam quality [53,601–603]. These concepts rely on the advantages that PWFA offers with respect to LWFA for the injection and acceleration of high-quality beams. PWFA drivers propagate through plasma at nearly the speed of

light, thus permitting to lock the phase position of the witness beam with respect to the wakefields. Besides, the strong focussing field generated by the driver allows for a diffraction-free propagation, which results in a remarkably steady wakefield generation. Both features combined make it possible to find persistent beam-loading conditions that suppress the build-up of correlated energy spread in the witness beam [329]. In addition, the relatively low electric fields (orders of magnitude lower than drive lasers, see Fig. 26.1) associated with the space charge of the drive beam can avoid the ionisation of high-ionisation-threshold species (e.g. helium), which can be then used as dopants for advanced injection techniques based on selective ionisation. The underdense plasma photo-cathode [603], also known as Trojan Horse injection, uses a low-intensity laser to rapidly induce ionisation over a small phase region of the wakefield, enabling the production of witness beams with ultra-low emittances, about two orders of magnitude below the state of the art. The wakefield-induced ionisation (WII) injection method [53,652] uses only the wakefields to induce ionisation and trapping of high-quality electron beams intrinsically synchronised with the driver, thus alleviating the pointing jitter requirements at high plasma densities, where normalised emittances as low as  $0.1 \mu\text{m}$  can be obtained. The optical plasma torch injection method [601] relies on a laser-ionised plasma density bump to induce the injection, even for lower-current drive beam scenarios. These injection techniques uniquely apply to PWFA and promise to deliver superior beam quality with respect to LWFA. As Trojan Horse injection, WII injection, and plasma torch methods rely on ionisation, they can be tuned to find optimal conditions for beam loading [48,53] resulting in beams with high current and low energy spread, which together with an intrinsic low emittance yield ultra-high brightness beams.

Hybrid plasma accelerators can improve the brightness of the electron beam output by a factor of up to 10,000 compared to the state of the art, and hence can fulfil the main EuPRAXIA aim of “Superior Beam Quality”.

Specific results considering different injection techniques for high-quality witness beam production in a conceptual design for a hybrid LWFA→PWFA staging are shown in Section 26.2.1.

## 26.2.1 Injector for a Hybrid Plasma Accelerator

### Introduction

Beam-driven plasma wakefield accelerators have unique features for the production of high-quality and high-energy electron beams. On the one hand, PWFAs allow for the generation of stable and dephasing-free plasma wakefields, which can be sustained over longer distances, therefore providing higher energy gains and improved control over accelerated witness beams and their characteristics, such as their energy spread. On the other hand, operating PWFAs in the blowout regime enables novel injection techniques specifically designed to deliver ultra-low emittance and ultra-high brightness witness beams [54,601,603,652,654,662] with much higher quality than the drivers.

The hybrid plasma accelerator is a combination of a laser-driven plasma-wakefield accelerator with a PWFA in a staged setup, which uses the output beam of the LWFA to drive a PWFA, rather than an external beam from an RF linac. Initially proposed as an energy booster for LWFA beams [651], the concept was further developed in the following years towards a beam brightness transformer [53,602,603,670,671], aiming to reach the demanding beam quality requirements of accelerator-driven light sources

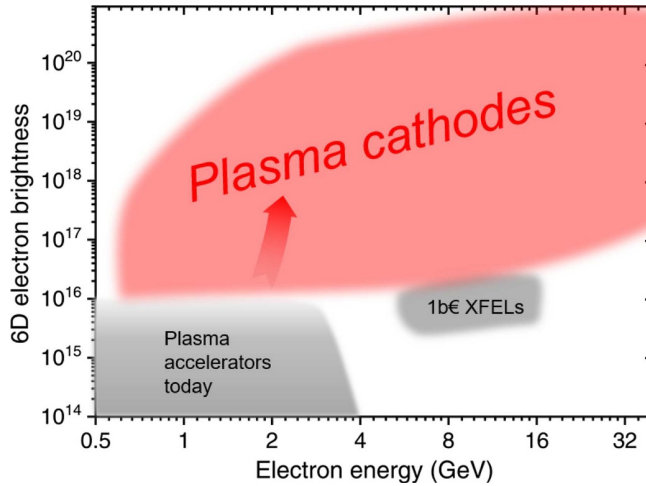


**Fig. 26.3.** The 6D brightness reach of the three related “plasma-cathode” schemes described here exceeds the state of the art by many orders of magnitude.

without sacrificing the small spatial footprint and the relatively low cost offered by LWFA.

One of the steps towards the realisation of such energy, emittance and brightness transformers is the implementation of advanced injection techniques for PWFAs delivering superior-quality witness beams. It should be noted that these concepts do also work for linac-driven PWFA and hence are solutions, which are accessible across LWFA and PWFA, and hence globally for the EuPRAXIA approach. In this chapter, we discuss three options for a hybrid plasma accelerator to deliver electron beams with superior quality. Various parameters determine the quality of electron beams, and the priorities may change from application to application, however, a key performance parameter is the brightness of the electron beam. Brightness is a composite parameter of key beam parameters involving the current,  $I$ , the normalised emittance,  $\varepsilon_n$ , and the relative energy spread,  $\bar{\sigma}_\gamma = \sigma_\gamma / \bar{\gamma}$ , with  $\bar{\gamma}$  the average energy and  $\sigma_\gamma$  the energy spread (RMS). The 5D-brightness is defined as  $B_{5D} = 2I / \varepsilon_{n,x} \varepsilon_{n,y}$  and the 6D-brightness as  $B_{6D} = B_{5D} / \bar{\sigma}_\gamma$ , which also includes the relative energy spread. A high current, low energy spread, and in particular a low normalised emittance are therefore key targets of these injector schemes. While short, kA-scale electron beams are the natural outcome of plasma accelerators, these “plasma-cathode” schemes stand out by being able to produce beams with an emittance (in both planes) orders of magnitude less than conventional methods. This is key to achieving peak brightness levels orders of magnitude better than the state of the art, and thus superior-quality electron beams, as shown in Figure 26.3.

The brightness enhancement of the PWFA output electron beam with respect to the input driver electron beam from LWFA or a linac is about five orders of magnitude.

### Plasma-Torch Injection

The use of a sharp density downramp for a localised injection had been first suggested for PWFA [15,54,676–678], but while today it is a standard method of injection in LWFA, until recently it never had been realised experimentally for PWFA. Supported

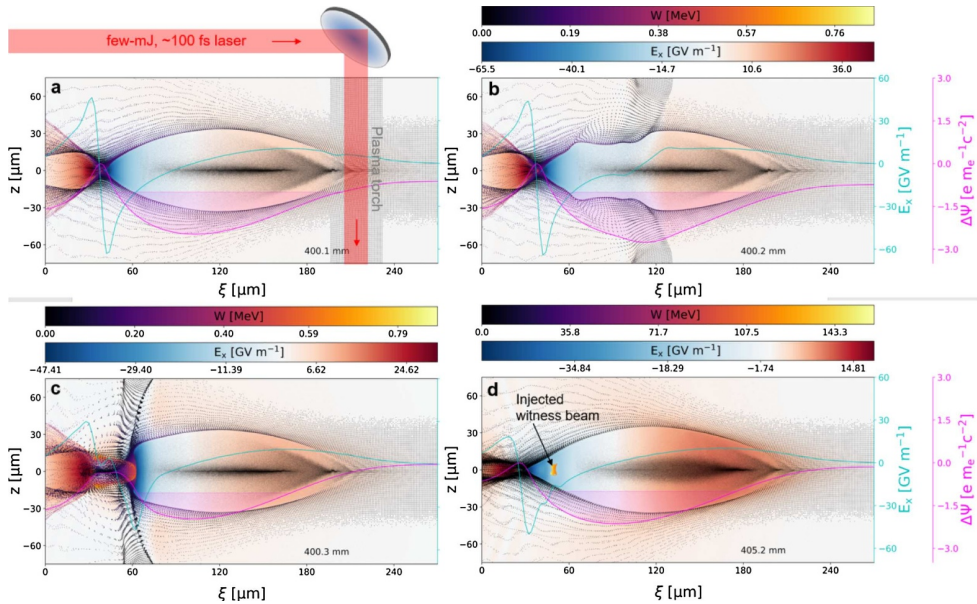


**Fig. 26.4.** 3D PIC-simulations reproducing the plasma-torch downramp injection experiment during the E-210: Trojan Horse programme at SLAC FACET ([654] and D. Ullmann, to be published).

by EuPRAXIA, as part of the “E-210: Trojan Horse” experiment at SLAC FACET, an advanced all-optical method of downramp injection has been developed and demonstrated [654], which does not require a *gaseous* density downramp. Instead, another fundamental advantage of PWFA has been exploited, namely the fact that the electric fields associated with even ultra-intense electron beam drivers have a ceiling at the scale of tens of GV/m, the same scale of the plasma wakefields they produce. This means that the electron driver beams themselves do not tunnel-ionise media or ionisation levels with high ionisation thresholds such as helium. For example, in a hydrogen / helium mixture, hydrogen with a comparably low ionisation threshold can be used to support the PWFA process, leaving the helium fraction in a neutral state. An additional low-power laser pulse can then be used to locally ionise helium and thereby generate a plasma density spike, with a sharp plasma density downramp. This avoids the necessity and complexity of hydrodynamic gas inhomogeneities, e.g. by shock-front production with a knife or a localised gas jet, which requires hydrodynamic timescales and interferes also with the hydrogen density, thus impacting on the PWFA process itself. We call the all-optical method of downramp injection plasma-torch injection [601,679].

At SLAC FACET in E-210, we demonstrated the concept experimentally by sending an ionising few-mJ-class,  $\sim 100$  fs scale Ti:Sapphire laser pulse perpendicularly across the beam-driven hydrogen plasma wave. At intensities of the order of only few  $10^{15}$  W/cm<sup>2</sup>, this non-relativistic laser pulse then ionises a helium plasma torch with tunable width and shape along its path on top of the hydrogen background plasma. The downramp at the end of this plasma spike then leads to the tunable injection of hydrogen and helium electrons. Figure 26.4 shows how this process works, based on 3D PIC-simulations with VSim.

Further details on how to achieve and tune the process is found in references [601,679] (theory), and [654] and [D. Ullmann, to be published] (experiments). The parameter space experimentally available by gas-density downramps is a subset of

what can be realised by plasma-torch downramps. Theoretical studies, which investigate PWFA downramp injection such as [15,54], indicate that very high quality electron bunches are possible. Beyond that, a wide, as of yet unexplored injector parameter space arises from the superior tunability of the plasma torch, e.g. as regards the peak density and steepness of gradients, and shapes. For example, since the helium (or another high ionisation threshold (HIT) gas) density is independently tunable from the hydrogen density, local peak plasma densities up to the critical density are possible. On the other hand, due to the direct dependency of the plasma profile on the generating laser pulse intensity profile, extremely sharp downramps and / or extremely thin or asymmetric plasma density profiles are possible [D. Ullmann, to be published]. The demands put on the driver beam current are comparably low, as the trapping threshold for density-downramp injection is around 1 kA, and the extreme tunability, e.g. as regards downramp steepness enabled by the all-optical plasma torch density transition, may allow to push this entry level further. Electron beams produced by LWFA, for example, naturally easily exceed currents of 1 kA scale and can therefore be used as plasma-torch-capable PWFA drivers. The plasma-torch injection method combines high feasibility and very high tunability with very high output beam quality.

Plasma-torch injection is a proven technique with low driver beam requirements, high tunability, and excellent output electron beam quality reach and high charge levels.

### Wakefield-Induced Ionisation Injection

The wakefield-induced ionisation (WII) injection method [53,652] exploits PWFAs operating at a high transformer ratio to induce ionisation and trapping of high-quality electron bunches by the accelerating wakefields of the plasma wake. By definition, in a high transformer ratio PWFA, the electric fields at the rear of the first plasma blowout are significantly higher than at the front. Thus, this configuration permits to trigger ionisation from the wakefields only while avoiding spurious contributions from the fields associated with the drive beam. In this way, the initial phase-space population of the injected electron bunch can be drastically constrained, resulting in low-emittance beams. The electrons forming the witness beam originate from field-induced ionisation of an atomic species with appropriate ionisation threshold, which is doped into the background plasma in a short axial region of the plasma target. Therefore, by tuning the concentration of the dopant, the total injected charge can be controlled to find near-optimal beam-loading conditions for a largely reduced time-correlated energy spread. As demonstrated in [329] and confirmed by simulations considering the WII injection method [53], the required peak currents are on the order of tens of kiloamperes, thus resulting in extremely high-brightness beams with a sub-percent energy spread.

The WII injection method is especially well suited for hybrid LWFA→PWFA staging, where drive beams above 10 kA peak current and around 10 fs duration can be produced in a dedicated LWFA stage [28]. The short duration of LWFA-produced beams make them suitable to operate as PWFA drivers at high plasma densities, close to  $10^{19} \text{ cm}^{-3}$ , where witness beams with normalised emittance as low as  $0.1 \mu\text{m}$  can be produced by means of WII injection. Another fundamental advantage of hybrid LWFA→PWFA staging with WII injection relies on its relative simplicity: since the injection is triggered by the wakefields themselves, there is no need for precise spatiotemporal alignment of external components, such as lasers, and thus the WII injection method becomes insensitive to the pointing jitter of the electron beam emerging from the LWFA stage.

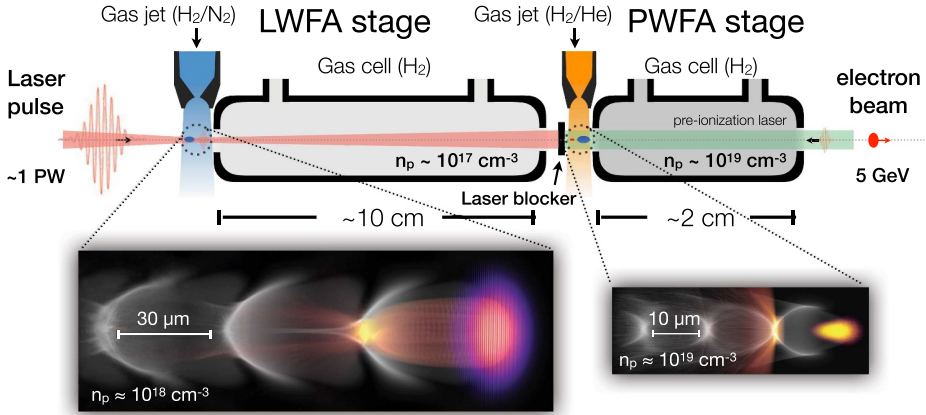


**Fig. 26.5.** Schematic of a hybrid LWFA→PWFA staged setup with wakefield-induced ionisation injection [602]. The setup consists of two quasi-identical plasma acceleration stages coupled to each other. In each stage, the injection of a witness beam is induced by field-ionisation from the dopant species contained in the gas jet. Immediately after the gas jet, a longer plasma cell with no dopant is used to further accelerate the generated witness beam.

A conceptual design study for hybrid LWFA→PWFA staging with WII injection, based on particle-in-cell (PIC) simulations and well-known scaling rules have been recently published [602]. There, we describe the schematics of a possible design consisting of two quasi-identical plasma acceleration modules coupled to each other with a minimal distance in between (Fig. 26.5). The first plasma stage is meant to be driven by a high-power laser (LWFA), and optimised for the production of a highly relativistic (order GeV energy) and high-current  $\gtrsim 10$  kA electron beam via ionisation injection [279,661]. The LWFA electron beam is then used as driver of the subsequent plasma stage (PWFA), where a new high-quality witness beam is produced via WII injection and then accelerated to high energies. Both plasma stages need to be sufficiently close to each other, such that the LWFA beam can be refocused into the second plasma by means of its self-driven plasma wakefields. A thin steel foil can be positioned at the entrance of the second plasma stage to reflect the spent laser, while letting the electron beam pass through and drive the PWFA stage. In addition, a counter-propagating low-intensity laser can be used to preionise the PWFA stage to facilitate the beam focusing, enhance the wakefield excitation and further constrain the dopant section.

PIC simulations considering a PWFA scenario as the one sketched above (Fig. 26.5) show that, by operating the PWFA stage with a short and high-current electron beam at plasma densities  $\sim 8 \times 10^{18} \text{ cm}^{-3}$ , it is possible to generate ultra-short electron beams (sub-femtosecond duration), which double the initial energy of the LWFA beam in just few cm of acceleration, for the parameters considered. Moreover, the normalised emittance of the newly generated PWFA beam can be on the order of hundred nanometers, at the same time that its current can reach values of tens of kiloamps, as required for optimum beam loading.

The WII injection method is especially well-suited for hybrid PWFA at high plasma densities, providing ultra-short and high 6D-brightness beams from a straightforward setup.

Figures 26.6 a and b show electron density snapshots of the simulation for the PWFA stage during the process of injection and acceleration, respectively. The parameters

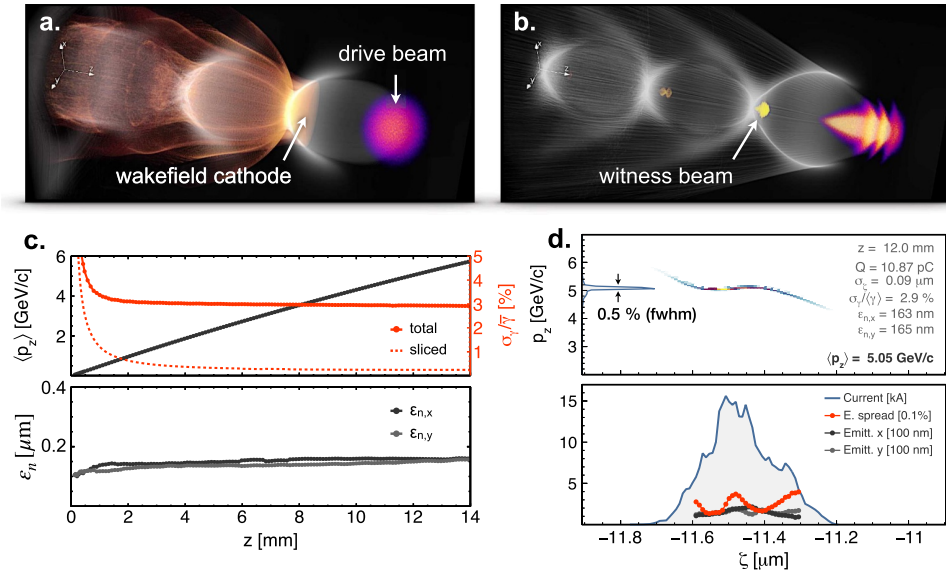


**Fig. 26.6.** 3D OSIRIS simulation [336] for a PWFA stage with wakefield-induced ionisation injection [53,652], driven by a high-current LWFA-produced beam. (a): electron density of the drive beam, the background plasma and the helium dopant during the injection process. (b): same quantities after injection and acceleration. (c) (top): evolution of the average longitudinal momentum of the witness beam (dark grey), the total relative energy spread (red) and the average sliced relative energy spread (dashed red). (c) (bottom): evolution of the projected normalised emittance of the beam in the  $x$  (dark grey) and  $y$  (light grey) planes. (b) (top): longitudinal phase space of the witness beam after 12 mm of propagation. (b) (bottom): sliced values of the current (blue), relative energy spread (red) and normalised emittance in the  $x$  (dark grey) and  $y$  (light grey) planes.

of the witness beam after 12 mm of propagation are shown in Figure 26.6d, featuring a peak current of 15 kA, 11 pC charge, 0.8 fs duration (fwhm),  $\sim 5$  GeV average energy and  $\sim 160$  nm normalised emittance in both transverse planes. The total relative energy spread of the witness beam is  $\sim 3\%$  in total, but only  $\sim 0.5\%$  within the fwhm of the energy peak. The average sliced relative energy spread is around 0.2%. Figure 26.6c shows the evolution of the witness beam parameters as a function of the propagation distance, showcasing an essentially constant energy gain rate and steady beam-loading conditions, derived from the unique wakefield stability of PWFA in the blowout regime. The brightness of the witness beam produced in the PWFA stage is about five orders of magnitude larger than that of the drive beam generated in the LWFA stage.

### Trojan Horse: Plasma Photo-cathode Injection

Complementary to the thinking behind the hybrid LWFA  $\rightarrow$  PWFA as an accelerator [651], the plasma photo-cathode also hybridises LWFA and PWFA elements and thus combines the best of both worlds to engender an injector [603]. It exploits electron beams – either from LWFA or from a linac – as superior plasma wakefield drivers, and the capability of focused laser pulses to produce localised plasma. The electron beam driver excites a plasma wakefield in low ionisation threshold (LIT) plasma such as hydrogen, and a spatiotemporally synchronised and aligned, focused laser

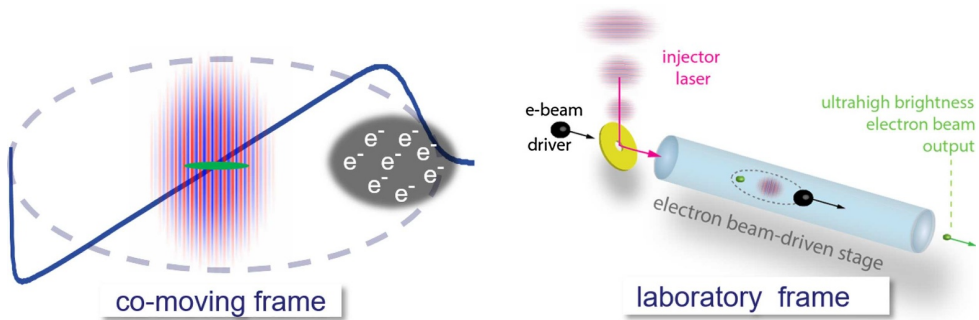


**Fig. 26.7.** The plasma photo-cathode mechanism in collinear geometry in the co-moving frame (left) and laboratory frame (right). The blue profile (solid line) is the longitudinal electric field, and the released electrons are shown in green as a small ellipse in the centre of the left-hand illustration.

pulse – the plasma photo-cathode laser pulse – is ionising a high ionisation threshold (HIT) medium such as helium *inside* the LIT plasma wakefield. The plasma photo-cathode laser pulse can propagate in arbitrary geometry with respect to the driver beam [680], and can be applied over a wide range of plasma densities such as from  $10^{15} - 10^{19} \text{ cm}^{-3}$  range and the position, shape and amount of plasma as well as the position of release within the plasma blowout can be tuned by tuning the laser pulse energy and other parameters. Sub-mJ laser pulse energies are sufficient to achieve the required peak intensities of  $10^{15} \text{ W/cm}^2$  for Ti:Sapphire laser pulses to ionise helium, for example. The liberated helium electrons are then captured by the plasma wakefield and produce an electron beam of ultralow emittance. The main reason for this is that the residual transverse momentum of these helium plasma electrons is negligible. Figure 26.7 visualises the plasma photo-cathode in co-moving and lab frame for collinear geometry.

The normalised emittance reach of this method goes down to the tens of nrad range [603] or even single digit nrad range in both planes by optically confining the laser pulse release region e.g. via SSTF [681,682] or with colliding laser pulses [662], but also in simple Gaussian laser geometry, in particular when working at larger plasma wavelengths. The obtainable emittances are up to three orders of magnitude better than with state-of-the-art plasma accelerators, or radiofrequency-based linac, with typical output electron beam normalised emittances of the order of  $\mu\text{mrad}$ . Due to the quadratic scaling, this corresponds to a 5D brightness improvement of up to six orders of magnitude. The initial plasma photo-cathode idea and considerations regarding e.g. the negligible residual momentum due to the vanishing ponderomotive potential of the release laser pulse [603] were in the following confirmed and e.g. scalings were further developed by various groups [683–685] and have spawned various variations of the scheme [662,681,682,686,687].

Great progress has also been made experimentally. The “E-210: Trojan Horse” collaboration at SLAC FACET has successfully demonstrated feasibility of the plasma photo-cathode process and first core results are now published [654]. These experiments have been carried out under sub-optimal boundary conditions as regards maximum available blowout size, and geometry. That the experiment nevertheless succeeded, is therefore extremely encouraging. By increasing the plasma blowout size and by improving spatiotemporal alignment and synchronization of electron driver beam and laser pulse, the stability and quality of the output electron beam can be systematically improved. With regard to stability, a key advantage of this injection method is that the injection is largely decoupled from the plasma wakefield strength

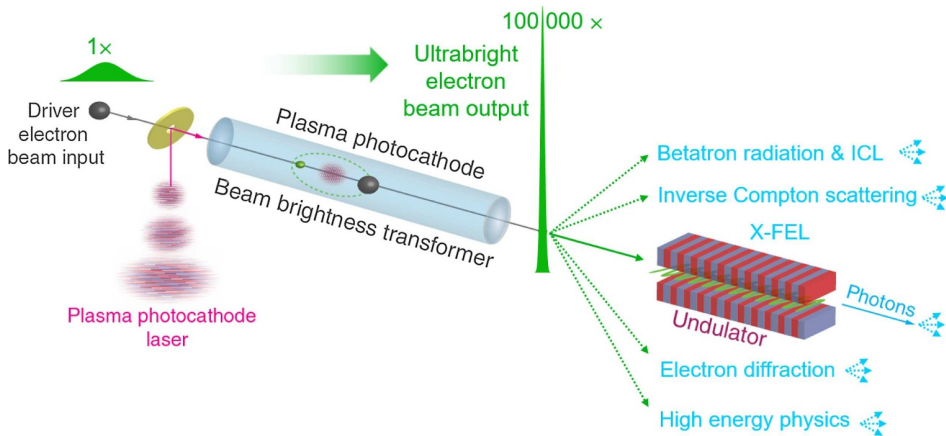


**Fig. 26.8.** Plasma photo-cathode beam brightness transformer based on the Trojan Horse mechanism as a transformative source for applications.

and that injection happens around the zero-crossing of longitudinal and transverse wakefields (see Fig. 26.7). Therefore, even in case of significant spatiotemporal jitter of the plasma photo-cathode laser, or driver electron beam jitter in terms of charge or current profile, the generated and accelerated output electron beam will be relatively unaffected by these jitters. For example, operation in a  $500\ \mu\text{m}$ -scale blowout with state-of-the-art input beam jitter suggests an output beam stability at the 1%-level around emittance levels of around  $10\ \text{nm rad}$ , few pC charge and 1-fs-scale electron beam duration.

Plasma photo-cathode injection is a proven mechanism which promises superior electron beam quality, stability and tunability.

It is applicable as a beam brightness transformer both with linac-generated electron beam drivers as well as with LWFA-generated electron beam drivers, where elegantly the inherent synchronization between electron beam and plasma photo-cathode can be exploited. The extreme beam quality, and stability, is a unique path towards key EuPRAXIA applications. In particular, various light sources profit immensely from dramatically higher electron beam brightness, and high energy physics profits from the much lower emittance. These considerations are visualised in Figure 26.8.

Generating the witness output beam within a single plasma stage e.g. via the plasma photo-cathode mechanism has a further advantage versus external injection or the use of multiple stages, namely that challenges with injection into a plasma stage are completely avoided and that only extraction from the single plasma stage has to be regarded e.g. as regards emittance preservation. This thinking has been extended to minimization of energy spread and optimization of 6D brightness [48]. This is based on tailored beam loading. Such beam loading can be achieved either with a single plasma photo-cathode process as charge values e.g. in the few hundred pC range are accessible just by increasing the HIT density and/or the plasma photo-cathode laser pulse intensity. The obtainable emittance and brightness values of such high-charge bunch generation are still excellent, the obtainable emittance values are increased somewhat due to non-negligible space-charge effects. We therefore conceived and developed a decoupled dechirping process which nevertheless takes place in a single plasma stage [48]. The underlying principle is the use of “escort” bunches, which are added on top of the ultralow emittance witness beam to provide the necessary beam loading. These allow to remove the energy chirp completely, and scaling laws suggest

that at larger plasma blowouts, residual energy spread can be reduced [48,685] and that energy spreads down to the sub-0.01% already at an energy of 2-3 GeV can be obtained. This corresponds to ultrahigh 6D brightness [48], again exceeding state-of-the-art by orders of magnitude.

### 26.3 Plasma Injection Mechanisms

To achieve high beam quality stably from LWFA, control over both electron injection into the accelerating buckets and acceleration processes are essential. Nowadays, electron injection schemes via field ionisation and plasma density gradients are widely applied in experiments due to their simplicity and robustness. However, the resulting electron beam quality is generally not high enough as compared to those beams produced by conventional accelerators. In the following, we discuss the possibility to achieve better control of electron injection by combining different schemes, which may enable one to control the electron bunch duration, charge, and energy spread in order to satisfy the requirements for a LWFA-based user facility.

#### 26.3.1 Optimisation of Ionisation Injection

Even though ionisation injection is stable and easy to implement in experiment, it often leads to broad beam energy spread mainly for two causes. First, electron injection can occur continuously as long as the injection thresholds are satisfied. Second, the trapped electrons are often released via ionisation at different wakefield phases, thereby undergoing very different accelerating fields. In the following, we discuss briefly three schemes to reduce the energy spread of accelerated electrons, i.e., self-truncated ionisation injection, two-colour laser ionisation injection, and magnetic-field-controlled ionisation injection.

#### Self-Truncated Ionisation Injection

In order to further reduce the ionisation injection length beyond the mechanical limit, a simple single-stage scheme called self-truncated ionisation injection (STII) was proposed, which predicts a small energy spread of the trapped electron beams well below 10% [661]. This scheme utilises the self-focussing of a laser beam in a plasma to truncate the ionisation injection process, so that the injection length can be reduced to just a few hundred micrometres. Usually, people choose the laser spot size satisfying the so called matching condition  $k_p w_0 = 2a_0^{1/2}$  [185], where  $k_p$  is the wavenumber of the plasma,  $w_0$  is the laser waist radius, and  $a_0$  is the amplitude of the normalised laser vector potential. If  $w_0$  is chosen to be larger than the above matching condition requirement, due to the development of laser self-focussing, the injection is suppressed at the distance of a few hundred micrometres. The reason is explained as follows. The wake strength can be expressed as the pseudo-potential  $\psi$ . To trap an electron, the pseudo-potential drop from the releasing point of the inner-shell electrons to the bottom of  $\psi$  should satisfy  $\Delta\psi > 1$ . For the unmatched case, this condition is satisfied at the beginning. But it is violated when the self-focussing occurs at a few hundred micrometers. Numerical simulations suggest that electron beams with energy spread within 5% can be produced with this scheme. The STII scheme has recently been experimentally verified by several groups with 100 TW scale laser systems, where electrons are trapped and accelerated stably to above 1 GeV with relatively smaller energy spread [28,660].

## Ionisation Injection with Two-Colour Lasers

To further reduce the energy spread to the sub-percent level, one needs to further reduce the ionisation injection length. It is found that the use of a dual-colour laser can limit the ionisation injection in a few separated regions [688]. The injection length of each of the regions is within 100  $\mu\text{m}$ , thus the energy spread can be reduced to the sub-percent level. Let us consider a dual-colour laser with its electric field in the form of  $E = E_{10} \left[ \sin(\omega t) + \sin\left(\frac{3\omega t}{3}\right) \right]$  (the first two terms of the Taylor series of a square wave). Because of the dispersion of the laser in plasma, the different frequency components of the laser propagate at different phase velocities. The wave transforms to  $E = E_{10} \left[ \cos(\omega t) + \cos\left(\frac{3\omega t}{3}\right) \right]$  after propagating a distance of  $\Delta z = \frac{3}{8} \lambda_p \frac{\omega}{\omega_p}$ , where  $\lambda_p$  is the plasma wavelength and  $\omega_p$  is the plasma frequency. With the change of the wave form, the amplitude increases by a factor of  $\sqrt{2}$ . According to the Ammosov-Delone-Krainov (ADK) model, the ionisation rate is exponentially dependent on the electric field. Thus, the  $\sqrt{2}$ -factor can largely influence the ionisation probability. Numerical simulations suggest that this scheme may lead to high-quality electron beams with an energy spread less than 1% [689]. An experimental demonstration of this scheme still remains to be carried out.

## Magnetic-Field-Assisted Ionisation Injection

The above studies make use of self-consistent laser evolutions to truncate the ionisation injection distance, generating high-quality electron beams of small energy spread. It is found that an external transverse magnetic field (ETMF) of a few tens of Tesla can be applied to further control the ionisation injection in LWFA [23]. The ETMF changes the trapping threshold, and the efficient electron injection occurs only if the self-generated magnetic field in the wakefield exceeds a certain critical threshold. For example, the ionisation injection is totally suppressed by a large ETMF at early stages when  $B_y^{ext} = 50$  T. At a later time, when the self-generated magnetic field in the wakefield exceeds the ETMF, the injection occurs at a higher rate, leading to a larger beam charge. The non-linear injection process also shapes the longitudinal charge profile of injected electron beams, as shown in Figure 26.10. When using a stronger ETMF of  $B_y^{ext} = 50$  T, for example, a trapezoidal-like charge profile can be generated. Such a beam profile is known to cause a nearly uniform beam-loading wakefield  $E_z$  [329], which can reduce the energy spread due to longitudinal phase mixing and accelerates the electron beam to a higher peak energy and a lower energy spread. When using  $B_y^{ext} = 50$  T, it is shown that the relative energy spread can gradually decrease from 6.2% ( $z = 4$  mm) to 4.3% ( $z = 5$  mm), while the peak energy increases from  $\sim 224$  MeV to  $\sim 290$  MeV. This is attributed to the uniform beam-loading wakefield. So far this scheme is only demonstrated by 3D PIC simulation.

### 26.3.2 Generation of Attosecond Electron Bunches by Density-Gradient-Controlled Injection

Generally, shorter electron bunches help to achieve higher beam brightness, and hold the promise of generating shorter radiation pulses [690], which are essential for ultra-fast science and applications. While it is common to produce fs-duration beams from LWFA [29], it remains a challenge to go to the sub-fs or attosecond regime. In order to have such extremely short bunches, it is expected to apply fine control over the wakefield acceleration, especially during the injection phase. The key requirement

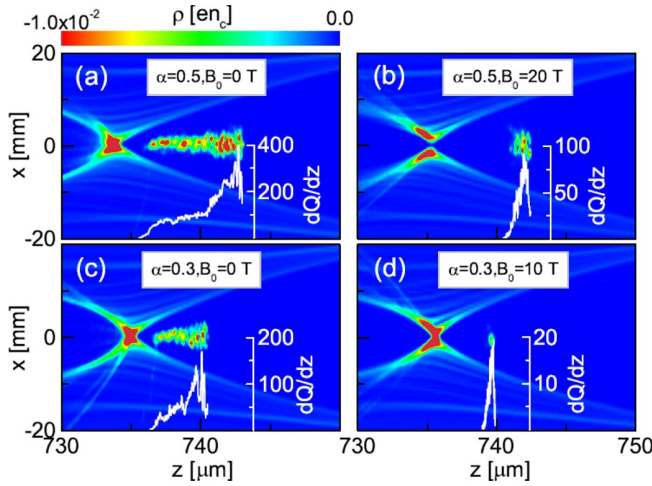


**Fig. 26.9.** Bubble structures and injected electron bunches in a density-profile-tailored plasma with  $n_0 = 0.0002n_{cr}$ , the density bump size  $100 \mu\text{m}$  and four different values of the external magnetic fields and height of the density bump  $\alpha$  over the background plasma [693] (copyright IOP Publishing, reprinted with permission).

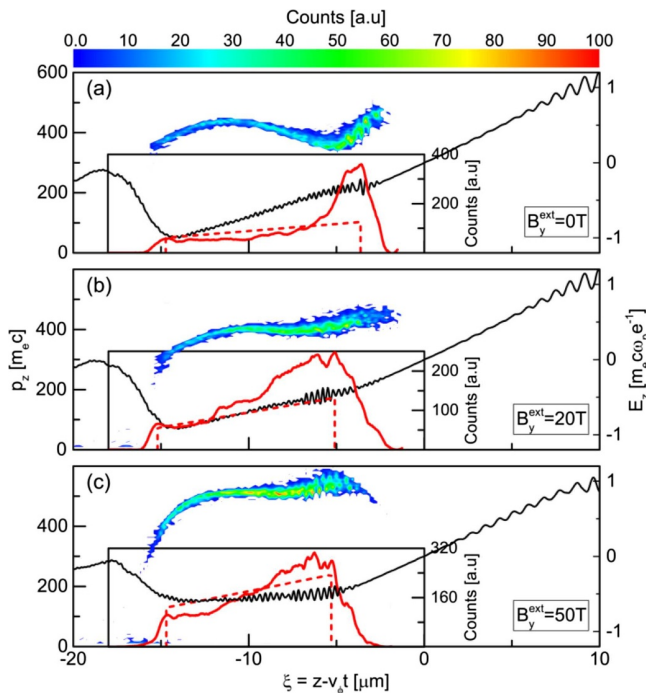


**Fig. 26.10.** (a)–(c) Phase space of injected electrons (colour contour) and the accelerating field  $E_z$  (black curve) for the external field  $B_y^{ext} = 0, 20, 50 \text{ T}$ . Insets compare the charge profiles of electron beams from the simulations (red solid curve) with the optimised trapezoidal-shaped profiles (red dash curve). The figure is taken from [23].

is to make the electron injection occur in a ultra-short period and in a very small area, meanwhile with a high rate so that there is a considerable number of electrons trapped. Following are several possible schemes based upon numerical simulations, which are yet to be demonstrated experimentally.

#### Attosecond Electron Bunches Injected at a Density Transition from an Up ramp to a Plateau

A density tailoring scheme was proposed that makes use of a highly non-linear plasma wave [31,662], which forms extremely short (well within attoseconds duration) high electron density peaks. Usually only a small fraction of electrons in the density peaks can be injected when plasma wave breaking occurs. To achieve injection of a whole density peak almost simultaneously, the plasma density is tailored to include an up ramp followed by a plateau. With such a density profile, the phase velocity of the plasma wave is changed abruptly along the wave-propagation direction from superluminal in the up ramp region to subluminal at the beginning of the density plateau. This can lead to the sudden injection of the first density peak behind the driving laser pulse, generating dense attosecond electron sheets. The above mechanism is essentially of a 1D nature, and in high dimensions it works well for a relatively broad laser spot size (larger than a plasma wavelength). Such dense electron sheets ( $\sim$  the critical plasma density,  $\sim 100$  attoseconds in duration) may be used as relativistic flying mirrors for generating attosecond X-ray pulses [691] or may self-consistently generate giant half-cycle attosecond light pulses [692].

#### Attosecond Electron Bunch Generation Using a Modulated Plasma Density Profile

In addition to injection control with a density up ramp, density down ramps have been widely used to control electron injection. If the density down ramp is steep enough, it is found that ultra-short bunches with attosecond duration can be produced [30]. Generally, the velocity of the back of the bubble can be manipulated through the plasma density, because the plasma bubble length scales as  $n_e^{-1/2}$ , where  $n_e$  is the electron density. As the density is increased, the bubble contracts, and the rear of the bubble speeds up, suppressing injection. In contrast, if the density decreases, then the back of the bubble slows down, and some electrons can overtake the rear of the bubble and be injected. Thus, by varying the plasma density, self-injection can be controlled. It is found that attosecond electron bunches can be generated by introducing a density bump in a homogeneous plasma. Simulations suggest that injected charge scales approximately linearly with bunch length. Under some optimised cases, it is possible to reduce the electron bunch duration to even less than 100 attoseconds.

#### Attosecond Electron Bunches via Injection Suppression with a Magnetic Field

The wakefield structure in the LWFA can be modified by a static external magnetic field. This provides an alternative approach to control the electron injection. Because of the suppression of the electron transverse motion, electron injection can be enhanced by use of a static longitudinal magnetic field of a few tens of tesla [693]. In particular, it is found that attosecond electron bunches can be produced by combining a density-profile-tailored plasma with a longitudinal magnetic field. The static longitudinal magnetic field modifies the transverse structure of the bubble, while the density gradient changes its longitudinal structure. The magnetic field induces a

radial density hole in the bubble rear, which expands as the bubble evolves along the density downramp. Electron injection is triggered by the decreasing phase velocity of the bubble along the density downramp, and then suppressed by the expanding hole at the bubble rear. In this way, the position of electron injection can be controlled, leading to injection of isolated sub-femtosecond electron bunches. Compared to the scheme of density modulation mentioned above [30], the longitudinal magnetic field enables the realisation of sub-femtosecond electron bunches with high charge and with readily accessible parameters both for density profiles and magnetic field strength. Figure 26.9 shows examples of sub-femtosecond electron bunch generation by use of a reasonable density modulation and a longitudinal magnetic field.

## 26.4 Compact Radiation Generation

Based upon energetic electrons from LWFA, X-rays and gamma-rays can be produced via different schemes, such as betatron radiation, non-linear Thomson scattering, undulator radiation, and bremsstrahlung radiation [690]. Among them, the betatron radiation from LWFA in plasma has been demonstrated as a unique source of X-ray emission typically up to 100 keV. It makes use of the wakefield structure, so that the electron acceleration and radiation are combined in a compact way. However, the brilliance and spectrum control needs to be further improved for practical applications. In addition, even though XFELs based upon LWFA-produced electrons have been proposed, the required electron beam quality is yet to be demonstrated in experiment. In this case, coherent X-ray emission based upon LWFA may be achieved in alternative ways rather than based upon the conventional XFEL concept. In the following, some unique potential opportunities with LWFA for X-ray radiation will be discussed.

### 26.4.1 Betatron Radiation Control in a Plasma Channel

Plasma channels have been used normally for guiding laser propagation for electron acceleration via LWFA, where the laser pulses are typically incident along the channel axis. When the laser pulse is off-axially injected or injected with a certain angle against the channel axis, its centroid oscillates transversely in the plasma channel. This results in a wiggler motion of the whole accelerating structure and the self-trapped electrons produced behind the laser pulse, leading to strong synchrotron-like radiation [694]. The produced photon energy or radiation spectrum depend upon the electron energy and betatron oscillation amplitude, where the latter can be controlled by the transverse offset of the laser pulse or the incident angle about the channel axis. Moreover, usually the X-rays from betatron radiation show random polarisation. When the plasma channel is used, the X-ray polarisation can be fixed and tuned from linear to circular polarisation. This is realised by controlling the electron trajectories. If the laser pulse is initially injected off-axially into the plasma channel or at some injection angle in a plane across the plasma channel axis, the laser centroid oscillation and electron betatron oscillation all will remain in this plane. The resulting X-rays will be linearly polarised in this plane. When the laser pulse axis is non-collinear within the plane of the channel axis, the laser centroid will perform a spiral trajectory around the channel axis as shown in Figure 26.11. The resulting X-rays will be elliptically polarised [480]. Therefore, by use of plasma channels, one can realise the control of betatron radiation spectra and polarisation, which is attractive for applications and make up the shortage of large synchrotron radiation facilities.

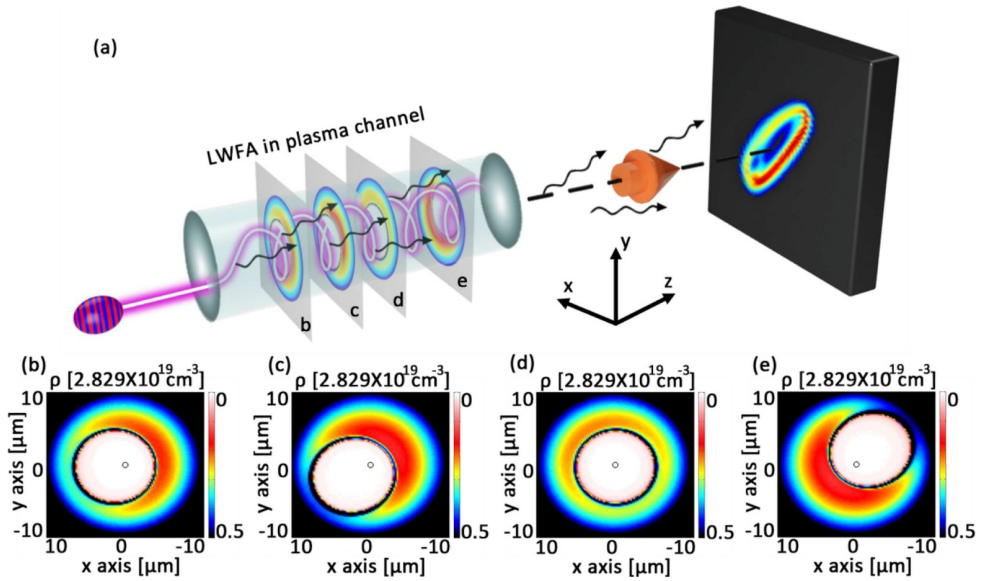


**Fig. 26.11.** Sketch of the radiation source from a helical plasma undulator based on LWFA in a plasma channel and the resulting far-field X-ray radiation distribution [480].

#### 26.4.2 Schemes for Enhanced Betatron Radiation

Betatron X-ray emission from LWFA usually utilises low-Z gases in the self-injection regime. In this regime, even though the electron energy can be controlled with the laser energy and acceleration distance, the betatron oscillation amplitude cannot be easily controlled. To enhance the betatron radiation yields and photon energy, a few schemes have been proposed to enhance the betatron oscillation amplitudes. For example, one may use two laser pulses, one to drive LWFA and another propagating behind to drive direct laser acceleration (DLA) [695]. The DLA or laser-assisted betatron resonance can considerably enhance betatron oscillation amplitudes and thus the X-ray yields and photon energy [71]. It is found that ionisation injection and the use of cluster targets can lead to enhanced betatron oscillation amplitudes, as demonstrated experimentally [646,696]. In these two cases, DLA is also involved at the later stage of electron acceleration, which increases the betatron oscillation amplitudes in addition to enhancing the electron energy.

#### 26.4.3 Coherent Bright XUV and X-Ray Radiation from LWFA

Laser-driven coherent XUV and X-ray radiation is produced so far via high-harmonics generation from laser-atom interactions at moderate laser intensity [697] or from relativistic laser-solid interactions [698]. However, their conversion efficiencies are usually low and fall off quickly with the harmonic order for both cases. Currently, coherent X-ray sources mainly rely on XFELs based upon conventional accelerator technologies. Nevertheless, there are some schemes proposed for coherent XUV and X-ray radiation generation based upon non-linear laser-wakefield excitation and LWFA-based ultra-short electron bunches. It was suggested that the high electron density spikes associated with the laser wakefields can be used as relativistic flying mirrors (RFM) to achieve laser pulse compression, frequency up-shift, and focussing in a counter-propagating geometry [699,700]. To realise coherent X-ray radiation, the flying mirror

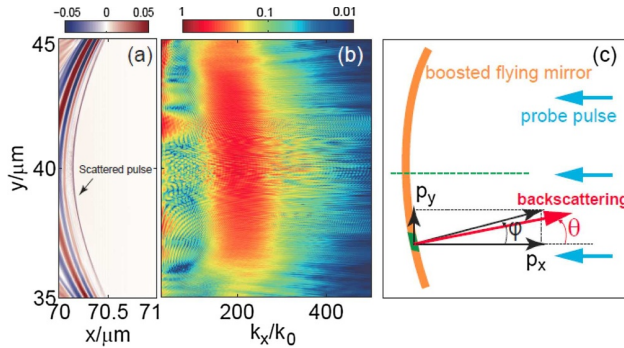


**Fig. 26.12.** Results of 2D PIC simulations of the X-ray generation from LWFA using flying mirrors [691] (reprinted with permission of AIP Publishing). (a) Spatial profile of the electric field of the scattered pulse and (b) the corresponding spectrum in space  $k_x$ - $y$ . (c) Schematic of the backscattering off the flying mirror.

(or the electron density spikes) must be dense enough and electrons in the mirror must have a uniform velocity or very small energy spread. This is technically very challenging.

On the other hand, it has been demonstrated numerically by PIC simulation that a relativistic dense electron sheet can be produced from LWFA with a tailored density profile composed of a density upramp and a density plateau [662]. With this density electron sheet, coherent Thomson scattering can be realised as demonstrated by integrated simulations including both the electron sheet formation and Thomson scattering. Simulations indicate that coherent X-ray emission at a keV photon energy can be realised with this scheme [691]. The required experimental conditions for the generation of dense electron beams from LWFA are within current technical capabilities. Typically multi-100 TW lasers will provide sufficiently high power for the required laser intensity and relatively broad focal spots larger than a plasma wavelength are preferable here. In addition, with the formation of dense electron sheets with a relatively large radius, they will be focused quickly by the transverse field in the laser wakefield. During this process, radially polarised coherent synchrotron radiation with  $\sim 100$  attosecond duration in the XUV regime ( $\sim 30$  eV) will be produced with an energy conversion efficiency as high as  $10^{-3}$  from the driving laser [692]. The emission has a conical angle typically less than  $10^\circ$ . As gas targets are used for this source, it has the potential to be produced with a high repetition rate.

## 26.5 Dielectric Technology for Diagnostics & Beam Control

While the study of particle acceleration in dielectrics is still limited to low energy gains, alternative use cases of dielectrics are being studied worldwide. The following lists three examples:

- Passive energy dechirper: The beam is sent through a dielectric structure. The induced wakefields act back on the electron beam and, if adjusted correctly, can compensate the correlated energy spread of the beam. This may be of great interest to the beams produced in laser-plasma accelerators due to their large correlated energy spread. On the other hand, in order to work best, these concepts require the charge and beam distribution not to vary from shot to shot, which is a currently not the case in LWFA. Therefore, its application is currently mainly studied in conventional accelerators, e.g. in [701].

- Diagnostic devices: The high frequency and high fields in THz dielectric structures make them an ideal candidate for transverse deflecting structures (TDS) to measure the longitudinal bunch length by applying a time-dependent transverse streaking to the beam. These applications are currently being studied theoretically [702] and experimental setups are under development. In principle, also DLAs can be used for this purpose, but there, the experimental progress is less advanced.
- DLA-type structures can be modified to act as beam position monitors [703] with a very good spacial resolution. Their small transverse aperture is a challenge for the integration into conventional accelerators, though.

## 26.6 Additional Application Beamlines

It could be envisaged in the future to extend the application beamlines foreseen in the EuPRAXIA baseline to broaden the scientific impact of the facility. Two options under particular consideration are (1) a high-field physics beamline at the construction site for laser-driven plasma acceleration and (2) a betatron source at the construction site focused on beam-driven plasma acceleration. The high-energy physics case is described briefly in the following and, as will be shown, could be integrated into the current EuPRAXIA design quite easily using only limited additional resources.

### High-Field Physics Beamline

High-field physics is the study of electrodynamics at fields close to the Schwinger field,  $E_{\text{cr}} = m_e^2 c^3 / (e\hbar) \approx 10^{18} \text{ V m}^{-1}$  [704]. The electric fields in the focus of a high-power laser are still far below this, but by colliding a high-intensity laser with a high-energy electron beam, the electric fields in the rest frame of the electron beam can approach a significant fraction of  $E_{\text{cr}}$ . In a head-on collision between the electron beam with energy  $\gamma m_e c^2$  and laser with peak electric field  $E_L$ , the field reaches  $4\gamma E_L$  in the electron rest frame. In such a collision, the electrons are made to oscillate in the laser field with such vigour that they lose a significant fraction of their energy through the emission of high-energy photons (gamma-rays). At high fields, the quantum nature of this emission must be taken into account and a definitive model of the radiation reaction process has not yet been established.

The electron beams produced by laser wakefield accelerators are ideally suited to these type of experiments as they can be naturally synchronised to the required femtosecond precision with a high-intensity laser pulse and their femtosecond duration and micrometre transverse size allow a large fraction of the electrons to overlap with a tightly focused laser pulse. Recent success in this area has been achieved with the first evidence for radiation reaction in a laser-electron beam collision [705] and first signatures of the quantum nature of that radiation [706].

The LWFA facility producing high-quality electron beams with GeV energies for the betatron beamline would be readily adapted to study high-field physics with the addition of a second high-power laser. This laser would be focussed near the exit of the wakefield accelerator (where the electron beam is small) and the key signature of radiation reaction would be the energy loss and change in spectral shape of the electron beam. The stability and reproducibility of the electron beam that will be produced at the dedicated user facility will allow the detailed discrimination of different models of quantum radiation reaction and so provide key insights into strong-field physics. [707]. This energy loss would be measured using the electron spectrometer on the betatron beamline. Additionally, on-axis measurements of the gamma-rays produced in the collision can be used to gain insight into the interaction. The gamma-ray

**Table 27.1.** Performance level and their respective average probability of dangerous failure per hour [709].

Performance level (PL)	Average probability of a dangerous failure per hour (PFH) in $\text{h}^{-1}$
a	$\geq 1 \times 10^{-5}$ to $< 1 \times 10^{-4}$
b	$\geq 3 \times 10^{-6}$ to $< 1 \times 10^{-5}$
c	$\geq 1 \times 10^{-6}$ to $< 3 \times 10^{-6}$
d	$\geq 1 \times 10^{-7}$ to $< 1 \times 10^{-6}$
e	$\geq 1 \times 10^{-8}$ to $< 1 \times 10^{-7}$

profile can be used to infer the on-shot laser intensity at the collision, and the spectrum can aid discrimination between models [705]. On-axis diagnostics to measure these can be placed outside the vacuum chamber behind a suitable vacuum window (e.g. Be or Kapton). Profile measurements of the gamma-rays can be made using pixelated scintillators and the spectra can be determined using pixelated scintillator stacks [708]. These on-axis diagnostics would go in place of the on-axis diagnostics of the betatron radiation, but they do not have demanding alignment requirements so this can be done rapidly. High-field experiments on the dedicated LWFA betatron beamline could be undertaken in relatively short access periods without major disruption to the main activities of the beamline, but could make significant impact in the rapidly growing field of experimental strong-field QED physics.

## 27 Safety and Environmental Impact

### 27.1 Safety Aspects

The EuPRAXIA facility will be built within an existing laboratory infrastructure, and therefore, will be governed by the local safety regulations. This includes entrance and access control systems to the laboratory perimeter and experimental areas, fire alarm systems, and evacuation systems.

Both the radiation safety system and the laser safety system are developed, analysed, and built according to the standards set to evaluate and monitor high-level safety systems. These standards ensure that a facility should be constructed in a manner that it is not able to present a hazard to the users or the general public. After this first goal has been achieved reducing further any risks of hazards which still exist is a secondary task any facility has to perform. These standards can be found in the functional safety of machine controls report [709] and are summarised below.

1. Identification of safety functions: In the first instance, the risk and dangers are assessed and necessary safety measures are identified. During the risk assessment, the assumption that no other protective measure has been put in place is assumed, so that the severity of each individual risk can be assessed correctly. Figure 27.1 shows an overview of the risk assessment and reduction procedure. Safety measures can be implemented via a control software system or via mechanical safety devices.
2. Specification of characteristics of each safety function: The second step lays out the individual specification each of the safety function needs to ensure the experimental environment is safe to operate for the users as well as for the public.

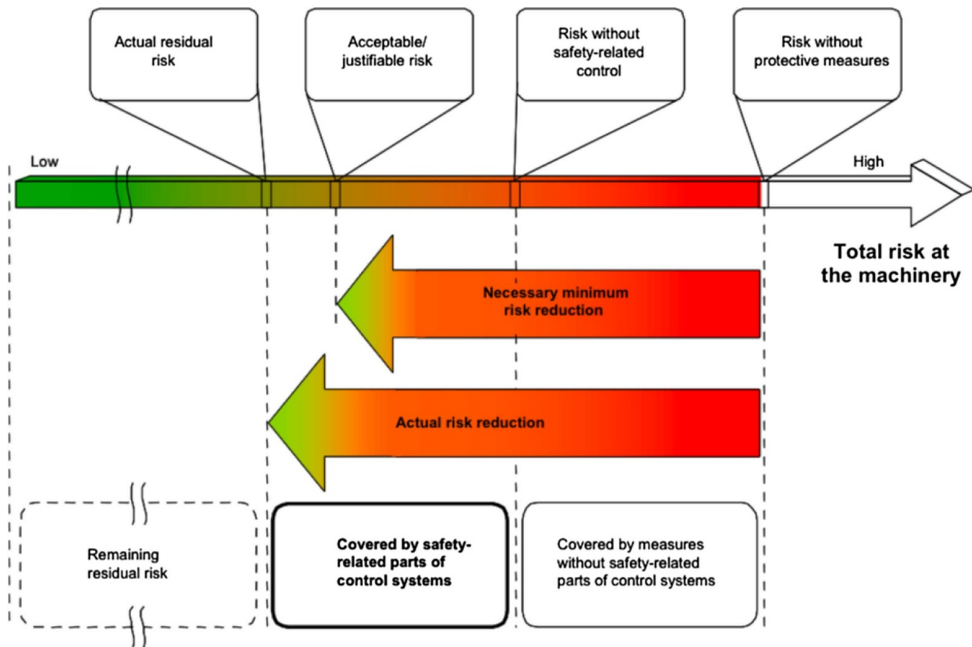


Fig. 27.1. Risk estimation and risk reduction (image credits: [709]).

3. Determination of required performance levels: Once the specifications are characterised, the necessary performance level or quality of the safety function needs to be assessed. The performance level can be placed in one of five categories, defined according to the “probability of a dangerous failure per hour (PFH)”. These levels are summarised in Table 27.1. As pointed out in [709], additional measures, such as software robustness or action-to-counter systematic failures, are required, in addition to PFH.
4. Realisation of safety function and identification of safety related parts of control system: After identifying the risks and hazards of the machine and defining what safety measures need to be implemented, the design of the proper safety-related parts of the protection system can be started.
5. Evaluation of performance level for safety related part of control system: The evaluation considers points such as the mean time to dangerous failure, average diagnostics coverage, and common cause of failure. This point also includes a software and systematic failure analysis.
6. Verification: The process checks if the performance level developed and built is higher than the required performance level for a subsystem. If the performance level is inferior to the required performance level, the safety function for this part of the machine has to be changed, until the required safety level has been attained.
7. Validation: The total safety system is checked for requirements met.
8. All safety functions analysed: The final point ensures that all systems have been analysed and implemented.

Points 1. to 7. are performed for each safety function separately. Point 8. ensures all functions laid out in the beginning of the safety assessment were implemented.

The safety of the accelerator parts of the machine will be implemented, based on local rules, by the research institutes hosting the different EuPRAXIA sites. We note in this context that the machine parameters of EuPRAXIA are well within the range of what has been safely handled at many of the partner institutes for

decades. No new records in beam energy, intensity, or brightness will be reached with the EuPRAXIA accelerators. For the laser system, however, the situation is different, as a high-repetition-rate, high-power regime is pursued. We thus describe in the following some key aspects of safety measures related to the EuPRAXIA laser specifically.

### *Laser*

The purpose of this section is to describe the risk of the laser beam on the EuPRAXIA facility and the means of protection put in place to reduce it to the minimum possible. It is not a full laser risk analysis that can not be led with the current definition of the laser.

The nine general principles of prevention are taken into account in the following manner:

- 1 – **Avoid risks:** Each zone is filtered by an access control by name badge: only authorised persons will be able to enter the zones with presence of the laser. These areas are isolated from the outside (the beam cannot get out). Signage at the entrance of each zone indicates the level of risk with the instructions to be applied.
- 2 – **Assess risks that can not be avoided:** A laser risk analysis has to be written and will have to be updated regularly. This makes it possible to highlight the critical points on which it is necessary to make modifications. In no case should workers be exposed without adequate protection.
- 3 – **Fight risks at the source:** All beam sources are equipped with beam blockers. To limit exposure, collective protection is preferred. In addition, when the collective protections are insufficient or inadequate, we will use the individual protections.
- 4 – **Adapt the work to the Man:** No worker should be exposed to a risk that is not covered by collective or individual protection. The beam height has been defined in such a way that the risk is as low as possible. In addition, all equipment must be at a height very different from that of the beam.
- 5 – **Take into account the evolution of the technique:** Security systems will be monitored on a regular basis and at each major change. Anomalies will be recorded in a hygiene, safety, and working conditions committee register. Room access is only given after receiving adequate security training. The review of the laser risk analysis will take into account technological developments.
- 6 – **Replace what is dangerous with something that is not dangerous or less dangerous:** In the majority of cases, especially during alignment phases, laser sources are used at low energy.
- 7 – **Planning prevention:** If an outside company should work in an area with laser presence, a prevention plan will be systematically written. In addition, the level of risk will be minimised with the presence of an authorised person. Unauthorised persons should not be exposed to risk.
- 8 – **Take collective protection measures:** Many collective protection measures will be installed throughout the path of the beam. To complete these measures, the wearing of glasses adapted to the beam of the area is mandatory. In addition, the wearing of clean room equipment (ISO7 or 8) can hide any reflective objects (watch, bracelet, etc.) which will be prohibited anyway for the operators involved with the laser beams.
- 9 – **Give the appropriate instructions to the workers:** Each person who can work in the presence of a laser must have received training on laser safety. Regulatory signage is present at each zone entrance and inside.

All laser sources used will be Class 4. At the highest level of risk, these lasers are also capable of producing dangerous diffuse reflections. They can cause damage to the skin and can also be a fire hazard. Their use requires extreme caution.

Depending on the area, the beam characteristics will be different (power, energy, repetition rate, wavelength, beam diameter, and pulse duration). The protection will have to be suitable for those characteristics.

There will be two different levels of protection: (1) collective protection, and (2) individual protection.

## Collective Protection

The collective protection consists of three types:

- Zonal protection at each zone: At the entrance of each zone, signalling of the current risk level of the zone by jack and scrolling panels and displays of safety instructions (e.g. to wear safety glasses) will be present. Each zone is accessible through a door with access control. Depending on the level of risk, the persons authorised to enter are different. The list of personnel with their access is validated by the facility management. At the entrance of the zone, an airlock is present to prevent the propagation (direct or by diffusion) of the laser beam out of the zone. Some areas may have windows for visitor tours. These are obscured by components with the same purpose. These protections will be installed before the commissioning of the first laser sources in each zone.
- Global protection at the optical tables: The goal is to add additional protection to local protections that will be linked to the personal security system. This protection is of the hood type encompassing one or more optical tables. These covers will be installed once all equipment on the optical table is installed. In any case, they will be installed before the first tests with the final laser beam.
- Local protection: The objective is to isolate the beam locally using the most appropriate means, such as a single tube to isolate the beam, hoods to isolate a complete block of the optical path, or beam blockers, some of which will be connected to the PSS. These protections will be installed as the optical path progresses. The search for leaks is systematically carried out to guarantee their opacity. In the case where the beam is under vacuum, it is the entire empty system that ensures the protection of personnel. The beam is isolated by tubes or enclosures. The empty system connected to the PSS automatically manages the safety of personnel in the case of a return to atmospheric pressure.

The protection type “hood” will be different and especially adapted to each situation, for example, through the use of:

- a tube for a simple insulation of the beam,
- a hood to isolate a complete block of the optical path,
- a cover enclosing one or more optical tables,
- etc.

In all cases, the material used will allow the absorption and non-diffusion of the beam. The covers enclosing the optical tables are connected to the PSS. Their opening is allowed only for certain levels of risk. An unauthorised opening automatically triggers the zone to a safe level.

Two types of blockers will be used:

- Interzone, which protects staff from the upstream zone,
- Local, which allows to isolate a part of the optical path.

All interzone blockers will be controlled by the PSS. They make it possible to secure the zone in the event of a detected risk. Their functioning is controlled by the PSS. In the case of failure, the interlocks of the sources are opened automatically, which stops the emission of the laser beams.

### Individual Protection

Personal protection is used in addition to collective protection. Goggles are mandatory in areas where laser risk is present. The goggles will be placed in the access locks, on a suitable display. Filters will be selected to protect staff from sources used. Several types of frames will be available to best adapt to the morphology of each. The strongest attenuation will be covered by signals. Permanent staff will have named glasses. Other pairs will be available for casual users.

### Training

All personnel to work in the presence of lasers will have received training in laser safety. A training certificate will be requested from any external person exposed to the laser risk. A visit of the installations will be realised to visualise the locations of the individual protection measures, the various equipment of collective protections, emergency exits, etc.

### Security System

The main purpose of the “PSS” security system is to

- manage collective security loops in danger zones;
- allow the turn on and force the shut down of the laser beams by means of interlocks of the sources;
- report the danger through signaling equipment (verrine, scrolling panels, etc.);
- manage the opening and closing of laser beam blockers;
- control the access and in a general way all the openings of the laser zones; and
- check the closing of the blackout blinds.

Some blockers can be controlled by the supervision system with a link to the PSS.

Only authorised persons can pilot the PSS. Before any change in the level of risk, this person must ensure that those present are authorised and have the necessary protection. The signalling and access to the area concerned is automatically modified accordingly. An audible warning signal is emitted.

### Emergency Situations

Despite all the means of prevention put in place, zero risk does not exist. In the event of an accident, the following measures will be implemented:

- a first aid worker must be present per room;
- all personnel who can work with a laser presence will be trained to the risks as well as for aid measures;
- emergency calls can be accessed in all areas;
- first aid equipment is implemented in each room;
- equipment for fire fighting is present in each zone.

## 27.2 Environmental Impact

Although based on novel acceleration technologies, the proposed EuPRAXIA facility will be very similar to existing conventional accelerator infrastructures in the same beam energy range with regard to its radiological effects, materials and water consumption, environmental emissions, and most other environmental impact factors. As previous sections in this report, such as Chapter 27.1 (on safety), Chapter 11 (on the control-command system) and Chapter 22 (on the electron beam dump design), demonstrate first studies have been completed and strategies have been defined on how to design and implement safety and control systems in a comprehensive and thorough way to limit the facility's environmental effects. This will be carried out in close collaboration with dedicated technical groups at the various partner institutions of EuPRAXIA and will thus be built on extensive experience from other operational machines.

The energy consumption will be a particular factor to be investigated in detail as part of the technical machine design. In a short-term view, the operation of laser systems at average powers beyond the current state of the art certainly presents challenges in this respect; on the other hand, EuPRAXIA's mission to strive for a considerable miniaturisation of the accelerator footprint is expected to have positive effects on energy usage, especially in the long run. EuPRAXIA will use RF systems and laser systems at the highest available efficiency; RF power schemes, for example, can achieve 70% efficiency and the EuPRAXIA laser technology is foreseen to reach an efficiency at the few percent level (wall-plug to RF / laser power). The total power consumption of the proposed facility will stay well within the available power at existing research institutes and is therefore not a fundamental issue for the implementation of EuPRAXIA. However, measures to improve the overall system efficiency are highly important and will be pursued in the technical design phase.

## Part 5

# EuPRAXIA Pre-Construction R&D and Technical Design Phase

## 28 Necessary Experiments and Prototypes for the EuPRAXIA Design

With the EuPRAXIA design featuring a wide range of cutting-edge technologies, a thorough experimental campaign of conceptual tests and prototyping activities will be an essential and unavoidable step in the technical design phase of the project.

In the following section we will provide a list summarising the most important R&D activities identified so far in this context. For reader convenience, we have separated them by main topics with R&D on laser systems, plasma components, RF and accelerator technology, and diagnostics. The following list must be considered as a list of ideas to be tested (and possibly improved) before and during the project's technical design and preparatory phases.

### 28.1 Laser System

EuPRAXIA requires a petawatt laser working at a minimum of 20 Hz and ideally at 100 Hz as a baseline. Such a laser does not exist at the moment and hence several proof-of-principle tests need to be carried out, along with the prototyping of critical components in order to de-risk the project.

#### Pointing stability of drive laser and feedback control

Beams from plasma accelerators are known to have pointing fluctuations. This is a major issue that will limit the applicability of plasma accelerators. Further, this also has safety implications as it is possible for the pointing of the particle and radiation beams from the plasma to exceed the acceptable range beyond which there could be safety implications for the facility as well as the personnel working in the area. For laser-driven plasma accelerators, it is known that the pointing stability of the driver laser affects that of the electron beam. However, the effect of the driver and the inherent fluctuations coming from the plasma medium have not yet been delineated. It is therefore essential to make sure that the effect of laser-beam pointing on the pointing of particle and radiation beams from the plasma accelerator is fully understood and controlled. It is also necessary to test feedback control loops that control the laser pointing to maintain the electron beam pointing within a safe limit. Experiments that test such genetic-algorithm-based loops are underway and are encouraging.

#### Generation of controlled pulse trains

A single pulse of a typical photo-cathode laser has about 200 mJ in energy in the infra-red (800 nm) region. Afterwards, the laser beam has to be compressed, sent to a third harmonic generator (to go from 800 nm to 266 nm), and then it goes through a UV stretcher to be able to switch easily from short pulse to long pulse depending on the linac operation requirements. The final maximum UV energy will be about 2 mJ but it must be possible to reduce it down to a few  $\mu\text{J}$  using filters to have

the possibility to explore a big range of energies. Such systems are nowadays quite standard and do not require additional R&D. Other tasks and schemes, however, may require producing 3D-shaped laser pulses (formation of triangular, cylindrical, ellipsoidal, etc. pulses), R&D on which may be carried out, e.g. by staff at the Institute of Applied Physics of the Russian Academy of Sciences (IAP-RAS).

The EuPRAXIA beam-driven plasma acceleration schemes rely on the possibilities of generating ps-spaced pulse trains, each pulse having the characteristics mentioned before. The driver pulses in the train shall be equally spaced to resonantly drive the plasma wave, while the witness pulse delay should be easily tuned to maximise the acceleration performance. Moreover some schemes foresee also an increasing charge in the driving electron beam, and with this a non-constant intensity in the corresponding optical pulses. Solutions and optical schemes have already been tested for some time, but additional experiments are still needed to find the optimal and most versatile solution.

### Damage testing of optical components

Optical components in the beam transport line, including the last grating in the compressor, highly reflective mirrors and parabolas, are exposed to the highest unfocussed intensities in the laser system. Typically, the laser beam diameter is chosen so as to have a fluence on these optics just below the damage threshold of the components. Although high-damage threshold coatings exist, their behaviour at these fluence levels at high repetition rate is unknown. Joint R&D efforts with optical manufacturing companies are thus required for developing and testing high-damage threshold optics in the system.

### Prototype of a 100 Hz laser system

The repetition rates of a high-power laser system such as the one envisaged in EuPRAXIA are currently limited by the availability of pump laser technologies that can drive these petawatt lasers at high repetition rate. The repetition rate of petawatt and petawatt-class lasers is currently limited to 10 Hz, in both flash-lamp-pumped as well as diode-pumped solid-state laser (DPSSL) technologies. R&D works are thus ongoing to extend this further. Although EuPRAXIA could begin with a 20 Hz petawatt laser system, it aspires to have a 100 Hz petawatt laser for driving plasma accelerators in its next phase. Significant advancements in high-average-power laser technology are required to achieve this. Some of these technologies include, for example, the use of multiple optical fibres, phase-locked to deliver the required brightness. Such systems are not currently available at sufficiently high energy and power, but may offer advantages from a systems engineering aspect in the future if the anticipated performance and cost improvements are realised. It is envisaged that multiple pump laser technologies (DPSSL thin-disk, Big-Aperture Thulium, etc.) will need to be tested in this regard in order to build a prototype for such a system.

### Thermal load and cooling of critical laser components

Even with the right pump laser technology, the thermal management of key components in the laser system becomes a bottleneck for driving high-power lasers at high repetition rates as at such high repetition rates the thermal load induced in the system invariably induces a thermal lens effect that will detrimentally affect the laser

beam quality. For example, the final amplifier, where the maximum pump energy is dumped, needs an active cooling system that can take away the excess heat generated in the gain medium, while maintaining the wavefront quality of the laser beam. This means that turbulent flows of liquid and cryogenics, which are usually used to cool optical systems, need to be employed carefully so that they do not affect the transmitted wavefront quality of the amplifier. Amplifier technologies such as OPCPA, which do not rely on energy storage, will need to be explored in this regard.

The pulse compressor is the final link in the laser chain, one of the most critical and often acts as a fuse in terms of damage threshold for the entire laser chain. The gratings used in high-power laser compressors are typically metallic (gold) although, with the expansion in the numbers of CPA laser systems around the world, grating technology is developing quite rapidly with the goal of increasing the damage threshold of gratings for use in pulse compressors. Recent reports on hybrid / dielectric gratings for petawatt-class laser systems are very encouraging.

While the damage threshold is one key issue with the compressor gratings, their very diffracting nature causes issues with heat absorption. With gold gratings, typically around 94-95% of the energy is diffracted into the first order, and 3% into the zeroth order. The remaining 3% is absorbed by the grating, which can lead to issues with substrate heating and deformation. For example, a compressor grating in a petawatt laser running at 20 Hz can be exposed to as much as 900 W of average power, and there is a significant risk that it will absorb enough energy to deform as a consequence of thermal gradients set up in the substrates. A solution needs to be developed to address this problem in EuPRAXIA.

## 28.2 Plasma Components

### High-throughput plasma targets and plasma mirrors

For LWFA applications at high repetition rates, gas targets that can provide the acceleration medium are a prerequisite. Depending on the necessary acceleration gradient, it is often required to fill gas targets ranging from gas-filled capillaries, which operate at few millibars, and gas-cells with few bar backing pressures to pulsed gas jets, which operate at several tens of bar backing pressure. This creates a significant load on the pumping system as the gas release into the vacuum chamber with pulsed nozzles, running at high repetition rates, and gas cells, leaking continuously through the apertures for laser inlet and exit, must be handled. At high repetition rates, this might require differential pumping systems or techniques that isolate the high-pressure region from the rest of the vacuum beamline. Such systems will be tested and prototyped.

Similarly, it is essential to remove the drive laser pulse after the interaction with the gas target. Current technology (such as plasma mirrors) needs to be able to operate at high repetition rate. While it is possible to use tape-drives as plasma mirrors, their reliability at high repetition rate, subjected to high-pressure and high-radiation environments, needs to be checked. Recent experiments suggest that liquid crystals could provide an alternative but this again needs to be tested at appropriate repetition rates.

Due to dephasing issues in a single stage of a laser-plasma accelerator, adding multiple stages of acceleration will be required to produce electron beams of energies around and beyond 5 GeV. The requirement of high-repetition-rate plasma mirrors is important for not just the driver removal but also for enabling staged acceleration at high repetition rate. The current technology for staged acceleration involves the drive laser for the second or additional stage to be reflected into the plasma target by

a plasma mirror. This requires highly reflective and thin optics in order to minimise energy loss from the laser as well as reducing the disturbance of the electron bunch. The development and testing of such plasma mirrors will be an essential aspect of the technical design phase.

### Stability and reliability of active plasma lenses

Active plasma lenses represent compact and affordable tools with radially symmetric focusing and magnetic field gradients up to several kT/m. Such devices represent a reliable and affordable solution because of their compactness, strong focussing, and high tunability.

To be used as focussing devices, however, their effects on the particle beam distribution must be well characterised. Some studies are already reported in literature (e.g. in [305]) and first experimental results focussing a high-brightness electron beam by means of a discharge-capillary of a few centimetres length (pre-filled with hydrogen gas) are available. The magnetic focussing field, when operating at low discharge currents, can be highly non-linear at increasing distance from the lens centre, leading to an emittance increase due to spherical aberrations.

The necessary additional experimental and prototyping studies will focus on the reduction of beam emittance increases due to non-linearities in the focussing field during lensing and / or the possible partial ionisation of the gas in the capillary. To achieve a full optimisation of such a device and a high quality of the focussed beam, a viable solution could be the experimental study of different capillary geometries and discharge circuits. Experiments are also needed to refine the numerical model of the phenomenon to account for the effects, for instance, of misalignment on the properties of the out-coming beam or to design optimised capillaries.

## 28.3 RF and Accelerator Technology

Additional issues that need to be tested concern practical aspects of the implementation of EuPRAXIA as a test facility. We underlined three classes of problems that have emerged during the work towards the present CDR.

### Laser-electron beam synchronisation for external injection schemes

The most stringent requirement for the timing and synchronisation systems concerns the injection and acceleration of a single bunch in a plasma wave excited by a laser pulse. In this case, the relative jitter between laser pulse and electron bunch must be a fraction of the plasma wavelength (i.e. smaller than 20 fs RMS). Once such requirement is met, all other subsystems could benefit of such a high-quality synchronisation performance.

The synchronisation system usually generates and distributes a reference signal to provide a fine temporal alignment among all the relevant sub-system oscillators that guarantees a temporal coherence of their outputs with a precision of 10 ps–10 fs (coherence between RF accelerating fields, laser oscillator frequencies, ADC / DAC clocks, etc.). A typical system is based on industrial standard devices, common to many accelerator infrastructures based on room-temperature RF (e.g. European XFEL, FLASH, LCLS, SwissFEL, ELI\_NP GBS, etc.). Testing is still needed to assess that the required <20 fs jitter can be routinely achieved in a complex accelerator environment.

Moreover, the proposed sub-femtosecond synchronisation technique, proposed in Chapter 15 and expecting to achieve even better timing synchronisation, will also need to be tested experimentally and optimised.

### Performance and reliability of a plasma-based beam dump

A plasma beam dump uses the collective oscillations of plasma electrons to absorb the kinetic energy of a particle beam. Recent studies [581] proposed a modified passive plasma beam dump scheme using either a gradient or stepped plasma profile to maintain a higher decelerating gradient compared with a uniform plasma. The improvement is a result of the plasma wavelength change preventing the re-acceleration of low energy particles. Particle-in-cell simulation results show that both stepped and gradient plasma profiles can achieve improved energy loss compared with a uniform plasma for an electron bunch of parameters compatible with those expected for EuPRAXIA.

Plasma beam dumps show great promise both in providing compact deceleration to complement high-gradient novel accelerators and in reducing the complexity of beam dumps in conventional accelerators. Although passive plasma beam dumps are not capable of decelerating the head of the bunch, the rapid reduction in total beam energy would allow for a conventional beam dump to absorb the remaining energy with greatly reduced radio-activation and cooling requirements. Experiments are now needed to assess the reliability of the scheme, which has to satisfy also the radio-protection standards to be included in the final technical design of EuPRAXIA.

### Automatic feedback systems for optimising electron beam properties

The achievement of a high quality of laser-wakefield-accelerated beams comparable with conventional accelerators is an open experimental issue and many innovative ideas have been proposed and tested.

For instance, Dann et al. [710] recently proposed a genetic algorithm to apply active feedback to a laser wakefield accelerator at a higher power (10 TW) and a lower repetition rate (5 Hz) than previous work. The temporal shape of the drive laser pulse has been adjusted automatically to optimise the properties of the electron beam. By changing the software configuration, different properties could be improved. This included the total accelerated charge per bunch, which was doubled, and the average electron energy, which was increased from 22 to 27 MeV.

Moreover, using experimental measurements directly to provide feedback allows the system to work even when the underlying acceleration mechanisms are not fully understood, and, in fact, studying the optimised pulse shape might reveal new insights into the physical processes responsible.

Reference [710] already identifies other promising algorithms to be used in the same way as the genetic one to improve beam parameters. Similar ideas can be used also to design the generation and transport of high-charge, higher-energy laser-driven electron beams. Such an approach needs to be further tested since it may be a practical way to run EuPRAXIA as a user facility.

## 28.4 Diagnostics

The diagnostics for both the beam-driven and laser-driven design options of EuPRAXIA will face similar problems. First of all the (laser or particle) driver will

strongly affect any measurement if the driver is not properly removed. Typically the driver is “intense” enough to trigger efficiently the acceleration mechanism; thus its removal must be quite complete in order not to blind or even damage the diagnostics detectors. Another non-negligible requirement is the compactness of the diagnostic station, which may be not trivial at high energies.

Due to the powerful focussing strength of the plasma channel, which the electron beam exits after acceleration, the beam will have a quite high divergence. Such a characteristic, joined with the high energy spread possible during the commissioning phase, may result in complex capture optics, possibly affecting the accuracy of beam parameter measurements. Additionally, to have an energy spread competitive with conventional accelerators, plasma-accelerated beams must be extremely short (on the fs scale); therefore, fs resolution is required in any time-related measurements (e.g. for the bunch length as well as phase jitters).

Especially in the commissioning phase, the accelerated beam may experience some shot-to-shot instabilities connected to the high accelerating fields acting on the beam itself. Therefore, the measurement techniques should be as much as possible independent on pointing, energy, and time jitters.

Most of these issues as well as possible solutions are extensively discussed in Chapter 21 and [711], where the authors report on the design study of diagnostics for a high-brightness accelerator, based on an X-band linac and a plasma accelerator stage, to be delivered in the framework of the INFN-LNF initiative towards beam-driven plasma accelerators.

The development and implementation of most of the ideas reported in [711] should be experimentally studied to be a baseline also for the technical design phase of EuPRAXIA. Some activities have already started during the EuPRAXIA CDR phase. Although they are of paramount importance to assess EuPRAXIA concepts, some of these experiments are focused on demonstrating reliability or on investigating implementation issues. Therefore, some of them may not have the potential for world-class scientific publications, which is a prerequisite for a successful application to many of Europe’s top test laboratories. It is thus likely that some of these proof-of-principle tests will not get experimental time in the open slots in some of the major user facilities through direct application. A proposed strategy is to establish collaborations between EuPRAXIA partners and associate labs in order to facilitate such experiments.

As a general statement, single-shot measurements are preferable for plasma-accelerated beams, including for emittance diagnostics, while a measurement resolution at the  $\mu\text{m}$ -level and fs-scale (for beam size and bunch length respectively) are requested. In the following, we will report on the necessary beam measurements trying to give a fast overview of the main issues to be included in the systematic experimental studies needed to complete the technical design of EuPRAXIA.

## Longitudinal phase space

The conventional way to measure longitudinal phase space in high-brightness linacs involves transverse (RF) deflectors for length measurements and dipoles as spectrometers for energy measurement; they are often used together for full longitudinal phase-space measurements and / or as diagnostics for slice energy spread. X-band frequency (i.e. more compact) devices should be tested for EuPRAXIA-like beams to verify that they can be considered as an option for the final design.

Such techniques are intercepting and typically require multiple shots. Single-shot, non-intercepting bunch length measurements may be useful, for instance, when the beam is sent into a plasma module to correlate input and output properties of the

bunch. Such a feature is believed to be very useful in the commissioning phase. In this context, extensive testing and / or prototyping of novel ideas can help significantly.

One idea to be tested could be the use of diffraction radiation, which is emitted when a charged particle passes through a hole with transverse dimension smaller than the radial extension of the electromagnetic field travelling with the charge. There are some studies reported in [312,551,673], but optimisation and testing with a EuPRAXIA-like beam is still to be performed. Similar comments hold for devices for non-destructive bunch length measurements based on Smith-Purcell radiation [712]. A systematic prototyping of devices using both approaches can help significantly for the next EuPRAXIA phases.

Another quite interesting option for single-shot, bunch length measurements is electro-optical sampling. The bunch electric field can rotate the polarisation of a laser impinging on a crystal, and thus it is possible to retrieve the longitudinal beam profile in one shot [713]. Experiments are needed to reduce the temporal resolution (now on the order of 40–50 fs), limited by the crystal bandwidth or by the length of the laser probe.

Since plasma-accelerated beams are in the femtosecond range, the synchronisation with an external RF pulse (e.g. in a transverse RF deflector) is not at all trivial. A class of novel devices, namely passive streakers, are now starting to be discussed. The idea is to deflect the tail of the beam by means of self-induced wake-fields when the beam travels close to properly designed structures, such as dielectric or corrugated pipes. Such devices were conceived to compensate correlated energy spread in free-electron lasers; wakefields are naturally synchronous with the beam and thus researchers consider to use them for deflecting the bunch as in a RF deflector. Interesting and non-trivial R&D is still needed but such an idea could also have an impact for EuPRAXIA.

## Transverse phase space

There are two main measurements for transverse diagnostics: emittance and envelope (i.e. beam size along the machine).

The envelope measurement is needed to properly match the beam along the machine; comparing the measured dimensions with the simulated ones typically helps considerably in the commissioning phase. Beam size measurements in high-brightness linear accelerators is typically done with optical transition radiation. Such an approach is still valid also for EuPRAXIA, even if some testing / prototyping is needed to verify the technique's reliability for  $\mu\text{m}$ -size beams, as the ones expected at the entrance or exit from the plasma channel.

Emittance measurement is a more difficult issue; the resolution must be better than 1 mm mrad and, ideally, one needs single-shot, non-destructive measurement means to be used in the tuning of the machine to control the emittance increase possible during the plasma acceleration. A viable solution could be to use betatron radiation for the emittance measurement just at the end of the plasma channel, while other single-shot methods must be proven before a final design and implementation.

Conventional betatron radiation systems were able to measure just the beam profile and divergence, neglecting the correlation term. Only recently a new algorithm has been developed to retrieve the correlation term [711]. By using the simultaneous measurement of the electron and radiation energy spectra, it is possible to have a better reconstruction of the phase space.

A kind of optical pepper pot, based on optical transition radiation produced when a charge passes through a metallic foil, has also been proposed for single-shot emittance measurement [711]. The angular distribution of the emerging radiation contains information about the angular divergence of the beam. By using an optical

system to reproduce outside the vacuum chamber the source radiation field and sample it by means of a microlens array, it is possible to retrieve the value of the beam divergence in different transverse positions.

Such ideas need careful testing, with conventional beams as well as with high-divergence and high-energy-spread beams, which do not preserve emittance in a drift [379].

### Beam trajectory and beam charge monitors

Plasma accelerators require control of the charge and the trajectory at resolutions of a few pC and a few micrometres. Such accuracy is needed at the entrance of plasma channel, since misalignment can induce instabilities in the beam, but also at the entrance of the undulator sections.

Even if commercial systems (e.g. integrated current transformers) allow the measurement of a charge as low as 50 fC, we still need testing devices able to measure both charge and beam position, seeking the most compact solution.

Cavity beam position monitors (BPM) can have  $\mu\text{m}$ -level resolution, even at very low charge (few pC), while taking up little space longitudinally. There exist many kinds of cavity BPMs working in different frequency ranges; one of the difficulties is the monitor calibration in an operating machine environment and thus a systematic experimental study of the possibilities is believed to be mandatory.

## 29 EuPRAXIA Consortium Facilities

### 29.1 APOLLON (France)

The APOLLON facility [714] will deliver a set of laser beams, synchronised and possibly overlapped at one single focal spot, for a maximum total energy on target of 265 J. This laser setup includes:

- a main laser beam (“F1”), delivering pulses of 150 J at maximum in 15 fs, i.e. with a peak power of 10 PW (1 shot per minute),
- an intense auxiliary laser beam (“F2”), delivering pulses of 15 J at maximum in 15 fs, i.e. with a peak power of 1 PW,
- an uncompressed “creation” laser beam (“F3”), delivering pulses of duration 1 ns with a maximum energy of 250 J,
- and a fs probe laser beam (“F4”), delivering pulses of 250 mJ at maximum in 20 fs (10 TW).

These beams will be directed into two experimental areas:

- HE1, which – using short focal length focusing optics ( $f/2.5$ ) – will be more focussed on the study of laser interaction with solid targets at intensities close to  $1 \times 10^{22} \text{ W/cm}^2$  to generate proton, ion and X-ray radiation secondary sources for pump-probe experiments,
- HE0, which will be more specialised for studying particle acceleration using long-focal-length focusing optics ( $f/75$ ).

This facility is located on the Orme des Merisiers site, reusing the ALS building (dismantled in 2006).

The facility will be open to users in 2020 after first experiments devoted to equipment validation and reliability tests. The laser chain and the associated experimental areas will thus be at the heart of a unique centre for experiments at the forefront of research on various topics related to high-power ultra-high intensity lasers and to the sources they allow creating.



**Fig. 29.1.** Map of European EuPRAXIA consortium facilities. Divided into laser, accelerator and computing laboratories, these could be used for prototyping and testing concepts and components during the planned technical design phase of the project.

## 29.2 CLARA (United Kingdom)

CLARA (Compact Linear Accelerator for Research and Applications) is a purpose-built dedicated accelerator test facility at STFC Daresbury Laboratory in the UK [715]. Currently CLARA operates at up to 50 MeV, providing electron beams into two independent radiation bunkers for exploitation by accelerator researchers, including LWFA and PWFA experts. One bunker also has the capability to combine the electron beam with a 10 TW laser which is particularly attractive for plasma accelerator experiments. In the future, it is planned to upgrade the beam energy to 250 MeV (the main parameters are summarised in Tab. 29.1), again with a dedicated bunker and high peak power laser, for a range of electron beam experiments including plasma acceleration studies. The electron beams are generated by a high-gradient photo-injector, with a repetition rate up to 400 Hz, and so the electron beam brightness will be very high, with peak currents beyond 5 kA, ideally matched to PWFA experiments. In addition, CLARA has space reserved for an FEL to be installed in the future, enabling advanced FEL concepts to be developed and tested prior to implementation in an X-ray facility. The layout of CLARA, showing the 250 MeV electron exploitation beamline and radiation bunker, and the space reserved for an FEL in the straight-ahead geometry, is shown in Figure 29.3. Access to beam time at CLARA is granted competitively through a call for proposals, open to any researcher (subject to eligibility). Proposals are assessed by an allocation panel, who advise the facility based upon certain criteria, such as scientific excellence and impact.



**Fig. 29.2.** View of the laser facilities at APOLLON (image courtesy of APOLLON).

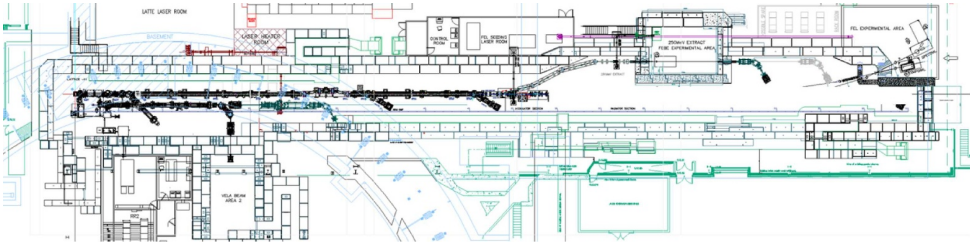


**Fig. 29.3.** Layout of the CLARA facility, including the 250 MeV electron exploitation beamline, radiation bunker, and the space reserved for an FEL (image courtesy of CLARA).

**Table 29.1.** Main parameters for the CLARA operating modes.

	Units	
<b>Bunch charge</b>	pC	25–250
<b>Energy</b>	MeV	250
<b>Bunch length</b>	fs RMS	<30–850
<b>Energy Spread</b>	keV	25–100
<b>Repetition rate</b>	Hz	100–400
<b>Normalised emittance</b>	mm–mrad	<1

### 29.3 COXINEL (France)

COXINEL [65,716] is a test experiment set up by a collaboration of Synchrotron SOLEIL, Laboratoire d’Optique Appliquée (LOA), PhLAM of the University of Lille (all France), and the Weizmann Institute of Science (Israel). It is based at the *Salle Jaune* hall of LOA, where a 10 m electron transport beamline was designed and installed by SOLEIL. The laser-plasma accelerator uses the 60 TW, 800 nm, 30 fs Ti:Sapphire laser of LOA, and an additional laser beam of several mJ is provided to seed the FEL. The electron beam is handled by a series of permanent-magnet variable-gradient quadrupoles designed for this experiment, followed by a decompressing magnetic chicane, electro-quadrupoles and the 18 mm-period undulator U18 of SOLEIL. The chicane-based beam transport follows the strategy of the longitudinal sorting of electron energies to enable FEL amplification for high beam energy spreads.

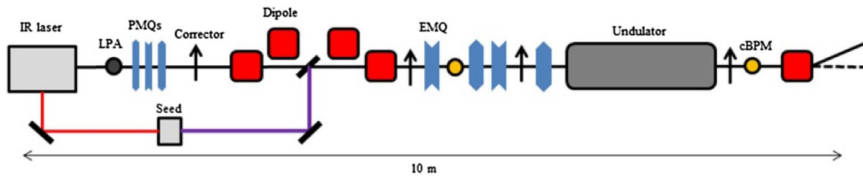


**Fig. 29.4.** Schematic view of the COXINEL beamline. The following abbreviations are used to describe the beamline components: LPA = laser-plasma accelerator, PMQ = permanent magnet quadrupole, EMQ = electromagnetic quadrupole, cBPM = cavity beam position monitor (image credits: [716]).

## 29.4 ELBE Centre for High Power Radiation Sources (Germany)

The ELBE Centre for High Power Radiation Sources of the Helmholtz-Zentrum Dresden-Rossendorf (HZDR) [717] combines advanced laser-plasma accelerator research with the user operation of accelerator-driven radiation sources serving a range from intense THz pulses via IR FEL beams and X-rays to pulsed positrons. Basic research as well as interdisciplinary applications of societal relevance, like image-guided cancer radiotherapy, benefit from the leading in-house expertise of the centre. Highest fields are offered at the dual-beam petawatt laser DRACO with key applications in ion and electron acceleration and are complemented by the development of the fully diode-laser-pumped petawatt laser Penelope. Unique synergies of ultra-fast probing and plasma preparation are exploited by the installation and operation of the Helmholtz International Beamline for Extreme Fields (HIBEF) at the European XFEL. Basic research as well as applied experimental projects are complemented by innovative and open-source computing activities focussing on GPU-accelerated simulation tools (PIConGPU), aiming for predictive capabilities and big data management. HZDR operates the DRACO petawatt laser facility providing  $\sim 30$  fs laser pulses in two independent pulse-cleaned beams of 4 J and 25 J laser energy on target. The main beams can be used individually or combined and are routinely complemented by an independent suite of synchronised probe beams at different non-harmonic wavelengths and pulse durations as well as by ELBE-accelerator electron bunches of ps duration. Two fully equipped target areas are served with a focus on the laser interaction with solid and gaseous targets at short and long focal lengths. With the topical focus of the facility on the development of advanced plasma accelerators and related applications, a key advantage is the provision of single-shot reference diagnostics and probes for the routine on-shot characterisation of the laser-matter interaction and particle beams as well as a variety of targets and target support. A dedicated pulsed magnet infrastructure enables the investigation of magnetised plasmas as well as ion beam transport for the dose-controlled external irradiation of samples like radiobiological probes. For the latter, an integrated biology lab supports handling and evaluation of, for example, cell samples. The development of next-generation high-power lasers is performed with the diode-pumped Yb:CaF<sub>2</sub> petawatt laser project Penelope. Pulses of 150 J in 150 fs will be available first for ion acceleration applications within the joint Helmholtz ATHENA project at final repetition rates of up to 1 Hz. One aspect of ATHENA is the implementation of a series of different front-end technologies for advanced temporal pulse cleaning.

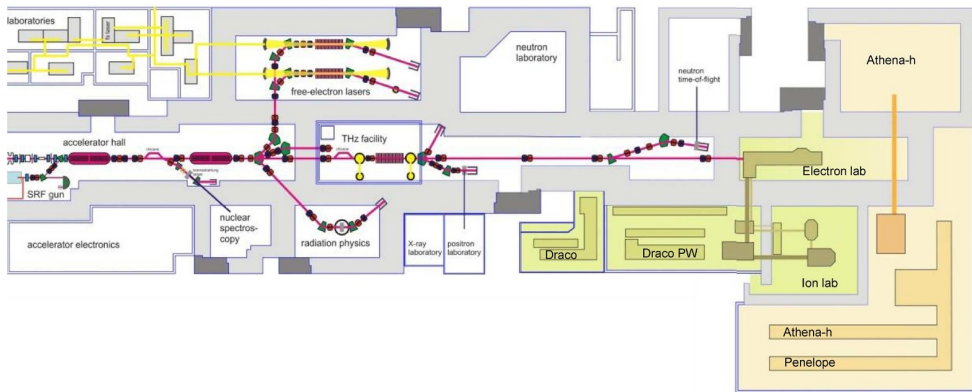


**Fig. 29.5.** Footprint of the ELBE Centre for High Power Radiation Sources, showing from the left the cw superconducting 40 MeV electron accelerator with the SRF photo-gun and downstream experimental areas for secondary radiation (total scale about 100 m). Experimental areas for the Draco petawatt laser system are coloured in green (including areas labelled as “Draco”, “Draco PW”, “Electron lab”, “Ion lab”), providing bunkers for multi-source experiments. The Penelope laser area and lab space hosting ATHENA\_h are coloured in orange (including areas labelled as “Athena-h”, “Penelope”) (image courtesy of Helmholtz-Zentrum Dresden-Rossendorf).



**Fig. 29.6.** The L1 “Allegra” laser developed in-house by the ELI Beamlines laser team (100 mJ, 1 kHz) (image courtesy of ELI Beamlines).

## 29.5 ELI – Extreme Light Infrastructure

### ELI Beamlines

The main goal at ELI Beamlines [718] is to develop the most advanced laser equipment in the world for basic research as well as for areas such as medical imaging and diagnostics, radiotherapy, new materials, and X-ray optics. The development of a compact laser-driven free-electron laser is one of the main topics of the ELI Beamlines team. All these research activities at ELI Beamlines are based on the laser systems, which are under operation or preparation.

The L1 “Allegra” laser has been developed in-house by the ELI Beamlines laser team (see Fig. 29.6). The concept of the laser is based on the amplification of frequency-chirped picosecond pulses in an optical parametric chirped-pulse amplification (OPCPA) chain consisting of a total of seven amplifiers. The laser system is designed to generate  $<20$  fs pulses with energy exceeding 100 mJ per pulse at a high repetition rate of 1 kHz. The central wavelength of the “Allegra” laser is  $830 \text{ nm} < \lambda < 860 \text{ nm}$  with the linear horizontal polarisation of the output beam. The output laser pulse energy stability (RMS) is better than 5%. The output laser beam



**Fig. 29.7.** The L2 “Amos” laser system is under development now at ELI-Beamlines (20 J, 10 Hz) (image courtesy of ELI Beamlines).



**Fig. 29.8.** The L3 “HAPLS” laser system at ELI-Beamlines (30 J, 10 Hz) (image courtesy of ELI Beamlines).



**Fig. 29.9.** The L4 “Aton” laser system is under development now at ELI-Beamlines (2 kJ, 1 shot/min) (image courtesy of ELI Beamlines).

pointing stability (RMS) is less than  $10 \mu\text{rad}$ . The L3 “HAPLS” laser system of ELI Beamlines (see Fig. 29.8) is designed to deliver petawatt pulses with energy of at least 30 J and a pulse duration of 30 fs at a repetition rate of 10 Hz. This system was developed at the Lawrence Livermore National Laboratory (LLNL, USA) with ELI Beamlines cooperating on the development of the petawatt pulse compressor, the short-pulse diagnostics, and the short-pulse controls and timing. The current parameters, achieved now (August 2019) are a peak power of 0.4 PW, a pulse energy of 11.5 J for a pulse length of 28 fs at a repetition rate of 3.3 Hz.

The L2 “Amos” (see Fig. 29.7) and L4 “Aton” (see Fig. 29.9) laser systems are under development now at ELI Beamlines. The L2 “Amos” laser system is designed to generate ultra-short laser pulses with peak power up to 0.5 PW. The laser will be able to operate at a high repetition rate of 10 Hz due to the full utilisation of new technologies, such as laser diode pumping and cryogenic cooling of the laser material. In the nearest future, this laser system will be upgraded to provide an output pulse energy of 10 J with a repetition rate up to 25 Hz and with a pulse compression down

**Table 29.2.** Typical beam parameters at the FLASHForward facility.

	<b>Units</b>	
<b>Bunch Charge</b>	pC	50–800
<b>Energy</b>	MeV	400–1250
<b>Bunch Length</b>	fs RMS	50–6000
<b>Chirp</b>	% RMS	$\pm 0.5$
<b>Transverse Emittance</b>	mm mrad RMS proj	1–3
<b>Focal Spot size</b>	$\mu\text{m} \times \mu\text{m}$	5×5 (spec.), 30×30 (meas.)
<b>Energy resolution</b>	%	0.02
<b>Macro repetition rate</b>	Hz	1–10
<b>Micro repetition rate</b>	MHz	0.040–3

to 30 fs. The L4 “Aton” laser system is designed to generate an extremely high and unprecedented peak power of 10 PW during pulse durations of about 130 fs with a repetition rate of 1 shot per minute. The expected stability of the output laser pulse energy (RMS) is better than 10% with the output laser beam pointing stability (RMS) less than 10  $\mu\text{rad}$ . The delivery of the L4 “Aton” laser system was contracted with the United States-Lithuanian consortium of National Energetics and EKSPILA in September 2014. The main subcontractors of this laser system are Schott and the Lawrence Livermore National Laboratory. ELI Beamlines is in charge of the full diagnostics of the compressed 10 PW beam, the laser timing platform, as well as the design and delivery of opto-mechanics for the 10 PW compressor.

In parallel with the development of the different laser systems of ELI Beamlines, the preparation of the experimental halls for different research activities is on the way. The user operation of the L1 “Allegra” laser for material and bio-molecular applications started at ELI Beamlines in summer 2019. The usage of the L3 “HAPLS” laser for plasma physics and for ion acceleration should start in the second half of 2019. The electron acceleration and development of the undulator X-ray source will start from the middle of 2020.

## ELI-ALPS

The research infrastructure at ELI-ALPS [719] is based on four main laser sources: three operating in the 100 W average power regime in the near-infrared (NIR) and one 10 W mid-IR (MIR) source. These systems are designed to deliver pulses with unique combinations of pulse duration, repetition rate, and pulse energy. The hallmarks of this next-generation laser architecture are the use of sub-ps fibre oscillators: pulse amplification in fibres and white-light-generated seeding pulses which exhibit passive carrier-envelope phase (CEP) stability. Each laser will run synchronised to the central facility clock and is guaranteed to run continuously for at least 8 hours per day. All lasers have been optimised for different regions in the parameter space.

## 29.6 FLASHForward (Germany)

FLASHForward (Future-Oriented Wakefield Accelerator Research and Development at FLASH) [720] is a beam-driven plasma wakefield experiment at DESY that aims to

produce, in a few centimetres of ionised hydrogen, electron beams of energies exceeding 1.5 GeV, which are of sufficient quality to demonstrate gain in a free-electron laser. Situated at the free-electron laser FLASH, the experimental beamline allows for milestone studies assessing several types of plasma internal particle injection regimes, external injection, and controlled beam capturing and release for subsequent applications. The facility provides a combination of low-emittance GeV-class electrons from a superconducting MHz repetition rate accelerator synchronised to a 25 TW laser interacting in a windowless, optically accessible, versatile plasma target. Experiments commenced in 2018, aiming to open up new avenues in the highly dynamic research field of plasma wakefield acceleration.

Through parallel operation with FLASH FEL users and dedicated accelerator R&D beam time, FLASHForward plans to operate for >1000 hours per year, opening up new avenues in the highly dynamic research field of beam-driven plasma wakefield acceleration (PWFA).

To this end, FLASHForward research is composed of an ever-expanding scientific programme, comprised of a number of core experiments starting with both internal and external injection studies, and culminating in the exploration of FEL gain from a PWFA. In addition to these experiments, a number of novel diagnostics and prototypes are in development to diagnose these novel beams, both at FLASHForward and beyond. Table 29.2 summarises some meaningful beam parameters.

## 29.7 HI Jena (Germany)

The Helmholtz Institute Jena and the Institute of Optics & Quantum Electronics at Friedrich-Schiller-University Jena are conducting research on the development of high-power laser systems as well as laser-plasma interactions. Their foci in laser development lie, on the one hand, in petawatt laser systems and their improvement of beam quality, repetition rate, and energy efficiency. On the other hand, the labs investigate the development of novel fibre laser systems with MHz-scale repetition rates and high average power, among others, as FEL seeding sources. In laser-plasma interactions, Jena has a strong track-record in particle acceleration using laser-plasma interactions, both using electrons and protons / ions. A topic of particular focus is the development and application of novel plasma diagnostics, such as shadowgraphy to better understand the dynamics inside plasma accelerators [721].

HI Jena hosts three different high-power laser systems (see Tab. 29.3) that are used on a day-to-day basis for laser particle acceleration experiments as well as the generation of high-order surface harmonics and secondary XUV and X-ray radiation.

The POLARIS (Petawatt Optical Laser Amplifier for Radiation Intensive Experiments) laser [723] is the world's only fully diode-pumped laser system to generate pulses of peak power up to 200 TW. It currently boasts a temporal intensity contrast on the order of  $1 \times 10^{-13}$  for amplified spontaneous emission, which is, however, subject to future improvement together with a planned energy upgrade.

The JETI40 and JETI200 lasers, on the other hand, are both Ti:Sapphire-based systems. Each beamline has two experimental chambers available and includes a few-cycle probe beam that can be used, for example, for pump-probe experiments or as a diagnostic tool. Based on a double chirped-pulse-amplification system in combination with a plasma mirror, JETI200 also features improved temporal contrast on the order of  $1 \times 10^{-13}$  for amplified spontaneous emission and  $1 \times 10^{-10}$  for pre-pulses.



**Fig. 29.10.** Control room of the POLARIS laser at the Helmholtz Institute Jena (image credits: FSU Jena and HI-Jena [722]).

**Table 29.3.** Overview parameters of the three high-power laser systems at Helmholtz Institute Jena. Both the POLARIS and JETI200 systems produce pulses with around 200 TW peak power, while JETI40 can reach around 40 TW peak powers.

	<b>POLARIS</b> [722]	<b>JETI40</b> [724]	<b>JETI200</b> [725]
Wavelength	1030 nm	800 nm	800 nm
Bandwidth (FWHM)	19 nm	40 nm	
Pulse duration	$\leq 100$ fs	$\geq 25$ fs	17 fs
Energy on target	$\geq 17$ J	1.0 J	4 J
Max. intensity	$1 \times 10^{21}$ W cm $^{-2}$	$1 \times 10^{20}$ W cm $^{-2}$	$\geq 1 \times 10^{21}$ W cm $^{-2}$
Repetition rate	1/50 Hz	10 Hz	5 Hz

## 29.8 ILIL (Italy)

The research activities of the Intense Laser Irradiation Laboratory (ILIL) [726] are focused on fundamental studies of high-intensity laser interactions with matter and their applications. The laboratory not only participates in the European infrastructure projects EuPRAXIA and ELI, but it is also part of the European consortium engaged in laser-driven fusion research.

Since 2015, the lab is engaged in the upgrade of the laser and target area facility, in the framework of the Italian Network of the Extreme Light Infrastructure (ELI-Italy), to enable laser-matter interaction studies at extreme laser intensities. Fundamental studies include plasma formation and heating by laser beams, laser-induced instabilities and other non-linear processes, atomic physics of highly-ionized plasmas, ultra-short X-ray emission and the acceleration of charged particles. The laboratory has well-established collaborations with many leading international high-power laser laboratories and facilities, as well as academic groups. The Intense Laser Irradiation Laboratory has long-term experience in the training of young scientists through several schemes including European Union RT Networks.

The ILIL-PW interaction area is equipped with a 140 cm diameter octagonal vacuum chamber connected to the compressor chamber by a two-mirror chicane. Energies on target up to 4 J in  $<30$  fs pulse duration are focused with an f/10

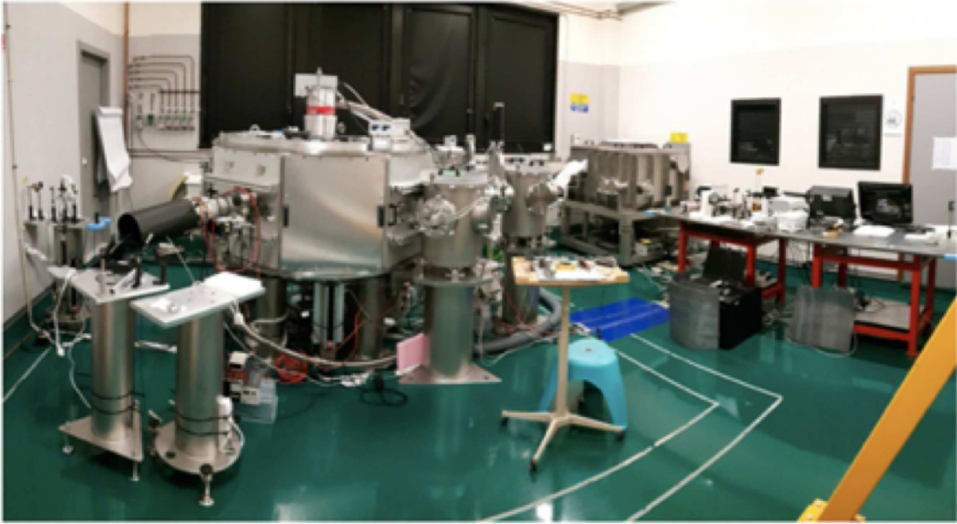


**Fig. 29.11.** ILIL experimental area (image courtesy of CNR-INO).

off-axis parabolic mirror, with a spot radius down to  $10\ \mu\text{m}$  and an intensity exceeding  $3 \times 10^{19}\ \text{W}/\text{cm}^2$ . Alternatively, the beam can be focused with an  $f/3$  off-axis parabolic mirror, delivering a spot radius of  $3\ \mu\text{m}$  and an intensity exceeding  $2 \times 10^{20}\ \text{W}/\text{cm}^2$ .

The ILIL-TW interaction area is equipped with two 80 cm diameter interaction vacuum chambers. One of the interaction chambers is configured with an  $f/10$  off-axis parabolic mirror, with an energy on target of 400 mJ in a 35 fs pulse duration and a focal spot radius of  $10\ \mu\text{m}$ , for an intensity of  $3 \times 10^{18}\ \text{W}/\text{cm}^2$ . The set-up is optimised for repetitive operation (1 Hz) of LWFA with multi-tens of MeV electron energy for applications, gamma-ray generation and detector tests and development. The other chamber is configured with an  $f/3$  off-axis parabolic mirror, with an energy on target of 400 mJ in a 35 fs pulse duration and a focal spot radius of  $3\ \mu\text{m}$ , for an intensity of  $2 \times 10^{19}\ \text{W}/\text{cm}^2$ .

## 29.9 Imperial College London (United Kingdom)

The John Adams Institute at Imperial College hosts a laboratory that is dedicated only to the development of targetry and diagnostics for plasma acceleration experiments. The laboratory hosts an in-house-developed laser system for testing these devices at the repetition rates required for next-generation wakefield facilities, such as EuPRAXIA. The laser is a CPA system based on Titanium:Sapphire as a gain medium and currently delivers:

- a 10 mJ, 30 fs arm that will produce a low-energy ( $<10\ \text{MeV}$ ) source of electrons,
- a 50 mJ, 30 fs arm that will produce up to 50 MeV electrons on a table top,
- a 500 mJ, 30 fs arm that can produce up to 200 MeV electron beams in a separate wakefield interaction chamber.

The system currently operates at 10 Hz, which is just below the minimum operation level of the EuPRAXIA facilities and upgrades will allow the first two stages to be operated at 100 Hz. This will thus allow the development of targets and diagnostics that can operate within the full scale of operating rates expected for EuPRAXIA.



**Fig. 29.12.** The Zhi lab set up at the John Adams Institute at Imperial College (image courtesy of Imperial College).

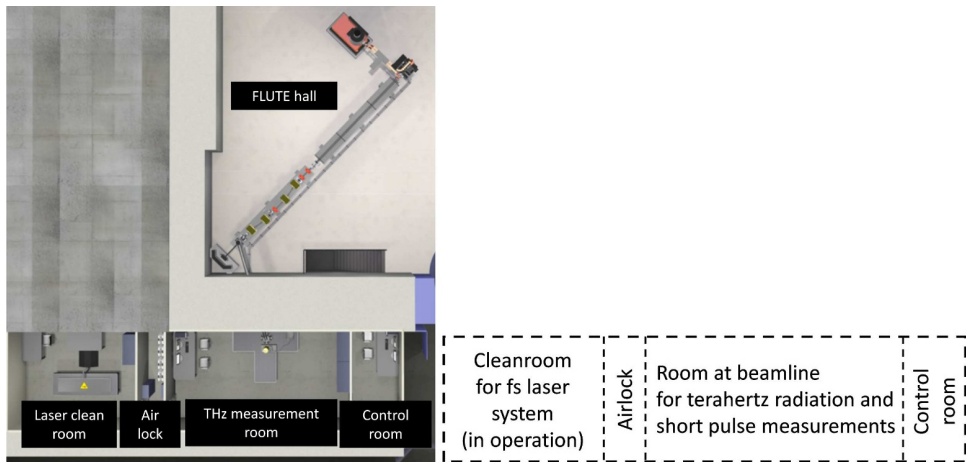


**Fig. 29.13.** Left: Layout of FLUTE facility. Right: Layout of support rooms as part of the FLUTE facility in front of the bunker: laser room, beamline room for experiments with low energy, soft photons in fs pulses, and control room. The area is to approximate scale with the cleanroom of  $30 \text{ m}^2$  housing the fs laser system for photo-injection of the FLUTE accelerator (image courtesy of KIT).

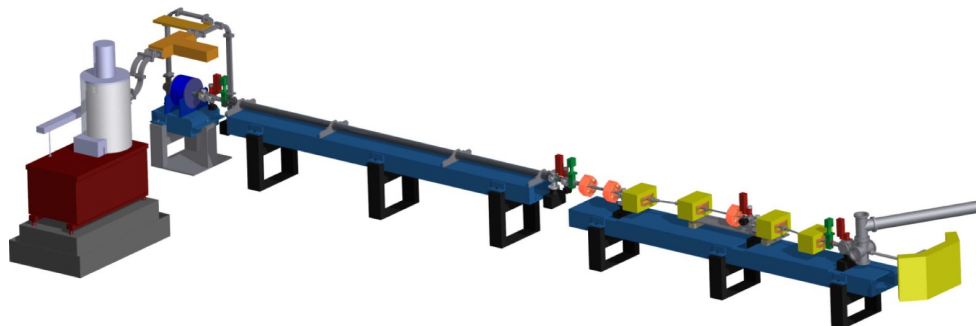


**Fig. 29.14.** Layout of FLUTE accelerator to be placed on 21 m diagonal of the bunker ground level (image courtesy of KIT).

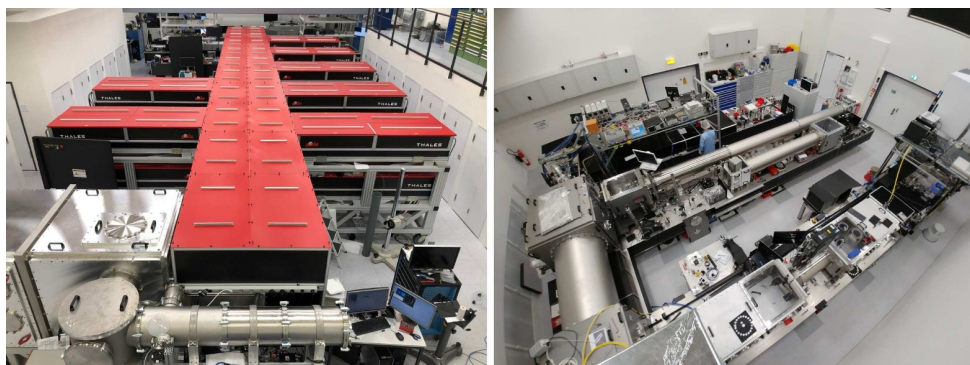


**Fig. 29.15.** Left: ATLAS-3000 main amplifier and compressor (60 J, 25 fs, 1Hz). Right: PFS-pro (200 mJ/800fs/5kHz) and PFS (8J, 800 fs, 10 Hz) lasers (image courtesy of Ludwig-Maximilians-Universität München).

### 29.10 KIT (Germany)

The FLUTE facility at KIT [727] is comprised of a two-level bunker, which is fully radiation protected at the ground and at the lower level with near square dimensions, and several support rooms in front of the bunker. The ground level houses the FLUTE accelerator on a 21 m diagonal in a  $210\text{ m}^2$  area bunker with a free height of 5 m. The VLA compact Storage Ring design fits perfectly within the ground level bunker. The lower level of the bunker, with the same overall area of  $210\text{ m}^2$ , is sectioned and a  $140\text{ m}^2$  area with a height of 2.5 m is exclusively reserved for the dedicated laser system of the Plasma Injector, while the remaining area with a height of 2.2 m can be used e.g. for support electronics and other installations. FLUTE develops in several phases to benefit from novel technologies including those from Helmholtz partners. In the final phase besides an additional life sciences laboratory, the PICCO-LO mode operation will enhance the capabilities of FLUTE to provide pulse lengths towards 1 fs by implementing a tenfold improved high performance optical synchronization system. Thus, covering the spectral band up to 300 THz and beyond with pulse energies well into the GW range.

### 29.11 LMU-CALA (Germany)

The CALA laboratory at the Ludwig-Maximilians-Universität München (LMU) is dedicated to fundamental and applied research into particle and photon sources for medical applications [728]. The building will host two laser systems:

- ATLAS-3000 is a 2.5 PW Ti:Sa laser currently under commissioning. Its target parameters are 60 J, 25 fs at 1 Hz repetition rate delivered to four target bunkers (LION, LUX, HF, ETTF). LION and HF are dedicated to solid-target interactions such as ion acceleration, using short-focal-length geometry to achieve intensities beyond the  $1 \times 10^{22} \text{ W/cm}^2$ -range. ETTF is a general-purpose electron acceleration and betatron/Compton scattering beamline with a 14 m long vacuum chamber for long-focal-length and colliding-pulse interactions, while LUX is a dedicated undulator radiation beamline. ATLAS-3000 will have a synchronised 200 TW output that will be coupled into the experiment bunkers on demand.
- PFS/PFS-pro is a Yb-YAG-based laser system under development. In one output, it will provide 200 mJ, 1 ps pulses at a 5 kHz repetition rate, the other one will deliver 8 J, 800 fs pulses at 10 Hz. Ways of converting both outputs to a few-cycle pulse duration are currently being investigated, either by direct compression of by pumping of an OPCPA arm. The short pulses and an unconverted part of the ps-pulses will drive a fifth experimental area called SPECTRE, dedicated to the development of an all-optical Thomson source for imaging purposes.

### 29.12 LPA-UHI100 (France)

The LIDYL laboratory operates the Saclay Laser-Matter Interaction Center (SLIC) infrastructure, including the UHI100 laser facility and experimental area opened for access to ARIES and LASERLAB-Europe users. UHI100 is a Ti/Sa laser system and delivers a laser power of 100 TW at 10 Hz with a 25 fs pulse duration. Intensities on target in the  $1 \times 10^{18}$ – $1 \times 10^{19} \text{ W cm}^{-2}$  range have been obtained using a deformable mirror. UHI100 also features a very high temporal contrast obtained thanks to a double plasma mirror inserted between the compressor and the experimental chamber. The short pulse duration, ultra-high contrast, and intensity together with the radiation-protected experimental area – fully equipped for ultra-high intensity experiments under vacuum – make this facility unique. The whole facility (laser and experimental area) will be moved to a new location at Orme des Merisiers (CEA) in a completely renovated area, at the beginning of 2020. In this new configuration, there will be the possibility to send the laser at full power into one experimental chamber or to split the energy into two beams with a chosen ratio making it possible to work with two laser beams in one experimental chamber. The two laser beams will benefit from the same performance-improving equipment, such as a double plasma mirror to increase the temporal contrast, if required, and a deformable mirror to optimise the spatial profile of the laser at the interaction point. A probe beam with few mJ energy will also be available.

Services currently offered by the infrastructure include: the UHI100 laser and experimental area fully equipped with diagnostics for the laser (duration, energy, and position after compression); two double plasma mirror chambers, two deformable mirrors, and associated wave front sensors; two experimental chambers of which one will be more dedicated to solid-target interaction and the other dedicated to laser-plasma acceleration. A set of parabolas with variable focal length is also available to explore different interaction regimes. Diagnostics and tools are present to study electron generation (e.g. electron spectrometers and a magnetic transport line for

70 MeV electron beams). The radioprotection has been specifically dimensioned for electron acceleration and the survey is insured by radioprotection services from CEA.

The facility is operated by a team of two technicians, one engineer and one local co-investigator in charge of the access to the experimental room. Users receive complete technical and scientific assistance, from the conceptual design of the experiment to its realisation. A workshop will be accessible during campaigns as well as administrative assistance, if needed.

### 29.13 Lund Laser Centre (Sweden)

The Lund Laser Centre (LLC) is the largest unit in the Nordic countries within the field of lasers, optics, and spectroscopy [729].

Research is performed in basic atomic, molecular and chemical physics as well as in applications to the fields of energy, environmental, medical and information technology. The LLC is characterised by its interdisciplinary nature, fostering a strong exchange of ideas, techniques, and resources. The Centre has extraordinary resources in terms of scientific expertise, advanced laser systems (more than 30 major systems, including a 10 Hz, 40 TW laser), detection, and auxiliary equipment. Experimental techniques range from high-resolution (CW) to ultra-fast (attosecond) spectroscopy with an accessible spectral region from THz radiation to X-rays.

LLC provides access to laboratories which cover a broad range of research activities. High-intensity laser-matter interactions and attosecond science are investigated using three different systems:

- a 40 TW, 10 Hz, 40 fs Ti:Sapphire system with active beam-pointing stabilisation,
- a CEP-stable 1 kHz, 20 fs, 5 mJ tunable Ti:Sapphire system equipped with pulse compression,
- and an OPA to reach mid-IR wavelength with a CEP-stable 200 kHz, 7 fs 10  $\mu$ J OPCPA.

The laboratories include pump/probe setups, X-ray and electron spectrometers for advanced time-resolved and particle acceleration studies. Time-resolved atomic and molecular laser spectroscopy experiments can be carried out thanks to a unique laser spectroscopic set-up. Quantum optics/information topics are studied using coherent transient techniques and spectroscopy of low-temperature rare-earth-ion doped crystals. Femtochemistry laser experiments are used for studies of, e.g. natural and artificial photosynthesis, natural pigments, novel types of solar cells and their constituent materials, reaction dynamics and coherent control. Time-resolved diffraction studies are carried out for solids, and advanced single molecule spectroscopy of polymers and biomolecules. Biomedical applications with fluorescence diagnostics, tissue optics and photodynamic tumour therapy can also be accommodated within LLC as well as time-resolved scattering media spectroscopy and gas-in-scattering-media studies. Environmental monitoring can be carried out using a mobile laser radar system, which can be used for atmospheric mapping, marine and vegetation monitoring. Combustion diagnostics of reactive flows using fluorescence and scattering techniques are possible using high-repetition rate and short pulse laser systems.

### 29.14 LUX (Germany)

LUX [66] is a laser-plasma accelerator developed and operated in a collaboration of Hamburg University and DESY. Driven by the 200 TW peak power ANGUS laser system, it provides a continuous-flow plasma-cell target to generate few-100 MeV electron beams at 1 Hz repetition rate. The generated plasma electron beam is captured,

transported, and diagnosed using modern accelerator technology. A miniature undulator provides spontaneous (synchrotron-type) emission down to a few nanometres. The whole facility is fully integrated into a controls system, which provides unique capabilities to correlate drive laser and electron beam parameters.

### 29.15 Queen's University of Belfast (United Kingdom)

The Centre for Plasma Physics at Queen's University Belfast hosts the high-power laser TARANIS, together with the fs-scale system TARANIS-X [730]. The TARANIS laser provides two twin beams originating from the same oscillator and sharing most of the amplification chain. The oscillator delivers a train of 44 fs-long pulses, each with an energy of approximately 5 nJ, at 76 MHz (average power of 400 mW), and a broadband spectrum from 1020 to 1120 nm. The beam is stretched to 1.2 ns and first amplified by a regenerative amplifier up to 0.6 mJ at a repetition rate of 500 Hz (average power of 300 mW). Two Nd:phosphate rod amplifiers take the energy of the beam up to the Joule level, before it is split into two beamlets, each going onto their own third phosphate-glass rod amplifier that takes the energy up to 25 J per beam. A dazzler is used to correct high-order phase distortions, allowing to reach pulse durations as short as 600 fs. An energy efficiency of the compressors of the order of 60 % brings the energy of each beam after compression to approximately 15 J (25 TW peak power). Due to the glass-based technology of the laser, the repetition rate of the system is relatively low, of the order of one full-power shot every 12 minutes.

The TARANIS-X system instead relies on a different architecture, heavily based on an OPCPA system pumped by one of the arms of TARANIS. In a nutshell, TARANIS-X provides two main outputs: one at low-power and high-repetition rate, and one at high-power and low-repetition rate. The first mode of operation provides a train of mJ-scale pulses at 1 kHz, with each pulse having a sub-10 fs duration (2-3 optical cycles). The second mode provides a beam with maximum energy of the order of 1 J and approximately 10 fs duration. Since the final amplification stage of this mode is pumped by one arm of TARANIS, the repetition rate in this case is relatively low, of the order of one full-power shot every 5 minutes.

All these beams can then be directed into two separate target areas, featuring large vacuum vessels (inner diameter of the chambers of the order of 1.5 m) and a whole suite of diagnostics for on-shot monitoring of the main characteristics of the beams. F/3 off-axis parabolas are available together with an adaptive optics system that allows for focusing as tight as 5  $\mu\text{m}$  FWHM. Extension pipes can be attached to the chambers, enabling long-focal length focusing.

Different diagnostics can be implemented for laser-plasma experiments including particle spectroscopy (either based on magnetic dipoles or Thomson parabolas) using different detectors, such as: LANEX scintillation screens, imaging plates, radiochromic films, and CR-39.

The system allows for different beams to be directed, already synchronised, in the target areas. This provides a high-degree of flexibility in the beam configurations available for experiments (i.e., two sub-ps beams, two ns beams, one sub-ps beam and one ns beam, one fs and one ns beam, or one fs and one sub-ps beam). A highly synchronised (<0.1 ps jitter) probe beam capability with variable pulse duration from 400 fs to 1.2 ns, 100 mJ energy, and 2.5 cm beam size is also available.

In the following, a summary of the main parameters for the different modes of operation is given:

**Table 29.4.** Beam parameters of the TARANIS laser system at the Queen's University of Belfast.

	TARANIS (compressed)	TARANIS (stretched)	TARANIS-X (low-energy mode)	TARANIS-X (high-energy mode)
Wavelength	1053 nm	1053 nm	820 nm	820 nm
Pulse duration	600 fs	1.2 ns	10 fs	10 fs
Energy on target	15 J	25 J	0.3 mJ	1 J
Max. intensity	$2 \times 10^{19} \text{ W cm}^{-2}$	$2 \times 10^{16} \text{ W cm}^{-2}$	$3 \times 10^{16} \text{ W cm}^{-2}$	$1 \times 10^{20} \text{ W cm}^{-2}$
Repetition rate	1 shot / 12 min.	1 shot / 12 min.	1 kHz	1 shot / 5 min.

## 29.16 Rutherford Appleton Laboratory (United Kingdom)

### Facility Description

The Central Laser Facility (CLF) at STFC-RAL [731] hosts the 350 TW Gemini Ti:Sapphire laser that is used extensively for laser wakefield acceleration experiments by visiting user groups. Gemini has two beams with energy of 15 J in a 40 fs pulse with a maximum repetition rate of 1 shot per 20 seconds. These beams are fed into a dedicated target area (TA3) containing a large vacuum chamber which can be configured to suit individual experimental needs. For gas target experiments, the standard laser focusing uses a long focal length off-axis parabola ( $f/20$ ) for a spot radius ( $1/e^2$ ) of  $16.7 \mu\text{m}$  with intensity  $\sim 2.8 \times 10^{19} \text{ Wcm}^{-2}$  (normalised vector potential  $a_0=3.6$ ). A beam layout is also available using an  $f/40$  off-axis parabola reducing the intensity to  $\sim 6 \times 10^{18} \text{ Wcm}^{-2}$ . The second Gemini target area (TA2) receives the laser beam that is split off before the final amplifier with an energy of 1 J and compressed to 40 fs. This is focused with an  $f/17$  off-axis parabola to a  $20 \mu\text{m}$  spot with intensity  $3 \times 10^{18} \text{ Wcm}^{-2}$  (normalised vector potential  $a_0=1.1$ ). The maximum repetition rate in TA2 is 5 Hz provided that experiments do not exceed radiological safety limits.

Both target areas are equipped with adaptive optics and have independent control of the spectral phase of the pulse allowing user-defined control over the spatial and temporal properties of the laser pulse. CLF experiments are supported throughout the planning stages and implementation by a team of laser staff, plasma physicists, engineering design and support staff. Specialist target requirements are provided by a dedicated Target Fabrication department.

### Mode of Access

A call for proposals, open to any researcher (subject to eligibility), is issued twice per year for access to Gemini. Proposals are assessed by an independent panel who advise the facility based on certain defined criteria. Experiments in TA3 are allocated a number of weeks (typically 4–6) of access fully supported by a team of specialist scientific and engineering staff. TA2 is operated with longer access slots (8 – 12 weeks) with a lower level of facility support.

## 29.17 SCAPA (United Kingdom)

### Facility Description

The Scottish Centre for the Application of Plasma-based Accelerators (SCAPA) [732] at the University of Strathclyde houses two high-power Ti:Sapphire laser systems for

laser wakefield acceleration experiments. Visiting user groups can conduct experiments in collaboration with the Strathclyde group. The laser systems are:

- (a) 40 TW at a 10 Hz pulse repetition rate (1.4 J per pulse, 35 fs pulse duration). This laser drives two laser wakefield accelerator beamlines in Bunker C (including the ALPHA-X beamline). For ALPHA-X, the laser is focused by an f/16 spherical mirror to a spot radius ( $1/e^2$ ) of  $20\ \mu\text{m}$  with an intensity of  $\sim 4 \times 10^{18}\ \text{Wcm}^{-2}$  (normalised vector potential  $a_0 = 1.4$ ).
- (b) 350 TW at a 5 Hz pulse repetition rate (8.75 J per pulse, 25 fs pulse duration). This laser drives two laser wakefield accelerator beamlines in Bunker A and, in each case, the laser is focussed by an f/17 off-axis parabola to a spot radius ( $1/e^2$ ) of  $22\ \mu\text{m}$  with an intensity of  $\sim 3.5 \times 10^{19}\ \text{Wcm}^{-2}$  (normalised vector potential  $a_0 = 4.0$ ). One beamline is able to support longer focal lengths (up to f/34) for larger focal spot size.

Both lasers feature adaptive optics and online full power attenuation of the pulse energy in the 10–100% range. Synchronised probe laser pulses (up to 30 mJ uncompressed) are also available for both systems. Experiments are supported by SCAPA core staff (management, laser and technical) and by the collaborating Strathclyde research team. SCAPA houses a number of auxiliary labs that are at the disposal of users for experimental preparation and post-analysis studies.

### Mode of Access

Proposals for laser beam time are submitted to SCAPA management and assessed by an access management panel. For each laser system, there are six nominal experimental slots per year (each for a nominal duration of 6 weeks). SCAPA supports a flexible approach to scheduling in order to respond rapidly to users' needs. SCAPA operations are sustained with access fee income that must come from the user group and / or collaborating Strathclyde team (those parties determine the relative contributions). Travel and subsistence costs are not covered by SCAPA but may be so by the collaborating Strathclyde team. As a first step regarding access, users are encouraged to contact SCAPA management and the relevant collaborating Strathclyde teams.

## 29.18 SINBAD (Germany)

The Helmholtz Association has set up an accelerator R&D program across six accelerator laboratories in Germany, providing sustained funding for project-independent accelerator research. According to this mission, DESY is currently in the process of setting up the central, long-term dedicated accelerator research facility SINBAD (Short INnovative Bunches and Accelerators) [733] in the very centre of the DESY-Hamburg campus (see Fig. 29.16). The main beam parameters are reported in Table 29.5. This area will provide the necessary space for multiple independent experiments accessing a common infrastructure. SINBAD will provide a future-proof home to the accelerator R&D efforts at DESY while providing sufficient room for developing the setup into one of the two flagship projects of ATHENA, the Helmholtz collaboration for laser-plasma acceleration for large infrastructure investments. For this purpose, for example, the high-repetition-rate, high-average-power KALDERA laser will be installed in the central hall until the end of 2020.

SINBAD will initially host two main, independent experiments: ARES & AXSIS. At the core of the ARES (Accelerator Research Experiment at SINBAD) experimental area, a conventional S-band electron linac will accelerate ultra-short electron



**Fig. 29.16.** 3D visualisation of the SINBAD facility. The ARES and AXSIS experiments as well as the KALDERA laser system will be hosted in this site (image courtesy of DESY).

**Table 29.5.** Design parameters of the SINBAD facility.

	<b>Units</b>	
<b>Bunch Charge</b>	pC	0.5–20
<b>Energy</b>	MeV	100
<b>Bunch Length</b>		sub-fs to few fs
<b>Rep. rate</b>	Hz	10–50
<b>Electron Time arrival Jitter</b>	fs (RMS)	<10

bunches to 100 MeV with an RMS arrival time jitter of less than 10 fs. While the design is optimised for low-charge (pC), ultra-short (sub/single fs) beams, bunch charges with several tens of pC can also be accelerated at the cost of longer bunch duration. Once this goal is achieved, the accelerated electron bunches will be injected into advanced acceleration structures like dielectric structures or plasma cells. The commissioning of the ARES-linac has started and first beams at the linac exit are expected at the end of 2019.

As a second initial experiment, SINBAD will also host the AXSIS experiment which is a collaborative effort of DESY, CFEL, and Arizona State University funded by an ERC synergy grant. It aims to set up an ultra-compact light source based on electron acceleration by a THz-laser in a dielectric loaded waveguide and subsequent inverse Compton scattering.

Finally, SINBAD will host a 400 m<sup>2</sup> laser laboratory which will be used for the KALDERA laser project. KALDERA is developing kHz laser technology with 3 J single pulse energy for plasma wakefield accelerators, thus enabling high average power.

### 29.19 SPARC\_LAB (Italy)

SPARC\_LAB (Sources for Plasma Accelerators and Radiation Compton with Lasers and Beams) [734] is an interdisciplinary laboratory and its layout is shown in

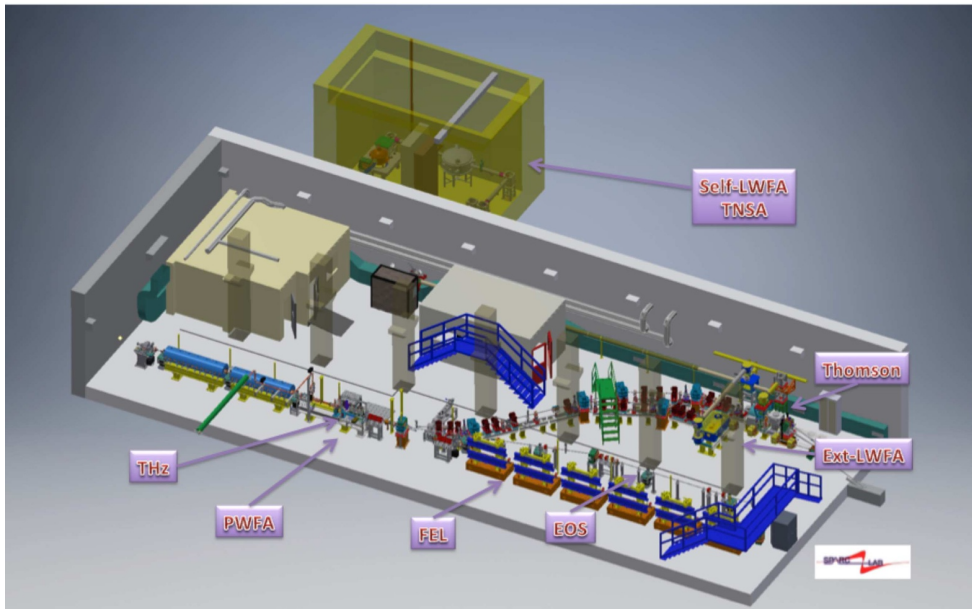


**Fig. 29.17.** Layout of the SPARC\_LAB facility (image courtesy of SPARC\_LAB).

**Table 29.6.** Typical parameters of the SPARC linear accelerator.

	Units	
<b>Bunch charge</b>	pC	10–1000
<b>Energy</b>	MeV	30–180
<b>Bunch length</b>	fs RMS	10–10000
<b>Energy spread</b>	% RMS	$\pm 0.1$
<b>Repetition rate</b>	Hz	1–10

Figure 29.17. It was born from the integration of a high-brightness photo-injector (SPARC) able to produce high-quality electron beams up to 170 MeV energy with high peak current ( $>1$  kA) and low emittance ( $<2$  mm mrad), and of a high-power laser ( $>200$  TW) (FLAME) able to deliver ultra-short laser pulses ( $<30$  fs).

The SPARC photo-injector is characterised by a copper photo-cathode, illuminated by a UV laser (266 nm) and embedded in a 1.6-cell standing wave RF gun (BNL/UCLA/SLAC type), operating at 2.856 GHz (S-band, normal conducting technology). The high peak field on the photo-cathode ( $\geq 120$  MV/m) allows beam acceleration up to  $\geq 5.6$  MeV. The beam is then properly focussed and matched into three constant gradient  $2\pi/3$  travelling wave (TW) structures of the SLAC type, which boost the beam energy up to 180 MeV. The first accelerating section is also used as an RF compressor (in the velocity bunching regime) by varying the beam arrival time. Solenoid coils embedding the first two sections can be powered to provide additional magnetic focussing to better control the beam envelope and the emittance oscillations under RF compression. Typical beam parameters of the SPARC linear accelerator are reported in Table 29.6.

In autumn 2015 the last 3 m long low-gradient ( $\approx 15$  MV/m) S-band TW accelerating section has been replaced by a 1.4 m long structure operating in the C-band at 5.712 GHz, with an average accelerating field of  $\approx 35$  MV/m, and a plasma chamber

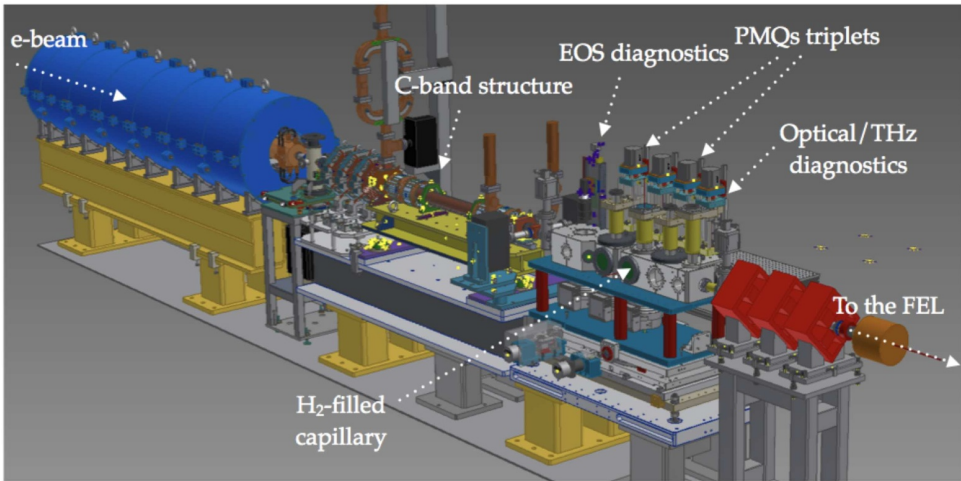


**Fig. 29.18.** SPARC PWFA test station (image courtesy of SPARC\_LAB).

**Table 29.7.** Typical parameters of the FLAME laser at SPARC\_LAB.

	Units	
<b>Energy</b>	J	7 (after compression)
<b>Energy stability</b>	% RMS	±0.1
<b>Wavelength</b>	nm	800
<b>Repetition rate</b>	Hz	10
<b>Pulse duration</b>	fs RMS	25
<b>Synchronisation with linac</b>	fs RMS	50
<b>Beam quality</b>	M2	<1.5

for PWFA experiments, hosting diagnostics, permanent magnet quadrupoles, and the capillary, i.e. the plasma accelerating structure (see Fig. 29.18).

The integration of the SPARC high-brightness photo-injector and the high-intensity FLAME laser has driven the development and characterisation of a  $\gamma$ -ray source from Thomson backscattering. Electron and photon beams have been synchronised at the scale of  $<50$  fs, an essential requirement for the recent successful operation of the X-ray ( $\approx 50$  keV) Thomson backscattering source and for the future investigation of new ultra-compact acceleration techniques ( $>1$  GV/m) based on the external injection of high-quality electron beams in a plasma cell.

The operation of the FLAME laser alone has led to successful electron acceleration up to 400 MeV in 2–4 mm long plasma cells with less than 20 % energy spread. Innovative electron beam transverse diagnostics based on betatron radiation have been conceived and tested, and experiments on ion acceleration by target normal sheath acceleration (TNSA) have been carried out. Typical beam parameters are reported in Table 29.7.

**29.20 University of Oxford (United Kingdom)**

The University of Oxford currently houses a TW laser laboratory used as a test bed for laser wakefield experiments, diagnostic and target development, and high-harmonic generation. A new laboratory is currently under construction which will



**Fig. 29.19.** The new laser laboratory at the University of Oxford under construction (image courtesy of the University of Oxford).

host an upgraded Ti:Sa laser system and will allow the generation of 10 Hz, 200 MeV electron beams. This facility will also house a separate long-pulse laser which will be used in lab astrophysics experiments.

The laser consists of a Ti:Sa oscillator which delivers a mode-locked train of pulses at a repetition rate of 84 MHz with a spectrum from 780 to 820 nm. This output is currently divided between two regenerative amplifiers outputting multi-mJ level pulses at a rate of 1 kHz. One arm is used for the generation of XUV high harmonics, whilst the other is stepped down to 10 Hz and sent to a multi-pass amplifier. The multi-pass is due to be upgraded in December 2019 during the commissioning of the new laboratory, housed in the basement of the Denys Wilkinson Building, to supply a compressed output of 600 mJ, <50 fs pulses at a repetition rate of 10 Hz.

The new laser line will also include an adaptive optic and wavefront measurement device, a 10 mJ, 50 fs probe beam with the option to be frequency doubled, and a laser machining rig for the manufacturing of targets which will use the 1 kHz pulses that are rejected from the multi-pass. A dedicated target area will house a vacuum chamber and beam dump to perform experiments in controlled injection and plasma channel waveguides with diagnostics including visible/IR spectrometers, interferometry, a magnetic dipole electron spectrometer and LANEX scintillation screens, as well as an X-ray camera for betatron measurements.

### 29.21 Wigner Institute (Hungary)

The Wigner Datacenter (WDC) is a large-scale investment project of the Wigner Research Centre (WRC) for Physics [735]. Our data centre aims to conform to the dynamically changing needs of research and innovation by providing a cutting-edge infrastructure with exceptional energy efficiency, in an environmentally friendly way. For the next decade, the pillars of the European research-related IT infrastructure will be high-security data centres that follow a sustainable operating model. The physical and IT security at the Csillebérc campus – which is outstanding even in international comparison – ensures extremely high availability and service quality to the research projects supported by the data centre. The WDC has the capability to store a huge amount of data in the Wigner Cloud system up to the terabyte scale.

Beyond the WDC, the WRC institute also hosts a GPU grid [736] which is available to develop fast diagnostic tools and perform beam analysis methods in various GPU/Xeon/Phi/FPGA platforms. The experts of Wigner RCP are also capable to run, e.g. PIC simulations on the cloud, thus being able to contribute either to start-to-end simulations or computational studies of smaller, specific parts of the EuPRAXIA project. For CPU computations, we have a total of 4.8384 TFlops computational capacity. For GPU computations, we have 603.444 Tflops and 57.932 Tflops for



**Fig. 29.20.** The building of the Wigner Datacenter (image courtesy of Wigner Research Centre for Physics).

single (32 bit) and double (64 bit) precision calculations, respectively. Finally, our MIC system can provide a total of 12.184 Tflops computational capacity.

## 30 International Consortium Facilities

### 30.1 Berkeley Lab Laser Accelerator Center (United States)

The Berkeley Lab Laser Accelerator (BELLA) Center at Lawrence Berkeley National Laboratory is focused on research in applications of femtosecond, high-power lasers, including in electron acceleration, ion acceleration, and the production of secondary photon and particle sources. Currently, there are four laser systems in operation or planned at BELLA: 1) the 1 PW BELLA laser with parameters listed in Table 30.1; 2) a 10–50 TW, 40 fs Ti:Sapphire CPA laser system at 5 Hz operation with two amplifier arms designed for Thomson scattering and other photon generation experiments; 3) a 100 TW laser system in operation since fall 2018 and designed for investigating a laser-plasma-driven FEL; 4) k-BELLA, a 1kHz, 1kW-average-power laser system currently proposed and under design.

Both the BELLA PW-laser and the 10–50 TW-system are equipped with target chambers as well as various electron, photon, neutron and laser diagnostics. While the former features a long focal length beamline to deliver the laser to the target chamber, the lower power system uses paraboloid mirrors with focal length between 1.1 and 1.5 m for beam focusing. User access to both systems is available through the LaserNetUS program.

Besides its experimental capabilities, LBNL also has strong expertise in theoretical and simulation work. Worth mentioning in this context is the BLAST (Berkeley Lab Accelerator Simulation Toolkit) package, an open-access suite of codes developed as part of the LBNL Accelerator and Modeling Program for plasma acceleration simulation optimised to HPC and next generation computing systems.

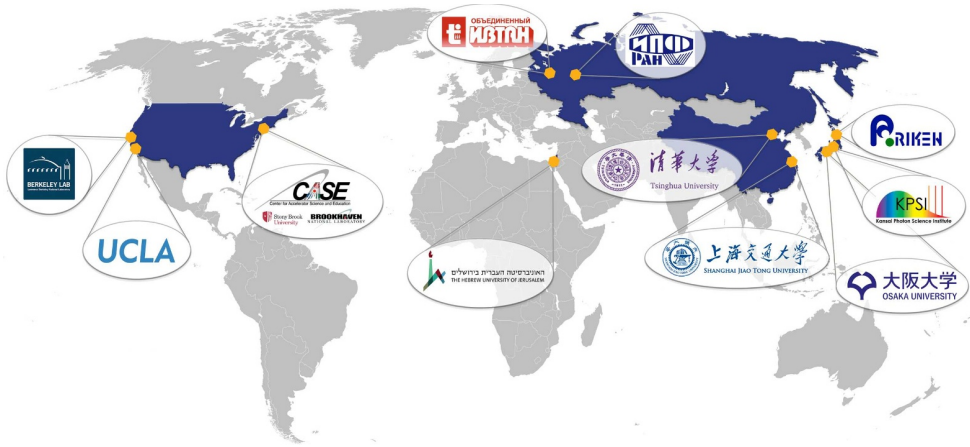


**Fig. 30.1.** Map of international EuPRAXIA consortium facilities. Divided into laser and accelerator laboratories, these could be used for prototyping and testing experiments during the planned technical design phase of the project.

**Table 30.1.** Parameters of the BELLA PW-laser system [737,738].

Wavelength [ $\mu\text{m}$ ]	800
Pulse energy [J]	>42
Pulse duration [fs]	<40
Repetition rate [Hz]	1
Energy stability [%]	$\approx 1$
Pointing stability [ $\mu\text{rad}$ ]	<2
Strehl ratio	$\approx 0.8$

### 30.2 Institute of Applied Physics at the Russian Academy of Sciences (Russia)

Laser-plasma acceleration of charged particles is studied in the Institute of Applied Physics at the Russian Academy of Sciences (IAP-RAS) with two laser facilities. The key element of the first one is a sub-PW laser PEARL [739]. It is an optical parametric chirped pulse amplification (OPCPA) laser system with pulse durations of 50–60 fs, wavelength of 910 nm and power up to 0.56 PW. The temporal contrast in intensity, and in the nanosecond range, of the laser system after compression is  $1/(2 \times 10^8)$  between the main short pulse and the amplified spontaneous emission generated in the OPCPA stages. The facility includes optical lines with adaptive optics providing focal lengths in a wide range from 0.8 m to 8 m ( $f/4 - f/40$ ), as well as a target chamber with a target positioning system and diagnostic systems (Thomson parabola spectrometer, two-screen single-shot electron spectrometer, etc.). The PEARL facility has been used to study electron acceleration [740] and ion acceleration [741] in laser-driven plasmas. There are several projects focused on plasma-based methods of charged particle acceleration supported by Russian funds, such as RSCF and RSBF.

A second IAP-RAS laser facility is capable of generating 1 TW, 60 fs laser pulses with 10 Hz repetition rate. Electron acceleration in plasma wakefields generated in gas-filled capillary tubes by laser pulses [742] and in laser-solid interaction [743] is explored with this facility.

Finally, at IAP-RAS, active work is underway to create lasers with a pulse shape in the form of a 3D ellipse for photo-cathodes [744]. In addition, it is planned to create a laser-plasma accelerator system with external injection based on a radiofrequency

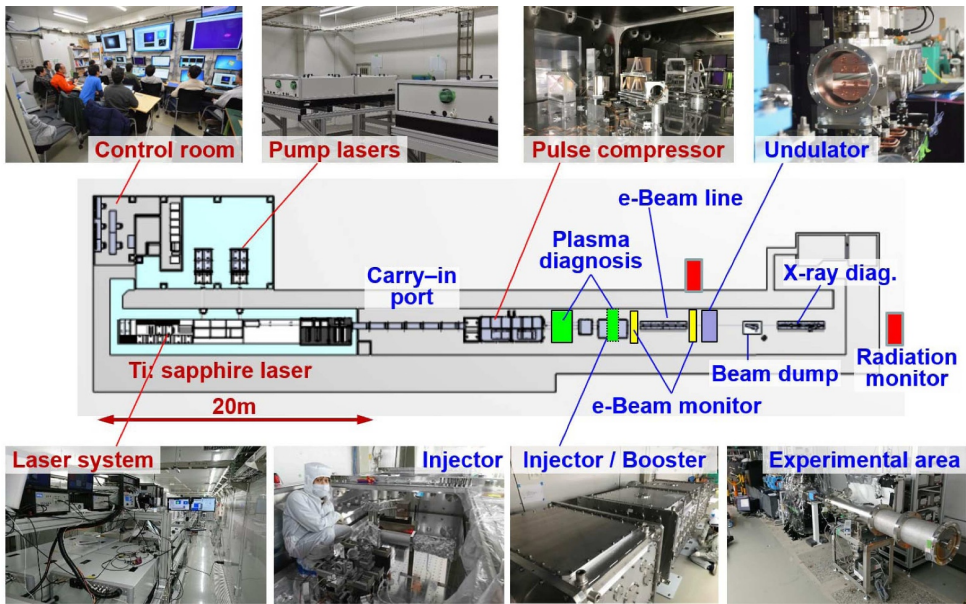


**Fig. 30.2.** Layout of the platform for LWFA of electrons at the RIKEN SPring-8 Centre (image credits: Y. Sano).

accelerator. For this purpose, a unique synchronisation system of the petawatt laser source PEARL with an external radiofrequency accelerator is being developed, providing a jitter of tens of femtoseconds. Since the EuPRAXIA project also implies a system with external injection, interaction in this direction can be very fruitful.

### 30.3 Osaka University / KPSI-QST / RIKEN (Japan)

Large R&D efforts in laser-plasma wakefield acceleration of electrons were carried out as a part of the national program ImPACT (2014–2018) under the Cabinet Office of the Japanese government. In ImPACT, major Japanese players in this field, namely Osaka University, KPSI-QST, RIKEN, KEK, and Tohoku University jointly worked to demonstrate stable electron acceleration, including a staging scheme and synchrotron radiation generation with undulators. An electron acceleration platform spanning 60 m was built in RIKEN SPring-8 Centre (see Fig. 30.2), which contains three different laser systems: a 1 J system (50 TW, 20 fs, 10 Hz), a 2 J system (40 TW, 50 fs, 5 Hz), and a 10 J system (100 TW, 100 fs, 0.1 Hz). The laser pulses from these three laser systems are precisely synchronised by means of a common front end. All three offer an energy stability of around 1% (RMS) and a pointing stability of 8  $\mu$ rad (RMS). The facility also already features an undulator beamline.

The platform is now being used effectively for R&D of electron acceleration as part of the MIRAI program (2017–2026) under NEXT/JST among Osaka University, RIKEN, and KPSI-QST together with several other Japanese institutions. Aiming to develop basic technologies for compact X-ray FEL and ion cancer therapy systems, research foci of the program lie in laser-based small electron and ion accelerator development. Although many of the program member institutes have their own dedicated facilities (RIKEN, Osaka University, KPSI-QST, and KEK), an experimental platform for laser-based ion acceleration is under planning. Electron acceleration up to 1 GeV, two-stage acceleration with a separation of 2 m between stages, and

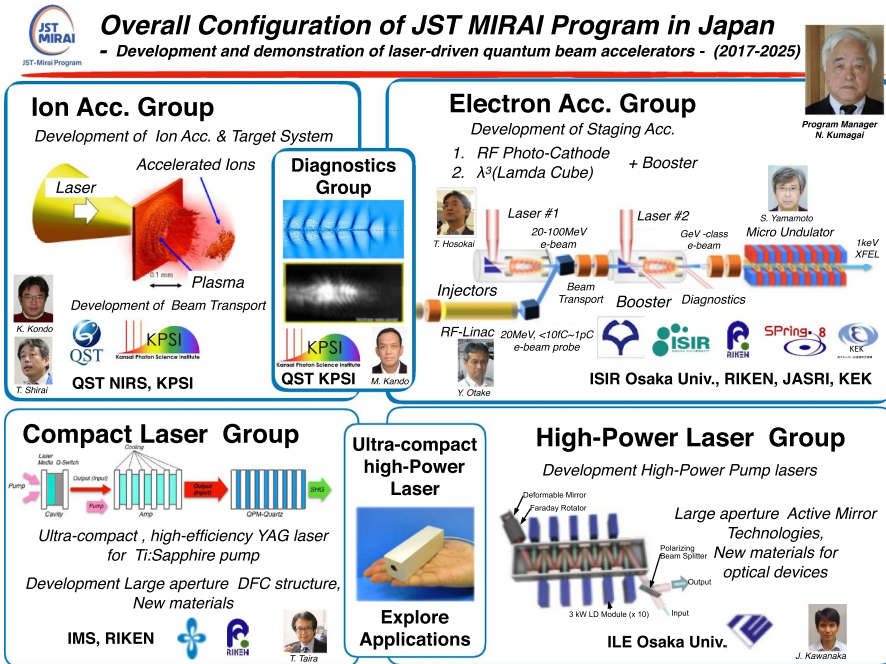


Fig. 30.3. Structure and key topics of the MIRAI program (image credits: Y. Sano).

synchrotron radiation generation from compact undulators were confirmed. High-power laser systems for downsizing the facilities are also developed in IMS (Institute for Molecular Science), RIKEN, and Osaka University.

### 30.4 Shanghai Jiaotong University (China)

Research in the Key Laboratory for Laser Plasmas (LLP) at Shanghai Jiao Tong University is mainly focussed on laser-plasma-based particle acceleration and radiation. LLP provides cutting-edge research facilities, including two 800 nm high-power femtosecond laser systems (200 TW, 5 J, 25 fs, 10 Hz and 20 mJ, 40 fs, 1 kHz), one mid-infrared (2.2  $\mu\text{m}$ ) intense laser system (100 TW, 8 J/100 fs), three multifunctional target chambers, and a high-performance scientific computing system (30 Tflops). Ion acceleration from laser-solid interaction, electron acceleration and betatron radiation generation from laser-driven wakefields in under-dense plasma are carried out on the 200 TW laser and target system. Terahertz radiation generation and its applications from laser filaments in air are carried out on the kHz laser system. Wakefield acceleration will also be investigated on the mid-infrared laser and target system in the coming years.

### 30.5 Tsinghua University Beijing (China)

Tsinghua University Beijing has its own facilities suitable for plasma wakefield acceleration research with a high-power pulsed laser at 30 TW/1 J/30 fs and an electron linac reaching up to 45 MeV. Additionally, it has set up strong collaborations for experimental studies with other institutes in East Asia, including the National Central University (NCU) in Taiwan (multi-pulse laser facility at 100 TW, and 10 Hz)

and the SXFEL facility in Shanghai, China (electron beams with 840 MeV,  $\leq 0.1\%$  energy spread,  $\leq 1$  ps duration, 0.5 nC charge, and 10 Hz repetition rate). Research activities at these facilities are focussed on laser- and beam-driven plasma acceleration techniques and applications, ranging from external injection and staging studies to beam manipulation and diagnostics as well as radiation generation. In a joint effort with Qifeng New Light Source Co. and NCU Taiwan, Tsinghua University is also developing compact and robust turn-key laser systems suitable as commercial systems for laser-plasma experiments. The expected performance includes 20–40 TW power, less than 30 fs pulse duration, and better-than 0.7% energy stability.

## 31 Computing Facilities

During the conceptual design study of EuPRAXIA, a significant number of simulations was carried out, some of which, especially particle-in-cell (PIC) simulations of plasma injectors and accelerator stages, are computationally so demanding that they required the use of high-performance computing (HPC) systems. These computational studies were carried out in some cases at smaller, local supercomputing systems, which several of EuPRAXIA's partner institutes host (e.g. the MAXWELL cluster at DESY (<https://maxwell.desy.de/>)). In other cases, they were integrated as activities into dedicated computing time grants at larger facilities.

An example of the latter case are the activities of some of the EuPRAXIA Consortium partners at the Juelich Supercomputing Centre (JSC). The JSC provides high-performance computer capacity for scientists at the Research Centre Jülich, at universities and research laboratories in Germany and in Europe – as well as for industrial partners [745]. Since 2012, DESY, the University of Hamburg and IST have led dedicated computing grants for high-performance simulations on plasma wakefield acceleration. Between the years 2016 and 2018, for example, the computing project entitled “Electron-injection techniques in plasma-wakefield accelerators for driving FELs” involved the participation of 20 scientists from four different international institutions (DESY, IST, University of Hamburg and University of Strathclyde) and involved the consumption of more than 30 million CPU-hours in the supercomputer JUQUEEN, using the particle-in-cell (PIC) code OSIRIS. The project included many activities and computational studies relevant or directly related to EuPRAXIA. In 2016, it received an Award for Excellence by the John von Neumann Institute for Computing. Today, the JSC has expanded its capabilities through the implementation of the new state-of-the-art supercomputer JUWELS, which provides more than 2500 computing nodes with 48 Intel Xeon Platinum 8168 CPUs each, enabling parallel computing capabilities beyond 1 Petaflops per second. In addition, 56 accelerated compute nodes counting on 4x Nvidia V100 GPUs each are available in JUWELS, enabling outstanding computing capabilities for highly parallelised PIC codes based on GPUs, such as PICongPU and, eventually, FBPIC.

For the future of the EuPRAXIA project, especially the technical design phase, such resource-intensive computational studies will become even more important. While a variety of test experiments and prototyping activities at different European and international facilities are foreseen, as described in the previous chapters, simulation-based work will be as essential, for example, for the detailed optimisation of component and machine performances as well as for error & tolerance studies and new code development activities. A short overview of the supercomputing facility landscape on national and European levels is thus presented in the following outlining possible future opportunities.

The national landscapes for high-performance computing in Europe are diverse. In Germany, for example, the main organisational structure is the Gauss Alliance

**Table 31.1.** Some of the largest supercomputing facilities in Europe based on the Top500 list of supercomputers worldwide (June 2019) [746].  $R_{max}$  describes the maximal LINPACK performance achieved, where LINPACK is a type of benchmark measuring a system's floating point computing power.

Facility	No. of cores	$R_{max}$ [TFlop/s]	Application
Piz Daint (Swiss National Supercomputing Centre, Switzerland)	$3.9 \times 10^5$	$2.1 \times 10^4$	Research
SuperMUC-NG (Leibniz Rechenzentrum, Germany)	$3.1 \times 10^5$	$1.9 \times 10^4$	Research
PANGAEA III (Total Exploration Production, France)	$2.9 \times 10^5$	$1.8 \times 10^4$	Industry
HPC4 (Eni S.p.A., Italy)	$2.5 \times 10^5$	$1.2 \times 10^4$	Industry
Tera-1000-2 (CEA, France)	$5.6 \times 10^5$	$1.2 \times 10^4$	Research

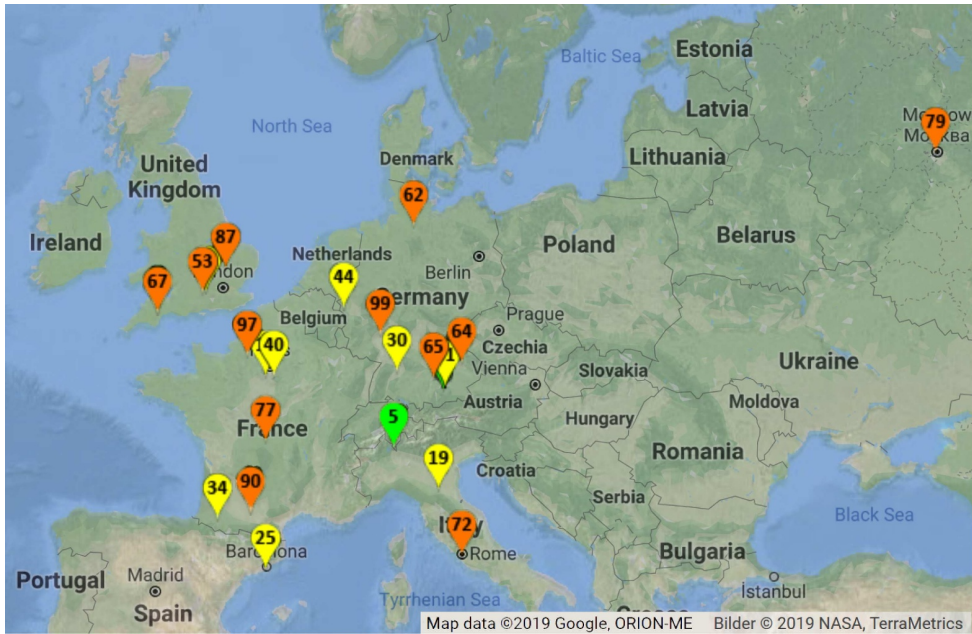


**Fig. 31.1.** Map of European supercomputing facilities ranked in the Top 100 worldwide (based on [746], list of Nov 2018; image adapted from [747]).

with its three-level system of HPC infrastructures [748], the first level being the national supercomputing centres. Many of these systems have user access driven by the evaluation of user proposals. Some of these systems belong to universities or research organisations, such as the Max-Planck and Helmholtz societies. For the field of novel plasma accelerators, local installations at the participating partners, in particular, play a key role in developing and optimising simulation codes, while providing a smaller amount for production runs. Examples include the systems at DESY (as mentioned above), GSI and HZDR for the Helmholtz EuPRAXIA

partners. Large-scale simulations are largely run on the level one Gauss Alliance systems, with the main installations the Jülich Supercomputing Centre (JSC) in Jülich, the Leibniz Supercomputing Centre (LRZ) in Garching/Munich and the High Performance Computing Centre (HLRS) in Stuttgart. All of these allow for large-scale user access. Strategically, EuPRAXIA aims to maintain and foster access to both the systems for code development as well as those for large-scale production runs. National access could be coordinated with the access to European resources via the European PRACE initiative [749] that also provides access to some of the Gauss Alliance systems. Using EuPRAXIA as an applicant for computing time rather than individual users within the EuPRAXIA consortium could potentially even allow for a more stable and strategic allocation of computing resources at scales not accessible to individual groups.

There are, however, also investments on a national level in supercomputing facilities to be foreseen. In the United Kingdom, the government has recently decided to spend £79 million to purchase and operate the ARCHER2 supercomputer which will replace the currently operating ARCHER supercomputer at the University of Edinburgh. With a peak performance between 20 and 28 petaflops, it will offer about a five-fold increase in capability related to various numerical simulations, but for the same power consumption. It will have a homogeneous architecture powered by CPUs. Once the system is installed and the service is opened early 2020, ARCHER2 will represent a significant step forward on the road to Exascale computing which should be available by the mid-2020s [750].

Finally, looking at the European scale, several large-scale high-performance computing systems with several hundred thousand computing cores exist across Europe (compared to 2.4 Mio. computing cores at the worldwide largest supercomputer Summit at the Oak Ridge National Laboratory in the US), as has been mentioned above. Table 31.1 and Figure 31.1 give a good overview of the capabilities of the most highly ranked of these systems. On the other hand, the United States and Asia remain dominant as leaders in large HPC facilities as well as in the manufacturing of HPC components and systems. To coordinate the European landscape and resources better, the European Union has thus initiated a number of programmes in recent years, such as HPC-Europa [751]. Another new initiative aiming to boost the supercomputing ecosystem in Europe has been launched in 2018 with the EuroHPC Joint Undertaking [752]. With a 1 billion euro investment from the EU and European countries, this project focuses on two topics: firstly, to develop a world-class European supercomputing infrastructure through the construction of new supercomputers; and secondly, to enable a long-term R&D program to continue the development of the European HPC landscape towards higher performance, but also to foster a more independent European supercomputing supply industry. The first aspect follows, more specifically, the goal to buy and implement, by 2020, three new pre-exascale machines (which would rank within the top 5 globally) as well as five new peta-scale computers in Europe (to be located in Bulgaria, Czech Republic, Finland, Italy, Luxembourg, Portugal and Slovenia). This initiative would double the supercomputing resources available for European users from academia, industry and the public sector [753]. In the long-term, further supercomputing systems on the exascale and beyond are foreseen to be installed with a strong focus on using European technology at this point. For EuPRAXIA, such a development is of great interest and could be pursued further in parallel to activities and opportunities at national scales.

## Part 6

### Appendix

## 32 Further Working Package Results

### 32.1 Assumptions and Numerical PIC Codes Used

The theoretical framework of most of the studies presented in this report is based on plasma and accelerator theory which has been developed in the last decades and copiously documented in the literature. In the context of plasma acceleration theory in particular, some key features that the EuPRAXIA design makes use of include:

- linear and non-linear plasma waves,
- propagation, self-focusing, and guiding of laser pulses in plasmas,
- methods of injection and trapping plasma electrons in plasma waves, by means of plasma density gradients, ionization, etc.
- limits to electron energy gain, including electron dephasing and laser pulse depletion.

The plasma acceleration scaling laws, in particular the expected energy gain in specific conditions are reported and discussed in Chapters 7, 13 and 16. However, as the wakefield formation and electron acceleration in an underdense plasma cannot be fully predicted by analytic theory owing to non-linear effects of laser pulse propagation, plasma wakes and motion of the accelerated electrons, only numerical simulations taking into account all combined effects can provide the real properties of the excited wave and of the electron bunch exiting the plasma structure.

Particle in Cell (PIC) simulations are a widely used tool for the investigation of both laser- and beam-driven plasma acceleration: a large number of macro-particles are distributed with positions within a grid and momenta. Each time step, the currents are “deposited” onto the appropriate corners or segments of the grid. Maxwell’s equations are then advanced forward to calculate new electric and magnetic fields by using commonly the finite difference time domain (FDTD) method. The force on each particle is then calculated so that their momentum and position can be advanced forward to the next time step after which the current can be determined and the whole sequence can be repeated the desired number of time steps. Some well-known PIC codes are quoted below:

- OSIRIS: R.A. Fonseca et al., “OSIRIS: A Three-Dimensional, Fully Relativistic Particle in Cell Code for Modeling Plasma Based Accelerators”, ICCS 2002, LNCS, vol. 2331, 2002, pp. 342–351
- CALDER: E. Lefebvre et al., “Electron and photon production from relativistic laser-plasma interactions”, Nucl. Fusion 43 (2003) 629–633
- WARP: J.-L. Vay et al., “Novel methods in the Particle-In-Cell accelerator Code-Framework Warp”, Comp. Sci. & Discovery 014019 (2012)
- HiPACE: T. Mehrling et al., “HiPACE: a quasi-static particle-in-cell code”, Plasma Phys. Control. Fusion 56 084012 (2014)
- AlaDyn C. Benedetti et al., “ALaDyn: A High Accuracy Code for the Laser-Plasma Interaction”, Proceedings of EPAC08, Genoa, Italy (2008).
- SMILEI J. Derouillat et al., “SMILEI: a collaborative, open-source, multi-purpose particle-in-cell code for plasma simulation”, 2017, arXiv:1702.05128v1 [www.maisondelasimulation.fr/smilei](http://www.maisondelasimulation.fr/smilei)

**Table 32.1.** PIC codes used by different partners for EuPRAXIA simulation studies.

PIC code used	Users
OSIRIS	IST, DESY
WARP	CNRS-LPGP, CEA
CALDER-Circ	LOA
SMILEI	CNRS-LLR
ALaDyn, Architect	INFN, CNR
HiPACE	DESY
PIConGPU	DESY
FBPIC	DESY
LAPLAC	JiHT

In order to reduce the amount of computational resources (number of cores and computation time) required for full PIC simulations, various methods have been developed. To quote only a few of them:

- Fourier decomposition along the poloidal direction with respect to the laser propagation axis, first implementation in CALDER-CIRC; A.F. Lifschitz et al, *Journal of Computational Physics* 228 (2009) 1803–1814
- Boosted Lorentz Frame: In this method the simulation is done in a Lorentz frame moving at a speed near the speed of light; as a result, the plasma is Lorentz contracted and the laser wavelength is Lorentz expanded; J.-L. Vay, *Phys. Rev. Lett.* 98, 130405 (2007)
- Hybrid kinetic-fluid approach, where the relativistic beams are treated kinetically and the background plasma electrons as a fluid (example: Architect, ALaDyn)
- Ponderomotive guiding center (PGC) approximation, where the optical cycles of the laser are averaged out (examples: WAKE, HiPACE, ALaDyn, and optional in OSIRIS); P. Mora, T.M. Antonsen, *Phys. Plasmas* 4, 217 (1997)
- Quasi-static approximation when the characteristic timescales of the beam evolution are significantly greater than the characteristic timescales of the plasma evolution (examples: WAKE, HiPACE)

The simulation codes that will be used in WP2 making use of laser-driven plasma acceleration, as well in WP9 and WP14 using an electron beam as driver are listed in Table 32.1.

A short description of the codes used as part of the EuPRAXIA project is reported in the following. Detailed simulation results are presented in Part 4.

### Description of the code OSIRIS

OSIRIS [336] is a state-of-the-art massively parallel particle-in-cell code (or particle-mesh) highly optimised for a wide range of architectures and that has been successfully used for the past fifteen years to support high impact scientific results. It is an object-oriented PIC code, written in Fortran 90. Parallelisation is achieved using domain decomposition with MPI, and HDF5 is used for diagnostics. The code contains algorithms for 1D, 2D, and 3D simulations in Cartesian coordinates and for 2D simulations in azimuthally symmetric cylindrical coordinates. The algorithm can be divided into four key steps: (i) particle push using the self-consistent electro-magnetic fields and the relativistic Lorentz force (ii) current deposit into the numerical grid, (iii) electric and magnetic field advance using the full discrete set of Maxwell's equations and (iv) interpolation of up-dated fields at particles positions. OSIRIS makes no

physical approximations up to the extent where quantum mechanical effects can be neglected. It captures the full laser pulse/particle beam and plasma particle dynamics and it is thus ideally suited for the work associated with this research proposal. OSIRIS is a proprietary code, being developed by the OSIRIS Consortium (IST and UCLA), and being available for development and scientific work to collaborators and partners of the OSIRIS consortium, all team members in this proposal. OSIRIS incorporates advanced physical algorithms including the boosted frames technique to relax computational requirements of plasma-based accelerators, a hybrid algorithm for efficient modeling of fast ignition related scenarios, a new additional laser solver algorithm using the ponderomotive guiding center (PGC), a quasi-3D algorithm that uses a finite number of cylindrical field harmonics to speed up calculations, a hybrid field solver employing finite-differences in the transverse directions and Fourier transforms in the longitudinal direction to ensure perfect dispersion properties in scenarios in order to mitigate the numerical Cerenkov instability and a radiation back reaction algorithm. The new PGC laser solver can lead to computational speedups larger than two orders of magnitude in comparison to the standard OSIRIS algorithm in the conditions relevant for EuPRAXIA.

### Description of the code CALDER CIRC

The code CALDER-CIRC [589,754] is a PIC (Particle in Cell) code. It numerically solves Maxwell's equations coupled to Vlasov equation to describe laser-plasma interaction. A kinetic description of the plasma is necessary for LWFA simulations in non-linear regimes, hence the use of Vlasov equation, which describes, for each species in the plasma, the evolution of the distribution function in the phase space (6 dimensions, 3 dimensions for position, 3 for momenta). To avoid a too heavy computational load, a method of characteristics is used (specifically, a particle method), which avoids to directly discretise the distribution function in a six-dimensional space. The phase space is approximated by an ensemble of  $N$  "macroparticles", each one with given position, momentum and charge weight. Maxwell's equations are discretised on a uniform grid in  $(r,z)$ , separating the multiple azimuthal modes. The code is explicit in time. At each time iteration, the processors perform in a loop the following steps:

- Computation of the electromagnetic fields on the grid nodes by integration of Maxwell's equations
- Interpolation of the fields at the position of each of the  $N$  macroparticles
- Advance of the macroparticles in phase space by integration of the equations of motion
- Projection of the charge and current density on the grid nodes from the updated particle positions and momenta

The code has the possibility to save and restart a simulation. CALDER-CIRC code has not been developed to be used on vectorial machines. Instead, the code is parallelised for distributed memory architectures. In a parallel simulation, the spatial domain is divided into sub-domains, each assigned to one processor. The initial inputs are read and then processed by a master processor, which distributes the data needed for the simulation to all the other processors. Each processor then solves Maxwell's equations in the subdomain to which it has been assigned and performs the position and momentum evolution of the macroparticles located in its subdomain. Communications between processors are performed when macroparticles exit the spatial subdomain managed by the processor, when the processors exchange the values of the fields at the boundary cells, or when the global diagnostics are saved on files. The communications thus only occur at the boundaries between the subdomains, or in

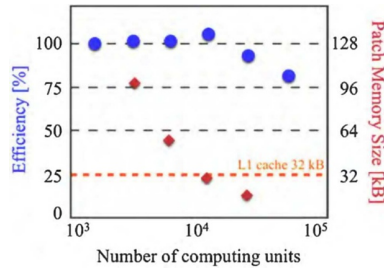


**Fig. 32.1.** Performance scalings for SMILEI code [587].

the (not frequent) iterations when global diagnostics act. The code is also well suited for a highly parallel machine. The code has already been used on supercomputers, among which the supercomputers Curie of TGCC and JADE of CINES.

### Description of the code SMILEI

SMILEI [587] is an explicit Particle-In-Cell (PIC) code written in C++. It uses finite difference schemes to solve Maxwell equations on a grid. Particles, sampling the plasma phase space and able to move freely in the whole domain, are then moved according to the fields evaluated on their local surrounding cells. Once particles have moved, they can deposit their current on the grid. These currents are used as source terms to solve the Maxwell equations again and so goes the PIC cycle. This code uses at most 2 Gb of memory per core and in average less than 1 Gb per core. Two layers of parallelisation are implemented. The first one is a classical MPI domain decomposition. Fields and particles are exchanged only between neighbors and global communications are only needed when reductions are done for outputs. Each MPI process has a copy of its local grid part and a copy of the particles living in this local grid part. As seen in Figure 32.1, the MPI parallelisation has already proven a very good strong scalability on the OCCIGEN system over 50 thousand cores. OCCIGEN is a Bull system. Each node holds 2 Haswell processors of 12 cores 2.6 Gbytes of memory per core. The network is a fat tree Infinyband (IB 4x FDR). The second layer of parallelisation deals with the load division within an MPI process between the several openMP threads it owns. In order to spread the computational load as homogeneously as possible between openMP threads, MPI domains are further divided into many patches which can be seen as sub-domains. They also own their own copy of local grid and particles array. There are many more patches than openMP threads so that the openMP dynamic schedule can keep all threads busy at all times, dispatching the load efficiently between all threads. It is important to note that the number of openMP threads is limited by the number of cores per CPU and that, the efficiency of the load balancing increases with the number of threads. This method therefore benefits a lot from recent CPU with high core counts. But in order to have a real dynamic load balancing, the load must also be balanced between MPI processes. In order to do so, patches exchanges between MPI processes are implemented. An overloaded process is able to offload some of its work to neighbor processes. Patches are ordered along an Hilbert Space-Filing curve, and each MPI process owns a continuous sequences of patches of similar total load. Patches are dynamically exchanged along this curve as their load evolves in order to keep the total load of every single MPI process to a similar level.

## Description of the code WARP

WARP [755] is both a code and a general purpose framework for parallel three-dimensional Particle-In-Cell simulations of beams in accelerators, plasmas, laser-plasma systems, non-neutral plasma traps, sources, and other applications. It contains multiple field solvers (electrostatic FFT, multigrid, electromagnetic), internal conductors (cut-cell method with electrostatic solver), surface physics (space-charge limited emission, secondary emission of electrons or gas from impact of electrons or ions), volumetric ionization. It employs advanced methods such as cutcell boundaries, Adaptive Mesh Refinement, a “warped” coordinate system with no paraxial assumption nor reference orbit required, and boosted-frame support, to name a few. Warp has already been used and experimentally tested on various laser facilities as the Lund Laser Center in Sweden or the UHI100 laser at CEA-Saclay. It is worth noting that the research with Warp is done in close collaboration with the development Team of Lawrence Berkeley National Laboratory (LBNL), especially with J.L. Vay et R. Lehe who are specialists in the laser plasma acceleration modeling and PIC-like numerical methods. The main computationally expensive loops are parallelised using MPI. Warp is written in a combination of i) Fortran for efficient implementation of computationally intensive tasks, ii) Python for high-level specification and control of simulations, and iii) C for interfaces between Fortran and Python. As all computationally relevant tasks are implemented in Fortran, OpenMP will be used on the Fortran level (i.e., there will only be one python interpreter per MPI task, each of which utilises many threads to further parallelise node-level computations). Strong scaling has been demonstrated on various computers. A demonstration example performed by the LBNL Team is shown on Figure 32.2. Warp spectral solver is currently parallelised at subdomain level using MPI (coarse grain parallelism). In turn, every subdomain calls the sequential FFTW 3 library. Additional threadlevel concurrency needs to be added inside the subdomain computations (fine grain parallelism). The spectral solver can use other FFT libraries and we may have to replace the FFTW library calls by calls to a FFT library, like the MKL one, which is better tuned for Knights Landing. One of the special feature of WARP is the possibility to use the boosted-frame technique, reducing the computation time by a large factor, especially for the long accelerator stage. The code can be also used in various geometries, in particular the cylindrical one by including a limited number of azimuthal modes has been implemented. As a result, a quasi-3D computation can be performed with a computing time of two orders of magnitude lower than a full 3D computation. This method was initially implemented in the code Calder-CIRC and is operational in Warp since 2014.

## Description of HiPACE – A 3D quasi-static PIC code

HiPACE (Highly efficient Plasma Accelerator Emulation) [756] is a relativistic, fully electromagnetic, three-dimensional (3D) and fully MPI-parallelised particle-in-cell (PIC) code. It uses the quasistatic approximation to efficiently model particle-beam driven plasma-wakefield accelerators. HiPACE exploits the disparity of time scales in the interaction of highly relativistic particle beams with plasma to decouple beam and plasma evolution. This enables time steps which are many times greater than those used in FDTD PIC codes and therefore renders possible a reduction of the required number of core hours by orders of magnitude. While the axial magnetic field was neglected in the original version of HiPACE, it is now computed along with all other field quantities, so as to allow for the fully consistent simulation of non-cylindrically-symmetric phenomena, such as the hose instability.

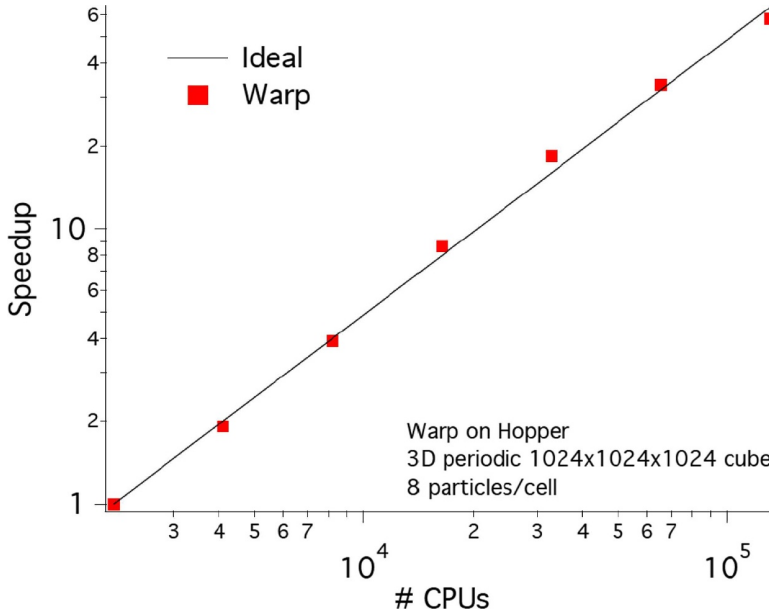


**Fig. 32.2.** Strong parallel scaling of Warp EM solver on 3D periodic 1024x1024x1024 grid with 8 particles/cell, on up to 131,072 cores (image credits: Jean-Luc Vay).

### Description of the code Architect

The Architect code [600,621] belongs to the family of hybrid approach for plasma and laser wakefield acceleration, where to reduce the computational cost the electron background plasma is treated as a cold fluid. The use of a fluid background significantly reduces the computational cost. Architect uses the particle-in-cell (PIC) approach to evolve the electron bunches to preserve the kinetic nature of bunches, particles are evolved in a 3D3V phase-space. Electromagnetic fields are evolved accordingly to Maxwell's equations. To further reduce calculation time without loss of accuracy the fluid and electromagnetic equations are solved assuming cylindrical symmetry. The integrated equations can be written, in a compact way, as follows:

$$\begin{aligned} \partial_t n_e + \nabla \cdot (\beta n_e) &= 0 \\ \partial_t \mathbf{p}_e + c\beta_e \nabla \cdot \mathbf{p}_e &= qn_e(\mathbf{E} + c\beta + e \times \mathbf{B}) \end{aligned} \quad (32.1)$$

$$\nabla \times \mathbf{E} + \partial_t \mathbf{B} = 0 \quad (32.2)$$

$$\nabla \times \mathbf{B} - c^2 \partial_t \mathbf{E} = q\mu_0 c(n_e \beta_e + n_b \beta_b) \quad (32.3)$$

$$d_t \mathbf{p}_{particle} = q(\mathbf{E} + c\beta_{particle} \times \mathbf{B}) \quad (32.4)$$

$$d_t \mathbf{x}_{particle} = \mathbf{v}_{particle} \quad (32.5)$$

where  $\mathbf{E}$  is the electric field,  $\mathbf{B}$  the magnetic field,  $c$  the speed of light,  $\beta_e = u_e/c$  the relativistic  $\beta$  for the background electrons,  $\beta_b$  the relativistic  $\beta$  for the electron bunch,  $\mathbf{p}_e$  the fluid relativistic momentum for electrons,  $n_e$  is the electron density and  $n_b$  the bunch density. For each single particle of the kinetic bunch(es) we identify a relativistic momentum,  $\mathbf{p}_{particle}$ , a relativistic  $\beta$ ,  $\beta_{particle}$ , a velocity,  $\mathbf{v}_{particle}$ , and a position,  $\mathbf{x}_{particle}$ . The first and second equations are the fluid mass conservation and the fluid momentum conservation respectively. The third and the fourth are Faraday's law and Ampere's law respectively. The last two equations are the kinetic compound to the model, the relativistic Newton's law for each

single particle composing the bunch(es): the momentum equation and the position-velocity equation. The fluid velocity classically written as  $u_e$  has been written as a function of  $\beta$ . Ions are assumed as a static background. The code algorithms are presented in Reference [600], and a full comparison with a PIC code is presented in Reference [621]. Dynamic in plasma-based accelerators spans over a large range of timescales, while beams evolve on a timescale on the order of the inverse betatron oscillations, the background plasma evolves on a timescale on the order of the inverse of the plasma frequency. The shortest dominating timescale is the background plasma frequency. The hybrid approach permits to overcome the computational cost imposed by the shortest timescale without renouncing to the full time-explicit formulation. A time-explicit formulation permits to take into account for background density modulation: plasma density ramps and radial plasma channel modulation. We observe background electrons have locally similar behaviour. The evolution of a single particle around the ion bubble resemble the behaviour of the local ensemble averaged behaviour, a fluid description holds. The hybrid approach algorithmic strength consists on the combination of mature state-of-the-art numerical techniques both for the kinetic description as well as for the fluid part. The novelty that a hybrid approach consists is the wise combination of the different algorithms using different timescales. The interaction between the kinetic and fluid scale is made possible via the bunch current, calculated and weighted on the fluid mesh. The novelty introduced by architect is the resolution of evolution equation in a time explicit domain, there is no quasi-static approximation. Moreover, electron bunches are initialised in vacuum with their self-consistent field, we treat the transition from vacuum to plasma.

### Description of the code ALaDyn

The code ALaDyn [362,592,757,758] is a Particle in Cell (PIC) code designed to investigate three main physical regimes:

- Laser-plasma interaction in under-dense gas targets for electron acceleration (LWFA);
- Beam-plasma interaction in under-dense gas targets for electron acceleration (PWFA);
- Laser-plasma interaction in over-dense solid targets for proton(ions) acceleration and related phenomenologies.

A PIC method is based on a hybrid formal setting, whereby plasma particles are represented on a Lagrangian framework whereas self-consistent fields are represented on the Eulerian framework given by Maxwell equations. As most other PIC codes, ALaDyn discretise particle and field dynamical equations by centered finite differences on a staggered space and time grid (Yee's module) using one step second order leap-frog integrator. To connect Lagrangian particles to Eulerian fields collocated on the spatial grid, finite order B-splines are used. B-splines are local polynomials with compact support, allowing to represent delta-like point particles on a grid for charge deposition and, by converse, to assign field grid data to a point particle. Energy preserving PIC schemes do not satisfy local charge conservation and the related Poisson equation. By converse, using one of the many numerical recipes to enforce the continuity equations, energy conservation is heavily damaged. ALaDyn code implements both charge or energy preserving schemes, letting the user to choose, depending on the problem at hand. Besides the standard leap-frog integrator, ALaDyn also implements a fourth order in space and time Runge-Kutta integrator. This scheme requires larger computational resources, of course, but can be of help to improve on accuracy and reduce dispersive effects of wave propagation. The code implements also reduced models based on:

- the envelope (two-scale) approximation of the laser fields and of the particle dynamics;
- a cold fluid approximation of the background plasma dynamics;
- hybrid fluid-kinetic simulations (kinetic particles on top of a fluid background).

Reduced models have been intensively tested from a linear up to a strongly non-linear regime, showing that they are reliable and robust. In particular it has been shown that the breakdown of the implemented numerical models usually is closely related to the breakdown of the physical assumption underlining the theoretical model. In all of the above configurations, field induced ionization (tunneling) is also implemented and can be activated, if requested by the user. All ionization models are based on the ADK scheme plus barrier suppression (BSI) for higher  $Z$  ions. For solid targets, impact (collisional) ionization is under development.

### Implementation

ALaDyn is almost completely written in Fortran 90, but a couple of utility modules are written in C++. C can also be easily used to extend code functionalities. Fortran 90 is the most popular computational language in PIC codes, probably because of the higher efficiency in handling multidimensional arrays on a grid. Finite difference integration allows to exploit efficient parallelism by domain decomposition using MPI technique to distribute the computational work among CPU units. ALaDyn has been successfully ported to many HPC architectures, both in Italy at CINECA and in Europe through PRACE Partnerships. From the CINECA IBM-SP6 system in 2011, to the test system at CINECA based on IBM/BGP in 2012, then CINECA FERMI in 2014 and MARCONI in 2016, ALaDyn run on a multitude of HPC architectures, always extracting top range performances. A new version has been recently released open source on the web, with a GPLv3 license. In part it has been rewritten from scratch and it is the basis for future development. Sources can be found, together with other codes, in our organization GitHub page at [github.com/AlaDyn](https://github.com/AlaDyn)

### Description of the code PIConGPU

PIConGPU [759] is a fully relativistic Particle-in-Cell (PIC) code developed and maintained by the Computational Radiation Physics group at the Institute for Radiation Physics at HZDR, Dresden, Germany. The code is written in C++ and it is designed to run on Graphical Processing Units (GPUs) based on the NVIDIA CUDA library, which are in general better suited for heavy parallelisation due to a much higher number of individual cores, as compared to CPUs, allowing a significant speed up of the simulations. The code supports a hybrid architecture consisting of single computation nodes interconnected in a standard cluster topology, with each node carrying one or more GPUs. The internode communication is realised using the message-passing interface (MPI). PIConGPU implements various numerical schemes to solve the PIC cycle. Its features for the electro-magnetic PIC algorithm include:

- A central or Yee-lattice for fields.
- Particle pushers that solve the equation of motion for charged and neutral particles, e.g., the Boris- and the Vay-Pusher.
- Maxwell field solvers, e.g. Yee's and Lehe's scheme.
- Rigorously charge conserving current deposition schemes, such as Villasenor-Buneman, Esirkepov and ZigZag.

- Macro-particle form factors ranging from NGP (0th order), CIC (1st), TSC (2nd), PSQ (3rd) to P4S (4th).

and the electro-magnetic PIC algorithm is further self-consistently coupled to:

- Classical radiation reaction.
- QED synchrotron radiation (photon emission).
- Advanced field ionization methods.

The code is open source and licensed under the GPLv3+.

### Description of the code FBPIC

FBPIC [489,760] is an open-source Particle-In-Cell (PIC) code for relativistic plasma physics. By design, the code is especially well-suited for simulations of plasma-based particle acceleration. It implements a unique algorithm that uses an azimuthal mode decomposition of the electromagnetic fields in a cylindrical geometry, to reduce the computational costs of simulations with close-to-cylindrical symmetry. For typical cases of plasma acceleration, this method results in orders-of-magnitude speed-up when compared to conventional, fully three-dimensional algorithms. By advancing the fields in spectral space, it furthermore avoids numerical errors common to traditional field solvers that are based on finite-difference methods. The implemented Galilean-PSATD (Pseudo-Spectral Analytical Time Domain) solver mitigates artificial beam quality degradation by numerical Cherenkov radiation (NCR) [761] and is free of the numerical Cherenkov instability (NCI) for relativistically drifting plasmas [762,763]. The latter characteristic allows to model the process of plasma acceleration in an optimal, relativistic frame of reference. For many simulation cases, the so-called Lorentz-boosted frame technique leads to orders-of-magnitude reductions in runtime, thereby increasing the overall efficiency of a simulation even more. In order to make all of these algorithmic features available to the user, FBPIC exposes an easy-to-use API to setup a simulation, providing many helper functions to initialise pre-defined physical objects, such as particle beams or laser profiles. The code is written in Python and uses on-the-fly compilation to machine code for high performance. On a first level, the algorithm is optimised to run efficiently on highly parallel hardware, such as GPUs and multi-core CPUs. On a second level, the computation is scaled to distributed compute nodes using MPI (Message Parsing Interface). FBPIC supports the OpenPMD standard [764], which defines a common format for structured output files. This open-source standard allows to use the same post-processing tools for output generated by different codes, facilitating compatibility and comparability of results.

### Description of the code LAPLAC

In the hybrid code LAPLAC [765,766] the electron background plasma, like in the code Architect, is treated as a cold fluid. To describe self-consistently the wakefield generation by a short intense laser pulse propagating in an ionising gas the laser pulse non-linear dynamics and plasma formation due to tunneling ionisation of the gas are taken into account. The Maxwell equation for the total electric field (which includes high-frequency laser fields and also slowly varying plasma wakefields)

$$\nabla \times \nabla \mathbf{E} + \frac{1}{c^2} \frac{\partial^2 \mathbf{E}}{\partial t^2} = -\frac{4\pi}{c^2} \frac{\partial}{\partial t} (\mathbf{J} + \mathbf{J}_{\text{ion}}) \quad (32.6)$$

contains the electric current density of free electrons  $\mathbf{J} = en_e\mathbf{V}_e$ , determined by the momentum of free electrons  $\mathbf{P}_e$  :  $\mathbf{V}_e = \mathbf{P}_e/(m_e^2 + \mathbf{P}_e^2/c^2)^{1/2}$ , and also the ionisation current, which provides the momentum and energy changes of the laser pulse due to direct ionisation losses in the process of tunnel gas ionisation [767]. The hydrodynamic equations for the electron plasma density and the electron momentum can be written in the form of equation (32.1) with additional terms describing the impact of optical field ionisation [768]. The laser pulse propagation and the wakefield generation are described in terms of the slowly varying amplitude approximation which implies that the laser pulse duration is in excess of a few optical cycles.

The PIC method is used to study the motion of the electron beam particles, which is described by the extended equations (32.4–32.5), where the radiation strength in the Landau-Lifshitz form is taken into account. The code also allows to investigate the dynamics of the electron spin precession, which is calculated based on the T-BMT equations [769].

## 32.2 Further Considerations for High-Gradient Plasma-Accelerator Structures

### 32.2.1 Introduction

Several options are envisaged in the frame of EuPRAXIA for a plasma based multi-GeV accelerator. Four concepts in particular are currently under study:

1. Beam generation and acceleration in a single-stage laser-driven plasma injector / accelerator.
2. External injection of an electron bunch into a laser-driven plasma accelerator.
3. External injection of an electron bunch into a beam-driven plasma accelerator.
4. Hybrid schemes including both laser-driven and beam-driven plasma acceleration.

In this frame, the role of WP3 has been to define laser-driven plasma accelerating structures *(i) to achieve an injector, by generating a source of electrons of energy 150 MeV or 1 GeV*, producing bunches of short duration with reliable parameters, suitable for injection into a laser-plasma accelerating structure; *(ii) to achieve a high gradient accelerating structure providing energy gain from 1 to 5 GeV*, with controllable plasma parameters, compatible with laser propagation over the acceleration length, and scalable to high electron energy requirements. This section provides additional background information for the plasma target design presented in Chapters 13 and 16.

### 32.2.2 Plasma Stage Parameters

#### Regime of Operation and Parameter Range

Laser and plasma parameters need to be identified to achieve the different types of plasma stages considered in the EuPRAXIA design. They can be classified as:

- Laser wakefield *injectors* to generate electron bunches at an energy of
  - 150 MeV, so that the energy gain in the plasma structure is  $\Delta W = 150$  MeV
  - 1 GeV, i.e.  $\Delta W = 1$  GeV
- Laser-plasma *accelerator* stages to increase the energy of the electrons
  - from 150 MeV to 1 GeV :  $\Delta W = 0.85$  GeV
  - from 150 MeV to 5 GeV :  $\Delta W = 4.85$  GeV
  - from 1 GeV to 5 GeV :  $\Delta W = 4$  GeV

Laser wakefield injectors, by definition, generate relativistic electrons bunches as a result of laser-plasma interaction, without external injection from an external electron source. Therefore, they operate in a non-linear regime, such that the laser normalised vector potential  $a_0 > 1$ , corresponding to a peak laser intensity on target  $I_L$  larger than  $2.1 \times 10^{18} \text{ W/cm}^2$ , for a laser of wavelength  $\lambda = 800 \text{ nm}$ .

Laser-plasma accelerator stages by definition provide an accelerating structure where externally injected electron bunches gain energy. Injection or trapping of plasma electrons in this structure should be avoided so that they operate in the quasi-linear regime with  $a_0$  of the order of 1.

The maximum energy gain an electron can experience can be estimated by  $\Delta W = eE_{acc}L_{acc}$  with  $e$  the electron charge,  $E_{acc}$  the average electric field and  $L_{acc}$  the acceleration length. The optimum acceleration length is the dephasing length  $L_\varphi$ , defined as the distance after which electrons slip out of the accelerating and focussing phase. The acceleration process is the most efficient when it is equal to the laser energy depletion length,  $L_{dpl}$ , defined as the length over which half of the laser energy is used to excite the plasma wave.

The energy gain over the dephasing length, can be estimated from scaling laws established by Lu et al. [185]. In the non-linear regime relevant for LPI,  $a_0$  is larger than 2, and the energy gain evaluated over the dephasing length, is given by :

$$\Delta W(/m_e c^2) \simeq \frac{2}{3} \frac{n_c}{n_e} a_0. \quad (32.7)$$

This is an upper limit, as for  $a_0 > 2$  the depletion length is always smaller than the dephasing length. If we consider a laser intensity high enough to inject electrons in the wakefield ( $a_0 \gtrsim 2$ ), we obtain estimates in agreement with experimental achievements:

$$\Delta W = 150 \text{ MeV} : n_e \simeq 7.9 \times 10^{18} \text{ cm}^{-3} \text{ and } L_{acc} \simeq 1 \text{ mm for } a_0 = 2$$

$$\Delta W = 1 \text{ GeV} : n_e \simeq 1.8 \times 10^{18} \text{ cm}^{-3} \text{ and } L_{acc} \simeq 9 \text{ mm for } a_0 = 3$$

In the linear regime relevant for LPAS,  $a_0 \simeq 1$ ,  $L_\varphi$  and  $L_{dpl}$  scale as follow [185]

:

$$L_\varphi \simeq \frac{n_c}{n_e} \frac{1}{k_p} \quad (32.8)$$

and

$$L_{dpl} \simeq \frac{n_c}{n_e} \frac{1}{k_p} \frac{\omega_p \tau_L}{a_0^2} \quad (32.9)$$

The use of laser energy on the dephasing length is optimum for  $\omega_p \tau_L \simeq 1$  and  $a_0 \simeq 1$ .

For LPAS, the energy gain is estimated over the dephasing length for externally injected electrons trapped in the structure, and  $a_0 = 1$ , using  $\Delta W(/m_e c^2) = n_c/n_e$ :

$$\Delta W = 0.85 \text{ GeV} : n_e \simeq 1 \times 10^{18} \text{ cm}^{-3} \text{ and } L_\varphi \simeq 9 \text{ mm}$$

$$\Delta W = 4 \text{ GeV} : n_e \simeq 2.2 \times 10^{17} \text{ cm}^{-3} \text{ and } L_\varphi \simeq 88 \text{ mm}$$

$$\Delta W = 4.85 \text{ GeV} : n_e \simeq 1.8 \times 10^{17} \text{ cm}^{-3} \text{ and } L_\varphi \simeq 118 \text{ mm}$$

These scalings are approximate, and for example they do not take completely into account the evolution of the wakefield amplitude due to laser self-focussing which is significant in most experiments. However they provide estimates of the density and acceleration length corresponding to a given energy gain close to experimental achievements as discussed by S. Mangles [770].

## Overview of Relevant Experimental Efforts

Most of the experimental work to date in the field of LWFA is related to the injector class, and studies the acceleration of small populations of relativistic electrons issued

from the bulk of plasma electrons, with which the intense laser interacts. These accelerated electron bunches are relatively easy to achieve experimentally with existing laser systems, but the properties of the electron bunches are difficult to control and may not be suitable for demanding applications.

Over the past fifteen years, successive improvements have been proposed theoretically and demonstrated experimentally. The use of various physical mechanisms provides different levels of control of the electron beam properties at the expense of simplicity.

A selected number of processes or mechanisms are discussed in this report, based on their strong potential for improving the electron beam quality. Published experimental results were examined and compared not only in terms of achieved electron properties, but also regarding their reliability, stability, or scalability to larger electron energy, or repetition rate.

External injection and acceleration of electrons in a LWFA have been attempted by only a few groups, and its achievement is complex as it involves femtosecond range timing and micron precision on alignment and stability of beams. The early work of Amiranoff et al. [771] has demonstrated the need of short electron bunches for injection into a plasma structure, and the extension of the plasma length to the dephasing length in order to fully exploit this scheme. Recent work [181] has further demonstrated the potential and challenges of external injection, emphasising the need for compact electron beam transport and shaping.

Following the first tentative experiments for external injection, laser guiding techniques have been developed and demonstrated experimentally in order to provide plasma media able to sustain accelerating structures over dephasing lengths much longer than the Rayleigh length.

Accurate comparison of experimental and simulation results is also extremely challenging as it requires a precision not currently available for two main reasons: on one hand, experimental parameters are not completely known from usual measurements as diagnostics are not necessarily available on the scales required; on the other hand, simulations need sizeable computing capacity to correctly describe 3D situations taking into account realistic and non perfect inputs. Undergoing efforts aim at a better knowledge of experimental parameters and the development of numerical tools to provide a more realistic description.

### 32.2.3 Plasma Creation

Targets for laser-driven plasma accelerators can be broadly classified as waveguide or non-waveguide targets; each can be further divided into targets which are pre-ionised or are ionised by the driving laser. It should be emphasised that guiding of the driving laser pulse can, and in general will, still occur in “non-guiding” targets through relativistic self-focussing.

The plasma target can incorporate important additional features such as: structures for controlling injection of electrons into the wakefield; longitudinal variation of the plasma density for extending acceleration beyond the dephasing length [196], or for controlling the properties of the electron bunch as it leaves the acceleration stage. The criteria to be considered when choosing a plasma target are described in the following.

#### Criteria for Choosing Plasma Targets

The choice of the plasma target depends on the constraints on the plasma stage considered:

**Required plasma length:** To achieve a given energy gain, the target must be at least as long as the expected gain divided by the mean accelerating gradient. For optimised operation, the accelerating length is limited by electron dephasing and the accelerating gradient is controlled by plasma density and laser intensity values. As the plasma electron density, the laser intensity and the laser power are the main parameters that determine the dynamics of the interaction, a valid strategy would be to fix those parameters according to the desired energy gain. The length of the target must then be set to match the dephasing length. A variable length target provides a degree of freedom to adjust the plasma length independently from the density, for example to tune finely the electron energy without changing the other parameters.

**Appropriate density profile:** For a laser wakefield electron injector, a tailored density profile can be useful. For example when the density gradient injection scheme is used, the plasma target should exhibit a steep density gradient to limit the volume of injection to a controlled area. When the laser amplitude  $a_0$  in vacuum is lower than the injection threshold, self-focusing and self-compression play a significant role to achieve injection. As these mechanisms depend on the local plasma density, the shape of the density profile along the propagation direction provides a way to control the injection length. Moreover gradients can be used in the injector to compensate the energy chirp of the injected electron bunch and therefore reduce the energy spread [32].

In an accelerator stage, an upward gradient can be used to keep the externally injected electrons in phase with the plasma wave driven by laser, and a downward gradient to control the beam properties at the transition between plasma and vacuum.

**Stability of the plasma density:** In order to use the electron beam for applications, the stability of its properties is crucial. All sources of fluctuations of experimental parameters should be characterised and minimised to reduce the electron bunch property fluctuations. However, determining contributions of each parameter fluctuations on the electron bunch fluctuations is difficult to achieve experimentally. A study by Desforges et al. [197,198] shows that the plasma electron density is a key parameter for the stability of the injector. The acceptable level of fluctuations on the value of the density could be investigated numerically in conjunction with WP2.

**The lifetime of the target and the repetition rate it can sustain:** The target should be able to sustain a 10 Hz repetition rate and to be used for at least a day. From these considerations, two strategies can be adopted : a robust target that can sustain a large number of shots (typically hundreds of thousands of shots assuming a 10 Hz repetition rate during a day of operation) or a remotely interchangeable target that can sustain a smaller number of shots but can be replaced without interrupting operation.

**Possibility to probe the target:** It can be useful to have the possibility to probe the target, either to trigger the injection in the case of colliding pulse injection for the injector(s), to monitor the density of the plasma, or to discriminate sources of trouble in the case of abnormal operation.

**Compactness and compatibility with diagnostics:** Finally, the target design must be compatible with other diagnostics that may be implemented in the experimental chamber such as laser or electron diagnostics.

## Gas Cells and Gas Jets

### *Gas jets*

Gas jets have seen a very wide use as targets for laser-plasma interactions. Much early work in laser wakefield acceleration was performed with gas jets, for example the three seminal experiments presenting electron beams with narrow peaked energy spectrum (PES) employed gas jets as the target [11,12,273]. Kneip et al. [772] used gas jets as targets to obtain narrow PES electron beams with energies to the GeV level. More recently a novel dual gas jet design has been used to obtain stable, narrow PES electron beams with central energy tunable in 50 – 300 MeV range [773].

Supersonic gas jet nozzles can be optimised to provide nearly flat-top density profiles required for laser wakefield acceleration, where a plateau in plasma density can be many millimetres long. Semushin and Malka [289] showed this can be done by optimising the opening angle of the conical nozzle  $\theta$ , the throat diameter  $d_C$  and the diameter of the exit  $d_E$ . Simulations agree with experimental measurements and show a 5 mm long flat density plateau is obtained. However, as the density profile is generated by a supersonic expansion, density is typically only flat to  $\approx 10\%$ . Schmid and Veisz [276] further show that the scale length of density gradients on either side of the density plateau follow a linear dependence on the product  $Ld_E$ , where  $L$  is the length of the divergent section.

The peak plasma density is controlled by changing the backing pressure of the jet; the plasma density varies linearly with backing pressure. Typically pressures up to 100 bar are used to obtain plasma densities up to  $n_e \simeq 1 \times 10^{20} \text{ cm}^{-3}$ . For a fixed throat diameter, increasing the nozzle diameter results in lower density plateau values. As an example, for an optimised nozzle with  $d = 2$  (15) mm, a backing pressure of 100 bar results in peak electron density of  $n_e = 2 \times 10^{20}$  ( $4 \times 10^{18}$ )  $\text{cm}^{-3}$ . The high pressure solenoid valves usually used to control the gas flow out of the jet are typically open for a few tens of milliseconds which presents heavy vacuum system loads. This can be reduced through the use of faster solenoids and careful design of the valve/nozzle system to minimise the volume of gas released per shot.

Gas jets rely on expansion into vacuum and as such provide an entirely open geometry for diagnostic access. This allows for the plasma density profile to be measured for every high power shot. In addition, by using ultra-short, nearly single-cycle probe pulses, Buck et al. [532] directly measured the phase of the self-injected electrons within the accelerator cavity.

For very high repetition rate ( $f > 100 \text{ kHz}$ ) operation of laser wakefield accelerators, it will be desirable to remove plasma from the beam path prior to the arrival of the next laser pulse. In gas jet targets, the supersonic flow perpendicular to the accelerator axis means that plasma removal occurs naturally.

### *Gas cells*

Osterhoff et al. [774] have investigated laser-wakefield acceleration in steady-state flow gas cells. In this work the gas “cell” is a gas-filled capillary, but it is important to note that, unlike the waveguides described in this section, reflections from the capillary wall play no role in guiding the laser since the capillary diameter is much larger than the laser spot size.

The capillaries are constructed by laser-machining channels of semi-circular cross-section in sapphire plates; additional channels are machined into the plates to provide a route for gas to flow into the main capillary. Contacting two such plates together forms the capillary.

Fluid simulations show that within a few hundred milliseconds of the gas valve opening, the gas within the central 80% of the capillary is highly homogeneous and stationary. Further, turbulence in the gas plumes formed immediately outside the

capillary is low, and supersonic shock fronts of the type found in some high-Mach number gas jets, are avoided.

As an example, Osterhoff et al. [774] constructed steady-state 15 mm long gas cells from capillaries of 250  $\mu\text{m}$  diameter. Using 850 mJ, 42 fs full width at half maximum (FWHM) laser pulses from a Ti:sapphire laser they generated electron beams of up to 200 MeV. These beams were emitted within a low-divergence cone of  $(2.1 \pm 0.5)$  mrad FWHM, and had shot-to-shot stabilities of 2.5% RMS in energy, 1.4 mrad RMS pointing, and 16% RMS in charge. The high stability of gas cell targets was used by Weingartner et al. [569] to perform a quadrupole focussing scan to measure the emittance of laser wakefield accelerated electron beams.

A different approach was introduced by Vargas et al. [775], presenting the use of three-dimensional printing of gas cells. Single-stage or two-stage gas cells can be printed with ease. Due to the cell being a rectangular enclosure windows can be used to allow for diagnostic access. Improved stability as compared to gas jets is observed, along with higher electron beam energies.

## Waveguide Targets

In general terms waveguides utilise a transverse variation of the refractive index to guide the driving laser pulse, and these may usefully be divided into step-index and gradient refractive index waveguides. In the context of plasma accelerators, gradient refractive index guiding can be achieved by creating a transverse variation of the plasma density to form a “plasma channel”. Step-index waveguides can be achieved via grazing-incidence reflections from the inner wall of a gas-filled capillary tube [350]. A key difference between the operation of plasma channels and hollow-core capillary waveguides is that the guiding properties of the former usually depend on the on-axis density, whereas in hollow-core capillaries the guiding is much less strongly dependent on the plasma density. Confinement of the driving laser pulse in waveguides, and by relativistic self-guiding, is considered in detail in this section.

## Complex or Novel Structures

### *Variable-length gas cells*

It can be useful to be able to adjust the length of the target, either: (i) to match the target length to the dephasing or pump depletion lengths, without also changing the gas density; or (ii) to study the evolution of the particle with longitudinal position in the plasma accelerator.

One example has been provided by Heigoldt et al. [776]. In their design, the rear gas cell pinhole was mounted on a cylinder which could be driven longitudinally within the gas cell, thereby varying the length of the gas cell between 2 mm and 4 mm. This cell was used to study the evolution of the longitudinal bunch profile with longitudinal position within the plasma accelerator.

Hydrodynamic simulations of a variable-length gas cell with two separate chambers have been reported by Kononenko et al. [286]: an “injector section”, and an “accelerator section”. In such a target the plasma density in the accelerator region is always below the self-trapping threshold. A single laser pulse is self-guided throughout the interaction, with the density and length of the first injection section determining the phase space volume of the accelerated beam. Such cells of varying density, driven by a single pulse, can have a number of applications. In the case of an increasing plasma density between the steps, the shortening of the plasma wave wavelength can rephase electrons into the accelerating phase of the wakefield, thus increasing the

maximum dephased energy (as described in the paragraph below). By contrast, density decreases can help make injection easier, thus potentially reducing the trapping threshold even for relatively low intensity laser drivers.

#### *Tapered density targets*

Targets in which the plasma density varies with longitudinal position could be used to extend acceleration beyond the dephasing length  $L_\varphi$ . In this approach, the plasma density increases longitudinally, so that the plasma wavelength decreases as the particle bunch slips forward with respect to the laser driver. For the correct longitudinal variation of the plasma density, the particles maintain their location (i.e. phase) relative to the plasma wave.

This idea was first described for particle-driven plasma accelerators by Katsouleas [188]. Sprangle et al. have derived an expression for the longitudinal density profile for the case of a laser-wakefield accelerator driven in a plasma channel [777]. Rittershofer et al. [196] extended this work to account for the *transverse* variation of the plasma density in the plasma response, and derived conditions for phase locking the location of the bunch to the transverse or longitudinal accelerating fields, or both. We note that Pukhov and Kostyukov [778] have also considered the use of layered plasmas to optimise simultaneously the energy gain and quality of laser-accelerated electron bunches, and Yoon et al. have studied quasi-phase-matched laser wakefield acceleration [779].

Varying density, steady-state flow gas cells were investigated by Rittershofer [780]. Gas cells were formed from 15 mm long, laser-machined capillaries with an inner diameter of 200–300  $\mu\text{m}$ . Gas was introduced into the capillaries via 500  $\mu\text{m}$  diameter inlets located 750  $\mu\text{m}$  from the capillary ends. The gas pressure at each end could be set independently, allowing the formation of a close-to-linear variation with a ratio as high as approximately two in gas density between the gas inlets. For example, using hydrogen, a change in the atomic density from  $3 \times 10^{18}$  to  $1.5 \times 10^{18} \text{ cm}^{-3}$  over a distance of 10.8 mm was demonstrated. The density ramps formed in this way were found to agree with fluid flow simulations.

Tapered *plasma channels* have also been investigated. For example, Kaganovich et al. [781] have described a segmented discharge-ablated capillary discharge. In this device, three plastic capillaries of inner diameter 500  $\mu\text{m}$  were joined coaxially to form a capillary with a total length of a 60 mm. By driving different current pulses in each section it was possible to generate three, coaxial plasma channels of different axial density. The mean plasma density was approximately  $2 \times 10^{19} \text{ cm}^{-3}$ .

Abuazoum et al. [782] have described a tapered gas-filled capillary discharge waveguide which utilises an alumina capillary with a linearly-varying inner diameter. Measurements of the variation of the transmitted laser spot size as a function of the input spot size indicated the formation of a plasma channel with an axial plasma density which changed from  $1.8 \times 10^{18}$  to  $2.9 \times 10^{18} \text{ cm}^{-3}$  over the 40 mm length of the waveguide.

#### *Targets incorporating structures for localised injection*

Different approaches to controlling injection by density transitions have been proposed. Gonsalves et al. [658] use an integrated gas jet within a capillary discharge waveguide to produce localised injection via density gradient injection. Narrow PES beams with 5% energy spread and charge of  $\simeq 10 \text{ pC}$  were observed with peak energies up to 400 MeV.

Schaper et al. [783] have incorporated multiple gas inlets or outlets to steady-state gas cells, with the objective of tailoring the longitudinal profile of the gas density. Similarly to above a nozzle has been included for controlling electron injection. Additionally, the density profile for exiting electron beam can be tailored to ensure optimum electron beam quality.

The density tailoring approaches above rely on the phase velocity of the wakefield changing and thus electrons becoming injected. Alternatively one can introduce a localised section of an impurity gas to employ ionisation injection. This approach was first explored by Pollock et al. [282] to demonstrate the generation of PES beams of 5% energy spread at 0.5 GeV using a 200 TW laser. The concept was also tested by de la Ossa et al. [652] in the context of beam-driven wakefield acceleration. Through simulations, a 2.6 GeV, 6% RMS energy spread beam is predicted as a result of localised ionisation injection.

### 32.2.4 Laser Confinement

At the intensity required for high gradient plasma acceleration, the laser beam has to be focussed to a spot size in the range 10 – 100  $\mu\text{m}$  corresponding in vacuum to a diffraction length of the order of  $3 \times 10^{-4}$  to 0.03 m. Assuming an average accelerating gradient in the range 1 – 10 GV/m, the distance required to achieve 1 (5) GeV is in the range 1 – 0.1 (5 – 0.5) m. As the laser diffraction in free space limits the volume over which a high intensity can be achieved, the laser beam has to be confined transversely to prevent diffraction. This can be achieved by employing the non-linear self-guiding effect or by imposing external guiding structures, such as waveguides. Two main types of waveguides are of interest at the intensity and plasma parameters required: plasma channels and capillary tubes or a combination of both.

### Self-Guiding

#### *Guiding mechanism*

The self-guiding of short laser pulses in an underdense plasma is based on refractive guiding. This is achieved by laser-driven modifications to the refractive index of plasma yielding a maximum on axis, i.e.  $\partial\eta/\partial r < 0$ . This causes self-focussing of the pulse as laser wavefronts will curve towards the axis, where the phase velocity is the lowest. When the self-focussing effect induced by the laser balances the natural diffraction of the pulse, self-guiding can be achieved.

The refractive index response in the standard self-guiding theory is due to relativistic electron quiver motion [784,785] or self-channelling [786]. In the weakly relativistic regime ( $a_0 < 1$ ) the refractive index of the plasma is given by,

$$\eta \simeq 1 - \frac{\omega_p^2}{2\omega_0^2} \left( 1 - \frac{a^2}{4} + \frac{\Delta n_p}{n_e} + \frac{\delta n}{n_e} \right) \quad (32.10)$$

for a linearly polarised laser. Laser pulses with an intensity maximum on-axis can undergo self-focussing; this is described by the  $-a^2/4$  term in equation (32.10). The mass of the electrons in the laser field is increased by a factor of  $\gamma_\perp = \sqrt{1 + a_0^2}/2$ , meaning the axial electrons will have higher mass and thus respond slower to the laser field. This results in a spatially varying  $\eta$ , with the highest refractive index being in the regions with highest intensity. For laser pulses with durations much longer than a plasma wavelength, the laser can expel a fraction of electrons from the axis and set up a density channel. For very high intensities ( $a_0 > 1$ ), self-channelling can also occur for short pulses, where the laser is guided in its own self-generated density cavity, which is sometimes known as a plasma “bubble” [787]. These effects are accounted for in the laser pulse guiding by the  $\delta n/n_e$  term above; a reduced density on-axis results in a higher axial value for  $\eta$ . A pre-generated density channel, characterised by the  $\Delta n_p/n_e$  term in equation (32.10), will also guide the pulse.

### *Main properties of guided pulses*

Self-guiding relies on non-linear self-focussing, which occurs for pulses with an intensity maximum on-axis. The guided spot size depends weakly on the laser power, with  $k_p w_m = 2(2P/P_c)^{1/6}$  in the weakly relativistic regime [344] and  $k_p w_m = 2(P/P_c)^{1/6}$  in the 3D non-linear regime [363]. Here,  $w_m$  is the matched or guided mode size. As the laser power is usually chosen to be close to or a few times higher than  $P_c$ , the transverse extent of guided spots is of the order of a plasma wavelength  $\lambda_p$ . For ultra-short very intense pulses, the guided spot size can be recast to read  $k_p w_m = 2\sqrt{a_0}$ , showing that the matched mode size depends also on laser intensity.

### *Parameters range*

Self-focussing is possible for laser pulses with power that is larger than the critical power for self-focussing,  $P_c = (n_c/n_e)17.4$  GW. The critical power is a function of plasma electron density; requiring higher laser powers for self-focussing to occur at lower background densities. For an example, a 30 TW laser can self-focus at  $n_e = 1 \times 10^{18} \text{ cm}^{-3}$  whereas the critical power for self-focussing at  $n_e = 1 \times 10^{17} \text{ cm}^{-3}$  is 300 TW.

The matched mode size will depend on the laser power and the plasma density. Thomas et al. [788] show that in order to achieve optimum coupling, the laser vacuum waist size  $w_0$  should be close to the matched value in plasma. Given a fixed power laser for  $w_0 < \lambda_p$ , the laser diffraction is too fast for the plasma to provide a sufficient guiding response leading to pulse filamentation and breakup. Only when  $w_0 \simeq \lambda_p$  is stable self-guiding achieved, which in turn results in high quality electron beams. In general, there exists no upper limit for the laser intensity for self-guiding as long as  $w_0$  is suitably matched to the guided mode size.

Self-focussing is effective for the body of long pulses ( $c\tau_L \gg \lambda_p$ ), but the tail of such pulses may undergo other laser-plasma instabilities. Early theoretical work [343,344] raised doubt on the effectiveness of relativistic self-guiding for short pulses ( $c\tau_L \lesssim \lambda_p$ ). However, simulations [185] and experimental [789] work have shown guiding of the body of short pulses can be achieved via self-channelling and non-linear blowout.

It has been shown theoretically [790] and experimentally [791] that only the energy contained within the central spot is self-guided. For poor quality focal spots, where a lot of energy is displaced from the central FWHM of the pulse, the energy contained in the wings is lost. Hence maximising the energy in the focal spot enhances the guiding efficiency.

The guiding length is mainly limited by energy depletion of the main pulse. As the intense pulse propagates in the plasma, the front edge of the laser loses energy to the plasma and continuously etches away. This happens in a length characterised by the pulse depletion length  $L_{\text{dpl}} = c\tau_L \omega_0^2 / \omega_p^2$ . Once the pulse power falls below  $P_c$ , self-focussing will no longer occur and thus the pulse will undergo slow diffraction.

### *State-of the art*

Many experimental results have been obtained by employing self-guiding in laser wakefield accelerators. Two of the initial demonstrations of PES electron acceleration in 2004 used self-guiding [12,273]; details regarding these experiments are presented in Table 32.2. Kneip et al. [772] measured 0.8 GeV electron beams generated by 200 TW laser self-guided over  $1 \text{ cm} \gtrsim 10z_R$  with plasma electron density  $n_e = 5 \times 10^{18} \text{ cm}^{-3}$ . Clayton et al. [19] report electron ionisation assisted injection and acceleration beyond GeV energies driven by a 250 TW self-guided over  $1.3 \text{ cm} \simeq 15z_R$  at  $n_e = 1.5 \times 10^{18} \text{ cm}^{-3}$ . Wang et al. [792] reported the acceleration to 2 GeV of PES beams using a PW laser. However, they also noted that with that available laser power, theoretically they should be able to reach the 10 GeV level,

thus highlighting the importance of good focal beam quality for good self-guiding and acceleration.

A detailed study of self-guiding was performed by Ralph et al. [789]. It was shown that guiding over tens of Rayleigh lengths can be achieved by choosing a suitable plasma density. Self-guided laser modes over a distance of 8.5 mm were measured with  $n_e = 4.5 \times 10^{18}$  cm<sup>-3</sup>.

#### *Expected extension of performance*

The scalability of self-guiding has been experimentally verified in the density range of  $1 \times 10^{18} - 2 \times 10^{19}$  cm<sup>-3</sup>. Experimental characterisations of self-guiding at lower plasma densities have not been performed to date. However, simulations [793] predict self-guiding of petawatt pulses at plasma densities as low as  $n_e = 1 \times 10^{17}$  cm<sup>-3</sup>. Lowering the plasma density will require higher laser powers to facilitate self-guiding as  $P_c \propto n_e^{-1}$ .

The *reliability* of self-guiding is determined by the driving laser itself. As self-focussing is an inherently non-linear process high input laser stability is essential. However, as the guiding is driven by the laser pulse itself and relies on no external equipment, since the gas medium is typically ionised by the leading edge of the pulse, it is reliable so long as there is gas present in the target with a controlled value and distribution.

The *stability* of self-guiding is determined by the stability of the laser pulse intensity profile and the reproducibility of gas distribution.

The *repetition rate* of self-guided experiments has to date been limited by the laser repetition rate. The highest repetition rate, determined by the plasma relaxation time, has been discussed by authors presenting beam-driven collider designs and is typically of the order of 10s kHz [794]. Repetition rates nearer 1 MHz could be possible provided fast removal of the gas (100 m/s) is performed.

Additional repetition rate limitations will be imposed by the thermal load in the target. If 10% of a 10 J laser pulse firing at 10 kHz is left behind in the wakefields, this represents a thermal load of 10 kW in the target. Such a high heat load will require efficient cooling, or removal of unused wakefield energy by one or more trailing laser pulses.

## Guiding in Plasma Channels

Here we give a brief overview of the optical properties of plasma channels before describing several methods for creating them.

### *Guiding mechanism*

A plasma channel is a cylindrical plasma in which the electron density  $n_e(\mathbf{r}_\perp)$  varies with the transverse coordinate  $\mathbf{r}_\perp$ ; of course, the electron density may also vary with the longitudinal position,  $z$ , but this is usually of secondary importance.

For non-relativistic intensities, the refractive index of a plasma varies as,

$$\eta = \sqrt{1 - n_e(\mathbf{r})/n_{cr}} \approx 1 - n_e(\mathbf{r})/2n_{cr}. \quad (32.11)$$

Hence a column of plasma in which  $n_e(\mathbf{r}_\perp)$  increases smoothly with radial distance from the axis will have a refractive index which decreases away from the axis. As such, each transverse slice of the plasma column acts as a positive lens, which focuses light as it propagates along the axis. A plasma channel, therefore, is an example of a gradient refractive index (GRIN) waveguide.

An alternative configuration, known as a ‘‘hollow plasma channel’’, is one in which the plasma column comprises a uniform density core surrounded by a coaxial cylinder

of higher density. Light propagating at sufficiently small angles to the axis of this structure will suffer total internal reflection at the core-cladding boundary, and hence be guided. This is an example of a step-index waveguide, and is analogous to a standard silica optical fibre.

Unless otherwise specified, we will use the term “plasma channel” when the electron density varies continuously with the transverse coordinate, and “hollow plasma channel” when the density varies discontinuously.

### Main Properties of Guided Modes

The mode structure of plasma channels has been described in detail by Milchberg et al. [795–797]. If we write the electric field of a mode as  $E(\mathbf{r}_\perp, z) = u(\mathbf{r}_\perp) \exp(i\beta z)$ , then the modes are given by solutions of,

$$\nabla_\perp^2 u(\mathbf{r}_\perp) + k_\perp^2 u(\mathbf{r}_\perp) = 0, \tag{32.12}$$

where  $\nabla_\perp^2$  is the transverse Laplacian, and  $k_\perp$  is given by,

$$k_\perp^2(\mathbf{r}_\perp, \omega) = k_0^2 - \beta^2 - 4\pi r_e n_e(r_\perp) + 4\pi k_0^2 \chi(\mathbf{r}_\perp, \omega), \tag{32.13}$$

in which  $k_0 = \omega/c$  is the angular wavenumber in vacuum,  $r_e$  is the classical electron radius, and  $\chi(\mathbf{r}_\perp, \omega)$  is the total electric susceptibility of ions and neutrals in the plasma. Three categories of modes can be identified:

- **Radiation modes:**  $k_\perp^2 > 0$  for all  $\mathbf{r}_\perp$ . In this case the solutions to (32.12) are freely propagating waves.
- **Bound modes:**  $k_\perp^2 > 0$  within some region, say  $|\mathbf{r}_\perp| < r_m$ , and  $k_\perp^2 < 0$  outside this. In this case, radiation in the inner region is trapped and propagates without loss. This is an idealisation, however, since in most real plasma channels the electron density falls to zero at large distances from the axis or there is a material boundary.
- **Leaky modes:**  $k_\perp^2 < 0$  for  $r_m < |\mathbf{r}_\perp| < r_{out}$  but  $k_\perp^2 > 0$  elsewhere. In other words, the modes are partially confined for some inner region ( $|\mathbf{r}_\perp| < r_m$ ), but some of this radiation can tunnel through the intermediate region to the outer region ( $|\mathbf{r}_\perp| > r_{out}$ ) where it radiates away from the axis.

It is worth noting that, provided the contribution of the ions and neutrals to the refractive index can be ignored, the *transverse profiles of the modes of the plasma channel are independent of wavelength*. To see this we note that in this case (32.12) can be written as,

$$[\nabla_\perp^2 - 4\pi r_e n_e(r_\perp)] u(\mathbf{r}_\perp) = [\beta^2 - k_0^2] u(\mathbf{r}_\perp). \tag{32.14}$$

The left-hand side of this equation is independent of wavelength, and hence so must be the eigenvalues ( $\zeta^2 = \beta^2 - k_0^2$ ) and the eigenmodes  $u(\mathbf{r}_\perp)$ . Of course, the propagation constant  $\beta$  will depend on wavelength since  $\zeta$  depends on  $k_0$ .

### Infinite Parabolic Channels

The infinite parabolic channel is an idealisation in which the electron density increases quadratically with radial distance to infinity. The electron density can be written in the form,

$$n_e(\rho) = n_{e0} + \frac{1}{\pi r_e w_m^2} \left( \frac{\rho}{w_m} \right)^2, \tag{32.15}$$

where  $\rho$  is the radial distance from the axis,  $n_{e0}$  is the electron density on axis, and  $w_m$  describes the curvature of the channel.

In this idealised case the modes are bound, and described by Laguerre-Gaussian functions:

$$u(\rho, \phi) = \exp(im\phi) \left(2 \frac{\rho^2}{w_m^2}\right)^{\frac{m}{2}} L_l^m \left[2 \left(\frac{\rho}{w_m}\right)^2\right] \exp\left[-\left(\frac{\rho}{w_m}\right)^2\right], \quad (32.16)$$

where  $l = 0, 1, 2, 3, \dots$  and  $m = 0, 1, 2, 3, \dots$  are the radial and azimuthal mode numbers, and  $L_l^m(x)$  is a Laguerre-Gaussian function. The propagation constant is given by,

$$\beta_{l,m}^2 = k_0^2 - 4\pi r_e n_{e0} - (2l + m + 1) \frac{4}{w_m^2}. \quad (32.17)$$

We see that the channel parameter  $w_m$  is related to the transverse size of the modes. In particular, the lowest-order mode ( $l = 0, m = 0$ ) is a *gaussian beam of spot size* (radius at which the *amplitude* of the field falls to  $1/e$  of the value on axis)  $w_m$ . Hence the parameter  $w_m$  is also known as the “matched spot size” of the channel.

### Infinite Power Law Channels

The parabolic channel described above can be generalised to the case of an infinite power-law channel in which the electron density is described by,

$$n_e(\rho) = n_{e0} + \frac{1}{\pi r_e w_m^2} \left(\frac{\rho}{w_m}\right)^s, \quad (32.18)$$

where  $s \geq 2$ . Calculating of the modes of such channels requires numerical solution of (32.12). However, it can be shown [795] that the lowest order modes of channels of this type are very close to Gaussian beam with a matched spot size of  $w_m$ . This is an important result since it shows that the transverse profile of the lowest-order mode does not depend strongly on the *shape* of the channel.

### Truncated Parabolic Channels

Real plasma channels are not infinite in extent. To gain an understanding of a more realistic scenario, Durfee et al. have also considered [795,796,798] the case of a plasma channel in which the electron density increases quadratically for  $\rho \leq r_m$ , but has a constant value of  $n_e(r_m)$  outside this region. Their analysis shows that low-loss propagation requires that the mode numbers satisfy:

$$2l + m + 1 < \frac{r_m}{w_m}. \quad (32.19)$$

### Capillary Discharge Waveguides

In a capillary discharge waveguide, a pulsed electrical discharge is used to create, and heat, a plasma contained within the capillary. In early work the plasma was formed by discharge ablation of a polypropylene capillary [799,800]. This approach has the disadvantages that: (i) the plasma contains partially ionised carbon ions which can

become further ionised by the guided laser pulse, leading to distortion or destruction of the plasma channel [801]; (ii) the capillary wall is ablated on each shot, limiting the electrical lifetime of the device.

These short-comings were overcome by forming the capillary in a refractory material, to reduce ablation, and filling it with gas: the gas-filled capillary discharge waveguide (CDW). Of particular interest is the case of a hydrogen-filled CDW [802] since the plasma formed by the discharge is nearly fully ionised, and hence the plasma channel is not distorted by further ionisation by the guided laser pulse [801].

In discharge-ablated and gas-filled CDWs, the plasma channel is formed by conduction of heat to the capillary wall. Since pressure across the capillary is equilibrated rapidly, the temperature gradient formed by heat conduction creates a density gradient: the plasma is hot, and of lower density, near the axis; and cooler and denser near the capillary wall [803–805].

### *Parameter ranges*

The guiding properties of hydrogen-filled CDWs have been measured interferometrically by Gonsalves et al. [806], yielding the following approximate scaling laws for the on-axis density and the matched spot size in square cross-section capillaries of side  $X$ :

$$n_{e0}[\text{m}^{-3}] = 0.87n_{\text{H}_2}^i m^{-3} = 0.11 \times 10^{24} \quad (32.20)$$

$$w_m[\mu\text{m}] = 6.6 \times 10^4 \left( \frac{X[\mu\text{m}]}{2} \right)^{0.651} (n_{\text{H}_2}^i m^{-3})^{-0.1875}, \quad (32.21)$$

where  $n_{\text{H}_2}^i$  is the initial density of hydrogen *molecules*. Although these scaling laws were determined for square cross-section capillaries, they are expected to be approximately correct for circular cross-section capillaries of diameter  $X$  [805]. The scalings were determined from measurements in the range  $2 \times 10^{17} \text{ cm}^{-3} \leq n_{e0} \leq 3 \times 10^{18} \text{ cm}^{-3}$ , and for capillaries of side  $210 \mu\text{m} \leq X \leq 465 \mu\text{m}$ ; *they should therefore be used with caution outside this domain*.

The Berkeley group [518,807] have also deduced the axial electron density and the matched spot size of hydrogen-filled CDWs from measurements of the transverse oscillations of the centroid of low-intensity laser pulses and by spectral interferometry. These measurements were found to be in approximate agreement with eqns (32.20) and (32.21); however, there are differences, which illustrate that the properties of the channel depend in detail on the design of the capillary and of the discharge circuit.

### *State-of the art*

Hydrogen-filled CDWs have been operated with axial plasma densities in the range  $n_{e0} = 7 \times 10^{17} - 10^{19} \text{ cm}^{-3}$  [27,808,809]. The matched spot is typically in the range  $w_m = 40 - 60 \mu\text{m}$ . Plasma channels with lengths up to 90 mm have been demonstrated and used in electron acceleration experiments [27].

Hydrogen-filled CDWs have successfully guided relativistically intense laser pulses [351]. They have also been used extensively in electron acceleration experiments [27, 277,290,808,809], generating electron beams with energies up to 4.2 GeV.

Plasma density evolution of hydrogen-filled capillaries has been investigated using spectroscopic analysis of Balmer lines showing a good shot to shot reproducibility (shot to shot variations of the order of  $\sim 10\%$ ) and reliability [810].

### *Expected extension of performance*

The Berkeley group have increased the pulse repetition rate of hydrogen-filled CDWs up to 1 kHz [811]. This was achieved by: (i) reducing the peak discharge current from the few hundred ampères used in early work to around 100 A; and (ii) water

cooling the capillary. No erosion of the capillary wall was observed within the 0.6  $\mu\text{m}$  measurement error after 10 million shots. Given that the wall could be eroded by a few microns without affecting the guiding performance, operation at a 1 kHz repetition rate should be possible for at least 20 hours [812].

Although the parameters have not yet been achieved simultaneously, the summary of the state of the art is that plasma channels with lengths of order 100 mm, an axial density as low as  $n_{e0} \approx 5 \times 10^{17} \text{ cm}^{-3}$ , a matched spot size of 50–60  $\mu\text{m}$ , and a pulse repetition rate up to 1 kHz would seem to be possible with this approach.

It is worth noting that one disadvantage of the CDW is that optical access to the plasma channel is difficult owing to surface roughening of the inner wall by the electrical discharge, although it may be that this can be alleviated by using lower discharge currents [812]. A second issue to be aware of is that jitter in the pointing of the driving laser can lead to laser-induced damage at the entrance to the capillary. Finally, it is not known whether it will be possible to decrease the axial electron density below  $n_{e0} \approx 5 \times 10^{17} \text{ cm}^{-3}$ .

## Plasma Channels Formed by Hydrodynamic Expansion

### *Channel formation*

As first described by Durfee and Milchberg [345], plasma channels can also be formed by hydrodynamic expansion of a hot plasma column into a cold gas. If a well defined boundary is formed between the heated plasma and the surrounding gas, the large pressure gradient drives a shock wave as the hot electrons move out, pulling the ions at the ion sound speed  $c_s = (Zk_B T_e / M_{\text{ion}})^{1/2}$ . Behind the shock front the electron density increases with radial distance, and hence a plasma channel is formed.

### *Parameter ranges*

In early work the initial plasma column was formed and heated using  $\approx 100$  ps pulses from a Nd:YAG laser; an extended focus was produced using an axicon lens [345, 795, 796, 813, 814]. In this approach the initial plasma is formed by a seeded avalanche breakdown, the seed electrons being formed by multiphoton ionisation of the target gas. These seed electrons are rapidly heated by inverse bremsstrahlung, leading to additional collisional ionisation and heating of the plasma.

Efficient plasma heating requires that the intensity of the heating laser is less than approximately  $10^{13} \text{ W cm}^{-2}$ , and in order to reach temperatures of 10–100 eV it is necessary that the laser pulse duration is of order 100 ps. These parameters limit the target to reasonably high-Z gases (e.g. Ar), for which the weakest bound valence electrons can be ionised by multi-photon or barrier suppression ionisation. As a consequence the plasma channel will not be fully ionised, although the ions in the plasma channel will typically have a closed shell (e.g.  $\text{Ar}^{8+}$ ). The plasma channel would, ideally, be fully ionised so that it cannot be distorted by further ionisation by a guided laser pulse with an intensity of order  $10^{18} \text{ W cm}^{-2}$ . To address this issue, Volbeyn et al. developed the “ignitor-heater” technique, in which the target gas is ionised by a short, intense laser pulse (e.g. 100 fs,  $10^{14} \text{ W cm}^{-2}$ ), and subsequently heated by a long, energetic laser pulse (10–100 fs, 100 mJ) [815]. This approach has been used to generate plasma channels in nitrogen and fully-ionised hydrogen [11, 815].

Efficient plasma heating by collisions also requires that the initial target density is relatively high, which restricts the axial electron density of the plasma channel to  $n_{e0} \gtrsim 10^{19} \text{ cm}^{-3}$ . To overcome this limit, the Milchberg group have studied the formation of plasma channels by hydrodynamic expansion of laser-heated clusters [816, 817]. Within each cluster, the local density is near that of a solid, and hence it can be ionised, then rapidly collisionally heated by a picosecond-duration laser pulse;

once heated, the gas clusters explode to form a uniform, hot plasma column, which will expand radially to form a plasma channel. The use of a clustered gas therefore allows the use of a target gas with a low initial *average* density. This approach has been used to generate fully ionised plasma channels with  $n_{e0} \approx 10^{18} \text{ cm}^{-3}$ .

### *State-of the art*

Durfee et al. have reported [796] the formation of plasma channels of lengths up to 15 mm with  $n_{e0} \approx 5 \times 10^{18} \text{ cm}^{-3}$  and  $w_m = 25\text{--}30 \mu\text{m}$ . The  $1/e$  intensity attenuation length for waveguides of this type has been measured to be  $L_{1/e} \approx 350 \text{ mm}$ . Geddes et al. [11] used the ignitor-heater approach to generate quasi-monoenergetic electron of energy 80 MeV in 2 mm long,  $n_{e0} \approx 2 \times 10^{19} \text{ cm}^{-3}$  plasma channels formed in hydrogen gas. The Milchberg group has also demonstrated the formation of longitudinally modulated plasma channels in clustered-gas targets [817] suitable for quasi-phase-matched electron acceleration [818].

### *Expected extension of performance*

It is worth noting two significant advantages of plasma channels formed by hydrodynamic expansion which both arise from the fact that the channels are formed in free space: (i) it is straightforward to probe the channels transversely; and (ii) fresh channels can, in principle, be created with a high repetition rate, the upper limit being determined by the repetition rate of the channel-forming laser, and the time taken for fresh gas to replace a used channel. It should therefore be possible to produce plasma channels of this type at kilohertz pulse repetition rates. The channels can also be expected to be reliable, with a stability determined by that of the channel-forming laser.

Previous work suggests that hydrodynamic plasma channels could be generated with an axial density as low as  $n_{e0} \approx 10^{18}\text{--}5 \times 10^{18} \text{ cm}^{-3}$ , with lengths of a few tens of mm, and a matched spot size of  $w_m = 25\text{--}30 \mu\text{m}$ .

A significant issue with this approach is the difficulty in reducing the on-axis plasma density below  $n_{e0} = 10^{18} \text{ cm}^{-3}$ . It may be possible to reduce the axial plasma density by using optical field ionisation (OFI) to form the initial plasma column [348], since with this ionisation mechanism the heating of the electrons depends on the polarisation of the laser field, and not on the initial density. Initial simulations of OFI-heated hydrodynamic plasma channels are promising [348], but more remains to be done. It is worth noting that Lemos et al. have shown that hydrodynamic plasma channels with  $n_{e0} \approx 10^{18} \text{ cm}^{-3}$  can be formed in hydrogen and helium following OFI [346,347], but generation of plasma channels at lower density has not been reported.

## Hollow Plasma Channels

An ideal hollow plasma channel comprises a cylindrical, evacuated core surrounded by a uniform “cladding” of plasma with an electron density  $n_w$ . As first described by Chiou et al. [819,820], an intense laser pulse (or a particle beam) propagating along the axis will excite surface currents on the core-cladding boundary which generate electromagnetic fields which extend into the core. These wakefields are therefore fundamentally different from the electrostatic fields arising from the density modulations generated by a driving beam propagating in a homogeneous plasma. The wakefields generated in a hollow plasma channel are about a factor of two lower [819] in amplitude than than would be generated by the same driver propagating in a uniform plasma of density  $n_w$ , but they offer several distinct advantages:

- The accelerating field is transversely uniform in the core region
- For a relativistic particle the transverse focussing forces are weak and linear, helping to preserve emittance

- Scattering of the accelerating bunch is avoided, preventing emittance growth; this is likely to be particularly important for plasma-based colliders.

Schroeder et al. [821] have considered the case of a *partially filled* hollow channel, in which the core region has an electron density  $n_{core}$ . They show that the accelerating fields are governed by  $n_w$ , but that the focussing is determined by  $n_{core}$ , and that therefore matched beam propagation is in principle possible.

### *Guiding mechanism*

In a hollow plasma channel the refractive index of the core ( $\eta_1 = 1$ ) is greater than that of the cladding ( $\eta_2 = (1 - n_w/n_{cr})$ ), and hence light can be guided through the core by total internal reflection, exactly as in a conventional step-index fibre.

### *Main properties of guided modes*

The modes of a hollow plasma channel are the same as in a step-index fibre; since in this case  $\eta_1 - \eta_2 \ll 1$ , these can be approximated by the linearly-polarised modes. For radiation polarised in the  $x$ -direction the lowest order linearly-polarised mode (LP<sub>01</sub>) can be written as,

$$E_x = E_0 \begin{cases} J_0(hr) \exp(i\beta z) & r < a \\ \frac{J_0(ha)}{K_0(qa)} K_0(qr) \exp(i\beta z) & r > a \end{cases} \quad (32.22)$$

where  $a$  is the core radius,  $h^2 = k_0^2 - \beta^2$  and  $q^2 = \beta^2 - \eta_2^2 k_0^2$ . The propagation constant  $\beta$  is determined from the following characteristic equation:

$$h \frac{J_1(ha)}{J_0(ha)} = q \frac{K_1(qa)}{K_0(qa)}, \quad (32.23)$$

where  $J_n(x)$  is the Bessel function of the first kind, and  $K_n(x)$  is the modified Bessel function of the second kind.

The group velocity of the mode is found to be  $v_g = (\beta/k_0)c$ , which, for typical parameters, is close to  $c$ .

### *Parameter ranges and state of the art*

Although hollow plasma channels have been much discussed there are only a few examples of their generation in practice. Kimura et al. [822] have described a method for generating a partially-filled hollow plasma channel by directing a high-order Bessel beam through a target gas: in a high-order Bessel beam the locus of peak intensity is a narrow ring; this can ionise a target gas to form an annulus of plasma, surrounding an un-ionised core. Kimura et al. describe the parameters for a partially-filled hollow channel of length 100 mm and 22  $\mu\text{m}$  wall radius. The Ti:sapphire laser parameters required to generate this channel are: an energy of 50 mJ and a pulse duration of 60 fs.

Gessner et al. [51] have demonstrated the use of this method to create a partially-filled hollow plasma channel of length 80 mm and wall radius  $\approx 256 \mu\text{m}$ . This was used to generate a plasma wakefield with a positron driver beam.

### *Expected extension of performance*

It is difficult to predict the future performance of hollow plasma channels since they would seem to be at an early stage in their development.

It is worth noting that for the channels described by Kimura et al. the core has the same atomic density as the wall; as such, full ionisation of the core would destroy the channel, and hence these channels can only be used with low intensity drivers.

For example, in the work described by Gessner et al. it was necessary to reduce the density of the positron driver beam to prevent ionisation of the gaseous core. Similar considerations would apply to the application of these channels to laser-driven plasma wakefields; in this context it is worth pointing out that the driving the wakefield by a train of low-intensity laser pulses [607] could be advantageous since it might be possible to prevent additional ionisation of the core, whilst driving a wakefield of useful amplitude.

## Guiding in Capillary Tubes

### *Guiding mechanism*

When a capillary tube is used the laser beam is guided by reflections at the inner capillary wall [350], and laser guiding can thus be achieved in vacuum or at low plasma density. This guiding scheme does not rely on laser power, or plasma density, and provides the opportunity to explore a large domain of laser-plasma parameters. Laser guiding can, in principle, be achieved inside capillary tubes with total or partial reflection at the inner wall, depending on the material of the tube wall, which may be either a conductor or a dielectric material. Metallic tubes could be used to guide the laser beam without loss at the inner wall. In practice, their surface is usually not optically smooth for the laser wavelength and tube diameters used for laser guiding at high intensities. Dielectric capillaries, such as glass capillaries, are optically smooth and can be manufactured with a good reliability for a large range of inner diameter (10  $\mu\text{m}$  to several mm), wall thickness (50  $\mu\text{m}$  to several mm) and lengths (mm to meter).

### *Main properties of guided modes*

Quasi transverse electromagnetic waves with wavelength smaller than the tube radius are eigenmodes, described by Bessel functions for cylindrical dielectric capillary tubes. An incident linearly polarised gaussian laser beam can be efficiently coupled to the linearly polarised family of hybrid modes, namely the  $\text{EH}_{1m}$  modes [350].

The electric field is damped along the direction of propagation,  $z$ , as each reflection at the dielectric capillary wall is associated with a refracted fraction of the laser beam inside the dielectric wall. This refracted fraction is minimum for the smallest perpendicular wavenumber, corresponding to the grazing incidence. Laser damping is usually described by the *attenuation length*  $L_m^l$ , defined as

$$L_m^l = \frac{1}{k_m^l} = \frac{2k_{z0}^2 R_{\text{cap}}^3 \sqrt{\varepsilon_r - 1}}{u_m^2 (1 + \varepsilon_r)}. \quad (32.24)$$

After a propagation distance of  $L_m^l$ , the field magnitude decreases by a factor  $1/e$  and the beam energy by a factor  $1/e^2$ , owing to refraction losses.  $L_m^l$  drops rapidly with increasing mode order, which means that higher-order modes are damped over shorter distances. Therefore, the use of the fundamental mode is preferable to achieve laser guiding over a long propagation distance.

The *group velocity* is determined from the dispersion relation of an electromagnetic wave in a capillary tube,  $k_0^2 = (k_z^2 + k_{\perp m}^2)$ , for  $k_{\perp m}^2 \ll k_0^2$ , as

$$v_{gm} \simeq c \left( 1 - \frac{k_{\perp m}^2}{k_0^2} \right)^{1/2}. \quad (32.25)$$

The group velocity is close to the velocity of light in free space, and decreases as the mode order increases. This again supports the use a lower-order mode with higher group velocity, corresponding to a higher phase velocity for the wakefield.

Another important aspect associated with the use of a capillary tube is the threshold of material damage at the inner wall where reflection occurs, which determines the ability of capillary tubes to guide intense lasers. It is linked to the *contrast* between the intensity at the capillary axis and at the wall, which is one order of magnitude larger for the fundamental mode compared to the ninth mode. Once again, it emphasises the advantage of using the fundamental mode. For a glass capillary, the ionisation threshold is of the order of  $10^{14} \text{ Wcm}^{-2}$  for an  $800 \mu\text{m}$  laser pulse with duration shorter than or of the order of 100 fs. [823]. The maximum intensity on-axis which can be guided by a capillary of  $50 \mu\text{m}$  radius on the fundamental  $\text{EH}_{11}$  mode without wall ionisation is thus of the order of  $10^{19} \text{ Wcm}^{-2}$ .

### *Coupling*

When a laser beam is focussed at the entrance of a capillary tube, its energy has to be coupled to the capillary eigenmodes before propagation. The *coupling coefficient* of an incident Gaussian beam on the first four eigenmodes depends on the ratio of capillary radius to laser waist,  $R_{\text{cap}}/w_0$ . Monomode coupling can be achieved when  $R_{\text{cap}}/w_0 \simeq 1.55$  (or  $w_0/R_{\text{cap}} \simeq 0.65$ ). In this case, almost 98% of the incident laser energy is coupled to the fundamental  $\text{EH}_{11}$  mode, and only 1% of laser energy is coupled to higher-order modes. The remaining 1% of laser energy is the energy contained in the wings of the gaussian function outside the capillary diameter, and it is lost into the material at the front surface of capillary tube.

The *quality of coupling* of laser energy to the capillary tube depends on the contrast in time and space in the entrance plane of the capillary tube, and on the pointing stability. At high intensity, the lifetime of the capillary tube can also be shortened by pointing fluctuations. The effect of pointing fluctuations and symmetry variations on the coupling of a laser beam to a capillary tube radius have been studied theoretically and confirmed experimentally [824]. The angle between the laser axis and the capillary tube axis has to be smaller than 5 mrad and the displacement of the laser spot centre to the centre of the tube should be smaller than 10% of the tube radius for matched condition to the fundamental mode.

### *Electron acceleration*

Simulations [353] show that electron acceleration to several GeV can be achieved. Some issues occurring at coupling were pointed out: the excitation of higher modes by a gaussian pulse at the % level introduces transverse modulation of the laser envelope, which can in turn defocus electrons. To mitigate this issue, either the pulse structure in the entrance plane should be closer to a Bessel function, selecting only the fundamental mode, or electrons could be injected into the accelerating structure a few cm after the entrance, when the modulation is smoothed out.

Alternatively, a slightly non linear regime favours a compensation by the plasma of this locally transverse modulation. An other potential solution is the presence of a low density plasma channel [825].

To summarise, quasi-monomode guiding can be selected by coupling the input laser energy to the fundamental  $\text{EH}_{11}$  mode: 98% of the energy of a gaussian beam can be coupled to the fundamental mode for a waist size  $w_0 = 0.645R_{\text{cap}}$ . This mode is preferable for laser wakefield acceleration as its group velocity is close to the velocity of light in free space, its damping factor is a minimum for a given capillary radius and wavelength, and the transverse electric field exhibits a variation similar to a gaussian beam.

*Parameter range*

Laser guiding on the fundamental mode exhibits the best properties for laser-plasma acceleration. Conditions on the main parameters are determined as follows:

Laser intensity: maximum value determined by material damage at the wall. Higher for larger diameter capillary tube.

Spot size: matched value depends on energy distribution, usually a fraction of the capillary radius (from 0.6 to 1 for a Gaussian function or Airy function respectively).

Plasma density: can be chosen from zero to the value where self-focussing is significant as determined by laser power becoming of the order of the critical power.

Plasma can be homogeneous or exhibit a density profile: the condition for mode coupling in varying density profile needs to be studied.

Damping length of laser energy along the propagation direction: is proportional to the cube of the tube radius and can be extended to several metres.

*State-of-the-art*

Guiding in capillary tubes at low intensity has been measured and corresponds to theoretical predictions in terms of coupling and transmission. The sensitivity of the coupling and transmission to misalignments has been studied theoretically: predictions are in excellent agreement with experimental results and are discussed in Ref. [824].

*Monomode guiding* has been demonstrated experimentally for laser intensities of the order of  $I_0 \simeq 10^{16} \text{ Wcm}^{-2}$  in a vacuum [826] and the transmission has been measured for different values of the capillary tube radius. The measured transmissions correspond to the predicted values for quasi-monomode guiding, which was thus measured in a vacuum over a distance of 100 Rayleigh lengths. Analytical predictions for coupling conditions and damping length have been confirmed experimentally for tubes under vacuum.

The excitation of plasma waves over a length of up to 8 cm was demonstrated by guiding intense laser pulses through hydrogen-filled glass capillary tubes [525]. Laser guiding at input intensities up to  $10^{18} \text{ Wcm}^{-2}$  was achieved with more than 90% energy transmission in evacuated or hydrogen-filled gas tubes up to 8 cm long, with a radius of  $R_{\text{cap}} = 50 \mu\text{m}$ . To investigate the linear regime, the input intensity was kept below  $3 \times 10^{17} \text{ Wcm}^{-2}$ , and the electron density was varied in the range  $0.05 - 5 \times 10^{18} \text{ cm}^{-3}$ . The plasma wave amplitude was diagnosed by analysing the spectrum of the transmitted laser radiation.

The longitudinal accelerating field, inferred from a detailed analysis of laser wake-field dynamics in capillary tubes and numerical simulations [827], is in the range of 1–10 GV/m for an input laser intensity of the order of  $I_0 \simeq 10^{17} \text{ Wcm}^{-2}$ . The average product of gradient and length achieved in this experiment was thus of the order of 0.4 GV at a pressure of 50 mbar; it could be increased to several gigavolts by increasing the length and diameter of the capillary tube with higher laser energy.

*Expected extension of performance*

Scalability can be achieved easily by the use of longer capillary tube. The damping length due to refraction losses limits the maximum value of propagation to values which can be larger than the dephasing length. As the damping length is strongly dependent on capillary radius, the tube radius should also be increased. Typically, guiding can be extended to the metre range for capillary tube radius of the order of 100 microns. Plasma density has no lower limit for guiding, and it can be matched to resonant conditions for plasma wave excitation independently of guiding condition.

Reliability, stability, repetition rate: these three properties mainly depend on laser beam quality at the entrance of the capillary tube and reproducibility of plasma density.

As guiding is passive the reliability of the accelerating structure is related to the reliability of plasma wave characteristics, determined by the stability of laser coupling, and the reproducibility of the gas concentration at the time of interaction with the laser.

Stability of laser parameters in the focal plane is required. The required laser pointing stability at the entrance of the capillary was calculated and measured by Veysman et al. [824], to achieve a transmission of laser energy within 5% of the maximum value, the angle  $\theta_{inc}$  between the laser and tube axis should be smaller than 5 mrad, with a displacement between the centre of the laser spot and the centre of the tube smaller than 10% of capillary tube radius. Most of the energy is guided within the fundamental mode for a symmetrical spot at the entrance with angle  $\theta_{inc}$  smaller than 1.5 mrad.

The stability of plasma density is mostly determined by the gas injection system. The standard deviation of density fluctuations was measured by Ju et al. [352] to be of the order of 15% in the stationary state following the injection of gas. It should be possible to reduce this value to a few percent by improving the gas feed system.

A repetition rate at 10 Hz should be possible provided the laser quality and pointing is controlled.

### 32.2.5 Injection Techniques for the LPI

#### Self-Injection (SI)

##### *Physical mechanism*

In the self-injection scheme a large amplitude plasma wave is excited in the wake of the laser pulse. With the laser intensities currently achieved, the self-injection process relies on the laser self-focussing leading to a lengthening of the bubble. As a consequence, some electrons passing through the bubble during its lengthening gain enough energy to be injected in the plasma wave [533]. For sufficiently high laser intensities ( $a_0 > 3 - 4$ ) [185,639] electrons at the back of the bubble near the laser axis can be injected in the cavity, where they experience a longitudinal accelerating field.

Perturbation of the accelerating field due to the field generated by the accelerated electron beam can lead to increased energy spread and unintended trapping of background electrons generating the so-called “dark current”. Beamloading effects can eventually cancel the accelerating field and limit the charge of the accelerated beam.

In experiments, for a given laser system, a density threshold is commonly observed, below which no electron beam is generated. The highest beam quality (energy spread, stability) and electron energy are achieved for a working point just above the density injection threshold [828]. Nevertheless, the plasma density needs to be high enough to accelerate a significant charge and to reach electron self-injection conditions sufficiently early in the interaction for acceleration to occur after injection. Mangles et al. [828] determined a threshold on laser power to achieve self-injection, taking into account the proportion of laser energy contained in the FWHM of the laser pulse  $\alpha$ , as a function of plasma electronic density. This threshold is illustrated in Figure 32.3.

##### *State-of-the-art*

Sävert et al. [533] use gas jets as targets to measure non-linear lengthening of the first plasma period behind the laser. These measurements provided experimental

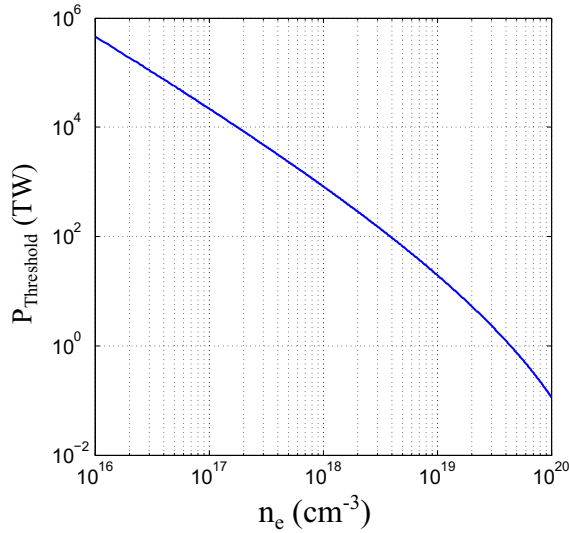


**Fig. 32.3.** Laser power threshold for self-injection as a function of plasma electronic density for a laser wavelength of  $\lambda = 0.8 \mu\text{m}$  and assuming a gaussian energy distribution ( $\alpha = 0.5$ ).

evidence that in that regime, self-injection was caused by the lengthening of the first plasma period. Electron acceleration to energies of hundreds of MeV are achieved experimentally by SI [11, 12, 273, 533, 829, 830]. The generation of high quality electron beams with a charge of tens of pC is rarely observed, as the highest charge (50-100 pC) is accompanied by large energy spread. However the highest electron energy achieved in LWFA was obtained with SI combined with laser guiding, demonstrating 6 pC of charge at 4.2 GeV in a single stage with an energy spread as low as 6% (RMS) and a divergence below 1 mrad [27].

#### *Advantages and disadvantages*

Self-injection is the simplest and most straight-forward injection scheme to be implemented in Laser Wakefield Acceleration (LWFA) [180]. However, in the self-injection scheme, electron injection and trapping in the plasma wave continues until the amplitude of the wakefield is reduced through beam loading, that is the electric field generated by the trapped electrons reduces and finally cancels the wakefield, or laser energy depletion. Typically, self-injection is accompanied by a large energy spread of the accelerated electron bunch. Within the self-injection scheme highest quality electron beams are achieved in the bubble regime [787], where the laser with relativistic laser intensity is focussed to a sphere of radius shorter than the plasma wave wavelength. The laser and plasma parameter range for the generation of high-quality electron beams is generally narrow [533] and shot-to-shot fluctuations are typically large in this acceleration regime.

As the self-injection scheme relies on the non-linear evolution of the plasma wave, the stability of the electron beam can be unacceptable for many applications.

#### *Expected extension of performance: scalability, reliability, stability*

With this injection scheme, electron energy can be increased to the 5 GeV level, considering 4.2 GeV have already been achieved [27]. However, since this scheme relies on the non-linear evolution of the plasma wave, it needs precise control of the laser and plasma parameters to ensure stability and reproducibility of the electron bunch properties.

## Colliding-Pulse Injection (CPI)

### *Physical mechanism*

The colliding-pulse injection scheme is based on the use of two laser pulses: a drive laser pulse creates the plasma wave without injecting electrons and a second laser pulse, called the injection pulse, is used to locally trigger the injection [368]. The interaction of the two laser pulses creates a beat-wave pattern, which can, if the intensity is high enough, give a sufficient velocity to some electrons for them to be trapped.

### *State-of-the-art*

This technique was used to produce electron bunches of  $\sim 100$  to  $\sim 200$  MeV. Relative energy spread as low as  $\sigma_E/E \sim 1\%$  have been produced for a beam charge of the order of  $Q \sim 10$  pC [657,831,832].

### *Advantages and disadvantages*

This technique allows control of the location of injection by adjusting the location of the laser pulses interference and consequently provides a mean to control the acceleration length and the electron energy. Though relatively low charge electron bunches are produced with current experimental parameters. this scheme also allows control of the injection volume by controlling the intensities of the laser pulses, and therefore the energy spread. This technique imposes particular challenges on the laser system. It requires the use of two laser pulse with good stability for both laser pulses to achieve low fluctuations of electron bunches properties. Furthermore, in a directly counter propagating geometry, laser systems would require extra protection to prevent propagation of laser energy back down the laser amplifier chain.

### *Expected extension of performance: scalability, reliability, stability*

Colliding pulse injection can potentially be used to inject and accelerate electrons to energy levels similar to SI given the same length of plasma. However as this scheme relies on two laser pulses, a good stability of the two laser pulses is required for stable operation.

## Density Gradient Injection (DGI)

### *Physical mechanism*

Control of electron injection can be achieved through tailoring of the plasma density profile [275,833]. The relativistic plasma wave wavelength,  $\lambda_p = 2\pi c \sqrt{\epsilon_0 m_e / n_e e^2}$ , being inversely proportional to the electronic density, a decreasing density gradient leads to an increase in this plasma wave wavelength, which reduces the wake phase velocity. In general, injection of electrons in the plasma wave occurs when the velocity of the background electrons approaches the wake phase velocity. The reduction of the phase velocity lowers the injection threshold and some background electrons can then be injected in the wakefield.

Injection through plasma density profile tailoring has been investigated both numerically and experimentally for a number of plasma density profiles and/or laser parameters. In most cases, plasma density profiles consist of two plasma density plateaux of electron density  $n_{e1}$  and  $n_{e2}$ , both below the self-injection threshold, with  $n_{e1} > n_{e2}$  and connected by a negative density gradient. Depending on the density gradient length  $L_g$  two regimes can be distinguished. For  $L_g > \lambda_p$ , a slowing down of the plasma wave phase velocity occurs that lowers the threshold for wave-breaking and causes trapping of background electrons at a specific position. For a sharp density transition ( $L_g \leq \lambda_p$ ), a sudden increase in the plasma wavelength is

produced leading to rephasing of the plasma electrons into the accelerating phase of the plasma wave.

### *State-of-the-art*

The density gradient can be the falling edge of a single gas jet [17]: in this case the electron energy is low as electrons are injected at the exit of the density profile.

The density gradient can also be produced by using a secondary laser pulse [16, 834], by a shock generated by introducing a sharp object in the gas flow of a jet [18,381,659], or by using two separate overlapping gas jets [32,835]. In those cases, the location of the density gradient can be changed relative to the density profile and the energy of the electrons can thus be tuned.

DGI has been used to achieve electron beams with energy in the range  $E \simeq [25 - 600]$  MeV, with energy spreads of the order of  $\sigma_E/E \simeq [1 - 25]\%$ , and with a charge in the range  $Q \simeq [1 - 1000]$  pC [17,32,381,659,834].

### *Advantages and disadvantages*

With respect to self-injection in a homogeneous plasma, in the scheme based on injection in a steep density downramp, higher quality, nearly dark-current free electron beams are obtained. Injection probabilities close to 100% and improved (with respect to self-injection) shot-to-shot stability are generally achieved in experiments. Shot-to-shot fluctuations as low as  $\sim 2\%$  of the electron energy,  $\sim 6\%$  of the charge and pointing stability better than 1 mrad have been reported [658].

Experimental studies indicate that a good control of the plasma density profile is needed, small changes can affect the electron beam quality and the stability. One of the major difficulties of this injection technique is the realisation and the control of the sharp density downramp. More investigation on the realisation of the density transition is needed, with particular attention to the robustness and the life-time of the adopted technique.

### *Expected extension of performance: scalability, reliability, stability*

This scheme relies on a precise density profile and the stability of this scheme is therefore linked to the reproducibility of the density profile as well as the laser stability. The possibility that it can lead to injection at lower densities than self-injection could lead to higher energy gain.

## Ionisation-Induced Injection (III)

### *Physical mechanism*

The ionisation-induced injection scheme depends on the addition of a small fraction of high-Z gas to the low-Z gas, Z being the atomic number. Outer shells of the high-Z atoms are ionised at relatively low intensities (typically below  $I_L = 10^{16}$  W/cm<sup>2</sup>) so that electrons appear at the front of the laser pulse and contribute to the plasma wake. Inner-shell electrons are ionised closer to the laser intensity peak and are more likely to be injected in the wake. As illustrated in Figure 32.4, an electron born close to the laser peak intensity (at  $k_p\xi_1$  in Fig. 32.4) experiences a larger difference of potential than an electron born at the front of the laser pulse (at  $k_p\xi_2$ ) and is thus more likely injected into the wake. Chen et al. [281] describe how an electron born stationary inside the wake is turned around by the potential of the non-linear wake provided that the wakefield driving laser potential exceeds:

$$a_0 \gtrsim 1.7(1 - n_e/n_c) \quad (32.26)$$

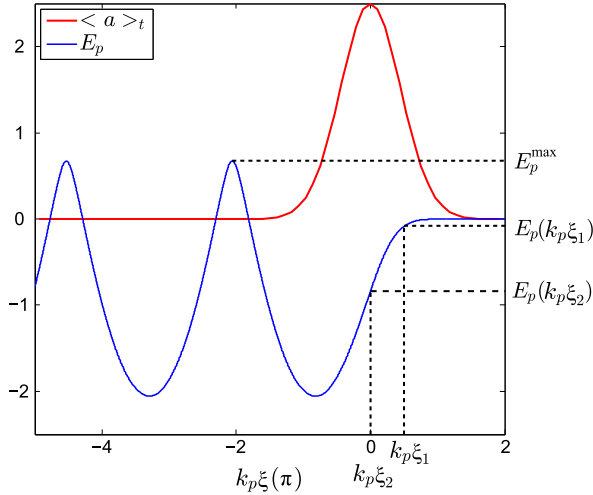


**Fig. 32.4.** Example of laser envelope and wake potential energy for  $a_0 = 2.5$ .

### *State-of-the-art*

This technique was first observed in plasma wakefield experiments to observe the acceleration of very narrow energy spread electron beams directly from a plasma in the blow-out regime [836]. A laser wakefield experiment performed in hydrogen filled capillaries measured 150 MeV electrons with  $< 10\%$  energy spread at very low laser intensity  $a_0 < 1$ , which was coupled to rapid ionisation of the target with arrival of the driving laser pulse [277]. Simulations performed later demonstrated that III of impurity atoms from the surface of the capillary walls, coupled with laser pulse intensity amplification such that the trapping threshold was just reached, could explain the appearance of these PES beams [837]. Subsequent experiments were able to utilise this technique with purposely introduced dopant species to produce electron bunches of  $Q \simeq 1$  pC to  $Q \simeq 100$  pC and relative energy spreads of the order of  $\sigma_E/E \sim 5$  to  $\sim 10\%$  [278,282,773,838,839].

### *Advantages and disadvantages*

This technique provides a way to trigger electron injection into the accelerating phase; injection continues as long as the laser intensity is high enough to ionise inner shell electrons, leading to accelerated electrons with broad energy distributions [278,279,840].

The energy spread can be reduced by tuning the laser intensity to be above the threshold only in a small volume of interaction, at the expense of the accelerated charge. Using carefully controlled low laser intensities, the maximum intensity achieved through pulse compression can be enough to allow trapping for only a small duration [837]. It is also possible to use structured targets composed of a region containing a gas mixture for the injection followed by a region of pure gas to further accelerate injected electrons [282,773], or tailored density profile to combine ionisation-induced injection to a density gradient [838]. A similar effect has been suggested by using a secondary high-intensity laser pulse which acts to ionise atomic electrons which otherwise would not be liberated by the wakefield driving pulse. By using fast focussing, the volume of which this electron liberation occurs can be small leading to PES beams [681,841].

The main benefits of the III technique are that it is very easy to implement experimentally, the charge can be increased compared to self-injection[840], it can

lower the intensity threshold compared to SI [281] (which is beneficial for a potential increase in repetition rate) and can potentially reduce the transverse emittance [281].

*Expected extension of performance: scalability, reliability, stability, repetition rate*

This scheme can potentially be scaled up to higher energies but generally produces broad electron energy distributions. However, combined with either DGI or CPI, it is a way to increase the injected charge. This combination of mechanisms offers tunability of charge, energy, energy spread, and emittance by increasing the number of control parameters, together with increased complexity of implementation and higher constraints on stability.

### Comparison of Injector Performance

In Tables 32.2–32.5 a summary of electron properties achieved by each injection technique is presented, corresponding to experimental results found in the cited references. Selected publications were chosen for electron parameters close enough (less than one order of magnitude in electron energy) to the range expected for EuPRAXIA. The last two columns on the right hand side of each table are the target parameters for plasma, laser and electrons, identified in the EuPRAXIA baseline as injectors at 150 MeV and 1 GeV.

References in these tables were selected for their proximity to EuPRAXIA target parameters, first using the energy, then the energy spread. Some references were included because they highlight an original experimental implementation of the scheme considered such as ref [834] in Table 32.4. However there may be other publications relating results closer to EuPRAXIA target parameters that the authors are unaware of.

#### *Discussion of Table 32.2 Self-Injection*

Faure *al.* [273] observed 170 MeV energy beams with 24% energy spread, 10 mrad divergence and a charge of 0.5 nC. Geddes et al. [11] obtained electron beams with 86 MeV energy, 300 pC, 2% energy spread and 1–2 mm mrad normalised RMS emittance. In this work the laser is guided over  $10 z_R$  in a laser-preformed channel. It should be noted that the total charge in references [11] and [273] was evaluated with an Integrating Current Transformer (ICT). In a later publication [536], it is highlighted that the ICT used in such conditions yield values for charge that are on average an order of magnitude too high. To take this into account the values included in Table 32.2 for these reference are the published results divided by ten.

Banerjee et al. [829] reported on electron beams with 100–800 MeV energies, 1–4 mrad divergence and 5–25% energy spread.

Mangles et al. [12] obtained 50–80 MeV beams with down to 3% energy spread, 90 mrad divergence and a charge of 22 pC. Froula et al. [830] observed electron energies up to 720 MeV with divergence 2.85 mrad, an estimated normalised emittance of 5 mm mrad and a charge of 6.7 pC.

#### *Discussion of Table 32.4 Density-Gradient Injection*

In Faure et al. [834] a relatively sharp (30  $\mu\text{m}$  density gradient) transition is generated using a crossing laser beam to create a channel. Electron beams with 50 – 200 MeV energy,  $40 \pm 20$  pC charge and  $5 \pm 2$  mrad divergence are produced. The injection probability is 95%, but large shot-to-shot fluctuations of the energy and the energy spread are observed. In particular, the energy spread increases with charge, which is attributed to beamloading effects. A comparison with the colliding pulse injection scheme at the same density is performed. The colliding pulse scheme leads to better stability, whereas better collimation of the electron beam occurs in the density gradient injection scheme.

In Schmid et al. [18] a knife edge is inserted into the gas jet to produce a shock front with estimated density transition width of  $5\ \mu\text{m}$ . Electron beams with 23 MeV energy, 9% energy spread, 8.9 mrad divergence and 3.3 pC charge are generated with up to 95% injection probability.

Buck et al. [659] produce a sharp density transition by insertion of a knife edge into the gas-jet target. They obtain up to 133 MeV energy electron beams with 6.5 MeV energy spread and 1.2 pC charge. Higher charge beams are obtained with 50 MeV energy and 5.3 MeV energy spread.

Gonsalves et al. [658] report on experiments with a gas-jet followed by a capillary discharge. Electron beams with energy 300–400 MeV, average divergence (FWHM) 2.2 mrad and energy spread (FWHM) 11% are obtained with 100% injection probability. The highest quality beams obtained have 1.8% energy spread and 1.4 mrad divergence with a charge of 1 pC. Shot-to-shot RMS variations were measured to be 1.9% in energy, 45% in charge and 0.57 mrad pointing stability. By small changes in the plasma density profiles, a charge stability of 6% is achieved.

In Fourmaux et al. [842] a crossing high-intensity laser is used to generate the plasma density gradient with an estimated gradient length of  $25\ \mu\text{m}$ . Electron beams with 280 MeV energy, energy spread 11%, divergence 6 mrad and more than 300 pC charge are accelerated. The shot-to-shot standard deviations are measured to be 28% in energy and 40% in charge.

In Thauray et al. [20] a comparison of density transition injection with (gas mixture 99% He + 1% N<sub>2</sub>) and without (pure He) ionisation injection is performed. Electron beams with 123 MeV energy and 11% energy spread, divergence of 5 mrad and 2.6 mrad (elliptical beam) and 1 pC charge are generated. The shot-to-shot charge stability (12%), energy stability (2.5%), RMS pointing stability (1.5 mrad) and injection probability (100%) are improved in the case of the gas mixture with respect to pure He (24%, 7%, 3.2 mrad, < 100%). Additional lower energy peaks are present in the case of the gas mixture, indicating that regular ionisation injection occurs after the density transition. An increased percentage of N<sub>2</sub> in the gas mixture leads to increased charge in the electron beam without affecting the beam quality.

Burza et al. [843] create a more complex density profile by the insertion of a thin ( $25\ \mu\text{m}$ ) wire into the gas-jet. The life-time of the wire is 60–100 shots. The obtained density profile is characterised by three density plateaus (the second plateau having half the density of the first and third plateau) connected by two transition regions consisting of a shock and a downward gradient each. Electron beams with energies up to 100 MeV, energy spread below 4% at 100 MeV, divergence 2–8 mrad, 10–100 pC charge and 95% injection probability are obtained.

Recent results reported by Wang et al. [32] are obtained with a different approach showing very promising results. With the use of two gas-jets and a wall inserted at the end of the first gas-jet, a density profile consisting of a first plateau, a density bump followed by a density downramp and a second plateau is generated. Injection occurs in the first plateau and reversal of the electron beam chirp is achieved in the density downramp. Electron beams with 200–600 MeV energy, 0.4–1.2% RMS energy spread, 0.2 mrad RMS divergence and 10–80 pC charge are observed.

*Comments*

The properties of electron bunches reported in Tables 32.2–32.5 illustrate the main features of each injection technique. However, other properties can also be relevant, such as the electron bunch pointing fluctuations, its transverse slice emittance or its length (*i.e.* longitudinal size).

In Tables 32.2–32.5, the “traffic light system” is used to highlight results corresponding to EuPRAXIA parameter requirements (in green), close to requirements but with further improvements needed (in yellow) and far from EuPRAXIA requirements (in red).

Most experimental studies focus on the control of the injection to reduce the energy spread, the transverse emittance or increase the energy. The stability of electron properties has not yet been intensively studied. To develop a reliable electron beam, stability and reproducibility of electron properties are needed. They are currently limited by the stability and reproducibility of the parameters of the laser and plasma target. More work is necessary to quantify clearly the main mechanisms and propose ways to stabilise acceleration processes.



**Table 32.3.** Comparison of selected published performances to EuPRAXIA baseline for colliding pulse injection (CPI).

Injection technique		CPI		Baseline 150 MeV	Baseline 1 GeV
References		[657]	[831]	Report D 1.2.	Report D 1.2.
Plasma	Target	Jet	Jet	Cell / capillary / jet	Cell / Capillary
	Gas	He	He	H <sub>2</sub>	H <sub>2</sub>
	$n_e$ (cm <sup>-3</sup> )	$7.5 \times 10^{18}$	$5.7 \times 10^{18}$	$3 \times 10^{18}$	$2 \times 10^{17}$
	Length (mm)	2	3	$\geq 5$	$> 10$
	$E_L$ (J)	0.72 and 0.25	N/A	0.4	100
Laser	$\tau_L$ (fs)	30	30	42	100
	$P_L$ (TW)	$\sim 24$	N/A	10	1000
	$I_L$ (W/cm <sup>2</sup> )	$3.4 \times 10^{18}$ and $4 \times 10^{17}$	$4.6 \times 10^{18}$ and $4 \times 10^{17}$	$\sim 3 \times 10^{18}$	-
	$a_0$	1.3 and 0.4	1.5 and 0.4	1.2 and 0.6	-
	$w_0$ ( $\mu\text{m}$ )	$16 \times 21$ and 31 (FWHM)	N/A	N/A	-
Electrons	Guiding	No	No	No	-
	$E$ (MeV)	117	206	$\sim 150$	1000
	$\sigma_E/E$ (%)	11 (FWHM)	$\sim 7$ (FWHM)	$\sim 1.4$ (FWHM)	5 (RMS)
	$Q$ (pC)	19	13	7.6	$\sim 11.8$ (gaussian FWHM)
	$\sigma_{\perp}$ (mrad)	5.8 (FWHM)	4.5	$\sim 1$	100
Comments	$\epsilon_{N,\perp}$ (mm.mrad)	N/A	N/A	N/A	1
	$\Delta E/E$ (%)	6	5 (RMS)	N/A	-
	$\Delta Q/Q$ (%)	36	30 (RMS)	25 (RMS)	-
	$f$ (Hz)	N/A	N/A	N/A	10
	$P_i$ (%)	100	N/A	N/A	-
Comments		Tunable	-	Tunable	-

**Table 32.4.** Comparison of selected published performances to EuPRAXIA baseline for density-gradient injection (DGI).

Injection technique		DGI				Baseline 150 MeV	Baseline 1 GeV	
References	[834]	[842]	[659]	[843]	[32]	Report D 1.2.	Report D 1.2.	
Target	Jet	Jet	Jet	Jet	Two jets	Cell / capillary / jet	Cell / capillary	
Plasma	Gas	He	He	He	He	H <sub>2</sub>	H <sub>2</sub>	
	$n_e$ (cm <sup>-3</sup> )	$1 \times 10^{19}$	$5.2 \times 10^{18}$	$3.3 \times 10^{18}$	$6 \times 10^{18}$ then $3 \times 10^{18}$	$3 \times 10^{18}$	$2 \times 10^{17}$	
	Plasma Length (mm)	2.1	5	$\sim 1$	3	$\geq 5$	$> 10$	
	$E_L$ (J)	1	2.5	0.77	1	N/A	5	
Laser	$\tau_L$ (fs)	30	30	28	42	33	100	
	$P_L$ (TW)	30	80	$\sim 28$	$\sim 24$	100	1000	
	$I_L$ (W/cm <sup>2</sup> )	$3.6 \times 10^{18}$	$1.2 \times 10^{19}$	$8.5 \times 10^{18}$	N/A	$\sim 3.6 \times 10^{18}$	-	
	$a_0$	1.3	2.4	2.0	N/A	1.3	-	
	$w_0$ ( $\mu\text{m}$ )	$17 \times 22$ (FWHM)	18 (FWHM)	13.5 (FWHM)	15 (FWHM)	32 (FWHM)	-	-
	Guiding	No	No	No	No	No	-	-
Electrons	$E$ (MeV)	100	335	$\sim 133$	100	$\sim 550$	150	
	$\sigma_E/E$ (%)	$\sim 10$	8 (1/e)	$\sim 5$ (FWHM)	$\sim 4$ (FWHM)	$\sim 1$	5 (RMS) $\sim 11.8$ (gaussian FWHM)	
	$Q$ (pC)	40	335	1.2	$\sim 43$	$\sim 30$	100	
	$\sigma_{\perp}$ (mrad)	5	5	$\sim 3$	4	0.2 (RMS)	5.8 (RMS) $\sim 13.7$ (gaussian FWHM)	
Comments	$\varepsilon_{N,\perp}$ (mm.mrad)	N/A	N/A	N/A	N/A	N/A	1	
	$\Delta E/E$ (%)	100	$\sim 33$	$\sim 5.5$	N/A	$\pm 5$	-	
	$\Delta Q/Q$ (%)	50	$\sim 50$	$\sim 83$	$\sim 44$	$\sim 50$	-	
	$f$ (Hz)	N/A	N/A	N/A	N/A	N/A	10	
	$P_i$ (%)	95	40	99	95	N/A	-	
Comments	-	Tunable	Tunable	-	Tunable	-	-	

**Table 32.5.** Comparison of selected published performances to EuPRAXIA baseline for ionisation-induced injection (III).

Injection technique		III				Baseline 150 MeV	Baseline 1 GeV
References		[278]	[282]	[773]	[839]	Report D 1.2.	Report D 1.2.
Target	Jet	Two-stage cell	Two jets	Jet	Cell / capillary / jet	Cell / Capillary	
Plasma	99%He + 1%Ar	99.5%He + 0.5%N <sub>2</sub>	99.5He + 0.5%N <sub>2</sub> / He	99.5%He + 0.5%N <sub>2</sub>	H <sub>2</sub>	H <sub>2</sub>	H <sub>2</sub>
	$n_e$ (cm <sup>-3</sup> )	$2 \times 10^{19}$	$3 \times 10^{18}$	$3.4 \times 10^{18} + 1.2 \times 10^{18}$	$5 \times 10^{18}$	$3 \times 10^{18}$	$2 \times 10^{17}$
	Plasma Length (mm)	3	8	0.5 + 2	4	$\geq 5$	>10
	$E_L$ (J)	N/A	N/A	1.7	N/A	5	100
Laser	$\tau_L$ (fs)	30	60	34	30	30	100
	$P_L$ (TW)	24	40	47	30	167	1000
	$I_L$ (W/cm <sup>2</sup> )	$\sim 2.8 \times 10^{19}$	$\sim 10^{19}$	N/A	$\sim [1.8 - 5.0] \times 10^{18}$	-	-
	$a_0$	$\sim 3.6$	$\sim 2 - 2.8$	2.5 (sim)	$[0.9 - 1.5]$	-	-
	$w_0$ ( $\mu\text{m}$ )	10 (FWHM)	15 ( $1/e^2$ )	10 ( $1/e^2$ )	28 ( $1/e^2$ )	-	-
	Guiding	No	No	No	No	-	-
	$E$ (MeV)	$\sim 115$	460	175	300	150	1000
	$\sigma_{E/E}$ (%)	$\sim 20$ (FWHM)	$\sim 5$ (FWHM)	$\sim 17$ (FWHM)	5 (FWHM)	5 (RMS)	5 (RMS)
	$Q$ (pC)	$\sim 12$	35	$\sim 20$	N/A	$\sim 11.8$ (gaussian FWHM)	$\sim 11.8$ (gaussian FWHM)
	$\sigma_{\perp}$ (mrad)	$2.9 \pm 0.8$	2.3	N/A	N/A	5.8 (RMS)	0.71 (RMS)
Electrons	$\varepsilon_{N,\perp}$ (mm.mrad)	N/A	N/A	N/A	N/A	$\sim 13.7$ (gaussian FWHM)	$\sim 1.7$ (gaussian FWHM)
	$\Delta E/E$ (%)	N/A	N/A	N/A	N/A	1	1
	$\Delta Q/Q$ (%)	$\sim 40$	N/A	N/A	N/A	-	-
	$f$ (Hz)	N/A	N/A	N/A	N/A	10	10
	$P_i$ (%)	N/A	N/A	75	N/A	-	-
	Comments	-	-	Tunable	-	-	-

### 32.2.6 Summary: Preliminary Design Elements

Table 32.6 summarises the main properties (state-of-the-art or expected to be achieved soon) of four general type of plasma targets of interest for EuPRAXIA design:

**Table 32.6.** Summary of plasma targets main properties

Target type	Length mm	$n_e$ value $\text{cm}^{-3}$	$n_e$ tailoring	$n_e$ stability	rep rate	life time
Gas jet	< 20 self-foc.	$10^{18}$	multiple jets	turbulent flow	10 Hz	> 24 h
Gas cell	> 1 self-foc.	$10^{17}$ – $10^{19}$	machining	gas feed dependent	10 Hz	laser quality dependent
Plasma channel HE	< 30 guiding	$(1 - 5) \times 10^{18}$ parabolic	similar to gas jet	laser quality dependent	10 Hz	>24h
Plasma channel discharge	10 – –90 guiding	$5 \times 10^{17}$ – $10^{19}$ parabolic	multiple gas feed	discharge dependent	10 Hz	laser quality dependent
Cap tube	10–1000 guiding	$(0 - 5) \times 10^{17}$ homogeneous	multiple gas feed	gas feed static	10 Hz	laser quality dependent

Although current operation of experiments is lower than 10Hz, the listed targets have the capability, in terms of gas feed, to operate at 10 Hz provided an adequate evacuation system is used to minimise the gas load inside the interaction chamber. Gas jets and gas cells can be used in a range of gas length and density, and laser power where self-focussing is effective, otherwise the distance of high intensity interaction is limited to the diffraction length. Consequently gas jets and gas cells are better suited for injectors. The comparison of gas cell and gas jets for similar conditions of plasma density shows that gas cells are more stable, essentially due to a smoother gas feed system.

Gas jets exhibit an open geometry interesting for diagnostics, and provides robustness against laser beam defects in quality of instability. Heavy gas load may prevent large repetition rate. Plasma channels HE, formed by hydrodynamic expansion, are able to guide intense pulses over a moderate distance at intermediate density, and have the advantage of open geometry, similar to gas jets. Plasma channels created by discharge and grazing incidence capillary tubes are the two main types of wave-guides adequate for intense laser guiding in the 10 cm range, scalable to longer lengths. They can operate in the quasi-linear regime and are suited for accelerator structures. Multiple gas feeds along the propagation axis could be used to tailor the density profile for controlled acceleration. 10Hz repetition rate should not be an issue in terms of gas load. Energy deposition and flow in the waveguides should be studied to determine if cooling systems should be implemented.

A critical issue for the lifetime of gas cell and waveguides is the laser beam quality and stability. As the laser properties also play a crucial role in the reproducibility of the acceleration process, this seems to be an absolutely necessary requirement for the design of the laser system.

Finally, systematic studies of the stability of the gas/plasma density should be performed for each type of target: it is a parameter which is not well documented although it is crucial for the stability of the acceleration process. Figure 32.5

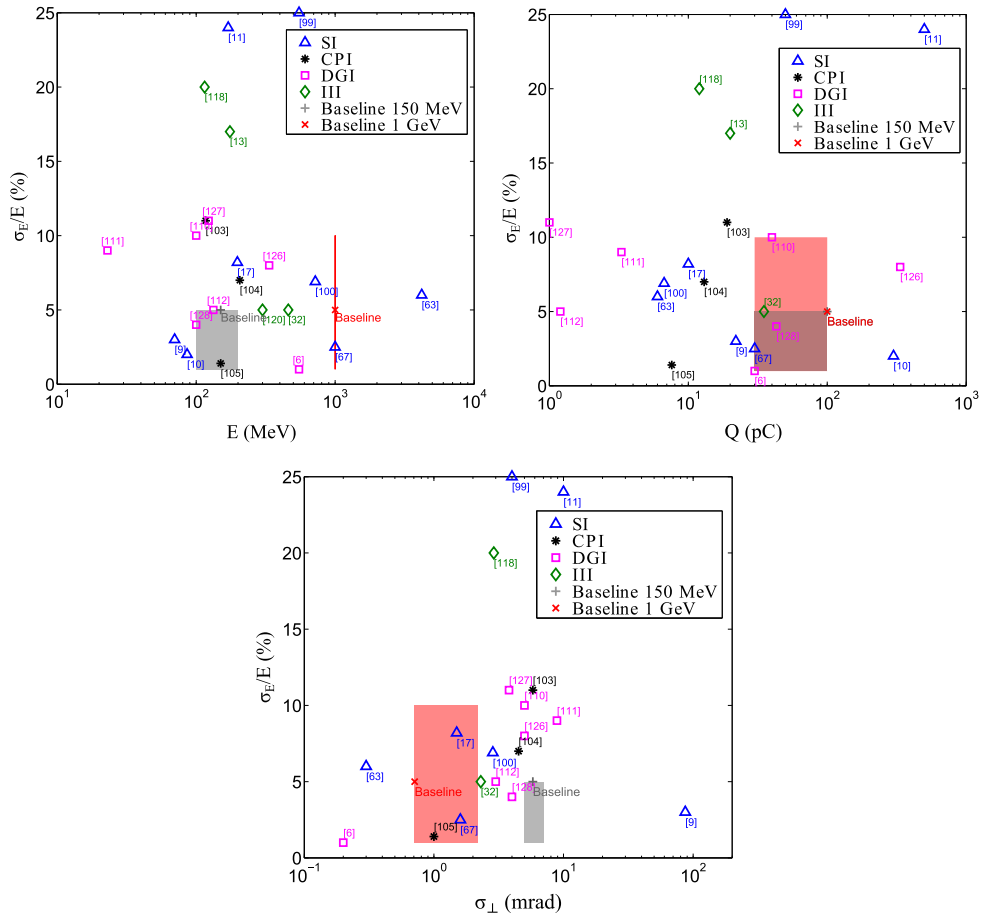


**Fig. 32.5.** Comparison of published results with EuPRAXIA injector parameters. Operation points of published results are indicated in 3 parameter spaces: energy spread vs energy (a), energy spread vs charge (b), and energy spread vs divergence space (c); symbols indicate different injection mechanisms; the two EuPRAXIA baseline injectors are indicated as grey area for 150 MeV and red area for 1 GeV.

summarises the properties of published electron beams for four parameters relevant for the EuPRAXIA design.

It shows that among the examined results for all injection schemes, none has all four parameters within the range of EuPRAXIA design. It indicates that more efforts are necessary in particular to reduce the beam divergence of the injector. However we can see that reference [843] is close to EuPRAXIA target parameters for an injector at 150 MeV. We can also see that reference [832] presents parameters within the range of EuPRAXIA target but produced too low charge electron bunches.

### 32.3 Enabling Laser Design and Optimisation

#### 32.3.1 Introduction

The EuPRAXIA infrastructure relies on a range of laser systems to drive plasma acceleration in a set of different configurations, including the 150 MeV injector, and

the 1 and 5 GeV accelerators. The “Laser Design and Optimisation” Work Package (WP4) has delivered the design of the laser systems and all required subsystems to fulfil the specifications starting from the “Benchmarking of existing technology and comparison with the requirements” (EuPRAXIA Deliverable Report D4.1, see also Sect. 7.2), where a major effort was dedicated to the identification and definition of the most promising approaches. This process of selection was also strongly driven by some of the physics specifications requiring pulse duration as short as 30 fs to be available. Indeed, this requirement, combined with the significant energy per pulse needed by the three LPA schemes, made Ti:Sa emerge as the most suitable technology, with main components featuring a high TRL.

Based on the foreseen temporal constraints, the design of the main EuPRAXIA lasers could be delivered using Ti:Sa laser technology and exploiting the dramatic ongoing developments in pump lasers, i.e. lasers capable of delivering ns pulses with  $\approx 100$  J level energy per pulse at a 100 Hz pulse repetition rate. An overview of the full conceptual design is given in Chapter 10.

Conceptual laser design and optimisation was driven by the physics specifications set by the acceleration schemes.

Here we further discuss main issues behind the conceptual laser design that concern enabling key components.

The first issue concerns the thermal management of the main amplifier heads. Here a combination of conductive cooling through the crystal mounts and convective cooling in air of the amplifying crystal, the most commonly used cooling techniques in low repetition rate systems, may be found to be insufficient for high repetition rate operation at the required energy levels. Other more aggressive cooling strategies must then be envisaged, such as fluid (i.e. liquid or gas) forced flow cooling. Indeed, for these reasons, the amplifying crystals considered are not monolithic, but are divided into two identical sub-crystals face-cooled by a liquid flow, to increase the available cooling surface. This fractioning of the crystal has no impact on the overall energy amplification performances. A quantitative evaluation is given in Chapter 10 for such a configuration with water cooling. Preliminary simulations indeed show that this scheme may provide the appropriate heat extraction with a manageable wavefront aberration. More detailed, full-scale simulations are however needed in combination with a set of validation experiments on real samples to reduce design uncertainties and support the technical design.

Beam transport from the final amplifier to the target final focus includes a set of issues currently still under quantitative evaluation. An overview of these important issues is included in Chapter 10. The main challenges are certainly the thermal and spectral issues in the compressor, and the pointing stability at the interaction plane. Regardless of the grating technology, cooling of the gratings will most likely be necessary. While numerical modelling is being implemented and preliminary small-scale experiments are just emerging, a reliable compressor design with cooled gratings will require full-scale components tests at the required average power level. Moreover, depending on the laser beamline, wide bandwidth acceptance will be needed. New grating technologies are emerging, like hybrid gratings with metal and multi-layer dielectric coatings or new configurations for pure multilayer dielectric gratings. Among these issues, compressor grating performance at high average power levels is certainly of concern and grating cooling technology will be necessary to control the impact on beam quality.

Regarding the pointing stability, in general, the requirements depend on the specific application, involving possibly super-position of two laser focal spots or a laser focal spot and an electron beam in the focal region. These specifications will require a major design effort, still under investigation. In general, pointing stability will be

affected by the whole system and several strategies can be considered. Active stabilisation of PW-scale lasers using closed loops between stability detection on the interaction point and crucial transport optics is being considered. At the same time, passive stabilisation adopting self-stabilizing optics mounts, is also being considered.

### 32.3.2 Pump Laser Technology

The availability of the required pump laser power is a critical issue in the design. It should be noted that the diode laser pump units considered in our design currently use commercially available diode laser technology, either directly or with small changes in use condition. These pump sources use low-cost passively cooled arrays of 1-cm diode laser bars, which were developed for low repetition rate and low duty cycle use and have limited cooling capacity by design (for low cost and compactness). The low heat extraction rate leads to restrictions in either duty cycle, output power, spatial brightness or power conversion efficiency, meaning that in general the diode laser pumps are marginal in performance for the EuPRAXIA system. In the solutions presented here, these limitations are proposed to be overcome by accepting reduced performance or by interleaving many sources at the expense of substantially increased cost. Alternative solutions without these performance restrictions are also available, but these are either research prototypes that require technology transfer to industry [Platz, 2018] or require the use of microchannel cooling of bars, which is not preferred on cost and reliability grounds.

#### DIPOLE-Like Technology

DiPOLE is a diode-pumped, solid state laser amplifier architecture developed at the Central Laser Facility. It is based on an end-pumped stack of ceramic Yb:YAG slabs, cooled by a flow of low-temperature, high-pressure helium gas [Ertel 2011]. This technology was recently demonstrated at the 1kW level with the DiPOLE100 system (STCF, UK, HiLASE, CZ), showing 100 J output energy @ 10 Hz, 1030 nm with > 60 J expected conversion @ 515 nm [Mason 2017]. This architecture and gain material exhibit reduced reabsorption loss and increased absorption and emission cross-sections in Yb:YAG, with a low quantum defect due to the very close pump and emission wavelengths being 940 nm and 1030 nm, respectively. These advantages enable efficient energy extraction and potential scalability to high average power. A scaled version of this architecture has already been considered as a pump source for the 30 J, 30 fs, 10 Hz Gemini upgrade at STFC (EPAC project). The main specs of the Gemini upgrade are very relevant to the Laser 2 (P0) of EuPRAXIA and will constitute an extremely interesting reference system in view of the final design.

At this stage we can envisage a possible schematic approach to the main EuPRAXIA amplifier module, (AMP3(P0)) where, scaling the DiPOLE system to the 150 J level (IR), we can consider up to three pumping units, delivering the required 280 J each (@0.5  $\mu\text{m}$ ) on the final Ti:Sa crystal. This will be discussed in more details in the following paragraph.

#### P60-Like Technology

The P60 is a commercial system produced by Amplitude Technologies as a part of the P-series systems, using an improved “active mirror” configuration, the so-called Disk Amplifier Heads (DAH), based on Nd:YAG. Currently operated with flash lamp

pumping, conversion to diode pumping has been developed by Amplitude and a preliminary design has been produced. The general architecture of the P60 includes a seeder, followed by 6 identical Nd:YAG DAH amplifiers. The main features of the system are 1) enhanced and simple thermal management without cryogenic cooling. Longitudinal liquid cooling in gain/heat load distributed disks; 2) compatibility with diode pumping, 3) compact footprint 1.5 x 4.8 m and beam specifications suitable for Ti:Sa pumping.

The demonstrated performances include  $>70\text{J}$  at  $1064\text{nm}$  with a  $0.41\%$  RMS shot-to-shot stability and  $75\%$  SHG efficiency with  $5\text{-}6\text{ns}$  Gaussian temporal pulse @  $2.8\text{J}/\text{cm}^2$  incident fluence with a  $65\text{ mm}$  diameter and  $18\text{ mm}$  thick LBO type I crystal. These values indicate that an array of a limited number of P60-like systems could deliver the required pump energy for Laser1 and Laser2. Laser3 will require additional development to reach the  $>100\text{ J}$  level after SHG so that an array of up to 4-5 units would provide sufficient pump energy.

The DPSSL version of the P60 is envisaged to operate at an ultimate rep. rate of  $100\text{ Hz}$ . However, current heat load performances would already enable  $3.5\text{ kW}$  average power with  $75\text{ J}$  per pulse (IR) at  $50\text{ Hz}$  with no risk. In fact, the thermal load extraction capability demonstrated in disk amplifiers with flashlamps pumping is similar to the heat load at  $50\text{ Hz}$  with diode pumping. Moreover, diodes with required brilliance and power supplies are existing and qualified. One important issue concerns the lifetime of diodes for high rep rate. Assuming a diode lifetime of  $\sim 2$  billions shots at a  $2\%$  duty cycle, diodes should be replaced every  $700/230$  days at  $8/24\text{H}$  operation at  $100\text{ Hz}$  rep-rate and every  $1400/460$  days at  $8/24\text{H}$  operation at  $50\text{ Hz}$  rep-rate.

### HAPLS-Like Technology

The HAPLS system was developed by the LLNL for ELI Beamlines (Prague). The system is based on a diode pumped, He cooled Nd:APG-1 glass with cooled ASE edge cladding and currently can operate at  $>100\text{ J}$  output energy demonstrated @  $3.3\text{ Hz}$ ,  $1053\text{ nm}$ , with  $0.7\%$  RMS stability and  $80\text{ J}$  SHG energy @  $526.5\text{ nm}$ . Ramping up to  $10\text{ Hz}$ ,  $200\text{ J}$  (IR) the design limit is currently in progress. In the HAPLS system, the diode pumped system is used to pump a Ti:Sa system to deliver  $30\text{ J}$  in  $30\text{ fs}$  at  $10\text{ Hz}$ . This technology is derived from Inertial Fusion Energy Laser architectures and can be aperture scaled to single aperture, kilojoule,  $>100\text{kW}$  output. For the HAPLS preamplifier, LLNL took a first step towards increasing the repetition rate of J-class Ti:sapphire lasers by working with Northrup Grumman Cutting Edge Optronics (NG CEO) to produce a green pump laser that is fully diode-pumped and capable of producing  $2\text{ J}$  at  $10\text{ Hz}$ . Based on this experience and the data obtained from the design, construction, and operation of this laser system, increasing the repetition rate by  $10\times$  to  $100\text{ Hz}$  is straightforward. This design is compatible with the mandatory (P0) requirements for AMP1 and AMP2, possibly even at  $100\text{ Hz}$  (P1).

#### 32.3.3 Pump Array Layouts

The two systems P60 and DiPOLE described above have been considered as the main building blocks for the pump laser system for the Ti:Sapphire laser chain. An analysis was then carried out to determine the most efficient arrangements of the pump arrays fitting the pump energy requirements, minimizing the number of required devices and the energy in excess which is lost. In this analysis further assumptions were made, that is:

- For the Amplitude P60 system, it was assumed possible to scale down the system to lower energy levels, taking advantage of the modularity of the system;

- The DiPOLE 100 was considered capable to readjust the rep rate and the pulse energy at the same average power (e.g. running at 20 Hz with 50 J of pulse energy in the infrared)

Regarding the operation at the P1 performance level, a diode pumped version of the P60 system was considered, capable to operate at 50 Hz at the same output pulse energy.

### P0 Performance Level

The P0 operation regime has a pulse repetition rate of 20 Hz. The two pump sources considered above feature a repetition rate of only 10 Hz. To circumvent this problem (in view of the development of devices operating at higher rep rate) we consider the use of two (or two sets) of pump sources operating in interleaved mode. In this way the repetition rate of the pump pulses arriving to the amplifiers is effectively doubled.

Moreover, pump energies higher than about 60 J (as needed by the AMP3 module) require the use of more than a single pump source. In turn, this calls for specific arrangements to multiplex the input from several pump units to the amplification crystals.

### P1 Performance Level

The P1 operation regime considers a pulse repetition rate of 100 Hz, along with higher energies than P0. Currently no solutions for pump sources are available to meet these requirements and will have to be developed for the purpose. Speculatively, we have considered the availability of a system similar to Amplitude P60 but operating at 50 Hz, resulting from the conversion to diode laser pumping of the available P60 (which is flashlamp pumped), with an output energy of 60 J/pulse in the second harmonic. Again, reaching 100 Hz requires the time interleaving of a pair of twin sources. This analysis did not include the DiPOLE 100 system, as no developments are currently planned toward a high energy, high rep rate system.

### 32.3.4 Conclusive Remarks

The requirement of 20/100 Hz of repetition rate respectively at the P0/P1 performance level has a very significant impact on the pump laser arrays: as the available/foreseen pump devices have a repetition rate of 10Hz/50Hz; this requires the doubling of the pump sources to achieve the required repetition rate by temporally interleaving the shots. As a secondary point, the pump pulses must be routed to the amplifying crystals using angular multiplexing of the input directions. This introduces some complexity in the design of the optical layout of the amplifiers. Also, shot to shot energy stability issues can become more critical when the pump pulses are delivered alternatively by two different sets of devices. It is clear that the availability of pump sources natively operating at 20 Hz / 100 Hz would introduce a large simplification in the architecture of the whole laser amplifier.

Summarising the current and expected performances of kW-scale DPSSL pumping systems currently available, we can say that the three selected systems are in a highly advanced development stage. All of them have demonstrated performances required to fulfil part of the pumping needs of the main EuPRAXIA laser P0 specifications. Some of these technologies are being considered independently for scaled

operation at higher rep rate and higher energy per pulse, making them good candidates for pump lasers to reach the P1 specifications. However, a significant targeted development will be needed to address scaling of candidate systems at the desired 100 Hz repetition rate. In view of this, a dedicated de-risking activity is foreseen as discussed in Chapter 10.

## 32.4 Outreach and Liaison

The EuPRAXIA consortium has established an Outreach and Liaison group based at the University of Liverpool/Cockcroft Institute. The group holds weekly online meetings with the Management Support Team at DESY to ensure that communication activities are always on the agenda and to continuously monitor progress.

### 32.4.1 Resources

#### The EuPRAXIA Brand

The group produced a collection of materials to assist the partners with the dissemination of the project and its objectives, creating a visual language to facilitate the prompt identification of the EuPRAXIA brand.

In order to ensure a consistent message the group created some informative slides about the project and made them available to all project partners. A template for presentations was also created and all partners were encouraged to use it in order to reinforce the project branding.

Following the same visual identity idea, the group produced a poster template to advertise all EuPRAXIA-related events and a series of roll-up banners that were displayed prominently at project meetings, workshops and conferences around the world.

#### Website and social media

The project website [www.eupraxia-project.eu](http://www.eupraxia-project.eu) is the main portal of information of EuPRAXIA for the external world. It is regularly updated with news and upcoming events. Relevant news about EuPRAXIA are also promoted via social media, using the Facebook pages of the [Cockcroft Institute](#) and the [Quasar group](#) as well as the corresponding twitter accounts [@cockcroft\\_news](#) and [@QUASAR\\_group](#), with the hashtags [#EuPRAXIA](#), [#plasma](#), and [#accelerator](#).

#### Intranet

A repository of documents was set up in the University of Liverpool's Sharepoint system to facilitate the internal exchange of documents among the project partners. The intranet is linked to the website and all participants in the project have been provided with a password to access the information. Apart from the repository of documents, Sharepoint offers a news blog and a collaborative work space (wikipraxia).



Fig. 32.6. EuPRAXIA leaflet.

## Leaflets

The group produced an informative leaflet about EuPRAXIA which can be downloaded from the website (<http://www.eupraxia-project.eu/downloads.html>). All partners were encouraged to use the leaflet for promoting the project among colleagues, national authorities, policy makers, and the public in general. In order to facilitate the local promotion, the leaflet was translated to German, French, Portuguese, Italian, and Spanish. Moreover a non-technical version of the leaflet was produced to assist in the communication of the project objectives to non-scientific audiences.

## Brochure

A glossy 28-page brochure of the EuPRAXIA project was prepared and focuses on the key technologies to be developed by EuPRAXIA (high-power lasers, accelerator technology, free-electron lasers, high-energy physics and other applications) highlighting their challenges and potential for innovation, and includes information about the project and its partners in general.

The brochure was designed to appeal to a very broad audience. Its primary targets are members of the technology industry, but it also addresses European policy makers, potential users, broader scientific community and the general public.

The brochure informs members of the technology industry of the opportunities offered by EuPRAXIA for innovation and business. It is particularly relevant for the laser industry, manufactures of accelerator components (magnets, vacuum systems, etc.), feedback and control software developers, and system engineers. It also informs potential users of free-electron lasers and the high-energy physics community of the unique opportunities presented by EuPRAXIA. The brochure was distributed to all project partners and at international conferences and workshops. It is also available for [download](https://issuu.com/quasar-group/docs/eupraxia_brochure_web/2) via the project website and available in electronic form via ISSUU ([https://issuu.com/quasar-group/docs/eupraxia\\_brochure\\_web/2](https://issuu.com/quasar-group/docs/eupraxia_brochure_web/2)) for easy access by various device platforms. Several A0 posters were also produced on the basis of the brochure and used to communicate the challenges across the different scientific work packages.

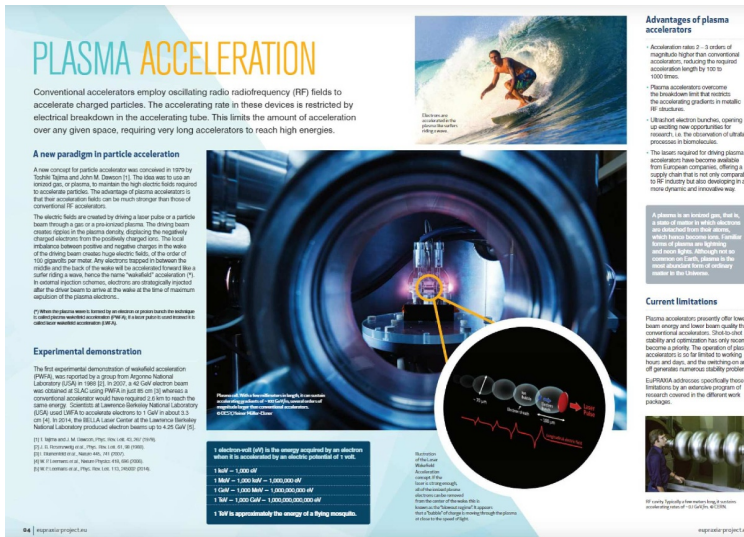


Fig. 32.7. EuPRAXIA brochure.

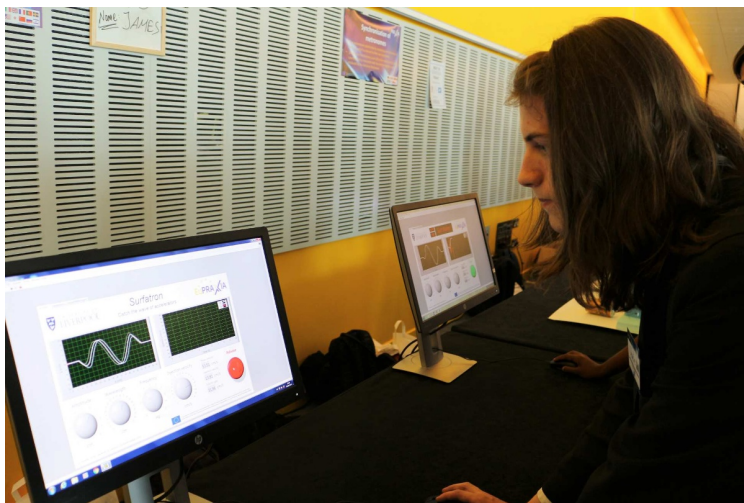


Fig. 32.8. Demonstration of the *Surfatron* game at a past outreach event.

Video

A short video clip about EuPRAXIA, styled as an action movie trailer, was produced. The aim of the video was to create a sense of anticipation for the potential impact of plasma accelerators on society. The video has been shown at numerous outreach events, scientific conferences and meetings, and it is available on Youtube (<https://www.youtube.com/watch?v=vDkkKt1MUvs>). It also features on the European Commission’s “EU-funded R&I projects” playlist.

## The *Surfatron*

A computer game called *Surfatron* was created to demonstrate the concept of wake-field acceleration. The game simulates the motion of a particle in a travelling wave, likened to the motion of a surfer riding a wave at sea.

The player can control the parameters of the wave (amplitude, wavelength, and frequency), as well as the injection velocity of the particle into the wave.

By finding the optimum parameters and releasing the particle at the right time, the aim is to obtain maximum acceleration for the particle. The game also includes some information about the science of EuPRAXIA. The *Surfatron* attracted large crowds at outreach events and international conferences where a leaderboard and prizes helped audience engagement.

### 32.4.2 Publications

#### Feature articles

A number of feature articles about EuPRAXIA have been published on websites and magazines around the world. This included for example:

- [EuPRAXIA Design Study comes of age](#), Accelerating News (October 2018)
- [Plasma accelerators could overcome size limitations of LHCarge Hadron Collider](#), Horizon (July 2018)
- [EuPRAXIA@SPARC\\_LAB: verso la prima generazione di acceleratori da tavolo](#), SIF Prima Pagina (July 2018).
- [Charting a course for advanced accelerators](#), CERN Courier (November 2017)
- [Boosting the electron beam brightness: NeXource](#), Accelerating News (September 2017)
- [Acceleration re-defined once again in Pisa](#), INFN News (July 2016)
- [EuPRAXIA consortium paves way for next generation laser technology](#), Accelerating News (July 2016)
- [Three million euros for European Plasma Research Accelerator with eXcellence In Applications \(EuPRAXIA\) project](#), Laserlab Newsletter (June 2016)
- [Consortium sets out to build European laser plasma accelerator](#), Physics World (April 2016)
- [World's first high energy plasma-based accelerator to be built](#), Electro Optics (April 2016)
- [What will the world's first plasma accelerator look like?](#), Design Products & Applications (April 2016)
- [Innovation news in brief: Scientists to build world's first plasma accelerator](#), The Maven (April 2016)
- [Compact modern accelerators for big science](#), Accelerating News (November 2015)
- [EU consortium to develop plasma accelerator](#), Horizon 2020 Projects (November 2015)
- [EU launches plasma particle accelerator](#), Semiconductor Engineering (November 2015)
- [EU funds design study for European plasma accelerator](#), Deutsches Wissenschafts- und Innovationshaus (November 2015)
- [EU funds design study for European plasma accelerator](#), phys.org (November 2015)

## Newsletter

The Outreach and Liaison group created a [newsletter](#) called *EuPRAXIA Files* to reinforce the sense of community, help with the work of the EuPRAXIA researchers, and strengthen the links with other communities. *EuPRAXIA Files* is a collection of abstracts from published papers that are relevant to the EuPRAXIA study. The newsletter has become a platform for all the research articles generated within the project. *EuPRAXIA Files* is produced every four months and sent by email to all project partners and associate partners. It is also made available for download from the website (<http://www.eupraxia-project.eu/the-eupraxia-files.html>).

### 32.4.3 Activities

#### Active promotion

The Outreach and Liaison group has contributed actively to the promotion of the project by participating in industrial exhibitions associated to major conferences of accelerator science and technology. Using a booth sponsored by the University of Liverpool, they distributed informative material and answered questions about EuPRAXIA in the *International Particle Accelerators Conference – IPAC*, the world’s largest conference in the field, in Busan, South Korea (2016), Copenhagen (2017), and Vancouver (2018) as well as in the *International Beam Instrumentation Conference – IBIC* in Barcelona (2016) and Grand Rapids, USA, (2017).

Individual members of the consortium have also been very active in the promotion of EuPRAXIA with contributions at a large number of conferences, for example *Lab Innovations* in Birmingham, UK (2018).

The project brochure and leaflets actively distributed among national authorities, policy makers and the wider scientific community with a focus on Germany, UK, Portugal, Italy and France.

#### Outreach events

The EuPRAXIA Consortium has been strongly committed to public engagement and endeavours to communicate its objectives and results to the general public through the organisation of outreach events. By communicating the specific research challenges and opportunities of plasma accelerators, this has helped increase the attractiveness of the field overall.

##### *Marie Curie Day 2017*

On 7 November 2017, an event was organised to celebrate the 150<sup>th</sup> birth anniversary of Marie Skłodowska Curie, as well as the EU funding program that bears her name. This pan-European event was held simultaneously at the University of Liverpool, CERN, and the Ludwig Maximilian University in Munich. All talks were recorded and are available via the event website (<https://marie-curie-day-2017.org/>).

In Liverpool, almost 100 local high school students attended a series of activities at the University: an introductory talk by an actress playing the role of Madame Curie, a live connection with CERN where Dr Marco Silari presented the impact of MSCA on research at CERN, a set of hands-on demonstrations on radioactivity, and a poster session about our research and training. The children also participated in a poster competition about “Women in Science”. The event next featured a talk by Prof Carsten Welsch about “Accelerating Researcher Training” that was live streamed for



**Fig. 32.9.** Outreach activities on the “Physics of Star Wars” in Nov 2017.

world-wide access. Among other topics, it covered the physics challenges and opportunities of the EuPRAXIA project. An evening talk at LMU Munich by Professor Katia Parodi on “Research in ion beam cancer therapy” concluded the event.

### *Physics of Star Wars*

The University of Liverpool team organised a “Physics of Star Wars” event on 27 November 2017 at the University’s Central Teaching Laboratory. The aim of the event was to introduce cutting-edge science to hundreds of secondary school children, undergraduate and PhD students, as well as university staff. The day started with a lecture which first presented iconic scenes from the movies to then link them to the group’s research projects on particle acceleration.

After the lecture, all attendees were given the opportunity to understand the science behind Star Wars through numerous hands-on activities. This was then linked to ongoing research activities, including EuPRAXIA. Laser and beam-driven acceleration were motivated through the enormous acceleration “gradient” achieved when spacecraft in the famous films jump to hyperspeed.

### *Symposium*

The symposium “[Quantum Leap towards the Next Generation of Accelerators](#)” took place at the Liverpool Arena Convention Centre on 6 July 2018 as part of the 3<sup>rd</sup> EuPRAXIA Collaboration Week. Its aim was to bring together scientists, industry, and policy makers involved in the development of novel accelerators, and to raise the public profile of the project through widespread coverage in the media.

Over 120 high school students were invited to the symposium which offered them an excellent opportunity to learn about the societal impact of particle accelerators, while meeting and interacting with scientists.

The event featured talks from research leaders about accelerators and their applications in an accessible and entertaining way. The talks were streamed live over the internet and are now available on [YouTube](#). The talks were followed by a two-hour long interactive session with scientists and engineers, featuring a poster session showcasing the main results from EuPRAXIA, and hands-on demonstrations for the students, illustrating the concepts of wakefield acceleration.

The Symposium was the occasion to bring together for the first time the scientists of the consortium with members of relevant companies. The symposium included an industry exhibition with 20 exhibitors. The afternoon session was especially addressed

to the industry and it presented the main technological challenges and innovation opportunities offered by EuPRAXIA. Representatives from more than 40 companies were present at the event.

#### *Audiences and impact*

The outreach events organised by the University of Liverpool have been targeted mostly at local high school students (ages 14 – 17). The participation of girls was encouraged by targeting girls' schools and ensuring a balanced representation of female demonstrators and speakers.

Apart from the direct participation in the events listed above, which for logistical reasons is limited to a few hundred people, the reach and scope of the activities has been greatly multiplied by intensive dissemination campaigns before, during, and after each of the events.

Traditional media coverage (press, radio, and TV), as well as social media (Twitter, Facebook and Instagram) have made it possible for the EuPRAXIA outreach activities organised from Liverpool to have an international impact.

The *Marie Curie Day* was an international success: more than 500,000 people read about the event via the internet, social media and wider press coverage, and the *Physics of Star Wars* event reached more than one Million people. The total reach of communication about the Symposium in 2018 was also in excess of 100,000.

## **32.5 Experience from PWFA Test Experiments**

Plasma-based technology promises a tremendous reduction in size of accelerators used for research, medical, and industrial applications, making it possible to develop tabletop machines accessible for a broader scientific community. In addition to the acceleration purposes, plasmas are very useful to shape the beam longitudinal phase space and can be used also as strong focusing devices. In both cases the required structures are very compact and allow for a wide tunability. In the following sections, the main results obtained from beam-plasma interaction at the INFN's SPARC\_LAB facility and a number of DESY experiments will be presented and discussed.

### 32.5.1 Active Plasma Lenses

While overcoming the limits of conventional accelerators and pushing particles to higher energies, plasma-based accelerators usually produce beams of large angular divergence. Rapid and degradation-free capture of such bunches requires strong and tunable focusing optics. Active plasma lenses (APLs) represent a compact and affordable tool to generate radially symmetric magnetic field gradients, several orders of magnitude larger than what conventional quadrupoles and solenoids can provide. Originating at the Berkeley Radiation Lab in 1950 [399], the technology was not widely adopted until its recent resurrection by the same laboratory [38,181] in the context of advanced accelerators. INFN and DESY have recently taken lead in this research with a number of recent results.

Two previous works from SPARC\_LAB [305,844] show that APL focusing can be highly non-linear and induce a dramatic emittance growth. Starting from these findings we have studied in detail the problem and developed an improved system with which we obtained experimental results showing how these non-linearities can be minimised and lensing improved [845]. These achievements represent a major breakthrough toward the miniaturisation of next-generation focusing devices.

At SPARC\_LAB, the APL consists of a 3 cm-long sapphire tube with 500  $\mu\text{m}$  hole radius. The capillary is filled at 1 Hz with  $\text{H}_2$  gas (produced by an electrolytic

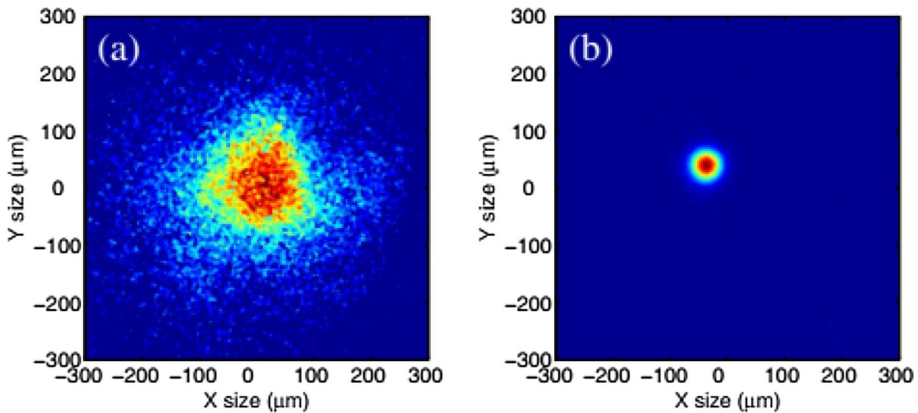


**Fig. 32.10.** Beam spot on a screen downstream of the lens with the discharge turned off (a) and on (b) [845] (copyright (2018) by the American Physical Society).

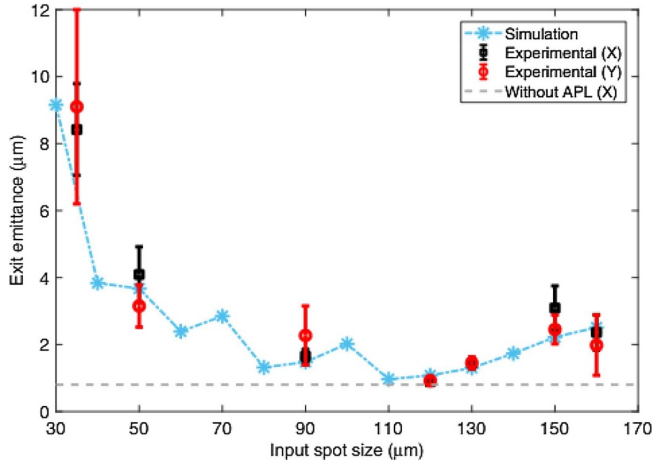
generator) through two inlets. The two capillary electrodes are then connected to a discharge circuit fed by a 20 kV pulser. To test the APL focusing we varied the bunch transverse spot size at the capillary entrance from 35  $\mu\text{m}$  up to 160  $\mu\text{m}$ . This is the largest spot size that ensures to transport the entire beam charge across the capillary clear aperture.

Figure 32.10 shows the resulting focused and unfocused beams after the APL. What we found is that to improve the focusing and preserve the beam emittance the discharge-current flowing through the capillary must be high enough to fully ionise the gas and produce a more linear magnetic field. In addition to this, the interaction with plasma generates beam-driven wakefields that can strongly affect the bunch dynamics. In this context, passive plasma lenses are able to produce a net beam focusing through the plasma neutralisation of the space-charge fields. When dealing with active plasma lenses we have therefore to consider their combined effect. The non-linearities of the overall focusing can be minimised by manipulating both the bunch shape and the capillary-discharge setup.

Figure 32.11 shows the bunch emittance measured downstream of the capillary as a function of the spot size at its entrance. Each point is obtained for the minimum spot provided by the APL on the first screen downstream. According to simulations, the best compromise in terms of resulting emittance is obtained by entering into the plasma with a transverse spot size of 110  $\mu\text{m}$ . We thus followed this expectation and tuned the magnetic optics along the photo-injector to achieve an experimental spot size at capillary entrance of 115  $\mu\text{m}$ . When the discharge is turned on and its delay adjusted to provide the minimum spot size on such a screen (70 A), the beam is squeezed down to 17.5  $\mu\text{m}$ . These conditions corresponded also to the best results in terms of beam emittance (0.9  $\mu\text{m}$ ), which is almost preserved with respect to the unperturbed beam.

Plasma lens studies at DESY are broad and diversified. The discharge capillaries, with varying length (15–195 mm) and diameter (300  $\mu\text{m}$  to 1.5 mm) are manufactured centrally, then installed and tested across several laboratories: at the Mainz Microtron (MaMi), at CERN’s CLEAR User Facility and on site at the FLASHForward facility.

First results came from MaMi [846], where a 30 mm long, 1 mm diameter capillary milled from two sapphire slabs was used to demonstrate stable APL operation with magnetic field gradients up to 823 T/m. These experiments were done using hydrogen, and found evidence of a radial field non-linearity towards the capillary walls [847].



**Fig. 32.11.** Resulting emittance as a function of beam spot size at capillary entrance. The black square and red circle data points refer to the experimentally measured emittances. The blue dash-dotted line represents the expected emittance from numerical simulations. The grey dashed line shows the unperturbed (X) beam emittance without APL [845] (copyright (2018) by the American Physical Society).

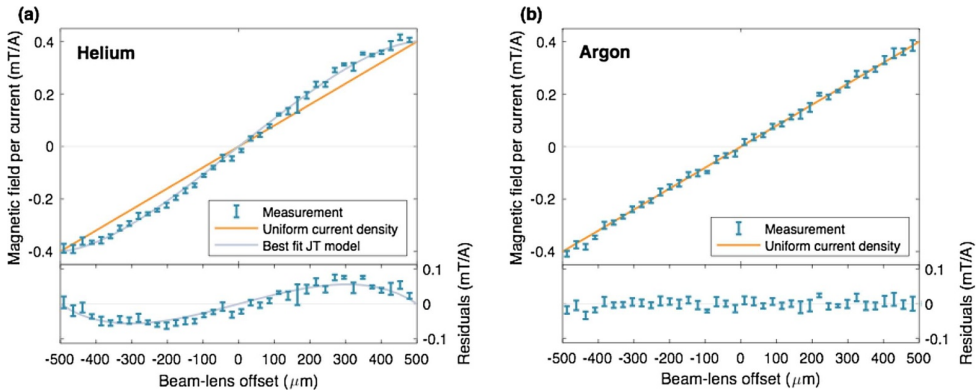


**Fig. 32.12.** Direct measurements of the radial magnetic field profile in an APL. A non-linearity is observed in the helium-filled APL (a), caused by a radial plasma temperature non-uniformity, which leads to aberration and emittance growth. This aberration is suppressed in an argon-filled APL (b) [849].

This problem was further investigated and eventually overcome by a series of experiments at the CLEAR User Facility [848], which utilised a similar 15 mm long, 1 mm diameter sapphire capillary. By using a tightly focused electron beam and offsetting the capillary transversely, the local magnetic field could be measured by observing the angular deflection of the 200 MeV electron beam [849]. Figure 32.12 shows high-precision measurements of the full radial magnetic field profile.

Crucially, this measurement was performed in both helium (expected to behave exactly like hydrogen) as well as in argon – a much heavier gas species. The measurements show that the field non-linearity in helium is consistent with theoretical prediction, whereas in argon, the field is linear to within the precision of the measurement.

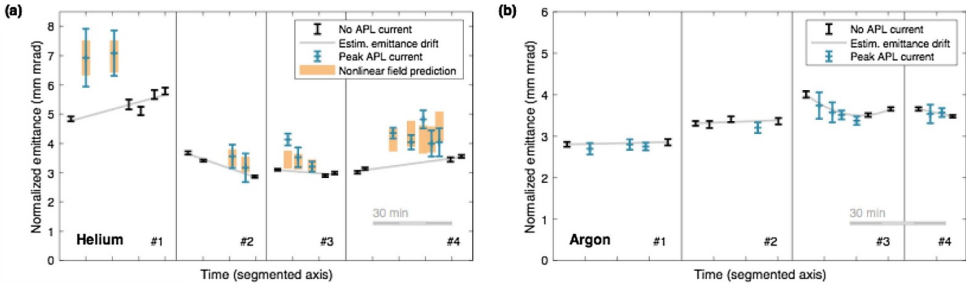


**Fig. 32.13.** Emittance measurements from a series of quadrupole scans in both (a) helium and (b) argon. The beam emittance is observed to grow in the helium-filled APL, as expected from the non-linear fields, whereas in the argon-filled APL no emittance growth is observed [849].

This finding suggests that the aberration and consequent emittance growth can be fully suppressed by an appropriate choice of gas species, given that a sufficiently low beam current to avoid plasma wakefields is used. This prediction was confirmed by measuring the beam emittance before and after lensing in both a helium and argon lens (see Fig. 32.13), successfully demonstrating emittance preservation in the argon-filled APL.

At FLASHForward, plasma density profile of the APL is carefully characterised, both longitudinally and transversely, using two independent techniques: laser interferometry and Stark broadening. This, together with magnetohydrodynamical (MHD) simulations, has led to an increased understanding of the complex evolution of the plasma over  $\mu\text{s}$  timescales, from initial ionisation and heating to the eventual diffusion and recombination.

### 32.5.2 Plasma Dechirper

The wakefield structure in a plasma-based particle accelerator offers distinct advantages for future free-electron laser (FEL) and high energy physics (HEP) applications, such as strong intrinsic focusing and high accelerating gradients. These, in principle, allow for the stable propagation and acceleration of an injected bunch to required energies over distances orders of magnitude shorter than those possible in conventional accelerator designs. A challenge of plasma-based concepts, however, is the development of the longitudinal phase-space (LPS) of the beam, accelerated in an environment that may imprint a large linear energy-time dependency – the so-called “chirp” – on the beam up to the GeV/mm level. Upon exit of the plasma section this large negative remnant chirp will halt FEL gain or lead to a beam size increase limiting luminosity in HEP experiments. Ideally the chirp ought to be mitigated in order to utilise plasma wakefield acceleration techniques in future facilities. At SPARC\_LAB we have developed a new plasma-based device that allows tuning of the beam LPS by using the wakefields excited in a plasma channel [305]. Such a solution is based on the use of the wakefields created by the beam in the plasma and can be employed both to remove the energy chirp (acting like a dechirper) or tune it by adjusting the plasma density. The basic idea of the LPS manipulation is shown in Figure 32.14, where the LPS and computed plasma wakefield (red line) produced by a 200 pC bunch in a plasma whose density is  $10^{14}\text{cm}^{-3}$  are shown. In such a configuration, the tail of the beam experiences a decelerating electric field and loses its energy, while the head moves along an unperturbed plasma, keeping its energy constant.

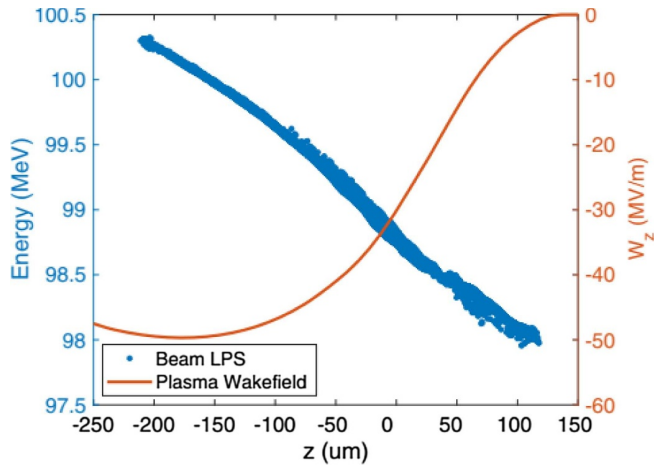


**Fig. 32.14.** LPS of the beam and longitudinal plasma wakefield  $W_z$  (red line) produced in a plasma channel by a moving electron bunch (blue dots) [613] (copyright (2019) by the American Physical Society).

To measure the effect on the energy spectrum of the beam induced by the plasma, the beam was transported to the magnetic spectrometer downstream of the capillary and several measurements were made at different plasma densities. Once the  $H^2$  is ionised it takes almost  $10 \mu\text{s}$  to recombine. During this time, the plasma density slowly decreases. Thus by choosing the time of arrival by delaying the beam the plasma density observed by the electron bunch was varied. Figure 32.15a shows the unperturbed energy spectrum when there is no plasma in the capillary. In this case the overall energy spread is 0.6 MeV. When the plasma is turned on and its density tuned to  $\text{np } 10^{14} \text{ cm}^{-3}$  (corresponding to a delay on the order of  $4.5 \mu\text{s}$ ), a maximum reduction of the beam energy spread was observed, reduced to 0.1 MeV as shown in Figure 32.15b.

Because of the high flexibility of the plasma dechirper by manipulating the parameters of the system (e.g. plasma density) and parameters of the beam (by changing its density with focusing), the system can be tuned in order to remove the given correlated energy spread. It represents an essential feature in order to make the plasma-accelerated beams usable with conventional magnetic optics and for applications involving the generation of FEL radiation.

The FLASHForward experiment [850], attached to the FLASH FEL facility, is designed to generate the characteristically high accelerating fields in the wake of FLASH electron beams interacting with a plasma. This setup was used to perform a proof-of-principle experiment in which the correlated energy spread of a chirped FLASH electron bunch was completely removed by the electric fields generated in plasma. This world-first demonstration was shown to generate dechirping strengths orders of magnitude higher than competing state-of-the-art techniques [851,852] and strengths much larger than subsequent plasma-based dechirping examples [613].

In this experiment an electron bunch, with length  $63 \mu\text{m}$  and a linear chirp of  $60.5 \text{ MeV/mm}$ , was transported from FLASH to the FLASHForward beamline. Once in FLASHForward the chirped bunch was injected into a 33 mm-long plasma, generated by firing a high-voltage discharge through pumped argon gas. After the discharge pulse ends the density of the plasma electrons exponentially decays due to plasma recombination and expansion into vacuum. The plasma density can, therefore, be controlled by delaying the arrival time of the electron beam relative to the discharge,

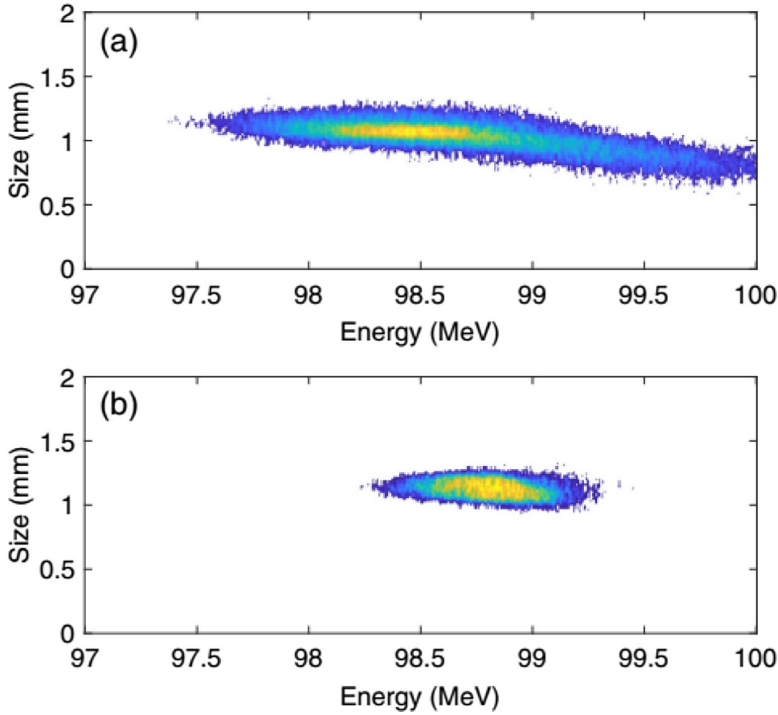


**Fig. 32.15.** Energy spectrum of the electron beam after the capillary without (a) and with (b) plasma in the channel. A significant reduction in energy spread is observed [613] (copyright (2019) by the American Physical Society).

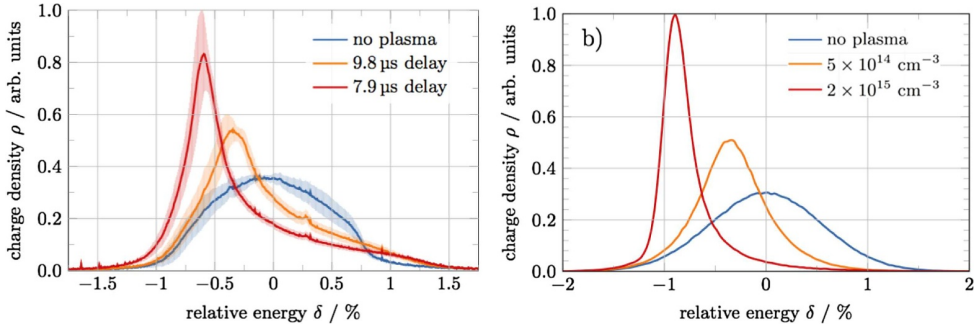


**Fig. 32.16.** A series of energy spectra, as recorded by the optical system surrounding the dipole spectrometer (shown in (a)), for no interaction with plasma as well as two dechirping plasma densities. The standard deviation for each energy slice – an average over 50 consecutive shots – is shown by the error ranges. The simulated energy spectra for the corresponding plasma densities are shown in (b) [850] (copyright (2019) by the American Physical Society).

with the electron beam experiencing lower densities – and therefore lower dechirping gradients – at ever longer times after discharge.

An electron spectrometer located downstream of the plasma capillary was used to disperse the bunch in energy and record the dechirping effect. The energy spectrum of the chirped bunch without interaction with plasma, as well as two cases after interaction with plasma, can be seen in Figure 32.16.

The experimentally derived parameters were used to simulate the dechirping effect using a particle-in-cell code. The plasma density was varied with the maximum dechirping effect observed at a plasma density of  $2 \times 10^{15} \text{ cm}^{-3}$ . The spectra and dechirping effect in these two cases show good agreement. In addition, the fluctuation of the spectra over 50 consecutive shots with and without plasma interaction is consistent, suggesting that the plasma dechirper does not decrease the stability of the incoming beam, increasing the technique's applicability to future FEL and HEP facilities.

Simulations of the chirped bunch interacting with plasma over the full discharge delay time can be seen in Figure 32.17. A comparison between the profile and absolute values of dechirping for both the experimental and simulated data sets shows excellent agreement. The incoming 60.5 MeV/mm chirp is fully compensated 7.9  $\mu\text{s}$  after discharge, implying a dechirping strength of 1.8 GeV/mm/m; two orders of magnitude greater than competing state-of-the-art techniques, with the potential to compensate even greater chirps in shorter distances in future experiments. As such, this principle may be used to mitigate the large energy chirps of electron bunches generated in plasma, thus drastically improving the applicability of plasma wakefield schemes to future experiments where a negligible correlated energy spread is required.

### 32.5.3 Plasma Sources

The parallel development of plasma sources is another essential area of research for the development of practical plasma accelerators. A region of plasma in which the species, density, ionisation state, uniformity, length and longitudinal and/or transverse profile of the plasma density are all well defined is required for both PWFAs and LWFAs. Additionally, the plasma source will need to be reproducible and highly reliable.

For the 1 GeV case, we foresee a single stage of plasma acceleration, 40 cm long (1 mm in diameter), coupled with the RF linac operating at about 500 MeV. Such a goal can be obtained with a plasma density around  $1 \times 10^{16} \text{ cm}^{-3}$  (corresponding to a wave breaking field  $E_0$  around 13 GV/m), that can be used to produce electric fields of 1–2 GV/m and characterised by a plasma wavelength of  $\lambda_p \approx 300 \mu\text{m}$ . In our plasma module, these operating conditions will be obtained by producing a neutral gas pressure around 50 mbar, that will be ionised by using a voltage around 25–27 kV, corresponding to a plasma current pulse through the capillary of 500 A. The maximum allowed voltage in this design is around 40 kV, which can be used to ionise up to 70-cm long capillaries.

For the 5 GeV case, if we maintain the plasma density around  $1 \times 10^{16} \text{ cm}^{-3}$ , the structure of the capillary plasma source has to be changed with respect to the previous case. In fact, this value of density allows to reach accelerating gradients around 1–2 GV/m, that entails the use capillaries up to 2–3 m in length in order to achieve 5 GeV. In this operating conditions, the requested breakdown voltage for a conventional single stage capillary could become larger than 100–150 kV. This high voltage may damage the capillary surface, therefore using a trigger discharge which will reduce the breakdown threshold as well as the jittering time of the discharge is planned.

This proposed scheme is based on the gas filled capillary discharge in which we pre-ionise the gas with a preformed plasma prior to the main discharge. Similar mechanisms have been studied in the past for different purposes, such as cold cathode thyratron [853], trigatron [854] and segmented laser trigger ablative capillaries [781].

With this scheme, which may be referred as segmented capillary discharge, we aim to combine the advantages of the segmented discharge with gas-filled capillary

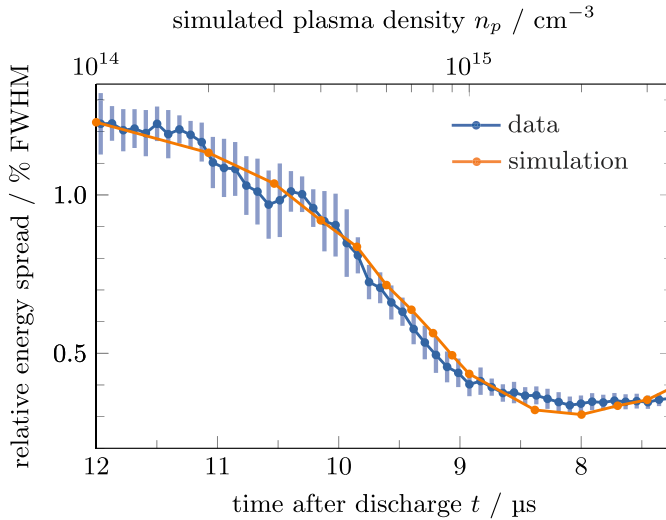


**Fig. 32.17.** The FWHM of the chirped bunch energy as a function of discharge time relative to the arrival time of the electron bunch. The standard deviation, representing the shot-to-shot fluctuations per delay step, is plotted. Simulated FWHM of the chirped bunch energy spectra as a function of electron plasma density over the identical range are shown for comparison [850] (copyright (2019) by the American Physical Society).

technology to produce long plasma channel (m-scale) for plasma-based acceleration schemes of the EuPRAXIA project.

The segmented capillary discharge proposed for this project will use a trigger discharge obtained with a pulsed high voltage signal to overcome the limits of the Paschen's law. The scheme in Figure 32.18 shows a possible implementation of this technique. A voltage of few kVs is imposed between the two external electrodes. The voltage is not enough to ignite the discharge because is still lower than the breakdown threshold obtained with the Paschen's curves. The initial plasma, instead, is formed in a short primary capillary (first stage). Part of this plasma and free electrons expand into the long capillary (the second stage) being accelerated by the potential of the last electrode. The electrons then gain in a short distance enough energy to ionise the neutral molecules, producing an avalanche-like effect in the neutral gas which lets the discharge to ionise the entire gas column. The proposed technique led to produce m-scale plasma channel with reasonable applied voltage. Due to the reduced requirement on the breakdown voltage, the basic structure of the segmented capillary discharge can be repeated to create a multi-stage capillary without particular attention on the high voltage generator. The multistage capillary is then just a chain of few assembled segmented capillaries.

A single segmented capillary unit can be extended by adding more units obtaining up to m-scale capillaries homogeneously ionised and controlled independently one to each other, leading to the desired length of plasma with the proper density ( $1 \times 10^{16} - 1 \times 10^{17} \text{ cm}^{-3}$ ) required for this project. The possible interference between the electrodes is avoided by the use of the stripline in the discharge circuit, which allows to carry high voltage without crosstalk.

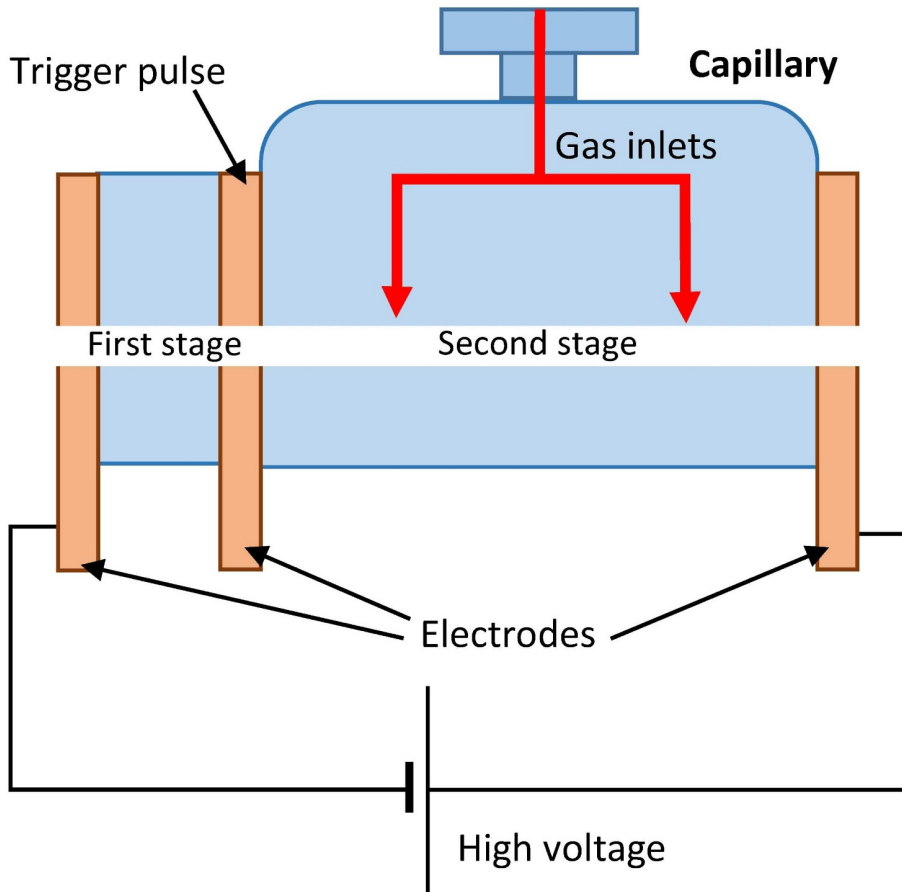


**Fig. 32.18.** Scheme of the segmented capillary: in the first stage the trigger discharge starts the ionisation of the entire gas confined into the capillary (second stage). This single unit can be extended by adding more units to reach m-scale capillaries.

#### 32.5.4 Beam-Driven Plasma Wakefields

One of the main goals of DESY's FLASHForward facility is to accelerate an externally injected witness bunch without degrading the longitudinal and transverse beam quality (i.e., while preserving charge, energy spread and emittance). This challenging task has seen significant progress in recent experiments. While much of this work is currently on-going, one particularly striking preliminary result is shown in Figure 32.19, demonstrating fine control over the longitudinal phase space resulting in very low-energy spread acceleration – on the sub-per-mille level.

Reaching this result involved finding the sweet spot in a large parameter space of beam- and plasma parameters. It should be emphasised that performing a multi-dimensional scan over thousands of shots demands ultra-stable beams and plasmas and a high level of machine tunability.

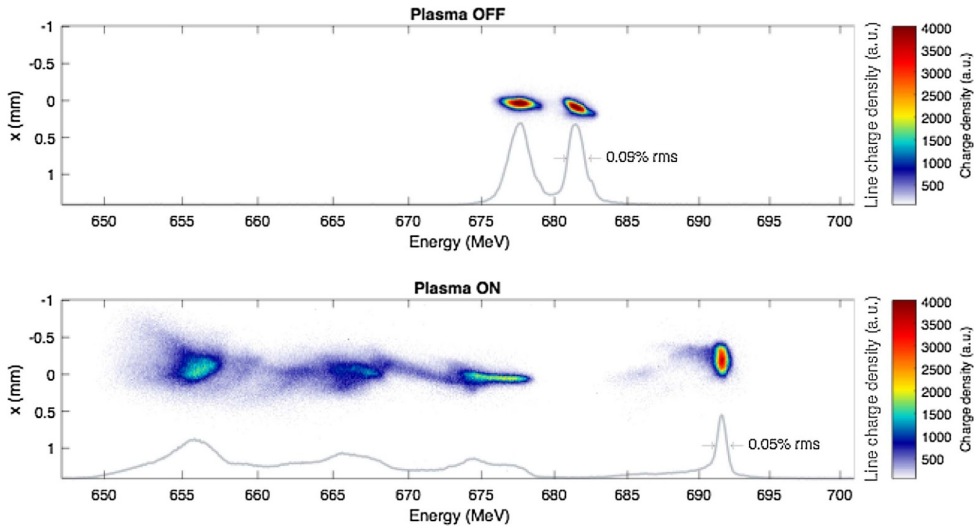


**Fig. 32.19.** Sample shots showing energy spectrum of a two-bunch beam, with a driver (left) and a witness bunch (right), with no interaction (top) and after passing through 33 mm of plasma (bottom). This working point was the result of an optimisation procedure to preserve energy spread. In fact, the initial (correlated) energy spread was approximately halved during acceleration, from 0.09% RMS to 0.05% RMS (spectral peak).

## 32.6 Use of Other Novel Technologies

### 32.6.1 Possible Alternative Injector Concepts

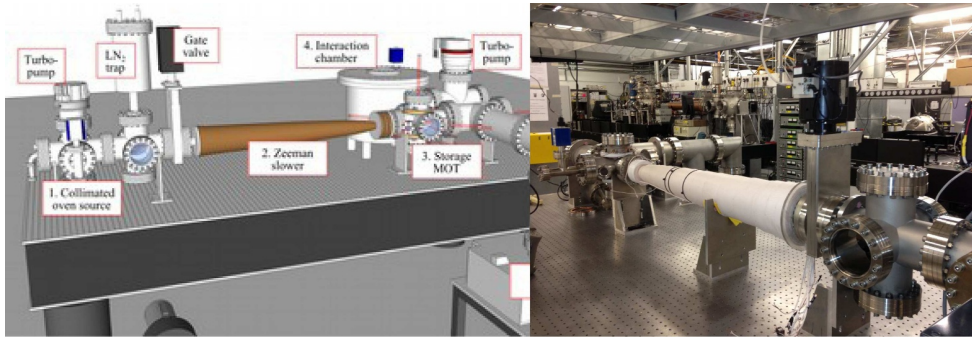
One of the objectives of the non-EU-funded EuPRAXIA work package WP10 is to monitor the world-wide efforts on the alternative injector concepts. This survey is performed as part of EuPRAXIA in order to present a complete picture of the competing advanced acceleration schemes and to evaluate if one of these concepts may serve as an alternative external injector in the future. This CDR-chapter lists some of the most prominent efforts in this field and shows some simulation and experimental results. While the efforts on ultra-cold electron sources will also be covered here, the current world-wide efforts can be split into two main directions:

- Dielectric laser acceleration (DLA)
- THz acceleration in dielectric loaded wave-guides

It must be noted that beam-driven dielectric wakefield accelerators are not within the scope of this report.

### 32.6.2 Ultra-Cold Electron Source

Electron sources are the basic components for many applications from electron diffraction and electron microscopy systems to state-of-the-art scientific research facilities utilizing particle accelerators, such as X-ray free-electron lasers, injector for laser-plasma based accelerators and high-energy electron-positron colliders, e.g. the International Linear Collider (ILC) and the Compact Linear Collider (CLIC). Here a brief description of the preliminary results undertaken at the University of Manchester is given.



(a) Sketch of the experimental setup.

(b) Photo of the experimental setup

**Fig. 32.20.** Sketch and photo of the experimental setup for the ultra cold electron source at Manchester University.

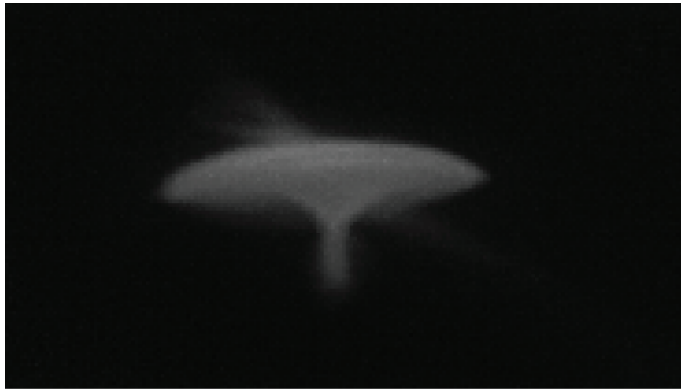


**Fig. 32.21.** The first electrons measured on 2nd March 2017 at Manchester University.

Cold atom electron source (CAES) have been proposed as an alternative to conventional photo-injectors or thermionic electron guns, which are widely used in today's particle accelerators. The CAES can produce electron beams with temperatures as low as 10 K ( $\Delta E \approx 1\text{meV}$ ), which is several orders of magnitude lower than for both thermionic and photo-emitter sources. The resultant beam emittance (which is a measure of beam quality in position and momentum phase space) is hence markedly improved, allowing ultra-high brightness electron bunches to be produced. These features are crucial for the next generation particle accelerators, e.g. free-electron lasers, plasma-based accelerators and the future high luminosity linear colliders, and for structure studies using high resolution electron diffraction. Figure 32.20 shows a schematic of the cold atom electron source and a picture of the setup.

First electrons were measured in spring 2017 (see Fig. 32.21) with the further characterisation of the source still ongoing.

Given the very experimental stage of this concept, it cannot be seen as a viable alternative for use at EuPRAXIA at the moment.

### 32.6.3 Dielectric Laser Acceleration (DLA)

Dielectric laser-driven acceleration (DLA) refers to the acceleration of electrons in photonic micro-structures made of dielectric and semiconductor materials which are

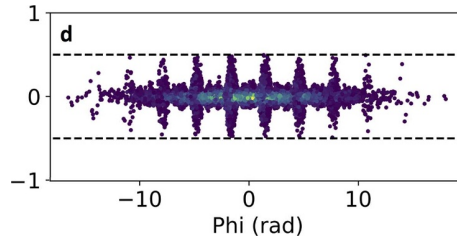


**Fig. 32.22.** Example of the modulation of the transverse beam size due to the phase-dependence of the focusing field. For more details see [859]

driven by lasers in the  $0.8\mu\text{m}$ – $10\mu\text{m}$  range. A good review can be found in [855]. Compared to laser plasma acceleration (LWFA), each individual laser is very low power, but the goal is to stage multiple DLAs with each powered by a dedicated laser at high repetition rate (MHz). First steps towards staging of these accelerators have been shown e.g. by the University of Erlangen, Germany. While the overall acceleration length achieved experimentally so far is still very limited (sub-cm length, sub-MeV overall energy gain), significant acceleration gradients (hundreds of MeV/m) have been observed [856].

Multiple leading groups have recently joined in the “Accelerator on a Chip International Program” (ACHIP) to combine the efforts on this topic. This program covers all aspects of building such an accelerator, thus not only acceleration, but also electron guns, transverse focusing, diagnostic and light generation [857]. With the transverse focusing of the electron beam also being performed by DLAs, Figure 32.22 shows a result of the simulation of an externally injected beam with a length of multiple laser-periods. Due to the phase-dependent transverse focusing, the transverse beam size gets modulated. While most of the studied concepts are driven by side-coupled lasers, currently studies on longitudinally coupled structures are being revitalised aiming to make use of the recent progress in manufacturing technology [858].

Given the current limitation of experimentally achieved energy gain of  $\leq 1\text{MeV}$ , it cannot be seen as a viable alternative for use at EuPRAXIA at the moment.

## THz Acceleration in Dielectric Lined Waveguides

A different concept of dielectric acceleration is the acceleration of electrons by THz lasers in dielectric loaded waveguides. Lasers are used to create THz fields, e.g. by optical rectification, which are then coupled into the waveguides. These structures consist of metallic waveguides which are lined with suitable dielectric material (e.g. quartz) to slow down the phase-velocity in the structures. Given the high frequency and the dielectric material, field levels of the order of several hundred MeV should be achievable without breakdown. As suitable THz sources are only currently being developed, only proof of principle experiments have been done so far [860]. At DESY, the AXISIS [861] project currently aims to set up the required laser and accelerator infrastructure to develop an all-THz driven light source.

All-optical solutions require the development of corresponding electron sources such as described in e.g. [862]. First experimental steps towards this goal have been achieved [863] but are still very limited in energy as well as beam quality. While these results are still far from fulfilling the requirements, they are an important stepping stone. On the other hand, simulation studies on the combination of a conventional S-band RF-gun with a THz linac also show promising results [864].

Given the current limitation of experimentally achieved energy gains of few 10ns of MeV, it cannot be seen as a viable alternative for use at EuPRAXIA at the moment. This may be revised if more powerful THz sources should become available.

#### 32.6.4 State of the Art in Fibre Optics Lasers

Another main task of WP10 is to monitor the progress of fiber lasers (FL) and to judge their applicability to the EuPRAXIA project. Currently almost all LWFA experiments are performed using Ti:Sa laser systems. While these systems are capable to deliver the required laser parameters for single shots, they feature the following main disadvantages:

- Low repetition rate. PW-class Ti:Sa systems are currently limited to the few Hz range, mainly limited by thermal issues.
- Low efficiency. PW-class TiSa systems have a very poor conversion efficiency from wall plug power to laser power.

In fiber lasers, optical fibers doped with rare earth ions (e.g. ytterbium) are used as gain materials. These lasers are wide spread in industry use due to their robustness, high repetition rate (CW possible) and high efficiency [865–869]. There are efforts ongoing to increase the power obtained from a single fiber, e.g:

- double clad fibers to allow increasing the pumping power
- large core fibers. If used, one loses the advantage of having a single mode fiber and additional tricks must be applied to compensate the associated disadvantages (e.g. strong coiling of the fibers, asymmetric fiber designs, ...).

Still, the power from a single fiber is limited to the mJ level. Several groups worldwide pursue efforts to combine multiple FL to reach higher laser power. In the next section some of this concepts are described.

While most currently used fiber lasers today operate in CV or short pulse mode, ultra-short pulse generation from fiber lasers is possible and was demonstrated using e.g. rare-earth-doped fibers providing the required bandwidth.

In summary FL feature the following key advantages:

- very high ratio of surface to volume and thus a well controllable cooling of the gain material.
- Ability to use materials with low quantum defect
- Laser guiding effect.
  - The fibers guides the laser and pump light and thus a good laser quality is obtained. (up to 90% for kW systems)
  - This allows using the very efficient diode lasers as pump lasers.
- high efficiency. (due to low intrinsic losses, usability of materials with low quantum defect)

The applicability of fiber lasers to LWFA has been studied e.g. in [870,871]

#### Combination Methods

In order to increase the maximal power obtainable from a fiber laser based system, there are multiple options to combine the power from multiple fibers.

- The possibility to resonantly drive the plasma wake with multiple comparably low-power lasers pulses spaced in time has been studied e.g. in [607]. While this is an interesting concept, it does not bring down the power per pulse to the level achievable by today's fiber laser systems and the rep-rate is also not suitable.

- The use of incoherently combined laser pulses has been studied in [872]. While the presented results achievable by the incoherent combination are better than one may expect, the disadvantages are too dominant.
- There are currently several groups worldwide trying to coherently combine the power of multiple fiber lasers. The central issues are the required high control over the individual fibers and the fast feedback [873–876] and e.g. the Jena group managed to combine multiple rod-type fiber lasers [877,878]. In France, the X-CAN project (which is a follow-up of the ICAN-project) is using thin fibers and is currently aiming to combine 64 fibers. While these concepts can in principle scaled to much more fibers, still significant engineering work must be done.

## Conclusion

While the fiber lasers have very promising results, their individual power is too small for LWFA applications. While they may be used as pumps for TiSa systems, the world-wide development of the coherent combination of multiple fibers has not yet achieved the required level and must be monitored for further developments. On the long run, the high rep-rate of fiber lasers will be crucial to the success of LWFA, not only because of the obvious benefits for the users, but also as it will allow to implement kHz-feedback concepts around the laser and LWFA.

## 32.7 Experience from FEL Test Experiments

As discussed in Chapter 1, there are currently three experimental projects towards an LWFA-based FEL – SOLEIL-LOA, CFEL-DESY (Lux) and KIT-FSU. The first two programs involve the longitudinal beam decompression, and KIT-FSU collaboration aims at the transverse gradient undulator scheme. The scientific programs of these projects are very different from each other, and therefore, they provide different experiences and teach us different lessons.

### SOLEIL-LOA

The SOLEIL-LOA project has FEL amplification as its final goal, and the intermediate steps include equipment commissioning, beam dynamics and incoherent radiation studies, weak and high-gain FEL processes. In this experiment, the regime with moderate electron energies of 150-200 MeV, and UV-XUV radiation 200-300 nm is explored in order to relief the amplification constraints which become more challenging as the radiation wavelength becomes shorter. The beamline is designed to provide tight and sophisticated control of the beam properties.

During the commissioning runs, different regimes of LWFA were explored, including usage of different target designed – a variable-length gas cell and super-sonic gas nozzle. For the further work the preference was given to the nozzle target, as it allows more flexibility for the setup and alignment. The nozzle setup was tested in the different regimes, using the pure low-Z gas (helium), or a mixture of low- and high-Z gases (helium + 1-2% nitrogen) for ionisation injection, with and without a plastic wafer for the shock-injection. For the final work the nozzle with gas mixture was chosen as a most straightforward and repeatable way of operation.

In this project a strong accent is made on the electrons manipulation beamline and it starts with the three specially designed variable strength quadrupoles (QUAPEVA) placed only a few millimetres downstream the LWFA nozzle. These

quadrupoles were shown to play a major role in the beam dynamics and manipulation of the beam transverse phase space. Due to the plasma effects on the laser propagation, LWFA beam intrinsically acquires some angle with the laser axis, which was shown to be reproducible along the session of shots. This effect may deviate from session-to-session and practically represents an important problem for the beamline alignment. It was shown that controlling the positions of QUAPEVA quadrupoles it is possible to separately correct orbit mis-steerings and minimise beam dispersion. This correction technique was realised with a help of a specially developed procedure of beam pointing alignment compensation (BPAC), which takes advantage of the motorised translations of the QUAPEVA quadrupoles. Performing this procedure at the beginning of each shooting session has proven to be a very useful tool for the dynamics control of the beamline alignment and beam transverse dispersions.

This manipulation of the longitudinal electron phase space is realised via a magnetic chicane. Besides the longitudinal beam decompression, the chicane allows to use a tuneable slit in the dispersive section for electron energy range selection. This part was essential for the photon observation, as it allows to select a single percent energy window and correlate it to the undulator radiation spectral features.

Therefore the beamline has proven to provide a tight and sophisticated control of the beam properties, and is able to correct the intrinsic limitations of the LWFA beam, such as relatively low pointing stability, emittance growth and energy spread. The matched electron beam leads to the successful observation of undulator synchrotron radiation after an 8 m transport path. In the experiments targeting the photon generation it was shown, that the proper advance beam manipulation is essential for the successful studies of the amplification. Several of the most relevant recent results are presented in [879–882].

## CFEL-DESY

The scientific programme of CFEL-DESY projects covers a wide range of tasks. It goes from the development of the plasma target and high-repetition-rate LWFA, to the spontaneous X-ray emission and FEL amplification, also including some aspects of software development.

A first challenging part of this work is the development of the dedicated LWFA scheme using a multi-inlet gas-cell with the tailored pressure profile and pulsed discharge. Such a scheme should allow the separate injector and accelerator stages and it targets the high-energy 600 MeV and high quality electron beams. The compatibility of the *Lux* beamline with the *Regae* linac machine also requires a dedicated gas evacuation system and limits the size of the interaction chamber.

As an intermediate step on the way to FEL amplifier, the *Lux* projects, also targets generation of the keV-level X-rays at a moderately high repetition-rate of 5 Hz.

## KIT-FSU

The KIT-FSU project aims – as a major milestone on the path towards a LWFA-driven transverse gradient undulator (TGU)-FEL – at demonstrating and investigating the TGU scheme for the case of spontaneous undulator radiation. Besides the continuous work on improving the LWFA performance at the JETI laser facility in Jena, it encompasses the development and realisation of a well-adapted beam transport line, the design, realisation and characterisation of a superconducting TGU and the theoretical and experimental investigation of the beam dynamics inside the TGU and subsequently the characteristics of the generated radiation.

The TGU scheme requires a beam transport line with adjustable dispersion at the entrance of the TGU for matching the electron energy to the TGU's magnetic flux density amplitude. That is achieved by a dogleg chicane, composed of a quadrupole triplet for beam capture and an achromat-like cell, in the first experimental approach consisting of two dipole magnets with a quadrupole triplet centred between them. Similar to the SOLEIL-LOA approach, the pointing uncertainty of the LWFA is coped with in particular by making the quadrupole magnets positionally adjustable and applying a beam-based alignment scheme. For this purpose dedicated in-vacuum quadrupole electromagnets have been designed and built. The described linear transport line and alignment procedure were successfully experimentally demonstrated. Our concept for the beam transport is currently being expanded to a non-linear scheme allowing for chromatic correction and proper matching of a wide electron energy distribution in order to take full advantage of the TGU scheme.

On the side of the TGU, various options of realising such a device had been investigated before a 40-period superconducting TGU with cylindrical pole shape was built. The device has been successfully quench-tested in a liquid Helium bath and is currently under commissioning in its own, conduction cooling-based cryostat. Two complementary experimental tests of the TGU are planned in order to gain a comprehensive understanding of the beam dynamics inside the TGU as well as of the TGU radiation properties: (1) A test with a well-defined electron beam at a conventional accelerator to be performed at the ARES linac which is a part of the SINBAD test facility in collaboration with DESY, Hamburg, and (2) a test at the laser wakefield accelerator at the JETI laser facility in Jena. While with the former “analytical” experiment the properties of the TGU in terms of beam dynamics and generated radiation will be mapped out in detail, the latter “synthetic” experiment will be the actual proof of principle for a LWFA-driven TGU light source.

## 32.8 Accelerator Prototyping – Report on Test Experiments

### 32.8.1 Introduction

In this chapter we report on the prototyping and experimental activity that some of the EuPRAXIA partners pursued to get information relevant for the present Conceptual Design Report (CDR). At the moment of writing the CDR, some of the experiments have already shown interesting results, others have been approved and already assembled; this chapter accounts for all of them with some examples. The experiments we cover here are focused on improving the plasma accelerated beam quality in terms of beam parameters, reproducibility and reliability.

One of these experiments will test advanced plasma cells to assess the sensitivity of the electron beam quality and reliability on impinging laser pulse and plasma parameters. This is a critical issue for EuPRAXIA as the dependencies of electron beam parameters on the driving laser and plasma conditions need to be understood fully.

The second experiment proposes a single shot, compact, non-destructive bunch length measurement. The electron bunch length is a crucial parameter in generating the plasma bubble typical of particle driven plasma accelerators; indeed, the driver bunch length needs to be finely tuned to trigger the plasma acceleration of the witness beam. Moreover, the high brightness beam of EuPRAXIA relies on high current, that is short bunch length. The single shot feature can be particularly useful for monitoring the reproducibility of plasma accelerated beams helping in adjusting the many key parameters. At the same time, having compact diagnostics is mandatory if one wants to build a compact accelerator.

The third experiment addresses the issues of capillary manufacturing to minimise mainly aging problems in all the schemes using capillaries (both laser- or beam-driven as well as in staged plasma accelerators). The multiple discharge may damage the capillaries affecting the plasma distribution and thus the accelerated beam parameters.

### 32.8.2 Testing Laser Wakefield Accelerator Sources for EuPRAXIA

A joint experiment, involving different institutes of the EuPRAXIA consortium, have been proposed; its main goal is to examine the electron beam quality and reproducibility from laser-driven plasma wakefield acceleration in a double gas cell. This is a key component of the development work required for EuPRAXIA, aiming to deliver compact, high quality, high rep-rate electron beam sources based on plasma acceleration technology.

Recent progresses in Laser Wakefield Acceleration (LWFA) have demonstrated acceleration of electron beams to  $> \text{GeV}$  energies. However, in order to build a facility based on LWFA-driven beams, their stability, reproducibility, energy spread, etc. need to be improved further. In LWFA, an intense laser pulse propagates through an underdense plasma and drives a plasma wave. It leads to large longitudinal and transverse fields, which are capable of accelerating and focusing electrons.

Typically, the plasma is formed by ionisation of a gaseous medium provided by a supersonic gas jet, a gas-filled capillary or a gas cell. Along with the stability of the driving laser, the properties of the plasma medium and its stability affect the beam quality in LWFA. In order to produce stable, high-quality electron beams for applications, it is essential to delineate the effects of the laser driver from that of the plasma medium. The determination of tolerances in the variation of several key parameters is crucial for designing an accelerator such as EuPRAXIA and is poorly documented: such an experiment may provide data which are much needed to benchmark simulations and speed up LWFA development.

The experiment will investigate the influence of laser parameters on controlling the electron beam parameters for given tailored plasma profiles; this is of paramount importance to EuPRAXIA.

The experiment will be hosted in the Lund Laser Centre (LLC). In order to have a meaningful test, it is important that the drive laser is well characterised for all its parameters, including energy, pulse length, spectrum, wave-front and pointing fluctuations on every shot in order to delineate the driver effects from those induced by the plasma. The 20TW laser at the LLC is ideal for this test in this regard as it not only fields all the necessary diagnostics for this experiment but also employs fast pointing control in order to stabilise the laser pointing from shot to shot.

The experiment will use the 20TW laser facility at LLC. The high-power laser beam will be focused using an  $F/20$  parabolic mirror to a spot size of  $\sim 20 \mu\text{m}$  yielding a normalised vector potential in vacuum of 1.4. The gas cell will be pressurised through two separate fill tubes to  $\leq 1 \text{bar}$  to give electron densities in the range  $0\text{--}2 \times 10^{19} \text{cm}^{-3}$ . One tube will be used to fill the first cell with a helium (or hydrogen)-nitrogen mix, and the second tube will fill the second cell with pure helium (hydrogen). This will allow to investigate the performance of the acceleration under different injection conditions.

A short pulse transverse probe will be used to diagnose the performance of the gas cell (plasma density) and to characterise online the plasma profile with a Mach-Zehnder interferometer. The stability of the gas cell during the acceleration will be monitored shot-to-shot. The transmitted laser pulse will be sampled onto a spectrometer to measure the effects on the laser spectrum due to the plasma wave formation.

A magnetic spectrometer with scintillator-based detectors will measure the produced electron spectrum and angular distribution.

The experimental team is composed of researchers from Imperial College London, CNRS, CEA, INFN and CLF. Each collaborator has proven expertise in LWFA and gas cell design and is actively involved with the EuPRAXIA design project.

The proposal will be partially funded by the ARIES network and 4 weeks of access at the laser facility in Lund has been planned. The highly characterised, pointing-stabilised laser in the Lund Laser Centre is of fundamental importance for this experiment.

### 32.8.3 Non-Destructive Bunch Length Measurement Based on Smith-Purcell Radiation

Non-destructive bunch measurements are a very important diagnostics in a plasma accelerator to improve reliability and repeatability by tuning the (many) parameters affecting the acceleration process. The experiment aims to measure the bunch length at the SPARC LAB linear accelerator by using Coherent Smith-Purcell radiation and comparing the results with other diagnostic tools. The innovative Smith-Purcell detectors are designed by the LAL group.

Smith-Purcell radiation is emitted when an electron bunch is traveling close to a corrugated planar device; from the peculiarity of the emitted radiation spectrum it is possible to measure the bunch length. The beam trajectory is a fundamental parameter and the beam axis will be adjusted with two BPMs, one upstream and one downstream as well as a charge monitor that is installed downstream. Downstream optical transition radiation (OTR) screens will be used as well.

The installed detectors are described in Figure 32.23. since there is a correlation between the Smith-Purcell radiation angle and its frequency, it is possible to measure the whole emitted radiation spectrum in one single shot.

To look for the signal, the accelerator was delivering the maximum possible charge (to minimise the signal noise) and the beam axis was set as close as possible to the grating. Afterwards the grating position has been moved to understand the background and it has been changed to measure the signal with different dynamic ranges. The bunch profile could also be changed using the low energy bunch compressor (first two Linac sections). The results are being analyzed and compared to standard bunch length measurements with an RF deflector.

The fully coherent signal due to the very large pitch grating has been observed. The measurement of the fully coherent signal is always coupled with the measurement of the background by replacing the grating by a blank plane (grating without teeth). Measuring the partially coherent signal with several gratings having different pitches allows a measurement of the signal yield on a large dynamic range. By comparing this signal yield with the fully coherent signal the form factor of the bunch can be extracted while eliminating most theoretical uncertainties on the description of the single electron yield.

### 32.8.4 3D-Printed Capillary for a Hydrogen-Filled Discharge for Plasma Acceleration

Plasma-based acceleration experiments require capillaries with a radius of a few hundred microns to confine plasma up to a centimetre scale capillary length. A long and controlled plasma channel allows to sustain high fields which may be used for the manipulation of the electron beam or to accelerate electrons. The production of these capillaries is relatively complicated and expensive since they are usually made with hard materials whose manufacturing requires highly specialised industries. Fine

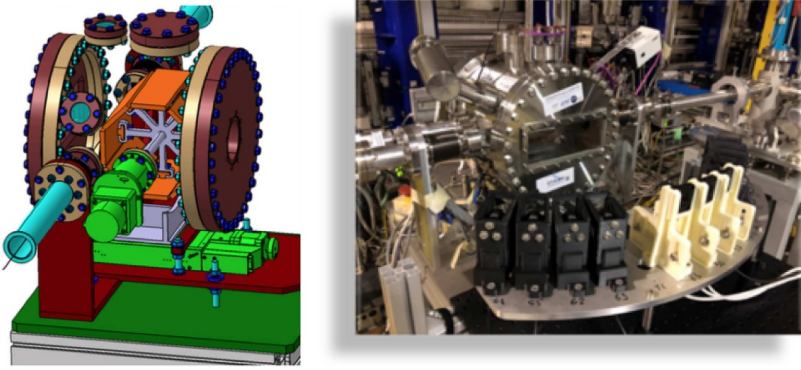


**Fig. 32.23.** The SPARC\_LAB experimental apparatus (right) and conceptual drawing (left), as seen after its installation in 2018.

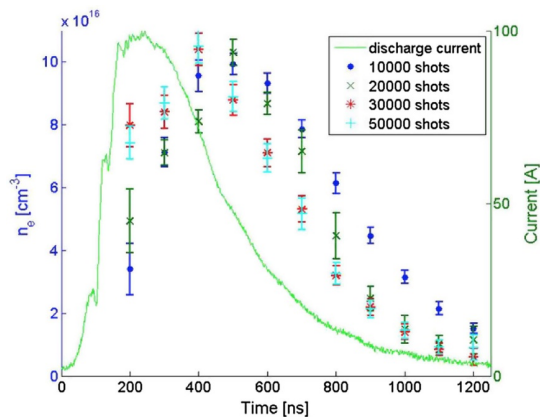


**Fig. 32.24.** Discharge current profile and averaged density along the entire capillary length acquired every 100 ns of delay from the discharge trigger. Each point is averaged over 10 shots and over the entire capillary length. The error bars represent the standard deviation around the mean value [883] (reprinted with permission of AIP Publishing).

variations of the capillary shape may significantly increase the cost and time needed to produce them.

SPARC\_LAB demonstrated the possibility of using 3D printed polymeric capillaries to drive a hydrogen-filled plasma discharge up to 1 Hz repetition rate in an RF-based electron linac [883]. The plasma density distribution has been measured after several shot intervals, showing the effect of the surface ablation on the plasma density distribution. This effect is almost invisible in the earlier stages of the discharge. After more than 55,000 shots (corresponding to more than 16 h of working time), the effects of the ablation on the plasma density distribution are not evident and the capillary can still be used.

The use of these capillaries may significantly reduce the cost and time for prototyping, allowing us to easily manipulate their geometry, laying another building block for future cheap and compact particle accelerators.

The effects of the ablation of the capillary can be observed by measuring the average electron plasma density variation after thousands of shots, as shown in Figure 32.24. The density has been acquired by varying the trigger of the Intensified Charge-Coupled Device (ICCD) with respect to the discharge trigger with 100

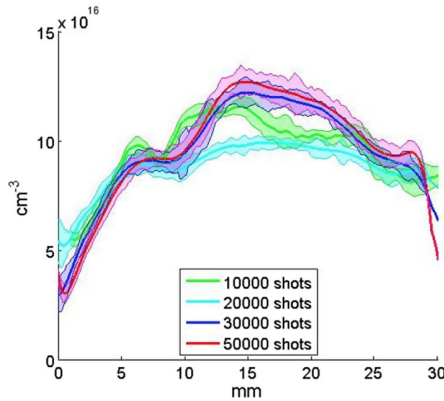


**Fig. 32.25.** Plasma electron density distribution along the capillary measured at the maximum density value for an increasing number of shots [883] (reprinted with permission of AIP Publishing).

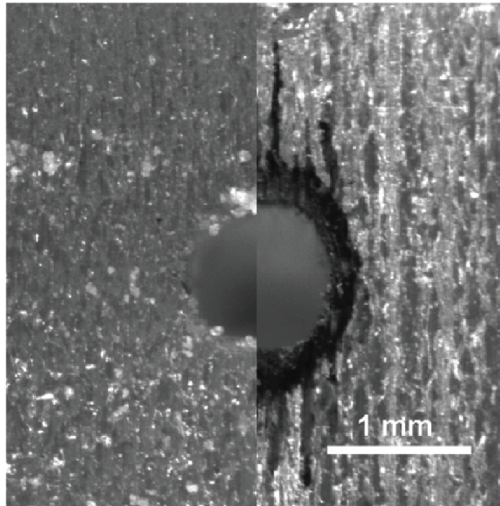


**Fig. 32.26.** Entrance of the capillary after the print (left) and after more than 55,000 shots (right). The burns on the entrance are probably caused by the electrons impinging on the plastic during the alignment [883] (reprinted with permission of AIP Publishing).

ns steps. Each point is averaged over 10 shots, and each density value is averaged over the entire capillary length. The error bars represent the standard deviation around the mean value. As can be seen from the earliest measurements taken after 10,000 shots, the electron density in the earlier shots reached its maximum of  $\approx 10^{17} \text{ cm}^{-3}$  around 500 ns after the discharge, and then it started to decrease exponentially at 600 ns. By increasing the number of shots, the electron density peak moves to an earlier time (almost 400 ns after the trigger), but its value does not change.

Due to the burns caused by the earlier discharges, when the thermal conduction is higher and the heat flux can penetrate more easily into the capillary walls, the capillary surface becomes harder and it changes its thermal conductivity reducing the possibility to be ablated and increasing the heat transfer to the gas letting it be ionised faster. The shot-to-shot error on the averaged plasma density around the maximum, i.e. between 300 and 600 ns, is lower than 7% even for the measurements obtained

at 50,000 shots. The plasma density profiles along the capillary acquired when the plasma density reached its maximum, i.e., at 500 ns delay for the earlier shots and 400 ns for the latest, have been plotted in Figure 32.25. After more than 50,000 shots (corresponding to more than 16h of working time), no significant degradation of the longitudinal plasma distribution has been revealed.

The high plasma temperature which heats the capillary surface also altered the optical properties of the capillary. The optical transmission in the range between 400 and 700 nm has been measured before and after 55,000 shots. The burns caused by the discharges reduce the transmission of light, especially at the lower wavelengths, possibly due to surface modification because of hardening. This is not pronounced enough to prevent the observation of the plasma emitted light, but the transmittance of the Balmer beta line is reduced by almost 17%. The changes in the transmittance may also be caused partly by the electrons of the accelerated beams which during the alignment have hit the capillary surface or by the ablation caused by the plasma itself. The different transmittance of the light has been taken into account during the spectroscopic analysis.

The picture of the entrance hole of the capillary has been acquired before and after more than 55,000 shots (Fig. 32.26) by using a microscope with a magnification of 12.5. On the left side of Figure 32.26, it is possible to see the capillary before its use. The entrance of the capillary has a 1 mm diameter, and the internal surface is not perfectly smooth due to the printing process. On the right, the figure shows the same hole after 55,000 shots placed in high vacuum and exposed to electron bunches. The radius of the capillary has been changed during the operation, and it is larger by  $79 \pm 8 \mu\text{m}$  than in the left image. A microscope was also used to observe the transverse profile of the capillary. From the comparison between the edge (on the right of the picture) and the middle part of the capillary, it was observed that the ablation affects the capillary uniformly. The radius gets larger by 1.4  $\mu\text{m}$  per shot, which is comparable with the values obtained with sapphire capillaries.

### 32.9 CAD Model of the Conceptual EuPRAXIA Facility Layout

Some example screenshots of the CAD model of the proposed EuPRAXIA facility layout are shown below. The current model is conceptual, but will form a basis for the detailed technical layout to be developed in the next phase of EuPRAXIA. The full CAD model is available upon request.

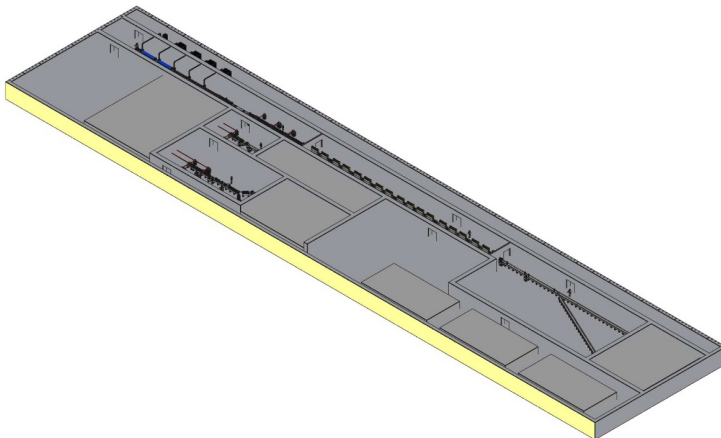


**Fig. 32.27.** Screenshot of the CAD model of the proposed EuPRAXIA facility layout. Here, the laser-driven plasma acceleration construction is shown in a perspective view.

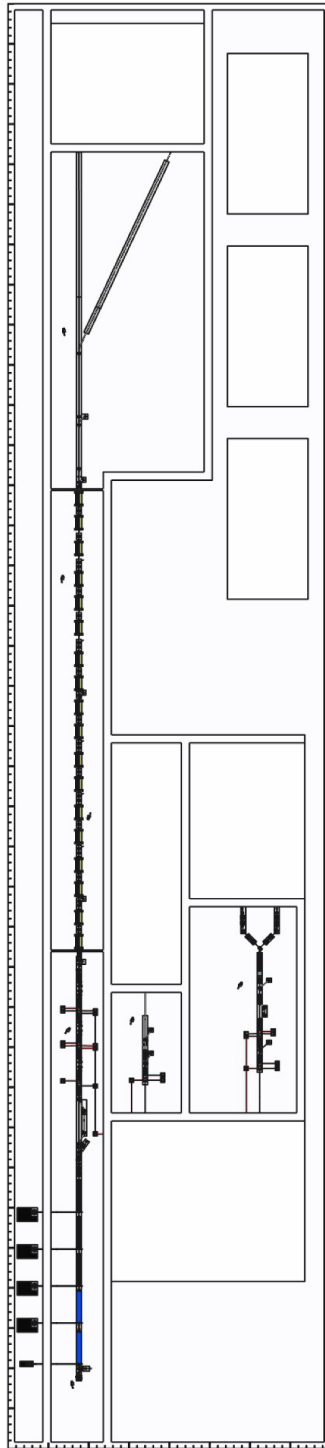


**Fig. 32.28.** Screenshot of the CAD model of the proposed EuPRAXIA facility layout. Here, the laser-driven plasma acceleration construction site is shown in a top view.

### 33 EuPRAXIA Publications and Conference Contributions

The following list provides an overview of the journal publications and conference proceedings published as part of the EuPRAXIA design study. Many more papers were published and presented in the past four years on topics and results related to the project, these could not all be included here but are mentioned in many cases as references throughout this report.

#### 33.1 List of EuPRAXIA Peer-Reviewed Publications

1. Xia G., Bonatto A., Pizzato Nunes R., Liang L., Jakobsson O., Zhao Y., Williamson B., Davut C., Wang X. **Plasma Beam Dumps for the EuPRAXIA Facility**. *Instruments* 4(2) 10 (2020). [10.3390/instruments4020010](https://doi.org/10.3390/instruments4020010)
2. Ghaith A., Loulergue A., Oumbarek-Espinos D., Marcouille O., Valteau M., Labat M., Corde S., Couprie M.-E. **Electron Beam Brightness and Undulator Radiation Brilliance for a Laser Plasma Acceleration Based Free Electron Laser**. *Instruments* 4 1 (2020). [doi:10.3390/instruments4010001](https://doi.org/10.3390/instruments4010001)
3. Nguyen F., Bernhard A., Chance A., Couprie M.-E., Dattoli G., Lechner C., Marocchino A., Maynard G., Petralia A., Rossi A.R. **Free electron laser performance within the EuPRAXIA facility**. *Instruments* 4(1) 5 (2020). [doi:10.3390/instruments4010005](https://doi.org/10.3390/instruments4010005)
4. Siders C.W., Galvin T., Erlandson A., Bayramian A., Reagan B., Sistrunk E., Spinka T., Haefner C. **Wavelength Scaling of Laser Wakefield Acceleration for the EuPRAXIA Design Point**. *Instruments* 3(3) 44 (2019). [10.3390/instruments3030044](https://doi.org/10.3390/instruments3030044)
5. Toci G., Mazzotta Z., Labate L., Mathieu F., Vannini M., Patrizi B., Gizzi L.A. **Conceptual Design of a Laser Driver for a Plasma Accelerator User Facility**. *Instruments* 3(3) 40 (2019). [10.3390/instruments3030040](https://doi.org/10.3390/instruments3030040)
6. Huebner M., Will I., Koerner J., Reiter J., Lenski M., Tuemmler J., Hein J., Eppich B., Ginolas A., Crump P. **Novel High-Power, High Repetition Rate Laser Diode Pump Modules Suitable for High-Energy Class Laser Facilities**. *Instruments* 3(3) 34 (2019). [10.3390/instruments3030034](https://doi.org/10.3390/instruments3030034)
7. Ghaith A., Oumbarek D., Kitegi C., Valteau M., Marteau F., Couprie M.-E. **Permanent Magnet Based Quadrupoles for Plasma Acceleration Sources**. *Instruments* 3(2) 27 (2019). [doi:10.3390/instruments3020027](https://doi.org/10.3390/instruments3020027)
8. Ghaith A. et al. **Tunable High Spatio-Spectral Purity Undulator Radiation from a Transported Laser Plasma Accelerated Electron Beam**. *Scientific Reports* 9 19020 (2019). [10.1038/s41598-019-55209-4](https://doi.org/10.1038/s41598-019-55209-4)
9. Tomassini P., Terzani D., Labate L., Toci G., Chance A., Nghiem P.A.P., Gizzi L.A. **High quality electron bunches for a multi-stage GeV accelerator with the Resonant Multi-Pulse Ionization injection**. *Physical Review Accelerators and Beams*, in press (2019).
10. Weikum M. et al. **EuPRAXIA – a compact cost-efficient particle and radiation source**. *AIP Conference Proceedings* 2160 040012 (2019). [10.1063/1.5127692](https://doi.org/10.1063/1.5127692)
11. Terzani D., Londrillo P. **A fast and accurate numerical implementation of the envelope model for laser-plasma dynamics**. *Computer Physics Communications* 242 49 – 59 (2019). [10.1016/j.cpc.2019.04.007](https://doi.org/10.1016/j.cpc.2019.04.007)
12. Ferran Pousa A., Martinez de la Ossa A., Brinkmann R., Assmann R.W. **Compact Multistage Plasma-Based Accelerator Design for Correlated Energy Spread Compensation**. *Physical Review Letters* 123 (5) 054801 (2019). [10.1103/PhysRevLett.123.054801](https://doi.org/10.1103/PhysRevLett.123.054801)

13. Kokurewicz K., Brunetti E., Welsh G. H., Wiggins S. M., Boyd M., Sorensen A., Chalmers A. J., Schettino G., Subiel A., DesRosiers C., Jaroszynski D. **A. Focused very high-energy electron beams as a novel radiotherapy modality for producing high-dose volumetric elements.** Scientific Reports 9 10837 (2019). [10.1038/s41598-019-46630-w](https://doi.org/10.1038/s41598-019-46630-w)
14. Hidding B., Beaton A., Boulton L., Corde S., Doepp A., Habib F. A., Heinemann T., Irman A., Karsch S., Kirwan G., Knetsch A., Manahan G. G., de la Ossa A. M., Nutter A., Scherkl P., Schramm U., Ullmann D. **Fundamentals and Applications of Hybrid LWFA-PWFA.** Applied Sciences-Basel 9 (13) 2626 (2019). [10.3390/app9132626](https://doi.org/10.3390/app9132626)
15. Hidding B., Foster B., Hogan M. J., Muggli P., Rosenzweig J. B. **Directions in plasma wakefield acceleration.** Philosophical Transactions of The Royal Society A – Mathematical Physical and Engineering Sciences 377 (2151) 20190215 (2019). [10.1098/rsta.2018.0215](https://doi.org/10.1098/rsta.2018.0215)
16. Panetta D., Labate L., Billeci L., Di Lascio N., Esposito G., Faita F., Mettivier G., Palla D., Pandola L., Pisciotta P., Russo G., Sarno A., Tomassini P., Salvadori P. A., Gizzi L. A., Russo P. **Numerical simulation of novel concept 4D cardiac microtomography for small rodents based on all-optical Thomson scattering X-ray sources.** Scientific Reports 9 8439 (2019). [10.1038/s41598-019-44779-y](https://doi.org/10.1038/s41598-019-44779-y)
17. Brandi F., Gizzi L. A. **Optical diagnostics for density measurement in high-quality laser-plasma electron accelerators.** High Power Laser Science and Engineering 7 e26 (2019). [10.1017/hpl.2019.11](https://doi.org/10.1017/hpl.2019.11)
18. Shalloo R. J., Arran C., Picksley A., von Boetticher A., Corner L., Holloway J., Hine G., Jonnerby J., Milchberg H. M., Thornton C., Walczak R., Hooker S.M. **Low-density hydrodynamic optical-field-ionized plasma channels generated with an axicon lens.** Physical Review Accelerators and Beams 22 (4) 041302 (2019). [10.1103/PhysRevAccelBeams.22.041302](https://doi.org/10.1103/PhysRevAccelBeams.22.041302)
19. Alejo A., Walczak R., Sarri G. **Laser-driven high-quality positron sources as possible injectors for plasma-based accelerators.** Scientific Reports 9 5279 (2019). [10.1038/s41598-019-41650-y](https://doi.org/10.1038/s41598-019-41650-y)
20. Mehrling T. J., Fonseca R. A., Martinez de la Ossa A., Vieira J. **Mechanisms for the mitigation of the hose instability in plasma-wakefield accelerators.** Physical Review Accelerators and Beams 22 (3) 031302 (2019). [10.1103/PhysRevAccelBeams.22.031302](https://doi.org/10.1103/PhysRevAccelBeams.22.031302)
21. Shpakov V. et al. **Longitudinal Phase-Space Manipulation with Beam-Driven Plasma Wakefields.** Physical Review Letters 122 (11) 114801 (2019). [10.1103/PhysRevLett.122.114801](https://doi.org/10.1103/PhysRevLett.122.114801)
22. Wilson T. C., Li F. Y., Weng S. M., Chen M., McKenna P., Sheng Z. M. **Laser pulse compression towards collapse and beyond in plasma.** Journal of Physics B-Atomic Molecular and Optical Physics 52 (5) 055403 (2019). [10.1088/1361-6455/ab0132](https://doi.org/10.1088/1361-6455/ab0132)
23. Balerna A. et al. **The Potential of EuPRAXIA@SPARC LAB for Radiation Based Techniques.** Condensed Matter 4 (1) 30 (2019). [10.3390/condmat4010030](https://doi.org/10.3390/condmat4010030)
24. Biagioni A. et al. **Temperature analysis in the shock waves regime for gas-filled plasma capillaries in plasma-based accelerators.** Journal of Instrumentation 14 C03002 (2019). [10.1088/1748-0221/14/03/C03002](https://doi.org/10.1088/1748-0221/14/03/C03002)
25. Hussein A. E. et al. **Laser-wakefield accelerators for high-resolution X-ray imaging of complex microstructures.** Scientific Reports 9 3249 (2019). [10.1038/s41598-019-39845-4](https://doi.org/10.1038/s41598-019-39845-4)
26. Li X., Chance A., Nghiem P.A.P. **Preserving emittance by matching out and matching in plasma wakefield acceleration stage.** Physical Review

- Accelerators and Beams 22 (2) 021304 (2019). [10.1103/PhysRevAccelBeams.22.021304](https://doi.org/10.1103/PhysRevAccelBeams.22.021304)
27. Tomassini P., De Nicola S., Labate L., Londrillo P., Fedele R., Terzani D., Nguyen F., Vantaggiato G., Gizzi L. A. **High-quality GeV-scale electron bunches with the Resonant Multi-Pulse Ionization Injection**. Nuclear Instruments & Methods in Physics Research Section A-Accelerators Spectrometers Detectors and Associated Equipment 909 1 – 4 (2018). [10.1016/j.nima.2018.03.002](https://doi.org/10.1016/j.nima.2018.03.002)
  28. Couprie M.-E. **Towards compact Free Electron-Laser based on laser plasma accelerators**. Nuclear Instruments & Methods in Physics Research Section A-Accelerators Spectrometers Detectors and Associated Equipment 909 5 – 15 (2018).
  29. Chiadroni E. et al. **Overview of plasma lens experiments and recent results at SPARC LAB**. Nuclear Instruments & Methods in Physics Research Section A-Accelerators Spectrometers Detectors and Associated Equipment 909 16 – 20 (2018). [10.1016/j.nima.2018.02.014](https://doi.org/10.1016/j.nima.2018.02.014)
  30. Li X., Mosnier A., Nghiem P.A.P. **Design of a 5 GeV laser-plasma accelerating module in the quasi-linear regime**. Nuclear Instruments & Methods in Physics Research Section A-Accelerators Spectrometers Detectors and Associated Equipment 909 49 – 53 (2018). [10.1016/j.nima.2018.02.104](https://doi.org/10.1016/j.nima.2018.02.104)
  31. Rossi A. R., Petrillo V., Bacci A., Chiadroni E., Cianchi A., Ferrario M., Giribono A., Marocchino A., Conti M. Rossetti, Serafini L., Vaccarezza C. **Plasma boosted electron beams for driving Free Electron Lasers**. Nuclear Instruments & Methods in Physics Research Section A-Accelerators Spectrometers Detectors and Associated Equipment 909 54 – 57 (2018). [10.1016/j.nima.2018.02.092](https://doi.org/10.1016/j.nima.2018.02.092)
  32. Gizzi L.A., Koester P., Labate L., Mathieu F., Mazzotta Z., Toci G., Vannini M. **A viable laser driver for a user plasma accelerator**. Nuclear Instruments & Methods in Physics Research Section A-Accelerators Spectrometers Detectors and Associated Equipment 909 58 – 66 (2018). [10.1016/j.nima.2018.02.089](https://doi.org/10.1016/j.nima.2018.02.089)
  33. Romeo S., Chiadroni E., Croia M., Ferrario M., Giribono A., Marocchino A., Mira F., Pompili R., Rossi A. R., Vaccarezza C. **Simulation design for forthcoming high quality plasma wakefield acceleration experiment in linear regime at SPARC LAB**. Nuclear Instruments & Methods in Physics Research Section A-Accelerators Spectrometers Detectors and Associated Equipment 909 71 – 75 (2018). [10.1016/j.nima.2018.02.081](https://doi.org/10.1016/j.nima.2018.02.081)
  34. Svystun E., Assmann R. W., Dorda U., Ferran Pousa A., Heinemann T., Marchetti B., Martinez de la Ossa A., Walker P.A., Weikum M.K., Zhu J. **Beam quality preservation studies in a laser-plasma accelerator with external injection for EuPRAXIA**. Nuclear Instruments & Methods in Physics Research Section A-Accelerators Spectrometers Detectors and Associated Equipment 909 90 – 94 (2018). [10.1016/j.nima.2018.02.060](https://doi.org/10.1016/j.nima.2018.02.060)
  35. Walker P. A., Assmann R. W., Brinkmann R., Chiadroni E., Dorda U., Ferrario M., Kocon D., Marchetti B., Pribyl L., Specka A., Walczak R. **Layout considerations for a future electron plasma research accelerator facility EuPRAXIA**. Nuclear Instruments & Methods in Physics Research Section A-Accelerators Spectrometers Detectors and Associated Equipment 909 111 – 113 (2018). [10.1016/j.nima.2018.02.028](https://doi.org/10.1016/j.nima.2018.02.028)
  36. Vantaggiato G., Labate L., Tomassini P., Gizzi L. A. **Modelling of pulse train generation for resonant laser wakefield acceleration using a delay mask**. Nuclear Instruments & Methods in Physics Research Section A-Accelerators Spectrometers Detectors and Associated Equipment 909 114 – 117 (2018). [10.1016/j.nima.2018.02.024](https://doi.org/10.1016/j.nima.2018.02.024)

37. Costa G., Anania M. P., Bisesto F., Chiadroni E., Cianchi A., Curcio A., Ferrario M., Filippi F., Marocchino A., Mira F., Pompili R., Zigler A. **Characterization of self-injected electron beams from LWFA experiments at SPARC LAB**. Nuclear Instruments & Methods in Physics Research Section A-Accelerators Spectrometers Detectors and Associated Equipment 909 118 – 122 (2018). [10.1016/j.nima.2018.02.008](https://doi.org/10.1016/j.nima.2018.02.008)
38. Ferrario M. et al. **EuPRAXIA@SPARC LAB Design study towards a compact FEL facility at LNF**. Nuclear Instruments & Methods in Physics Research Section A-Accelerators Spectrometers Detectors and Associated Equipment 909 134 – 138 (2018). [10.1016/j.nima.2018.01.094](https://doi.org/10.1016/j.nima.2018.01.094)
39. Pompili R. et al. **Recent results at SPARC LAB**. Nuclear Instruments & Methods in Physics Research Section A-Accelerators Spectrometers Detectors and Associated Equipment 909 139 – 144 (2018). [10.1016/j.nima.2018.01.071](https://doi.org/10.1016/j.nima.2018.01.071)
40. Giribono A., Bacci A., Chiadroni E., Cianchi A., Croia M., Ferrario M., Marocchino A., Petrillo V., Pompili R., Romeo S., Conti M. Rossetti, Rossi A. R., Vaccarezza C. **RF injector design studies for the trailing witness bunch for a plasma-based user facility**. Nuclear Instruments & Methods in Physics Research Section A-Accelerators Spectrometers Detectors and Associated Equipment 909 229 – 232 (2018). [10.1016/j.nima.2018.01.042](https://doi.org/10.1016/j.nima.2018.01.042)
41. Scifo J. et al. **Nano-machining surface analysis and emittance measurements of a copper photocathode at SPARC LAB**. Nuclear Instruments & Methods in Physics Research Section A-Accelerators Spectrometers Detectors and Associated Equipment 909 233 – 238 (2018). [10.1016/j.nima.2018.01.041](https://doi.org/10.1016/j.nima.2018.01.041)
42. Diomede M. et al. **Preliminary RF design of an X-band linac for the EuPRAXIA@SPARC LAB project**. Nuclear Instruments & Methods in Physics Research Section A-Accelerators Spectrometers Detectors and Associated Equipment 909 243 – 246 (2018). [10.1016/j.nima.2018.01.032](https://doi.org/10.1016/j.nima.2018.01.032)
43. Biagioni A. et al. **Wake fields effects in dielectric capillary**. Nuclear Instruments & Methods in Physics Research Section A-Accelerators Spectrometers Detectors and Associated Equipment 909 247 – 251 (2018). [10.1016/j.nima.2018.01.028](https://doi.org/10.1016/j.nima.2018.01.028)
44. Giribono A., Bacci A., Chiadroni E., Cianchi A., Croia M., Ferrario M., Marocchino A., Petrillo V., Pompili R., Romeo S., Conti M. Rossetti, Rossi A. R., Vaccarezza C. **EuPRAXIA@SPARC LAB: The high-brightness RF photo-injector layout proposal**. Nuclear Instruments & Methods in Physics Research Section A-Accelerators Spectrometers Detectors and Associated Equipment 909 282 – 285 (2018). [10.1016/j.nima.2018.03.009](https://doi.org/10.1016/j.nima.2018.03.009)
45. Villa F., Cianchi A., Coreno M., Dabagov S., Marcelli A., Minicozzi V., Morante S., Stellato F. **Design study of a photon beamline for a soft X-ray FEL driven by high gradient acceleration at EuPRAXIA@SPARC LAB**. Nuclear Instruments & Methods in Physics Research Section A-Accelerators Spectrometers Detectors and Associated Equipment 909 294 – 297 (2018). [10.1016/j.nima.2018.02.091](https://doi.org/10.1016/j.nima.2018.02.091)
46. Vaccarezza C. et al. **EUPRAXIA@SPARC LAB: Beam dynamics studies for the X-band Linac**. Nuclear Instruments & Methods in Physics Research Section A-Accelerators Spectrometers Detectors and Associated Equipment 909 314 – 317 (2018). [10.1016/j.nima.2018.01.100](https://doi.org/10.1016/j.nima.2018.01.100)
47. Delbos N., Werle C., Dornmair I., Eichner T., Huebner L., J alas S., Jolly S. W., Kirchen M., Leroux V., Messner P., Schnepf M., Trunk M., Walker P. A., Winkler P., Maier A.R. **Lux – A laser-plasma driven undulator beamline**. Nuclear Instruments & Methods in Physics Research Section A-Accelerators Spectrometers Detectors and Associated Equipment 909 318 – 322 (2018). [10.1016/j.nima.2018.01.082](https://doi.org/10.1016/j.nima.2018.01.082)

48. Cianchi A., Andreani C., Bedogni R., Festa G., Sans-Planell O., Senesi R. **A complementary compact laser based neutron source.** Nuclear Instruments & Methods in Physics Research Section A-Accelerators Spectrometers Detectors and Associated Equipment 909 323 – 326 (2018). [10.1016/j.nima.2018.01.052](https://doi.org/10.1016/j.nima.2018.01.052)
49. Filippi F., Anania M. P., Biagioni A., Brentegani E., Chiadroni E., Cianchi A., Deng A., Ferrario M., Pompili R., Rosenzweig J., Zigler A. **Tapering of plasma density ramp profiles for adiabatic lens experiments.** Nuclear Instruments & Methods in Physics Research Section A-Accelerators Spectrometers Detectors and Associated Equipment 909 339 – 342 (2018). [10.1016/j.nima.2018.04.037](https://doi.org/10.1016/j.nima.2018.04.037)
50. Filippi F., Anania M. P., Biagioni A., Brentegani E., Chiadroni E., Cianchi A., Ferrario M., Marocchino A., Zigler A. **Plasma ramps caused by outflow in gas-filled capillaries.** Nuclear Instruments & Methods in Physics Research Section A-Accelerators Spectrometers Detectors and Associated Equipment 909 346 – 349 (2018). [10.1016/j.nima.2018.02.102](https://doi.org/10.1016/j.nima.2018.02.102)
51. Cianchi A. et al. **Conceptual design of electron beam diagnostics for high brightness plasma accelerator.** Nuclear Instruments & Methods in Physics Research Section A-Accelerators Spectrometers Detectors and Associated Equipment 909 350 – 354 (2018). [10.1016/j.nima.2018.02.095](https://doi.org/10.1016/j.nima.2018.02.095)
52. Marongiu M., Castellano M., Chiadroni E., Cianchi A., Franzini G., Giribono A., Mostacci A., Palumbo L., Shpakov V., Stella A., Variola A. **Energy measurements by means of transition radiation in novel Linacs.** Nuclear Instruments & Methods in Physics Research Section A-Accelerators Spectrometers Detectors and Associated Equipment 909 355 – 358 (2018). [10.1016/j.nima.2018.02.093](https://doi.org/10.1016/j.nima.2018.02.093)
53. Audet T. L., Lee P., Maynard G., Dufrenoy S., Dobosz, Maitrallain A., Bougeard M., Monot P., Cros B. **Gas cell density characterization for laser wakefield acceleration.** Nuclear Instruments & Methods in Physics Research Section A-Accelerators Spectrometers Detectors and Associated Equipment 909 383 – 386 (2018). [10.1016/j.nima.2018.01.053](https://doi.org/10.1016/j.nima.2018.01.053)
54. Bisesto F. G., Anania M. P., Botton M., Chiadroni E., Cianchi A., Curcio A., Ferrario M., Galletti M., Henis Z., Pompili R., Schleifer E., Zigler A. **Evolution of the electric fields induced in high intensity laser-matter interactions.** Nuclear Instruments & Methods in Physics Research Section A-Accelerators Spectrometers Detectors and Associated Equipment 909 398 – 401 (2018). [10.1016/j.nima.2018.03.040](https://doi.org/10.1016/j.nima.2018.03.040)
55. Brentegani E., Anania M. P., Atzeni S., Biagioni A., Chiadroni E., Croia M., Ferrario M., Filippi F., Marocchino A., Mostacci A., Pompili R., Romeo S., Schiavi A., Zigler A. **Numerical studies on capillary discharges as focusing elements for electron beams.** Nuclear Instruments & Methods in Physics Research Section A-Accelerators Spectrometers Detectors and Associated Equipment 909 404 – 407 (2018). [10.1016/j.nima.2018.03.012](https://doi.org/10.1016/j.nima.2018.03.012)
56. Marocchino A., Chiadroni E., Ferrario M., Mira F., Rossi A. R. **Design of high brightness Plasma Wakefield Acceleration experiment at SPARC\_LAB test facility with particle-in-cell simulations.** Nuclear Instruments & Methods in Physics Research Section A-Accelerators Spectrometers Detectors and Associated Equipment 909 408 – 413 (2018). [10.1016/j.nima.2018.02.068](https://doi.org/10.1016/j.nima.2018.02.068)
57. Lee P., Audet T. L., Lehe R., Vay J. -L., Maynard G., Cros B. **Investigation of the dynamics of ionization induced injected electrons under the influence of beam loading effects.** Nuclear Instruments & Methods in Physics Research Section A-Accelerators Spectrometers Detectors and Associated Equipment 909 428 – 432 (2018). [10.1016/j.nima.2018.02.004](https://doi.org/10.1016/j.nima.2018.02.004)

58. Mira F., Ferrario M., Londrillo P., Marocchino A. **Characterisation of beam driven ionisation injection in the blowout regime of plasma acceleration.** Nuclear Instruments & Methods in Physics Research Section A-Accelerators Spectrometers Detectors and Associated Equipment 909 441 – 445 (2018). [10.1016/j.nima.2018.01.019](https://doi.org/10.1016/j.nima.2018.01.019)
59. Bisesto F. G. et al. **The FLAME laser at SPARC\_LAB .** Nuclear Instruments & Methods in Physics Research Section A-Accelerators Spectrometers Detectors and Associated Equipment 909 452 – 455 (2018). [10.1016/j.nima.2018.02.027](https://doi.org/10.1016/j.nima.2018.02.027)
60. Shpakov V., Chiadroni E., Curcio A., Fares H., Ferrario M., Marocchino A., Mira F., Petrillo V., Rossi A.R., Romeo S. **Plasma acceleration limitations due to betatron radiation.** Nuclear Instruments & Methods in Physics Research Section A-Accelerators Spectrometers Detectors and Associated Equipment 909 463 – 466 (2018). [10.1016/j.nima.2018.02.058](https://doi.org/10.1016/j.nima.2018.02.058)
61. Brandi F., Marsili P., Giammanco F., Sylla F., Gizzi L.A. **Measurement of the particle number density in a pulsed flow gas cell with a second-harmonic interferometer.** IOP Conf. Series: Journal of Physics: Conf. Series 1079 012006 (2018) [doi:10.1088/1742-6596/1079/1/012006](https://doi.org/10.1088/1742-6596/1079/1/012006)
62. Li X., Nghiem P.A.P., Mosnier A. **Toward low energy spread in plasma accelerators in quasilinear regime.** Physical Review Accelerators and Beams 21 (11) 111301 (2018). [10.1103/PhysRevAccelBeams.21.111301](https://doi.org/10.1103/PhysRevAccelBeams.21.111301)
63. Pompili R. et al. **Focusing of High-Brightness Electron Beams with Active-Plasma Lenses.** Physical Review Letters 121 (17) 174801 (2018). [10.1103/PhysRevLett.121.174801](https://doi.org/10.1103/PhysRevLett.121.174801)
64. Dopp A., Thaury C., Guillaume E., Massimo F., Lifschitz A., Andriyash I., Goddet J.-P., Tazfi A., Phuoc K. Ta, Malka V. **Energy-Chirp Compensation in a Laser Wakefield Accelerator.** Physical Review Letters 121 (7) 074802 (2018). [10.1103/PhysRevLett.121.074802](https://doi.org/10.1103/PhysRevLett.121.074802)
65. Filippi F., Anania M. P., Biagioni A., Chiadroni E., Cianchi A., Ferber Y., Ferrario M., Zigler A. **3D-printed capillary for hydrogen filled discharge for plasma based experiments in RF-based electron linac accelerator.** Review of Scientific Instruments 89 (8) 083502 (2018). [10.1063/1.5010264](https://doi.org/10.1063/1.5010264)
66. Zhao Q., Weng S. M., Sheng Z.M., Chen M., Zhang G.B., Mori W.B., Hidding B., Jaroszynski D.A., Zhang J. **Ionization injection in a laser wakefield accelerator subject to a transverse magnetic field.** New Journal of Physics 20 063031 (2018). [10.1088/1367-2630/aac926](https://doi.org/10.1088/1367-2630/aac926)
67. Labate L., Vantaggiato G., Gizzi L.A. **Intra-cycle depolarization of ultraintense laser pulses focused by off-axis parabolic mirrors.** High Power Laser Science and Engineering 6 e32 (2018) [10.1017/hpl.2018.27](https://doi.org/10.1017/hpl.2018.27)
68. Lee P., Maynard G., Audet T.L., Cros B., Lehe R., Vay J.-L. **Optimization of laser-plasma injector via beam loading effects using ionization-induced injection.** Physical Review Accelerators and Beams 21 (5) 052802 (2018). [10.1103/PhysRevAccelBeams.21.052802](https://doi.org/10.1103/PhysRevAccelBeams.21.052802)
69. Cianchi A. et al. **Frontiers of beam diagnostics in plasma accelerators: Measuring the ultra-fast and ultra-cold.** Physics of Plasmas 25 (5) 056704 (2018). [10.1063/1.5017847](https://doi.org/10.1063/1.5017847)
70. Yang X., Brunetti E., Jaroszynski D.A. **High-energy coherent terahertz radiation emitted by wide-angle electron beams from a laser-wakefield accelerator.** New Journal of Physics 20 043046 (2018). [10.1088/1367-2630/aab74d](https://doi.org/10.1088/1367-2630/aab74d)
71. Luo J., Chen M., Wu W. Y., Weng S. M., Sheng Z.M., Schroeder C.B., Jaroszynski D.A., Esarey E., Leemans W.P., Mori W.B., Zhang J. **Multistage Coupling of**

- Laser-Wakefield Accelerators with Curved Plasma Channels.** Physical Review Letters 120 (15) 154801 (2018). [10.1103/PhysRevLett.120.154801](https://doi.org/10.1103/PhysRevLett.120.154801)
71. Andre T. et al. **Control of laser plasma accelerated electrons for light sources.** Nature Communications 9 1334 (2018). [10.1038/s41467-018-03776-x](https://doi.org/10.1038/s41467-018-03776-x)
  73. Ghotra H.S., Jaroszynski D., Ersfeld B., Saini N.S., Yoffe S., Kant N. **Transverse electromagnetic Hermite-Gaussian mode-driven direct laser acceleration of electron under the influence of axial magnetic field.** Laser and Particle Beams 36 (1) 154 – 161 (2018). [10.1017/S0263034618000083](https://doi.org/10.1017/S0263034618000083)
  74. Pompili R., Anania M. P., Chiadroni E., Cianchi A., Ferrario M., Lollo V., Notargiacomo A., Picardi L., Ronsivalle C., Rosenzweig J.B., Shpakov V., Vannozzi A. **Compact and tunable focusing device for plasma wakefield acceleration.** Review of Scientific Instruments 89 (3) 033302 (2018). [10.1063/1.5006134](https://doi.org/10.1063/1.5006134)
  75. Massimo F., Lifschitz A. F., Thauray C., Malka V. **Numerical study of laser energy effects on density transition injection in laser wakefield acceleration.** Plasma Physics and Controlled Fusion 60 (3) 034005 (2018). [10.1088/1361-6587/aaa336](https://doi.org/10.1088/1361-6587/aaa336)
  76. Pompili R., Castorina G., Ferrario M., Marocchino A., Zigler A. **Guiding of charged particle beams in curved capillary-discharge waveguides.** AIP Advances 8 (1) 015326 (2018). [10.1063/1.5011964](https://doi.org/10.1063/1.5011964)
  77. Marocchino A. et al. **Experimental characterization of the effects induced by passive plasma lens on high brightness electron bunches.** Applied Physics Letters 111 (18) 184101 (2017). [10.1063/1.4999010](https://doi.org/10.1063/1.4999010)
  78. Subiel A., Moskvina V., Welsh G.H., Cipiccia S., Reboredo D., DesRosiers C., Jaroszynski D.A. **Challenges of dosimetry of ultra-short pulsed very high energy electron beams.** Physica Medica-European Journal of Medical Physics 42 327 – 331 (2017). [10.1016/j.ejmp.2017.04.029](https://doi.org/10.1016/j.ejmp.2017.04.029)
  79. Tomassini P., De Nicola S., Labate L., Londrillo P., Fedele R., Terzani D., Gizzi L.A. **The resonant multi-pulse ionization injection.** Physics of Plasmas 24 (10) 103120 (2017). [10.1063/1.5000696](https://doi.org/10.1063/1.5000696)
  80. Chiadroni E. et al. **Beam manipulation for resonant plasma wakefield acceleration.** Nuclear Instruments & Methods in Physics Research Section A-Accelerators Spectrometers Detectors and Associated Equipment 865 139 – 143 (2017). [10.1016/j.nima.2017.01.017](https://doi.org/10.1016/j.nima.2017.01.017)
  81. Wang W.-M., Sheng Z.-M., Li Y.-T., Zhang Y., Zhang J. **Terahertz emission driven by two-color laser pulses at various frequency ratios.** Physical Review A 96 (2) 023844 (2017). [10.1103/PhysRevA.96.023844](https://doi.org/10.1103/PhysRevA.96.023844)
  82. Massimo F., Lifschitz A. F., Thauray C., Malka V. **Numerical studies of density transition injection in laser wakefield acceleration.** Plasma Physics and Controlled Fusion 59 (8) 085004 (2017). [10.1088/1361-6587/aa717d](https://doi.org/10.1088/1361-6587/aa717d)
  83. Tooley M.P., Ersfeld B., Yoffe S.R., Noble A., Brunetti E., Sheng Z.M., Islam M.R., Jaroszynski D.A. **Towards Attosecond High-Energy Electron Bunches: Controlling Self-Injection in Laser-Wakefield Accelerators Through Plasma-Density Modulation.** Physical Review Letters 119 (4) 044801 (2017). [10.1103/PhysRevLett.119.044801](https://doi.org/10.1103/PhysRevLett.119.044801)
  84. Pinheiro M.J. **A reformulation of mechanics and electrodynamics.** Heliyon 3 (7) e00365 (2017). [10.1016/j.heliyon.2017.e00365](https://doi.org/10.1016/j.heliyon.2017.e00365)
  85. Shpakov V., Chiadroni E., Curcio A., Fares H., Ferrario M., Marocchino A., Petrillo V., Rossi A.R., Romeo S. **Study of the beam tolerance for plasma based ion channel lasers.** Nuclear Instruments & Methods in Physics Research Section B-Beam Interactions With Materials and Atoms 402 384 – 387 (2017). [10.1016/j.nimb.2017.03.107](https://doi.org/10.1016/j.nimb.2017.03.107)
  86. Manahan G.G., Habib A.F., Scherkl P., Delinikolas P., Beaton A., Knetsch A., Karger O., Wittig G., Heinemann T., Sheng Z.M., Cary J.R., Bruhwiler D.L.,

- Rosenzweig J.B., Hidding B. **Single-stage plasma-based correlated energy spread compensation for ultrahigh 6D brightness electron beams.** *Nature Communications* 8 15705 (2017). [10.1038/ncomms15705](https://doi.org/10.1038/ncomms15705)
87. Wilson T.C., Li F.Y., Weikum M., Sheng Z.M. **Influence of strong magnetic fields on laser pulse propagation in underdense plasma.** *Plasma Physics and Controlled Fusion* 59 (6) 065002 (2017). [10.1088/1361-6587/aa6941](https://doi.org/10.1088/1361-6587/aa6941)
88. Mehrling T.J., Fonseca R.A., Martinez de la Ossa A., Vieira J. **Mitigation of the Hose Instability in Plasma-Wakefield Accelerators.** *Physical Review Letters* 118 (17) 174801 (2017). [10.1103/PhysRevLett.118.174801](https://doi.org/10.1103/PhysRevLett.118.174801)
89. Yang X., Brunetti E., Reboredo Gil D., Welsh G.H., Li F.Y., Cipiccia S., Ersfeld B., Grant D.W., Grant P.A., Islam M.R., Tooley M.P., Vieux G., Wiggins S.M., Sheng Z.M., Jaroszynski D.A. **Three electron beams from a laser-plasma wakefield accelerator and the energy apportioning question.** *Scientific Reports* 7 43910 (2017). [10.1038/srep43910](https://doi.org/10.1038/srep43910)
90. Filippi F., Anania M. P., Brentegani E., Biagioni A., Cianchi A., Chiadroni E., Ferrario M., Pompili R., Romeo S., Zigler A., GP IOP. **Gas-filled capillaries for plasma-based accelerators.** *Journal of Physics Conference Series* 874 (2017). [10.1088/1742-6596/874/1/012036](https://doi.org/10.1088/1742-6596/874/1/012036)
91. Ferran Pousa A., Assmann R., Brinkmann R., Martinez de la Ossa A. **External injection into a laser-driven plasma accelerator with sub-femtosecond timing jitter.** *Journal of Physics Conference Series* 874 UNSP 012032 (2017). [10.1088/1742-6596/874/1/012032](https://doi.org/10.1088/1742-6596/874/1/012032)
92. Walker P.A. et al. **Horizon 2020 EuPRAXIA design study.** *Journal of Physics Conference Series* 874 UNSP 012029 (2017). [10.1088/1742-6596/874/1/012029](https://doi.org/10.1088/1742-6596/874/1/012029)
93. Vieira J., Trines R.M.G.M., Alves E.P., Fonseca R.A., Mendonca J.T., Bingham R., Norreys P., Silva L. O. **High Orbital Angular Momentum Harmonic Generation.** *Physical Review Letters* 117 (26) 265001 (2016). [10.1103/PhysRevLett.117.265001](https://doi.org/10.1103/PhysRevLett.117.265001)
94. Massimo F., Atzeni S., Marocchino A. **Comparisons of time explicit hybrid kinetic-fluid code Architect for Plasma Wakefield Acceleration with a full PIC code.** *Journal of Computational Physics* 327 841 – 850 (2016). [10.1016/j.jcp.2016.09.067](https://doi.org/10.1016/j.jcp.2016.09.067)
95. Labate L., Ferrara P., Fulgentini L., Gizzi L.A. **Effects of small misalignments on the intensity and Strehl ratio for a laser beam focused by an off-axis parabola.** *Applied Optics* 55 (23) 6506 – 6515 (2016). [10.1364/AO.55.006506](https://doi.org/10.1364/AO.55.006506)
96. Brandi F., Giammanco F., Conti F., Sylla F., Lambert G., Gizzi L.A. **Real-time monitoring via second-harmonic interferometry of a flow gas cell for laser wakefield acceleration.** *Review of Scientific Instruments* 87 (8) 086103 (2016). [10.1063/1.4960399](https://doi.org/10.1063/1.4960399)
97. Luo J., Chen M., Zeng M., Vieira J., Yu L.L., Weng S.M., Silva L.O., Jaroszynski D.A., Sheng Z.M., Zhang J. **A compact tunable polarized X-ray source based on laser-plasma helical undulators.** *Scientific Reports* 6 29101 (2016). [10.1038/srep29101](https://doi.org/10.1038/srep29101)
98. Huang K., Li Y.F., Li D.Z., Chen L.M., Tao M.Z., Ma Y., Zhao J.R., Li M.H., Chen M., Mirzaie M., Hafz N., Sokollik T., Sheng Z.M., Zhang J. **Resonantly Enhanced Betatron Hard X-rays from Ionization Injected Electrons in a Laser Plasma Accelerator.** *Scientific Reports* 6 27633 (2016). [10.1038/srep27633](https://doi.org/10.1038/srep27633)
99. Zeng M., Luo J., Chen M., Mori W.B., Sheng Z.-M., Hidding B. **High quality electron beam acceleration by ionization injection in laser wakefields with mid-infrared dual-color lasers.** *Physics of Plasmas* 23 (6) 063113 (2016). [10.1063/1.4953895](https://doi.org/10.1063/1.4953895)

100. Yu L.-L., Zhao Y., Qian L.-J., Chen M., Weng S.-M., Sheng Z.-M., Jaroszynski D.A., Mori W.B., Zhang J. **Plasma optical modulators for intense lasers**. *Nature Communications* 7 11893 (2016). [10.1038/ncomms11893](https://doi.org/10.1038/ncomms11893)
101. Vieira J., Trines R. M.G.M., Alves E.P., Fonseca R.A., Mendonca J.T., Bingham R., Norreys P., Silva L.O. **Amplification and generation of ultra-intense twisted laser pulses via stimulated Raman scattering**. *Nature Communications* 7 10371 (2016). [10.1038/ncomms10371](https://doi.org/10.1038/ncomms10371)

### 33.2 List of EuPRAXIA Conference Proceedings

1. Nghiem P.A.P. et al. **EuPRAXIA, a step toward a plasma-wakefield based accelerator with high beam quality**. 10th International Particle Accelerator Conference (IPAC) May 19 – 24 2019 Melbourne, Australia. Proceedings of IPAC'19 WEZZPLS2 (2019). [doi:10.18429/JACoW-IPAC2019-WEZZPLS2](https://doi.org/10.18429/JACoW-IPAC2019-WEZZPLS2)
2. Ferran Pousa A., Assmann R., Martinez de la Ossa, A. **WAKE-T: A fast particle tracking code for plasma-based accelerators**. 10th International Particle Accelerator Conference (IPAC) May 19 – 24 2019 Melbourne, Australia. Proceedings of IPAC'19 THPGW012 (2019). [doi:10.18429/JACoW-IPAC2019-THPGW012](https://doi.org/10.18429/JACoW-IPAC2019-THPGW012)
3. Weikum M.K. et al. **Status of the HORIZON 2020 EuPRAXIA Conceptual Design Study**. 10th International Particle Accelerator Conference (IPAC) May 19 – 24 2019 Melbourne, Australia. Proceedings of IPAC'19 THPGW026 (2019). [doi:10.18429/JACoW-IPAC2019-THPGW026](https://doi.org/10.18429/JACoW-IPAC2019-THPGW026)
4. Walker P.A. **Facility Considerations For A European Plasma Accelerator Infrastructure (EuPRAXIA)**. 10th International Particle Accelerator Conference (IPAC) May 19 – 24 2019 Melbourne, Australia. Proceedings of IPAC'19 THPGW025 (2019). [doi:10.18429/JACoW-IPAC2019-THPGW025](https://doi.org/10.18429/JACoW-IPAC2019-THPGW025)
5. Zhu J., Assmann R.W., Ferran Pousa A., Marchetti B., Walker P.A. **Simulation study of an RF injector for the LWFA configuration of EuPRAXIA**. 9th International Particle Accelerator Conference (IPAC) April 29 – May 4 2018 Vancouver, Canada. Proceedings of IPAC'18 THPAF032 (2018). [doi:10.18429/JACoW-IPAC2018-THPAF032](https://doi.org/10.18429/JACoW-IPAC2018-THPAF032)
6. Ferran Pousa A., Assmann R.W., Martinez de la Ossa, A. **Beam quality limitations of plasma-based accelerators**. 9th International Particle Accelerator Conference (IPAC) April 29 – May 4 2018 Vancouver, Canada. Proceedings of IPAC'18 TUXGBE4 (2018). [doi:10.18429/JACoW-IPAC2018-TUXGBE4](https://doi.org/10.18429/JACoW-IPAC2018-TUXGBE4)
7. Ferran Pousa A., Assmann R.W., Martinez de la Ossa, A. **VisualPIC: A New Data Visualizer and Post-Processor for Particle-in-Cell Codes**. 8th International Particle Accelerator Conference (IPAC) May 14-19 2017 Copenhagen, Denmark. Proceedings of IPAC'17 TUPIK007 (2017). <https://doi.org/10.18429/JACoW-IPAC2017-TUPIK007>
8. Kokurewicz K., Welsh G. H., Brunetti E., Wiggins S. M., Boyd M., Sorensen A., Chalmers A., Schettino G., Subiel A., Desrosiers C., Jaroszynski D. A., Ledingham K.W.D. **Laser-plasma generated very high energy electrons (VHEEs) in radiotherapy**. MEDICAL APPLICATIONS OF LASER-GENERATED BEAMS OF PARTICLES IV: REVIEW OF PROGRESS AND STRATEGIES FOR THE FUTURE. Proceedings of SPIE 10239 UNSP 102390C (2017). Conference on Medical Applications of Laser-Generated Beams of Particles IV – Review of Progress and Strategies for the Future APR 24-25 2017 Prague CZECH REPUBLIC. [10.1117/12.2271183](https://doi.org/10.1117/12.2271183)
9. Brunetti E., Yang X., Li F. Y., Reboredo Gil D., Welsh G.H., Cipiccia S., Ersfeld B., Grant D.W., Grant P.A., Islam M.R., Shahzad M., Tooley M.P., Vieux G., Wiggins S.M., Sheng Z.M., Jaroszynski D.A. **Wide-angle electron beams**

- from laser-wakefield accelerators.** LASER ACCELERATION OF ELECTRONS PROTONS AND IONS IV. Proceedings of SPIE 10240 UNSP 102400P (2017). Conference on Laser Acceleration of Electrons Protons and Ions IV APR 24-26 2017 Prague CZECH REPUBLIC. [10.1117/12.2269314](https://doi.org/10.1117/12.2269314)
10. Tomassini P., Labate L., Londrillo P., Fedele R., Terzani D., Gizzi L.A. **High-Quality electron bunch production for high-brilliance Thomson Scattering sources.** LASER ACCELERATION OF ELECTRONS PROTONS AND IONS IV. Proceedings of SPIE 10240 UNSP 102400T (2017). Conference on Laser Acceleration of Electrons Protons and Ions IV APR 24-26 2017 Prague CZECH REPUBLIC. [10.1117/12.2266938](https://doi.org/10.1117/12.2266938)
  11. Macleod A.J., Noble A., Jaroszynski D.A. **On the energy-momentum tensor of light in strong fields: an all optical view of the Abraham-Minkowski controversy.** RELATIVISTIC PLASMA WAVES AND PARTICLE BEAMS AS COHERENT AND INCOHERENT RADIATION SOURCES II Proceedings of SPIE 10234 UNSP 102340F (2017). Conference on Relativistic Plasma Waves and Particle Beams as Coherent and Incoherent Radiation Sources II APR 27 2017 Prague CZECH REPUBLIC. [10.1117/12.2269630](https://doi.org/10.1117/12.2269630)
  12. Yoffe S.R., Noble A., Macleod A.J., Jaroszynski D.A. **Electron beam cooling in intense focussed laser pulses.** RELATIVISTIC PLASMA WAVES AND PARTICLE BEAMS AS COHERENT AND INCOHERENT RADIATION SOURCES II Proceedings of SPIE 10234 UNSP 102340E (2017). Conference on Relativistic Plasma Waves and Particle Beams as Coherent and Incoherent Radiation Sources II APR 27 2017 Prague CZECH REPUBLIC. [10.1117/12.2265812](https://doi.org/10.1117/12.2265812)

## Acknowledgements

Open access funding enabled and organized by Projekt DEAL. The completion of the EuPRAXIA design study and this Conceptual Design Report has been possible only because of the efforts and hard work of many people.

We would in particular like to thank the Scientific Advisory Committee:

Caterina Biscari (ALBA)	Constantin Haefner (LLNL)
Franck Falcoz (Amplitude Technologies)	Knut Michel (Trumpf Scientific)
Luca Giannessi (FERMI)	Christophe Simon-Boisson (Thales)
Edda Gschwendtner (CERN)	Thomas Tschentscher (European XFEL)

We also thank the EuPRAXIA Steering Committee (SC) and Collaboration Board (CB):

Ralph Assmann (CB,SC)	Victor Malka (SC)
Reinhard Brinkmann (CB)	Barbara Marchetti (SC)
Antoine Chancé (CB,SC)	Alberto Martinez de la Ossa (SC)
Enrica Chiadroni (SC)	François Mathieu (SC)
Alessandro Cianchi (SC)	Alban Mosnier (CB)
Jim Clarke (CB,SC)	Andrea Mostacci (CB,SC)
Marie-Emmanuelle Couprie (CB,SC)	Zulfikar Najmudin (CB,SC)
Brigitte Cros (SC)	Phu Anh Phi Nghiem (SC)
Giuseppe Dattoli (SC)	Federico Nguyen (CB)
Nicolas Delerue (SC)	Jens Osterhoff (SC)
Ulrich Dorda (SC)	Rajeev Pattathil (CB,SC)
Massimo Ferrario (chair CB,SC)	Zheng-Ming Sheng (SC)
Leonida Antonio Gizzi (CB,SC)	Luís Silva (SC)
Florian Grüner (SC)	Arnd Specka (CB,SC)
Bernhard Hidding (CB,SC)	Ricardo Torres (CB)
Simon Hooker (CB)	Cristina Vaccarezza (SC)
Dino Jaroszynski (CB,SC)	Jorge Vieira (CB,SC)
Roger Jones (CB,SC)	Roman Walczak (CB,SC)
Luca Labate (SC)	Carsten Welsch (CB,SC)
Agustin Lifschitz (SC)	Mark Wiggins (SC)
Andreas Maier (CB,SC)	Guoxing Xia (CB,SC)

The efforts of the Work Package leaders and co-leaders in coordinating the detailed technical design work have been essential to the success of this project.

Further special thanks go to

- the technical, scientific and administrative staff as well as the many early career researchers at our partner institutions who contributed to the conceptual work and organisation;
- the groups and researchers at our associated partners who dedicated their time and resources entirely as in-kind contributions to EuPRAXIA;
- the DESY EU Office, in particular Tom Minniberger and Ute Krell, for their continued support in funding and reporting matters;
- and the many colleagues and researchers who offered their advice in fruitful discussions – the editors would like to name in particular J. Collier, H. Dosch, G. Mourou, W. Sandner, T. Tajima, C.-G. Wahlström and O. Wiestler.

Finally, we would like to acknowledge with much appreciation the European Union's Horizon 2020 programme for our funding of this design study. Some of this work was also partially funded by the Center of Advanced Systems Understanding (CASUS)

which is financed by Germany's Federal Ministry of Education and Research (BMBF) and by the Saxon Ministry for Science, Culture and Tourism (SMWK) with tax funds on the basis of the budget approved by the Saxon State Parliament.



This project has received funding from the European Union's Horizon 2020 research and innovation programme under grant agreement No. 653782. The information herein reflects only the views of its authors and the European Commission is not responsible for any use that may be made of the information contained.

**Open Access** This is an open access article distributed under the terms of the Creative Commons Attribution License (<https://creativecommons.org/licenses/by/4.0/>), which permits unrestricted use, distribution, and reproduction in any medium, provided the original work is properly cited.

**Publisher's Note** The EPJ Publishers remain neutral with regard to jurisdictional claims in published maps and institutional affiliations.

## References

1. Wideroe, R. Über ein neues Prinzip zur Herstellung hoher Spannungen. *Arch. für Elektrotechnik* 21, 387–406 (1928).
2. Van der Meer, S. Stochastic Damping of Betatron Oscillations tech. rep. (CERN, Geneva, 1972), CERN/ISR-PO/72-31.
3. Nobel Media AB. The Nobel Prize in Physics 1984 2019. <https://www.nobelprize.org/prizes/physics/1984/summary/> (2019).
4. Tajima, T. & Dawson, J. M. Laser Electron Accelerator. *Phys. Rev. Lett.* 43, 267–270. doi:10.1103/PhysRevLett.43.267. <http://link.aps.org/doi/10.1103/PhysRevLett.43.267> (1979).
5. Nobel Media AB. The Nobel Prize in Physics 2018 2019. <https://www.nobelprize.org/prizes/physics/2018/summary/> (2019).
6. European Commission. Open innovation, open science, open to the world – EU Law and Publications <https://ec.europa.eu/digital-single-market/en/news/open-innovation-open-science-open-world-vision-europe> (2016).
7. DESY. European Network for Novel Accelerators EuroNNAc3 2019. <https://www.euronnac.eu/> (2019).
8. Henning, W. & Shank, C. Accelerators for America’s future tech. rep. (2010). <http://scholar.google.com/scholar?hl=en&btnG=Search&q=intitle:Accelerators+for+America?s+Future#0>.
9. Gonsalves, A. J. et al. Petawatt Laser Guiding and Electron Beam Acceleration to 8 GeV in a Laser-Heated Capillary Discharge Waveguide. *Phys. Rev. Lett.* 122, 84801. doi:10.1103/PhysRevLett.122.084801. <https://doi.org/10.1103/PhysRevLett.122.084801> (2019).
10. Tajima, T. & Dawson, J. M. Laser electron accelerator. *Phys. Rev. Lett.* 43, 267–270. doi:10.1103/PhysRevLett.43.267 (1979).
11. Geddes, C. G. R. et al. High-quality electron beams from a laser wakefield accelerator using plasma-channel guiding. *Nature* 431, 538–541. doi:10.1038/nature02900 (2004).
12. Mangles, S. P. D. et al. Monoenergetic beams of relativistic electrons from intense laser-plasma interactions. *Nature* 431, 535–538. doi:10.1038/nature02939 (2004).
13. Faure, J. et al. A laser – plasma accelerator producing monoenergetic electron beams. *Nature* 431, 541–544. doi:10.1038/nature02900.1. (2004).
14. Strickland, D. & Mourou, G. Compression of amplified chirped optical pulses. *Opt. Commun.* 55, 447–449 (1985).
15. Suk, H., Barov, N., Rosenzweig, J. B. & Esarey, E. Plasma Electron Trapping and Acceleration in a Plasma Wake Field Using a Density Transition. *Phys. Rev. Lett.* 86, 1011–1014. doi:10.1103/PhysRevLett.86.1011. <http://link.aps.org/doi/10.1103/PhysRevLett.86.1011> (Feb. 2001).
16. Chien, T.-Y. et al. Spatially Localized Self-Injection of Electrons in a Self-Modulated Laser- Wakefield Accelerator by Using a Laser-Induced Transient Density Ramp. *Phys. Rev. Lett.* 94, 115003. doi:10.1103/PhysRevLett.94.115003. <http://link.aps.org/doi/10.1103/PhysRevLett.94.115003> (2005).
17. Geddes, C. G. R. et al. Plasma-Density-Gradient Injection of Low Absolute-Momentum- Spread Electron Bunches. *Phys. Rev. Lett.* 100, 215004. doi:10.1103/PhysRevLett.100.215004. <https://link.aps.org/doi/10.1103/PhysRevLett.100.215004> (May 2008).
18. Schmid, K. et al. Density-transition based electron injector for laser driven wakefield accelerators. *Phys. Rev. ST Accel. Beams* 13, 091301. doi:10.1103/PhysRevSTAB.13.091301. <https://link.aps.org/doi/10.1103/PhysRevSTAB.13.091301%20> <http://link.aps.org/doi/10.1103/PhysRevSTAB.13.091301> (Sept. 2010).
19. Clayton, C. E. et al. Self-Guided Laser Wakefield Acceleration beyond 1 GeV Using Ionization-Induced Injection. *Phys. Rev. Lett.* 105, 105003. doi:10.1103/PhysRevLett.105.105003. <http://link.aps.org/doi/10.1103/PhysRevLett.105.105003> (2010).
20. Thaury, C. et al. Shock assisted ionization injection in laser-plasma accelerators. *Sci. Rep.* 5, 16310–. doi:10.1038/srep16310. <http://www.nature.com/articles/srep16310%20> <http://www.ncbi.nlm.nih.gov/pmc/articles/PMC4637871/> (Oct. 2015).

21. Wenz, J. et al. Dual-energy electron beams from a compact laser-driven accelerator. *Nat. Photonics* 13, 263–269. doi:10.1038/s41566-019-0356-z. <http://www.nature.com/articles/s41566-019-0356-z> (Apr. 2019).
22. Kuschel, S. et al. Controlling the Self-Injection Threshold in Laser Wakefield Accelerators. *Phys. Rev. Lett.* 121, 154801. doi:10.1103/PhysRevLett.121.154801. <https://link.aps.org/doi/10.1103/PhysRevLett.121.154801> (Oct. 2018).
23. Zhao, Q. et al. Ionization injection in a laser wakefield accelerator subject to a transverse magnetic field. *New J. Phys.* 20, 063031. doi:10.1088/1367-2630/aac926. <http://stacks.iop.org/1367-2630/20/i=6/a=063031?key=crossref.c14dc6c28c72a55dc177dad55fd2b21e> (June 2018).
24. Svystun, E., Assmann, R. W., Dorda, U., Marchetti, B. & Martinez de la Ossa, A. Numerical Studies on Electron Beam Quality Optimization in a Laser-Driven Plasma Accelerator with External Injection at SINBAD for ATHENAe in Proc. 10th Int. Part. Accel. Conf. (Melbourne, Australia, 2019), THPGW023. doi:10.18429/JACoW-IPAC2019-THPGW023.
25. Wang, K. et al. Longitudinal compression and transverse matching of electron bunch for external injection LPWA at ESCULAP. *Nucl. Instruments Methods Phys. Res. Sect. A Accel. Spectrometers, Detect. Assoc. Equip.* 909, 266–270. <https://www.sciencedirect.com/science/article/pii/S0168900217313682?via%3Dihub%20> <https://linkinghub.elsevier.com/retrieve/pii/S0168900217313682> (Nov. 2018).
26. Hua, J., Wu, Y. & Lu, W. External injection from a Linac into a LWFA with  $\sim 100\%$  capture efficiency (Conference Presentation) in Laser Accel. Electrons, Protons, Ions V (eds Esarey, E., Schroeder, C. B. & Schreiber, J.) 11037 (SPIE, May 2019), 31. doi:10.1117/12.2520697. <https://www.spiedigitallibrary.org/conference-proceedings-of-spie/11037/2520697/External-injection-from-a-Linac-into-a-LWFA-with-100/10.1117/12.2520697.full>.
27. Leemans, W. P. et al. Multi-GeV Electron Beams from Capillary-Discharge-Guided Subpetawatt Laser Pulses in the Self-Trapping Regime. *Phys. Rev. Lett.* 113, 245002. doi:10.1103/PhysRevLett.113.245002. <http://link.aps.org/doi/10.1103/PhysRevLett.113.245002> (2014).
28. Couperus, J. et al. Demonstration of a beam loaded nanocoulomb-class laser wakefield accelerator. *Nat. Commun.* 8, 487. doi:10.1038/s41467-017-00592-7. <http://www.nature.com/articles/s41467-017-00592-7> (Dec. 2017).
29. Islam, M. R. et al. Near-Threshold Electron Injection in the Laser-Plasma Wakefield Accelerator Leading to Femtosecond Bunches. *New J. Phys.* 17. doi:10.1088/1367-2630/17/9/093033 (2015).
30. Tooley, M. P. et al. Towards Attosecond High-Energy Electron Bunches: Controlling Self- Injection in Laser-Wakefield Accelerators Through Plasma-Density Modulation. *Phys. Rev. Lett.* 119, 044801. doi:10.1103/PhysRevLett.119.044801. <http://link.aps.org/doi/10.1103/PhysRevLett.119.044801> (July 2017).
31. Weikum, M., Li, F., Assmann, R., Sheng, Z. & Jaroszynski, D. Generation of attosecond electron bunches in a laser-plasma accelerator using a plasma density upramp. *Nucl. Instruments Methods Phys. Res. Sect. A Accel. Spectrometers, Detect. Assoc. Equip.* 829, 33–36. doi:10.1016/J.NIMA.2016.01.003. <https://www.sciencedirect.com/science/article/pii/S0168900216000061?via%3Dihub> (Sept. 2016).
32. Wang, W. T. et al. High-Brightness High-Energy Electron Beams from a Laser Wakefield Accelerator via Energy Chirp Control. *Phys. Rev. Lett.* 117, 124801. doi:10.1103/PhysRevLett.117.124801. <https://link.aps.org/doi/10.1103/PhysRevLett.117.124801> (Sept. 2016).
33. Brinkmann, R. et al. Chirp mitigation of plasma-accelerated beams by a modulated plasma density. *Phys. Rev. Lett.* 118, 214801 (2017).
34. Ferran Pousa, A., Martinez de la Ossa, A., Brinkmann, R. & Assmann, R. Compact Multistage Plasma-Based Accelerator Design for Correlated Energy Spread Compensation. *Phys. Rev. Lett.* 123, 054801. doi:10.1103/PhysRevLett.123.054801. <https://link.aps.org/doi/10.1103/PhysRevLett.123.054801> (July 2019).

35. Mehrling, T., Grebenyuk, J., Tsung, F. S., Floettmann, K. & Osterhoff, J. Transverse emittance growth in staged laser-wakefield acceleration. *Phys. Rev. ST Accel. Beams* 15, 111303. doi:10.1103/PhysRevSTAB.15.111303. <https://link.aps.org/doi/10.1103/PhysRevSTAB.15.111303> (Nov. 2012).
36. Dornmair, I., Floettmann, K. & Maier, a. R. Emittance conservation by tailored focusing profiles in a plasma accelerator. *Phys. Rev. Spec. Top.-Accel. Beams* 18, 1–6. doi:10.1103/PhysRevSTAB.18.041302 (2015).
37. Xu, X. L. et al. Physics of Phase Space Matching for Staging Plasma and Traditional Accelerator Components Using Longitudinally Tailored Plasma Profiles. *Phys. Rev. Lett.* 116, 1–5. doi:10.1103/PhysRevLett.116.124801 (2016).
38. Van Tilborg, J. et al. Active plasma lensing for relativistic laser-plasma-accelerated electron beams. *Phys. Rev. Lett.* 115, 184802. doi:10.1103/PhysRevLett.115.184802. <https://link.aps.org/doi/10.1103/PhysRevLett.115.184802> (Oct. 2015).
39. Zhang, C. J. et al. Probing plasma wakefields using electron bunches generated from a laser wakefield accelerator. *Plasma Phys. Control. Fusion* 60, 044013. doi:10.1088/1361-6587/aaabfd. <http://stacks.iop.org/0741-3335/60/i=4/a=044013?key=crossref.64defbb275912d2c3bd43e3bb163231c> (Apr. 2018).
40. Audet, T. L. et al. Electron injector for compact staged high energy accelerator. *Nucl. Instruments Methods Phys. Res. Sect. A Accel. Spectrometers, Detect. Assoc. Equip.* doi:<http://dx.doi.org/10.1016/j.nima.2016.01.035>. <http://www.sciencedirect.com/science/article/pii/S0168900216000516> (2016).
41. Steinke, S. et al. Staging of laser-plasma accelerators. *Phys. Plasmas* 23, 056705. doi:10.1063/1.4948280. <http://aip.scitation.org/doi/10.1063/1.4948280> (May 2016).
42. Pathak, V. B., Kim, H. T., Vieira, J., Silva, L. O. & Nam, C. H. All optical dual stage laser wakefield acceleration driven by two-color laser pulses. *Sci. Rep.* 8, 11772. doi:10.1038/s41598-018-30095-4. <http://www.nature.com/articles/s41598-018-30095-4> (Dec. 2018).
43. Gonsalves, A. J. et al. Generation and pointing stabilization of multi-GeV electron beams from a laser plasma accelerator driven in a pre-formed plasma waveguide. *Phys. Plasmas* 22, 056703. doi:10.1063/1.4919278. <http://scitation.aip.org/content/aip/journal/pop/22/5/10.1063/1.4919278> (May 2015).
44. Shalloo, R. J. et al. Hydrodynamic optical-field-ionized plasma channels. *Phys. Rev. E* 97, 053203. doi:10.1103/PhysRevE.97.053203. <https://link.aps.org/doi/10.1103/PhysRevE.97.053203> (May 2018).
45. Blumenfeld, I. et al. Energy doubling of 42 GeV electrons in a metre-scale plasma wakefield accelerator. *Nature* 445, 741–744. doi:10.1038/nature05538. <http://www.nature.com/nature/journal/v445/n7129/full/nature05538.html> (2007).
46. Litos, M. et al. High-efficiency acceleration of an electron beam in a plasma wakefield accelerator. *Nature* 515, 92–95. doi:10.1038/nature13882. <http://www.nature.com/articles/nature13882> (Nov. 2014).
47. Litos, M. et al. 9 GeV energy gain in a beam-driven plasma wakefield accelerator. *Plasma Phys. Control. Fusion* 58, 034017. doi:10.1088/0741-3335/58/3/034017. <http://stacks.iop.org/0741-3335/58/i=3/a=034017?key=crossref.62a219d7ccc3fd7f12ea5cb18a4f3d73> (Mar. 2016).
48. Manahan, G. G. et al. Single-Stage Plasma-Based Correlated Energy Spread Compensation for Ultrahigh 6D Brightness Electron Beams. *Nat. Commun.* 8. doi:10.1038/ncomms15705. <http://www.nature.com/doi/10.1038/ncomms15705> (2017).
49. Loisch, G. et al. Observation of High Transformer Ratio Plasma Wakefield Acceleration. *Phys. Rev. Lett.* 121, 064801. doi:10.1103/PhysRevLett.121.064801. <https://link.aps.org/doi/10.1103/PhysRevLett.121.064801> (Aug. 2018).
50. Doebert, S. & al., E. The Proton Driven Advanced Wake Field Acceleration Experiment (AWAKE) at CERN in Proc. 10th Int. Part. Accel. Conf. (Melbourne, Australia, 2019), 642– 646. doi:10.18429/JACoW-LINAC2018-TH1A04.
51. Gessner, S. et al. Demonstration of a positron beam-driven hollow channel plasma wakefield accelerator. *Nat. Commun.* 7, 11785. doi:10.1038/ncomms11785. <http://www.nature.com/articles/ncomms11785> (Sept. 2016).

52. Corde, S. et al. Multi-gigaelectronvolt acceleration of positrons in a self-loaded plasma wakefield. *Nature* 524, 442–445. doi:10.1038/nature14890. <http://www.nature.com/articles/nature14890> (Aug. 2015).
53. Martinez de la Ossa, A., Mehrling, T. J., Schaper, L., Streeter, M. J. V. & Osterhoff, J. Wakefield-induced ionization injection in beam-driven plasma accelerators. *Phys. Plasmas* 22, 093107. doi:10.1063/1.4929921. <http://aip.scitation.org/doi/10.1063/1.4929921> (Sept. 2015).
54. Martinez de la Ossa, A. et al. Optimizing density down-ramp injection for beam-driven plasma wakefield accelerators. *Phys. Rev. Accel. Beams* 20, 091301. doi:10.1103/PhysRevAccelBeams.20.091301. <https://link.aps.org/doi/10.1103/PhysRevAccelBeams.20.091301> (Sept. 2017).
55. Hidding, B. et al. Beyond injection: Trojan horse underdense photocathode plasma wakefield acceleration in AIP Conf. Proc. 1507 (American Institute of Physics, Dec. 2013), 570–575. doi:10.1063/1.4773760. <http://aip.scitation.org/doi/abs/10.1063/1.4773760>.
56. Schlenvoigt, H.-P. et al. A compact synchrotron radiation source driven by a laser-plasma wakefield accelerator. *Nat. Phys.* 4, 130–133 (2008).
57. Fuchs, M. et al. Laser-driven soft-X-ray undulator source. *Nat. Phys.* 5, 826–829 (2009).
58. Anania, M. P. et al. Transport of ultra-short electron bunches in a free-electron laser driven by a laser-plasma wakefield accelerator in SPIE Eur. Opt. Optoelectron. (2009), 735916.
59. Lambert, G. et al. Progress on the generation of undulator radiation in the UV from a plasma-based electron beam in Proceed. FEL conf., Nara, Japan (2012), 2.
60. Nakajima, K. Compact X-ray sources: Towards a table-top free-electron laser. *Nat. Phys.* 4, 92–93 (2008).
61. Grüner, F. et al. Design considerations for table-top, laser-based VUV and X-ray free electron lasers. *Appl. Phys. B* 86, 431–435 (2007).
62. Maier, A. R. et al. Demonstration scheme for a laser-plasma-driven free-electron laser. *Phys. Rev. X* 2, 31019 (2012).
63. Loulergue, A. et al. Beam manipulation for compact laser wakefield accelerator based free-electron lasers. *New J. Phys.* 17, 23028 (2015).
64. Huang, Z., Ding, Y. & Schroeder, C. B. Compact X-ray free-electron laser from a laserplasma accelerator using a transverse-gradient undulator. *Phys. Rev. Lett.* 109, 1–5. doi:10.1103/PhysRevLett.109.204801 (2012).
65. André, T. et al. Control of laser plasma accelerated electrons for light sources. *Nat. Commun.* 9, 1334 (2018).
66. Delbos, N. et al. LUX – A laser–plasma driven undulator beamline. *Nucl. Instruments Methods Phys. Res. Sect. A Accel. Spectrometers, Detect. Assoc. Equip.* (2018).
67. Bernhard, A. et al. Progress on experiments towards LWFA-driven transverse gradient undulator-based FELs. *Nucl. Instruments Methods Phys. Res. Sect. A Accel. Spectrometers, Detect. Assoc. Equip.* 909, 391–397 (2018).
68. Cole, J. M. et al. High-resolution mCT of a mouse embryo using a compact laser-driven X-ray betatron source. *Proc. Natl. Acad. Sci.* 115, 6335–6340. doi:10.1073/PNAS.1802314115. <https://www.pnas.org/content/115/25/6335#sec-6> (June 2018).
69. Döpp, A. et al. Stable femtosecond X-rays with tunable polarization from a laser-driven accelerator. *Light Sci. Appl.* 6, e17086–e17086. doi:10.1038/lsa.2017.86. <http://www.nature.com/articles/lsa201786> (Nov. 2017).
70. Kneip, S. et al. Bright spatially coherent synchrotron X-rays from a table-top source. *Nat. Phys.* 6, 980–983. doi:10.1038/nphys1789. <http://www.nature.com/articles/nphys1789> (Dec. 2010).
71. Cipiccia, S. et al. Gamma-rays from harmonically resonant betatron oscillations in a plasma wake. *Nat. Phys.* 7, 867–871. doi:10.1038/nphys2090. <http://www.nature.com/articles/nphys2090> (Nov. 2011).

72. Albert, F. et al. Observation of Betatron X-Ray Radiation in a Self-Modulated Laser Wakefield Accelerator Driven with Picosecond Laser Pulses. *Phys. Rev. Lett.* 118, 134801. doi:10.1103/PhysRevLett.118.134801. <http://link.aps.org/doi/10.1103/PhysRevLett.118.134801> (Mar. 2017).
73. Guo, B. et al. Generation of Coherent Monochromatic Betatron Radiation by Laser-triggered Ionization Injection in Plasma Accelerators in 2018 IEEE Adv. Accel. Concepts Work. (IEEE, Aug. 2018), 1–4. doi:10.1109/AAC.2018.8659443. <https://ieeexplore.ieee.org/document/8659443/>.
74. Kneip, S. et al. X-ray phase contrast imaging of biological specimens with femtosecond pulses of betatron radiation from a compact laser plasma wakefield accelerator. *Appl. Phys. Lett.* 99, 093701. doi:10.1063/1.3627216. <http://aip.scitation.org/doi/10.1063/1.3627216> (Aug. 2011).
75. Cole, J. M. et al. Laser-wakefield accelerators as hard x-ray sources for 3D medical imaging of human bone. *Sci. Rep.* 5, 13244. doi:10.1038/srep13244. <http://www.nature.com/articles/srep13244> (Oct. 2015).
76. Schwoerer, H., Liesfeld, B., Schlenvoigt, H.-P., Amthor, K.-U. & Sauerbrey, R. Thomson- Backscattered X Rays From Laser-Accelerated Electrons. *Phys. Rev. Lett.* 96, 014802. doi:10.1103/PhysRevLett.96.014802. <https://link.aps.org/doi/10.1103/PhysRevLett.96.014802> (Jan. 2006).
77. Chen, S. et al. MeV-Energy X Rays from Inverse Compton Scattering with Laser-Wakefield Accelerated Electrons. *Phys. Rev. Lett.* 110, 155003. doi:10.1103/PhysRevLett.110.155003. <https://link.aps.org/doi/10.1103/PhysRevLett.110.155003> (Apr. 2013).
78. Yu, C. et al. Ultrahigh brilliance quasi-monochromatic MeV g-rays based on self-synchronized all-optical Compton scattering. *Sci. Rep.* 6, 29518. doi:10.1038/srep29518. <http://www.nature.com/articles/srep29518> (Sept. 2016).
79. Geddes, C. G. R. et al. Compact quasi-monoenergetic photon sources from laser-plasma accelerators for nuclear detection and characterization. *Nucl. Instrum. Meth. B* 350, 116–121. doi:10.1016/j.nimb.2015.01.013. <http://www.sciencedirect.com/science/article/pii/S0168583X15000269> (2015).
80. DesRosiers, C., Moskvina, V., Cao, M., Joshi, C. J. & Langer, M. Laser-plasma generated very high energy electrons in radiation therapy of the prostate in (eds Neev, J., Nolte, S., Heisterkamp, A. & Schaffer, C. B.) 6881 (International Society for Optics and Photonics, Feb. 2008), 688109. doi:10.1117/12.761663. <http://proceedings.spiedigitallibrary.org/proceeding.aspx?doi=10.1117/12.761663>.
81. Nicolai, M. et al. Realizing a laser-driven electron source applicable for radiobiological tumor irradiation. *Appl. Phys. B* 116, 643–651. doi:10.1007/s00340-013-5747-0. <http://link.springer.com/10.1007/s00340-013-5747-0> (Sept. 2014).
82. Chiu, C. et al. Laser electron accelerators for radiation medicine: A feasibility study. *Med. Phys.* 31, 2042–2052. doi:10.1118/1.1739301. <http://doi.wiley.com/10.1118/1.1739301> (June 2004).
83. Schroeder, C. B., Esarey, E., Geddes, C. G. R., Benedetti, C. & Leemans, W. P. Physics considerations for laser-plasma linear colliders. *Phys. Rev. Spec. Top.-Accel. Beams* 13, 101301. doi:10.1103/PhysRevSTAB.13.101301. <https://link.aps.org/doi/10.1103/PhysRevSTAB.13.101301> (Oct. 2010).
84. Schroeder, C., Benedetti, C., Esarey, E. & Leemans, W. Laser-plasma-based linear collider using hollow plasma channels. *Nucl. Instruments Methods Phys. Res. Sect. A Accel. Spectrometers, Detect. Assoc. Equip.* 829, 113–116. doi:10.1016/J.NIMA.2016.03.001. <https://www.sciencedirect.com/science/article/pii/S0168900216002667> via%3Dihub (Sept. 2016).
85. European Commission. Open innovation, open science, open to the world-EU Law and Publications <https://ec.europa.eu/digital-single-market/en/news/open-innovation-open-science-open-world-vision-europe> (2016).
86. LBG OIS Center. Why Open Innovation in Science? 2019. <https://ois.lbg.ac.at/en/about/mission-history> (2019).

87. OpenInnovation.eu. Open Innovation-What is Open Innovation? 2019. <https://www.openinnovation.eu/open-innovation/> (2019).
88. Research England. Research and knowledge exchange funding for 2019-20 tech. rep. (2019), RE-P-2019-05. <https://re.ukri.org/documents/finance/2019-20-funding-allocations/research-and-knowledge-exchange-funding-for-2019-20/>.
89. European Commission. European Cloud Initiative -Building a competitive data and knowledge economy in Europe tech. rep. (2016), COM(2016) 178. <http://eur-lex.europa.eu/legal-content/EN/TXT/PDF/?uri=CELEX:52016DC0178&from=EN>.
90. Weikum, M. K. et al. Status of the Horizon 2020 EuPRAXIA conceptual design study. *J. Phys. Conf. Ser.* 1350. doi:10.1088/1742-6596/1350/1/012059 (Dec. 2019).
91. Argyropoulos, T. et al. Design, fabrication, and high-gradient testing of an X-band, travelingwave accelerating structure milled from copper halves. *Phys. Rev. Accel. Beams* 21, 061001. doi:10.1103/PhysRevAccelBeams.21.061001. <https://link.aps.org/doi/10.1103/PhysRevAccelBeams.21.061001> (June 2018).
92. Gizzi, L. A. et al. A Viable Laser Driver for a User Plasma Accelerator. *Nucl. Instruments Methods Phys. Res. Sect. A Accel. Spectrometers, Detect. Assoc. Equip.* 909, 58–66. doi:10.1016/j.nima.2018.02.089. <https://linkinghub.elsevier.com/retrieve/pii/S0168900218302717> (2018).
93. Nanni, E. A. et al. Terahertz-driven linear electron acceleration. *Nat. Commun.* 6, 8486. doi:10.1038/ncomms9486. <http://www.nature.com/articles/ncomms9486> (Dec. 2015).
94. Peralta, E. A. et al. Demonstration of electron acceleration in a laser-driven dielectric microstructure. *Nature* 503, 91–94. doi:10.1038/nature12664. <http://www.nature.com/articles/nature12664> (Nov. 2013).
95. Korn, G. Future perspectives of ELI Beamlines Hamburg, Germany, 2018. [https://ard.desy.de/sites2009/site\\_ard/content/e157650/e271962/GeorgKorn\\_ELI.pdf](https://ard.desy.de/sites2009/site_ard/content/e157650/e271962/GeorgKorn_ELI.pdf).
96. Office of High Energy Physics, Office of Science & U.S. Department of Energy. Preliminary Conceptual Design Report for the FACET-II Project at SLAC National Accelerator Laboratory tech. rep. (2015), SLAC-R-1067. <http://slac.stanford.edu/pubs/slacreports/reports21/slac-r-1067.pdf>.
97. SLAC National Accelerator Laboratory. Facility for Advanced Accelerator Experimental Tests (FACET)-Proposals Overview 2019. <https://facet.slac.stanford.edu/proposals> (2019).
98. Dorda, U. SINBAD-Status & Plans in Beschleuniger-Betriebsseminar 2019 (Travemuende, Germany, 2019). <https://indico.desy.de/indico/event/21928/session/5/contribution/1/material/slides/0.pdf>.
99. Deutsches Elektronensynchrotron DESY. FLASHFORWARD-Experimental Proposals 2018. [https://forward.desy.de/experimental\\_proposals/](https://forward.desy.de/experimental_proposals/) (2019).
100. Vaccarezza, C. The SPARC\_LAB Thomson Source in Eur. Adv. Accel. Concepts Work. (Elba, Italy, 2015). [https://agenda.infn.it/event/8146/contributions/71629/attachments/51945/61358/The\\_SPARC\\_LAB\\_Thomson\\_SOURCE.pptx](https://agenda.infn.it/event/8146/contributions/71629/attachments/51945/61358/The_SPARC_LAB_Thomson_SOURCE.pptx).
101. CERN. CLEAR-Beam Line Description <https://clear.web.cern.ch/content/beamline-description> (2019).
102. Ferran Pousa, A., Aßmann, R. & Martinez de la Ossa, A. VisualPIC: a new data visualizer and post-processor for particle-in-cell codes. *Proc. IPAC 2017*, 1696–1698. doi:10.18429/JACOW-IPAC2017-TUPIK007. <http://jacow.org/ipac2017/doi/JACoW-IPAC2017-TUPIK007.html> (2017).
103. Rocca, J. J. et al. in *Free Electron Lasers 2002* 515–522 (Elsevier, 2003).
104. McPherson, A. et al. Studies of multiphoton production of vacuum-ultraviolet radiation in the rare gases. *JOSA B* 4, 595–601 (1987).
105. Ferray, M. et al. Multiple-harmonic conversion of 1064 nm radiation in rare gases. *J. Phys. B At. Mol. Opt. Phys.* 21, L31 (1988).
106. Paul, P. M. et al. Observation of a train of attosecond pulses from high harmonic generation. *Science* (80-. ). 292, 1689–1692 (2001).

107. Dromey, B. et al. High harmonic generation in the relativistic limit. *Nat. Phys.* 2, 456 (2006).
108. Couprie, M.-E. & Filhol, J.-M. X radiation sources based on accelerators. *Comptes Rendus Phys.* 9, 487–506 (2008).
109. Couprie, M. E. New generation of light sources: present and future. *J. Electron Spectros. Relat. Phenomena* 196, 3–13 (2014).
110. Couprie, M. E. Short wavelength free-electron laser sources. *Comptes Rendus l'Académie des Sci. IV-Physics* 1, 329–345 (2000).
111. Madey, J. M. J. Stimulated Emission of Bremsstrahlung in a Periodic Magnetic Field. *J. Appl. Phys.* 42, 1906–1913. doi:10.1063/1.1660466. <http://dx.doi.org/10.1063/1.1660466> (1971).
112. Schawlow, A. L. & Townes, C. H. Infrared and optical masers. *Phys. Rev.* 112, 1940 (1958).
113. Maimain, T. Stimulated optical radiation in Ruby. *Nature* 187, 493–494 (1960).
114. Deacon, D. A. G. et al. First operation of a free-electron laser. *Phys. Rev. Lett.* 38, 892 (1977).
115. Emma, P. et al. First lasing and operation of an ångstrom-wavelength free-electron laser. *Nat. Photonics* 4, 641–647. doi:10.1038/nphoton.2010.176. <http://www.nature.com/doi/10.1038/nphoton.2010.176> (2010).
116. Ishikawa, T. et al. A compact X-ray free-electron laser emitting in the sub-ångstrom region. *Nat. Photonics* 6, 540–544 (2012).
117. Kang, H.-S. et al. Hard X-ray free-electron laser with femtosecond-scale timing jitter. *Nat. Photonics* 11, 708 (2017).
118. Milne, C. J. et al. SwissFEL: The Swiss X-ray free electron laser. *Appl. Sci.* 7, 720 (2017).
119. Weise, H. & Decking, W. Commissioning and first lasing of the European XFEL in Proc. FEL2017, St. Fe, NM, USA (2017).
120. Ackermann, W. et al. Operation of a free-electron laser from the extreme ultraviolet to the water window. *Nat. Photonics* 1, 336–342 (2007).
121. Allaria, E. et al. Highly coherent and stable pulses from the FERMI seeded free-electron laser in the extreme ultraviolet. *Nat. Photonics* 6, 699–704 (2012).
122. Wang, G. Commissioning Status of the Dalian Coherent Light Source in 8th Int. Part. Accel. Conf. (IPAC'17), Copenhagen, Denmark, 14-19 May, 2017 (2017), 2709–2712.
123. McNeil, B. Free electron lasers: First light from hard X-ray laser. *Nat. Photonics* 3, 375–377 (2009).
124. Pellegrini, C., Marinelli, A. & Reiche, S. The physics of X-ray free-electron lasers. *Rev. Mod. Phys.* 88, 15006 (2016).
125. Bostedt, C. et al. Linac coherent light source: the first five years. *Rev. Mod. Phys.* 88, 15007 (2016).
126. Chapman, H. N. et al. Femtosecond X-ray protein nanocrystallography. *Nature* 470, 73–77 (2011).
127. Seibert, M. M. et al. Single mimivirus particles intercepted and imaged with an X-ray laser. *Nature* 470, 78–81 (2011).
128. Kirian, R. A. et al. Structure-factor analysis of femtosecond microdiffraction patterns from protein nanocrystals. *Acta Crystallogr. Sect. A Found. Crystallogr.* 67, 131–140 (2011).
129. Young, L. et al. Femtosecond electronic response of atoms to ultra-intense X-rays. *Nature* 466, 56–61 (2010).
130. Berrah, N. et al. Non-linear processes in the interaction of atoms and molecules with intense EUV and X-ray fields from SASE free electron lasers (FELs). *J. Mod. Opt.* 57, 1015–1040 (2010).
131. Doumy, G. et al. Nonlinear atomic response to intense ultrashort X rays. *Phys. Rev. Lett.* 106, 83002–83006 (2011).
132. Richter, M., Bobashev, S. V., Sorokin, A. A. & Tiedtke, K. Multiphoton ionization of atoms with soft X-ray pulses. *J. Phys. B At. Mol. Opt. Phys.* 43, 194005–194012 (2010).

133. Zewail, A. H. Femtochemistry: Atomic-scale dynamics of the chemical bond. *J. Phys. Chem. A* 104, 5660–5694 (2000).
134. Meyer, M., Costello, J. T., Düsterer, S., Li, W. B. & Radcliffe, P. Two-colour experiments in the gas phase. *J. Phys. B At. Mol. Opt. Phys.* 43, 194006–194015 (2010).
135. Günther, C. M. et al. Sequential femtosecond X-ray imaging. *Nat. Photonics* 5, 99–102 (2011).
136. Roy, S. et al. Lensless X-ray imaging in reflection geometry. *Nat. Photonics* 5, 243–245 (2011).
137. Glowina, J. M. et al. Time-resolved pump-probe experiments at the LCLS. *Opt. Express* 18, 17620–17630 (2010).
138. Galtier, E. et al. Decay of crystalline order and equilibration during the solid-to-plasma transition induced by 20 ~fs microfocused 92 ~eV free-electron-laser pulses. *Phys. Rev. Lett.* 106, 164801–164806 (2011).
139. Molodozhentsev, A. & Pribyl, L. Progress on the generation of undulator radiation in the UV from a plasma-based electron beam in Proc. IPAC2016, Busan, Korea (2016), 4005–4007.
140. Marteau, F. et al. Variable high gradient permanent magnet quadrupole (QUAPEVA). *Appl. Phys. Lett.* 111, 253503 (2017).
141. Couprie, M.-E., Loulergue, A., Labat, M., Lehe, R. & Malka, V. Towards a free electron laser based on laser plasma accelerators. *J. Phys. B At. Mol. Opt. Phys.* 47, 234001 (2014).
142. ALEGRO Collaboration. Towards an Advanced Linear International Collider 2019. <https://arxiv.org/abs/1901.10370>.
143. Liu, J. S. et al. All-Optical Cascaded Laser Wakefield Accelerator Using Ionization-Induced Injection. *Phys. Rev. Lett.* 107, 35001. doi:10.1103/PhysRevLett.107.035001. <http://link.aps.org/doi/10.1103/PhysRevLett.107.035001> (2011).
144. U.S. Department of Energy-Office of Science. Advanced Accelerator Development Strategy Report in DOE Adv. Accel. Concepts Res. Roadmap Work. Febr. 2 – 3, 2016 (2016).
145. PWASC. Plasma wakefield accelerator steering committee 2019. <http://pwasc.org.uk/> (2019).
146. Hogan, M. J. et al. Plasma wakefield acceleration experiments at FACET. *New J. Phys.* 12, 055030. doi:10.1088/1367-2630/12/5/055030. <http://stacks.iop.org/1367-2630/12/i=5/a=055030?key=crossref.72f665d9f313301607de16ff3f559a55> (May 2010).
147. U.S. Department of Energy. Technical Design Report for the FACET-II Project at SLAC National Accelerator Laboratory tech. rep. (SLAC National Accelerator Laboratory, 2016), SLAC-R-1072.
148. Alejo, A., Walczak, R. & Sarri, G. Laser-driven high-quality positron sources as possible injectors for plasma-based accelerators. *Sci. Rep.* 9, 5279. doi:10.1038/s41598-019-41650-y. <http://www.nature.com/articles/s41598-019-41650-y> (Dec. 2019).
149. Keeble, D. J. et al. Identification of A-and B -Site Cation Vacancy Defects in Perovskite Oxide Thin Films. *Phys. Rev. Lett.* 105, 226102. doi:10.1103/PhysRevLett.105.226102. <https://link.aps.org/doi/10.1103/PhysRevLett.105.226102> (Nov. 2010).
150. Helmholtz-Zentrum Dresden-Rossendorf. Positronen-Annihilations-Spektroskopie am HZDR 2018. <https://www.hzdr.de/db/Cms?pNid=3225> (2019).
151. Helmholtz-Zentrum Dresden-Rossendorf. The Slow-Positron System of Rossendorf-SPONSOR 2019. <https://www.hzdr.de/db/Cms?pOid=35320&pNid=3225> (2019).
152. Heinz Maier-Leibnitz-Zentrum. NEPOMUC-Neutron induced positron source Munich 2019. <https://www.mlz-garching.de/nepomuc>.
153. Heinz Maier-Leibnitz-Zentrum. PLEPS-Pulsed low energy positron system 2019. <https://www.mlz-garching.de/pleps>.
154. Sarri, G. et al. Table-Top Laser-Based Source of Femtosecond, Collimated, Ultrarelativistic Positron Beams. *Phys. Rev. Lett.* 110, 255002. doi:10.1103/PhysRevLett.110.255002. <https://link.aps.org/doi/10.1103/PhysRevLett.110.255002> (June 2013).

155. Sarri, G. et al. Spectral and spatial characterisation of laser-driven positron beams. *Plasma Phys. Control. Fusion* 59, 014015. doi:10.1088/0741-3335/59/1/014015. <http://stacks.iop.org/0741-3335/59/i=1/a=014015?key=crossref.5e376211abe22b4718389b5279783e9e> (Jan. 2017).
156. Sarri, G. et al. Overview of laser-driven generation of electron–positron beams. *J. Plasma Phys.* 81, 455810401. doi:10.1017/S002237781500046X. [https://www.cambridge.org/core/product/identifier/S002237781500046X/type/journal\\_article](https://www.cambridge.org/core/product/identifier/S002237781500046X/type/journal_article) (Aug. 2015).
157. Deutsches Elektronensynchrotron-DESY. FLASH [http://photon-science.desy.de/facilities/flash/index\\_eng.html](http://photon-science.desy.de/facilities/flash/index_eng.html).
158. SwissFEL Collaboration. SwissFEL Conceptual Design Report tech. rep. (). [https://www.psi.ch/sites/default/files/import/swissfel\\_old/CurrentSwissFELPublications/EN/SwissFEL\\_CDR\\_V20\\_23.04.1](https://www.psi.ch/sites/default/files/import/swissfel_old/CurrentSwissFELPublications/EN/SwissFEL_CDR_V20_23.04.1).
159. Wilkinson, M. D. et al. The FAIR Guiding Principles for scientific data management and stewardship. *Sci. Data* 3, 160018. doi:10.1038/sdata.2016.18. <http://www.nature.com/articles/sdata201618> (Dec. 2016).
160. e-Infrastructure Reflection Group. e-IRG Roadmap 2016 tech. rep. (2016), Version 5.3. <http://e-irg.eu/documents/10920/12353/Roadmap+2016.pdf>.
161. UK Data Service. The ‘FAIR’ principles for scientific data management. <https://www.ukdataservice.ac.uk/news-and-events/newsitem/?id=4615> (June 2016).
162. Alesini, D., Anania, M. P., Artioli, M. & Bacci, A. EuPRAXIA@SPARCLAB Conceptual Design Report tech. rep. LNF-1803 (Istituto Nazionale di Fisica Nucleare INFN, 2018). <http://www.lnf.infn.it/sis/preprint/pdf/getfile.php?filename=INFN-18-03-LNF.pdf>.
163. Ferrario, M. et al. EuPRAXIA@ SPARC\_LAB Design study towards a compact FEL facility at LNF. *Nucl. Instruments Methods Phys. Res. Sect. A Accel. Spectrometers, Detect. Assoc. Equip.* 909, 134–138 (2018).
164. Wuensch, W. Advances in High Gradient Accelerating Structures and in the Understanding Gradient Limits in *Proc. Int. Part. Accel. Conf. IPAC 17* (2017).
165. Bisesto, F. G. et al. The FLAME laser at SPARC\_LAB. *Nucl. Instruments Methods Phys. Res. Sect. A Accel. Spectrometers, Detect. Assoc. Equip.* 909, 452–455 (2018).
166. Institut Curie. Institut Curie – Recombination, Repair and Cancer: Team Dutreix <https://science.institut-curie.org/research/biology-chemistry-of-radiations-cell-signaling-and-cancer-axis/umr-3347-normal-and-pathological-signaling/team-dutreix/>.
167. Derouillat, J. et al. SMILEI: A Collaborative, Open-Source, Multi-Purpose Particle-in-Cell Code for Plasma Simulation. 222, 351–373. doi:10.1016/j.cpc.2017.09.024. <http://arxiv.org/abs/1702.05128>.
168. Intense Laser Irradiation Laboratory. Laboratorio di Laser Intensi – Istituto Nazionale di Ottica – Consiglio Nazionale delle Ricerche 2019. [http://research.ino.it/Groups/ilil/it/about\\_it/](http://research.ino.it/Groups/ilil/it/about_it/) (2019).
169. Gizzi, L. A. et al. Laser-Plasma Acceleration: First Experimental Results from the Plasmon- X Project in Charg. Neutral Part. Channeling Phenom. (*WORLD SCIENTIFIC*, Apr. 2010), 485–501. doi:10.1142/9789814307017\_0045. [http://www.worldscientific.com/doi/abs/10.1142/9789814307017\\_0045](http://www.worldscientific.com/doi/abs/10.1142/9789814307017_0045).
170. Tomassini, P. et al. The resonant multi-pulse ionization injection. *Phys. Plasmas* 24, 103120. doi:10.1063/1.5000696. <http://aip.scitation.org/doi/10.1063/1.5000696> (Oct. 2017).
171. Nghiem, P. A. et al. Eupraxia, A Step Toward A Plasma-Wakefield Based Accelerator with High Beam Quality. *J. Phys. Conf. Ser.* 1350. doi:10.1088/1742-6596/1350/1/012068 (2019).
172. Rossi, A. et al. A concept for an active plasma undulator in Eur. Adv. Accel. Concepts Work. (Elba, Italy, 2019).
173. European Commission. HORIZON2020-Work Programme 2018-2020: Technical Readiness Levels (TRL) tech. rep. (2017), C(2017)7124. [https://ec.europa.eu/research/participants/data/ref/h2020/other/wp/2018-2020/annexes/h2020-wp1820-annex-g-trl\\_en.pdf](https://ec.europa.eu/research/participants/data/ref/h2020/other/wp/2018-2020/annexes/h2020-wp1820-annex-g-trl_en.pdf).

174. Particle Physics Project Prioritization Panel (P5). Building for Discovery – Strategic Plan for U.S. Particle Physics in the Global Context tech. rep. (2014). [http://inspirehep.net/record/1299183/files/FINAL\\_P5\\_Report\\_053014.pdf](http://inspirehep.net/record/1299183/files/FINAL_P5_Report_053014.pdf).
175. Ellis, R. & al., E. Physics Briefing Book: European Strategy for Particle Physics Preparatory Group tech. rep. (CERN, Geneva, Switzerland, 2019), CERN–ESU–004. [http://cds.cern.ch/record/2691414/files/Briefing\\_Book\\_Final.pdf](http://cds.cern.ch/record/2691414/files/Briefing_Book_Final.pdf).
176. League of European Accelerator-based Photon Sources (LEAPS). LEAPS Strategy 2030 tech. rep. (2018). [https://www.leaps-initiative.eu/sites/sites\\_custom/site\\_leaps-initiative/content/e49102/e65282/e65283/LEAPS\\_Strategy2030\\_180611.pdf](https://www.leaps-initiative.eu/sites/sites_custom/site_leaps-initiative/content/e49102/e65282/e65283/LEAPS_Strategy2030_180611.pdf).
177. Hidding, B. et al. Plasma Wakefield Accelerator Research 2019-2040: A community-driven UK roadmap compiled by the Plasma Wakefield Accelerator Steering Committee (PWASC) 2019. [https://www.researchgate.net/publication/332553759\\_Plasma\\_Wakefield\\_Accelerator\\_Research\\_2019\\_-\\_2040\\_A\\_community-driven\\_UK\\_roadmap\\_compiled\\_by\\_the\\_Plasma\\_Wakefield\\_Accelerator\\_Steering\\_Committee\\_PWASC](https://www.researchgate.net/publication/332553759_Plasma_Wakefield_Accelerator_Research_2019_-_2040_A_community-driven_UK_roadmap_compiled_by_the_Plasma_Wakefield_Accelerator_Steering_Committee_PWASC).
178. European Network for Novel Accelerators. A European Roadmap tech. rep. (2017), (published as EU EuCARD2 deliverable report). [https://edms.cern.ch/ui/file/1325207/2/EuCARD2\\_Del7-2-Final.pdf](https://edms.cern.ch/ui/file/1325207/2/EuCARD2_Del7-2-Final.pdf).
179. Cros, B., Muggli, P. & (on behalf of the ALEGRO collaboration). ALEGRO input for the 2020 update of the European Strategy 2019. <https://arxiv.org/abs/1901.08436>.
180. Esarey, E., Schroeder, C. B. & Leemans, W. P. Physics of laser-driven plasma-based electron accelerators. *Rev. Mod. Phys.* 81, 1229–1285. doi:10.1103/RevModPhys.81.1229 (2009).
181. Steinke, S. et al. Multistage coupling of independent laser-plasma accelerators. *Nature* 530, 190–193. doi:10.1038/nature16525. <http://www.nature.com/articles/nature16525> (Feb. 2016).
182. Nakajima, K. Seamless multistage laser-plasma acceleration toward future high-energy colliders. *Light Sci. Appl.* 7 (2018).
183. Cros, B. et al. Laser plasma acceleration of electrons with multi-PW laser beams in the frame of CILEX. *Nucl. Instr. Meth. Phys. Res., Sect. A* 740, 27–33. doi:10.1016/j.nima.2013.10.090 (2014).
184. Leemans, W. P. et al. The BERkeley Lab Laser Accelerator (BELLA): A 10 GeV Laser Plasma Accelerator. *AIP Conf. Proc.* 1299 (2010).
185. Lu, W. et al. Generating multi-GeV electron bunches using single stage laser wakefield acceleration in a 3D nonlinear regime. *Phys. Rev. ST Accel. Beams* 10, 61301. doi:10.1103/PhysRevSTAB.10.061301. <http://link.aps.org/doi/10.1103/PhysRevSTAB.10.061301> <https://link.aps.org/doi/10.1103/PhysRevSTAB.10.061301> (June 2007).
186. Lu, W., Huang, C., Zhou, M., Mori, W. B. & Katsouleas, T. Nonlinear Theory for Relativistic Plasma Wakefields in the Blowout Regime. *Phys. Rev. Lett.* 96, 165002. doi:10.1103/PhysRevLett.96.165002. <https://link.aps.org/doi/10.1103/PhysRevLett.96.165002> (Apr. 2006).
187. Bane, K., Wilson, P. & Weiland, T. Wake fields and wake field acceleration tech. rep. (Stanford Linear Accelerator Center, 1984), SLAC–PUB–3528.
188. Katsouleas, T. Physical mechanisms in the plasma wake-field accelerator. *Phys. Rev. A* 33, 2056–2064. doi:10.1103/PhysRevA.33.2056. <http://link.aps.org/doi/10.1103/PhysRevA.33.2056> (Mar. 1986).
189. Chen, P., Su, J. J., Dawson, J. M., Bane, K. L. F. & Wilson, P. B. Energy Transfer in the Plasma Wake-Field Accelerator. *Phys. Rev. Lett.* 56, 1252–1255. doi:10.1103/PhysRevLett.56.1252. <https://link.aps.org/doi/10.1103/PhysRevLett.56.1252> (Mar. 1986).
190. Bane, K. L. F., Chen, P. & Wilson, P. B. On Collinear Wake Field Acceleration. *IEEE Trans. Nucl. Sci.* 32, 3524–3526. doi:10.1109/TNS.1985.4334416. <http://ieeexplore.ieee.org/document/4334416> (Oct. 1985).

191. Jiang, B., Jing, C., Schoessow, P., Power, J. & Gai, W. Formation of a novel shaped bunch to enhance transformer ratio in collinear wakefield accelerators. *Phys. Rev. Spec. Top.–Accel. Beams* 15, 011301. doi:10.1103/PhysRevSTAB.15.011301. <https://link.aps.org/doi/10.1103/PhysRevSTAB.15.011301> (Jan. 2012).
192. Tsakanov, V. M. On collinear wake field acceleration with high transformer ratio. *Nucl. Instruments Methods Phys. Res. Sect. A Accel. Spectrometers, Detect. Assoc. Equip.* 432, 202–213 (1999).
193. Van der Meer, S. Improving the power efficiency of the plasma wakefield accelerator tech. rep. CERN–PS–85–65–AA ; CLIC–Note–3 (CERN, Geneva, 1985), CERN–PS–85–65–AA, CLIC–Note–3.
194. Floettmann, K. Some basic features of the beam emittance. *Phys. Rev. Spec. Top.–Accel. Beams* 6. doi:10.1103/PhysRevSTAB.6.034202 (2003).
195. Courant, E. D. & Snyder, H. S. Theory of the Alternating–Gradient Synchrotron. *An. Phys.* 3 (1958).
196. Rittershofer, W., Schroeder, C. B., Esarey, E., Grüner, F. J. & Leemans, W. P. Tapered plasma channels to phase–lock accelerating and focusing forces in laser–plasma accelerators. *Phys. Plasmas* 17, 63104. doi:10.1063/1.3430638. <http://dx.doi.org/10.1063/1.3430638> (June 2010).
197. Desforges, F. G. et al. Reproducibility of electron beams from laser wakefield acceleration in capillary tubes. *Nucl. Instrum. Meth. A* 740, 54–59. doi:10.1016/j.nima.2013.10.062. <http://www.sciencedirect.com/science/article/pii/S0168900213014538> (2013).
198. Desforges, F. G. Injection induite par ionisation pour l’accélération laser–plasma dans des tubes capillaires diélectriques PhD thesis (Université Paris–Sud, 2015).
199. Strickland, D. & Mourou, G. Compression of amplified chirped optical pulses. 56, 219–221 (1985).
200. Heyl, C. M., Arnold, C. L., Couairon, A. & L’Huillier, A. Introduction to macroscopic power scaling principles for high–order harmonic generation. *J. Phys. B At. Mol. Opt. Phys.* 50, 013001. doi:10.1088/1361–6455/50/1/013001. <http://stacks.iop.org/0953–4075/50/i=1/a=013001?key=crossref.7fde8adcd056897664c8553591f789d8> (Jan. 2017).
201. Giambruno, F., Radier, C., Rey, G. & Chériaux, G. Design of a 10PW (150J/15fs) peak power laser system with Ti:sapphire medium through spectral control. *Appl. Opt.* 50, 2617–2621. doi:10.1364/AO.50.002617. <http://ao.osa.org/abstract.cfm?URI=ao-50-17-2617> (2011).
202. Ros, D. et al. LASERIX : A Multi X–Ray/XUV Beamline High Repetition–Rate Facility. *X–Ray Lasers 2006*, Springer, Dordr. (2007).
203. Leemans, W. P. et al. Bella Laser and Operations in Proc. PAC2013, Pasadena, CA USA (2013), THYAA1.
204. Lee, S. K., Sung, H. J., Lee, H. W., Yoo, J. Y. & Nam, C. H. Extreme light at CoReL–Sand its application to single cycle pulse generation [https://indico.cern.ch/event/531896/contributions/2223472/attachments/1328915/1996120/LEE\\_SK.pdf](https://indico.cern.ch/event/531896/contributions/2223472/attachments/1328915/1996120/LEE_SK.pdf).
205. Wang, Z. et al. High–contrast 1.16 PW Ti: sapphire laser system combined with a doubled chirped–pulse amplification scheme and a femtosecond optical–parametric amplifier. *Opt. Lett.* 36, 3194–3196 (2011).
206. Keppler, S. et al. Full characterization of the amplified spontaneous emission from a diodepumped high–power laser system. *Opt. Express* 22, 11228–11235 (2014).
207. Siebold, M., Roeser, F., Loeser, M., Albach, D. & Schramm, U. PEnELOPE—a high peak–power diode–pumped laser system for laser–plasma experiments in High–Power, High–Energy, High–Intensity Laser Technol. Res. Using Extrem. Light Enter. New Front. with Petawatt–Class Lasers, Proc. SPIE Vol. 8780 (2013), 878005.
208. Liebetrau, H. et al. Ultra–high contrast frontend for high peak power fs–lasers at 1030 nm. *Opt. Express* 22, 24776–24786 (2014).
209. Gaul, E. et al. Improved pulse contrast on the Texas Petawatt Laser in *J. Phys. Conf. Ser.* 717 (2016), 12092.

210. Ross, I. N. et al. Generation of terawatt pulses by use of optical parametric chirped pulse amplification. *Appl. Opt.* 39, 2422–2427 (2000).
211. Dubietis, A., Rytis Butkus & Algis, P. P. Trends in Chirped Pulse Optical Parametric Amplification. *IEEE J. Sel Top. Quantum Electron.* 12, 163–172 (2006).
212. Xie, X. et al. Multi petawatt laser design for the SHENGUANG II laser facility in High–Power, High–Energy, High–Intensity Laser Technol. II 9513 (2015), 95130A.
213. Danson, C., Hillier, D., Hopps N. & Neely, D. Petawatt class lasers worldwide. *High Power Laser Sci. Eng.* 3, e3 (2015).
214. McNeil, B. W. J. & Thompson, N. R. X–Ray Free–Electron Lasers. *Nat. Photonics* 4, 814–821. doi:10.1038/nphoton.2010.239. <http://www.nature.com/doi/10.1038/nphoton.2010.239> (2010).
215. Haus, H. Noise in free–electron laser amplifier. *IEEE J. Quantum Electron.* 17, 1427–1435 (1981).
216. Dattoli, G., Marino, A., Renieri, A. & Romanelli, F. Progress in the Hamiltonian picture of the free–electron laser. *IEEE J. Quantum Electron.* 17, 1371–1387 (1981).
217. Bonifacio, R., Pellegrini, C. & Narducci, L. M. Collective instabilities and high–gain regime in a free electron laser. *Opt. Commun.* 50, 373–378 (1984).
218. Kim, K.–J. An analysis of self–amplified spontaneous emission. *Nucl. Instruments Methods Phys. Res. Sect. A Accel. Spectrometers, Detect. Assoc. Equip.* 250, 396–403 (1986).
219. Dattoli, G., Ottaviani, P. L. & Pagnutti, S. Booklet for FEL design: a collection of practical formulae. Ed. Sci. Frascati (2007).
220. Walker, P. A. et al. EuPRAXIA Deliverable Report 1.2 Report defining preliminary study concept 2016.
221. Toci, G. et al. EuPRAXIA Deliverable Report: D4.1 Benchmarking of existing technology and comparison with the requirements tech. rep. (EuPRAXIA, 2016).
222. Nagymihaly, R. S. et al. Liquid–cooled Ti:Sapphire thin disk amplifiers for high average power 100–TW systems. *Opt. Express* 25, 6664. doi:10.1364/OE.25.006664. <https://www.osapublishing.org/abstract.cfm?URI=oe-25-6-6664> (Mar. 2017).
223. Chvykov, V., Nagymihaly, R. S., Cao, H., Kalashnikov, M. & Osvey, K. Design of a thin disk amplifier with extraction during pumping for high peak and average power Ti:Sa systems (EDP–TD). *Opt. Express* 24, 3721. doi:10.1364/OE.24.003721. <https://www.osapublishing.org/abstract.cfm?URI=oe-24-4-3721> (Feb. 2016).
224. Chu, Y. et al. High–contrast 20 Petawatt Ti:sapphire laser system. *Opt. Express* 21, 29231. doi:10.1364/OE.21.029231. <https://www.osapublishing.org/oe/abstract.cfm?uri=oe-21-24-29231> (Dec. 2013).
225. Gizzi, L. et al. A viable laser driver for a user plasma accelerator. *Nucl. Instruments Methods Phys. Res. Sect. A Accel. Spectrometers, Detect. Assoc. Equip.* 909, 58–66. doi:10.1016/J.NIMA.2018.02.089. <https://www.sciencedirect.com/science/article/pii/S0168900218302717?via%3Dihub> (Nov. 2018).
226. Morice, O. Miro: Complete modeling and software for pulse amplification and propagation in high–power laser systems. *Opt. Eng.* 42, 1530. doi:10.1117/1.1574326. <http://opticalengineering.spiedigitallibrary.org/article.aspx?doi=10.1117/1.1574326> (June 2003).
227. Gizzi, L. et al. A New Line for Laser–Driven Light Ions Acceleration and Related TNSA Studies. *Appl. Sci.* 7, 984. doi:10.3390/app7100984. <http://www.mdpi.com/2076-3417/7/10/984> (Sept. 2017).
228. Toci, G. et al. Conceptual Design of a Laser Driver for a Plasma Accelerator User Facility. *Instruments* 3, 40 (2019).
229. Ferrara, P. et al. 3–D numerical simulation of Yb:YAG active slabs with longitudinal doping gradient for thermal load effects assessment. *Opt. Express* 22, 5375. doi:10.1364/OE.22.005375. <https://www.osapublishing.org/oe/abstract.cfm?uri=oe-22-5-5375> (Mar. 2014).
230. Alessi, D. A., Nguyen, H. T., Britten, J. A., Rosso, P. A. & Haefner, C. Low–dispersion low–loss dielectric gratings for efficient ultrafast laser pulse compression at high average powers. *Opt. Laser Technol.* 117, 239–243. doi:10.1016/J.OPTLASTEC.

- 2019.04.005. <https://www.sciencedirect.com/science/article/pii/S0030399218320218> (Sept. 2019).
231. De Vido, M. et al. A scalable high-energy diode-pumped solid state laser for laser-plasma interaction science and applications. *J. Phys. Conf. Ser.* 717, 012090. doi:10.1088/1742-6596/717/1/012090. <http://stacks.iop.org/1742-6596/717/i=1/a=012090?key=crossref.7a785c45870b7afba9fa905eb32e8ec2> (May 2016).
  232. Leemans, W. Progress on Petawatt level experiments at BELLA Center for electron and ion acceleration Elba, Italy, 2017.
  233. Mathieu, F. et al. Device and method for the measurement of inclination and angular stability of electromagnetic radiation beams (patent no: 102019000020562) 2019.
  234. Galvin, T. et al. Scaling of petawatt-class lasers to multi-kHz repetition rates in *Proc. SPIE 11033, High-Power, High-Energy, High-Intensity Laser Technol. IV* (2019), 1103303. doi:10.1117/12.2520981.
  235. Honea, E. C. et al. 115 W Tm:YAG CW diode-pumped solid-state laser in *Adv. Solid State Lasers* (OSA, Washington, D.C., Jan. 1997), HP8. doi:10.1364/ASSL.1997.HP8. <https://www.osapublishing.org/abstract.cfm?URI=ASSL-1997-HP8>.
  236. Dergachev, A. et al. Review of Multipass Slab Laser Systems. *IEEE J. Sel. Top. Quantum Electron.* 13, 647-660. doi:10.1109/JSTQE.2007.897177. [http://ieeexplore.ieee.org/document/4244415/\(2007\)](http://ieeexplore.ieee.org/document/4244415/(2007)).
  237. International Electrotechnical Commission (IEC). Functional safety and IEC 61508 : A basic guide tech. rep. May (IEC, 2004). [https://www.google.com/url?sa=t & rct=j & q=&srsc=s & source=web & cd=1 & cad=rja & uact=8 & ved=0ahUKEwi9x4Oky6TNAhUEKcAKHQZ2BQIQFggfMAA&url=http%3A%2F%2Fweb.archive.nationalarchives.gov.uk%2F20111005155017%2Fhttp%3A%2Fwww.dft.gov.uk%2Fpgr%2Ffrail%2Fpassenger%2Ffranchis](https://www.google.com/url?sa=t&rc=1&q=&srsc=s&source=web&cd=1&cad=rja&uact=8&ved=0ahUKEwi9x4Oky6TNAhUEKcAKHQZ2BQIQFggfMAA&url=http%3A%2F%2Fweb.archive.nationalarchives.gov.uk%2F20111005155017%2Fhttp%3A%2Fwww.dft.gov.uk%2Fpgr%2Ffrail%2Fpassenger%2Ffranchis).
  238. Gizzi, L. et al. EuPRAXIA Milestone Report: M4.4 Final Laser and Controls Requirement Table tech. rep. (EuPRAXIA, 2018).
  239. Palmer, D. T. et al. The next generation photoinjector tech. rep. (Stanford Linear Accelerator Center (SLAC), 2005).
  240. Palmer, D. T. et al. Simulations of the BNL/SLAC/UCLA 1.6 cell emittance compensated photocathode rf gun low energy beam line tech. rep. (Stanford Linear Accelerator Center SLAC-PUB-95-6800, 1995).
  241. Adriani, O. et al. Technical Design Report EuroGammaS proposal for the ELI-NP Gamma beam System (2014).
  242. Limborg-Deprey, C. RF Design of the LCLS Gun tech. rep. (SLAC National Accelerator Laboratory (SLAC), 2010). <http://www-ssrl.slac.stanford.edu/lcls/technotes/lcls-tn-05-3.pdf>.
  243. Dolgashev, V. A., Tantawi, S. G., Nantista, C. D., Higashi, Y. & Higo, T. RF breakdown in normal conducting single-cell structures in *Part. Accel. Conf. 2005. PAC 2005. Proc.* (2005), 595-599.
  244. Palmer, D. T. et al. Microwave measurements of the BNL/SLAC/UCLA 1.6 cell photocathode RF gun in *Part. Accel. Conf. 1995., Proc. 1995 2* (1995), 982-984.
  245. Guan, X. et al. Study of RF-asymmetry in photo-injector. *Nucl. Instruments Methods Phys. Res. Sect. A Accel. Spectrometers, Detect. Assoc. Equip.* 574, 17-21 (2007).
  246. Chae, M. S. et al. Emittance growth due to multipole transverse magnetic modes in an rf gun. *Phys. Rev. Spec. Top. Beams* 14, 104203 (2011).
  247. A. Bacci and A. Giribono, private communications
  248. Los Alamos Accelerator Code Group. Download Area for Poisson Superfish [http://laacg.lanl.gov/laacg/services/download\\_sf.phtml](http://laacg.lanl.gov/laacg/services/download_sf.phtml).
  249. ANSYS Inc. ANSYS <http://www.ansys.com>.
  250. Alesini, D., Lollo, V. & Battisti, A. Process for manufacturing a vacuum and radiofrequency metal gasket and structure incorporating it (patent no: WO2016147118A1, PCT/IB2016/051464) 2016.
  251. Alesini, D. et al. New technology based on clamping for high gradient radio frequency photogun. *Phys. Rev. Spec. Top. Beams* 18, 92001 (2015).

252. Kuroda, R. et al. Quasi-monochromatic hard X-ray source via laser Compton scattering and its application. *Nucl. Instruments Methods Phys. Res. Sect. A Accel. Spectrometers, Detect. Assoc. Equip.* 637, S183–S186 (2011).
253. Kong, S. H., Kinross-Wright, J., Nguyen, D. C. & Sheffield, R. L. Photocathodes for free electron lasers. *Nucl. Instruments Methods Phys. Res. Sect. A Accel. Spectrometers, Detect. Assoc. Equip.* 358, 272–275 (1995).
254. Dowell, D. H. & Schmerge, J. F. Quantum efficiency and thermal emittance of metal photocathodes. *Phys. Rev. Spec. Top. Beams* 12, 74201 (2009).
255. Cultrera, L. et al. Mg based photocathodes for high brightness RF photoinjectors. *Appl. Surf. Sci.* 253, 6531–6534 (2007).
256. Lorusso, A. et al. Pulsed laser deposition of yttrium photocathode suitable for use in radiofrequency guns. *Appl. Phys. A* 123, 779 (2017).
257. Zhou, F. et al. Recent photocathode R&D for the LCLS injector in FEL Conf. 2014, Proc. (2014), 771–773.
258. Carlsten, B. New photoelectric injector design for the Los Alamos National Laboratory XUV FEL accelerator. *Nucl. Instruments Methods Phys. Res. Sect. A Accel. Spectrometers, Detect. Assoc. Equip.* 285, 313–319. doi:10.1016/0168-9002(89)90472-5. <https://www.sciencedirect.com/science/article/pii/016890028904725> (Dec. 1989).
259. Billen, J. H. & Young, L. M. Poisson Superfish. Los Alamos Nat. Lab tech. rep. (LA-UR-96-1834, revised, 2006).
260. Serafini, L. & Ferrario, M. Velocity bunching in photo-injectors in AIP Conf. Proc. 581 (AIP, Sept. 2001), 87–106. doi:10.1063/1.1401564. <http://aip.scitation.org/doi/abs/10.1063/1.1401564>.
261. Ferrario, M. et al. Experimental demonstration of emittance compensation with velocity bunching. *Phys. Rev. Lett.* 104, 54801 (2010).
262. Neal, R. B. THE STANFORD 2-MILE LINEAR ACCELERATOR. *Phys. Today* 20, 27–41 (1966).
263. Flottmann, K., Piot, P., Ferrario, M. & Grigorian, B. The TESLA X-FEL injector in Proc. Part. Accel. Conf. 2001 (2001), 2236f2238.
264. Wuensch, W. Ultimate Field Gradient in Metallic Structures in Proc. Int. Part. Accel. Conf. (IPAC'17), Copenhagen, Denmark, 14–19 May, 2017 (2017), 24–29.
265. Higo, T. et al. Advances in X-band TW accelerator structures operating in the 100 MV/m regime in IPAC 2010–1st Int. Part. Accel. Conf. (Kyoto, Japan, 2010), THPEA013/SLAC-PUB-15150.
266. Delahaye, J.-P. Towards CLIC feasibility tech. rep. (2010), CERN-OPEN-2010-024, CLIC-Note-822.
267. Shintake, T. in *Synchrotron Light Sources Free. Lasers Accel. Physics, Instrum. Sci. Appl.* 1–48 (Springer International Publishing, 2014).
268. Löhl, F. et al. Status of the SwissFEL C-band Linac in 36th Int. Free Electron Laser Conf. FEL 2014 (FEL 2014) (2014), 322–326.
269. Alesini, D. et al. The C-Band accelerating structures for SPARC photoinjector energy upgrade. *J. Instrum.* 8, P05004 (2013).
270. Farkas, Z. D., Hoag, H. A., Loew, G. A. & Wilson, P. B. SLED: A Method of Doubling SLAC's Energy in Proceedings, 9th Int. Conf. High-Energy Accel. (HEACC 1974) Stanford, California, May 2–7, 1974 (1974), 576.
271. Chao, A. W. *Physics of collective beam instabilities in high-energy accelerators* (Wiley, New York, USA, 1993).
272. Bane, K. L. F. Short range dipole wakefields in accelerating structures for the NLC tech. rep. (2003).
273. Faure, J. et al. A laser-plasma accelerator producing monoenergetic electron beams. *Nature* 431, 541–544. doi:10.1038/nature02963. <http://dx.doi.org/10.1038/nature02963> (2004).
274. Vieira, J. M. et al. Magnetic Control of Particle Injection in Plasma Based Accelerators. *Phys. Rev. Lett.* 106, 225001. doi:10.1103/PhysRevLett.106.225001. <http://link.aps.org/doi/10.1103/PhysRevLett.106.225001> (2011).

275. Bulanov, S. V., Naumova, N., Pegoraro, F. & Sakai, J. Particle injection into the wave acceleration phase due to nonlinear wake wave breaking. *Phys. Rev. E* 58, R5257–R5260. doi:10.1103/PhysRevE.58.R5257. <http://link.aps.org/doi/10.1103/PhysRevE.58.R5257> (1998).
276. Schmid, K. & Veisz, L. Supersonic gas jets for laser–plasma experiments. *Rev. Sci. Instrum.* 83, 53304. doi:10.1063/1.4719915. <http://scitation.aip.org/content/aip/journal/rsi/83/5/10.1063/1.4719915> (2012).
277. Rowlands–Rees, T. P. et al. Laser–driven acceleration of electrons in a partially ionized plasma channel. *Phys Rev Lett* 100, 105005. doi:10.1103/PhysRevLett.100.105005 (2008).
278. McGuffey, C. et al. Ionization Induced Trapping in a LaserWakefield Accelerator. *Phys. Rev. Lett.* 104, 25004. doi:10.1103/PhysRevLett.104.025004. <http://link.aps.org/doi/10.1103/PhysRevLett.104.025004> (2010).
279. Pak, A. et al. Injection and Trapping of Tunnel–Ionized Electrons into Laser–Produced Wakes. *Phys. Rev. Lett.* 104, 25003. doi:10.1103/PhysRevLett.104.025003. <http://link.aps.org/doi/10.1103/PhysRevLett.104.025003> (2010).
280. Audet, T. L. et al. Investigation of ionization–induced electron injection in a wakefield driven by laser inside a gas cell. *Phys. Plasmas* 23. doi:<http://dx.doi.org/10.1063/1.4942033>. <http://scitation.aip.org/content/aip/journal/pop/23/2/10.1063/1.4942033> (2016).
281. Chen, M., Esarey, E. H., Schroeder, C. B., Geddes, C. G. R. & Leemans, W. P. Theory of ionization–induced trapping in laser–plasma accelerators. *Phys. Plasmas* 19, 33101. doi:10.1063/1.3689922. <http://link.aip.org/link/?PHP/19/033101/1> (2012).
282. Pollock, B. B. et al. Demonstration of a Narrow Energy Spread,  $\sim 0.5$  GeV Electron Beam from a Two–Stage Laser Wakefield Accelerator. *Phys. Rev. Lett.* 107, 45001. doi:10.1103/PhysRevLett.107.045001. <http://link.aps.org/doi/10.1103/PhysRevLett.107.045001> (2011).
283. Mehrling, T. J., Robson, R. E., Erbe, J.–H. & Osterhoff, J. Efficient numerical modelling of the emittance evolution of beams with finite energy spread in plasma wakefield accelerators. *Nucl. Instruments Methods Phys. Res. Sect. A Accel. Spectrometers, Detect. Assoc. Equip.* 829, 367–371. doi:<https://doi.org/10.1016/j.nima.2016.01.091>. <http://www.sciencedirect.com/science/article/pii/S0168900216001418> (2016).
284. Swanson, K. K. et al. Control of tunable, monoenergetic laser–plasma–accelerated electron beams using a shock–induced density downramp injector. *Phys. Rev. Accel. Beams* 20, 1–6. doi:10.1103/PhysRevAccelBeams.20.051301 (2017).
285. Lee, P. et al. Optimization of laser–plasma injector via beam loading effects using ionizationinduced injection. *Phys. Rev. Accel. Beams* 21, 052802. doi:10.1103/PhysRevAccelBeams.21.052802. <https://link.aps.org/doi/10.1103/PhysRevAccelBeams.21.052802> (May 2018).
286. Kononenko, O. et al. 2D hydrodynamic simulations of a variable length gas target for density down–ramp injection of electrons into a laser wakefield accelerator. *Nucl. Inst. Methods Phys. Res. A* 829, 125–129. doi:10.1016/j.nima.2016.03.104. <http://dx.doi.org/10.1016/j.nima.2016.03.104> (Sept. 2016).
287. Lee, P. et al. Modeling laser–driven electron acceleration using WARP with Fourier decomposition. *Nucl. Instruments Methods Phys. Res. Sect. A Accel. Spectrometers, Detect. Assoc. Equip.* 829, 358–362. doi:10.1016/j.nima.2015.12.036 (2016).
288. Lee, P. et al. Dynamics of electron injection and acceleration driven by laser wakefield in tailored density profiles. *Phys. Rev. Acc. Beams* 19, 112802. doi:10.1103/PhysRevAccelBeams.19.112802 (2016).
289. Semushin, S. & Malka, V. High density gas jet nozzle design for laser target production. *Rev. Sci. Instrum.* 72, 2961. doi:10.1063/1.1380393. <http://scitation.aip.org/content/aip/journal/rsi/72/7/10.1063/1.1380393> (2001).
290. Leemans, W. P. et al. GeV electron beams from a centimetre–scale accelerator. *Nat. Phys.* 2, 696–699. doi:10.1038/nphys418. <http://www.nature.com/doi/10.1038/nphys418> (2006).

291. Audet, T. et al. EuPRAXIA Milestone Report: M3.2 Design for Interaction Chambers Proposed tech. rep. (EuPRAXIA, 2017).
292. Streeter, M. J. V. et al. Temporal feedback control of high-intensity laser pulses to optimize ultrafast heating of atomic clusters. *Appl. Phys. Lett.* 112, 244101. doi:10.1063/1.5027297. <http://aip.scitation.org/doi/10.1063/1.5027297> (2018).
293. Kallos, E. et al. High-Gradient Plasma-Wakefield Acceleration with Two Subpicosecond Electron Bunches. *Phys. Rev. Lett.* 100, 074802. doi:10.1103/PhysRevLett.100.074802. <https://link.aps.org/doi/10.1103/PhysRevLett.100.074802> (Feb. 2008).
294. Aschikhin, A. et al. The FLASHForward facility at DESY. *Nucl. Instruments Methods Phys. Res. Sect. A Accel. Spectrometers, Detect. Assoc. Equip.* 806, 175–183. doi:10.1016/J.NIMA.2015.10.005. <https://www.sciencedirect.com/science/article/pii/S0168900215012103> (Jan. 2016).
295. Walker, P. A. et al. Horizon 2020 EuPRAXIA design study. *J. Phys. Conf. Ser.* 874, 012029. doi:10.1088/1742-6596/874/1/012029. <http://stacks.iop.org/1742-6596/874/i=1/a=012029?key=crossref.38f8a3aa8a83e5e841762fbfd0deb590> (July 2017).
296. Ferrario, M. et al. SPARC LAB present and future. *Nucl. Instruments Methods Phys. Res. Sect. B Beam Interact. with Mater. Atoms* 309, 183–188. doi:10.1016/J.NIMB.2013.03.049 (Aug. 2013).
297. Benedetti, C., Schroeder, C., Esarey, E. & Leemans, W. Emittance preservation in plasmabased accelerators with ion motion. *Phys. Rev. Accel. Beams* 20, 111301. doi:10.1103/PhysRevAccelBeams.20.111301. <https://link.aps.org/doi/10.1103/PhysRevAccelBeams.20.111301> (Nov. 2017).
298. Tzoufras, M. et al. Beam loading by electrons in nonlinear plasma wakes. *Phys. Plasmas* 16. doi:10.1063/1.3118628 (May 2009).
299. Serafini, L. & Rosenzweig, J. B. Envelope analysis of intense relativistic quasilaminar beams in rf photoinjectors: A theory of emittance compensation. *Phys. Rev. E* 55, 7565–7590. doi:10.1103/PhysRevE.55.7565. <http://link.aps.org/doi/10.1103/PhysRevE.55.7565> (1997).
300. Ferrario, M. et al. Direct Measurement of the Double Emittance Minimum in the Beam Dynamics of the Sparc High-Brightness Photoinjector. *Phys. Rev. Lett.* 99, 234801. doi:10.1103/PhysRevLett.99.234801. <https://link.aps.org/doi/10.1103/PhysRevLett.99.234801> (Dec. 2007).
301. Aune, B. & Miller, R. H. New Method for Positron Production At Slac in 1979 Linear Accel. Conf. (1979), 0–3.
302. Emma, P. Accelerator Physics challenges of X-ray FEL SASE Sources in Proc. EPAC 2002, Paris, Fr. (2002), 49–53.
303. Chiadroni, E. et al. Beam manipulation for resonant plasma wakefield acceleration. *Nucl. Instruments Methods Phys. Res. Sect. A Accel. Spectrometers, Detect. Assoc. Equip.* –. doi:<http://dx.doi.org/10.1016/j.nima.2017.01.017>. <http://www.sciencedirect.com/science/article/pii/S0168900217300165> (2017).
304. Rossi, A. R. et al. The External-Injection experiment at the SPARC LAB facility. *Nucl. Instrum. Meth. A* 740, 60–66. doi:10.1016/0030-4018(93)90611-8. <http://www.sciencedirect.com/science/article/pii/S016890021301454X> (2014).
305. Pompili, R. et al. Experimental characterization of active plasma lensing for electron beams. *Appl. Phys. Lett.* 110, 04101. doi:10.1063/1.4977894. <http://dx.doi.org/10.1063/1.4977894> (2017).
306. Giannessi, L. et al. Self-Amplified Spontaneous Emission Free-Electron Laser with an Energy-Chirped Electron Beam and Undulator Tapering. *Phys. Rev. Lett.* 106, 144801. doi:10.1103/PhysRevLett.106.144801. <https://link.aps.org/doi/10.1103/PhysRevLett.106.144801> (Apr. 2011).
307. Giannessi, L. et al. Superradiant Cascade in a Seeded Free-Electron Laser. *Phys. Rev. Lett.* 110, 044801. doi:10.1103/PhysRevLett.110.044801. <https://link.aps.org/doi/10.1103/PhysRevLett.110.044801> (Jan. 2013).
308. Labat, M. et al. High-Gain Harmonic-Generation Free-Electron Laser Seeded by Harmonics Generated in Gas. *Phys. Rev. Lett.* 107, 224801. doi:10.1103/

- PhysRevLett.107.224801. <https://link.aps.org/doi/10.1103/PhysRevLett.107.224801> (Nov. 2011).
309. Ronsivalle, C. et al. Large-bandwidth two-color free-electron laser driven by a comb-like electron beam. *New J. Phys.* 16, 033018. doi:10.1088/1367-2630/16/3/033018. <http://stacks.iop.org/1367-2630/16/i=3/a=033018> ? key=crossref.a08948663f61174c2a249ec7d2efde8b (Mar. 2014).
  310. Giribono, A. X-ray generation at SPARC\_LAB Thomson backscattering source. *Nuovo Cim. C- Colloq. Commun. Phys.* 38. <https://www.sif.it/riviste/sif/ncc/econtents/2015/038/02/article/22> (2015).
  311. Vaccarezza, C. et al. The SPARC\_LAB Thomson source. *Nucl. Instruments Methods Phys. Res. Sect. A Accel. Spectrometers, Detect. Assoc. Equip.* 829, 237-242. <https://www.sciencedirect.com/science/article/pii/S0168900216001303> ? via %3Dihub (2016).
  312. Chiadroni, E. et al. Characterization of the THz radiation source at the Frascati linear accelerator. *Rev. Sci. Instrum.* 84, 22703. doi:10.1063/1.4790429. <https://doi.org/10.1063/1.4790429> (2013).
  313. Chiadroni, E. et al. The SPARC linear accelerator based terahertz source. *Appl. Phys. Lett.* 102, 094101. doi:10.1063/1.4794014. <http://aip.scitation.org/doi/10.1063/1.4794014> (Mar. 2013).
  314. Alesini, D. et al. Status of the SPARC project. *Nucl. Instruments Methods Phys. Res. Sect. A Accel. Spectrometers, Detect. Assoc. Equip.* 528, 586-590. doi:10.1016/J.NIMA.2004.04.107. <https://www.sciencedirect.com/science/article/pii/S0168900204007831> (Aug. 2004).
  315. Young, L. TStep: An electron linac design code
  316. Zhu, J., Assmann, R., Dorda, U. & Marchetti, B. Lattice design and start-to-end simulations for the ARES linac. *Nucl. Instruments Methods Phys. Res. A* 909, 467-470. doi:10.1016/j.nima.2018.02.045 (Nov. 2018).
  317. Dorda, U. et al. Status and objectives of the dedicated accelerator R&D facility "SINBAD" at DESY. *Nucl. Instruments Methods Phys. Res. Sect. A Accel. Spectrometers, Detect. Assoc. Equip.* 909, 239-242 (2018).
  318. Zhu, J. Design Study for Generating Sub-Femtosecond to Femtosecond Electron Bunches for Advanced Accelerator Development at SINBAD PhD thesis (University of Hamburg).
  319. Lemery, F. et al. Overview of the ARES Bunch Compressor at SINBAD in Proc. 10th Int. Part. Accel. Conf. (Melbourne, 2019), MOPTS025. doi:10.18429/JACoW-IPAC2019- MOPTS025.
  320. Floettmann, K. et al. Astra: A space charge tracking algorithm. Manual, Version 3, 2014. [http://www.desy.de/%5Csim\\$mpyflo/Astra\\_manual/Astra-Manual\\_V3.2.pdf](http://www.desy.de/%5Csim$mpyflo/Astra_manual/Astra-Manual_V3.2.pdf) (2011).
  321. Qiang, J., Lidia, S., Ryne, R. D. & Limborg-Deprey, C. Three-dimensional quasistatic model for high brightness beam dynamics simulation. *Phys. Rev. Spec. Top.-Accel. Beams* 9, 044204. doi:10.1103/PhysRevSTAB.9.044204. <https://link.aps.org/doi/10.1103/PhysRevSTAB.9.044204> (Apr. 2006).
  322. Zhu, J., Assmann, R., Dorda, U., Marchetti, B. & Elektronen-synchrotron, D. MATCHING SPACE-CHARGE DOMINATED ELECTRON BUNCHES INTO THE PLASMA ACCELERATOR AT SINBAD in IPAC 2017, Copenhagen (2017), 4429-4431.
  323. Ferrario, M. et al. Laser comb with velocity bunching: Preliminary results at SPARC. *Nucl. Instruments Methods Phys. Res. Sect. A Accel. Spectrometers, Detect. Assoc. Equip.* 637, S43-S46. doi:10.1016/J.NIMA.2010.02.018. <https://www.sciencedirect.com/science/article/pii/S0168900210002160?via%3Dihub> (May 2011).
  324. Villa, F. et al. Laser pulse shaping for high gradient accelerators. *Nucl. Instruments Methods Phys. Res. Sect. A Accel. Spectrometers, Detect. Assoc. Equip.* 829, 446-451. doi:10.1016/J.NIMA.2016.01.010. <https://www.sciencedirect.com/science/article/pii/S0168900216000139?via%3Dihub> (Sept. 2016).

325. Mostacci, A. et al. Advanced Beam Manipulation Techniques at SPARC in IPAC 2011 (San Sebastian, Spain, 2011), 2877–2881.
326. Giorgianni, F. et al. Tailoring of Highly Intense THz Radiation Through High Brightness Electron Beams Longitudinal Manipulation. *Appl. Sci.* 6, 56. doi:10.3390/app6020056. <http://www.mdpi.com/2076-3417/6/2/56> (Feb. 2016).
327. Petrillo, V. et al. Observation of Time-Domain Modulation of Free-Electron-Laser Pulses by Multi-peaked Electron-Energy Spectrum. *Phys. Rev. Lett.* 111, 114802. doi:10.1103/PhysRevLett.111.114802. <https://link.aps.org/doi/10.1103/PhysRevLett.111.114802> (Sept. 2013).
328. Petralia, A. et al. Two-Color Radiation Generated in a Seeded Free-Electron Laser with Two Electron Beams. *Phys. Rev. Lett.* 115, 014801. doi:10.1103/PhysRevLett.115.014801. <https://link.aps.org/doi/10.1103/PhysRevLett.115.014801> (June 2015).
329. Tzoufras, M. et al. Beam Loading in the Nonlinear Regime of Plasma-Based Acceleration. *Phys. Rev. Lett.* 101, 145002. doi:10.1103/PhysRevLett.101.145002. <https://link.aps.org/doi/10.1103/PhysRevLett.101.145002> (Sept. 2008).
330. Assmann, R. & Yokoya, K. Transverse beam dynamics in plasma-based linacs. *Nucl. Instruments Methods Phys. Res. Sect. A Accel. Spectrometers, Detect. Assoc. Equip.* 410, 544–548. doi:10.1016/S0168-9002(98)00187-9. <https://www.sciencedirect.com/science/article/pii/S0168900298001879?via%3Dihub> (June 1998).
331. Ferran Pousa, A., Assmann, R., Brinkmann, R. & Martinez de la Ossa, A. External Injection into a Laser-Driven Plasma Accelerator with Sub-Femtosecond Timing Jitter. *J. Phys. Conf. Ser.* 874, 012032. doi:10.1088/1742-6596/874/1/012032. <http://stacks.iop.org/1742-6596/874/i=1/a=012032?key=crossref.eb0dce28a7460e9cef823dfa84a31f93> (2017).
332. Clayton, C. & Serafini, L. Generation and transport of ultrashort phase-locked electron bunches to a plasma beatwave accelerator. *IEEE Trans. Plasma Sci.* 24, 400–408. doi:10.1109/27.510004. <http://ieeexplore.ieee.org/document/510004/> (Apr. 1996).
333. Katsouleas, T. et al. A plasma klystron for generating ultra-short electron bunches. *IEEE Trans. Plasma Sci.* 24, 443–447. doi:10.1109/27.510009. <http://ieeexplore.ieee.org/document/510009/> (Apr. 1996).
334. Ferrario, M., Katsouleas, T., Serafini, L. & Zvi, I. Adiabatic plasma buncher. *IEEE Trans. Plasma Sci.* 28, 1152–1158. doi:10.1109/27.893295. <http://ieeexplore.ieee.org/document/893295/> (2000).
335. Gorbunov, L. M. & Kirsanov, V. I. Excitation of plasma waves by an electromagnetic wave packet. *Sov. Phys. JETP* 66, 290–294. [http://www.jetp.ac.ru/cgi-bin/dn/e\\_066\\_02\\_0290.pdf](http://www.jetp.ac.ru/cgi-bin/dn/e_066_02_0290.pdf) (1987).
336. Fonseca, R. et al. OSIRIS: A three-dimensional, fully relativistic particle in cell code for modeling plasma based accelerators. *Comput. Sci.* 2002, 342–351. doi:10.1007/3-540-47789-6\_36. [http://link.springer.com/10.1007/3-540-47789-6\\_36](http://link.springer.com/10.1007/3-540-47789-6_36) [http://link.springer.com/chapter/10.1007/3-540-47789-6\\_36](http://link.springer.com/chapter/10.1007/3-540-47789-6_36) (2002).
337. Gordon, D., Mori, W. & Antonsen, T. A ponderomotive guiding center particle-in-cell code for efficient modeling of laser-plasma interactions. *IEEE Trans. Plasma Sci.* 28, 1135–1143. doi:10.1109/27.893300. <http://ieeexplore.ieee.org/document/893300/> (Aug. 2000).
338. Bryant, P. AGILE—a tool for interactive lattice design in Proc. 7th Eur. Part. Accel. Conf. (EPAC 2000) (Vienna, Austria, 2000), 1357–1359.
339. Grote, H. & Schmidt, F. MAD-X—An upgrade from MAD8 in Proc. IEEE Part. Accel. Conf. 5 (2003), 3497–3499.
340. Borland, M. Elegant: A flexible SDDS-compliant code for accelerator simulation. *Adv. Phot. Source LS-287*, 1–11. doi:10.2172/761286. [http://www.osti.gov/bridge/product.biblio.jsp?osti\\_id=761286](http://www.osti.gov/bridge/product.biblio.jsp?osti_id=761286) (Sept. 2000).
341. Assmann, R. et al. SINBAD—A proposal for a dedicated accelerator research facility at DESY in IPAC 2014 Proc. 5th Int. Part. Accel. Conf. (2014), 1466–1469. doi:10.18429/JACoW-IPAC2014-TUPME047.

342. Zhu, J., Assmann, R. W., Dohlus, M., Dorda, U. & Marchetti, B. Sub-fs electron bunch generation with sub-10-fs bunch arrival-time jitter via bunch slicing in a magnetic chicane. *Phys. Rev. Accel. Beams* 19, 054401. doi:10.1103/PhysRevAccelBeams.19.054401. <https://link.aps.org/doi/10.1103/PhysRevAccelBeams.19.054401> (May 2016).
343. Sprangle, P. & Esarey, E. H. Interaction of ultrahigh laser fields with beams and plasmas. *Phys. Fluids B-Plasma* 4, 2241–2248. doi:10.1063/1.860192. <http://scitation.aip.org/content/aip/journal/pofb/4/7/10.1063/1.860192> (1992).
344. Sprangle, P., Tang, C.-M. & Esarey, E. H. Relativistic Self-Focusing of Short-Pulse Radiation Beams in Plasmas. *IEEE T. Plasma Sci.* 15, 145–153. doi:10.1109/TPS.1987.4316677. <http://ieeexplore.ieee.org/xpl/articleDetails.jsp?arnumber=4316677> (1987).
345. Durfee, C. G. & Milchberg, H. M. Light pipe for high intensity laser pulses. *Phys. Rev. Lett.* 71, 2409–2412. doi:10.1103/PhysRevLett.71.2409. <http://link.aps.org/doi/10.1103/PhysRevLett.71.2409> (1993).
346. Lemos, N. et al. Plasma expansion into a waveguide created by a linearly polarized femtosecond laser pulse. *Phys Plasmas* 20, 63102–63110. doi:10.1063/1.4810797 (2013).
347. Lemos, N. et al. Effects of laser polarization in the expansion of plasma waveguides. *Phys Plasmas* 20, 103106–103109. doi:10.1063/1.4825228 (2013).
348. Hooker, S. M. et al. Low Density Plasma Channels Created by Hydrodynamic Expansion of OFI-heated Plasma Columns in *Adv. Accel. Concepts Work.* (2016).
349. Shaloo, R. et al. Low-density hydrodynamic optical-field-ionized plasma channels generated with an axicon lens. *Phys. Rev. Accel. Beams* 22, 41302. doi:10.1103/PhysRevAccelBeams.22.041302. <https://doi.org/10.1103/PhysRevAccelBeams.22.041302> (2019).
350. Cros, B. et al. Eigenmodes for capillary tubes with dielectric walls and ultraintense laser pulse guiding. *Phys. Rev. E* 65, 26405. doi:10.1103/PhysRevE.65.026405. <http://link.aps.org/doi/10.1103/PhysRevE.65.026405> (2002).
351. Butler, A., Spence, D. J. & Hooker, S. M. Guiding of High-Intensity Laser Pulses with a Hydrogen-Filled Capillary Discharge Waveguide. *Phys Rev Lett* 89, 185003. doi:10.1103/PhysRevLett.89.185003. <http://link.aps.org/doi/10.1103/PhysRevLett.89.185003> (Oct. 2002).
352. Ju, J. & Cros, B. Characterization of temporal and spatial distribution of hydrogen gas density in capillary tubes for laser-plasma experiments. *J. Appl. Phys.* 112, 113102. doi:10.1063/1.4768209. <http://link.aip.org/link/?JAP/112/113102/1> (2012).
353. Paradkar, B. S., Cros, B., Mora, P. & Maynard, G. Numerical modeling of multi-GeV laser wakefield electron acceleration inside a dielectric capillary tube. *Phys. Plasmas* 20, 083120. doi:10.1063/1.4819718. <http://aip.scitation.org/doi/10.1063/1.4819718> (2013).
354. Vay, J. L. et al. Modeling of 10 GeV–1 TeV laser-plasma accelerators using Lorentz boosted simulations. *Phys. Plasmas* 18, 1–16. doi:10.1063/1.3663841 (2011).
355. Kapteyn, H. C., Szoke, A., Falcone, R. W. & Murnane, M. M. Prepulse energy suppression for high-energy ultrashort pulses using self-induced plasma shuttering. *Opt. Lett.* 16, 490. doi:10.1364/OL.16.000490. <http://www.osapublishing.org/viewmedia.cfm?uri=ol-16-7-490&seq=0&html=true> (1991).
356. Marocchino, A., Massimo, F., Rossi, A. R., Chiadroni, E. & Ferrario, M. Efficient modeling of plasma wakefield acceleration in quasi-non-linear-regimes with the hybrid code Architect. *Nucl. Instruments Methods Phys. Res. Sect. A Accel. Spectrometers, Detect. Assoc. Equip.* 829, 386–391 (Sept. 2016).
357. Massimo, F., Atzeni, S. & Marocchino, A. Comparisons of time explicit hybrid kinetic-fluid code Architect for Plasma Wakefield Acceleration with a full PIC code. *J. Comput. Phys.* 327, 841–850 (2016).
358. Massimo, F. et al. Transformer ratio studies for single bunch plasma wakefield acceleration. *Nucl. Inst. Methods Phys. Res. A* 740, 242–245 (Mar. 2014).

359. Tzoufras, M. et al. Beam Loading in the Nonlinear Regime of Plasma-Based Acceleration. *Phys. Rev. Lett.* 101, 145002 (Sept. 2008).
360. Katsouleas, T., Wilks, S., Chen, P., Dawson, J. M. & Su, J. J. Beam loading in plasma accelerators. *Part. Accel.* 22, 81–99. <http://cds.cern.ch/record/898463/files/p81.pdf> (1987).
361. Rosenzweig, J. B., Barov, N., Thompson, M. C. & Yoder, R. B. Energy loss of a high charge bunched electron beam in plasma: Simulations, scaling, and accelerating wakefields. *Phys. Rev. Spec. Top. Beams* 7, 61302 (2004).
362. Londrillo, P., Gatti, C. & Ferrario, M. Numerical investigation of beam-driven PWFA in quasi-nonlinear regime. *Nucl. Inst. Methods Phys. Res. A* 740, 236–241. doi:10.1016/J.NIMA.2013.10.028. <https://www.sciencedirect.com/science/article/pii/S0168900213013740> (Mar. 2014).
363. Lu, W. et al. A nonlinear theory for multidimensional relativistic plasma wave wakefields. *Phys. Plasmas* 13, 56709. doi:10.1063/1.2203364. <http://scitation.aip.org/content/aip/journal/pop/13/5/10.1063/1.2203364>(2006).
364. Barov, N. & Rosenzweig, J. B. Propagation of short electron pulses in underdense plasmas. *Phys. Rev. E* 49, 4407 (1994).
365. Ting, A., Esarey, E. & Sprangle, P. Nonlinear wakefield generation and relativistic focusing of intense laser pulses in plasmas. *Phys. Fluids B* 2, 1390–1394. doi:http://dx.doi.org/10.1063/1.859561. <http://scitation.aip.org/content/aip/journal/pofb/2/6/10.1063/1.859561> (1990).
366. Feit, M. D., Komashko, A. M., Musher, S. L., Rubenchik, A. M. & Turitsyn, S. K. Electron cavitation and relativistic self-focusing in underdense plasma. *Phys. Rev. E* 57, 7122 (1998).
367. Rosenzweig, J. B., Breizman, B., Katsouleas, T. & Su, J. J. Acceleration and focusing of electrons in two-dimensional nonlinear plasma wake fields. *Phys. Rev. A* 44, R6189–R6192. doi:10.1103/PhysRevA.44.R6189. <http://link.aps.org/doi/10.1103/PhysRevA.44.R6189> (1991).
368. Umstadter, D., Kim, J. K. & Dodd, E. Laser Injection of Ultrashort Electron Pulses into Wakefield Plasma Waves. *Phys. Rev. Lett.* 76, 2073–2076. doi:10.1103/PhysRevLett.76.2073. <http://link.aps.org/doi/10.1103/PhysRevLett.76.2073> (1996).
369. Modena, A. et al. Electron acceleration from the breaking of relativistic plasma waves. *Nature* 377, 606–608. doi:10.1038/377606a0. <http://dx.doi.org/10.1038/377606a0> (1995).
370. Esarey, E. H., Hubbard, R. F., Leemans, W. P., Ting, A. & Sprangle, P. Electron Injection into Plasma Wakefields by Colliding Laser Pulses. *Phys. Rev. Lett.* 79, 2682–2685. doi:10.1103/PhysRevLett.79.2682. <http://link.aps.org/doi/10.1103/PhysRevLett.79.2682> (1997).
371. Maier, A. R. et al. Demonstration scheme for a laser-plasma-driven free-electron laser. *Phys. Rev. X* 2, 1–7. doi:10.1103/PhysRevX.2.031019 (2012).
372. Couprie, M. E. et al. in *X-Ray Lasers 2012* 55–62 (Springer, 2014).
373. O’Shea, F. H. et al. Short period, high field cryogenic undulator for extreme performance x-ray free electron lasers. *Phys. Rev. Spec. Top. Beams* 13, 70702 (2010).
374. Walker, R. P. Interference effects in undulator and wiggler radiation sources. *Nucl. Instrum. Methods Phys. Res.* 335, 328–337. doi:10.1016/0168-9002(93)90288-S (1993).
375. Walker, R. P. Phase errors and their effect on undulator radiation properties. *Phys. Rev. Spec. Top. Beams* 16, 10704 (2013).
376. Couprie, M.–E., Andre, T. & Andriyash, I. COXINEL: Towards free electron laser amplification to qualify laser plasma acceleration. *Reza Kenkyu* 45, 94–98 (2017).
377. Antici, P. et al. Laser-driven electron beamlines generated by coupling laser-plasma sources with conventional transport systems. *J. Appl. Phys.* 112. doi:10.1063/1.4740456 (2012).
378. Liu, T., Zhang, T., Wang, D. & Huang, Z. Compact beam transport system for free-electron lasers driven by a laser plasma accelerator. *Phys. Rev. Accel. Beams* 20, 20701 (2017).

379. Migliorati, M. et al. Intrinsic normalized emittance growth in laser-driven electron accelerators. *Phys. Rev. ST Accel. Beams* 16, 11302. doi:10.1103/PhysRevSTAB.16.011302. <http://link.aps.org/doi/10.1103/PhysRevSTAB.16.011302> (2013).
380. Hosokai, T. et al. Optical guidance of terrawatt laser pulses by the implosion phase of a fast Z-pinch discharge in a gas-filled capillary. *Opt. Lett.* 25, 10–12 (2000).
381. Thaury, C. et al. Demonstration of relativistic electron beam focusing by a laser-plasma lens. *Nat Commun* 6, ——. <http://dx.doi.org/10.1038/ncomms7860> (Apr. 2015).
382. Iwashita, Y. et al. Super strong adjustable permanent magnet quadrupole for the final focus in a linear collider in Proc. 10th Eur. Part. Accel. Conf. EPAC 6 (2006), 2550–2552.
383. Eichner, T. et al. Miniature magnetic devices for laser-based, table-top free-electron lasers. *Phys. Rev. Spec. Top. Beams* 10, 82401 (2007).
384. Lou, W., Hartill, D., Rice, D., Rubin, D. & Welch, J. Stability considerations of permanent magnet quadrupoles for CESR phase-III upgrade. *Phys. Rev. Spec. Top. Beams* 1, 22401 (1998).
385. Lim, J. K. et al. Adjustable, short focal length permanent-magnet quadrupole based electron beam final focus system. *Phys. Rev. Spec. Top. Beams* 8, 72401 (2005).
386. Modena, M. et al. Design, assembly and first measurements of a short model for CLIC final focus hybrid quadrupole QD0 in Conf. Proc. 1205201 (2012), THPPD010.
387. N’gotta, P., Le Bec, G. & Chavanne, J. Hybrid high gradient permanent magnet quadrupole. *Phys. Rev. Accel. Beams* 19, 122401 (2016).
388. Ghaith, A. et al. Permanent Magnet-Based Quadrupoles for Plasma Acceleration Sources. *Instruments* 3, 27. doi:10.3390/instruments3020027. <https://www.mdpi.com/2410-390X/3/2/27> (2019).
389. Mihara, T., Iwashita, Y., Kumada, M. & Sugiyama, E. A superstrong adjustable permanent magnet quadrupole for the final focus lens in a linear collider in Proc. 1st Annu. Meet. Part. Accel. Soc. Japan 29th Linear Accel. Meet. Japan (2004).
390. Shepherd, B., Clarke, J. & Collomb, N. CONSTRUCTION AND MEASUREMENT OF NOVEL ADJUSTABLE PERMANENT MAGNET QUADRUPOLES FOR CLIC in Proc. 3h Int. Part. Accel. Conf. (New Orleans, USA, 2016), THPPD016.
391. Gottschalk, S. C., Kangas, K., DeHart, T. E., Volk, J. T. & Spencer, C. M. Performance of an adjustable strength permanent magnet quadrupole in Proc. 2005 Part. Accel. Conf. (2005), 2071–2073.
392. Tosin, G., Sanchez, P. P., Citadini, J. F. & Vergasta, C. C. Super hybrid quadrupoles. *Nucl. Instruments Methods Phys. Res. Sect. A Accel. Spectrometers, Detect. Assoc. Equip.* 674, 67–73 (2012).
393. Rago, C. E., Spencer, C. M., Wolf, Z. & Yocky, G. High reliability prototype quadrupole for the Next Linear Collider. *IEEE Trans. Appl. Supercond.* 12, 270–273 (2002).
394. Benabderrahmane, C., Couprie, M., Forest, F. & Cosson, O. Multi-pôle magnétique réglable 2016.
395. Ghaith, A. et al. Cryogenic Permanent Magnet Undulator for an FEL Application in Proc. FEL2017 (Santa Fe, USA, 2017), WEP065.
396. Kitegi, C. et al. QUAPEVA: Variable High Gradient Permanent Magnet Quadrupole in 60th ICFA Adv. Beam Dyn. Work. Futur. Light Sources (Shanghai, China, 2018), WEA2WD01.
397. Ghaith, A. et al. Tunable high gradient quadrupoles for a laser plasma acceleration based FEL. *Nucl. Instruments Methods Phys. Res. Sect. A Accel. Spectrometers, Detect. Assoc. Equip.* 909, 290–293 (2018).
398. Oumbarek Espinos, D. et al. Skew Quadrupole Effect of Laser Plasma Electron Beam Transport. *Appl. Sci.* 9, 2447. doi:10.3390/app9122447. <https://www.mdpi.com/2076-3417/9/12/2447> (2019).
399. Panofsky, W. K. H. & Baker, W. R. A focusing device for the external 350-MeV proton beam of the 184-inch cyclotron at Berkeley. *Rev. Sci. Instrum.* 21, 445–447 (1950).

400. Autin, B. et al. A z-pinch plasma lens for focusing high-energy particles in an accelerator. *IEEE Trans. plasma Sci.* 15, 226–237 (1987).
401. Van Tilborg, J. et al. Comparative study of active plasma lenses in high-quality electron accelerator transport lines. *Phys. Plasmas* 25, 56702 (2018).
402. Tatchyn, R. et al. Design considerations for a 60 meter pure permanent magnet undulator for the SLAC linac coherent light source (LCLS) in *Proc. Int. Conf. Part. Accel. (PAC 93)* (1993), 1608–1610.
403. Halbach, K. Permanent magnet undulators. *Le J. Phys. Colloq.* 44, C1–211 (1983).
404. Robinson, K. E. et al. Hybrid undulator design considerations. *Nucl. Instruments Methods Phys. Res. Sect. A Accel. Spectrometers, Detect. Assoc. Equip.* 250, 100–109 (1986).
405. Gudat, W., Pflueger, J., Chatzipetros, J. & Peatman, W. An undulator/multipole wiggler for the BESSY storage ring. *Nucl. Instruments Methods Phys. Res. Sect. A Accel. Spectrometers, Detect. Assoc. Equip.* 246, 50–53. doi:10.1016/0168-9002(86)90043-4 (1986).
406. Tanaka, T. et al. In-vacuum undulators in *Proc. 27th Int. Free Electron Conf.* (2005), 370–377.
407. Yamamoto, S. et al. Construction of an in-vacuum type undulator for production of undulator x rays in the 5–25 keV region. *Rev. Sci. Instrum.* 63, 400–403 (1992).
408. Kersevan, R., Hahn, M., Parat, I. & Schmied, D. Machine operation issue related to the vacuum system of the ESRF. *EPAC08*, 3705 (2008).
409. Hara, T. et al. In-vacuum undulators of SPring-8. *J. Synchrotron Radiat.* 5, 403–405 (1998).
410. Hara, T. et al. SPring-8 in-vacuum undulator beam test at the ESRF. *J. Synchrotron Radiat.* 5, 406–408 (1998).
411. De Lacheisserie, é. d. T. *Magnétisme* (S/I. Collection Grenoble Sciences, 1999).
412. Coey, J. M. D. *Rare-earth iron permanent magnets* 54 (Oxford University Press, 1996).
413. Pan, S. in *Rare Earth Perm. Alloy. High Temp. Phase Transform.* 27–93 (Springer, 2013).
414. Givord, D., Li, H. S. & De La Bâthie, R. P. Magnetic properties of Y2Fe14B and Nd2Fe14B single crystals. *Solid State Commun.* 51, 857–860 (1984).
415. Sagawa, M., Hirosawa, S., Yamamoto, H., Fujimura, S. & Matsuura, Y. Nd-Fe-B permanent magnet materials. *Jpn. J. Appl. Phys.* 26, 785 (1987).
416. Sagawa, M. et al. Dependence of coercivity on the anisotropy field in the Nd2Fe14B-type sintered magnets. *J. Appl. Phys.* 61, 3559–3561 (1987).
417. Bizen, T. et al. Baking effect for NdFeB magnets against demagnetization induced by highenergy electrons. *Nucl. Instruments Methods Phys. Res. Sect. A Accel. Spectrometers, Detect. Assoc. Equip.* 515, 850–852 (2003).
418. Bizen, T. et al. High-energy electron irradiation of NdFeB permanent magnets: Dependence of radiation damage on the electron energy. *Nucl. Instruments Methods Phys. Res. Sect. A Accel. Spectrometers, Detect. Assoc. Equip.* 574, 401–406 (2007).
419. Hara, T. et al. Cryogenic permanent magnet undulators. *Phys. Rev. Spec. Top. Beams* 7, 50702 (2004).
420. Dufeu, D. & Lethuillier, P. High sensitivity 2~T vibrating sample magnetometer. *Rev. Sci. Instrum.* 70, 3035–3039 (1999).
421. Abache, C. & Oesterreicher, H. Magnetic properties of compounds R2Fe14B. *J. Appl. Phys.* 57, 4112–4114 (1985).
422. Hirosawa, S. et al. Magnetization and magnetic anisotropy of R2Fe14B measured on single crystals. *J. Appl. Phys.* 59, 873–879 (1986).
423. García, L. M., Chaboy, J., Bartolomé, F. & Goedkoop, J. B. Orbital magnetic moment instability at the spin reorientation transition of Nd 2 Fe 14 B. *Phys. Rev. Lett.* 85, 429 (2000).
424. Hiroyoshi, H. et al. High-field magnetization of R2Fe14B single crystals. *J. Magn. Magn. Mater.* 54, 583–584 (1986).

425. Goll, D., Seeger, M. & Kronmüller, H. Magnetic and microstructural properties of nanocrystalline exchange coupled PrFeB permanent magnets. *J. Magn. Mater.* 185, 49–60 (1998).
426. Couprie, M. E. No Title. *SPIE Opt. Optoelectron.* 951204.
427. Tanaka, T., Tsuru, R., Nakajima, T. & Kitamura, H. Magnetic characterization for cryogenic permanent-magnet undulators: a first result. *J. Synchrotron Radiat.* 14, 416–420 (2007).
428. Tanabe, T. et al. Cryogenic Field Measurement of Pr<sub>2</sub>Fe<sub>14</sub>B Undulator and Performance Enhancement Options at the NSLS-II in AIP Conf. Proc. 1234 (2010), 29–32.
429. Kitegi, C. A. et al. Development of a PrFeB cryogenic undulator at NSLS-II. *Proc. IPAC2012, New Orleans, Louisiana, USA*, 762–764 (2012).
430. Valléau, M. et al. Development of Cryogenic Permanent Magnet Undulators at SOLEIL. *Synchrotron Radiat. News* 31, 42–47 (2018).
431. Benabderrahmane, C. et al. Nd<sub>2</sub>Fe<sub>14</sub>B and Pr<sub>2</sub>Fe<sub>14</sub>B magnets characterisation and modelling for cryogenic permanent magnet undulator applications. *Nucl. Instruments Methods Phys. Res. Sect. A Accel. Spectrometers, Detect. Assoc. Equip.* 669, 1–6 (2012).
432. Couprie, M. E. et al. The status of the LUNEX5 project in *Proc. FEL 14* (2014).
433. Kitegi, C. A. et al. COXINEL Task 2.9, U15 COXINEL Task 2.9 U15 Undulator Report: U15 cryogenic undulator progress report. *Proc. IPAC2012, New Orleans, Louisiana, USA*, 762–764 (2012).
434. Bahrtdt, J. et al. Cryogenic undulator for a table top FEL in AIP Conf. Proc. 1234 (2010), 499–502.
435. Bahrtdt, J. et al. Cryogenic design of a PrFeB-based undulator. *proc. IPAC*, 3111–3113 (2010).
436. Kuhn, C., Schulz, B., Bahrtdt, J., Scheer, M. & Gaupp, A. Developing of Advanced Magnet Structures for Cryogenic in Vacuum Permanent Magnet Undulators (2014).
437. Holy, F. et al. First spectral measurements of a cryogenic high-field short-period undulator. *Phys. Rev. ST Accel. Beams* 17, 50704. doi:10.1103/PhysRevSTAB.17.050704. <http://link.aps.org/doi/10.1103/PhysRevSTAB.17.050704> (2014).
438. Chavanne, J. et al. Construction of a cryogenic permanent magnet undulator at the ESRF in *Proc. EPAC Conf.* (2008), 2243–2245.
439. Chavanne, J., Penel, C. & Elleaume, P. Development and operation of a prototype cryogenic permanent magnet undulator at the ESRF (2009).
440. Chavanne, J., Lebec, G., Penel, C., Revol, F. & Kitegi, C. First operational experience with a cryogenic permanent magnet undulator at the ESRF in 23rd Part. *Accel. Conf.* (2009), 2414–2416.
441. Kitegi, C. et al. Development of a cryogenic permanent magnet in-vacuum undulator at the ESRF. *Proc. EPAC 2006, Edinburgh, Scotl.* 3559–3561 (2006).
442. Tanaka, T. et al. In situ correction of field errors induced by temperature gradient in cryogenic undulators. *Phys. Rev. Spec. Top. Beams* 12, 120702 (2009).
443. Calvi, M. et al. Commissioning results of the U14 cryogenic undulator at SLS. *J. Phys. Conf. Ser.* 425, 32017 (2013).
444. Schmidt, T., Reiche, S. et al. Undulators for the SwissFEL. *Proc. FEL2009, Liverpool, UK*, 706–713 (2009).
445. Benabderrahmane, C. et al. Development of a 2 m Pr<sub>2</sub>Fe<sub>14</sub>B cryogenic permanent magnet undulator at SOLEIL. *J. Phys. Conf. Ser.* 425, 32019 (2013).
446. Benabderrahmane, C. et al. Development of a PrFeB cryogenic undulator at SOLEIL. *Proc. IPAC2010, Kyoto, Japan* 3096 (2010).
447. Couprie, M. E. et al. An application of laser-plasma acceleration: towards a free-electron laser amplification. *Plasma Phys. Control. Fusion* 58, 34020 (2016).
448. André, T. et al. First electron beam measurements on coxinel in 7th Int. Part. *Accel. Conf. (IPAC'16), Busan, Korea* (2016), 712–715.
449. Schouten, J. C., Rial, E. C. M. et al. Electron beam heating and operation of the cryogenic undulator and superconducting wigglers at DIAMOND in *Proc. 2nd Int. Part. Accel. Conf. IPAC 11* (2011).

450. Ostenfeld, C. W. & Pedersen, M. Cryogenic in-vacuum undulator at Danfysik. Proc. IPAC2010, Kyoto, Japan 3093 (2010).
451. Bahrtdt, J. & Kuhn, C. Cryogenic permanent magnet undulator development at HZB/BESSY II. *Synchrotron Radiat. News* 28, 9–14 (2015).
452. Bahrtdt, J. et al. Measurements of the lattice modifications for the cryogenic undulator CPMU17 in Proc. 7th Int. Part. Accel. Conf. (Busan, Korea, 2016).
453. Bahrtdt, J. et al. A canted double undulator system with a wide energy range for EMIL in Proc. 6th Int. Part. Accel. Conf. (Richmond, USA, 2015).
454. Bahrtdt, J. et al. Characterisation and implementation of the cryogenic permanent magnet undulator CPMU17 at BESSY II in Proc. 10th Int. Part. Accel. Conf., IPAC2019, Melbourne, Aust. (2019), 1415–1418. doi:10.18429/JACoW-IPAC2019-TUPGW014.
455. Yang, Y., Zhang, X., Sun, S. & Lu, H. Field error correction considerations of cryogenic permanent magnet undulator (CPMU) for high energy photon source test facility (HEPS-TF) (2016).
456. Yang, C.-K. et al. Design of a System at NSRRC to Measure the Field for an In-vacuum Cryogenic Undulator with Permanent Magnet (2014).
457. Chubar, O., Elleaume, P. & Chavanne, J. A three-dimensional magnetostatics computer code for insertion devices. *J. Synchrotron Radiat.* 5, 481–484 (1998).
458. Clarke, J. & Bradshaw, T. Superconducting Undulator Workshop Report. ICFA Beam Dyn. Newsl. 65, 148 (2014).
459. Casalbuoni, S. et al. Recent developments on superconducting undulators at ANKA (2015).
460. Ivanyushenkov, Y. et al. Development and performance of 1.1-m long superconducting undulator at the Advanced Photon Source (2015).
461. Emma, P. et al. A plan for the development of superconducting undulator prototypes for LCLS-II and future FELs in FEL 2014 Conf. Proceedings, Basel, Switz. (2014).
462. Ivanyushenkov, Y. Magnetic Simulation of a Superconducting Undulator for the Advanced Photon Source in Part. Accel. Proceedings, 23rd Conf. PAC'09, Vancouver, Canada, May 4–8, 2009 (2010), MO6PFP077. <http://accelconf.web.cern.ch/AccelConf/PAC2009/papers/mo6pfp077.pdf>.
463. Elwood, G., Bayliss, V., Clarke, J., Canfer, S. & Bradshaw, T. FINAL PROTOTYPE SC HELICAL UNDULATOR MEASURED tech. rep. (2013).
464. Corlett, J. et al. Design concepts for a next generation light source at LBNL. Proc. FEL2013 (2013).
465. Clarke, J. et al. Status of the UK superconducting planar undulator project in Proc. 4th Int. Part. Accel. Conf. (Shanghai, China, 2013), WEPWA062.
466. Ivanyushenkov, Y. et al. Advances in Superconducting Undulators in 2013 Part. Accel. Conf. Conf. Proc. (2013).
467. Plettner, T. & Byer, R. L. Proposed dielectric-based microstructure laser-driven undulator. *Phys. Rev. Spec. Top. Beams* 11, 30704 (2008).
468. Harrison, J., Joshi, A., Lake, J., Candler, R. & Musumeci, P. Surface-micromachined magnetic undulator with period length between 10 mm and 1 mm for advanced light sources. *Phys. Rev. Spec. Top. Beams* 15, 70703 (2012).
469. Paulson, K. Micro-undulator research at UCSB. *Nucl. Instruments Methods Phys. Res. A Accel. Spectrometers, Detect. Assoc. Equip.* 296, 624–630. doi:10.1016/0168-9002(90)91278-J (1990).
470. Tachyn, R. Perspectives on micropole undulators in synchrotron radiation technology. *Rev. Sci. Instrum.* 60, 1796–1804. doi:10.1063/1.1140907 (1989).
471. Arnold, D. P. & Wang, N. Permanent magnets for MEMS. *J. microelectromechanical Syst.* 18, 1255–1266 (2009).
472. Tantawi, S. Microwave-based Undulator: A New Tool for Free Electron Lasers and Synchrotron Light Sources. HBEB Work. Puerto-Rico (2013).
473. Bacci, A., Ferrario, M., Maroli, C., Petrillo, V. & Serafini, L. Transverse effects in the production of x rays with a free-electron laser based on an optical undulator. *Phys. Rev. Spec. Top.-Accel. Beams* 9, 1–9. doi:10.1103/PhysRevSTAB.9.060704 (2006).

474. Whittum, D. H., Sessler, A. M. & Dawson, J. M. Ion-channel laser. *Phys. Rev. Lett.* 64, 2511 (1990).
475. Williams, R. L., Clayton, C. E., Joshi, C. & Katsouleas, T. C. Studies of classical radiation emission from plasma wave undulators. *IEEE Trans. plasma Sci.* 21, 156–166 (1993).
476. Joshi, C., Katsouleas, T., Dawson, J., Yan, Y. & Slater, J. Plasma wave wigglers for freeelectron lasers. *IEEE J. Quantum Electron.* 23, 1571–1577 (1987).
477. Corde, S. & Ta Phuoc, K. Plasma wave undulator for laser-accelerated electrons. *Phys. Plasmas* 18, 33111 (2011).
478. Rykovanov, S., Schroeder, C., Esarey, E., Geddes, C. & Leemans, W. Plasma Undulator Based on Laser Excitation of Wakefields in a Plasma Channel. *Phys. Rev. Lett.* 114, 145003. doi:10.1103/PhysRevLett.114.145003. <https://link.aps.org/doi/10.1103/PhysRevLett.114.145003> (Apr. 2015).
479. Rykovanov, S. G. et al. Tunable polarization plasma channel undulator for narrow bandwidth photon emission. *Phys. Rev. Accel. Beams* 19, 90703 (2016).
480. Luo, J. et al. A compact tunable polarized X-ray source based on laser-plasma helical undulators. *Sci. Rep.* 6, 29101. doi:10.1038/srep29101. <http://www.nature.com/articles/srep29101> (Sept. 2016).
481. Andriyash, I. A. et al. An ultracompact X-ray source based on a laser-plasma undulator. *Nat. Commun.* 5, 4736 (2014).
482. Ciocci, F., Dattoli, G. & Sabia, E. Transverse Gradient Undulators and FEL operating with large energy spread. *Opt. Commun.* 356, 582–588 (2015).
483. Smith, T. I., Madey, J. M. J., Elias, L. R. & Deacon, D. A. G. Reducing the sensitivity of a free-electron laser to electron energy. *J. Appl. Phys.* 50, 4580–4583 (1979).
484. Liu, T. et al. Beam Transport Line of the LPA-FEL Facility Based on Transverse Gradient Undulator in Proceedings, 7th Int. Part. Accel. Conf. (IPAC 2016) Busan, Korea, May 8–13, 2016 (2016), THPMB027. doi:10.18429/JACoW-IPAC2016-THPMB027.
485. Bernhard, A. et al. Radiation emitted by transverse-gradient undulators. *Phys. Rev. Accel. Beams* 19, 90704. doi:10.1103/PhysRevAccelBeams.19.090704 (2016).
486. Ferrario, M., Migliorati, M. & Palumbo, L. Space Charge Effects, 331–356. 26 p. <http://cds.cern.ch/record/1982426> (Jan. 2016).
487. Van Tilborg, J. et al. Nonuniform discharge currents in active plasma lenses. *Phys. Rev. Accel. Beams* 20, 32803. doi:10.1103/PhysRevAccelBeams.20.032803 (2017).
488. Lindstrøm, C. A. & Adli, E. Analytic plasma wakefield limits for active plasma lenses (2018).
489. Lehe, R., Kirchen, M., Andriyash, I. A., Godfrey, B. B. & Vay, J.–L. A spectral, quacylindrical and dispersion-free Particle-In-Cell algorithm. *Comput. Phys. Commun.* 203, 66–82. doi:10.1016/J.CPC.2016.02.007. <https://www.sciencedirect.com/science/article/pii/S0010465516300224> (June 2016).
490. Akre, R., Bentson, L., Emma, P. & Krejcik, P. A transverse RF deflecting structure for bunch length and phase space diagnostics in PACS2001. *Proc. 2001 Part. Accel. Conf. (Cat. No.01CH37268)* 3 (June 2001), 2353–2355 vol.3. doi:10.1109/PAC.2001.987379.
491. Kennedy, J. & Eberhart, R. Particle swarm optimization in *Proc. ICNN'95-Int. Conf. Neural Networks* 4 (Nov. 1995), 1942–1948 vol.4. doi:10.1109/ICNN.1995.488968.
492. Hestenes, M. R. & Stiefel, E. Methods of conjugate gradients for solving linear systems. *J Res NIST* 49, 409–436. doi:10.6028/jres.049.044. <http://dx.doi.org/10.6028/jres.049.044> (1952).
493. Uriot, D. & Pichoff, N. Status of TraceWin Code in Proceedings, 6th Int. Part. Accel. Conf. (IPAC 2015) Richmond, Virginia, USA, May 3–8, 2015 (2015), MOPWA008. doi:10.18429/JACoW-IPAC2015-MOPWA008. <http://accelconf.web.cern.ch/AccelConf/IPAC2015/papers/mopwa008.pdf>.
494. Ferran Pousa, A., de la Ossa, A., Brinkmann, R. & Assmann, R.W. Correlated Energy Spread Compensation in Multi-Stage Plasma-Based Accelerators. *arXiv Prepr. arXiv1811.07757* (2018).

495. Ferran Pousa, A., Aßmann, R. W. & Martinez de la Ossa, A. Wake-T: A Fast Particle Tracking Code for Plasma-Based Accelerators in Proc. 10th Int. Partile Accel. Conf. (IPAC'19), Melbourne, Aust. 19–24 May 2019 (Geneva, Switzerland, 2019), 3601–3604. doi:10.18429/JACoW-IPAC2019-THPGW012.
496. Feister, S. et al. A novel femtosecond-gated, high-resolution, frequency-shifted shearing interferometry technique for probing pre-plasma expansion in ultra-intense laser experiments. *Rev. Sci. Instrum.* 85, 11D602. doi:10.1063/1.4886955. <http://dx.doi.org/10.1063/1.4886955> (2014).
497. Park, J., Baldis, H. & Chen, H. The implementation and data analysis of an interferometer for intense short pulse laser experiments. *High Power Laser Sci. Eng.* 4. doi:10.1017/hpl.2016.21 (2016).
498. Ruiz-Camacho, J., Beg, F. N. & Lee, P. Comparison of sensitivities of Moiré deflectionometry and interferometry to measure electron densities in z-pinch plasmas. *J. Phys. D. Appl. Phys.* 40, 2026. <http://stacks.iop.org/0022-3727/40/i=7/a=026> (2007).
499. Kalal, M., Slezak, O., Martinkova, M. & Rhee, Y. J. Compact design of a Nomarski interferometer and Its application in the diagnostics of coulomb explosions of deuterium clusters. *J. Korean Phys. Soc.* 56, 287–294 (2010).
500. Chanteloup, J.-C. Multiple-wave lateral shearing interferometry for wave-front sensing. *Appl. Opt.* 44, 1559–1571. doi:10.1364/AO.44.001559. <http://ao.osa.org/abstract.cfm?URI=ao-44-9-1559> (Mar. 2005).
501. Mollica, F. et al. Direct, real-time and sensitive plasma density diagnostic by quadri-wave lateral shearing interferometry in 42nd Eur. Phys. Soc. Conf. Plasma Physics, EPS 2015 (2015).
502. Phasics Corp. Plasma & Gas Density Measurement: SID4 HR 2019. <http://phasicscorp.com/product/plasma-density-measurement-using-phase-shift/>.
503. Plateau, G. R. et al. Wavefront-sensor-based electron density measurements for laser-plasma accelerators. *Rev. Sci. Instrum.* 81, 33108. doi:10.1063/1.3360889. <http://scitation.aip.org/content/aip/journal/rsi/81/3/10.1063/1.3360889> (2010).
504. Hopf, F. A., Tomita, A. & Al-Jumaily, G. Second-harmonic interferometers. *Opt. Lett.* 5, 386–388. doi:10.1364/OL.5.000386. <http://ol.osa.org/abstract.cfm?URI=ol-5-9-386> (Sept. 1980).
505. Alum, K., Kovalchuk, I. & Ostrovskaja, G. Nonlinear dispersive interferometer. *Pisma v Zhurnal Tekhnicheskoi Fiz.* 7, 1359–1364 (Nov. 1981).
506. Brandi, F. & Giammanco, F. Versatile second-harmonic interferometer with high temporal resolution and high sensitivity based on a continuous-wave Nd:YAG laser. *Opt. Lett.* 32, 2327–2329. doi:10.1364/OL.32.002327. <http://ol.osa.org/abstract.cfm?URI=ol-32-16-2327> (Aug. 2007).
507. Jobs, F. C. & Bretz, N. L. A prototype imaging second harmonic interferometer. *Rev. Sci. Instrum.* 68, 709–712. doi:10.1063/1.1147681. <http://dx.doi.org/10.1063/1.1147681> (1997).
508. Abraham, E., Minoshima, K. & Matsumoto, H. Femtosecond laser-induced breakdown in water: time-resolved shadow imaging and two-color interferometric imaging. *Opt. Commun.* 176, 441–452. doi:http://dx.doi.org/10.1016/S0030-4018(00)00547-2. <http://www.sciencedirect.com/science/article/pii/S0030401800005472> (2000).
509. Brandi, F. et al. Electron density measurements of a field-reversed configuration plasma using a novel compact ultrastable second-harmonic interferometer. *Rev. Sci. Instrum.* 80, 113501. doi:10.1063/1.3258199. <http://dx.doi.org/10.1063/1.3258199> (2009).
510. Van Tilborg, J., Gonsalves, A. J., Esarey, E., Schroeder, C. B. & Leemans, W. P. Highsensitivity plasma density retrieval in a common-path second-harmonic interferometer through simultaneous group and phase velocity measurement. *Phys. Plasmas* 26, 23106. doi:10.1063/1.5080269. <https://aip.scitation.org/doi/full/10.1063/1.5080269> (2019).
511. Peck, E. R. & Huang, S. Refractivity and dispersion of hydrogen in the visible and near infrared. *J. Opt. Soc. Am.* 67, 1550–1554. doi:10.1364/JOSA.67.001550. <http://www.osapublishing.org/abstract.cfm?URI=josa-67-11-1550> (Nov. 1977).

512. Brandi, F. & Giammanco, F. Temporal and spatial characterization of a pulsed gas jet by a compact high-speed high-sensitivity second-harmonic interferometer. *Opt. Express* 19, 25479–25487. doi:10.1364/OE.19.025479. <http://www.opticsexpress.org/abstract.cfm?URI=oe-19-25-25479> (Dec. 2011).
513. Brandi, F. et al. Note: Real-time monitoring via second-harmonic interferometry of a flow gas cell for laser wakefield acceleration. *Rev. Sci. Instrum.* 87, 86103. doi:10.1063/1.4960399. <http://dx.doi.org/10.1063/1.4960399> (2016).
514. Minoshima, K. & Matsumoto, H. In-situ measurements of shapes and thicknesses of optical parts by femtosecond two-colour interferometry. *Opt. Commun.* 138, 6–10. doi:[http://dx.doi.org/10.1016/S0030-4018\(97\)00029-1](http://dx.doi.org/10.1016/S0030-4018(97)00029-1). <http://www.sciencedirect.com/science/article/pii/S0030401897000291> (1997).
515. Couperus, J. P. et al. Tomographic characterisation of gas-jet targets for laser wakefield acceleration. *Nucl. Instruments Methods Phys. Res. Sect. A Accel. Spectrometers, Detect. Assoc. Equip.* 830, 504–509. doi:<http://dx.doi.org/10.1016/j.nima.2016.02.099>. <http://www.sciencedirect.com/science/article/pii/S0168900216300171> (2016).
516. Gautam, G. & Parigger, C. G. Electron density and temperature diagnostics in laser-induced hydrogen plasma. *J. Phys. Conf. Ser.* 810, 12055. <http://stacks.iop.org/1742-6596/810/i=1/a=012055> (2017).
517. Van Tilborg, J. et al. Measurement of the laser-pulse group velocity in plasma waveguides. *Phys. Rev. E-Stat. Nonlinear, Soft Matter Phys.* 89, 1–5. doi:10.1103/PhysRevE.89.063103 (2014).
518. Daniels, J. et al. Plasma density diagnostic for capillary-discharge based plasma channels. *Phys. Plasmas* 22, 73112. doi:10.1063/1.4926825. <http://dx.doi.org/10.1063/1.4926825> (2015).
519. Benedetti, C., Rossi, F., Schroeder, C. B., Esarey, E. & Leemans, W. P. Pulse evolution and plasma-wave phase velocity in channel-guided laser-plasma accelerators. *Phys. Rev. E* 92, 23109. doi:10.1103/PhysRevE.92.023109. <http://link.aps.org/doi/10.1103/PhysRevE.92.023109> (Aug. 2015).
520. Daniels, J. et al. Plasma control and diagnostics for 10 GeV electron beams on BELLA. *AIP Conf. Proc.* 1812, 40008. doi:10.1063/1.4975855. <http://aip.scitation.org/doi/abs/10.1063/1.4975855> (2017).
521. Murphy, C. D. et al. Evidence of photon acceleration by laser wake fields. *Phys. Plasmas* 13, 1–8. doi:10.1063/1.2178650 (2006).
522. Cros, B. Laser-driven Plasma Wakefield: Propagation Effects. *Cern Yellow Reports* 1, 207. <https://e-publishing.cern.ch/index.php/CYR/article/view/221> (2016).
523. Wilks, S. C., Dawson, J. M., Mori, W. B., Katsouleas, T. & Jones, M. E. Photon Accelerator. *Phys. Rev. Lett.* 62, 2600–2603. doi:10.1103/PhysRevLett.62.2600 (1989).
524. Andreev, N. E. & Chegotov, M. V. Wakefield generation as the mechanism behind spectral shift of a short laser pulse. *J. Exp. Theor. Phys.* 101, 56–63. doi:10.1134/1.2010661. <https://doi.org/10.1134/1.2010661> (July 2005).
525. Wojda, F. et al. Laser-driven plasma waves in capillary tubes. *Phys. Rev. E* 80, 66403. doi:10.1103/PhysRevE.80.066403. <http://link.aps.org/doi/10.1103/PhysRevE.80.066403> (2009).
526. Kasim, M. F. et al. Simulation of density measurements in plasma wakefields using photon acceleration. *Phys. Rev. Spec. Top.-Accel. Beams* 18, 1–9. doi:10.1103/PhysRevSTAB.18.032801 (2015).
527. Schreiber, J. et al. Complete Temporal Characterization of Asymmetric Pulse Compression in a Laser Wakefield. *Phys. Rev. Lett.* 105, 235003. doi:10.1103/PhysRevLett.105.235003. <http://link.aps.org/doi/10.1103/PhysRevLett.105.235003> (2010).
528. Marques, J. R. et al. Temporal and Spatial Measurements of the Electron Density Perturbation Produced in the Wake of an Ultra-Short Laser Pulse. *EQEC'96. 1996 Eur. Quantum Electron. Conf.* 1–4. doi:10.1109/EQEC.1996.561779 (1996).

529. Siders, C.W. et al. Laser wakefield excitation and measurement by femtosecond longitudinal interferometry. *Summ. Pap. Present. Quantum Electron. Laser Sci. Conf.* 76, 0–3. doi:10.1109/QELS.1996.865582. <http://www.ncbi.nlm.nih.gov/pubmed/10061001> (1996).
530. Matlis, N. H. et al. Snapshots of laser wakefields. *Nat. Phys.* 2, 749–753. doi:10.1038/nphys442 (Nov. 2006).
531. Kaluza, M. et al. Measurement of Magnetic-Field Structures in a Laser-Wakefield Accelerator. *Phys. Rev. Lett.* 105, 115002. doi:10.1103/PhysRevLett.105.115002. <http://link.aps.org/doi/10.1103/PhysRevLett.105.115002> (Sept. 2010).
532. Buck, A. et al. Real-time observation of laser-driven electron acceleration. *Nat. Phys.* 7, 543–548. doi:10.1038/nphys1942. <http://dx.doi.org/10.1038/nphys1942> (2011).
533. Sävert, A. et al. Direct Observation of the Injection Dynamics of a Laser Wakefield Accelerator Using Few-Femtosecond Shadowgraphy. *Phys. Rev. Lett.* 115, 55002. doi:10.1103/PhysRevLett.115.055002. <http://link.aps.org/doi/10.1103/PhysRevLett.115.055002> (July 2015).
534. Unser, K. B. Design and preliminary tests of a beam intensity monitor for LEP in *Proc. 1989 IEEE Part. Accel. Conf. Sci. Technol.* (1989), 71–73.
535. Hidding, B. et al. Novel method for characterizing relativistic electron beams in a harsh laser-plasma environment. *Rev. Sci. Instrum.* 78, 83301 (2007).
536. Glinec, Y. et al. Absolute calibration for a broad range single shot electron spectrometer. *Rev. Sci. Instrum.* 77, 103301 (2006).
537. Nakamura, K. et al. Electron beam charge diagnostics for laser plasma accelerators. *Phys. Rev. Spec. Top. Beams* 14, 62801 (2011).
538. Mazzoni, S. et al. Beam Instrumentation Developments for the Advanced Proton Driven Plasma Wakefield Acceleration Experiment at CERN (2017).
539. Simon, C. et al. Design and Beam Test Results of the Reentrant Cavity BPM for the European XFEL. *Proc. IBIC* (2016).
540. Dolgashev, V. A. & Wang, J. RF design of X-band RF deflector for femtosecond diagnostics of LCLS electron beam in *AIP Conf. Proc.* 1507 (2012), 682–687.
541. Swinson, C., Fedurin, M., Palmer, M. A., Pogorelsky, I. et al. ATF Facilities Upgrades and Deflector Cavity Commissioning. *Energy (MeV)* 57, 80 (2018).
542. Behrens, C. et al. Few-femtosecond time-resolved measurements of X-ray free-electron lasers. *Nat. Commun.* 5. doi:10.1038/ncomms4762. <http://www.nature.com/doi/10.1038/ncomms4762> (2014).
543. Christie, F., Rönsch-Schulenburg, J., Schreiber, S. & Vogt, M. Generation of Ultra-Short Electron Bunches and FEL Pulses and Characterization of Their Longitudinal Properties At FLASH2 in *Proc. IPAC 2017, Copenhagen, Denmark* (2017), 2600–2603.
544. D’Arcy, R., Aschikhin, A., Gonzalez Caminal, P., Libov, V. & Osterhoff, J. Longitudinal Phase Space Reconstruction at FLASHForward Using a Novel X-Band Transverse Deflection Cavity, *PolariX. Int. Part. Accel. Conf. 2018, 4.* doi:10.18429/JACoW-IPAC2018-TUPML017 (2018).
545. Marchetti, B. et al. X-band TDS project in *Proc. IPAC 17* (2017).
546. Grudiev, A. Design of compact high power rf components at x-band tech. rep. (2016).
547. Craievich, P. et al. Status of the PolariX-TDS Project in 9th Int. Part. Accel. Conf.(IPAC’18), Vancouver, BC, Canada, April 29–May 4, 2018 (2018), 3808–3811.
548. Marx, D. et al. Reconstruction of the 3D charge distribution of an electron bunch using a novel variable-polarization transverse deflecting structure (TDS) in *J. Phys. Conf. Ser.* 874 (2017), 188–191. doi:10.1088/1742-6596/874/1/012077.
549. Marx, D., Aßmann, R., D’Arcy, R. & Marchetti, B. Simulations of 3D charge density measurements for commissioning of the PolariX-TDS in *J. Phys. Conf. Ser.* 1067 (2018), 72012.
550. Lundh, O. et al. Few femtosecond, few kiloampere electron bunch produced by a laserplasma accelerator. *Nat. Phys.* 7, 219–222. doi:10.1038/nphys1872. <http://dx.doi.org/10.1038/nphys1872> (2011).

551. Maxwell, T. J. et al. Coherent-radiation spectroscopy of few-femtosecond electron bunches using a middle-infrared prism spectrometer. *Phys. Rev. Lett.* 111, 184801 (2013).
552. Wesch, S., Schmidt, B., Behrens, C., Delsim-Hashemi, H. & Schmüser, P. A multi-channel THz and infrared spectrometer for femtosecond electron bunch diagnostics by single-shot spectroscopy of coherent radiation. *Nucl. Instruments Methods Phys. Res. Sect. A Accel. Spectrometers, Detect. Assoc. Equip.* 665, 40–47 (2011).
553. Smith, S. J. & Purcell, E. M. Visible Light from Localized Surface Charges Moving across a Grating. *Phys. Rev.* 92, 1069. doi:10.1103/PhysRev.92.1069. <http://link.aps.org/doi/10.1103/PhysRev.92.1069> (1953).
554. Brownell, J. H., Walsh, J. & Doucas, G. Spontaneous Smith-Purcell radiation described through induced surface currents. *Phys. Rev. E* 57, 1075 (1998).
555. Blackmore, V. et al. First measurements of the longitudinal bunch profile of a 28.5 GeV beam using coherent Smith-Purcell radiation. *Phys. Rev. Spec. Top. Beams* 12, 32803 (2009).
556. Andrews, H. L. et al. Reconstruction of the time profile of 20.35 GeV, subpicosecond long electron bunches by means of coherent Smith-Purcell radiation. *Phys. Rev. Spec. Top. Beams* 17, 52802 (2014).
557. Delerue, N. et al. Longitudinal Profile Monitor using Smith-Purcell-Radiation: Recent Results from the E-203 Collaboration tech. rep. (SLAC National Accelerator Lab., Menlo Park, CA (United States), 2013).
558. Delerue, N. et al. Bunch Length Measurements Using Coherent Smith-Purcell Radiation With Several Gratings at CLIO in 9th Int. Part. Accel. Conf.(IPAC'18), Vancouver, BC, Canada, April 29-May 4, 2018 (2018), 2239–2242.
559. Bock, M. K. Measuring the electron bunch timing with femtosecond resolution at FLASH 2013.
560. Wilke, I. et al. Single-shot electron-beam bunch length measurements. *Phys. Rev. Lett.* 88, 124801 (2002).
561. Berden, G. et al. Electro-optic technique with improved time resolution for real-time, nondestructive, single-shot measurements of femtosecond electron bunch profiles. *Phys. Rev. Lett.* 93, 114802 (2004).
562. Cavalieri, A. L. et al. Clocking femtosecond X rays. *Phys. Rev. Lett.* 94, 114801 (2005).
563. Pompili, R. et al. Femtosecond timing-jitter between photo-cathode laser and ultra-short electron bunches by means of hybrid compression. *New J. Phys.* 18, 83033 (2016).
564. Löhl, F. et al. Measurements of the transverse emittance at the FLASH injector at DESY. *Phys. Rev. Spec. Top. Beams* 9, 92802 (2006).
565. Delerue, N. Single shot transverse emittance measurement of multi-MeV electron beams using a long pepper-pot. *Nucl. Instruments Methods Phys. Res. Sect. A Accel. Spectrometers, Detect. Assoc. Equip.* 644, 1–10 (2011).
566. Thomas, C., Delerue, N. & Bartolini, R. Single shot 3 GeV electron transverse emittance with a pepper-pot. *Nucl. Instruments Methods Phys. Res. Sect. A Accel. Spectrometers, Detect. Assoc. Equip.* 729, 554–556 (2013).
567. Thomas, C., Delerue, N. & Bartolini, R. Single shot transverse emittance measurement from OTR screens in a drift transport section. *J. Instrum.* 6, P07004 (2011).
568. Pompili, R. et al. Focusing of High-Brightness Electron Beams with Active-Plasma Lenses. *Phys. Rev. Lett.* 121, 174801 (2018).
569. Weingartner, R. et al. Ultralow emittance electron beams from a laser-wakefield accelerator. *Phys. Rev. Spec. Top.-Accel. Beams* 15, 111302. doi:10.1103/PhysRevSTAB.15.111302. <http://link.aps.org/doi/10.1103/PhysRevSTAB.15.111302> (Nov. 2012).
570. Barber, S. K. et al. Measured emittance dependence on the injection method in laser plasma accelerators. *Phys. Rev. Lett.* 119, 104801 (2017).
571. Li, F. et al. Transverse phase space diagnostics for ionization injection in laser plasma acceleration using permanent magnetic quadrupoles. *Plasma Phys. Control. Fusion* 60, 44007 (2018).

572. Kieffer, R. et al. Direct observation of incoherent Cherenkov diffraction radiation in the visible range. *Phys. Rev. Lett.* 121, 54802 (2018).
573. Rousse, A. et al. Production of a keV X-ray beam from synchrotron radiation in relativistic laser–plasma interaction. *Phys. Rev. Lett.* 93, 135005. doi:10.1103/PhysRevLett.93.135005. <http://link.aps.org/doi/10.1103/PhysRevLett.93.135005> (2004).
574. Plateau, G. R. et al. Low-emittance electron bunches from a laser–plasma accelerator measured using single-shot x-ray spectroscopy. *Phys. Rev. Lett.* 109, 64802 (2012).
575. Kneip, S. et al. Characterization of transverse beam emittance of electrons from a laserplasma wakefield accelerator in the bubble regime using betatron x-ray radiation. *Phys. Rev. Spec. Top.–Accel. Beams* 15, 2–6. doi:10.1103/PhysRevSTAB.15.021302 (2012).
576. Curcio, A. et al. Trace-space reconstruction of low-emittance electron beams through betatron radiation in laser–plasma accelerators. *Phys. Rev. Accel. Beams* 20, 12801 (2017).
577. Cianchi, A. et al. Frontiers of beam diagnostics in plasma accelerators: Measuring the ultra-fast and ultra-cold. *Phys. Plasmas* 25, 56704 (2018).
578. Takei, H. & Takeda, Y. Conceptual Design of Beam Dump for High Power Electron Beam in Proc. the XVIII Int. Linear Accel. Conf. (Geneva, Switzerland, 1996).
579. Wu, H.-C., Tajima, T., Habs, D., Chao, A. W. & Meyer-ter-Vehn, J. Collective deceleration: Toward a compact beam dump. *Phys. Rev. Spec. Top.–Accel. Beams* 13, 101303. doi:10.1103/PhysRevSTAB.13.101303. <https://link.aps.org/doi/10.1103/PhysRevSTAB.13.101303> (Oct. 2010).
580. Bonatto, A. et al. Passive and active plasma deceleration for the compact disposal of electron beams. *Phys. Plasmas* 22, 083106. doi:10.1063/1.4928379. <http://aip.scitation.org/doi/10.1063/1.4928379> (Aug. 2015).
581. Hanahoe, K. et al. Simulation study of a passive plasma beam dump using varying plasma density. *Phys. Plasmas* 24, 023120. doi:10.1063/1.4977449. <http://aip.scitation.org/doi/10.1063/1.4977449> (Feb. 2017).
582. Li, X., Mosnier, A. & Nghiem, P. A. P. Design of a 5 GeV laser–plasma accelerating module in the quasi-linear regime. *Nucl. Instruments Methods Phys. Res. Sect. A Accel. Spectrometers, Detect. Assoc. Equip.* 909, 49–53. doi:10.1016/J.NIMA.2018.02.104. <https://www.sciencedirect.com/science/article/pii/S0168900218302924> (Nov. 2018).
583. Arber, T. D. et al. Contemporary particle-in-cell approach to laser–plasma modelling. *Plasma Phys. Control. Fusion* 57, 113001. doi:10.1088/0741-3335/57/11/113001. <http://stacks.iop.org/0741-3335/57/i=11/a=113001?key=crossref.907aa156b73b99b125b1a0ae886c4c22> (Nov. 2015).
584. Cowley, J. et al. Excitation and Control of Plasma Wakefields by Multiple Laser Pulses. *Phys. Rev. Lett.* 119, 044802. doi:10.1103/PhysRevLett.119.044802. <http://link.aps.org/doi/10.1103/PhysRevLett.119.044802> (July 2017).
585. Zhu, J., Assmann, R.W., Marchetti, B., Ferran Pousa, A. & Walker, P. A. Simulation Study of an RF Injector for the LWFA Configuration at EuPRAXIA in Proc. 9th Int. Part. Accel. Conf. (Vancouver, Canada, 2018), 3025–3028. doi:10.18429/JACoW-IPAC2018-THPAF032. <http://accelconf.web.cern.ch/AccelConf/ipac2018/papers/thpaf032.pdf>.
586. Beck, A. et al. Physical processes at work in sub-30 fs, PW laser pulse-driven plasma accelerators: Towards GeV electron acceleration experiments at CILEX facility. *Nucl. Instruments Methods Phys. Res. Sect. A Accel. Spectrometers, Detect. Assoc. Equip.* 740, 67–73. doi:10.1016/J.NIMA.2013.11.003. <https://www.sciencedirect.com/science/article/pii/S0168900213015039?via%3Dihub> (Mar. 2014).
587. Derouillat, J. et al. Smilei : A collaborative, open-source, multi-purpose particle-in-cell code for plasma simulation. *Comput. Phys. Commun.* 222, 351–373. doi:10.1016/J.CPC.2017.09.024. <https://www.sciencedirect.com/science/article/pii/S0010465517303314?via%3Dihub> (Jan. 2018).

588. Massimo, F., Lifschitz, A. F., Thaury, C. & Malka, V. Numerical studies of density transition injection in laser wakefield acceleration. *Plasma Phys. Control. Fusion* 59, 085004. doi:10.1088/1361-6587/aa717d. <http://stacks.iop.org/0741-3335/59/i=8/a=085004?key=crossref.89c9b609a7e3009a70897b539b7cbbfa> (Aug. 2017).
589. Lifschitz, A. F. et al. Particle-in-Cell modelling of laser-plasma interaction using Fourier decomposition. *J. Comput. Phys.* 228, 1803-1814. doi:<http://dx.doi.org/10.1016/j.jcp.2008.11.017>. <http://www.sciencedirect.com/science/article/pii/S002199108005950> (2009).
590. Audet, T. et al. Gas cell density characterization for laser wakefield acceleration. *Nucl. Instruments Methods Phys. Res. Sect. A Accel. Spectrometers, Detect. Assoc. Equip.* 909, 383-386. doi:10.1016/J.NIMA.2018.01.053. <https://www.sciencedirect.com/science/article/pii/S0168900218300706?via%3Dihub> (Nov. 2018).
591. Tomassini, P. et al. High quality electron bunches for a multi-stage GeV accelerator with the Resonant Multi-Pulse Ionization injection. *Phys. Rev. Accel. Beams* 22, 111302. doi:10.1103/PhysRevAccelBeams.22.111302 (2019).
592. Benedetti, C., Sgattoni, A., Turchetti, G. & Londrillo, P. ALaDyn : A High-Accuracy PIC Code for the. *IEEE Trans. plasma Sci.* 36, 1790-1798 (2008).
593. Tomassini, P. & Rossi, A. R. Matching strategies for a plasma booster. *Plasma Phys. Control. Fusion* 58, 034001. doi:10.1088/0741-3335/58/3/034001. <http://stacks.iop.org/0741-3335/58/i=3/a=034001?key=crossref.a8863e6d422c259f9ac2dd382dbbd396> (Mar. 2016).
594. Tomassini, P. et al. High-quality 5GeV electron bunches with the resonant multi-pulse ionization injection. *Plasma Phys. Control. Fusion* 62, 014010. doi:10.1088/1361-6587/ab45c5. <http://iopscience.iop.org/article/10.1088/1361-6587/ab45c5> (Sept. 2019).
595. Li, X., Nghiem, P. A. P. & Mosnier, A. Toward low energy spread in plasma accelerators in quasilinear regime. *Phys. Rev. Accel. Beams* 21, 111301. doi:10.1103/PhysRevAccelBeams.21.111301. <https://link.aps.org/doi/10.1103/PhysRevAccelBeams.21.111301> (Nov. 2018).
596. Rossi, A. R. et al. Stability study for matching in laser driven plasma acceleration. *Nucl. Instruments Methods Phys. Res. Sect. A Accel. Spectrometers, Detect. Assoc. Equip.* 829, 67-72. doi:10.1016/j.nima.2016.02.015 (2016).
597. Andreev, N., Baranov, V. & Matevosyan, H. Trapping and acceleration of short electron bunches in the laser wakefields. *Laser Part. Beams* 35, 569-573. doi:10.1017/S0263034617000556. [https://www.cambridge.org/core/product/identifier/S0263034617000556/type/journal\\_article](https://www.cambridge.org/core/product/identifier/S0263034617000556/type/journal_article) (Dec. 2017).
598. Pugacheva, D. V. & Andreev, N. E. Effect of synchrotron radiation on the dynamics of electron spin precession in the process of laser-plasma acceleration. *Quantum Electron.* 48, 291-294. doi:10.1070/QEL16673. <http://stacks.iop.org/1063-7818/48/i=4/a=291?key=crossref.ea55805acb28868e972fe35dc3b99d6c> (Apr. 2018).
599. Dohlus, M., Kabel, A. & Limberg, T. Efficient field calculation of 3D bunches on general trajectories. *Nucl. Instr. Meth. Phys. Res., Sect. A* 445, 338-342. doi:[https://doi.org/10.1016/S0168-9002\(00\)00139-X](https://doi.org/10.1016/S0168-9002(00)00139-X). <http://www.sciencedirect.com/science/article/pii/S016890020000139X> (2000).
600. Marocchino, A., Massimo, F., Rossi, A., Chiadroni, E. & Ferrario, M. Efficient modeling of plasma wakefield acceleration in quasi-non-linear-regimes with the hybrid code Architect. *Nucl. Instruments Methods Phys. Res. Sect. A Accel. Spectrometers, Detect. Assoc. Equip.* 829, 386-391. doi:10.1016/J.NIMA.2016.03.005. <https://www.sciencedirect.com/science/article/pii/S0168900216300237%20> <https://www.sciencedirect.com/science/article/pii/S0168900216300237?via%3Dihub> (Sept. 2016).
601. Wittig, G. et al. Optical plasma torch electron bunch generation in plasma wakefield accelerators. *Phys. Rev. ST Accel. Beams* 18, 81304. doi:10.1103/PhysRevSTAB.18.081304. <https://link.aps.org/doi/10.1103/PhysRevSTAB.18.081304> (Aug. 2015).

602. Martinez de la Ossa, A. et al. Hybrid LWFA–PWFA staging as a beam energy and brightness transformer: conceptual design and simulations. *Philos. Trans. R. Soc. A Math. Phys. Eng. Sci.* 377, 20180175. doi:10.1098/rsta.2018.0175. <https://royalsocietypublishing.org/doi/10.1098/rsta.2018.0175> (Aug. 2019).
603. Hidding, B. et al. Ultracold Electron Bunch Generation via Plasma Photocathode Emission and Acceleration in a Beam–Driven Plasma Blowout. *Phys. Rev. Lett.* 108, 35001. doi:10.1103/PhysRevLett.108.035001. <http://link.aps.org/doi/10.1103/PhysRevLett.108.035001> (Jan. 2012).
604. Nieter, C. & Cary, J. R. VORPAL: a versatile plasma simulation code. *J. Comput. Phys.* 196, 448–473. doi:10.1016/J.JCP.2003.11.004. <https://www.sciencedirect.com/science/article/pii/S0021999103006041?via%3Dihub> (May 2004).
605. Scisciò, M. et al. Parametric study of transport beam lines for electron beams accelerated by laser–plasma interaction. *J. Appl. Phys.* 119, 094905. doi:10.1063/1.4942626. <http://aip.scitation.org/doi/10.1063/1.4942626> (Mar. 2016).
606. Li, X., Chancé, A. & Nghiem, P. A. P. Preserving emittance by matching out and matching in plasma wakefield acceleration stage. *Phys. Rev. Accel. Beams* 22, 021304. doi:10.1103/PhysRevAccelBeams.22.021304. <https://link.aps.org/doi/10.1103/PhysRevAccelBeams.22.021304> (Feb. 2019).
607. Hooker, S. M. et al. Multi–pulse laser wakefield acceleration: a new route to efficient, highrepetition– rate plasma accelerators and high flux radiation sources. *J. Phys. B–Atomic Mol. Opt. Phys.* 47, 234003. doi:10.1088/0953–4075/47/23/234003. <http://stacks.iop.org/0953–4075/47/i=23/a=234003> (Nov. 2014).
608. Shaloo, R. J. et al. Generation of laser pulse trains for tests of multi–pulse laser wakefield acceleration. *Nucl. Instruments Methods Phys. Res. Sect. A Accel. Spectrometers, Detect. Assoc. Equip.* 829, 383–385 (2016).
609. Siders, C. W., Siders, J. L. W., Taylor, A. J., Park, S.–G. & Weiner, A. M. Efficient highenergy pulse–train generation using a 2 n–pulse Michelson interferometer. *Appl. Opt.* 37, 5302–5305 (1998).
610. Sprangle, P., Esarey, E. & Krall, J. Self–guiding and stability of intense optical beams in gases undergoing ionization. *Phys. Rev. E* 54, 4211–4232. doi:10.1103/PhysRevE.54.4211. <https://link.aps.org/doi/10.1103/PhysRevE.54.4211> (Oct. 1996).
611. Schroeder, C. et al. Thermal emittance from ionization–induced trapping in plasma accelerators. *Phys. Rev. Spec. Top.–Accel. Beams* 17, 101301. doi:10.1103/PhysRevSTAB.17.101301. <https://link.aps.org/doi/10.1103/PhysRevSTAB.17.101301> (Oct. 2014).
612. Rossi, A. et al. Plasma boosted electron beams for driving Free Electron Lasers. *Nucl. Instruments Methods Phys. Res. Sect. A Accel. Spectrometers, Detect. Assoc. Equip.* 909, 54–57. doi:10.1016/J.NIMA.2018.02.092. <https://www.sciencedirect.com/science/article/pii/S0168900218302730> (Nov. 2018).
613. Shpakov, V. et al. Longitudinal Phase–Space Manipulation with Beam–Driven Plasma Wakefields. *Phys. Rev. Lett.* 122, 114801. doi:10.1103/PhysRevLett.122.114801. <https://link.aps.org/doi/10.1103/PhysRevLett.122.114801> (Mar. 2019).
614. Döpp, A. et al. Energy–Chirp Compensation in a Laser Wakefield Accelerator. *Phys. Rev. Lett.* 121, 74802. doi:10.1103/PhysRevLett.121.074802. <https://link.aps.org/doi/10.1103/PhysRevLett.121.074802> (Aug. 2018).
615. D’Arcy, R. et al. Tunable Plasma–Based Energy Dechirper. *Phys. Rev. Lett.* 122, 034801. doi:10.1103/PhysRevLett.122.034801. <https://link.aps.org/doi/10.1103/PhysRevLett.122.034801> (Jan. 2019).
616. Wu, Y. P. et al. Phase Space Dynamics of a Plasma Wakefield Dechirper for Energy Spread Reduction. *Phys. Rev. Lett.* 122, 204804. doi:10.1103/PhysRevLett.122.204804. <https://link.aps.org/doi/10.1103/PhysRevLett.122.204804> (May 2019).
617. Xu, X. L. et al. Physics of Phase Space Matching for Staging Plasma and Traditional Accelerator Components Using Longitudinally Tailored Plasma Profiles. *Phys. Rev. Lett.* 116, 124801. doi:10.1103/PhysRevLett.116.124801. <https://link.aps.org/doi/10.1103/PhysRevLett.116.124801> (Mar. 2016).

618. Okada, T. & Ogawa, K. Saturated magnetic fields of Weibel instabilities in ultraintense laser–plasma interactions. *Phys. Plasmas* 14, 72702. doi:10.1063/1.2746023. <https://doi.org/10.1063/1.2746023> (2007).
619. Poole, P. L. et al. Experiment and simulation of novel liquid crystal plasma mirrors for high contrast, intense laser pulses. *Sci. Rep.* 6, 32041. <http://dx.doi.org/10.1038/srep32041> <http://10.0.4.14/srep32041> (Aug. 2016).
620. Reid, M. B. Electron beam emittance growth in thin foils: A betatron function analysis. *J. Appl. Phys.* 70, 7185–7187. doi:10.1063/1.349761. <https://doi.org/10.1063/1.349761> (1991).
621. Massimo, F., Atzeni, S. & Marocchino, A. Comparisons of time explicit hybrid kinetic–fluid code Architect for Plasma Wakefield Acceleration with a full PIC code. *J. Comput. Phys.* 327, 841–850. doi:10.1016/J.JCP.2016.09.067. <https://www.sciencedirect.com/science/article/pii/S0021999116305010?via%3Dihub> (Dec. 2016).
622. Couprie, M. E. et al. Strategies towards a compact XUV free electron laser adopted for the LUNEX5 project. *J. Mod. Opt.* 63, 309–323. doi:10.1080/09500340.2015.1075617. <http://www.tandfonline.com/doi/full/10.1080/09500340.2015.1075617> (Feb. 2016).
623. Nguyen, F. et al. Free Electron Laser Performance within the EuPRAXIA Facility. *Instruments* 4, 5. doi:10.3390/instruments4010005 (2020).
624. Tomassini, P. et al. High–quality GeV–scale electron bunches with the Resonant Multi–Pulse Ionization Injection. *Nucl. Instruments Methods Phys. Res. Sect. A Accel. Spectrometers, Detect. Assoc. Equip.* 909, 1–4. doi:10.1016/J.NIMA.2018.03.002. <https://www.sciencedirect.com/science/article/pii/S016890021830319X?via%3Dihub> (Nov. 2018).
625. Giribono, A. et al. EuPRAXIA@SPARC\_LAB: The high–brightness RF photo–injector layout proposal. *Nucl. Instruments Methods Phys. Res. Sect. A Accel. Spectrometers, Detect. Assoc. Equip.* 909, 282–285. doi:10.1016/J.NIMA.2018.03.009. <https://www.sciencedirect.com/science/article/pii/S0168900218303267> (Nov. 2018).
626. Marocchino, A. & al., E. High Brightness Electron Beams from Plasma–based Acceleration in LINAC’18 (Beijing, China, 2018), TH1A03.
627. Rossetti Conti, M. et al. Electron beam transfer line design for plasma driven Free Electron Lasers. *Nucl. Instruments Methods Phys. Res. Sect. A Accel. Spectrometers, Detect. Assoc. Equip.* 909, 84–89. doi:10.1016/J.NIMA.2018.02.061. <https://www.sciencedirect.com/science/article/pii/S0168900218302158> (Nov. 2018).
628. Dattoli, G., Letardi, T., Madey, J. & Renieri, A. Limits on the single–pass higher harmonics FEL operation. *IEEE J. Quantum Electron.* 20, 1003–1005. doi:10.1109/JQE.1984.1072516. <http://ieeexplore.ieee.org/document/1072516/> (Sept. 1984).
629. Ming Xie. Design optimization for an X–ray free electron laser driven by SLAC linac in *Proc. Part. Accel. Conf. 1 (IEEE, 1995)*, 183–185. doi:10.1109/PAC.1995.504603. <http://ieeexplore.ieee.org/document/504603/>.
630. Dattoli, G., Renieri, A., Torre, A. & Caloi, R. Inhomogeneous broadening effects in highgain free electron laser operation: A simple parametrization. *Nuovo Cim. D* 11, 393–404. doi:10.1007/BF02450989. <http://link.springer.com/10.1007/BF02450989> (Mar. 1989).
631. Dattoli, G., Giannessi, L., Ottaviani, P. L. & Ronsivalle, C. Semi–analytical model of self–amplified spontaneous–emission free–electron lasers, including diffraction and pulsepropagation effects. *J. Appl. Phys.* 95, 3206–3210. doi:10.1063/1.1645979. <http://aip.scitation.org/doi/10.1063/1.1645979> (Mar. 2004).
632. Dejus, R., Jaski, M. & Kim, S. On–Axis Brilliance and Power of In–Vacuum Undulators for the Advanced Photon Source tech. rep. (Argonne National Laboratory, 2009), ANL/APS/LS– 314.
633. Moog, E., Dejus, R. & Sasaki, S. Comparison of Achievable Magnetic Fields with Superconducting and Cryogenic Permanent Magnet Undulators – A Comprehensive Study of Computed and Measured Values tech. rep. (Argonne National Laboratory, 2017), ANL/APS/LS– 348.

634. Giannessi, L. Overview of PERSEO, a system for simulating FEL dynamics in Mathematica in 28th Int. Free Electron Laser Conf. FEL 2006 (Berlin, Germany, 2006), 91–94.
635. Thomas, A. G. R. Scalings for radiation from plasma bubbles. *Phys. Plasmas* 17, 56708. doi:10.1063/1.3368678. <http://scitation.aip.org/content/aip/journal/pop/17/5/10.1063/1.3368678> (2010).
636. Esarey, E. H., Shadwick, B. A., Catravas, P. & Leemans, W. P. Synchrotron radiation from electron beams in plasma-focusing channels. *Phys. Rev. E* 65, 56505. doi:10.1103/PhysRevE.65.056505. <http://link.aps.org/doi/10.1103/PhysRevE.65.056505> (2002).
637. Kneip, S. et al. Bright spatially coherent synchrotron X-rays from a table-top source. *Nat. Phys.* 7, 737. doi:10.1038/nphys2093. <http://dx.doi.org/10.1038/nphys2093> (2011).
638. Najmudin, Z. et al. Compact laser accelerators for X-ray phase-contrast imaging. *Philos. Trans. R. Soc. A Math. Phys. Eng. Sci.* 372. doi:10.1098/rsta.2013.0032 (2014).
639. Mangles, S. P. D. et al. On the stability of laser wakefield electron accelerators in the monoenergetic regime. *Phys. Plasmas* 14, 56702. doi:10.1063/1.2436481. <http://dx.doi.org/10.1063/1.2436481> (May 2007).
640. Wang, S. et al. X-Ray Emission from Betatron Motion in a Plasma Wiggler. *Phys. Rev. Lett.* 88, 135004. doi:10.1103/PhysRevLett.88.135004. <http://link.aps.org/doi/10.1103/PhysRevLett.88.135004> (2002).
641. Phuoc, K. T. et al. Imaging Electron Trajectories in a Laser-Wakefield Cavity Using Betatron X-Ray Radiation. *Phys. Rev. Lett.* 97, 225002. doi:10.1103/PhysRevLett.97.225002. <http://link.aps.org/doi/10.1103/PhysRevLett.97.225002> (2006).
642. Fourmaux, S. et al. Demonstration of the synchrotron-type spectrum of laser-produced Betatron radiation. *New J. Phys.* 13, 33017. doi:10.1088/1367-2630/13/3/033017. <http://stacks.iop.org/1367-2630/13/i=3/a=033017> (2011).
643. Wenz, J. et al. Quantitative X-ray phase-contrast microtomography from a compact laserdriven betatron source. *Nat. Commun.* 6, 7568. doi:10.1038/ncomms8568. <http://dx.doi.org/10.1038/ncomms8568> (2015).
644. Phuoc, K. T. et al. All-optical Compton gamma-ray source. *Nat. Photon.* 6, 308–311. doi:10.1038/nphoton.2012.82. <http://dx.doi.org/10.1038/nphoton.2012.82> (2012).
645. Powers, N. D. et al. Quasi-monoenergetic and tunable X-rays from a laser-driven Compton light source. *Nat. Photonics* 8, 28–31. doi:10.1038/nphoton.2013.314. <http://www.nature.com/articles/nphoton.2013.314> (Jan. 2014).
646. Chen, H. et al. Emittance of positron beams produced in intense laser plasma interaction. *Phys. Plasmas* 20, 13111. doi:10.1063/1.4789621. <http://link.aip.org/link/?PHP/20/013111/1> (2013).
647. Sarri, G. et al. Ultrahigh Brilliance Multi-MeV g -Ray Beams from Nonlinear Relativistic Thomson Scattering. *Phys. Rev. Lett.* 113, 224801. doi:10.1103/PhysRevLett.113.224801. <https://link.aps.org/doi/10.1103/PhysRevLett.113.224801> (Nov. 2014).
648. Petrillo, V. et al. Photon flux and spectrum of g-rays Compton sources. *Nucl. Instruments Methods Phys. Res. Sect. A Accel. Spectrometers, Detect. Assoc. Equip.* 693, 109–116. doi:10.1016/J.NIMA.2012.07.015. <https://www.sciencedirect.com/science/article/pii/S0168900212007772> (Nov. 2012).
649. Ranjan, N. et al. Simulation of inverse Compton scattering and its implications on the scattered linewidth. *Phys. Rev. Accel. Beams* 21, 030701. doi:10.1103/PhysRevAccelBeams.21.030701. <https://link.aps.org/doi/10.1103/PhysRevAccelBeams.21.030701> (Mar. 2018).
650. Deutsches Elektronen-Synchrotron DESY. Test Beams at DESY 2019. [http://particle-physics.desy.de/test\\_beams\\_at\\_desy/](http://particle-physics.desy.de/test_beams_at_desy/).
651. Hidding, B. et al. Monoenergetic Energy Doubling in a Hybrid Laser-Plasma Wakefield Accelerator. *Phys. Rev. Lett.* 104, 195002. doi:10.1103/PhysRevLett.104.195002 (2010).

652. Martinez de la Ossa, A., Grebenyuk, J., Mehrling, T., Schaper, L. & Osterhoff, J. High-Quality Electron Beams from Beam-Driven Plasma Accelerators by Wakefield-Induced Ionization Injection. *Phys. Rev. Lett.* 111, 245003. doi:10.1103/PhysRevLett.111.245003. <http://link.aps.org/doi/10.1103/PhysRevLett.111.245003> (Dec. 2013).
653. Gilljohann, M. F. et al. Direct Observation of Plasma Waves and Dynamics Induced by Laser-Accelerated Electron Beams. *Phys. Rev. X* 9, 11046. doi:10.1103/PhysRevX.9.011046. <https://link.aps.org/doi/10.1103/PhysRevX.9.011046> (Mar. 2019).
654. Deng, A. et al. Generation and acceleration of electron bunches from a plasma photocathode. *Nat. Phys.* doi:10.1038/s41567-019-0610-9. <http://www.nature.com/articles/s41567-019-0610-9> (Aug. 2019).
655. Mehrling, T. J., Fonseca, R. A., de la Ossa, A. & Vieira, J. Mitigation of the Hose Instability in Plasma-Wakefield Accelerators. *Phys. Rev. Lett.* 118, 174801. doi:10.1103/PhysRevLett.118.174801. <https://link.aps.org/doi/10.1103/PhysRevLett.118.174801> (Apr. 2017).
656. Martinez de la Ossa, A., Mehrling, T. J. & Osterhoff, J. Intrinsic Stabilization of the Drive Beam in Plasma-Wakefield Accelerators. *Phys. Rev. Lett.* 121, 64803. doi:10.1103/PhysRevLett.121.064803. <https://link.aps.org/doi/10.1103/PhysRevLett.121.064803> (Aug. 2018).
657. Faure, J. et al. Controlled injection and acceleration of electrons in plasma wakefields by colliding laser pulses. *Nature* 444, 737–739. doi:10.1038/nature05393. <http://dx.doi.org/10.1038/nature05393> (2006).
658. Gonsalves, A. J. et al. Tunable laser plasma accelerator based on longitudinal density tailoring. *Nat. Phys.* 7, 862–866. doi:10.1038/nphys2071. <http://dx.doi.org/10.1038/nphys2071> (2011).
659. Buck, A. et al. Shock-Front Injector for High-Quality Laser-Plasma Acceleration. *Phys. Rev. Lett.* 110, 185006. doi:10.1103/PhysRevLett.110.185006. <http://link.aps.org/doi/10.1103/PhysRevLett.110.185006> (May 2013).
660. Mirzaie, M. et al. Demonstration of self-truncated ionization injection for GeV electron beams. *Sci. Rep.* 5, 1–9. doi:10.1038/srep14659 (2015).
661. Zeng, M., Chen, M., Sheng, Z. M., Mori, W. B. & Zhang, J. Self-truncated ionization injection and consequent monoenergetic electron bunches in laser wakefield acceleration. *Phys. Plasmas* 21. doi:10.1063/1.4868404 (2014).
662. Li, F. Y. et al. Dense Attosecond Electron Sheets from Laser Wakefields Using an Up-Ramp Density Transition. *Phys. Rev. Lett.* 110, 135002. doi:10.1103/PhysRevLett.110.135002. <https://link.aps.org/doi/10.1103/PhysRevLett.110.135002> (Mar. 2013).
663. Heinemann, T. et al. Investigating the Key Parameters of a Staged Laser- and Particle Driven Plasma Wakefield Accelerator Experiment, TUPIK010. doi:10.18429/JACOW-IPAC2017-TUPIK010. <http://inspirehep.net/record/1626947> (2017).
664. Sears, C. M. S. et al. Emittance and divergence of laser wakefield accelerated electrons. *Phys. Rev. ST Accel. Beams* 13, 92803. doi:10.1103/PhysRevSTAB.13.092803. <http://link.aps.org/doi/10.1103/PhysRevSTAB.13.092803> (2010).
665. Kuschel, S. et al. Demonstration of passive plasma lensing of a laser wakefield accelerated electron bunch. *Phys. Rev. Accel. Beams* 19, 71301. doi:10.1103/PhysRevAccelBeams.19.071301. <https://link.aps.org/doi/10.1103/PhysRevAccelBeams.19.071301> (July 2016).
666. Lindstrøm, C. A. et al. Emittance Preservation in an Aberration-Free Active Plasma Lens. *Phys Rev Lett* 121, 194801. doi:10.1103/PhysRevLett.121.194801 (Nov. 2018).
667. Chou, S. et al. Collective Deceleration of Laser-Driven Electron Bunches. *Phys. Rev. Lett.* 117, 144801 (Sept. 2016).
668. Raj, G. et al. Probing Ultrafast Magnetic-Field Generation by Current Filamentation Instability in Femtosecond Relativistic Laser-Matter Interactions. *arXiv*, 1–7. <http://arxiv.org/abs/1907.12052> (July 2019).
669. Corde, S. et al. Multi-gigaelectronvolt acceleration of positrons in a self-loaded plasma wakefield. *Nature* 524, 442 EP —. <https://doi.org/10.1038/nature14890> (Aug. 2015).

670. Hidding, B. et al. Ultrahigh brightness bunches from hybrid plasma accelerators as drivers of 5th generation light sources. *J. Phys. B At. Mol. Opt. Phys.* 47, 234010. <http://stacks.iop.org/0953-4075/47/i=23/a=234010> (2014).
671. Hidding, B. et al. Fundamentals and Applications of Hybrid LWFA–PWFA. *Appl. Sci.* 9. doi:10.3390/app9132626. <https://www.mdpi.com/2076-3417/9/13/2626> (2019).
672. Masson–Laborde, P. E. et al. Giga–electronvolt electrons due to a transition from laser wakefield acceleration to plasma wakefield acceleration. *Phys. Plasmas* 21, 123113. doi:10.1063/1.4903851. <http://scitation.aip.org/content/aip/journal/pop/21/12/10.1063/1.4903851> (2014).
673. Heigoldt, M. et al. Temporal evolution of longitudinal bunch profile in a laser wakefield accelerator. *Phys. Rev. Spec. Top.–Accel. Beams* 18. doi:10.1103/PhysRevSTAB.18.121302 (2015).
674. Corde, S. et al. Controlled Betatron X–Ray Radiation from Tunable Optically Injected Electrons. *Phys. Rev. Lett.* 107, 255003. doi:10.1103/PhysRevLett.107.255003. <http://link.aps.org/doi/10.1103/PhysRevLett.107.255003> (2011).
675. Schramm, U. et al. First results with the novel petawatt laser acceleration facility in Dresden. *J. Phys. Conf. Ser.* 874. <https://iopscience.iop.org/article/10.1088/1742-6596/874/1/012028/meta> (2017).
676. England, R. J., Rosenzweig, J. B. & Barov, N. Plasma electron fluid motion and wave breaking near a density transition. *Phys. Rev. E* 66, 016501. doi:10.1103/PhysRevE.66.016501. <https://link.aps.org/doi/10.1103/PhysRevE.66.016501> (July 2002).
677. Thompson, M. C., Rosenzweig, J. B. & Suk, H. Plasma density transition trapping as a possible high–brightness electron beam source. *Phys. Rev. Spec. Top.–Accel. Beams* 7, 011301. doi:10.1103/PhysRevSTAB.7.011301. <https://link.aps.org/doi/10.1103/PhysRevSTAB.7.011301> (Jan. 2004).
678. Baxevanis, P. et al. Operation and applications of a plasma wakefield accelerator based on the density down–ramp injection technique in AIP Conf. Proc. 1812 (AIP Publishing LLC, Mar. 2017), 100013. doi:10.1063/1.4975911. <http://aip.scitation.org/doi/abs/10.1063/1.4975911>.
679. Wittig, G. et al. Electron beam manipulation, injection and acceleration in plasma wakefield accelerators by optically generated plasma density spikes. *Nucl. Instruments Methods Phys. Res. Sect. A Accel. Spectrometers, Detect. Assoc. Equip.* 829, 83–87. doi:<https://doi.org/10.1016/j.nima.2016.02.027>. <http://www.sciencedirect.com/science/article/pii/S0168900216001893> (2016).
680. Hidding, B., Pretzler, G., Bruhwiler, D. & Rosenzweig, J. B. Method for generating electron beams in a hybrid plasma accelerator 2011.
681. Bourgeois, N., Cowley, J. & Hooker, S. M. Two–Pulse Ionization Injection into Quasilinear Laser Wakefields. *Phys. Rev. Lett.* 111, 155004. <http://link.aps.org/doi/10.1103/PhysRevLett.111.155004> (Oct. 2013).
682. Manahan, G. G. et al. Advanced schemes for underdense plasma photocathode wakefield accelerators: pathways towards ultrahigh brightness electron beams. *Phil. Trans. R. Soc. A* 377, 20180182. doi:10.1098/rsta.2018.0182. <https://royalsocietypublishing.org/doi/10.1098/rsta.2018.0182> (Aug. 2019).
683. Xi, Y., Hidding, B., Bruhwiler, D., Pretzler, G. & Rosenzweig, J. B. Hybrid modeling of relativistic underdense plasma photocathode injectors. *Phys. Rev. ST Accel. Beams* 16, 31303. doi:10.1103/PhysRevSTAB.16.031303. <http://link.aps.org/doi/10.1103/PhysRevSTAB.16.031303> (Mar. 2013).
684. Schroeder, C. B. et al. Thermal emittance from ionization–induced trapping in plasma accelerators. *Phys. Rev. ST Accel. Beams* 17, 101301. doi:10.1103/PhysRevSTAB.17.101301. <https://link.aps.org/doi/10.1103/PhysRevSTAB.17.101301> (Oct. 2014).
685. Moon, K., Kumar, S., Hur, M. & Chung, M. Longitudinal phase space dynamics of witness bunch during the Trojan Horse injection for plasma–based particle accelerators. *Phys. Plasmas* 26, 073103. doi:10.1063/1.5108928. <http://aip.scitation.org/doi/10.1063/1.5108928> (July 2019).

686. Yu, L.-L. et al. Two-Color Laser-Ionization Injection. *Phys. Rev. Lett.* 112, 125001. doi:10.1103/PhysRevLett.112.125001. <http://link.aps.org/doi/10.1103/PhysRevLett.112.125001> (2014).
687. Hidding, B. et al. Tunable Electron Multibunch Production in Plasma Wakefield Accelerators. *arXiv*, 1403.1109 (2014).
688. Zeng, M. et al. Multichromatic Narrow-Energy-Spread Electron Bunches from Laser-Wakefield Acceleration with Dual-Color Lasers. *Phys. Rev. Lett.* 114, 084801. doi:10.1103/PhysRevLett.114.084801. <https://link.aps.org/doi/10.1103/PhysRevLett.114.084801> (Feb. 2015).
689. Zeng, M. et al. High quality electron beam acceleration by ionization injection in laser wakefields with mid-infrared dual-color lasers. *Phys. Plasmas* 23, 063113. doi:10.1063/1.4953895. <http://aip.scitation.org/doi/10.1063/1.4953895> (June 2016).
690. Corde, S. et al. Observation of longitudinal and transverse self-injections in laser-plasma accelerators. *Nat. Commun.* 4, 1501. doi:10.1038/ncomms2528. <http://dx.doi.org/10.1038/ncomms2528> (2013).
691. Li, F. Y. et al. Coherent kilo-electron-volt backscattering from plasma-wave boosted relativistic electron mirrors. *Appl. Phys. Lett.* 105, 161102. doi:10.1063/1.4899136. <http://aip.scitation.org/doi/10.1063/1.4899136> (Oct. 2014).
692. Li, F. Y. et al. Radially polarized, half-cycle, attosecond pulses from laser wakefields through coherent synchrotronlike radiation. *Phys. Rev. E* 90, 043104. doi:10.1103/PhysRevE.90.043104. <https://link.aps.org/doi/10.1103/PhysRevE.90.043104> (Oct. 2014).
693. Zhao, Q. et al. Sub-femtosecond electron bunches in laser wakefield acceleration via injection suppression with a magnetic field. *Plasma Phys. Control. Fusion* 61, 085015. doi:10.1088/1361-6587/ab249c. <https://iopscience.iop.org/article/10.1088/1361-6587/ab249c> (Aug. 2019).
694. Chen, M. et al. Tunable synchrotron-like radiation from centimeter scale plasma channels. *Light Sci. Appl.* 5, e16015-e16015. doi:10.1038/lsa.2016.15. <http://www.nature.com/articles/lsa201615> (Jan. 2016).
695. Zhang, X., Khudik, V. N. & Shvets, G. Synergistic Laser-Wakefield and Direct-Laser Acceleration in the Plasma-Bubble Regime. *Phys. Rev. Lett.* 114, 184801. doi:10.1103/PhysRevLett.114.184801. <https://link.aps.org/doi/10.1103/PhysRevLett.114.184801> (May 2015).
696. Huang, K. et al. Resonantly Enhanced Betatron Hard X-rays from Ionization Injected Electrons in a Laser Plasma Accelerator. *Sci. Rep.* 6, 27633. doi:10.1038/srep27633. <http://www.nature.com/articles/srep27633> (Sept. 2016).
697. Krausz, F. & Ivanov, M. Attosecond physics. *Rev. Mod. Phys.* 81, 163-234. doi:10.1103/RevModPhys.81.163. <https://link.aps.org/doi/10.1103/RevModPhys.81.163> (Feb. 2009).
698. Tsakiris, G. D., Eidmann, K., Meyer-ter-Vehn, J. & Krausz, F. Route to intense single attosecond pulses. *New J. Phys.* 8, 19-19. doi:10.1088/1367-2630/8/1/019. <http://stacks.iop.org/1367-2630/8/i=1/a=019?key=crossref.65a890ec861c69659d7da6087740162d> (Jan. 2006).
699. Bulanov, S. V., Esirkepov, T. & Tajima, T. Light Intensification towards the Schwinger Limit. *Phys. Rev. Lett.* 91, 085001. doi:10.1103/PhysRevLett.91.085001. <https://link.aps.org/doi/10.1103/PhysRevLett.91.085001> (Aug. 2003).
700. Kando, M. et al. Enhancement of Photon Number Reflected by the Relativistic Flying Mirror. *Phys. Rev. Lett.* 103, 235003. doi:10.1103/PhysRevLett.103.235003. <https://link.aps.org/doi/10.1103/PhysRevLett.103.235003> (Dec. 2009).
701. Bettoni, S. Passive Streaking Using Transverse Wakefield for Ultrashort Bunch Diagnostics in Proc. Int. Part. Accel. Conf. (IPAC'17), Copenhagen, Denmark, 14-19 May, 2017 (JACoW, Geneva, Switzerland, May 2017), FRXCA1.
702. Lemery, F., Assmann, R., Floettmann, K. & Vinatier, T. A Transverse Deflection Structure with Dielectric-Lined Waveguides in the Sub-THz Regime IPAC'17. Copenhagen, Denmark, 2017.

703. Soong, K., Byer, R. L., Peralta, E. A., England, R. & Wu, Z. Beam Position Monitor for Micro-Accelerators in Proc. Part. Accel. Conf. (2013), MOPAC32.
704. Di Piazza, A. Nonlinear Breit–Wheeler Pair Production in a Tightly Focused Laser Beam. *Phys. Rev. Lett.* 117, 213201. doi:10.1103/PhysRevLett.117.213201. <https://link.aps.org/doi/10.1103/PhysRevLett.117.213201> (Nov. 2016).
705. Cole, J. et al. Experimental Evidence of Radiation Reaction in the Collision of a High-Intensity Laser Pulse with a Laser-Wakefield Accelerated Electron Beam. *Phys. Rev. X* 8, 011020. doi:10.1103/PhysRevX.8.011020. <https://link.aps.org/doi/10.1103/PhysRevX.8.011020> (Feb. 2018).
706. Poder, K. et al. Experimental Signatures of the Quantum Nature of Radiation Reaction in the Field of an Ultraintense Laser. *Phys. Rev. X* 8, 031004. doi:10.1103/PhysRevX.8.031004. <https://link.aps.org/doi/10.1103/PhysRevX.8.031004> (July 2018).
707. Arran, C. et al. Optimal parameters for radiation reaction experiments. *Plasma Phys. Control. Fusion* 61, 074009. doi:10.1088/1361-6587/ab20f6. <https://iopscience.iop.org/article/10.1088/1361-6587/ab20f6> (July 2019).
708. Behm, K. T. et al. A spectrometer for ultrashort gamma-ray pulses with photon energies greater than 10 MeV. *Rev. Sci. Instrum.* 89, 113303. doi:10.1063/1.5056248. <http://aip.scitation.org/doi/10.1063/1.5056248> (Nov. 2018).
709. Hauke, M. & al., E. Functional safety of machine controls report—Application of EN ISO 13849 2008.
710. Dann, S. J. D. et al. Laser wakefield acceleration with active feedback at 5 Hz. *Phys. Rev. Accel. Beams* 22, 41303. doi:10.1103/PhysRevAccelBeams.22.041303. <https://link.aps.org/doi/10.1103/PhysRevAccelBeams.22.041303> (Apr. 2019).
711. Cianchi, A. et al. Conceptual design of electron beam diagnostics for high brightness plasma accelerator. *Nucl. Instruments Methods Phys. Res. Sect. A Accel. Spectrometers, Detect. Assoc. Equip.* 909, 350–354. doi:<https://doi.org/10.1016/j.nima.2018.02.095>. <http://www.sciencedirect.com/science/article/pii/S0168900218302754> (2018).
712. Malovytsia, M. & Delerue, N. Comparison of the Smith-purcell Radiation Yield for Different Models in Proceedings, 7th Int. Part. Accel. Conf. (IPAC 2016) Busan, Korea, May 8-13, 2016 (2016), MOPMB004. doi:10.18429/JACoW-IPAC2016-MOPMB004.
713. Pompili, R. et al. First single-shot and non-intercepting longitudinal bunch diagnostics for comb-like beam by means of Electro-Optic Sampling. *Nucl. Instruments Methods Phys. Res. Sect. A Accel. Spectrometers, Detect. Assoc. Equip.* 740, 216–221. doi:<https://doi.org/10.1016/j.nima.2013.10.031>. <http://www.sciencedirect.com/science/article/pii/S0168900213013776> (2014).
714. Apollon Research Infrastructure. About Apollon 2019. <http://www.apollon-laser.fr/>.
715. UK Research and Innovation – Science and Technology Facilities Council. CLARA – Compact Linear Accelerator for Research and Applications 2016. <https://stfc.ukri.org/research/accelerator-science/clara-compact-linear-accelerator-for-research-and-applications/>.
716. Labat, M. et al. Robustness of a Plasma Acceleration Based Free Electron Laser. *Phys. Rev. Accel. Beams* 21, 114802. doi:10.1103/PhysRevAccelBeams.21.114802. <https://link.aps.org/doi/10.1103/PhysRevAccelBeams.21.114802> (2018).
717. Helmholtz-Zentrum Dresden-Rossendorf e.V. Strahlungsquelle am ELBE-Zentrum für Hochleistungs-Strahlenquellen 2019. <https://www.hzdr.de/db/Cms?pNid=145>.
718. ELI Beamlines. eli beamlines 2019. <https://www.eli-beams.eu/>.
719. ELI-HU Nonprofit Kft. ELI Alps 2019. <https://www.eli-alps.hu>.
720. Deutsches Elektronen-Synchrotron. FLASHFORWARD 2018. <https://forward.desy.de/>.
721. Sävert, A. et al. Direct Observation of the Injection Dynamics of a Laser Wakefield Accelerator Using Few-Femtosecond Shadowgraphy. *Phys. Rev. Lett.* 115, 055002. doi:10.1103/PhysRevLett.115.055002. <https://link.aps.org/doi/10.1103/PhysRevLett.115.055002> (July 2015).

722. Helmholtz Institute Jena. POLARIS Laser 2019. [https://www.hi-jena.de/en/helmholtz\\_institute\\_jena/about-the-helmholtz-institute-jena/experimental\\_facilities/local/polaris/](https://www.hi-jena.de/en/helmholtz_institute_jena/about-the-helmholtz-institute-jena/experimental_facilities/local/polaris/) (2019).
723. Hornung, M. et al. 54 J pulses with 18 nm bandwidth from a diode-pumped chirped-pulse amplification laser system. *Opt. Lett.* 41, 5413. doi:10.1364/OL.41.005413. <https://www.osapublishing.org/abstract.cfm?URI=ol-41-22-5413> (Nov. 2016).
724. Helmholtz Institute Jena. JETI40 Laser 2019. [https://www.hi-jena.de/en/helmholtz\\_institute\\_jena/about-the-helmholtz-institute-jena/experimental\\_facilities/local/jeti40-laser/](https://www.hi-jena.de/en/helmholtz_institute_jena/about-the-helmholtz-institute-jena/experimental_facilities/local/jeti40-laser/) (2019).
725. Helmholtz Institute Jena. JETI200 Laser 2019. [https://www.hi-jena.de/en/helmholtz\\_institute\\_jena/about-the-helmholtz-institute-jena/experimental\\_facilities/local/jeti200-laser-kopie/](https://www.hi-jena.de/en/helmholtz_institute_jena/about-the-helmholtz-institute-jena/experimental_facilities/local/jeti200-laser-kopie/) (2019).
726. Laboratorio di Laser Intensi. Laboratorio di Laser Intensi 2019. [http://research.ino.it/Groups/ilil/it/about\\_it/](http://research.ino.it/Groups/ilil/it/about_it/).
727. KIT. FLUTE 2019. <http://www.ibpt.kit.edu/flute.php>.
728. Centre for Advanced Laser Applications. CALA - Centre for Advanced Laser Applications: Mainpage 2019. <http://www.cala-laser.de/> (2019).
729. Lund University. Lund Laser Centre - Lund University 2019. <http://www.llc.lu.se/>.
730. Queen's University Belfast. Centre for Plasma Physics - Projects & Facilities 2019. <https://www.qub.ac.uk/research-centres/CentreforPlasmaPhysics/ProjectsFacilities/>.
731. UK Research and Innovation - Science and Technology Facilities Council. Central Laser Facility 2016. <https://stfc.ukri.org/research/lasers-and-plasma-physics/central-laser-facility/>.
732. SCAPA. Scottish Centre for the Application of Plasma-Based Accelerators 2019. <http://www.scapa.ac.uk/>.
733. Deutsches Elektronen-Synchrotron. SINBAD 2018. <https://ard.desy.de/e225180/>.
734. INFN-LNF. SPARC LAB 2019. [http://w3.lnf.infn.it/lab/sparc\\_lab/](http://w3.lnf.infn.it/lab/sparc_lab/).
735. Wigner Datacenter. Wigner Datacenter <https://wignerdc.hu/home> (2019).
736. Kacsokovics, B. Wigner GPU lab 2019. <http://gpu.wigner.mta.hu/en> (2019).
737. Berkeley Lab. BELLA Petawatt Laser <http://bella.lbl.gov/facilities/bella-center-facilities-bella-laser/>.
738. Nakamura, K. et al. Diagnostics, Control and Performance Parameters for the BELLA High Repetition Rate Petawatt Class Laser. *IEEE J. Quantum Electron.* 53 (2017).
739. Lozhkarev, V. V. et al. Compact 0.56 Petawatt laser system based on optical parametric chirped pulse amplification in KD\*P crystals. *Laser Phys. Lett.* 4, 421–427. doi:10.1002/lapl. 200710008. <http://stacks.iop.org/1612-202X/4/i=6/a=003?key=crossref.b360373a803c9dc5192641f4d4556273> (June 2007).
740. Soloviev, A. et al. Fast electron generation using PW-class PEARL facility. *Nucl. Instruments Methods Phys. Res. Sect. A Accel. Spectrometers, Detect. Assoc. Equip.* 653, 35–41. doi:10.1016/J.NIMA.2011.01.180. <https://www.sciencedirect.com/science/article/pii/S0168900211003329?via%3Dihub> (Oct. 2011).
741. Soloviev, A. et al. Experimental evidence for short-pulse laser heating of solid-density target to high bulk temperatures. *Sci. Rep.* 7, 12144. doi:10.1038/s41598-017-11675-2. <http://www.nature.com/articles/s41598-017-11675-2> (Dec. 2017).
742. Eremin, V. et al. Study of the plasma wave excited by intense femtosecond laser pulses in a dielectric capillary. *Phys. Plasmas* 19, 093121. doi:10.1063/1.4754868. <http://aip.scitation.org/doi/10.1063/1.4754868> (Sept. 2012).
743. Malkov, Y. A. et al. Generation of quasi-monochromatic beams of accelerated electrons during interaction of weak-contrast intense femtosecond laser radiation with a metalfoil edge. *Quantum Electron.* 43, 226–231. doi:10.1070/QE2013v043n03ABEH015100. <http://stacks.iop.org/1063-7818/43/i=3/a=226?key=crossref.49da99fea29a4b721c6222f086f1f2bf> (Mar. 2013).
744. Mironov, S. Y. et al. Spatio-temporal shaping of photocathode laser pulses for linear electron accelerators. *Physics-Uspekhi* 60, 1039–1050. doi:10.3367/UFNe.2017.03.038143. <http://stacks.iop.org/1063-7869/60/i=10/a=1039?key=crossref.0d052239e15e19b0ec3120cf7ba2dfc2> (Oct. 2017).

745. Institute for Advanced Simulation - Jülich Supercomputing Centre. Forschungszentrum Jülich - JSC - Supercomputers 2019. [https://www.fz-juelich.de/ias/jsc/EN/Expertise/Supercomputers/supercomputers\\_node.html](https://www.fz-juelich.de/ias/jsc/EN/Expertise/Supercomputers/supercomputers_node.html) (2019).
746. TOP500.org. TOP500 List - June 2019 | TOP500 Supercomputer Sites 2019. <https://www.top500.org/list/2019/06/> (2019).
747. Elbattah, M. Explore the World's Supercomputers 2018. <http://supercompviz.apphb.com/index.html#> (2019).
748. Gauß-Allianz e.V. Gauß-Allianz - HPC in Deutschland: Wissens- & Technologietransfer 2019. <https://gauss-allianz.de/> (2019).
749. PRACE. PRACE - Partnership for Advanced Computing in Europe 2019. <http://www.prace-ri.eu/> (2019).
750. EPCC (press release). £79m supercomputer set to boost UK capability Edinburgh, Mar. 2019. <https://www.epcc.ed.ac.uk/news/79m-supercomputer-set-boost-uk-capability>.
751. HPC-Europa3. HPC-Europa3 - Pan-European Research Infrastructure on High Performance Computing 2017. <http://www.hpc-europa.eu/> (2019).
752. EuroHPC Joint Undertaking. EuroHPC - Leading the way in the European Supercomputing. <https://eurohpc-ju.europa.eu/index.html> (2019).
753. European Commission (press release). Digital Single Market: Europe announces eight sites to host world-class supercomputers Luxembourg, June 2019. [https://europa.eu/rapid/press-release\\_IP-19-2868\\_en.htm](https://europa.eu/rapid/press-release_IP-19-2868_en.htm).
754. Lefebvre, E. et al. Electron and photon production from relativistic laser-plasma interactions. *Nucl. Fusion* 43, 629–633. doi:10.1088/0029-5515/43/7/317. <http://stacks.iop.org/0029-5515/43/i=7/a=317?key=crossref.3611b3a5dcb0c8c90a988479af5f3cd3> (July 2003).
755. Vay, J.-L., Grote, D. P., Cohen, R. H. & Friedman, A. Novel methods in the Particle-In-Cell accelerator Code-Framework WARP. *Comput. Sci. Disc.* 5, 14019. doi:10.1088/1749-4699/5/1/014019. <http://stacks.iop.org/1749-4699/5/i=1/a=014019> (2012).
756. Mehrling, T., Benedetti, C., Schroeder, C. B. & Osterhoff, J. HiPACE: a quasi-static particle-in-cell code. *Plasma Phys. Control. Fusion* 56, 084012. doi:10.1088/0741-3335/56/8/084012. <http://stacks.iop.org/0741-3335/56/i=8/a=084012?key=crossref.70bffd7eee174a2aacc367aee0a7216> (Aug. 2014).
757. Londrillo, P., Benedetti, C. & Sgattoni, A. Charge preserving high order PIC schemes. *Nucl. Instruments Methods Phys. Res. Sect. A Accel. Spectrometers, Detect. Assoc. Equip.* 620, 28–35. doi:10.1016/J.NIMA.2010.01.055. <https://www.sciencedirect.com/science/article/pii/S0168900210001233> (Aug. 2010).
758. Terzani, D. & Londrillo, P. A fast and accurate numerical implementation of the envelope model for laser-plasma dynamics. *Comput. Phys. Commun.* 242, 49–49. doi:10.1016/J.CPC.2019.04.007. <https://www.sciencedirect.com/science/article/pii/S0010465519301195?via%3Dihub> (Sept. 2019).
759. Burau, H. et al. PICongPU: A Fully Relativistic Particle-in-Cell Code for a GPU Cluster. *IEEE Trans. Plasma Sci.* 38, 2831–2839. doi:10.1109/TPS.2010.2064310. <http://ieeexplore.ieee.org/document/5556015/> (Oct. 2010).
760. Github. Fourier-Bessel Particle-In-Cell code (FPIC) 2019. <https://github.com/fbpic/fbpic>.
761. Jalas, S. et al. Accurate modeling of plasma acceleration with arbitrary order pseudospectral particle-in-cell methods. *Phys. Plasmas* 24, 033115. doi:10.1063/1.4978569. <http://aip.scitation.org/doi/10.1063/1.4978569> (Mar. 2017).
762. Kirchen, M. et al. Stable discrete representation of relativistically drifting plasmas. *Phys. Plasmas* 23, 100704. doi:10.1063/1.4964770. <http://aip.scitation.org/doi/10.1063/1.4964770> (Oct. 2016).
763. Lehe, R., Kirchen, M., Godfrey, B. B., Maier, A. R. & Vay, J.-L. Elimination of numerical Cherenkov instability in flowing-plasma particle-in-cell simulations by using Galilean coordinates. *Phys. Rev. E* 94, 053305. doi:10.1103/PhysRevE.94.053305. <https://link.aps.org/doi/10.1103/PhysRevE.94.053305> (Nov. 2016).

764. Github. The openPMD Standard 2019. <https://github.com/openPMD/openPMD-standard>.
765. Andreev, N. E. & Kuznetsov, S. V. Guided propagation of short intense laser pulses and electron acceleration. *Plasma Phys. Control. Fusion* 45, A39–A57 (2003).
766. Andreev, N. E. & Kuznetsov, S. V. Laser Wakefield Acceleration of Finite Charge Electron Bunches. 36, 1765–1772 (2008).
767. Andreev, N. E., Veisman, M. E., Cadjan, M. G. & Chegotov, M. V. Generation of a wakefield during gas ionization. 26, 947–959 (2000).
768. Andreev, N. E. et al. Nonadiabatic heating of a plasma produced by the ionization of a gas by a short intense laser pulse. *JETP Lett.* 68, 592–598 (1998).
769. Pugacheva, D. V. & Andreev, N. E. Effect of synchrotron radiation on the dynamics of electron spin precession in the process of laser-plasma acceleration. *Quantum Electron.* 48, 291 (2018).
770. Mangles, S. P. D. An Overview of Recent Progress in LaserWakefield Acceleration Experiments. *Cern Yellow Reports* 1, 289. <https://e-publishing.web.cern.ch/index.php/CYR/article/view/224> (2016).
771. Amiranoff, F. et al. Observation of Laser Wakefield Acceleration of Electrons. *Phys. Rev. Lett.* 81, 995–998. doi:10.1103/PhysRevLett.81.995. <http://link.aps.org/doi/10.1103/PhysRevLett.81.995> (1998).
772. Kneip, S. et al. Near-GeV Acceleration of Electrons by a Nonlinear Plasma Wave Driven by a Self-Guided Laser Pulse. *Phys. Rev. Lett.* 103, 35002. doi:10.1103/PhysRevLett.103.035002. <http://link.aps.org/doi/10.1103/PhysRevLett.103.035002> (July 2009).
773. Golovin, G. et al. Tunable monoenergetic electron beams from independently controllable laser-wakefield acceleration and injection. *Phys. Rev. Spec. Top. - Accel. Beams* 18, 1–6. doi:10.1103/PhysRevSTAB.18.011301 (2015).
774. Osterhoff, J. et al. Generation of Stable, Low-Divergence Electron Beams by Laser-Wakefield Acceleration in a Steady-State-Flow Gas Cell. *Phys. Rev. Lett.* 101, 85002. doi:10.1103/PhysRevLett.101.085002. <http://link.aps.org/doi/10.1103/PhysRevLett.101.085002> (2008).
775. Vargas, M. et al. Improvements to laser wakefield accelerated electron beam stability, divergence, and energy spread using three-dimensional printed two-stage gas cell targets. *Appl. Phys. Lett.* 104, 174103. doi:10.1063/1.4874981. <http://scitation.aip.org/content/aip/journal/apl/104/17/10.1063/1.4874981> (2014).
776. Heigoldt, M. et al. Temporal evolution of longitudinal bunch profile in a laser wakefield accelerator. *Phys Rev Spec Top-Ac* 18, 121302–121306. doi:10.1103/PhysRevSTAB.18.121302. <http://link.aps.org/doi/10.1103/PhysRevSTAB.18.121302> (Dec. 2015).
777. Sprangle, P. et al. Wakefield generation and GeV acceleration in tapered plasma channels. *Phys Rev E* 63, 56405 (May 2001).
778. Pukhov, A. & Kostyukov, I. Control of laser-wakefield acceleration by the plasma-density profile. *Phys Rev E* 77, 25401–25404. doi:10.1103/PhysRevE.77.025401 (Feb. 2008).
779. Yoon, S. J., Palastro, J. P. & Milchberg, H. M. Quasi-Phase-Matched Laser Wakefield Acceleration. *Phys Rev Lett* 112, 134803. doi:10.1103/PhysRevLett.112.134803 (Apr. 2014).
780. Rittershofer, W. Laser wakefield acceleration in tapered plasma channels: Theory, simulation and experiment PhD thesis (University of Oxford, 2014).
781. Kaganovich, D., Zigler, A., Hubbard, R. F., Sprangle, P. & Ting, A. Velocity control and staging in laser wakefield accelerators using segmented capillary discharges. *Appl. Phys. Lett.* 78, 3175–3177. doi:10.1063/1.1373407. <http://aip.scitation.org/doi/10.1063/1.1373407> (May 2001).
782. Abuazoum, S. et al. Linearly tapered discharge capillary waveguides as a medium for a laser plasma wakefield accelerator. *Appl. Phys. Lett.* 100, 14106. doi:10.1063/1.3674309. <http://link.aip.org/link/APPLAB/v100/i1/p014106/s1&Agg=doi> (2012).
783. Schaper, L., Goldberg, L., Kleinwächter, T., Schwinkendorf, J.-P. & Osterhoff, J. Longitudinal gas-density profilometry for plasma-wakefield acceleration

- targets. Nucl. Instrum. Meth. A 740, 208–211. doi:10.1016/0030-4018(93)90611-8. <http://www.sciencedirect.com/science/article/pii/S0168900213014332> (2014).
784. Litvak, A. G. Finite amplitude wave beams in a magneto-active plasma tech. rep. (Gorky State Univ., USSR, 1969). [http://jetp.ac.ru/cgi-bin/dn/e\\_030\\_02\\_0344.pdf](http://jetp.ac.ru/cgi-bin/dn/e_030_02_0344.pdf).
785. Max, C. E., Arons, J. & Langdon, A. B. Self-Modulation and Self-Focusing of Electromagnetic Waves in Plasmas. Phys. Rev. Lett. 33, 209–212. doi:10.1103/PhysRevLett.33.209. <http://link.aps.org/doi/10.1103/PhysRevLett.33.209> (1974).
786. Sun, G.-Z., Ott, E., Lee, Y. C. & Guzdar, P. Self-focusing of short intense pulses in plasmas. Phys. Fluids 30, 526–532. doi:10.1063/1.866349. <http://scitation.aip.org/content/aip/journal/pof1/30/2/10.1063/1.866349> (1987).
787. Pukhov, a. & Meyer-ter-Vehn, J. Laser wake field acceleration: The highly non-linear brokenwave regime. Appl. Phys. B Lasers Opt. 74, 355–361. doi:10.1007/s003400200795 (2002).
788. Thomas, A. G. R. et al. Effect of Laser-Focusing Conditions on Propagation and Monoenergetic Electron Production in Laser-Wakefield Accelerators. Phys. Rev. Lett. 98, 95004. doi:10.1103/PhysRevLett.98.095004. <http://link.aps.org/doi/10.1103/PhysRevLett.98.095004> (Mar. 2007).
789. Ralph, J. E. et al. Self-Guiding of Ultrashort, Relativistically Intense Laser Pulses through Underdense Plasmas in the Blowout Regime. Phys. Rev. Lett. 102, 175003. doi:10.1103/PhysRevLett.102.175003. <http://link.aps.org/doi/10.1103/PhysRevLett.102.175003> (Apr. 2009).
790. Vieira, J. M. et al. Magnetically assisted self-injection and radiation generation for plasmabased acceleration. Plasma Phys. Control. Fusion 54, 124044. doi:10.1088/0741-3335/54/12/124044. <http://stacks.iop.org/0741-3335/54/i=12/a=124044> (2012).
791. Mangles, S. P. D. et al. Controlling the spectrum of x-rays generated in a laser-plasma accelerator by tailoring the laser wavefront. Appl. Phys. Lett. 95, 181106. doi:10.1063/1.3258022. <http://scitation.aip.org/content/aip/journal/apl/95/18/10.1063/1.3258022> (2009).
792. Wang, X. et al. Quasi-monoenergetic laser-plasma acceleration of electrons to 2 GeV. Nat. Commun. 4, 1988. doi:10.1038/ncomms2988. <http://dx.doi.org/10.1038/ncomms2988> (2013).
793. Kalmykov, S. Y. et al. Numerical modelling of a 10-cm-long multi-GeV laser wakefield accelerator driven by a self-guided petawatt pulse. New J. Phys. 12, 45019. <http://stacks.iop.org/1367-2630/12/i=4/a=045019> (2010).
794. Sahai, A. A. et al. Excitation of wakefields in a relativistically hot plasma created by dying non-linear plasma wakefields. AIP Conf. Proc. 1507, 618–622. doi:10.1063/1.4773768. <http://aip.scitation.org/doi/abs/10.1063/1.4773768> (2012).
795. Durfee, C. G., Lynch, J. & Milchberg, H. M. Mode properties of a plasma waveguide for intense laser pulses. Opt Lett 19, 1937–1939. <http://www.opticsinfobase.org/ol/fulltext.cfm?uri=ol-19-23-1937> (1994).
796. Durfee, C. G., Lynch, J. & Milchberg, H. M. Development of a plasma waveguide for high-intensity laser pulses. Phys. Rev. E 51, 2368–2389. doi:10.1103/PhysRevE.51.2368. <http://link.aps.org/doi/10.1103/PhysRevE.51.2368> (1995).
797. Clark, T. R. & Milchberg, H. M. Optical mode structure of the plasma waveguide. Phys Rev E 61, 1954–1965. doi:10.1103/PhysRevE.61.1954 (Feb. 2000).
798. Durfee, C. G., Clark, T. R. & Milchberg, H. M. Mode control in a two-pulse-excited plasma waveguide. J Opt Soc Am B 13, 59–67. doi:10.1364/JOSAB.13.000059 (Jan. 1996).
799. Ehrlich, Y. et al. Guiding of High Intensity Laser Pulses in Straight and Curved Plasma Channel Experiments. Phys. Rev. Lett. 77, 4186–4189. doi:10.1103/PhysRevLett.77.4186. <http://www.ncbi.nlm.nih.gov/pubmed/10062470> (1996).
800. Kaganovich, D. et al. High efficiency guiding of terawatt subpicosecond laser pulses in a capillary discharge plasma channel. Phys Rev E 59, R4769–R4772. doi:10.1103/PhysRevE.59.R4769 (Apr. 1999).

801. Spence, D. J., Butler, A. & Hooker, S. M. Gas-filled capillary discharge waveguides. *J Opt Soc Am B* 20, 138–151. <http://www.opticsinfobase.org/abstract.cfm?id=70837> (2003).
802. Spence, D. J. & Hooker, S. M. Investigation of a hydrogen plasma waveguide. *Phys. Rev. E* 63, 15401. doi:10.1103/PhysRevE.63.015401 (Dec. 2000).
803. Bobrova, N. A. et al. Simulations of a hydrogen-filled capillary discharge waveguide. *Phys Rev E* 65, 16407. doi:10.1103/PhysRevE.65.016407 (Jan. 2002).
804. Broks, B., Garloff, K. & van der Mullen, J. Nonlocal-thermal-equilibrium model of a pulsed capillary discharge waveguide. *Phys Rev E* 71, 16401. doi:10.1103/PhysRevE.71.016401 (Jan. 2005).
805. Broks, B. H. P. et al. Modeling of a square pulsed capillary discharge waveguide for interferometry measurements. *Phys Plasmas* 14, 23501. doi:10.1063/1.2432053 (2007).
806. Gonsalves, A. J., Rowlands-Rees, T. P., Broks, B. H. P., van der Mullen, J. J. A. M. & Hooker, S. M. Transverse interferometry of a hydrogen-filled capillary discharge waveguide. *Phys Rev Lett* 98, 25002. doi:10.1103/PhysRevLett.98.025002 (Jan. 2007).
807. Gonsalves, A. J. et al. Plasma channel diagnostic based on laser centroid oscillations. *Phys Plasmas* 17, 56706. doi:10.1063/1.3357175 (2010).
808. Ibbotson, T. P. A. et al. Investigation of the role of plasma channels as waveguides for laserwakefield accelerators. *New J Phys* 12, 45008. doi:10.1088/1367-2630/12/4/045008 (2010).
809. Karsch, S. et al. GeV-scale electron acceleration in a gas-filled capillary discharge waveguide. *New J. Phys.* 9, 415. <http://stacks.iop.org/1367-2630/9/i=11/a=415> (2007).
810. Filippi, F. et al. Spectroscopic measurements of plasma emission light for plasma-based acceleration experiments. *J. Instrum.* 11, C09015. <http://stacks.iop.org/1748-0221/11/i=09/a=C09015> (2016).
811. Gonsalves, A. J. et al. Demonstration of a high repetition rate capillary discharge waveguide. *J Appl Phys* 119, 33302–33312. doi:10.1063/1.4940121 (Jan. 2016).
812. Gonsalves, A. J. Investigation of a Hydrogen-filled Capillary Discharge Waveguide for Laser-driven Plasma Accelerators PhD thesis (University of Oxford, 2006).
813. Milchberg, H. M., Clark, T. R., Durfee, C. G., Antonsen, T. M. & Mora, P. Development and applications of a plasma waveguide for intense laser pulses. *Phys Plasmas* 3, 2149. doi:10.1063/1.871668 (1996).
814. Clark, T. R. & Milchberg, H. M. Time-and space-resolved density evolution of the plasma waveguide. *Phys Rev Lett.* <http://journals.aps.org/prl/abstract/10.1103/PhysRevLett.78.2373> (1997).
815. Volfbeyn, P., Esarey, E. & Leemans, W. P. Guiding of laser pulses in plasma channels created by the ignitor-heater technique. *Phys Plasmas* 6, 2269–2277. doi:10.1063/1.873503. <http://scitation.aip.org/content/aip/journal/pop/6/5/10.1063/1.873503> (1999).
816. Sheng, H., Kim, K. Y., Kumarappan, V., Layer, B. D. & Milchberg, H. M. Plasma waveguides efficiently generated by Bessel beams in elongated cluster gas jets. *Phys Rev E* 72, 36411. doi:10.1103/PhysRevE.72.036411. <http://link.aps.org/doi/10.1103/PhysRevE.72.036411> (Sept. 2005).
817. Yoon, S. J. et al. Shock formation in supersonic cluster jets and its effect on axially modulated laser-produced plasma waveguides. *Opt. Express* 21, 15878. doi:10.1364/OE.21.015878. <http://www.opticsinfobase.org/abstract.cfm?URI=oe-21-13-15878> (2013).
818. Yoon, S. J., Palastro, J. P., Gordon, D., ANTONSEN, T. M. & Milchberg, H. M. Quasiphase- matched acceleration of electrons in a corrugated plasma channel. *Phys Rev Spec Top-Ac* 15, 81305–81311. doi:10.1103/PhysRevSTAB.15.081305. <http://link.aps.org/doi/10.1103/PhysRevSTAB.15.081305> (Aug. 2012).
819. Chiou, T. C. et al. Laser wake-field acceleration and optical guiding in a hollow plasma channel. *Phys. Plasmas* 2, 310–318. doi:10.1063/1.871107. <http://aip.scitation.org/doi/10.1063/1.871107> (Jan. 1995).

820. Chiou, T. C. & Katsouleas, T. High beam quality and efficiency in plasma-based accelerators. *Phys Rev Lett* 81, 3411–3414. doi:10.1103/PhysRevLett.81.3411. <http://link.aps.org/doi/10.1103/PhysRevLett.81.3411> (1998).
821. Schroeder, C. B., Esarey, E., Benedetti, C. & Leemans, W. P. Control of focusing forces and emittances in plasma-based accelerators using near-hollow plasma channels. *Phys Plasmas* 20, 80701. doi:10.1063/1.4817799. <http://link.aip.org/link/PHPAEN/v20/i8/p080701/s1&Agg=doi> (2013).
822. Kimura, W., Milchberg, H., Muggli, P., Li, X. & Mori, W. Hollow plasma channel for positron plasma wakefield acceleration. *Phys Rev Spec Top-Ac* 14, 41301. doi:10.1103/PhysRevSTAB.14.041301. <http://link.aps.org/doi/10.1103/PhysRevSTAB.14.041301> (Apr. 2011).
823. Du, D., Liu, X., Korn, G., Squier, J. & Mourou, G. A. Laser-induced breakdown by impact ionization in SiO<sub>2</sub> with pulse widths from 7 ns to 150 fs. *Appl. Phys. Lett.* 64, 3071–3073. doi:10.1063/1.111350. <http://scitation.aip.org/content/aip/journal/apl/64/23/10.1063/1.111350> (1994).
824. Veysman, M. et al. Theoretical and experimental study of laser beam propagation in capillary tubes for non-symmetrical coupling conditions. *J. Opt. Soc. Am. B* 27, 1400–1408. doi:10.1364/JOSAB.27.001400. <http://josab.osa.org/abstract.cfm?URI=josab-27-7-1400> (2010).
825. Paradkar, B. S. et al. A comparative study of plasma channels for a 100 GeV electron accelerator using a multi-petawatt. *Plasma Phys. Control. Fusion* 56, 84008. <http://stacks.iop.org/0741-3335/56/i=8/a=084008> (2014).
826. Dorchies, F. et al. Monomode Guiding of 1016Wcm..2 Laser Pulses over 100 Rayleigh Lengths in Hollow Capillary Dielectric Tubes. *Phys. Rev. Lett.* 82, 4655–4658. <http://link.aps.org/doi/10.1103/PhysRevLett.82.4655> (June 1999).
827. Andreev, N. E. et al. Analysis of laser wakefield dynamics in capillary tubes. *New J. Phys.* 12, 45024. <http://stacks.iop.org/1367-2630/12/i=4/a=045024> (2010).
828. Mangles, S. P. D. et al. Self-injection threshold in self-guided laser wakefield accelerators. *Phys. Rev. Spec. Top. - Accel. Beams* 15, 2–7. doi:10.1103/PhysRevSTAB.15.011302 (2012).
829. Banerjee, S. et al. Generation of tunable, 100–800 MeV quasi-monoenergetic electron beams from a laser-wakefield accelerator in the blowout regime. *Phys. Plasmas* 19, 56703. doi:10.1063/1.4718711. <http://dx.doi.org/10.1063/1.4718711> (May 2012).
830. Froula, D. H. et al. Measurements of the Critical Power for Self-Injection of Electrons in a Laser Wakefield Accelerator. *Phys. Rev. Lett.* 103, 215006. doi:10.1103/PhysRevLett.103.215006. <http://link.aps.org/doi/10.1103/PhysRevLett.103.215006> (2009).
831. Rechatin, C. et al. Controlling the Phase-Space Volume of Injected Electrons in a Laser- Plasma Accelerator. *Phys. Rev. Lett.* 102, 164801. <http://link.aps.org/doi/10.1103/PhysRevLett.102.164801> (Apr. 2009).
832. Geddes, C. G. R. et al. High energy, low energy spread electron bunches produced via colliding pulse injection. *AIP Conf. Proc.* 1777, 40003. doi:10.1063/1.4965605. <http://aip.scitation.org/doi/abs/10.1063/1.4965605> (2016).
833. Tomassini, P. et al. Production of high-quality electron beams in numerical experiments of laser wakefield acceleration with longitudinal wave breaking. *Phys. Rev. ST Accel. Beams* 6, 121301. <http://link.aps.org/doi/10.1103/PhysRevSTAB.6.121301> (Dec. 2003).
834. Faure, J., Rechatin, C., Lundh, O., Ammoura, L. & Malka, V. Injection and acceleration of quasimonoenergetic relativistic electron beams using density gradients at the edges of a plasma channel. *Phys. Plasmas* 17, 83107. doi:10.1063/1.3469581. <http://scitation.aip.org/content/aip/journal/pop/17/8/10.1063/1.3469581> (2010).
835. Hansson, M. et al. Down-ramp injection and independently controlled acceleration of electrons in a tailored laser wakefield accelerator. *Phys. Rev. ST Accel. Beams* 18, 71303. doi:10.1103/PhysRevSTAB.18.071303. <http://link.aps.org/doi/10.1103/PhysRevSTAB.18.071303> (July 2015).

836. Oz, E. et al. Ionization-Induced Electron Trapping in Ultrarelativistic Plasma Wakes. *Phys. Rev. Lett.* 98, 84801. doi:10.1103/PhysRevLett.98.084801. <http://link.aps.org/doi/10.1103/PhysRevLett.98.084801> (2007).
837. Kamperidis, C., Dimitriou, V., Mangles, S. P. D., Dangor, A. E. & Najmudin, Z. Low energy spread electron beams from ionization injection in a weakly relativistic laser wakefield accelerator. *Plasma Phys. Control. Fusion* 56, 84007. <http://stacks.iop.org/0741-3335/56/i=8/a=084007> (2014).
838. Hansson, M. et al. Localization of ionization-induced trapping in a laser wakefield accelerator using a density down-ramp. *Plasma Phys. Control. Fusion* 58, 55009. <http://stacks.iop.org/0741-3335/58/i=5/a=055009> (2016).
839. Hafz, N. A. M. et al. Generation of high-quality electron beams by ionization injection in a single acceleration stage. *High Power Laser Sci. Eng.* 4. doi:10.1017/hpl.2016.25. <https://www.cambridge.org/core/article/div-class-title-generation-of-high-quality-electron-beams-by-ionization-injection-in-a-single-acceleration-stage-div/C77983BABA7C750654DCB69A3C83257C> (2016).
840. Desforges, F. G. et al. Dynamics of ionization-induced electron injection in the high density regime of laser wakefield acceleration. *Phys. Plasmas* 21, 120703. doi:10.1063/1.4903845. <http://scitation.aip.org/content/aip/journal/pop/21/12/10.1063/1.4903845> (2014).
841. Chen, M., Sheng, Z. M., Ma, Y. Y. & Zhang, J. Electron injection and trapping in a laser wakefield by field ionization to high-charge states of gases. *J. Appl. Phys.* 99, 1–4. doi:10.1063/1.2179194 (2006).
842. Fourmaux, S. et al. Quasi-monoenergetic electron beams production in a sharp density transition. *Appl. Phys. Lett.* 101, 111106. doi:10.1063/1.4752114. <http://dx.doi.org/10.1063/1.4752114> (Sept. 2012).
843. Burza, M. et al. Laser wakefield acceleration using wire produced double density ramps. *Phys. Rev. ST Accel. Beams* 16, 11301. doi:10.1103/PhysRevSTAB.16.011301. <http://link.aps.org/doi/10.1103/PhysRevSTAB.16.011301> (2013).
844. Marocchino, A. et al. Experimental characterization of the effects induced by passive plasma lens on high brightness electron bunches. *Appl. Phys. Lett.* 111, 184101. doi:10.1063/1.4999010. <http://aip.scitation.org/doi/10.1063/1.4999010> (Oct. 2017).
845. Pompili, R. et al. Focusing of High-Brightness Electron Beams with Active-Plasma Lenses. *Phys. Rev. Lett.* 121, 174801. doi:10.1103/PhysRevLett.121.174801. <https://link.aps.org/doi/10.1103/PhysRevLett.121.174801> (Oct. 2018).
846. Röckemann, J.-H. et al. Direct measurement of focusing fields in active plasma lenses. *Phys. Rev. Accel. Beams* 21, 122801. doi:10.1103/PhysRevAccelBeams.21.122801. <https://link.aps.org/doi/10.1103/PhysRevAccelBeams.21.122801> (Dec. 2018).
847. Van Tilborg, J. et al. Nonuniform discharge currents in active plasma lenses. *Phys. Rev. Accel. Beams* 20, 032803. doi:10.1103/PhysRevAccelBeams.20.032803. <https://link.aps.org/doi/10.1103/PhysRevAccelBeams.20.032803> (Mar. 2017).
848. Lindström, C. et al. Overview of the CLEAR plasma lens experiment. *Nucl. Instruments Methods Phys. Res. Sect. A Accel. Spectrometers, Detect. Assoc. Equip.* 909, 379–382. doi:10.1016/J.NIMA.2018.01.063. <https://www.sciencedirect.com/science/article/pii/S0168900218300809> (Nov. 2018).
849. Lindström, C. A. et al. Emittance Preservation in an Aberration-Free Active Plasma Lens. *Phys. Rev. Lett.* 121, 194801. doi:10.1103/PhysRevLett.121.194801. <https://link.aps.org/doi/10.1103/PhysRevLett.121.194801> (Nov. 2018).
850. D’Arcy, R. et al. FLASHForward: plasma wakefield accelerator science for high-averagepower applications. *Philos. Trans. R. Soc. A Math. Phys. Eng. Sci.* 377, 20180392. doi:10.1098/rsta.2018.0392. <https://royalsocietypublishing.org/doi/10.1098/rsta.2018.0392> (Aug. 2019).
851. Bane, K. & Stupakov, G. Corrugated pipe as a beam dechirper. *Nucl. Instruments Methods Phys. Res. Sect. A Accel. Spectrometers, Detect. Assoc. Equip.* 690, 106–110. doi:10.1016/J.NIMA.2012.07.001. <https://www.sciencedirect.com/science/article/pii/S0168900212007310> (Oct. 2012).

852. Antipov, S. et al. Experimental Demonstration of Energy-Chirp Compensation by a Tunable Dielectric-Based Structure. *Phys. Rev. Lett.* 112, 114801. doi:10.1103/PhysRevLett.112.114801. <https://link.aps.org/doi/10.1103/PhysRevLett.112.114801> (Mar. 2014).
853. Frank, K. et al. High-power pseudospark and BLT switches. *IEEE Trans. Plasma Sci.* 16, 317–323. doi:10.1109/27.3831. <http://ieeexplore.ieee.org/document/3831/> (Apr. 1988).
854. Sletten, A. & Lewis, T. Characteristics of the trigatron spark-gap. *Proc. IEE-Part C Monogr.* 104, 54–61 (1957).
855. England, R. J. et al. Dielectric laser accelerators. *Rev. Mod. Phys.* 86, 1337–1389. doi:10.1103/RevModPhys.86.1337. <http://link.aps.org/doi/10.1103/RevModPhys.86.1337> (Dec. 2014).
856. Leedle, K. J., Pease, R. F., Byer, R. L. & Harris, J. S. Laser acceleration and deflection of 96.3 keV electrons with a silicon dielectric structure. *Optica* 2, 158–161. doi:10.1364/optica.2.000158 (2015).
857. McNeur, J. et al. Elements of a dielectric laser accelerator. *Optica* 5, 687–690. doi:10.1364/OPTICA.5.000687. <http://www.osapublishing.org/optica/abstract.cfm?URI=optica-5-6-687> (June 2018).
858. England, R., Kwiatkowski, A., Ng, C.-K. & Wu, Z. Input Coupling for Photonic Bandgap Fiber Accelerators. *IEEE J. Sel. Top. QUANTUM Electron.* 22 (2016).
859. Mayet, F., Assmann, R., Dorda, U. & Kuropka, W. Simulation of phase-dependent transverse focusing in dielectric laser accelerator based lattices. *J. Phys. Conf. Ser.* 1067. doi:10.1088/1742-6596/1067/4/042002 (2018).
860. Nanni, E. A. et al. Linear electron acceleration in THz waveguides. *IPAC 2014 Proc. 5th Int. Part. Accel. Conf.* 1896–1899. doi:10.18429/JACoW-IPAC2014-WEOAB03 (2014).
861. Kärtner, F. et al. AXISIS: Exploring the frontiers in attosecond X-ray science, imaging and spectroscopy. *Nucl. Instruments Methods Phys. Res. Sect. A Accel. Spectrometers, Detect. Assoc. Equip.* 829 (2016).
862. Fallahi, A., Fakhari, M., Yahaghi, A., Arrieta, M. & Kärtner, F. X. Short electron bunch generation using single-cycle ultrafast electron guns. *Phys. Rev. Accel. Beams* 19, 81302. doi:10.1103/PhysRevAccelBeams.19.081302. <https://link.aps.org/doi/10.1103/PhysRevAccelBeams.19.081302> (Aug. 2016).
863. Vashchenko, G. et al. Performance analysis of the prototype THz-driven electron gun for the AXISIS project. *Nucl. Instruments Methods Phys. Res. Sect. A Accel. Spectrometers, Detect. Assoc. Equip.* (2018).
864. Vinatier, T., Assmann, R. W., Dorda, U., Lemery, F. & Marchetti, B. Simulations on a potential hybrid and compact attosecond X-ray source based on RF and THz technologies. *Nucl. Instruments Methods Phys. Res. Sect. A Accel. Spectrometers, Detect. Assoc. Equip.* 909, 185–192. doi:10.1016/j.nima.2018.03.025. <https://doi.org/10.1016/j.nima.2018.03.025> (2018).
865. Limpert, J. et al. High Repetition Rate Gigawatt Peak Power Fiber Laser Systems: Challenges, Design, and Experiment. *IEEE J. Sel. Top. Quantum Electron.* 15, 159–169. doi:10.1109/JSTQE.2008.2010244 (Jan. 2009).
866. Jauregui, C., Limpert, J. & Tunnermann, A. High-power fibre lasers. *Nat Phot.* 7, 861–867. <http://dx.doi.org/10.1038/nphoton.2013.273> (Nov. 2013).
867. Müller, M. et al. 1 kW 1 mJ eight-channel ultrafast fiber laser. *Opt. Lett.* 41, 3439–3442. doi:10.1364/OL.41.003439. <http://ol.osa.org/abstract.cfm?URI=ol-41-15-3439> (Aug. 2016).
868. Tünnermann, A., Schreiber, T. & Limpert, J. Fiber lasers and amplifiers: an ultrafast performance evolution. *Appl. Opt.* 49, F71–F78. doi:10.1364/AO.49.000F71. <http://ao.osa.org/abstract.cfm?URI=ao-49-25-F71> (2010).
869. Zervas, M. N. & Codemard, C. A. High Power Fiber Lasers: A Review. *IEEE J. Sel. Top. Quantum Electron.* 20, 219–241. doi:10.1109/JSTQE.2014.2321279 (Sept. 2014).
870. Mourou, G., Tajima, T., Quinn, M. N., Brocklesby, B. & Limpert, J. Are fiber-based lasers the future of accelerators? *Nucl. Instruments Methods Phys. Res. Sect.*

- A Accel. Spectrometers, Detect. Assoc. Equip. 740, 17–20. doi:<http://dx.doi.org/10.1016/j.nima.2013.10.041>. <http://www.sciencedirect.com/science/article/pii/S0168900213014228> (2014).
871. Mourou, G. A., Brocklesby, B., Tajima, T. & Limpert, J. The future is fibre accelerators. *Nat. Photon.* 7, 258–261. doi:[10.1038/nphoton.2013.75](https://doi.org/10.1038/nphoton.2013.75). <http://dx.doi.org/10.1038/nphoton.2013.75> (2013).
872. Benedetti, C., Schroeder, C. B., Esarey, E. & Leemans, W. P. Plasma wakefields driven by an incoherent combination of laser pulses: A path towards high-average power laser-plasma accelerators. *Phys. Plasmas* 21. doi:<http://dx.doi.org/10.1063/1.4878620>. <http://scitation.aip.org/content/aip/journal/pop/21/5/10.1063/1.4878620> (2014).
873. Augst, S. J., Fan, T. Y. & Sanchez, A. Coherent beam combining and phase noise measurements of ytterbium fiber amplifiers. *Opt. Lett.* 29, 474–476. doi:[10.1364/OL.29.000474](https://doi.org/10.1364/OL.29.000474). <http://ol.osa.org/abstract.cfm?URI=ol-29-5-474> (Mar. 2004).
874. Bellanger, C. et al. Collective phase measurement of an array of fiber lasers by quadriwave lateral shearing interferometry for coherent beam combining. *Opt. Lett.* 35, 3931–3933. doi:[10.1364/OL.35.003931](https://doi.org/10.1364/OL.35.003931). <http://ol.osa.org/abstract.cfm?URI=ol-35-23-3931> (Dec. 2010).
875. Daniault, L. et al. XCAN - A coherent amplification network of femtosecond fiber chirped-pulse amplifiers. *Eur. Phys. J. Spec. Top.* 224, 2609–2613. doi:[10.1140/epjst/e2015-02571-y](https://doi.org/10.1140/epjst/e2015-02571-y). <http://dx.doi.org/10.1140/epjst/e2015-02571-y> (2015).
876. Mourou, G. A., Hulin, D. & Galvanauskas, A. The Road to High Peak Power and High Average Power Lasers: Coherent-Amplification-Network (CAN). *AIP Conf. Proc.* 827, 152–163. doi:<http://dx.doi.org/10.1063/1.2195207>. <http://scitation.aip.org/content/aip/proceeding/aipcp/10.1063/1.2195207> (2006).
877. Klenke, A. et al. Coherently combined 16-channel multicore fiber laser system. *Opt. Lett.* 43, 1519–1522. doi:[10.1364/OL.43.001519](https://doi.org/10.1364/OL.43.001519). <http://ol.osa.org/abstract.cfm?URI=ol-43-7-1519> (Apr. 2018).
878. Klenke, A. et al. Coherent Beam Combination of Ultrafast Fiber Lasers. *IEEE J. Sel. Top. Quantum Electron.* 24, 1–9. doi:[10.1109/JSTQE.2018.2808540](https://doi.org/10.1109/JSTQE.2018.2808540) (2018).
879. Ghaith, A. et al. Tunable High Spatio-Spectral Purity Undulator Radiation from a Transported Laser Plasma Accelerated Electron Beam. *Sci. Rep.* 9, 19020. doi:[10.1038/s41598-019-55209-4](https://doi.org/10.1038/s41598-019-55209-4) (2019).
880. Ghaith, A. et al. Electron Beam Brightness and Undulator Radiation Brilliance for a Laser Plasma Acceleration Based Free Electron Laser. *Instruments* 4, 1. doi:[10.3390/instruments4010001](https://doi.org/10.3390/instruments4010001) (2020).
881. Oumbarek Espinos, D. et al. COXINEL transport of laser plasma accelerated electrons. *Plasma Phys. Control. Fusion* 62, 034001 (2020).
882. Roussel, E. et al. Energy spread tuning of a laser-plasma accelerated electron beam in a magnetic chicane. *Plasma Phys. Control. Fusion* 62, 074003 (2020).
883. Filippi, F. et al. 3D-printed capillary for hydrogen filled discharge for plasma based experiments in RF-based electron linac accelerator. *Rev. Sci. Instrum.* 89, 83502. doi:[10.1063/1.5010264](https://doi.org/10.1063/1.5010264). <https://doi.org/10.1063/1.5010264>

### List of EuPRAXIA Partner and Associated Partner Institutes

The EuPRAXIA Consortium consists of the following 16 partner institutes and 25 associated partner organisations. Partners are those institutes that joined the project from its beginning and received funding through the European Union's Horizon 2020 programme, while associated partners have joined the design study entirely with in-kind contributions.

#### EuPRAXIA Partners

- CEA:** Commissariat à l'Énergie Atomique et aux Énergies Alternatives, 91191 Gif sur Yvette, France
- CNR:** Consiglio Nazionale delle Ricerche - Istituto Nazionale di Ottica, Via Moruzzi, 1, 56124 Pisa, Italy
- CNRS:** Centre National de la Recherche Scientifique: LPGP – LOA – LULI – LLR, Orsay & Palaiseau, France
- DESY:** Deutsches Elektronensynchrotron, Notkestr. 85, 22607 Hamburg, Germany
- ENEA:** Agenzia Nazionale per le Nuove Tecnologie, l'Energia e lo Sviluppo Economico Sostenibile – Centro Ricerche Frascati, Via Enrico Fermi, 45, 00044 Frascati (Roma), Italy
- ICL:** Imperial College London, South Kensington Campus, London SW7 2AZ, United Kingdom
- INFN:** Istituto Nazionale di Fisica Nucleare - Laboratori Nazionali di Frascati, Via Enrico Fermi, 40, 00044 Frascati RM, Italy
- IST:** Instituto Superior Técnico, Av. Rovisco Pais 1, 1049-001 Lisboa, Portugal
- SOLEIL:** Synchrotron SOLEIL, L'Orme des Merisiers, 91190 Saint-Aubin, France
- STFC:** Science and Technology Facilities Council: Central Laser Facility - ASTeC, Didcot & Warrington, United Kingdom
- UHH:** Universität Hamburg, Mittelweg 177, 20148 Hamburg, Germany
- ULIV:** University of Liverpool, Brownlow Hill, Liverpool, L69 7ZX, United Kingdom
- UMAN:** University of Manchester, Oxford Rd, Manchester M13 9PL, United Kingdom
- UOXF:** University of Oxford, Oxford OX1 2JD, United Kingdom
- URLS:** Sapienza Università di Roma, Piazzale Aldo Moro, 5, 00185 Roma, RM, Italy
- USTRATH:** University of Strathclyde, 16 Richmond St, Glasgow G1 1XQ, United Kingdom

**EuPRAXIA Associate Partners**

- CASE:** Centre for Accelerator Science and Education at Stony Brook University and Brookhaven National Laboratory, Stonybrook & Upton, United States of America
- CERN:** European Organisation for Nuclear Research, Espl. des Particules 1, 1211 Meyrin, Switzerland
- ELI:** Extreme Light Infrastructure – Beamlines, Za Radnicí 835, Dolní Břežany, 252 41 Czech Republic
- FBH:** Ferdinand-Braun-Institut, Leibniz-Institut für Höchstfrequenztechnik, Gustav-Kirchhoff-Str. 4, 12489 Berlin, Germany
- FZJ:** Forschungszentrum Jülich, Wilhelm-Johnen-Straße, 52428 Jülich, Germany
- HIJ:** Helmholtz-Institut Jena, Fröbelstieg 3, 07743 Jena, Germany
- HUJI:** Hebrew University of Jerusalem, Jerusalem, Israel
- HZDR:** Helmholtz-Zentrum Dresden-Rossendorf e.V., Bautzner Landstr. 400, 01328 Dresden, Germany
- IAP-RAS:** Institute of Applied Physics of the Russian Academy of Sciences, 603950 Nizhnij Novgorod, Russia
- JIHT:** Joint Institute for High Temperatures of the Russian Academy of Sciences, 125412, Izhorskaya st. 13 Bd.2, Moscow, Russia
- KIT:** Karlsruher Institut für Technologie, Karlsruhe, Germany
- KPSI:** National Institutes for Quantum and Radiological Science and Technology – Kansai Photon Science Institute, Kyoto & Hyogo, Japan
- LBNL:** Lawrence Berkeley National Laboratory, 1 Cyclotron Rd, Berkeley, CA 94720, United States of America
- LMU:** Ludwig-Maximilians-Universität München, Geschwister-Scholl-Platz 1, 80539 Munich, Germany
- LU:** Lund University, 221 00 Lund, Sweden
- OU:** Osaka University, 1-1 Yamadaoka, Suita, Osaka 565-0871 Japan
- PHLAM:** Laboratoire de Physique des Lasers Atomes et Molécules, Université de Lille 1, 2 Avenue Jean Perrin, 59650 Villeneuve-d’Ascq, France
- QUB:** Queen’s University Belfast, University Rd, Belfast BT7 1NN, United Kingdom
- RSC:** RIKEN SPring-8 Center, 1-1-1 Kouto, Sayo-cho Sayo-gun, Hyogo 679–5148 Japan
- SJTU:** Shanghai Jiao Tong University, 800 Dongchuan RD. Minhang District, Shanghai, China
- TUB:** Tsinghua University Beijing, 30 Shuangqing Rd, Haidian Qu, Beijing Shi, China
- UCLA:** University of California Los Angeles, Los Angeles, CA 90095, United States of America
- URTV:** Università degli Studi di Roma “Tor Vergata”, Via Cracovia, 50, 00133 Roma RM, Italy
- WIGNER:** Wigner Research Centre of the Hungarian Academy of Science, Konkoly-Thege Miklós út 29-33, 1121 Budapest, Hungary
- YORK:** University of York, Heslington, York YO10 5DD, United Kingdom

## Commonly Used Acronyms

- ALS Alignment System
- APL Active Plasma Lens
- ASTRA a 3D particle-tracking code [K. Floettmann, March 2017. [http://www.desy.de/~mpyflo/Astra\\_manual/Astra-Manual\\_V3.2.pdf](http://www.desy.de/~mpyflo/Astra_manual/Astra-Manual_V3.2.pdf)]
- BPA Beam-Driven Plasma Accelerator / Acceleration (typically referring to an entire machine or concept instead of a single stage)
- BPM Beam Position Monitor
- CA Clear Aperture
- CB Collaboration Board
- CDW Capillary Discharge Waveguide
- CPA Chirped Pulse Amplification
- DKDP Deuterated Potassium Dihydrogen Phosphate
- DLS Diagnostics Laser System
- elegant* a 3D particle-tracking code [Borland, M. United States, 2000. doi:10.2172/761286]
- EuXFEL European X-ray Free-Electron Laser, located in Hamburg, Germany
- FBPIC a 3D particle-in-cell code [R. Lehe et al. Computer Physics Communications 203 (2016) 66-82, doi: 10.1016/J.CPC.2016.02.007]
- FCC Facility Control-Command
- FEL free-electron laser
- FEP Front End Processor fs femtosecond, 1 fs=1×10<sup>-15</sup> s
- FWHM full width at half maximum
- GRIN Gradient Refractive Index
- HEP High-energy physics
- HETL High-Energy Transfer Line
- ICS inverse Compton scattering
- ICT Integrated Current Transformer
- LCC Laser Control-Command
- LETL Low-Energy Transfer Line
- LPA Laser-Driven Plasma Accelerator / Acceleration (typically referring to an entire machine or concept instead of a single stage)
- LPAS Laser-Driven Plasma Acceleration Stage
- LPI Laser-Plasma Injector
- LPS Longitudinal Phase-Space, typically energy vs. time
- LWFA laser-driven wakefield acceleration
- OFI Optical Field Ionisation
- PES Peaked Energy Spectrum
- PIC Particle-In-Cell, a type of simulation code relevant for plasma accelerator studies
- PPAS Particle-driven Plasma Acceleration Stage
- PSO Particle Swarm Optimisation
- PSS Personal Safety System
- PW Petawatt (1PW=1×10<sup>15</sup> W)
- PWFA beam-driven wakefield acceleration
- R&D research and development
- RF Radiofrequency
- RFI Radiofrequency Injector
- RI research infrastructure
- RMS root mean square (also as rms)
- S2E Start-to-End (in the context of simulations)

SC Steering Committee  
SSS Synchronisation and Sequencing System  
TAS Target Areas Systems  
TDS Transverse Deflecting Structure  
*TraceWin* a 3D particle-tracking code [D. Uriot, N. Pichoff. Proc. 6th Int. Part.  
Acc. Conf. 2015, MOPWA008]  
TW Terawatt (1 TW= $1 \times 10^{12}$  W)  
VFS Vacuum and Fluids Systems  
WP Working Package

## List of Figures

1.1	Partners and associated partners of the EuPRAXIA Consortium. . .	3701
1.2	Project management structure of the EuPRAXIA design study. . . .	3701
1.3	Participants in the EuroNNAc and EuPRAXIA Workshop on a European Plasma Accelerator in Pisa, June 2016. . . . .	3703
1.4	Comparison of size and achievable electron beam energy for different existing radiofrequency and plasma accelerators. . . . .	3703
1.5	Basic principle of a plasma accelerator. . . . .	3703
1.6	Small, novel plasma accelerator compared to the FLASH accelerator at DESY. . . . .	3703
1.7	Livingston curve for accelerators, showing the maximum reach in beam energy versus time. . . . .	3706
1.8	Schematic of the COXINEL experiment . . . . .	3708
1.9	Tomographic imaging of a mouse embryo carried out at the Gemini laser at the STFC Rutherford Appleton Laboratory. . . . .	3709
1.10	Schematic of an open innovation model for EuPRAXIA. . . . .	3711
2.1	Length comparison of a typical RF-based accelerator facility with the EuPRAXIA 5 GeV design. . . . .	3716
2.2	Size, frequency, and field strength comparison of different types of RF cavities. . . . .	3717
2.3	Comparison of different lasers and applications in terms of stored energy in a single laser pulse and repetition rate of the laser. . . . .	3717
2.4	Comparison of user concepts in light sources and the EuPRAXIA laser-driven plasma accelerator concept. . . . .	3718
2.5	Summary of the electron beam energy and relative energy spread for the different EuPRAXIA schemes. . . . .	3718
2.6	Scientific fields for which the EuPRAXIA research infrastructure would be interesting based on an initial survey of potential future EuPRAXIA users. . . . .	3720
2.7	Word cloud describing scientific fields and topics of interest relevant to potential future users of the EuPRAXIA research infrastructure. . . .	3720
2.8	Types of activities for which the EuPRAXIA research infrastructure would be interesting based on an initial survey of potential future EuPRAXIA users. . . . .	3720
2.9	3D visualisation of a plasma wave excited by a high-intensity laser pulse and accelerating an electron beam generated with the VisualPIC code. . . . .	3723
2.10	HAPLS laser at Lawrence Livermore National Laboratory. . . . .	3724
2.11	Diffraction image of a complex biomolecule under high-intensity X-ray light. . . . .	3725
2.12	CMS detector at the Large Hadron Collider. . . . .	3727
2.13	Phase-contrast X-ray image of a spider. . . . .	3730
2.14	Accelerators used for inspection and material testing. . . . .	3731
2.15	Physical principle and context of positron annihilation spectroscopy as a material inspection technique. . . . .	3732
2.16	Variety of possible topics and application fields at the EuPRAXIA Research Infrastructure. . . . .	3735
3.1	EuPRAXIA facility concept. . . . .	3740
3.2	Overview of EuPRAXIA technical clusters. . . . .	3741
3.3	Overview of EuPRAXIA construction and excellence sites. . . . .	3752
3.4	Schematic facility layout for the flagship construction site based on beam-driven plasma acceleration. . . . .	3753

3.5	Size comparison of the EuPRAXIA infrastructure in relation to a hospital in Copenhagen. . . . .	3753
3.6	Comparison of the expected EuPRAXIA machine length with other facilities of equivalent beam energies. . . . .	3753
3.7	Schematic facility layout for the flagship construction site based on laser-driven plasma acceleration. . . . .	3756
3.8	Summary of some key strategies to make data management within the EuPRAXIA collaboration more consistent with the FAIR principles. . . . .	3759
3.9	Overview of EuPRAXIA construction and excellence sites. . . . .	3759
3.10	Layout of the EuPRAXIA@SPARC_LAB infrastructure. . . . .	3762
3.11	Overview of the different partners and activities involved in the LAPLACE and PALAS projects. . . . .	3763
3.12	ELI Beamlines facility in Dolni Brezany. . . . .	3769
3.13	Visualisation and areal view of the EPAC facility under development. . . . .	3773
3.14	The L3 “HAPLS” laser system at the ELI Beamlines laser hall. . . . .	3775
3.15	Possible allocation of the “laser-driven” FEL elements in the ELI Beamlines experimental areas E5 and E6. . . . .	3775
3.16	Map and aerial view of the CNR campus in Pisa. . . . .	3777
3.17	Layout of the Intense Laser Irradiation Laboratory at CNR-INO. . . . .	3777
3.18	Interaction target chamber and control room at the Intense Laser Irradiation Laboratory. . . . .	3777
3.19	Map of the CNR campus showing the INO laboratories. . . . .	3777
3.20	The five main pillars of the EuPRAXIA long-term science programme. . . . .	3780
4.1	Temporal profile of the foreseen investment costs. . . . .	3782
4.2	Temporal profile of the foreseen person-power. . . . .	3783
4.3	Preliminary study of resource distribution in Europe. . . . .	3784
4.4	Breakdown of PWFA investment cost into technical categories. . . . .	3786
4.5	Breakdown of LWFA investment cost into technical categories. . . . .	3786
5.1	Main technical milestones to achieve during the EuPRAXIA technical design phase. . . . .	3789
5.2	Preliminary project timeline. . . . .	3791
5.3	Implementation and re-evaluation process for the EuPRAXIA project structure. . . . .	3792
5.4	Planned management structure for the EuPRAXIA Consortium. . . . .	3792
5.5	Main user categories expected at EuPRAXIA. . . . .	3794
5.6	Summary of the proposed access modes for users at EuPRAXIA. . . . .	3795
5.7	List of the main technical risks associated with each major sub-system of EuPRAXIA. . . . .	3801
6.1	Map of large-scale user facilities providing access to similar types of particle and radiation sources as EuPRAXIA will offer. . . . .	3804
6.2	Map of areas of impact expected through EuPRAXIA. . . . .	3807
6.3	Positioning of EuPRAXIA in the technological accelerator landscape of the next decades. . . . .	3811
7.1	Wakefield generation and electron beam acceleration in a plasma accelerator. . . . .	3813
7.2	Examples of different types of plasma sources used in plasma injectors and accelerators. . . . .	3819
7.3	Operating principle of chirped pulse amplification (CPA) and optical parametric chirped pulse amplification (OPCPA). . . . .	3820
7.4	Operating principle of a free-electron laser (FEL). . . . .	3823
8.1	Overview layout of the EuPRAXIA site for beam-driven plasma acceleration. . . . .	3826

8.2	Overview layout of the EuPRAXIA site for laser-driven plasma acceleration. . . . .	3826
8.3	Beam distribution and acceleration configurations under consideration for the various EuPRAXIA beamlines. . . . .	3830
10.1	Block diagram of the three laser driver chains. . . . .	3839
10.2	Amplifier head geometries. . . . .	3843
10.3	Schematic structure of the twin amplifying crystals in the transmission geometry, along with the cooling flow arrangement. . . . .	3844
10.4	Top view of the general layout of the amplifier crystals for the transmission geometry for a six-pass arrangement. . . . .	3845
10.5	Beam paths for the injection in the Ti:Sapphire crystals. . . . .	3845
10.6	AMP3 multipass layout. . . . .	3846
10.7	Overview of the synchronisation scheme for the implementation of the EDP strategy. . . . .	3847
10.8	Simulation of the fluid velocity distribution in the cooling channel. . . . .	3849
10.9	Temperature profile along the crystal surface and effective film coefficient for different flow speeds. . . . .	3849
10.10	Ridge fluid simulations. . . . .	3849
10.11	Wall-plug efficiency comparison between different laser architectures. . . . .	3855
10.12	Extraction efficiency . . . . .	3855
11.1	Hardware architecture for the control-command system. . . . .	3860
11.2	Schematic of the beamline divided into different zones. . . . .	3867
11.3	Scheme of timing and synchronisation. . . . .	3869
12.1	Gun fields. . . . .	3871
12.2	SPARC Gun Solenoid. . . . .	3873
12.3	Solenoid coils embedding the first accelerating S-band structure. . . . .	3875
12.4	Layout of the EuPRAXIA S-band RF power station. . . . .	3877
12.5	Pulse compression with a SLED-type system. . . . .	3880
12.6	Effective shunt impedance as a function of the section attenuation and resulting accelerating field profile. . . . .	3880
12.7	Basic EuPRAXIA X-band accelerating cell. . . . .	3881
12.8	Characteristics of the TW accelerating section as a function of iris radius. . . . .	3882
12.9	Schematics of an 8-section X-band RF module. . . . .	3883
13.1	Plasma density profile for the LPI using a density downramp. . . . .	3887
13.2	Beam properties for the density downramp LPI. . . . .	3888
13.3	Schematic view of the target cell used in the simulation. . . . .	3889
13.4	Longitudinal density profile for different lengths of the exit tube. . . . .	3889
13.5	Laser evolution inside the ionisation injection plasma target. . . . .	3890
13.6	Energy distribution of the electrons at the exit of the ionisation injection plasma target. . . . .	3890
13.7	Schematic of the laser removal and coupling in a multi-stage configuration. . . . .	3894
14.1	Layout of the SPARC-like RF photo-injector. . . . .	3899
14.2	Charge distribution at the cathode surface produced by the photo-cathode laser pulse. . . . .	3900
14.3	Evolution of the witness beam parameters along the injector in the case of pure RF compression. . . . .	3900
14.4	Beam distribution at the photo-injector exit. . . . .	3902
14.5	Longitudinal phase space of the LWFA-accelerated electron beam at the L2 linac exit. . . . .	3902
14.6	Start-to-end simulation results for the witness bunch from the photo-cathode to the undulator entrance. . . . .	3902

14.7	Start-to-end simulation results for the witness bunch from the photo-cathode to the undulator entrance. . . . .	3902
14.8	Injection layout for the hybrid compression scheme. . . . .	3904
14.9	Transverse beam size and normalised emittance evolutions from the photo-cathode to the linac exit. . . . .	3905
14.10	Beam optics from the linac exit to the injection point. . . . .	3905
14.11	Transverse and longitudinal phase spaces of the beam at the linac exit and the injection point. . . . .	3906
14.12	Longitudinal phase space of the PWFA-accelerated electron beam at the L2 linac exit. . . . .	3907
14.13	Transverse and longitudinal distributions of the photo-cathode laser at the cathode surface. . . . .	3907
14.14	Transverse distribution of the comb beam used for PWFA . . . . .	3908
14.15	Driver and witness beam energy and current profiles after velocity bunching. . . . .	3908
14.16	Horizontal and vertical phase-space distribution of the PWFA driver and witness beams at the L1 linac entrance. . . . .	3910
14.17	Transverse RMS size of the electron beam (driver plus witness) along the linac. . . . .	3910
14.18	Horizontal and vertical phase-space distribution of the PWFA driver and witness beams at the capillary entrance. . . . .	3910
14.19	Transverse horizontal and vertical distribution of the PWFA driver and witness beams at the capillary entrance. . . . .	3910
14.20	Start-to-end simulation results for the driver bunch from the photo-cathode to the undulator entrance showing emittance and spot size. . . . .	3910
14.21	Start-to-end simulation results for the witness beam from the photo-cathode to the undulator entrance showing emittance and spot size. . . . .	3910
14.22	Start-to-end simulation results for the driver bunch from the photo-cathode to the undulator entrance showing energy, energy spread and bunch length. . . . .	3910
14.23	Start-to-end simulation results for the witness beam from the photo-cathode to the undulator entrance showing energy, energy spread and bunch length. . . . .	3910
15.1	Schematic view of the synchronising stage. . . . .	3914
15.2	On-axis longitudinal electric field after 1.2 mm of propagation in the plasma, with the electron beam placed at the zero crossing. . . . .	3916
15.3	Beta function and emittance evolution for beams with different offsets. . . . .	3917
15.4	Jitter correction thanks to plasma stage and chicane. . . . .	3918
16.1	Schematic of the proposed developments at the two EuPRAXIA construction sites, with the plasma accelerator stages circled. . . . .	3919
16.2	Example and simulation of different capillary tubes. . . . .	3922
16.3	Schematic of the laser removal and coupling in a multi-stage configuration. . . . .	3924
17.1	Electron bunch and background density after 5 mm of propagation in the plasma. . . . .	3929
17.2	Phase-space and slice analysis of the driver and witness at the plasma exit. . . . .	3930
17.3	Electron bunch and background density after 15 mm of plasma. . . . .	3930
17.4	Evolution of the witness parameters and phase space in the 5 GeV case. . . . .	3932
17.5	Rolling slice analysis for the witness bunch at the plasma input and exit for the 5 GeV case. . . . .	3934
18.1	RADIA model and magnetic field of a cryogenic undulator with a 12 mm period. . . . .	3944

18.2	Deflection parameter versus gap for different period undulators using RADIA. . . . .	3945
18.3	Typical magnet design for an SCU viewed from the side. . . . .	3946
18.4	Transverse gradient undulator scheme. . . . .	3949
19.1	Layout of the low-energy beam transfer line. . . . .	3951
19.2	Beam parameters along a low-energy transfer line of six quadrupoles. . . . .	3951
19.3	Beam slice parameters along a low-energy transfer line of six quadrupoles. . . . .	3952
19.4	Beam parameters along a low-energy transfer line of eight quadrupoles. . . . .	3954
19.5	Beam slice parameters along a low-energy transfer line of eight quadrupoles. . . . .	3954
19.6	Magnetic field profile in a 1 mm diameter active plasma lens. . . . .	3956
19.7	Beam parameters along a low-energy transfer line of two active plasma lenses. . . . .	3956
19.8	Beam slice parameters along a low-energy transfer line of two active plasma lenses. . . . .	3956
19.9	Layout of the high-energy beam transfer line. . . . .	3959
19.10	Beam parameters along the high-energy transfer line for Scheme 1. . . . .	3961
19.11	Beam slice parameters along the high-energy transfer line for Scheme 1. . . . .	3962
19.12	Beam parameters along the high-energy transfer line for Scheme 2. . . . .	3963
19.13	Beam slice parameters along the high-energy transfer line for Scheme 2. . . . .	3963
19.14	Beam parameters along the high-energy transfer line for Scheme 3. . . . .	3963
19.15	Beam slice parameters along the high-energy transfer line for Scheme 3. . . . .	3963
19.16	Illustrative representation of the accelerator beamline of Scheme 4. . . . .	3963
19.17	Beam parameters along the high-energy transfer line between the two LPAS for Scheme 4. . . . .	3967
19.18	Current profile of the beam before and after the chicane in Scheme 4. . . . .	3967
19.19	Beam parameters along the high-energy transfer line after the second LPAS for Scheme 4. . . . .	3967
19.20	Beam slice parameters along the high-energy transfer line after the second LPAS for Scheme 4. . . . .	3967
19.21	Beam parameters along the high-energy transfer line for Scheme 5. . . . .	3967
19.22	Beam slice parameters along the high-energy transfer line for Scheme 5. . . . .	3967
20.1	Interferometric measurement capability for neutral molecular hydrogen. . . . .	3976
20.2	Interferometric measurement capability for free electrons. . . . .	3976
21.1	Temporary beamline for the electron diagnostics after the LPI. . . . .	3988
21.2	Layout of the permanent beamline for electron diagnostics between the LPI and LPAS. . . . .	3989
21.3	Layout of the diagnostics in the electron gun section of SINBAD-ARES. . . . .	3990
21.4	Layout of the diagnostics in the linac section of ARES. . . . .	3990
21.5	Layout of the diagnostics in the beam-matching section of SINBAD-ARES. . . . .	3990
21.6	Layout of the diagnostics for the RF injector at EuPRAXIA@SPARC_LAB. . . . .	3990
21.7	Layout of the diagnostics for a section of the linac at EuPRAXIA@SPARC_LAB. . . . .	3991
21.8	Layout of the matching optics and diagnostics setup behind the plasma booster. . . . .	3992
22.1	SwissFEL Aramis beam stopper. . . . .	3996
22.2	Beam longitudinal phase space after 8.5 cm in plasma. . . . .	3999
22.3	Density profile used to eliminate the re-acceleration of particles in the bunch tail. . . . .	3999
22.4	Beam longitudinal phase space after 21 cm in plasma. . . . .	3999
22.5	Energy plots as a function of propagation distance in plasma. . . . .	3999

23.1	The accelerator schemes under investigation. . . . .	4002
23.2	Beam parameters obtained at the LPI exit. . . . .	4006
23.3	Beam parameters obtained at the LPAS exit. . . . .	4006
23.4	Scheme 1 using a single-stage injector / accelerator generating an FEL-quality 5 GeV beam. . . . .	4012
23.5	Visualisation of the ReMPI scheme . . . . .	4012
23.6	Driver train evolution. . . . .	4014
23.7	On-axis snapshot at the early stage of bunch trapping. . . . .	4015
23.8	Phase space of the bunch at the end of the 25 cm long capillary. . . .	4016
23.9	Phase-space cuts of the final beam. . . . .	4017
23.10	Longitudinal phase-space plot and current profile of the final beam. . .	4017
23.11	Slice analysis with a slice thickness of 0.1 $\mu\text{m}$ . . . . .	4017
23.12	Evolution of the beam parameters from Scheme 1 along the HETL. . .	4017
23.13	Sensitivity of the accelerating field on the resonance condition mismatch.	4020
23.14	Scheme 2 combining a 150 MeV laser-plasma injector with an LPAS to 5 GeV. . . . .	4021
23.15	The longitudinal normalised electric field, resonantly excited by a train of laser pulses. . . . .	4021
23.16	The longitudinal phase-space density of the bunch close to the end of the injection process and at the end of the acceleration phase. . . . .	4021
23.17	Electron beam phase space (position vs. normalised momentum $p/mc$ ) at the end of the acceleration phase. . . . .	4022
23.18	Twiss parameters and chromatic length along the plasma downramp and the passive plasma lens. . . . .	4023
23.19	Evolution of the beam size and emittance along the LETL. . . . .	4025
23.20	Transverse and longitudinal phase spaces at the plasma exit of Scheme 2.	4025
23.21	Beam emittance and RMS size evolution along the upramp of the LPAS.	4026
23.22	Evolution of the Twiss parameter $\gamma$ and the normalised phase-space emittance $\varepsilon_{ph,n}$ along the downramp and the downstream drift. . . . .	4027
23.23	Evolution of the beam parameters from Scheme 2 along the HETL. . .	4028
23.24	Scheme 3 combining a 500 MeV RF injector with an LPAS to 5 GeV. . .	4028
23.25	Evolution of the beam parameters along the RF injector. . . . .	4030
23.26	Beam properties at the capillary entrance. . . . .	4031
23.27	Transverse and longitudinal phase spaces at the accelerator exit in Scheme 3. . . . .	4032
23.28	Evolution of beam parameters during plasma acceleration. . . . .	4032
23.29	Slice characteristics along the beam. . . . .	4032
23.30	Evolution of the beam parameters from Scheme 3 along the HETL. . .	4033
23.31	Overview of the proposed acceleration scheme and the evolution of the longitudinal phase space of the beam along the two-stage dechirping concept. . . . .	4035
23.32	Overview of the two-stage accelerator beamline for EuPRAXIA. . . . .	4036
23.33	On-axis density profile of the two plasma stages. . . . .	4036
23.34	Transverse and longitudinal phase space of the electron beam as delivered by the RF linac at the entrance of the first plasma. . . . .	4037
23.35	Evolution of the longitudinal phase space of the externally injected electron beam along the beamline. . . . .	4037
23.36	Comparison of the current profiles of the original and smoothed beams.	4038
23.37	Evolution of the parameters of the core part of the beam along both plasma stages. . . . .	4038
23.38	Transverse and longitudinal phase space of the improved (smoothed) beam after the second plasma stage. . . . .	4039

23.39	Transverse and longitudinal phase space of the improved (smoothed) beam at the undulator entrance. . . . .	4039
23.40	Scheme 5 combining a 500 MeV RF injector with a PPAS to 1 GeV. . .	4040
23.41	Horizontal and vertical phase-space distribution of the PWFA driver and witness beams at the capillary entrance. . . . .	4041
23.42	Transverse horizontal and vertical distribution of the PWFA driver and witness beams at the capillary entrance. . . . .	4041
23.43	Driver and witness density contour plots with the position of the accelerating electric field overlaid. . . . .	4043
23.44	Transverse and longitudinal phase spaces at the plasma exit of Scheme 5. . . . .	4044
23.45	Evolution of the beam parameters from Scheme 5 along the HETL. . .	4046
24.1	Magnetic unit cell of a system made up of an undulator as well as focussing and defocussing quadrupoles for the $\lambda_u = 3$ cm configuration. . . . .	4050
24.2	Energy, current, energy spread, and normalised emittance slice profiles for Schemes 3-5 GeV and 2-5 GeV. . . . .	4051
24.3	Energy, current, energy spread, and normalised emittance slice profiles for Schemes 3-1 GeV and 5-1 GeV . . . . .	4051
24.4	Growth of the SASE FEL energy per pulse of Scheme 2-5 GeV and Scheme 3-5 GeV for the short-undulator-period configuration. . . . .	4051
24.5	Growth of the SASE FEL energy per pulse of Scheme 5-1 GeV and Scheme 3-1 GeV for the short-undulator-period configuration. . . . .	4051
24.6	Growth of the SASE FEL energy per pulse of Scheme 2-5 GeV and Scheme 3-5 GeV for the long-undulator-period configuration. . . . .	4054
24.7	Growth of the SASE FEL energy per pulse of Scheme 5-1 GeV and Scheme 3-1 GeV for the long-undulator-period configuration. . . . .	4055
24.8	Cartoon of the trajectory of an electron with maximum Lorentz factor $\gamma_{z0}$ being accelerated in a non-linear wakefield leading to betatron emission . . . . .	4057
24.9	Conceptual visualisation of a betatron beamline at the proposed EuPRAXIA laser-driven construction site. . . . .	4060
24.10	Cartoon of the collision of an electron with Lorentz factor $\gamma$ with a laser resulting in MeV radiation emission. . . . .	4064
25.1	Schematic layout for the electron test beamline. . . . .	4067
25.2	Simulated evolution of the transverse size of the positron beam through the low-energy beamline. . . . .	4067
25.3	Conceptual visualisation of the positron and test electron beamline at the proposed EuPRAXIA laser-driven construction site. . . . .	4069
25.4	Conceptual design of the low-energy positron beamline to be installed at the laser-driven plasma acceleration construction site. . . . .	4070
25.5	Conceptual design of the high-energy positron beamline designed for the PWFA construction site. . . . .	4072
25.6	Simulated evolution of the transverse size of the beam through the high-energy beamline. . . . .	4072
26.1	Three-dimensional electron density maps, extracted from particle-in-cell simulations for LWFA and PWFA. . . . .	4074
26.2	Schematic of the double-jet plasma target for the LPWFA proof-of-concept experiment at HZDR. . . . .	4077
26.3	The 6D brightness reach of the three related “plasma-cathode” schemes described here exceeds the state of the art by many orders of magnitude. . . . .	4079
26.4	3D PIC-simulations reproducing the plasma-torch downramp injection experiment during the E-210: Trojan Horse programme at SLAC FACET. . . . .	4080
26.5	Schematic of a hybrid LWFA→PWFA staged setup with wakefield-induced ionisation injection. . . . .	4081

26.6	3D OSIRIS simulation for a PWFA stage with wakefield-induced ionisation injection. . . . .	4082
26.7	The plasma photo-cathode mechanism in collinear geometry in the co-moving frame and laboratory frame. . . . .	4084
26.8	Plasma photo-cathode beam brightness transformer based on the Trojan Horse mechanism as a transformative source for applications. . . . .	4085
26.9	Bubble structures and injected electron bunches in a density-profile-tailored plasma. . . . .	4087
26.10	Phase space of injected electrons and the accelerating field $E_z$ for the external field $B_y^{ext} = 0, 20, 50$ T. . . . .	4087
26.11	Sketch of the radiation source from a helical plasma undulator based on LWFA in a plasma channel and the resulting far-field X-ray radiation distribution. . . . .	4090
26.12	Results of 2D simulations of the X-ray generation from LWFA using flying mirrors. . . . .	4092
27.1	Risk estimation and risk reduction. . . . .	4094
29.1	Map of European EuPRAXIA consortium facilities. . . . .	4108
29.2	View of the laser facilities at APOLLON. . . . .	4109
29.3	Layout of the CLARA facility. . . . .	4109
29.4	Schematic view of the COXINEL beamline. . . . .	4110
29.5	Footprint of the ELBE Centre for High Power Radiation Sources at the Helmholtz Zentrum Dresden-Rossendorf. . . . .	4111
29.6	The L1 “Allegra” laser developed in-house by the ELI Beamlines laser team (100 mJ, 1 kHz). . . . .	4111
29.7	The L2 “Amos” laser system is under development now at ELI-Beamlines (20 J, 10 Hz). . . . .	4111
29.8	The L3 “HAPLS” laser system at ELI-Beamlines (30 J, 10 Hz). . . . .	4112
29.9	The L4 “Aton” laser system is under development now at ELI-Beamlines (2 kJ, 1 shot/min). . . . .	4112
29.10	Control room of the POLARIS laser at the Helmholtz Institute Jena. . . . .	4114
29.11	ILIL experimental area. . . . .	4116
29.12	The Zhi lab set up at the John Adams Institute at Imperial College. . . . .	4116
29.13	Layout of the FLUTE facility and support rooms. . . . .	4116
29.14	Layout of FLUTE accelerator to be placed on 21 m diagonal of the bunker ground level. . . . .	4116
29.15	Laser systems at CALA. . . . .	4118
29.16	3D visualisation of the SINBAD facility. . . . .	4123
29.17	Layout of the SPARC LAB facility. . . . .	4125
29.18	SPARC PWFA test station. . . . .	4126
29.19	The new laser laboratory at the University of Oxford under construction. . . . .	4126
29.20	The building of the Wigner Datacenter (image courtesy of Wigner Research Centre for Physics). . . . .	4127
30.1	Map of international EuPRAXIA consortium facilities. . . . .	4128
30.2	Layout of the platform for LWFA of electrons at the RIKEN SPring-8 Centre. . . . .	4130
30.3	Structure and key topics of the MIRAI program. . . . .	4130
31.1	Map of European supercomputing facilities ranked in the Top 100 worldwide. . . . .	4132
32.1	Performance scalings for SMILEI code. . . . .	4138
32.2	Strong parallel scaling of Warp EM solver. . . . .	4139
32.3	Laser power threshold for self-injection as a function of plasma electronic density. . . . .	4163
32.4	Example of laser envelope and wake potential energy for $a_0 = 2.5$ . . . . .	4167

32.5	Comparison of published results with EuPRAXIA injector parameters.	4176
32.6	EuPRAXIA leaflet.	4182
32.7	EuPRAXIA brochure.	4182
32.8	Demonstration of the <i>Surfatron</i> game at a past outreach event.	4183
32.9	Outreach activities on the “Physics of Star Wars” in Nov 2017.	4186
32.10	Beam spot on a screen downstream of the lens with the discharge turned off and on.	4188
32.11	Resulting emittance as a function of beam spot size at capillary entrance.	4188
32.12	Direct measurements of the radial magnetic field profile in an APL.	4189
32.13	Emittance measurements from a series of quadrupole scans in both helium and argon.	4190
32.14	LPS of the beam and longitudinal plasma wakefield produced in a plasma channel.	4190
32.15	Energy spectrum of the electron beam after the capillary without and with plasma in the channel.	4191
32.16	A series of energy spectra for no interaction with plasma as well as two dechirping plasma densities.	4192
32.17	The FWHM of the chirped bunch energy as a function of discharge time relative to the arrival time of the electron bunch.	4193
32.18	Scheme of the segmented capillary.	4194
32.19	Sample shots showing energy spectrum of a two-bunch beam, with a driver and a witness bunch, with no interaction and after passing through 33 mm of plasma.	4196
32.20	Sketch and photo of the experimental setup for the ultra cold electron source at Manchester University.	4197
32.21	The first electrons measured on 2nd March 2017 at Manchester University.	4197
32.22	Example of the modulation of the transverse beam size due to the phase-dependence of the focusing field.	4198
32.23	The SPARC_LAB experimental apparatus and conceptual drawing, as seen after its installation in 2018.	4204
32.24	Discharge current profile and averaged density along the entire capillary length acquired every 100 ns of delay from the discharge trigger.	4204
32.25	Plasma electron density distribution along the capillary measured at the maximum density value for an increasing number of shots.	4205
32.26	Entrance of the capillary after the print and after more than 55,000 shots.	4205
32.27	Screenshot of the CAD model of the proposed EuPRAXIA facility layout in a perspective view.	4207
32.28	Screenshot of the CAD model of the proposed EuPRAXIA facility layout in a top view.	4209

## List of Tables

2.1	Summary of the electron beam properties of several accelerator test facilities currently in operation or under development. . . . .	3722
2.2	Main positron beam parameters obtainable in FACET and FACET-II compared with those achievable with EuPRAXIA. . . . .	3729
2.3	Calculated positron lifetimes (ps) for perfect lattice (bulk) and monovacancy defects in selected materials. . . . .	3732
3.1	Performance summary of the EuPRAXIA design. . . . .	3738
3.2	Institutes with interests in particular EuPRAXIA cluster topics. . . .	3742
3.3	Comparison of the expected EuPRAXIA machine length with other facilities of equivalent beam energies. . . . .	3753
3.4	Parameters achieved with the start-to-end simulations for the EuPRAXIA@SPARC_LAB facility. . . . .	3761
4.1	EuPRAXIA Cost Estimate. . . . .	3782
4.2	Cost split beam-driven plasma accelerator. . . . .	3784
4.3	Cost split laser-driven plasma accelerator. . . . .	3786
4.4	Costs for various scenarios. . . . .	3789
5.1	General risks for EuPRAXIA project. . . . .	3799
7.1	Main parameters of some PW laser systems worldwide. . . . .	3822
8.1	Naming convention of the different accelerator schemes investigated as part of the EuPRAXIA conceptual design study. . . . .	3830
9.1	Estimated goal parameters of the electron beam at the entrance of an undulator for FEL lasing. . . . .	3832
9.2	Summary table of parameters and technical data of the laser system. . .	3833
9.3	Summary table of parameters and technical data of the RF injector and accelerator. . . . .	3833
9.4	Summary table of parameters and technical data of the plasma injector. .	3834
9.5	Summary table of parameters and technical data of the plasma accelerator stages. . . . .	3834
9.6	Summary table of parameters and technical data of the beam transport. .	3835
9.7	Summary table of parameters and technical data of the free-electron laser. . . . .	3836
9.8	Summary table of parameters and technical data of the betatron and inverse Compton scattering sources. . . . .	3837
9.9	Summary table of parameters and technical data of the secondary particle sources. . . . .	3837
9.10	Summary table of parameters from the start-to-end simulations of different acceleration schemes. . . . .	3838
10.1	Laser parameters for the three EuPRAXIA laser driver beamlines. . . .	3841
10.2	Setup and component characteristics for the various amplification stages. .	3843
10.3	Main design and operational parameter for the amplifier AMP3 in the reflection configuration. . . . .	3846
11.1	Set of laser diagnostics, their proposed positioning along the beamline, and data taking rates. . . . .	3865
11.2	A strategic view of protection measures put into place along the laser chains. . . . .	3866
12.1	Main parameters of the RF gun. . . . .	3871
12.2	Parameters of the gun solenoid. . . . .	3873
12.3	Characteristics of the solenoid focussing magnets per linac section. . .	3875
12.4	Technical specifications of the S-band accelerating sections. . . . .	3875
12.5	Main specifications of the S-band klystrons. . . . .	3877
12.6	Characteristics of the EuPRAXIA constant gradient accelerating section. .	3882

12.7	Main parameters of the X-band linac RF system. . . . .	3883
13.1	Target parameters for electron bunches generated by LPIs. . . . .	3885
13.2	LPI using a density downramp: beam parameters at the end of the plasma lens. . . . .	3888
13.3	Main characteristics of the electron bunch for different values of CN2. . . . .	3891
13.4	Experimental parameters for the low-energy LPI. . . . .	3893
13.5	Experimental parameters for the 1 GeV LPI. . . . .	3894
13.6	Beam parameters and the accelerator properties that impact their stability. . . . .	3895
14.1	Target values for the 1 GeV electron beam parameters to drive a SASE FEL. . . . .	3898
14.2	Main photo-injector parameters. . . . .	3899
14.3	Witness beam parameters at the end of the photo-injector in the case of pure RF compression. . . . .	3900
14.4	L1 and L2 linac parameter list. . . . .	3902
14.5	Beam parameters at the linac exit and the injection point. . . . .	3906
14.6	L1 and L2 linac parameter list for the PWFA external injection scheme. . . . .	3907
14.7	Main photo-injector parameters. . . . .	3908
14.8	Driver and witness beam parameters at the end of the photo-injector. . . . .	3910
16.1	Example of parameter sets to achieve an energy gain of the order of 5 GeV in a laser-driven plasma-accelerator stage. . . . .	3923
17.1	Total and best slice PWFA bunch parameters at plasma entrance and exit. . . . .	3930
18.1	Typical quadrupole specifications. . . . .	3937
18.2	Characteristics of fixed-gradient quadrupoles. . . . .	3938
18.3	Characteristics of variable gradient quadrupoles. . . . .	3939
18.4	Typical characteristics of permanent magnets used for undulators. . . . .	3941
18.5	Width of magnets and poles for different periods and coefficients of the fitting curves, a, b and c, shown in Figure 18.2. The magnetic field is fitted with the equation $B_{peak} = a \exp(b \frac{g}{\lambda_u} + c(\frac{g}{\lambda_u})^2)$ , where $g$ is the magnetic gap. . . . .	3943
19.1	Parameters of the focusing elements in the low-energy transport line using six quadrupoles. . . . .	3952
19.2	Parameters of the focusing elements in the low-energy transport line using eight quadrupoles. . . . .	3954
19.3	Parameters of the focusing elements in the low-energy transport line using two active plasma lenses. . . . .	3958
19.4	Comparison of the beam parameters at the end of the LPI and at the entrance of the LPAS for the four different low-energy transfer line configurations. . . . .	3958
19.5	Electron beam matching parameters at the entrance of the undulator section in the case of a short-undulator-period design. . . . .	3959
19.6	Matching parameters at the entrance of the undulator section in the case of a long-undulator-period setup. . . . .	3959
19.7	Parameters of the focusing elements in the high-energy transport line to the undulator for the case of Scheme 1. . . . .	3961
19.8	Comparison between the beam parameters at the LPI exit and at the entrance of the undulator for Scheme 1. . . . .	3962
19.9	Parameters of the focusing elements in the transport line to the undulator for the case of Scheme 2. . . . .	3963
19.10	Comparison between the beam parameters at the LPAS exit and at the entrance of the undulator for Scheme 2. . . . .	3963

19.11	Parameters of the focusing elements in the transport line to the undulator for the case of Scheme 3. . . . .	3963
19.12	Comparison between the beam parameters at the LPAS exit and at the entrance of the undulator for Scheme 3. . . . .	3963
19.13	Parameters of the focusing elements in the transport line between the two LPAS stages in Scheme 4. . . . .	3967
19.14	Parameters of the focusing elements in the transport line to the undulator for the case of Scheme 4. . . . .	3967
19.15	Comparison between the beam parameters at the exit of the second LPAS and at the undulator entrance for Scheme 4. . . . .	3967
19.16	Parameters of the focusing elements in the high-energy transport line to the undulator for the case of Scheme 5. . . . .	3967
19.17	Comparison between the beam parameters at the PPAS exit and at the entrance of the undulator for Scheme 5. . . . .	3967
20.1	Measuring capability of interferometric methods. Phase shift after passing through 1 cm of medium. . . . .	3975
20.2	Comparison of interferometric methods. . . . .	3977
21.1	Electron bunch parameters at different diagnostic points (DP1 to DP3) along the beamline. . . . .	3984
22.1	Parameters of the electron beam hitting the beam dump. . . . .	3996
23.1	Main requirements for the electron beam at the exit of the injector and accelerator. . . . .	4002
23.2	Naming convention of the different accelerator schemes investigated as part of the EuPRAXIA conceptual design study. . . . .	4002
23.3	Laser and electron input beam parameters of the LPAS. . . . .	4006
23.4	Requested beam quality and expected quality parameters obtained by means of simulations for Scheme 1. . . . .	4012
23.5	Parameters of the driver train and the ionisation pulse. . . . .	4013
23.6	Comparison between the beam parameters at the end of the LPI and at the entrance of the undulator for Scheme 1. . . . .	4018
23.7	Comparison between the beam parameters at the end of the LPAS and at the entrance of the undulator for Scheme 2. . . . .	4028
23.8	Comparison between the beam parameters at the end of the LPAS and at the entrance of the undulator for Scheme 3. . . . .	4033
23.9	Final parameters of the core of the improved (smoothed) beam at the end of the second plasma. . . . .	4039
23.10	Comparison between the beam parameters at the exit of the second LPAS and at the undulator entrance for Scheme 4. . . . .	4039
23.11	Main photo-injector parameters. . . . .	4041
23.12	Driver and witness beam parameters at the end of the photo-injector. . . . .	4041
23.13	Comparison between the beam parameters at the end of the PPAS and at the entrance of the undulator for Scheme 5. . . . .	4045
24.1	Best slice values of the relevant parameters at the plasma exit. . . . .	4048
24.2	Undulator configurations used for the FEL environment. . . . .	4049
24.3	Best slice values of the relevant parameters at the undulator entrance and expected cooperation lengths. . . . .	4050
24.4	FEL semi-analytical results for the short-undulator-period configuration based on the best slice parameters of Table 24.3. . . . .	4051
24.5	Results of the time-dependent simulations with longitudinal dynamics, obtained with PERSEO, for the short-undulator-period configuration. . . . .	4051
24.6	FEL semi-analytical results for the long-undulator-period configuration based on the best slice parameters of Table 24.3. . . . .	4054

24.7	Results of the time-dependent simulations with longitudinal dynamics, obtained with PERSEO, for the long-undulator-period configuration. . .	4054
24.8	Important properties of a plasma betatron-radiation source and their implications. . . . .	4059
24.9	Scalings for betatron radiation from established scaling laws. . . . .	4060
24.10	Unique properties of plasma-accelerator-based ICS radiation sources, and their implications. . . . .	4065
25.1	Expected properties of the low-energy positron beam generated at the EuPRAXIA beamline. . . . .	4069
27.1	Performance level and their respective average probability of dangerous failure per hour. . . . .	4094
29.1	Main parameters for the CLARA operating modes. . . . .	4109
29.2	Typical beam parameters at the FLASHForward facility. . . . .	4113
29.3	Overview parameters of the three high-power laser systems at Helmholtz Institute Jena. . . . .	4115
29.4	Beam parameters of the TARANIS laser system at the Queen's University of Belfast. . . . .	4122
29.5	Design parameters of the SINBAD facility. . . . .	4123
29.6	Typical parameters of the SPARC linear accelerator. . . . .	4125
29.7	Typical parameters of the FLAME laser at SPARC_LAB. . . . .	4126
30.1	Parameters of the BELLA PW-laser. . . . .	4128
31.1	Some of the largest supercomputing facilities in Europe based on the Top500 list of supercomputers worldwide. . . . .	4132
32.1	PIC codes used for EuPRAXIA. . . . .	4136
32.2	Comparison of selected published performances to EuPRAXIA baseline for self-injection (SI). . . . .	4171
32.3	Comparison of selected published performances to EuPRAXIA baseline for colliding pulse injection (CPI). . . . .	4172
32.4	Comparison of selected published performances to EuPRAXIA baseline for density-gradient injection (DGI). . . . .	4173
32.5	Comparison of selected published performances to EuPRAXIA baseline for ionisation-induced injection (III). . . . .	4174
32.6	Summary of plasma targets main properties. . . . .	4175